

Tubular Structures VIII

Y.S. Choo and
G.J. van der Vegte, editors

CRC Press
Taylor & Francis Group
A BALKEMA BOOK

TUBULAR STRUCTURES VIII



Taylor & Francis
Taylor & Francis Group
http://taylorandfrancis.com

PROCEEDINGS OF THE EIGHTH INTERNATIONAL SYMPOSIUM ON TUBULAR STRUCTURES
SINGAPORE/26-28 AUGUST 1998

Tubular Structures VIII

Edited by
Y.S.CHOO
CAE/CAD/CAM Centre, National University of Singapore
G.J.VAN DER VEGTE
Institute of High Performance Computing, Singapore
Delft University of Technology, Netherlands

CRC Press
Taylor & Francis Group
Boca Raton London New York

CRC Press is an imprint of the
Taylor & Francis Group, an **informa** business
A BALKEMA BOOK

Published by:
CRC Press/Balkema
P.O. Box 447, 2300 AK Leiden, The Netherlands
e-mail: Pub.NL@taylorandfrancis.com
www.crcpress.com – www.taylorandfrancis.com

© 1998 by Taylor & Francis Group, LLC
CRC Press/Balkema is an imprint of the Taylor & Francis Group, an informa business

No claim to original U.S. Government works

ISBN 13: 978-90-5809-001-0 (hbk)

This book contains information obtained from authentic and highly regarded sources. Reasonable efforts have been made to publish reliable data and information, but the author and publisher cannot assume responsibility for the validity of all materials or the consequences of their use. The authors and publishers have attempted to trace the copyright holders of all material reproduced in this publication and apologize to copyright holders if permission to publish in this form has not been obtained. If any copyright material has not been acknowledged please write and let us know so we may rectify in any future reprint.

Except as permitted under U.S. Copyright Law, no part of this book may be reprinted, reproduced, transmitted, or utilized in any form by any electronic, mechanical, or other means, now known or hereafter invented, including photocopying, microfilming, and recording, or in any information storage or retrieval system, without written permission from the publishers.

For permission to photocopy or use material electronically from this work, please access www. copyright.com (http://www.copyright.com/) or contact the Copyright Clearance Center, Inc. (CCC), 222 Rosewood Drive, Danvers, MA 01923, 978-750-8400. CCC is a not-for-profit organization that provides licenses and registration for a variety of users. For organizations that have been granted a photocopy license by the CCC, a separate system of payment has been arranged.

Trademark Notice: Product or corporate names may be trademarks or registered trademarks, and are used only for identification and explanation without intent to infringe.

Visit the Taylor & Francis Web site at
http://www.taylorandfrancis.com

and the CRC Press Web site at
http://www.crcpress.com

Cover photo:
Roof structure of the Singapore International Convention & Exhibition Centre at Suntec City

The texts of the various papers in this volume were set individually by typists under the supervision of each of the authors concerned.

Tubular Structures VIII, Choo & Van der Vegte (eds) © 1998 Balkema, Rotterdam, ISBN 90 5809 001 9

Table of contents

Preface XI

Organisation XIII

Acknowledgements XV

Kurobane lecture

Improvement of I beam-to-RHS column moment connections for avoidance of brittle fracture 3
Y. Kurobane

Papers in plenary sessions

The storm surge barrier in the 'Nieuwe Waterweg' near Rotterdam: Design aspects 21
J.S. Leendertz

The storm surge barrier in the 'Nieuwe Waterweg' near Rotterdam, Netherlands: Fabrication and assembling of the tubular trusses 31
A. Zondervan

State of the art of profiling technology for CHS tubular connections 41
P.C. Glijnis

The adventures of ZAPPI in the world of tubular structures 51
M. Eekhout

Tubular structures in railway architecture in the Netherlands 63
H.H. Snijder & L.I. Vákár

Design of prestressed roof structure suspended from tubular steel towers 73
K. Ikago, K. Hara & K. Ukai

SPACES: Structural behaviour and characteristics of a composite tubular steel space frame bridge deck system 81
A.E. Churchman & J.M.C. Cadei

Aluminium multi-planar hollow section traffic sign structures 89
F. Soetens & W.M.G. Courage

Fatigue design of welded aluminium rectangular hollow section joints 95
P.J.Haagensen & K.A.Macdonald

New code formulations for tubular joint static strength 107
A.F.Dier & M.Lalani

Commentary on the draft specification for fatigue design of hollow section joints 117
A.M.van Wingerde, J.Wardenier & J.A.Packer

Static strength

Experimental study of a full-scale multiplanar tubular XT-joint 131
T.K.Chan, C.K.Soh & T.C.Fung

Static strength of T-joints reinforced with doubler or collar plates 139
Y.S.Choo, B.H.Li, G.J.van der Vegte, N.Zettlemoyer & J.Y.R.Liew

Ultimate strength of ring stiffened T-joints – A theoretical model 147
M.M.K.Lee & A.Llewelyn-Parry

The static behaviour of multiplanar XX-joints loaded with in-plane bending moments and axial forces 157
Y.Yu, D.K.Liu & J.Wardenier

Fundamental behaviour of rectangular hollow sections with web openings 167
D.J.Ridley-Ellis, G.Davies & J.S.Owen

Tests of stiffened and unstiffened welded knee connections in cold-formed RHS 177
T.Wilkinson & G.J.Hancock

Tests of bolted and internal sleeve knee connections in cold-formed RHS 187
T.Wilkinson & G.J.Hancock

Investigations on stiffened and unstiffened L-joints made of circular hollow sections 197
R.Puthli, F.Mang & D.Karcher

Introduction to the database of gusset-plate to CHS tube joints 203
M.Ariyoshi, S.R.Wilmshurst, Y.Makino, G.J.van der Vegte & Y.S.Choo

A new ultimate capacity formula for unstiffened CHS T-, TT-, X-, K- and KK-joints under axial brace loads 213
Y.Yamada, M.Morita, Y.Makino & S.R.Wilmshurst

Effect of boundary conditions and chord preload on the strength of RHS uniplanar gap K-joints 223
D.K.Liu, Y.Yu & J.Wardenier

Effect of boundary conditions and chord preload on the strength of RHS multiplanar gap KK-joints 231
D.K.Liu, Y.Yu & J.Wardenier

Current understanding of completely overlap tubular joints 239
T.C.Fung, C.K.Soh, L.Y.Cheung & W.M.Gho

Effect of overlap on the behaviour of axially loaded CHS K-joints 249
E.M.Dexter & M.M.K.Lee

Ultimate capacity of axially loaded K-joints in CHS 259
E.M.Dexter & M.M.K.Lee

Static strength tests of CHS KT-joints under axial loading 269
S.R.Wilmshurst, M.Morita, S.Sakae, Y.Makino & Y.Kurobane

The effects of weld size on the ultimate strength of a double-tee tubular joint under brace axial compression or bending 277
C.T.Kang, D.G.Moffat, J.Mistry & K.T.Ong

Load-displacement characterisation and prediction for combined loading of a YT tubular joint with and without fillet weld 285
T.H.Hyde & S.B.Leen

A critical assessment of the finite element method for predicting the static strength of tubular T- and YT-joints 293
T.H.Hyde, S.B.Saad, Y.Khalid, S.B.Leen & N.A.Warrior

Fatigue strength

Prediction of stress concentration factors in in-plane moment loaded tubular K-joints 305
M.M.K.Lee & M.R.Morgan

Fatigue design and secondary bending moments in RHS K-joints with gap 315
S.Herion & R.Puthli

Nominal stress range fatigue of stainless steel fillet welds 323
K.E.Lahti, E.Niemi & H.Hänninen

Effects of weld profile on the fatigue life of thin-walled cruciform joint 331
F.R.Mashiri, X.L.Zhao & P.Grundy

Analysis of cracked T-tubular welded joints using finite and boundary element methods 341
S.T.Lie & G.Li

J estimation method for through cracked tubular T-joints 347
B.Wang, N.Hu, Y.Makino & Y.Kurobane

Factors affecting the fracture mechanics assessment of a cracked offshore tubular joint 353
D.Bowness & M.M.K.Lee

Guidance on the selection of stress intensity factor solutions for fracture mechanics assessment of cracked offshore tubular joints 361
D.Bowness & M.M.K.Lee

Members and columns

Dynamic failure of bent tubular cantilevers under dynamic tip loading 373
B.Wang, M.H.Yang & W.C.Fok

Cyclic inelastic behavior of compact steel tubular columns 381
I.H.P.Mamaghani & Y.Kajikawa

Void-filled SHS beams subjected to high amplitude cyclic bending 391
X.L.Zhao, R.Grzebieta & E.Sironic

Optimum design and comparison of hollow flange beams 399
K.Jármai, J.Farkas & T.Liszkai

Compact or Class 1 limits for rectangular hollow sections in bending 409
T.Wilkinson & G.J.Hancock

Influence of boundary conditions on the modeling of steel CHS columns 417
Y.X.Dong & S.P.Chiew

Service load deformations of concrete-filled steel RHS sections 425
M.A.Bradford

Use of tubular steel columns for high rise construction – A case study 433
H.P.Lai

The behaviour of cold-formed slender square hollow section beam-columns 445
R.M.Sully & G.J.Hancock

Frames

Study on out-of-plane rotational stiffness of CHS joints and effective column length of web members in CHS lattice girder 457
Y.Furukawa, Y.Makino & Y.Kurobane

Advanced inelastic analysis for the design of tubular structures 465
J.Y.R.Liew, L.K.Tang & Y.S.Choo

The elastic buckling behaviour of cellular columns 473
S.J.Wilkinson, K.Roodbaraky & G.Davies

Optimum design of a statically indeterminate tubular truss 481
J.Farkas & K.Jármai

Fire

The performance in fire of concrete filled SHS columns protected by Intumescent paint 491
M.Edwards

The effects of fire curves on the temperature of steel tubular members 499
M.B.Wong & J.I.Ghojel

Buckling strength of steel tubular frames under fire 505
N.L.Patterson & M.B.Wong

Advanced structural fire design of offshore structures 511
T.Holmas & J.Amdahl

Connections

Tests of portal frames in cold-formed RHS 521
T.Wilkinson & G.J.Hancock

Rotation capacity of joints for beam-to-column RR and RI welded connections 531
J.Szlendak

Design model for bolted moment end plate connections joining rectangular hollow sections 539
A.T.Wheeler, M.J.Clarke, G.J.Hancock & T.M.Murray

Finite element modelling of bolted moment end plate connections in tubular members 549
A.T.Wheeler, M.J.Clarke & G.J.Hancock

Rectangular hollow section column connections using the Lindapter HolloBolt 559
N.F.Yeomans

CHS column connections without stiffener 567
T.Kamba & C.Taclendo

Study of structural strength of column joints reinforced by welding ring-stiffeners in steel tubular transmission towers 577
E.Hongo, T.Fukasawa & Y.Matsuo

Experimental study of structural behavior of beam-to-column connections reinforced by increasing plate thickness of column without diaphragms 585
K.Morita, K.Ebato, K.Furusawa, K.Fujita & K.Hamano

Study on beam to box column connections with split diaphragms 595
K.Fukuda, M.Tabuchi & F.Otake

A moment-rotation model for connections of H-beams to concrete filled RHS columns 605
A.Kawano & C.Matsui

On the behaviour and design of composite column to beam connections under seismic loads 615
J.G.Beutel, D.P.Thambiratnam & N.J.Perera

High strength steel RHS, domestic flooring system 625
M.Alikhail, X.L.Zhao, L.Koss, P.Grundy, H.Dagg & A.Shield

Experimental study of connections between longitudinal plates and RHS columns 635
J.J.Cao, J.A.Packer & N.Kosteski

Parametric finite element study of connections between longitudinal plates and RHS columns 645
J.J.Cao, J.A.Packer & N.Kosteski

Author index 655



Taylor & Francis
Taylor & Francis Group
http://taylorandfrancis.com

Tubular Structures VIII, Choo & Van der Vegte (eds) © 1998 Balkema, Rotterdam, ISBN 90 5809 001 9

Preface

This publication contains the papers presented at the Eighth International Symposium on Tubular Structures (8th ISTS) held at Singapore on 26-28 August 1998. In particular, the Keynote Address of the 8th ISTS was presented by Professor Y. Kurobane, whose contribution and commitment to the work of both the IIW Subcommission XV-E and CIDECT is legendary.

The 8th ISTS provided the forum for the presentation and discussion of the current research results and applications, including the following themes: Architecture and engineering of tubular structures, static and fatigue strength of hollow section joints, beam-to-column connections, behaviour of tubular members and frames under static, dynamic or fire loads.

Structural hollow sections have inherently superior properties as compared to those of open profiles, and they offer special advantages with regards to application, fabrication, assembly and erection. The recent advancement in computer-aided engineering systems for design, and profiling and welding technologies for fabrication, has led to more wide spread use of tubular structures. Examples found in this book include the Storm Surge Barrier near Rotterdam, railway stations in the Netherlands, pre-stressed roof structures in Japan, and a composite tubular space frame bridge deck system.

We hope that this book will provide a good reference for architects, designers, engineers and manufacturers to design and construct more innovative and cost effective tubular structures.

Y.S.Choo
CAE/CAD/CAM Centre, National University of Singapore

G.J.van der Vegte
Institute of High Performance Computing, Singapore
Delft University of Technology, Netherlands

Publications of the previous Symposia on Tubular Structures

Coutie, M.G. & G.Davies (eds) 1993. *Tubular Structures V.* Proceedings of the 5th International Symposium, Nottingham, 1993. London etc.: E & FN Spon.

Farkas, J. & K.Jármai (eds) 1996. *Tubular Structures VII.* Proceedings of the 7th International Symposium, Miskolc, Hungary, 1996. Rotterdam: Balkema.

Grundy, P., A.Holgate & B.Wong (eds) 1994. *Tubular Structures VI.* Proceedings of the 6th Interntional Symposium, Melbourne, Australia, 1994. Rotterdam: Balkema.

International Institute of Welding (IIW) 1984. *Welding of Tubular Structures.* Proceedings of an International Conference, Boston, 1984. Oxford etc.: Pergamon Press.

Kurobane, Y. & Y. Makino (eds) 1987. *Safety Criteria in Design of Tubular Structures.* Proceedings of the International Meeting, Tokyo, 1986. Tokyo: Architectural Institute of Japan, IIW.

Niemi, E. & P. Mäkeläinen (eds), 1990. *Tubular Structures.* The Third Internationsal Symposium, Lappeenranta, 1989. London-New York: Elsevier Applied Science.

Wardenier, J. & E. Panjeh Shahi (eds) 1991. *Tubular Structures.* 4th International Symposium, Delft 1991. Delft: Delft University Press.

Tubular Structures VIII, Choo & Van der Vegte (eds) © 1998 Balkema, Rotterdam, ISBN 90 5809 001 9

Organisation

This volume contains the papers presented at the Eighth International Symposium on Tubular Structures (8th ISTS) held at Singapore, 26-28 August 1998. The 8th ISTS was organised by International Institute of Welding Subcommision XV-E: Tubular Structures, Comité International pour le Développement et l'Etude de la Construction Tubulaire (CIDECT), the National University of Singapore and the Institute of High Performance Computing, Singapore.

INTERNATIONAL PROGRAMME COMMITTEE

Prof. J.Wardenier, *Committee Chairman*
Delft University of Technology, Netherlands

Dr Y.S.Choo, *Local Organising Committee Chairman*
National University of Singapore, Singapore

E. Bollinger, *Chairman of CIDECT Technical Commission*
Tubeurop, Paris, France

Dr G. Davies
University of Nottingham, UK

Prof. P.Grundy
Monash University, Melbourne, Australia

Prof. Y. Kurobane
Kumamoto Institute of Technology, Japan

Dr P.W. Marshall
MHP Systems Engineering, Houston, USA

Prof. E. Niemi
Lappeenranta University of Technology, Finland

Prof. J.A. Packer, *Chairman of IIW Subcommission XV-E*
University of Toronto, Canada

Prof. R.S. Puthli
University of Karlsruhe, Germany

N.F. Yeomans, *Chairman of CIDECT Joints Working Group*
British Steel Tubes and Pipes, Corby, UK

Dr N. Zettlemoyer
Exxon Production Research Company, Houston, USA

LOCAL ORGANISING COMMITTEE

Dr Y.S.Choo, *Chairman*
National University of Singapore

Dr S.P.Chiew
Nanyang Technological University, Singapore

H.P.Lai
RSP Architects, Planners and Engineers, Singapore

Prof. K.Y.Lam
Institute of High Performance Computing, Singapore

Dr J.Y.R.Liew
National University of Singapore

Prof. N.E.Shanmugam
National University of Singapore

Prof. C.K.Soh
Nanyang Technological University, Singapore

Dr G.J.van der Vegte, *Secretary*
Institute of High Performance Computing, Singapore
Delft University of Technology, Netherlands

SUPPORTING ORGANISATIONS

Construction Industry Development Board, Singapore
Singapore Structural Steel Society
Malaysian Structural Steel Association

Tubular Structures VIII, Choo & Van der Vegte (eds) © 1998 Balkema, Rotterdam, ISBN 90 5809 001 9

Acknowledgements

The editors wish to acknowledge the financial assistance of CIDECT (Comité International pour le Développement et l'Etude de la Construction Tubulaire) and technical assistance of the International Institute of Welding Subcommission XV-E: Tubular Structures. The editors also acknowledge the support of the staff members of the National University of Singapore and Institute of High Performance Computing, Singapore.
The Guest-of-Honour for the Eighth International Symposium on Tubular Structures was Chua Koon Hoe, Director-General of Public Works, Singapore and Chairman, Construction Industry Development Board, Singapore.
The editors received the kind assistance of the following reviewers:

Dr G. Davies
Prof. P.Grundy
Prof. G.J. Hancock
Dr T. Holmas
Prof. Y. Kurobane
Dr M.M.K. Lee
Prof. K.H. Lee
Dr J.Y.R. Liew
Prof. Y. Makino
Prof. E. Niemi
Prof. J.A. Packer
Prof. R.S. Puthli
Dr A. Romeijn
Prof. N.E. Shanmugam
Prof. L. Twilt
Prof. J. Wardenier
Dr A.M. van Wingerde
N.F. Yeomans
Dr N. Zettlemoyer

Y.S. Choo
Chairman and Editor

G.J. van der Vegte
Co-Editor

Singapore
August 1998



Taylor & Francis
Taylor & Francis Group
http://taylorandfrancis.com

Kurobane lecture



Taylor & Francis
Taylor & Francis Group
http://taylorandfrancis.com

Tubular Structures VIII, Choo & Van der Vegte (eds) © 1998 Balkema, Rotterdam, ISBN 90 5809 001 9

Improvement of I beam-to-RHS column moment connections for avoidance of brittle fracture

Yoshiaki Kurobane
Kumamoto Institute of Technology, Japan

ABSTRACT: A large-scale research into beam-to-column connections with conventional and improved details is first summarized. An evaluation of factors influencing the deformation capacity of beam-to-column assemblies is made based on these research results. Further, simple formulae are proposed to predict the plastic deformation capacity of the assemblies. Two types of connections, developed from a new design concept, were found possible to avoid premature occurrences of brittle fracture.

1 INTRODUCTION

The 1994 Northridge and 1995 Kobe Earthquakes both revealed that steel moment connections in building frames were susceptible to brittle fracture under the influence of strong ground motions. One important difference in damage pattern between the two events is that: in Northridge fracture occurred with little visible sign of yielding of material in regions where cracks started; while in Kobe most cracks started with ductile tear, which changed to brittle fracture after plate elements in connections sustained extensive yielding or local buckling. Consequently, improvements of connection design proposed in the two countries appear somewhat contrasting. In the USA, beam-to-column connections are recommended to be configured with sufficient strength so that plastic hinges occur within the beam span and away from the face of the column (SAC 1995). One way to achieve the sufficient strength of connections is to reinforce the beam ends by additional members or plates. One of the alternatives to reinforced connections is to reduce the cross section of the beam intentionally, to produce an intended plastic hinge zone located away from the column face. So-called the dog bone connection is one example of the alternative design.

In Japan no emergency change of the current building code has been undertaken. Several proposals have been made to improve the performance of moment connections, as will be discussed later. Improvements to be made, however, are entirely left to the judgment and responsibility of designers.

This paper first discusses a large-scale research into beam-to-column connections with conventional and improved details. A critical evaluation of results of this research shows that, although proposed improvements in details are found effective, it is difficult to totally eliminate the possibility of brittle fracture by these improvements. The two other proposals, which are discussed subsequently, are based on a design concept different from the historic one. These two proposals use bolted connections, in place of welded connections, at critical sections. Brittle fracture may be avoided by using these connections. One of the proposals looks closer to the American proposal from the view point that a critical section is moved away from the column face. Since box section columns are used in over 90 % of steel moment frames in Japan, all the proposals discussed herein deal with connections between box section columns and wide flange beams.

2 COLLABORATIVE RESEARCH INTO BEHAVIOR OF CONNECTIONS WITH CONVENTIONAL AND IMPROVED DETAILS

2.1 *Purposes and issues*

A large-scale research project, in collaboration of 7 universities, was started a few months after the Kobe Earthquake and completed in July 1997 (AIJ Kinki 1997). The primary purpose of the project was to find viable improved details of connections so that beam-to-column assemblies would show a sufficient deformation capacity to meet severe inelastic demand from future earthquakes. The improvements in details, however, were proposed to be achievable by ordinary fabricators with only minor changes in their equipment and resources. More thorough investigations into connection design, to seek long term solutions for preventing brittle fractures in connections, were outside the scope of this project. Beam-to-column connections selected for the research were those between RHS

columns and wide flange beams, with the through diaphragms at the positions of beam flanges, because these connections were most commonly used in Japan.

A series of cyclic loading tests were performed on beam-to-column assemblies using 86 specimens. Variables incorporated in these tests are:

Main Variables

1. connections designed for shop and field welding applications
2. dimensions and material properties of beams
3. conventional and improved profiles of beam copes
4. thickness of through diaphragms

Supplementary Variables

5. steel weld tab and flux weld tab
6. stringer beads and weave beads
7. static loading and dynamic loading
8. test temperatures, room temperature and cryogenic temperature

For each of selected combinations of the main variables, 4 duplicate specimens were fabricated by two different fabricators and tested at two different institutions.

Test results are rather surprising because they showed that brittle fractures could not be prevented, if steel moment frames were subjected to strong ground motions equivalent in intensity to the Kobe Earthquake. Figure 1 shows the distributions of cumulative plastic deformation factors observed in these tests. The cumulative plastic deformation factor η, as defined in Appendix, represents the plastic deformation capacity under cyclic loading conditions. The test results gave the following statistics:

specimens with details for shop welding:
η_m=50.8 σ_η=20.6 n=70
specimens with details for field welding:
η_m=48.3 σ_η=20.8 n=16

in which η_m denotes the mean of the cumulative plastic deformation factor η, σ_η denotes the sample standard deviation of η, and n denotes the number of specimens.

As shown in Fig. 1, the coefficient of variation (COV) is quite large. A large scatter of data suggests the possibility that a few connections may show very low values of plastic deformation capacity. However, the test results also suggest that connections with combined improvements in connection details as well as in welding procedures may realize a good plastic deformation capacity (say, η being greater than 40).

The following discussion focuses on the deformation capacity of beam-to-column assemblies, when plastic hinges form at the beam ends next to the column faces. Factors deteriorating the deformation capacity are examined based on the test results from the collaborative research project. Quantitative importance factors are proposed to evaluate the cumulative plastic deformation factor of connections.

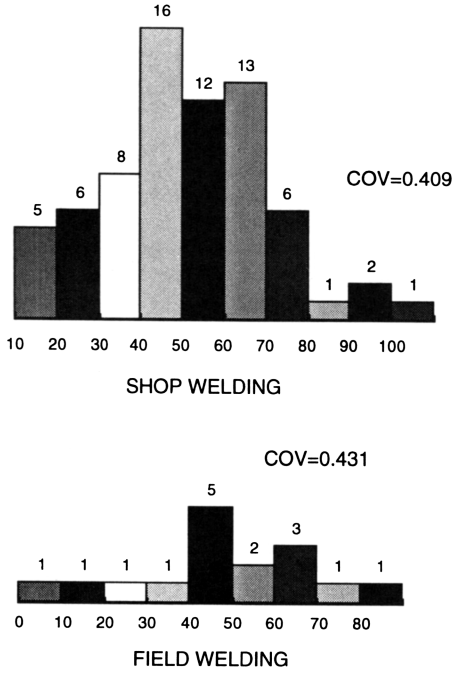

Figure 1. Histograms showing distributions of cumulative plastic deformation factors.

2.2 *Summary of test procedures and results*

2.2.1 *Test program*

All the specimens were configured to form a T-shaped assembly with a single wide flange beam connected to the one side of an RHS column. The details of connections can be subdivided into two large groups depending on the design applicable to either shop weld-

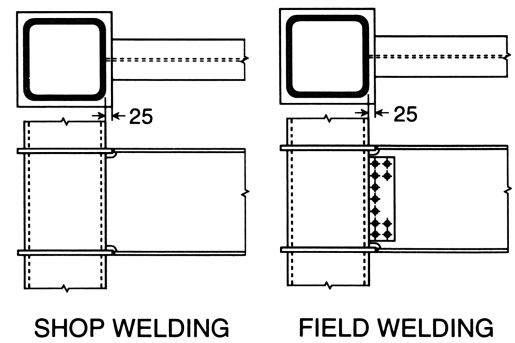

Figure 2. Examples of conventional connection designs.

Table 1. Dimensions and mechanical properties of beam materials.

DIMENSIONS (MATERIAL NO.)	STEEL GRADE	SPECIMENS EXTRACTED FROM	σ_y (MPa)	σ_u (MPa)	elong (%)	${}_vE_0$ (J)	${}_vT_E$ (°C)
W600x200x11x17		flange at1/4 of width	290	446	28	115	4
(E6)	SN400B	flange at intersection with web	252	436	31	73	27
		web	342	465	29	155	-44
W500x200x10x16		flange at1/4 of width	293	448	30	117	8
(E5)	SS400	flange at intersection with web	279	446	31	39	16
		web	313	446	31	-	-
W600x250x12x25		flange at1/4 of width	371	517	32	197	-42
(B6)	SN490	flange at intersection with web	344	513	28	165	-30
		web	425	553	23	-	-

Note:
elong=elongation; σ_y=yield stress; σ_u=ultimate tensile strength; ${}_vE_0$=absorbed energy at 0 degree C; ${}_vT_E$=energy transition temperature

ing or field welding. The beam flanges were groove welded to the through diaphragms, while the beam webs were either welded to the column faces or bolted to the columns via shear tabs. Figure 2 illustrates these two representative connection details.

Three different grades of steel were used for beams, of which the steel with the designation SS is ordinary low carbon steel for structural use, while the steel with the designation SN is new steel for which both the upper and lower limits of yield stress are specified in the Japanese Industrial Standard. Mechanical properties of beam materials are summarized in Table 1.

One of the important variables in connection details was the type of beam copes. The conventional beam cope and improved copes of Types A and B are shown in Fig. 3. The conventional cope was manufactured by a cutter with a radius of 35 mm. However, a return with a radius of about 10 mm was also prepared at the point where the cope hole contacted the beam flange. When the improved cope of Type A was used, a backing bar was interrupted by the beam web. Two pieces of backing bar were made to fit from the both sides of the beam flange. The improved cope for field welded connections was similar in shape to the improved Type B cope for shop welded connections as shown in Fig. 4. However, an additional improvement was made by extending a portion of the diaphragm towards the beam flange.

Backing bars were fillet welded to the beam flanges at points around a quarter of the beam width in accordance with the AIJ Recommendations (AIJ 1995) in all the conventional and improved specimens. This was because past test results as well as damage to connections due to the Kobe Earthquake indicated that existence of fillet welds right in front of the beam cope was harmful and frequently induced brittle fractures starting from the corners of the copes.

The thickness of the diaphragm was designed to be larger than the thickness of the beam flange by 3 mm or by about 7 mm.

Weld tabs used were of two kinds, steel tabs and flux tabs. Although steel tabs are commonly used everywhere, flux tabs are special to Japanese fabricators. Flux tabs are a kind of weld dams made of ce-

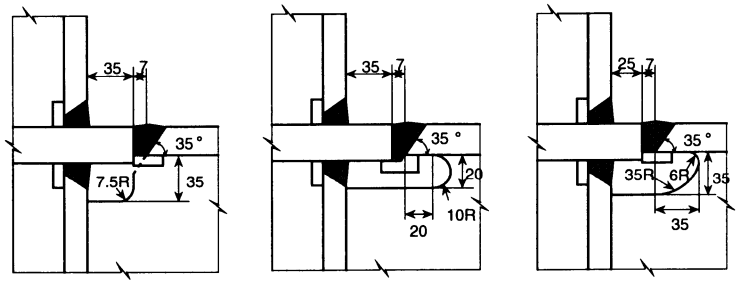

(a) Improved Type A cope (b) Improved Type B cope (c) conventional cope

Figure 3. Details of improved and conventional beam copes.

Table 2. Summary of test results.

1 SPECI -MEN	2 SHOP/ FIELD	3 BEAM MATE- RIAL	4 COPE	5 WELD TAB	6 STRINGER /WEAVE	7 FAIL- URE MODE	8 LOAD & TEMPER- ATURE	9 η ,TEST	10 η_e , PREDIC- TION	11 TEST/ PRE- DICTION
1	S	E5	C	F	S	A		42.0	50	0.84
2	S	E5	C	F	S	A		48.2	50	0.96
3	S	E5	C	F	W	A		37.6	50	0.75
4	S	E5	C	F	W	A		31.1	50	0.62
5	S	E5	A	F	S	E		59.9	67	0.89
6	S	E5	A	F	S	E		58.2	67	0.87
7	S	E5	A	F	W	B		64.0	53	1.21
8	S	E5	A	F	W	E		57.6	53	1.09
9	S	E5	A	S	W	B		48.8	31	1.57
10	S	E5	A	F	W	E		58.3	53	1.10
11	S	E5	A	F	W	E		58.6	53	1.11
12	S	E5	B	F	S	E		59.5	67	0.89
13	S	E5	B	F	S	E		58.7	67	0.88
14	S	E5	B	F	W	B		47.4	53	0.89
15	S	E5	B	F	W	B		50.3	53	0.95
16	S	E5	C	S	W	A*	L	20.7	31	0.67
17	S	E5	C	S	W	B*	L	21.0	31	0.68
18	S	E5	C	F	S	A	L	61.3	50	1.23
19	S	E5	C	F	S	A	L	45.9	50	0.92
20	S	E5	A	S	W	E	L	75.3	31	2.43
21	S	E5	A	S	W	A*	L	20.8	31	0.67
22	S	E5	A	F	S	E	L	95.7	67	1.43
23	S	E5	A	F	S	E	L	69.6	67	1.04
24	S	E5	B	S	W	F*	L	14.1	31	0.45
25	S	E5	B	S	W	A	L	68.0	31	2.19
26	S	E5	B	F	S	E	L	77.2	67	1.15
27	S	E5	B	F	S	E	L	65.7	67	0.98
28	S	B6	C	S	W	B		21.0	31	0.68
29	S	B6	C	S	W	B*		13.7	31	0.44
30	S	B6	C	S	W	B		44.5	31	1.44
31	S	B6	C	S	W	B		10.8	31	0.35
32	S	B6	C	S	S	B		43.4	45	0.96
33	S	B6	C	S	S	B		43.4	45	0.96
34	S	B6	C	S	S	B		60.4	45	1.34
35	S	B6	C	S	S	B		35.7	45	0.79
36	S	B6	C	F	S	B		61.4	50	1.23
37	S	B6	C	F	S	B		61.4	50	1.23
38	S	B6	A	S	W	B		21.9	31	0.71
39	S	B6	A	S	W	B		31.1	31	1.00
40	S	B6	A	S	S	B		44.5	45	0.99
41	S	B6	A	S	S	C		62.5	45	1.39
42	S	B6	A	F	S	C*		32.8	67	0.49
43	S	B6	A	F	S	B		78.4	67	1.17
44	S	B6	A	F	S	B		57.2	67	0.85
45	S	B6	A	F	S	E		85.5	67	1.28
46	S	B6	B	S	W	B		16.0	31	0.52
47	S	B6	B	S	W	C		14.7	31	0.47
48	S	B6	B	S	S	B		48.7	45	1.08
49	S	B6	B	S	S	B		43.4	45	0.96
50	S	B6	B	F	S	C		40.7	67	0.61
51	S	B6	B	F	S	B		67.8	67	1.01
52	S	B6	B	F	S	B		48.3	67	0.72
53	S	B6	B	F	S	B		63.6	67	0.95
54	S	B6	C	S	S	B		39.1	45	0.87
55	S	B6	C	S	S	B		42.4	45	0.94
56	S	B6	C	S	S	B	D	39.5	45	0.88
57	S	B6	C	S	S	B	D	37.1	45	0.82
58	S	B6	C	F	S	B	D	68.9	50	1.38
59	S	B6	C	F	S	B	D	63.6	50	1.27

Table 2. continued.

1 SPECI -MEN	2 SHOP/ FIELD	3 BEAM MATE- RIAL	4 COPE	5 WELD TAB	6 STRINGER /WEAVE	7 FAIL- URE MODE	8 LOAD & TEMPER- ATURE	9 η ,TEST	10 η_e, PREDIC- TION	11 TEST/ PRE- DICTION
60	S	B6	A	F	S	B		71.2	67	1.06
61	S	B6	A	F	S	B		48.7	67	0.73
62	S	B6	A	F	S	B	D	43.0	67	0.64
63	S	B6	A	F	S	B	D	72.0	67	1.07
64	S	B6	B	F	S	B		59.8	67	0.89
65	S	B6	B	F	S	E		78.5	67	1.17
66	S	B6	B	F	S	B	D	93.1	67	1.39
67	S	B6	B	F	S	B	D	102.0	67	1.52
68	S	E6	C	S	W	A		21.5	31	0.69
69	S	E6	A	S	W	E		52.5	31	1.69
70	S	E6	B	S	W	E		55.2	31	1.78
71	F	B6	C	S	S	A		49.8	45	1.11
72	F	B6	C	S	S	A		51.9	45	1.15
73	F	B6	C	F	S	B*		33.8	50	0.68
74	F	B6	C	F	S	B		47.7	50	0.95
75	F	B6	B	S	S	F		71.0	67	1.06
76	F	B6	B	S	S	A		68.9	67	1.03
77	F	B6	B	F	S	D		86.9	51	1.70
78	F	B6	B	F	S	D		62.5	51	1.23
79	F	B6	C	F	S	A		54.0	50	1.08
80	F	B6	C	F	S	C*		16.0	50	0.32
81	F	B6	C	F	S	A		45.0	50	0.90
82	F	B6	C	F	S	C*		8.5	50	0.17
83	F	B6	B	F	S	C		48.7	51	0.95
84	F	B6	B	F	S	B		44.0	51	0.86
85	F	B6	B	F	S	C*		21.2	51	0.42
86	F	B6	B	F	S	F		63.0	51	1.24

Note:

Column 2: S=shop welding; F=field welding

Column 4: A=improved Type A; B=improved Type B; C=conventional

Column 5: F=flux tab; S=steel tab

Column 6: S=stringer beads; W=weave beads

Column 7: A=fracture from corner of beam cope; B=fracture from HAZ or weld metal close to beam flange at termination of groove welds; C= fracture from HAZ or weld metal close to through diaphragm at termination of groove welds; D=fracture from HAZ or weld metal close to through diaphragm in central portion of beam flange; E=local buckling of beam flange; F=others; *=weld defect at points of crack initiation

Column 8: L=low temperature; D=dynamic loading

Column 10: η_e =67 for connections with recommended details

ramics but is called flux tabs. Two different welding procedures were specified for fabricating specimens, which were called multi-passes per each layer and single pass per each layer. Cross sections of weld beads are compared between these two in Fig. 5. In the later portion of this paper the former welding procedure is called stringer beads, while the latter one is called weave beads. The weave beads provide higher weld metal deposition rate and greater heat input, which promotes grain growth in the HAZ and attendant low notch toughness.

Of 86 specimens, 8 specimens were tested in dynamic loading with the rate varying between 1 Hz. and 0.6 Hz. while twelve specimens were tested at a temperature of -23 degrees C. The remainder of the specimens were subjected to slowly applied cyclic loading at room temperatures. All the specimens were tested in principle under the loading sequences predetermined as follows: at least 2 cycles of reversed loading in an elastic region and, subsequently, displacement controlled cyclic loading with the amplitude increased as $\pm 2\theta_p$, $\pm 4\theta_p$, $\pm 6\theta_p$, .. up to failure, where θ_p signifies the elastic beam rotation at the full plastic moment M_p (See Appendix). Two cycles of loading were applied at each displacement increment.

2.2.2 *Test results*

Test results are summarized in Table 2. Specimens showed various failure modes, which are classified into 6 groups (A through F) and summarized in the footnotes to Table 2. Specimen 72 with conventional beam copes and Specimen 78 with improved

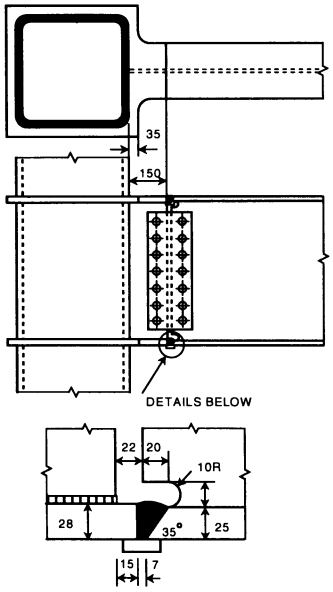

Figure 4. Improved connections for field welding application.

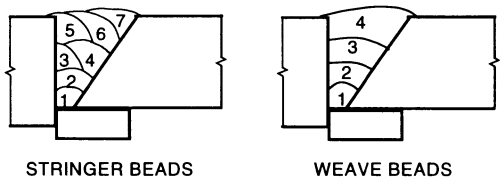

Figure 5. Cross section of weld beads.

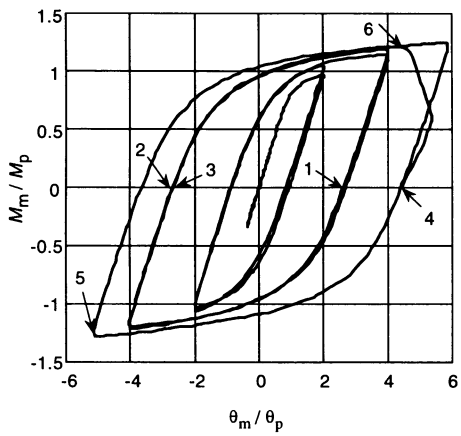

Figure 6. Moment vs. rotation hysteretic curves for Specimen 72.

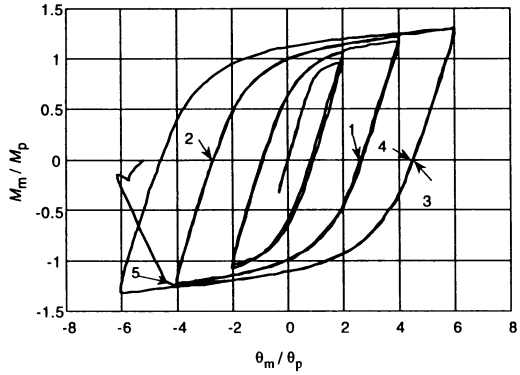

Figure 7. Moment vs. rotation hysteretic curves for Specimen 78.

beam copes are selected from those designed for field welding application to show details of the connection performance. Figures. 6 and 7 show the load vs. beam rotation hysteretic curves.

Specimen 72 showed the following failure sequences. The numbers in the following lists correspond to the numbers in Figs. 6 and 7.

1. A crack was found at a corner of the beam cope near the bottom flange.
2. A crack was found at a corner of the beam cope near the top flange.
3. A crack was found at the outer edges of the beam top flange next to the weld tabs.
4. A crack was found at the inner edges of the beam bottom flange next to the weld tabs.
5. The load was reversed at $5\theta_p$ due to a stroke limit of a hydraulic ram.
6. A crack extended from the corner of the beam cope and one of the cracks extended from the weld tab regions coalesced, which led to ductile tear of the beam bottom flange (See Fig. 8).

Specimen 78 showed the following failure sequences.

1. A crack was found at a corner of the beam cope near the bottom flange. The beam top flange sustained plastic bending deflection.
2. A crack was found at a corner of the beam cope near the top flange. The beam bottom flange sustained plastic bending deflection.
3. A crack occurred along the weld toes at the end of the bottom flange near the corner of the beam cope. Other cracks were found in the welds between the top diaphragm and the web.
4. A crack occurred in the base metal on the rounded surface of the beam cope near the top flange.
5. Brittle fracture ran through the welds at the end of the beam top flange (See Fig. 9).

2.3 *Factors affecting deformation capacity of connections*

First of all, let us examine effects of improving the profile of beam copes on the deformation capacity of connections. The following are statistics of the test results for all the 86 specimens.

specimens with improved beam copes:
η_m=56.7 σ_η=20.3 n=53
specimens with conventional beam copes:
η_m=40.1 σ_η=16.3 n=33

The above comparison shows that the improvement of cope profiles give significant effects in increasing the deformation capacity. The difference in η between the improved Types A and B profiles is only marginal. Specimens with the improved beam copes tended to evade a fracture starting from the corner of the beam cope, and change failure modes to other modes like local buckling or a fracture starting from the weld tab region.

The effect of the type of weld tabs on the deformation capacity is more composite. New screened database is created by omitting specimens tested at a low temperature and in dynamic loading and also specimens failed by a brittle or ductile fracture from the corner of the beam cope. The following comparisons are made with no regard to the type of beam copes because the performance of welded joints is of primary concern here. The screened database gives the following statistics on the effect of weld tabs. For connections for shop welding application,

specimens with flux tabs:
η_m=59.5 σ_η=11.8 n=24
specimens with steel tabs:
η_m=37.8 σ_η=15.8 n=21

Histograms showing distributions of η are also shown in Fig. 10. Clearly the deformation capacity improves appreciably by using flux tabs instead of steel tabs. When steel tabs are used, cracks frequently started from notch roots formed by the weld tabs and the beam flanges. Finite element analyses (AIJ Kinki 1997, Tanaka 1996a) indicated that stresses in the beam flanges and in the through diaphragms concentrated at points in the weld tab regions, and that these concentrated stresses were amplified much more by steel

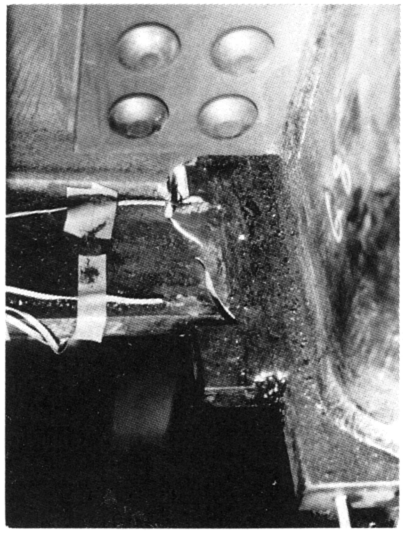

Figure 8. Failure mode of Specimen 72.

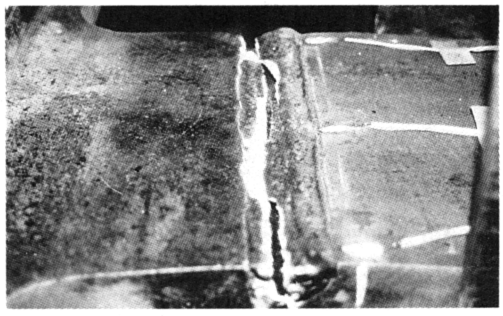

Figure 9. Failure mode of Specimen 78.

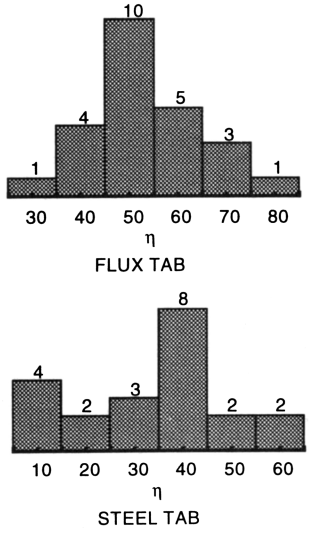

Figure 10. Histograms showing distributions of η.

tabs than by flux tabs.

On the contrary, specimens with field welding details show a different tendency that:

specimens with flux tabs:

η_m=43.5 σ_η=24.1 n=10

specimens with steel tabs:

η_m=71 n=1

The mean value of η for specimens with flux tabs are significantly smaller than that for specimens with flux tabs but with details for shop welding application. Although only one specimen with steel tabs exists in the screened database, the 3 other specimens that failed by fracture from beam copes showed greater deformation capacity than η_m=43.5 of specimens with flux tabs.

These opposite effects brought about by weld tabs were explained as follows: welders, who specialized field welding in practice, were unaccustomed to using flux tabs, which caused many local weld defects found at the start and stop of welded joints. Above all, field welded connections with improved copes have straight edges at the termination of groove welds. With this detail, welding procedure was simple and steel tabs should have given a much less harmful effect.

Stringer beads and weave beads are compared below based on the screened database.

specimens with stringer beads:

η_m=52.8 σ_η=17.5 n=39

specimens with weave beads:

η_m=39.2 σ_η=18.9 n=17

Stringer beads are definitely preferable for attaining better performance of welded joints.

Wide flange beams were fabricated by using 3 different grades of steel. Of these B6 steel (See Table 1) showed superior fracture toughness properties to the other two according to Charpy V notch tests. It is interesting to see that no shop welded specimen made of B6 steel sustained a fracture from corners of the beam copes regardless of the type of copes. However, effects of superior material properties were not demonstrated when fractures started from welded joints. This was because fracture toughness properties of the HAZ and weld metal showed no great difference between B6 steel and E5 and E6 steels.

Effects of the other variables were found to be rather insignificant. The results of dynamic loading tests showed no significant difference from the results obtained under slowly applied cyclic loading. This was because adverse effects of higher strain rate, namely the elevation of transition temperatures, were offset by the temperature elevation caused by plastic straining during dynamic loading (Toyoda 1997). The results of test at -23 degrees C showed no appreciable reduction in ductility as compared with test results obtained at room temperatures. Varying thickness of the through diaphragms gave no effect on the performance of specimens.

Specimens that showed the value of η smaller than 40 were carefully inspected after testing. Several discontinuities due to slag inclusions, an arc strike, incomplete fusion, porosity and a short bead just in front of the beam cope (removed before testing) were found. All the discontinuities did not constitute rejectable conditions per the AIJ UT criteria (AIJ 1979). Some of the discontinuities, however, were found to be responsible for inducing fractures of specimens. The specimens with these influential weld defects are shown by the * symbol in Table 2. The weld defects were found to be one of causes for a large scatter of test results.

3 EVALUATION OF REDUCTION FACTORS AND DEFORMATION CAPACITIES

Among several factors that would deteriorate the performance of connections, the present research results revealed that the following 4 factors significantly participated in reducing the deformation capacity of specimens. These factors include the conventional beam cope, steel weld tab, weave beads and unskilled welding operation. One of the other important factors is the material factor, of which effects were unable to be evaluated from these research results. However, it should be noted that the toughness properties of both base and welded materials used in these tests were above average according to Charpy V impact test results. Further, all the fabricators who provided specimens are commonly accepted as having sufficient capability to fabricate steel moment connections used for testing. The reduction of the deformation capacity due to poorer material quality and workmanship falls outside the scope of the present evaluation.

The reduction in η values is denoted by R with a subscript showing the cause for the reduction. Each value of R's is calculated as the difference in η_m between two opposite cases, which was assessed in the previous section for each influencing factor. The following are the evaluated R values.

$R_{\text{CONVENTIONAL COPE}}$ = 56.7-40.1 $\simeq$ 17

$R_{\text{STEEL TAB}}$ = 59.5-37.8 $\simeq$ 22

The above reduction factor is not applicable to field welded connections with the improved beam copes.

$R_{\text{WEAVE BEADS}}$ = 52.8-39.2 $\simeq$ 14

$R_{\text{UNSKILLED AT FLUX TAB}}$ = 59.5-43.2 $\simeq$ 16

The last reduction factor is applicable only to field welded connections so far as the present test results are concerned.

From the test results shown in Table 2 all the specimens that require no reduction in η values are selected. These specimens are called connections with recommended details and gave the following statistics:

connections with recommended details:

η_m=67.3 σ_η=16.8 n=24

Using the above η_m value an estimate of the cumulative plastic deformation factor, denoted by η_e, is given as the smallest of the values evaluated from the 3 equations as follows:

$$\eta_e = 67\text{-}R_{\text{CONVENTIONAL COPE}} \quad (1)$$

$$\eta_e = 67\text{-}R_{\text{WEAVE BEADS}}\text{-}R_{\text{STEEL TAB}} \quad (2)$$

$$\eta_e = 67\text{-}R_{\text{WEAVE BEADS}}\text{-}R_{\text{UNSKILLED AT FLUX TAB}} \quad (3)$$

Equation 1 and both Equations 2 and 3, respectively,

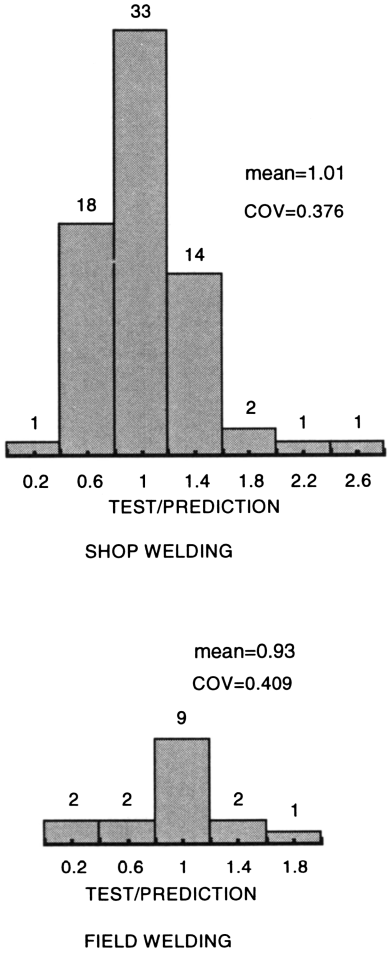

Figure 11. Histograms showing distributions of test to prediction ratios.

evaluate the cumulative plastic deformation factors of connections when failures are governed by a fracture starting from the corner of the beam cope and by a fracture starting from the HAZ or weld metal in the groove welds at the beam ends. Since 16 out of 86 specimens failed by local buckling, the above equations should give conservative estimates of η. This is because, if local buckling were completely prevented, specimens would have shown a greater deformation capacity.

The cumulative plastic deformation factors are calculated for all the specimens and shown in Table 2. The ratios of observed η to predicted η distribute as shown in Fig. 11. The above equations slightly overestimate the deformation capacity of field welded connections. However, these equations can predict the cumulative plastic deformation factor with reduced uncertainties as compared with the means of all the test results (Compare Fig. 1 with Fig. 11).

Connections studied here have welded joints at the positions where geometrical discontinuities exist (excepting field welled connections with improved copes). Furthermore, these positions coincide with the beam ends where bending moments become highest under earthquake loads. In this view the present connection design is considered inappropriate. If the connection design is improved more drastically, it would not be difficult to attain the cumulative plastic deformation factor of about 100. Examples of such drastically improved connections include connections with dog

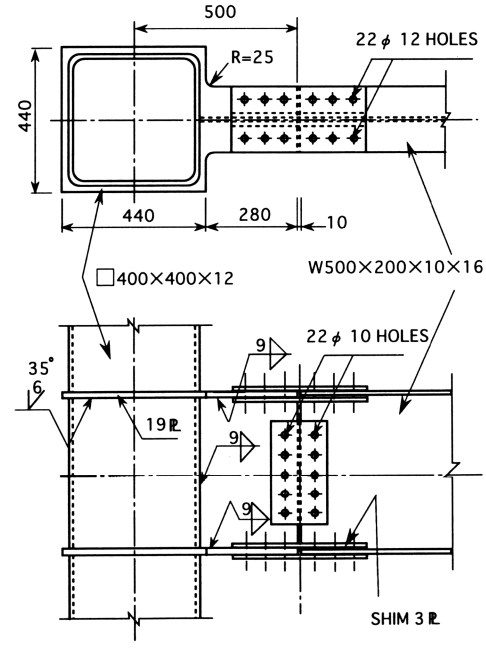

Figure 12. New bolted connection.

bone details (SAC Joint Venture 1995) and bolted moment connections described in the next section. Since the value of η_m for connections with recommended details were found to be 67, the reduction factor $R_{\text{INAPPROPRIATE DESIGN}}$ is considered to be even greater than 33.

4 NEW BOLTED BEAM TO COLUMN CONNECTIONS

Beam-to-column connections described here belong to one of the alternative approaches to the conventional connections that have welded joints at critical sections at the beam ends. The through diaphragms are extended sufficiently long to accommodate bolted beam splices used as field connections (See Fig. 12). The thickness of the through diaphragms can be chosen to be greater than the thickness of the beam flanges so that the weakest sections move from the beam sections adjacent to the column faces to the beam splices. The performance of new connections is largely governed by the performance of beam splices in cyclic loading.

A series of tests were conducted by the author and coworkers on beam-to-column assemblies with these new connection details (Kurobane et al. 1998). The reduced area of the beam flange due to bolt holes is only of 22% in these tests. Figure 13 shows examples of moment vs. rotation hysteretic curves, in which a new connection is compared with a conventional connection. Both the new and conventional connections use the same beam and column sections.

The conventional connection sustained cracks along the toes of welds at the outer edges of the beam flange (One crack initiated on the side of the beam flange and the other crack initiated on the side of the through diaphragm). The two cracks extended in a ductile manner and led to a separation of the beam flange from the connection, showing η of 56 (See Fig. 14). The conventional connection tested here had flux tabs, conventional copes and weave beads and is almost identical to some of the specimens tested in the collaborative research mentioned previously. Test results are also typical of those observed in the previous research.

The new connection sustained combined tensile yielding and local buckling of the beam flanges and web adjacent to the beam splice, of the splice plates and of the flanges and web of the stub beam connected to the column (See Fig. 15). Testing was terminated due to an excessive rotation of the beam reaching 0.09 radian. One of the beam flange sustained necking and was about to tear off at the final stage. Four major slips at the bolted beam splice occurred during the first 2 cycles of deformation controlled loading into inelastic regions. After these major slips the slip coefficient dropped to 50% of that at the first slip and stabilized during the following cyclic loading. After bolted connections slipped into bearing, the moment vs. rotation

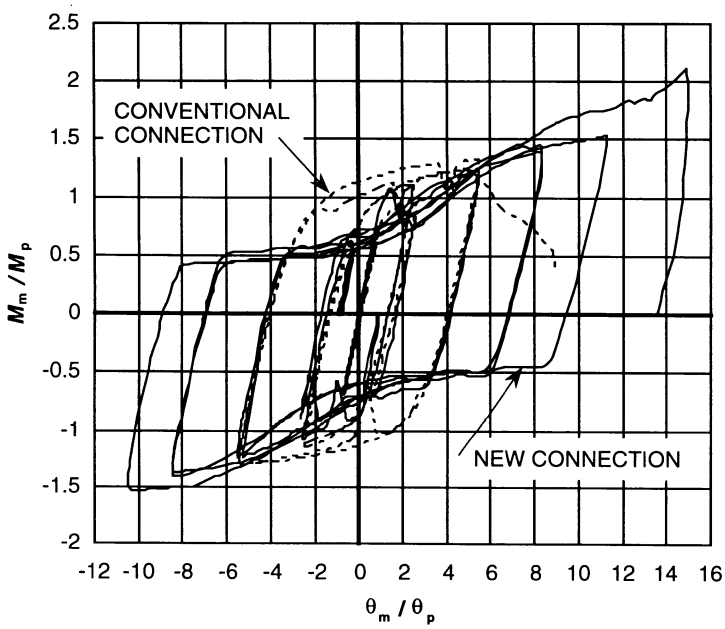

Figure 13. Comparison of moment vs. rotation hysteretic curves between conventional and new connections.



Figure 14. Failure mode of conventional connection by shop welding.

curves showed significantly hardening envelops and finally a moment capacity even greater than $2M_p$, where M_p signifies the full plastic moment of the beam (not of the stub beam). The cumulative plastic deformation factor η reached 158.

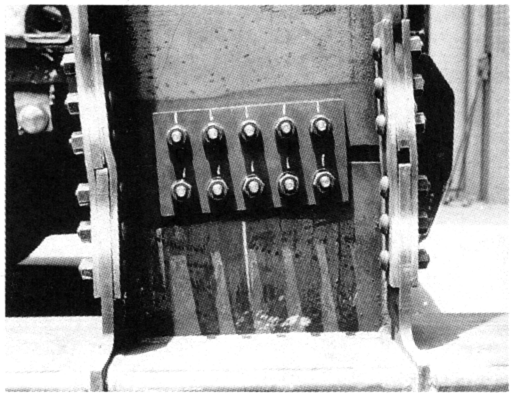

Figure 15. Failure mode of new bolted connection.

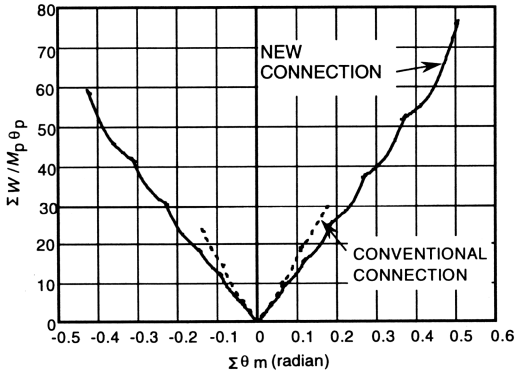

Figure 16. Cumulative plastic deformation factor based on dissipated energies.

Since the pattern of hysteresis loops is different between the new and conventional connections, comparison is made of the deformation capacities between the two in terms of dissipated energy. The area below the hysteresis curve represents the dissipated energy. However, since the area below an elastic unloading envelop represents the energy stored in the structure, this area is regarded as the negative dissipated energy (See Fig. A2). The dissipated energies, non-dimensionalized by $M_p\theta_p$, are plotted against the accumulated beam rotation $\Sigma\theta_m$ for the two specimens in Fig. 16, where $\Sigma\theta_m$ denotes the sum of rotations caused by either the positive or negative moment. It is interesting to see that dissipated energies at the same value of $\Sigma\theta_m$ are greater for the conventional connection than for the new connection. However, the final energies dissipated are much greater for the new connection than for the conventional connection.

Beam splices connected by high-strength bolts under cyclic loading were studied by a few investigators in the past (Igarashi et al. 1977, Tanaka et al. 1984, Takeuchi et al. 1997). All the test results showed hysteresis loops similar to those shown here, which were generally represented by bi-linear curves with a slightly pinched form due to slipping. Responses of moment frames having these connections to strong ground motions were also studied, which showed that the responses were similar to frames with bi-linear hysteresis loops, except that a sudden increase in displacement occurred at the instant when bolted connections slipped suddenly (Taniguchi et al 1980, Kaneta et al 1983).

Advantages of these new connections over conventional ones are found not only in a greater energy absorbing capacity but also in the fact that brittle fracture can be avoided by using sufficiently tough material for the beams. The beam flanges at bolted connections sustained plastic deformation largely in plain stress state, suggesting the flange would fail by plastic instability rather than by brittle fracture. The total cost required for fabrication, material and transportation is estimated to be reduced by about 5% by using new connections. Furthermore, since welding robots can be used extensively, the demand for skilled labor is less for the new connections. The last point may bear greater importance for the future from the quality control viewpoint.

5 END PLATE CONNECTIONS WITH BLIND BOLTS

Connections described here offer a straightforward solution for beam-to-RHS column connections by bolting. Beams with end plates are directly connected to column faces by tension bolts. Closed column sections necessitate the use of blind bolts. Further, the

Table 3. Dimensions of end plates for standard connections.

	SQUARE HOLLOW COLUMN SECTION							
	B=250		300			350		
	t=12	16	12	16	19	12	16	19
	PARTIALLY THICKENED COLUMN SECTION							
WIDEFLANGE	B=262	258	312	316	313	362	366	363
BEAM SECTION	t=24	24	24	32	32	24	32	32
250x125x6x9 248x124x5x8	450x200x19		450x250x19			450x300x19		
300x150x6.5x9 298x149x5.5x8	500x200x19		500x250x19			500x300x19		
350x175x7x11 346x174x6x9	550x200x28		550x250x19			550x300x19		
400x200x8x13 396x199x7x11	600x200x32		600x250x28			600x300x28		
450x200x9x14 446x199x8x12	650x200x36		650x250x32			650x300x28		

column walls have to be reinforced to prevent local distortion of the column walls and to fulfill the requirements for full moment connections. The column walls are partially thickened over the areas where the end plates are attached (See Fig. 17).

Two proprietary devices were developed to realize these connections. One of the devices concerns the development of new blind bolts, which had to be not only strong enough to carry bending moments at the beam ends but also easy for installation and tightening at erection sites. The new blind bolts being used for these connections are those called MUTF (Metric Ultra Twist Fastener) manufactured by Huck International Inc. (Huck 1994, Packer et al. 1997). MUTF27 bolts were exclusively used for the development of these connections. The number 27 represents the nominal diameter of the bolts. MUTF bolts are roughly equivalent in strength to ASTM A325 bolts with the same nominal diameter. However, the actual diameter of bolt heads and sleeves of these bolts is equal to 28.5 mm. The diameter of bolt holes is specified to be 30 mm to allow bolt heads to go through.

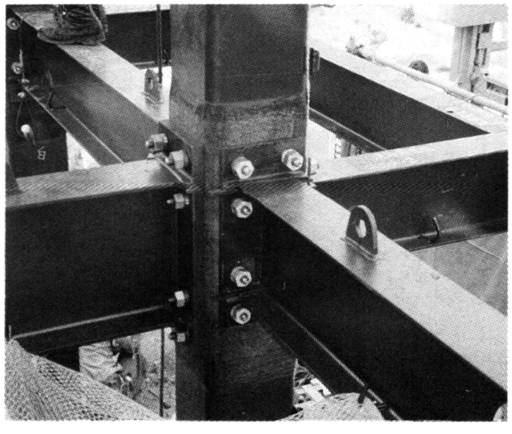

Figure 17. End plate connection with blind bolts.

The other device is for manufacturing partially thickened RHS. Hollow sections are heated by electromagnetic induction to a temperature at which material plastic flow can easily occur. The ends of the RHS are pushed by the hydraulic ram. While the induction coil travels towards the predetermined end point, water is sprayed just behind the coil to cool the sections for preventing buckling of the tube walls (See Fig. 18). The tube walls are tapered at the junctions between the thickened walls and the walls with original thickness. The rapid heating and cooling processes cause the tube material to be hardened. The thickened sections are post-heat treated to restore material properties. Since RHS's used for this type of construction are cold finished ones, original sections show a high yield stress to ultimate tensile strength ratio.

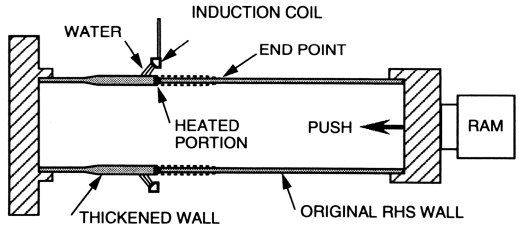

Figure 18. Manufacturing process for partially thickened sections.

The post heat treatments bring about improved material properties (e.g. higher toughness and greater ductility) as compared with original cold finished sections. Material properties of thickened sections with and without post-heat treatments are reported elsewhere (Tanaka et al. 1996b).

The standard connections shown in Table 3 were officially approved by the Japanese Ministry of Construction as the moment connections that fulfilled the requirements specified in the Japanese building code. All of these standard connections use 8 MUTF27 bolts. Table 3 shows dimensions of the end plate for each combination of beams and columns. Connections with beams and columns of larger dimensions probably require more bolts but have not been studied yet.

A series of tests were conducted on beam-to-column assemblies with the standard connections (Fukuda et al. 1997). The connections selected for these tests are the 4 connections shown by highlighting the dimensions of beams, columns and end plates in Table 3. Anti-symmetrical shear loads were applied to cruciform specimens as shown in Fig. 19. The dimensions shown in this figure are those of the specimen discussed in detail below. All the specimens finally failed by combined local and lateral buckling of beams. The specimen with the smallest column sizes (250x250x12 mm) sustained plastic bending deflection at the column end as well. The only specimen with the 350x350x12 mm column sustained ductile cracks extending from weld toes at the outer edge of the beam flange as shown in Fig. 20. However, no quick drop in load due to crack initiation was observed. The hysteresis curve for this particular specimen is shown in Fig. 21, in which the maximum load was governed by combined local and lateral buckling of the beams. Testing was terminated due to the limit of a ram stroke when the beam rotation reached 1/14 radian. It should be noted that the cumulative plastic deformation factors observed in these tests are incomparable with those discussed in the previous sections, because loading sequences are different between the two research projects.

Fukuda and Furumi (1997) are emphasizing the following advantages of these connections over conventional connections:

1. reduction in time to be taken to fabricate and erect a structure
2. flexibility to accommodate beams with different depths framing into each column
3. avoidance of brittle fracture

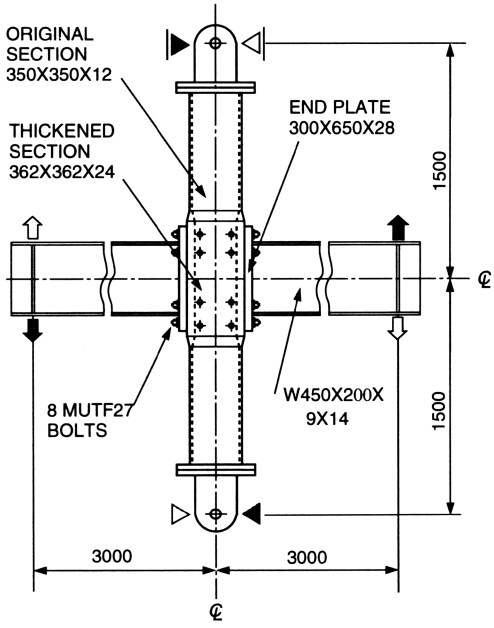

Figure 19. Schematic diagram for anti-symmetrical loading.

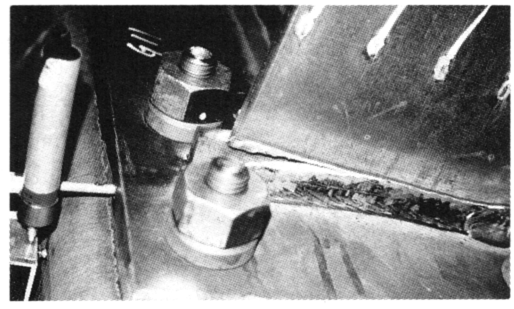

Figure 20. Tensile failure of end plate connection.

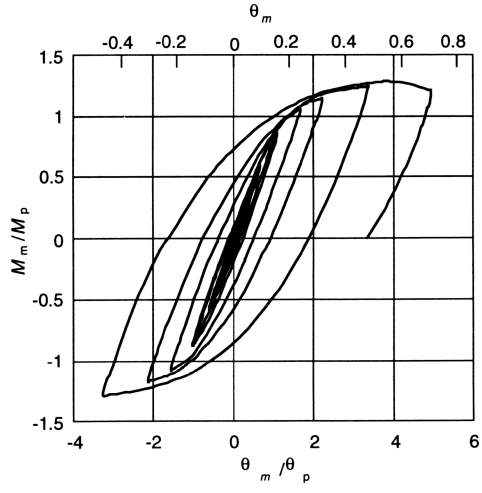

Figure 21. Moment vs. rotation hysteretic curves for end plate connection.

6 SUMMARY AND CONCLUSIONS

Well designed beam-to-column connections can easily show a plastic deformation capacity of 100, unless local and/or lateral buckling controls the ultimate limit state. The plastic deformation capacity is herein represented by the cumulative plastic deformation factor η as defined in Appendix. However, inadequately designed connections, such as connections in which welding is used at the junctions between columns and beam flange ends, η is reduced by 33 % even if the quality of welds is good and acceptable per ordinary quality control criteria.

Connections with conventional beam copes may sustain premature cracks developing at the corners of these copes, which entails a further reduction of η by 17%. However, these cracks can be avoided simply by improving the profile of copes. The total reduction in η of 50% may be attributed to the inappropriate design of connections.

Connections with improved beam copes are subjected to premature developments of cracks at other critical locations, which include the points along the weld toes at the edges and at central portion of each beam flange. When steel weld tabs are used and left as they are, notches formed by unfused regions between the weld tabs and the beam flanges enhance stress concentrations. The reduction in η due to steel tabs amounts to 22. When flux tabs are used and additionally when welders are insufficiently skilled at using flux weld tabs, weld defects may be created by nonmetallic inclusions. These defects, even if they are sufficiently small not to constitute rejectable conditions, reduce the deformation capacity by 16. Further, weave beads cause large heat input, and, thus, deteriorate the toughness of material in the HAZ and weld metal, which results in the reduction of η by 14%. The total reduction in η of 36% (steel tabs) or of 30 % (flux tabs) may be attributed to inappropriate welding procedures.

Brittle fracture may be avoided by moving welded joints away from critical sections at the beam ends adjacent to the column faces. One significant example is the newly developed connection in which welded joints at the beam flange ends are omitted by extending the through diaphragms long enough to accommodate a field bolted beam splice. This connection is superior in strength to the dog bone connection, because the diaphragms with thickness larger than the thickness of the beam flanges can be selected.

The end plate connection with blind bolts has details entirely different from conventional connections and was proven to have good performance as a moment connection. Standardized connections with larger sizes are planned to be developed.

ACKNOWLEDGMENTS

Section 2 of this paper summarizes a portion of the report published by Committee on Steel Building Structures, the Kinki Branch of the Architectural Institute of Japan (AIJ Kinki 1997). The author wishes to thank the chairman of the above mentioned committee, Professor Kazuo Inoue for providing him with raw data shown in Figs. 6-9. Thanks are extended also to Mr. Kenji Furumi, Daiwa House Industry Co. Ltd. for providing him with all the data shown in Figs. 17-21 as well as Table 3.

REFERENCES

AIJ 1979. *Standard for ultrasonic testing of welded joints in steel building structures*. Architectural Institute of Japan. Tokyo, in Japanese

AIJ 1995. *Technical recommendations for steel construction for buildings Part 1 Guide to steel-rib fabrications*. Architectural Institute of Japan. Tokyo, in Japanese

AIJ Kinki 1997. *Full-scale test on plastic rotation capacity of steel wide-flange beams connected with square tube steel columns*. Committee on Steel Building Structures. the Kinki Branch of the Architectural Institute of Japan. Osaka, in Japanese

Fukuda, A, & K. Furumi 1997. DSQ frame system. *Building letter*. Building Center of Japan. Tokyo. 365: 9-13, in Japanese

Huck 1994. *The ultra-twist fastening system*. Huck International Inc. Irvine

Igarashi, S., K. Wakiyama & E. Kawada 1977. *Preliminary Report of IABSE Symposium*. Lisboa

Kaneta, K. & H. Nishizawa 1983. Earthquake response analysis of steel frames with high strength bolted connection-Part 1 On the results of the on-line hybrid simulation. *Trans. AIJ*. 330: 78-85, in Japanese

Kurobane, Y., K. Ochi, Y. Yamashita, Y. Tokutome & M. Tanaka 1998. Testing of new bolted moment connections between RHS columns and I-section beams. *Structural Technology*. 11(115): 37-43, in Japanese

Packer, J.A. & J.E. Henderson 1997. *Hollow structural section connections and trusses*. Willowdale: Canadian Institute of Steel Construction

SAC Joint Venture 1995. *Interim Guidelines: Evaluation, repair, modification and design of steel moment frame structures*. Report SAC-95-02, SAC Joint Venture. Sacramento

Takeuchi, I., I. Inoue & N. Uno 1997. Experimental study on high strength bolted connections of H-shaped beams. *Summaries of Technical Papers of Annual Meeting of AIJ*. C-1:257-262, in Japanese

Tanaka, A & K. Takanashi 1984. Monotonic and cyclic behaviors of H.S. bolted moment connections

in wide flange beams. *Trans. AIJ.* 346: 101-111, in Japanese

Tanaka, T. & M. Tabuchi 1996a. Fracture on SHS column to beam connection by Hyogoken-Nangu Earthquake. *J. Constructional Steel.* JSSC: 151-158, in Japanese

Tanaka,T., M. Tabuchi, M. Maruyama, K. Furumi, T. Morita, K. Usami & Y. Matsubara 1996b. Experimental study on end-plate to SHS column connections reinforced by increasing wall thickness with one side bolts. Tubular Structures VII. J. Farkas & K. Jarmai eds.: 253-260. Rotterdam: Balkema

Taniguchi, H., K. Takanashi, S. Tanaka & A. Tanaka 1980. Non-linear earthquake response analysis of structures by a computer-actuator on-line system--Part IV Response analyses of one bay-one story frames with high strength bolted connections. *Trans. AIJ.* 291: 33-41, in Japanese

Toyoda, M . 1997. Effect of strain rate under seismic loading on fracture behavior of welded structures. *IIW Doc. XV-948-97, Doc. X-1379-97, Doc. XV-G-97-09.* International Institute of Welding. Cambridge

APPENDIX: DEFINITION OF CUMULATIVE PLASTIC DEFORMATION FACTOR

The bending moment M_m denotes the maximum beam moment at the column face. The rotation θ_m denotes the rotation of the beam segment between the loading point and the column face (See Fig. A1). The full plastic moment M_p is calculated by using the measured yield stresses of materials and measured dimensions of beam sections. The elastic beam rotation θ_p at the full plastic moment is defined as the elastic component of beam rotation at M_m=M_p (See Fig. A2). The plastic components of beam rotation at the i-th half cycle, non-dimensionalized by dividing it by θ_p, are denoted by η_i^+ and η_i^-, in which the + and - symbols distinguish positive and negative moments (See Fig. A2). The cumulative plastic deformation factor is defined as the sum of η_i^+ and η_i^- sustained by the specimen until failure occurs and written as:

$$\eta = \sum_i \left(\eta_i^+ + | \eta_i^- | \right)$$

The alternative definition of the cumulative plastic deformation factor is the sum of plastic energies dissipated during all the cycles, nondimensionalized by dividing the energy by $M_p\theta_p$. According to the latter definition η_i^+ and η_i^- are written as:

$$\eta_i^+ = \frac{\sum_i W_i^+}{M_p \theta_p} \quad \text{and} \quad \eta_i^- = \frac{\sum_i W_i^-}{M_p \theta_p}$$

where W_i denotes the energy absorbed at the ith cycle (See Fig. A2).

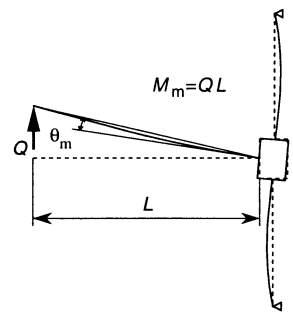

Figure A1

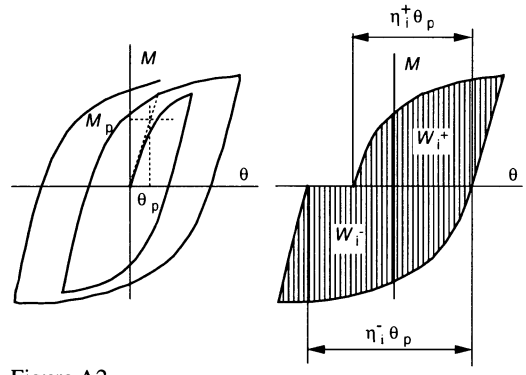

Figure A2



Taylor & Francis
Taylor & Francis Group
http://taylorandfrancis.com

Papers in plenary sessions



Taylor & Francis
Taylor & Francis Group
http://taylorandfrancis.com

Tubular Structures VIII, Choo & Van der Vegte (eds) © 1998 Balkema, Rotterdam, ISBN 90 5809 001 9

The storm surge barrier in the 'Nieuwe Waterweg' near Rotterdam: Design aspects

J.S. Leendertz
Ministry of Transport, Public Works and Watermanagement, Zoetermeer, Netherlands

ABSTRACT: The Storm surge barrier in the Nieuwe Waterweg protects the area around Rotterdam from being flooded by storm surges. It consists of two floating hemispherical gates which can be swung into the river and sunk on the river bed. Both curved retaining walls which consist of orthotropic plate structures are connected to pivots in the abutment by means of two triangular space trusses made of tubular sectons.

1 INTRODUCTION

1.1 *History*

After completion of the Eastern Scheldt Storm Surge Barrier 1986 the province of Zeeland was protected against flooding from the Norh Sea. However in the province of South Holland the area of Rotterdam failed to have an adequate protection. Figure 1 shows a map of the mentioned areas, the ending of the river (Rhine) is clearly seen.

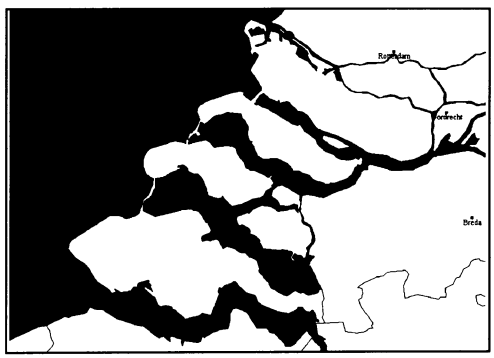

Figure 1. South West Holland and Zealand

In 1987 a committee was founded to investigate the possibilities in alternative of raising all dikes in the whole area. The results of a qualification procedure with bids for design and build contracts showed the construction of a storm barrier to be the most favorable solution.

The estimated costs not being of a different order: Approximately Dfl. 1,800,000.000 for raising all dikes and Dfl. 1,400.000,000, including raising a remaining part of the dikes and a second movable storm surge barrier in the Hartel Canal, the construction of a barrier was the more favorable solution.
Moreover the construction period turned out to be much shorter.

1.2 *Project Philosophy*

In the Ministry of Transport, Watermanagement and Public Works, the "Rijkswaterstaat" organisation developed in the last 200 years from "United Owners of Dyke Rings" to the organisation of today, that during the last 50 years planned and designed itself almost all works that have to protect the Netherlands from being flooded by the sea and rivers.

For this project Rijkswaterstaat wanted to use a maximum of creativity from private companies.

After the prequalification phase, two consortia have been selected to prepare a design and a final bid.

As a result the Bouwcombinatie Maeslantkering (BMK) has been selected for realisation of the barrier for a fixed price of Dfl. 700,000.000. Only a few specific influences could lead to additional costs. It has been commisioned to the Min. of Transport in May 1997, which after a 5 years maintenance contract will bear the full responsibility, including the design.

2 FUNCTIONAL REQUIREMENTS AND CONTRACT

In order to give a maximum of freedom and allowing the future contractors, Rijkswaterstaat brought the functional requirements as shown below to the highest abstraction level as possible.

Design Specifications:

- Indicated part of the river for possible locations of the barrier
- Design life: 100 years
- Closure Frequency
  First 50 years: 1 time in 10 years
  Second 50 years: 1 time in 5 years
- No obstruction for shipping and river discharge
- Specified maximum translation wave
- Failure rates:
  * Not closing: 1:1000 times
  * Not opening: 1:10.000 times
  * Collapse: 1:1,000.000 years
- 1.60m lowering of water level at Rotterdam, compared to situation without a barrier
- Width of riverbed 360m, depth at datum level 17.0m, no shipping height restrictions.

The design and build contract included:

- Preparations for construction
- Construction work
- Maintenance and operation manual & training
- Commissioning 1/7/'97 (realised 1/10/'97)

In addition the contractor needed to carry out all works under quality assurance.

3 DESIGN PHILOSOPY

Based on the requirements listed before, BMK preferred a full probabilistic approach. It meant that for each element of the structure the probability of loads and their combination effects had to be linked to the various failure modes. The contractors could choose between a full probalilistic approach or an approach with Load and Resistance Factor Design (LRFD).

In order to avoid doing new research into the failure probability of materials and structural elements, BMK decided to derive the failure probabilities by updating the failure probabilities as included in the various standards ie. NEN 6770, NEN 6771 and NEN6772, being $1.6*10^{-4}$/year and adapting them to the needed level for this structure. It changed the check according the standards:

$S_k*\gamma_S<R_k/\gamma_r$ into: $S_{bmk}<R_{nom}/\gamma_{m0}$

In which:

S_k = Characteristic load (5% exceedance probability)

γ_s = Partial safety factor for loads

R_k = Characteristic strength (95% exceedance probability)

γ_r = Partial safety factor for resistance

S_{bmk} = design value for loads by BMK

R_{nom} = Resistance according to the standards

γ_{m0} = Modelling factor, including: transfer R_{nom} to R_k; effects of the structural system; serial effects; parallel effects

In general this procedure leads to the fact that the incertainty in the loads as well as the strength with respect to standards are transferred into an additional safety, that is obtained by raising the loads.

For the proposed structure it was foreseen that a complete failure tree system had to be elaborated in order to define the failure probability on element level. Figure 2 shows the failure tree for the situation: Collapse under design load.

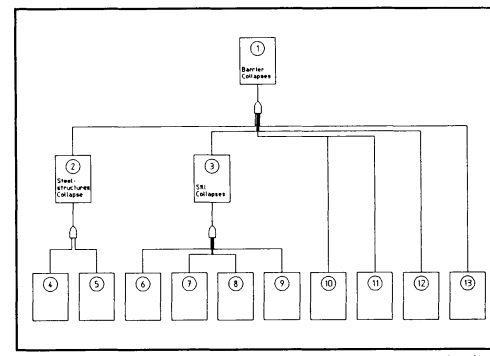

Figure 2. Failure tree for collapse under design load

Explanation of Failure tree:

Nr.	Collapse of Item	Failure rate
1.	Barrier	8.5e-7
2.	Steel struct. collapse	5.6e-7
3.	Sill	7.2e-8
4.	Retaining wall	2.0e-7
5.	Tubular space truss	3.9e-7
6.	Sill blocks	7.2e-8
7.	Sill protection	0.
8.	Filter	0.
9.	Riverbed protection	1.0e-10
10.	Ball joint	2.0e-7
11.	Adjadent dikes	1.0e-6
12.	Abutment	1.0e-8
13.	Others	0.

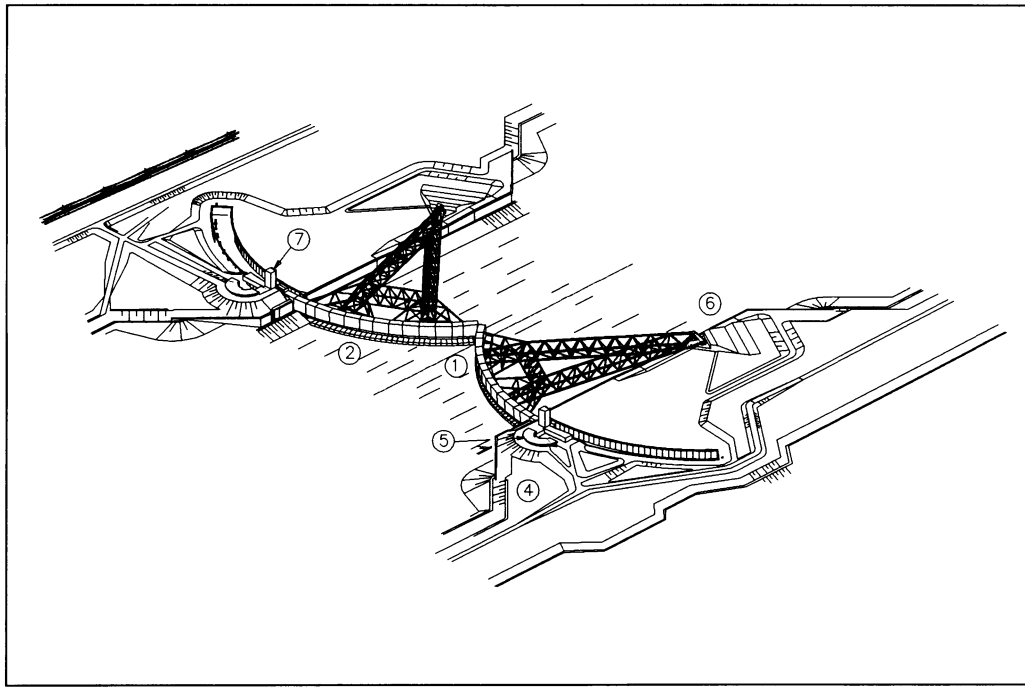

Figure 3. Perspective view

Finally the verification of the elements has been carried out by a calculation of the unity checks (u.c.) for all load combinations, which show the loading versus the capacity, values that may not exceed 1.0.

4 GENERAL PRINCIPLE OF THE STRUCTURE

4.1 *The structures*

The storm barrier consists of the following main parts, where the stuctures on the North and South bank are equal, but each other's reflected image. Figure 3 shows the main structural elements of the storm barrier in a perspective view:

1. Sill and river bed protection
2. Retaining wall detailed as a curved ships hull, length is 210m, steel weight approx. 7000tons
3. Tubular space truss, length 250m steel weight approx. 7000tons (in Figure 3 not indicated by a number)
4. Raised dikes towards North sea
5. Control building
6. Pivot or Ball joint, diameter 10m
7. Engine for horizontal movements

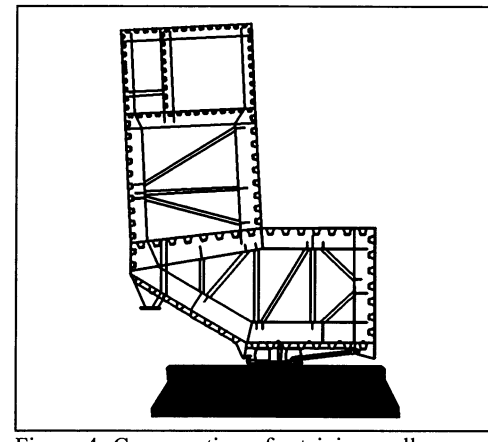
Figure 4. Cross section of retaining wall

4.1.1 *Retaining Wall*

Figure 4 shows a cross section of the retaining wall. The retaining wall which is effectively a curved ships hull.

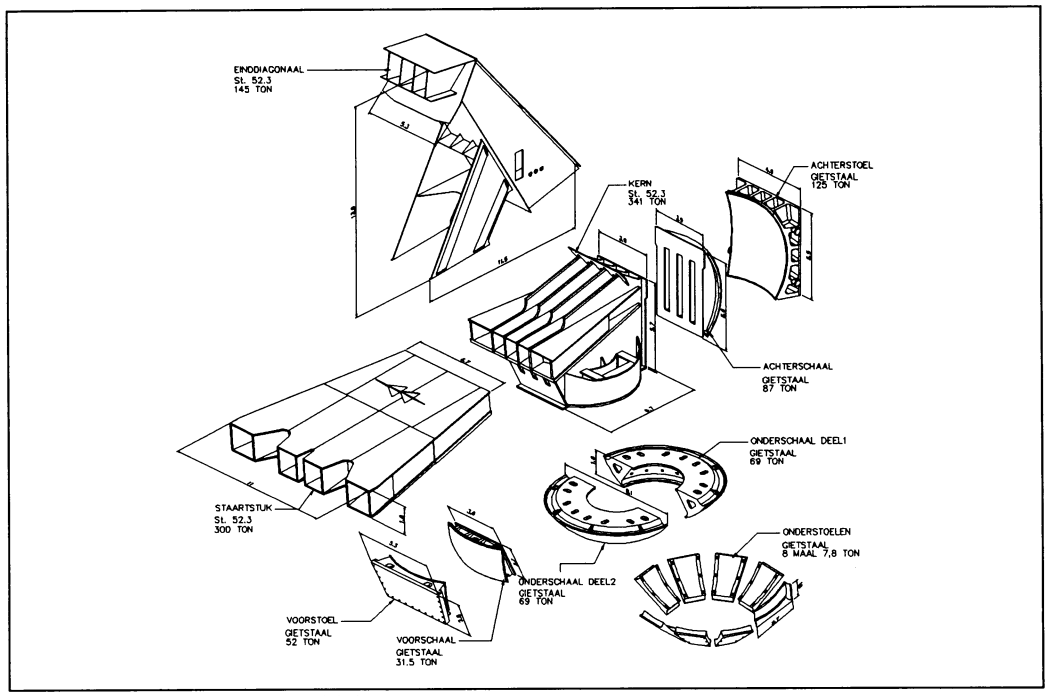

Figure 5. Exploded view of ball joint

It is made of plate structures, stiffened by trapezoidal sections. This structure showed a favorable amount of volume of welds and less surface for painting. The retaining wall has a height of 22.0m and a length of 210m. The width amounts 15.0m.

The lower part contains inlet valves and pumps for ballasting and deballasting, the upper part is a passive tank, where the front wall retains the waves and the wall at the riverside withstands the hydraulic head during operation. The upper tank as well as the lower tank for ballasting can be distinguished clearly.

During the phase "out of service" the retaining wall is supported by elastomeric bearings. During the phase "in service" the retaining wall is supported by fenders in sleighs, that can move over the sill blocks.

4.1.2 *Tubular space trusses*

The tubular space frame trusses that have triangular sections, transmit the horizontal forces from the curved retaining wall to the ball joint.

The details will be discussed later.

4.1.3 *Ball joint*

Figure 5 shows an exploded view of the parts of the ball joint. All horizontal forces are transmitted to the pivot, detailed as a facetted ball joint, which rests in an anchor block. The kernel of the ball joint is a rectangular box structure with four webs that transmit the horizontal forces directly to the front wall of the abutment and the vertical forces to a bearing element with the shape of a ring.The anchor block transfers the loads to the soil as it works as a gravity structure. The shape of the facetted ball joint with a diameter of 10.0m is achieved by means of convex steel casting elements, which are bolted to the kernel. The horizontal loads are taken by the rear bearing in case of a storm surge. Just after the storm surge a situation may occur with a so called "negative hydraulic head". Then the resultant force moves onto the front bearing.

The surfaces of the ball joint are covered with one layer which is a mixture of MoS_2 and Poly Tetra Fluor Ethylene (PTFE) in order to obtain a low dynamic and static design value for friction resistance (<0.15). For "run in" purposes, where the intial friction needs to be overcome, an additional layer of PTFE-spray has been applied.

In order to avoid damage of the cover layers by "fretting" or "pumping" during the phase "out of service", the ball joint is supported by coupled hydraulic jacks, which are permanently under pressure.

The horizontal movements of the gate are generated by an engine with electrical pumps and hydro-engines, which can give a maximum thrust of 1500kN.

The closing and opening operation is controlled by computer, which starts from the decision: "Close barrier SVKW". Unless emergency stops no human interference is possible.

The steel structure is protected against corrosion by a conventional environmently friendly system which consists of:

1 Layer primer 80μm;
2 Layers epoxy coating, each 200μm.

For esthetical reasons the upper parts of the retaining wall, the space truss and the housing of the ball joint have been painted white.

4.2 *Phases*

If a storm level which is expected to exceed 3.20m above datum, a closing operation is initiated.
The following phases in a closing operation are distinguished:

1. Out of service (parked), water level in dock 1.0m below ebb tide level.
2. Floating with outward horizontal movement (duration approx. 0.5hrs.)
3. Immersing (letting in water) (duration approx. 1.0hrs.)
4. In service
   Controlled support recactions on sill (duration max. 30hrs.)
5. Lifting (pumping out water) (duration approx. 2.0hrs.)
6. Floating with inward horizontal movement (duration approx. 0.5hrs.)
7. Floating for ball joint jacking purpose
8. Maintenance with dry dock

4.3 *Loadings*

Through all phases the following loads have been combined:

1. Hydraulic head
   Storm surge "Pos." approx: 6.5m
   "Negative" approx: 1.5m
2. Waves (with amplification trough reflection if applicable), Top, Crest and longitudinal distribution
   Initial wave heigth approx. 2.5m
3. Dead load
4. Uplift
5. Current
6. Wind
7. Traction

5 TUBULAR TRUSSES

5.1 *Geometry and dimensions*

Each gate includes two tubular space trusses with a total length of 250m. Figure 6 shows one gate.

The tubular space structures have a triangular section of 3 trusses. Two inclined vertical trusses with a common top chord and a horizontal truss with two chords. The distance between the top chord and the plane of the bottom chords amounts 18m and the distance between two bottom chords amounts 15m. The trusses contain no diagonals in order to avoid the secondairy effects related to contraction of the chords.

All sections are circular. The top and bottom chords have a diameter of 1800mm and wall thicknesses from 45mm to 90mm. Each tube has been has been fabricated out of rolled plates with a longitudinal weld seam, each part with a length of 4m. These parts were assembled to complete tubes with discontinnuous seams.

The diagonals have a diameter of 800mm and a wall thickness of 16mm. They have been fabricated from strip through a spiral rolling and welding process.

At the meeting points the spreader elements have been connected by another space truss, the "transverse coupling truss". This transverse truss acts as a bottom chord in a system where the retaining wall acts as a top chord.

5.2 *Development of the structure*

Originally the design consisted of rectangular hollow sections, the modification into circular sections had the following advantages:

- saving of material by better use of the sections
- cheaper fabrication, assembly and erection
- reduction of wind load effects
- easier maintenance
- esthetics

The original design did not comprise the transverse coupling truss, but the stress reversals in the retaining wall and the connection of the trusses near the ball joint made it necessary to add a horizontal load carrying structure.

5.3 *Load transfer*

The total load on the gate caused by the hydraulic

head amounts approx. 300MN and is mainly taken by all chords in the bottom plane. The top chords and diagonals mainly carry the dead load and work as stabilizers. Further all elements of the structure deal with wind forces.

The transverse coupling truss does not function as a main load carrying element, but it reduces the horizontal bending effects which could lead to fatigue problems, in the retaining wall and the space trusses that is caused by wave crest and trough along the retaining wall.
The front bearing of the ball joint has to take 50MN from "negative hydraulic head", which needed so much space, that the last bottom chords needed to be lifted at their connection to the ball bearing, the resultant of the horizontal compression force (300MN) continues in a straight line to the rear bearing.

The rectangular box girder elements of the top chords end in a end diagonal, which again has a rectangular box section. The last spacing between end diagonal and bottom chord contains an additional truss, which gives additional bending capacity needed for the eccentricity moments generated by the ball joint.

5.4 *Connections to retaining wall and ball joint*

The connection of the main trusses to the box sections of the retaining wall has been achieved by means of transition elements which are steel castings, that have a circular section at one end and a square section at the other end, they are shown in perspective in Figure 7.

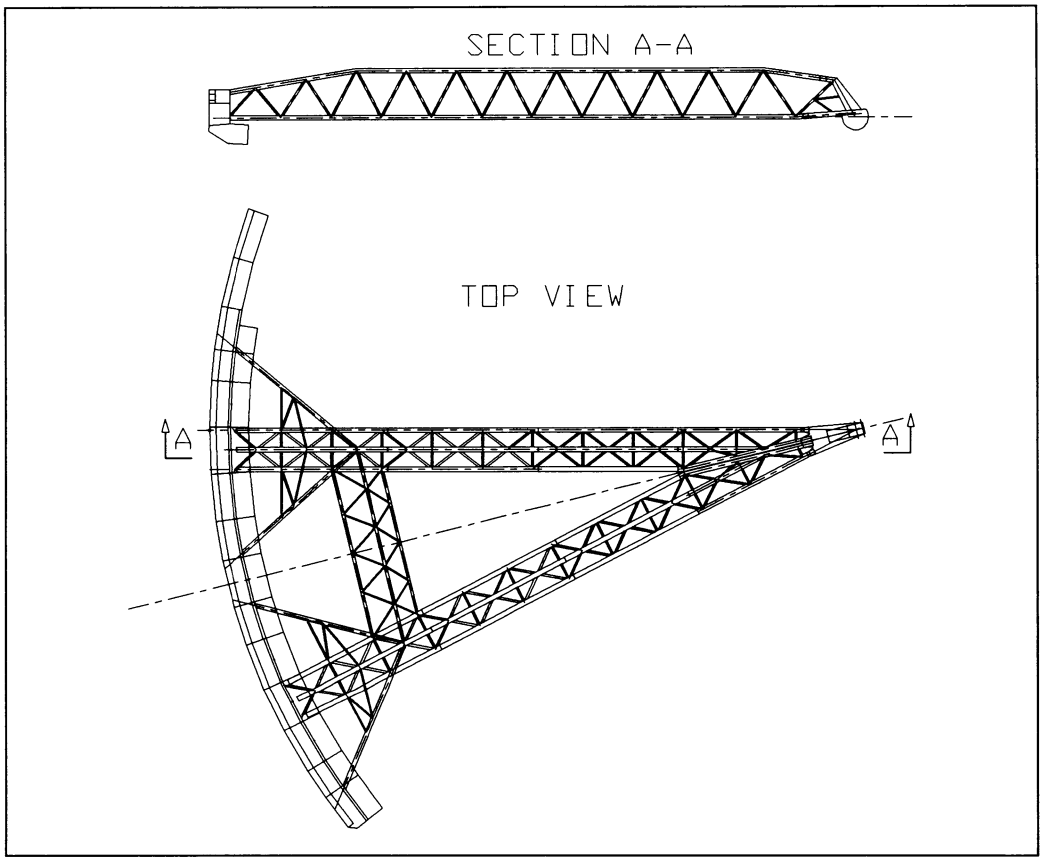

Figure 6. Tubular Space Trusses in plan and elevation

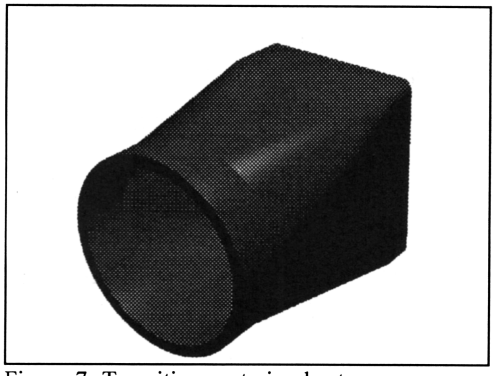

Figure 7. Transition part circular to square

The connection of the spreader elements to the retaining wall has been detailed with gusset plates in the tubular sections as shown in Figure 8.

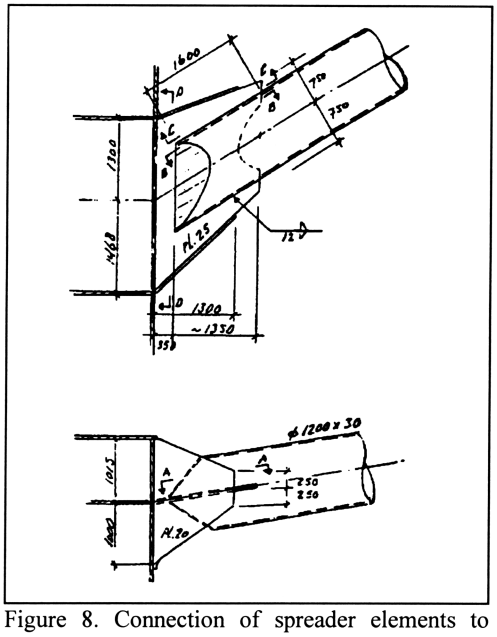

Figure 8. Connection of spreader elements to retaining wall

Near the ball joint, both trusses meet, are joined and transferred with sections of steel castings into square sections and subsequently connected to the ball joint. The meeting of the trusses has been detailed with two plates that form a flexible link in longitudinal direction and a rigid connection in transverse direction between the chords. In this way concentrations of forces are avoided.

The structure is shown in plan and in crosssection of the tubular sections in Figure 9.
The rectangular sections provide both the linking of the two space trusses to each other, as well as the connection to the rectangular box sections, which are the kernel of the ball joint, by means of bolted connections.

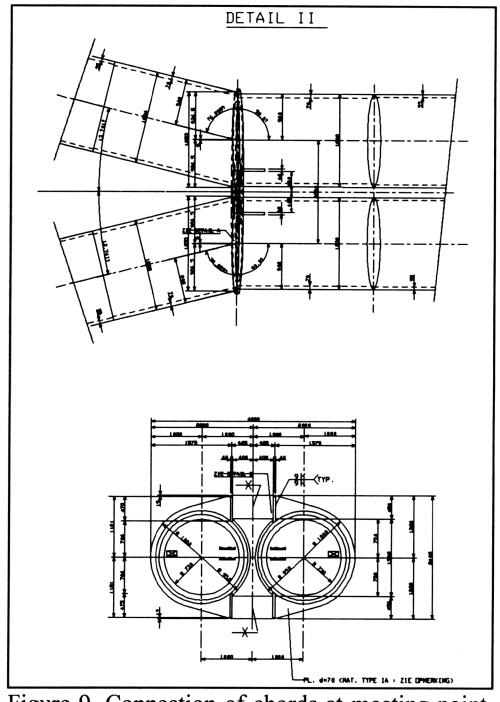

Figure 9. Connection of chords at meeting point

5.5 *Material*

The trusses have been made of two types of material, Type 1 and Type 2, which both are rolled thermo-mechanically. Both have a yielding stress of 355N/mm^2 for thicknesses of 16mm and less and 285N/mm^2 for thicknesses up to 250mm.

The relationship between yielding and break R_e/R_m does not exceed 0.85. The material Type 1 has guaranteed properties in transverse direction in order to avoid "lamellar tearing" (Z35) and has been selected for the "cans" with respect to "lamellar tearing', Z35. The material Type 2 has not and is used for all other elements.
The cast steel for the transition elements has a material comparable to GS 52.

6 DESIGN OF THE TRUSSES

6.1 *General*

The design of the whole storm barrier needed extensive hydraudynamic testing and investigations at the "Delft Hydraulic Laboratories" with the use of scale models.

Further a 3-dimensional Finite Element Model has been made which was analysed with ANSYS Release 4.4. It included both the steel and concrete structures. The connection between the ball joint and the abutment was simulated with "contact elements". Sub- and Superstructuring techniques made it possible to generate a general behaviour including dynamic analyses and 2nd order analyses as well as detail analyses with the appropriate loadings and boundaries.

6.2 *Mechanical Behaviour*

The trusses have been loaded by unity loads on the retaining wall, that could be scaled and combined. With the information of the "RAS-barrier" program which has been developed to calculate the hydraulic loads for each element the normal forces, shear forces and bending moments were obtained.

After the selection of the relevant loading combinations it was possible to derive the internal forces and moments in both the bars and the connections for all combinations.

Separately a non-linear analysis of the complete structure has been carried out in order to investigate the influence of overall buckling behaviour on the section forces in the elements.

It showed that the forces from the linear analyses had to be enlarged by a factor λ_n derived from the 2nd order calculations. The factor λ_n = 1.03 - 1.05 for the chords and λ_n = 1.03 - 1.35 for the diagonals. It means that the effects in the chords are maximal 3%, the deformations were found to be affected with 5%.

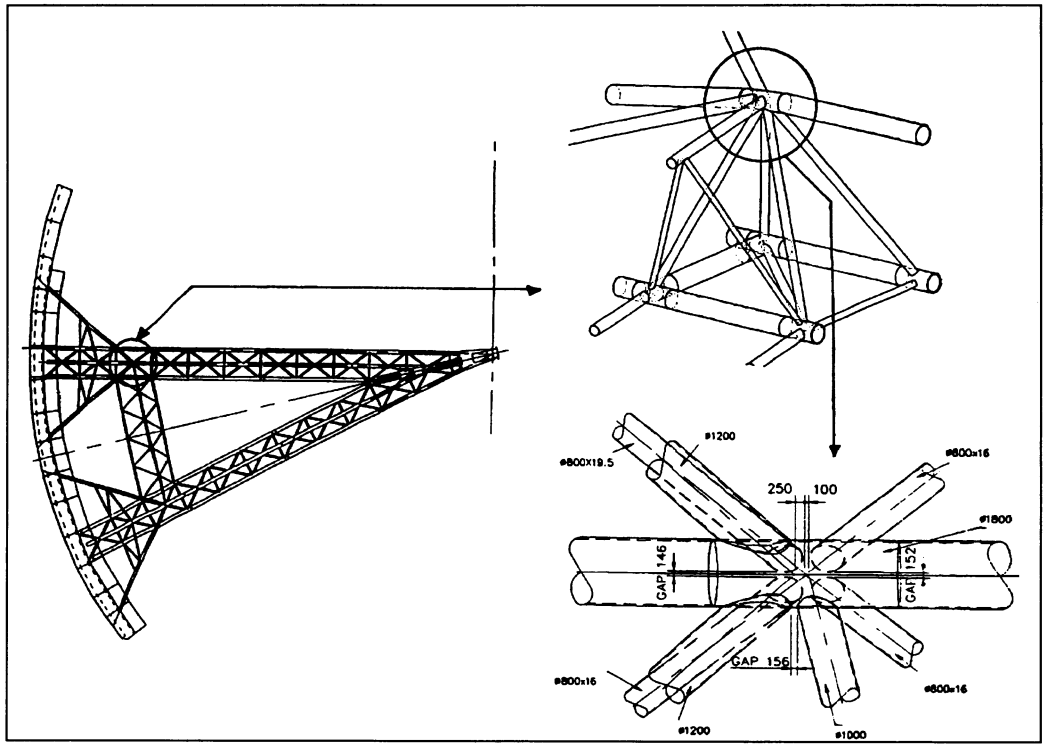

Figure 10. Connection of spreader element and transverse connection truss to top chord

6.2.1 *Static Strength*

For all bars and nodes the loads have been compared to the resistance available acc. to the updated strength according to the dutch standards: NEN 6770, NEN 6771 and NEN 6772, which in their approach are comparable to Eurocode 3.

Further the static strength of the bars has been reduced with a γ_m which takes account of the previously mentioned difference between the failure probabilities in the standards and the requirements for the barrier and in addition a factor which includes serial and parallel effects in the structure and leads to a lower strength of the individual elements when they take part in the load resistance of a large structure.

For the verification of the nodes an approach has been used, based on K-, N- or X-connections. Other connections like T- and Y-nodes that deviate from the standard approach have been calculated by simple calculations "by hand", using the standards. Figure 10 shows the connection of the top chord of the main truss with the top chord of the transverse coupling truss and the spreader element.

The transition elements from circular section to a square section (Fig. 7) have been analysed with 3D FE-models with solid elements.

The connection of the spreader elements (Fig. 8) to the retaining wall has been verified with the API-code.

The flexible connection of the chords at the meeting points (Fig. 9) have been checked separately by means of a 3D FE-model with solid elements.

As the trusses have been constructed from thermomechanically produced material which has a relationship between yielding f_y and breaking f_t of $f_y/f_t = 0.85$. The verification rules in the standards have been derived for: f_t of $f_y/f_t = 0.67$.
This relationship governs the ductile behaviour of the connections, so it was needed to investigate this effect.

Studies at the research institute TNO showed that the reduction in strength of 1.15 as derived by BMK was ample sufficiently.

In general the unity check does not exceed 0.85 which shows that there is some capacity left, but that the bars are not widely overdimensioned.

Once the stresses known, PD6493 was used to derive the acceptable defects for fabrication, assembly and erection.

6.2.2 *Fatigue*

Based on the information from the static analyses which showed which nodes possessed the largest unity checks, it was possible to calculate the fatigue resistance for these nodes.

The section forces and moments were divided by the section properties and multiplied with stress concentration factors (scf's by Efthymiu) which resulted in Hot Spot Stresses.

For the derived stress spectra, which mainly are caused by wave forces, it was shown that the design life of 75 years is met without any damage.

7 ORGANIZATION AND PROCEDURES

The combination of contractors Bouwcombinatie Maeslantkering (BMK) comprises of two branches:

1. BMK-Civil Works:
   - Hollandsche Beton en Waterbouw (HBW)
   - Van Hattum en Blankevoort
   - Dirk Verstoep
   - NBM Amstelland

2. BMK-Steel Works:
   - Hollandia Kloos nv.
   - Hollandsche Staalbouw Maatschappij bv.
   - Stapel bv.

The following subcontractors were involved:

- Dillinger Hütte, Dillingen (D)
  Rolled steel products
- Betonmortelcentrale Haringman,
  Concrete
- Croon Electrotechniek, Rotterdam
  Electrical Installation and Electronic Control Systems
- Dywidag Systems, Zaltbommel
  Reinforcement and prestress elements for concrete
- Hillson,
- Hydraudyne, Boxtel
  Hydraulic equipement
- Inter Techniek,
- Mebin, Rotterdam
  Concrete
- Mos Soil Drilling, Delft
  Soil mechanical investigations
- SIF Holland Offshore, Roermond
  Rolling and fabrication of Chord tubes
- TMI, Liege (B)
  Spiral welded bracings
- Ebroacero, Zaragoza (Sp)
  Steel casting transition parts
- SAF, Chalons s. Saône, (F)
  Welding consumables
- Sigma Coatings, Amsterdam
  Corrosion protection systems
- Škoda, Plzen (Cs)
  Steel castings for ball joint
- FIT, Madrid (Sp)
  Elastomeric bearings for ball joint

- OKS, München (D)
  Development and fabrication of low friction cover
- Menning, Soest
  Application of low friction covers
- Sarlin, Helsinki (Su)
  Deballasting pumps
- Econosto, Rotterdam
  Butterfly valves
- Trelleborg Bakker, Ridderkerk
  Fender units and elastomeric bearings for retaining wall
- Delft Hydraulics, de Voorst
  Hydraudynamic investigations
- TNO, Apeldoorn, Delft, Rijswijk
  Analyses of tolerances, ultimate limit capacity, fatigue strength. Testing of materials and welding procedures
- MME, Ridderkerk
  Non destructive testing of materials and welds

As mentioned before, the Ministry of Transport (Rijkswaterstaat) will take over the design responsibility in the end, which leads to the fact that the engineers and construction managers of BMK needed to have full agreement on all design aspects, method statements evaluation procedures etc. with the engineers of Rijkswaterstaat.

Therefore all documents and drawings as well as fabrication, assembly and erection documents have been subjected to an acceptance procedure which worked as follows:

1. BMK creates a concept
2. Informal meetings BMK and RWS
3. BMK makes final design documents, including calculations, reports and drawings
4. Last informal meeting BMK and RWS, if successful:
5. Offical application
6. RWS accepts
7. BMK draws further details
8. BMK drafts fabrication procedures, method statements and erection plan

The work started after a statement of acceptance of the plans by Rijkswaterstaat.

8 PRESENT SITUATION AND CONCLUSION

The Storm Surge Barrier has been completed and became a landmark near the coast of South Holland in the neighbourhood of Rotterdam.

The first tests have been completed at 11 and 12 May 1997 and although the design storm surges have not yet taken place, the design effort and testing makes Rijkswaterstaat confident about the way the barrier will fulfill the specifications.

9 ACKNOWLEDGEMENT

The author wishes to thank all internal BMK and RWS authors for the comprehensive internal documents and literature which allowed him to find all detailed information which was not directly at his disposal and the co-operation of BMK and RWS in getting the pictures.

REFERENCES

Ministry of Transport, Watermanagement and Public Works & Bouwcombinatie Maeslantkering 1995. Stormvloedkering Nieuwe Waterweg. Opvallendste beveiligingswerk voor Zuid-Holland (in dutch)

Noordzij, R. 1995. Evaluatie SVKW. De vakwerkarmen van de sectordeuren in de Stormvloedkering Nieuwe Waterweg (in dutch)

Rohde, A.A.J., A.F. Pruijssers, J. Kerstens, B. de Torbal, T. Bogers, J.P. Kottenhagen & M. Broeders 1993. Stormvloedkering Nieuwe Waterweg, Syllabus 4/5/1993 (in dutch) Staalbouwkundig Genootschap: Rotterdam.

Tubular Structures VIII, Choo & Van der Vegte (eds) © 1998 Balkema, Rotterdam, ISBN 90 5809 001 9

The storm surge barrier in the 'Nieuwe Waterweg' near Rotterdam, Netherlands: Fabrication and assembling of the tubular trusses

A.Zondervan
Hollandia BV, Krimpen aan den IJssel, Netherlands

ABSTRACT: Building a Storm Surge Barrier of dimensions and weights as the Storm Surge Barrier in the Nieuwe Waterweg requires a high design, fabrication and assembling standard. Due to the enormous dimensions with respect to lengths, thicknesses etc. BMK found out that available and commonly used standards would not lead to the quality and economic BMK was aiming at. To assure that the Storm Surge Barrier should be built in schedule, within the economical budget and fulfilling the design specifications the work has been performed under ISO 9001 quality regulations.

1 INTRODUCTION

1.1 *Contract & Organisation*

As the Netherlands have to be protected against flooding from the North Sea by a Storm Surge Barrier, BMK was selected and contracted by the Ministery of Transport, Watermanagement and Public works to build the barrier in the "Nieuwe Waterweg" the main entrance to the harbour of Rotterdam.

The construction work must take place without interrupting the shipping traffic.

In August 1989 BMK was informed that their proposal has been chosen to be the best one in relationship to technical and economical aspects.

After installation of the management team two separate branches were introduced, BMK-Staal, responsible for design, fabrication, assembling and testing of the steel parts of the project, and BMK-Civiel responsible for the civil works.

In October 1989 the design team was installed and started up to investigate all external design requirements.

1.2 *Tubular trusses*

The trusses designed for transferring the loads from the retaining wall to the pivot point, have with one top chord and two bottom chords, connected with diagonals according to the basic

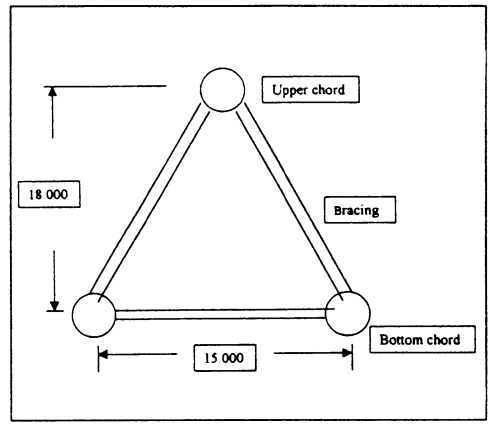

Figure 1, the typical section of the truss

design concept. The design team found out that available and existing specifications for materials and welding could not be used for this structure because of needed strength, thicknesses, expected assembling and welding conditions etc.
To cover these special aspects, specifications have been prepared by BMK-Staal to be used in this project by her sub-contractors, her fabricators and her own assembling department. For the tubular trusses the following specifications were prepared:

- Material specification, describing all material requirements
- Welding specification, describing all

requirements applicable for welding in the shops as well as on the assembling sites
- Dimensional specification giving all tolerances during fabrication and assembling,
- Non Destructive Examination specification, describing all examinations and criteria for acceptance of materials and welds
- Weldable castings specification, describing the requirements subject to the transition pieces
- Preservation specification describing the preservation requirements

2 MATERIAL SPECIFICATION

The material specification describes the requirements to which the materials to be used have to fulfil. Special attention has been given to the chemical and mechanical requirements.
The chemical requirements as shown in figure 2 are chosen in such a way that no preheating was required for all plate thicknesses during fabrication, assembly and welding.

Element		Max cont. t≤ 63 mm	Max. cont. t>63 mm	Addtional for Type I
Carbon	C	0.16	0.12	–
Phosphorus	P	0.025	0.025	–
Sulphur	S	0.015	0.015	0.008 max
Nitrogen	N	0.014	0.14	–
Manganese	Mn	1.7	1.7	–
Silicon	Si	0.55	0.45	–
Chromium	Cr	0.25	0.25	–
Molybdenum	Mo	0.08	0.08	–
Vanadium	V	0.08	0.08	–
Niobium	Nb	0.040	0.040	–
Titanium	Ti	0.02	0.02	–
Nickel	Ni	0.45	0.45	–
Copper	Cu	0.30	0.30	–
Aluminium	Al	0.06	0.06	–
Boron	B	0.0005	0.0005	–

Figure 2, Chemical material requirements

With respect to the material thickness of the chords which are in thickness varying between 50 mm up to 90 mm, the quantity of longitudinal, circumferencial welds and the number of node welds (bracings onto the chords) a lot of time and energy has been saved as preheating could be avoided at all, due to the weldability of the materials (as a result of the chemical composition) which has been based on the following values:

- CEN value (%) to be calculated to the following formula:

  $$CEN\ (\%) = C + A(C)\{(Si/24 + Mn/6 + Cu/15 + Ni/20 + (Cr+Mo+V+Nb)/5 + 5B\}$$

  Where: $A(C) = 0.75 + 0.25 \tanh\{20(C - 0.12)\}$

  For the A(C) factor in the formula following vallues have been used.

C (%)	0	0.08	0.12	0.16	0.20
A (C)	0.5	0.584	0.75	0.916	0.98

- Carbon equivalent to be calculated using the following formula:

  $$Ceq = C + Mn/6 + \frac{Cr+Mo+V}{5} + \frac{Ni+Cu}{15} + Si/24$$

  To obtain the optimal weldability the chemical composition has to fulfil the following additional requirements:

  CEN value: ≤ 0.34, for t > 80 mm: 0.36
  Nb+V+Ti : ≤ 0.08
  Cr+Mo+Cu+Ni: ≤ 0.8

  t = thickness of plate

The mechanical requirements especially for the chord members which had to be fulfilled by the fabricators have been drafted in such a way that testing of the Mechanical properties in the mill laboratories should be performed on specimens which were in the same condition as the plates in their rolled configuration to refer to a chord member in respect to the cold deformation and 5.5% permanently streched condition. This in comparison to the outside surface of the chord members to be used for the tubular trusses.
The outside diameter of the chords is 1800 mm and the wall thickness is from 50 mm up to 90 mm.The procedure of milling of the plates as well as the way of normalising (degassing procedure) has been described and was subjected to approval of the BMK organisation.

The connection of trusses to the retaining wall and the pivot has been featured with transitions pieces. These pieces allow the transformation from circular into square sections.

After investigation of all possibilities for this transition connection points, a choice has been made for transition castings.

The chemical requirements for these castings have been specified in such a way that welding without preheating could be performed. The checmial requirements are shown in figure 4.

The carbon equivalent of the castings has been calculated in accordance to the following formula:

$$Ceq = C + Mn/6 + \frac{Cr + Mo + V}{5} + \frac{Cu + Ni}{15} + Si/24$$

Type of material	Thickness mm	Yield strength (lower/0.2)/Nmm^2	Ultimate tensile N/mm^2	Ratio measured Yield/Ultimate max %	Elongation min %
I u/i IV	< 16	355	490-630	0.85	22
	> 16 ≤ 40	345	490-630	0.85	22
	> 40 ≤ 63	335	470-630	0.85	22
	> 63 ≤ 80	325	460-630	0.85	22
	> 80 ≤ 100	315	460-630	0.85	22
	> 100 ≤ 150	295	450 min	0.85	18
	> 150 ≤ 250	285	450 min	0.85	18

0.2 yield strength and ultimate tensile strength must be tested as follows:
t ≤ 100 mm : tensile test over full plate thickness
t > 100 mm : tensile test over full plate thickness or tensile test with one (1) plate surface and ½ plate thickness incl.

Figure 3, Mechanical requirements

Product analysis Elements	%		Tolerance for product analysis %	
Carbon	0.15	max	--	
Silicon	0.52	max	--	
Magnanese	1.35	max	--	
Phosphorus	0.020	max	--	
Sulphur	0.015	max	--	
Niobium	0.03	max	--	*
Vanadium	0.08	max	--	
Molybdenum	0.08	max	--	
Niobium + Vanadium	0.10	max	--	*
Niobium + Vanadium + Titanium	0.12	max	--	*
Nickel	1.00	max	--	
Copper	0.30	max	--	
Titanium	0.02	max	--	*
Chromium	0.25	max	--	
Aluminium (soluble)	0.06	max	--	
Nitrogen	0.014	max	--	*
Calcium	--	--	--	
Cerium	--	--	--	
Magnesium	--	--	--	
Perlit	--	--	--	
Ceq (incl. Si)	0.43	max	--	

- These values should be measured on the special testpiece only to be performed by TNO-Apeldoorn

Figure 4, Chemical testrequirements of the transition castings

The permissible product carbon equivalent (Ceq) has been restricted for (cold) weldability reasons to 0.43.

The mechanical tests have been carried out on all standard testcoupons which were attached to the castings and on the special testblock which has been produced for testing purposes only. This ensured that mechanical properties were known before production of the castings itself. The position of the test specimens used for the mechanical tests are both at sub-surface and mid-thickness positions (1 series of tests at each position per testblock). All mechanical tests are carried out after final heat treatment.
The mechanical requirements for the steel castings are as shown in figure 5.

Tests	Minimum requirements
Yield stress at 0.2 %	320 N/mm^2
Tesile strength	460 N/mm^2
Elongation	22%
Reduction of area	35%
Charpy-V notch impact Individual (max 1 specimen)	27 Joule at -20°C
Charpy-V notch impact 3 testspecimen (average)	40 Joule at -20°C
CTOD tests 3 testspecimen	min 0.20 mm at -10°C

Figure 5, Mechanical testrequirements for transition castings

After the testblocks have passed the tests succesfully, Ebroacero, Zaragoza, Spain has been contracted for the delivery of 32 high quality castings. All produced castings fulfilled the specification.

3 WELDING SPECIFICATION

Due to the special material requirements the

welding specification for welding the truss chords and bracings could be simplified in such a way that the arrangements and control of preheating elements was not longer necessary.

The welding specification pays special attention to the hydrogen content of the welding consumables which has been specified to a maximum of 5 ml per 100 gr deposit weld metal to be checked every half year by a independent laboratory.
Further, the welding specification requires procedures which fulfil a number of destructive tests to be demonstrated before this procedure was accepted to be used for the BMK project.
The requested tests are:

Fillet welds:
- 3 macro sections including hardness measurements HV 10
- measurement of deposit hydrogen content in the weld metal
- all weld tension test

Butt welds (full- and partial penetration welds):
- 3 macro sections including hardness
- measurement of deposit hydrogen content in the weld metal
- 2 weld tension tests
- 3 x 4 sets (3) of charpy-V impact tests to be tested at -20°C at following positions:
  - fusion line
  - fusion line + 2 mm
  - fusion line + 5 mm
  - centerweld
    all at surface, midweld and root position
- 3 bend tests
- 3 sets (3) of tensile tests at following positions:
  - surface
  - midweld
  - root
- 3 sets (3) CTOD (Crack Tip Opening Displacements) test (for chord node sections only)

Especially the welds of the nodes (longitudinal – circumference and bracing to node welds) have to be welded in the rolled (cold rolled tubulars) condition and real situations (welding positions) using the same materials as to be used in the project. In this way the most possible and representative mechanical values of the base materials in the heat affected zone and deposit weld material were known.

For the tests BMK used the sample nodes and bracing pieces.

Welders were only permitted to perform welding if they were certified by authorized persons by means of valid certificate (1/2 yearly updated).

The welds must be tested visual as well as by means of non destructive examination (ultrasonic-magnetic particle testings). The requirements for visual and non destructive acceptance for the welds of the chords and bracings as well have been a part of the welding specification.

4 MILLING OF THE PLATES

After having prepared and having received the acceptance of the material specification, knowing the dimensions of the plates (length, width and thickness etc.) and the approxmately tonnage necessary, worldwide, 5 mills were requested to demonstrate their capabilities:

BMK prefered to buy the material at a mill where the expected percentage of rejection was minimal For this purpose the following aspects were important items to accept or reject interested mills:
- Normal chemical analyses
- Normal reached mechanical proporties
- Lost percentage

As BMK intended to purchase 30.000 tons of steel all mills were invited to participate and to respond to the questions. After having received and studying the answers of the mills, three of them were deemed to be capable to deliver the steel to the requirements of BMK. After commercial negotations two of them were visited and auditted to check their facilities (rolling plant, laboratories) and the effectiveness and implementation of their quality system.

After investigation of the technical and economical aspects, Dillinger Hütte, Dillingen Germany has been contracted to deliver the 30.000 tons varying in thickness from 8 till 200 mm, of plate material for the Storm Surge Barrier.

The milling method used by Dillinger Hütte is the latest material milling procedure called Thermo Mechanical Controlled Processed. This production method "TMCP" is in principal based on strictly controlled deformation of steel under certain controlled temperatures. Due to the deformation and temperatures of the material by rolling and the chemical composition the material characteristics with respect to mechanical, fatique and weldability are excellent.

5 FABRICATION OF THE CHORDS

A truss consists of chords and bracings (figure 1) The chord tubulars are varying in thickness from 50 mm (near the retaining wall) up to 90 mm (near the pivot) with an outside diameter of 1800 mm. The tolerances in diameter were restricted to minimise high-low at the welds between the chord members. These tolerances are:

- out of roundness at connection sections of each chord member max. 3 mm
- high low at weld positions max. 3 mm.

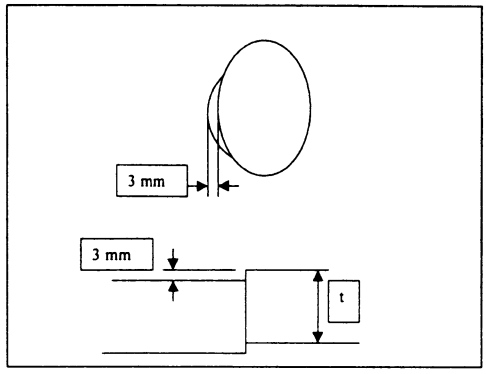

Figure 6, Tolerances at welding positions

After evalutation of three experienced company's for rolling of tubulars, SIF Roermond, Netherlands has been contracted to produce a complete sample chord for testing purposes only. After having passed the extensive destructive and non destructive tests of this sample chord member succesfully, SIF was contracted to roll all chord members, to weld the longitudinal welds and the circumferencial welds and to deliver 60 m pieces to BMK.

5.1 *Rolling of the chord members*

Before the start of rolling the plates to tubular chord members, the weld preparation for the inside of the longitudinal welds are machined and présetting of the longitudinal plate ends (which will form the longitudinal weld seams)has been done, Présetting has been performed to assure a good roundness of the whole chord member especially at both sides of the longitudinal weld. Rolling has been performed under cold conditions.

After rolling the chord member, the member has been checked at roundness, tackwelded from the outside and when acceptable, transported to the location for longitudinal welding.

5.2 *Longitudinal welds*

The weld preparation for the longitudinal weld is shown in figure 7 and is welded at first from the inside of the tubular.

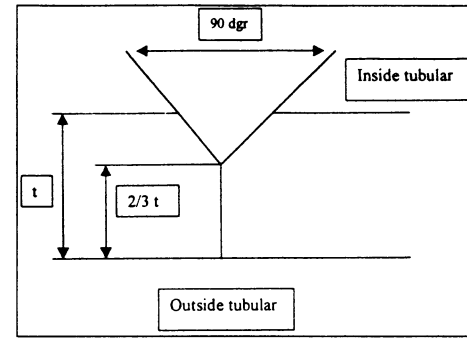

Figure 7, Weldconfiguration longitudinal welds

After completion of the inside, the weld preparation for outside welding has been machined with milling machines including as well as the root zone of the longitudinal weld. After finishing this machining, the rootzone has been inspected by Magnetic Particle Inspection. It was welded from the outside and 24 hours after completion of welding, Ultrasonic and Magnetic Particle Inspection has been carried out.

5.3 *Welding of the circumferencial welds*

Before to start the welding of the circumferencial welds, configurated as shown in figure7 on both ends of the chord member the weld configuration for the inside of the circumference welds were machined on milling machines. Thereafter two chord members are positioned and tackwelded from the outside and welding of the circumference weld was performed from the inside. Subsequently the weld has been machined from the outside to make a proper weld configuration and to clean the rootpass as well. The root has been checked by Magnetic Particle Inspection.
Further the weld now has been completed from the outside and 24 hours after completion subjected to Ultrasonic and Magnetic Particle Inspection. According to this procedure, specified lengths of chords have been fabricated. After

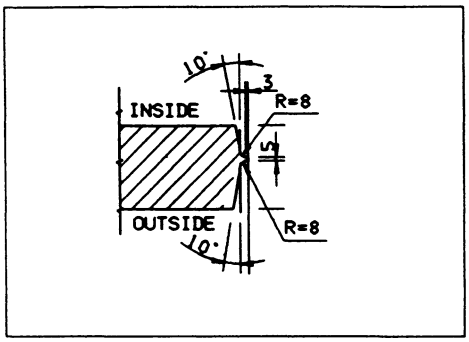

Figure 8, Weldconfiguration circumferencial welds

having passed the dimensional test they were released for shipping to the preservation site.

6 FABRICATION OF THE BRACINGS

The bracings, varying in length from 16 m up to 20 m and in thickness from 16 mm up to 22 mm were produced as spiralwelded tubulars.
The base material for the bracings has been delivered as coil material. Before contracting a company, three companies were requested to produce a sample, using the same material and welding parameters as to be used for the bracings. After testing the samples by means of non destructive and destructive testing (welds, roundness) two companies were requested to give their best price.
The company contracted to deliver the bracings was TMI, Liege, Belgium.

6.1 *Rolling and spiral welding*

The rolling and spiral welding has been performed using a specialised rolling and welding machine. The coil is positioned at the end of the machine being unrolled, the material is twisted in such a way that it is forming a tubular supported by guiding rolls. Directly after twisting the spiral weld is welded form the outside.
After welding the spiral welded bracing is flame cut with a overlength of approx 0,5 m and on spotcheck base tested by Ultrasonic and Magnetic Particle Inspection.

6.2 *Bevelling the bracing ends*

Due to the angles and positions of the bracings to the chords, complicated ends on the bracings were required.

See for example the weld configurations of figure 9.
To assure that these chosen weld configurations could be produced, a experienced company has been requested to develop computer programs to be used on bevelling machines. After several try-outs and welding tests from bracing to node welds, this company (HGG, Middenmeer, Netherlands) has been contracted to bevel all bracings ends for the project.
Number of bracings: 258 (both ends bevelled).

7 TRANSPORTATION OF CHORDS AND BRACINGS

The uncoated chords (length 60 m, weight: ± 170 tons) as well as the bracings were transported by barges on the river to the preservation site of Hollandia B.V., Krimpen a/d IJssel, Netherlands, unloaded with floating cranes, and prepared for preservation.

8 PRESERVATION OF CHORDS AND MEMBERS

The chords and bracings were steelblasted up to a cleaning grade of SA3 according SIS 5900 and thereafter a 4 layer paintsystem has been applied to a nominal dry film thickness of 1200 microns.
After steelblasting but before coating, the areas to be welded (site circumferencial welds) as well as the receiving positions of the bracings at the nodes were protected to with a temporary plastic seal to avoid paint on these positions.
After painting, the protective seal was removed and a easy to remove plastic coating has been applied on these areas to assure a temporary protection against rust and contamination during transport and storage.

9 TRANSPORTATION TO ASSEMBLING SITE

The assembling of the chords and bracings to form the trusses has been performed at the final position of the Storm Surge Barrier. The chords and bracings were loaded on river barges and sailed to the assembling sites (north and south shore of the barrier) unloaded with floating cranes and stored on such a way that multiwheel cars were able to load them and to transport them to their assembling position. See figure 11.

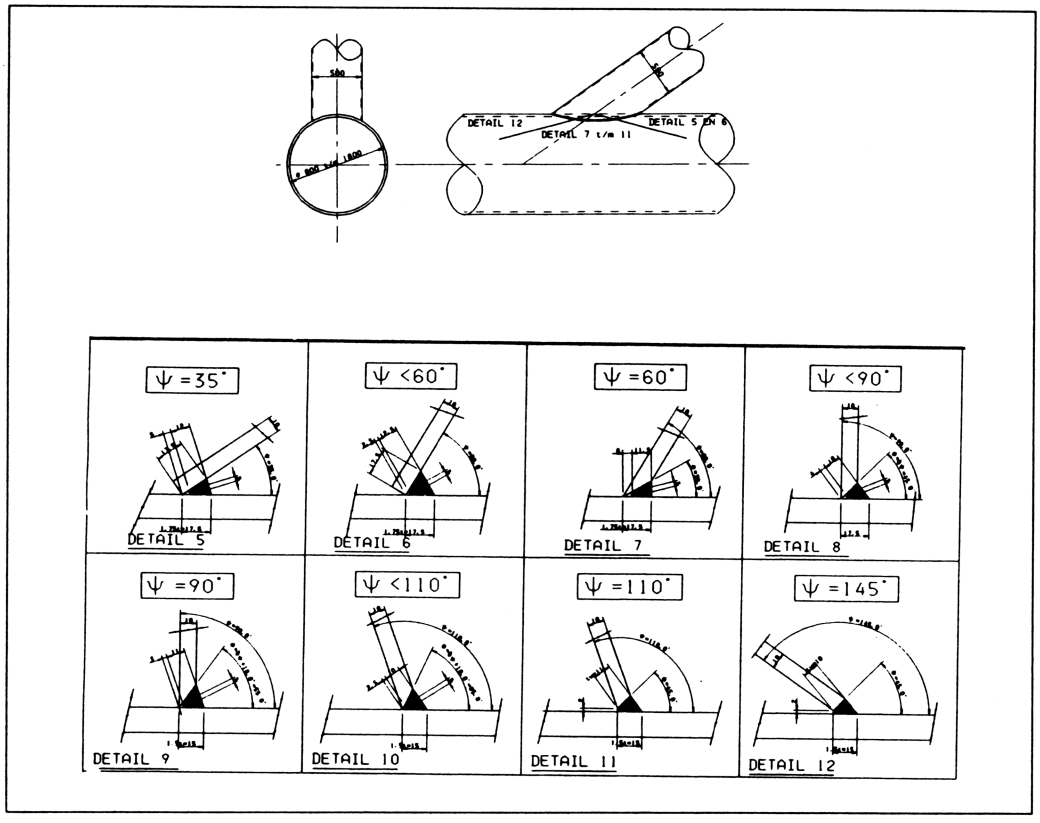

Figure 9, Example weld configuration bracings to nodes

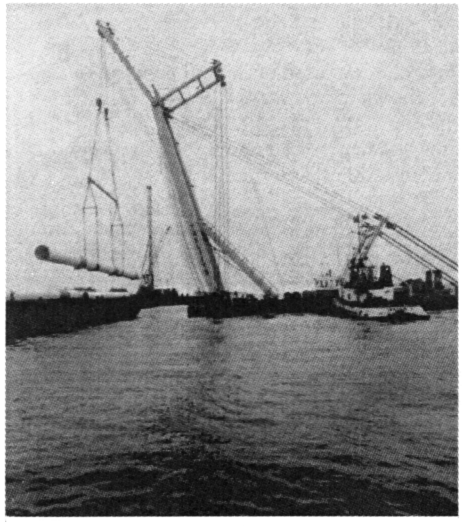

Figure 10, Unloading of chord section on site

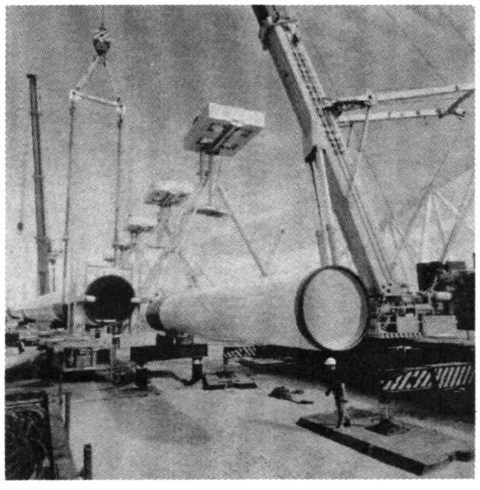

Figure 11, Transport of chords to their building position

10 TEMPORARY STRUCTURES AND SUPPORTS

To assure that the tubular trusses could be built within the required tolerances and within the tight schedule before starting, the assembling the possible methods were studied and reviewed extensivily. To perform the assembling, BMK felt it was necessary to take care for sufficient arrangements for supporting and welding at all stages of assembling.

The site was prepared with 48 steel piles into the bottom to assure a sufficiently horizontal plane base for assembling the bottom chords of the tubular trusses. On top of these piles, arrangements were positioned to assure that the bottom chords could be positioned in the horizontal and vertical direction.

To enable the assembling of the Upperchord adequate, A-frames were constructed which were a adequate help to position the upper chord in the exact position and to carry out the welding with the required result These A-frames therefore were constructed in such a way that while they are positioned on to the two bottom chords, the triangle section remains adequate.In addition the A-frames were equiped with a insulated housing that covered the welding area to assure that welding is possible under the most severe weather conditions. See figure 12.

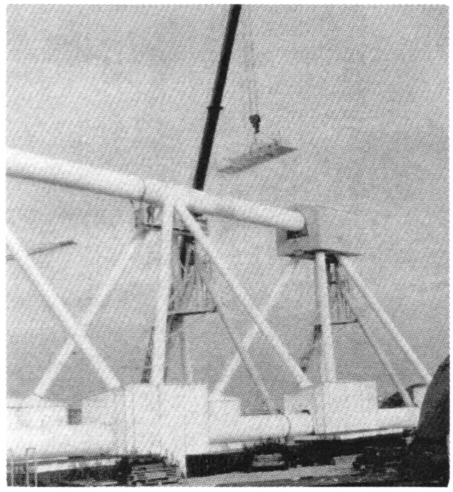

Figure 12, Positioning of A-frame

11 ASSEMBLING OF THE TRUSSES

The assembling of the trusses has been started at the North shore. Before starting, the site has been prepared in such a way that on all necessary areas movable cranes could perform their work.
The foundation required for the assembling of the bottom chords of the trusses had been installed. This foundation was made from 48 steel piles drilled 15 m in to the ground to create fixed arrangements in vertical and horizontal directions. On to the piles, arrangements have been placed to assure that the chords can be moved in the horizontal plane and to fix the chords on the exact dimensions. See figure 13.



Figure 13, Bottom chords installed on piles

The bottom chords are all placed on jacks to create in a later term the building camber.

Starting with two bottom chords sections of 60 m each, positioned on to the foundation arrangements, the first site welding was performed in June 1992.
The weld configuration of the full penetration welds is shown in figure 14. (for example at the wall thickness of 90 mm, 258 weld passes has to be made in a diameter of 1.8 m with a total weld length of ± 1450 m.

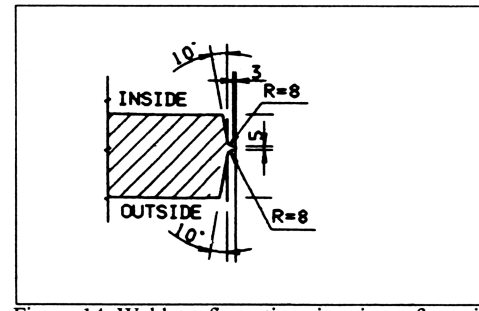

Figure 14, Weld configuration site-circumferencial welds

After connecting on both sides two bottom chord sections of 60 m the bottom bracings were positioned and welded, all in a exact horizontal plane. Now the calculated building camber of the bottom section has been created by means of releasing the jacks from both ends and using the self weight of the chords as acting as ballasting material.
At the position of each node point of the upperchord A-frames are positioned. These A-frames were placed on the bottom chords to assure a real triangular section of the truss. Further the A-frames are used as well to weld the bracings to the upper chord and therefore have been equiped with an insulated housing.

The upper chords of 60 m length each were lifted with movable cranes, placed on the A-frames and the circumferencial weld has been welded.

On the first 60 m section, the vertical bracings were positioned and welded at first to the bottom chords and thereafter to the upperchords.

Now the third 60 m section of the bottom chords were positioned, welded, jacked into the building camber and the A-frames were placed. Furhter the third 60 m upperchord was positioned on the A-frames, the circumferencial weld has been welded and placed in the building camber. At section two now the bracings were positioned and welded to the bottom and upperchord. According to this method the 2 trusses on the Northern shore as well as on the Southern shore have been completed within two years.

12 CONNECTION TO THE RETAINING WALL AND PIVOT

Simultaneously to the construction work of the trusses, the construction of the retaining wall and the pivot has been carried out. The trusses fitted exactly between the retaining wall and the pivot due to a continuous monitoring, a simultaneously carried out FE analysis of the weld and dimensional procedures during the connection process.

13 CONCLUSION

The transfer of the design requirements caused strict requirements for materials, fabrication and assembly as well as narrow tolerances which were anticipated during the preparation phase.
The realisation resulted in structures within the strict specifications and tolerances due to the consisently operating quality system.

14 ACKNOWLEDGEMENT

The author wishes to thank the BMK authors and operating crew for the documentation, literature and workmanship which allowed him to describe the methods followed as well as for the pictures which have been incorporated in this paper.

15 REFERENCES

- Material specification, internal doc. BMK
author A. Zondervan
- Welding specification internal doc. BMK
author A. Zondervan
- Fabrication and assembling specification, internal doc. BMK
author A. Zondervan
- Dimensional and tolerance specification, internal doc. BMK
author W. Post
- Non Destructive Examination specification, internal doc. BMK
author A. Zondervan



Taylor & Francis
Taylor & Francis Group
http://taylorandfrancis.com

Tubular Structures VIII, Choo & Van der Vegte (eds) © 1998 Balkema, Rotterdam, ISBN 90 5809 001 9

State of the art of profiling technology for CHS tubular connections

P.C.Glijnis
HGG Profiling Equipment B.V., Middenmeer, Netherlands

ABSTRACT: A brief history of the profiling technology for CHS tubes is given; from hand-cutting to a preview of the equipment presently available on the market. The various basic designs of the equipment with the range of production are explained i.e. in chuck, with a conveyor and mobile types. The cutting processes, such as oxyfuel, plasma, laser and water jet, with their specific advantages and disadvantages for profiling, are briefly considered. Since more and more designs are made on CAD systems, integration of the cutting equipment may lead to considerable savings possible in the production. This approach also gives the architect or designer more flexibility in shapes. A description of the available systems is given and some examples are shown. Another very important factor for profiled tube ends is the shape of the welds. Especially for thick wall sections, savings can be made by optimizing the bevelling. A brief preview of the possibilities is given, together with some examples. On one hand, the demands of the designer and architects are the basis for the design; however, on the other hand the available technology and the cost efficiency. Finally, the expected future developments for the profiling technology will be shown.

1 INTRODUCTION

1.1 *History*

The history of pipeprofiling machines does not go back very far. To determine when the pipeprofiling machine had been invented, it suffices to look at the two basic things required: pipes and cutting technology. Pipes exist for a long time, so the cutting technology is the factor that determines the age of the machine. The first available cutting technique was the oxy fuel cutting. This was developed in the first half of the 19th century. Therefore it was then that the first steps were made in the development of the pipeprofiling machines.

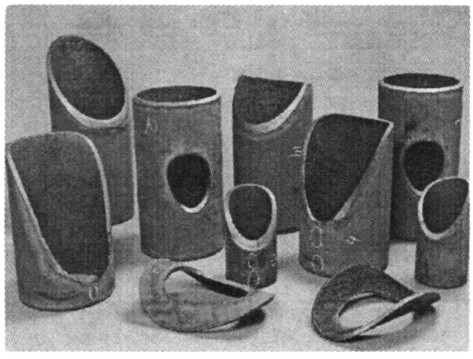

Figure 1 : Selection of profiles

1.2 *Cutting by hand*

Originally, people made an estimation of the profile that had to be cut and then cut these by hand. However, it was found out very soon that this was very labour intensive and besides that, the cuts were not very accurate. Therefore the technique of using templates was introduced. The profile was determined by a graphical method and the template was made in the office on paper on a scale of 1 to 1. If the templates had to be used more than once, these were copied on a thin steel plate. The template was wrapped around the pipe and the profile was marked. Then the operator cut the profile by hand on the marked line. With some grinding and testfitting the profile was made and if necessary they also cut a bevel by hand. The angle of the bevel was determined on the shopfloor, which made it very inaccurate. It is the author's experience that only in very few cases

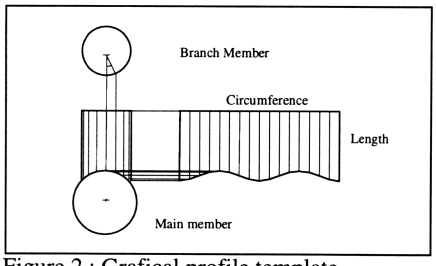

Figure 2 : Grafical profile template

the bevel was also marked on the templates. It was very complex to determine this graphically and therefore it was not done until it had become possible to generate the templates by computer. The technique of the templates was the first step in making profiling simpler and it is still used throughout the whole world. To produce a tubular construction in this way, was very time consuming, specially when there is little or no repetition at all.

1.3 *The first machines*

The first step in automation was to make a machine, in which a template could be used to make the cut in a mechanised way. This saved a lot of time in jobs with a lot of repetition.

The first real machine that was able to cut a profile, was a very ingenious mechanical system. Most of the shapes can be described as a function of superpositioned sinusoidal waves, i.e. the weighted sum. A sinusoidal wave can be generated by a mechanical crank mechanism. It is also possible to add these together into one movement. First these machines were 2- axis: the rotation of the pipe and the longitudinal movement of the cuttingtorch. With some calculations the crank settings could be determined and the machine was able to cut the profile. In this way templates were not necessary anymore and production became a little more flexible. Later developments of this system made it also possible to cut the bevel. In this way these machines became triple axle controlled. (Rotation, longitudinal movement and cuttingtorch angle). The number of driving rod mechanism varies from 1 to 4 depending upon the capabilities of the machine. Some of these mechanical types of machines are still produced and are useful in some specific applications.

The next step was the electrical analogue machine. The generation of the sinusoid could be done electronically by now, which eased the mechanical system and also the setting of the machine was faster and simpler. The basics of the machine were still the same as the former mechanical types.

1.4 *Computer controlled equipment*

Now it was time for the computer to be introduced in this type of machine and this happened in the 1970's.

The first machines were dramatically complex because of the bulky computers and complex electronics. But nevertheless, the profile could be cut on these machines by inputting just a few simple parameters and then the computer made the profile-calculation. In this way the settings for mechanical or analogue system did not have to be calculated anymore. Now profiling had become a bit more flexible.

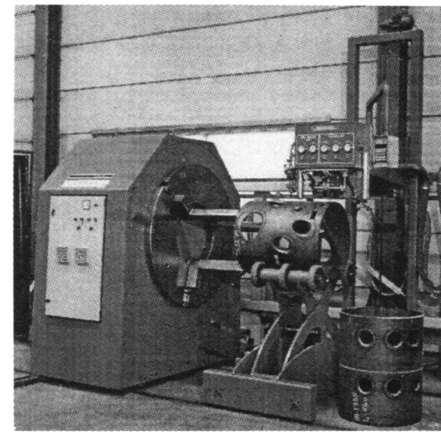
Figure 3 : Computer Controlled Pipeprofiler

The programming and the cutting were done profile after profile. Therefore the next step was to pre-program several cuts in advance and to have the computer move the torch from one cut to another also. This increased the productivity drastically and also made it more flexible. This was realised during late 80's, early 90's.

Parallel to the integration of computers into the machines, they were also introduced in the design of the tubular constructions.

Nowadays most of the designs of the more complex tubular constructions are made on a CAD system. This development has also enabled the designer (architect) to design more complex constructions. It is seen that the repetitiveness is getting less and less, which is the latest step in the development of the pipeprofiling machine: the CAD system and the machine are integrated to a CAD/CAM system.

This gives full freedom to the designer (architect) because the extra costs, if there is no repetitiveness, are low and the lead-time to production is shortened. These CAD/CAM solutions are the state of the art in profiling at the moment. Later on a more detailed description of these systems is given.

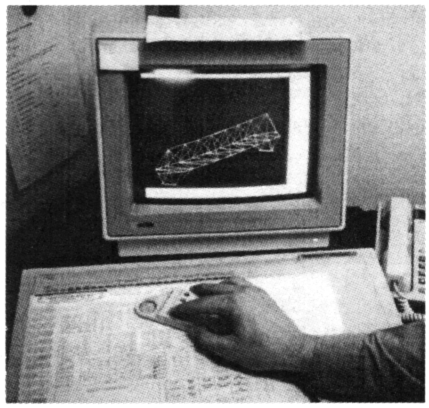

Figure 4 : Workpreparation system CAD/CAM

Another development, which can be seen in machining, is on the logistical side.

Principally two types of design can be distinguished: one is the chuck type of machine where the pipe is clamped by a chuck and rests on pipe trolleys and the other type is the rollerbed/conveyor type. This last mentioned has a completely integrated pipe handling system and has big advantages for cutting large quantities of material. A major disadvantage is that this type of machine is less accurate.In the last number of years machines have been developed, in which both machine types are combined into one machine. In this way the advantages of both are used.

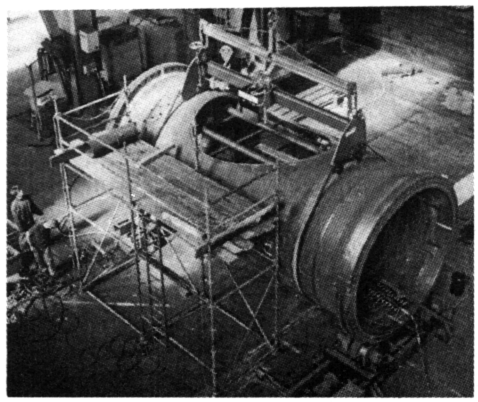

Figure 5: Computer Controlled Mobile Pipeprofiler

Another development started in the early 1980's, when the first mobile computer controlled pipe cutter was introduced. Normally the pipe was taken to the machine for profiling but for big and or heavy pipes this was costly and big machines were needed. Now men were able to bring the machine to the pipe instead of the other way around and the cutting could be done on the spot. In the United States pipes were cut with a diameter of 4500mm and a wall thickness of 200 mm. The only other option to do such a job is by hand but with such a wall thickness, this is not an easy task.

In general for small quantities and/or high quality cuts, chuck type stationary machines are used. If the quantities are big a system with an integrated pipe handling system will have its advantages. For very big, (over 1.500 mm diameter) and heavy (over 15 ton) pipes, a mobile unit is a good solution. However these are the general rules and in specific cases other machines or combinations might be a better solution.

2 THE CUTTING PROCESSES

The most used cutting processes for profiling are oxy fuel and plasma cutting. Other processes are also used but in less cases. These processes are Laser, Waterjet and grinding. The selection of a process can be a difficult task. A lot of different variables have their influence. Over the last period of time the heat input during the cutting has became an important factor due to the high grade steels that are used more and more.

2.1 *Oxyfuel Cutting*

The most common way of cutting is oxy fuel cutting. This is also often called autogenious cutting. The process is based upon the exothermic reaction between pure oxygen and steel. A gas is mixed with oxygen in order to get a flame. This flame is used to preheat the material before the cutting. Then pure oxygen is used to burn the material away in a small kerf, for which a thin jet of oxygen is needed. The burner required, consists of a ring with holes out of which the mixture of gas and oxygen flows for the preheating flame and of a hole in the middle out of which the cutting oxygen will flow. This process is exothermic, which means that the burning of the steel with the oxygen will generate heat in order to preheat the material around it so that the process will be continuos. Theoretically the preheating flame can be switched off when the cutting has been started.

The process as mentioned before exists already for a lot of years and is very widely used in the steel industry. However,only a few users know about the theoretical background. The process can be used on most of the carbon steels but not on stainless steel and

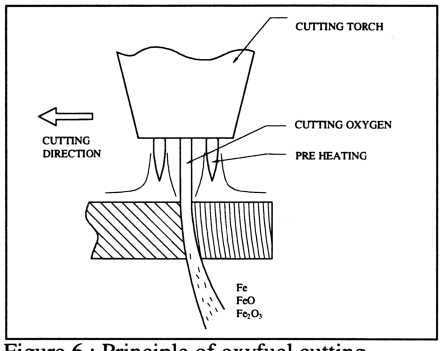

Figure 6 : Principle of oxyfuel cutting

aluminium. There is no real limitation for the thickness to be cut. The process is now able to cut a thickness of over 1000mm (1 m.). The speeds of cutting are limited to 700 mm per minute maximum. The oxyfuel process has considerable heat input. So the heat affected zone can be a problem in same materials. This can be avoided by preheating the material or by grinding the cut-surface. An advantage is that the process is quite simple and that the equipment that is needed, is simple too. In comparison to the other processes this one can be called fool proof.

2.2 *Plasma Cutting*

Another often-used process is the plasma process. The principle of this process is to make an electrical arc between the material that has to be cut and an electrode.

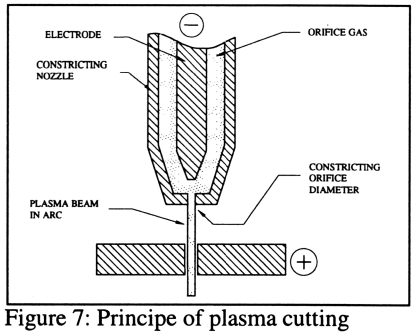

Figure 7: Principe of plasma cutting

Through the arc flows a gas, which is heated into its plasma condition. The arc where the gas leads through is a constricting nozzle. The temperatures are between 10.000 and 20.000 C. The gas will expand extensively when it is heated.and will have a very high velocity.The high velocity jet of the overheated gas (plasma) is used to melt the material away.

This is a different principle compared with the oxy fuel cutting, which is a burning process. The gasses used for plasma cutting are Air, Argon, Hydroxide, Nitrogen and oxygen or mixtures of these gases. Important factors for choosing the gas are how much energy can be put into a unit of gas, availability, reaction of the gas with the material and the thickness of the material. The main advantages of this process over the oxy fuel cutting are the speeds which can reach a 10 fold or more and the possibility of cutting all conducting materials thus including stainless steel, aluminium and copper.The head oaffected zone is less than by oxyfuel cutting, specially in thinmaterial. There is almost no difference in thick material. The equipment needed is considerably more complex and costly than for oxy fuel and asks for a better-trained operator. If used on a CNC machine (Computerised Numerical Control) this process will improve the productivity by a factor of 2 to 3 times if used on the thinner wall thickness (below 15 mm.) which makes it very attractive. The maximum thickness, which can be cut, is approximately 250mm. This is more than enough in case of pipeprofiling. However, the equipment gets very expensive if a thick material has to be cut. There is no real alternative for materials, which can not be cut with oxy fuel. However mild steel oxy fuel might be more interesting because the cutting speeds achieved with plasma cutting in a thick material are comparable. (See fig. 8)

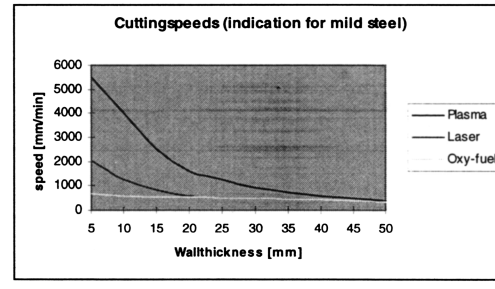

Figure 8 : Cutting speed diagram

So the main advantage is the speed in smaller thickness. Other advantages are that the process can be automated easier and a cleaner cut can be achieved, what makes it more suitable for CNC cutting machines.

Disadvantages are that the possibilities for cutting under an angle for weldseams are limited (approximately 45 deg. can be achieved in praxis), fumes and the light of the arc can be a problem so that normally the process is shielded and the fumes are extracted.

In general the following comparison chart can be made among the three processes.

comparision table

		oxy-fuel	plasma	laser
speed	thin wall	-	++	++
	thick wall	+	+/-	-
accuracy	thin wall	-	+	++
	thick wall	+	+/-	++
bevelcutting		++	+/-	-
cleanness of cut		+/-	+	++
heat affected zone		+/-	+	++

Figure 9 : Comparision chart

2.3 *Lasercutting*

The laser cutting process works with a laserbeam, which is focussed in the material that has to be cut and in this way melts or vaporises the material. An assist gasflow can be used to remove the molten or vaporised material. The equipment for laser cutting is considerably more expensive than for the plasma process. The thickness to be cut is limited to approximately 25 mm. and normally no cutting under an angle is possible. This is a process with very low heat input and therefore suitable for high-grade steels so the process is only used in special occasions. Due to the fast growing developments in this area it is certainly possible that the process is going to be used more. The main advantages are high speeds, very accurate and clean cuts.

2.4 *Waterjet Cutting*

Another process, which is sometimes used, is waterjet cutting. In this process water is used at a very high pressure (approximately 2000 to 4000 bar) and streams through a very small orifice thus creating a very thin jet of water. With this jet, steels with a small thickness can be cut. For thicker materials an abrasive is used. This means that an abrasive for example sand is mixed with the water. The main advantage is that no heat input is generated in the material to be cut and that the cuts are very clean. The equipment is quit expensive and the cutting speeds are very low on steel with a substantial thickness. A special problem is the device to collect the exhaust liquid, which must be positioned inside the tube. Also the noise is often a problem. It is used for pipeprofiling only in special occasions.

3 STATE OF THE ART EQUIPMENT

In tubular constructions very complex profiles (contours) can appear. For the welding a bevel has to be made also, which makes the profile even more complex. By using modern CNC pipeprofiling machines this is simplified. For instance to cut a saddle on a CNC machine (see fig. 10).

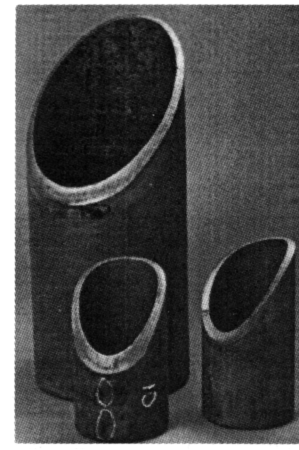

Figure 10 : Saddle piece

Only the diameter, wall thickness, connecting diameter, angle between the centrelines, eccentricity and bevel (6 numbers) have to be programmed in the machine which calculates the exact shape internally and cuts it.

Today most of the designs in tubular constructions are made in a CAD system. The most widely used CAD systems is AutoCAD but there are also others. The CAD systems can be divided into groups, which are used in the most important sectors for tubulars. These sectors are: the Steel construction industry, Petrochemical, Cranes, Offshore and Amusement constructions. A number of CAD systems are used in more than one sector. This also depends on the software modules, which are available for every CAD system.

At this moment only a few suppliers can make a real connection between the profiling machine and a CAD system, but developments in this area are growing fast. Most of the CAD packages have the possibility to develop intelligent solutions to generate data using the drawing (or model) as a base.

For systems as AutoCAD* and Pro-Engineering** are available but costly (the number of licences that can be sold is low). They are cost-efficient as the quantity and the complexity is big. The good thing with these systems is that the freedom for the designer is enlarged. The main advantages are:

- Even in jobs with no or very little repetition profiling can be done very efficiently.
- The time, needed from the design to the actual cutting, can be very short.
- The rejection rate is very low because the pipes are cut as they are drawn.
- Drawing changes can be followed better in the production phase.
- Multiple connections can be cut in almost the same time as single connections.
- By the use of nesting (to cut as many pieces as possible from one pipe, in order to get as little rest material as possible) software tube can be optimally used

Because of these advantages these systems will be used more and more which will decrease price in the near future and it will also initiate new developments, which will improve the available software. Another factor is that the construction industry is adopting the principle of using subcontractors for specialised jobs. Companies who offer profilingwork as a subcontractor are covering this hole in the market. These companies normally have the up to date equipment and can offer the work for a very competitive price because of the volume of work they do.
Factors that slow down the developments are:

- The market for profiling CHS material is not so big and so there is not too much coverage for development costs.
- There is no standard data format that describes the profiling of CHS material.

3.1 *Link to CAD Systems*

The CAD systems can be divided into two groups. The line based and the volumebased systems. It is normally the architect or designer who decides which system to use for the basic design. Than the engineer will decide, either to use the same system as the architect/designer or to convert the design into another system he wants to use. Especially this conversion can cause a lot of problems. Up to now there are no formats, which are widely adapted to convert designs (3 Dimensional), from one system to another. The Engineer will make the necessary calculations and detailed design so that he is able to see that the design is fit for purpose. This will be done in close co-operation with the architect or designer. In this stage it is very important that there is a good understanding of the possible production methods. As far as the profiling is concerned it saves a lot of time and cost if the construction is drawn in a 3 D CAD system, from which the data for the profiling can be generated automatically. If this is the case then the extra costs for multiple connections are not that high, because the original design drawing can be used the time from engineering to the first cuts can be very short (sometimes within a few days). Also the costs to adapt changes in the design during the production phase will be reduced considerably.

In the line-based Cad systems like AutoCAD the systems function by making a drawing of the tubular construction by drawing lines which represent the centrelines of the tubes. On each line, a data-tag is attached, on which the position number, diameter, wall thickness and material quality is noted and for both ends of the line it is described to which tubulars or surfaces they have to fit. In the more advanced systems, parameters like bevel, rootopening and weld shrinkage can be taken into account. All first CAD/CAM systems for pipeprofiling are line-based

The second generation is the system that can be connected to the volume based CAD systems. In this system a more actual model of the tubular structure is made. The drawing itself holds much more information so there is less to be done by data-tags. However these systems are much more complex to make connections. The only system, the author is aware of, where a connection is available, is Pro-Engineer. But work is in progress to make more and more systems to connect into full CAD/CAM systems.

4 THE BEVEL FOR WELDING

Another important aspect of producing a tubular construction is welding. This has effect on both the quality and the cost. Both factors are strongly influenced by the profilecutting. The exact shape has to enable the welder to make a high quality weld in as little time as possible. The time needed is directly related to the volume to be filled and in which position the welding will be executed. Normally the more difficult the position is, the more volume is needed to ensure a high quality weld and the speed of welding (grams per second) has to be lower. This means that the more difficult the position is the more savings can be made. Normally the position in which the welding has to be executed can not be changed. This leaves the possibility to optimalize the shape for the welding.

A situation, which is seen often, is when

two pipes have to be connected under an inclined angle. In the "heel" zone the angle between the material surfaces is very small also. In this case there is no space to make a good weld in the normal way. Research has shown that the "heel" zone is less critical with respect to fatigue. The available solutions are all based on the welding to be executed between the outside surfaces of the material. The first code in which such a solution was described was the AWS D 1.1 / 1972. This is a code, which is published by the American Welding Society. At this moment several solutions are available as shown in the sketch.

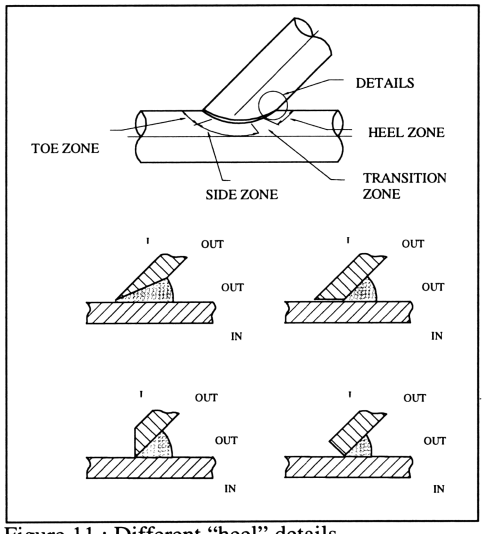

Figure 11 : Different "heel" details

The other details are also often used. Specially in the steel construction and the cranebuilding industry. For this kind of work the solution as described in the AWS D 1.1 is too expensive.

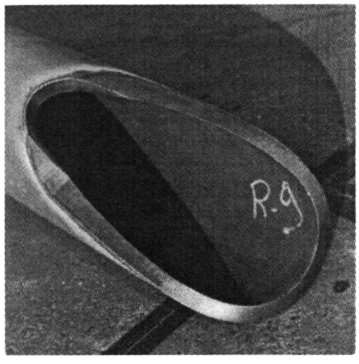

Figure 12 : A profile according AWS D1.1-96

The profile has to be burnt with two cuts. (see fig. 12) The other profile can be made in one cut. The only new development in this is that a new profile has been developed which has no bevel and rootgap in the "heel" zone and than transforms to a bevel and rootgap in the "side" and the "toe" zone. This type of profile makes fabrication reasonable and is easily weldable. It can be used in situation with wallthicknesses below 8 mm and in situations where fatigue is not critical.

Another example where important savings are obtained by using sophisticated cutting equipment is in the production of T pieces. Most of these are produced by forging or casting. But the special ones are produced by welding together two pieces of pipe.

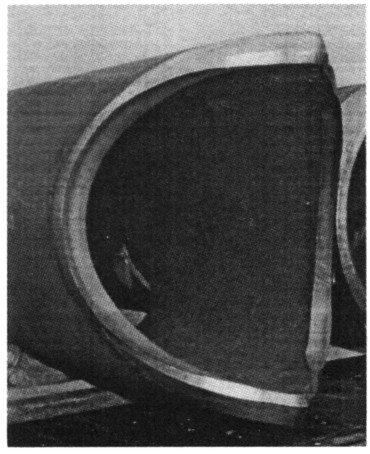
Figure 13 : Special saddle profile for D=D T-piece

Especially the ones for equal diameters can be very complicated. In the picture an example is shown of an equal T in pipe of a 1000mm diameter and a wallthickness of 80 mm. In this case 1/3 of the volume is at the inside and 2/3 outside. In this way approximately 40 % of the weldvolume is saved if compared to single sided welding from the outside. Also the stress in the material is less because of the double sided welding.

A limitation is that the diameter of the pipe has to be big enough to execute the welding from the inside in a save way. In the picture one can see the transitions very clearly of the several cuts flowing into each other. It is very costly to develop software in order to make such a profile but when it is available it is simple to work with. In this case only the diameter, wallthickness have to be programmmputer calculates the whole shape (hole and saddle).

In this case it is shown that big savings can be obtained by having the right equipment and software available.

5 THE FUTURE

The developments for the future can be split up in three fields, which have influence on the profiling of pipes. These fields are:

- Cutting technology (oxy fuel, plasma and others)
- Cutting machines with or without integrated pipe handling systems
- Work preparation systems (CAD, nesting and MDI (Manual Data Input)).

5.1 *The future of Cutting technology*

In the cutting technology the main developments will be seen in plasma and laser cutting. Although the oxy fuel process is already many years old, it should not be considered as old-fashioned. Its further developments will be in details such as camera vision systems to overcome the need of visual checking by an operator. In plasma cutting, more developments are expected. The most come down to concentrating the plasma jet further to cut a smaller kerf and to allow higher speeds with better accuracy. Also developments are expected with more sharp torches to allow for bevelcutting which is necessary in pipeprofiling.
For the laser cutting process developments are ongoing to allow for cutting bevels up to angles of approximately 45 deg., while the cost of the equipment and its running costs are decreasing. For some areas of pipeprofiling this process will penetrate the market especially in the area of thin wall thickness 6 mm and below.

5.2 *The future in CNC Pipeprofiling Equipment*

For the cutting machines we see that the robots are entering the area of work. At the moment the conventional CNC machines are cheaper and it is not certain that they will be outbeaten price wise by the robots. But one thing is sure that the robot has much more flexibility. For the future it is expected that much more SHS, RHS and for example elliptical shaped pipes will need profiling and for this the robot might be a good and flexible solution.

Another area in which the machines will be developed is in the integration of pipe handling system. Because the quantity of pipes to be profiled is increasing bringing down the logistical costs is getting more and more interesting.

5.3 *The future in workpreparation CAD/CAM*

For the development in the work preparation we will see that software modules will be available for much more CAD systems. This will make it possible to generate the data for the profiling directly from the model. In the beginning these modules will be costly but they will come down in price as the number of installations rises. With integration into nesting software this will save even more material and time. Also programming by Manual Data Input will be simplified as much as possible to enable the workshop to do the cutting of the simple constructions directly on the shopfloor without work preparation.

In general the profiling costs will come down and the extra costs for making a construction more complex artistic will come down even more. This will give the designer, architect more freedom in designing. In the near future also good profiling systems can be expected for SHS and RHS material.

6 PROJECT EXAMPLE THE MAASLAND STORM SURGE BARRIER

This project is a very good example of the use of computer controlled pipeprofiling technology. The design of the construction was done in a CAD system. At first sight, one may expect that there is a lot of repetition in this project but this is not the case. Because of a camber nearly all parts are a little different from each other. The camber was needed to build the structure so that after production when it is in free span it will be straight.

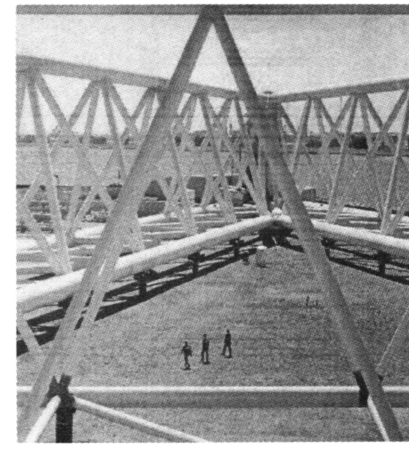

Figure 14 : Storm surge barrier construction

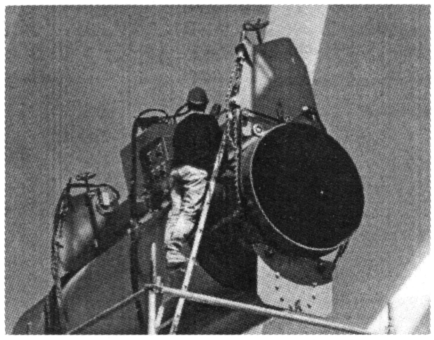

Figure 15 : Mobile computer controlled Pipeprofiler

The design model was used to generate all work preparation data for the cutting machines. For quality assurance reasons it was decided that the pipes would be drawn separately . These drawings are used to check the automatical generated data for the cutting machines. In all cases where the data was in contradiction it was found that a mistake had been made making the separate drawings of the pipes.

Because spiral welded tubes were used which could be produced in exact lengths suitable for each part no nesting was done. This means that one pipe was cut from each raw pipe.

Deviations of the circular shape of a pipe are normally in the area of the longitudinal weld so for the spiral-welded pipe they are in the area of the weld also. Due to these deviations the actual fit-up might not be as good as needed. Therefore it is necessary to have the direction of the weld as perpendicular as possible to profile. In co-operation a system was developed to achieve this.

In the project were a high number of repetitive welds, which were in the same position. Because of this we could optimalize the weldvolume to the position and the weldprocess. For easy fitup the design of the profile was done in such a way that no rootgap was needed in the "heel" zone. This was possible because the construction was not very dynamical so that fatigue was not critical. By doing this, the pipes could be fitted together by letting them touch in the "heel" zone and so automatically the right rootgap was established for the rest of the profile.

Another remarkable thing in this construction was that there where pipes that had to be profiled exceeding 100 tons. In a stationary machine normally pipes up to 15 tons can be profiled. For this mobile cutting machines where used at site. This saves the transport cost of the pipes for the profiling. Before cutting the theoretical dimensions where checked and if they has to be changed based on the actual dimensions this was done by changing the program at site also. In this way even the big pipes fitted perfectly and a lot of fitting and welding time was saved.

7 CONCLUSION

The production of tubular construction has become simpler since computer controlled pipeprofiling machines have been developed. Specially the connection of these machines to CAD systems will give the designer/architect much more freedom to make a design, that can be produced for a reasonable price. This process of growth will be pushed on, in order that in the near future even more complicated constructions can be made.

8 NOTES

- AutoCad is a registered trademark of Autodesk
- Pro/engineer is a registered trademark of Parametric Technology Corporation.

9 REFERENCES

- Autogeen snijden met Acetyleen

Author Ing. D.R. J. Lafèbre

- Welding Handbook Eight Edition, Volume 1

American Welding Society

- Welding Handbook Eight Edition, Volume 2

American Welding Society



Taylor & Francis
Taylor & Francis Group
http://taylorandfrancis.com

Tubular Structures VIII, Choo & Van der Vegte (eds) © 1998 Balkema, Rotterdam, ISBN 90 5809 001 9

The adventures of ZAPPI in the world of tubular structures

Mick Eekhout
Delft University of Technology, Faculty of Architecture & Octatube Space Structures bv, Netherlands

Abstract: Tubular structures at the change of the millennium are established as an experienced structural technology. Its virtues have been used regularly for more than one century. The last generation developed through research and applications its maturity. For visual structures in architecture tubular structures are the main material elements. However, the great leaps forward have been achieved in the pioneering phase. The interest of many contemporary designers are not so much focussed on mature and experienced technology but rather on discovering unknown territories of knowledge and insight. The discovery is structure with tubes as solitary structural elements. The eternal quest towards the unknown is what drives creative designers towards new horizons.

1. Introduction Zappi

The quest for the new and the unknown is some thing, which I have been consciously and unconsciously engaged on since starting my architectural studies in 1968. Since the last decade I have enjoyed the privilege of having my own design & production company with a motivated staff who allow themselves to be misused to realize the most exotic ideas and to perform the most unusual experiments.

In recent years I have built up an interesting relationship with *Zappi*. The term kept buzzing about in my head whenever a new idea had to be worked out. *Zappi* stands for the ultimate new and unknown, and the little creature with many undiscovered characteristics became known after being introduced to a wider audience in my inaugural lecture in 1992.
The term *Zappi* was launched by the former town architect of Haarlem, Thijs Asselbergs, while acting as moderator in January 1992 for a forum discussion where Professor Jaap Oosterhoff was my opponent. The topic was the cultural significance of *iron*. Thijs asked us to describe an ideal building material, as yet unknown to either of us. After that the term *Zappi* lived on as a sort of nickname, as the name of a famous artist or scientist you would like to meet sometime. Launched as a term for a new building material to be developed with superior qualities, it has also increasingly come to symbolize the adventurous quest itself. It stands for the unknown, the mysterious and challenging. It is both material and idea, it is both concrete and abstract. It is the unknown result the process leads you to. It is everything you suddenly find after looking too long in the wrong place. In short, it is a mentality that cares little about the apparent senselessness of ideas or about the practicality of inventions.

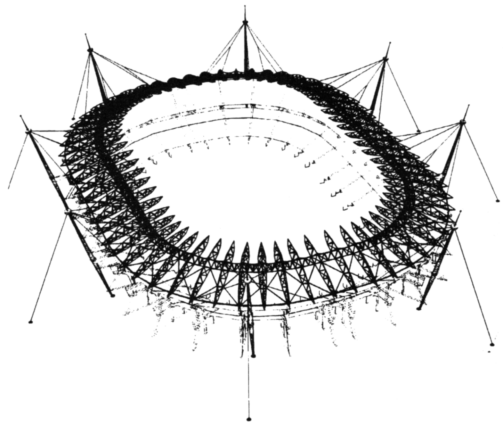

Fig. 1: Tubular steel structure composed as cigar-formed delta trusses on a ring truss suspended from 8 tubular masts for an Olympic stadium in Tunis. Arch. Arcadis / Schuurman.

Zappi has made its mark in my work in four ways.

Firstly, *Zappi* as it began: a long-term fundamental research project with the material goal of developing a strong, stiff and tough glass-like plate material that does not break suddenly under overloading. This material must be so reliable that engineers can work with it in such a way that structural loading do not form a problem. This research project has been started under the supervision of my chair of Product Development in the faculty of Architecture at the TU Delft. It is a joint operation with the faculties of Aeronautics and Chemical Technology. The phase was the detailed description of performances expected from architecture. This description was then converted into fundamental chemical and material technology research, followed by an extensive test program in the laboratory of the faculty of Aeronautics. The objective is a reliable transparent material suited for large frameless and structurally loaded glass envelopes.

Secondly, *Zappi* stands not only for goals but also for a mentality. *Zappi* is a friendly and somewhat comical bulldog combining intelligence and resoluteness. Only in such a mentality can the motivation be found to keep up a process of product design, development and research. *Zappi* wants to be noncorroding steel or non-breakable glass, however charming this rusting or breaking may be. Who is the best suited to look for this new product? The search by one individual has as many disadvantages as the search by a team. The individual needs a soundboard and servile assistance; the team can choke individual creativity. Capital resources are not always decisive.

It is my opinion that searching for *Zappi* may take an entire lifetime. I am someone who likes designing and building, but also likes researching. To my mind, joining short term and long term goals generates great strengths. The process of designing, producing and building usually gives more satisfaction than the great emptiness which comes into being after completion of a building or after production and launching of a newly developed product. Even though the ultimate goal, which Zappi represents always, remains, like the horizon, just one day ahead, it is as noble a goal as the Grail was for King Arthur's Knights of the Round Table.

Thirdly, *Zappi* is always close at hand. Each step towards *Zappi*, even because of the pleasure it gives when a distinct step has been taken, is *Zappi* itself. Such a step with a clear progression was the frameless glazing in the early nineties. In particular, the fixing of the double glass panels to the Quattro node, through glue technology instead of a bolted connection through both glass panes and the air space. Each further development in the direction of a perfect glass structural material is a piece of *Zappi*. Each result is achieved as *Zappi* immediately engages a new opportunity, never forgetting at the same time that reaching the formulated end goal also depends on a number of discrete steps. That is why this article has *Zappi* in its title: its publication reveals one step, to be followed, hopefully, by many other equally successful steps.

Fourthly, *Zappi* stands for the infectiousness of the activity of developing new products for the building industry. *Zappi* wants to get the entire audience laughing along at its jokes, to compel applause with its clever feats, to stimulate a larger circle of parties involved - those who are engaged in one way or another in product development in the building industry. This is done by spreading new ideas and products amongst professionals motivated to upgrade the technology of materials and products for architecture and for the building industry. *Zappi's* answer to the question 'would you ever do it again?' would always be 'Yes!'

2. Tubular Structures

From the late Sixties technical research has continued to investigate tubular structural systems, tube properties and connections and the use of tubular sections in construction is now an accepted

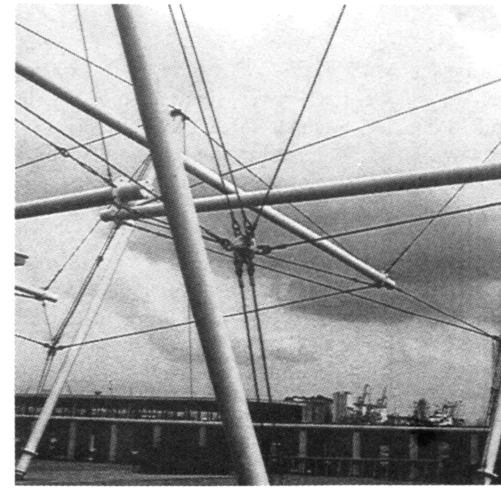

Fig.2: A tensigrity structure as an art work by Loes van der Horst and Mick Eekhout forming a sculptural and structural composition of tubes. Energy complex Amsterdam.

and exciting practice. As developments in tubular steel have progressed, structural engineers and manufacturers have been well informed of all changes. Architects are also kept up to date but are not encouraged within their own profession to use tubular sections in construction. The current depth of proven knowledge is such that further technical research will provide only diminishing returns and it is now an appropriate time to revue the current position in order to encourage and stimulate tubular construction and innovative design within the architectural profession.

The author is concerned with the current position of designing with tubular structures, when seen through the eyes of an architect. Grouped under the main headings of architectonic, structural and industrial design, the proposition is made that good design requires vision and the integration of all three concepts. In antiquity the Ionic order succeeded the Doric order where the more slender and detailed construction of the latter reflected the knowledge and culture of a more advanced society. Similarly the architectural use of slender tubular elements, using the latest product and design technologies, has led to the construction of delicate, attractive and exciting buildings suited to the ideals of the present. The objective of many technically curious architects for an architectonic expression of technology in their work has resulted in particular structural and technical iconography, culminating in the production of some outstanding architecture. The introduction of lightweight structures in modern architecture has proved to be a logical and inevitable solution, providing cover for mass assemblies of people, for traffic-related purposes and other large-scale events. But this suitability for function is only the beginning of the design process, which requires the study of technical solutions encompassing sectional choice and detail designs.

The aesthetics of tubular structures are a major contribution to their architectural image, but as designers strive for a heightened spatial enlightenment, designs are requiring ever more complex structural solutions and high standards in their elements and components. New designs are helped by combinations of intelligent detailing, by the application of computerized 3D design, by engineering improvements in materials, by fabrication techniques and by assembly procedures. Existing designs embrace the structural possibilities of material strength and jointing limitations in spatial conception and more attention is now paid to the integration with other components of the building, such as roof cladding, glass facades, paneled walls, interior wall partitioning, installations, etc. Next is to embed this technology in a cultural consciousness resulting in inspiring architectonic applications. The initiative is now with the architect. The architect's ideal is to generate ideas, perhaps surprising ideas, to design dazzling architectural schemes, to engineer an ingenious structural system, to develop the most intelligent steel details and to have it fabricated and built in the most economical way. He should be driven by inspiration to interpret a functional scheme to attain a result possessing more atmosphere and spirit, and ultimately a more striking presence. For architects to remain faithful to their creative task they need incitement, insight and vision in addition to technical instruction. They must harness technical knowledge to visual and spatial design that links cultural and philosophical ideals.

3. Architectonic Design

Throughout history architectural style has been closely related to the building materials available and to the associated construction techniques, but has been constrained by the theoretical and strength limitations they impose. Architectural vision questions established practices and brings a philosophical concern to influence building design, appearance and use, often stretching the boundaries of the current construction technologies. The influence of an individual over established common opinion and with theory over craft skills develops as skilled architectural designers exercise their professional role. As the abstract idea gained ground over material optimization in architecture, the issue whether to expose or to conceal the construction detail of a building is more frequently encountered. Usually tubular structures are perceived as slightly more expensive, more elaborate than structures with open profiles and to benefit from this increase in cost, their use is often seen in exposed locations and positions of visual appreciation. The issue to expose or to conceal is as much a philosophical as a technological consideration, but as there are only limited known ways for the architect to compose the internal and external character of the building, an exposed (inside or outside) structure may adequately serve that purpose.

The architect may think that fire protection regulations are restricting the use of exposed steel for multi-storey buildings, but developments to improve fire protection are becoming established. Intumescent coating and concrete or water filling is some techniques widely used to impart fire protection to tubular structures.

Architects with ideals of structural honesty, truth and beauty, in which each architect is free to develop his own style, usually defend exposure of the structure. Usually the contrast in a building between an abstract part and a material part can create a moment of tension, an important ingredient in a design. Increasingly a more philosophical position is being adopted; by deliberately showing elements of construction a design can bestow upon a building a charm and an appearance that generates thought in the design concept.

In recent years certain architects have stimulated the development of new technologies when working in close partnership with a manufacturer. Those architects with an awareness of technology and having imagination, combined with a drive for something new and exciting, have pushed current technology far. It is this reciprocity between architecture and technology that is important. For some architects and in some eras technology was allowed to develop quite independently and was only to be seen in unprestigious building. It was only later that there importance was recognized. A prime example is the revival of all kinds of neo-styles a century ago but the industrial revolution and its benefits for the building industry were not appreciated greatly by the architects of that era who were more or less interpreting architectural styles of preceding centuries. Only later the endeavor of so called non-experts, like Joseph Paxton, who designed and built the Crystal Palace; Josef Monier, who invented reinforced concrete and Gustave Eiffel who built the Eiffel tower were fully recognized. These men were not educated as architects or civil engineers, but learned the trade in practice or by trial and error. Now looking back from so many generations later, it is recognized that their influence on the progress of architectural technology was greater than many contemporary architects. However the opposite effect has been felt in the last three decades. The Olympic roof in Munich designed by Gunther Behnisch and Frei Otto, was a roof structure that was outside current technology. However it was a prize-winning design with worldwide exposure and with sufficient backing by clients and with model and test development it was possible to ensure its construction. This project provided inspiration for other designers and shortly after the Munich project, Richard Rogers and Renzo Piano designed the Centre Pompidou in Paris and an innovative an overwhelmingly technocratic building was constructed. The area has gradually blossomed and today the Centre Pompidou receives more visitors than any other building in Paris. This daring show of technology and the teasing challenge of the carnival of colors has contributed to make it the most debated piece of architecture from the decade. It returned to architecture and technology the use of cast steel elements in a prominent way. As the roof in Munich shaped a way in international architecture so that many less obvious architectural projects could follow in its wake, the Centre Pompidou building changed architectural fashion.

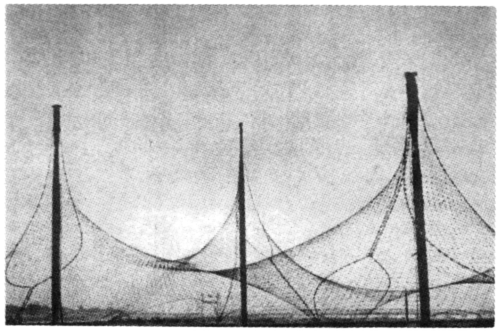

Fig. 3: Construction photograph of the German pavilion in Montreal, predecessor of the Munich roof by Rolf Gutbrot and Frei Otto.

In the technical architects' office, the working method of many is based upon the belief that decisions about the conceptual design for a building have to be accompanied by the appropriate choice of structural system and detailing for the elements of construction. Contemporary architects try to challenge the building industry and suppliers to go one step further, sometimes too far, but it is appreciated that improvements are being made in technology and architecture.

Although tube producers may like to have all steel members in tube, the architect still will retain open profiles for certain situations. However, whilst appreciating the crisp lines and rich shadow potential of the open profile, the charm and elegance of circular tubes and the robust and pragmatic nature of square tubes must not be forgotten. Each, with his or her own spatial characteristics, offers the architect a more varied and challenging means to conceive his design.

Architects more because of its ability to stimulate visual inspiration than its functional merit use technology. It is used to support the desire to build with aesthetic appeal. Advanced or newly developed technologies can feature in building design and sometimes dominate. Equally they can be successfully integrated with traditional and established building techniques. Both approaches

for architecture express the way structures and construction in building act and the way in which individual components are produced, assembled, erected and installed. The personal opinion of the designer is highly influential and can define whether an abstract line of design is sought or a material one with a desire to express the constituent parts of building, how it is composed and how it works, from detail to overall composition. It regards this readable information from the building, as an alternative to boredom in too abstract buildings and to elaboration in highly decorated buildings. Ideas and requirements for technical orientated architecture stimulate technological development.

4. Abstract Versus Material Approach

A tube is more abstract than an open steel profile. Since all material is located on the outside, it hides the thickness and the inner volume. Tubular design can choose to maintain this abstraction and conceal material cross section or react against it balancing abstraction with materialization. Here the softness and abstraction of tubes is made relative by introducing connections that are sharp, have plate thickness, reveal the inside of tubes and so thickness and show the strength of these constructions and how they are composed. Just by contrast sharpness can reinforce a global soft character. This has to be done consciously and not by accident. Indifference would lead to ad hoc designs and careless detailing. As tubular structures are visual structures, the structural system, the choice of elements and the details are one package in which all ingredients should reinforce each other. But negligence from the architect can affect the strength and conviction of a scheme. The architect should not relinquish the development of the structure to the structural engineer, however capable and proficient the engineer. Tubular structures are a dominant part of the visual structures and therefore need attention from the architect. When the inherent aspects of the tube are to be maintained connections should be outside, hiding the inside of the tube. Such connections however pose many technical problems, but lead to a philosophy of an abstract mode for structural design, compared with a mechanical one. For most architects an outstanding property of tubes is essentially their abstraction. It leads naturally to a design philosophy of equal abstraction in the design of the welded or bolted connections of the individual tube elements. Pursuing this abstraction is one of the challenges for technical architects. "The essential is invisible for the eyes" (St. Exupéry: "The little Prince"), means a denial of the visual material compared with material affirmation, both in system and in detail. In the opposite and widespread mechanical approach all from which the structure has been built is clearly visible. In the extreme, bolted open steel profiles show both the material thicknesses as well as the type and number of connections. But in abstraction the tubular structure is streamlined where the individual tubes seem to flow over from one element into the other without visual connecting elements. Throughout the history of architecture the balance between these two approaches has been apparent. The Gothic style was mechanical, all stones and bricks were exposed and the method of building was visible. In the Renaissance this changed with plastered surfaces being used to hide the structural material used.

All early structures of timber, cast iron and steel of the last century were made of separate elements and components that were prefabricated and connected on the building site. The bolts and nails were always shown. These structures were developed by pragmatic builders and structural designers, not architects and were not considered to warrant the close attention of good architectural commitment. Nowadays the 19th Century buildings are recognized as pieces of architecture, although they were conceived as just industrialized buildings, products of the industrial revolution. It was only later, after the development of reinforced concrete, that architects got the notion that there were structures with internal connections capable of producing smooth surfaces of a structural but abstract nature. Concrete structures were seen to be very abstract. For steel structures it was the invention of welding that made it possible to connect tubes without revealing a thickness. Yet welding on site has many problems requiring skills

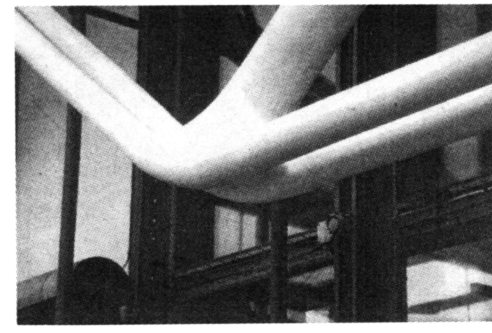

Fig. 4: Example of a complete abstract connection detail in the lower chord of a flat frame in the Centre Pompidou building in Paris, by Renzo Piano and Richard Rogers.

different to those normally found in site construction and is not a preferred option. The site-welded structures in the building of Ludwig Mies van der Rohe have required a lot of maintenance. The preferable option is for the majority of connections on the building site to be completed by bolting or pinning. However the architectural design stimulated by welding has emphasized abstraction in connections and has led to a series of tubular details with complex bolted connections hidden inside the tube to achieve a visual deception. The choice for an abstract connection within tubular structures has consequences for detailing with abstract building skins rather than mechanical building skins. It all leads to a very refined choice of materials, usually with a more complex method of connection, leading to less economical structures. Hiding required more skill than revealing. But with time and experience in this way of thinking the consequences of cost will reduce. A similar development has appeared in the airplane and car industry, where the demands for hidden connections originated from aerodynamic streamlining.

5. Glass and Steel Structures

The moment a structure is clad with a glass envelope, daylight floods into the space to reveal the elegance and beauty of a well designed tubular structure capturing an extreme expression of slender tubular construction. A complete glass envelope can be made to fit the structure like a transparent glove. Maximum attention is given to the chosen system and the elements and corresponding details. Here the strength and compactness of tubular steel structures gives great benefit as one are usually able to concentrate the material of the structure.

There is no need for glass to be used exclusively as a secondary covering material, it can be designed to behave like a prime structural element, receiving stresses from external climatic loading and its own dead loads. However due to the brittle nature of glass it can be employed as a structural plate with relatively low allowable stresses, though at present the level of understanding for glass as a structural material is in its infancy. Currently large thickness are required for any structural requirement but glass panels with plate dimensions like 2mx2m, are being used with mullions reinforcing their edges and fixing the individual glass panels to the main structure.

Aluminum is the preferred material for glazing mullions with only a small amount in steel tubular frame elements, but as aluminum has a lower modulus of elasticity than steel, aluminum profiles tend to be more bulky than steel. It is not so much the width of these profiles that makes designers think about an alternative, but the diagonal dimension of the internal and external part of the mullion, as most of the glazing mullions are seen from an oblique angle. Large mullion profiles tend to compress, which is not the concept of the transparent glass envelope. Also in some instances the graphic image of the aluminum mullions could conflict with the tubular structure and because of its smaller scale and higher frequency, it could overpower the tubular structure. Ultimately the highest degree of uninterrupted vision through a transparent envelope is more desirable. This leads to the recommendation that the alignment of the glazing mullions and of the tubular structure should

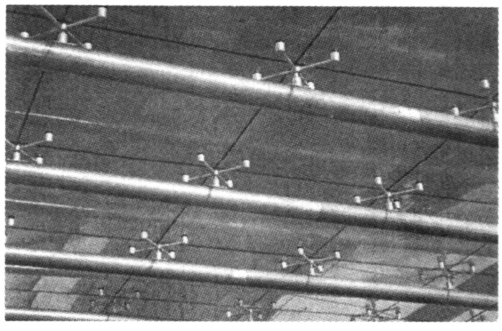

Fig. 5: A clear and simple tubular structure with Quattro nodes and a frameless glazing skin indicating slenderness:s Blaak Metro station in Rotterdam by Marja Haring.



Fig.6: A 50 meter span minimized space frame of interwoven delta trusses, for an indoor sub-tropical swimming pool in Bremen ,Germany, by Karel Hamming and Mick Eekhout

be integrated so that the two are not conflicting in a topological way.

In order to gain the most slender profile one way is to develop glazing mullion profiles in steel with underspanning stiffeners, so avoiding conflicting solutions with large glass surfaces near prime tubular steel members. It could be built of fully tempered glass panels, stabilized with a filigree secondary network or with short compression studs perpendicular to the glass plane and with longer tensile rods or cables to stiffen the whole assembly for wind and other external loading acting on the glass surface. In this way all attention is focused upon the tender play of the tensile element and the elegant circular hollow section. The circular tube is the natural choice, to allow the gentle flow of air around the shaft, as the compression strengths are equal in both axis perpendicular to the shaft.
In Mainz the roof structure of the new ZDF offices was designed by engineer Petar Reich and the author as a 'fishbone'-scheme, composed of a central circular tube and an overspanning and underspanning tensile rod structure with outriggers in between. For downward loading the tube plus lower 'belly'-rod form a rigid couple? For upward loading like wind gusts, the tube plus upper rod line makes the roof rigid. As the frameless glass planes are directly connected to four folded spiders, glass connectors fixed on top of the vertical outriggers, this glass envelope appears to float above the structure. In the new Glass Museum Hall for the Prinsenhof Museum at Delft, designed by the author, a tubular roof structure with spider connectors and frameless glass panels is split into two structural groups. For downward loading bent tubes with underspanned rods are active in one direction of the roof. For upward loadings straight bottom tubes with upward curved rods provide the rigidity. These two groups of tubular stabilizers are inter-linked only by means of vertical outriggers or compression studs. When there is no secondary staging or outriggers, the corners of the frameless glass panels can be fixed directly to the tubular elements by means of connection nodes.
Glass envelopes are very versatile, stretching over vertical or sloping facades and over flat roofs or shaped roofs, with a variety of options for glazing panels. The technology of glass envelopes that has been developed during the recent years, has progressed from fully bolted connections and complicated internally hinged stainless steel connectors, to metal elements glued directly onto the internal side of the glass panels without any perforation. It is a field of technology very much under the influence of new developments, all endeavoring to maximize the material elegance.

Usually glass panels are big enough to employ sizable tubular elements, so carrying major stresses. Again this is an application where an elliptical tube could offer benefits by providing a higher bending resistance in its deeper axis and be less restrictive of daylight in the shorter more slender axis. Such profiles would encourage the use of tubular elements in glass architecture.

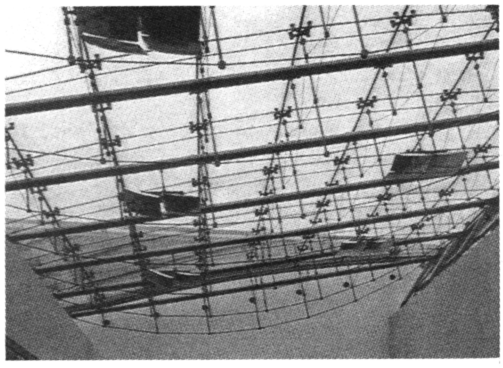

Fig.7: Fish-bone structure of central tube, and two bow strings for ZDF in Mainz, Germany, by Braun & Schlockermann and Mick Eekhout



Fig.8: Longitudinal view in the Glass Museum Hall of the Prinsenhof Museum in Delft, The Netherlands.

6. Future Developments

Designing tubular structures has a parallel in music where to play music well; one has to master the technique before one can perform. To perform excellently however and with true musical genius goes well beyond mastering techniques. The playing may become an improvisation, an on the spot invention by the performer, transcending the score, being the ultimate aspiration. All this is true in architectural design. Easier steps are being developed to move from simple to complicated designs, from technical to an architectural use of tubular structures, but in all cases the spirit of design to be developed by the project architect must be pursued.

Many future developments are related to design. Architects want to consider an optimal use for the potentially expressive tubular structure, as a balanced part of their design. Future designs of buildings can be increasingly freed from the orthogonal shackles of Modern Architecture. Keep what is worth keeping, but spend the rest of your time inventing.

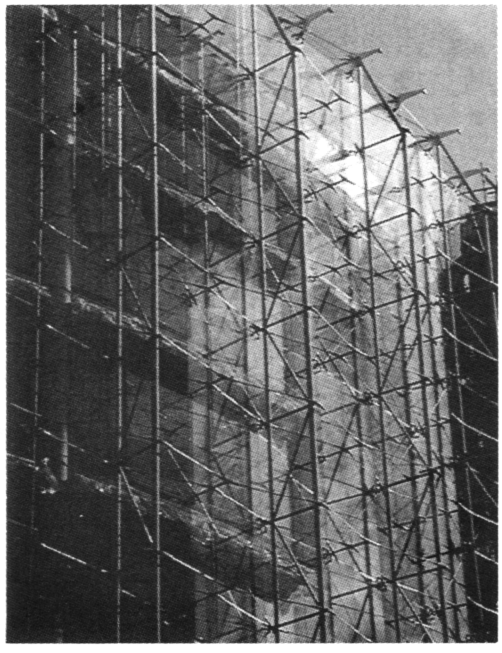

Fig.9: The expressive high-tech facade of the Helicon Building, at the Finnsbury Pavement, in London, by Sheppard Robson and Ove Arup.

Tubular structures are becoming more and more deformed in the design stage, from straight to undulating, from one and two dimensional form to three dimensional, supporting the spatial envelope of the building in a very specific and recognizable manner. Designers are changing their attitude from consumers of standard and system products to co-designers of project-based products. There will be a growing number of characteristic structural schemes and hence elements, components and details, that bear the signature of the particular project architect for the building that infuse the building with greater personality.

Architects can be very passionate about their design ideas out of spatial reasoning. They are living in a time where technology is no longer damned as it was in the Seventies, nor is applauded as in the Eighties. In the Nineties and at the start of the 21st Century a balance is required between function, appropriate technology and meaning in architecture. Let us achieve a blend of traditional and newly developed technology, of old and new elements, of abstract and mechanical components, all in a designed form to give an appropriate meaning and inspiration to the buildings.

Some architects will be inspired by alien technology outside of the building and construction environment, by bicycles, cars, yachts, ships, airplanes and even space technology to enrich their own designs. Some architects, however, are tired of technology and so develop their buildings in a more abstract and material-denying way. Abstraction may last long as has been proved by the 'classical' Modern Movement, but abstraction today only survive with good spatial concepts. Others are inspired by the technology revealed by nature, designing in similar principles and adapted natural forms and curved components. Others do it to be obstinate and shocking, protesting against the values of current society and existing principles of design and building. But there is no anarchy without discipline. The deconstructivists need discipline and systemization to enable their designs to be built. Under these influences there will be a large variation in ways to contemplate the material components of a building, a personal touch to the meaning. Architects are a part of the changing society, receptive to environmental influences in the shape of ethical, philosophical and cultural impulses, which they combine, with their abilities of technical knowledge and skill and their philosophical insight and vision. Global influences

are concentrated in the mind of the architect and are continuously changing. All this should not be ignored by the architect in the function of a consumer of building products. The times when only producers could dictate the form and finesses of structures are definitely over.

7. Computer Aided Design & Production

Other influences of our changing and developing society are based on technology. Architects, who see an improved technique to realize their designs, discover them and they will adapt their designs to encompass the state of the art of this improved technology. They will aim to solve problems that could not be solved before until the newness becomes an established part of main stream design. Progress is inevitable, and although architects will imagine design concepts in their heads and still sketch designs on paper, they must master computer drafting. Computer technology develops quickly; as each step is accommodated its users are anticipating the next improvement. The computer is an ever-refined tool to produce the drawings of the building and its components but it is also a mathematical tool and is capable of generating data at a rapid speed necessary for production and fabrication. Computers can generate complex geometry's that before were impossible to envisage, either preventing construction or only at high risks of many errors and they can do this quickly. In the coming decade the development of computer assistance for design and manufacturing will also enable non-standard and non-system structures to be built with composing elements and components individually fabricated and assembled in a desired shape at a modest extra cost. The computer will have elevated non-standard to the common building market.

8. Production & Assembly Techniques

Generally manufacturing methods will have to develop towards flexible industrial production, where varying product parameters can be met without causing the production to slide from industrial to hand craft. Of course there will be problems in this transition but jobs with increased variation will prevail.Small-scale producers will be asked to develop non-standard cross sections for tubular profiles, elliptical, triangular or any other irregular quadrangular form, to specifically answer requests from project architects. An adequate flexible rolling process still has to be developed for that purpose.

Some fabrication technologies have recently been developed like concealed bolting in the wall of tubes and are awaiting exploitation. Such a technique is 'Flow drilling', where the wall is deformed to become an integrated threaded nut. Friction welding may also be contemplated for attaching appropriate end pieces to circular tubes to facilitate assembly. The use of weldable steel castings for 3D connections is growing. Steel casting is increasing in popularity and element prices are becoming more acceptable. Cast connectors could be given special forms to give the tubular structure its own character; streamlined connections imbue the entire structure with their own elegance. A cumulative pattern catalogue of cast structural elements would provide a valuable architectural design reference.

To maintain abstraction of design with tubular structures, a concealed bolted or mechanical connection for two tubes in one line is needed. This would achieve a flush butt assembly prior to erection or be used to connect larger assemblies of tubular structures above ground and without welding. Laser or plasma cutting of flat plates to accommodate end pieces is becoming low cost as both its technique and computer operation develop making it as easy and popular as flame cutting. This also applies to counterformed ends of tubes to be welded with matching curvature in truss-like designs where complicated arrangements can then be constructed.

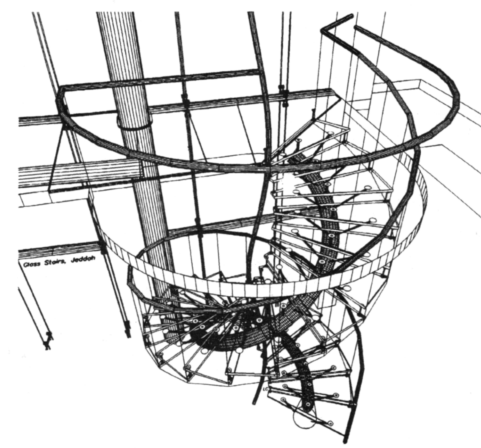

Fig.10: An all glass spiral stair, cantilivering from a spiral central tube, in Jeddah, by Areen and Mick Eekhout

Other technologies like bending of tubes need further development. Architects would welcome bending in two axes simultaneously, while keeping accurate size control. Fabrication is serviced by more automated welding machines accommodating larger structures and changing work pieces with flexibility in position in the fabrication process. But the more curved structures are designed, the higher the need for an intelligent measuring system to determine the shape of elements for fabrication and for the assembled geometry. During assembly complicated spatial elements have to be maneuvered into position and this requires accurate measurement. Enhanced fire-retarding paints are required that can be used both indoors and outdoors on tubular elements, are effective up to 90 min have a smooth appearance and a cost price that is not prohibitive. Spray applications will ensure that site damage will be restored easily.

9. Quality Assurance and Standards

To achieve a quality product the partners in a building team co-operating on a project, have to be quality conscious. All partners, the manufacturers, the architect, the engineers and the contractors have to establish their own quality assurance plans that should interlock to produce an optimal result.Quality is also governed by rules and requirements laid down in national, and increasingly, in European Standards. Although the background is always to assure a minimum quality that is fit for purpose the user must make sure that initiative in design is not inhibited by rigid interpretation. The increasing bureaucracy in the process of planning and manufacture must remain at a workable level so as not to smother and suffocate creativity.

10. Fundamental Material Research Zappi

A proposal has now been made for the fundamental material research, which is part of *Zappi's* objectives. However, the initiative has already been published, and through the marketing pull effect the first collaborations have already been set up. We will not go any deeper into the real material developments until the stage has been reached of the patent application for the first workable material concept of *Zappi*.

11. Conclusions

Zappi is till a long way off, but it believes the entire process is exciting and very convincing, despite the disappointments and the cautious maneuvering required at every step. What is so stimulating is that results can be realized bit by bit on the basis of diverse projects, where again and again project architects are encountered who show interest an participate. Major consideration with each bit of technical progress, whether this is Quattro or any other new building product, is its orientation to constructional value, practical application, and the improvement of the architectural quality. *Zappi* prefers its high technology product development to be applied in good buildings, which become even better or acquire more character. The value of developing something new is therefore not a thing apart. Real satisfaction in this development work comes, al in all cases, from those victories won by the skin of your teeth.Perhaps the best remedy for the disease of sterile architecture is joy in design, joy in performance, vigour and wit.

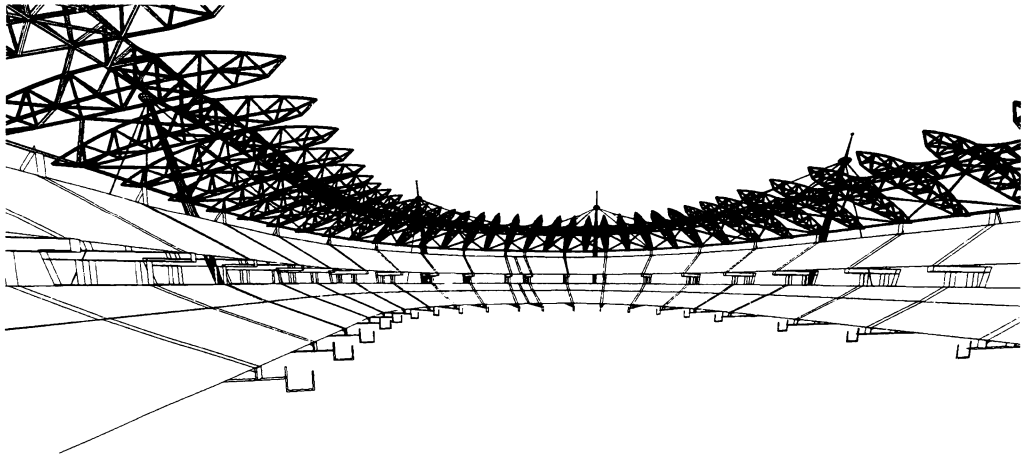

Fig.11: Interior view of Tunis stadium.

12. References

1. Mick Eekhout, *'Architecture in Space Structures'* , 010 Publishers, Rotterdam 1989, ISBN 90-6450-080-0.

2. Mick Eekhout, *'Product Development in Glass Structures'*, 010 Publishers, Rotterdam 1990 ISBN 90-6450-111-4.

3. Mick Eekhout, *'Architecture between Tradition and Technology,* Publications Architecture TU Delft, 1992, ISBN 90-5269-113-4

4. Mick Eekhout, *'Stressed Glass, Zappi or Product Development for the NAI'*, NAI Publishers Rotterdam, 1996, ISBN 90-72469-78-X

5. Mick Eekhout, *'Tubular Structures in Architecture'*, Cidect, Genève, 1996, ISBN 90-75095-26-0



Taylor & Francis
Taylor & Francis Group
http://taylorandfrancis.com

Tubular Structures VIII, Choo & Van der Vegte (eds) © 1998 Balkema, Rotterdam, ISBN 90 5809 001 9

Tubular structures in railway architecture in the Netherlands

H.H.Snijder
Holland Railconsult, Utrecht & Eindhoven University of Technology, Faculty of Architecture, Building and Planning, Netherlands

L.I.Vákár
Holland Railconsult, Utrecht, Netherlands

ABSTRACT: In the last decades many new railway stations were built in the Netherlands and many existing railway stations were enhanced and improved. This is due to increasing railway traffic and an upgrade of railway infrastructure to guarantee public transport and mobility. In these railway station projects tubular structures are often used, among other reasons, for their architectural quality in roofs. Applications of tubular structures in railway station architecture are shown. An overview is given of recently built railway station roofs in the Netherlands where tubular structures are used. Some railway station projects in the areas of Rotterdam and Amsterdam are discussed in more detail. Also attention is paid to fabrication, assembly and erection of these roofs. A tendency in the examples can be observed from space structure systems towards three dimensional trusses in hollow sections.

1 INTRODUCTION TO RAILWAY STATION ROOF DESIGN

In the 19th century, railway lines and stations were built on the outskirts of the city at ground level. A railway station usually consisted of a monumental building, functioning as a gate to the city, with right behind this building a roof structure over the platforms. To the passenger, the monumental building determines the sight of the so-called façade station. In the 20th century, the railway station became an obstacle in the city due to city development. The railway station was no longer situated on the outskirts and it did not turn its face to all passengers anymore: a front- and backside developed. Therefore, new railway stations in the Netherlands are usually designed as fly-over station. To avoid level crossings with road traffic, the railway track is elevated. Then, the railway station is built at ground level under the fly-over making it easily accessible from both sides. However, in that case the railway station loses its characteristic face towards passengers. This problem is solved by building an architecturally impressive roof structure which functions as an eye-catching beacon to passengers (Schoor et al. 1993). Also such a roof structure overcomes the difference between the entrance at ground level and the elevated platforms at the level of the fly-over.

In the last decade many new railway stations were built in the Netherlands and many existing railway stations were enhanced and improved. This is due to increasing railway traffic and an upgrade of railway infrastructure to guarantee public transport and mobility in the near future. The buildings of these railway stations and their roof structures over the platforms are designed in close co-operation between architect and structural engineer. The architect takes the lead in building design, the structural engineer takes the lead in roof design. Tubular structures are very popular to architects because of their smooth surface and because they are aesthetically attractive. They also offer good possibilities to structural engineers, having outstanding static properties regarding tension, compression, torsion and double axis bending, resulting in considerable material savings compared to open sections.

Tubular steel structures enable transparency when combined with glass, yielding a lot of daylight in the station. This is striven for to optimise social security for passengers and to help them to orient themselves. Tubular steel structures are often placed at the outside of the roof because of two reasons. Maintenance, e.g. painting against corrosion, can take place from the outside which is extremely important for undisturbed efficient operating of the railway lines within the station. Also, passengers are not distressed by pigeon's excrements: the roofing between structure and platform prevents this. An occasional shower cleans the tubes. Between roof structure and platform, façades in steel and glass protect passengers from the climate. Rectangular hollow sections (RHS) are often applied in these

façades since they combine an attractive appearance with sufficient stiffness to support the glass. Again, a lot of glass is preferred in the façades for reasons of social security and passenger orientation. On the platforms, the number of obstacles should be limited since they hinder passengers finding their way to the trains. Therefore, the number of columns is limited leading to large spans which ask for truss-like structures with tension and compression members. Steel tubes behave very well under tension; they also behave very well under compression with regard to buckling around all axes, with a lot of steel far away from the neutral axis. Tubular steel structures are therefore a logic solution for railway station roof designs. Because of their smooth appearance without sharp edges, tubular structures are also a good choice from maintenance point of view. The surface area to be painted is relatively small and the required corrosion protection can be applied more economically compared to structures of open sections.

Truss-like structures also have a disadvantage in having to make a lot of connections and the presence of a lot of steel members. A tendency can be observed towards less members and less connections: from space frame systems to three dimensional truss girders. The welding of connections of RHS is relatively easy because special profiling is not necessary. For Circular Hollow Sections (CHS) special profiling is required which complicates fabrication of connections.

However, nowadays use of automatic production equipment facilitates profiling of CHS connections considerably and overcomes this problem. It is also relatively difficult to connect other structural elements (like corrugated steel sheeting) to tubular sections when compared to open sections. However, the disadvantages are outweighed by the advantages: in railway station roof design, tubular steel structures dominate.

In the next paragraph an overview is given of recently built railway station roofs in the Netherlands, where tubular structures are used prominently.

2 OVERVIEW OF TUBULAR STRUCTURES IN RAILWAY STATION ROOFS

In the following railway stations in the Netherlands, tubular steel structures have been applied in a prominent way.

2.1 *Breda Station (1975)*

One of the first applications of tubular structures in railway station roofs is the Mero space frame system of Breda Station (Fig. 1). Only a limited number of columns was allowed on the platforms resulting in large spans where a space frame is appropriate. Nowadays the disadvantage of difficulty in maintenance shows in a lot of dust on the tubes.

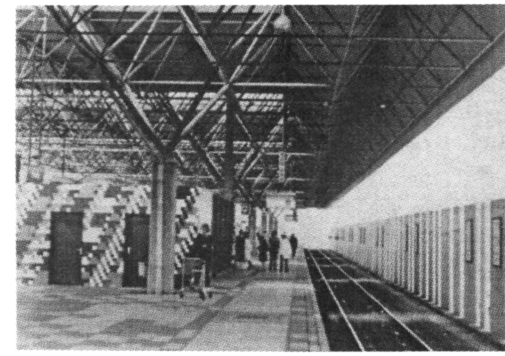

Figure 1. Breda Station.

2.2 *Zaandam Station (1983)*

Also a Mero space frame system was applied as a roof structure for Zaandam Station (Fig. 2). For the first time a striking bright colour was used which became common in later station projects.

2.3 *Lelylaan Station (1986)*

In Lelylaan Station (Fig. 3) the space frame system is replaced by three-dimensional trapezoidal truss girders (Schoor et al. 1993, Maas 1987). To facilitate maintenance, the structure is placed outside the roofing for the first time here. This also protects passengers against pigeon's excrements. Social security asking for a limited number of columns was an important criterion. Large column free spans (48 m – 18 m – 43 m) and cantilevers (20 m each) are made possible using the tubular truss girders.



Figure 2. Zaandam Station.

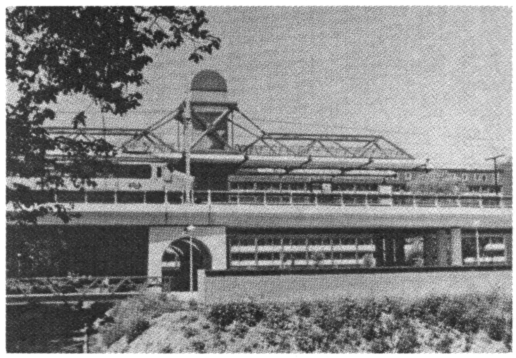

Figure 3. Lelylaan Station.

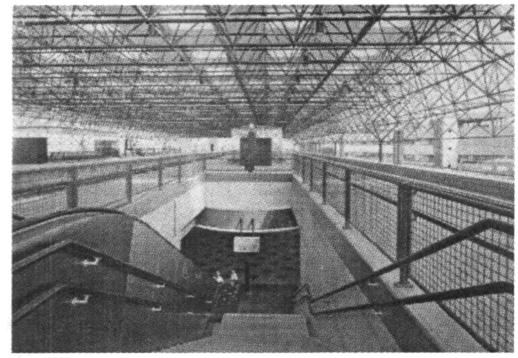

Figure 5. Almere Central Station (photo: Teo Krijgman).

2.4 *Amsterdam Sloterdijk Station (1986)*

Amsterdam Sloterdijk Station (Fig. 4) is a railway and metro station built as a table-like structure over a railway junction (Schoor et al. 1993, Maas 1987). It was necessary to create a lot of volume in relation to office buildings nearby. Tubular sections are applied prominently in the structure of this station's hall. The table of the hall consists of frames built up by welding tubular sections together to form three dimensional truss girders. The tabletop is again a Mero space frame system.

2.5 *Almere Central Station (1987)*

Almere Central Station (Fig. 5) is a typical fly-over station with a 150 m long Krupp Montal space frame roof (Schoor et al. 1993). The span in width direction is 42.5 m. The structure is located under the roofing yielding filthiness on the individual members. Birds cause passengers a lot of inconvenience. Moreover the number of 12,678 individual members is huge making maintenance difficult. The condescending sides of the frame offer passengers protection from wind and rain.

2.6 *Station Lelystad Centrum (1988)*

Also Station Lelystad Centrum (Fig. 6) is a fly-over station with a space frame system as a roof (Schoor et al. 1993). In the roof also three dimensional truss girders are included. The fold in the 143 m long roof gives it its strength. The structure spans three times 49.5 m in length direction and is designed to be easily redoubled in the future when the number of railway tracks is increased. It offers good protection from wind and rain but a disadvantage is again the huge number of individual members under the roofing, even though the net density is only 70% compared to the roof of Almere Central Station.

2.7 *Recent projects*

Some recent railway station projects in the Rotterdam and Amsterdam area, where tubular structures are prominently applied, are discussed in more detail in the next paragraph: Rotterdam Blaak

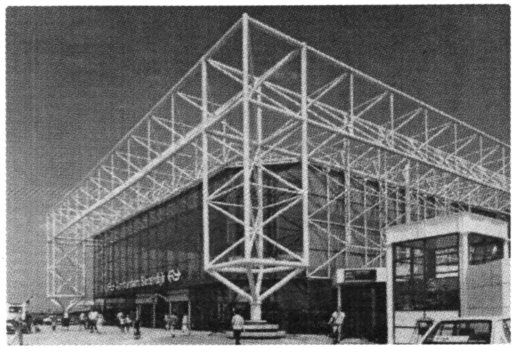

Figure 4. Amsterdam Sloterdijk Station (photo: Sybolt Voeten).



Figure 6. Lelystad Centrum Station.

Station (1993), Amsterdam Duivendrecht Station (1993) and Amsterdam Central Station's Intermediate Roof (1997). Also, attention is paid to fabrication, assembly and erection of these roofs.

3 RECENT RAILWAY STATION PROJECTS WITH TUBULAR STRUCTURES

3.1 *Rotterdam Blaak Station (1993)*

Rotterdam Blaak Station (Fig. 7) is situated at a public transport junction where a railway tunnel crosses a metro tunnel (Schoor et al. 1993, QA 1993, Binney 1995, Vákár 1993a, Loriers 1995). This railway station with its two island platforms offers the opportunity to change from train to metro or tram. Because of its underground location, the design of Rotterdam Blaak Station focussed on helping the passengers to orient themselves. At ground level, the roof over the main stairwell serves as a beacon for passengers. The roof consists of a transparent disc of 35 m diameter, which is hanging from a steel arch spanning 62.5 m. The arch is founded on the middle wall of the railway tunnel thus marking the tunnel axis. Also, the roof serves as an orientation point for passengers leaving the trains underground. The big transparent roof allows lots of daylight to pass through to tunnel level 14 m below ground level. The roof of Rotterdam Blaak Station forms the summit, the crown of the railway tunnel and materialises what The Netherlands Railways stand for: passengers are sacred and Rotterdam Blaak Station gives them an aureole.

The actual roof, the transparent disc of 35 m diameter, is carried by a steel shell structure with the shape of a spherical segment. The steel structure is placed outside the roofing, making maintenance easy to carry out, letting an occasional shower clean the structure and avoiding inconvenience due to birds. The spherical segment is hanging from the arch. Furthermore, the rims of the void of the main stairwell carry supports to the spherical segment. The hangers from arch to roof are stayed tubes and look like a ship's mast referring to the Rotterdam harbour. The arch consists of three chords ∅ 298.5 mm which were bent coldly into two radii. They are connected by CHS braces ∅ 60.3 to ∅ 108 mm. The design is such that the middle section has a nabla (∇) shape and both sections near the supports have a delta (Δ) shape. Two points exist where the three chords are in line, forming a bending and torsional hinge. Here tubes ∅ 168.3 mm are welded between the chords giving Vierendeel action.

Since the arch has torsional hinges at both ends, it tends to fall over. To prevent this, the suspension of the disc to the arch has been designed as a brace, so it fixes the middle of the arch laterally. Hence the arch and the spherical segment work as a unit: they keep each other upright.

The upper net of the spherical segment consists of triangles in CHS ∅ 193.7 mm; the lower net consists of triangles in square hollow sections 200 mm. The upper and lower net are interconnected by verticals. Between the supports on the rims of the void diagonals have been added to form a truss. The verticals are CHS ∅ 88.9 mm as well as the diagonals. The connection of the upper net members is difficult: six coldly bent members with three different radii and at least one vertical member meet. To facilitate fabrication of this connection, big cast steel ball joints ∅ 420 mm were preferred. The tubes were welded to these cast steel ball joints. They cover up inaccuracies of the spherical shape. After all, the members should follow a flowing line in three directions.

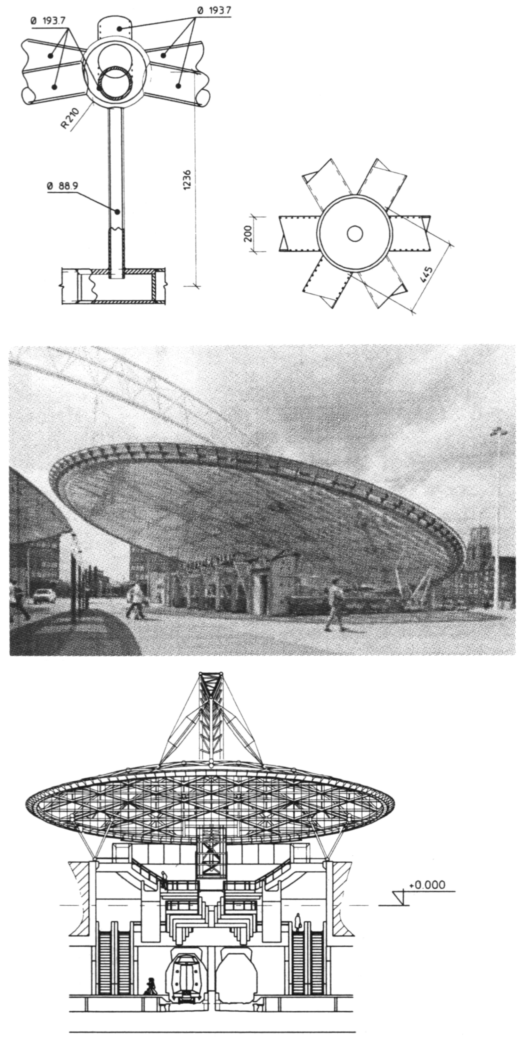

Figure 7. Rotterdam Blaak Station (photo: Frank van Dam).

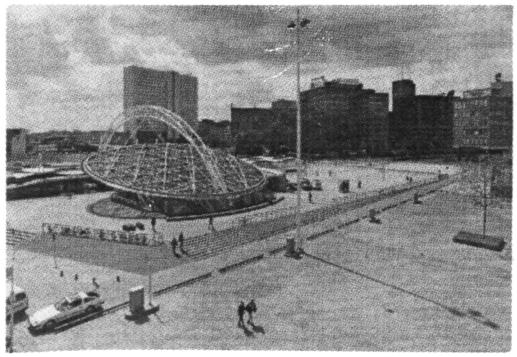

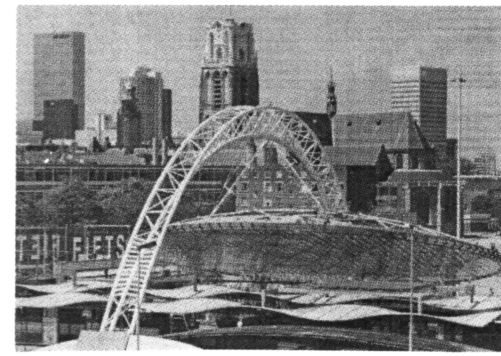

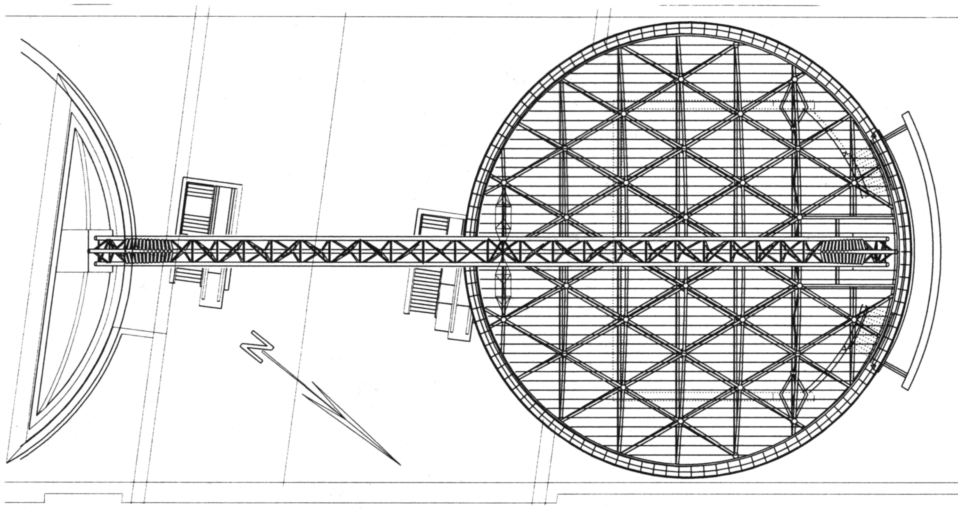

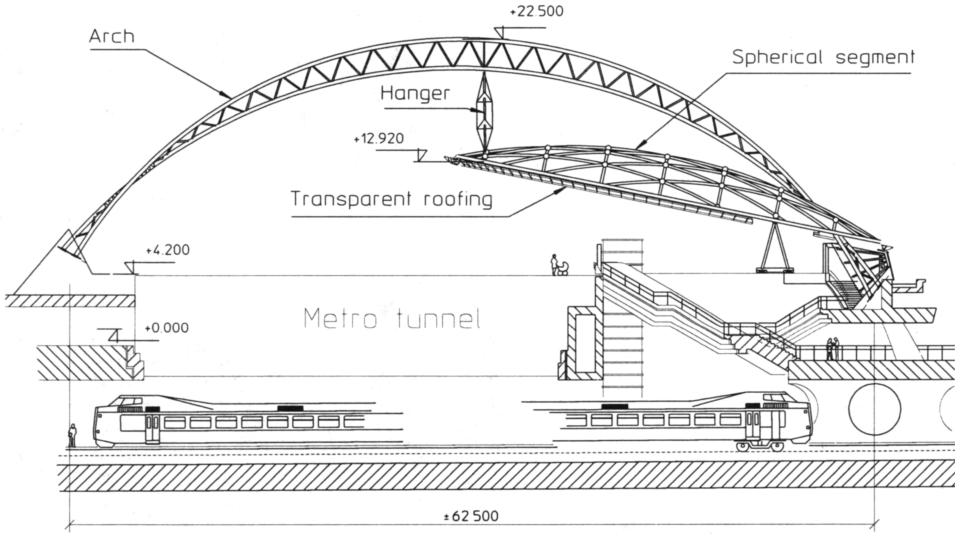

Figure 7 (continued). Rotterdam Blaak Station (photos:Frank van Dam).

3.2 *Amsterdam Duivendrecht Station (1993)*

Amsterdam Duivendrecht Station is a railway and metro junction station with three levels. The upper level has a roof which measures 150 × 47 m^2, having closed façades for as far as possible (Schoor et al. 1993, Binney 1995, Vákár 1993b). The steel structure consists mainly of three dimensional truss girders built up in CHS (Fig. 8). The possibilities for assembly and erection of the structure, with regard to railway and metro operation, governed the design. Therefore, the roof was prefabricated in structural parts which were as big as possible. At night these completely finished parts were assembled and erected.

The 47 m span is halved by placing a three dimensional delta (Δ) girder on four supports on the middle axis of the roof. This meant that only half the number of tracks had to be taken out of order while mounting secondary structural elements. The columns are designed three dimensionally in such a way that large hogging moments are topped and deflections are limited. Also for the almost 22 m long secondary girders placed at an intermediate distance of 11.5 m, three dimensional truss girders are used, but now in the shape of a nabla (∇). Each girder was mounted, complete with the part of the roof hanging underneath it. The nabla girders are supported in the façade on longitudinal steel beams which are supported in their turn on slender pin ended columns.

In the middle of both longitudinal façades, a triangular RHS frame stabilises the structure; the columns of the delta girder slide in length direction. V-shaped stabilising braces of CHS in the other two façades together with wind bracing elements of CHS in the roof plane, stabilise the structure in transverse direction.

Between the roof planes under the nabla girders, 3.8 m wide polycarbonate areas yielding daylight in the station, are supported by RHS. The delta and nabla girders are built up in CHS. The chords are of steel grade S355, the other members of steel grade S235. The delta girder has an upper chord ∅ 273 mm and lower chords ∅ 219.1 mm. The braces in both side areas are CHS ∅ 139.7 mm (∅ 193.7 mm near the supports); in the bottomside area RHS 200 × 100 and square hollow sections 80 mm are used as braces. The columns of the delta girder consist of CHS ∅ 273 mm. The nabla girders have chords in CHS ∅ 127 mm. The braces vary from CHS ∅ 76.1 mm to ∅ 108 mm. The bottomside area of the delta girder and the topside areas of the nabla girders coincide. In this area also the wind bracing elements are included. The nabla girders in the façades are placed on an edge beam designed as a box girder, welded together from sections W 530 × 165 × 85. This beam is supported by RHS columns 200 × 100 of about 5.1 m length. The nabla girders are braced to this edge beam to lead the forces from the wind bracing in the roof to the triangular RHS frame in the façade.

The steel weight is 21 kg/m2 for delta and nabla girders together. With supports, columns, façade beams and wind bracing this weight is almost redoubled.

The result is a light roof structure which is easy to maintain. Maintenance is very simple due to the closed roofing under the steel structure which serves as platform during maintenance operations.

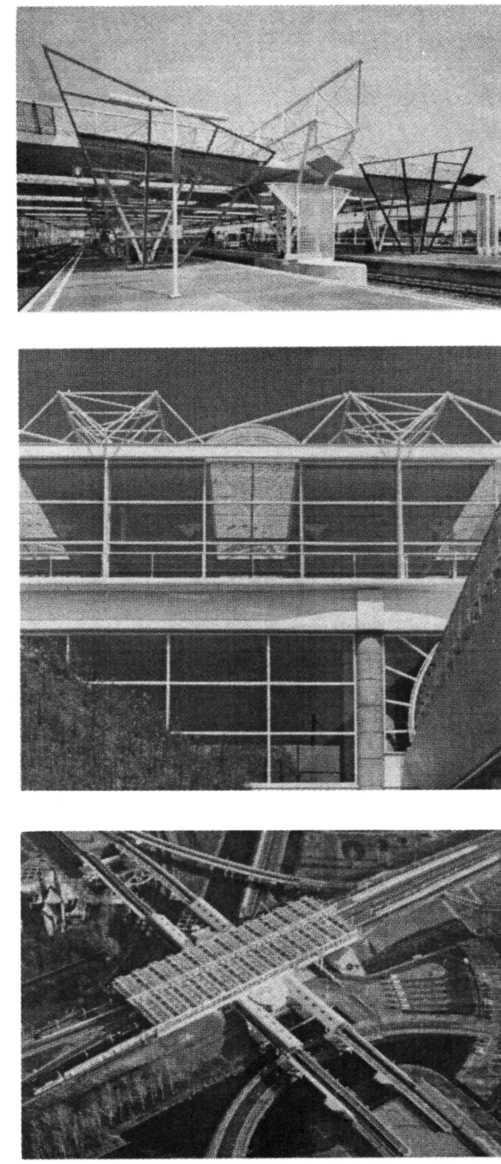

Figure 8: Amsterdam Duivendrecht Station (photos: Frank van Dam and bottom Aeroview, Dick Sellenraad).

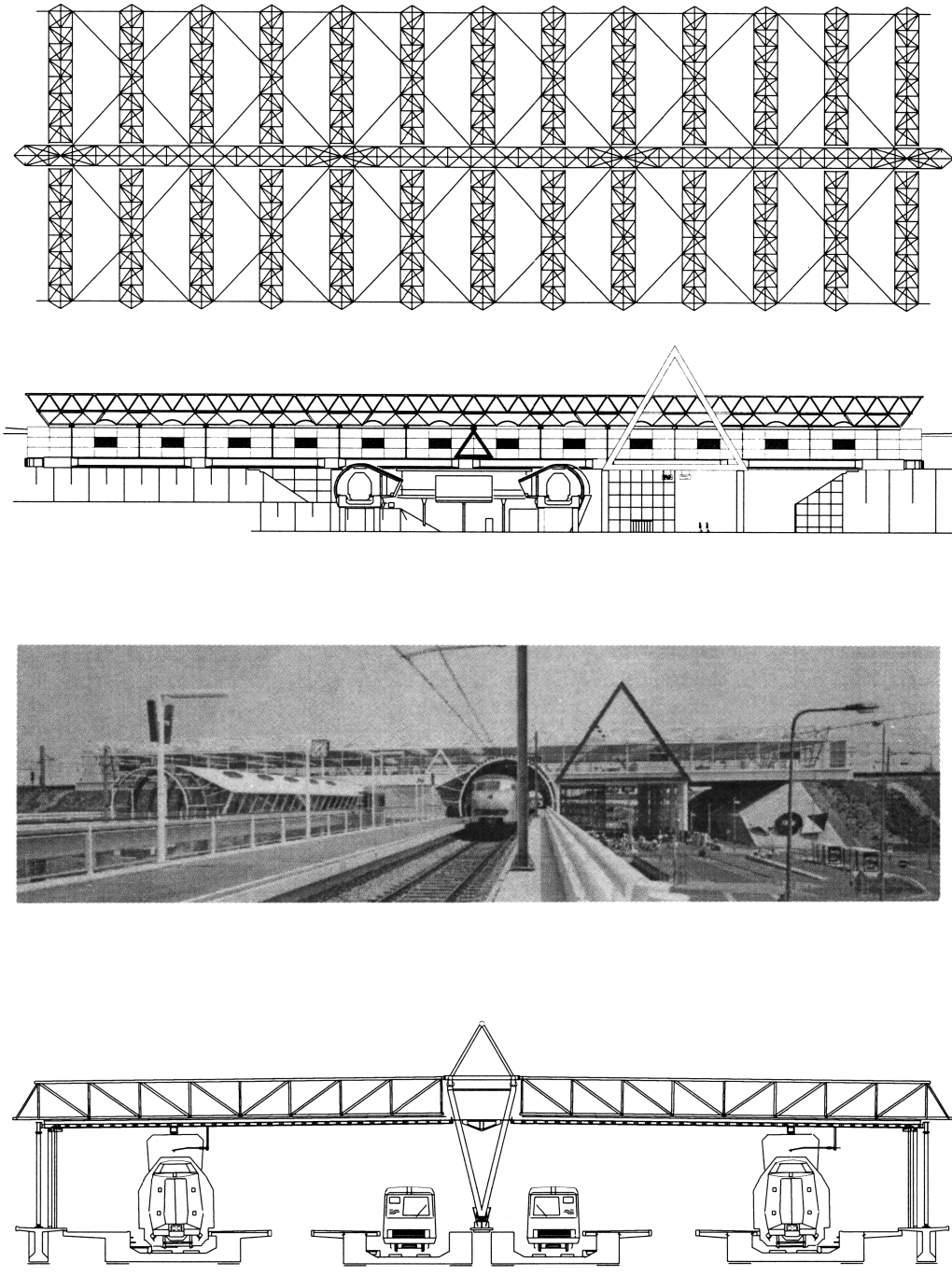

Figure 8 (continued). Amsterdam Duivendrecht Station (photo: Frank van Dam).

3.3 *Amsterdam Central Station's Intermediate Roof (1997)*

Amsterdam Central Station is a typical façade station built at the end of the 19th century. Behind the building a roof structure over tracks and platforms with three hinged arches spanning 44.5 m was built: the South Roof. Later, in 1922, the North Roof spanning 34 m was built. Between these roofs three tracks remained uncovered until 1997 when, due to international high-speed trains coming to Amsterdam, the so-called Intermediate Roof was finished (Fig. 9). The Intermediate Roof has a length of 354 m and consists mainly of tubular sections (Bilsen et al. 1997). Important requirements for the design were easy maintenance, no inconvenience due to birds and no additional obstacles on the platforms since available space is limited.

The Intermediate Roof spans 19.5 m making use of arches on supports connected to the North and South Roof, thus avoiding separate columns at platform level. Only at the south-west side the arches are continued as columns until platform level because the South Roof is shorter than the North Roof. On a macro scale the arch shape matches the North and South Roof. In detail a lot of differences are present. In the Intermediate Roof, wire glass, referring to the North and South Roof, is located above the platforms under the structure helping passengers to orient themselves and to protect them from bird inconvenience.

The arches are built up by welding tubular sections together to form three dimensional truss structures of the nabla (∇) type: two bent upper chords and one bent lower chord (3 ∅ 193.7 × 6.3) are connected by braces (∅ 101.6 × 5). In top and side view the arches taper.

The arches are connected by four three dimensional nabla (∇) truss girders in CHS of the same sizes. However, near the supports the chords have thicker wall sizes and the braces are heavier. System length of the girders is usually 12.5 m except where the CHS wind trusses are present.

Between the nabla girders, bent RHS (180 × 100 × 5) extended by steel strips welded to the bottom flange, carry the aluminium wire glass supporting structure every 2 m. The nabla girders also carry cold formed steel roof plates, positioned above the tracks in the middle of the Intermediate Roof.

The supports of the arches are hinges transferring the reactions to the North and South Roof, which could take these reactions easily. At the south-west side, where the columns are present, a horizontal beam takes the horizontal arch reaction leaving only the vertical reaction to be transferred by the column. The column is a continuation of the three chords of the arch. Where the chords meet, the column changes through a header plate into a triangular section with rounded corners and is tapered until platform level.

The structure is predominantly welded. The arches and the nabla girders were fabricated in the shop by welding. Profile cutting was of course

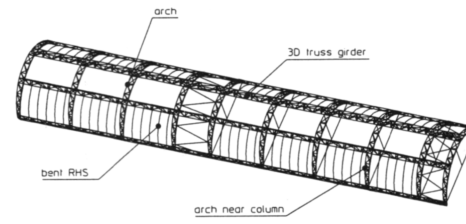



(photo: Chiel van Diest).

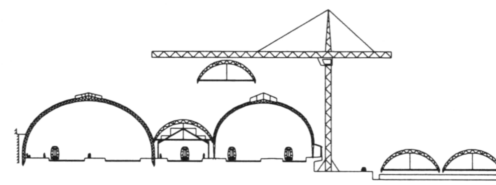

Assembly and erection

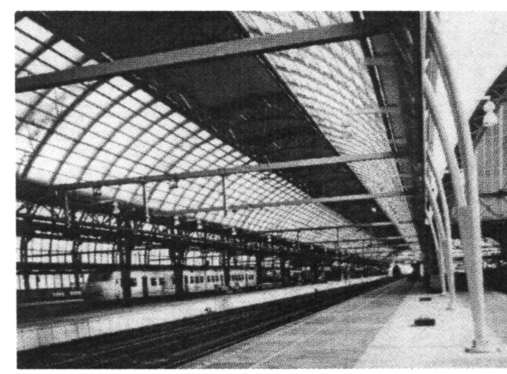

(photo: Rik Hoogewoud).

Figure 9. Amsterdam Central Station's Intermediate Roof.

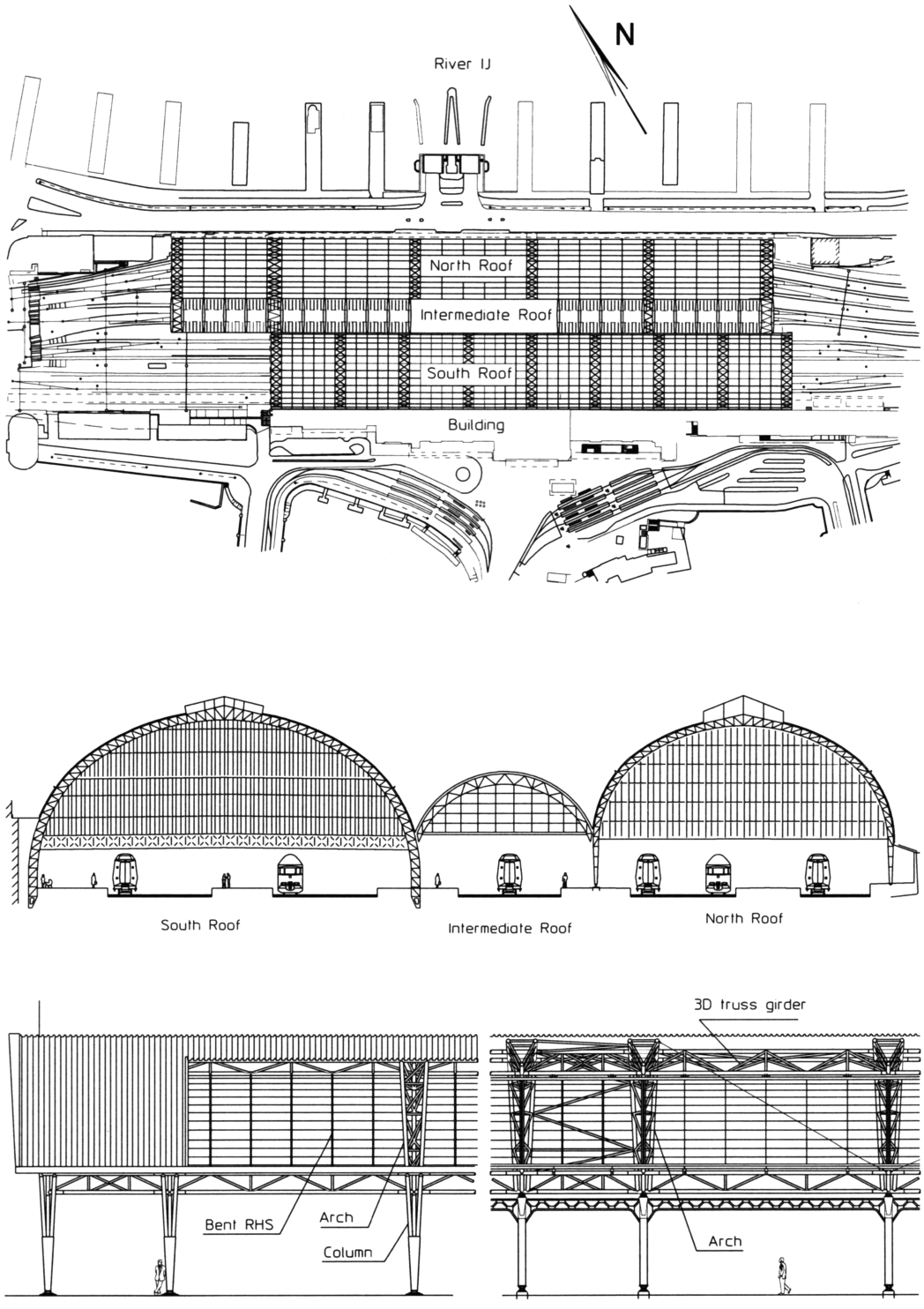

Figure 9 (continued). Amsterdam Central Station's Intermediate Roof.

necessary to make the connections in CHS. To be able to transport the structure from shop to site, divisions in the nabla girders were made between arch and nabla girders. The parts were joined by on site welding of chords and braces also. A possible change in wall thickness of chords, coincides with this division. The tube with the thickest wall is internally planed, yielding the same wall thickness as the one of the adjacent tube. Thus the weld can be made giving a smooth transition and making ultrasonic inspection possible. Special attention had to be paid to measurements and out of tolerance: moulds were used to make sure that the structure fits on site.

Especially in those cases where a new roof is built in an existing railway station, assembly and erection is extremely difficult because railway traffic and passenger transport must continue without obstruction. Amsterdam Central Station counts 150,000 passengers and 1400 train movements per day. The available building space was limited. This problem was solved building the structure on a temporary platform of 50 m length over the tracks and passenger platforms. After lifting the elements to this temporary platform by crane and after assembly there, the structure was shifted section by section into place using a (stuffing) press technique.

4 CONCLUSIONS

This paper reports on recently built railway station roofs in the Netherlands where tubular structures are predominantly applied. A lot of applications of tubular structures in railway stations is illustrated. In these cases tubular structures are preferred for their architectural quality and their structural properties. In railway stations, the number of columns on platform level should be limited, leading to large spans which ask for truss-like structures where hollow sections are appropriate. A tendency in the examples can be observed from space structure systems towards three dimensional trusses in hollow sections due to the need of minimising maintenance combined with reducing labour costs.

REFERENCES

Bilsen, H.P., Spoon, M., Bosch, J. van den & H.H. Snijder 1997. Middenkap Amsterdam CS – Kleiner maar niet minder groots dan de buren (Intermediate Roof Amsterdam Central Station – Smaller but not less spectacular than its neighbours). *Bouwen met Staal.* 136:20-25. (in Dutch).

Binney, M. 1995. *Architecture of Rail – The Way Ahead.* Academy Editions.

Loriers, M.-C. 1995. Figure de Liaisons – Station de transports Rotterdam. *Techniques & Architecture.* 420:88. (in French).

Maas, T. 1987. Three stations nearby Amsterdam. *Architecture and Urbanism.* 8(9):55-71.

Quaternario Award (QA) 1993. IAITA. International Award for Innovative Technology in Architecture. Singapore 1993. Elemond Editori Associati. Milano: Electa.

Schoor, H. van de, et al. 1993. *NS laat bouwen – stations sinds 1980 (The Netherlands Railways are having built – railway stations since 1980).* Sphinx Cultuurprijs 1993. Zutphen: Walburg Pers. (in Dutch).

Vákár, L.I. 1993a. Station Rotterdam Blaak - Overkapping vormt aureool boven hoofd van reiziger (Rotterdam Blaak Station - Roof forming an aureole above the traveller's head). *Bouwen met Staal.* 114:27-35. (in Dutch).

Vákár. L.I. 1993b. Station Duivendrecht, Amsterdam - Hechte samenwerking tussen architect en constructeur uit zich in logische stationskap (Amsterdam Duivendrecht Station - Close co-operation between architect and structural engineer expressed in a logical station roof). *Bouwen met Staal.* 111:31-39. (in Dutch).

Tubular Structures VIII, Choo & Van der Vegte (eds) © 1998 Balkema, Rotterdam, ISBN 90 5809 001 9

Design of prestressed roof structure suspended from tubular steel towers

Kohju Ikago, Katsumi Hara & Kunio Ukai
Nikken Sekkei Limited, Osaka, Japan

ABSTRACT : A Stadium with prestressed suspension roof is now completed in Kumamoto, Japan. Prestressed suspension structure system is adopted to make the roof light and pleasant. The roof structure is designed to be suspended from 59.7 m height tubular steel towers doubling as floodlight towers. The distinctive feature of this structure system is the prestresses introduced into the main steel arc at field side. 300 tons prestresses are introduced at both end of the main arc, consequently suspension cables and stay cables are tensioned inevitably. These tensions give stiffness to the roof structures which consist of slender steel girders and cables and make them stable against any external forces such as strong winds or earthquake motions.

1. STRUCTURAL DESIGN

1.1 *Outline of structural design*

A light and pleasant roof was intended to cover the upper space of the stands. The plan of the roof is shaped like a half moon with the field side line as the subtense (hereinafter called A-line) and the stands upper stage concourse side line as the arc (hereinafter called B-line).

The roof was planned to be suspended by cables tied to steel framed towers doubling as floodlight towers 59.7 m high from the ground level. The roof surface structure was to be built up of a light and pleasant arch shaped front steel edge (A-line) and a rear side steel frame (B-line) with steel beams connecting them.

The special design feature of this roof is introducing a tensile force of approximately 300 tons to front arch shaped steel and 310 tons to each side stay cable of the tower. Thus, a tensile force will be introduced to all cables to create a stable roof surface of prestressed suspension structure.

The roof surface is finished with membrane and holding cable spread between A-line and B-line to provide a bright membrane roof.

In this structural system, the downward load such as the roof dead load or snow load is resisted by the suspension cables and the front arch shaped steel. The upward load such as wind blow-up load will be transferred by the front steel arch to the lower structure. The horizontal load such as seismic force and sideways winds will be transferred by the steel members composing the roof surface to the lower structure.

1.2 *Roof structure*

The length direction roof span is approximately 178 m and the maximum width is 39 m (Figs. 2,4).The front field side elevation of the roof is arc-shaped, its rise being about 25 m, hence the rise-span ratio is $25/178 \fallingdotseq 1/7.1$

The A-line structural system consists of arch-shaped H-section steel erected in an arch-shape and it works as "holder" of the roof to prevent the roof surface from being blown up and to give rigidity to the roof, and suspension cables are connected to this steel to hold it up. This H-section steel and the suspension cables are in the same vertical plane, that is, in the A-line vertical plane, and to give rigidity to the structure, or in other words, to prevent a large deformation by the wind blow up force, prestress will be given to this arch-shaped steel and the side stay cable. Prestress force to be introduced is 300 tons and 310 tons respectively (Fig. 5).

On the rear side of the roof surface, bow-shaped B-line, together with its steel beams and the steel columns supporting them and the axial brace, supports the roof.

This B-line structure, together with the arch-shaped steel A-line and the steel beams on the roof surface, forms a half moon shaped truss configuration in the roof plane as shown in Fig. 4. Horizontal forces such as seismic force and wind force will be transferred to the lower structure by this truss.

Each steel tower consists of two (2) steel tube columns of 1,200 mm in diameter. A-line surface suspension cables are tied to this column top. The position on the column where cables are tied is approximately 36.5 m high from the column base.

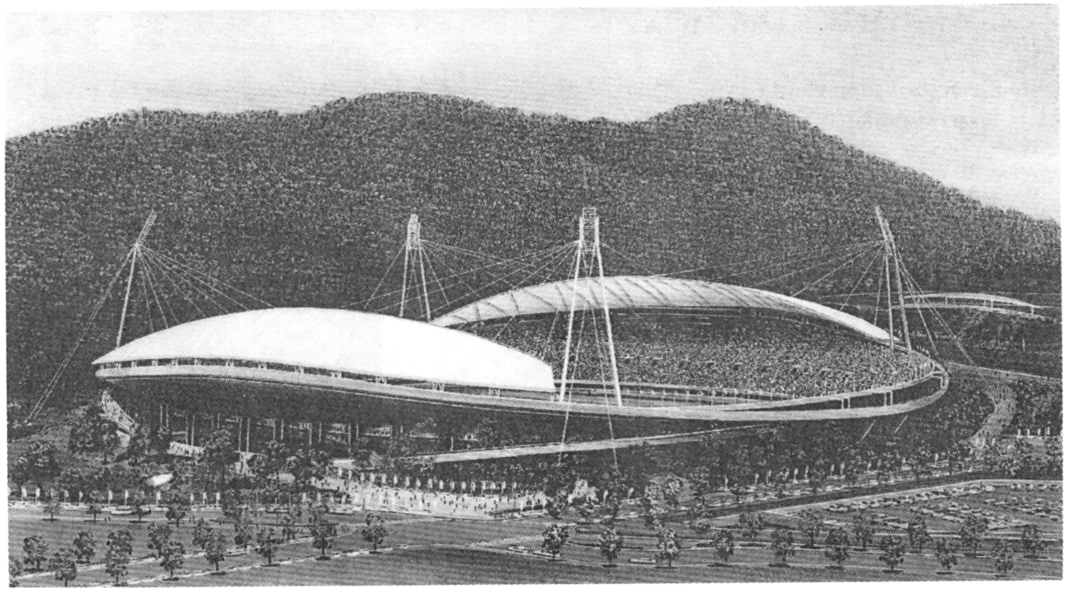

Fig. 1 Appearance rendering

Table 1. Outline of the facility

Owner	:Kumamoto Prefecture
Design	:Nikken Sekkei Ltd.
Construction supervision	:Nikken Sekkei Ltd.
Construction	:Kajima Corp. and others
Roof Steel work and cable installation	:Kajima Corp. and Yokogawa construction Co.Ltd.
Membrane work	:Kajima Corp. and Taiyo Kogyo Corp.
Site area	:214,599m^2
Building area	:20,241 m^2
Total floor area	:34,697 m^2
Seating capacity	:32,000 persons

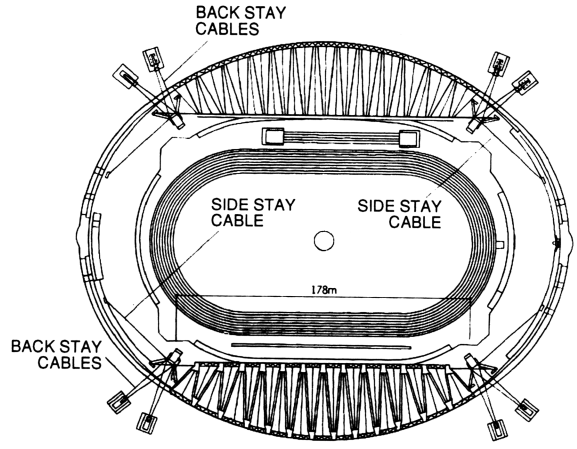

Fig. 2 Plan of the stadium

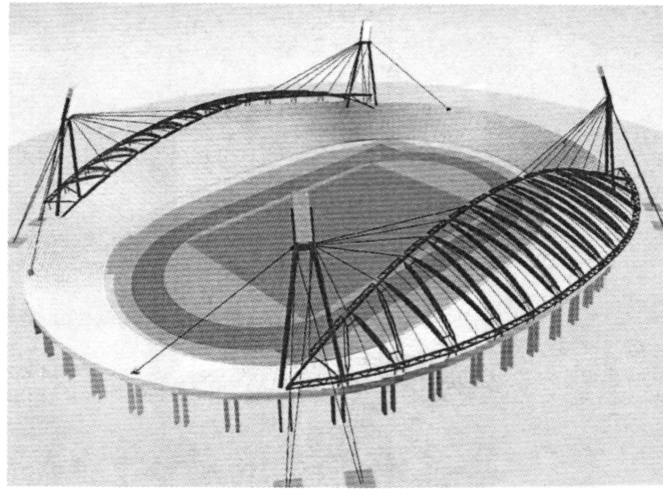

Fig. 3 Roof skeleton perspective

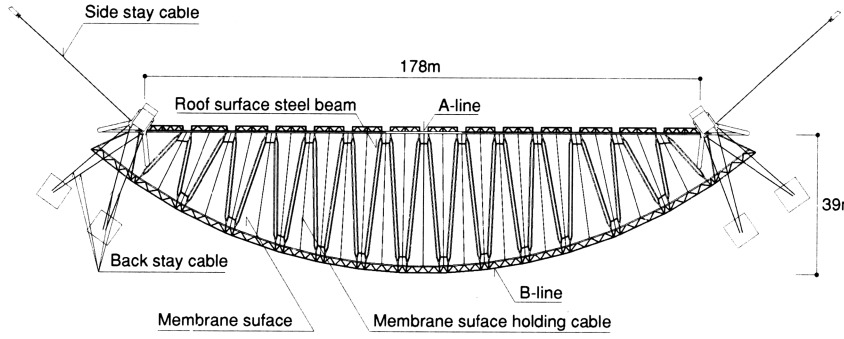

Fig. 4 Horizontal truss consisted of A-line,B-line and roof surface beams

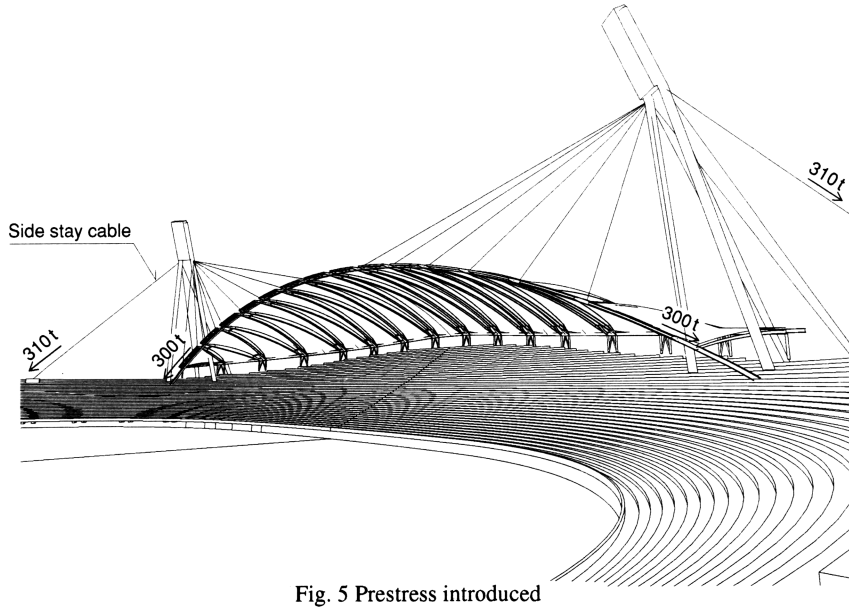

Fig. 5 Prestress introduced

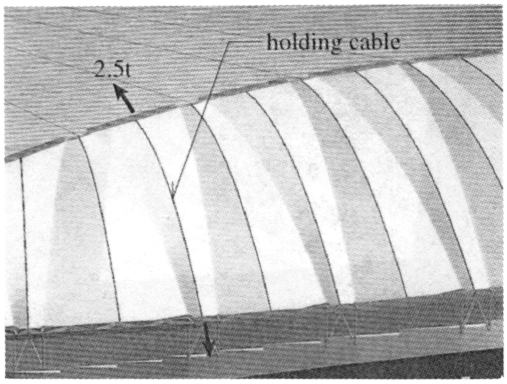

Fig. 6 Membrane finish

The two (2) tower column bases are pin bearing type. Since this tower doubles as a floodlight tower, the tower as a whole is tilted forward to produce the required lighting effect. Therefore, each of the two (2) columns is provided with two (2) each back stay cables totaling four (4) strung backward to prevent falling of the roof forward. In addition, to prevent overturn of the tower on its back, a side cable is provided in the direction shown in Figs. 3-5 . All these devices combined, each steel tower column received tensile force from three (3) directions by the A-line suspension cables, the side cable and the back stay cable. As a result, each steel tower column receives a compression force of approximately 900 tons at all times.

Light, pleasant and bright membrane finish was employed for the roof surface. The roof is made of integration of unit membrane roof pieces—each surrounded by A-line steel, steel beams in the roof surface plane and B-line steel—and holding cable. The entire roof surface is made by repetition of this unit membrane surface (Fig. 6).

The longitudinal section of the unit membrane surface is arc-shaped from the weather top to the downstream side. The tangent line is horizontal at the weather top and tilts downstream toward B-line. The cross-section has a shallow V-letter shape, and a holding cable is placed in the valley of the V-section to hold the membrane down. The ends of this holding cable are anchored to A-line and B-line respectively. To prevent the membrane surface from being largely deformed by wind, the rigidity of the holding cable is reinforced with a prestressing force of 2.5 tons.

As the result, the blow-up wind load is transferred to the A-line and B-line structures via holding cables and the steel beams on both sides of the unit membrane, and the vertical load by wind blow-down and snow is transferred by the membrane to the steel beams on both sides which further convey the load to the A-line and B-line structure.

2. ROOF STRUCTURE CONSTRUCTION PROGRAM

The construction procedure will be shown below.

1) Flood light tower erection(Fig. 7).
   Install the back stay cables.
   Install the side stay cables
2) Erect B-line steel frames(Fig. 8).
3) Erect A-line arch-type steel-structure(Fig. 9).
4) Install A-line suspension cables(Fig. 10), and introduce 310tons prestress force to side stay cables.
5) Introduce 300tons prestress force to A-line steel(Fig. 11).
6) Erect roof surface steel members(Fig. 12).
7) Install membrane roof (Fig. 13).

3. ANALYSIS OF SUSPENSION STRUCTURE

In the case of suspension structure, the rigidity and safeness of the structure largely depend upon the tensile stress distribution. Therefore, the geometrical nonlinear effect was considered in the stress deformation analysis.

The purpose of the analysis at the design stage was to determine the shape and structural members of the roof as well as said tension distribution, and also to confirm that the structure, after completion thereof be safe against wind and seismic load.

The following is a summary of the results of the analysis based on the construction sequence and the results of the analysis on stress under wind load:

1) A-line is jacked down and released from supports after the installation of the suspension cables to the steel towers. Axial force distribution in this construction stage is shown in Figure 14.
2) Installation of back stay cables (Fig. 15)
3) Installation of side stay cable CB13 (Fig. 16)
4) Introduction of A-line prestress (Fig. 17)
5) Installation of the roof surface girder and the application of dead load by membrane spread-out installation.
   Axial force distribution under dead load application including prestress force and the deformation by the dead load of the roof surface beam and the membrane only are shown in Figure 18.
6) Analysis of stress and deformation under wind load (Fig. 19)

The wind velocity pressure and wind force coefficient distribution for design of the roof structure was determined based on the result of the wind tunnel test. Figure 20 shows an example of the design wind pressure coefficient which is the sum of the wind pressure coefficients of both upper and lower surface of the roof.

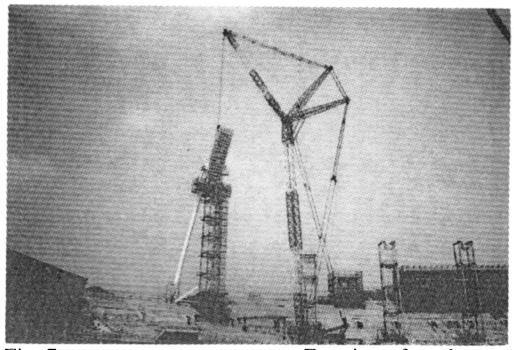

Fig. 7 Erection of steel tower

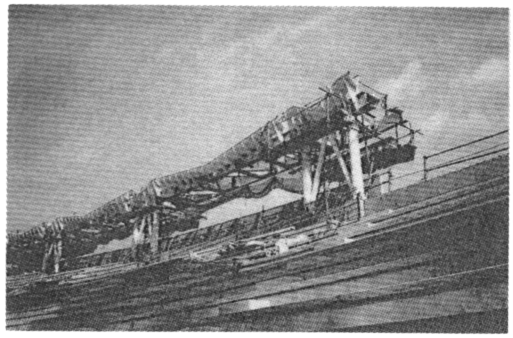

Fig. 8 Erection of B-line steel

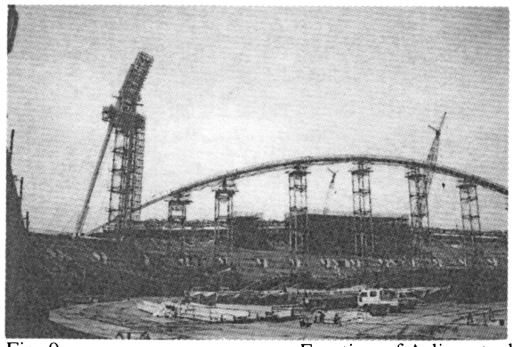

Fig. 9 Erection of A-line steel

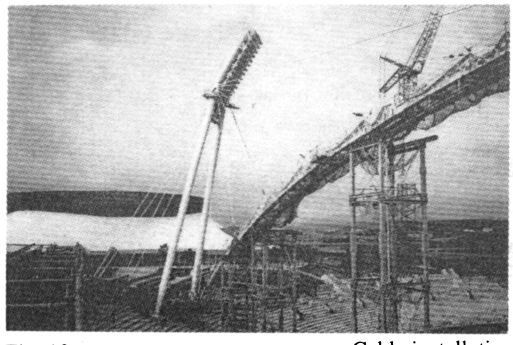

Fig. 10 Cable installation

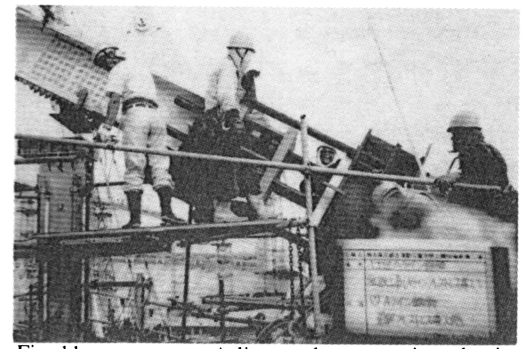

Fig. 11 A-line steel prestress introduction

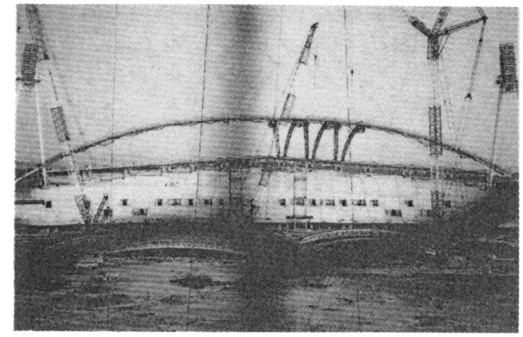

Fig. 12 Erection of roof steel beams

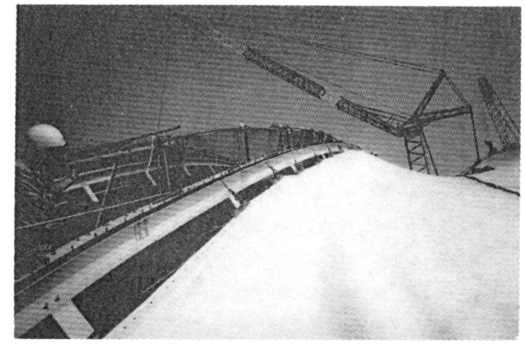

Fig. 13 Construction of membrane roof

4. COMPARISON BETWEEN ANALYSIS RESULTS AND ACTUAL MEASUREMENTS

During the actual construction work, the vertical displacement at three (3) points including the center of A-line, the pull-in force of the A-line tension end, the light tower base section stress and the top connector stress were centrally controlled at the measurement room in real time when the A-line prestress was introduced. Figure 21 shows the typical diagram of the automatic measurement system.

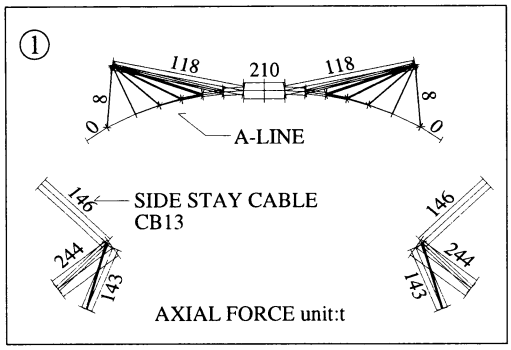

Fig. 14 Jack Down

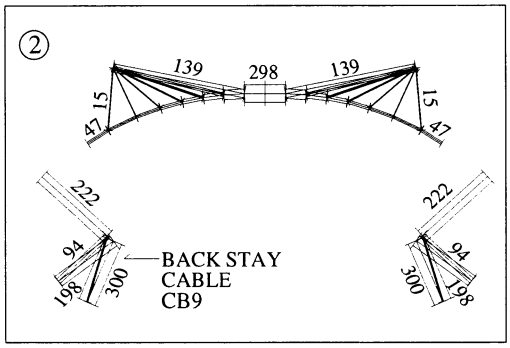

Fig. 15 Install CB9

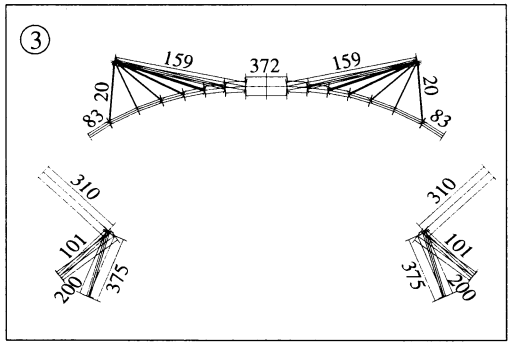

Fig. 16 Install CB13

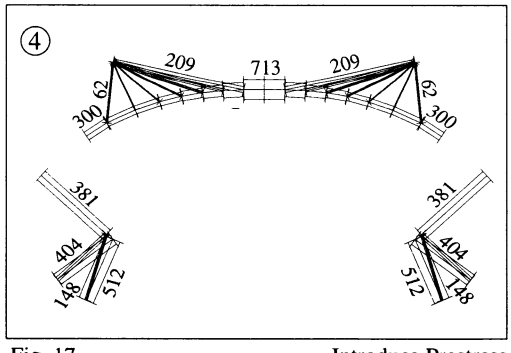

Fig. 17 Introduce Prestress

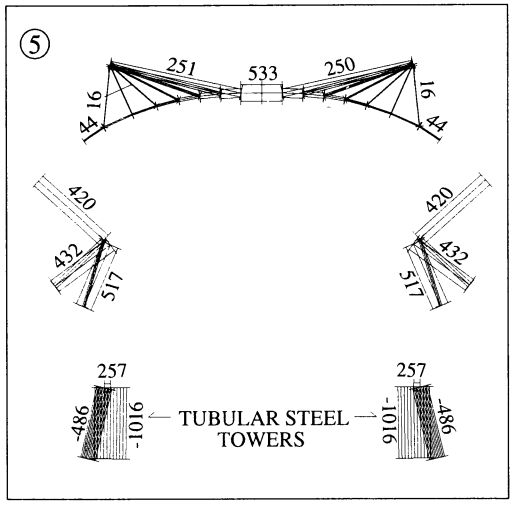

Fig. 18 Dead Load

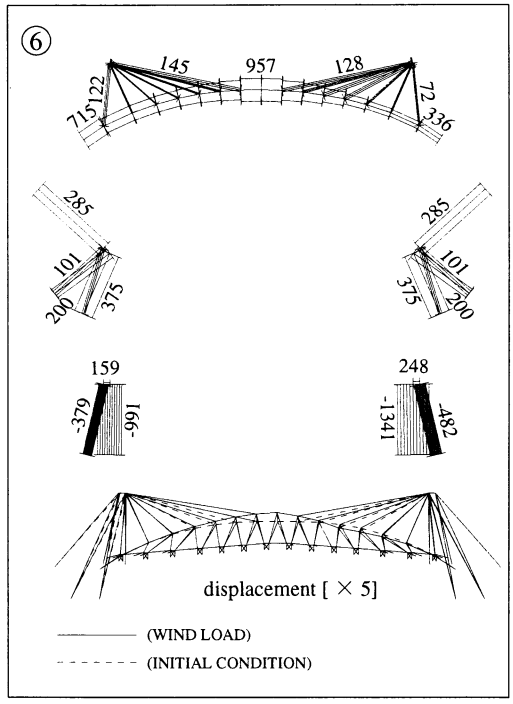

Fig. 19 Wind Load

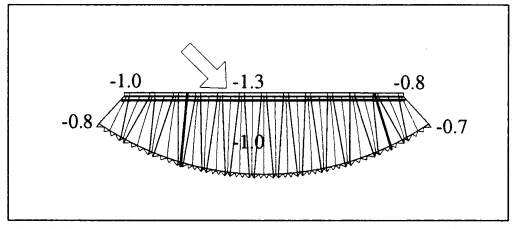

Fig. 20 Distribution of wind force coefficient

Figures 22-25 show the comparisons between the analytical results and the actual measurements. The horizontal axes of the graphs show construction steps, namely from left to right, 1) the time when suspension cable is installed and A-line is jacked down, 2) back stay cable CB9 installation time, 3) side stay cable CB13 installation time, 4) time when A-line tensile force reaches 250t, 5) time when A-line end tensile force reaches 285t ,and 6) when A-line end tensile force reaches 300t. The vertical axes show the analytical values and the actual measurement values at each construction stage.

Figure 22 shows the development, at each construction step, of the A-line tension end pull-in stroke. Figure 23 shows the development, at each construction step, of the vertical displacement at A-line center. Figure 24 and Figure 25 respectively show the development, at each construction step, of the inside and outside tower base stress. It is admissible that each set of analytical value and measurement value generally coincide with each other as to the tendency of change as the construction progresses and as to numerals.

5. FEM ANALYSIS OF STEEL TUBE TOWER TOP SUSPENSION CABLE HANGING SECTION

Eight (8) roof suspension cables and four (4) back stay cables and one (1) side stay cable concentrate at the light tower top made of two (2) steel tubes of 1200 mm each in diameter (Fig. 26).

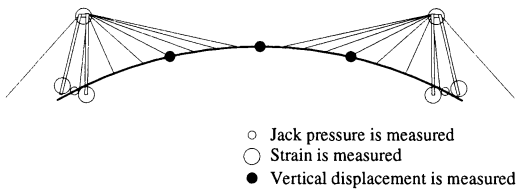

Fig. 21 Measurement system diagram

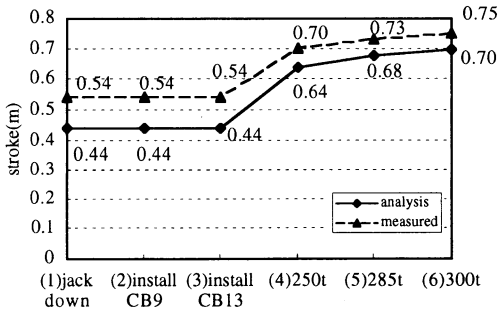

Fig. 22 STROKE OF A-LINE END

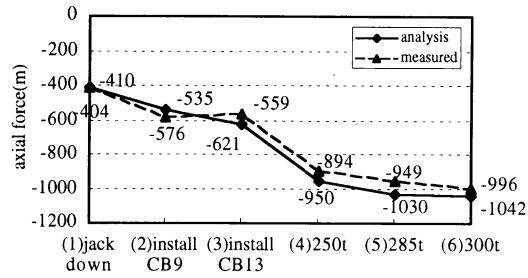

Fig. 23 VERTICAL DISPLACEMENT OF A-LINE TOP

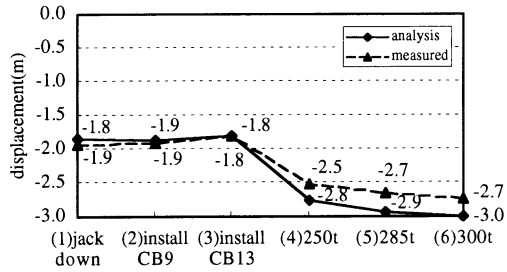

Fig. 24 INSIDE TUBULAR COLUMN

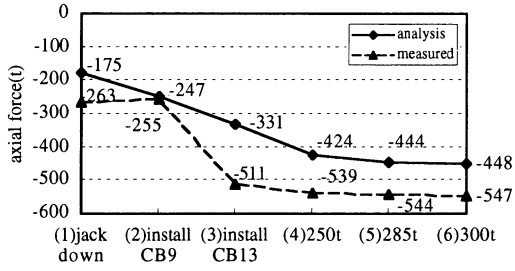

Fig. 25 OUTSIDE TUBULAR COLUMN

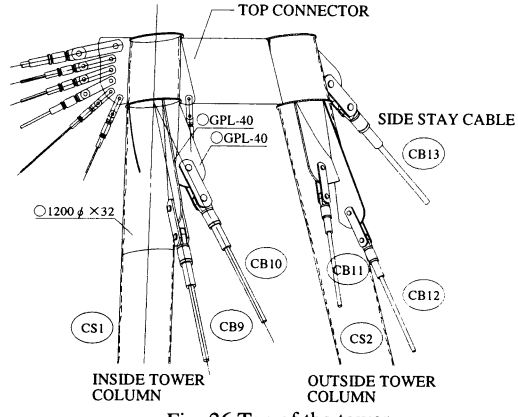

Fig. 26 Top of the tower

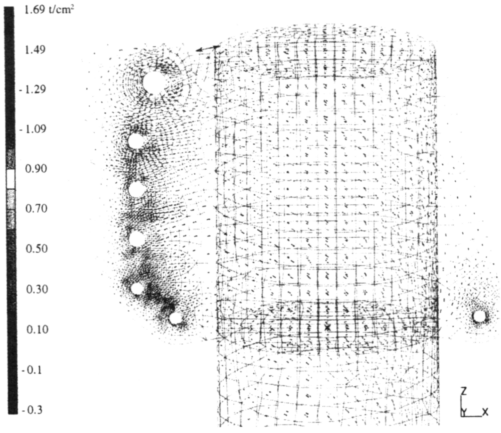

Fig. 27 Maximun principal stress

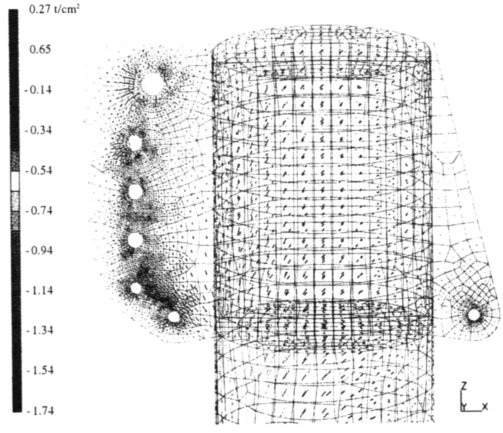

Fig. 28 Minimun principal stress

The gusset plate at the hanging section of each cable plays a very important role in gathering up this roof structure. Each of them is a through gusset plate wedged into the steel tube.

Further, this gusset plate has been modeled into a finite element model and has been confirmed to be safe at all times in all predictable loading cases(Figs. 27,28).

6. CONCLUSION

The roof of this track and field sports stadium has a suspended roof structure system introducing prestressed elements, and it really is an innovative structure without parallel. Because of its unprecedentedness, detailed analyses were conducted from the design stage taking the construction sequence factor into consideration so that the results thereof be reflected upon the design. The construction was executed with a very high accuracy carefully controlling the stress of each structural member as well as the coordinates, and the results of measurements during construction well coincided with the analytical data.

As of this date, this track and field sports stadium has been completed successfully and is waiting for the glorious days when it is to be used as the main arena for the National Athletic Meet next year.

Tubular Structures VIII, Choo & Van der Vegte (eds) © 1998 Balkema, Rotterdam, ISBN 90 5809 001 9

SPACES: Structural behaviour and characteristics of a composite tubular steel space frame bridge deck system

Allan E.Churchman & John M.C.Cadei
MSP-Maunsell, Beckenham, UK

ABSTRACT: The SPACES bridge system consists of a tubular steel space frame acting compositely with a concrete roadway slab enclosed by a shell in advanced Fibre Reinforced Plastic (FRP) material. The structural characterisation of the System is presented with particular reference to composite behaviour and associated stiffness and strength characteristics.

1. PRESENTATION OF THE SPACES SYSTEM

1.1 System profile

The SPACES bridge system (Ref. 1, 2, 3) combines an optimised steel tubular space frame, a concrete roadway slab acting compositely with the space frame, and a corrosion-free enclosure shell in advanced Fibre Reinforced Plastic material which permanently protects the steelwork against corrosion (Fig. 1). The System is designed to provide competitive solutions on initial and particularly life-cycle cost/benefit basis to a broad spectrum of bridging needs for highways, railways, and footways, ranging from girder bridges and viaducts over 50 m in span to long span cable-supported and overhead arch bridges.

The System has provision for post-tensioning by external cables running inside the enclosure. The post-tensioning allows further material weight savings to be achieved and reduces or eliminates tensile stresses in the concrete slab over supports in continuous construction.

1.2 Space frame

The space frame is normally configured as a double-layer rectangular grid connected by diagonal braces arranged on a tetrahedral pattern (Fig 2). It is an all-welded structure fabricated from tubular steel members connected either directly to each other or to cast steel nodes. Elements are connected by circumferential full penetration butt welds formed by semi-automated processes which deliver high weld quality.

1.3 Enclosure shell

The enclosure shell is formed from interlocking modular FRP components having the strength and stiffness to constitute a permanent structural platform for inspection and maintenance (Ref. 4). It is attached to the underside of the steel space frame by a system of hangers. It may be shaped to achieve particular architectural or aerodynamic objectives, and may be conformed to a variety of bridge alignments. Depending on the specific requirements

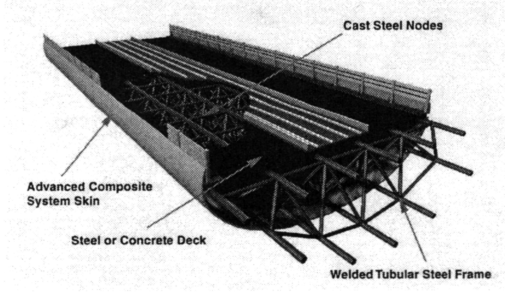

Figure 1. The SPACES System Technology

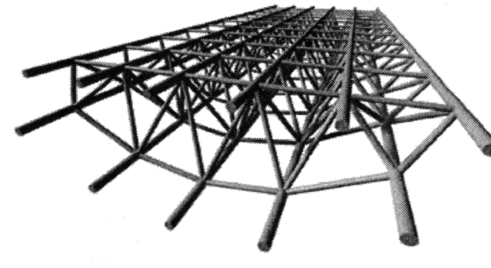

Figure 2. Space frame configuration

of the application it can be made to participate structurally with the rest of the structure to increase its torsional rigidity.

1.4 Roadway slab

The concrete roadway slab is connected to the top plane chord members by conventional shear studs. As a result of the composite action thereby obtained the stress resultants in the space frame top chord members due to concentrated loads on the roadway are reduced and the fatigue strength increased accordingly. Similarly the ultimate and fatigue strength of the space frame nodes in the top plane nodes are improved by composite action with the slab. The potential corrosion of the bottom layer of reinforcement of the slab is reduced by the presence of the enclosure.

1.5 Rational use of multiple materials

The System combines best available technologies and materials in a complementary manner so as to maximise the advantages of each whilst designing out any potential shortcomings. Concrete is used to form the top flange which is mostly in compression and is subject to the greatest fatigue loading. Steel is used to form web planes and the lower 'flange' plane of the deck where the numerically largest principal stresses are primarily tensile and therefore concrete affords little advantage.

Lightweight FRP protects the steelwork against corrosion and provides a permanent access platform for inspection and maintenance. The level of atmospheric protection within the enclosure reduces the rate of steel corrosion to about 5% of that of unenclosed steel.

1.6 Fields of application

The System is suitable for the construction of a broad spectrum of spans and usages, ranging from medium to long span bridges and viaducts (Fig. 3) to long span cable supported bridges (Fig. 4), whether for highway, railway or mixed use . The system is particularly suitable for high speed railway viaducts (Fig. 5,6).

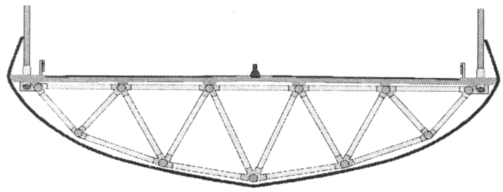

Figure 3. Long span viaduct application

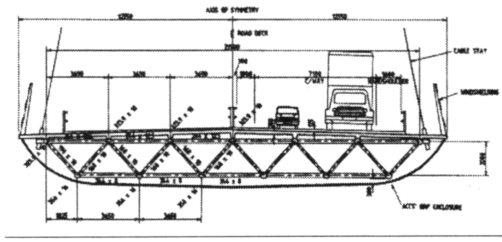

Figure 4. Cable-stayed bridge application

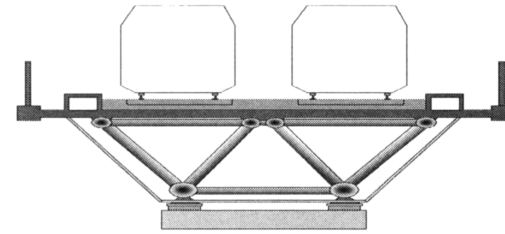

Figure 5. High speed railway viaduct cross-section

1.7 Advantages

Benefits include reduced time, cost and risk in construction and maintenance, and high quality and integrity of the completed structure. The major weight savings which the system delivers allows much larger units to be handled during construction, thereby increasing construction speed and reducing disruption caused by construction. The integrated enclosure shell enables subsequent inspection and maintenance to be carried out without causing disruption to traffic either over or under the bridge.

The enclosure shell uncouples the form from the structure opening up exciting architectural possibilities.

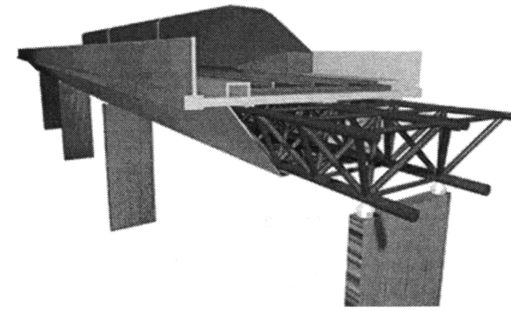

Figure 6. High speed rail viaduct visualisation

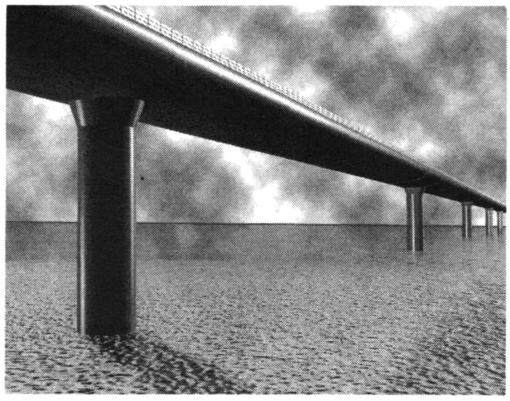

Figure 7. Visualisation of 100 m span marine viaduct

1.8 Aesthetic potential

The aesthetic potential of the System is exemplified by the bridge designs shown in Figs 7, 8, 9 which were developed as solutions within bridge competitions.

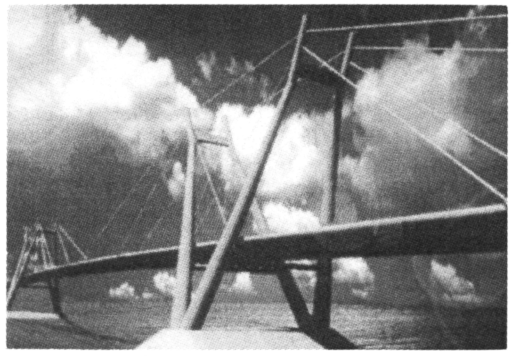

Figure 8. Visualisation of cable-stayed SPACES bridge

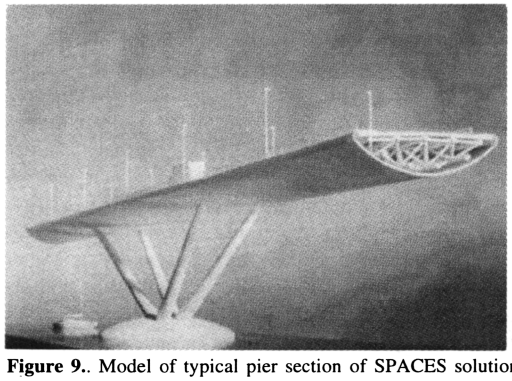

Figure 9.. Model of typical pier section of SPACES solution for visually slender crossing

2. STRUCTURAL RATIONALE

A well engineered steel space frame is a more efficient structural form than an equivalent plate or box girder, the advantage increasing with span length. The advantage is greatest in the webs, where as construction depth increases, stiffened web plates become less efficient in terms of material usage because of slenderness effects and the need for substantial stiffening.

The space frame acting compositely with the deck slab exhibits three dimensional rigidity, i.e. high torsional and transverse stiffness as well as longitudinal stiffness. Hence the deck can be handled in large erection units, typically whole spans. High torsional and transverse stiffness make for efficient distribution of concentrated load effects comparable to that obtained in a solid slab. There follows a greater ultimate load capacity and longer fatigue life for a given quantity of steel. There is no need for obstructive internal diaphragms of the type needed at piers of plate and box girder bridges. As a result, wide decks carrying dual carriageways can be carried on single central piers causing minimum visual blockage.

The high transverse stiffness is well suited for cable-supported bridge decks with widely spaced cable planes. High torsional stiffness makes the deck also suited to bridges which are skewed or curved in plan.

The greater flexural stiffness of tubular elements compared to plate and stiffener elements of comparable plate and box girders result in reduced vibration, fatigue damage, and noise emission under dynamic loadings. The concrete slab and FRP enclosure also contribute to structural damping and noise attenuation.

The static redundancy of the space frame improves safety with respect to fatigue, impact, and damage propagation. Fatigue effects in members directly under the deck slab are minimal due to composite action with the concrete slab and the use of cast steel nodes in critical high stress areas.

Circular hollow sections have optimal buckling strength in relation to weight and joints generally perform better than with other sectional shapes. The clean, stiffener-free fabrication has no corrosion traps or points which are difficult to inspect or paint.

3. BRIDGE CONFIGURATION

The objective sought in the geometric configuration of the space frame is to achieve maximum regularity and repetition of standard modules along with well-conditioned node geometry, within the overall functional and aesthetic criteria informing the design

of the bridge. The space frame grid and the enclosure can be readily configured for bridges skewed or curved in plan. The direction vector of the space frame diagonals (L_x, L_y, L_z) is selected to minimise the node and member density, thereby improving fabrication economy; and render the angles between members suitable from the point of view of node geometry and ease of fabrication. The relationship of tube diameters is selected to avoid intersection of brace footprints at nodes, maximise node strength, and facilitate automated cutting and welding. The deck span/depth ratio is chosen to optimise the weight of steel.

In girder bridges, the longitudinal chords are normally the primary members and may therefore run continuously through nodes with the other members branching off . In cable-supported bridges where there is more significant biaxial bending, chord sizes are sometimes varied across a section in order to achieve a clear separation between diameters of intersecting longitudinal and transverse chords, so as to maximise joint strength and fatigue resistance.

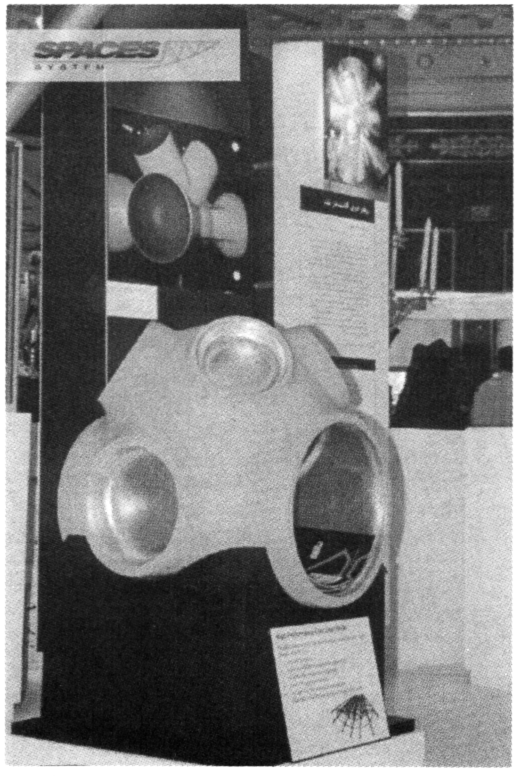

Figure 10. SPACES cast steel node *(Courtesy of River Don Castings Ltd)*

Cast steel nodes (Figure 10) are used where dictated by joint strength or fatigue endurance requirements, typically at points of high transverse load such as at bearings and in hogging moment regions of continuous viaducts. Diagonals are welded directly onto primary chord members or onto node stubs.

The cost of cast nodes is a function of the external volume of the nodes. Therefore one aims to minimise the diameter of the principal chords by adopting the minimum permissible diameter/thickness ratio in the most heavily loaded member.

4. STRUCTURAL PERFORMANCE

A naked rectangular grid space frame as used for roofs possesses considerable longitudinal and transverse stiffness due to the bi-directional array of chords but has negligible torsional stiffness. Moreover, if not properly restrained externally or braced, it can have a low global buckling strength due to lack of in-plane stiffness of the compression grid. However when the top grid is combined with a participating concrete slab, the structure acquires considerable torsional stiffness and global buckling strength. The high torsional stiffness results in low torsional rotation of the deck under eccentric lane loading, leading to a more uniform distribution of stress between longitudinal chords, the torsional moment being absorbed primarily by forces in the brace members.

The combination of high transverse and torsional stiffness gives the deck an excellent ability to distribute concentrated loads from vehicle axles and abnormal vehicles, thereby reducing fatigue stresses and other local effects. It also renders the deck particularly suitable for cable-supported bridges, where biaxial bending is more significant than in girder bridges and torsional stiffness may be required for adequate aeroelastic stability. The triangulation in the transverse plane ensures that the cross-section is relatively free from distortion.

As a result of the slab acting as a stiff shear plate in its own plane and the tetrahedral arrangement of braces, all the nodes are effectively restrained laterally. Hence the global critical buckling mode is limited to local buckling of members between nodes. Given the relatively low slenderness ratio of the tubular members, they can mobilise a high proportion of their yield strength in compression. This is in contrast to traditional thin-walled steel bridge structural forms based on steel plate and stiffeners, in which as the depth of the structure increases, the plates become progressively

weaker in buckling, and the stiffeners, which do not make very efficient use of material, become increasingly heavier, with a significant penalty in material usage. As a result, it has been found that in the 100 m span range, the weight of steel in SPACES decks approaches 50% of that in a conventional steel box girder structure.

Tubular members have the advantage of optimum compressive capacity in relation to weight; of being available in a wider range of weights than rolled steel sections, and of enabling three-dimensional joints to be readily formed without the need for complex fabrications involving stiffeners and corrosion traps. The lower slenderness of tubular brace members compared to equivalent stiffened plates also results in higher local natural vibration frequencies. As result there is less noise emission in dynamically loaded structures such as high speed railway viaducts.

5. MODELLING AND ANALYSIS

5.1 Modelling for preliminary design

Due to the resistance of the cross-section to distortion, the structure may be analysed sufficiently accurately for preliminary design purposes as an equivalent spine beam for global effects and an equivalent orthotropic plate for local effects of concentrated loads. The stiffness properties of the beam and plate can be readily determined by imposing the displacement field for the deformation mode associated with the stiffness property of interest, applying the virtual work or minimum strain energy method to determine any unknown modal parameters, and using equilibrium to obtain the stiffness value. The properties of interest for the beam model are the flexural and shear stiffnesses EI, and GA_s and the torsional and warping stiffnesses GK and EI_w, while for the orthotropic plate model the parameters are flexural stiffness D_{xx}, D_{yy}, D_{xy}, D_{33}, and shear stiffnesses S_x, S_y. Figure 11 shows the torsional behaviour mode for a uniform depth.

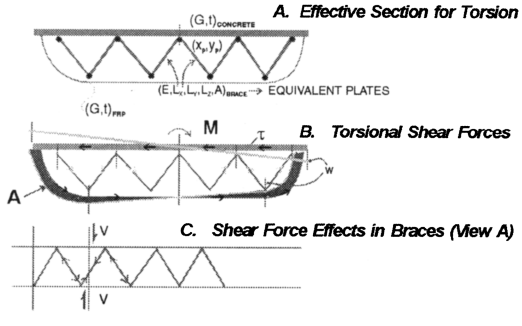

Figure 11. Torsional behaviour

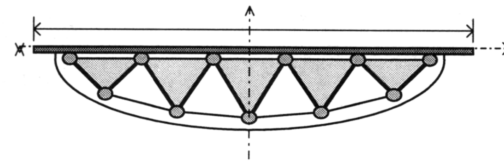

Figure 12. Transversally variable SPACES deck

The equivalent spine beam properties may readily accommodate space frames transversally variable in depth. (Figure 12.)

5.2 Loading patterns and analysis

Critical loading patterns and magnitudes are determined from beam influence lines and orthotropic plate influence surfaces which are readily obtained. Once the stress resultants in the equivalent continuous structure have been calculated by the usual methods of structural analysis (with a significantly reduced number of degrees of freedom), the stress resultants in the space frame members and the concrete slab may be derived on the basis of the methods outlined above. Thus an apparently complex structure, having a large number of degrees of freedom, can be analysed by simple methods which can be carried out manually or implemented on a spreadsheet, yielding results typically within 5% of a more accurate analysis.

5.3 Modelling for detailed design

For detailed design, the structure is analysed using the finite element method. The space frame members are modelled as three-dimensional beams and the slab by shell elements at the appropriate eccentricity from the top grid members. When used compositely, the enclosure is modelled by anisotropic shell elements. Joint elements may be used to represent the shear connectors, if required.

By virtue of the regularity and repetitiveness of the structural configuration, finite element models can be generated automatically with simple macros. The advantage of finite element modelling is that colour-coded stress resultant contour plots may be produced for specific families of elements (e.g. chords or braces), which can be also read as tube size distribution maps (Fig. 13).

The ease with which tube sizes can be varied to suit the load envelope pattern is another reason for the structural efficiency of the composite space frame. The finite element modelling takes into account the stage-by-stage incremental build-up of

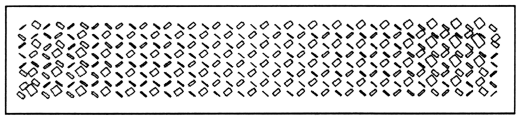

Figure 13. Typical brace maximum axial load plot

the structure, with the concrete slab being typically applied in various stages after the erection of the space frame.

5.4 Design of structural elements

Structural elements are designed for strength considering factored extreme load effects and ultimate strength, and for fatigue and durability under actual load spectra. Nodes are designed for strength and fatigue using when applicable parametric strength equations given in such references as [Ref. 7,8], modified for multiplanar joints [Ref. 6]. Otherwise nodes are analysed by finite element analysis, assuming the Von Mises yield criterion in the strength analysis and the hot spot stress criterion as defined in BS 7608:1993 in the fatigue analysis. Fig. 14 shows a typical FE mesh for a node in the outside edge.

6. CONTRIBUTION OF ENCLOSURE SHELL

The primary purpose of the FRP enclosure is to provide long-term corrosion protection to the tubular space frame and access for inspection and maintenance. In terms of material, it is typically equivalent to a 10 mm thick FRP plate weighing 20 kg/m^2 and the elastic properties of the e-glass/polyester composite material are in the order of E_x= 20 GPa, E_y= 8 GPa, ν_{xy}= 0.18, G_{xy}= 4.0 GPa.

The shell is not normally required to act compositely with the space frame, but can be made to do so if advantageous for the application. When not acting compositely, the fixings and joints are designed to accommodate relative movements between the steel and the composite. If connected so as to act compositely, the enclosure has little impact on the longitudinal stiffness of the lower grid because of its low longitudinal modulus and area. However in applications in which the lower grid is not triangulated, and therefore does not possess significant shear stiffness, the enclosure shell can make a significant contribution to the global torsional stiffness of the deck.

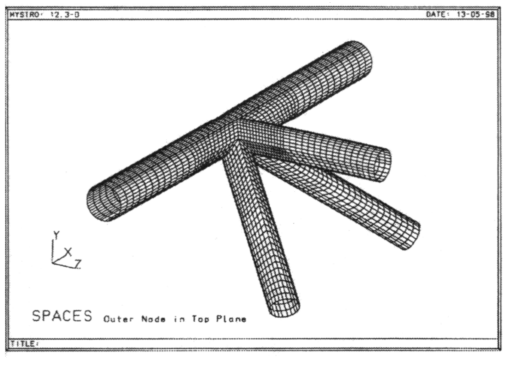

Figure 14. Node finite element model

7. KEY DESIGN ISSUES

7.1 Fatigue strength of connections

The fatigue strength of nodes can be critical particularly in cable stayed bridges where the state of stress is significantly biaxial resulting in the forces in primary and secondary chords having the same order of magnitude. The following approaches towards achieving the required fatigue strength may be adopted:

a) using cast steel nodes more extensively
b) varying the chord sizes across the section
c) reducing the moments in secondary chords by separating them structurally from the deck slab
d) passing the secondary chords through the primary chords.

On the basis of current cost profiles the first option is somewhat more costly. The other options are often economically more attractive and have been shown to greatly reduce the stress concentration factors in the tube walls.

7.2 Slab design and shear connection between space frame and slab

The slab is always connected to the primary chords by shear connectors and may or may not be connected to the secondary chords. Steel

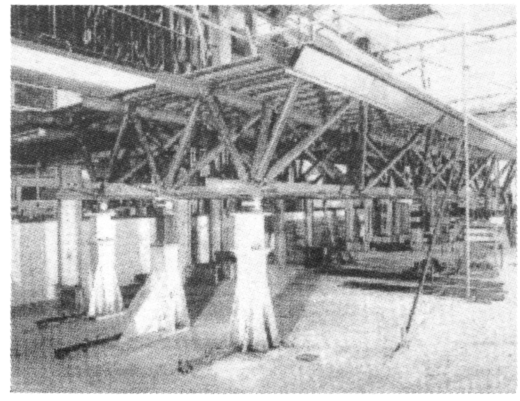

Figure 15. Cambridge half scale model of SPACES deck

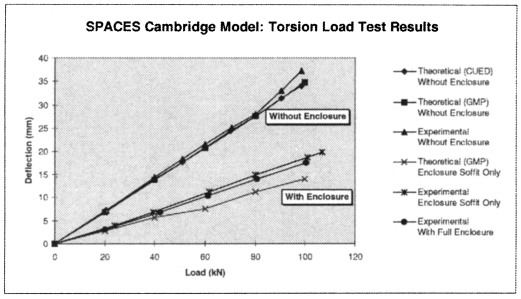

Figure 16. Comparison of experimental and theoretical results with and without participation of FRP shell

reinforcement free slabs using fibres as an alternative may be used when the slab span to depth ratio is suitable. When connected to both primary and secondary chords the slab spans two ways resulting in improved stiffness and distribution of concentrated wheel loads.

8. VALIDATION TESTS

Tests were carried out at the University of Cambridge [Ref. 9] on a half full scale model of a composite space frame deck (Fig. 15). These demonstrated that in that instance the shell increased the torsional stiffness by about 50% (Fig. 16). Clearly in larger bridges the enhancement would be less, and in general when it is necessary to increase the shear stiffness of the lower grid it is sometimes more economic to do so by adding in-plane bracing.

9. MATERIAL QUANTITIES

Fig. 17 shows a graph of steel quantity versus span length for optimised composite steel plated structures and SPACES structures. It can be seen that especially in spans exceeding 60m there is a significant saving in steel weight, approaching 50% in longer spans. The weight saving is particularly beneficial when the structure has to be erected over water, and/or when the deck is supported by primary

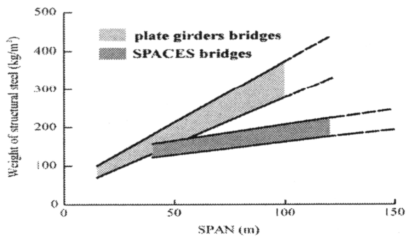

Figure 17. Steel quantity versus span for steel composite bridges

structures such as cable systems or arches, and in seismic areas.

The space frame normally has a lower volume of welding, greater standardisation of elements, and a lower fabrication component count than conventional steel box girder structures. Furthermore the weight of a typical deck unit is significantly lighter leading to lower handling installation and overall constructions costs. However, while the cost of a fabricated deck unit will normally be competitive with plated structures the increased cost of tubulars and nodes will lead to a higher unit rate per fabricated tonne of steelwork.

10. FABRICATION AND CONSTRUCTION

In the case of welded brace-to-chord connections Fig. 18), the detailed joint geometric data needed to define member end profiles and continuously variable member edge bevel angles is calculated by computer programme. The brace members are cut, profiled, and bevelled by automatic milling machines. Welding is carried out by semi-automated processes where convenient.

The space frame is erected in complete span units. The rigidity of the frame makes it possible to achieve good fit-up to facilitate in-place butt welding. Since SPACES decks are usually continuous over intermediate supports, the construction of the concrete slab is sequenced to minimise permanent tension in the slab. In some applications post-tensioning cables are used within the space frame to prestress the slab. Slab panels are typically cast on permanent formwork, which can be propped off the space frame lower grid. When there is a sufficient gap between the slab and the transverse chords, the slab can be cast on a travelling form.

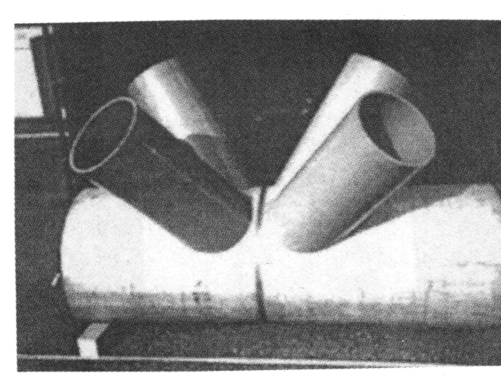

Figure 18. Assembly of fabricated node *(Courtesy of NKK)*

11. CONCLUDING REMARKS

The SPACES decking system is one of the most advanced bridge deck forms being structurally highly efficient due to its high transverse and torsional stiffness. For longer span bridges this leads to cost effective structures with significant savings in materials which in turn can significantly reduce erection weights of whole spans. The structure can be readily dimensioned for preliminary design by modelling it as an equivalent orthotropic plate or spine beam. The System allows for the separation of the primary structure and the aerodynamic profiling and opens up interesting aesthetic possibilities which also result in low cost of maintenance and operation.

12. REFERENCES

1. Churchman A E, Cadei J M C, "SPACES System: A new concept in bridge design, construction, and operation", 23rd European Transport Forum, 1995.
2. Churchman A E, Cadei J M C, "SPACES: A new concept in bridge construction", Int. Conf. New Technologies in Structural Engineering, Lisbon, July 1997
3. Cadei J M C, Churchman A E, "The Design Approach for a New Composite Space Frame Bridge System", IABSE Conference on Composite Construction- Conventional and Innovative, Innsbruck, 1997
4. Head P R, Thorpe J E, Irvine R A "The use of advanced composite materials for bridge enclosures", Int. Conf. New Technologies in Structural Engineering, Lisbon, July 1997
5. CIDECT, " Design guide for circular hollow section (CHS) joints under predominantly static loading"
6. Paul J, Makino Y, Kurobane, "New ultimate capacity formulae for multiplanar joints", Tubular structures V, 1993.
7. Efthymiou M, "Development of SCF formulae and generalised influence functions for use in fatigue analysis", 2nd Revision, Offshore Tubular Joints Conference (OTJ '88), USG Offshore Research, Englefield Green near Egham, UK
8. CIDECT, "Design Guide for Structural Hollow Sections in Mechanical Applications", 1995
9. McConnel R E, Sebastian R M, "Testing of a Composite Space Truss Bridge with GRP Panels", CUED/D - Struct/TR.149(1995), Technical Report, University of Cambridge, 1995

Tubular Structures VIII, Choo & Van der Vegte (eds) © 1998 Balkema, Rotterdam, ISBN 90 5809 001 9

Aluminium multi-planar hollow section traffic sign structures

F.Soetens
TNO Building and Construction Research, Delft & Eindhoven University of Technology, Netherlands
W.M.G.Courage
TNO Building and Construction Research, Delft, Netherlands

ABSTRACT: Currently, overhead highway traffic sign structures in The Netherlands are triangular space frame girders composed of circular hollow steel sections supported by two X-shaped columns consisting of rectangular hollow steel sections.
However, the Dutch Ministry of Transport has initiated the development of traffic sign structures focusing on the use of sustainable materials and low maintenance costs. Therefore, four aluminium gantries have been designed and built.
The predominant loading is wind which is reflected in the overall size of the space frame structure: the horizontal dimension of the triangular space frame is larger than its vertical dimension. In addition to the static design a fatigue analysis was carried out in order to assess the lifetime of the structure.

1 INTRODUCTION

Aluminium applications have rapidly increased in Europe the past decade and an even quicker growth is expected in the forthcoming years. In addition to well-known building applications like windows and doors, an important part of the above growth is foreseen for load-bearing applications. Aluminium has a lot of favourable properties for use in structural applications. However, its use is hampered by a number of reasons such as:

- Limited knowledge about the structural behaviour of aluminium.
- Design rules missing or not up-to-date.
- Knowledge transfer insufficient.

To overcome the above problems many national and international research projects have been carried out dealing with various topics such as fatigue (Soetens, Van Straalen & Dijkstra 1995). Most of these projects have resulted in improved design rules for structural applications (Eurocode 9 1998), (NEN 6710 1991). As far as knowledge transfer is concerned a European initiative was undertaken by the aluminium industry which resulted in a training program to be used for students but also for designers in industry (TALAT 1995).

Many structural concepts for aluminium are based on steel solutions, which is obviously not the best solution for an aluminium structure.

In order to take advantage of the beneficial properties of aluminium it is important to think aluminium from the beginning and optimise the structure with respect to design, material selection and fabrication process.

The next chapter is focused on the structural use of aluminium in general, while in chapter 3 the aluminium traffic sign structure is dealt with.

2 STRUCTURAL USE OF ALUMINIUM

The use of aluminium in structural applications is favoured by the following physical and mechanical properties:

- low density, about one-third for steel (see also Table 1);
- high strength and ductility, even with very low temperatures;
- optimum cross-section design in particular through extrusion;
- good machinability;
- high corrosion resistance as a result of a resistant oxide layer;
- very good recyclability , re-use at an equal level of application.

Some less favourable properties have to be taken into account, like:

- low modulus of elasticity, one-third of steel;

Table 1. Comparison material properties aluminium versus steel.

Material properties	Aluminium	Steel
Density [kg/m^3]	2700	7800
Modulus of elasticity [N/mm^2]	70000	210000
Shear modulus [N/mm^2]	27000	81000
Thermal elongation [K^{-1}]	23x10^{-6}	12x10^{-6}

- low melting point ($\pm$ 650^0 C), low strength at high temperatures;
- high thermal elongation, two times steel equivalent;
- fatigue sometimes determinant factor.

The most important aluminium properties compared to steel are given in Table 1.

For structural applications pure aluminium cannot be used because of its low mechanical properties. However, many aluminium alloys are available with mechanical properties comparable to structural steels.

As stated above one of the advantages of aluminium is an optimum cross-section design by means of extrusion. Aluminium is heated up to $\pm$ 400^0 C and then pressed through a die, which allows for simple, open cross-sections but also complicated, hollow sections including stiffeners as well as joint details. Examples of extrusions are given in Figure 1.

3 ALUMINIUM TRAFFIC SIGN STRUCTURES

3.1 *State of the art*

Up till now overhead traffic sign structures used at highways in The Netherlands consist of triangular space frame girders composed of circular hollow steel sections supported by two X-shaped columns consisting of rectangular hollow steel sections. Since the Dutch Ministry of Transport is looking for new sustainable materials in various applications, TNO and Alcoa Nederland - a subsidiary of Alcoa USA - developed an aluminium overhead traffic sign structure. According to a directive of the authorities the aluminium design had to look similar to the steel design i.e. a triangular space frame girder and X-shaped columns (see Figure 2).

However, the cross-section of the chord beams and the braces are typical aluminium extruded shapes (see Figure 3).

The flat surfaces of the chord beams have been chosen as such to facilitate welding of the braces while the bridges in the cross-sections of the chord beams should reduce the stress concentrations along the perimeter of the connection (see also 3.3).

3.2 *Static design*

To determine the static strength and deformations of the structure as indicated in Figure 2, finite element calculations were carried out using the TNO FEM-

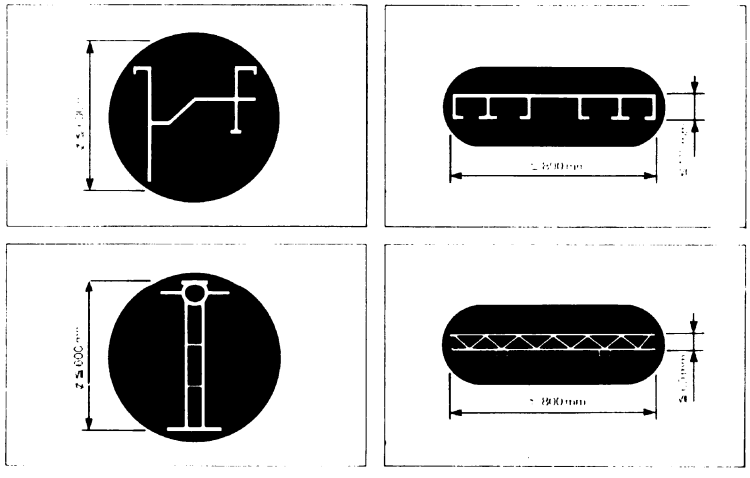

Figure 1. Cross-sections aluminium extrusions. Maximum dimensions in mm.

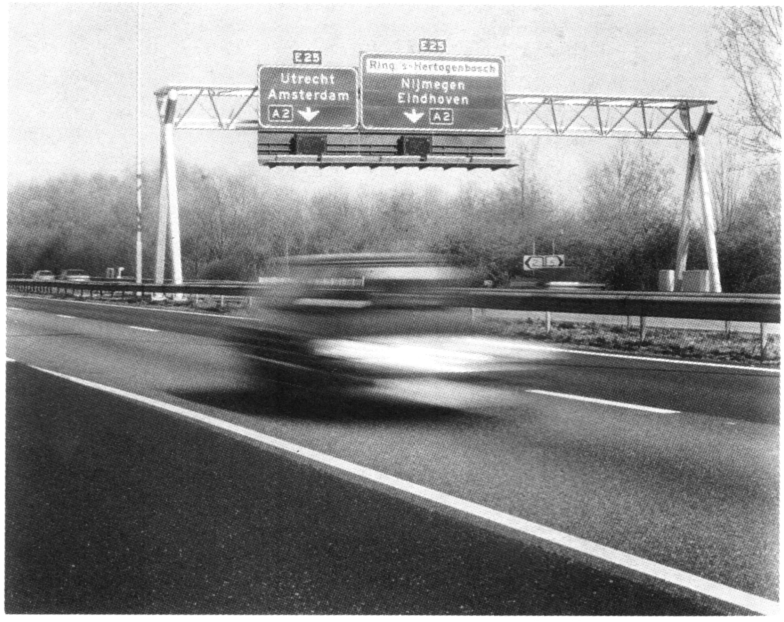

Figure 2. Aluminium overhead traffic sign structure.

program DIANA and applying 3-dimensional, 2-nodes Timoshenko beam elements. The aluminium alloy chosen was 6005A-T6 which has a proof strength $f_{0.2}$ = 210 N/mm^2; a tensile strength f_t = 260 N/mm^2; and a rupture strain ε_u = 8 %.

As far as loads and load combinations are concerned, wind loading is dominant. For the design wind loads and wind velocities at a height of 40 m were taken into account according to NEN 6702. The drag coefficients for the various parts of the structure were determined according to BS 8100.

The dynamic enhancement factor was fixed at 1.1, based on earlier calculations and measurements which varied between 1.04 and 1.08. Except for wind in three directions ($\perp$, $\parallel$ and under 45^0), the weight of the structure, and the settlements of the foundations were considered. In total 11 load combinations were applied.

The forces in the gantry as a result of the governing load combinations were checked according NEN 6710. The welded joints between braces and chords have been evaluated according NEN 6772 with yielding of the chord surface as the governing criterion. The bolted joints between the triangular space frame and the columns, and at the column base-plate have also been checked according NEN 6772.

3.3 *Fatigue design*

To determine the number and size of the stress ranges to be taken into account for the fatigue analysis, the dynamic response of the structure induced by wind loading is calculated according to (Staalduinen & Courage 1996). For the description of these loading cycles, an analytical description of the probability density functions of the long term wind climate has been used. Further, analytical descriptions of along wind turbulence have been employed. By using random generation of wind fields, the static, quasi-static and dynamic response of structures can be calculated. First the structure is assumed to have an quasi-static response to the wind load.

This quasi-static response can be assessed by calculating the dynamic pressure and combining this with force coefficients of the structure concerned. Combining these with the above mentioned description of the loading cycles, results in a quasi-static contribution of stress cycles in the structure. For the gantries the finite element-model was used in determining the relation between static wind load and static stress in a large number of members of the structure. For the dynamic response, frequency domain techniques are employed since the coherence functions of aerodynamic admittance functions can be easily taken into account in the frequency domain.

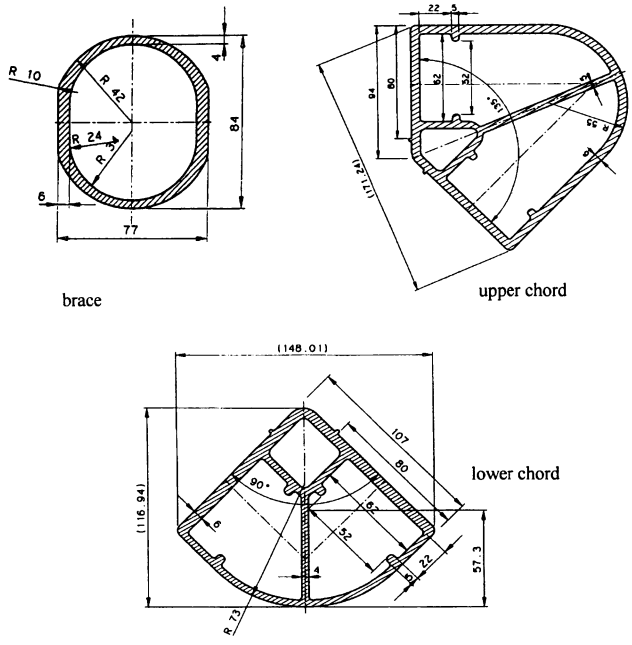

Figure 3. Cross-sections members triangular space frame.

Hence, the modal wind load on the structure can be assessed in terms of force spectra and the corresponding modal response can be calculated. Using the finite element-model, natural frequencies and mode shapes of the first four vibration modes were calculated.

In Figure 4 the eigenmode of the first natural frequency of a 21 m gantry is shown. Subsequently the relations between modal displacements and stress in the various members monitored were determined. Using these relations in the modal response due to the wind load then gives additional contributions the stress ranges for the structure. Additionally at the hot spots of the welded joints between braces and chords stress concentration factors (SCF) have been taken into account based on a detailed FEM-analysis (Gräf 1997), see also Figure 5.

Maximum SCF-values ranged up to 4.4 for example the chord saddle point in case of out of plane bending. Typical SCF-values were similar to steel

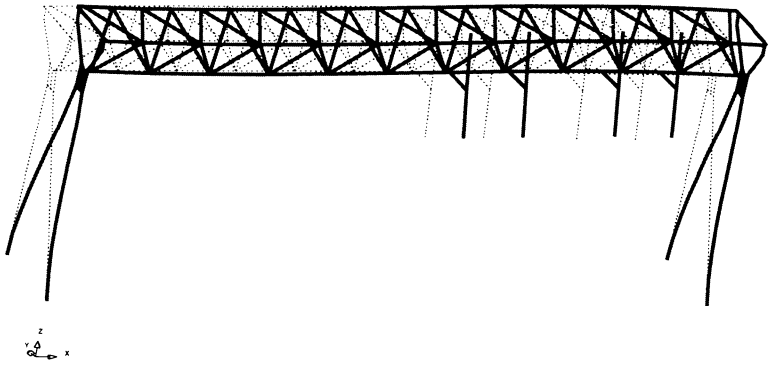

Figure 4. Eigenmode 1 aluminium gantry, frequency = 3.06 [Hz].

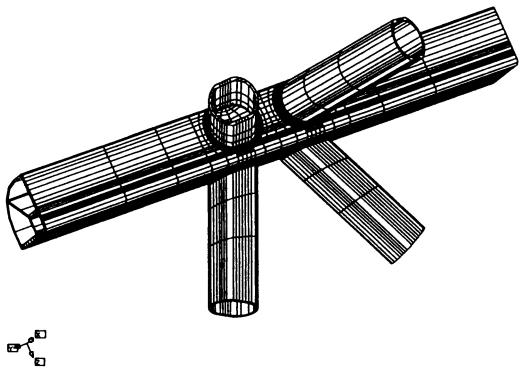

Figure 5. FEM-model welded space frame joint.

values. However, chord cross-sections without bridges showed much higher SCF-values (up to 8 times higher !)

Based on the above SCF-values quasi-static stress ranges have been determined as well as cumulative stress spectra. For the governing hot spots the fatigue damage due to quasi-static loading as well as due to the dynamic response has been evaluated taking into account the well-known Miner-rule and SN-curves according (ECCS 1992). The above evaluation demonstrated that the design of the aluminium gantry easily satisfied the required lifetime of 25 years (Courage, Soetens & Steenhuis).

4 CONCLUDING REMARKS

As elucidated in 3 the design of the aluminium overhead traffic sign gantry fulfils the requirements regarding static strength and fatigue life.

Based upon the above study a pilot project of 4 gantries was approved by the Ministry of Transport and subsequently those gantries were built by Alcoa Nederland. Finally, the gantries were put in place in March 1997. It is to be expected that the above aluminium alternative will be able to compete in the near future with the steel gantries used nowadays.

In general, the above described aluminium gantry underlines the statements of 2 regarding the structural use of aluminium. The aluminium gantry has a number of advantages compared to its steel equivalent of which the easy assembly and the sustainability without any corrosion protection are the most important in this case. And the disadvantages such as a lower E-modulus and a lower fatigue strength than steel are easily overcome.

REFERENCES

Soetens, F., IJ.J. van Straalen & O.D. Dijkstra 1995. European research on fatigue of aluminium structures. *Proceedings 6th International Conference on Aluminium Weldments.* Cleveland, Ohio.

Eurocode 9 1998. Design of aluminium structures. *CEN/CS.* February 1998, 1st edition. Brussels.

NEN 6710 1991. Aluminium structures. Basic requirements and basic rules for calculation of predominantly statically loaded structures. *NNI.* TGB 1990. Delft.

TALAT 1995. Training in aluminium application technologies. *European Aluminium Association.* Brussels.

NEN 6702 1991. Loadings and deformations. *NNI.* TGB 1990. Delft.

BS 8100 1986. Lattice towers and masts. Codes of practice for loading. Part 1. *British Standards Institution.* London.

NEN 6772 1991. Steel structures - connections. *NNI.* TGB 1990. Delft.

Staalduinen, P.C. & W.M.G. Courage 1996. Wind induced fatigue of slender light weight structures. In Structural dynamics-EURODYN '96. Augusti, Borri & Spinelli (eds). Rotterdam: Balkema.

Gräf, H. 1997. Stress concentration factors of a KK-joint in an aluminium road sign gantry. TNO-report 97-CON-R1282. Rijswijk.

ECCS 1992. European recommendations for aluminium alloy structures - fatigue design. Brussels.

Courage, W.M.G., F. Soetens & M. Steenhuis 1996. Design of Alcoa 22 m gantry. TNO-report 96-CON-R1202-01. Rijswijk.



Taylor & Francis
Taylor & Francis Group
http://taylorandfrancis.com

Tubular Structures VIII, Choo & Van der Vegte (eds) © 1998 Balkema, Rotterdam, ISBN 90 5809 001 9

Fatigue design of welded aluminium rectangular hollow section joints

P.J. Haagensen & K.A. Macdonald
Norwegian University of Science and Technology, Department of Structural Engineering, Trondheim, Norway

ABSTRACT: Fatigue design methods for welded aluminium joints are reviewed, including various approaches to fatigue life estimation currently adopted in design codes across a range of industrial applications. The applicability of these established methodologies to the fatigue design of automotive space frame structures is critically assessed. The hot spot stress method is identified as the most promising in terms of providing a coherent and comprehensive approach to design. Particular problems related to implementation are considered such as failure sites and determination of appropriate stress concentration factors from physical models, finite element calculations or parametric equations. Preliminary results from finite element stress analyses and fatigue test are also presented for rectangular hollow sections welded in a T-joint configuration. Recommendations are made for a design methodology for welded rectangular hollow-section joints in aluminium space frames, including use of a single hot spot *S-N* curve.

1 INTRODUCTION

Aluminium welded hollow section (RHS) joints are finding increased use in crane and bridge structures, transport vehicles and in automotive structures. Tubular structures are occasionally fabricated using forged or cast nodes but these are more expensive to produce than welded inter-tube connections which are consequently more common. However, the fatigue design basis for welded RHS joints in aluminium is limited and no design recommendations currently exist for such joints. An appropriate starting platform from which to establish a fatigue design methodology could be the experience recently gained with similar structures fabricated in steel. In particular, fatigue assessment based on the geometric hot spot stress range (or hot spot stress) concept could be adopted for aluminium structures. However, in automotive design the material thicknesses tend to be smaller than those used in civil engineering design and this difference might limit the possibilities for transfer of data from the steel industry.

This paper gives a brief overview of fatigue assessment procedures used in the design of steel tubular structures. The limited *S-N* data available for aluminium RHS joints are presented and the need for further experimental research is outlined.

Trends in the development of design codes are also discussed in light of the fact that international codes are rapidly harmonising through co-operation between organisations such as ISO (International Standards Organisation), CEN (Comité Européen de Normalisation) responsible for Eurocodes, IIW (International Institute of Welding) and API (American Petroleum Institute).

2 FATIGUE LIFE ASSESSMENT METHODS FOR WELDED TUBULAR JOINTS

In the majority of current fatigue design codes there are two generic types of *S-N* curve used. In conventional welded structures involving plates and beams the *nominal stress* approach is normally employed where the different fatigue behaviour of various structural elements or details is described by assigning to them different *S-N* curves, termed design categories or classes, and combining these with nominal stresses remote from the weld.

Since fatigue failure in welded constructions is not only related to geometry, the direction of loading and failure site also influences joint categorisation.

Examples of design categories are such basic connections are joints with butt or fillet weld, having different design categories dependent on the stress direction. The main advantage of the nominal stress approach is that the *S-N* curves for each weld category (or weld class) include of the notch effect of the weld as well as the effect of the component geometry. The main sources of scatter due to fabrication variables are thus included in the test data used to create the curve. Nominal stresses are calculated from a structural analysis and comprise membrane the stress range, S_m and the bending stress range S_b, in general $S = S_m + S_b$. The complexities of and interactions between geometry and loading found in some structures, e.g. in circular section tubular joints, give rise to a plethora of possible failure sites and here the *hot spot stress* approach is used to reduce the design to a common basis. Additionally, the difficulties encountered in defining a nominal stress in complex structures also makes the hot spot approach the only practicable method. Fatigue failure will occur at sites of high peak stress in such joints and it is assumed that fatigue life is related to the magnitude of these peaks. Fatigue design is accomplished by combining knowledge of these local stress peaks - usually in the form of a stress concentration factor (SCF) for a particular load configuration - with an *S-N* curve representing a simple weld without any structural SCF.

2.1 *The geometric hot spot stress approach - circular hollow-section (CHS) joints*

The hot spot approach has been used extensively in the offshore industry in the analysis of results from tests on steel tubular joints (Marshall 1996). Stresses in circular hollow -section (CHS) joints arise from three main sources:

- The basic stress response due to the global action of the remote applied load, i.e. the stress that can be calculated from a frame analysis disregarding the stress concentrating effects of both the joint and the weld.
- The geometric stresses resulting from local bending of the tube walls to maintain compatibility between the members.
- The highly local stress near the intersection lines between members. These local stresses are strongly influenced by the weld shape.

The maximum stress (or notch stress), located at the weld toe is the sum of the nominal stress, the geometric stress and the local stress components. The geometric hot spot stress range or hot spot stress concept has evolved as the most practical basis for fatigue design of welded joints. It captures fictitious local stress that characterizes the fatigue performance of the joint, but excludes the very local stress perturbations caused by changes in the weld toe geometry. Also excluded are the effects of any undectable defects. These effects are included in the *S-N* curve. The hot spot stress concept places different structural geometries on a common basis, enabling the use of a single *S-N* curve. The hot spot S_h is tied to the global loads in the structure through:

$$S_{HS} = SCF \times S_{nom} \qquad [1]$$

where S_{nom} is the nominal stress range and the stress concentration factor (SCF) is normally obtained from either finite element analyses or from strain gauge measurements. It is important hat consistency with the *S-N* curve is maintained by using the same method for estimating the hot spot in the fatigue test as used in obtaining SCFs. The hot spot stress method for steel CHS joints has been validated by *S-N* data for different types of joints and loading conditions that plot into a single scatter band (Marshall 1996).

There is general agreement that the hot spot is located at the weld toe but there are many opinions as to the proper method of determining the hot spot from strain gauge measurements. In the early US practice for offshore structures, the API and AWS codes defined the hot spot stress range as the total stress range measured by a strain gauge placed adjacent to the weld toe, perpendicular to the weld, i.e. an attempt was made to measure the maximum stress at the weld toe, including the notch effect of the weld. Typically hot spot gauges were placed within 6 mm to $0.1\sqrt{rt}$ of the weld toe with a gauge length of 3 mm, r and t referring to the outside radius and thickness of the instrumented member.

In the European Coal and Steel Community (ECSC) method (Radenkovic 1981), also for offshore steel structures, an extrapolation in made from two strain gauges placed just outside the weld notch zone and in the region of stress linearity to determine the geometric hot spot stress range. This method is also used for non-linear stress distributions. In the Det Norske Veritas (DNV) method (Gibstein & Moe

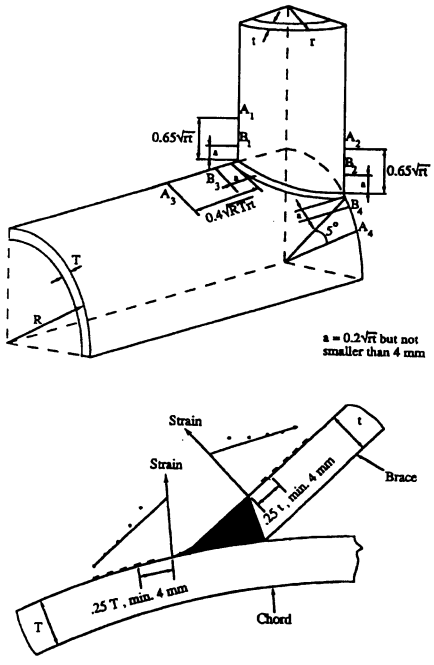

Figure 1 Recommended location of strain gauges to measure hot spot stress in tubular joints, ECSC (top) and DNV (bottom)

1985) for offshore structures many strain gauges are placed near the weld to allow for a more accurate determination of the region of hot spot stress. The ECSC and the DNV recommended locations for the strain gauges are shown in Figure 1. The ECSC definition is based on the maximum principal stress, i.e. the stress components are extrapolated to the weld toe and the maximum principal stress calculated. The stress normal to the weld used in the US definition is somewhat lower than this but in the regions of highest stress, the crown and saddle location the two are almost identical.
In the IIW design recommendations (Hobbacher 1996) a non-linear (quadratic) extrapolation procedure is recommended for cases of high local shell bending stresses caused for example by eccentric attachments in large diameter tubes or plane plates. The quadratic extrapolation requires a minimum of three strain gauges and is based on points on a curve, fitted to the strain gauge measurements by regression analysis.

The SCF is determined by several methods:

- Physical models using strain gauges, as outlined above.
- Finite element methods using appropriate meshes which model the overall joint geometry without actually modeling the weld.
- Parametric formulae, based on either strain gauge measurements or FEM.

In the finite element analysis care must be taken to obtain stresses at positions for extrapolation that are consistent with the definition of the hot spot stress used. In the IIW recommendations (Ref. 2) detailed instructions are given for the FEM analysis.

The value of the SCF is critical for the accuracy of the predicted life, and large efforts have therefore been made to assess available data to define sets of parametric equations for use in design codes. In the latest Health and Safety Executive revision (HSE 1995) of the guidance for offshore structures, two sets of parametric equations (Efthiumiou 1988, HSE 1991) are recommended for design of tubular CHS joints. A comprehensive survey of the changes in the HSE guidance has recently been presented (Stacey and Sharp 1995). Changes similar to those in the HSE guidance are likely to be implemented in the API code for offshore structures which is currently undergoing extensive revisions which are aimed at producing a new ISO code for offshore structures. The new ISO code is in turn intended to become the Eurocode 3 (steel structures) fatigue clauses for offshore structures (Baerheim & al. 1995). Since there is a trend towards harmonization of European design rules, the new ISO provisions in Eurocode 3 for hot spot based fatigue assessment of tubular structures are expected to influence the hot spot assessment procedures in future versions of Eurocode 9 for aluminium structures.

The *S-N* curve to be used with the hot spot concept is usually identical to or very similar to the *S-N* curve for a simple butt weld. In the early (1984) Department of Energy guidance on which NS 3472 (Norsk standard 1984) for steel structures are based, the T-curve for tubular joints is almost identical to the D-curve which applies to transverse butt welds in plate structures. This follows from the definition of the hot spot stress. For a transverse butt weld in a plate or pipe there is no geometric stress concentration and the SCF = 1. Therefore the associated hot spot stress *S-N* curve should only include the effect of the weld, i.e. the *S-N* curve for a transverse butt weld should be used.

The physical size of the joint under consideration is important because the size of the strain gauge limits the distance from the weld to the locations of the gauge. In thin-walled structures the gauge has therefore to be placed farther away from the weld than has been possible in offshore steel joints, and special guidance has therefore evolved for thin section welded joints

The effect of plate thickness is usually handled the same way in design recommendations for the hot spot stress method as for the nominal stress method. A thickness penalty factor is imposed for plate thicknesses greater than the reference thickness, t_o. The penalty factor, when applied to the stress range, is usually expressed as:

$$\frac{S}{S_o} = \left(\frac{t_o}{t}\right)^q \qquad [2]$$

where S is the stress range at thickness t.

In most of the older rules the value of thickness exponent q is 0.25. However, assessment of recent research data has indicated stronger influence of thickness and in the latest HSE and API/ISO revision for offshore structures a higher penalty factor of $q = 0.30$ is given

2.2 *Rectangular and square hollow-section joints*

The considerable knowledge gained regarding the static stress response of circular hollow-section joints is unfortunately not directly transferable to rectangular hollow-section joints because of marked differences in the behaviour of the latter(van Wingerde & al. 1993) The stiffness distribution in the flat sidewalls is different from that of cylindrical shells and the chord corners near to the brace walls have a strong influence on the maximum stress. Interest in joints of this type has been confined to those made in steel (van Wingerde et al.1995) and recommendation have been made on the selection of hot spot stress definition, parametric equations for SCFs and on appropriate *S-N* curves for RHS joints (van Wingerde 1996). In contrast, static stress and fatigue guidance for RHS joints in aluminium are absent in the literature and little data exists. Some fatigue test results have been reviewed (Kosteas & Gietl 1996) but the data are not analysed in terms of local or hot spot stress, but these data nonetheless indicate hat a design hot spot stress range (FAT value) of 40MPa would be applicable to welded square hollow-section joints.

2.3 *The hot spot stress concept applied to plate joints*

Recent fatigue design guidance for welded details in steel ship structures (Det Norske Veritas 1996a), and similar guidance for aluminium ships (Det Norske Veritas 1996b), have in both cases adopted a hot spot stress approach, due mainly to the geometric complexity of the internal hull structure of modern ships making it difficult to define nominal stresses. The guidance favours the maximum local stress at the weld toe (called the notch stress) over the extrapolated geometric stress described earlier, see Figure 3. The effect of the local weld geometry is therefore included in the notch stress, dictating that the same effects are excluded from the *S-N* curve, which is consequently elevated above that for a butt weld by a factor of approximately 1.5.

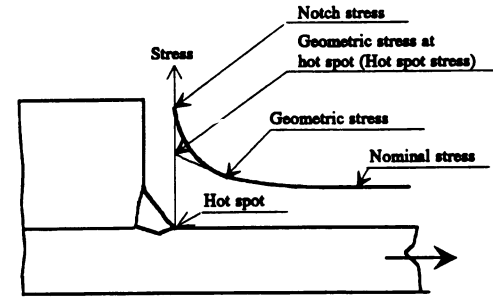

Figure 2 Notch hot spot stress (Det Norske Veritas 1996a)

The notch stress concept is attractive in that it is an actual stress, in contrast to the fictitious extrapolated hot spot stress already described. In both practical and numerical applications, however, the notch stress approach is problematic. The two most important parameters influencing the stress concentration factor for the weld are highly variable along the weld length, the weld toe radius, r, and the weld angle θ, and these parameters can only be readily described in terms of statistical distribution. Therefore, in a deterministic finite element analyses the variations in r and θ cannot be modelled, and some descriptive values (average or maximum) are employed as default values In the DNV rules for welded steel ship structures (Det Norske Veritas 1996b) these default values are $r/t = 0.15$ and $\theta =$

45° for butt welds, where t = plate thickness. Similar problems are encountered when the notch stress is to be determined experimentally from strain gage measurements since it cannot be measured directly at the weld because the strain gage would have to straddle the weld toe. Instead an extrapolated hot spot stress is obtained from strain gauges placed at distances of $0.5t$ and $1.5t$ from the weld. To account for the stress concentration effect of the weld the hot spot stress is multiplied by a default SCF of K_w = 1.5 for the weld. Thus the DNV notch stress approach is effectively the same as the hot spot approach since a factor of 1.5 is first applied to the *S-N* curve, then it is accounted for by multiplying the hot spot stress by the same factor of 1.5.

2.4 *Hot spot S-N curves for aluminium joints*

In the DNV guidance for welded aluminium ship structures (DNV 1996) two *S-N* curves are given for welded joints (three curves including one for welded joints in a corrosive environment), as shown in Figure 3.

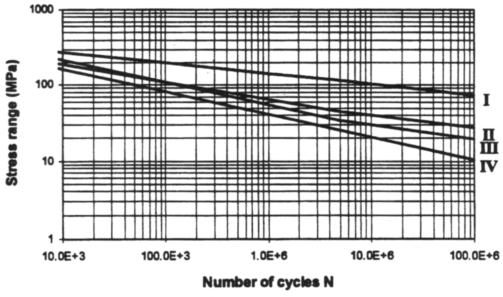

Figure 3 The DNV design S-N curves for aluminium ships (DNV 1996)

The applied stress range is the *notch stress range* as defined in Figure 2. Curve I applies to base material. The highest curve for welds (Curve II) represents butt welds while the lower curve, Curve III, which also has a steeper slope (m = 3.37), represents fillet welds as low strength (high severity) joints. Curve II is for welds in a corrosive environment. Since the slope of Curves II and III are close to the value of m = 3 in the IIW guidance, corresponding *S-N* curves, characterised by their FAT value, (FAT = Stress range at N = 2×10^6) can be obtained from the DNV curves. The stress range of curve III at 2×10^6 cycles is 45 MPa but this includes the K_w factor of 1.5 so the corresponding FAT value becomes 45/1.5 = 30 MPa. Similarly the FAT value Curve II is 55/1.5 = 37 MPa. These curves can now be compared with other curves for aluminium welded joints based on hot spot stresses.

S-N data from a large number of welded aluminium plate specimens with a variety of geometries and in thicknesses up to 6 mm have recently been collected (Ref.1) and analysed in terms of hot spot stresses obtained either from strain gauge measurements or from finite element analyses. The results plotted as hot spot stresses are summarised in Figure 4. It was concluded that a weld category curve corresponding to FAT 40 would constitute a conservative hot spot based design curve for welded aluminium structures.

In the US the Category B curve in the Aluminum Association Design Manual has recently been proposed (Sharp et al. 1996) for use as a general design hot spot stress based design curve for welded aluminium joints. This is the S-N curve for longitudinal butt welds. In Eurocode 9 (CEN 1996) and in BS 8118 (BSI 1991) the hot spot stress method is mentioned but no advice is given on the choice of S-N curve.

The DNV classification note for ships is the only known code using the hot spot stress concept for welded aluminium structures. However, by analogy with design codes for steel structures where the hot spot stress S-N curves are nearly identical to the curves for two sided butt welds, s-n curves for hot spot stress fatigue design can be obtained from

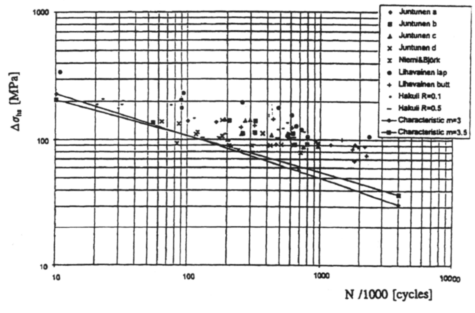

Figure 4 S-N data for small MIG welded aluminium plate specimens (Ref.1)

Table 1 Possible hot spot stress S-N curves for fatigue design of welded al structures

Source (Ref)	Stress at 2 mill cycles $S_{2\ mill}$ (MPa)	Design category	Slope m	Comments
Eurocode 9 (CEN 1996)	35	Class 35	4.0	Curve for two sided butt welds
BS 8118 (BS 1991)	35	Class 35	3.2	Curve for two sided butt welds
IIW (Hobbacher 1996)	32 or 40	Fat 32 or 40	3.0	Curves for two sided butt welds
(Nordmark et al . 1996)	46	AA Cat. B	4.75	Various types of welds
(Partanen and Niemi 1996)	46	-	3.0	Various types of welds
Det Norske Veritas (DNV 1997)	30 or 37	Curve III or II	3.37 or 4.32	Fillet or butt welds, resp.
(Kosteas et Gietl 1995)	40	-	3.5	Based on data for hollow section joints

other stress s-n obtained in this way are compared in Table 1.

3 FINITE ELEMENT ANALYSES

The determination of the state of stress at experienced by weldments is critical in design, but especially so where the hot spot stress method is used. Appropriate SCFs are pivotal in analysing experimental fatigue data for establishing hot spot *S-N* curves and are also critical in terms of relating structural or nominal stresses to hot spot stresses for use in fatigue design. The work reported here is primarily of an exploratory nature and was firstly aimed at determining the SCF for welded aluminium RHS T-joints, Figure 5, under simple membrane and bending loading of the chord member, and secondly to establish an *S-N* curve for this joint

3.1 *Determination of SCFs*

The FE analyses were performed using both the I-DEAS and Abaqus commercial codes. Three-dimensional solid models were used representing a quarter of the test specimen geometry by employing symmetry planes where possible. Geometrically linear elasto-static analysis routines were used. Two sets of models were used: I-DEAS based modelling of parametric variations in local weld

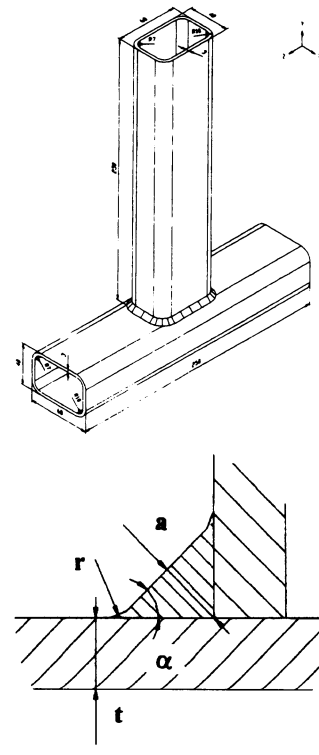

Figure 5 Specimen dimensions

geometry; and Abaqus based analyses of the nominal weld geometry to independently verify the SCFs determined. The two series of analysis separately employed 10-node tetrahedral and 20-node brick elements. Meshing rules suggested by IIW (Niemi 1995) were employed and the stresses for extrapolation were also extracted in accordance with these guidelines in order to maintain consistency between FE predictions and experimental stress analyses.

The following nominal parameters were used for the model: weld toe radius, $r = 0.8$mm; weld angle, $\alpha = 45°$; weld throat size, $a = 3$mm; tube wall thickness, $t = 3$mm. Subjected to pure bending of the chord member, a weld toe SCF value of 1.93 was calculated based on extrapoloation. The site of maximum stress along the weld toe is located near to the corner of the brace member towards the sidewall of the chord. An entirely separate FE analysis of the same geometry using a different program and different solid elements produced SCF values of 1.86 in bending and 1.51 under membrane loading.

3.2 *Parametric study*

In an investigation of the sensitivity of the SCF to parametric variations in the weld and section geometry, the four parameters r, α, a and t were systematically varied. Identical tube geometries were used on brace and chord members in a given analysis and during variation of t the external dimensions remained constant. The toe radius, r, was varied between 0.3mm and 3.0mm; α was varied from 35° to 55°; a ranged between 2mm and 4mm; and t was varied between 2mm and 3.5mm. Statistical analysis of the resulting distribution of SCF_Z (in this case defining the maximum stress at the weld toe), based on both maximum principal stress and axial stress component, revealed that r and t have the strongest influence while the SCF is only a weak function of both α and a. Examples are given in Figure 6. Models fitted to the data produced the equations:

$$SCF_z = 1.79 + 0.332\alpha + 0.73te^{-2r} + 0.33ta \quad [3]$$

$$SCF_{\sigma 1} = 1.17 + 0.759\alpha + 0.898te^{-2r} + 0.16a \quad [4]$$

with α in radians and t, r and a in mm. Equation 3 refers to the axial (Z-direction) stress component and Equation 4 refers to maximum principal stress at the weld toe. The bounds investigated (stated above) strictly apply as limits to these equations. These models behave in a similar way to established treatments for transverse fillet welds in plate (Niu & Glinka 1987) but, as the joint under consideration here is between hollow-sections, there is strictly no valid basis on which to make a direct comparison. The variation of SCF with both r and t is plotted in Figure 7 where it is clear that, as could be foreseen, combinations of small weld toe radius and large weld angle, weld throat and wall thickness lead to high SCFs. In particular, combinations of r and t have most influence.

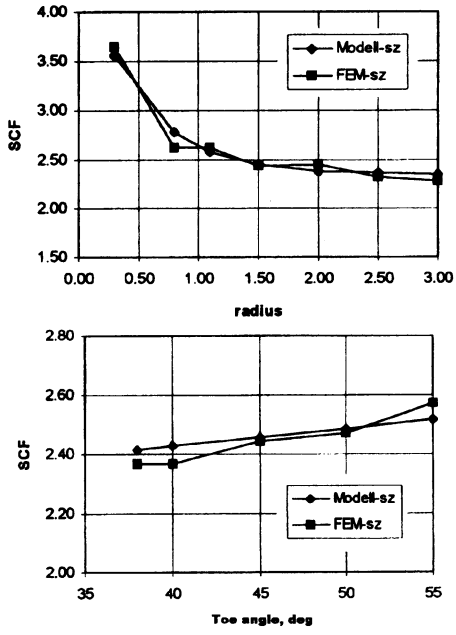

Figure 6 Examples of parametric variation of SCF (radius and toe angle)

4 FATIGUE TESTS

Test data were generated from welded T-joint specimens in bending and, because the hot spot stress method is being studied as the prime candidate for a design method, data from a test programme on welded lap-joints in aluminium are also reported. The test data are reported in an earlier publication (Macdonald & Haagensen 1998).

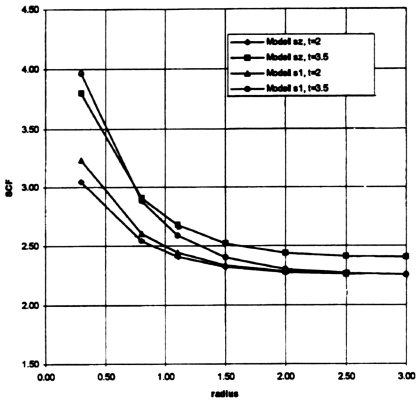

Figure 7 SCF as a function of r and t

4.1 *Welded extrusions (T-joints)*

Fatigue testing of T-joint specimens was performed on a series of four specimen groups covering two weld metals (4043 and 5183), and as-welded and improved (toe-ground) weldments. The specimen geometry, Figure 5 is identical to that studied earlier using FE, however, the unloaded brace member was shortened in order to facilitate testing. The parent material extrusions were 6082.26-T5 aluminium alloy that has specified minimum tensile properties of 290 MPa yield strength and 340 MPa ultimate tensile strength. The specimens were loaded in 4-point bending of the chord member. All tests were carried out at R=0.1 and under constant amplitude conditions using a 5 Hz sinusoidal waveform. The nominal stresses were calculated from simple elastic bending theory for the loaded cross-section. The hot spot stresses were determined from a simple multiplication of the nominal stresses by an SCF of 1.83, derived from the FE work described earlier. A limited number of specimens were instrumented with strain gauges on the chord, located close to the anticipated failure site using the IIW guidelines Hobbacher 1996) in order to measure the hot spot strain, Figure 9. A polynomial curve fitted to the strain data was linearly extrapolated to the weld toe from positions at 0.9mm and 3mm from the weld toe. Good agreement was found between the hot spot stresses based on experimental (SCF=1.83) and numerical (SCF=1.93) stress analyses. Endurance data generated in the test programme are given in Tables 2-5, presented in terms of both nominal and local (hot spot) stress ranges, using an SCF of 1.83.

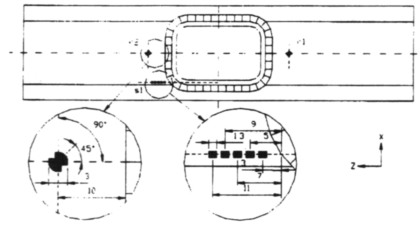

Figure 8 Strain gauge locations

Linear regression analysis of the test data produced the design lines (mean minus two standard deviations) plotted in Figure10 the corresponding S-N constants are noted in Table 2.

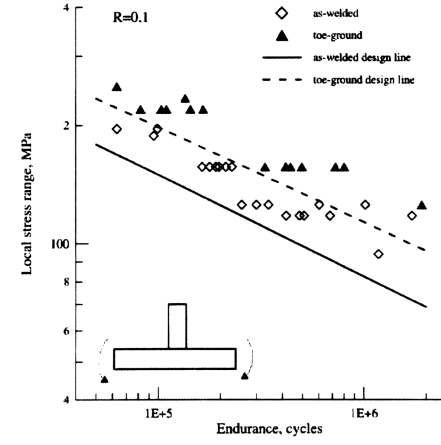

Figure 9 Fatigue test data from welded RHS T-joints

Table 2 Fatigue test results, *S-N* constants for mean and design lines.

Test series	*S-N* curves		
	Log C	$S_{2\ mill}$ MPa	m
As-welded, mean line	13.79		3.87
As-welded, design line	13.42	69.1	3.87
Toe ground, mean line	14.75		4.12
Toe ground, design line	14.46	95.5	4.12

Some data are available in the literature (Hagström & Sandström 1996) for welded T-joints in aluminium hollow profiles. Directly relevant data reviewed by Kosteas & Gietl were already expressed as local stress ranges but the Hagström & Sandström data had to be re-evaluated in terms of hot spot stress. This involved performing an FE analysis on the test geometry used (axial loading of the brace) to get an SCF value of 4.4. These data are all plotted in Figure 10 based on local stress range with the results of the present study for as-welded joints where it is clear that the hot spot stress approach appears to performing well in terms of reducing data from different loading configurations to a common basis.

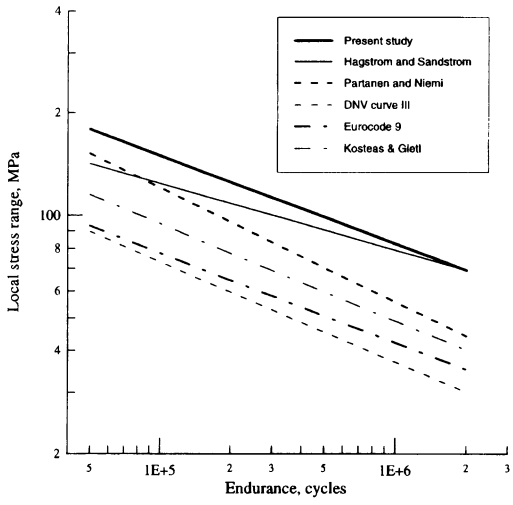

Figure10 Comparison of test data with published results, all are design (mean –2SD) curves

5 PROPOSED DESIGN METHODOLOGY

Based on an evaluation of the published literature the following recommendations are made for the first version of a design methodology for welded aluminium space frames made of rectangular hollow section joints:

5.1 *Definition of hot spot stress*

Use the IIW (Niemi 1995) definition.

5.2 *Determination of hot spot stress by strain gage measurements*

Use the IIW (Niemi 1995) extrapolation procedure

5.3 *Finite element analysis to determine SCFs*

Determine stress distribution by three-dimensional analysis, determine SCFs by linear extrapolation from two points on the curve in accordance with the IIW procedure. Use IIW (Niemi 1995) guidance for FEM analysis.

5.4 *Parametric formulae for SCFs*

Use equations proposed by van Wingerde et al. (van Wingerde et al. 1995) for RHS *T* and *K* joints as preliminary guidance.

5.5 *Hot spot stress design S-N curve*

Use the Partanen & Niemi curve with a stress range at 2×10^6 cycles of 40 MPa, slope $-1/3$. This curve is slightly higher than e.g. the proposed DNV curves (D, when corrected for the difference between hot spot and notch stresses.

6 CONCLUSIONS

The following conclusions are drawn:

Many different definitions of hot spot stress range exist and are used in the fatigue design of welded structures. The guidance recently published by IIW for derivation of the hot spot stress from strain gauge measurements and FEM analyses are recommended for use for preliminary fatigue design of thin walled aluminium structures.

The hot spot stress *S-N* curves for welded aluminium structures in design recommendations that give specific advice are remarkably similar, apparently converging on a design fatigue stress range at two million cycles in the region of 30 to 40 MPa.

The hot spot method appears well-suited to automotive space frames fabricated from welded aluminium RHS joints, however, the design database needs to be expanded. Specific parametric equations for SCFs need to be developed (or adapted from existing methodologies for steel structures).

Parametric FE analysis of a T-joint configuration under in-plane bending of the brace showed that combinations of small weld toe radius and large weld angle, weld throat and wall thickness lead to high SCFs. In particular, combinations of r and t have most influence.

Stress concentration factors determined from strain gauge measurements and FE analysis were in good agreement.

ACKNOWLEDGEMENTS

The authors wish to acknowledge the work of R. M Edvardsen and R. Trandum, both of whom made contributions to the work reported here as part of their M.Sc. thesis work.

REFERENCES

Aluminum Association 1994. *Aluminum design manual.* Washington D.C.

API 1993. API RP2A, Recommended practice for planning, designing and constructing fixed offshore platforms, 20th Edition, American Petroleum Institute.

Baerheim, M. et al. 1996. Proposed fatigue provisions in the new ISO code for offshore structures. Proc. 15th Int. Conf. Offshore Mechanics and Arctic Engineering, OMAE 199, Florence, Italy, June 16-20, 1996.

British Standards Institution 1991. *Structural use of aluminium.* Part 1. Code of practice for design.

CEN 1996. *Eurocode 9: Design of aluminium structures. Part 2 Structures susceptible to fatigue.* prENV 191-2, CEN/TC 250SC 9.

Det Norske Veritas, 1984. Classification note 30.2, "Fatigue strength analysis for mobile offshore units".

Det Norske Veritas, 1996a. Class Note: Fatigue assessment of ship structures. Report No. 93-0432, revised 1st Sept. 1996.

Det Norske Veritas, 1996b. Class Note: Fatigue assessment of aluminium structures. Report No. LIB-J-00010, Dec. 1995, revised 10th Jan. 1996.

Efthymiou, M. 1988. Development of SCF formulae and generalised influence functions for use in fatigue analysis". Proceedings of the Offshore Tubular Joint Conference. Surrey, UK,

Gibstein, M. B. & E. T. Moe 1985. Fatigue of tubular joints. Chapter 8, Fatigue Handbook, Ed. Almar-Naess, Tapir.

Hagström, J. & R. Sandström 1996. Fatigue properties of welded T-joints in thin-walled aluminium profiles. Proc. 5th Int. Conf. on Aluminium Alloys, ICAA-5, Grenoble, 1-5 July, 1996, Materials Science Forum, Vol. 217-222, No. 3, 1996: 1727-1732.

HSE 1990. Guidance on design, construction and certification". 4th Edition (including Feb.1995 amendments), HMSO, London, UK.

HSE 1992. Fatigue background guidance document, Report OTH 92 390, HMSO.

Health and Safety Executive 1990. Stress concentration factors for simple tubular joints: assessment of existing and development of new parametric formulae. Prepared by Lloyd's Register of Shipping, HSE Report OTH 91 357, HMSO, London.

Kosteas, D. & B. Gietl. 1996. A comparative analysis of existing test data on welded aluminium tubular joints. Fatigue and Fracture of Engineering Materials and Structures, Vol. 19: 731-738.

Marshall, P. W. 1992, Design of welded tubular connections. Basis and use of AWS code provisions. Elsevier, Amsterdam.

Macdonald, K.A. & P.J. Haagensen 1998, Progress in fatigue assessment of welded hollow-section aluminium structures, 7th Int. Conf. on Joints in Aluminium Structures (INALCO '98). Cambridge, UK, 15 17 April 1998: 431-449.

Niu, X. & G. Glinka 1987. The weld profile effect on stress intensity factors in weldments". Int. J. Fracture, Vol. 35, 1987: 3-20.

Niemi. E. 1995. Stress determination for fatigue analysis of welded components. Abington Publishing, Cambridge, UK.

Norsk standard 1984. NS 3472. Prosjektering av stålkonstruksjoner. Beregning og dimensjonering. 2. utg., Norges Standardiseringsforbund.

Partanen, T. & E. Niemi 1996. Hot spot *S-N* curves based on fatigue tests of small MIG welded aluminium specimens, IIW Doc. 1636-96.

Radenkovic, D. 1981. Stress analysis in tubular joints. Int. Conf. on Steels in Marine Structures, Paris 1981. Sharp, M.L. et al. 1996. *Fatigue design of aluminum components and structures*. McGraw-Hill

Stacey, A. & J. V. Sharp, 1995. The revised HSE fatigue guidance . Proceedings of the 14th International Conference on Offshore Mechanics and Arctic Engineering, OMAE 1995. Copenhagen, Denmark, June 18-22, 1995.

van Wingerde, A. M. et al.. Proposed revisions for fatigue design of planar welded connections made of hollow structural sections. Proc. 5th Int. Symp. on Tubular Structures, Nottingham,1993.

van Wingerde et al. 1995A. M., Packer and Wardenier, J., "Criteria for fatigue assessment of hollow structural section connections". J. Construct. Steel research, Vol. 35: 712-115.

van Wingerde, A. M. et al. 1996, Packer, Wardenier, J. and Dutta, D., The fatigue behaviour of K-joints made of square hollow sections. IIW Doc. *XIII*-1626-96.



Taylor & Francis
Taylor & Francis Group
http://taylorandfrancis.com

Tubular Structures VIII, Choo & Van der Vegte (eds) © 1998 Balkema, Rotterdam, ISBN 90 5809 001 9

New code formulations for tubular joint static strength

A. F. Dier & M. Lalani
MSL Engineering Limited, Ascot, Berkshire, UK

ABSTRACT: This paper presents the main findings of a major international joint industry project on the static strength of tubular joints. Based on the most extensive and carefully screened database ever assembled, the robustness of existing design formulations were examined, and new formulations were developed where present codes are found wanting. The formulations form the basis of much of the relevant recommendations of the Tubular Joint Committee of the Working Group charged with producing the new ISO offshore standard (ISO-13819 Part 2). The paper describes the databases and the screening criteria used in their preparation. The philosophy and strategy adopted for fitting functions (Q_u functions) to the data is explained, and the resulting design formulations are presented along with the associated statistical variables describing 'goodness of fit'.

1 INTRODUCTION

Commonly, tubular joints in offshore installations are designed to the formulations contained in the American recommended practice API RP2A. These were established in 1980 and no fundamental changes have been made since that time. Other codes also address joint design. The strengths predicted by the codes often differ due to the adoption of different philosophies during code formulation and to differences in the underlying databases used during curve fitting and calibration. It is recognised that a number of technological advances have taken place regarding the ultimate limit state of tubular joints from 1980 to date, including the generation of pertinent new data and information. With the much larger database now available, e.g. more than four times that in 1980, refined and more robust formulations for static strength can be established for use in the structural appraisal of existing installations and for consideration by code-drafting bodies. With the above observations in mind, a major international joint industry project (JIP) was initiated and which was completed earlier last year, MSL (1996). The JIP was funded by 10 Oil Companies, 1 Regulatory Authority and 1 Certification Authority. The objectives were two-fold:

1. to develop fully validated static strength formulations for tubular joints for use in the reappraisal of existing steel platforms or by code drafting committees
2. to develop closed-form expressions which enable non-linear load deformation curves to be readily created for the range of joint types, loadcases and geometries that commonly occur in practice.

This paper is concerned with the first of the above objectives; some information with respect to the second can be found in Dier & Lalani (1995).

2 DATABASES

Three types of databases were compiled during the project: unscreened database, screened database and finite element database. The first database contains all known test data and is validated against source reports where available. An initial lower limit of 100 mm on the chord diameter was used in assembling the database, this being lower than the limits of 140 mm and 125 mm used in the preparation of API RP2A and HSE Guidance Notes respectively. The argument for a cut-off limit stems from a concern that small scale specimens are not representative of fabricated joints found offshore, from a material,

weld and tolerance standpoint. However, it is recognised that failure modes for tubular joints subjected to static loading are generally dominated by gross, plastic ovalisation of the chord cross-section, and size effects would therefore be expected to be less of an issue for statically loaded joints when compared to joints subjected to fatigue loading. The suitability of the 100 mm limit was confirmed during appraisal exercises.

Adequate screening criteria are clearly important in establishing a reliable screened database. There are obvious criteria (e.g. chord yield strength and thickness should be measured and not just minimum specified or nominal values quoted) but many are more subtle such as ensuring that the test boundary conditions have not influenced the result or that chord/brace member yielding has not affected the measured response. The main criteria, which were vetted by acknowledged tubular joint experts world-wide, used in the project were as follows:

1. Chord yield strength and thickness should be measured values;

2. For K joints, gaps or overlaps should be at least twice the chord thickness (joints having near zero gap/overlap values were subsequently used to confirm the adequacy of interpolating between gapped and overlapped joint behaviour);

3. An initial lower limit on chord length/radius ratio (= α) of 3 was selected, although this limit was tightened to 8 following data appraisals;

4. An upper limit on brace to chord thickness ratio (= τ) of 1.1 was used to screen out data where the investigator had tried to force joint failure (rather than brace failure) by using thickened braces, the value of 1.1 allows for thickness tolerances for the case when the brace and chord thicknesses are nominally the same;

5. Similarly, joints with braces having stiffeners or grout in-fill were screened out;

6. Both chord and brace utilisations were checked and the data separated into two groups: one group where the stresses in both the chord and the brace were below yield and the other where the chord and/or brace stress did exceed yield. The first group was treated as true joint strength with no reservation whilst the second group was treated as lower bound. Joints under in-plane or out-of-plane bending in which the brace moment exceeded the plastic moment capacity were rejected. Likewise, axially loaded joints for which the axial capacity of the brace had been exceeded were rejected.

A total of 1072 simple joint specimens with D greater than 100 mm were validated. The corresponding number following screening was 659 which includes 118 and 541 specimens with and without additional chord load respectively. The size of the screened database is compared to those used in the preparation of API RP2A and the HSE Guidance Notes, which represent 1980 and 1985 status respectively, in Table 1. The distribution of the specimens to joint and load type is indicated in Table 2. The significance of establishing a suitably screened database cannot be over-emphasised. The differences in various code provisions on joint strength are partly due to differences in databases.

Table 1. Comparison of number of steel specimens used to prepare guidance.

Brace Load	Number of Specimens		
	API	HSE	Present Work
Axial	104	167	453
IPB	16	33	57
OPB	17	20	31
Total	137	220	541

Table 2. Number* of steel specimens in unscreened and screened databases.

Joint Type	Brace Compression	Brace Tension	Brace IPB	Brace OPB	Additional Chord Load	Total
T	134 (82)	49 (22)	64 (38)	26 (18)	6 (6)	279 (166)
Y	12 (12)	3 (3)	4 (0)	6 (0)	0 (0)	25 (15)
DT	93 (60)	55 (33)	17 (13)	4 (4)	33 (33)	202 (143)
X	17 (12)	13 (2)	0 (0)	0 (0)	0 (0)	30 (14)
K	368 (199)		6 (6)	5 (5)	51 (43)	430 (253)
YY	58 (28)		1 (0)	4 (4)	43 (36)	106 (68)
Total	802 (453)		92 (57)	45 (31)	127 (118)	1072 (659)

* The first number refers to the unscreened database and the second, bracketed, number to the screened database

3 APPRAISALS OF DATABASES

3.1 General

Subsequent to the compilation of the screened databases, the following general approach was used to derive recommended formulations for the assessment of tubular joint static strength:

1. Conduct curve-fitting exercises to the data. It was at this stage when additional or more stringent screening criteria were developed. An example of this is the tightening up of the chord length/radius ratio as discussed below. Also, extensive studies were conducted in an attempt to separate out the influence of chord stresses (inherent in all test data except for axially loaded DT/X joints) on joint strength. This aspect is further described below.

2. Examine the performance of existing formulations; this included an assessment of API, HSE, DNV, NPD, CSA and EC3 formulations.

3. Generate new data by FE analysis where appropriate to resolve certain potentially important issues identified during the course of the project.

4. Select appropriate formulations on the basis of the above studies and comparisons.

Curve fitting exercises essentially comprised finding the best mean fits of selected functional forms (e.g. linear, power law expressions, etc.) to the data. A multivariate least squares regression analysis based on percentage differences was used throughout. Multivariate means that the constants of an assumed expression form are found simultaneously, and not found independently in a piece-meal fashion. The regression analysis was based on minimising the sum of squares of the percentage error (between data points and the fitted function) rather than the absolute error to ensure that equal weighting was applied to all data points. A series of regression analyses was used in which each constant in turn was rounded off and thereafter held constant in the subsequent analyses. Having found the best fit mean curve, statistical calculations were conducted to establish the associated characteristic curve. For this work, the characteristic curve was defined as 95% survivability at the 50% confidence level, i.e. consistent with that being used for the characteristic strength of other components. The calculations took account of the number of test data in the sample.

In common with existing codes, characteristic strength formulations for uni-directional loaded joints were found in the form of:

$$P_k = Q_u Q_f \frac{F_y T^2}{\sin\theta} \qquad (1)$$

$$M_k = Q_u Q_f \frac{F_y T^2 d}{\sin\theta} \qquad (2)$$

in which Q_u is the basic joint strength parameter and Q_f is a factor to account for the effects of chord loads; both are non-dimensional parameters and are discussed below. F_y is the minimum specified yield stress of the chord material at the joint (or 0.8 of the tensile strength, if less). The factor of 0.8 is a relaxation of existing code requirements and follows a secondary study into the role of the yield/ultimate strength ratio. Other terms in Equations (1) and (2) relate to joint geometry, see Figure 1.

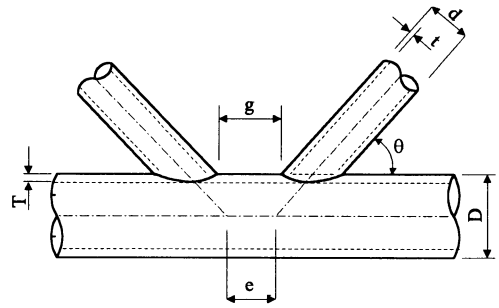

$$\beta = \frac{d}{D} \qquad \gamma = \frac{D}{2T}$$

Figure 1. Joint notation

In practice, a joint will normally be the subject of combined brace loading and the following interaction equation should be satisfied:

$$\left|\frac{P_d}{\Gamma P_k}\right| + \left(\frac{M_{di}}{\Gamma M_{ki}}\right)^2 + \left|\frac{M_{do}}{\Gamma M_{ko}}\right| \le 1.0 \qquad (3)$$

in which subscripts d refers to factored design load, i to in-plane bending (IPB) and o to out-of-plane bending (OPB). The partial factor of safety, Γ, may be taken as 0.95. For the purposes of evaluating the first term in Equation (3), the role of joint classification has to be recognised. This issue concerns the separation of brace axial loads into K, X and Y load components. A load-based classification scheme, such as used in API, is recommended. The recommended expansion of the axial load term is as follows:

$$\left|\frac{P_d}{\Gamma P_k}\right| = \frac{1}{\Gamma}\left|\frac{P_d}{\Sigma kP_K + yP_Y + xP_X}\right| \quad (4)$$

where P_K, P_Y and P_X are the characteristic K, Y and X strengths and k, y and x are the weighting factors according to the proportions in the classification (note $\Sigma k + y + x = 1.0$). A summation applies to K action because of the possibility of a particular brace interacting with two others by such action (e.g. consider a KT joint). The expanded axial load term has been corroborated against FE studies on DK joints which are presented elsewhere, Dier & Turner (1998). Dier & Turner (1998) also show that a linear expansion of the axial load term (i.e. taking the simple summation of individual utilisations) is an acceptable alternative to Equation (4). Unlike previous API practice where interpolation of Q_u was adequate for axially loaded braces with mixed classification, interpolation based on a weighted average of P_k is now required since Q_f also now varies with axial load classification.

An eccentric X joint (i.e. with staggered braces) will actually tend to behave more like two Y joints when the eccentricity is large. (This being similar to a K joint reverting to two Y joints at large gaps). Advantage may be taken of the increase in strength of eccentric X joints (there being a certain amount of Y action) by invoking the following correction to the nominal X classification of each brace:

$$R_x = 1 - \left|\frac{e}{3D}\right| \quad \text{but} \geq 0 \quad (5)$$

$$R_y = \left|\frac{e}{3D}\right| \quad \text{but} \leq 1.0 \quad (6)$$

where R_x and R_y are the correction factors to apply to the nominal X classification for determining the true proportions of X action and Y action respectively and e is the brace eccentricity measured along the chord axis. The justification for the above expressions follows from Finite Element studies which may be found in Dier & Turner (1998).

Existing codes give separate unity checks for joints and members. However, member failure often involves nonlinear behaviour at the location of a joint and therefore interaction effects between the member and joint cannot be ruled out. Concern has been expressed that separate unity checks on the joint alone and on the brace member alone may miss unfavourable interaction, see Healy & Zettlemoyer (1993). The unfavourable interaction could lead to an unsafe region, as shown schematically in Figure 2. Although the existence of such a region is unproven, it is prudent to limit the axial joint strength (Equation (1)) to the brace stub squash capacity and, for compression, the local buckling capacity of the brace stub. Similarly, the joint bending strength (Equation (2)) should be limited to the plastic moment capacity (for $D/T \leq 60$) or the sectional buckling moment capacity (for $D/T > 60$).

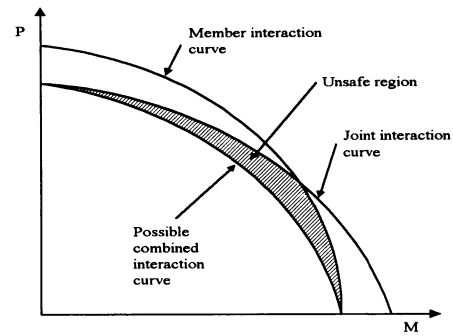

Figure 2. Unfavourable joint/member interaction

3.2 Determination of Q_f

It is reasonable to expect that the presence of moderate or high chord loads will have a deleterious effect on joint strength. Existing codes have a 'knock down' factor, i.e. the Q_f term, which is applied to the basic joint strength to allow for this effect. With the single exception of DT/X joints tested under brace axial loading, the chords of joints tested in the laboratory are necessarily subjected to equilibrium loads. Some tests have been conducted with additional chord loading applied in an effort to quantify chord stress effects. To date, the equilibrium chord loads in tested joints have generally been ignored when deriving the basic joint strength Q_u parameter. Specific test data, in which chord bending/axial loads have been additionally applied, have been used to formulate the Q_f correction term to apply with Q_u, thereby accounting for chord load effects. This approach is conservative in that it accounts for chord stress effects twice: firstly in the derivation of Q_u which is based on data containing the effect and secondly by correcting with the Q_f term.

In this work, attempts were made to find explicitly the Q_f functions and then adjust the database of measured joint strengths to account for chord load effects so that more appropriate Q_u functions could be found. The results of these

endeavours have resulted in the following formulation:

$$Q_f = 1.0 - \lambda U^2 \quad (7)$$

where λ = 0.030 for brace axial load
= 0.045 for brace IPB
= 0.021 for brace OPB

$$U = \frac{1}{\Gamma}\left[\alpha_1\left(\frac{P_{dc}}{P_y}\right)^2 + \alpha_2\left(\frac{M_{dc}}{M_p}\right)^2_{ipb} + \alpha_2\left(\frac{M_{dc}}{M_p}\right)^2_{opb}\right]^{0.5} \quad (8)$$

P_{dc} and M_{dc} (ipb and opb) are the factored axial load and bending moments in the chord; P_y and M_p are respectively the axial yield and plastic moment resistances of the chord and Γ is a partial factor of safety. The α factors are defined in Table 3.

Table 3. Recommended α factors to use in Equation 8.

Joint and load type	α_1	α_2
T/Y joints under brace axial loading	25	11
K joints under balanced axial loading	14	43
T/Y and K joints under brace moment loading and DT/X joints under any brace loading	25	43

Two values of the chord utilisation U should be calculated, corresponding to the loads either side of the joint, and the maximum value selected. Apart from DT/X joints with $\beta > 0.9$, Q_f may be set to unity if the magnitude of the chord axial tension stress is greater than the maximum combined stress due to chord moments.

Comparison of the above Q_f formulation with those of existing guidance such as API RP2A shows some differences. Some of the differences are of presentation only, others are identified and explained below.

1. The dependency of Q_f on γ has been removed. The γ dependency was introduced in codes following a careful set of test on DT joints with $\gamma = 25$ using various chord loads, Boone et al (1982), and forcing these results to align with those of K joints with γ = 16, Washio et al (1969). However, more recent K joint data with a wider range of γ, de Koning et al (1981), shows that the chord load effect for K joints does not substantially depend on γ. Furthermore, FE data on axially loaded T joints of various chord lengths and therefore various chord IPB, van der Valk (1988), again indicate that Q_f is independent of γ. The results for the DT joints are still valid of course, and the γ = 25 value is now explicitly included as a constant in Table 3. (The constant of 43 is obtained from the square of the shape factor times 25 i.e. $1.3^2 \times 25 = 43$, and reflects the change in presentation of the chord utilisations which are now expressed in terms of load ratios rather than stress ratios.)

2. The factor α_1 = 14 in Table 3 for K joints has been obtained from an examination of both test data for which equilibrium chord axial loads only existed and tests in which additional chord axial loads were applied. Substantial equilibrium chord loads can arise in K joints. For the boundary conditions used in tests, these equilibrium loads are generally induced on one side only of the joint. Analysis indicated that taking the maximum of the two U values either side of the joint gives marginally better matching of predicted and measured joint capacity. There are no relevant data for chord moment loaded K joints and therefore existing guidance is preserved (except for the γ-dependency).

3. For axially loaded T joints, the effect of chord IPB has been relaxed. Substantial equilibrium chord IPB may arise in T joints under axial loading. These chord moments can be expected, as confirmed in FE analyses (van der Valk (1988)), to affect joint strength. However, due to chord length and end plate effects, doubts over true chord boundary conditions and inherent experimental scatter, the extraction of a chord stress effect from the database proved most difficult. Trials using a Q_f function derived from the FE data did not seem to apply to the test data. There is a strong correlation between the chord IPB and joint failure with β. Since curve fitting was carried out empirically, the effect of higher chord IPB at higher β was automatically captured by the role of β in the Q_u function. In other words, the Q_f effect is hidden in the Q_u function. Recognising that chord IPB in structures may be higher than those attained in tests, it was felt prudent that some explicit allowance for Q_f should be made. This was achieved by assuming Q_f reaches 0.8 when the chord IPB reaches the yield moment.

The authors recognise that chord loading is one of the least understood parameters affecting joint

strength, there being little data to define properly the Q_f term. Recent FE work may resolve some of the issues involved, e.g. see Pecknold et al (1998).

3.3 Determination of Q_u

As explained in Section 3.1, Q_u factors were established from fitting curves to the screened data. Sensitivity plots of the ratios of experimental to predicted strengths against pertinent parameters (e.g. β, γ, θ etc.) were used to ensure that the prediction formulations had appropriately captured the effect of each parameter. The sensitivity plots were sometimes used to identify screening criteria. As an example, consider the role of α (α = L/2D, the chord length/radius ratio) on the axial strength of DT joints. It is to be expected that a specimen with a short chord length will record a lower measured strength as there is less resistance to chord wall deformation (ovalisation). This is clearly demonstrated in tests for which a strength reduction effect is apparent for α ratios below about 8. On the basis of this observation, it was decided to impose a (screening) lower limit of α = 8 for all joints. The subsequently derived strength formulations are considered valid for lower α ratios because in a platform the chord ends connect with other tubulars which effectively provide end plates to the chord. FE analysis, Roesset & Pan (1988), has shown that the presence of end plates more than counteracts the strength reduction due to the α effect.

Another example of additional screening criteria may be given. For tension loaded joints, application of the Yura deformation limit (= $2F_y(30d)/E$) showed that the ultimate strengths are almost certain to be governed by such rather than peak load. It was therefore appropriate to reject data where neither load-deformation curves nor stated loads at the deformation limit are given.

Following exhaustive appraisals of the screened steel model data, supplemented by FE data where appropriate, Q_u factors have been derived for each joint and load type as given in Table 4. Many of the Q_u factors are similar, at least in form, to those found in various existing codes although some slight modification of the coefficients may be noticed as a result of using the new and extensive database. In this paper only the significant differences between the Q_u factors in Table 4 and those in existing codes are discussed. These differences relate to K joints under balanced axial loading, DT/X joints under tension, and all joints subject to OPB.

Table 4. Basic strength factor Q_u.

Brace Loading	Joint Classification		
	Y	K	X
Axial compression	$(1.9 + 19\beta)\, Q_\beta^{0.5}$	$(1.9 + 19\beta)\, Q_\beta^{0.5}\, Q_g\, Q_{yy}$	$(2.8 + 14\beta)\, Q_\beta$
Axial tension	30β	$(1.9 + 19\beta)\, Q_\beta^{0.5}\, Q_g\, Q_{yy}$	23β for $\beta \le 0.9$ $21 + (\beta - 0.9)(17\gamma - 220)$ for $\beta > 0.9$ [but see text]
In-plane bending	$4.5\beta\gamma^{0.5}$	$4.5\beta\gamma^{0.5}$	$4.5\beta\gamma^{0.5}$
Out-of-plane bending	$3.2\gamma^{(0.5\beta^2)}$	$3.2\gamma^{(0.5\beta^2)}$	$3.2\gamma^{(0.5\beta^2)}$

Notes:

1. Q_β = $0.3 / (\beta(1-0.833\beta))$ for $\beta > 0.6$
   = 1.0 for $\beta \le 0.6$
2. Q_g = $1.9 - (g/D)^{0.5}$ for $g/T \ge 2.0$
   but $\not< 1.0$
   = $0.13 + 0.65\, \phi\, \gamma^{0.5}$ for $g/T \le -2.0$
   where $\phi = t\, F_{yb}/(TF_y)$
   = linear interpolated value between the limiting values of the above two expressions for $-2.0 < g/T < 2.0$
3. Q_{yy} = 1.0 when $\theta_t \le 4\theta_c - 90°$
   = $(110° + 4\,\theta_c - \theta_t)/200°$ when $\theta_t > 4\theta_c - 90°$

The derivation of the gapped K joint Q_u term has mainly followed traditional practice in that an enhancement factor, Q_g, has been quantified and is used with the corresponding Y joint Q_u formulation. The Q_g factor recognises the expectation that as the gap size increases, a K joint should revert to two Y joints. The gapped K joint strength database was corrected for chord load effects before deriving the Q_g term. However, a new coefficient, Q_{yy}, has been introduced into the formulation for K joints and becomes effective when the compression brace angle (θ_c) is less than 0.25 (θ_t + 90°) where θ_t is the tension brace angle. It may be noted that even for a maximum tension brace angle of 90°, no down-grading comes into effect if the compression brace angle is at least 45°. In practice, θ_c and θ_t may become interchanged due to load reversal as a wave passes through the structure. The down-grading of strength is significant for 30°/90° YT joints. The experimental data and new FE data on which Q_{yy} has been based are fully discussed in Dier & Turner (1998).

For the first time, a new formulation of Q_g is presented for overlapped K joints. Sensitivity plots of the measured strengths to the corresponding Y joint strengths ratios against various parameters indicate that the overlapped Q_g function is dependent on γ, τ and the ratio of brace to chord material yield stress. Regression analyses using a number of trial functions produced an appropriate characteristic Q_g function as given in Table 4. It is noted that this Q_g function does not contain a dependency on the degree of overlap and such independency is confirmed in the sensitivity plot in Figure 3. Sensitivity plots using other parameters (e.g. β, γ, τ, chord load, etc.) similarly show that the new Q_g function captures the effect, if any, of the various parameters.

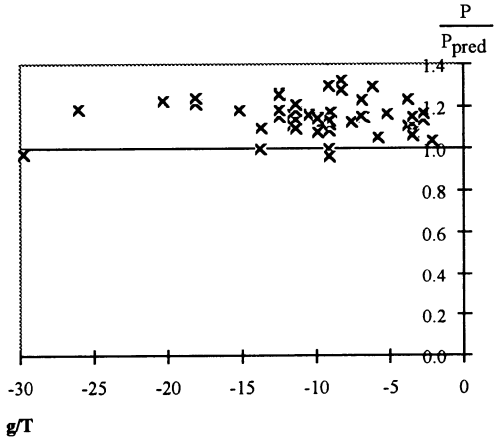

Figure 3. Sensitivity plot of overlap on K joint strength

Figure 4 shows the ratios of measured to predicted strengths for the complete range of K joints (gap and overlap). Two sets of predictions have been used, one based on the nominally lower bound API and the other on the new characteristic formulation. For the latter, interpolation between the gap and overlap Q_g functions is used for joints with near zero gap/overlap. The improvement of the new K joint formulations over API is quite evident in Figure 4, but especially for overlapped joints.

The Q_u formulations in Table 4 for tension loaded T/Y and DT/X joints have been derived on the basis of loads at which cracking has been observed in test data. However, tension loaded joints can sustain further loading beyond first crack. As an estimate of this reserve strength may be important in predominantly statically loaded joints, characteristic ultimate tensile strength Q_u expressions are given here. Note, however,

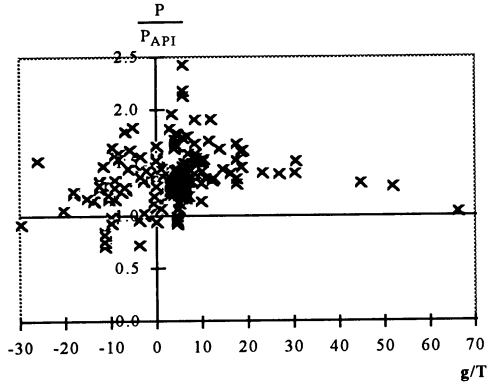

a) Prediction based on API

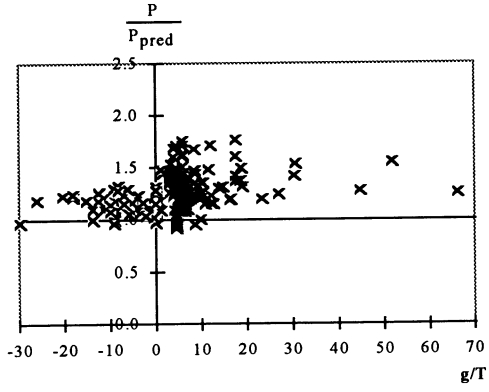

b) Prediction based on new formulation

Figure 4. Ratio of measured to predicted K joint strength against gap parameter

that reserve strength relies on ductility and probably a certain amount of material strain hardening.

For T/Y joints:

$$Q_u^{ult} = 42\,\beta - 4.1 \qquad (9)$$

For DT/X joints:

$$Q_u^{ult} = 41\,\beta - 2.2 \qquad \text{for } \beta \le 0.9 \qquad (10a)$$

$$= 35 + (\beta - 0.9)(32\,\gamma - 285) \qquad \text{for } \beta > 0.9 \qquad (10b)$$

The large increase in strength indicated in the second expression for DT/X joints at high β relies on membrane stresses in the chord as the load is essentially transferred directly from one brace to the other. Should there be any significant misalignment of the braces (say $e/D > 0.2$ where e is the eccentricity of the two braces) then load transfer by membrane action should not be relied upon, and the first expression (10a) should be invoked over the full range of β. This limitation on the second expression for DT joints also applies to the characteristic first crack formulation in Table 4.

A significant change from existing guidance may be noticed for joints under OPB. The form of the OPB Q_u formulation in Table 4 is based upon the FE work of Lee & Dexter (1994) although a simplified form of their recommendation was found appropriate after considering steel data. The OPB derivation perfectly illustrates the useful application of FE parametric studies in deriving design guidance where steel data are not extensive. Only ten steel OPB T/Y specimens passed all the screening criteria and these do not cover the high β with high γ region. The existing FE data, on the other hand, cover the whole geometric range in a systematic manner. In Figure 5, the experimental data are shown as grey columns, the FE data as black columns, and fitted Q_u functions (API and the new recommendations respectively) as white columns. The upper diagram shows the API fit whilst the lower relates to the new recommendation. The FE data are corroborated by the steel data and in particular the effect of γ at high β. The API surface in the upper diagram is independent of γ. The skewness of the surface has been understandingly missed before because of the lack of data. Whilst the form of the new OPB Q_u formulation was selected to follow the FE data, the leading constant was found from a regression analysis of the fully screened steel data only. It should be noted that the new formulation does not give a substantially improved coefficient of variation (COV) compared to API for the steel data, although it does for the FE data and presumably any new steel data and existing joints falling in the high β-γ region.

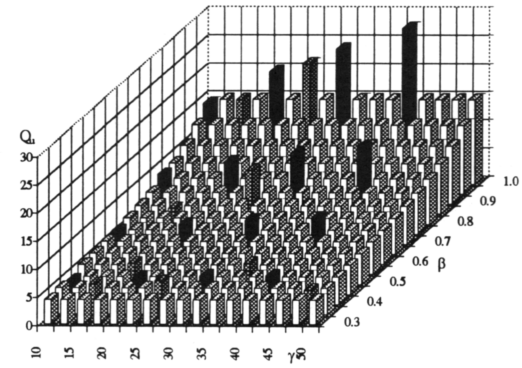

a) API Q_u (lower bound)

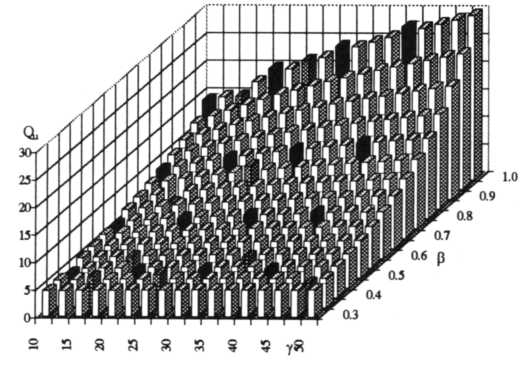

b) New formulation (mean)

Figure 5. Comparisons of experimental and FE data with fitted Q_u formulations (T joints under OPB)

3.4 Statistical variables

In certain circumstances, information relating to the mean, rather than the characteristic, value of joint strength may be required. Mean values may be obtained by multiplying the characteristic values calculated from earlier parts of this paper by the mean bias factors given below. For reliability studies, the coefficients of variation (COV) and the number of data are also tabulated.

3.5 Validity ranges

The validity ranges for the Q_u formulations in Table 4 are given below:

All joints:

$0.2 \leq \beta \leq 1.00$
$10 \leq \gamma \leq 50$
$30° \leq \theta \leq 90°$
$F_y \leq 500\ N/mm^2$

In addition, for K joints:

$g/D > -0.6$

4 IMPACT OF NEW FORMULATIONS

Clearly there are differences between the Q_u formulations of Table 4 with those contained in existing guidance; there are also differences relating to the Q_f formulations. These may be easily established by comparing plots of the respective formulations as, for example, in Figures 4 and 5. However, more pertinently, it is better to establish differences for practical geometries and loads that occur in 'real' structures. For this purpose Lloyds Register conducted, as part of the project, a comparative study of API, HSE and the new formulations for an existing Central North Sea jacket. The jacket comprises four vertical legs, X-braced in both elevation and plan, and supports some 16000 tons topsides. Taking factors of safety as unity, utilisations of the joints were calculated for extreme storm loads and the results of the API/new comparison for those joints having a utilisations ratio greater that two (based on the new formulations) are shown in Figure 6. As can be seen, the differences are modest and, for the more heavily stressed joints, there is a trend for the new formulations to result in slightly lower utilisations. This conclusion does not necessarily apply to different structural forms or with respect to guidance other than API. Although there would seem to little overall economic impact of the new formulations, they do improve overall reliability.

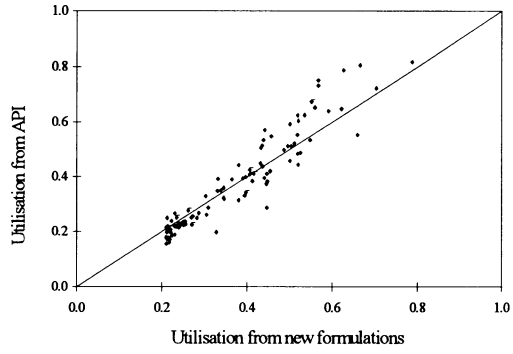

Figure 6. Comparison of joint utilisations resulting from API and new formulations

Table 5. Mean bias factors and coefficients of variation (COV).

Brace Loading	Parameter	Joint Classification					
		Y		K		X	
				Gapped	Overlapped		
Axial compression	Mean bias	1.265		1.300	1.154	1.158	
	COV	0.131		0.136	0.081	0.085	
	No. of data	66		125	55	72	
Axial tension(*)	Mean bias	1.708	(1.805)	As above		1.447	(1.138)
	COV	0.239	(0.263)			0.188	(0.071)
	No. of data	6	(14)			11	(21)
In-plane bending	Mean bias	1.213		1.243	No data	1.235	
	COV	0.106		0.105		0.075	
	No. of data	13		6		5	
Out-of-plane bending	Mean bias	1.268		1.217	No data	1.139	
	COV	0.118		0.155		0.060	
	No. of data	10		8		4	

* The values given in parentheses relate to ultimate tensile strength equations, as given earlier.

5 CONCLUSIONS

It is believed that the execution of the joint industry project has made good use of the available data on the static strength of tubular joints and that it has produced recommendations that are still simple and yet more robust that that contained in existing guidance. The presentation format of the guidance herein follows that of existing codes which should facilitate review by code drafting committees. In particular, the new guidance forms the basis of much of the relevant recommendations in the forthcoming offshore standard ISO-13819 Part 2.

Despite more that two decades of research into the static strength of tubular joints, the subject is still largely empirical. Although our knowledge has certainly increased during this time, it is still necessary to generate data (FE or steel model data) on which to carry out curve fitting exercises to derive new guidance. The greatest challenges facing researchers in this field are the generation of data, the formulation of robust guidance for multiplanar joints and the rapid and accurate analysis of structures allowing for joint non-linear flexibility effects. The last of these is being addressed in a second phase of the JIP. Technology developments in terms of computing power and appropriate software will surely be important in the medium term. However, in the near term, continuing research is necessarily slanted towards phenomenological modelling of joint behaviour.

ACKNOWLEDGEMENTS

The authors thank the JIP sponsors for permission to publish this paper. They also acknowledge the efforts of the hundreds of experimental researchers without whom this paper would not have been possible.

REFERENCES

American Petroleum Institute 1993. Recommended practice for planning, designing and constructing fixed offshore platforms. API-RP2A-LRFD, 1st Edition.

Boone, T. J. et al 1982. Chord stress effects on the ultimate strength of tubular joints. Texas Univ. report PMFSEL No. 82-1.

de Koning, C. et al 1981. The static strength of welded CHS K-joints. Stevin report 6-81-13, Delft University.

Dier, A. F. & Lalani, M. 1995. Strength and stiffness of tubular joints for assessment/design purposes. Paper OTC 7799, 27th Annual Offshore Technology Conference, Houston, 1 - 4 May 1995.

Dier, A. F. & Turner, T. E. 1998. FE studies on load classification, YY and eccentric X tubular joints. Paper presented at 17th OMAE Conference, Lisbon, Portugal, 5 - 9 July 1998.

Healy, B. E. & Zettlemoyer, N. 1993. In-plane bending strength of circular tubular joints. 5th Int. Symp. on Tubular Structures, Nottingham.

Lee, M. K. K. & E. Dexter 1994. A parametric study on the out-of-plane bending strength of T/Y joints. 6th Int. Symp. on Tubular Structures, Monash University, Australia, December 1994.

MSL Engineering Limited 1996. Assessment criteria and reserve strength of tubular joints - final report for JIP. MSL Document Reference C14200R018, March 1996.

Pecknold, D. A. et al 1998. Chord stress effects on ultimate strength of DT tubular joints. Paper presented at 17th OMAE Conference, Lisbon, Portugal, 5 - 9 July 1998.

Roesset, J. M. & Pan, C. P. 1988. Effect of chord lengths and boundary conditions on the behaviour of tubular x-joints. 7th Int. Conf. OMAE, Texas, February 1988.

van de Valk, C. A. C. 1988. Factors controlling the static strength of tubular T-joints. BOSS'88 Conf. Trøndheim, June 1988.

Tubular Structures VIII, Choo & Van der Vegte (eds) © 1998 Balkema, Rotterdam, ISBN 90 5809 001 9

Commentary on the draft specification for fatigue design of hollow section joints

A. M. van Wingerde & J. Wardenier
Faculty of Civil Engineering and Geo Sciences, Delft University of Technology, Netherlands
J. A. Packer
Department of Civil Engineering, University of Toronto, Canada

ABSTRACT: A new specification for fatigue design of welded tubular joints is being drafted by IIW Subcommission XV-E, which incorporates the results of numerous research projects carried out since the previous IIW specification, dating from 1985. A major analysis of the fatigue behaviour of hundreds of joints between round or square hollow sections revealed that it is possible to use one *S-N* line for all tubular joints as well as one thickness correction. The new design method leads to substantial savings for some cases while avoiding unconservative designs, which would be allowable under the older classification methods, in other cases. The new design specification, and related upcoming design guidelines by CIDECT and the EC, are a major step forward towards future use of tubular joints in fatigue critical applications in offshore and onshore structures.

1 INTRODUCTION

The existing IIW specification, IIW (1985), still stands as one of the most advanced fatigue design methods for tubular joints, since it is based on the hot spot stress method and contains SCF (Stress Concentration Factor) formulae for the designer, rather than just an *S-N* line, as is the case in most design guidelines (e.g. Eurocode 3 1992, AWS D1.1 1998).

However, the IIW design specification omits the knowledge gained from extensive research programmes in the eighties and nineties, especially for the fatigue design of joints made from square hollow sections. As a result, the SCF formulae are fairly crude compared to present research standards and indeed for square hollow sections may not offer a substantial gain in accuracy over the present day classification methods. Therefore, after many years of development, a new specification is being drafted by IIW Subcommission XV-E.

In terms of user-friendliness, the new method is comparable to the existing IIW specification, despite the more sophisticated formulae and extended range of validity, due to a large number of design graphs.

The underlying SCF formulae, which are given as well, allow for easy incorporation into spreadsheets and computer programs, for faster determination of the SCFs. On the other hand, the design graphs will provide the designer with a clearer understanding of the consequences of a change in geometry and which geometries are desirable or ought to be avoided.

2 CURRENT DESIGN RULES AND BACKGROUND

2.1 Classification method

Virtually all steel design specifications offer a fatigue design method based upon the classification method. The method is based on grouping construction details with a similar fatigue behaviour together in a so-called class, which is then attributed to an *S-N* line. A strong advantage of the classification method is its ease of use.

The stress range to be used in the *S-N* lines of the classification method is the nominal stress range, as found from beam theory: $\sigma_{nom} = F/A + M/W$.

As an example of the classification method, Eurocode 3 (EC3 1992) states that K-joints made with square hollow sections, with a gap within certain limits

($0.5 \cdot (b_0 - b_1) \le g \le 1.1 \cdot (b_0 - b_1)$, and $g \ge 2 \cdot t_0$), have the following class:

- a class of 71 for $\tau \le 0.5$ (τ is the ratio between the wall thickness of the brace(s) and the chord)
- a class of 36 for $\tau = 1.0$
- interpolate linearly between 36 and 71 for τ between 0.5 and 1.0.

A class in EC3 is simply the stress range corresponding to a fatigue life of two million cycles.

For the type of *S-N* line used for the classification method of tubular joints, the complete *S-N* line can be calculated from this value based on a 1:5 slope up to 10^8 cycles and after that a horizontal line. By

looking at the *S-N* line of the class for the nominal stress range in the braces, the fatigue life of the joint can be determined very easily.

A major disadvantage of the classification method for tubular joints is that they tend to have a very large variation in fatigue behaviour within one class.

For instance, some gapped K-joints made of square hollow sections of the example above would have a local stress range which is considerably higher than other joints within the class, for a given nominal stress range, (even with the τ influence included). Since, for instance, a factor of 3 on stress range would, for a 1:5 *S-N* line as used in the EC3, result in a change in the number of cycles to failure by a factor of 3^5, this is a serious drawback of this method. The classification method in AWS D1.1 (1998) suffers from similar problems.

To counter this, either many classes would have to be defined, or the class would have to be defined as a function of the geometry, as is actually already done to a certain degree for the factor τ in the example above.

2.2 Hot Spot (Geometric) Stress Method

The hot spot stress method takes the effect of the uneven stress distribution around the perimeter of the joint due to the overall joint geometry into account in a direct way. The stress range to be used in the *S-N* lines of this method is the hot spot stress range, which can be defined as the highest extrapolated stress range along a line perpendicular to the weld toe around the perimeter of the joint.

However, determining the stress ranges along a large number of lines perpendicular to the weld toe by means of strings of strain gauges or FE (Finite Element) Analysis is typically not feasible for the designer. Therefore, Stress Concentration Factors (SCFs) are used as simple multiplication factors on the nominal stress range. The SCF is simply the ratio between the hot spot stress range and the nominal stress range.

The SCF can be determined from formulae or graphs which are based upon large numbers of FE analyses calibrated with test results. Since the SCF can be a complex function of the joint geometry, it offers the opportunity for vastly superior accuracy in fatigue assessment over the classification method, at the expense of the extra step necessary in determining the SCF. The classification method can be thought of as a particular case of the hot spot stress method, where the SCF is assumed to be constant for (sometimes large) variations in geometry. This is the essence of the large inaccuracy of the classification method.

If the SCF can be easily, yet sufficiently accurately, determined by the designer, the basis for a superior fatigue design method is laid.

2.3 Existing IIW guidelines (IIW 1985)

The IIW is one of the few organisations which has complete tubular joint fatigue design recommendations based on a hot spot stress method which includes SCF formulae. However, a number of deficiencies mar the current design guidelines:

- For joints between round hollow sections, the SCF in the braces is determined from the SCF in the chord by a simple equation:
  $SCF_1 = SCF_0 \cdot 0.63 + 1$, based on the Lloyds formulae (Wordsworth 1981).
- The method still includes traces of the classification method, in that the designer also has to check the nominal stress range against a different (lower) *S-N* line. This hybrid approach is confusing to the designer and does not have much justification except for covering the influence of chord stresses. Although it is readily recognised that, especially for low SCFs where the stress distribution is rather diffuse, the highest stress might occur at other locations (for instance at the inside of the joint), this is more readily countered by specifying a minimum SCF as in the current proposal, presented in this paper.
- The formulae for square hollow sections in the existing IIW guidelines are quite primitive, not even distinguishing between chord and brace(s) and only dependent upon τ. In reality, the EC3 classification method seems directly related to the existing IIW hot spot stress guidelines. The aforementioned advantages of the hot spot stress method over the classification method disappear completely if the SCF formulae are overly simplistic. Hence, the existing IIW "hot spot stress method" design guidelines for joints made of square hollow sections, based upon evidence available in 1985, are probably no better than the EC3 classification method! Therefore, the largest improvements over current IIW recommendations can be expected in the area of tubular joints between square members.

2.4 Hot spot stress definition

A more extensive description of the hot spot stress definition, FE model and derivation of the parametric formulae advocated herein can be found in (van Wingerde et al. 1996b). Only the main issues will be repeated here.

The hot spot stress method employed in this study couples the fatigue life of a joint to the maximum hot spot stress at the weld toe of the joint. The stress concentration factor (SCF) is the ratio between the hot spot stress (at the weld toe) for a line of measurement on the joint and the nominal stress, where the latter is determined from simple beam analysis of the loading which is causing the hot spot stress.

Similar to previously proposed design rules for T- and X-joints (van Wingerde 1992), the method used is based upon parametric equations which give the relationship between the geometry of the joint and SCF for a line of measurement. As such, these SCF equations incorporate the unequal stiffness distribution around the perimeter of the weld. The fatigue life is then found from *S-N* lines (Wöhler curves), which give the relationship between the hot spot stress range and the number of cycles to failure.

SCFs are based upon a quadratic extrapolation being performed on stresses, perpendicular to the weld toe (this is a departure from the current IIW guidelines which are based on principal stresses), and along fixed lines of measurement (van Wingerde 1992).

3 SCF EQUATIONS

3.1 SCF equations along lines of measurement

For the 90° T- and X-joints made of square hollow structural sections studied by van Wingerde et al. (1992), five lines of measurement were identified, as shown in Figure 1. However, these five lines are only for one corner. All other corners have the same SCFs, due to symmetry.

Note that for X-joints only symmetric brace loads are considered. Due to eliminating some equations and combining other equations, 10 parametric equations or design graphs are sufficient to describe arbitrary (in-plane) load cases on 90° T- and X-joints (see van Wingerde 1992). Note that this method may slightly underestimate the "true" hot spot stress which could occur at positions between two lines of measurement.

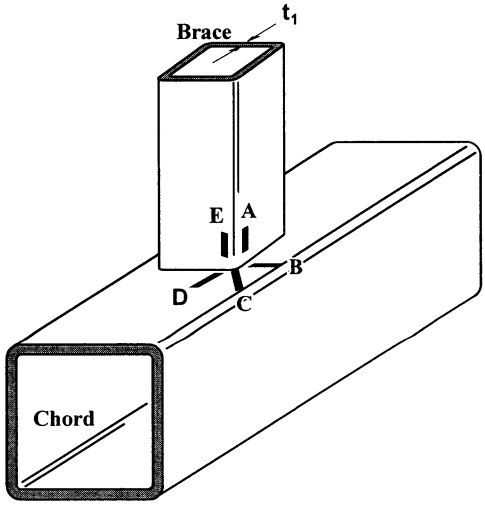

Figure 1. Measurement lines for 90° T- and X-joints

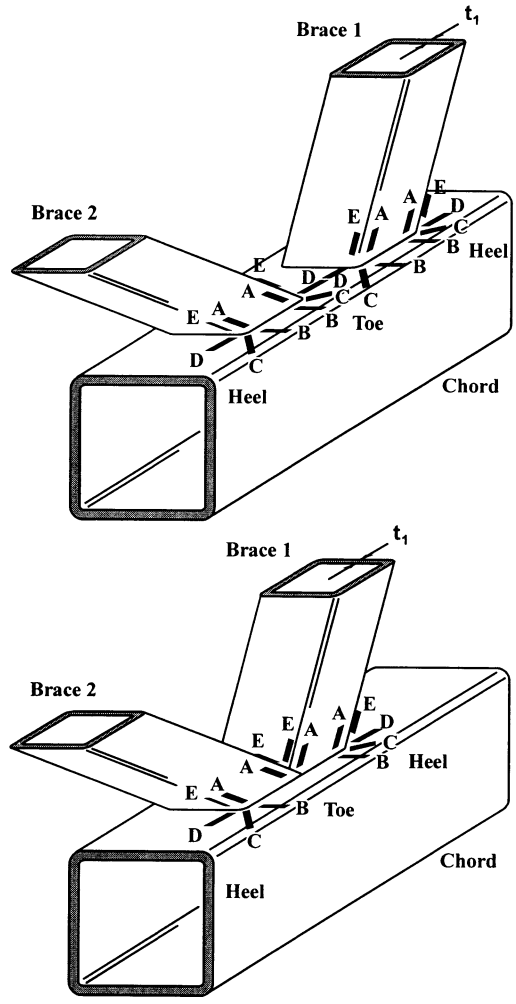

Figure 2. Measurement lines for K-joints with gap and overlap

With K-joints, the same lines A to E are used. However, there are now four corners to be considered and thus up to 20 lines of measurement (14 for overlapped joints), as shown in Figure 2.

For joints between round hollow sections, only saddle and chord locations are typically used. For T- and X-joints only axial load or in-plane bending on the braces has been covered as well as a simple equation to cater for in-plane chord loads. For K-joints six in-plane load cases exist: axial force or in-plane bending moment on brace 1, brace 2 or chord respectively.

In order to analyse a joint for a given load case the following steps are necessary:

1. For each line of measurement, the hot spot stress range is derived by multiplying the nominal

stresses which affect the hot spot stress by the appropriate SCF for the line of measurement and load case and then adding the results for different load cases together per line.
2. The highest hot spot stress ranges in the chord have to be selected from the measurement lines on the chord. Using the *S-N* line for the wall thickness of the chord, the fatigue life (number of cycles) for the chord is found.
3. For the braces, the same procedure is followed.

A balanced axial load case on a K-joint of square hollow sections, for example, involves axial loads on both braces and the chord. Therefore a hot spot stress range, along up to 20 lines of measurement, is calculated using three hot spot stress range components. An analysis of this case for one joint therefore involves deriving up to 60 SCFs. Thus, a large number of equations are necessary, even if locations with low SCFs are omitted.

In a recently completed CIDECT study (van Wingerde et al. 1996a, 1996b), 36 SCF equations were derived for gapped K-joints and 60 SCF equations for overlapped K-joints. Since these equations are dependent upon five independent geometric parameters (β, 2γ, τ, θ and g' or O_v), the equations tend to be complex, with up to 11 terms.

Although this method allows the flexibility of superposition of arbitrary load cases, it must be deemed unacceptably complex for inclusion in a manual design method, although it makes a suitable basis for a computer-based design program.

One should note that this method can still potentially underestimate the maximum hot spot stress range slightly, because the maximum hot spot stress range could occur at a position somewhere between two lines of measurement.

3.2 SCF equations for maximum SCFs in braces and chord

Given the overly complex set of equations for SCFs in K-joints, determined along the fixed lines of measurement shown in Figure 2, a simplification was necessary for inclusion into design guidelines. Based on the observation that K-joints typically carry a predominantly balanced axial load (see Figure 3a), with only minor other loads, the SCFs for that load case can be determined (van Wingerde et al. 1997).

Since no superposition of load cases is required, only the maximum SCFs in the braces (all lines A and E in Figure 3) and chord (all lines B, C and D in Figure 3) need to be determined, rather than providing SCFs for all lines of measurement. Following this method, two SCF equations were derived for the balanced axial load case for braces and chord respectively, as well as a SCF equation for additional axial load in the chord. In this way two

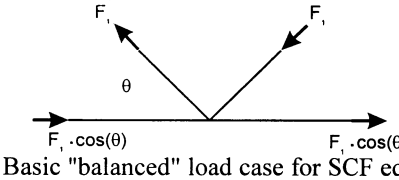

a) Basic "balanced" load case for SCF equations



b) "Additional" chord load

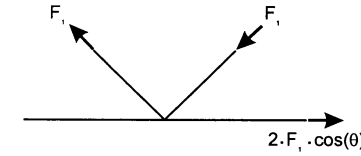

c) Typical load case for axially loaded tests

Figure 3. Combining balanced and additional chord load cases to obtain practical load cases

sets of three equations cover gapped and overlapped K-joints, as presented in Table 1, rather than the 96 of the previous CIDECT research programme (van Wingerde et al. 1996b).

Similar equation sets have been derived for various types of joints between round hollow sections (Karamanos et al. 1997). Also, for gapped K-joints made of square tubes practical alternative parametric formulas exist (Herion 1996, see also van Wingerde et al. 1997) and other formulas were taken from other sources, such as Efthymiou (1988), and hence are given in another form. For 90° T- and X- joints made from square hollow sections, where, as stated before, only 5 lines need to be considered but where bending plays a more prominent role, different SCF formulae are given for axial load and in-plane bending for lines B, C and D and only lines A and E were combined.

3.3 Form of the SCF equations and design graphs for basic "balanced" axial load case

Originally, the aim was to derive formulae that were as compact as possible, so that the designer would have less trouble using them. However, it is even better to eliminate intensive and error-prone use of parametric equations (except for computer-based calculations) and have the designer read the SCF from simple graphs. Graphs also give a better feeling for the influence of various parameters upon the SCF.

In general, the SCF is a function of β, 2γ, τ, θ and g' or O_v (see Table 1 for a description of these

parameters). It is obvious that directly plotting the SCF against 5 parameters is impossible and would lead to unreadable graphs. Therefore, an attempt was made to separate the parameters into 2 sets, of 2 and 3 parameters respectively, by defining the SCFs as: $SCF = f_1 \bullet f_2$.

In case of overlapped joints, there is a strong and complex relationship between β, θ, and O_v. These three parameters were selected for the first set, f_1. The remaining parameters, τ and 2γ, were used in the second set, f_2. Note that the first set describes the outer geometry of the joints, whereas the second set describes the wall thicknesses of the members. The procedure was optimised further by multiplying the factor f_1 by the value of f_2 for $2\gamma = 24$ and $\tau = 0.5$, while dividing the f_2 by this number. The graphs of the f_1 set then directly show the SCF for the case of $2\gamma = 24$ and $\tau = 0.5$. The procedure is analogous to Karamanos et al. (1997), an example is shown in Figure 4. f_2 becomes a correction factor for other values of 2γ and τ (see Figure 5 as an example).

For gapped joints, the SCF of the chord was plotted against β, with different lines for $\theta = 30°$, 45°, 60°, and 75° in different graphs for $g' = 1,2,4$ and 8. For the brace, one graph (shown in Figure 4) containing the SCF against β for $\theta = 30°$, 45°, 60°, and 75° was sufficient, since the gap had only a very small influence on the maximum SCF of the brace.

For overlapped joints, three graphs were made for the braces and three graphs for the chord. The graphs show the SCF against β, with different lines for $\theta = 30°$, 45° and 60°, in graphs for 50%, 75% and 100% overlap.

The whole set f_1 can thus be presented in a total of 11 graphs. The second set, f_2, consists of four graphs in total: for gap and overlap, chord and brace. Each graph shows a correction factor on the SCF against τ for six lines, for $2\gamma = 10$, 15, 20, 25, 30 and 35 (see for example Figure 5).

Table 1. Simplified Parametric SCF Formulae for K-Joints made of Square Hollow Sections

K-Joints with Gap

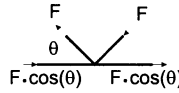

Basic balanced Axial Loading — Use SCF ≥2.0.

Brace $SCF = \{-0.008+0.45\bullet\beta-0.34\bullet\beta^2\}\bullet 2\gamma^{+1.36}\bullet\tau^{-0.66}\bullet\sin(\theta)^{+1.29}$

Chord $SCF = \{+0.48\bullet\beta-0.5\bullet\beta^2-0.012/\beta+0.012/g'\}\bullet 2\gamma^{+1.72}\bullet\tau^{+0.78}\bullet g'^{+0.2}\bullet\sin(\theta)^{+2.09}$



Axial Load on the Chord

Chord $SCF = \{2.45+1.23\bullet\beta\}\bullet g'^{-0.27}$ — Brace: negligible SCF

K-Joints with Overlap

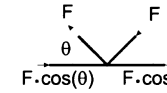

Basic balanced Axial Loading — Use SCF ≥2.0.

Brace $SCF = \{0.15+1.1\bullet\beta-0.48\bullet\beta^2-0.14/O_v\}\bullet 2\gamma^{+0.55}\bullet\tau^{-0.3}\bullet O_v^{-2.57+1.62\bullet\beta^2}\bullet\sin(\theta)^{+0.31}$

Chord $SCF = \{0.5+2.38\bullet\beta-2.87\bullet\beta^2+2.18\bullet\beta\bullet O_v+0.39\bullet O_v-1.43\bullet\sin(\theta)\}\bullet 2\gamma^{+0.29}\bullet\tau^{+0.7}\bullet O_v^{+0.73-5.53\bullet\sin^2(\theta)}\bullet\sin(\theta)^{-0.4-0.08\bullet O_v}$

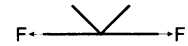

Axial Load on the Chord

Chord $SCF = \{1.2+1.46\bullet\beta-0.028\bullet\beta^2\}$ — Brace: negligible SCF

Notation and Range of Validity

β = Width ratio brace to chord	0.35	$\le\beta$	$\le$	1.00	
2γ = Width to wall thickness ratio chord	10	$\le 2\gamma$	$\le$	35	(for smaller 2γ: use $2\gamma = 10$)
τ = Wall thickness ratio brace to chord	0.25	$\le\tau$	$\le$	1.00	
θ = Angle between brace and chord	30°	$\le\theta$	$\le$	75° (gap), 60° (overlap)	
g' = Gap width to chord wall thickness ratio	$2\bullet\tau$	$\le g'$			($g \ge 2\bullet t_1$)
O_v = Overlapping percentage of braces	0.50	$\le O_v$	$\le$	1.00	(=50% to 100% overlap)
e = eccentricity of joint	−0.55	$\le e/b_0$	$\le$	0.25	(b_0 is chord width)

Notes : Although e is not used in the formulae, it still needs to be checked, for compliance with the static design specification.
Formulae give maximum SCFs at either the braces or the chord and are valid for square braces only.
Both braces are to have the same dimensions and same angle to the chord.
The formulae are also valid for rectangular chord members, within the parameter range of the static design specification.

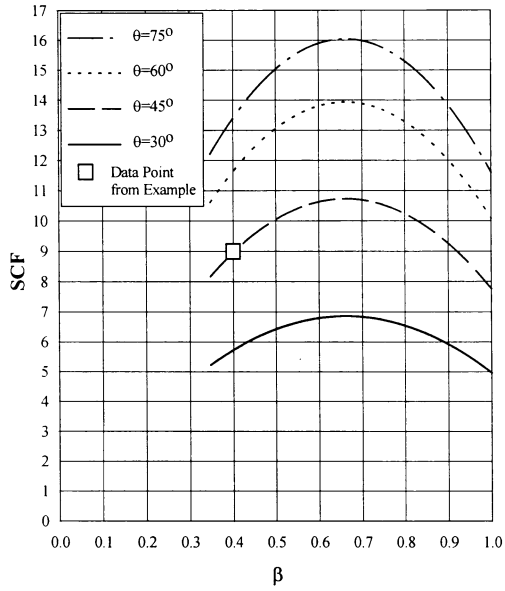

Figure 4. SCF in Braces of RHS K-Joints with Gap. "Balanced" Axial Loading (see Figure 3a).
Valid for $2\gamma = 24$ and $\tau = 0.5$. For other values of 2γ or τ, multiply the SCF found by a correction factor from Figure 5. The minimum value of the SCF (if necessary after multiplication with the correction factor) is 2.0.

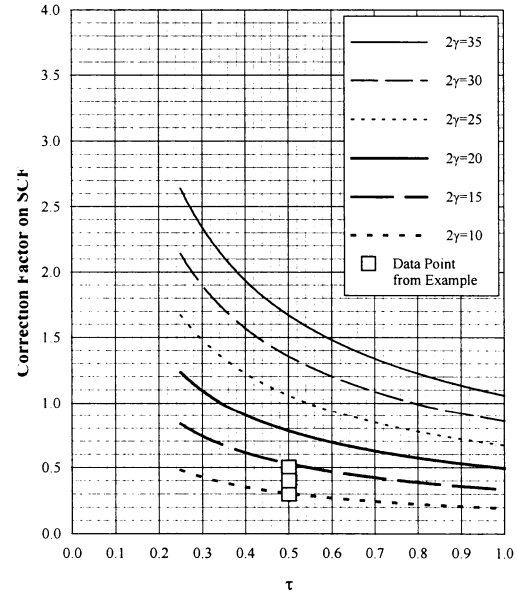

Figure 5. Correction Factor for SCF in Braces of RHS K-Joints with Gap. "Balanced" Axial Loading (see Figure 3a), for different values of 2γ and τ.
Note: For use with SCFs from Figure 4.

The complete set of graphs for the SCF and correction factors is given in van Wingerde et al. (1997). The equations are given in Table 1. Interpolation is allowed between the lines for other angles and between the graphs for other gaps or overlaps. For gap joints, extrapolation for larger or smaller gaps can even be performed, but one should check the validity range given in Table 1.

3.4 Other load cases

Some load cases are not covered by the basic SCF formulae of Table 1, but can still be analysed:

1. Bending moments in the braces. Lacking separate functions and possibilities for superposition, the stresses have to be calculated based upon the maximum nominal stress in the braces, even if this bending moment might not contribute fully to the critical hot spot stress range. For instance, a bending stress σ_{m1} of 30% of the axial stress σ_{a1} could be incorporated by multiplying σ_{a1} caused by the axial load case by 1.3 and using this value in the balanced axial load procedure of Table 1 and Figure 3a.

   This assumes that $SCF_{m1} = SCF_{a1}$, which is typically conservative, as well as occurrence of the highest SCF of both load cases in the same position which is always either correct or conservative. The degree of bending is often difficult to assess (Herion 1994) and therefore it is more practical for the designer to use correction factors, such as those provided in IIW (1985), EC3 (1992) and Wardenier (1982).
2. In the case of a different axial load to that assumed for the balanced load case (as shown in Figure 3a) or bending moment in the chord, an extra component for the stress range in the chord has to be determined (the influence in the braces is small). This requires two additional formulae, one for gapped and one for overlapped joints (given in Table 1). The nominal stress to be used for this additional hot spot stress range is the maximum bending stress plus maximum axial stress in the chord minus the stress caused by the "balanced" load case (which is already included in the basic formulae).

   So one uses the maximum of: $(\sigma_{m0}+\sigma_{a0})_{left}$ and $(\sigma_{m0}+\sigma_{a0})_{right}$ and subtracts $\sigma_{a1} \cdot \cos(\theta) \cdot A_1/A_0$. Note that the stress ranges in the brace are hardly affected by the load in the chord, so no additional adjustment is necessary there. For the "additional" load in the chord the equations are fairly simple, as most parameters had a negligible influence and the SCF could directly be plotted against β for various gaps.

   For the overlapped joints, the degree of overlap had little influence on the SCF, so only one line (SCF vs. β) was necessary. Together with

the 11+4 graphs of the SCFs for the basic "balanced" axial load case, this means that 16 graphs can fairly accurately describe the SCFs for all K-joints of square hollow sections within the (fairly large) range of validity. As was mentioned for braces earlier on, for the chord $SCF_{m0} = SCF_{a0}$ is assumed.

As was the case for the braces, adding up the maximum hot spot stress ranges in the chord due to the basic load case of Figure 3a and the "additional" chord load of Figure 3b can yield conservative results since the maximum stress may well occur along different lines of measurement for these load cases.

Consider a gapped K-joint which is loaded by axial loads as shown in Figure 3c (a typical set-up for tests). Since the load in the chord on the right hand side is higher than the load of the basic "balanced" load case of Figure 3a, an additional load on the chord has to be considered, as shown in Figure 3b. It is quite likely that the highest stress ranges due to the basic "balanced" axial load of Figure 3a occur along line B near the toe of brace 1 (see Figure 2). On the other hand, an "additional" axial force in the chord of Figure 3b may well result in the highest stress ranges occurring along line D at the heel of brace 1.

The maximum stress range in the chord is now found by adding the stress ranges of line B at the toe of brace 1 and line D at the heel of brace 1. Since the maximum stress ranges which are added in fact occur at different locations, it is obvious that this method can overestimate the actual maximum stress ranges occurring in the joint. Nevertheless, it is a fairly simple method of load superposition and always on the conservative side.

4 *S-N* LINES AND THICKNESS CORRECTION

4.1 Introduction to the thickness effect

The thickness effect is the result of several complex factors, which explains why results obtained by various researchers and implementation of the thickness correction varies considerably and discussions about the effect between researchers have always been quite lively. Haagensen (1989) and Marshall (1984) claim that the thickness effect is larger for joints with a higher stress gradient K_t. There seems to be evidence indicating that there might be a relationship between the thickness effect and the SCF, as indeed might be expected from fracture mechanics analyses.

Based on a statistical analysis of European fatigue test data, van Delft et al.(1985) have found a thickness effect of $t^{-0.075 \cdot \log(N)}$ for tubular joints between circular members, whereas van Wingerde (1992) established a factor of $t^{-0.11 \cdot \log(N)}$ for tubular joints between square members (t between 4 and 16 mm). Other researchers used a constant thickness correction (independent of N) of $t^{-0.3}$, as was derived for the new DEn guidelines (Thorpe & Sharp 1989).

A major factor is the complexity of the analysis of the thickness effect, since the thickness is an influencing factor on the fatigue behaviour, which itself is subject to considerable scatter. So if a smaller specimen achieves better fatigue performance it is difficult to determine how much the thickness effect contributes to the improved behaviour and how much is due to other factors.

4.2 Database used for the analysis of tubular joints

It is not possible for any single organisation to perform enough tests for well-founded conclusions on the influence of the thickness effect. Therefore, data needs to be gathered from as many sources as possible.

Although ideally only three parameters are needed from each test (S, N and t), in reality many more parameters are necessary for a detailed analysis: are certain data points higher than the average because of the smaller wall thickness, or because the test specimens were subjected to, for instance, TIG dressing or peening before testing? This means that many, often unpublished, parameters need to be gathered from a large number of sources. Fortunately, an existing database for tubular joints made of circular members could be used, namely that gathered by Dimitrakis and Lawrence of the University of Illinois (Dimitrakis et al. 1995).

The database used in this paper has been extended further since publication of that paper in 1995. The data for the tubular joints made of square members is obtained from European research projects, which were sponsored by the ECSC (European Coal and Steel Community) and CIDECT (Comité International pour le Développement et l' Étude de la Construction Tubulaire, an organisation of hollow section manufacturers). All the data used in this paper is from experimental laboratory tests, on either isolated joints or joints within complete trusses.

The data for circular hollow sections in particular needed an extensive amount of screening to arrive at valid conclusions, since this data originated from a very large number of organisations, each with different test methods, hot spot stress range definitions and number of cycles to failure definitions, weld treatments, materials, etc.

The total number of data points for which N, plus an extrapolated or locally measured strain or stress range is given, is 515, of which only the 418 points with extrapolated strains or stresses are used for the *S-N* lines and scatter bands.

4.3 Screening criteria

- No joints tested in water
- No reinforced joints
- No special weld treatments
- No tests which were subjected to high tensile loads prior to testing (known to improve the fatigue life)
- No retested joints
- No random test sequences
- No joints of which the failed member is not reported, so that the wall thickness of the member which failed is unknown.

The requirements above reduced the data set for circular hollow sections further to 173 valid test results.

For the tubular joints between square members, only a few overloaded tests and weld failures needed to be excluded, as the definition used for S (extrapolated) and N were uniform for all tests considered. One problem occurring for certain K-joints between square hollow sections was that, probably due to incorrect strain gauge measurements, the measured stress ranges were known to be incorrect (van Wingerde et al. 1997). In this case, the nominal stress range was multiplied instead by SCFs found from parametric design formulae (van Wingerde et al. 1996a). Altogether there were 65 valid data test results left for joints between square hollow sections.

4.4 Resulting S-N line definition for tubular joints

On contrast to earlier work by the authors (for instance van Wingerde 1992), a new S-N line and thickness correction have been established. Based on the analysis in the data sets for square and circular hollow sections, the DEn T' line (EC3 class 114) is recommended as a reference S-N line (for 16 mm wall thickness) for joints between both square and circular members, to allow for easier implementation in design guidelines. The equations for the S-N lines are therefore dependent upon the wall thickness, as given in Table 2:

Table 2. S-N line Equations for Tubular Joints

$10^3 < N < 5 \cdot 10^6$
$\log(S) = \frac{1}{3} \cdot (12.476 - \log(N)) + 0.06 \cdot \log(N) \cdot \log\left(\frac{16}{t}\right)$
$5 \cdot 10^6 < N < 10^8$ (variable amplitude only)
$\log(S) = \frac{1}{5} \cdot (16.327 - \log(N)) + 0.402 \cdot \log\left(\frac{16}{t}\right)$

Instead of the equations shown in Table 2, the $S - N$ lines, including the thickness correction, can be presented in the form of a set of $S - N$ lines for different wall thicknesses, see Figure 6. The presentation in the graphs is likely easier to use for most designers. Note that the S-N lines for EC3 are horizontal after N = 5 million cycles for constant amplitude loading (fatigue limit). The S-N lines shown in Figure 6 are for variable amplitude loading.

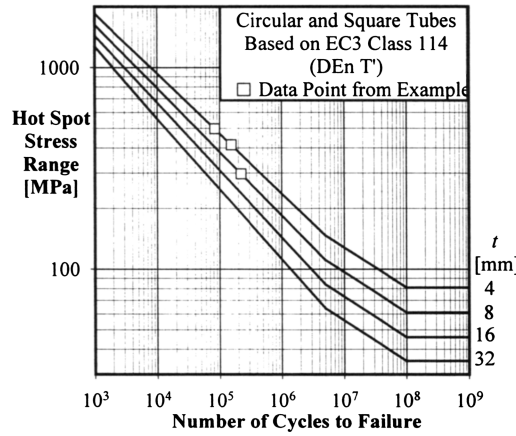

Figure 6. Recommended $S - N$ lines for tubular joints (circular and square hollow sections)

To check the validity of the recommended reference $S - N$ line and the thickness correction, all data is corrected with (the inverse of) the recommended thickness correction and plotted together with the reference $S - N$ line (which is plotted for t = 16 mm) in Figure 7.

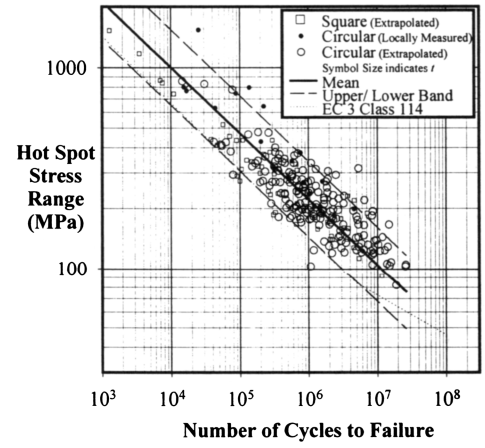

Figure 7. $S - N$ data for tubular joints between both circular and square members, with a thickness correction of $S_{plotted} = S_{test} \cdot \left(\frac{16}{t}\right)^{-0.06 \cdot \log N}$

5 EXAMPLE OF USE OF THE FORMULAE AND DESIGN GRAPHS

As an example, a K-joint for which the test results are known (Puthli et al. 1989) will be analysed here using the design graphs.

The test specimen has the following dimensions:

- Chord: 100x100x8 mm ($A_0 = 2889$ mm^2)
- Braces of 40x40x4 mm ($A_1 = 562$ mm^2)
- Angles between the braces and chord are 45°
- Gap between the braces = 25.4 mm.

The nominal axial stress range in the braces is 113 MPa. Loading is as shown in Figure 3c.

1. Determine the non-dimensional parameters:
   - $\beta = b_1 / b_0 = 40 / 100 = 0.4$
   - $2\gamma = b_0 / t_0 = 100 / 8 = 12.5$
   - $\tau = t_1 / t_0 = 4 / 8 = 0.5$
   - $g' = g / t_0 = 25.4 / 8 = 3.18$.
2. Determine the SCFs in the braces due to "balanced" axial loading (Figure 3a), as well as the SCF in the chord due to "additional" axial force in the chord (Figure 3b).
   - In the graph for SCFs in the braces of K-joints with gap (see symbol in Figure 4), for the line for $\theta = 45°$ and for $\beta = 0.4$, SCF = 9.0. This would be valid for $2\gamma = 24$ and $\tau = 0.5$.
   - Since $2\gamma = 12.5$ and $\tau = 0.5$, one must multiply by a factor, taken from the graph for correction factors to SCFs in braces of gapped K-joints (see symbols in Figure 5). For $2\gamma = 10$ and $\tau = 0.5$ a correction factor of 0.3 is obtained, and for $2\gamma = 15$ and $\tau = 0.5$ the correction factor is 0.5. Interpolating for $2\gamma = 12.5$ gives a factor of 0.4. So the resulting SCF = 9.0 • 0.4 = 3.6 in the braces. (Use of the first formula in Table 1 results in an SCF of 3.7, the difference being due to inaccuracies in reading the graphs).
   - Similarly for the chord under "balanced" axial loading an SCF of 2.3 is found (using the second formula in Table 1).
   - For the additional component of axial force in the chord, for $\beta = 0.4$ and $g' = 3.15$ an SCF = 2.2 is found (using the third formula in Table 1).
3. Determine the "additional" nominal stress range in the chord. The test specimen had the axial load case of Figure 3c. The tension force range in the right side was:
   $2 \bullet \sigma_{a1} \bullet \cos(\theta) \bullet A_1 = 2 \bullet 113 \bullet \cos(45°) \bullet 562 =$ 89.8 kN.
   Since the force range at the other chord end is zero, this is the maximum force range in the chord. The "balanced" axial load case is based on an axial force range in the chord which is the result of $(\sigma_{m1} + \sigma_{a1}) \bullet \cos(\theta) \bullet A_1 =$ 44.9 kN. Therefore the force range to be used for determination of the "additional" axial force range in the chord is 89.8-44.9 = 44.9 kN, resulting in an additional stress range of $44.9 \bullet 10^3 / 2889 =$ 15.5 MPa.
4. Determine the hot spot stress ranges in braces and chord.
   Braces:
   $S = (\sigma_{m1} + \sigma_{a1}) \bullet SCF = (0 + 113) \bullet 3.6 =$ 407 MPa.
   Chord:
   $S = \sigma_{a1} \bullet SCF_{bal.} + (\sigma_{a0,bal.}) \bullet SCF_{add.}$
   $= 113 \bullet 2.3 + 15.5 \bullet 2.2 =$ 294 MPa.
5. Determine the fatigue life of the joint. Using the S- N lines of Figure 6 (see also the symbols in Figure 6), t = 4 mm for the braces and S= 407 MPa, results in a fatigue life of slightly under 200,000 cycles for the braces Similarly, for t = 8 mm for the chord and S = 294 MPa, one obtains a fatigue life of slightly over 200,000 cycles for the chord. Using the more accurate formulae for the S- N lines and using the hot spot stress ranges based upon SCF formulae yields: for the braces, t = 4 mm, 415 MPa, and a fatigue life = 153,000 cycles, whereas for the chord, t = 8 mm, 298 MPa, and a fatigue life = 220,000 cycles.

For this test, a chord failure at N =153,000 cycles would therefore be predicted.

The test specimen failed in the chord at N = 361,000 cycles, or at about twice the number of cycles predicted. This is a perfectly normal discrepancy between prediction and test result (or indeed between various test results, even within one series of tests). On a stress basis, assuming an S- N line with a slope of 1:3, the error is a factor of $(361{,}000/153{,}000)^{1/3} = 1.33$, or 33%.

However, it should be noted that:

- A certain degree of bending was present in the test. For instance, if 20% bending is assumed in the braces ($\sigma_{m1} = 0.2 \bullet \sigma_{a1}$), the hot spot stress range in the braces becomes: 1.2•415 = 498 MPa, resulting in of fatigue life of 83,000 cycles. Note that the resulting bending moments in the brace would result in a smaller increase in nominal stress ranges in the chord. Since the brace was already determining the fatigue life of the joint, the chord needs not be checked for the influence of bending moments in the braces.
- The S- N lines of Figure 6 give a characteristic value and therefore typically underestimates the actual fatigue life.

On a stress basis, the error now becomes a factor of $(361{,}000/83{,}000)^{1/3} = 1.63$, or 63%. It is clear that assumptions on the degree of bending have an important influence on the predicted fatigue life of a joint.

6 CONCLUSIONS

- A simplified and comprehensive set of fatigue design recommendations has been provided for welded tubular joints, covering both circular and square hollow sections. For circular hollow sections, existing recommendations resulting from research on offshore tubular structures have been adopted, whereas for square hollow sections recent research on T-, X- and K-joints has been adopted.
- Recommended S- N lines are given, which have been verified by comparison with numerous test results and the SCF formulae proposed, for joints between both square and circular hollow sections. These S- N lines are presented in the form of both equations and graphs for the convenience of the designer and include a correction for the thickness effect (scale effect).
- The new method offers a superior appreciation of the fatigue strength of a given tubular joint.
- Although the underlying formulae are more complex than in the previous version of the IIW specification, the new method is comparable in terms of user-friendliness, due to the use of design graphs.

ACKNOWLEDGEMENTS

Prof. F. Lawrence and Dr. S. Dimitrakis from the University of Illinois are thanked for sharing their database of fatigue test results on joints between circular hollow sections, which was of great help in enhancing the analyses contained in this paper.

The experimental results from previous research programmes, used as a basis for the verification of the SCF formulae for K-joints between square hollow sections, were carried out with financial support of the ECSC (European Coal and Steel Community) and CIDECT (Comité International pour le Développement et l'Étude de la Construction Tubulaire).

The numerical research to produce the SCF parametric formulae, and analysis of the results, was carried out with the financial support of CIDECT Programs 7P and 7R, NSERC (the Natural Sciences and Engineering Research Council of Canada) and NATO (the North Atlantic Treaty Organisation) CRG No. 930101.

NOTATION

β = Brace (web) to chord width ratio = b_1/b_0

2γ = Width to wall thickness ratio of the chord = b_0/t_0 (γ = chord radius to wall thickness ratio for circular sections)

θ = Angle between brace (web) and chord.

σ = Nominal stress

τ = Brace (web) to chord wall thickness ratio = t_1/t_0

SCF = Stress Concentration Factor

A = Cross sectional area of member

F = Axial force in member

K_t = Stress gradient

M = In-plane bending moment in member

N = Number of cycles to failure

O_v = The overlapping percentage

W = Elastic section modulus of member considered

S = Hot spot stress range

b = External width of member considered

e = Eccentricity, with positive being towards the "outside of the truss", away from the braces (web members)

g = Gap between toes of braces (web members), ignoring the welds

g' = Gap to chord wall thickness ratio = g/t_0

t = Wall thickness of member considered

Subscripts

0 = Chord

1 = Brace(s)

a = Axial (stress)

m = In-plane bending (stress)

As an example, SCF_{a1} is the SCF due to an axial force in brace.

REFERENCES

AWS 1998. *Structural Welding Code - Steel.* ANSI/AWS D1.1-98. American Welding Society, Miami, USA.

DEn 1990. *Offshore Installation: Guidance on Design and Construction.* Department of Energy, London, UK.

Dimitrakis, S.D., Lawrence, F.V. & Mohr, W.C. 1995. S-N Curves for Welded Tubular Joints. *Proceedings of the 14th International Offshore Mechanics and Arctic Engineering Symposium (OMAE '95).* III:209-222.

EC3 1992. European Committee for Standardization, Eurocode 3: *Design of Steel Structures - Part 1.1: General Rules and Rules for Buildings.* ENV 1993-1-1: 1992E.

Efthymiou, M. 1988. Development of SCF Formulae and Generalised Influence Functions for use in Fatigue Analysis. *Proceedings of the Offshore Tubular Joints Conference (OTJ '88)*, UEG Offshore Research, Englefield Green, Near Egham, UK. (with subsequent corrections by Shell Co.).

Haagensen, P.J. 1989. Improvement Techniques. *Proceedings of the International Symposium on the Occasion of the Retirement of Prof. J. de Back*, Delft, The Netherlands:77-95.

Herion, S. 1994. *Raümliche K-Knoten aus rechteck-Hohlprofilen*. Ph.D. thesis, University of Karlsruhe, Germany.

Herion, S. 1996. Personal correspondence with the author..

IIW 1985. *Recommended Fatigue Design Procedure for Hollow Section Joints. Part 1 - Hot Spot Stress Method for Nodal Joints*. IIW Doc. XIII-1158-85, XV-582-85, International Institute of Welding Subcommission XV-E, IIW Annual Assembly, Strasbourg, France.

Karamanos, S.A, A. Romeijn & J. Wardenier 1997. Stress Concentration Factors for the Fatigue Design of Multi-Planar Welded Tubular Connections. *Proceedings of the 8th International Conference on Behaviour of Offshore Structures*. Delft, the Netherlands. III:63-76.

Marshall, P.W. 1984. Connections for Tubular Structures. *Proceedings of the 2nd International Conference on Welding of Tubular Structures*, Boston, USA:1-54.

Puthli, R.S., C.H.M. de Koning, A.M. van Wingerde, J. Wardenier & D. Dutta 1989. Fatigue Strength of Welded Unstiffened RHS-Joints in Latticed Structures and Vierendeel Girders - Final Report Part III: Evaluation for Design Rules. *Stevin Report 25-6-89-36/A1, TNO-IBBC Report BI-89-097/63.5.3820*, Delft University of Technology, the Netherlands.

Thorpe, T.W. & J.V. Sharp 1989. The fatigue performance of tubular joints in air and seawater *MaTSU*, Harwell Laboratory, Oxfordshire, UK (presented during the OMAE '89, but not included in the proceedings)

van Delft, D.R.V., Noordhoek, C. & de Back, J. 1985. Evaluation of the European Fatigue Test Data on Large-sized Welded Tubular Joints for Offshore Structures. *Proceedings of the Offshore Technology Conference (OTC '85)*, Houston, USA, paper OTC 4999.

van Delft, D.R.V., C. Noordhoek & M. L. Da Re. 1987. The Results of the European Fatigue Tests on Welded Tubular Joints compared with SCF Formulas and Design Lines. *Proceedings of Steel In Marine Structures (SIMS '87),* Delft, the Netherlands:565-577.

Wardenier, J. 1982. *Hollow Section Joints*. Delft: Delft University Press.

van Wingerde, A.M. 1992. The Fatigue Behaviour of T- and X-Joints made of Square Hollow Sections. *Heron*, the Netherlands.37(2):1-180.

van Wingerde A.M., J.A. Packer & J. Wardenier 1996a. Determination of Stress Concentration Factors for K-Connections between Square Hollow Sections. *Proceedings of the 6th International Offshore and Polar Engineering Conference*, Los Angeles, USA. IV:52-59.

van Wingerde A.M., J.A. Packer, J. Wardenier & D. Dutta 1996b. The Fatigue Behaviour of K-Joints made of Square Hollow Sections. *CIDECT Report 7P-19/96*, University of Toronto, Canada.

van Wingerde A.M., J.A. Packer, J. Wardenier & D. Dutta 1997. Simplified Design Graphs for the Fatigue Design of Multiplanar K-Joints with Gap - Interim Report: Simplified Design Graphs and Comparison of Fatigue Design Guidelines for Uniplanar RHS K-Joints. *CIDECT Report 7R-01/97*, University of Toronto, Canada.

Wordsworth A.C. 1981. Stress Concentration Factors at K- and KT- Tubular Joints. *Proceedings of the Conference on Fatigue in Offshore Structural Steel.* London, UK: 49-56.



Taylor & Francis
Taylor & Francis Group
http://taylorandfrancis.com

Static strength



Taylor & Francis
Taylor & Francis Group
http://taylorandfrancis.com

Tubular Structures VIII, Choo & Van der Vegte (eds) © 1998 Balkema, Rotterdam, ISBN 90 5809 001 9

Experimental study of a full-scale multiplanar tubular XT-joint

T.K.Chan, C.K.Soh & T.C.Fung
School of Civil and Structural Engineering, Nanyang Technological University, Singapore

ABSTRACT: This paper reports on a full-scale test of a multiplanar tubular XT-joint conducted using the multiplanar ultimate strength test rig at the Nanyang Technological University. The XT-joint is made up of a chord with a pair of out-of-plane braces and a single in-plane brace welded to the chord. The geometric parameters for this joint are α (2L/D)=21.86, β (d/D)=0.6, γ (D/2T) = 24.07 and τ (t/T) = 0.98. A constant axial tension load was applied to the out-of-plane braces and an axial compression load was applied to the in-plane brace and increased until failure. This specimen failed by plastification of the chord wall under the compression brace and through cracks at the weld toes of the tension braces. The ultimate axial compression load was significantly reduced by the tension load in the out-of-plane braces when compared to a corresponding uniplanar T-joint.

1 INTRODUCTION

Steel offshore structures are conventionally three-dimensional frames composed of cylindrical steel members. The main load bearing components are tubular members which are very efficient structural shapes, however, the connections of these tubular members are complex and difficult to analyse accurately. In the past, much research work have been carried out on uniplanar joints leading to their incorporation into design codes such as the API (1991) and AWS (1992). Relatively few research and testing of multiplanar joints have been initiated mainly because of their higher costs and test complexities. The lack of data on multiplanar joints is reflected in a different treatment of multiplanar joints in the various design codes. Most of design codes treat multiplanar joints as a series of uniplanar joints. The interaction between the different planes is ignored. This may result in over-conservative or unsafe actual strengths, depending on the loading, configuration and parameter of the multiplanar joints, because recent studies have shown that the multiplanar effect was a significant factor contributing to the strength of multiplanar joints. Multiplanar joint is an intrinsic feature in steel tubular construction, and the understanding of its behaviour is important for more efficient and economical design.

A review of existing literature reveals that there is a limited number of experimental studies on the behaviour of multiplanar tubular joints. No experimental test results on full-scale multiplanar XT-joints can be found. Davies (1994) and Vegte (1995) have modelled axially loaded multiplanar XT-joints using finite element analyses and have carried out numerical parametric studies. Based on the finite element results and the proposed ring model, ultimate strength formulae were established for axially loaded multiplanar XT-joints.

The objective of this investigation is to provide experimental data on the behaviour of multiplanar joints at ultimate loads, and is part of a series of tests to investigate the various failure modes of multiplanar joints. This specimen was loaded with a constant axial tension load to the East-West braces (out-of-plane load) and an axial compression load to the North brace (in-plane load). The observed failure load was then compared to values predicted by current design codes for a uniplanar T-joint and a multiplanar XT-joint to investigate the effects of the out-of-plane axial tension.

2 TEST SPECIMEN AND SET-UP

Figure 1 shows the geometry and dimensions of the multiplanar XT-joint. The geometric parameters for this joint are:

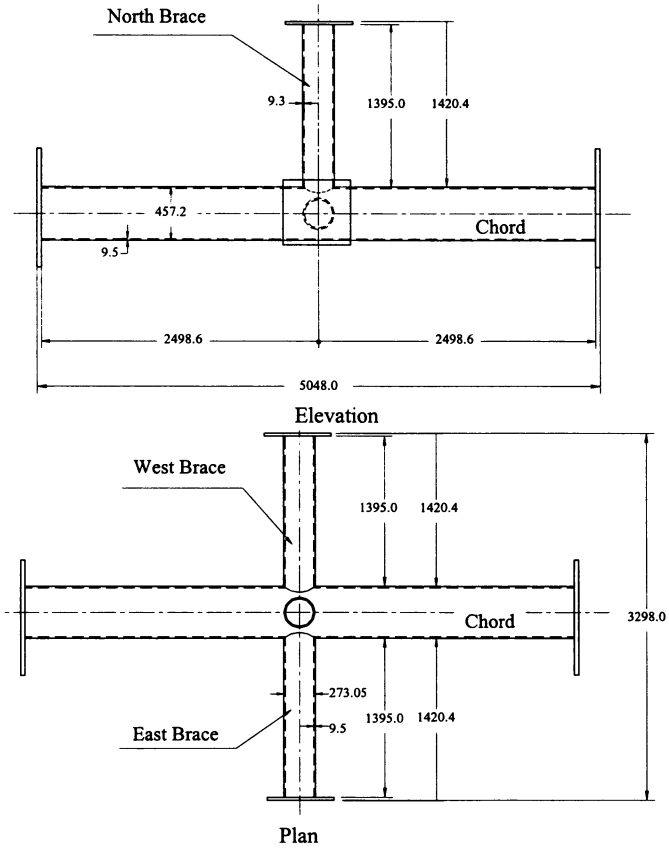

Figure 1 Detail of the XT-joint specimen
* All braces have the same diameter and thickness; all dimensions in mm

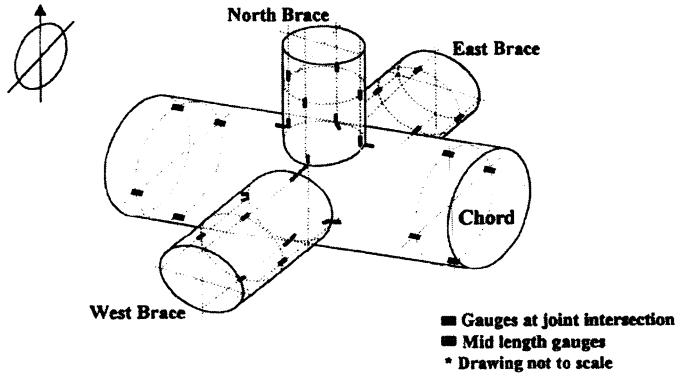

Figure 2 Strain gauge locations

α (2L/D)=21.86,β (d/D)=0.6,
γ (D/2T) = 24.07, and τ (t/T) = 0.98.

The XT-joint was made up of a 457.28mm dia. (18 inch) chord with a pair of East-West braces (out-of-plane) and a single North brace (in-plane) welded to the chord. The brace diameter is 273.05mm (10.75 inch). The β (d/D) value of 0.6 for this specimen is the upper range for non-overlapping multiplanar joint based on the limitation imposed by API (1991) for a minimum of 50mm clearance between adjacent braces. The thickness ratio, τ (t/T) was chosen to prevent premature brace failure. The end effects of the chord was reduced with a choice of a high α (2L/D) value.

2.1 *Materials*

Standard API 5L Grade B pipe was used for the specimen. Test coupons were machined from the pipes and tested in accordance with ASTM A370 (1992). The coupons were cut along the longitudinal axis of the pipe section and a flat specimen (12.48 x 7.70mm) was machined from the curved profile with a gauge length of 50mm. The mechanical properties derived from the tensile test are shown below.

Table 1 Mechanical properties of joint specimen

	Mill Cert.	Coupon Test	API Spec.
Yield stress (MPa)	312.2	361.8	250 min.
Ultimate stress (MPa)	482.8	478.5	415 min.
Elongation (%)	36	33	21 min.

The coupon test confirmed the mechanical properties reported in the manufacturer's certificate and were found to comply with the API specification. The elastic modulus obtained from the coupon test was observed to be 195GPa.

2.2 *Welding*

The brace and chord intersections were prepared and welded with full penetration welds in accordance with the AWS code (1992). The welds were ultrasonically tested for defects after fabrication.

2.3 *Strain measurements*

A total of 205 strain gauges were attached to the XT-joint to obtain the stress intensities at the various locations around the joint. A large number of gauges were attached to this specimen as it was previously used in another project to investigate the stress concentration factors. However, only 44 strain gauges were used in this test and are located as shown in Figure 2. Four linear strain gauges were placed longitudinally along each axes of the braces at its mid-length to record the correct application of load into the individual braces; and another 2 sets of four longitudinally along the axes of the chord. Any eccentricity in the application of load into the braces would cause bending and be reflected as uneven strain distribution in the brace. Twenty four strain gauges were placed at the intersection region of the braces and chord to determine the onset of plastic yielding in this region.

2.4 *Loading arrangement*

Figure 3 shows the test set-up for the XT-joint in the NTU multiplanar ultimate strength test rig. Additional details and capabilities of the NTU test facility were reported by Chiew *et.al* (1997). The chord ends were connected to the main frame of the test rig with 48mm dia. bolts to maintain the chord centre-line at the same alignment throughout the test. This end connection may be described as partially fixed as the bolts and end plate may deform slightly when loaded. The free ends of the braces were connected to the actuators by swivel heads which allow for brace rotation during load application. The swivel heads were mounted on the end plates of the braces by bolts.

2.5 *Instrumentation*

A total of 16 displacement transducers (LVDT) were placed at locations shown in Figure 4 to provide a plot of the joint load vs. displacement behaviour and to monitor the inclination of the East and West braces. The load readings were obtained from the integral load cells in the actuators.

Four transducers were placed around the chord at the NE, NW, SE and SW location (C1, C2, C3 and C4) to measure the deformation of the chord section during loading. The inclination of the chord (C5, C6 and C7), and the East and West braces were monitored by two transducers (E2 & E3 and W2 & W3) at each segment. No transducers were placed on the North brace as it was expected to remain vertical throughout the test. However, additional transducers (N1 and N2) were placed at the ends of the braces to confirm the displacement of the brace ends due to the applied loads.

The strain gauges and displacement transducers were connected to a TML data logger and interfaced to a personal computer running the Lab Windows software to automatically record the readings in conjunction with the load readings from the actuators.

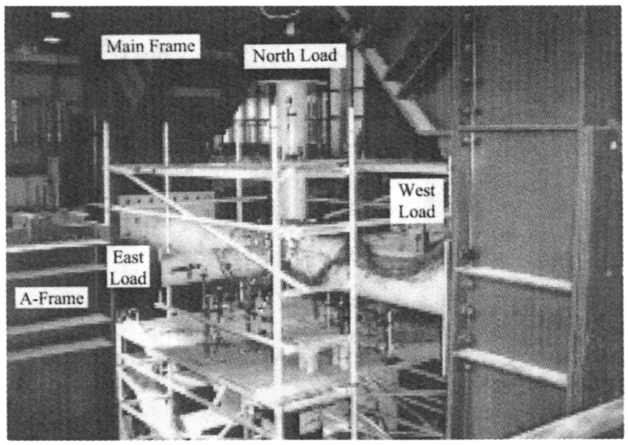

Figure 3 XT-joint specimen in the test rig

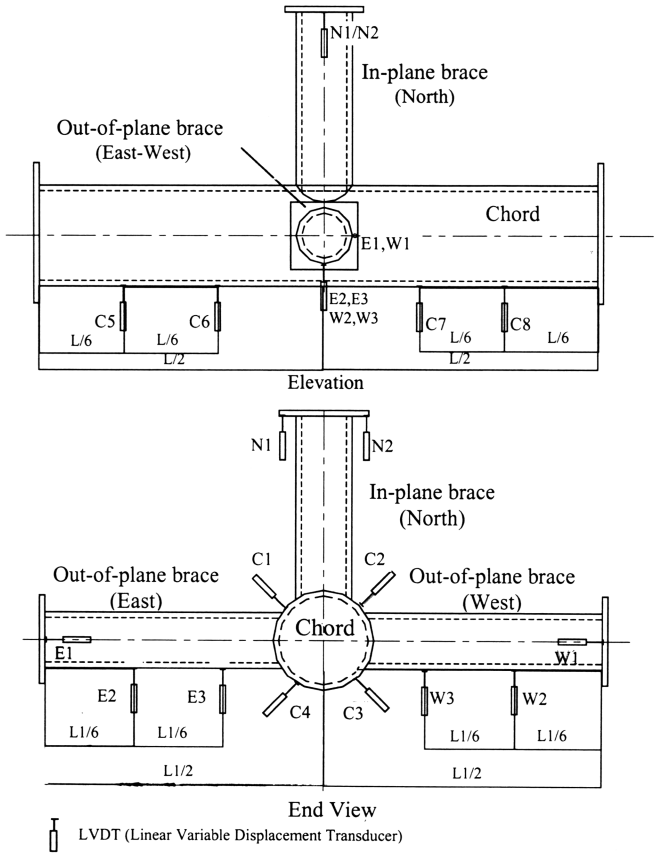

Figure 4 Locations of LVDT

2.6 *Test procedure*

Figure 5 shows the load arrangement applied to the XT-joint. The East and West braces (out-of-plane) were loaded with a constant axial tensile load of 300kN throughout the test and this was dynamically maintained by the actuators. The axial compressive load in the North brace (in-plane) was increased until failure occurred.

The test procedure was divided into 3 stages. For the first stage, the 300kN tensile load was applied to the East and West braces by 10 increments of 30kN, at a rate of 10kN per minute. At the second stage, the load in the North brace was increased at a rate of 20kN per minute until 200kN while maintaining the 300kN tension in the East-West braces. At the final stage, the test rig was switched to displacement control and the North brace was loaded at a rate of 1mm per minute up to joint failure and continued until the maximum travel of the actuator. The use of displacement control is to prevent sudden movements of the actuator during instability or joint failure.

3 RESULTS

The load-displacement curve for the multiplanar XT-joint is shown in Figure 6. The initial displacement of 3.08mm was due to the Stage 1 300kN tensile load into the East-West braces. At the initial part of the load-displacement curve, it is shown that the load increases with increasing displacement until the load reaches a peak of 374.5kN with a corresponding vertical displacement of 59.27mm at point 1. The load drops to a lower value of 321.0kN at point 2. After point 2, the load increases slightly with further vertical displacement before the test was stopped at a maximum displacement of 190 mm due to the stroke limitation of the actuator.

The stresses in all three braces were monitored by the mid-length strain gauges and were found to be almost the same indicating that the loads were correctly applied.

3.1 *Failure type*

Figure 7 shows the cross sectional view of the failed chord mid-section of the tested multiplanar XT-joint. The North in-plane brace has penetrated and buckled the chord wall while the East and West out-of-plane braces under the 300kN tensile force have caused the chord wall to bulge out. It is believed that after the point of maximum load, plastic hinges occurred at various points around the chord and thus the North brace was unable to sustain any additional load. The load carrying capacity decreased as the North brace moved into the chord until further deformation was prevented by membrane action in the material around the North brace. This consequently led to a slight increase in load carrying capacity.

It was also noted that after the point of maximum load, cracks were observed at the saddle of the out-of-plane braces and these cracks extended and widened as the test progressed into the post-buckling stage. The average length of the cracks at the weld toe of both the saddle points of the out-of-plane braces is approximately 200mm.

4 DISCUSSION OF RESULTS

4.1 *Comparison of experimental result with uniplanar T-joint predictions*

Over the last twenty years, a variety of ultimate strength formulae for uniplanar T-joints have been proposed. The most recent formulae are those published by Yura *et. al.*(1980), Billington *et. al.* (1982) and Kurobane *et. al.* (1984) and AWS (1992). The differences in the three strength formulae are due to differences in database screening, in the definition of the ultimate limit state and in the precision of the analysis. The AWS formulation, being a design code, is based on a lower bound interpretation of test data.

The comparison of the experimental result for multiplanar XT-joint with the predictions according to above ultimate strength formulae for uniplanar T-joints is shown in Table 2. The prediction from Kurobane *et. al.* was not included because the geometric parameter α (=21.86) of the test specimen exceeds the validity range ($6.0<\alpha<16.0$).

The experimental failure load was found to be significantly lower than all three predictions; about 70% of the load predicted for a uniplanar T-Joint. The test result for the XT-joint is only approximately 80% of the most conservative prediction using the AWS equation. This clearly indicates that the multiplanar effect of a high tension force in the out-of-plane braces is to reduce the load carrying capacity of a T-joint.

4.2 *Comparison of the experimental result with multiplanar ultimate strength predictions*

Only two existing design codes give recommendations which take into account multiplanar effects for tubular joints; AWS (1992) and Eurocode 3 (1992).

Table 2 The comparison of the experimental result for XT-joint with predictions of T-joints

Joint configuration and loading condition	T (mm)	α	β	γ	τ
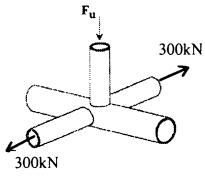	9.5	21.86	0.6	24.07	0.98
	$F_{u,TEST}$ (kN)	$F_{u,AWS,T}$ (kN)	$F_{u,Yura,T}$ (kN)	$F_{u,Billington,T}$ (kN)	
	374.54	480.1	510.7	531.6	
		$F_{u,TEST,XT}$ /$F_{u,AWS,T}$	$F_{u,TEST,XT}$ /$F_{u,Yura,T}$	$F_{u,TEST,XT}$ /$F_{u,Billington,T}$	
		0.78	0.73	0.70	

Table 3 Experimental and numerical results and ultimate strength formula's predictions

Joint configuration and loading condition	D (mm)	d (mm)	T (mm)	t (mm)	L (mm)
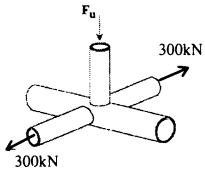	457.2	273.05	9.5	9.3	4997.2
		α	β	γ	τ
		21.86	0.6	24.07	0.98
	$F_{u,TEST}$ (kN)	$F_{u,AWS}$ (kN)	$F_{u,VEGTE}$ (kN)	$F_{u,AWS}$ / $F_{u,TEST}$	$F_{u,VEGTE}$ / $F_{u,TEST}$
	374.54	318.87	362.8	0.85	0.97

The AWS code proposes design recommendations for non-overlapping axially loaded multiplanar joints. Eurocode 3 only considers a few of multiplanar joints, such as the TT-, KK- and XX-joints. A number of researchers have investigated ultimate behaviour of multiplanar joints but only Vegte (1995) has proposed the ultimate strength formulae for axially loaded multiplanar XT-joints based on finite element analyses and ring model theory.

The experimental ultimate load is compared to that predicted using the AWS code and Vegte's ultimate strength formula as shown in Table 3. The AWS code prediction is conservative with a $F_{u,AWS}$ /$F_{u,TEST}$ ratio of 0.85 after removing the safety factors.

Although Vegte's formulation is only valid for an out-of-plane tension less than 60% of the in-plane axial compression ($-0.60 \leq J \leq 1.0$) while this test was carried out with a tension load ratio of -0.80 ($J = F_{2u}/F_{1u} = -300/374.54$), we have included a comparison as this is the only available formula based on a simplified analytical model. In this respect, Vegte's equation predicts an ultimate strength very close (a difference of only 3%) to the experimental result. This result serves to confirm that the multiplanar effect can be significant and a deeper understanding of the various failure modes of a multiplanar joint is pertinent.

5 CONCLUSIONS

The following conclusions can be drawn from this investigation:

1. For a multiplanar XT-joint subjected to an out-of-plane axial tensile load and an in-plane axial compressive load, the failure mode was a plastification of the chord wall with snap-through at the connection of the in-plane brace and bulging-out at the vicinity of the out-of-plane braces. Cracks also developed at the weld toe of the saddle points of the out-of-plane braces during the post-buckling stage.
2. For this multiplanar XT-joint configuration, pre-tensioning of the out-of-plane braces will reduce the strength as compared to the uniplanar T-joint

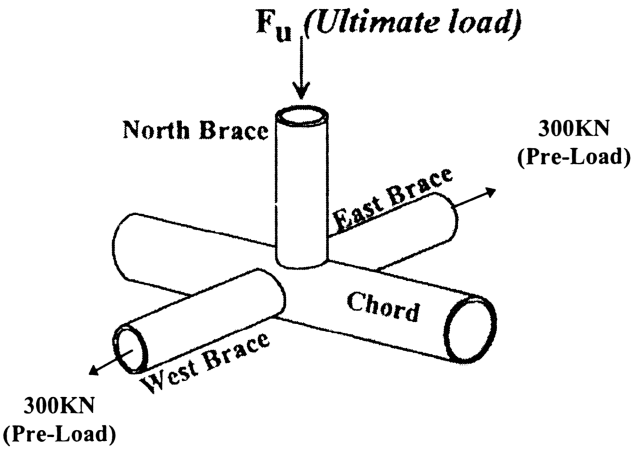

Figure 5 Load combination for multiplanar XT-joint specimen

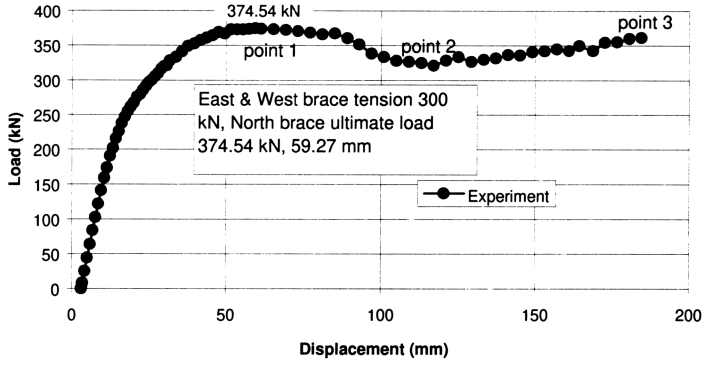

Figure 6 Load-displacement curve for the XT-joint

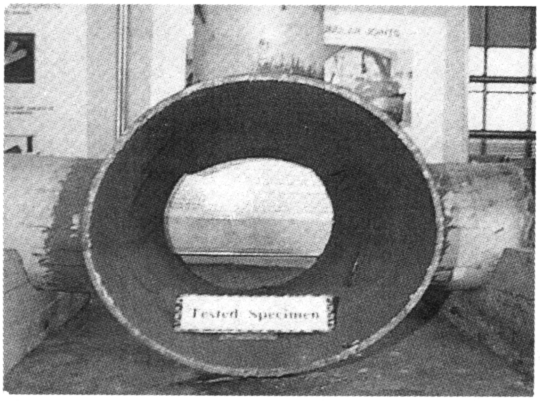

Figure 7 Cross section of failed multiplanar XT-joint

of the same dimension. This shows that the multiplanar effect can have a significant effect on the strength of multiplanar joints.

3. The AWS code predicts conservative values for the strength for XT-joints.

6 ACKNOWLEDGEMENT

The authors wish to thank the National Science and Technology Board and the Nanyang Technological University, Singapore for their financial support in this research project. The authors also wish to thank Luo Chang-Wei, Yu Sheng-Kai and the technical staff of the CSE Structures Laboratory for their assistance in carrying out the experimental testing work described in this paper.

REFERENCES

American Petroleum Institute 1991. *Recommended Practice for Planning, Designing and Construction of Fixed Offshore Platforms,* API Recommended Practice 2A(RP-2A), 19th Edition, Washington, USA.

American Welding Society 1992. *Structural Welding Code - Steel*, 14th Edition, ANSI/AWI D1.1-92, Miami, USA.

ASTM A370 1992 *Standard Method and Definitions for Mechanical Testing of Steel Products*, American Society for Testing Materials.

Billington, G. J., Lalani, M. & Tebbett, I.E. 1982. *Background to New Formulae for the Ultimate Limit State of Tubular Joints,* Proceedings Offshore Technology Conference, Paper OTC 4189, Houston, USA.

British Standards Institution, 1992. *Eurocode 3 Design of steel structures, Part 1: General rules and rules for buildings,* BSI London.

Chiew, S.P, Soh, C. K. & Fung, T. C. 1997. *Large Scale Testing of a Multiplanar Tubular DX-Joint,* Proceedings of the 7th International Offshore and Polar Engineering Conference, Honolulu, Hawaii, USA, pp.112-118.

Davies, G. & Crockett, P. 1994. *Interaction Diagrams for CHS T-DT Multiplanar Joints Under Axial Loads*, 4th International Offshore Polar Engineering Conference, Osaka, Japan, Vol. IV:15-20.

Kurobane, Y., Makino, Y. & Ochi, K. 1984. *Ultimate Resistance of Unstiffened Tubular Joints*, Journal of Structural Engineering, ASCE, Vol.110, No.2, pp.385-400.

Scola, S. & Redwood, R.G. 1989. *Behaviour of Axially Loaded Tubular V-Joints*, Journal Construct Steel Research, Vol.16, pp. 89-109.

van der Vegte, G.J. 1995. *The Static Strength of Uniplanar and Multiplanar Tubular T- and X-Joints*, Ph.D Thesis, Delft University, the Netherlands.

Yura, J.A., Zettlemoyer, N. & Edwards I.F. 1980, *Ultimate Capacity Equations for Tubular Joints*, Proceedings Offshore Technology Conference, Paper OTC 3690, Houston, USA

Tubular Structures VIII, Choo & Van der Vegte (eds) © 1998 Balkema, Rotterdam, ISBN 90 5809 001 9

Static strength of T-joints reinforced with doubler or collar plates

Y.S.Choo, B.H.Li & J.Y.R.Liew
National University of Singapore, Singapore

G.J.van der Vegte
Institute of High Performance Computing, Singapore & Delft University of Technology, Netherlands

N.Zettlemoyer
Exxon Production Research Company, Houston, USA

ABSTRACT: This paper presents the results of an experimental study on the behaviour of T-joints reinforced with a doubler plate or collar plate. At present, the design approach for these types of reinforced joints is very rudimentary. The general test arrangement, specimen details and results are presented. The test results are also compared with calculated strengths of un-reinforced T-joints using various equations. The experimental results show that there is significant strength enhancement for both types of reinforced T-joints.

1 INTRODUCTION

There are various components in offshore platform structures, such as boat landings, risers and sacrificial anodes, in which the connection to the structure (T-joint) is reinforced by provision of a *doubler plate*. At present, the design approach for doubler plate connections is very rudimentary and not based on test evidence.

An alternative reinforcement scheme, termed a *collar*, is also addressed in this paper. This scheme may be suitable to provide reinforcement to a pre-fabricated T-joint that is found to be under-designed. The collar concept also has potential applications for reinforcing joints in older offshore platforms.

Figure 1 illustrates the schematic arrangement for the two reinforcement types. For a T-joint reinforced with a doubler plate (Figure 1a), the brace is welded directly to the plate through a penetration weld, whereas the doubler plate is fillet welded to the chord. For the collar plate type of reinforcement (Figure 1b), the brace is first welded directly to the chord. Then the collar plate parts are fitted and welded to the chord and brace. There is no reinforcement within the brace foot print in this case.

This paper presents the results of an experimental program, partly sponsored by Exxon Production Research Company, to investigate the behaviour of T-joints reinforced by doubler or collar plates. The overall research program involves both experimental tests and parametric finite element studies. The results from additional tests and finite element studies will be reported in subsequent papers.

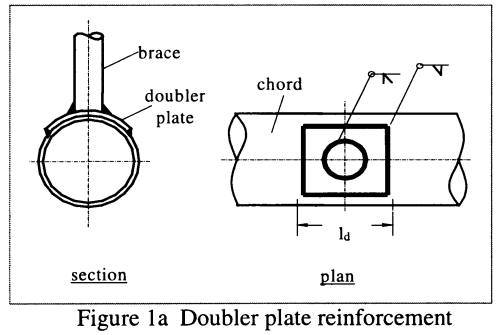

Figure 1a Doubler plate reinforcement

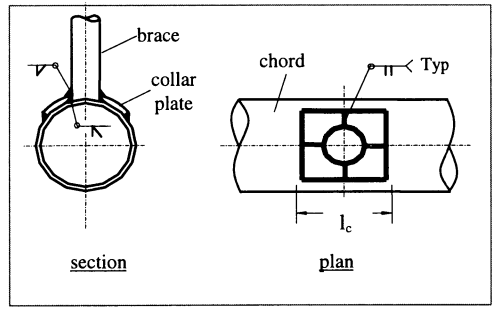

Figure 1b Collar plate reinforcement

2 EXPERIMENTAL PROGRAM

2.1 Specimen Details

The experimental program investigates the strength enhancement to a simple T-joint by provision of reinforcement around the intersection region, in the form of a doubler plate or a collar plate. The schematic view of the T-joint specimen is shown in Figure 2. Preliminary nonlinear finite element analyses were carried out to determine the appropriate geometric dimensions of the test specimens. Zettlemoyer (1988) and Madros et al. (1995) highlighted the need to consider an appropriate chord length to ensure joint failure occurring prior to chord member failure.

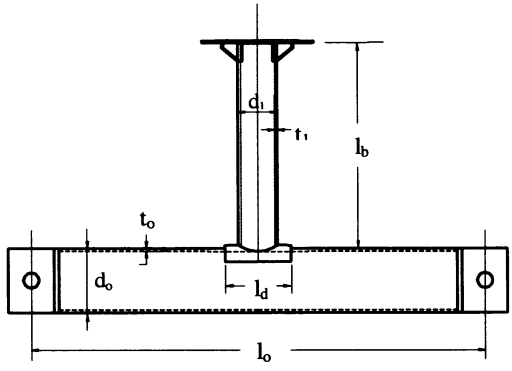

Figure 2. Schematic arrangement of specimen

The experimental program consists of eight tests with brace axial load. There are four pairs of tests, each pair with brace compression and tension. In Table 1 , it can be noted that specimens EX-01 and EX-02 are un-reinforced T-joints, which serve as references. There are four specimens reinforced with collar plates and two with doubler plates. The chords are API 16" (406.4 mm nominal) Schedule 20 and 40 pipes, whereas the braces are API 8" (219.1 mm nominal) Schedule 20 and 40 pipes. The chord length between pin supports is l_o=2840 mm (with $\alpha=2.l_o/d_o=13.9$) while the brace length is l_b=1100 mm. The reinforcement length is l_d=305 mm (with $l_d/d_o=0.74$). In this study, $l_c = l_d$. The chosen geometric parameters (with $2\gamma = d_o/t_o = 31.7$ and 50; $\beta = d_1/d_o = 0.54$; $\tau = t_1/t_o = 0.64$ and 0.79; and $\tau_d = t_d/t_o = 0.62$ and 0.73) correspond to typical values for T-joints with doubler plates in offshore platforms.

Table 1 Specimen details

Specimen	Type	d_o	d_1	t_o	t_1	t_d
EX-01	Un-reinforced	409.5	221.9	8.2	6.5	-
EX-02	Un-reinforced	409.5	221.9	8.2	6.5	-
EX-03	Collar	409.5	221.9	8.2	6.5	6
EX-04	Collar	409.5	221.9	8.2	6.5	6
EX-05	Collar	409.5	221.4	12.9	8.2	8
EX-06	Collar	409.5	221.4	12.9	8.2	8
EX-07	Doubler	409.5	221.9	8.2	6.5	6
EX-08	Doubler	409.5	221.9	8.2	6.5	6

Note: all dimensions in mm, measured
l_o=2840 mm; l_b=1100 mm; l_d=305mm

Table 2 Material properties and geometric ratios

Specimen	Brace load	$f_{y,c}$ (MPa)	$f_{y,b}$ (MPa)	$f_{y,d}$ (MPa)	$2\gamma=d_o/t_o$	$\tau=t_1/t_o$	$\tau_d=t_d/t_o$
EX-01	C	282	296	-	50	0.81	-
EX-02	T	282	296	-	50	0.81	-
EX-03	C	282	296	463	50	0.81	0.76
EX-04	T	271	296	463	50	0.81	0.76
EX-05	C	280	273	463	31.7	0.64	0.63
EX-06	T	280	273	463	31.7	0.64	0.63
EX-07	C	271	296	463	50	0.81	0.76
EX-08	T	299	296	463	50	0.81	0.76

Note: C – Compression; T - Tension

The chord and brace of each T-joint is fabricated from seamless, hot finished, carbon steel pipe, manufactured in accordance to API 5L Gr. B/ASTM A106-94A. The welding procedure follows AWS D1.1, with 7018 welding consumable. Table 2 summarises the measured yield stress (corresponding to 0.2% proof stress) for each of the chord, brace and doubler materials. For each chord pipe or brace pipe with the same heat number, four test coupons were made from the four diametrical positions of pipe and then tested.

2.2 Test arrangement

Figure 3 shows the general arrangement for the T-joint tests. The specimen is pin-supported at the chord ends and the brace end is bolted to the Instron actuator mounted on top of the four-column test frame. The pin supports, with the provision for sliding at the chord ends, minimise the possibility of chord axial load.

The displacement-controlled actuator has rated compression capacity of 2000 kN and tension capacity of 1200 kN, with a sensitivity within ±1% of full scale range, and a stroke of ±200 mm. For

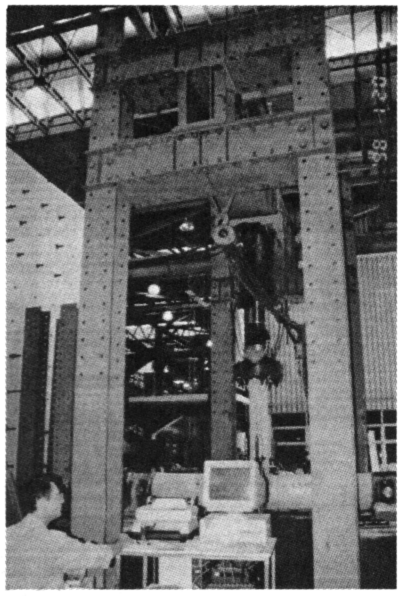

Figure 3. General test arrangement

each test, the brace load is applied at an initial stroke rate of 0.3 mm/minute for the linear load range, and then progressively increased up to 1.2 mm/minute at higher load ranges through the Instron 8800 controller.

For each specimen, the instrumentation includes strain gauging around the crown and saddle points to measure the strain distributions at the hot spots, and transducers to measure the displacements at selected points. Figure 4 shows the general arrangement of the transducers, with four of these measuring the brace displacements around the brace-chord intersection, and one transducer at each chord end.

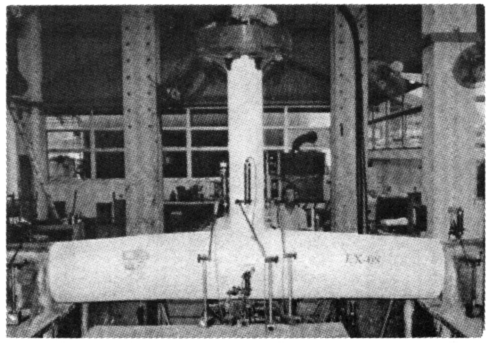

Figure 4. General arrangement of transducers

3 OBSERVATIONS & RESULTS

The observed behaviour and strength of each of the T-joints are reported in this section. The approach taken in this paper to present the load-deformation data is to refer to the ovalisation of chord section by subtracting the transducer reading at the chord bottom, δ_3 (at the brace centre-line) from the average of four transducer readings, δ_1, at the brace end that attaches to the chord. In this case, ovalisation=δ_1-δ_3.

3.1 Specimens Subjected to Brace Compression

Figure 5 shows the final deformed shape of specimen EX-03 (with collar reinforcement). There is the significant deformation around the brace-chord intersection, while the bottom of the chord is relatively straight.

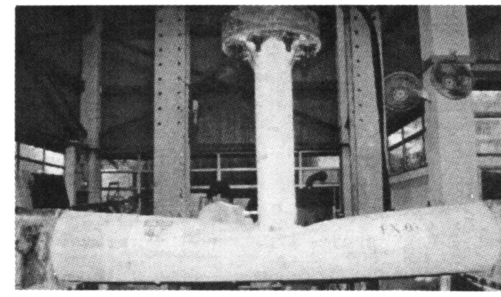

Figure 5. Overall deformed shape of EX-03

A close-up view of the brace-chord deformation can be observed in Figures 6a and 6b for specimens EX-03 and EX-07 (with doubler reinforcement), respectively. Both types of reinforcement are found to be effective in distributing the brace axial load to a larger region of the chord, with an associated strength enhancement. Most yielding in the reinforced specimens is in the chord around the perimeter of the reinforcement. The significant indentation at the brace-chord intersection requires the compatible deformation of the reinforcement plate. For specimen EX-07, there was a loud bang towards the end of the test and the doubler plate was observed to bulge out from the chord (Figure 6b).

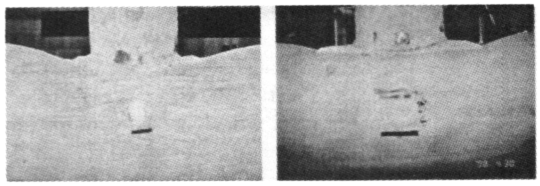

a. Detail of EX-03 b. Detail of EX-07

Figure 6 Detailed view of the deformed shape at the brace-chord intersection

Figure 7 presents the load-ovalisation curves for each of the specimens subjected to brace compression. The vertical axis refers to the normalised load with respect to the chord properties ($f_{y,c}\ t_o^2$), whereas the horizontal axis refers to the chord ovalisation (δ_1-δ_3). The peak load for each of the specimens is observed to occur at an ovalisation of 15 to 20 mm.

For the three specimens with the same 2γ (=50) ratio: EX-01 (un-reinforced), EX-03 (with collar reinforcement) and EX-07 (with doubler plate reinforcement), the following results are observed. The load-ovalisation curves for the reinforced specimens (EX-03 and EX-07) match closely and show that both reinforcement types perform similarly. There is a strength enhancement of around 40% as compared to the referenced strength of the un-reinforced joint. The observed strength enhancement appears to indicate that an effective β, based on the size of doubler/chord diameter, may be used to provide a good estimation of the compressive strength of these reinforced joints.

The normalised load R, defined here as $R=F_{u,test}/(f_{y,c}*t_o^2)$, for Specimen EX-05 (with 2γ=31.7) is R=16.7, whereas the values for Specimens EX-03 and EX-07 are respectively R=22.5 and R=22.8 (as tabulated in Table 3). The lower ratio may be due to the effect of γ, and the interaction between local joint failure and failure due to overall chord bending (van der Vegte, 1995).

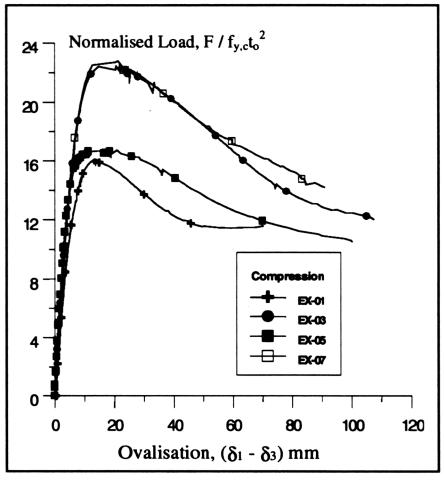

Figure 7. Load-ovalisation plots for compression cases

Table 3: Strength enhancement due to doubler or collar plates

Specimen	Type	Brace Load	$R = \frac{F_{u,test}}{f_{y,c}\,t_o^2}$	$\frac{R_{collar}}{R_{reference}}$	$\frac{R_{doubler}}{R_{reference}}$
EX-01	Reference	C	16.1	-	-
EX-02	Reference	T	29.0	-	-
EX-03	Collar	C	22.5	1.40	-
EX-04	Collar	T	33.5	1.15	-
EX-07	Doubler	C	22.8	-	1.42
EX-08	Doubler	T	35.3	-	1.22

3.2 Specimens Subjected to Brace Tension

The final deformed shape of each of the specimens (EX-02, EX-04 and EX-08) are shown in Figures 8 to 10. It can be observed that the failure mode corresponds to inelastic compressive buckling of the chord in bending. The change in chord diameter at the brace centre-line, up to the final stage of loading, is about $0.25d_o$ for specimen EX-02. The overall deformed shape of EX-08 can be observed in Figure 4.

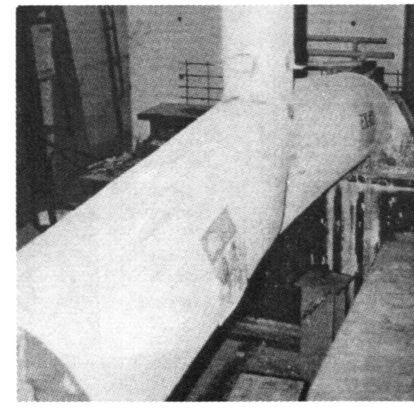

Figure 8. Deformed shape of specimen EX-02

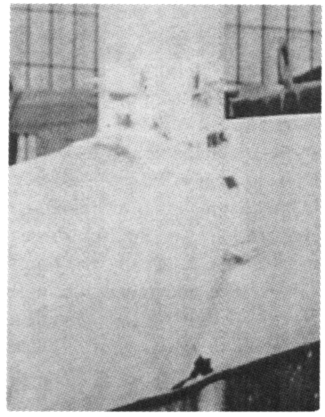

Figure 9. Detailed view of deformed shape of specimen EX-04 (with collar reinforcement)

It was observed during the test that a minor crack developed at the saddle points for specimen EX-02 as the maximum load was reached. For specimens EX-04, EX-06 and EX-08, no crack was found at the brace-chord intersection and the reinforcement region at the end of the tests.

Figure 11 presents the load-ovalisation curves for each of the specimens subjected to brace tension. It can be observed that specimens with $2\gamma=50$, i.e. EX-02 (un-reinforced), EX-04 (with collar reinforcement) and EX-08 (with doubler reinforcement), show a definite peak after large deformations of the chord. The load-ovalisation curves for both EX-04 and EX-08 are similar.

For specimen EX-06 with $2\gamma=31.7$, the test was stopped after the tensile capacity of the actuator was reached at 1200 kN. The lower normalised load for EX-06 is due to chord yielding occurring at $R\cong16$. (In Table 4, the plastic moment of the chord section is $M_p=568$ kNm, which translates to an equivalent normalised brace load of $R\cong16$).

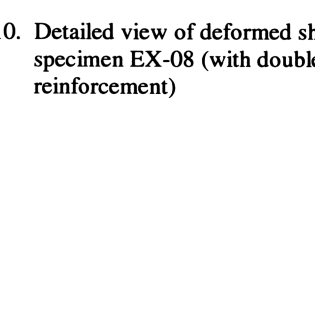

Figure 10. Detailed view of deformed shape of specimen EX-08 (with doubler reinforcement)

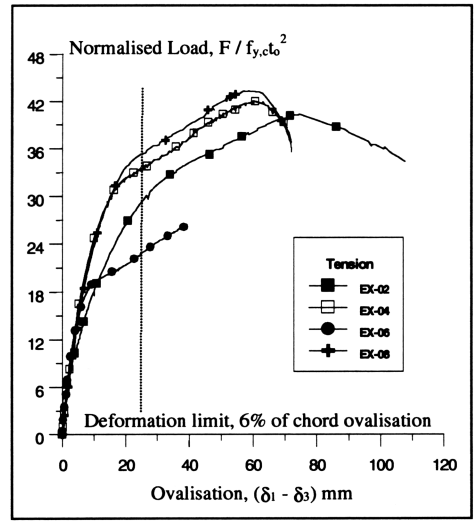

Figure 11. Load-ovalisation plots for tension cases

As a basis of comparison, the deformation limit as proposed by Lu et al. (1994) is considered here, but with a modification to a chord ovalisation (as a diametrical reference) of 6%, as compared to the 3% indentation (relative to the chord centre-line). The 6% ovalisation line is drawn in Figure 11, and the corresponding reference strength values are tabulated in Table 3. The strength enhancement due to the collar or doubler plate is observed to range from 15% to 22% for brace tension.

4 COMPARISON WITH STRENGTH EQUATIONS

The maximum compressive strength or the tensile strength (obtained using the 6% ovalisation limit) of the reference specimens are compared with calculated strengths from various references in Table 4. The *mean* strength of an un-reinforced T-joint is calculated using each of the following

equations from Dier & Lalani (1998), Kurobane et al. (1980) and Makino et al. (1981):

Dier & Lalani (1998):

$$F_{u,ISO} = Q_u f_{y,c} t_o^2 \quad (1)$$

with $Q_u = (1.9+19\beta)Q_\beta^{0.5}$ for *compression*, with mean bias factor=1.265

and $Q_u = 30\beta$ for *tension*, with mean bias factor=1.708 at first crack

$Q_\beta = 1.0$ for $\beta \leq 0.6$

Kurobane et al. (1980):

for axial *compression*, (2)

$$F_{u,Kurobane}=4.83(1+4.94\beta^2)(2\gamma)^{0.233}(0.5\alpha)^{-0.45}. f_{y,c} t_o^2$$

Makino et al. (1981): for axial *tension*, (3)

$$F_{u,Makino}=1.61(1+4.94\beta^2)(2\gamma)^{0.765}(0.5\alpha)^{-0.45}. f_{y,c} t_o^2$$

Table 4. Summary table for experimental results

Specimen	$F_{u,test}$ (kN)	$F_{u,ISO}$ (kN)	$F_{u,Kurobane}$ or $F_{u,Makino}$ (kN)	$M_{u,test}$ (kNm)	M_y (kNm)	M_p (kNm)
EX-01	305	291	262	217	287	372
EX-02	550	524	672	390	287	372
EX-03	426	-	-	302	287	372
EX-04	610	-	-	433	276	358
EX-05	780	-	-	554	433	568
EX-06	1050	-	-	745	433	568
EX-07	416	-	-	295	276	358
EX-08	710	-	-	504	304	395

Note: $M_{u,test} = F_{u,test} * l_o / 4$
(computed for chord at brace centre-line)

Although the calculated values for an un-reinforced T-joint from the above equations, $F_{u,ISO}$, $F_{u,Kurobane}$ and $F_{u,Makino}$ are based on different databases and approaches to data interpretation, the scatter of the values as compared to the test result $F_{u,test}$ for brace tension is noticeable.

From the reference load $F_{u,test}$, the corresponding moment, $M_{u,test}$, is compared to the bending moment to cause first yield of chord member, M_y, and plastic moment capacity of the chord member M_p. It is seen in Table 4 that specimens subjected to brace tension (EX-02, EX-04, EX-06 and EX-08) have achieved equal or higher capacities than the chord strength. For specimen EX-05 that is subjected to brace compression, $M_{u,test} \cong M_p$. The enhancement in joint strength resulting from the collar-plate or doubler-plate reinforcement is noticeable from the tests reported. The strength enhancement is especially large for specimens subjected to brace compression.

5 CONCLUSIONS

The experimental tests reported in this paper show that there is significant strength enhancement for a T-joint reinforced by a doubler plate or a collar plate. The strength enhancement, as observed from the test results, is around 40% for brace compression and 15% for brace tension. The load-ovalisation responses for both types of reinforcement are similar. The results have also been compared with calculated compressive and tensile strengths of un-reinforced T-joints using various equations. The large scatter in the calculated values, especially for brace tension, is noticeable.

The reported tests are only part of the research activities on joints reinforced with doubler or collar plates. The experimental results will be used as references for the parametric finite element study of reinforced T-joints subjected moments as well as axial loadings. These results will be presented in future publications.

NOMENCLATURE

d_o	outer diameter of the chord
d_1	outer diameter of the brace
$f_{y,b}$	yield stress of brace member
$f_{y,c}$	yield stress of chord member
$f_{y,d}$	yield stress of doubler-/collar- plate
$f_{u,b}$	ultimate stress of brace member
$f_{u,c}$	ultimate stress of chord member
$f_{u,d}$	ultimate stress of doubler-/collar- plate
$F_{u,ISO}$	compressive/tensile strength calculated from Dier (1998) equations
$F_{u,Kurobane}$	compressive strength calculated from Kurobane (1980) equation
$F_{u,Makino}$	tensile strength calculated from Makino (1981) equation
$F_{u,test}$	compressive/tensile strength from test
l_o	length of the chord
l_b	length of the brace
l_d	length of doubler-/collar-plate
M_p	plastic moment capacity of chord member
$M_{u,test}$	equivalent moment on chord member at brace centre-line computed from test load $F_{u,test}$
M_y	moment to cause first yield of chord member
R	Normalised load, $R = F_{u,test} / (f_{y,c} t_o^2)$
t_o	wall thickness of the chord
t_1	wall thickness of the brace
t_d	thickness of doubler-/collar- plate
α	chord length parameter $2.l_o/d_o$

β diameter ratio d_i/d_o
δ_i vertical displacement at location i
2γ chord diameter to thickness ratio d_o/t_o
τ brace to chord wall thickness ratio t_i/t_o
τ_d reinforcement plate to chord wall thickness ratio t_d/t_o

ACKNOWLEDGEMENTS

The reported work is partially sponsored by Exxon Production Research Company (Houston, U.S.A.). The specimens were contributed by Sembawang Marine & Offshore Engineering (Singapore). The experimental investigation was conducted in the Structural Engineering Laboratory, Department of Civil Engineering, National University of Singapore. The National University of Singapore provided a research scholarship to Mr B. H. Li.

REFERENCES

Dier, A.F. and Lalani, M. 1998. New code Formulations for tubular joint static strength. Eighth International Symposium on Tubular Structures, Singapore.

Kurobane, Y., Makino, Y. Mitsui, Y. 1980. Re-analysis of ultimate strength data for truss connections in circular hollow sections. IIW Doc. XV-461-80.

Lu, L.H., Windkel, G.D. de, Yu, Y., Wardenier, J. 1994. Deformation limit for the ultimate strength of hollow section joints. Sixth International Symposium on Tubular Structures, Melbourne, Australia.

Madros, M.S.Z., Zettlemoyer, N. and Healy, B.E. 1995. Effect of chord can length on strength of T joints. Offshore Technology Conference, OTC7800, Houston, USA.

Makino, Y., Kurobane, Y., Minoda, Y. 1981. Design of CHS X- and T-joints under tensile brace loading, IIW Doc. XV-487-81.

Van der Vegte, G.J. 1995. The Static Strength of Uniplanar and Multiplanar Tubular T- and X-Joints. Delft: Delft University Press.

Zettlemoyer, N. 1988. Developments in ultimate strength technology for simple tubular joints. Offshore Tubular Joints Conference (OTJ'88), Surrey, UK.

Zettlemoyer, N. 1996. ISO harmonisation of offshore guidance on strength of tubular joints, Sixth International Offshore & Polar Engineering conference (ISOPE-96), Los Angeles, USA.



Taylor & Francis
Taylor & Francis Group
http://taylorandfrancis.com

Tubular Structures VIII, Choo & Van der Vegte (eds) © 1998 Balkema, Rotterdam, ISBN 90 5809 001 9

Ultimate strength of ring stiffened T-joints – A theoretical model

M.M.K.Lee & A.Llewelyn-Parry
University of Wales Swansea, UK

ABSTRACT: Internal stiffeners are commonly employed to enhance the strength of tubular joints found in offshore steel jacket structures. However, no detailed design guidance on the determination of their strengths can be found in any major offshore code or design guide because of a lack of research effort. This paper first summarises the results of an extensive finite element study on CHS T-joints with internal T shaped stiffeners. The study generated a database of forty-two stiffened joints, some of which included multiple stiffeners. Observations on the development of plastic zones in the stiffeners show that the failure mechanism is the formation of plastic hinges from bending. A theoretical model based on the observed failure mechanism is then presented. The model is based on upper bound theorem, with a postulated five-hinge collapse mechanism. The proposed theoretical model was found to provide strength predictions to a very high degree of accuracy

1 INTRODUCTION

It is common practice in offshore steel jacket structures to stiffen tubular connections using internal stiffeners to enhance their static capacities. Internally stiffened joints also have the added advantage of reducing stress concentration, which would lead to a longer fatigue life. In spite of the many thousands of internally stiffened joints in service world-wide, no major offshore design code (such as API, 1993 and DEn, 1990) provides any substantial design guidance, particularly in the area of static strength requirements. This is due partly to the vast variety of possible stiffening arrangements and partly to the dearth of information available on such joints in research literature (limited work has been carried out recently on ring-stiffened X-joints (van der Vegte et al (1997)). In the design of stiffened joints, careful consideration is required of stiffener shapes, sizes and locations, construction sequence, economy etc.. This paper first reports on an extensive finite element (FE) study on stiffened T-joints with over forty analyses, some included multiple stiffeners. Based on the observed failure mechanism, which consists of discrete plastic zones forming in the stiffener(s), a theoretical model for predicting strength is presented.

2 FINITE ELEMENT STUDY

A convergence study was first carried out to establish the accuracy of the numerical procedure. The meshes were created following guidelines established in previous work at Swansea on other tubular joint types (Lee et al. 1995, Lee & Wilmshurst 1995, Dexter et al. 1996). Having established a cost-effective mesh layout, numerical models of five test joints from Sawada et al. (1979) – one unstiffened and four stiffened T-joints – were analysed to validate the finite element procedure.

The validated numerical procedure was first used to analyse the unstiffened version of an in-service T/Y-joint in the main leg of a jacket structure. This joint has the following dimensions:

brace inclination θ (measured from the chord axis)	= 83°
chord diameter D	= 3000 mm
chord thickness T	= 50 mm
chord length L	= 15000 mm
brace diameter d	= 1000 mm
brace thickness t	= 35 mm

With the above dimensions, the non-dimensional geometric ratios are α (=2L/D) = 10.0, β (= d/D) = 0.333, γ (= D/2T) = 30 and τ (= t/T) = 0.7. The numerical strength of this unstiffened joints was

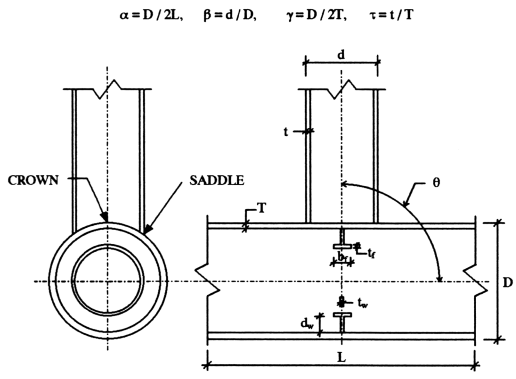

Fig. 1 Configuration and geometric ratios of a stiffened joint

compared with that obtained from the mean strength equation of the DEn Guide (1990).

T-shape stiffeners (see Fig. 1) of various dimensions were inserted into the above unstiffened T-joint for a parametric study. The ranges of dimensions used for the stiffeners were determined by comparison with the dimensions of the (unstiffened) joint. By restricting to what were considered to be reasonable and practical, the following ranges were established: $0.1 \leq d_w/D \leq 0.205$; $0.5 \leq t_w/T \leq 0.8$; $0.4 \leq t_f/T \leq 1.0$; $0.05 \leq b_f/D \leq 0.1$. A total of forty joints, each with a single stiffener, were analysed, which investigated:

a) the effects of the thickness t_w and the depth d_w of the web,
b) the effects of the thickness t_f and the width b_f of the flange,
c) the effects of the joint ratios β and γ, and
d) the influence of the position of the stiffener on strength

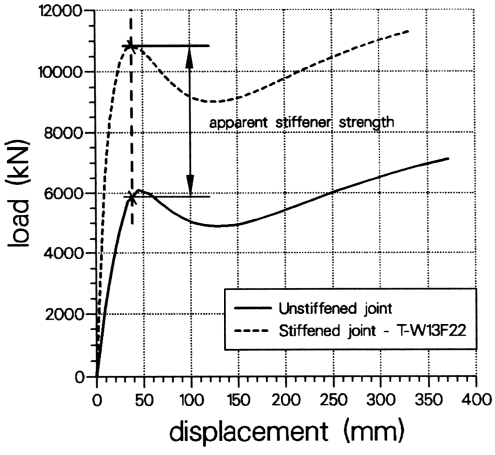

Fig. 2 Typical load-displacement curves for unstiffened and stiffened T-joints

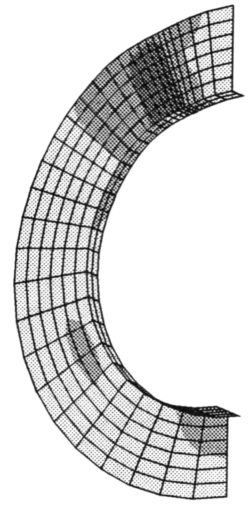

a. $\beta = 0.333$

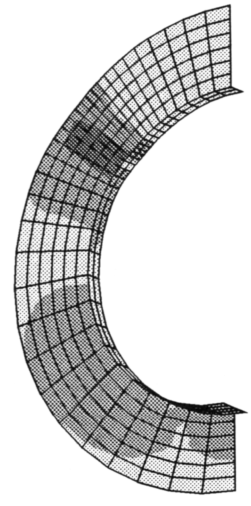

b. $\beta = 0.7$

Fig. 3 Plastic zones in stiffeners

Further details of the parametric study can be found in Lee & Llewelyn-Parry (1998). The results of the study are summarised as follows:

a) Internal ring stiffeners do not significantly affect the ductility of tubular joints as stiffened joints reach their peak strengths at similar deformation level as their unstiffened counterparts, Fig. 2.
b) The development of plastic zones, Fig. 3, suggests that the failure mechanism is the formation of plastic hinges in the stiffeners from bending, rather than from shear yielding.
c) The joint ratios β and γ have a significant influence on the strength enhancement given by the stiffeners, Fig. 2.
d) Determination of the strengths of stiffeners based on shear yielding is very conservative and the degree of conservatism increases as the stiffener becomes shallower.
e) The flange of a T-shape stiffener makes a contribution to the strength of stiffener, but the influence is larger from the thickness than from the width.
f) Compared with stiffeners positioned at the crown positions, those at the saddle position of the joint provide a better strength enhancement.

3 A THEORETICAL MODEL TO PREDICT STRENGTH

From the results of the finite element study, it has been established that the failure mechanism of a ring stiffened joint is one of chord yielding at the brace-chord intersection, and plastic hinges forming in the stiffener(s) due to bending. The proposed theoretical model first assumes that the strength of a stiffened joint is the sum of the strengths of the unstiffened joint and the stiffener. It then analyses the stiffener statically using simple plastic theory via upper bound theorem, by postulating a five-hinge failure mechanism, which leads to the collapse of the centrally stiffened joint. At the positions of the hinges, the geometry of the cross-section, which carries only a bending moment, is assumed to be an unsymmetrical I-section. This assumption is justified as previous work on stiffened joints from Sawada et al. (1979) and Krasenberg (1990) has shown that the unstiffened joint and the ring stiffener behave synergistically. It is therefore not unreasonable to suggest that, as the joint chord interacts with the stiffener in producing the strength enhancement, the stiffener acts in conjunction with a certain portion of the chord wall. The shape of the stiffener is, therefore, assumed to be that of an unsymmetrical I-section, with the width of its top flange to be determined from the theoretical model.

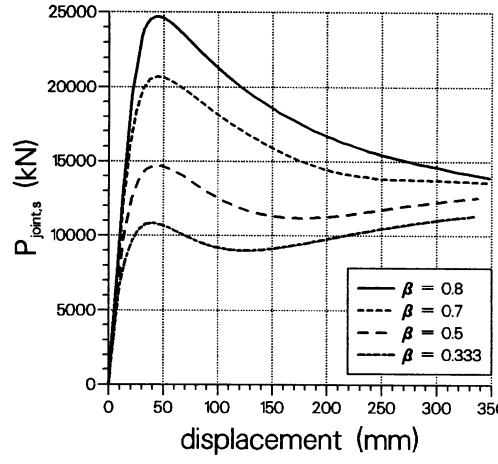

a. joints with varying β

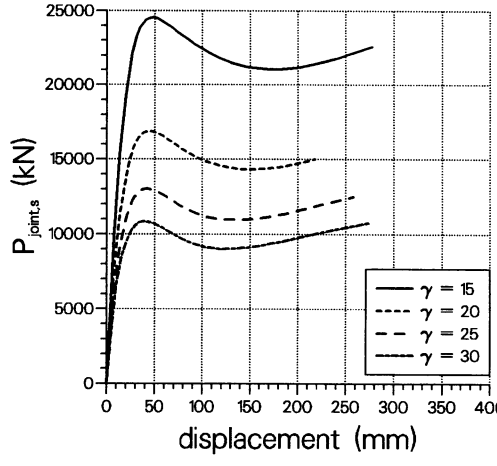

b. joints with varying γ

Fig. 4 Typical load-displacement curves for joints with varying β and γ

3.1 Upper bound analysis

Consider the five-hinge collapse mechanism of the stiffener shown in Fig. 5. (Note that in Fig. 5, for ease of visualisation and calculation of changes in rotation, the curved rigid links between the hinges are also shown as straight links.) The total load carried by the stiffener, 2P, is reacted by the shear flow along the circumference. The positions of the plastic hinges 1, 3 and 5 are fixed whereas those for hinges 2 and 4 are left free and to be determined by

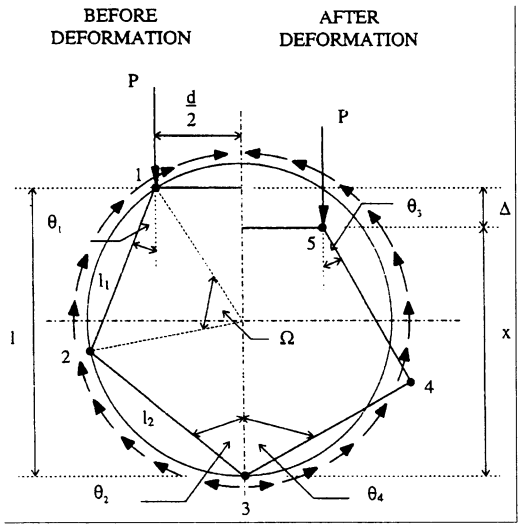

Fig. 5 A five-hinge collapse mechanism

minimising P. It is further assumed that there is no vertical displacement at hinge 3, i.e. the invert of the stiffener. This constraint is justified as results of finite element analyses (Lee & Llewelyn-Parry 1998) have shown negligible displacement of the joint at this position at peak load.

It is assumed that the chord and the stiffener are all made of an elastic-perfectly plastic material with yield stress σ_y in simple tension, which yields according to von Mises yield criterion. By equating the external work done $P\Delta$, where Δ is the vertical displacement of the load, to the internal work absorbed as plastic deformation in the hinges $2M_p[(\theta_3-\theta_1)+(\theta_4-\theta_2)]$, where M_p is the full plastic moment of the unsymmetrical I-section and θ_i, i=1 to 4, are the small rotations of the rigid links between the hinges, the following work equation is obtained

$$P = \frac{2M_p\theta_{diff}}{\Delta} \qquad (1)$$

where $\theta_{diff} = [(\theta_3-\theta_1) + (\theta_4-\theta_2)]$. (It is worth noting here that by virtue of a theorem of plasticity, there is no change in elastic strain energy, and all the energy contributed by the loads is spent in plastic deformation of the hinges.)

Using the geometry of Fig. 5, we have $x = l_1 \cos\theta_1 + l_2 \cos\theta_2$, giving

$$\theta_1 = \cos^{-1}\left(\frac{x - l_2\cos\theta_2}{l_1}\right) \qquad (2)$$

From $x(D-x) = d^2/4$, x is calculated as

$$x = 0.5\left(D - \sqrt{D^2 - d^2}\right) \qquad (3)$$

In addition, l_2 is given by

$$l_2 = D\cos\theta_2 \qquad (4)$$

and l_1 given by

$$l_1 = D\sin\left(\frac{\Omega}{2}\right) \qquad (5)$$

where $\Omega = 2\theta_2 - \sin^{-1}(d/D)$. Substituting equations (3)-(5) into equation (2), θ_1 is expressed in terms of θ_2 and the known joint geometrical values d and D. By considering the geometry of the hinge mechanism before and after deformation, Fig. 5, further geometric relationships can be established as follows. Firstly, resolving vertically, $l_1\cos\theta_1 + l_2\cos\theta_2 = l_1\cos\theta_3 + l_2\cos\theta_4 + \Delta$, which leads to

$$\theta_4 = \cos^{-1}\left\{\frac{\left(l_1(\cos\theta_1 - \cos\theta_3) + l_2\cos\theta_2 - \Delta\right)}{l_2}\right\} \qquad (6)$$

Secondly, resolving horizontally, $l_1\sin\theta_1 + 0.5d = l_2\sin\theta_2$ and $l_1\sin\theta_3 + 0.5d = l_2\sin\theta_4$, which leads to

$$\theta_4 = \sin^{-1}\left\{\frac{\left(l_1(\sin\theta_3 - \sin\theta_1) + l_2\sin\theta_2\right)}{l_2}\right\} \qquad (7)$$

By assuming a value for θ_2, i.e. an arbitrary collapse mechanism, equations (2)-(5) give values for l_1, l_2 and θ_1, which, with an assumed value for Δ (=$D/30$), will produce values for θ_3 and θ_4 from equations (6) and (7).

Since M_p is constant, equation (1) implies that P is proportional to θ_{diff}/Δ. The final value of θ_2, which gives the desired collapse mechanism, is obtained by minimising the value of θ_{diff}/Δ, which also leads to the smallest value for P. In this study minimisation was obtained through the use of Microsoft Excel (1993) and its 'solver' option.

For the calculations to minimise the values of θ_{diff}/Δ, involving the use of equations (1)-(7), the effective width of the top flange of the section b_c is determined using Roark's (1965) equation for the length of the flange outstand $\lambda = 0.55\sqrt{(DT)}$, which leads to

$$b_c = 1.1\sqrt{(DT)} + t_w \qquad (8)$$

Having determined b_c, the position of the plastic neutral axis can be determined. The diameter of the ring shown in Fig. 5 is thus the diameter of the plastic neutral axis D_p, which is used in equations (3)-(5). The value of θ_{diff} obtained for the geometries of the joints considered in this study, for a constant $\Delta = D/30$, varies slightly, but, for simplicity, a value of 4.6° (in equivalent radians) was used.

3.2 Evaluation of moment capacity

In the analysis presented in the preceding, the full plastic moment of resistance, M_p, is assumed to have

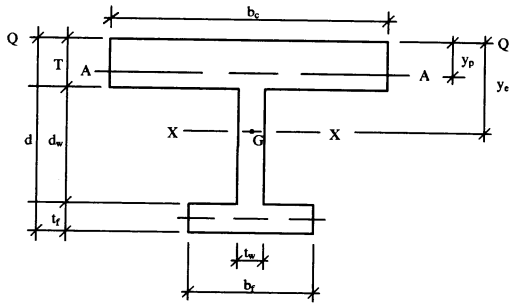

Fig. 6 Unsymmetrical I-section assumed at the plastic hinges

derived from an unsymmetrical I-section formed from the stiffener and part of the chord wall, Fig. 6. The determination of the effective width, b_c, of the top flange of the section shown in Fig. 6 will be performed in the next section, here an expression for the plastic moment of resistance, M_p, is derived as follows.

In Fig. 6, y_e, the distance between the centroidal axis X-X and QQ, is given by:

$$y_e = \frac{0.5\left(b_c T^2 + t_w d_w^2 + b_f t_f^2\right) + T t_w d_w + b_f t_f \left(T + d_w\right)}{A} \tag{9}$$

where A is the cross-sectional area of the I-section. The neutral axis at full plasticity for the section is the equal area axis A-A, at a distance y_p from QQ. In the context of the current study, A-A may lie in the top flange (the chord) or the web and its position given by:

in the top flange $$y_{p,c} = \frac{A}{2b_c} \tag{10}$$

(and lies with the range $0 < y_{p,c} \le T$)

in the web $$y_{p,w} = \frac{A + 2T\left(t_w - b_c\right)}{2t_w} \tag{11}$$

(and lies with the range $T < y_p \le (T + d_w)$)

Accordingly, the plastic section modulus is given by either

$$Z_{p,c} = b_c y_{p,c}^2 - A y_{p,c} + A y_e \tag{12}$$

or $$Z_{p,w} = \left(t_w - b_c\right)T^2 + A y_e - t_w y_{p,w}^2 \tag{13}$$

M_p is, hence, given by either

$$M_p = \sigma_y Z_{p,c} \tag{14}$$

or $$M_p = \sigma_y Z_{p,w} \tag{15}$$

3.3 Determination of the effective top flange width

In order to begin the analysis detailed in the preceding sections, a definitive width of the top flange has to be determined. For each of the forty stiffened joints analysed, and presented in Lee & Llewelyn (1998), the effective width of the top flange was determined using the following iterative process, implemented using a FORTRAN program:

1. Assume an initial effective width, b_c, using Roark's formula (equation (8)).
2. Determine the position of the plastic neutral axis and calculate M_p.
3. Calculate the load P_i that the unsymmetrical I-section can accommodate using the work equation (equation (1)).
4. Compare $2P_i$ with the strength of the stiffener determined from finite element calculations.
5. Increase or decrease b_c as required.
6. Go to Step 2 with the new value of b_c.
7. Repeat the process until there is no significant change in the value of b_c in successive iterations.

The values of b_c obtained from the above procedure, $b_{c,th}$, are given in Table 1. To enable the stiffener strengths to be obtained from the theoretical model, an equation by which b_c can be readily calculated is required. This is achieved by non-dimensionalising $b_{c,th}$ by D and then examining the variation of $b_{c,th}/D$ with the non-dimensional geometric parameters t_w/T, d_w/D, t_f/T, b_f/D, β and γ, shown in Figs. 7(a)-(d). The trends exhibited in each of the plots are summarised as follows:

1. $b_{c,th}/D$ decays with increasing d_w/D, Fig. 7(a); for the larger t_w/T, the decay is exponential; but for the smallest t_w/T, the decay is almost linear. The relationship can be best represented by a power law of the form $b_{c,th}/D = A(d_w/D)^B$, where both A and B are functions of t_w/T. (It is noted that the data point $t_w/T = 0.8$, $d_w/D = 0.1$ does not follow the general trend; rather than ignoring this point, it was decided to include it in the regression analysis, which would have some influence on accuracy.)
2. The relationship between $b_{c,th}/D$, t_f/T and b_f/D, Fig. 7(b), is very similar to that observed in Fig. 7(a) – again a power law of the form $b_{c,th}/D = C(t_f/T)^E$, where both C and E are functions of b_f/D, will give the best fit.
3. $b_{c,th}/D$ can be seen in Fig. 7(c) to increase exponentially with β, i.e. $b_{c,th}/D = F \exp(G\beta)$, where F and G are constants.
4. Fig. 7(d) shows a near linear relationship between $b_{c,th}/D$ and γ.

Based on the above observations, multiple regression analyses were carried out, using the database of $b_{c,th}$, which resulted in the following equation for $b_{c,eq}$ (predicted values of b_c):

Table 1 Theoretical and predicted chord lengths, FE and predicted stiffener strengths

Joint Ref.	T mm	t_w mm	d_w mm	b_f mm	t_f mm	$b_{c,th}$ mm	$b_{c,eqn}$ mm	$b_{c,eqn}/b_{c,th}$	$P_{stiff,fe}$ kN	$P_{stiff,th}$ kN	$P_{stiff,th}/P_{stiff,fe}$
T-W11F22	50	25	300	225	35	437	499	1.14	3379	3424	1.01
T-W12F22	50	25	380	225	35	257	345	1.34	4118	4372	1.06
T-W13F22	50	25	457.5	225	35	236	257	1.09	4957	5101	1.03
T-W14F22	50	25	535	225	35	208	201	0.97	5709	5643	0.99
T-W15F22	50	25	615	225	35	177	162	0.92	6396	6205	0.97
T-W21F22	50	30	300	225	35	756	818	1.08	3789	3826	1.01
T-W22F22	50	30	380	225	35	464	536	1.16	4781	4839	1.01
T-W23F22	50	30	457.5	225	35	297	385	1.30	5598	5960	1.06
T-W24F22	50	30	535	225	35	265	291	1.10	6540	6742	1.03
T-W25F22	50	30	615	225	35	219	227	1.04	7293	7389	1.01
T-W31F22	50	35	300	225	35	1544	1338	0.87	4436	4324	0.97
T-W32F22	50	35	380	225	35	1055	834	0.79	5491	5356	0.98
T-W33F22	50	35	457.5	225	35	597	576	0.96	6628	6610	1.00
T-W34F22	50	35	535	225	35	354	421	1.19	7526	7875	1.05
T-W35F22	50	35	615	225	35	256	319	1.25	8110	8723	1.08
T-W41F22	50	40	300	225	35	1850	2190	1.18	4807	4987	1.04
T-W42F22	50	40	380	225	35	1727	1298	0.75	6190	5951	0.96
T-W43F22	50	40	457.5	225	35	1014	861	0.85	7370	7268	0.99
T-W44F22	50	40	535	225	35	414	609	1.47	8256	8829	1.07
T-W45F22	50	40	615	225	35	302	448	1.48	8995	10161	1.13
T-W11F32	50	25	300	300	35	214	288	1.35	3419	3820	1.12
T-W12F32	50	25	380	300	35	213	199	0.93	4374	4251	0.97
T-W13F32	50	25	457.5	300	35	177	148	0.84	4982	4624	0.93
T-W14F32	50	25	535	300	35	161	116	0.72	5760	5098	0.89
T-W15F32	50	25	615	300	35	144	93	0.65	6566	5687	0.87
T-W13F11	50	25	457.5	150	20	1633	1656	1.01	4374	4386	1.00
T-W13F12	50	25	457.5	150	35	409	535	1.31	4573	4670	1.02
T-W13F13	50	25	457.5	150	50	231	260	1.13	4870	5057	1.04
T-W13F21	50	25	457.5	225	20	722	667	0.92	4466	4432	0.99
T-W13F23	50	25	457.5	225	50	184	140	0.76	5254	4692	0.89
T-W13F31	50	25	457.5	300	20	281	321	1.14	4609	4728	1.03
T-W13F33	50	25	457.5	300	50	153	91	0.59	5312	4218	0.79
T-W11F12	50	25	300	150	35	1139	1037	0.91	3085	3030	0.98
T-W15F12	50	25	615	150	35	255	336	1.32	6309	6780	1.07
T-W13F22(γ15)	100	25	457.5	225	35	96	88	0.92	4798	4637	0.97
T-W13F22(γ20)	75	25	457.5	225	35	129	138	1.07	4715	4841	1.03
T-W13F22(γ25)	60	25	457.5	225	35	176	191	1.09	4816	4957	1.03
T-W13F22(β0.5)	50	25	457.5	225	35	405	665	1.64	5591	5797	1.04
T-W13F22(β0.7)	50	25	457.5	225	35	2175	2074	0.95	6645	6592	0.99
T-W13F22(β0.8)	50	25	457.5	225	35	3607	3664	1.02	7388	7418	1.00
						Maximum		1.64			1.13
						Minimum		0.59			0.79
						Mean		1.055			1.002
						CoV		0.220			0.064

$$\frac{b_{c,eq}}{D} = 0.0005\left(\exp\left(\frac{t_w}{T}\right)^{63.66}\right)\left(\frac{d_w}{D}\right)^{\left(-2.14\left(\frac{t_w}{T}\right)-0.50\right)}\ldots$$

$$\left(\frac{b_f}{D}\right)^{-1.52}\left(\frac{t_f}{T}\right)^{\left(12.79\left(\frac{b_f}{D}\right)-2.66\right)}\left(\exp(5.69\beta)\right)\ldots$$

$$(0.00068\gamma - 0.0061) \qquad (16)$$

The validity ranges of equation (16) are $0.1 \le d_w/D \le 0.205$; $0.5 \le t_w/T \le 0.8$; $0.4 \le t_f/T \le 1.0$; $0.05 \le b_f/D \le 0.1$, $0.333 \le \beta \le 0.8$ and $15 \le \gamma \le 30$.

Table 1 gives the values of $b_{c,eq}$ for the forty joints in the database. Also included in the table are the ratio $b_{c,eq}/b_{c,th}$ and the results of statistical analysis of this ratio. With a mean $b_{c,eq}/b_{c,th}$ = 1.055, equation (16) is seen, on average, to under-predict the effective chord length. The coefficient of variation (CoV) of 0.22 also indicates a significant scatter in the predictions. However, as to be shown later, the scatter in predicting the effective chord length will not be reflected fully in the prediction of the strength of the stiffener. This is because the stiffener strength is directly proportional to the M_p (see equation (1)), but which is not particularly sensitive to the variation of b_c. For example, for joint T-W13F22(β0.5), although the effective chord length is some 64% over-predicted, M_p only changes from 17431 kNm to 18073 kNm, an error of only 3.7%.

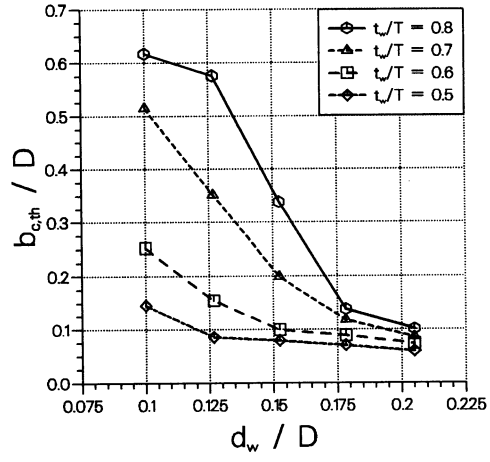

a. Effect of t_w/T and d_w/T on $b_{c,th}/D$

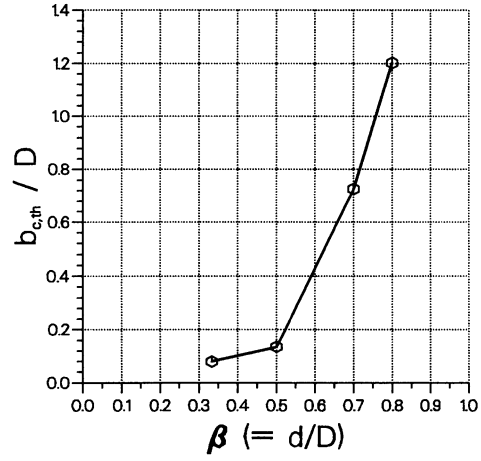

c. Effect of β on $b_{c,th}/D$

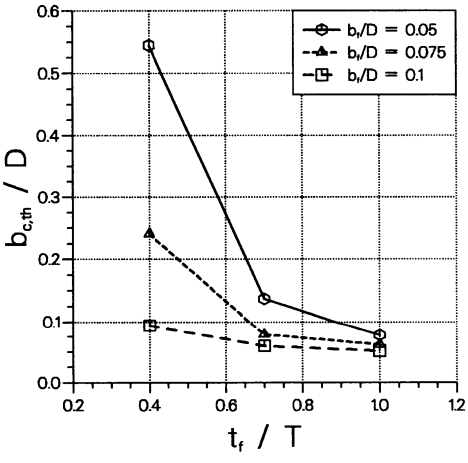

b. Effect of t_f/T and b_f/D on $b_{c,th}/D$

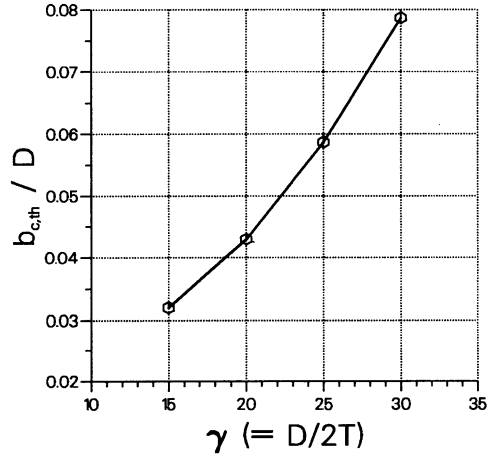

d. Effect of γ on $b_{c,th}/D$

Fig 7. Effects of various geometric ratios on b_c/D

4 STRENGTH PREDICTION OF STIFFENED JOINT USING THE THEORETICAL MODEL

4.1 Strength of stiffeners

With b_c calculated using equation (16), (as $b_{c,eq}$ in Table 1), the geometry of the unsymmetrical I-section thus defined, and the full plastic moment of resistance, M_p, determined using equations (9)-(15), the strength of the stiffeners $P_{stiff,th}$ can then calculated as $2P$ (P is obtained from equation (1)).

Using the proposed model, the strengths of the stiffeners, $P_{stiff,th}$, of the forty centrally stiffened joints are calculated and compared with the numerically determined strengths, $P_{stiff,fe}$, in Table 1. A statistical analysis of the ratio $P_{stiff,th}/P_{stiff,fe}$ yields a mean of 1.002 and a CoV of 6.4%. As mentioned in the foregoing, the errors in predicting the effective chord length are not fully reflected in the prediction of the strength of the stiffener. For joint T-W13F22(β0.5), which gives the worse over-prediction of 64% in b_c, the over-prediction in stiffener strength is only 4%. For joint T-W13F33, an under-prediction in b_c of over 40% produces an error of 21% in strength, which is the worse case. Figure 8 shows that the majority of the predicted strengths lie within the 10% error bands.

It is worth noting here that the strengths have been predicted using simple plastic theory, which, necessarily, assumes rigid-perfectly plastic behaviour. The majority of the offshore steels used in practice, however, work harden after yielding, with a typical yield stress to ultimate tensile strength ratio of around 0.7, and the use of the yield stress in calculating M_p, and hence the strength, will produce unacceptably conservative results. A finite element analysis of joint T-W13F22, in the database (Table 1), using the stress-strain curve for a typical mild steel with a yield stress of 254 N/mm^2 and an ultimate tensile strength of 403 N/mm^2 gives a stiffener strength of 6767 kN. The predicted strength of the stiffener is 5101 kN, 75% of the calculated value. However, if the flow stress (average of the yield stress and the ultimate tensile strength) is used in the prediction, the strength will increase to 6587 kN, giving an error of only 3%. To reduce conservatism in prediction, it is therefore proposed that the flow stress should be used.

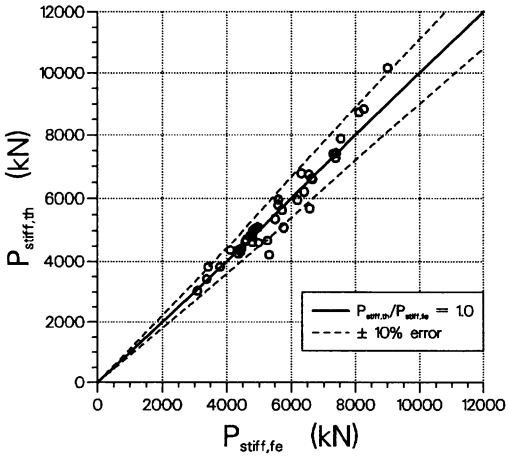

Fig 8. Comparison of theoretical and numerical stiffener strengths

4.2 Strength of stiffened joints

The theoretical model assumes that the joint strength is the sum of the strengths of the stiffener and the unstiffened joint. With the stiffener strength obtained from the upper bound analysis, calculating the strength of the stiffened joint is therefore a matter of adding to it the strength of the unstiffened joints estimated using an appropriate equation. There are several sets of equations in existence that can be used to estimate strength of unstiffened T-joints:

(1) from major design codes such as API (1993), DEn (1990), and ISO (1997);
(2) from Kurobane et. al. (1984), which forms the basis of the design equation in the CIDECT Design Guide by Wardenier et al. (1991) and the more recent research from van der Vegte, which takes into account the interaction between joint strength and overall chord bending.

Equations from (1) above are lower bound or characteristic strength equations, whereas those from (2) are mean strength equations. Here no attempt is made to give a detailed evaluation of the appropriateness, or otherwise, of these equations in estimating strengths of unstiffened T-joints, as it is outside the scope of the current work. However, the equations, in conjunction with the proposed upper bound analysis, were used to calculate the strengths of the stiffened joints in the database. Table 2 gives the results of the statistical analysis of the ratio of the predicted strength of stiffened joint $P_{joint,s,th}$ to the numerical strength of stiffened joint $P_{joint,s,fe}$. It is not possible to establish the relative accuracy of the equations because, as pointed out earlier, the finite element results were obtained using an elastic-perfectly plastic stress-strain curve and should, therefore, be low when compared with the strengths

Table 2 Statistical analysis of the ratio of the predicted strength of stiffened joint, $P_{joint,s,th}$, to the numerical strength of stiffened joint, $P_{joint,s,fe}$.

	Mean Strength Equations		Characteristic/Lower Bound Strength Equations		
	Kurobane	van der Vegte	API	DEn	ISO
Maximum	1.10	1.14	1.20	1.03	1.05
Minimum	0.90	0.95	0.78	0.75	0.77
Mean	1.0058	1.0572	1.0219	0.9108	0.9370
CoV	0.0344	0.0311	0.0662	0.0588	0.0575

obtained from the equations. The only observation, perhaps, that can be made is the scatter produced by the equations. van der Vegte's equation, despite its sophistication, produces a CoV that is only marginally better than that of Kurobane's. As far as the design equations are concerned, the CoV produced by API is slightly worse that those from DEn and ISO, which are very similar in magnitude.

6 CONCLUSIONS

Based on the results, and the observations on failure mechanism, of forty ring-stiffened T-joints analysed using the finite element method, a theoretical model for strength prediction has been proposed. The model assumes that the joint strength is the sum of the strengths of the T-shaped stiffener and the unstiffened joints; the latter can be easily estimated from equations currently available from design codes and research literature.

The strength of the T-shaped ring stiffener was analysed using simple plastic theory, via upper bound theorem, by postulating a five-hinge failure mechanism. At the position of the hinges, the stiffener is assumed to act in conjunction with part of the joint chord wall to form an unsymmetrical I-section; and the width of the flange of this I-section which comes from the chord wall was determined using an empirical equation. This simple model has been shown to be able to predict strengths of stiffeners obtained from finite element analysis with good accuracy. Information on existing strength equations for unstiffened T-joints that can be used together with the proposed model to obtain strengths of stiffened joints is also given. To reduce conservatism in design, it is proposed that the flow stress (the average of the yield stress and the ultimate tensile strength) should be used in the model to predict strengths.

7 ACKNOWLEDGEMENT

The authors thank Mr. M. Lalani and his colleagues at MSL Engineering for discussions, at the initial stage of the work, on stiffened joints in general. Financial support from both the University of Wales Swansea and MSL Engineering are gratefully acknowledged.

8 NOTATION

Joint parameters

d	brace outer diameter
D	chord outer diameter
L	chord length
t	brace wall thickness
T	chord wall thickness
α	chord length parameter ($2L/D$)
β	diameter ratio (d/D)
γ	chord thickness ratio ($D/2T$)
θ	in-plane brace angle
τ	wall thickness ratio (t/T)

Stiffener parameters

bf	width of flange
tf	thickness of flange
dw	depth of web
tw	thickness of web

$P_{joint,s,fe}$	numerical strength of stiffened joint
$P_{joint,s,th}$	predicted strength of stiffened joint
$P_{joint,u}$	strength of unstiffened joint
$P_{stiff,fe}$	numerical strength of stiffener
$P_{stiff,th}$	predicted strength of stiffener

9 REFERENCES

American Petroleum Institute 1993. API RP2A:

Planning, Designing and Constructing Fixed Offshore Platforms. 19th Edition.

Department of Energy 1990. Background to New Static Strength Guidance for Tubular Joints in Steel Offshore Structures. OTH 89 308.

Dexter E.M., Lee M.M.K. and Kirkwood, M.G. 1996. Overlapped K joints in circular hollow sections under axial loading. Journal of Offshore Mechanics and Arctic Engineering, Transactions of The American Society of Mechanical Engineers, Vol. 118, No.1, 53-61.

ISO 1997. 13819-2/Draft C.

Krasenberg R.W. 1990. Ring stiffeners in circular hollow section joints. Final Thesis, Delft University of Technology.

Lee M.M.K., Dexter E.M. and Kirkwood M.G. 1995. Strength of moment loaded tubular T/Y-joints in offshore platforms. The Structural Engineer, Journal of the Institution of Structural Engineers, Vol. 73, No. 15, 239-246.

Lee M.M.K. and Llewelyn-Parry A. 1998. Strength of ring-stiffened tubular T-joints in offshore structures - Part I: a numerical parametric study, submitted to Structures and Buildings, Proc. of I.C.E.

Lee M.M.K. and Wilmshurst S.R. 1995. Numerical modelling of CHS joints with multiplanar double-K configuration. Journal of Constructional Steel Research, 32, 281-301.

Kurobane Y., Makino Y. and Ochi K. 1984. Ultimate resistance of unstiffened tubular joints. Journal of Structural Engineering, American Society of Civil Engineers, Vol. 110, No. 2, 385-400.

Microsoft Excel, Version 5.0 1993. Microsoft Corporation.

Roark R.J. 1965. Formulas for stress and strains. McGraw-Hill Publishing.

Sawada Y., Idogaki S. Sketia K. 1979. Static and fatigue tests on T-joints stiffened by an internal ring. Offshore Technology Conference, Houston, USA, paper OTC 3422.

van der Vegte G.J. 1995. The Static Strength of Uniplanar and Multiplanar Tubular T- and X-joints, PhD Thesis, Delft University of Technology.

van der Vegte G.J., Leray, D.H. and Choo, Y.S. 1997. The axial strength of uniplanar X-joints reinforced by T-shaped ring-stiffeners. International Offshore and Polar Engineering Conference, Honolulu, USA.

Wardenier J., Kurobane Y., Packer J.A., Dutta D. and Yeomans N. 1991. Design Guide for Circular Hollow Section (CHS) Joints under Predominantly Static Loading, CIDECT.

Tubular Structures VIII, Choo & Van der Vegte (eds) © 1998 Balkema, Rotterdam, ISBN 90 5809 001 9

The static behaviour of multiplanar XX-joints loaded with in-plane bending moments and axial forces

Y.Yu, D.K.Liu & J.Wardenier
Delft University of Technology, Netherlands

ABSTRACT: This paper deals with an extensive numerical parameter study on the static behaviour of multiplanar XX-joints where the in-plane braces are loaded with in-plane bending moments and the out-of-plane braces with axial forces. Due to asymmetry in deformation, the behaviour of such joints is more complicated than that of multiplanar XX-joints loaded only with axial forces or only with in-plane bending moments. The influence of the boundary conditions on the ultimate moment capacity of the joints is investigated. Based upon the numerical results of the parameter study, functions for the multiplanar geometrical stiffening effect and for the multiplanar load effect of multiplanar joints are recommended.
KEYWORDS: Static Strength, Rectangular Hollow Sections, Multiplanar Connections.

1 INTRODUCTION

Experimental tests and numerical parameter studies on multiplanar XX-joints of rectangular hollow sections loaded with in-plane bending moments on the in-plane braces and axial forces on the out-of-plane braces were carried out within an ECSC programme (de Koning et al 1992) and a CIDECT research programme (Yu 1997).

The behaviour of such joints is influenced by the boundary conditions applied on the out-of-plane braces. In this paper, three boundary conditions are included: the out-of-plane braces are free to rotate; the out-of-plane braces are fixed in the direction parallel to the length of the chord and "follow force" (the applied loads N_2 are always in the direction of the longitudinal axis of the out-of-plane braces), see Figure 1.

Due to the in-plane bending moments on the in-plane braces, the out-of-plane braces will rotate. If the ends of the out-of-plane braces are free (Fig. 1) and loaded in tension, additional secondary bending moments on the out-of-plane braces occur which reduce the rotation somewhat. Thus, the rotation of the out-of-plane braces is not very much in such a case. If the ends of the out-of-plane braces are free and loaded in compression, the secondary bending moments increase the rotation. As a result, failure of the out-of-plane braces may occur due to a combination of the compression forces and the secondary bending moments in the out-of-plane braces. In such a case, the rotation of the out-of-plane braces may reduce largely the ultimate moment capacity of the joints.

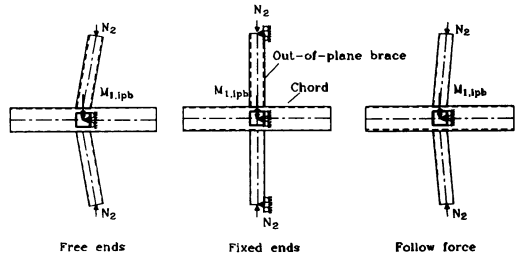

Figure 1. Three different boundary conditions

If the ends of the out-of-plane braces are restrained (Fig. 1) in a direction parallel to the chord length, secondary bending moments due to rotation of the out-of-plane braces are prevented. However, reaction forces on the ends of the out-of-plane braces result in secondary bending moments too. Such restraints have been applied in the experimental test for joint DX7 (de

Koning et al. 1992). Due to the application of the restraints, the ultimate moment capacity of the joints may increase for a large positive load ratio.

If the method of "follow force" (Fig. 1) is used, the applied forces on the out-of-plane braces are always in the direction along the longitudinal axis of the out-of-plane braces. As a result, no secondary bending moments on the out-of-plane braces occur.

2 RESEARCH PROGRAMME

The configuration of a multiplanar XX-joint loaded with in-plane bending moments on the in-plane braces and axial forces on the out-of-plane braces is shown in Figure 2.

The research programme is summarised in Table 1. The load ratio is defined as $J_{1\lambda}=N_2/(M_1/h_1)$. For each multiplanar XX-joint, five load ratios are applied with $J_{1\lambda}$=-1.0, -0.5, 0, 0.5 and 1.0 respectively. If the out-of-plane braces are loaded in compression, the load ratio is defined as positive, as shown in Figure 2. There are three groups of analyses based upon the three boundary conditions: group one with the out-of-plane braces free, group two with the out-of-plane braces fixed at their ends in the direction parallel to the chord length, group three with the axial loads always following the axes of the out-of-plane braces. Furthermore, the corresponding uniplanar joints are included for a comparison. Butt welds are included for joints with $\beta \neq 1.0$. The leg length of the weld along the chord is $0.5*t_1$ and that along the braces is (t_1+2) mm. For joints with β=1.0, the welds along the chord length are not included.

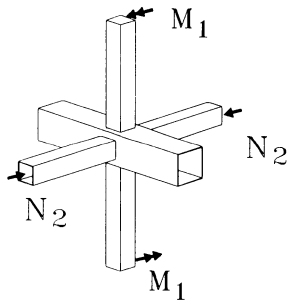

Figure 2. Configuration of an XX-joint loaded with in-plane bending moments and axial forces

3 THE FE ANALYSIS

The finite element model used is based upon previous studies (Yu et al. 1994, Yu 1997). Eight noded thick shell elements are used to model the chord, the braces and the weld. Both geometrical and material non-linearities are included. The thickness of the weld element is equal to the throat thickness of the fillet part of the butt weld. A quarter of each joint is modelled considering symmetry of loads and geometry, see Figure 3. A pure bending moment on the in-plane brace and a proportional axial load on the out-of-plane brace (a load ratio of $J_{1\lambda}=N_2h_1/M_1$) is applied at each increment.

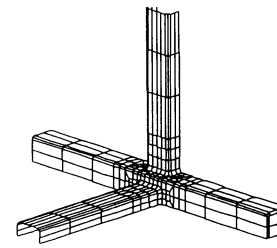

Figure 3. Finite element meshes

Table 1. Research programme for XX-joints loaded with in-plane bending moments and axial forces

Uniplanar joints	Multiplanar joints	Geometrical parameters	
Name	Name	β	2γ
x1i	xx1ia	0.4	15
x2i	xx2ia	0.4	24
x3i	xx3ia	0.4	35
x4i	xx4ia	0.6	15
x5i	xx5ia	0.6	24
x6i	xx6ia	0.6	35
x7i	xx7ia	0.8	15
x8i	xx8ia	0.8	24
x9i	xx9ia	0.8	35
x10i*	xx10ia*	1.0	15
x11i*	xx11ia*	1.0	24
x12i*	xx12ia*	1.0	35

f_{y0} = 355 N/mm^2, $b_0 = h_0$ = 150 mm, $b_2 = b_1 = h_1$, $t_2 = t_1$
l_0 = 900 mm, $J_{1\lambda}$ = -1, -0.5, 0, 0.5, 1.0

*: Without weld

Where, f_{y0} is the yield strength of the chord; b_i (i=0, 1, or 2) is the width of the chord or the in- and out-of-plane braces; h_i is the depth of the chord or the in- and out-of-plane braces; l_0 is the chord length.

4 NUMERICAL RESULTS AND OBSERVATIONS

The numerical results are presented in two groups: group 1 includes the joints with the out-of-plane braces free to rotate; group 2 includes the joints with the out-of-plane braces fixed at the ends in the direction parallel to the chord length. The results from group 3 are presented later on as a comparison.

4.1 Joints with the out-of-plane brace free (Group 1)

For joints with the out-of-plane braces free, the FE results of the non-dimensional in-plane bending moment vs. chord top face indentation curves are illustrated in Figure 4. The ultimate moment capacity of the joints is determined as the maximum moment or the moment at the ultimate deformation limit of $3\%b_0$ or the moment at the joint rotation of φ=0.1 rad., whichever is smaller (Yu & Wardenier 1996, Yu 1997). The ultimate moment capacity of each joint is listed in Table 2. For each multiplanar joint, five load ratios are included. The corresponding uniplanar joints are also included as comparison. Observations from Figure 4 are :

- For joints with a β=0.4 and 0.6 no geometrical multiplanar effects are observed.
- For the joints with small β values, the ultimate moment capacity is increased with an increase of the load ratios ($-1 \le J_{1A} \le 0.5$). For joints with a load ratio of J_{1A}=1.0, the ultimate moment capacity is decreased due to the increased rotation of the out-of-plane braces which results in unfavourable secondary bending moments in the out-of-plane braces. In such a case, the joint fails in the chord at the compression side of the out-of-plane braces next to the weld toe.
- The influence of the load ratio is larger for joints with smaller β values (β=0,4 and 0.6) than that for joints with larger β values (β=0.8 and 1.0) due to the rotation effects. Especially for joints with β=1, the influence of the load ratio is so small that the curves for different load ratios are overlapping.

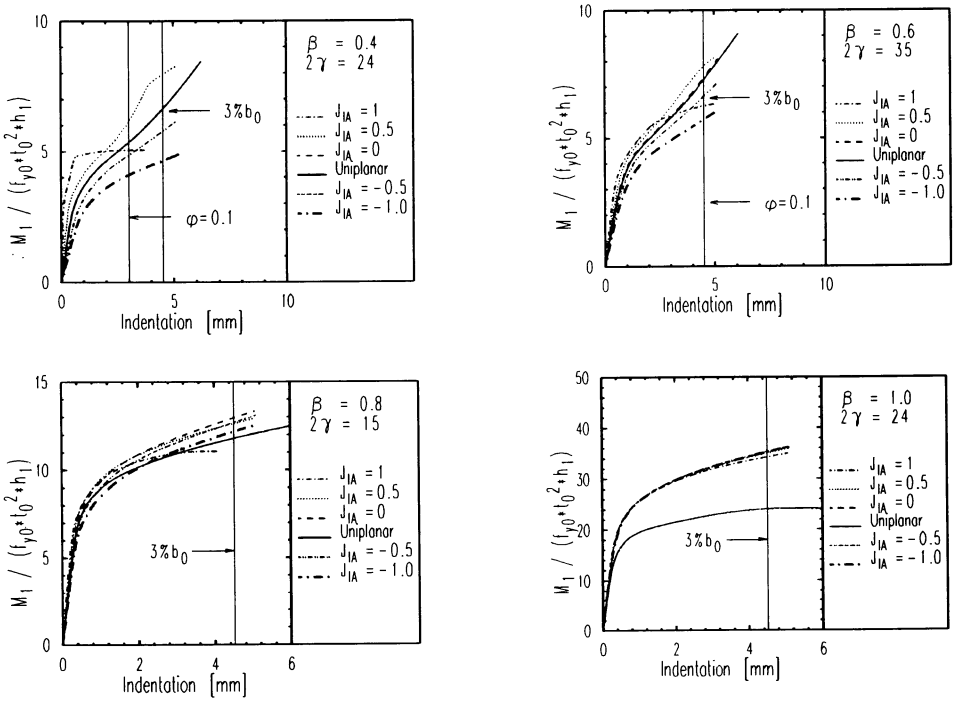

Figure 4. Numerical results of multiplanar XX-joints with the out-of-plane braces free (Group 1)

4.2 Joints with the out-of-plane braces fixed (Group 2)

In order to prevent failure due to the rotation of the out-of-plane brace, the end of the out-of-plane brace is restrained in the direction parallel to the chord length. The numerical results of these joints are shown in Figure 5. The ultimate moment capacities of the joints are listed in Table 3. Observations from Figure 5 are as follows:

- For multiplanar joints with $\beta \leq 0.6$, no or minor multiplanar geometrical effects are found compared to the results of the uniplanar joints. For multiplanar joints with $\beta=0.8$ and 1.0, larger multiplanar geometrical effects exist. The multiplanar geometrical effects are somewhat higher than those of joint group 1 depending upon the geometrical parameters.
- For joints with $\beta \leq 0.8$, the ultimate moment capacity of the joints is increased with the increase of the load ratios. For multiplanar joints with $\beta \leq 0.8$ and $J_{1A}=1.0$, the ultimate moment capacity of the joints is increased largely due to the restraints on the out-of-plane braces which results in high numerical results.
- For joints with $\beta=1.0$, the influence of the load ratio is very small which agrees with the results from joint group one.

5 COMPARISON BETWEEN THE RESULTS OF JOINTS WITH DIFFERENT BOUNDARY CONDITIONS

5.1 The results of joints with fixed and free ends

The influence of the restraints on the out-of-plane braces is shown in Figure 6. The vertical axis represents the ratio between the ultimate moment capacities of the joints with fixed and those with free ends of the out-of-plane braces.

For joints with load ratios J_{1A}=-1.0, -0.5, 0 and 0.5, the influence of the restraints is about 20% for joints with $\beta=0.8$ and is within 10% for joints with $\beta=0.4$, 0.6 and 1.0 independent on the load ratios, see Figure 6. The 2γ influence is neglectable.

For joints with $J_{1A}=1.0$ and $\beta \leq 0.8$, a much larger influence of the restraints is found, see Figure 6. When the out-of-plane braces are free to rotate, the ultimate moment capacity of the joints is reduced largely due to the large secondary bending moments on the out-of-plane braces for joints with $J_{1A}=1.0$, see Figure 4. Failure occurs in the chord at the compression side of the out-of-plane braces. However, when the out-of-plane braces are restrained and rotation is thus avoided, the ultimate moment capacity is increased as shown in Figure 5. In practice, the out-of-plane braces have a restraining effect between the free and fixed

Table 2. Numerical results of joint group 1

	Uniplanar $\frac{M_{1,ipb,u}}{f_{y0}t_0^2h_1}$	Multiplanar joints $\frac{M_{1,ipb,u}(J_{1A})}{f_{y0}t_0^2h_1}$					
		J_{1A}=	-1.0	-0.5	0.0	0.5	1.0
x1i	5.71	xx1ia	4.45	5.27	5.72	6.38	-----
x2i	5.35	xx2ia	4.09	4.86	5.36	6.15	5.05
x3i	5.21	xx3ia	3.75	4.51	5.22	6.48	5.95
x4i	7.56	xx4ia	6.49	7.14	7.61	7.71	5.95
x5i	7.17	xx5ia	5.90	6.66	7.20	7.50	5.72
x6i	7.25	xx6ia	5.72	6.62	7.34	7.79	6.25
x7i	11.80	xx7ia	12.18	12.68	12.94	12.63	11.07
x8i	11.40	xx8ia	11.18	11.76	12.12	11.92	10.22
x9i	10.87	xx9ia	10.35	10.99	11.41	11.31	9.79
x10i*	16.85	xx10ia*	22.36	23.18	23.38	-----	-----
x11i*	24.04	xx11ia*	35.20	35.27	34.62	33.37	30.87
x12i*	29.21	xx12ia*	47.68	47.70	47.58	47.31	46.52

*: Without weld, ---- : convergency failure.

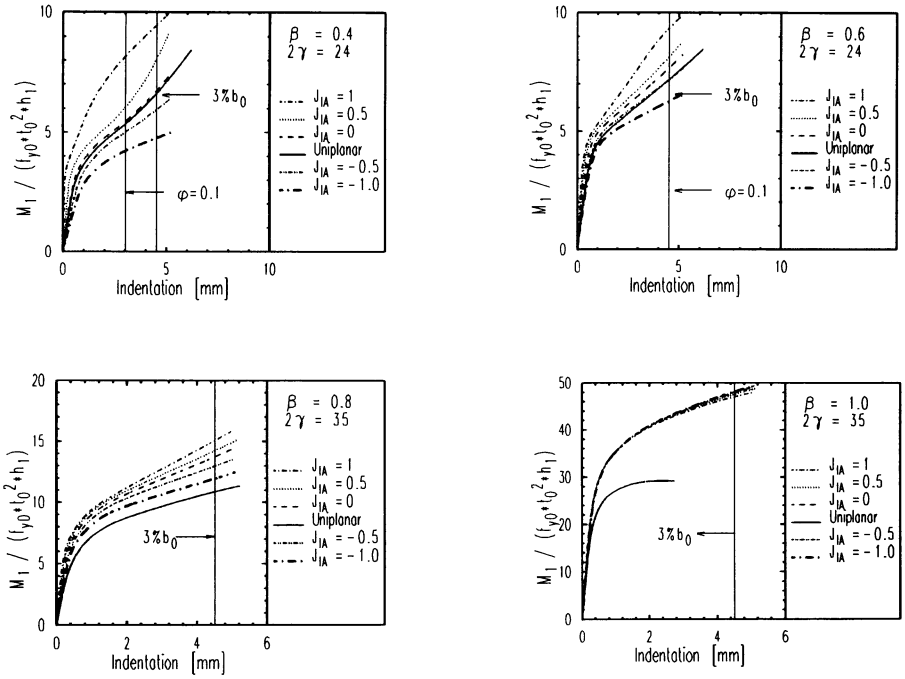

Figure 5. Numerical results of joint group 2

Table 3. Numerical results of joint group 2

	Uniplanar $\frac{M_{1,ipb,u}}{f_{y0}t_0^2h_1}$	Multiplanar joints $\frac{M_{1,ipb,u}(J_{IA})}{f_{y0}t_0^2h_1}$					
		J_{IA}=	-1	-0.5	0.0	0.5	1.0
x1i	5.71	xx1ia	4.60	5.44	5.83	6.25	9.37
x2i	5.35	xx2ia	4.22	5.01	5.46	6.05	8.17
x3i	5.21	xx3ia	3.84	4.67	5.36	6.36	7.70
x4i	7.56	xx4ia	6.93	7.69	8.19	8.56	9.56
x5i	7.17	xx5ia	6.27	7.16	7.66	8.13	9.35
x6i	7.25	xx6ia	6.05	7.13	7.75	8.41	9.16
x7i	11.80	xx7ia	-----	-----	15.28	-----	-----
x8i	11.40	xx8ia	12.86	13.86	14.62	15.15	15.76
x9i	10.87	xx9ia	11.95	12.97	13.72	14.22	15.05
x10i*	16.85	xx10ia*	23.04	24.01	24.27	24.00	23.16
x11i*	24.04	xx11ia*	35.65	35.68	35.61	35.45	35.04
x12i*	29.21	xx12ia*	48.10	48.03	47.84	47.55	47.01

*: Without weld; ---- : Convergency failure.

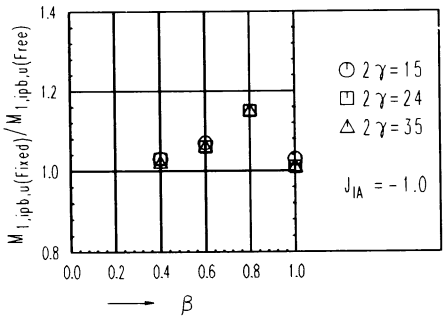

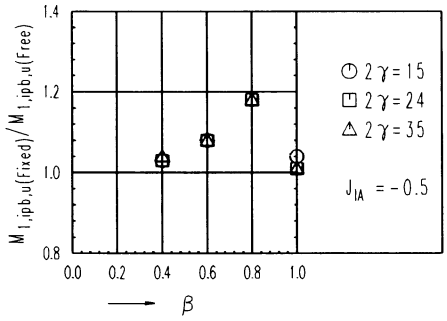

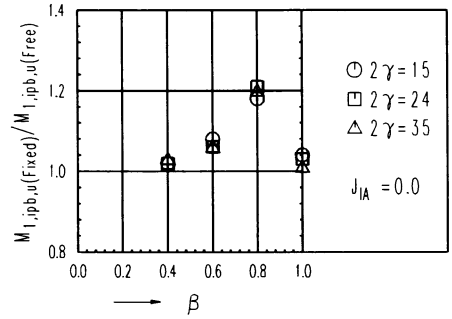

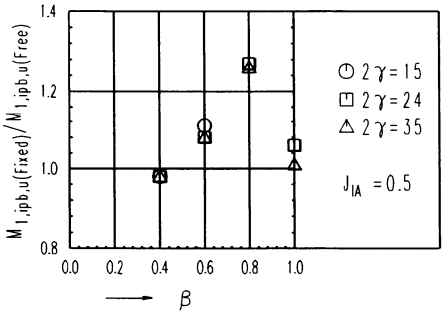

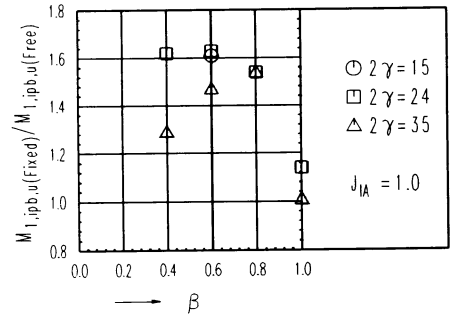

Figure 6. Comparison between the results of joints with fixed and free ends

boundary conditions. Thus, the influence of the restraints shown in Figure 6 is higher than that in the practice.

5.2 The results of joints with fixed ends, free ends and "follow force"

A comparison between the results of joints with fixed ends, free ends and "follow force" on the out-of-plane braces is shown in Figure 7. It can be seen that the ultimate moment capacity of joints with "follow force" is higher than that of joints with free ends and lower than that of joints with fixed ends.

For a joint with load ratio J_{IA}=0.5 and β=0.6, the ultimate moment capacity of a joint with "follow force" is 5% higher than that of a joint with free ends and 3% lower than that of a joint with fixed ends. For a joint with load ratio J_{IA}=0.5 and β=0.8, the ultimate moment capacity of a joint with "follow force" is 8% higher than that of a joint with free ends and 15% lower than that of a joint with fixed ends.

For a joint with J_{IA}=1.0 and β=0.6, the ultimate moment capacity of a joint with "follow force" is 62% higher than that of a joint with free ends and only 1% lower than that of a joint with fixed ends. For a joint with J_{IA}=1.0 and β=0.8, the ultimate moment capacity of a joint with "follow force" is 31% higher than that of a joint with free ends and 15% lower than that of a joint with fixed ends.

As indicated in Figure 7, for low load ratios the ultimate moment capacity of joints with "follow force" is close to that of joints with free ends. For high load ratios, it is close to that of joints with fixed ends.

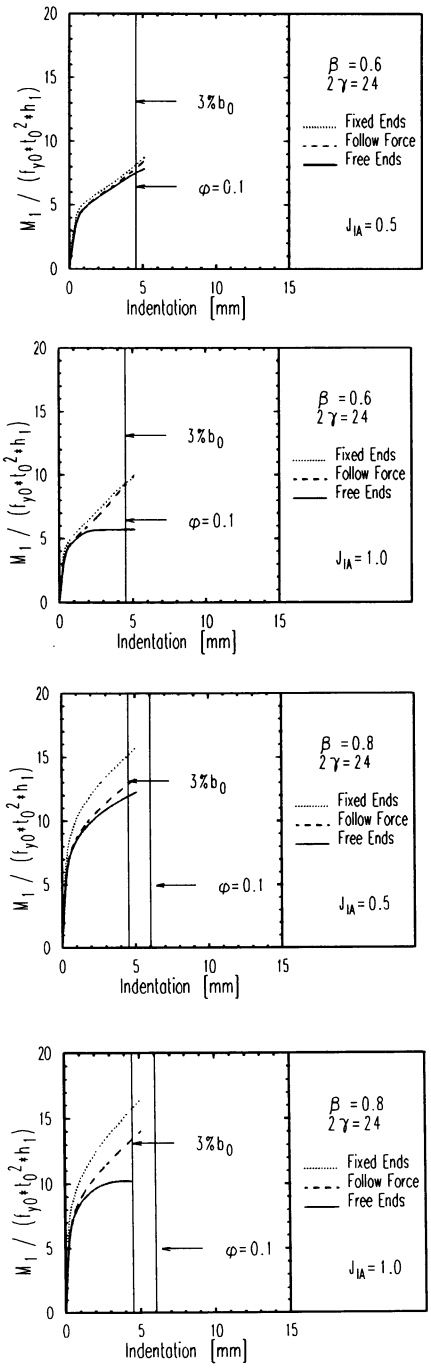

Figure 7. Comparison between the results of joints with fixed ends, free ends and "follow force"

6 THE JOINT ULTIMATE MOMENT CAPACITY

The general formulae for the ultimate moment capacity of the joints are determined as follows:

$$M_{1.ipb,u}\ (J_{1A}=0) = c_m * M_{1.ipb,u} \quad (1)$$

$$M_{1.ipb,u}\ (J_{1A}) = f\ (J_{1A}) * M_{1.ipb,u}\ (J_{1A}=0) \quad (2)$$

Where $M_{1.ipb,u}$ is the ultimate moment capacity of uniplanar X-joints;
c_m is a factor considering the multiplanar geometrical stiffening effects;
$M_{1.ipb,u}(J_{1A}=0)$ is the ultimate moment capacity of XX-joints with a load ratio $J_{1A}=0$;
$M_{1.ipb,u}(J_{1A})$ is the ultimate moment capacity of XX-joints with a load ratio J_{1A}.

6.1 The multiplanar geometrical stiffening effects

Joints with the out-of-plane braces free

According to definition, the factor for the multiplanar geometrical stiffening effects is defined as the ratio between the ultimate moment capacity of multiplanar XX-joints with $J_{1A}=0$ and that of the corresponding uniplanar X-joints. Based upon a previous study (Yu & Wardenier 1996), the factor for the multiplanar geometrical stiffening effects is given as:

$$c_m = 1 + 0.4\beta^x \quad (3)$$

Joints with the out-of-plane braces fixed

For joints with the out-of-plane braces restrained to rotate, the multiplanar geometrical stiffening effects are somewhat larger than those of the corresponding joints with the out-of-plane braces free due to the secondary bending moments on the out-of-plane braces. In practice, the boundary conditions of the out-of-plane braces are between fixed and free situations.

6.2 The multiplanar load effects

Joints with the out-of-plane braces free

The multiplanar load effects for joints with the out-of-plane braces free are illustrated in Figure 8.

For joints with negative load ratios ($J_{1A} \leq 0.0$), a clear negative multiplanar load effect is found. The function for the multiplanar load effects is defined as follows:

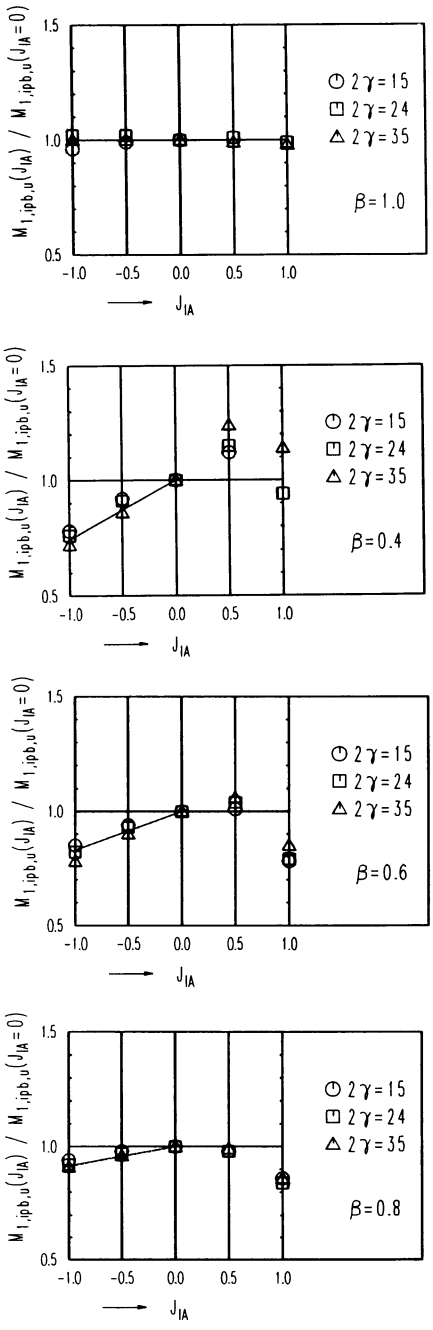

Figure 8. The multiplanar load effects (joints with the out-of-plane braces free)

$$f(J_{IA}) = 1 + 0.43(1 - \beta)J_{IA} \quad (J_{IA} \leq 0) \qquad (4)$$

As already discussed, due to the similar influence of the restraints for joints with different load ratios (J_{IA}=-1.0, -0.5 and 0 etc.), the multiplanar load effects of joints with and without restraints are similar. Thus, the regression formula of equation (4) is based upon all the numerical results of joint groups 1 and 2. Equation (4) is plotted in Figure 8.

For joints with a positive load ratio of J_{IA}=0.5, the multiplanar load effect is positive or small. For joints with a positive load ratio of J_{IA}=1.0 and $\beta \leq 0.8$, a negative multiplanar load effect is found in many cases due to the large secondary bending moments on the out-of-plane braces. The influence of the secondary bending moments depends not only on the load of the out-of-plane braces but also on the length of them. If the method of "follow force" is used, the secondary bending moments are excluded and the multiplanar load effects will be positive. For example, for a joint with β=0.6, 2γ=24 and J_{IA}=1.0, the multiplanar load effect according to Figure 8 is -21%, however if "follow force" is used, the joint ultimate moment capacity is increased by 62% compared to that of the corresponding joint with the out-of-plane braces free, see Figure 7. As a result, the ultimate moment capacity of the joint with "follow force" (J_{IA}=1.0) is 29% higher than that of the joint with the out-of-plane braces free and unloaded.

Similarly, for the joint with β=0.8, 2γ=24 and J_{IA}=1.0, the multiplanar load effect for the joint with the out-of-plane braces free is -16%, while the multiplanar load effect for the joint with "follow force" is 11%. Based upon these considerations, a lower bound of $f(J_{IA})$=1.0 is recommended for joints with $J_{IA} \geq 0.0$.

Joints with the out-of-plane braces restrained

The results of joints with the out-of-plane braces restrained are illustrated in Figure 9.

For joints with negative load ratios ($J_{IA} \leq 0$), equation (4) is applied, because a similar tendency of the multiplanar load effects is found. Equation (4) is also plotted in Figure 9.

For joints with positive load ratios ($J_{IA} \geq 0.0$), the multiplanar load effects in Figures 8 and 9 are about the same for J_{IA}=0.5, while for joints with J_{IA}=1.0, the multiplanar load effect for joints with the out-of-plane

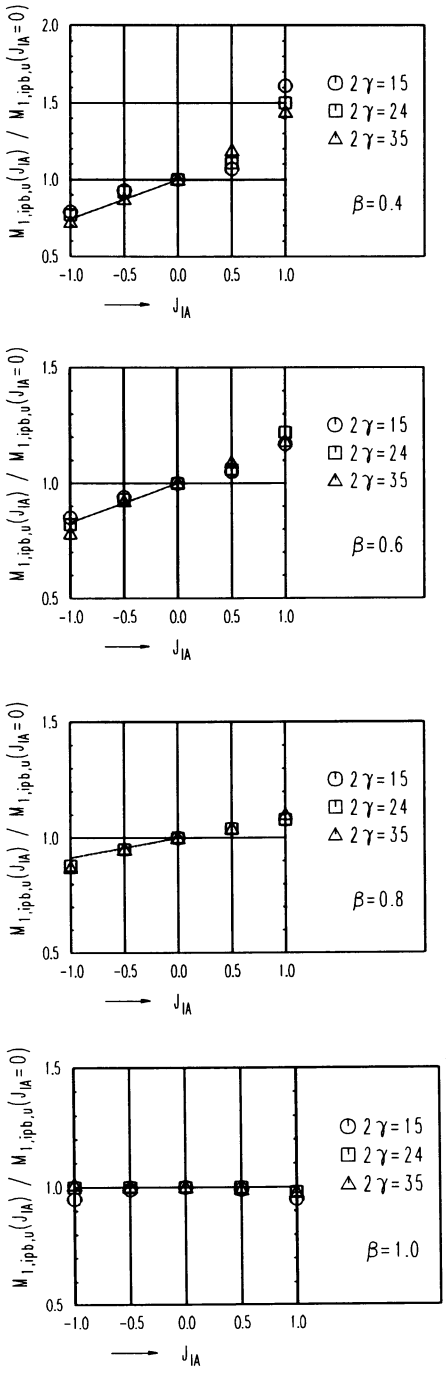

Figure 9. The multiplanar load effects (joints with the out-of-plane braces restrained)

braces free (Fig. 8) is negative and it is positive for joints with the out-of-plane braces restrained (Fig. 9). Thus, the behaviour of the joints is largely influenced by the boundary conditions of the out-of-plane braces

In practice, the out-of-plane braces are restrained between free and fixed boundary conditions. Based upon Figures 7 to 9, a lower bound of $f(J_{IA})=1.0$ is recommended for joints with $J_{IA} \geq 0.0$.

7 SUMMARY AND CONCLUSIONS

The behaviour of multiplanar XX-joints loaded with in-plane bending moments on the in-plane braces and axial forces on the out-of-plane braces has been analysed for different joint geometrical parameters and three groups of boundary conditions. It is summarised as follows:

1. The multiplanar geometrical stiffening effect can be given by $c_m = 1 + 0.4\beta^8$.

2. For joints loaded with negative load ratios $J_{IA} = N_2h_1/M_1 < 0$, i.e. the out-of-plane braces loaded in tension, a clear negative multiplanar load effect is found with the same tendency for joints with and without the out-of-plane braces restrained. The function for the multiplanar load effects is :

$$f(J_{IA}) = 1 + 0.43(1 - \beta)J_{IA} \quad (\text{for } J_{IA} \leq 0)$$

3. For joints loaded with positive load ratios $J_{IA} = N_2h_1/M_1 > 0$, i.e. the out-of-plane braces loaded in compression, the multiplanar effects depend upon the value of the load ratios and the boundary conditions. For joints with $J_{IA}=1.0$, the multiplanar load effects are largely influenced by the boundary conditions i.e. due to the secondary bending moment they are negative for most of the joints with the out-of-plane braces free and are positive for joints with the out-of-plane braces fixed. If "follow force" is used the secondary bending moments are excluded and the multiplanar load effects are between the two extreme cases, but still with a positive influence. As a lower bound, a function of $f(J_{IA})=1.0$ is recommended for the multiplanar load effects .

8 LIST OF SYMBOLS

c_m	Factor considering the multiplanar geometrical stiffening effects
b_i	Width of chord and braces (i=0,1,2)
f_{yo}	Yield stress of chord
h_i	Depth of chord and braces (i=0,1,2)
J_{IA}	Load ratio factor, $J_{IA} = N_2/(M_1 h_1)$
l_0	Chord length
M_1	In-plane bending moment (fig. 2)
$M_{1,ipb}$	In-plane bending moment (fig. 1)
$M_{1,ipb,u}$	Ultimate moment capacity
N_2	Axial force applied to brace
t_i	Thickness of chord and braces (i=0,1,2)
β	Width ratio between bracing member(s) and chord
γ	Half width to thickness ratio of the chord

9 REFERENCES

Koning, C.H.M. de, D.K. Liu, R.S. Puthli & J. Wardenier 1992. The development of design methods for the cost-effective applications of multiplanar joints, - experimental and numerical investigation on the static strength of multiplanar welded DX- and X-joints in R.H.S.. Stevin report No. 6.92.28, Delft University of Technology, The Netherlands.

Liu, D.K., R.S. Puthli & J. Wardenier 1993. Static strength of multiplanar DX-joints in rectangular hollow sections, Tubular Structures V, Proceedings of the Fifth International Symposium, 419-428, Nottingham, United Kingdom.

Yu, Y. & J. Wardenier 1996. Parameter study on the static strength of multiplanar XX-joints in rectangular hollow sections loaded with in-plane bending moments, Proceedings of the Sixth International Offshore and Polar Engineering Conference (ISOPE), vol. IV, 105-112, Los Angeles, California, USA.

Yu, Y. 1997. The static strength of uniplanar and multiplanar connections in rectangular hollow sections. PhD Thesis, Delft University Press, Delft.

Tubular Structures VIII, Choo & Van der Vegte (eds) © 1998 Balkema, Rotterdam, ISBN 90 5809 001 9

Fundamental behaviour of rectangular hollow sections with web openings

D.J. Ridley-Ellis, G. Davies & J.S. Owen
Department of Civil Engineering, University of Nottingham, UK

ABSTRACT: The influence of web openings on the fundamental structural behaviour of Rectangular Hollow Sections is introduced. The results of small scale tests on specimens in torsion and the development of analytical finite element models to predict behaviour are summarised allowing for the effect of single and multiple holes of various diameters and spacing placed symmetrically and asymmetrically. The finite element work has confirmed the experimental results in relation to stiffness, ultimate capacity and failure modes. This paper shows that torsion, bending and shear are inherently linked by asymmetry and geometric nonlinearity, even in simple torsion tests. The research is applicable to any field of engineering where it is advantageous to cut holes in the webs of load bearing hollow rectangular steel sections, although the primary aim is to develop a set of design rules for Rectangular Hollow Section Slim Floor edge beams with web openings.

1 INTRODUCTION

The use of Rectangular Hollow Sections (RHS) as edge beams in steel frame building construction is becoming increasingly common. In addition to their inherent torsional rigidity, RHS edge beams also offer architectural advantages, since they provide a flat steel outer face to the building perimeter; hence an improved aesthetic appearance. Additionally the option of a slender method of side wall construction with greater facility for cladding and future re-cladding is made available. Often, RHS edge beams are provided as an integrated element of a Slim Floor type construction eg. Slimdek® (See Figure 1).

One of the features of the Slimdek® system and certain other types of Slim Floor is the capacity to incorporate basic building services within the structural zone; a further economy of vertical space. The rectangular void within an RHS edge beam offers an ideal opportunity for efficient service integration. However this presents the need for openings in the web to allow passage of the service runs between the voids in the beams and the voids in the deck. Other cut-outs may be necessary if service runs are required to pass beyond the building perimeter, as is the case with some ventilation systems.

The consequences of cutting away parts of the webs of I section beams have been well researched eg. Gibson & Jenkins (1956), Kolosowski (1964), Redwood (1969), and Frost & Leffler (1971), but there has been little study into the effects of holes in the webs of Rectangular Hollow Sections. A sizeable opening in the web of an RHS Slim Floor beam will significantly alter the performance of the section. This paper presents the preliminary findings of a research project aimed at quantifying the influence of holes in the webs of load bearing RHS. The investigation is primarily concerned with the development of understanding as a preliminary to obtaining rules for the design of RHS Slimdek® beams with web openings. However, the findings will have other applications where load bearing

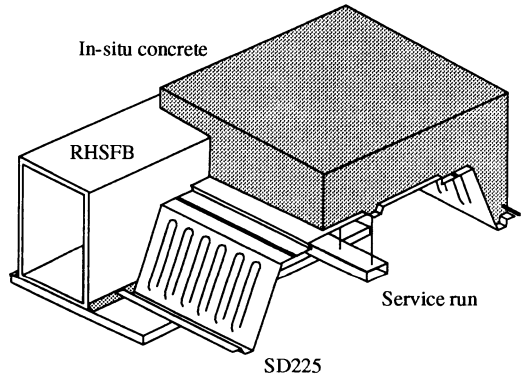

Figure 1. The Slimdek® system: RHS edge beam arrangement.

hollow, rectangular steel sections are required to have openings; eg., vehicle chassis and large machine beds.

This study into the fundamental behaviour of Rectangular Hollow Sections with web cut-outs will include the influence of the size, shape, number, position and relative position of holes upon strength and stiffness in bending, shear and torsion. The research will involve testing of full size RHS (in bending, shear and torsion) in addition to a comprehensive finite element study.

Full scale tests are expensive to undertake if a full range of parameters are to be examined. The availability of a torsion testing machine, and the limited amount of machining needed has enabled a large number of small scale tests on 38 mm square cold formed steel tube in torsion to reveal the effects of various arrangements of circular cut-outs on torsional capacity and modes of failure (See Section 4). This has been particularly valuable during the stage of developing the finite element modelling, both with regard to qualitative comparison and identification of modes of failure.

2 SLIM FLOOR: AN EXPLANATION.

2.1 *The Slim Floor approach*

Slim Floor is a method of steel frame multi-storey building construction in which the structural depth of each floor is minimised by incorporating the steel floor beams within the depth of the concrete floor slab. Conventional steel frame construction places the floor slab above the (downstand) beam such that the actual structural floor depth is the sum of the slab depth and the depth of the beam (See Figure 2). The Slim Floor approach permits a more efficient use of vertical space, which can result in a significant reduction in cladding costs. Since the Slim Floor beams are integrated into the floor structure there are no downstand beams and the floor can be prepared with either a flat soffit, or a false ceiling with no obstructions for service runs.

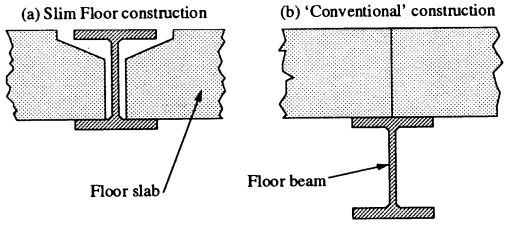

Figure 2. Slim Floor and 'conventional' steel frame construction.

Floor slabs may comprise of pre-cast units or in-situ concrete placed on profiled metal decking. The use of such a steel deck can reduce the weight of the floor and allow the accommodation of minor services within the slab depth in the voids between the ribs of the deck.

There are a number of alternative forms of Slim Floor beam, some of which are marketed as proprietary systems. The technique was originally developed in Scandinavia during the 1980's where it has markedly increased the market share for steel framed multi-storey buildings.

2.2 *The Slimdek® system*

British Steel markets a proprietary Slim Floor system under the registered trademark Slimdek®. Slimdek® is a development of British Steel's Slimflor® with new elements specifically designed for Slim Floor construction. The major element of the system is a range of asymmetric rolled I-beam sections, each with a 190 mm wide top flange and 300 mm wide bottom flange. The complete Slimdek® system consists of the 'Asymmetric Slimflor Beam' (ASB) used in conjunction with a composite slab of in-situ concrete placed on a profiled metal deck.

The asymmetric beam (See Figure 3) can be up to 25% lighter than conventional Slimflor® beams, and will permit larger openings for services in the web. An embossed diamond pattern rolled on to the beam is said to provide composite action with the floor slab without the need for welded shear connectors (Lawson et al. 1997). ASB sections are designed for use only with deep deck composite slabs. An improved deck profile (SD225) has recently been developed, which has a greater load carrying capacity, and a longer span range than the old CF210 system. The SD225 deck also has an improved ceiling fixing and service integration capability.

The ASB is intended for use as an internal member. Beams on the perimeter of a building are loaded, chiefly, on one side only. ASB and similar open

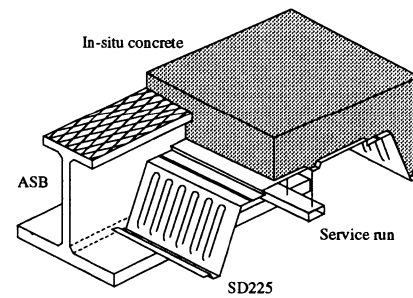

Figure 3. The Slimdek® system: internal beam arrangement.

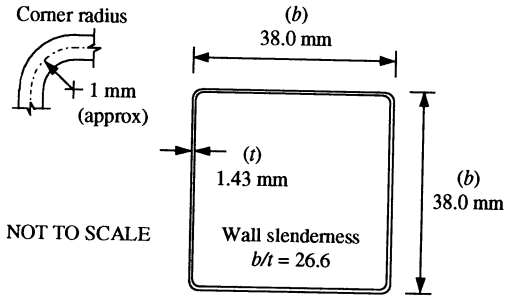

Figure 4. Cross section dimensions of the tube.

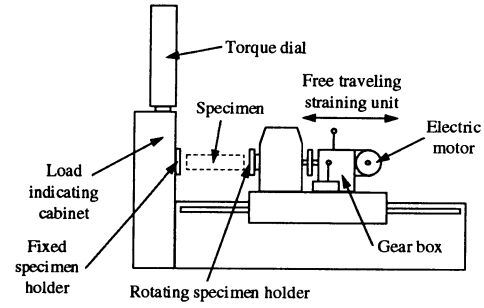

Figure 6. The torsion rig.

section beams are generally inefficient when subjected to out of balance loads and, if used inappropriately, may develop high degrees of rotational twist, causing damage to the building finishes and cladding. The Steel Construction Institute recommends the use of an edge beam based on a Rectangular Hollow Section (See Figure 1). Preliminary studies (Mullett et al. 1995) have shown that there is sufficient weight saving to compensate for the higher steel basis cost. In addition to their inherent torsional rigidity, RHS edge beams offer architectural advantages over downstand beam alternatives (Mullett 1997).

3 TORSION TESTING OF SCALE MODELS

3.1 *Experimental approach*

The preliminary torsion tests were performed on lengths of square section cold formed mild steel tube to provide a qualitative understanding of how a circular opening in the web can influence torsional strength and stiffness. The significance of hole size and the effect of relative hole position were examined.

Figure 4 shows the dimensions of tube tested. The wall slenderness ratio (26.6) is similar to that of the full size hot rolled RHS which would be used in typical edge beam construction. All specimens were 300 mm in length, but were restrained at either end by solid metal inserts and stiff clamping plates (See Figure 5). In all the tests described in this paper the length of the portion of the specimen free to twist under load was 240 mm. The inserts provided connectivity with the testing rig (See Figure 6). Torque (T) was applied at a constant rate of twist ($3^1/_3$ degrees per minute).

3.2 *Types of test piece; scope of study*

The test specimens have been classified according to the number and position of holes. Figures 7-10 show the types of test pieces. The figures show all four faces of the tube as if it were opened out; the dotted lines represent corners and the tube is such that the lines labelled AB coincide. Table 1 is a summary of the dimensions of the specimens tested.

Specimens of type I (See Figure 7) formed the control group. They had no holes and their torsional strength and stiffness can therefore be predicted by established formulae. The behaviour of the

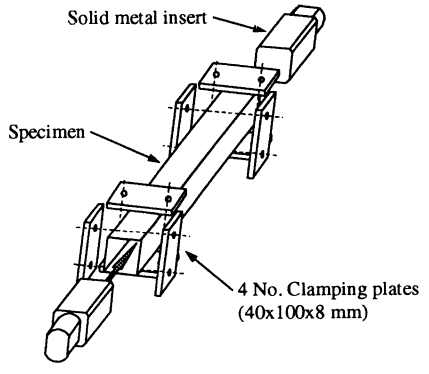

Figure 5. End conditions; clamping of the specimen.

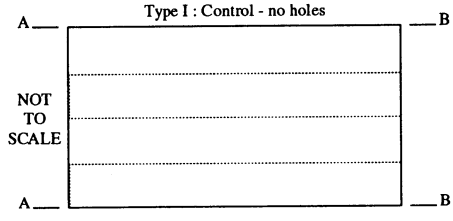

Figure 7. Developed view of type I specimens (control).

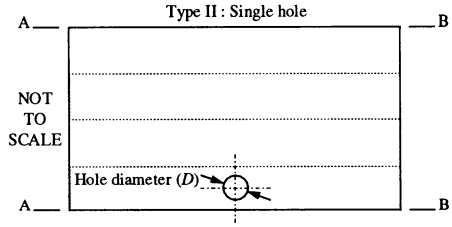

Figure 8. Developed view of type II specimens (one hole).

specimens with web openings can be compared directly with the behaviour of the control group to quantify the influence of the hole(s).

Specimens of type II (See Figure 8) had a single circular hole. The diameter (D) varied, but the hole was always placed centrally in one face.

Specimens of type III (See Figure 9) had two circular holes. The diameter (D) varied, but the holes were always placed centrally in opposing faces.

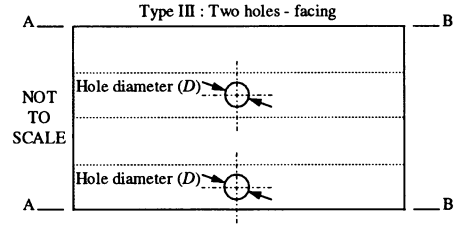

Figure 9. Developed view of type III specimens (two holes; facing).

Specimens of type IV (See Figure 10) had two circular holes. The holes are placed symmetrically in the same face at a distance s apart.

The material properties of the test pieces were determined from tensile testing of coupons cut from the tube. Tensile test piece dimensions were specified in accordance with BS EN 10 002-1 : 1990.

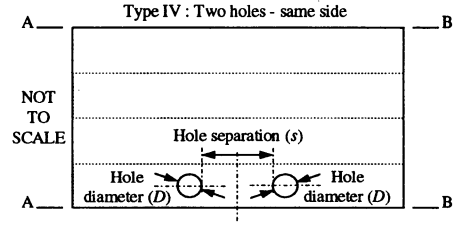

Figure 10. Developed view of type IV specimens (two holes; same side).

Table 1. Specimens tested.

Type	Number of specimens. tested	Hole diameter D (mm)	Hole diameter D/b (%)	Hole separation s (mm)	Hole separation s/D (%)
I	6	-	-	-	-
II	2	5	13.1	-	-
	2	10	26.3	-	-
	2	15	39.5	-	-
	2	20	52.6	-	-
	2	25	65.8	-	-
	2	30	78.9	-	-
III	2	5	13.1	-	-
	2	10	26.3	-	-
	2	15	39.5	-	-
	2	20	52.6	-	-
	2	25	65.8	-	-
	2	30	78.9	-	-
IV	1	20	52.6	5	25
	1	20	52.6	10	50
	1	20	52.6	15	75
	1	20	52.6	20	100
	1	20	52.6	25	125

4 RESULTS; EXPERIMENTAL OBSERVATIONS

4.1 *Torque-rotation relationships*

The results of coupon tests for material properties of the rectangular tube are shown in Figure 11.

Figures 12 and 13 include the torque-rotation histories for the control specimens (Type I). The initial elastic behaviour is followed by extensive plastic deformation (10 to 15 times the elastic rotation). This shows marginally positive stiffness slope which may be associated with strain hardening or the effects of large deflection This is followed by a significant drop in torque, associated with large out-of-plane distortion of the walls. This usually initiates near the ends of the tube adjacent to the ends of the metal inserts.

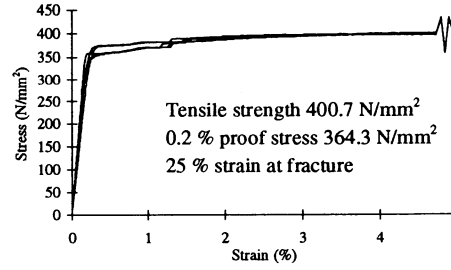

Figure 11. Coupon test; stress-strain relationship.

Ignoring radius effects, the theoretical fully plastic torque of the square section without cut-outs is given by:

$$T_p = \frac{2t\sigma_y}{\sqrt{3}}(b-t)^2 \qquad (1)$$

Where b = width (Figure 4)
t = wall thickness
T_p = theoretical fully plastic torque
σ_y = yield stress

As the coupon tests did not show a clearly defined yield point, the value of T_p used to compare the experimental results (Figures 12-16) was based on the 0.2 % proof stress. It should be noted that sections fail by buckling before the full strain hardened tensile strength observed in the coupon tests can develop.

Figure 12 also shows the behaviour of specimens with single holes (Type II). The effect of the diameter of the hole is seen to be important, small holes have little effect on the overall strength but decrease the extent of plastic behaviour. However for larger holes (*D/b* greater than 0.3) the reduction in strength is seen to be significant, although the subsequent negative stiffness in the collapse stage is seen to be reduced, so that it hardly exists for *D/b* greater than 0.6.

Onset on non-linearity is seen to be more pronounced in the specimens with larger holes. This is probably due to both initial local yielding and large displacements, although it is not possible to identify the point at which permanent damage first occurs from these test results alone. A finite element study, described later, is being developed to examine the distribution of stress.

Web openings reduce the initial stiffness of the section, although the reduction is less pronounced for a hole of small diameter than for one of large diameter.

Figure 13 shows the torque-rotation histories for the control specimens (type I) and the specimens with two holes facing (type III). The results show the double holes influencing torsional performance in a similar way to the single holes. Interestingly a double hole appears to have a similar effect to that of a single hole of equal diameter (Figure 14). The negative stiffness effect as shown in Figure 13 remains strong for all the specimens tested compared with the single sided holes shown in Figure 12.

The complete torque-rotation relationship for type IV specimens (two holes in the same side) is shown in Figure 15. Figure 16 shows how the distance between the holes affects peak torque. For large separations the capacity is similar to that of a specimen with a single hole of equal diameter. However, for smaller separations the holes begin to interact and the capacity is reduced. Type IV specimens also show a greater rotation before the peak torque is reached and reduced subsequent negative stiffness.

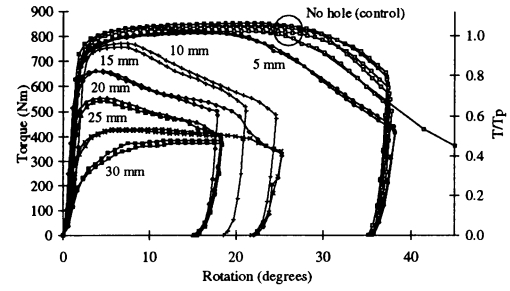

Figure 12. Torque rotation curves - One hole (Type II).

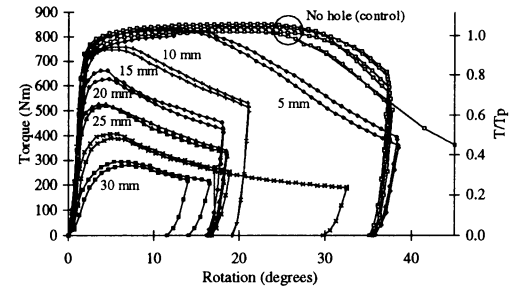

Figure 13. Torque rotation curves - Two holes facing (Type III).

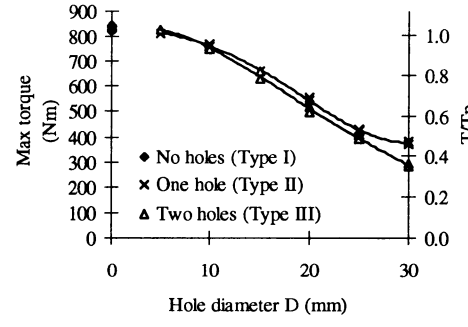

Figure 14. Peak torque and hole diameter - Types I, II & III.

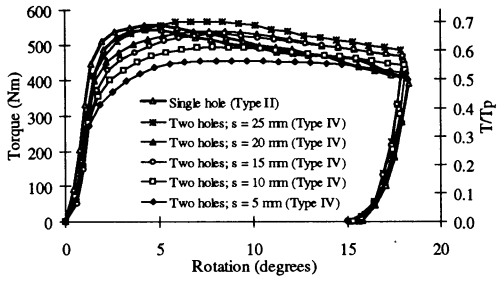

Figure 15. Torque rotation curves for Type IV specimens: 20 mm diameter hole (D/b = 0.53).

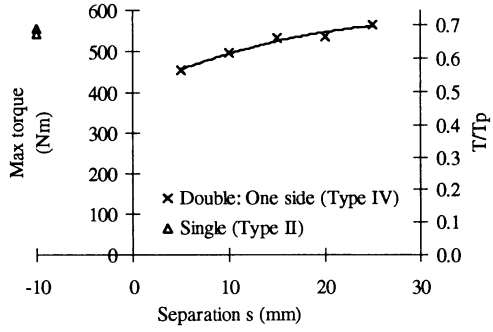

Figure 16. Peak torque and hole separation (Type IV) : 20 mm diameter hole (D/b = 0.53).

4.2 *Mechanisms of failure*

The specimens all failed in one of two ways; either a local end failure after global plastic strain, or a local failure in the region of the hole due to the weakening influence of the cut-out.

The failure of the stronger sections (those without holes or with D/b less than 0.13) was accompanied by the formation of a buckle on each of the four faces at 45° to the longitudinal axis of the section as shown in Figure 17. Sections with larger holes failed in the region of the hole in the manner shown in Figures 18 (Type II) & 19 (Type III). The failure mode of the type IV specimens is seen in Figure 20.

Figure 17 shows local failure initiated adjacent to and at the metal insert and clamp. Plastic strain occurred along the whole length of the specimens which failed in this manner. Hence it may be assumed with reasonable confidence that such sections had developed full torsional capacity prior to the formation of the buckle. All four buckles formed simultaneously.

In type II specimens (unsymmetrical) most of the rotation took place in the region of the hole and was about an axis parallel to, but offset from the longitudinal axis of the section. The face opposite the cut-out remained essentially plane, which resulted in bending of the section. It was observed that the unsymmetrical mode of failure caused the cross-section to lozenge (Figure 18).

In type III specimens (symmetrical, two holes facing. Figure 19) the rotation took place about the longitudinal axis of the section, and there was no bending or lozenging effect.

The mode of failure for type IV specimens seen in Figure 20 strongly resembles that of type II specimens, but with a shearing of the material between the holes. Initial plastic deformation was observed to occur at equal rates at both holes before the diagonal inward buckles form around the weaker of the two cut-outs.

A feature common to all the modes of failure in the local region around the hole is the sudden change in curvature at the distorted corners of the section marked * in Figures 17-20. This zone is associated with the high tensile stresses that develop around the hole (See Figure 21). Necking and even tearing could be seen in this region in the specimens with larger holes.

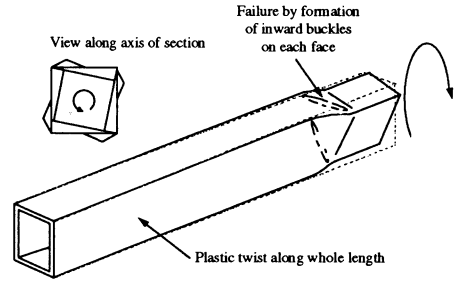

Figure 17. Post yield failure by buckling.

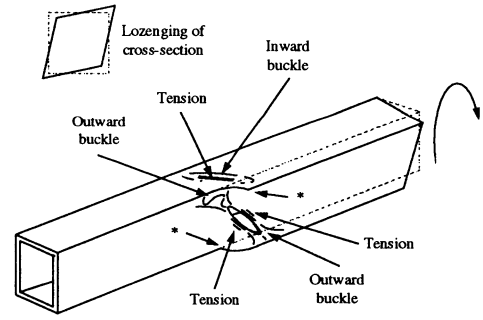

Figure 18. Failure of type II specimens.

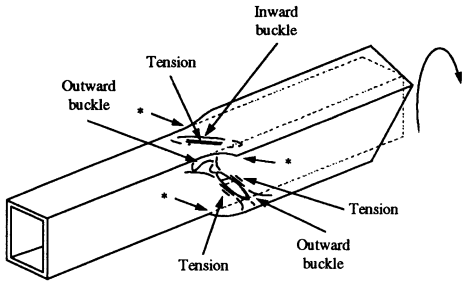

Figure 19. Failure of type III specimens.

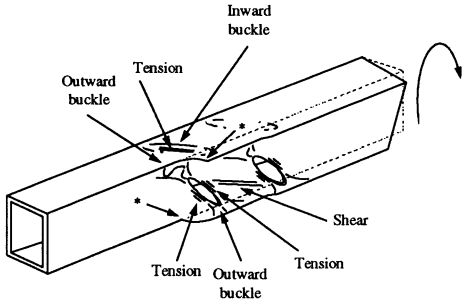

Figure 20. Failure of type IV specimens.

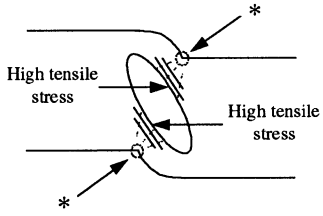

Figure 21. Regions of high tensile stress around the hole.

The tests have shown that web openings can have a profound effect on the torsional performance of the specimens. They also show failure by several different mechanisms depending on the number, diameter and position of the holes. This has clear implications for design, in particular, that for values of $D/b > 0.3$ some additional strengthening may be required around the hole.

5 ANALYTICAL MODELLING OF THE TORSION TESTS WITH FINITE ELEMENTS

Finite Element (FE) analysis provides a useful method of examining the effect of holes in tubular members. It allows combined shear, torsion and bending loads to be considered for a wide range of parameters.

The ABAQUS® FE package (version 5.5-1) has been used in the numerical studies. The models consist of 8-noded reduced integration thick shell elements (S8R). A finer mesh (See Figure 22) is required around the holes in order to correctly model stress concentrations and consequently models are quite detailed having typically 900 to 1500 elements, despite the apparent simplicity of the geometry. The magnitude of the FE problem coupled with the requirement for large displacement analysis (geometric non-linearity) means that models have needed large amounts of run time (more than 10 hours of CPU time). The use of symmetry and skew symmetry to reduce computational time had little effect, and so was not used.

The boundary conditions in the experimental study have been approximated in the FE model. Only the 240 mm long portion of the test piece which is free to twist was modelled. The restraint provided by the solid metal inserts and clamps was represented by multiple point constraints which prevent distortion of the cross section at the ends. The model was free to shorten with twist and was permitted to bend since no significant resistance to bending had been observed in the apparatus used for the experimental study.

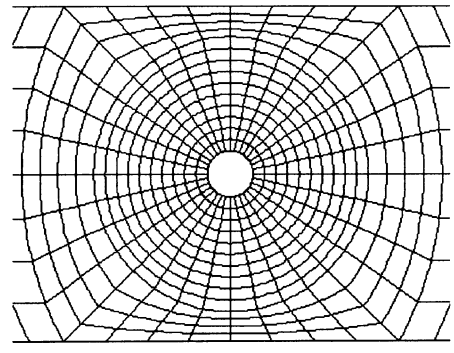

Figure 22. Mesh detail around the web opening; 5 mm hole ($D/b = 0.13$).

6 CALIBRATION OF THE FINITE ELEMENT MODEL

The FE models have been calibrated against the experimental observations by comparing torque-rotation histories (torsional stiffness and strength) and deformed shapes. In some instances, some features of the failure mechanism can be identified such as localised high tensile stress (manifesting as visible local tensile failure of the material).

The deformed shapes obtained from the numerical models match closely those observed during the experimental testing (compare Figures 23 and 19 for example). Close agreement was also obtained with respect to the torque-rotation histories (Figures 24-26). However, post yield behaviour proved problematic to model correctly, with most numerical models predicting an earlier drop is resistance than that experimentally observed.

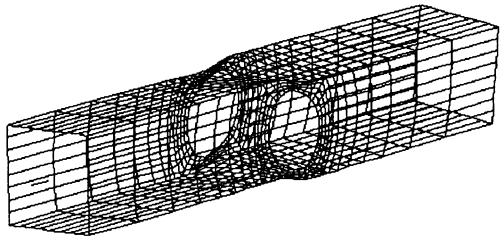

Figure 23. The distorted mesh (Type III specimen : 30 mm holes).

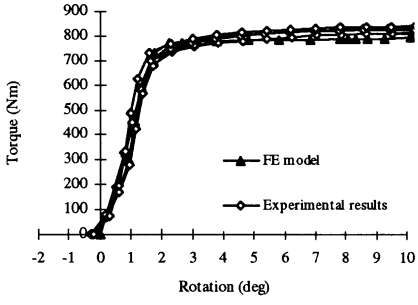

Figure 24. A comparison of experimental results and FE prediction - Type I : No holes.

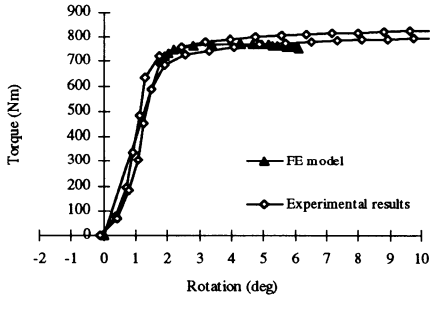

Figure 25. A comparison of experimental results and FE prediction - Type II : Two holes facing 5 mm diameter.

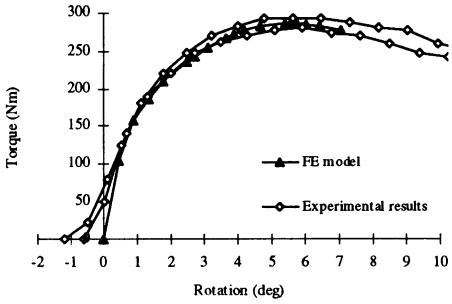

Figure 26. A comparison of experimental results and FE prediction - Type II : Two holes facing 30 mm diameter.

Once fully calibrated with the experimental data the finite element models will be used to investigate aspects of behaviour which would be impractical to study experimentally. Stress concentrations will be examined around the cut-outs. Factors such as hole shape and section size will also be considered and the scope of study will be expanded to include members of rectangular cross section.

7 CONCLUSIONS

Experimental investigation and numerical finite element modelling have shown that circular openings in the walls of square section steel tube can have a significant influence on the torsional strength and stiffness of the section.

A single sided circular opening can reduce the ultimate torsional capacity by as much as 70%. A small opening (*D/b* less than 0.1) will not reduce ultimate strength or stiffness, but will reduce the extent of plastic deformation at peak torque. A larger opening (*D/b* greater than 0.3) will reduce significantly both ultimate capacity and stiffness and will result in non-linear behaviour with asymmetry causing secondary bending effects at high twist due to differential shear in the webs.

A double sided circular opening has been shown to have a similar effect to that of a single sided opening with a slight reduction in capacity (0 to 10%). The symmetry of the condition means there are no bending effects at high twist although there is a more rapid loss of post failure stiffness.

A section with a web opening can behave in a largely non-linear manner. The presence of the hole(s) and associated stress concentrations constitute a flexible zone about which the majority of twist occurs and govern the nature of the failure mechanism.

Good agreement has been obtained between finite element models and experimental data with respect to the torque-rotation relationships and the deformed shapes at failure. Once calibrated, the numerical models will be used to investigate stress distributions and the significance tube aspect ratio and slenderness.

The loss in torsional strength of a section resulting from the provision of a cut out has important consequences in design. It is likely that small holes (*D/b* less than 0.3) may be specified without the need for additional strengthening, but larger holes will require strengthening to prevent localised high stresses.

The loss of stiffness of a cross-section with a web opening may prove to be more problematic than the loss of ultimate strength. The bulk of the deformation occurs in the region of the hole. High values of twist per unit length could cause damage to the fabric of the structure.

ACKNOWLEDGEMENT

This research is funded jointly by British Steel Tubes and Pipes plc and the University of Nottingham (UK).

REFERENCES

BS EN 10 002-1 : 1990. *Tensile testing of metallic materials, part one: Method of test at ambient temperatures,* British Standards Institution, 1990.

Frost R.W. & R.E. Leffler. 1971. Fatigue tests on beams with rectangular web holes. *Journal of the Structural Division. Proc ASCE.* 97(ST2) 509-527.

Gibson, J.E. & W.M. Jenkins. 1956. The Stress Distribution in a Simply Supported Beam with a Circular Hole. *The Structural Engineer.* 34: 443-449.

Kolosowski, J. 1964. Stresses and deflections in castellated beams. *Structural Engineer.* 42(1): 19-24.

Lawson, R.M., D.L. Mullett & J.W. Rackham. 1997. *Design of Asymmetric Slimflor beams using deep composite decking.* The Steel Construction Institute. Ref SCI-P-175.

Mullett, D.L., R.G. Ogden & J. Kerry. 1995. *Design of structural hollow sections for edge beams in Slimflor construction.* Report to British Steel (Tubes & Pipes). Steel Construction Institute. Doc RT481. Draft 01.

Mullett, D.L. 1997. *Design of RHS Slimflor edge beams.* The Steel Construction Institute. Ref SCI-P-169.

Redwood R.G. 1969. The strength of steel beams with unreinforced web holes. *Civil Engineering & Public Works Review.* 64: 559-562.

ABAQUS is a registered trademark of Hibbit, Karlsson and Sorrensen Inc.

Slimdek and Slimflor are registered trademarks of British Steel plc.



Taylor & Francis
Taylor & Francis Group
http://taylorandfrancis.com

Tubular Structures VIII, Choo & Van der Vegte (eds) © 1998 Balkema, Rotterdam, ISBN 90 5809 001 9

Tests of stiffened and unstiffened welded knee connections in cold-formed RHS

Tim Wilkinson & Gregory J. Hancock
Centre for Advanced Structural Engineering, The Department of Civil Engineering, The University of Sydney, N.S.W., Australia

ABSTRACT: This paper describes a series of tests on welded stiffened and unstiffened rigid knee connections for use in RHS portal frames. The RHS tested were cold-formed Grade C350 and Grade C450 specimens. The connection details and welding procedures are discussed. The rotation capacity of the connections for use in plastic design is examined. It was found that in tension (opening moment), there was often fracture in the heat affected zone of the RHS at low rotation values, whilst in compression (closing moment), web buckling occurred adjacent to the connection. The unstiffened connections were incapable of reaching the plastic moment. There was variability in the rotation capacity of the stiffened connections in tension, and so they were considered unsuitable for plastic hinge formation since the behaviour could not be guaranteed. For compression, only Grade C350, and not the Grade C450 joints, demonstrated rotation capacity suitable for use in plastic design.

KEYWORDS: cold-formed steel, hollow sections, welded connections, joints, plastic design, bending, rotation capacity, local buckling, fracture, heat affected zone.

1 INTRODUCTION

In plastic design, a statically indeterminate frame can carry extra load after some point has reached the plastic moment (M_p). A plastic hinge forms and can rotate further, redistributing load to other parts of the structure. Additional hinges may form as other regions in the frame become fully plastic. All hinges must be able maintain M_p for sufficiently large rotations to enable the plastic collapse mechanism to form. Plastic hinges often form at the connections of frames, since connections are sometimes points of maximum moment. However local effects can reduce the rotation capacity (R) of a connection compared to the rotation capacity of the member itself. R is defined as $\kappa/\kappa_p - 1$, where κ/κ_p is the dimensionless curvature at which the moment drops below M_p, $\kappa_p = M_p/EI$ (the plastic curvature), and EI is the elastic rigidity. Values of $R = 3$, or $R = 4$ are often considered suitable for plastic design (Wilkinson and Hancock (1997a)).

CIDECT has produced a design guide (Packer *et al* (1992)) for rectangular hollow section (RHS) connections which includes recommended details for stiffened and unstiffened welded knee connections suitable for a rigid portal frame. This advice is based on tests by Mang *et al* (1980). The CIDECT design guide gives the following recommendations:
"*... it could be expected that the rotation capacity of some unstiffened connections might be low, and in structures in which reasonable rotational capacity is required, a stiffened knee connection should be used... It is suggested to use, for unstiffened connections, only RHS members which satisfy plastic design requirements for rigid frames.*"

This paper examines a series of tests on stiffened and unstiffened welded knee connections constructed from cold-formed RHS. In particular, the ability of the connections to act as plastic hinges in a portal frame is discussed.

2 TEST SPECIMENS

Following a series of plastic bending tests on cold-formed RHS (Wilkinson and Hancock (1997a)), 150 x 50 x 4.0 RHS was chosen as an appropriate size for the joint tests. This section had exhibited rotation capacity ($R \approx 7$ for Grade C450, $R \approx 10$ for Grade C350) deemed suitable for plastic design. Two strength grades were selected, Grade C350L0 and C450L0 (nominal yield stress f_{yn} of 350 MPa and 450 MPa respectively), manufactured to Australian Standard AS 1163 (Standards Australia (1991a)). The Grade C450 specimens are called *DuraGal* sections, produced by BHP Structural and Pipeline Products using a unique cold-forming and in-line galvanising process. Figure 1 shows a typical RHS and defines the dimensions d, b, and t of the section.

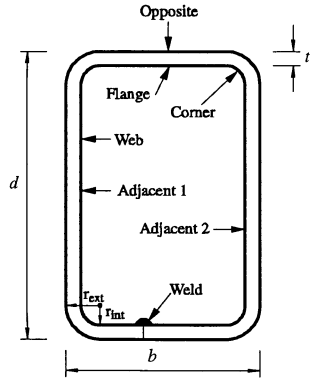

Figure 1: RHS Section

The yield stress used in calculations was obtained from coupons cut from the flat faces adjacent to the weld (Figure 1) and is included in Table 1. Full details on coupon tests and the RHS dimensions are given in Wilkinson and Hancock (1997b).

3 WELDING PROCEDURES

Welding procedures, including the joint preparation, welding consumables, workmanship and welding techniques may be prequalified by Clause 4.3 of Australian / New Zealand Standard AS/NZS 1554.1 (Standards Australia (1995)) using a welding procedure sheet. A variety of welding procedures was used. Some samples were welded by an independent fabricator (R. K. Engineering). This provided a useful benchmark as to the quality of welding that would be found in practice as performed by a typical steel fabricator. All other welding was performed in the Department of Civil Engineering, The University of Sydney. Full details on the welding procedures can be found in Wilkinson and Hancock (1997b). Extracts from welding procedures are included in Section 12 of this paper.

4 CONNECTION DETAILS

4.1 *Stiffened Welded Connection (SW)*

The SW connection detail is similar to that given in the CIDECT RHS joint design guide (Packer *et al* (1992)) as shown in Figure 2. One end of each leg of the connection was cut at an angle of 52.5° to create a total of 105° to match the obtuse angle of a typical portal frame column - rafter knee connection. A 10 mm stiffening plate was welded between the two legs. The plate protruded approximately 10 mm from each side of the RHS. Different welding procedures were used incorporating either full penetration butt or fillet welds between the stiffening plate and the RHS. The acute angle between the plate and the RHS on the inside corner of the knee (heel) was difficult to weld, particularly a butt weld. An alternative detail was then adopted ("Alternative Detail B" of Figure 2) in which the plate extended only a small amount beyond the inside corner of the knee. The alternative of using fillet welds in place of butt welds was investigated by a separate test as described later, and found not to produce a significant improvement in performance.

4.2 *Unstiffened Welded Connection (UW)*

The CIDECT design guide also includes an unstiffened mitred knee connection. The UW connection was similar to the stiffened welded joint, except that the two legs were butt welded directly together without a stiffening plate. The detail is shown in Figure 3. Since there was no backing plate against which to weld, weld blow-through was a common problem during the qualification process of the welding for the unstiffened connection.

5 TEST PROCEDURE

The aim of the connection tests was to simulate the behaviour of the knee joint in a portal frame under both opening and closing moments. Figure 4 shows the dimensions of the test specimens and a schematic diagram of the general test set up. It can be seen that unequal leg lengths have been used. The point of contraflexure (zero moment) in the rafter of a portal frame under typical loads is closer to the joint than the base of the column. Hence unequal leg lengths more accurately simulate the distribution of bending moment, axial force and shear force in the connection than an equal leg specimen. Tensile and compressive tests were performed on the sample joints, simulating gravity and wind loads on a portal frame structure (opening and closing moments respectively). Compression tests simulate the design actions on a connection under gravity or snow loads. Tension tests recreate the loads on the joint under wind uplift.

Tests were performed in a 2000 kN capacity DARTEC testing machine, using a servo-controlled hydraulic ram. A compressive or tensile load was applied through pins inserted through the webs of the RHS. The eccentricity of this load produced a bending moment at the joint. A constant crosshead speed of 0.03 mm/s was used at all times. Near the ultimate load, the test was halted for approximately 1 minute to obtain a value of the static load. A transducer measured the horizontal displacement at the joint, and the total vertical stroke of the DARTEC ram was obtained from the testing machine. Strain gauges were placed near the joint for curvature determination. Data

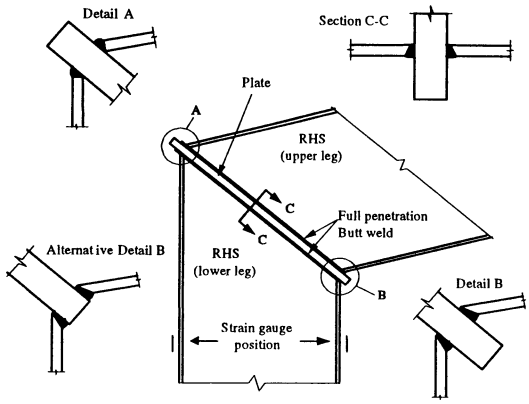

Figure 2: Stiffened welded connection (SW) (butt welded detail only)

was recorded by a SPECTRA data acquisition system.

After initial tests on 4 mm Grade C450 RHS (KJ01 (external fabricator), KJ02 (external fabricator), KJ03, KJ04), the steel was changed to 4 mm Grade C350 (KJ07, KJ08), and the thicker 5mm Grade 350 (KJ09, KJ10). Tests were also performed on fillet welded Grade C450 RHS (KJ11), and butt welded Grade C350 RHS with the alternative Detail B (KJ12). The abovementioned joints were stiffened. The unstiffened connections (KJ05, KJ06) were butt welded.

6 RESULTS

The results of the knee joint tests are summarised in Table 1. The results are separated into tension and compression tests. The maximum moment (M_{max}) reached at the knee and the maximum axial force (N_{max}) and shear force (V_{max}) induced at the connection

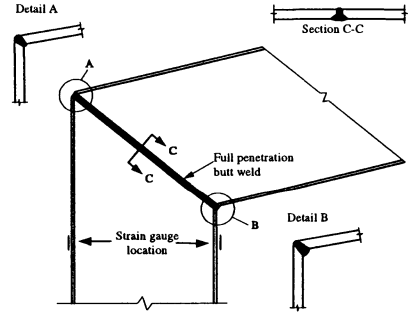

Figure 3: Unstiffened welded connection (UW)

centreline are listed. M_{max} is the second order moment and includes the effect of changing eccentricity at the joint as the connection deforms. N_{max} and V_{max} were obtained from a first order elastic analysis of the test joint and the applied load. These are compared to the plastic moment (M_p), the squash load ($A_g f_y$) and the shear yield load ($V_p = 2dtf_y/\sqrt{3}$). The maximum loads are *static* loads, which represent the recorded load after the testing machine has been halted for approximately one minute. The web slenderness (λ_w) and flange slenderness (λ_f) determined to Eurocode 3 (European Committee for Standardisation (1992)) are tabulated, and the mode of failure is described. The proportion of the web in compression (α), assuming full plasticity is given for compression tests only. The value of α is important, since the Class 1 web slenderness limit in Eurocode 3 is reduced from 72 when webs are under bending and compression (Table 5.3.1 of Eurocode 3). The reduced Class 1 limit, and the rotation capacity based on the curvature at the strain gauges (R_g) and the connection angle change (R_α) are also given.

6.1 *Failure Modes*

Figure 5 gives diagrammatic representations of the failure modes. Under *compression* loads web local buckling was the failure mode in all cases. As expected, local buckling occurred on the inside of the knee (the compression side due to the applied moment)

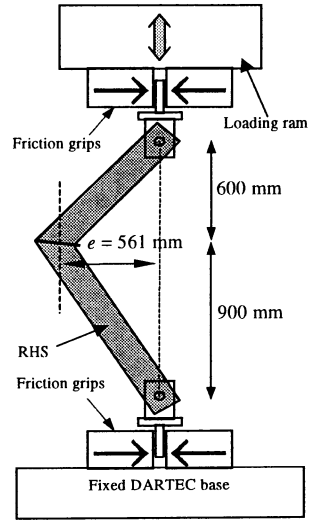

Figure 4: Test rig for knee joint tests

Table 1: Summary of Results for Knee Joint Tests

Speci-men	Section	Type	f_y (MPa)	λ_w	λ_f	α	λ	P_{max} (kN)	M_{max} (kNm)	$\frac{M_{max}}{M_p}$	N_{max} (kN)	$\frac{N_{max}}{A_g f_y}$	V_{max} (kN)	$\frac{V_{max}}{V_p}$	R_g	R_α	Failure Mode
							COMPRESSION										
KJ01	150x50x4.0 C450	SW	436	49.7	13.9	0.55	64.9	56.4	32.6	1.08	47.8	0.071	52.5	0.17	0.8	2.1	Local buckle inside of knee
KJ03	150x50x4.0 C450	SW	436	49.7	13.8	0.55	64.6	59.2	34.1	1.14	50.2	0.074	55.1	0.18	0.8	2.7	Local buckle inside of knee
KJ05	150x50x4.0 C450	UW	436	49.4	13.7	0.53	67.3	36.1	20.6	0.68	30.6	0.045	33.6	0.11	-	-	Local buckle across joint
KJ07	150x50x4.0 C350	SW	349	43.2	12.0	0.56	62.7	57.9	33.8	1.48	49.1	0.096	53.9	0.23	2.8	6.0	Local buckle inside of knee
KJ09	150x50x5.0 C350	SW	348	33.7	8.8	0.56	63.0	68.2	39.8	1.44	57.8	0.092	63.4	0.21	5.2	8.5	Local buckle inside of knee
							TENSION										
KJ02	150x50x4.0 C450	SW	436	49.8	13.8			69.6	38.9	1.30	59.0	0.088	64.7	0.21	0.9	2.0	Tube fracture in HAZ
KJ04	150x50x4.0 C450	SW	436	50.5	14.1			72.2	40.2	1.36	61.2	0.092	67.2	0.22	1.7	2.5	Tube fracture in HAZ
KJ06	150x50x4.0 C450	UW	436	49.5	13.7			42.1	23.2	0.77	35.7	0.052	39.2	0.12	-	-	Tube fracture in HAZ Tearing of butt weld
KJ08	150x50x4.0 C350	SW	349	43.4	12.0			67.1	35.3	1.56	56.9	0.11	62.4	0.26	10	5.0	Weld tearout from plate Local buckle outside of knee
KJ10	150x50x5.0 C350	SW	348	33.7	8.8			63.3	34.8	1.26	53.7	0.086	58.9	0.20	0.9	1.0	Weld tearout from plate
KJ11	150x50x4.0 C450	SW	436	50.2	14.0			67.9	36.0	1.21	57.6	0.086	63.2	0.20	2.5	2.6	Tube fracture in HAZ
KJ12	150x50x4.0 C350	SW	349	43.7	12.6			61.6	33.3	1.47	52.2	0.10	57.3	0.24	2.5	3.1	Tube fracture in HAZ

Note: Web slenderness = $\lambda_w = \frac{d-3t}{t}\sqrt{\frac{f_y}{235}}$, Flange slenderness = $\lambda_f = \frac{b-3t}{t}\sqrt{\frac{f_y}{235}}$, calculate to Eurocode 3

for type SW connections. The local buckle formed in the lower (longer) leg adjacent the stiffening plate for all stiffened welded joints as shown in Figure 5(a). For the unstiffened connection the buckle formed across the butt weld as shown in Figure 5(b). After local buckling, the applied load dropped slowly with increased deflection. There was no evidence of lateral buckling or out-of-plane deflections in any test.

Most joints loaded in *tension* failed at or near the weld. Failure always occurred on the inside of the knee as this side had the higher tension due to the axial force and bending moment. There was a sudden drop in load whenever there was a weld failure due to the reduction in cross-sectional area resisting the load. For some of the SW type connections, tube fracture occurred in the heat affected zone (HAZ) next to the weld. The HAZ fracture always initiated in the corner of the RHS. Another mode of failure observed was tearout of the weld from the stiffening plate. For the unstiffened welded connection, the weld fractured, but this may have been caused by poor welding, as this weld was difficult to manufacture. The failure modes are illustrated in Figure 5. No lateral buckling or out-of-plane deflections was observed.

6.2 *Load-stroke curves*

The load and stroke (vertical displacement) were recorded at regular intervals during each test. The load stroke curves are given in Figure 6 (Compression) and Figure 7 (Tension). The load has been non-dimensionalised with respect to the plastic load P_p where $P_p = M_p/e$ and e = 561 mm, the initial eccentricity of the joint. The stroke has been non-dimensionalised with respect to δ_p, so that a load of P_p corresponds to a non-dimensional stroke of unity, based on a first order linear elastic analysis of the specimen. Values of P_p and δ_p are given next to the relevant graph.

6.3 *Moment - curvature graphs*

The moment curvature relationships are required to determine the rotation capacity (R) of the connections. Figure 8 (Compression) and Figure 9 (Tension) show the moment curvature graphs for the tests. The graphs depict the second order moment and curvature *at the strain gauge location on the lower leg*. The curvature (κ) was calculated from the strains (obtained from the strain gauges) on opposite flanges of the RHS. The curvature was non-dimensionalised with respect to the plastic curvature (κ_p), where $\kappa_p = M_p/EI$.

Since the strain gauges were placed a finite distance from the connection centreline (150 mm for type SW and 100 mm for type UW) and not at the position of maximum curvature (or the buckle), the graphs do not represent the curvature and moment at the point of failure. Due to the extra eccentricity, the moment would be approximately 10 - 20 % higher at the failure location (compared to the gauge location). Additionally, more plasticity occurs closer to the joint and hence curvatures were higher closer to the connection centreline compared to the gauge location.

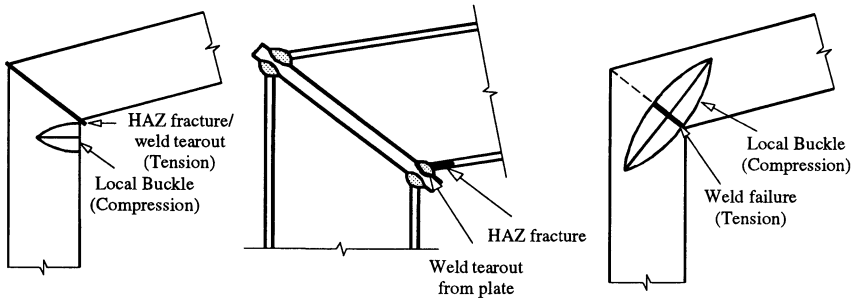

(a) Stiffened (SW) (b) Unstiffened (UW)

Figure 5: Failure modes for knee joints

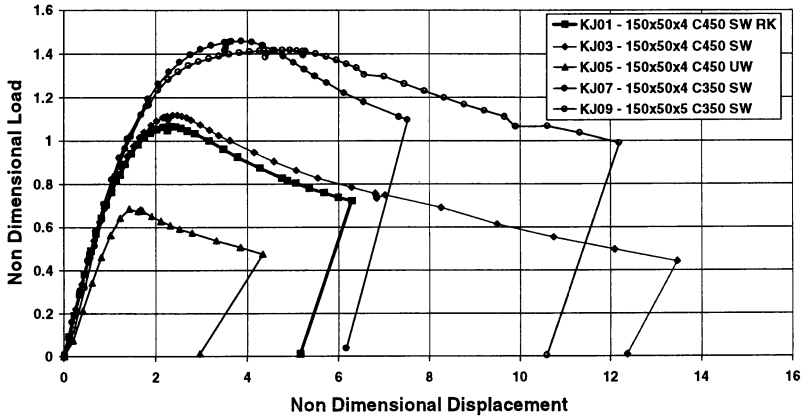

Specimen	P_p (kN)	δ_p (mm)
KJ01	53.73	12.97
KJ03	53.55	12.99
KJ05	53.68	13.00
KJ07	40.73	10.44
KJ09	49.22	10.80

Non-dimensional constants

Figure 6: Load Displacement Curves (Compression)

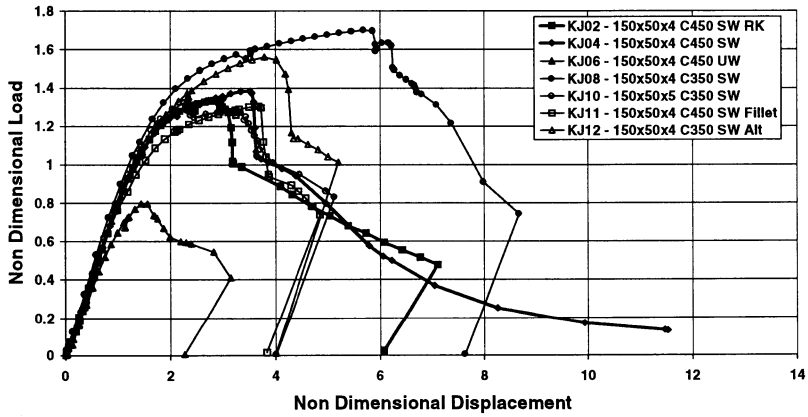

Specimen	P_p (kN)	δ_p (mm)
KJ02	53.30	13.00
KJ04	52.86	12.98
KJ06	53.94	12.98
KJ08	40.36	10.46
KJ10	49.13	10.81
KJ11	53.19	12.97
KJ12	40.47	10.43

Non-dimensional constants

Figure 7: Load Displacement Curves (Tension)

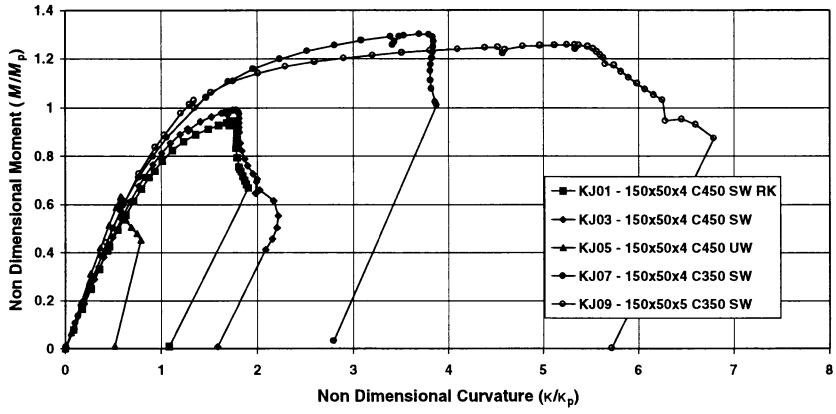

Figure 8: Moment curvature curves (Compression)

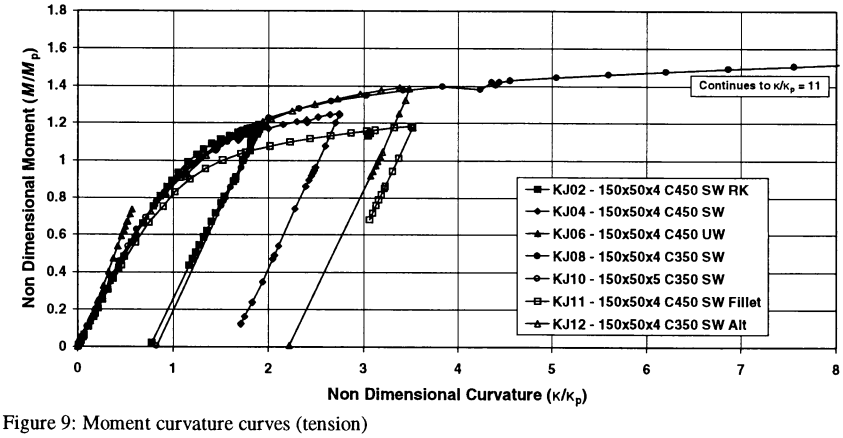

Figure 9: Moment curvature curves (tension)

Preliminary analysis using the advanced analysis program NIFA (Clarke and Hancock (1991)) indicates that at the ultimate load, the curvature at the joint is much higher than at the strain gauge position. However, NIFA is a frame analysis program and uses line elements for members. NIFA cannot model the complex local effects that occur close to connections.

The values of rotation capacity in Table 1 are based on the curvature at the strain gauge (R_g) and hence the "true" value at the joint (R) is higher.

6.4 *Moment - angle curves*

It is possible to plot the angle of the deformed member against the moment. In Figure 10(a), the undisplaced angle ($\alpha_0 = 105°$) is shown. Using a first order elastic analysis, the angle at which the plastic moment is reached (α_p) is given in Figure 10(b). Figure 10(c) shows the angle at any load (α_d). Each angle is calculated assuming that all rotation occurs at a single point at the joint centreline. The non-dimensional angle change ($\bar{\alpha}$) is given by:

$$\bar{\alpha} = \frac{\alpha_d - \alpha_0}{\alpha_p - \alpha_0} \qquad (1)$$

Figures 11 and 12 show the angle change versus moment graphs for compression and tension respectively. From these curves, the rotation capacity based on the angle change (R_α) was calculated. Values of R_α are given in Table 1. R_α is based on the behaviour of the whole joint and is not a "localised" value like R_g. For tension tests, R_α is defined as $R_\alpha = \bar{\alpha}_f - 1$, where fracture occurred at $\bar{\alpha}_f$, while in compression $R_\alpha = \bar{\alpha}_1 - 1$, where the moment drops below M_p at $\bar{\alpha}_1$.

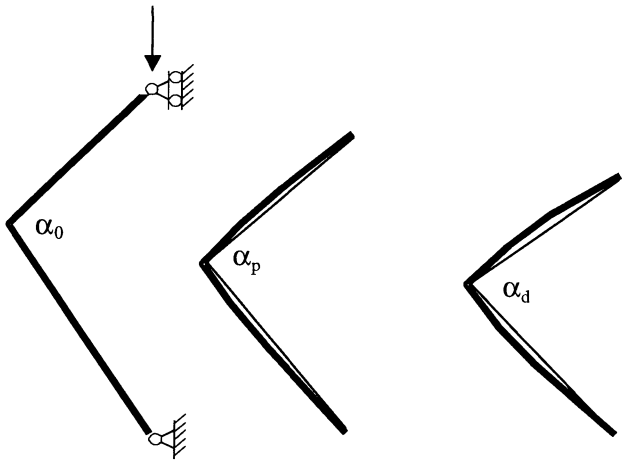

(a) Undisplaced (b) Displaced at plastic moment (c) Displaced at any load

Figure 10: Angle of connection at various load levels

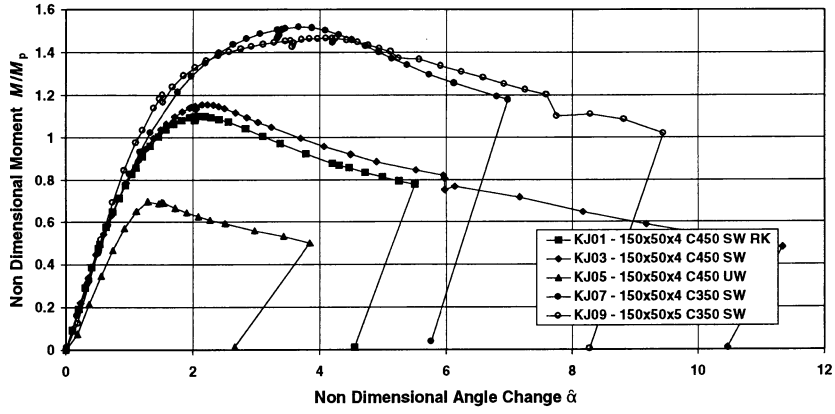

Figure 11: Moment versus angle change: compression

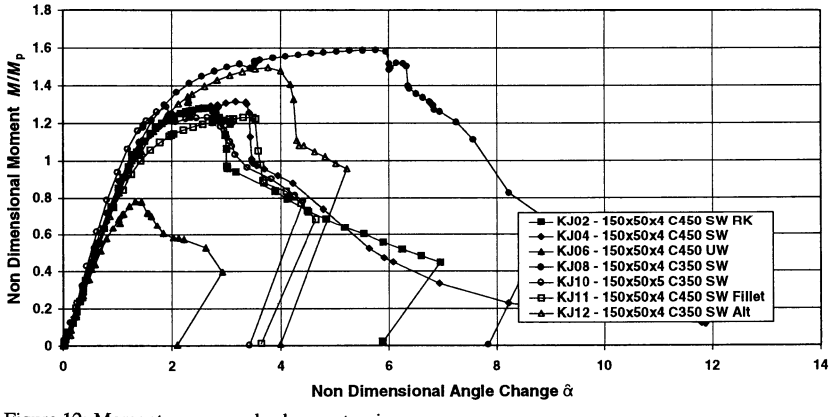

Figure 12: Moment versus angle change: tension

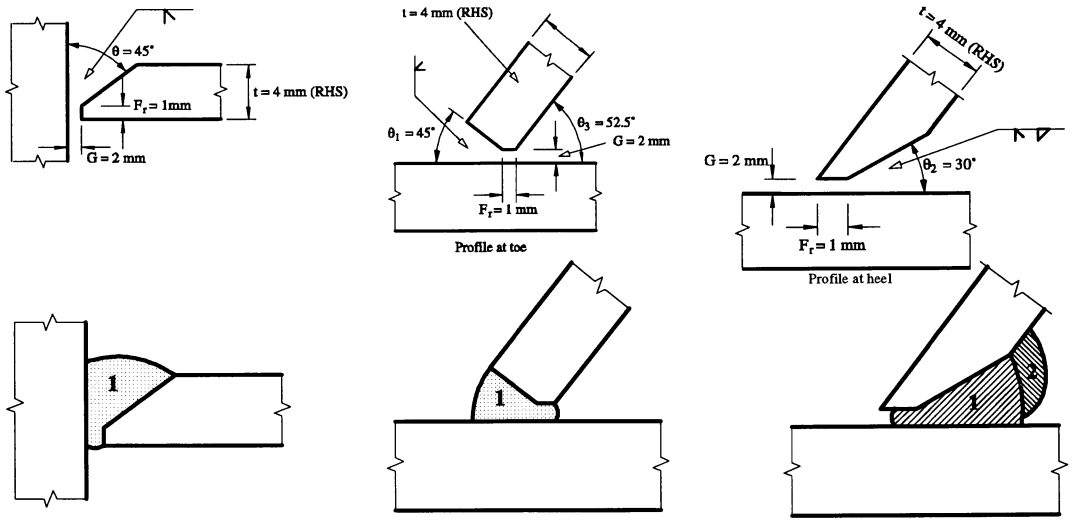

Figure 13: Typical weld preparation and weld run location and sequence for stiffened welded joint (butt welded)

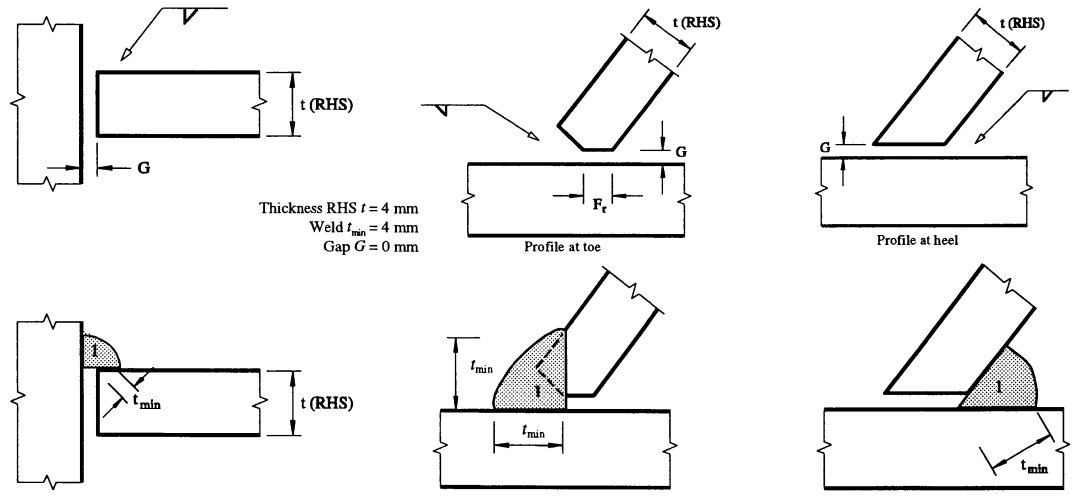

Figure 14: Typical weld preparation and weld run location and sequence for stiffened welded joint (fillet welded)

7 DISCUSSION

It can be seen from Table 1 that the axial force in the RHS is low (approximately 5 - 10 % of the squash load). In most current steel design specifications the reduction of plastic moment capacity due to this low axial force would be zero or small. All stiffened connections reached a moment greater than M_p. Combined compression and bending reduces the Class 1 limit in Eurocode 3 from the value of 72 for bending alone. All sections can still be classified as Class 1 and are deemed suitable for plastic design. The ratios of the shear force to the shear load capacity in the stiffened connections are less than the 0.5 limit given in the CIDECT design guide.

The unstiffened connections (KJ05 and KJ06) are most unsuitable for plastic hinge formation. Both failed at approximately 70-80 % of the plastic moment and hence cannot be used at a plastic hinge location.

There was considerable variation in the behaviour of the stiffened welded connections in both tension and compression.

Table 2: Heat Input

Specimen	Section	Type	Welding Procedure	Heat Input (kJ/mm)	R_g	R_α	Failure Mode
KJ02	150x50x4.0 C450	SW	RKE - 138	1.00/1.00	0.9	2.0	HAZ fracture
KJ04	150x50x4.0 C450	SW	TJW01	1.49/1.22	1.7	2.5	HAZ fracture
KJ06	150x50x4.0 C450	UW	TJW02	0.53	-	-	HAZ fracture Tearing of butt weld
KJ08	150x50x4.0 C350	SW	TJW04	1.33/1.26	10	5.0	Weld tearout from plate Local buckle outside of knee
KJ10	150x50x5.0 C350	SW	TJW03	1.37/1.20	0.9	1.0	Weld tearout from plate
KJ11	150x50x4.0 C450	SW (fillet)	TJW05	0.93	2.5	2.6	HAZ fracture
KJ12	150x50x4.0 C350	SW (alternate)	TJW04	1.33/1.26	2.5	3.1	HAZ fracture

Notes: Refer to Wilkinson and Hancock (1997b) for welding procedures.
For welding procedures involving two welding runs, two values of heat input are given.

7.1 *Compression*

Under compression, the Grade C450 specimens (KJ01 and KJ03) exhibited notably less rotation than the corresponding Grade C350 specimen (KJ07). It has been identified (Wilkinson and Hancock (1998)) that the rotation capacity of beams is affected by steel grade for very stocky sections. The thicker 5mm specimen in Grade C350 (KJ09) displayed more rotation capacity than the 4 mm thick specimen (KJ07), as would be expected from a stockier section. Only the stiffened welded connections in Grade C350 for both thicknesses (KJ07 and KJ09) were suitable for maintaining a plastic hinge for a sufficiently large rotation ($R_\alpha > 4$) suitable for plastic design.

The stiffened welded connections exhibit less rotation capacity than simple beams constructed from the same sections. The values for beams given in Wilkinson and Hancock (1998) illustrate this: (150x50x4.0 C450 $R \approx 7$; 150x50x4.0 C350 $R \approx 11$ as beams only, compared to 150x50x4.0 C450 $R_g = 0.8$, $R_\alpha = 2.1$ and 2.7; 150x50x4.0 C350 $R_g = 2.8$, $R_\alpha = 6.0$ for the connections). Possible reasons for this include:

(i) It has been documented that the rotation capacity under uniform moment (as for the beams) is greater than the rotation capacity under a moment gradient (as for the connections) (Lay and Galambos (1965, 1967))
(ii) There is net axial compression in the section which will initiate local buckling earlier.
(iii) Imperfections induced into the section by the welding process can affect the local buckling behaviour of the RHS.
(iv) The values of R_g are lower than the true values of rotation capacity.

7.2 *Tension*

Under tension the failure was always associated with the weld. It is difficult to establish the effect the different welding procedures had on the rotation capacity of the connections. There can be small differences between each welding run, even using the same procedure, that can affect the performance of the connection. Imperfections in the weld, or small regions in which extra heat was input, can affect the ductility of the connection markedly.

It has been shown that welded connections in C450 *DuraGal* have less ductility than Grade C350 (Zhao and Hancock (1995a,b). The results are generally in agreement with this. The Grade C350 specimen KJ10 had a low rotation capacity, but the failure was weld tearout from the plate, indicating poor welding was the probable cause. Table 2 summarises the heat input of the various welding procedures used in the manufacture of the different connections (Wilkinson and Hancock (1997b)).

HAZ fracture was the main cause of failure in the tension tests. The heat input during welding is an important parameter in assessing the likelihood of HAZ failure. Specimen KJ01, which was welded by an independent fabricator, had the lowest heat input for the butt welded specimens, yet had a low rotation capacity. Specimen KJ08 had a very large rotation capacity, and did not experience HAZ fracture, but failed by weld tearout. The detail of the connection was slightly modified (Figure 2) and the new connection (KJ12) experienced a much lower rotation capacity. The fillet welded C450 connection (KJ11) had less heat input than the other Grade C450 specimens and exhibited slightly higher rotation capacity, but still failed by HAZ fracture.

Although some specimens did show sufficient rotation capacity to be suitable for plastic hinge formation, the variability in behaviour meant that it was not possible to guarantee that the rotation capacity could be repeated.

Samples KJ01 and KJ02 were examined by BHP Structural and Pipeline Products after testing and

the welds were closely examined. Vickers Hardness tests showed that on average the hardness of the parent metal was 177 HV 5, while in the heat affected zone (HAZ) the average hardness was 150 HV 5. The drop in hardness indicates that the HAZ experienced softening, corresponding to a reduction in the ultimate stress (f_u) of approximately 80 MPa, and a reduction of at least 80 MPa in the yield stress (f_y).

8 CONCLUSION

The rotation capacity of stiffened and unstiffened welded knee joints for portal frames were examined. It was found that in tension (opening moment: simulated wind uplift loading), there was often fracture in the heat affected zone of the cold-formed RHS at low rotation values. In compression (closing moment: simulated gravity loading), web buckling occurred at the connection. There was variability in the behaviour of the stiffened welded connection in tension, while in compression only the Grade C350 connections could be considered suitable for plastic hinge formation. This contradicts the CIDECT design guide, which suggests that stiffened welded connections from Class 1 sections are suitable for plastic hinge formation. The unstiffened welded joints could not achieve the plastic moment, and are not suitable for plastic hinge formation.

ACKNOWLEDGEMENTS

This research project is funded by CIDECT (Comité International pour le Developpement et l'Étude de la Construction Tubulaire). Tube specimens were provided by BHP Structural and Pipeline Products. The experiments were carried out in the J. W. Roderick Laboratory for Materials and Structures, Department of Civil Engineering, The University of Sydney.

NOTATION

A_g	Gross cross section area
b	Width of RHS
d	Depth of RHS
E	Young's modulus of elasticity
e	Eccentricity
f_u	Ultimate tensile strength
f_y	Yield stress
f_{yn}	Nominal yield stress
I	Second moment of area
M_{max}	Maximum bending moment
M_p	Plastic bending moment
N_{max}	Maximum axial force
N_y	Yield load ($=A_g f_y$)
P_p	Plastic load
R	Rotation capacity
R_g	Rotation capacity at strain gauge location
R_g	Rotation capacity based on angle change
r_e	External corner radius of RHS
t	Thickness of RHS
V_{max}	Maximum shear force
V_p	Plastic shear capacity
α	Proportion of web in compression
α_0	Undisplaced connection angle
α_d	Connection angle at plastic load P_p
α_p	Connection angle at any load
$\bar{\alpha}$	Non-dimensional angle change
$\bar{\alpha}_f$	Non-dimensional angle change when moment drops below M_p (compression)
$\bar{\alpha}_f$	Non-dimensional angle change at fracture (tension)
κ	Curvature
κ_p	Plastic curvature ($= M_p/EI$)
λ_f	Flange slenderness
λ_w	Web slenderness

REFERENCES

European Committee for Standardisation, (1992), *Design of Steel Structures: Part 1.1 - General Rules and Rules for Buildings*, DD ENV. 1993-1-1, Eurocode 3 Editorial Group.

Lay M. G. and Galambos T. V. (1965), "Inelastic Steel Beams under Uniform Moment", *Journal of the Structural Division*, ASCE, Vol. 91, No. ST6, pp 67 - 93, December 1965.

Lay M. G. and Galambos T. V. (1967), "Inelastic Steel Beams under Moment Gradient", *Journal of the Structural Division*, ASCE, Vol. 93, No. ST1, pp 381 - 399, February 1967.

Mang F., Steidl G., and Bucak, O., (1980), "Design of Welded Lattice Joints and Moment Resisting Knee Joints Made of Hollow Sections", International Institute of Welding, *Document XV-463-80*, University of Karlsruhe, Germany.

Packer J. A., Wardenier J., Kurobane Y., Dutta D, and Yeomans N., (1992), *Design Guide for Rectangular Hollow Section (RHS) Joints under Predominantly Static Loading*, CIDECT Design Guide No. 3, Verlag TÜV Rheinland GmbH, Köln, Germany.

Standards Australia, (1990), Australian Standard *AS 4100 Steel Structures*, Standards Australia, Sydney.

Standards Australia, (1991), Australian Standard *AS 1163 Structural Steel Hollow Sections*, Standards Australia, Sydney.

Standards Australia / Standards New Zealand (1995), Australian / New Zealand Standard *AS 1554.1 Structural Steel Welding, Part 1: Welding of Steel Structures*, Standards Australia, Sydney.

Wilkinson T. and Hancock G. J., (1997a), "Tests for the Compact Web Slenderness of Cold-Formed Rectangular Hollow Sections", *Research Report*, No. R744, Department of Civil Engineering, University of Sydney, Sydney, Australia.

Wilkinson T. and Hancock G. J., (1997b), "Plastic Design of Cold-Formed RHS", CIDECT Project 2S, *Interim Report No. 3*, Centre for Advanced Structural Engineering, Department of Civil Engineering, University of Sydney, Sydney, Australia.

Wilkinson T. and Hancock G. J., (1998), "Compact or Class 1 Limits for Rectangular Hollow Sections in Bending", *Proceedings*, 8th International Symposium on Tubular Structures, Singapore, (Balkema, publ.).

Zhao X. L. and Hancock G. J., (1995a) "Butt Welds and Transverse Fillet Welds in Thin Cold-Formed RHS Members", *Journal of Structural Engineering*, ASCE, Vol. 121, No. 11, November 1995, pp. 1674-168

Zhao X. L. and Hancock G. J., (1995b) "Longitudinal Fillet Welds in Thin Cold-Formed RHS", *Journal of Structural Engineering*, ASCE, Vol. 121, No. 11, November 1995, pp. 1683-1690.

APPENDIX: WELDING PROCEDURES

Figures 13 and 14 show *extracts* from welding procedures for a butt welded and fillet welded stiffened joint, to show the typical joint preparation and weld run location at the heel and toe of the connection. Full details on the welding procedures can be found in Wilkinson and Hancock (1997b).

Tubular Structures VIII, Choo & Van der Vegte (eds) © 1998 Balkema, Rotterdam, ISBN 90 5809 001 9

Tests of bolted and internal sleeve knee connections in cold-formed RHS

Tim Wilkinson & Gregory J. Hancock
Centre for Advanced Structural Engineering, The Department of Civil Engineering, The University of Sydney, N.S.W., Australia

ABSTRACT: This paper examines different knee connections for portal frames constructed from cold-formed rectangular hollow sections: bolted plate connections, and welded and bolted internal sleeve connections. The specimen joints were tested in both tension and compression (opening and closing moments) to simulate wind uplift or gravity loading. It was found that the sleeve connections were capable of sustaining the plastic moment for large rotations considered suitable for plastic design. The use of an internal sleeve moved the plastic hinge in the connection away from the connection centreline and reduced the stress on the weld between the RHS. However, at present, the sleeve connection may not be a commercially viable possibility. The bolted plate connection achieved plastic rotations but failed in the heat affected zone in tension.

KEYWORDS: cold-formed steel, hollow sections, welded connections, bolted connections, joints, plastic design, bending, rotation capacity, local buckling, heat affected zone, fracture, internal sleeve.

1 INTRODUCTION

A statically indeterminate frame can carry extra load after a point has reached the plastic moment (M_p), by the creation of plastic hinges in the structure. All hinges, which often form at the connections in a structure, must be able maintain M_p for sufficiently large rotations to enable the plastic collapse mechanism to form. This is known as rotation capacity (R). R is defined as κ/κ_p - 1, where κ/κ_p is the dimensionless curvature at which the moment drops below M_p, $\kappa_p = M_p/EI$ (the plastic curvature), and EI is the elastic rigidity. The companion paper (Wilkinson and Hancock (1998a)) to this paper examines stiffened and unstiffened welded knee connections. It was found that most of the welded connections did not exhibit sufficient rotation capacity suitable for plastic hinge formation. Consequently different types of connections had to be considered.

This paper examines different knee joints for portal frames: bolted plate connections in which plates are welded flush against one RHS, and along the flange of the other RHS, then bolted together: and welded and bolted internal sleeve connections, in which a "V" shaped box section is fabricated to fit inside each leg of the connection, hammered into place, and welded or bolted. The specimen joints were tested in both tension and compression, inducing opening and closing moments respectively.

The main aim of the test series is to establish a suitable connection for an RHS portal frame test series (Wilkinson and Hancock (1998b)). The connection would need to be suitable for plastic hinge formation.

2 TEST SPECIMENS

The same size RHS as was used in the welded connection tests (Wilkinson and Hancock (1998a)), 150 x 50 x 4.0 RHS was chosen for the test series. In the beam tests (Wilkinson and Hancock (1997a)), this section had exhibited rotation capacity ($R \approx 7$ for Grade C450, $R \approx 10$ for Grade C350) suitable for plastic design (values of $R = 3$, or $R = 4$ are often considered suitable for plastic design).

The RHS were manufactured by BHP Structural and Pipeline Products. Two strength grades were selected, Grade C350L0 and C450L0 (nominal yield stress f_{yn} of 350 MPa and 450 MPa, and nominal ultimate stress f_{un} of 430 MPa and 500 MPa respectively), manufactured to Australian Standard AS 1163 (Standards Australia (1991a)). The Grade C450 specimens are called *DuraGal* sections, produced using a unique cold-forming and in-line galvanising process. The measured yield stress is used in all calculations, obtained from coupons cut from the flat faces adjacent to the longitudinal weld of the RHS, and is included in Table 1. Full details on tensile coupon tests and the RHS dimensions are available in Wilkinson and Hancock (1997b).

3 WELDING PROCEDURES

Welding procedures may be prequalified by Clause 4.3 of Australian / New Zealand Standard AS/NZS 1554.1 (Standards Australia (1995)). Welding was performed in the Department of Civil Engineering, The University of Sydney. Welding procedures can be found in Wilkinson and Hancock (1997b).

4 CONNECTION DETAILS

4.1 *Bolted end plate (BP)*

The bolted end plate connection shown in Figure 1 is denoted type BP. One RHS leg of the connection was mitre cut at 15° and a 10 mm steel plate was butt welded onto the mitred end. Another 10 mm plate was welded to the flange of the other RHS leg. The plate thickness of 10 mm was chosen to reduce excess plate deformation, but thin enough to avoid welding the 4 mm RHS to a much thicker plate. The second RHS leg was not mitred. The two sections were bolted together with eight fully tensioned high strength bolts. Coronet® load indicating washers ensured correct tensioning of the bolts. Stiffeners under the flange plate were employed against local bearing failure of the RHS web.

4.2 *Welded internal sleeve (WS)*

The welded internal sleeve connection is denoted type WS and is shown diagrammatically in Figure 2. An internal hollow steel sleeve was fabricated to fit inside the mitred knee connection. Two open "V" shaped pieces of 10 mm steel were profile cut at the same angle (105°) as the whole joint. Flange plates were fillet welded to "V" pieces to create a box section. After fabrication, the edges of the sleeve were ground to ensure that the sleeve would fit into the RHS legs. A groove was cut into the sleeve to allow for the internal seam weld of the RHS. The sleeve was fitted snugly inside each RHS leg of the joint. The sleeve was slightly oversized so that substantial sledgehammer blows were required to insert the sleeve into the RHS. The tight fit ensured that load could be transferred between the RHS and the sleeve mainly by friction. The sleeve thickness was chosen so that the plastic moment of the RHS was slightly smaller than the plastic moment of the sleeve itself. Finally, the two legs were butt welded together with the sleeve acting as a backing plate for the weld.

Since the junction of the two legs was strengthened by the sleeve, the plastic moment at the junction was approximately twice the value of M_p of the RHS alone. Hence, the plastic zone would be forced to form in the RHS outside the region of the sleeve and away from the weld. The tests on stiffened

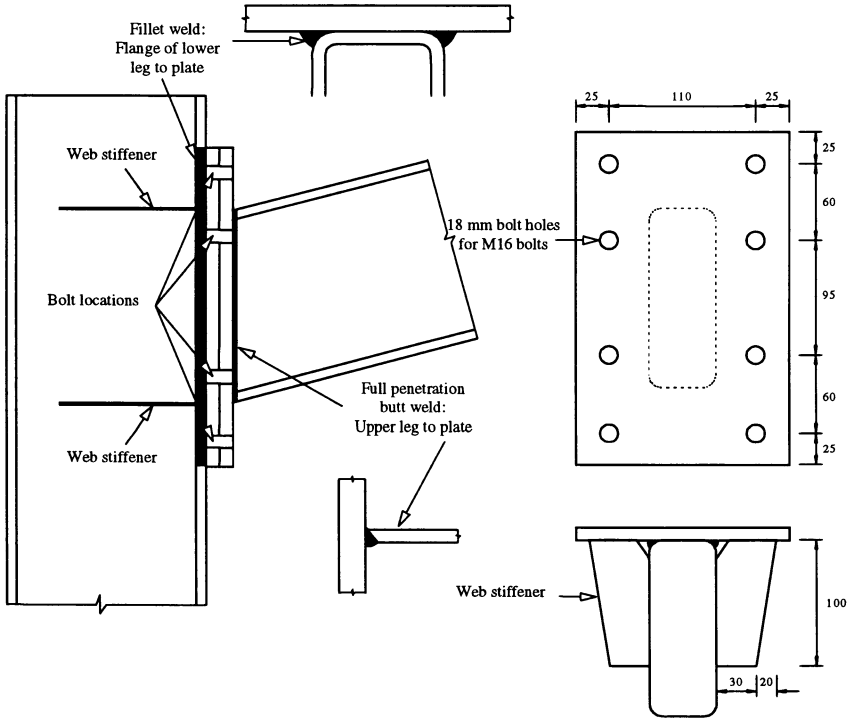

Figure 1: Connection details for bolted plate (BP) connection

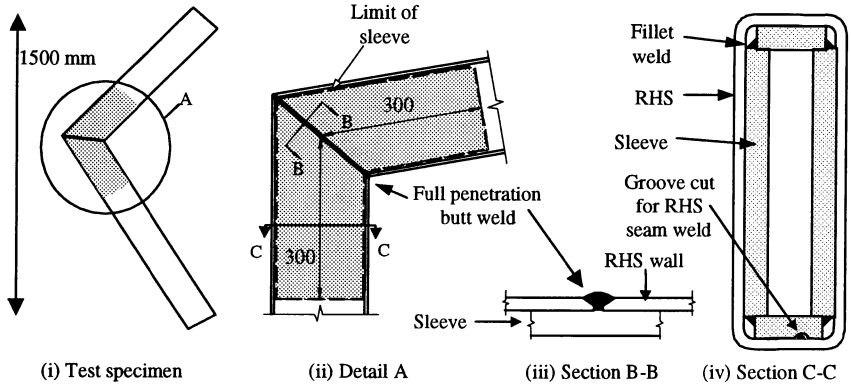

Figure 2: Details for welded sleeve (WS) connection

welded connections (Wilkinson and Hancock (1998a)) suggested that there was insufficient ductility at or near the weld to maintain a plastic hinge. Since the region near the weld was much stiffer, and the plastic zone was forced to move away from the weld, it was anticipated that the strain on the weld would be significantly reduced, and probably elastic.

4.3 *Bolted internal sleeve (BS)*

For a larger frame structure, the span of each roof rafter could be approximately 6 m, and the height of the column approximately 3 m. It would be difficult to manoeuvre such large elements in order to weld them together after inserting a sleeve. Hence a bolted alternative, as shown in Figure 3, was trialed.

The internal sleeve in this connection (denoted type BS) is identical to the sleeve described in Section 4.2. The two RHS legs were not welded together at the mitre line as for the WS connection. Four 4.6 Grade M16 bolts passed through each leg and the internal sleeve.

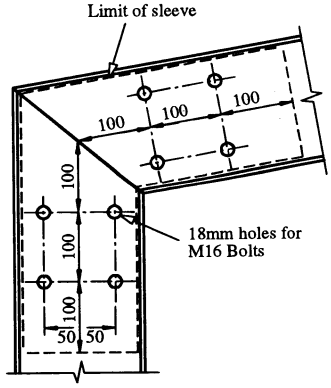

Figure 3: Bolt locations for BS connection

5 TEST PROCEDURE

The aim of the connection tests was to simulate the behaviour of the knee joint in a portal frame under both uplift and gravity load. Figure 4 shows the total dimensions of the test specimens and a schematic diagram of the general test set up. The test specimens were tested in both tension and compression (opening and closing moments) to simulate uplift and gravity loading respectively. Full details on the test procedure can be found in the companion paper (Wilkinson and Hancock (1998a)). Strain gauges were placed on the specimens as shown in Figure 5. It can be seen that for the WS connections, the gauges were within the region including the sleeve, while for the BS connection the gauges were positioned outside the sleeve region.

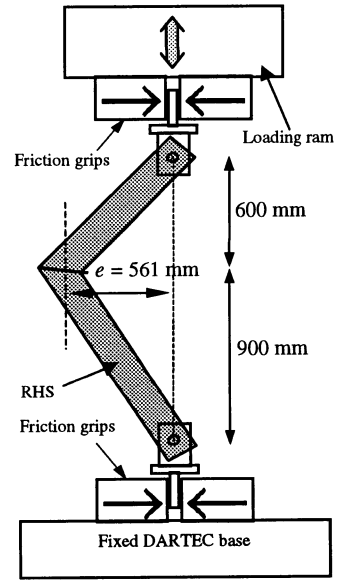

Figure 4: Test rig for knee joint tests

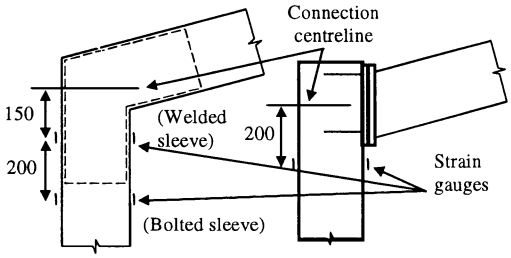

Figure 5: Strain gauge locations

6 RESULTS

The results of the knee joint tests are summarised in Table 1. The maximum moment (M_{max}) at the knee, and the maximum axial force (N_{max}) and shear force (V_{max}) induced at the connection centreline are listed and are compared to the plastic moment (M_p), the squash load ($A_g f_y$) and the shear yield load ($V_p = 2dtf_y/\sqrt{3}$). M_{max} is the second-order moment caused by the eccentricity of the applied axial load and therefore includes the effect of changing eccentricity at the joint as the connection deforms. N_{max} and V_{max} were obtained from a first order elastic analysis of the test joint and the applied load. The web slenderness (λ_w) and flange slenderness (λ_f) determined to Eurocode 3 (European Committee for Standardisation (1992)) are tabulated (refer to Table 1 for the definition of λ_w and λ_f), and the mode of failure is described. The proportion of the web in compression (α), assuming full plasticity, and the reduced Class 1 web limit is given for the compression tests only. The value of α is important, since the Class 1 web slenderness limit in Eurocode 3 is reduced from 72 when webs are under bending and compression (Table 5.3.1 of Eurocode 3). The reduced Class 1 limit (λ), and the rotation capacity based on the curvature at the strain gauges (R_g) and the connection angle change (R_α) are also given.

6.1 *Failure modes*

Figure 6 gives diagrammatic representations of the failure modes. For all *compression* tests, web local buckling on the inside of the knee was the failure mode. For the bolted plate connection, the buckle formed at the end of plate welded to the flange of the lower leg. For both the welded and bolted sleeve joints, the buckle formed just outside the limit of the sleeve. On the opposite tension face, the sleeve had pushed against the inside face of the flange of the RHS and caused a small outwards bulge in that face. As the load increased on the bolted sleeve connection, the two legs of the connection separated at the sleeve as shown in Figure 7. There was no evidence of lateral buckling or out-of-plane deflections in any test.

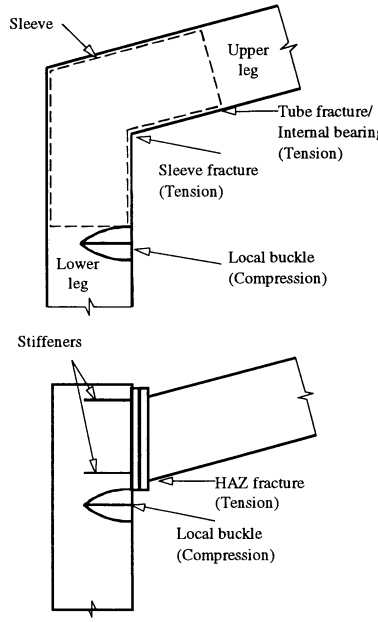

Figure 6: Failure modes

Table 1: Summary of results for knee joint tests

Specimen	Section	Type	f_y (MPa)	λ_w	λ_f	α	λ	P_{max} (kN)	M_{max} (kNm)	$\frac{M_{max}}{M_p}$	N_{max} (kN)	$\frac{N_{max}}{A_g f_y}$	V_{max} (kN)	$\frac{V_{max}}{V_p}$	R_g	R_α	Failure Mode
COMPRESSION																	
KJ13	150x50x4.0 C350	WS	429	48.3	13.5	0.57	62.1	75.5	44.2	1.57	64.0	0.10	70.2	0.24	1.7	8.3	Local buckle at end of sleeve
KJ15	150x50x4.0 C350	BP	429	48.0	13.5	0.55	64.3	57.1	34.2	1.21	48.4	0.077	53.1	0.18	1.0	5.1	Local buckle at end of flange plate
KJ17	150x50x5.0 C450	BS	436	48.0	13.3	0.56	62.4	74.8	47.0	1.64	63.4	0.099	69.6	0.23	2.0	23.0	Local buckle at end of sleeve
TENSION																	
KJ14	150x50x5.0 C350	WS	429	48.9	13.7			99.5	51.5	1.84	84.4	0.14	92.6	0.33	1.0	12.5	Tube fracture at end of sleeve (internal bearing)
KJ16	150x50x4.0 C350	BP	429	48.1	13.5			61.9	32.5	1.15	52.5	0.083	57.6	0.20	0.2	3.4	Tube fracture in HAZ (butt weld)
KJ18	150x50x4.0 C450	BS	436	47.8	13.3			78.3	41.1	1.43	66.4	0.10	72.8	0.24	0.3	13.0	Sleeve fracture

Note: Web slenderness = $\lambda_w = \frac{d-3t}{t}\sqrt{\frac{f_y}{235}}$, Flange slenderness = $\lambda_f = \frac{b-3t}{t}\sqrt{\frac{f_y}{235}}$, calculated to Eurocode 3

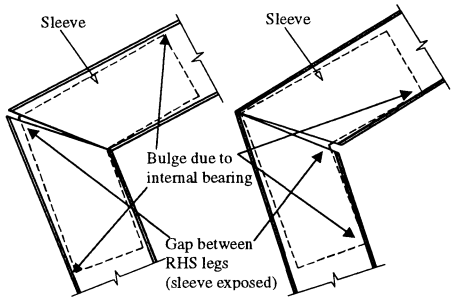

Figure 7: Opening of bolted sleeve during testing

In *tension*, the bolted plate connection failed by tube fracture in the heat affected zone adjacent to the RHS - plate butt weld in the upper leg. The fracture initiated in the corner of the RHS. A large bulge formed on the inside flange at the end of the sleeve in the welded sleeve connection. Eventually, the tube fractured at this point due to combined tension and internal bearing. As the load increased on the bolted sleeve connections, slippage of the connection was evident. Loud "bangs" were heard as the bolts and the sleeve slipped with respect to the RHS itself. The RHS began to open up at the junction (refer to Figure 7). Ultimately the internal sleeve fractured in the middle. No lateral buckling or out-of-plane deflections was observed in any of the tension tests.

6.2 *Load - stroke curves*

The load and stroke (vertical displacement) were recorded during each test. The load - stroke curves are given in Figure 8 (Compression) and Figure 9 (Tension). The load has been non-dimensionalised with respect to the plastic load P_p where $P_p = M_p/e$ and $e = 561$ mm, the initial eccentricity of the joint, and M_p is the plastic moment of the RHS alone. The stroke has been non-dimensionalised with respect to δ_p, so that a load of P_p corresponds to a non-dimensional stroke of unity, based on a first order linear elastic analysis of the specimen. Values of P_p and δ_p are given next to the relevant graph.

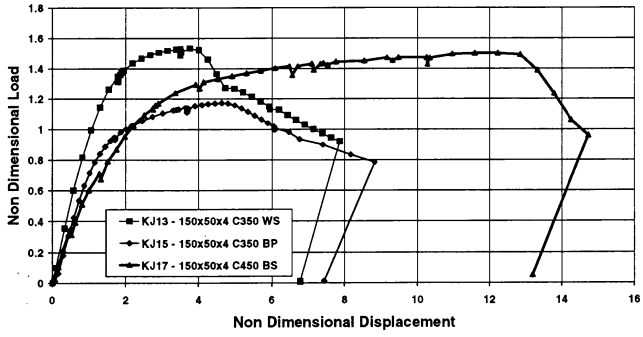

Figure 8: Load - stroke curve (compression)

Specimen	P_p (kN)	δ_p (mm)
KJ13	50.33	12.45
KJ15	53.55	12.48
KJ17	51.01	12.75

Non-dimensional constants

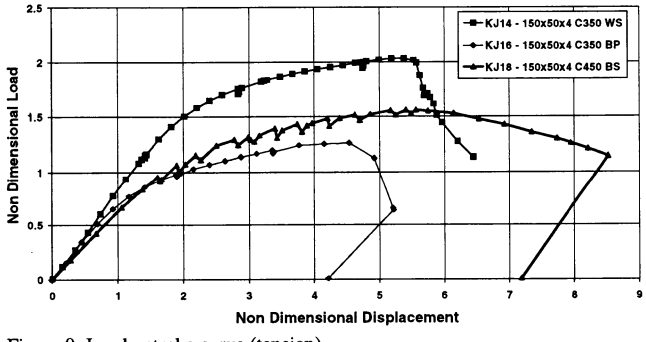

Figure 9: Load - stroke curve (tension)

Specimen	P_p (kN)	δ_p (mm)
KJ14	49.77	12.45
KJ16	50.25	12.47
KJ18	51.30	12.74

Non-dimensional constants

6.3 *Moment - curvature graphs*

Moment curvature relationships are needed to determine the rotation capacity (R_g) of the connections. Figures 10 and 11 show the moment curvature graphs for the knee joint tests. The graphs depict the second order moment and the curvature *at the strain gauge location on the lower leg* (Figure 5). The curvature (κ) was calculated from the strain gauge readings on opposite flanges of the RHS. The curvature was non-dimensionalised with respect to the plastic curvature (κ_p), where $\kappa_p = M_p/EI$. Since the strain gauges were placed a finite distance from the connection apex, the graphs do not represent the curvature and moment at the failure location. For the type WS connection, the strain gauges were placed in the region including the sleeve, while for the BS connection, the gauges were placed outside the sleeve region. Since the curvatures were highly localised at the end of the sleeve, both sets of strain gauges gave much lower values of curvature than were occurring at the sleeve end. Hence R_g underestimates the "true" value of R.

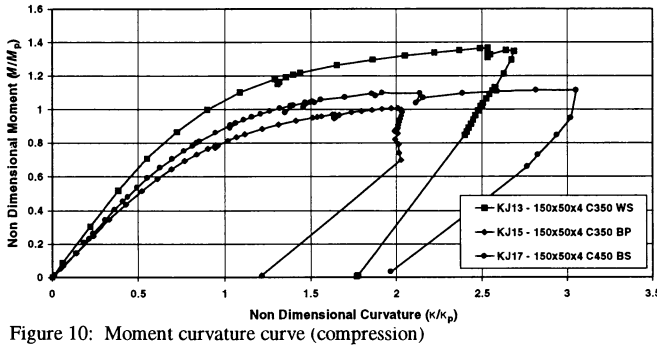

Figure 10: Moment curvature curve (compression)

Note: For Figures 10 and 11, the moment and curvature are calculated at the strain gauge location on the lower leg (refer to Figure 5). Refer to Section 6.4 for the definition of angle change. The moment is non dimensionalised with respect to the plastic moment of the RHS only, and not the RHS and the sleeve combined

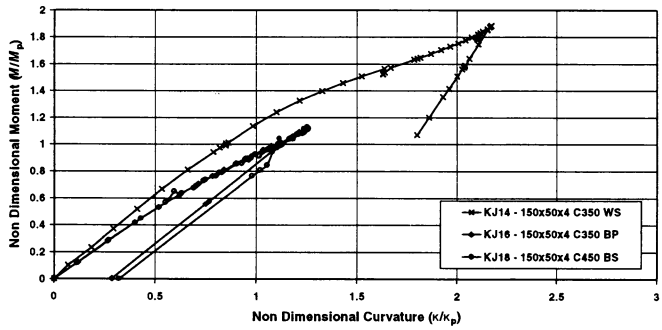

Figure 11:Moment curvature curve (tension)

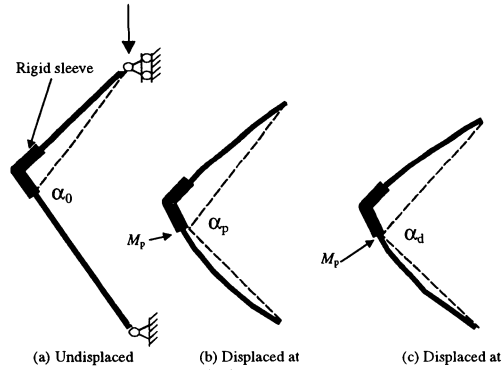

Figure 12: Angle change for sleeve connections (for BP connection refer to Figure 10 of Wilkinson & Hancock (1998a)

6.4 *Moment - angle curves*

It is possible to plot the angle of the deformed member against the moment. In Figure 12(a), the undisplaced angle (α_0) is shown. Using a first order elastic analysis, the angle at which the plastic moment at the end of the sleeve is reached (α_p) is given in Figure 12(b). Figure 12(c) shows the angle at any load (α_d). Note that for the sleeve connections (Figure 12), it is assumed that all the plastic rotation occurs at the end of one sleeve only. For the bolted plate (BP) connection, the analysis assumes all plastic rotation occurs at the joint centreline (Figure 10 of Wilkinson and Hancock (1998a). The moment has been calculated at the point where the rotation has been assumed. The non-dimensional angle change ($\bar{\alpha}$) is given by:

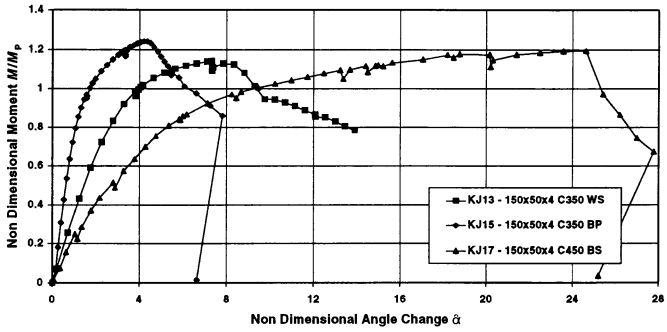

Figure 13:Moment angle-change curve (compression)

Note: For Figures 13 and 14, the moment is non dimensionalised with respect to the plastic moment of the RHS only, and not the RHS and the sleeve combined. Refer to Section 6.4 for the definition of angle change.

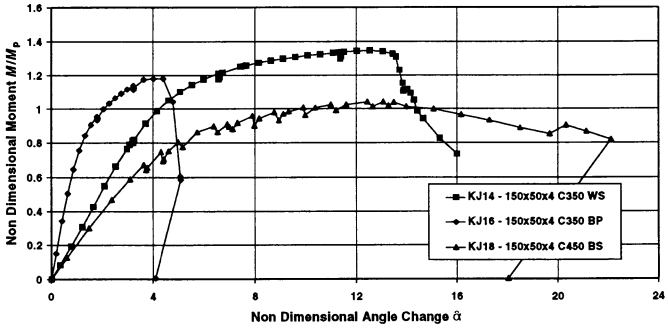

Figure 14:Moment angle-change curve (tension)

$$\bar{\alpha} = \frac{\alpha_d - \alpha_0}{\alpha_p - \alpha_0} \qquad (1)$$

Figures 13 and 14 show the angle change versus moment graphs for compression and tension respectively. From these curves, the rotation capacity based on the angle change (R_α) was calculated. Values of R_α are given in Table 1. R_α is based on the behaviour of the whole joint and is not a "localised" value like R_g. For tension tests, R_α is defined as $R_\alpha = \bar{\alpha}_f - 1$, where fracture occurred at $\bar{\alpha}_f$, while in compression $R_\alpha = \bar{\alpha}_1 - 1$, where the moment drops below M_p at $\bar{\alpha}_1$.

7 DISCUSSION

All connections reached a moment greater than M_p (of the RHS only). Since the sleeve connections had a much thicker region at the apex, the maximum moment reached is notably higher than M_p of the RHS. The axial force in the RHS is low (approximately 5 - 10 % of the squash load), and hence any reduction in the plastic moment capacity due to the presence of axial force would be small. In addition, all sections can still be classified as Class 1, even though the Class 1 limit has been reduced due to the presence of axial compression, and hence are classified as suitable for plastic design.

It is difficult to assess the rotation capacity of the different joints, particularly the sleeve connections. Since the point of maximum curvature in the sleeve connections was not at the apex, but at the end of the sleeve, the total vertical deflection of the test specimen was lower compared to a connection in which the curvature was concentrated at the apex. The total deflection of the bolted connection was increased by the opening of the connection at the junction of the two legs (refer to Figure 7). The welded sleeve connection was stiffer than either the bolted sleeve or the bolted plate connections.

The values of rotation capacity based on the strain gauges (R_g) do not give reliable estimates of the true rotation capacity of any of the connections. The values shown in Table 1 are very low, since the strain gauges were not at the point of maximum curvature. The curvature was highly localised, at the end of the sleeve, or the end of the plates.

Consequently, the rotation capacity based on

angle change (R_α) is a more appropriate measure to use. It can be seen in Figures 13 and 14, that the sleeve connections appear to be much less stiff than the bolted plate connection. This is due to the angle change analysis, in which it is assumed that all plastic rotation occurs at the end of one sleeve. Large curvatures were observed at the ends of both sleeves, but more rotation was visible at the end of the sleeve in the lower leg. The end of the sleeve in the lower leg was more eccentric to the line of action of the applied load than the upper leg. Another analysis (not included in this paper) was performed assuming that equal plastic rotation occurred at both ends of the sleeve. Similar curves to those in Figures 13 and 14 were achieved.

The assumption that all plastic rotation occurs at the end of the sleeve and that the sleeve remains perfectly rigid is incorrect. However it is very difficult to model the behaviour of the sleeve. As previously stated the deformations of the bolted sleeve connection are magnified as the connection began to open up (refer to Figure 7). It is unknown whether the RHS and sleeve act prismatically or non-prismatically. (Prismatic action is defined as the two objects acting as a unit with the stiffness of the combined unit, while non-prismatic action occurs when the two elements act independently and slip occurs between the two). Additionally, the sleeve does not act purely rigidly, and the deformation of the sleeve increases the angle change calculated in the analysis.

Regardless of the difficulties in quantifying the rotation capacity exactly, it is evident that large plastic rotations, much larger than those of the stiffened connections (Wilkinson and Hancock (1998a)), were achieved by the sleeve connections.

The bolted plate connection displayed plasticity, however the problem of weld or heat affected zone failure under tension loads was not overcome. The BP connection exhibited less stiffness in tension compared to compression, caused by the small opening up of the two plates during the test.

One major benefit of the welded sleeve connection was that it forced the plastic hinge to form away from the junction of the two RHS. The stress and strain on the weld was reduced as the sleeve took some of the load.

It was decided that the welded sleeve connection was the most suitable for the portal frame tests. However, this did pose difficulties with the construction of the frame. It was hard to insert the sleeve into the long column and rafter of the frame (both over 3 metres long). It was important that the sleeve fitted snugly into the RHS legs. The angle grinding of the sleeve was a labour intensive operation. At present, the sleeve connection may not be a commercially viable possibility. Since it fits inside the RHS, different sizes are required for the same outer size RHS, since the different thickness of RHS results in different inner dimensions. It is labour intensive and expensive to produce. For the purposes of this test series though, it is considered appropriate for the portal frames.

The welded sleeve has been used in cold-formed RHS portal frames. As expected, the plastic hinge formed at the end of the sleeve, and a plastic collapse mechanism formed in the entire frame. The connection performed adequately and there was no sign of distress or failure in the connection after the portal frame test. More details on the portal frame tests can be found in Wilkinson and Hancock (1998b).

8 CONCLUSION

This paper has presented three different details for knee connections for portal frames constructed from cold-formed RHS: bolted plate connections, and welded and bolted internal sleeve connections. The specimen joints were tested in both tension and compression (opening and closing moments) to simulate wind uplift or gravity loading. The use of an internal sleeve moved the plastic hinge in the connection away from the connection centreline and reduced the stress on the weld between the RHS. It was found that the sleeve connections were capable of sustaining the plastic moment for large rotations considered suitable for plastic design. However, the production of the internal sleeves used in this test program was labour intensive and lengthy, and not suitable for mass production. The bolted plate connection achieved plastic rotations suitable for plastic design but failed in tension in the heat affected zone of the RHS near the weld. The main aim of this test series was to produce a joint capable of sustaining hinge for subsequent use in tests of cold-formed RHS portal frames. The welded sleeve connection was deemed suitable for this purpose.

NOTATION

A_g	Gross cross section area
b	Width of RHS, or width of plate
d	Depth of RHS
E	Young's modulus of elasticity
f_u	Ultimate tensile strength
f_{un}	Nominal ultimate tensile strength
f_y	Yield stress
f_{yn}	Nominal yield stress
I	Second moment of area
M_{max}	Maximum bending moment
M_p	Plastic bending moment
N_{max}	Maximum load in stub column test
N_y	Yield load ($=A_g f_y$)
R	Rotation capacity
r_e	External corner radius of RHS
t	Thickness of RHS, or thickness of plate
κ	Curvature

κ_p Plastic curvature (= M_p/EI)
λ_f Flange slenderness
λ_w Web slenderness

ACKNOWLEDGEMENTS

This research project is funded by CIDECT (Comité International pour le Developpement et l'Étude de la Construction Tubulaire). Tube specimens were provided by BHP Structural and Pipeline Products. The experiments were carried out in the J. W. Roderick Laboratory for Materials and Structures, Department of Civil Engineering, the University of Sydney.

REFERENCES

European Committee for Standardisation, (1992), *Design of Steel Structures: Part 1.1 - General Rules and Rules for Buildings*, DD ENV. 1993-1-1, Eurocode 3 Editorial Group.

Standards Australia, (1990), Australian Standard *AS 4100 Steel Structures*, Standards Australia, Sydney.

Standards Australia, (1991), Australian Standard *AS 1163 Structural Steel Hollow Sections*, Standards Australia, Sydney.

Standards Australia / Standards New Zealand (1995), Australian / New Zealand Standard *AS 1554.1 Structural Steel Welding, Part 1: Welding of Steel Structures*, Standards Australia, Sydney.

Wilkinson T. and Hancock G. J., (1997a), "Tests for the Compact Web Slenderness of Cold-Formed Rectangular Hollow Sections", *Research Report*, No. R744, Department of Civil Engineering, University of Sydney, Sydney, Australia.

Wilkinson T. and Hancock G. J., (1997b), "Plastic Design of Cold-Formed RHS", CIDECT Project 2S, *Interim Report No. 3*, Centre for Advanced Structural Engineering, Department of Civil Engineering, University of Sydney, Sydney, Australia.

Wilkinson T. and Hancock G. J., (1998a), "Tests of Stiffened and Unstiffened Knee Connections in Cold-Formed RHS", *Proceedings*, 8th International Symposium on Tubular Structures, Singapore, (Balkema, publ.).

Wilkinson T. and Hancock G. J., (1998b), "Tests of Portal Frames in Cold-Formed RHS", *Proceedings*, 8th International Symposium on Tubular Structures, Singapore, (Balkema, publ.).



Taylor & Francis
Taylor & Francis Group
http://taylorandfrancis.com

Tubular Structures VIII, Choo & Van der Vegte (eds) © 1998 Balkema, Rotterdam, ISBN 90 5809 001 9

Investigations on stiffened and unstiffened L-joints made of circular hollow sections

R. Puthli, F. Mang & D. Karcher
University of Karlsruhe, Germany

ABSTRACT: In the scope of a CIDECT and a DFG (German research foundation) research project the behaviour of CHS L-joints is being investigated. This paper presents an overview of the whole project. Experimental tests and FE-analyses have been carried out at Karlsruhe University. Design of L-joints have so far only been dealt with in an unsatisfactory manner. For instance, in the CIDECT design guide, the capacity of unstiffened L-joints should be reduced. However, no information is given about the value of this reduction. The reduction factor α for compression loading (closing moments) is already given in the CIDECT final report of project 5BE. Some information is also provided by Puthli et al (1997).

1 GENERAL OVERVIEW

In this paper an overview of the whole work is given. The final results are not all available yet as the work is still in progress. They will be published when the work is completed. Therefore, special formulae for design are not presented in this paper.

Table 1 presents an overview of the research program.

2 RESEARCH PROGRAMME

2.1 *Rotational stiffness (Part 1)*

Each joint has a rotational flexibility which affects the load distribution. If this rotational (spring) stiffness is used in the analysis of framed structures, the load distribution can be more accurately predicted, without recourse to complex modelling of joints. The non-dimensional rotational stiffness c_{rel} is independent of D/t ratios for the stiffened and the unstiffened L-joints. The actual stiffness C of the joint can be calculated by using equation (1).

$$C = E \cdot W \cdot c_{rel} \quad (1)$$

where E = Modulus of Elasticity; W = Elastic Section Modulus.
The relationship between the joint moment and the actual stiffness is given by equation (2).

$$M = C \cdot \Delta\Theta \quad (2)$$

where $\Delta\Theta$ is the rotation of the joint.

2.2 *Ultimate load behaviour under compression loading (Part 2)*

Tests with stiffened and unstiffened specimens have been carried out according to Table 1. FE-analyses have also been carried out. Bending moment and axial loading are induced as shown in the Figures in Table 1. The test specimens with the stiffener plate maintain the original shape in the joint area due to the high plate stiffness. Failure is associated with plastic deformation in the compression zone. The unstiffened test specimen, on the other hand, ovalizes and a buckling failure occurs. With increasing D/t ratios the influence of buckling becomes more and more predominant. In Figure 1, two specimens after failure can be seen. The difference in the modes of failure for stiffened and unstiffened L-joints can be observed.
The test specimens are simulated by FE modelling to calibrate the numeric work. Measured material properties are used to model the elastic and the plastic behaviour. In the FE material law the Ludwig relationship is used to determine the true stress-strain behaviour from the Engineering stress-strain relationship.

$$\varepsilon_{True} = \ln(1+\varepsilon_{Engineering}) \quad (3)$$

$$\sigma_{True} = \sigma_{Engineering} \cdot (1+\varepsilon_{Engineering}) \quad (4)$$

Different steel grades have been investigated as given in Table 1. For FE-analyses (Parametric

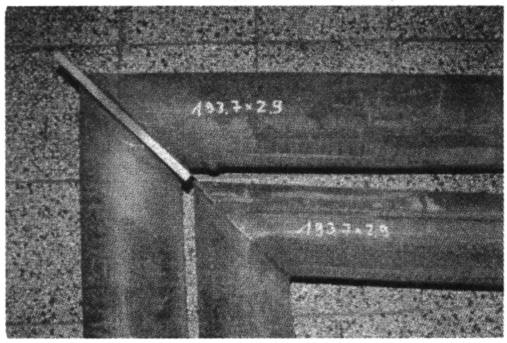

Figure 1: Typical modes of failure (stiffened and unstiffened specimens)

study), the values given in the codes of practice have been used. The reduction factor α is determined as the ratio of the ultimate moment capacities.

$$\alpha = \frac{M(\text{unstiffened})}{M(\text{stiffened})} \qquad (5)$$

For compression loading (closing moments), the maximum load is clearly defined, since the moment increases with the load and the maximum load is defined as failure. A second maximum load level corresponding to a new state of equlibrium cannot be reached. In Figure 2, a typical load-deformation plot can be seen.

The dependence of the ratio D/t and the steel grade on α is shown in Figure 3. The evaluation of part 2 of this research project (see Table 1) is also given in Figure 3. The dependence of the reduction factor α on the geometric parameter can be clearly seen. The analyses have been carried out for an angle Θ of 90°. If the two legs of the joint are connected to each other with an angle Θ greater than or equal to 90°, equation (6) can be used for modifying the reduction factor α.

$$\alpha_\Theta = 1 - \left[\sqrt{2}\cdot\cos\left(\frac{\Theta}{2}\right)\cdot(1-\alpha_{90°})\right] \qquad (6)$$

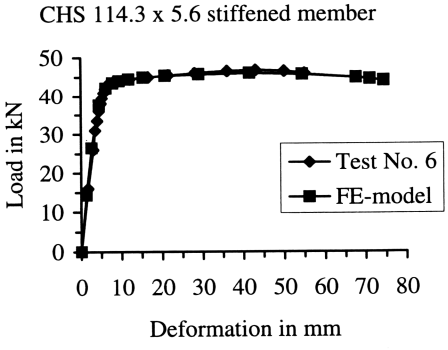

Figure 2: Typical Load-deformation behaviour under compression loading

2.3 *Bultimate load behaviour under tensile loading (Part 3)*

Tests with stiffened and unstiffened specimens have been carried out according to Table 1. FE-analyses have also been carried out. Bending moment and axial loading are induced as shown in the Figures in Table 1. For the FE-analyses, the same material law as for compression loading is used.

The dependence of the reduction factor α on the ratio D/t is not as significant as for compression loading (see part 2). The point of failure is also not clearly defined, because of tension stiffening. For some D/t ratios, an initial peak load can be reached (maximum moment capacity). On further load incrementation, a strong deformation occurs, followed by a significant load increase due to a new equilibrium state where tensile membrane stresses predominate. For other D/t ratios, the initial peak load is not clearly defined but strong deformation also occurs without a drop in load. The point of inflexion of the load-deformation-curve is therefore defined as failure in such cases. In Figure 4, two typical curves can be seen. Because of the load stiffening effect under tensile membrane stresses, the final ultimate load is about the same for stiffened and unstiffened members.

2.4 *Comparison with L-joints with through chords (Part 4)*

Altogether, 6 FE-models of L-joints with through chords will be analysed and compared with the L-joints. From initial work, it is observed that the ultimate load of such joints is comparable with that of stiffened L-joints.

2.5 *Formulae for SNCF/SCF (Parts 5 and 6)*

Work is presently under way to determine the fatigue behaviour. Strip gauges are applied to the test specimens. The FE-models are quite different from those for ultimate strength. In the FE linear analyses, solid elements are used to obtain correct hot spot stresses. For stiffened members, the location of the highest tensile stress in clearly defined as the crown positions of the tube (top for compression, bottom for tension). For unstiffened members, the highest tensile hot spot stresses occur at positions away from the crown points due to the lack of bending stiffness locally. The stress concentration, however, is not as

Table 1: Overview of the research project

RESEARCH PLAN: L-JOINTS MADE OF CIRCULAR HOLLOW SECTIONS					
	Description	Type of joints	Material	Tests	FEA
Part 1	Rotational Capacity	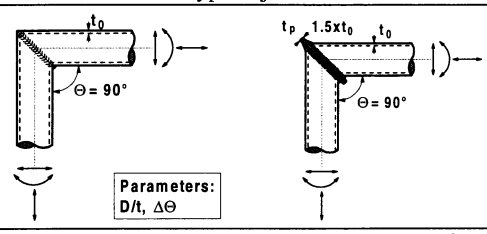	linear		43 No.
Part 2	Ultimate Load in Compression (closing moments)	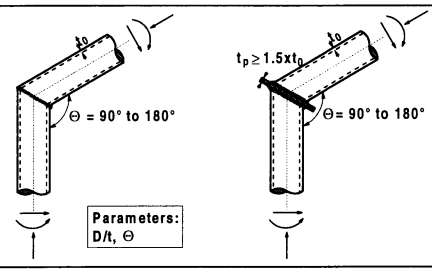	S 235 S 355 S 460 S 690 S 890	12 no. 8 no. --- 2 No. ---	43 No. 43 No. 43 No. 43 No. 43 No.
Part 3	Ultimate Load in Tension (opening moments)	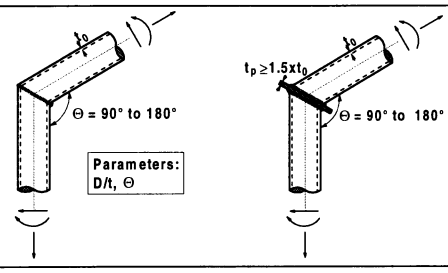	S 235 S 355 S 460 S 690 S 890	3 no. 3 no. --- 1 No. ---	43 No. 43 No. 43 No. 43 No. 43 No.
Part 4	Ultimate Load Tension + Compression	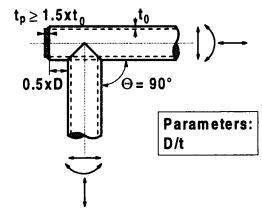	S 355 S 460	--- ---	6 no. 6 no.
Part 5	Fatigue Behaviour Compression (closing moments)	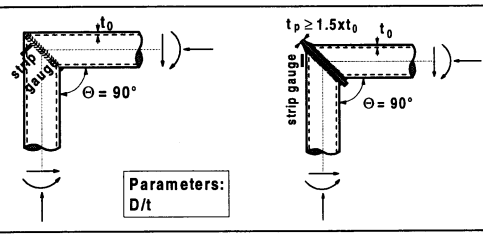	S 235 S 355 S 690	4 no. 2 no. 2 no.	linear 43 no.
Part 6	Fatigue Behaviour Tension (opening moments)	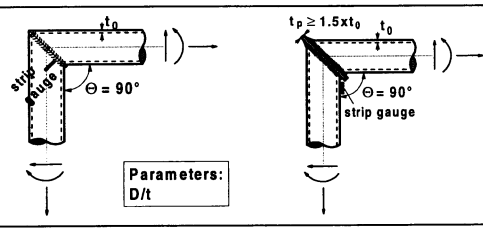	S 235 S 355 S 690	4 no. 2 no. 2 no.	linear 43 no.

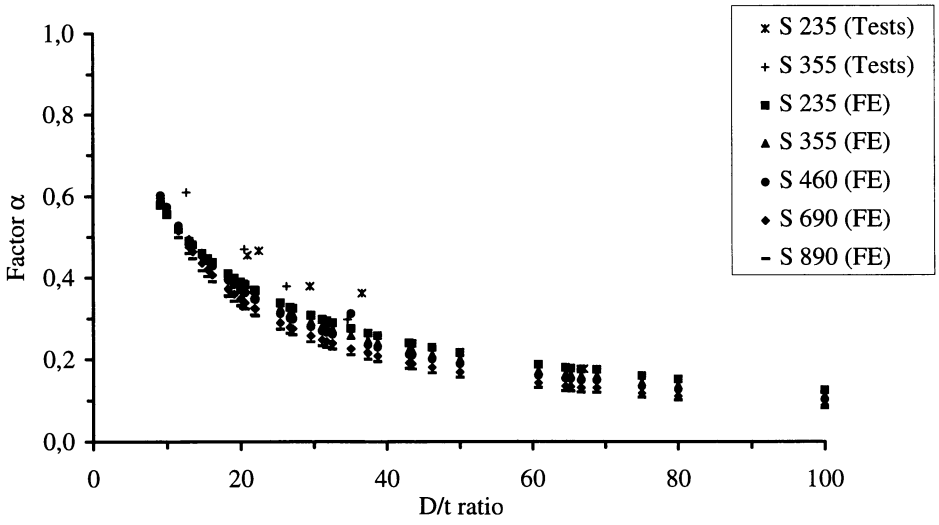

Figure 3: Dependence of the reduction factor α of the D/t ratio and the steel grade for Θ = 90° under compression loading (closing moments)

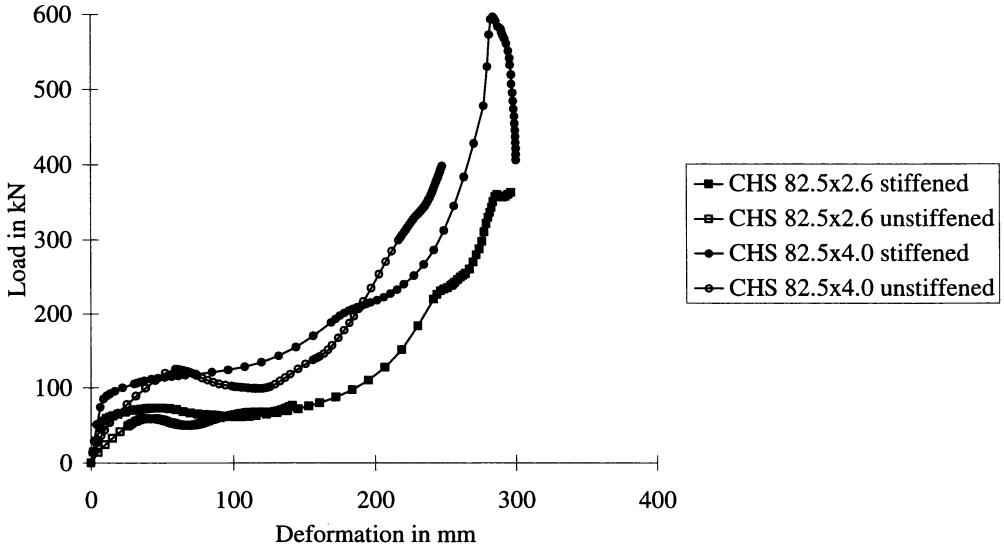

Figure 4: Load-Bearing behaviour under tension loading (opening moments)

high as for stiffened members so that the fatigue behaviour is better.

3 FABRICATION DETAILS

3.1 *Thickness of the stiffening plate*

The stiffening plate is fabricated according to the stipulations of DIN 18808 (1984). In clause 5.3 of DIN 18808 (1984) the plate size should comply with:

$$t_p \geq 1.5 \times t_i \quad (i = 1,2..) \tag{7}$$

$$t_p \geq 10 \text{ mm} \tag{8}$$

A stiffener plate thickness of 15 mm is used for all

test specimens so that the requirements in the DIN are fullfilled, since the maximum wall thickness of the tested tubes is 10 mm. The lateral dimensions of the stiffening plate are chosen on the basis of welding requirements. The distance from the outer edge of the tube to the edge of the plate should be at least two times the side length of the fillet weld to guarantee proper weld toes.

3.2 *Weld preparation*

Stiffened L-joints are welded by using fillet welds. The miter is cut at an angle of 45°. Therefore, the angle between the stiffening plate and the tube varies from 45° to 135°. At sharp corners, the welding is to be carried out with care. The throat thickness of the welds should comply with all important standards:

$$a_W = t \qquad (9)$$

where t = wall thickness of the tube.

The following Figure shows the weld preparation:

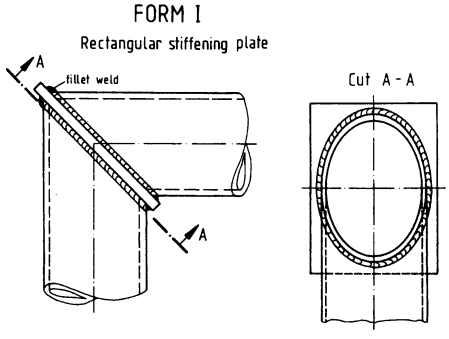

Figure 5: Weld preparation for stiffened L-joints

If the stiffening plate is to be invisible to satisfy architectural requirements, Figure 6 shows the details when an ellipsoidal plate is welded inside.
The unstiffened specimens are welded by a combination of butt and fillet welds with a smooth transition between the two. Edge preparation of the CHS wall as shown in Figure 7 is carried out. The inner (sharp) corner is a fillet weld and the outermost corner a butt weld. There is a smooth and gradual transition between fillet and butt weld around the two half circumferences.

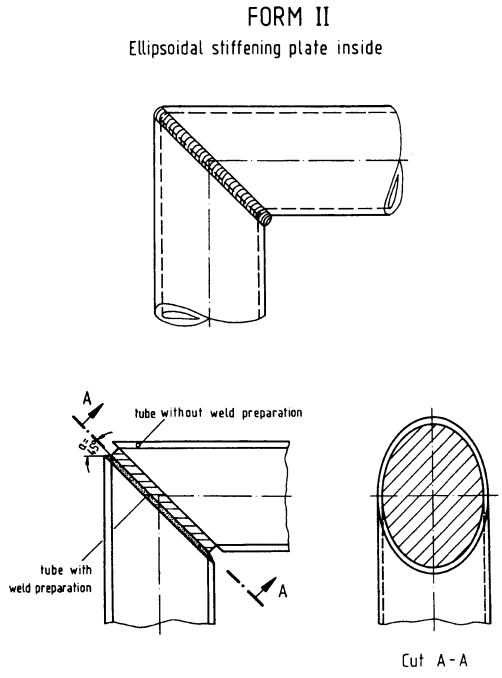

Figure 6: Weld preparation for stiffened L-joints using ellipsoidal plates inside

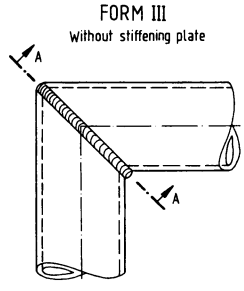

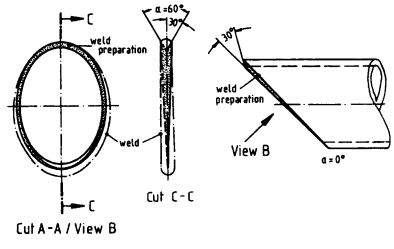

Figure 7: Weld preparation for unstiffened L-joints

4 Conclusions

In this paper an overview of the research project on L-joints made of CHS is given. FE studies have been carried out, where a non-linear material law based on tensile test data is used. Tests have also been carried out to calibrate FE-meshing and to study the behaviour of different loadings, different geometrical

parameters and different steel grades. The capacity of unstiffened L-joints has to be reduced by a factor α in relation to that of stiffened joints. This factor depends on the ratio D/t. A simple design concept is developed based upon this relationship.

The results of this work will form the basis of design recommendations for static strength as well as fatigue strength. The German standard DIN 18808 (1984) as well as the European Standard Eurocode 3 (1993) will include the results of this work. The first publication will be given in a CIDECT report. In this final report all design recommendations including design formulae for fatigue loading will be presented.

REFERENCES

DIN 18 808 (1984): Stahlbauten, Tragwerke aus Hohlprofilen unter vorwiegend ruhender Beanspruchung (Steel structures consisting of hollow sections under predominantly static loads). Beuth-Verlag, Berlin, Oktober 1984.

Dutta, Kurobane, Packer, Wardenier, Yeomans (1991): Constructions with Hollow Steel Sections, Design Guide for Circular Hollow Section (CHS) joints under predominantly static loading. CIDECT, Köln 1991.

Dutta, Kurobane, Packer, Wardenier, Yeomans (1992): Constructions with Hollow Steel Sections, Design Guide for Rectangular Hollow Section (RHS) joints under predominantly static loading. CIDECT, Köln 1992.

Eurocode 3 (1993): Design of steel structures, part 1.1: General rules and rules for buildings. 1993.

Karcher, D. (1998): Tragverhalten von Rahmenecken aus Rundhohlprofilen. PhD Thesis at the University of Karlsruhe, to be completed in 1998

Mang, F., Bucak Ö., Knödel, P. (1991): Ermittlung des Tragverhalten von biegesteifen Rahmenecken aus Rechteck-Hohlprofilen (St 37, St 52) unter statischer Belastung. AIF-research program No. 4117, Final report, April 1981, Studiengesellschaft für Anwendungstechnik Stahl und Eisen, Düsseldorf.

Mang, F., Herion, S., Karcher, D. (1996): L-joints made of Circular Hollow Sections. Final report of CIDECT project No. 5 BE, Karlsruhe University, June 1996, Rev. May 1997

Mang, F., Steidl, G., Bucak, Ö. (1980): Design of welded lattice joints and moment resisting knee joints made of hollow sections. International Institute of Welding Doc. XV-436-80, University of Karlsruhe, Germany, 1980.

Puthli, R., Mang, F., Karcher, D. (1997): The Static strength of stiffened and unstiffened L-joints made of Circular Hollow Sections. Proceedings of the 7th International Offshore and Polar Engineering Conference, Honolulu, Hawaii, USA, May 25-30 1997

Tubular Structures VIII, Choo & Van der Vegte (eds) © 1998 Balkema, Rotterdam, ISBN 90 5809 001 9

Introduction to the database of gusset-plate to CHS tube joints

M.Ariyoshi, S.R.Wilmshurst & Y.Makino
Kumamoto University, Japan

G.J.van der Vegte
Institute of High Performance Computing, Singapore & Delft University of Technology, Netherlands

Y.S.Choo
National University of Singapore, Singapore

ABSTRACT: This paper presents an introduction to a newly compiled database of gusset-plate to CHS tube joints. The database was compiled as a result of the large amount of data that had been generated in Japan, which may be inaccessible to many researchers due to publication of the results in Japanese. The database contains only data for joints where the capacity is governed by loads acting to radially deform the cross-section of the main tube. It contains data for geometry, load patterns and capacities, and material properties. Also presented in the paper are the original references, examples of load-deformation curves, and methods of determining the yield load and joint stiffness. A discussion of some problems arising during the compilation of the database with regard to the original references is made.

1. INTRODUCTION

A database for unstiffened CHS tubular joints was produced at Kumamoto University (1996) with the purpose of providing other researchers with the starting blocks for their own work on tubular joints. Tubular joint research over the previous thirty to forty years had resulted in a proliferation of data and, although published, the data had to collected and compiled by each researcher wishing to use it. Thus, a comprehensive database of uniplanar and multiplanar joint data was assembled.

It was realized soon afterwards by the authors that a considerable amount of work had been carried out on gusset-plate to tube joints. Many of the studies had been carried out in Japan with the results being published in Japanese journals and conferences. The obvious handicap of language prevented these results being found and subsequently utilized in any research programs outside of Japan itself. Therefore, the authors compiled a database of gusset-plate to CHS tube joints with similar aims to the tubular joint database mentioned previously.

This paper presents a database containing as much acquired data on a number of common configurations of gusset-plate to CHS tube joints. In addition, a commentary on the testing methods, load patterns, failure types, material properties, and examples of load-deformation relationships, are given. The database currently contains a total of 220 test and numerical results.

A future aim of the work is to produce simple load-deformation relationships based upon the results of

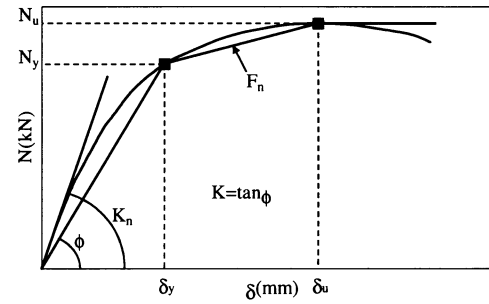

Fig. 1 Load-deformation relationship

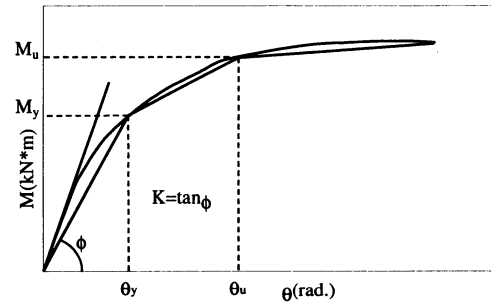

Fig. 2 Moment-rotation relationship

i.e. $F_n = f_0(N_y, N_u, \delta_y, \delta_u)$

where: $N_y = f_1(\alpha, \beta, \gamma, \ldots)$ $\quad \delta_y = f_3(\alpha, \beta, \gamma, \ldots)$

$N_u = f_2(\alpha, \beta, \gamma, \ldots)$ $\quad \delta_u = f_4(\alpha, \beta, \gamma, \ldots)$

connections within the database as shown in Fig. 1and Fig. 2. From these simplified load-deformation and moment-rotation relationships, functions can be derived using the geometrical parameters that describe the connection. Hence, the loads and deformations at yield and collapse could be estimated for gusset-plate to tube joints of any given geometry from these relationships.

Another use for the load-deformation relationships would be in a truss system constructed of CHS chords and interconnecting plates for the bracing (e.g. a Vierendeel truss). The truss could be idealized as a series of beams connected by springs (both axial and torsional) at the nodes to simulate the joint stiffness. The load-deformation relationships could then be used to prescribe the spring stiffness data. An analysis program (to be developed) could then be used for simple design of trusses that contain these plate-to-tube connections. An example of such a truss is a Vierendeel truss (see Fig. 3 and Fig. 4).

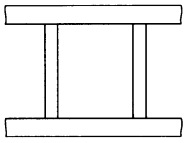

Fig. 3 Section of Vierendeel truss

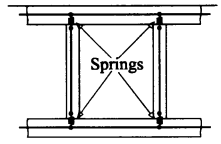

Fig. 4 Modelling with beams and springs

The database is stored in electronic format so that it can be easily downloaded and used by other researchers. Anyone is welcome to use the database, and feedback to the authors will be appreciated so that the quality and content of the database can be improved.

1.1 *Typical examples of gusset-plate to CHS tube connections*

Three main types of gusset-plate to tube connections are:

1. A through gusset plate, where the tubes are welded to each side of the plate, as in Fig. 5. This is often used in beam-column connections such as that shown in Fig. 6. The plates are designed to resist the shear forces and bending moments transmitted to the column from the I-beam whilst reducing the amount of shell buckling of the tube. A butt-plate is welded to the I-beam, and this is in turn welded to the square diaphragm plates.
2. A diaphragm stiffener, where a ring stiffener is welded to the outside of the tube. There are numerous configurations of this type of connection, of which two common types are shown in Fig. 7.
3. A connection where the end of the plate is welded directly to the outer surface of the tube. Examples of these are shown in Table 1.

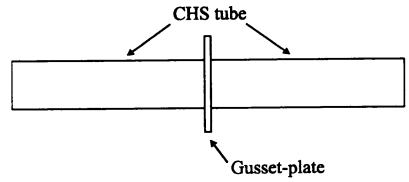

Fig. 5 Gusset plate to tube connection

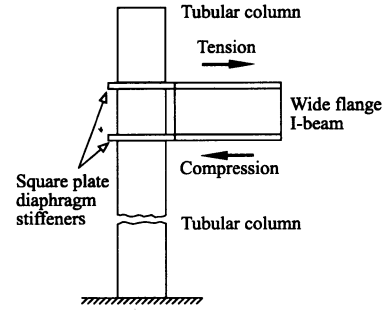

Fig. 6 Beam-column connection

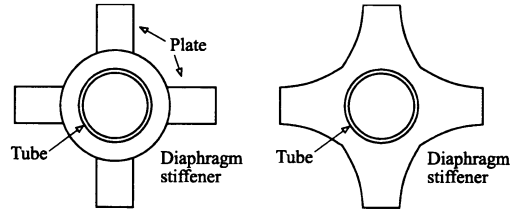

Fig. 7 Two examples of outer diaphragm stiffeners

1.2 *Information on previous database*

The only existing database, to the authors' knowledge is that of Makino (1984), in which the connection types are similar to those shown in Table 1 (i.e. the plate is welded to the outer surface of the tube). The total number of data was 103, and were used only to compare the strengths with tubular connections (i.e. tube to tube).

2. CLASSIFICATION OF JOINTS TYPES AND NUMBERS IN EACH DATA-SET

2.1 *Included and excluded joint types*

The database contains only those configurations where the stiffener aids the tube to resist shear and bending moments across the tube cross-section. Other configurations, such as the example shown in Fig. 8, where the load-transmission is axial and the connection strength does not depend upon the deformation of the cross-section, are not included in the database.

Table 1 Classification of joints and Loading configurations

	TP-joint	XP-joint
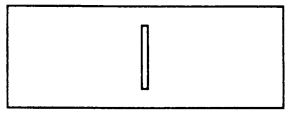	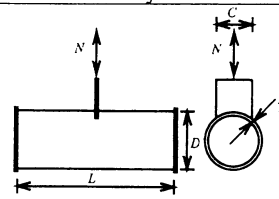 TP1	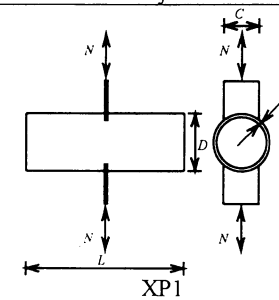 XP1
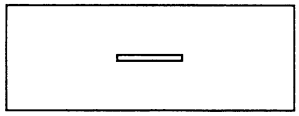	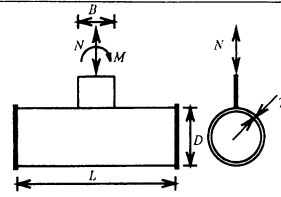 TP2	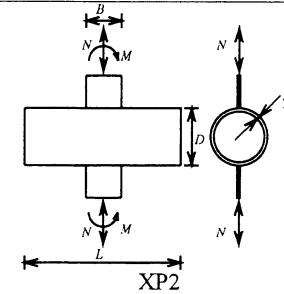 XP2
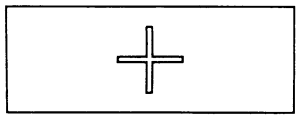	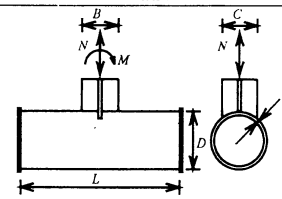 TP3	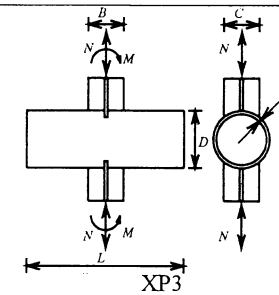 XP3
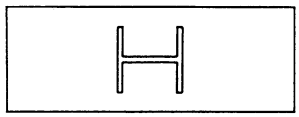	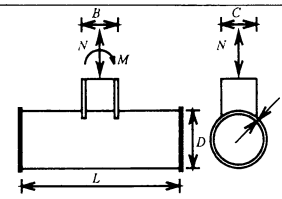 TP4	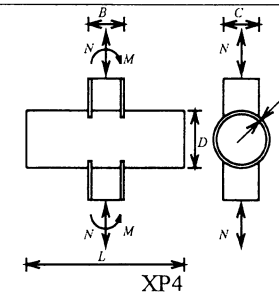 XP4
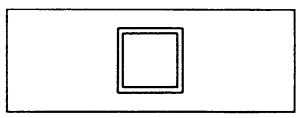	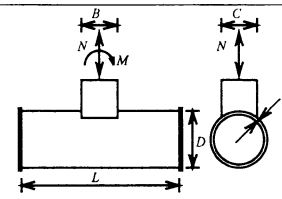 TP5	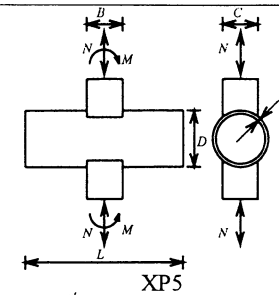 XP5

Table 2 Numbers of data-sets

	Compressive Axial Force		Tensile Axial Force		In-plane Bending Moment		Total
	Test	Analysis	Test	Analysis	Test	Analysis	
TP-joints	27	0	14	0	9	0	50
XP-joints	30	30	35	30	15	30	170
Total	57	30	49	30	24	30	220

2.2 *Classification of joints and Numbers of data-sets*

Table 1 shows ten configurations of plate to tube connections that are included in the database; 5 TP-joints and 5 XP-joints. Numbers of data for each joint type and loading are shown in Table 2.

2.3 *Loading configurations*

Generally the joints are subjected not only to simple loads but also to combined loads. In this paper, only joints subjected to simple loads are considered. The loads are compressive or tensile axial forces and in-plane bending moments, which are shown in Table 1.

3. DEFINITION OF SYMBOLS FOR GUSSET-PLATE TO CHS TUBE JOINTS

The definitions of the geometric parameters are presented in Table 1.

D : chord diameter (mm)
T : chord thickness (mm)
B,C : width of flange* (mm)
* in case of TP4 and XP4, B is the I-section web width, and C is the flange width
L : chord length (mm)

4. MATERIAL PROPERTIES

The material properties shown in the database are the values obtained from tests on tensile coupons taken in the longitudinal direction of each tubular member.

σ_y : yield stress according to tensile coupon test (MPa)
σ_u : ultimate stress according to tensile coupon test (MPa)

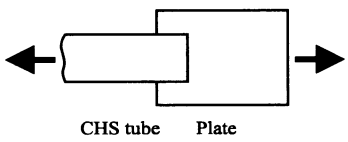

Fig. 8 Example of a plate-to tube connection excluded from the database

5. DEFINITIONS OF LOADS, DEFORMATION AND ULTIMATE STRENGTH

5.1 *Load symbols*

The loads are denoted by the following symbols, and are shown in Table 1. In the paper, tensile forces are represented as positive. For in-plane bending moments, the arrow direction shows the positive direction.

N_y : yield capacity of joint measured as the axial load in the gusset-plate (kN)
N_u : ultimate capacity of joint measured as the axial load in the gusset-plate (kN)
$M_{u,i}$: in-plane bending moment capacity of joint measured at surface of tube member (kN*m)

5.2 N_y *defined by Kurobane et al. (1984)*

Kurobane's definition of the yield strength is based on the results of tests on actual joints and tests on ring models. After plotting load-deformation relationships on double logarithmic paper, it was found that these load-deformation curves could be approximately described by two straight lines. The yield strength then was defined as the load at the intersection of the two lines, representing the point of maximum curvature variation of the load-deformation curve. However, in those cases where the load-deformation curve could not be approximated by two straight lines, the yield strength was taken as the load at the intersection of the load-deformation curve and the line with a slope of 0.779 K_n (initial stiffness), as shown in Fig. 9.

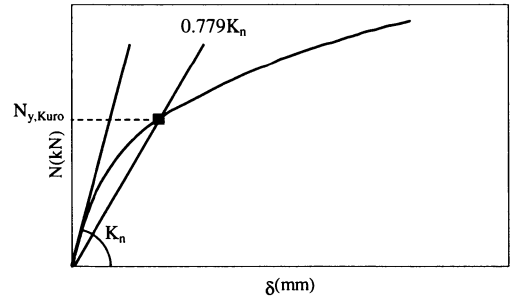

Fig. 9 Load-deformation relationship

5.3 N_y, N_u *defined by Kamba (1997)*

Kamba (1997) defined a third of the initial stiffness as the second stiffness. Subsequently, he assumed the yield load as the load where the slope of the load-deformation curve equalled the second stiffness (see Figs. 10 to 12). For load-deformation curves without a peak load (usually observed for joints under tensile loading), the ultimate strength was defined as 1.31 times the yield strength whereas the corresponding deformation was defined as ${}_t\delta_{max}$, as shown in Fig. 10.

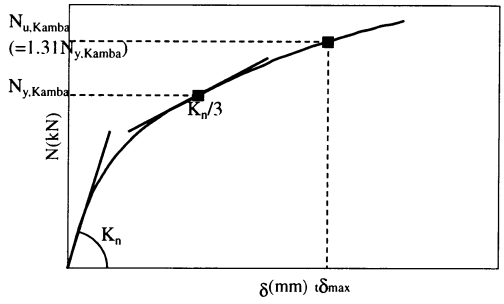

Fig. 10 Load-deformation relationship

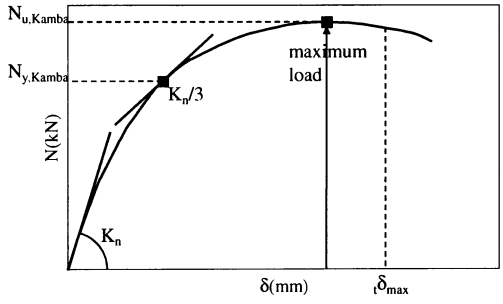

Fig. 11 Load-deformation relationship (maximum load < ${}_t\delta_{max}$)

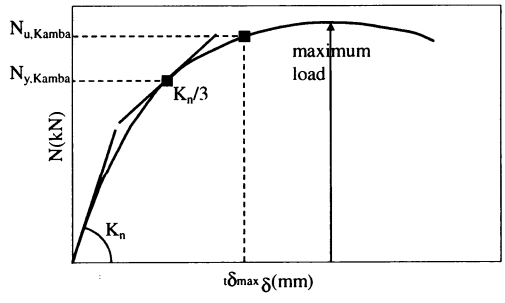

Fig. 12 Load-deformation relationship (maximum load > ${}_t\delta_{max}$)

For joints where the load-deformation curves showed a peak load (generally found for joints loaded in compression), the ultimate strength was taken as the maximum load (see Fig. 11). However, if the deformation at maximum load exceeded ${}_t\delta_{max}$, ultimate load was defined as the load at a deformation of ${}_t\delta_{max}$, as shown in Fig. 12.

5.4 *Deformation limit by Lu et al. (1994)*

From the experimental and the numerical load-deformation curves obtained for different joint types under different loading cases (van der Vegte et al. (1991), de Winkel et al. (1993) and Yu et al. (1994)), it was found that for connections where a peak load was reached, the corresponding local indentation of the chord face at the cross section varied between 2.5 % - 4 % D. Therefore, a local deformation limit of 3 % D (chord diameter) of the chord face was suggested by Lu (1994) as the ultimate deformation limit (see Fig. 13).

$$\delta_{u,Lu} = 0.03 * D$$

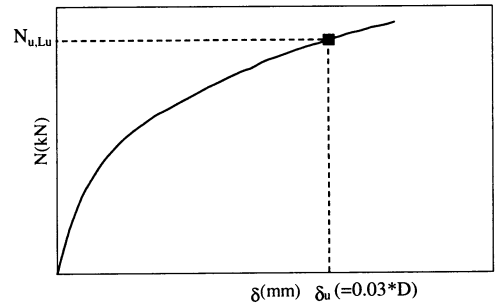

Fig. 13 Load-deformation relationship

5.5 N_y, *defined by Akiyama (1974)*

Section 5.2 to 5.4 described several methods that researchers have employed to determine the deformations and load values at the yield and the ultimate load states. However, Akiyama et al. (1974) use a very different method to determine the yield load (see Fig. 14). A line is drawn tangentially to the load-deformation curve at the point at which the crack was determined. Another line is drawn horizontally from the load value representing two-thirds of the value of the intersection point of the first line with the load-axis. A third line is drawn from the origin through the point where this second line intersects the curve. Where the third line intersects the first line is the value taken to be the yield load.

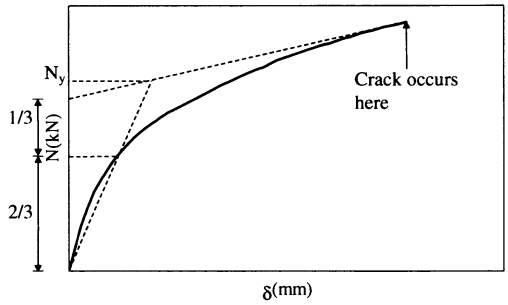

Fig. 14 Example of definition of N_y from Akiyama et al (1974)

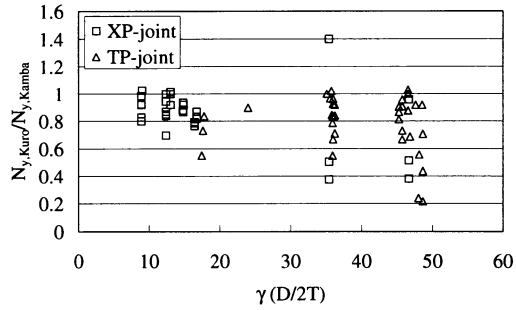

Fig. 15 Comparison between $N_{y,Kuro}$ and $N_{y,Kamba}$ (parameter γ)

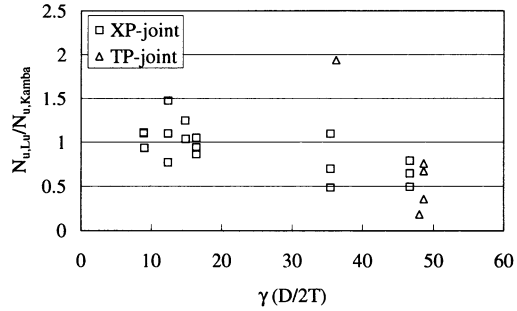

Fig. 16 Comparison between $N_{u,Lu}$ and $N_{u,Kamba}$ (parameter γ)

5.6 *Deflection and Stiffness of joints*

In the test results found in the available literature, the load-deformation relationships usually display the applied loads against the joint deformation in the direction of the acting loads. In the database the load-deformation relationships are described by N_y, N_u, $M_{u,i}$ and following symbols:

K_n : initial joint stiffness under axial force (mm)

δ_y : local deformation of joint reached at yield load (mm)

δ_u : local deformation of joint reached at ultimate strength (mm)

θ_y : in-plane rotation of joint reached at yield moment capacity (rad.)

θ_u : in-plane rotation of joint reached at ultimate moment capacity (rad.)

5.7 *Comparison between definitions for yield strength and ultimate strength*

Fig. 15 shows the comparison between the yield strengths using both Kurobane's and Kamba's method. The yield strengths determined with Kamba's definition are larger than the values given by Kurobane's formulae. In Fig. 16, the comparison between the ultimate strengths obtained from Lu's and Kamba's methods is shown. Although the ultimate strength predictions only slightly differ for γ values less than 20, it appears that for γ values larger than 35, Kamba's method results in higher ultimate strengths than the values predicted by Lu's deformation limit.

6. TYPICAL PROBLEMS ARISING FROM THE INTERPRETATION OF OTHER RESEARCHERS DATA AND METHODS

The interpretation of other researchers work can often present a host of problems. Although the work is published as fully as circumstances will allow, there are often details omitted which may be of importance to future studies. In this section several typical problems are highlighted and recommendations for future tests and studies are proposed, *viz*:

1. Definitions of the displacements, deformations, and loads.
2. Material property data.
3. Weld sizing, material, and detailing.

6.1 *Problems*

Section 5 described several methods that researchers have employed to determine the deformations and load values at the yield and the ultimate load states. It would appear from Figs 15 and 16 that there is no consistency for the predictions of the yield and ultimate loads. Within each differing methodology lies certain assumptions, but the most striking of these are those employed in the methods of Kamba (1997) and Akiyama (1974).

The method of Kamba appears to rely upon the fact that the designer or researcher has a corresponding tension loaded specimen with which to calculate the yield load in a compression-loaded specimen. This is almost invariably not the case.

In the Akiyama method, the particular tension

Table 3 Extract from the database

No.	Specimen	D	T	B	C	L	σ_y	σ_u	N_y	$N_{y,Kuro}$	$N_{y,Kamba}$	N_u	$N_{u,Kamba}$	$N_{u,Lu}$	$\delta_{u,Lu}$	θ_y	θ_u	$M_{u,i}$	K_n	δ_y/D	δ_u/D	Test/	Failure	Reference
		(mm)	(mm)	(mm)	(mm)	(mm)	(MPa)	(MPa)	(kN)	(kN)	(kN)	(kN)	(kN)	(kN)	(mm)	(rad.)	(rad.)	(kN*m)	kN/mm)			Analysis	Type	No.
XP1-C-1	XP1-C	267.1	9.02	-	138.9	2150	479	517	-168	-220.6	-255	-401	-334	-	-	-	-	-	75.0	0.011	0.087	Test	CLD	7
XP1-C-6	sc54-69	216.3	4	-	150	1000	354	519	-	-	-62.1	-	-80.4	-	-	-	-	-	18.4	0.025	0.082	Analysis	CLD	9
XP1-C-7	sc54-58	216.3	4	-	125	1000	354	519	-	-	-58.7	-	-69.2	-	-	-	-	-	12	0.036	0.076	Analysis	CLD	9
XP1-C-8	sc54-46	216.3	4	-	100	1000	354	519	-	-	-52.1	-	-57.7	-	-	-	-	-	8.6	0.043	0.069	Analysis	CLD	9
XP1-C-9	sc54-35	216.3	4	-	75	1000	354	519	-	-	-41.4	-	-44.6	-	-	-	-	-	6.6	0.05	0.069	Analysis	CLD	9
XP2-C-1	XP2-C	267.0	9.04	139.1	-	2150	479	517	-177	-176.5	-201	-289	-263.3	-	-	-	-	-	35.3	0.024	0.104	Test	CLD	7
XP2-C-2	A-10	101.6	3.04	101.6	-	600	365	-	-	-19.61	-23.53	-33	-30.83	-	-	-	-	-	-	-	-	Test	CLD	2
XP2-C-3	A-15	101.6	3.04	152.4	-	600	365	-	-	-23.04	-26.48	-37	-34.68	-	-	-	-	-	-	-	-	Test	CLD	2
XP2-C-4	A-20	101.6	3.04	203.2	-	600	365	-	-	-24.52	-29.91	-41	-39.18	-	-	-	-	-	-	-	-	Test	CLD	2
XP3-C-1		165.2	5.2	247.8	115.6	990	308	-	-	-	-	-123	-	-	-	-	-	-	-	-	-	Test	CLD	4
XP3-C-2		165.2	5.2	247.8	148.7	990	308	-	-	-	-	-187	-	-	-	-	-	-	-	-	-	Test	CLD	4
XP4-C-1		165.2	5.2	247.8	115.6	990	308	-	-	-	-	-179	-	-	-	-	-	-	-	-	-	Test	CLD	4
XP4-C-2		165.2	5.2	247.8	148.7	990	308	-	-	-	-	-265	-	-	-	-	-	-	-	-	-	Test	CLD	4
XP5-C-1	XP-B-1	114.3	4.39	85.7	91.4	772	377	-	-	-112.8	-122.6	-149	-160.6	-	-	-	-	-	196.1	-	-	Test	CLD	5
XP5-C-2	XP-B-2	114.3	4.39	171.5	91.4	858	377	-	-	-139.2	-137.3	-197	-179.8	-	-	-	-	-	264.8	-	-	Test	CLD	5
XP5-C-3	XP-B-3	114.3	4.39	342.9	91.4	1029	377	-	-	-225.5	-225.5	-300	-295.5	-	-	-	-	-	411.9	-	-	Test	CLD	5
XP1-T-1	XP1-T	267.4	9	-	136.9	2150	479	517	316	343.2	372.6	641	488.1	505.7	8.022	-	-	-	70.1	0.022	-	Test	CC	7
XP1-T-8	1-4	216.3	12	-	100	1000	349	-	343	331.4	323.6	448.2	423.9	396	6.489	-	-	-	150.9	0.02	0.129	Test	CC	6
XP1-T-9	st54-69	216.3	4	-	150	1000	354	519	-	-	99.3	-	130.1	-	6.489	-	-	-	18.9	0.039	0.103	Analysis		9
XP1-T-10	st54-58	216.3	4	-	125	1000	354	519	-	-	90.7	-	118.9	-	6.489	-	-	-	12.3	0.051	0.111	Analysis		9
XP1-T-11	st54-46	216.3	4	-	100	1000	354	519	-	-	80.3	-	105.2	-	6.489	-	-	-	8.8	0.061	0.132	Analysis		9
XP1-T-12	st54-35	216.3	4	-	75	1000	354	519	-	-	72.3	-	94.7	-	6.489	-	-	-	6.7	0.074	0.161	Analysis		9
XP2-T-1	XP2-T	267.3	9.04	139.2	-	2150	479	517	170	174.5	186.3	520	244.1	304.4	8.019	-	-	-	31.9	0.026	0.199	Test	CC	7
XP2-T-2	A-10	101.6	3.1	101.6	-	600	358	-	-	26.48	33.34	86	43.68	37.8	3.048	-	-	-	-	-	-	Test	CC	2
XP2-T-3	A-15	101.6	3.1	152.4	-	600	358	-	-	26.97	35.3	98	46.25	43.4	3.048	-	-	-	-	-	-	Test	CC	2
XP2-T-4	A-20	101.6	3.1	203.2	-	600	358	-	-	28.44	36.28	158	47.53	49.8	3.048	-	-	-	-	-	-	Test	CC	2
XP3-T-1		114.3	4.29	114.3	99.1	457	369	-	-	-	-	178	-	-	3.429	-	-	-	-	-	-	Test		1
XP3-T-2		114.3	4.08	228.6	99.1	571	369	-	-	-	-	203	-	-	3.429	-	-	-	-	-	-	Test		1
XP3-T-3		76.3	3.2	152.6	66.4	600	360	-	-	-	-	149	-	-	2.289	-	-	-	-	-	-	Test		3
XP4-T-1		114.3	4.12	114.3	99.1	457	369	-	-	-	-	243	-	-	3.429	-	-	-	-	-	-	Test		1
XP4-T-2		114.3	4	228.6	99.1	571	369	-	-	-	-	295	-	-	3.429	-	-	-	-	-	-	Test		1
XP4-T-3		76.3	3.2	152.6	66.4	600	360	-	-	-	-	222	-	-	2.289	-	-	-	-	-	-	Test		3
XP2-M-1	XP2-B-1	216.5	4.26	201.0	-	1500	395	-	-	-	-	-	-	-	-	-	-	9.9	-	-	-	Test	CLD	8
XP2-M-2	XP2-B-2	216.5	4.26	400.7	-	1700	395	-	-	-	-	-	-	-	-	-	-	22.9	-	-	-	Test	CLD	8
XP4-M-1	XP4-B-1	216.5	4.26	201.4	99.4	1500	395	-	-	-	-	-	-	-	-	-	-	19.1	-	-	-	Test	CLD	8
XP4-M-2	XP4-B-2	216.5	4.26	400.0	100.3	1700	395	-	-	-	-	-	-	-	-	-	-	34.8	-	-	-	Test	CLD	8

specimen represented in the figure shows a reasonable approximation of the yield load, but it relies upon the slope of the load-displacement curve at failure. The failure point for such a tension specimen is also dependent upon the crack formation, which can be in turn dependent upon the weld material and detailing (discussed later). In addition, the ultimate tensile strength values for the materials were not reported for some of the specimens. This was often a failing in earlier test programs, probably due to the design methods being based upon allowable stresses.

One obvious observation is that there does not appear to be a consistent point taken for the measurement of joint deformations in tests. This lack of consistency can therefore lead to serious discrepancies in the determination of the joint stiffness.

Often, the weld detailing is not reported in publications of test results. It has been shown in research on tube to tube connections that weld sizes can influence the joint strength. In particular, weld material strengths are not reported in the results of tests on tension specimens. The question then arises as to whether some specimens failed by cracking in the weld, prior to the actual ultimate strength.

6.2 *Tentative guidelines and recommendations for future tests and numerical work*

1. Consistent points for the measurement of the joint deformations must be determined, so that consistent joint stiffness values can be calculated. In any case, the positions and deformation data for all measured points should be archived.
2. Unique methods of determining the yield and ultimate loads from the load-displacement curves must be ascertained.
3. Material properties must be reported in full, i.e. yield stress and ultimate tensile stress values, elastic moduli, and, if possible, stress-strain curves should be archived for future reference by researchers using numerical methods to extend the database.
4. Details of the weld procedure, weld material, and sizing should be reported.

7. FAILURE MODES AND TYPES

Many failure types can be observed in tubular joints. Some failures do not take place in the joints but in one of the members, or are due to poor fabrication or testing, etc. In this paper, failure types are classified according to the data reported in the original papers. Data without a clear description of the failure type are excluded from the database.

CC : Crack at weld toes on Chord surface
CLD : Local Deformation of Chord

8. EXTRACT FROM THE DATABASE

An example from the database is shown in Table 3, and shows a section of the XP-joint data.

9. CONCLUSIONS

This paper presents an introduction to the database of gusset-plate to CHS tube joints. Only those joint types are included in the database where the loads act across the main tube. Connections with axially loaded tubes are not considered. The paper discusses some of the problems encountered during the compilation of the database, and tentative recommendations are made for future studies. Also discussed are some of the methods used by other researchers to determine the yield and ultimate loads and deformations. The paper is stored in electronic format as an EXCEL file and may be used freely by other researchers. The internet address is

http://www.arch.kumamoto-u.ac.jp/maki_lab/database.html

REFERENCES

Akiyama, N., Yajima, M., Akiyama, H. & Ohtake, A., (1974) "Experimental Study on Strength of Joints in Steel Tubular Structures", *Journal of Society of Steel Construction*, Vol. 10, No.102, pp.37-68 (in Japanese)

Kamba, T., (1997) "Prediction Equation for Initial Stiffness and Ultimate Capacity of Unstiffened CHS column and H-Beam Connections", *Doc. For Tubular Structure Committee of the AIJ* (in Japanese)

Kurobane, Y., Makino, Y. & Ochi, K., (1984) "Ultimate Resistance of Unstiffened TubularJoints", Journal of Structural Engineering, *Proc. of the American Society of Civil Engineers (ASCE)*, U.S.A., Vol.110, No.2, pp385-400

Lu, L. H., Winkel, G. D. de, Yu, Y. & Wardenier, J., (1994) "Deformation Limit for Ultimate Strength of Hollow Section Joints", *Proc. of 6th Int. Symposium on Tubular Structures*, Melbourne, Australia, pp.341-347

Makino, Y., (1984) "Experimental Study on Ultimate Capacity and Deformation for Tubular Joints", Doctoral Dissertation, Osaka University (in Japanese)

Makino, Y., Kurobane, Y., Ochi, K., Vegte, G. J. van der & Wilmshurst, S. R., (1996) "Database of Test and Numerical Analysis Results for Unstiffened Tubular Joints", IIW Doc. XV-E-96-220, Miskolc, Hungary

Vegte, G. J. van der, Puthli, R. S. & Wardenier, J., (1991) "The Static Strength and Stiffness of Uniplanar Tubular Steel X-joints", *Proc. International Conference on Steel & Aluminium Structures*, Singapore, pp.620-631

Winkel, G. D. de, Rink, H. D., Puthli, R. S & Wardenier, J., (1993) "The Behavior and the Static Strength of Unstiffened I-Beam to Circular Column Connections Under Multiplanar In-plane Bending Moments", *Proc. 3rd International Offshore and Polar Engineering Conference (ISOPE-93)*, Colorado, U.S.A

Yu, Y. & Wardenier, J., (1994) "Influence of the Types of Welds on the Static Strength of RHS T- and X- joints Loaded in Compression", *Proc. of 6th Int. Symposium on Tubular Structures*, Melbourne, Australia, pp.597-605

REFERENCES FOR DATABASE

(1) Naka, T., Kato, B., Tada, H. & Yamazaki, Y., (1960) "A Study of Welded Tubular Structures: Part5", Research Report, *Kanto Branch of the AIJ*, No.27 (in Japanese)

(2) Togo, T., (1967) "Experimental Study on Mechanical Behavior of Tubular Joints", Doctoral Dissertation, Osaka University, Osaka, Japan (in Japanese)

(3) Yoshida, Y., Kominami, T. & Nishimura, M., (1969) "Tests on Ultimate Strength of Brace Joints Intersected at Right Angles - Part1 and 2", Summary Papers, *Annual Conference of the AIJ* (in Japanese)

(4) Washio, K., Kurobane, Y., Togo, T., Mitsui, Y. & Nagao, N., (1970) "Experimental Study of Ultimate Capacity for Tube to Gusset Plate Joints - Part1", Summary Papers, *Annual Conference of the AIJ* (in Japanese)

(5) Makino, Y., Kurobane, Y. & Mitsui, Y., (1976) "Ultimate Capacity Equations for Tubular Cross Joints", Research Report, *Kyushu Branch of the AIJ*, No.22, pp. 253-256 (in Japanese)

(6) Kamba, T., Kanatani, H., Fujiwara, K. & Tabuchi, M., (1982) "Tests on Local Failures of Tubular Column to H-Beam Connections in Steel Structures – A Study on Tubular Column to Beam Connections Part 1", *Transactions of the AIJ*, No.322, pp. 44-51 (in Japanese)

(7) Makino, Y., (1984) "Experimental Study on Ultimate Capacity and Deformation for Tubular Joints", Doctoral Dissertation, Osaka University (in Japanese)

(8) Makino, Y., Kurobane, Y., Paul, J. C., Orita, Y & Hiraishi, K., (1991) "Ultimate Capacity of Gusset Plate-To-Tube Joints under Axial and In- Plane Bending Loads", *Proc. of 4th Int. Symposium on Tubular Structures*, Delft, The Netherlands, pp. 424-434

(9) Kamba, T., (1997) "Prediction Equation for Initial Stiffness and Ultimate Capacity of Unstiffened CHS Column and H-Beam Connections", *Doc. for Tubular Structure Committee of the AIJ* (in Japanese)



Taylor & Francis
Taylor & Francis Group
http://taylorandfrancis.com

Tubular Structures VIII, Choo & Van der Vegte (eds) © 1998 Balkema, Rotterdam, ISBN 90 5809 001 9

A new ultimate capacity formula for unstiffened CHS T-, TT-, X-, K- and KK-joints under axial brace loads

Y.Yamada, M.Morita, Y.Makino & S.R.Wilmshurst
Kumamoto University, Japan

ABSTRACT: This study presents continuous design equations for axially loaded CHS joints relating T-, TT-, X-, K- and KK-joints. The new equations are an extension to those previously derived by Morita et al (1997) and include KK-joints under symmetrical axial loading. The equations were derived using multiple non-linear regression analyses and the tubular joint database of Makino et al (1996). It is shown that although the accuracy of each of the strength predictions is slightly lower, the equations adequately capture the effects of the geometric parameters upon the joint strengths.

1. INTRODUCTION

Current design formulae such as AWS (1994), API (1993), CIDECT (1991), and AIJ (1990) are both simple and inaccurate, or in order to obtain reasonable accuracy are too complicated for use. In addition, some guidance documents, such as CIDECT, give individual formulae to be applied to each joint type for which the strength is to be determined. AWS presents a continuous formula to be applied to arbitrary joint types and loading, but lacks the accuracy to make it effective as a design formulation. It has been shown in many studies that the AWS formulation predictions can be grossly unsafe in some cases.

Therefore, it is desirable to have new ultimate capacity formulae with the following requirements:

(1) The new ultimate capacity formula should be simpler than existing formulae, even if the accuracy of the ultimate capacity equation is lower than that of existing formulae.

(2) It is better that new ultimate capacities are continuous equations for various joints. For example, the ultimate capacity of a TT-joint with $2\Phi = 0$ would be equal to half that of a T-joint, and with $2\Phi = 180$ the capacity would be equal to that of a X-joint as shown in Fig. 1. The ultimate capacity of K-joint with a large in-plane gap between the braces should approximate to that of a T/Y-joint as shown in Fig. 2, and so on. The main reason for a continuous equation is the potential to easily estimate the ultimate capacities of other joint configurations.

(3) New ultimate capacity formulae must deal not only with simple load cases, such as axial loading, but also with combined loads. (Only axially loaded cases are considered in this study).

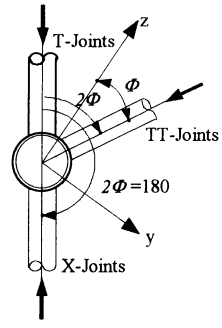

Fig. 1 Configurations showing the relationships between T-, TT-, and X-joints

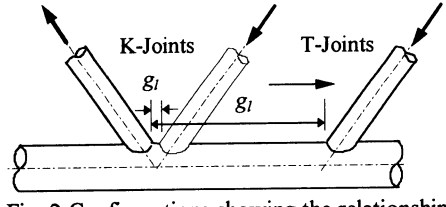

Fig. 2 Configurations showing the relationships between T- and K-joints

Table. 1 Number and parameter ranges for the data used in the regression analyses

Joint type	numbers		Parameter ranges											
	Test	FE	D (mm)	T (mm)	d (mm)	θ (deg.)	Φ (deg.)	β	γ	ζ_1	n_0	m_0	σ_y	σ_y/σ_u
T	29	40	113.9 ~1400	3.42 ~28.0	42.7 ~800	45 ~90	—	0.19 ~1.00	7.26 ~46.7	—	—	0.0 ~0.97	295 ~441	0.64 ~0.83
TT (Type 1)	2	6	190.8 ~406.4	5.20 ~11.0	60.6 ~244.5	—	30 ~45	0.22 ~0.60	18.3 ~18.5	—	—	0.05 ~0.80	355 ~384	0.70 ~0.86
K	437	1	59.7 ~558.8	1.62 ~12.7	22.0 ~326.4	30 ~90	—	0.19 ~1.00	7.77 ~51.0	-14.4 ~66.2	-0.69 ~0.94	-0.69 ~0.90	231 ~826	0.55 ~0.94
KK (Type 1)	13	44	120.0 ~216.1	1.50 ~7.9	38.4 ~101.7	49.1 ~63.4	30 ~45	0.29 ~0.47	9.00 ~40.0	0.83 ~25.3	—	—	278 ~404	0.69 ~0.88
X	97	52	60.5 ~408.0	2.97 ~28.0	21.7 ~407.4	60 ~90	—	0.21 ~1.00	7.3 ~36.2	—	-0.97 ~0.97	0 ~0.23	292 ~82.6	0.68 ~0.94
TT (Type 2)	8	17	190.8 ~406.4	5.2 ~11	42.8 ~244.5	—	30 ~60	0.22 ~0.73	18.3 ~18.5	—	—	0.01 ~1.05	355 ~384	0.70 ~0.86
KK (Type 2)	26	22	120.0 ~217.2	1.5 ~7.9	28.8 ~89.0	49.1 ~90	30 ~45	0.22 ~0.47	12.0 ~40.0	1.6 ~25.3	—	—	278 ~472	0.69 ~0.91

2. DATA FOR REGRESSION ANALYSIS

Local deformation of chord under axial brace loads can be distinguished into two failure types: Failure type 1 (Fig. 3 (a)), in which the two compression braces act together with no local deformation of chord wall in the transverse gap area between them; and Failure type 2 (Fig. 3 (b)), in which there is significant local deformation of chord wall in the transverse gap area in the form of a radial fold.

Data for regression analysis were screened according to the following conditions from the database for the tubular joints (Makino et al. 1996).

(1) Joints where the predominant failure mode was Local Deformation of Chord (CLD), Local Deformation of Chord with no deflections in transverse gap area on multiplanar joints (CLD1) in Failure type 1 and Local Deformation of Chord with deflections forming a fold in transverse gap area on multiplanar joints.(CLD2) in Failure type 2 were used.

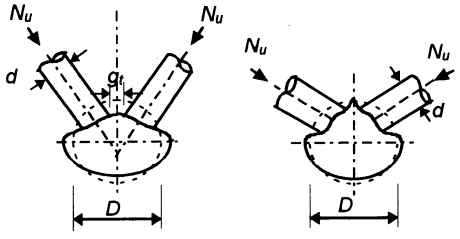

(a) Failure type 1 (b) Failure type 2

Fig.3 Illustrations of joint failure types for TT and KK-joints

(2) Test/FE results that did not have a first peak in the load-deformation history were omitted.

(3) Test/FE results with partially thickened chord/canned members were omitted.

(4) Test/FE results with concrete filled/grouted members were omitted.

(5) Test/FE results without measurements of the chord material yield and ultimate tensile stresses and chord length were omitted.

(6) Test results with unclear support conditions were omitted.

(7) Only T- and X-joints having α greater than 10 and TT-joints having larger than 8.9 were included in the database. (According to van der Vegte (1995), if α is greater than these values chord end effects on the ultimate capacity can be neglected. However, the number of tests for which $\alpha > 12$ is small.)

(8) Test/FE results with strength determined by Yura's deformation limit were omitted.

(9) The ultimate strengths of X-joint with the chord end plates are factored down by 1.192. (Usually X-joint test specimens do not have chord end plates, but the ultimate capacities of X-joints with chord end plates are. Thus the de-rating factor of 1.192 (Togo et al, (1967)) was used to reduce the capacity to be comparable with specimens without end-plates)

The resulting number of data sets and the ranges of data are as shown in Table 1. The parameter matrices for the KK-joints are shown in Figs. 4(a)-(d). The other joints (e.g. T-, K-, etc.) are not shown for clarity, but the matrices for these joints can be found in Morita et al (1997).

3. MATHEMATICAL MODEL OF FAILURE TYPE 1 FOR REGRESSION ANALYSIS

Fig.5 shows the relationships between the ultimate strength of K-joints from test and numerical analysis and the predictions according to the T-joint estimation equation of Morita et al. (1996). In a former paper (Morita et al. 1997), the mathematical model of K-joints for regression analysis was proposed as Eq. 1. However, the ultimate capacity estimations of joints with large overlaps were much greater than the joint strengths. Therefore, according to Fig.5, the mathematical model of K-joints for regression analysis was modified to that shown in Eq. 2. Fig.6 shows the relationship between the ultimate strength of KK-joints from tests and numerical analyses and the predictions according to the estimation equation for K-joints led from the result of regression analysis. According to Fig.6, the mathematical model for regression analysis was proposed as shown in Eq. 3.

$$ {}_K N_{u,c} = \left(1 + R_1 \exp(R_2\zeta_l)\beta^{R_3}\right) \cdot {}_T N_{u,c} \cdot \varepsilon \qquad (1) $$

$$ {}_K N_{u,c} = \left(1 + \frac{R_1 \beta^{R_2} \gamma^{R_3}}{\exp(R_4\zeta_l) + 1}\right) \cdot {}_T N_{u,c} \cdot \varepsilon \qquad (2) $$

$$ {}_{KK} N_{u,c} = \left(1 + R_1\gamma \sin\Phi + R_2\gamma \sin^2\Phi\right) \cdot {}_K N_{u,c} \cdot \varepsilon \qquad (3) $$

The final mathematical model is shown in Eq. 4. An explanation of each term is given in Table.2, since it was necessary to improve the overall accuracy of the ultimate capacity equation.

$$ \frac{N_u \sin\theta \cos\Phi}{\sigma_y T^2} = f_1 f_2 f_3 f_4 f_5 f_6 f_7 \cdot \varepsilon \qquad (4) $$

$$ f_1 = \frac{R_1}{1 + R_2\beta} \beta^{R_3} \gamma^{R_4} $$

$$ f_2 = 1 + \frac{R_5 \beta^{R_6} \gamma^{R_7}}{\exp(R_8\zeta_l) + 1} $$

$$ f_3 = 1 + R_9 \cos\theta $$

$$ f_4 = 1 + R_{10}\gamma \sin\Phi + R_{11}\gamma \sin^2\Phi $$

$$ f_5 = 1 + R_{12} n_0 + R_{13} n_0^2 $$

$$ f_6 = 1 + R_{14} m_0 $$

$$ f_7 = 1 + R_{15} \frac{\sigma_y}{\sigma_u} $$

Table.2 Definitions of terms in the ultimate capacity formula

$N_u \sin\theta$	Component force in the axis perpendicular to the chord for K-, KK-, and Y-joints.
$\cos\Phi$, $\sin\Phi$	Component force in the direction of z-axis for TT- and KK-joints of Failure type 1 and the direction of y-axis for X-, TT-, and KK-joints of Failure type 2 (see Fig.1).
$\frac{R_1}{1 + R_2\beta} \beta^{R_3} \gamma^{R_4}$	Basic term for ultimate capacity equations for hub joints derived from ring-model analysis.
$\left(1 + \frac{R_5 \beta^{R_6} \gamma^{R_7}}{\exp(R_8\zeta_l) + 1}\right)$	Correction factor for K- and KK-joints with in-plane gaps between the compression braces and the tension braces.
$(1 + R_9 \cos\theta)$	Correction factor for the component force in the direction of chord axis
$(1 + R_{10}\gamma \sin\Phi + R_{11}\gamma \sin^2\Phi)$, $(1 + R_{10} \cos\Phi + R_{11} \cos^2\Phi)$	Correction factor the component force in the direction perpendicular to chord axis for TT- and KK-joints. For failure type 2, the γ parameter was omitted, as there was no significant trend of the strength with this parameter.
$(1 + R_{12} n_0 + R_{13} n_0^2)$	Function to account for chord pre-stress.
$(1 + R_{14} m_0)$	Reduction factor for chord member global bending effects. For failure type 2, this term was omitted, because R_{14} from regression analysis was approximately 0.
$\left(1 + R_{15} \frac{\sigma_y}{\sigma_u}\right)$	Correction function for chord materials, since there is a mix of hot finished, cold finished, and high strength tubes in the database. For failure type 2, this term was omitted, as a relationship could not be established with the limited data.
ε	Error term in the regression equation

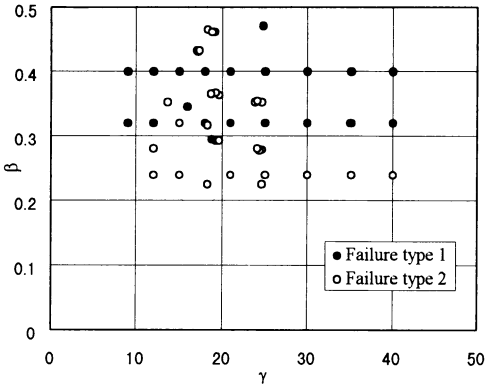

Fig.4(a) β versus γ

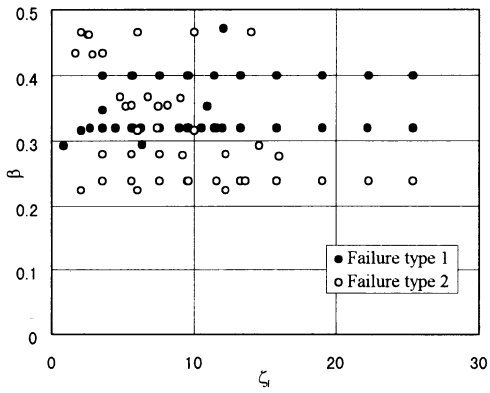

Fig.4(b) β versus ζ_l

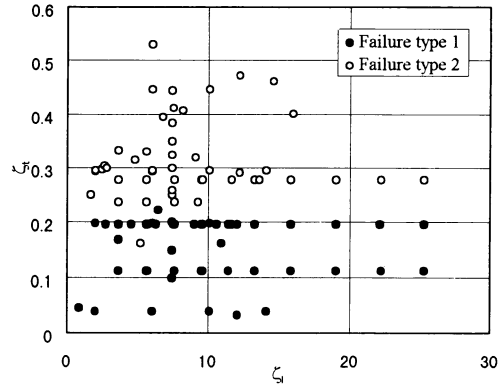

Fig.4(c) ζ_{st} versus ζ_l

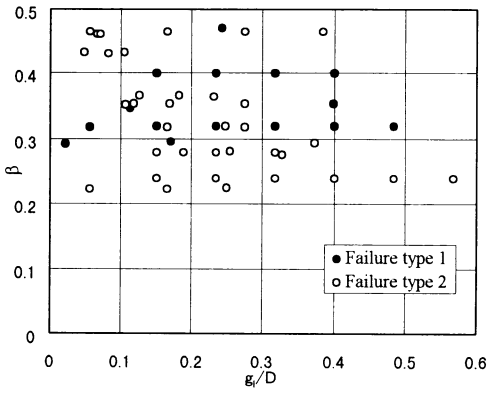

Fig.4(d) β versus g_l/D

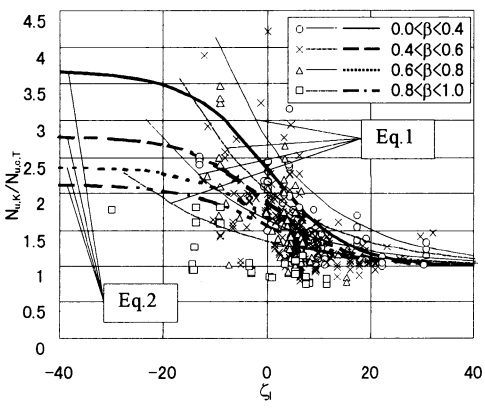

Fig.5 Ultimate strength interaction between T-joints and K-joints

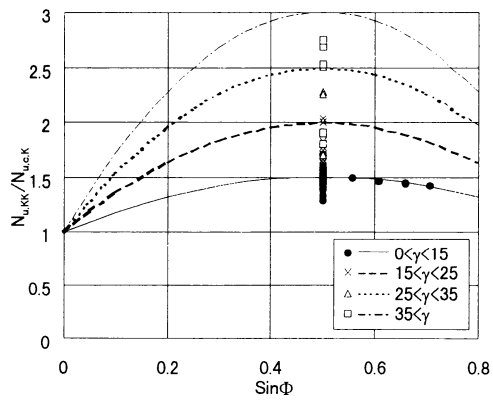

Fig.6 Ultimate strength interaction between K-joints and KK-joints

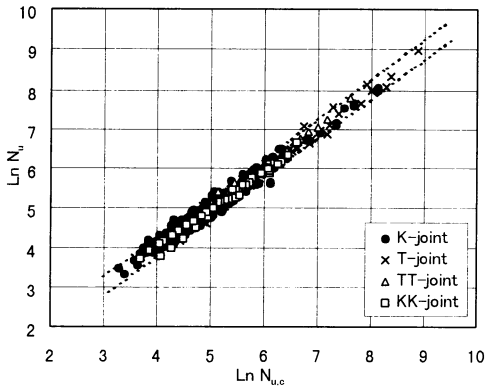

Fig.7 Relationships between test and numerical result and prediction equation (Type 1)

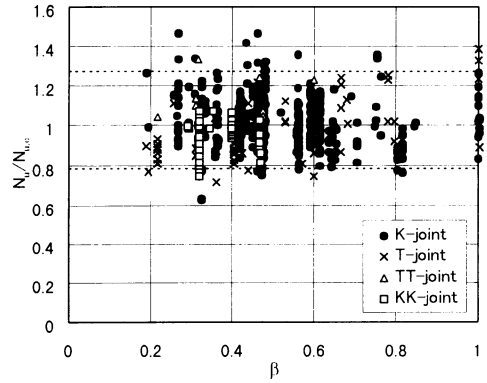

Fig. 8(a) Test and numerical results to prediction ratios against β (Type 1)

4. RESULTS OF REGRESSION ANALYSIS FOR FAILURE TYPE 1

The ultimate capacity formula derived by regression analysis for failure type 1 is shown in Eq.5, together with the mean and CoV. Fig.7 shows a comparison between test and numerical results and the predictions according to Eq. 5, plotted on log-log axes. The dotted line represents the approximate 95% confidence limits, which are given by $N_{u,c} \cdot e^{\pm 1.96\sigma}$ (where σ is the standard deviation).

$$N_{u,c} = f_1 f_2 f_3 f_4 f_5 f_6 f_7 \cdot \sigma_y T^2 \qquad (5)$$

$$f_1 = \frac{16.4}{1-0.390\beta}\beta^{0.710}\gamma^{0.246}$$

$$f_2 = 1 + \frac{0.134\beta^{-0.800}\gamma^{0.678}}{\exp(0.133\zeta_1)+1}$$

$$f_3 = \frac{1-0.136\cos\theta}{\sin\theta}$$

$$f_4 = \frac{1+0.122\gamma\sin\Phi - 0.0941\gamma\sin^2\Phi}{\cos\Phi}$$

$$f_5 = 1 + 0.275n_0 - 0.338n_0^2$$

$$f_6 = 1 - 0.229m_0 \qquad f_7 = 1 - 0.491\frac{\sigma_y}{\sigma_u}$$

number of data = 572
mean = 1.008
CoV = 0.125

Figs 8(a)-(c) show plots of the test and numerical results to prediction ratios against the parameters β, γ and ζ_1, respectively. It can be seen from the figures that there are no residual trends with the geometrical parameters indicating that Eq. 5 can accurately predict the ultimate capacities for T-joints, K-joints, and TT- and KK-joints failing with type 1.

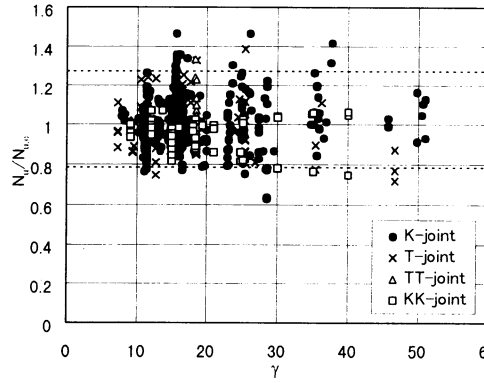

Fig.8(b) Test and numerical results to prediction ratios against γ (Type 1)

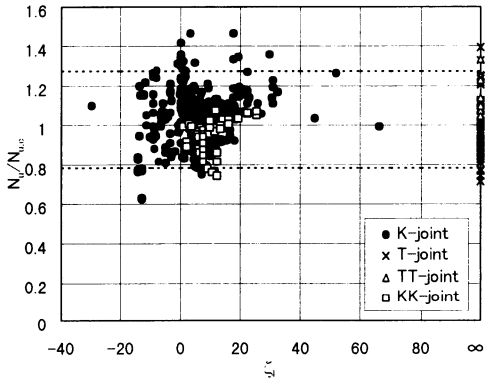

Fig.8(c) Test and numerical results to prediction ratios against ζ_1 (Type 1)

5. MATHEMATICAL MODEL OF FAILURE TYPE 2 FOR REGRESSION ANALYSIS

Eq. 6 shows the proposed mathematical model of failure type 2

$$\frac{N_u \sin\theta \sin\Phi}{\sigma_y T^2} = f_1 f_2 f_3 f_4 f_5 \cdot \varepsilon \qquad (6)$$

$$f_1 = \frac{R_1}{1+R_2\beta}\beta^{R_3}\gamma^{R_4}$$

$$f_2 = 1 + \frac{R_5\beta^{R_6}\gamma^{R_7}}{\exp(R_8\zeta_1)+1}$$

$$f_3 = 1 + R_9\cos\theta$$

$$f_4 = 1 + R_{10}\cos\Phi + R_{11}\cos^2\Phi$$

$$f_5 = 1 + R_{12}n_0 + R_{13}n_0^2$$

6. RESULTS OF REGRESSION ANALYSIS IN FAILURE TYPE 2

The ultimate capacity formula for failure type 2 was derived as Eq. 7, using all the applicable TT-, X-, and KK-joint data. Also shown are the mean and CoV values.

Fig.9 shows the comparison between test and numerical results and predictions according to the equation plotted on log-log axes. Figs 10(a), (b) and (c) show the ratios of the test and numerical results to the predictions against the parameters β, γ and ζ_1, respectively. It can be seen from Fig.9 that nearly all the data lies within the dotted lines indicating the 95% confidence limits. Figs 10(a)-(c) show that there are no residual trends of the capacity ratios with the geometrical parameters defining the formula.

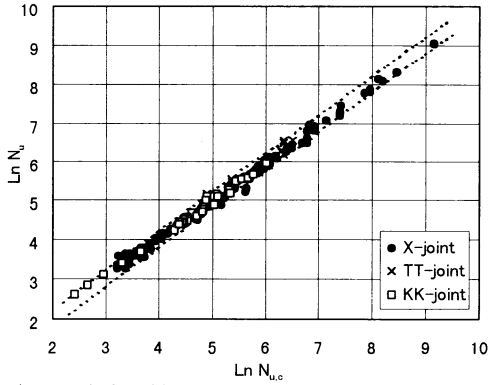

Fig.9 Relationships between test and numerical results and prediction equation (Type 2)

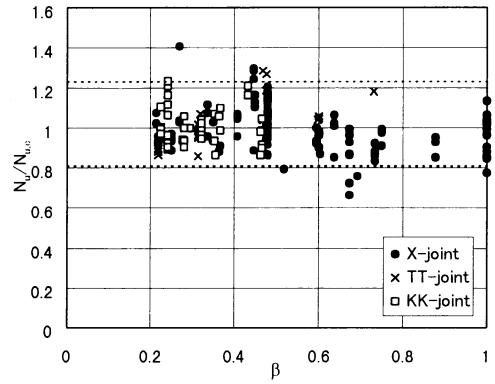

Fig.10(a) Test and numerical results to prediction ratios against β (Type 2)

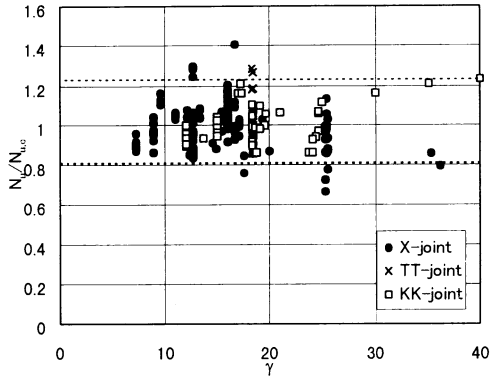

Fig.10(b) Test and numerical results to prediction ratios against γ (Type 2)

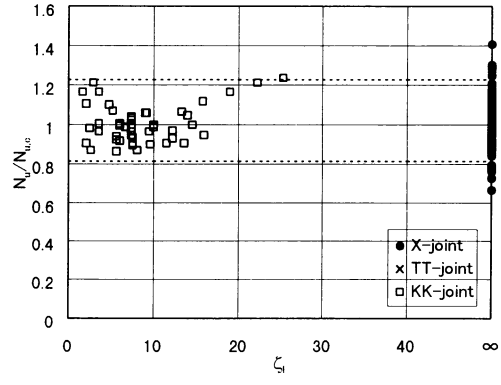

Fig.10(c) Test and numerical results to prediction ratios against ζ_1 (Type 2)

$$N_{u,c} = f_1 f_2 f_3 f_4 f_5 \cdot \sigma_y T^2 \quad (7)$$

$$f_1 = \frac{6.45}{1-0.763\beta}\beta^{0.259}\gamma^{0.101}$$

$$f_2 = 1 + \frac{1.89\beta^{3.24}\gamma^{0.830}}{\exp(0.119\zeta_l)+1}$$

$$f_3 = \frac{1+0.186\cos\theta}{\sin\theta}$$

$$f_4 = \frac{1+0.340\cos\Phi - 0.816\cos^2\Phi}{\sin\Phi}$$

$$f_5 = 1+0.200n_0 - 0.0898n_0^2$$

number of data = 222
mean = 1.005
CoV = 0.106

7. COMPARISON WITH EXISTING ULTIMATE CAPACITY FORMULAE

The formulae for K- and KK-joints of Kurobane et al (1984, 1996) are shown in Eqs (8)-(10):

For K-joints:

$$_K N_{u,c} = f_0 f_1 f_2 f_3 f_4 f_5 \cdot \sigma_y T^2 \quad (8)$$

$$f_0 = 2.11\left(1+5.66\frac{d}{D}\right)$$

$$f_1 = \left(\frac{D}{T}\right)^{0.209}$$

$$f_2 = 1 + \frac{0.00904\left(\frac{D}{T}\right)^{1.24}}{\exp\left(0.508\frac{g_l-3.04}{T}-1.33\right)+1}$$

$$f_3 = \frac{1-0.376\cos^2\theta}{\sin\theta}$$

$$f_4 = 1+0.305n_0 - 0.285n_0^2$$

$$f_5 = \left(\frac{\sigma_y}{\sigma_u}\right)^{-0.723}$$

For KK-joints (Failure type 1):

$$\frac{_{KK}N_{u,c}}{_K N_{u,c}} = 0.233\left(\frac{D}{T}\right)^{0.402} \quad (9)$$

For KK-joints (Failure type 2):

$$\frac{_{KK}N_{u,c}}{_K N_{u,c}} = 0.539\left(1-0.31\frac{g_l}{D}\right)\left(\frac{D}{T}\right)^{0.18} \quad (10)$$

Comparisons between the predictions from the proposed equation and the Kurobane K- and KK-joint equations are shown in Figs.11 and 12. Table 3 shows quality of the predictions by the Kurobane equations and the equations derived in this paper, in the form of the mean and CoV. The mean values of the predictions from the Kurobane K- and KK-joint equations against the same data are 0.995 and 0.993, and CoV values of that are 0.056 and 0.103, respectively.

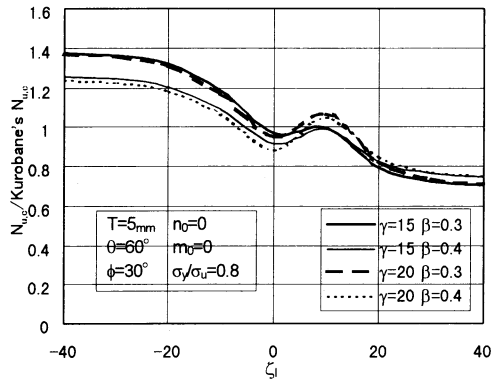

Fig.11 Comparison between the proposed equation and the Kurobane (1996) KK-joint of Failure type 1 equation

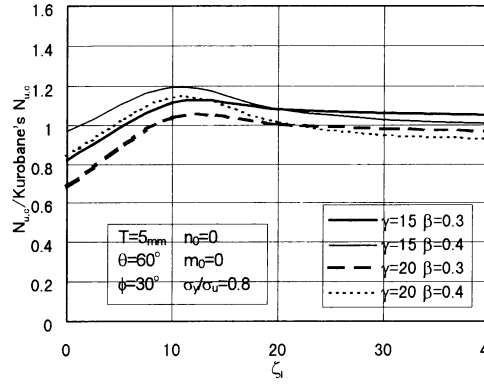

Fig.12 Comparison between the proposed equation and the Kurobane (1996) KK-joint of failure type 2 equation

The following observations can be made from the figures and the table:

(1) When $\zeta_l<0$, the K-joint strength predictions from the proposed equation are slightly higher than those from Kurobane (1984) formulae (see Fig.11). When $\zeta_l>0$ the predictions are lower

Table.3 The mean and CoV values of the strength predictions for each joint type using the derived formula and the Kurobane formulae (1984,1996)

Joint type	all data			$\zeta_l > 0$			$\zeta_l \leqq 0$		
	numbers	mean	CoV	numbers	mean	CoV	numbers	mean	CoV
T-joint	69	0.970	0.150	—	—	—	—	—	—
TT-joint (Type 1)	8	1.151	0.094	—	—	—	—	—	—
K-joint	438	1.016 (1.000)	0.124 (0.104)	359	1.011 (0.999)	0.113 (0.097)	79	1.040 (1.004)	0.165 (0.129)
KK-joint (Type 1)	57	0.990 (0.995)	0.080 (0.056)	57	0.990 (0.995)	0.080 (0.056)	—	—	—
X-joint	149	0.994	0.108	—	—	—	—	—	—
TT-joint (Type 2)	25	1.003	0.121	—	—	—	—	—	—
KK-joint (Type 2)	48	1.004 (0.993)	0.095 (0.103)	48	1.004 (0.993)	0.095 (0.103)	—	—	—

Means and CoV's determined from the predictions using the Kurobane formulae (1984, 1996) are shown in parentheses.

than those from the Kurobane formula.

(2) There is no available data for KK-joints with $\zeta_l<0$, thus, it is recommended that the prediction equation is not used for KK-joints with $\zeta_l<0$ at present.

(3) The higher CoV values for the T-joints and the TT-joints failing with type 2 may be due to a residual effect of bending moments in the chord.

8. CONCLUSIONS

This paper presents two new continuous equations for determining the ultimate capacities of T-, TT-, K-, and KK-joints failing with type 1 failure, and for X-, TT-, and KK-joints failing with type 2 failure. The ultimate capacities can now be predicted by only one equation for each failure type. The ultimate capacity formula consists of a basic equation and some multiplicative correction terms that have clear meanings. Consequently, ultimate capacities of arbitrary joints may be estimated easily.

Although the accuracy of each of the new ultimate capacity formulae is lower than the individual K-joint and KK-joint equations of Kurobane (1984, 1996) this can be attributed to the simpler regression models used.

Upon inspection of the CoV's for each of the derived equations and their 95% confidence limits for the capacity ratios, it can be seen that in each case the CoV is less than 15% and the confidence limits are in the range of 0.8 to 1.3. Therefore, these equations could be used to determine characteristic strength formulae suitable for design.

In the future, the continuous equations will be extended for various multiplanar joints. Eventually, the authors hope to propose an ultimate capacity formula for all joint types and loading conditions.

9. NOMENCLATURE

D	chord diameter
d	brace diameter
e	eccentricity between the point where two in-plane brace axes meet and the chord axis
g_l	longitudinal gap between two in-plane braces
g_t	transverse gap between two out-of-plane braces
L	chord length
M_0	bending moment in chord at center of joint
M_p	full plastic moment capacity in the chord member
m_0	bending moment ratio (M_0/M_p)
N_u	ultimate axial force in the brace
$N_{u,c}$	estimated ultimate axial force in the brace
N_0	axial force in the chord (pre-stressing force)
n_0	$\frac{N_0}{\pi(D-T)T\sigma_y}$
R_i	regression constants (i=1...n)
T	chord thickness
t	brace thickness

α chord length ratio (2L/D)
β diameter ratio (d/D)
γ chord thinness ratio (D/2T)
ε error term in regression analysis
Φ out-of-plane angle
θ in-plane angle between compression brace and chord
σ_y yield stress of chord material
σ_u ultimate tensile stress of chord material
ζ_l longitudinal gap ratio (g_l/T)
ζ_t transverse gap ratio (g_t/T)

10. REFERENCES

Architecture Institute of Japan, (1990) "Recommendations for the Design and Fabrications of Tubular Structures in Steel," AIJ, Tokyo, Japan (in Japanese)

American Petroleum Institute, (1991) "Recommended Practice for Planning, Designing and Construction of Fixed Offshore Platforms," API Recommended Practice 2A (RP-2A), 19th ed. Washington, DC.

American Welding Society, (1994) "Structural Welding Code-steel", ANSI/AWS D1.1-94, Miami.

Kurobane, Y., and Ochi K. (1996) "AWS vs International Design Rules for Circular Tubular K-Connections", Engineering Structures, Vol.19, No.3, pp.259-266.

Makino, Y., Kurobane, Y., Ochi, K., van der Vegte, G.J., and Wilmshurst, S.R. (1996) "Data of Test and Numerical Analysis Results for Unstiffened Tubular Joints", IIW Doc.XV-E-96-220, Miskolc, Hungary.

Morita, M., Makino, Y., Kurobane, Y., and van der Vegte, G.J. (1996) "A new Ultimate Capacity Formula for Unstiffened CHS Joints under Compression - Continuous Formula between T-, TT-, and X-joints", Proc. of 7th Int. Symposium on Tubular Structures, Miskolc, Hungary.

Morita, M., Yamada, Y., Makino, Y., Wilmshurst, S.R., Kurobane, Y., and Lee M.M.K. (1997) "A New Ultimate Capacity Formula for Unstiffened CHS K-Joints under Brace Axial Loads", Proc. of 7th ISOPE Conf., Honolulu, Hawaii.

Togo, T., (1967) "Experimental Study on Mechanical Behavior of Tubular Joints", Doctoral Dissertation, Osaka University, Japan (in Japanese)

Wardenier, J., Kurobane, Y., Packer, J.A., Dutta, D. and Yoemans, N., (1991) "Design Guide for Circular Hollow Section (CHS) Joint under Predominantly Static Loading", Verlag TUV Reinland, Koln, Germany

11. REFERENCES FOR THE DATABASE

Akiyama, N., Yajima, M., Akiyama, H. and Ohtake, A., (1974) "Experimental Study on Strength of Joints in Steel Tubular Structures", Journal of JSSC, Vol. 10, No. 102, pp. 37-68 (in Japanese)

Boone, T. J., Yura, J. A. and Hoadley, P. W., (1982) "Chord Stress Effects on the Ultimate Strength of Tubular Joints", Phil M. Ferguson Structural Eng. Lab. (PMFSEL), Report 82-1, Univ., of Texas, Austin, USA

Dexter E.M., (1994) "Overlapped Tubular Joints in C.H.S.: F.E. Validation and the Effect of Overlap on Strength", Civil Eng. Research Report No. CR/825/94, Univ. College of Swansea

Hlavacek, V., (1970) "Strength of Welded Tubular Joints in Lattice Girders", Construzioni Metalliche, No. 6

Ishikawajima-Harima Heavy Industries Co. Ltd., (1978) "Fatigue Strength of K, T and Y Joints in Tubular Structures", unpublished report (in Japanese)

Koning, C. H. M. de, and Wardenier, J., (1981) "The Static Strength of Welded CHS K-Joints", Stevin Report 6-81-13, Stevin Laboratory, Delft Univ. of Tech., Delft, The Netherlands

Kurobane, Y., (1964) "Welded Truss Joints of Tubular Structural Members", Memoirs, Faculty of Eng., Kumamoto Univ., Japan, Vol. 12, No. 1, pp. 1-39

Kurobane, Y. and Makino, Y., (1965) "Local Stress in Tubular Truss Joints", Research Report, Kyushu Branch of AIJ, No. 4, pp. 75-80 (in Japanese)

Kurobane, Y., Makino, Y., Honda, T. and Mitsui, Y., (1980) "Additional Tests on Tubular K-Joints - with CHS Members under Static Loads", IIW, Doc. XV-460-80, London, pp. 1-15

Makino, Y., Kurobane, Y., Mitsui, Y. and Yasunaga, M., (1978) "Experimental Study on Ultimate Strength of Tubular Joints with High Strength Steel and Heavy Walled Chord", Research Report, Chugoku-Kyushu Branch of AIJ, No. 4, pp. 255-258 (in Japanese)

Makino, Y. (1982) unpublished test results

Makino, Y., Kurobane, Y. and Ochi, K., (1984) "Ultimate Capacity of Tubular Double K-Joints", IIW, Int. Conference on Welding of Tubular Structures, Boston, pp. 451-458

Makino, Y., Kurobane, Y., Takizawa, S., Yamamoto, N. and Oki, H., (1987) "Behavior of Tubular K-Joints - Part 3: Test Results and Estimation of Ultimate Capacity", Research Report, Chugoku-Kyushu Branch of AIJ, No. 7, pp. 321-324 (in Japanese)

Makino, Y., Kurobane, Y. and Paul, J. C., (1993) "Ultimate Behavior of Diaphragm Stiffened Tubular KK-Joints", Proc. of 5th Int. Symposium on Tubular Structures, Nottingham, UK, pp. 465-472

Makino, Y., Kurobane, Y. and Paul, J. C., (1994) "Further Tests on Unstiffened Tubular KK-Joints", Proc. of 5th Int. Conference on Steel Structures, Jakarta, Indonesia, pp.183-190

Nakajima, T., Ishimaru, K., Shimizu, M., Koshihara, T. and Suzuki, K., (1972) "Study on Strength of Welded Joint in Thin-Walled Steel Pipe", Nihon Kokan Technical Report, No. 58, Nihon Kokan Co. Ltd. (in Japanese)

Nishida, Y., Sakamoto, S., Ohtake, A. and Minoshima, N., (1978) "Method for Reinforcing Tubular Truss Joints (Investigation into Optimum Area of Chord Walls with Partially Increased Thickness)", Summary Papers, Annual Conference of AIJ, pp. 1303-1304 (in Japanese)

Ochi, K., Kurobane, Y. and Makino, Y., (1981) "Further Tests on CHS K-Joints with Various d/D ratios", Technical Reports, Vol.30, No.3, Kumamoto Univ., Japan, pp. 119-124

Okushima S., (1984) "Actual Size Tests of Large Scale Tubular K-Joints - Main Roof Trusses of New Osaka International Trade Center No. 3", Nihon Kenchiku Sougo Sikensyo, Report No. IIA-83-58 (in Japanese)

Paul, J. C., Makino, Y. and Kurobane, Y., (1993) "Ultimate Resistance of Tubular Double T-Joints under Axial Brace Loading", Journal of Constructional Steel Research, Vol. 24, No. 3, pp. 205-228

Paul, J. C., Ueno, T., Makino, Y. and Kurobane, Y., (1993) "Ultimate Behavior of Multiplanar Double K-Joints", Int. Journal of ISOPE, Vol. 3, No. 1, pp. 43-50

Reber, J. B., (1972) "Ultimate Strength Design of Tubular Joints," Proc., Offshore Technology Conference, Paper No. OTC 1664

Sanders, D. H. and Yura, J. A., (1986) "Ultimate Strength and Behavior of Double-Tee Tubular Joints in Tension", Phil M. Ferguson Structural Eng. Lab. (PMFSEL), Report 86-2, Univ., of Texas, Austin, USA

Stamenkovic, A. and Sparrow, K.D., (1983) "Load Interaction in T-Joints of Steel Circular Hollow Sections", Journal of Structural Engineering, ASCE, Vol.109, No.9

Sumitomo Metal Industries Co. Ltd., (1976) unpublished report (in Japanese)

Takizawa, S., Yamamoto, N., Mihara, J. and Ohkata, S., (1979) " Full Scale Experiments of Tee and Cross Type Tubular Joints under Static and Cyclic Loading", Tech. Reports, Kawasaki Steel Tech. Review, Vol. 11, No. 2, Kawasaki Steel Corp., pp. 115-125

Togo, T., (1967) "Experimental Study on Mechanical Behavior of Tubular Joints", Doctoral Dissertation, Osaka Univ., Japan (in Japanese)

Toprac, A. A. and Louis, B. G., (1970) "Research on the Fatigue Behaviour of Tubular Connections", Structures Fatigue Research Lab. (SFRL), Tech. Report P550-13, Univ. of Texas, Austin, USA

Vegte, G. J. van der, Koning C. H. M. de, Puthli, R. S. and Wardenier, J., (1990) "Static Behaviour of Multiplanar Welded Joints in Circular Hollow Sections", Stevin Report 25.6.90.13/A1/11.03, TNO-IBBC Report BI-90-106/63.5.3860, Delft, The Netherlands

Vegte, G. J. van der, Puthli. R. S. and Wardenier, J., (1991) "The Influence of the Chord and Can Length on the Static Strength of Uniplanar Tubular Steel X-Joints", Proc. of 4th Int. Symposium on Tubular Structures, Delft, The Netherlands, pp. 435-447

Vegte, G. J. van der, (1995) "The Static Strength of Uniplanar and Multiplanar Tubular T- and X-Joints", Doctoral Thesis, Delft Univ. of Tech., The Netherlands

Wardenier, J. and Koning, C. H. M., (1977) "Investigation into the Static Strength of Welded Warren Type Joints Made of Circular Hollow Sections", Stevin Report No. B1-77-19, Stevin Lab., Delft Univ. of Technology, Delft, The Netherlands

Washio, K. and Kurobane, Y., (1963) "Truss Joint in Tubular Steel Structures (Preliminary Report)", Tech. Reports, Osaka Univ., Japan, Vol. 13, No. 553, pp. 147-163

Wilmshurst, S. R. (1995) "The Ultimate Load Behavior of Multiplanar KK-joints Subjected to Symmetrical and Anti-Symmetrical Axial Loading", Doctoral Thesis, University of Wales, Swansea, U.K..

Yura, J. A., Howell, L. E. and Frank, K. H., (1978) "Ultimate Load Tests on Tubular Connections", Civil Engineering Structures Research Lab., Univ. of Texas, Report No.78-1, Univ. of Texas

Tubular Structures VIII, Choo & Van der Vegte (eds) © 1998 Balkema, Rotterdam, ISBN 90 5809 001 9

Effect of boundary conditions and chord preload on the strength of RHS uniplanar gap K-joints

D.K. Liu, Y.Yu & J.Wardenier
Delft University of Technology, Netherlands

ABSTRACT: It is known that the boundary conditions implemented in tests and / or numerical analyses may have an effect on the strength of RHS and CHS K-joints. The boundary condition effect therefore should be given careful consideration when using a database containing tests or numerical data for joints having different boundary conditions. The objective of the current study is to investigate more in detail the sensitivity of the strength of RHS uniplanar gap K-joints to the boundary conditions and the chord preloads.

1 INTRODUCTION

The load and boundary conditions applied at the brace and chord ends are intended to reflect boundary conditions a joint encounters within a girder. Various load and boundary conditions have been applied in tests and / or numerical calculations of RHS and CHS K-joints. The boundary condition effects on the capacity of K-joints have been studied in previous investigations [1,2,3,4,5]. The conclusion from these studies seems different.

Bjornoy [2] indicated that there is a strong influence of boundary conditions on the capacity of K-joints in CHS, especially for eccentric overlapped joints. Connelly [3] discovered the same phenomenon and attributed the highest capacities to those joints embedded within a frame. Healy [4] studied the influence of so-called "single" boundary conditions and "double" boundary conditions on the capacity of overlapped CHS K-joints and found that the difference between "single" and "double" boundary conditions is negligible when the lateral movement of the braces is restrained. Dexter and Lee [1] concluded that boundary conditions may have a large effect on joint strength, even for the relatively large chord length used. Davies and Kelly [5] investigated boundary condition effect on the capacity of overlapped RHS K- and X-joints. Their results indicated that the boundary condition effects vary with the inclination of brace members to the chord.

A finite element (FE) parametric study has been initiated with the aim of studying the boundary condition and chord preload on the capacity of RHS uniplanar and multiplanar gap K-joints more in detail. The first stage of the study was aimed at RHS uniplanar gap K-joints. In the FE study a basic gap K-joint has been considered. The brace/chord width ratio β is 0.6, the angle of the brace member to the chord is 45 degrees and the eccentricity e is zero. For the chord width to chord thickness ratio three values are considered i.e. 2γ is 15.5, 24.5 and 34.5 respectively.

2 THE JOINT AND THE BOUNDARY CONDITIONS

2.1 *Joint configuration*

The configuration of the joint is shown in Figure 1.

The dimensions of the joint are simply copied from the multiplanar K-joint KK06 published in [6], in order to facilitate the investigation on the effect of multiplanarity on the capacity of the joint which will be published in a separate paper at this conference. The steel grade is taken as S 355 with a nominal f_y = 355N/mm^2.

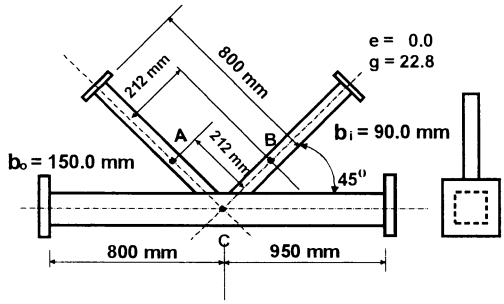

Figure 1 Configuration of the joint.

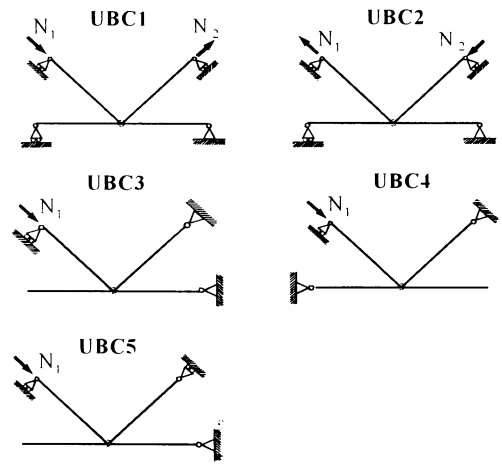

Figure 2 Boundary conditions.

To investigate the possible interaction between the boundary conditions and the chord width to chord thickness ratio 2γ three different groups of joints listed in Table 1 are numerically studied for various boundary conditions.

2.2 *Boundary conditions*

The boundary conditions considered in the study are shown in Figure 2.

The boundary conditions considered here are meant to be representative for the basic configurations commonly used in tests and numerical analyses. The reaction force in the chord for boundary conditions UBC1, UBC3 and UBC5 is compressive, while for boundary conditions UBC2 and UBC4 the reaction force in the chord is tensile.

2.3 *Finite element modelling*

Due to symmetry of the joint only half of the joint was modelled. Eight noded isoparametric thick shell elements (MARC element type 22) were used to model the chord, the braces as well as the welds, based on the experience from massive previous numerical analyses [8,10]. A typical finite element mesh used in the analyses is shown in Figure 3, having a total of 948 elements. Both geometrical and material nonlinearity, simulated by true stress-strain relationship, were used throughout. The same material property is used for the chord, the braces and the welds. Thick end plates were included in the model at the chord and brace ends to apply the loads and the boundary conditions. Corner radii were modelled for both the chord and the braces.

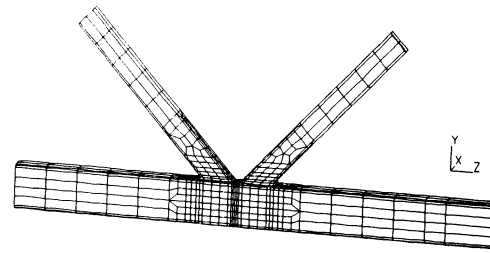

Figure 3 Finite element mesh.

3. RESULTS AND DISCUSSIONS

3.1 *Results for the joints without a chord preload*

Fifteen analyses (three series; one series for each 2γ) were undertaken. The capacities of the joints were determined based on a perpendicular indentation of 3% of the chord width, and compared with the CIDECT [7] design capacity predictions in Tables 2, 3 and 4 for 2γ=15.5, 24.5 and 34.5 respectively. Load-deformation curves for the three series are shown in Figures 4, 5 and 6. The deformations are taken as the change in length between two points A and C for the left brace and B and C for the right brace, as indicated in Figure 1. The results are plotted in Figure 7 in relation to the CIDECT design capacity.

Table 1 Joints dimensions.

JOINT	b_o (mm)	t_o (mm)	b_i (mm)	t_i (mm)	β (≈)	2γ	f_{yo} (N/mm^2)	f_{yi} (N/mm^2)
UBC-15	151	9.74	89	8.1	0.6	15.5	355	355
UBC-25	147	6	89	8.1	0.6	24.5	355	355
UBC-35	145	4.2	89	8.1	0.6	34.5	355	355

Table 2 FE capacities for different boundary conditions. 2γ=15.5. N_{OP} = 0.

JOINT	$N_u(3\%b_o)$ (kN)	FAILURE MODE	$N_{CIDECT,DES}$ (kN)	$N_u/N_{CIDECT,DES}$
UBC1-15	674	CHORD FACE FLEXURAL FAILURE	637	1.06
UBC2-15	693	CHORD FACE FLEXURAL FAILURE	699	0.99
UBC3-15	677	CHORD FACE FLEXURAL FAILURE	637	1.06
UBC4-15	695	CHORD FACE FLEXURAL FAILURE	699	0.99
UBC5-15	677	CHORD FACE FLEXURAL FAILURE	637	1.06

Table 3 FE capacities for different boundary conditions. 2γ=24.5. N_{OP} = 0.

JOINT	N_u ($3\%b_o$) (kN)	FAILURE MODE	$N_{CIDECT,DES}$ (KN)	$N_u/N_{CIDECT,DES}$
UBC1-25	307	CHORD FACE FLEXURAL FAILURE	336	0.91
UBC2-25	338	CHORD FACE FLEXURAL FAILURE	342	0.99
UBC3-25	308	CHORD FACE FLEXURAL FAILURE	336	0.92
UBC4-25	338	CHORD FACE FLEXURAL FAILURE	342	0.99
UBC5-25	307	CHORD FACE FLEXURAL FAILURE	336	0.91

Table 4 FE capacities for different boundary conditions. 2γ=34.5. N_{OP} = 0.

JOINT	$N_u(3\%b_o)$ (kN)	FAILURE MODE	$N_{CIDECT,DES}$ (KN)	$N_u/N_{CIDECT,DES}$
UBC1-35	175	CHORD FACE FLEXURAL FAILURE	202	0.87
UBC2-35	206	CHORD FACE FLEXURAL FAILURE	202	1.02
UBC3-35	174	CHORD FACE FLEXURAL FAILURE	202	0.86
UBC4-35	208	CHORD FACE FLEXURAL FAILURE	202	1.03
UBC5-35	173	CHORD FACE FLEXURAL FAILURE	202	0.86

3.2 Results for the joints with a chord preload

In order to study the effects of a tensile chord preload, twenty two analyses were undertaken. For the first fifteen analyses (three series; one series for each 2γ), the chord preload (in tension) is taken as $N_{OP} = N_1 COS(\pi/4)$. The ultimate loads based on an indentation of 3% of the chord width are tabulated and compared with the CIDECT design capacity predictions in Tables 5, 6 and 7 for 2γ=15.5, 24.5 and 34.5 respectively. Load-deformation curves for three series are shown in Figures 8, 9 and 10. The same deformation limit as mentioned above are considered and the indentations are calculated based on the measured deformation and the undeformed joint configuration. The ultimate loads related to the CIDECT design strengths vs parameter 2γ plots are shown in Figure 11.

In addition, four analyses were carried out for the joints of UBC1-15, UBC2-15, UBC1-35 and UBC2-35 with a chord preload (in tension) N_{OP} =

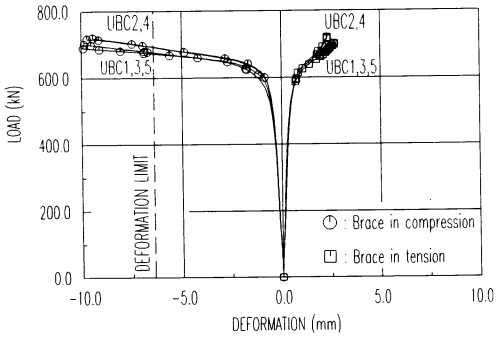

Figure 4 Load vs deformation plots for various boundary conditions. N_{OP} = 0. 2γ=15.5.

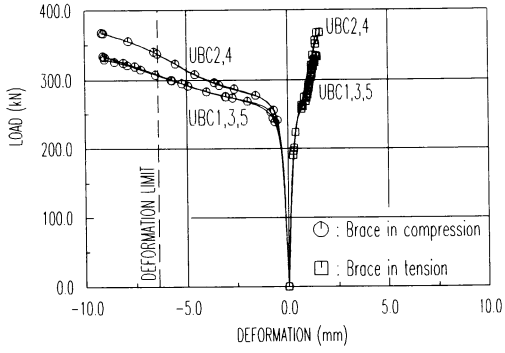

Figure 5 Load vs deformation plots for various boundary conditions. N_{OP} = 0. 2γ=24.5.

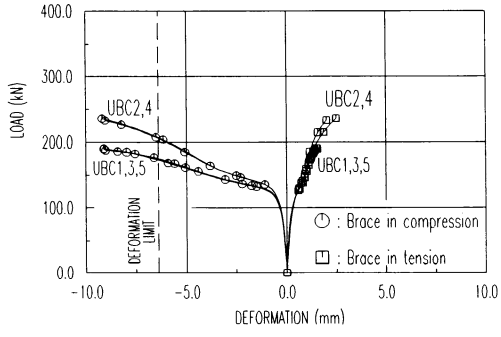

Figure 6 Load vs deformation plots for various boundary conditions. N_{OP} = 0. 2γ=34.5.

$2N_1COS(\pi/4)$. Load-deformation curves for these four analyses are shown in Figures 12 to 15 alongside with the load-deformation curves obtained for N_{OP}= $N_1COS(\pi/4)$ and N_{OP} = 0.

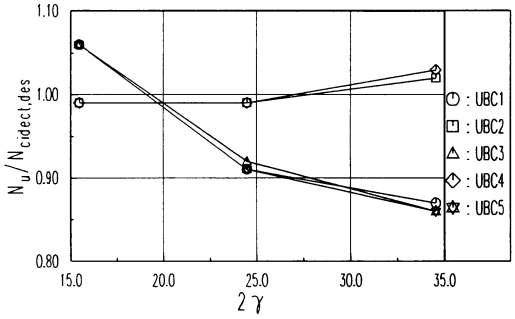

Figure 7 Load vs 2γ plots for various boundary conditions. N_{OP} = 0.

3.3 *Discussion*

3.3.1 *Discussion for the joints without a chord preload*

As can be observed from Table 2 to 4 the failure mode for the joints modelled with boundary conditions UBC1 to UBC5 is chord face flexural failure, as expected.

Two different groups of load-deformation relationships are observed in Figures 4 to 6. One group is for the joint modelled with boundary conditions UBC2 and UBC4 for which the chord is loaded in tension. The second group is for the joint modelled with boundary conditions UBC1, UBC3 and UBC5 for which the chord is loaded in compression combined with a potential secondary bending moment. It can be seen from Figures 4 to 7 that the difference between the two groups increases with increasing value of 2γ. Variations in capacity of up to 8% and 17% have resulted for 2γ=24.5 and 2γ=34.5 respectively, when the capacity of the joint is determined based on a deformation limit of $3\%b_0$.

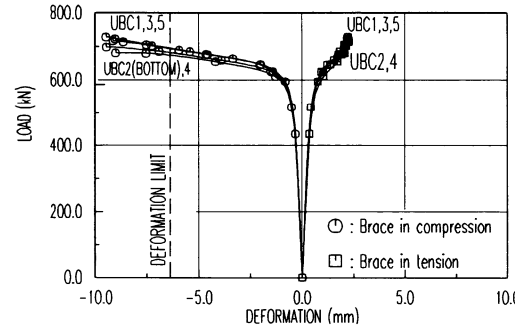

Figure 8 Load vs deformation plots for various boundary conditions. $N_{OP}=N_1$ COS(π/4). 2γ=15.5.

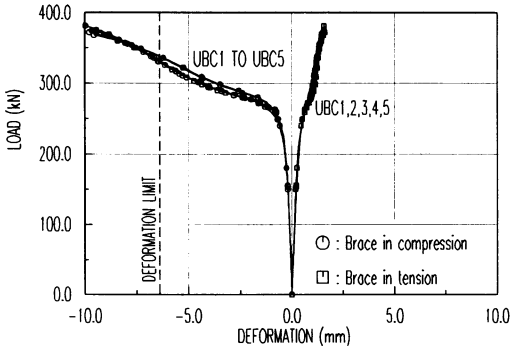

Figure 9 Load vs deformation plots for various boundary conditions. $N_{OP} = N_1 \cos(\pi/4)$. $2\gamma=24.5$.

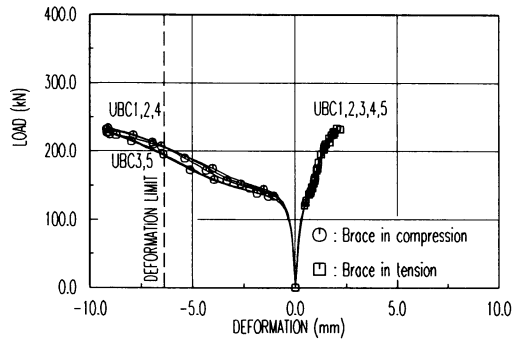

Figure 10 Load vs deformation plots for various boundary conditions. $N_{OP} = N_1 \cos(\pi/4)$. $2\gamma=34.5$.

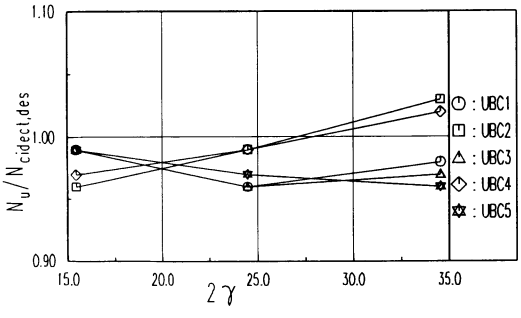

Figure 11 Load vs 2γ plots for various boundary conditions. $N_{OP} = N_1 \cos(\pi/4)$.

3.3.2 *Discussion for the joints with a chord preload*

As indicated in Tables 5 to 7 the failure modes for the joints with a tensile chord preload ($N_{OP} = N_1 \cos(\pi/4)$) are characterized by the chord face flexural failure for all boundary conditions.

Figures 8 to 11 show that there is little difference for the strength behaviour of the joint modelled with different boundary conditions if the chord is loaded by a tensile chord preload $N_{OP} = N_1 \cos(\pi/4)$. For the joint with $2\gamma = 15.5$ the maximum difference for the capacities of the joint for the different boundary conditions is about 3%. The same variation is found for the joint with $2\gamma = 24.5$. For the joint with $2\gamma = 34.5$, the maximum difference is increased to 7%.

Figure 13 shows that a large N_{OP}, for instance $N_{OP} = 2N_1 \cos(\pi/4)$, could lead to a chord plastic failure. For the joint UBC1-35, Figure 14 indicates that applying a tensile chord preload ($N_{OP} = N_1 \cos(\pi/4)$ or $N_{OP} = 2N_1 \cos(\pi/4)$) influences the strength behaviour of the joint if the chord is originally loaded in compression. If the chord was already in tension the effect of N_{OP} is very limited, as indicated in Figure 15 for UBC2-35.

Figures 4 to 7 and Figures 8 to 11 also show that the ultimate joint load capacity is dependent upon the deformation criteria which are used to determine the ultimate joint load capacity. It has been shown [9] that a variation in capacity of up to 11% may be conducted for the joint with $2\gamma=34.5$ if e.g. the deformation limit used would be $4\%b_0$ instead of $3\%b_0$.

4 CONCLUSIONS

In this paper the effect of boundary conditions and the chord preload on the strength behaviour of RHS uniplanar gap K-joint has been investigated for the joint shown in Figure 1.

(a) For the particular joint investigated ($\beta=0.6$, $\theta=45°$ and $e=0$), boundary conditions may have a considerable effect on the joint strength. The effect varies with the chord width to thickness ratio, and the effect is highly dependent on the chord axial load.

(b) As shown in Figure 7 the numerically determined joint strengths at a deformation limit of $3\%b_0$ for the joints for which the chords are in tension are more in agreement with the predicted CIDECT design capacities than those for which the chords are in compression.

(c) For this particular joint the ultimate joint load capacity is dependent upon the ultimate deformation criterion used, particularly for the joint with high chord width to chord thickness ratio.

Table 5 FE capacities for different boundary conditions. $2\gamma=15.5$. $N_{OP} = N_1 COS(\pi/4)$.

JOINT	$N_u(3\%b_o)$ (kN)	FAILURE MODE	$N_{CIDECT,DES}$ (kN)	$N_u/N_{CIDECT,DES}$
UBC1-15-Nop	694	CHORD FACE FLEXURAL FAILURE	699	0.99
UBC2-15-Nop	672	CHORD FACE FLEXURAL FAILURE	699	0.96
UBC3-15-Nop	693	CHORD FACE FLEXURAL FAILURE	699	0.99
UBC4--15-Nop	681	CHORD FACE FLEXURAL FAILURE	699	0.97
UBC5-15--Nop	693	CHORD FACE FLEXURAL FAILURE	699	0.99

Table 6 FE capacities for different boundary conditions. $2\gamma=24.5$. $N_{OP} = N_1 COS(\pi/4)$.

JOINT	$N_u(3\%b_o)$ (kN)	FAILURE MODE	$N_{CIDECT,DES}$ (KN)	$N_u/N_{CIDECT,DES}$
UBC1-25-Nop	330	CHORD FACE FLEXURAL FAILURE	342	0.96
UBC2-25-Nop	338	CHORD FACE FLEXURAL FAILURE	342	0.99
UBC3-25-Nop	328	CHORD FACE FLEXURAL FAILURE	342	0.96
UBC4-25-Nop	338	CHORD FACE FLEXURAL FAILURE	342	0.99
UBC5-25-Nop	330	CHORD FACE FLEXURAL FAILURE	342	0.97

Table 7 FE capacities for different boundary conditions. $2\gamma=34.5$. $N_{OP} = N_1 COS(\pi/4)$.

JOINT	$N_u(3\%b_o)$ (kN)	FAILURE MODE	$N_{CIDECT,DES}$ (kN)	$N_u/N_{CIDECT,DES}$
UBC1-35-Nop	198	CHORD FACE FLEXURAL FAILURE	202	0.98
UBC2-35-Nop	207	CHORD FACE FLEXURAL FAILURE	202	1.03
UBC3-35-Nop	195	CHORD FACE FLEXURAL FAILURE	202	0.97
UBC4-35-Nop	206	CHORD FACE FLEXURAL FAILURE	202	1.02
UBC5-35-Nop	193	CHORD FACE FLEXURAL FAILURE	202	0.96

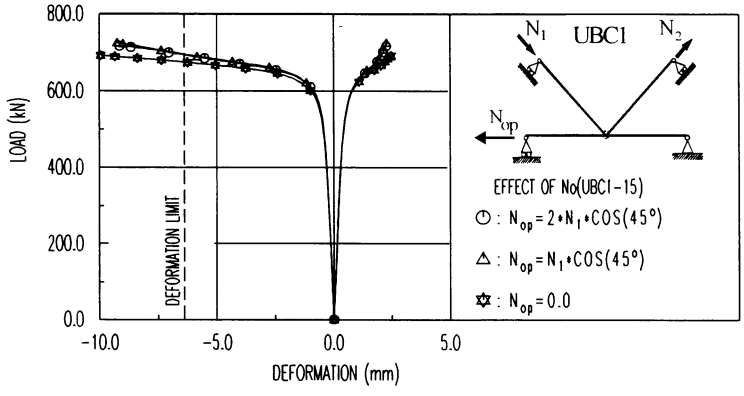

Figure 12 Load vs deformation plots for joint UBC1-15 for different chord preload N_{OP}. $2\gamma=15.5$.

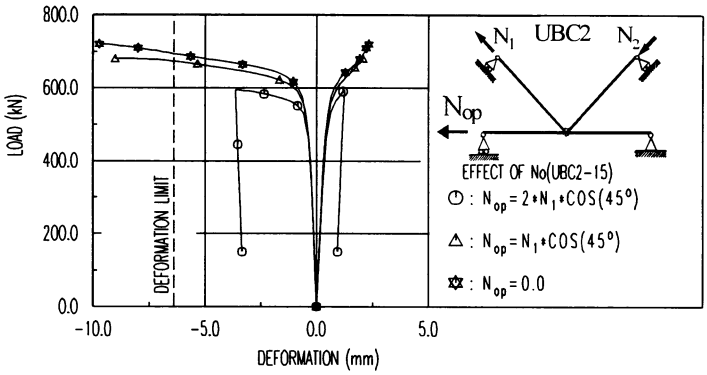

Figure 13 Load vs deformation plots for joint UBC2-15 for different chord preload N_{OP}. 2γ=15.5.

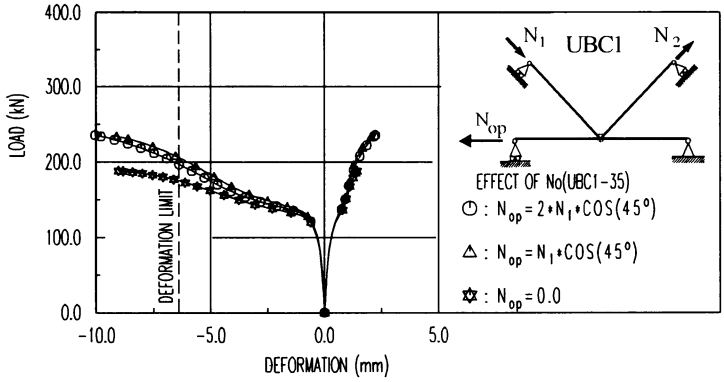

Figure 14 Load vs deformation plots for joint UBC1-35 for different chord preload N_{OP}. 2γ=34.5.

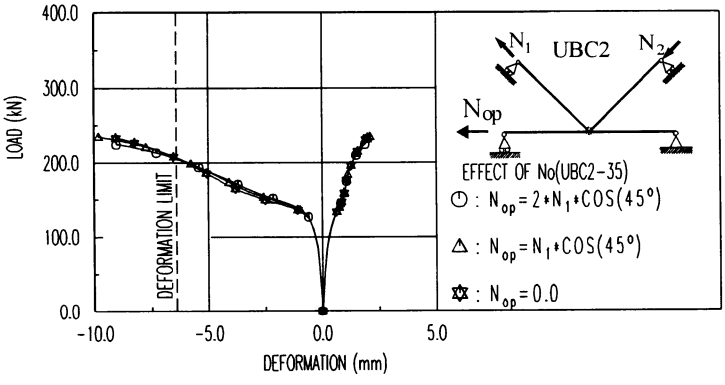

Figure 15 Load vs deformation plots for joint UBC2-35 for different chord preload N_{OP}. 2γ=34.5.

5 LIST OF SYMBOLS

A_o	Cross-section area of chord
N_{OP}	Chord preload
N_1, N_2	Axial force applied to brace
N_u	Connection resistance
$N_{CIDECT,DES}$	CIDECT design connection resistance
b_o	External width of square hollow section chord
b_i	External width of square hollow section brace i
e	Noding eccentricity for a connection
f_{yo}	Yield stress of chord
f_{yi}	Yield stress of brace i
g	Gap between the bracing members of a K-(KK-)connection
t_o	Thickness of square hollow section chord
t_i	Thickness of square hollow section brace i
β	Width ratio between bracing member(s) and chord
γ	Half width to thickness ratio of the chord
θ	Included angle between bracing member and the chord

REFERENCES

[1] E.M. Dexter et al. 1994. "Effect of overlap on strength of K-joints in CHS tubular members", Tubular structures VI, Proceedings of Sixth International Symposium on Tubular Structures, Australia.

[2] O.H. Bjornoy 1991. "Static strength of tubular joints, Phase II. Analyses and tests of gap and overlap K-joints", Veritec Report No. 91-3393, A.S. Veritec.

[3] M. Connelly et al. 1989. "Frame behaviour effects on tubular joints capacity", Tubular Structures III, Proceedings of Third International Symposium on Tubular Structures, Finland.

[4] B.E. Healy 1994. "A numerical investigation into the capacity of overlapped circular K-joints", Tubular Structures VI, Proceedings of Sixth International Symposium on Tubular Structures, Australia.

[5] G. Davies et al. 1996. "Effect of angle on the strength of overlapped RHS K- and X-joints", Tubular Structures VII, Proceedings of Seventh International Symposium on Tubular Structures, Hungary.

[6] M.A. O'connor 1993. "Static strength of multipanar K- joints in rectangular hollow sections", Tubular Structures V, Proceedings of Fifth International Symposium on Tubular Structures, United Kingdom.

[7] J. Packer et al. 1992. "CIDECT - Design guide for rectangular hollow section (RHS) joints under predominantly static loading". Verlag TÜV Rheinland GmbH, Koln.

[8] D. K. Liu et al. 1993. "Static strength of multiplanar DX joints in rectangular hollow sections", Tubular Structures V, Proceedings of Fifth International Symposium on Tubular Structures, United Kingdom.

[9] D. K. Liu et al. 1997. "Effect of boundary conditions and chord loads on the strength of RHS uniplanar GAP K- joints", Stevin Report No. 6-97-21, Faculty of Civil Engineering and Geosciences, Delft University of Technology.

[10] Y. Yu 1997. "The static strength of uniplanar and multiplanar connections in rectangular hollow sections", Ph. D thesis, Delft University Press, The Netherlands.

Tubular Structures VIII, Choo & Van der Vegte (eds) © 1998 Balkema, Rotterdam, ISBN 90 5809 001 9

Effect of boundary conditions and chord preload on the strength of RHS multiplanar gap KK-joints

D.K. Liu, Y.Yu & J.Wardenier
Delft University of Technology, Netherlands

ABSTRACT: It has been shown that the boundary conditions and the chord preloads may sometimes have a considerable effect on the strength of rectangular hollow section (RHS) uniplanar gap K-joints. The objective of the current study is to investigate in more detail the sensitivity of the strength of RHS multiplanar gap K-joints with respect to the boundary conditions and the chord preload.

1 INTRODUCTION

The load and boundary conditions applied at the brace and chord ends are intended to reflect the boundary conditions a joint encounters within a girder. Various load and boundary conditions have been applied in tests and/or numerical calculations of rectangular hollow section (RHS) and circular hollow section (CHS) K-joints. The boundary condition effects on the capacity of uniplanar K-joints have been studied in previous investigations [1 to 6]. These indicate that the boundary conditions and the chord preload may sometimes have a considerable effect on the strength of RHS uniplanar gap K-joints.

Less attention has been devoted to multiplanar connections between RHS compared to connections between CHS. Based on limited experimental evidence a correction factor of 0.9 has been recommended by CIDECT [9] to apply to the uniplanar connection resistance. To address this deficiency in the design process, an ECSC funded research programme was carried out to investigate the effect of the multiplanar interactions on the static strength of RHS KK-joints [7,8]. It is noted [7,8] that for all specimens in this investigation the chord is supported at the chord ends and a tension force is applied to the chord to prevent a failure by yielding of the chord.

A finite element (FE) parametric study has been initiated with the aim to study the effect of the boundary conditions and the chord preload on the capacity of RHS uniplanar and multiplanar gap K-joints. This second stage of the study deals with RHS multiplanar gap KK-joint. In the FE study a basic KK-gap joint has been considered. The nominal value of the chord width to chord thickness ratio i.e. 2γ is 15. The nominal brace to chord width ratio β is 0.6, the angle of the brace member to the chord is 45 degrees and the eccentricity e is zero. Consequently the value of gap is g=22.8 mm.

2 THE JOINT AND THE BOUNDARY CONDITIONS

2.1 *Joint configuration*

The configuration of the joint is shown in Figure 1.

The dimensions of the joint are the same as the multiplanar KK-joint KK06 published in [7] for which the measured dimensions are as follows : b_o = 150.6, b_i = 89.0, t_o = 9.74 and t_i = 8.09. The FE model is based on the measured dimensions. The steel grade S 355 with a design value f_y =355 N/mm^2 is used in the analyses.

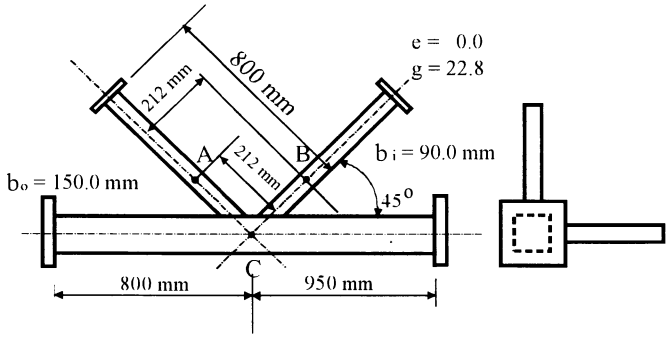

Figure 1 Configuration of the joint

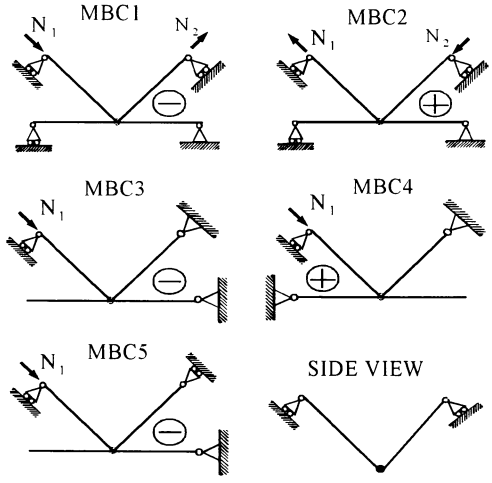

Figure 2 Boundary conditions

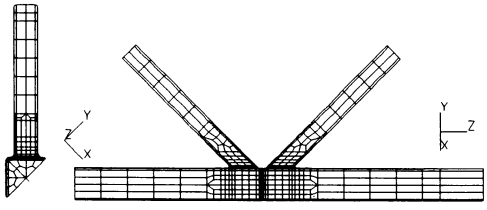

Figure 3 Finite element mesh

2.2 *Boundary conditions*

The boundary conditions considered in the study are shown in Figure 2.

The boundary conditions considered here are meant to be representative for the basic configurations commonly used in tests and numerical analyses. The reaction force on the chord for boundary conditions MBC1, MBC3 and MBC5 is compressive, while for boundary conditions MBC2 and MBC4 the reaction force in the chord is tensile.

2.3 *Finite element modelling*

Due to symmetry of the joint only half of the joint was modelled. Based on the experience from massive previous numerical analyses [10,12] eight noded isoparametric thick shell elements (MARC element type 22) were used to model the chord, the braces as well as the welds. A typical finite element mesh used in the analyses is shown in Figure 3, having a total of 1332 elements. Both geometrical and material nonlinearity, simulated by true stress-strain relationship were used throughout. The same material property was used for the chord, the braces and the welds. Thick end plates were included in the model at the chord and brace ends to apply the loads and the boundary conditions. Corner radii were modelled for both the chord and the braces.

3 RESULTS AND DISCUSSIONS

3.1 Numerical results

Twenty analyses (four for each boundary condition) were undertaken. The capacities of the joints are tabulated in Table 1 for different boundary conditions with different chord preloads N_{OP}. It should be noted that a positive value for N_{OP} represents a tensile chord preload. The capacities of the joints were determined either by the maximum load if it appears before the

deformation limit, or based on a perpendicular indentation of 3% of the chord width. The indentations were calculated based on the measured deformation. The theoretical chord reactions (axial loading), $N_{o,t}$, associated with the ultimate capacity, N_u , are listed in Table 2 for the different boundary conditions, and compared with the numerical results in Table 3. In Table 4 the ultimate loads obtained in the multiplanar model are compared with those obtained in the uniplanar model in [1] to assess the multiplanar effect.

The plots of the joint capacities and the chord reactions (axial loading) are displayed in Figure 5 for different boundary conditions with different chord preloads. As an example, the load-deformation curves for boundary condition MBC1, together with the load-deformation plots obtained for the comparable uniplanar joint, are shown in Figure 4. The deformations are measured as the change in length between two points A and C for the left brace and B and C for the right brace, as indicated in Figure 1. The deformation modes for the different boundary conditions with $N_{OP} = 0$ are plotted in Figure 6. An amplification factor of 5 is used in the figures.

3.2 Discussion

3.2.1 Discussion for the joint without a chord preload

As for uniplanar joints two different groups of joint behaviour are observed in Table 1 and in Figure 5. One group is for the joint modelled with boundary conditions MBC2 and MBC4 for which the chord is loaded in tension. The second group is for the joint modelled with boundary conditions MBC1, MBC3 and MBC5 for which the chord is loaded in compression. The ultimate capacities found for the group MBC2 and MBC4 are higher in comparison with the ultimate capacities found for the group of MBC1, MBC3 and MBC5.

Based on the numerical results in [11] and the plots shown in Figure 5 it is concluded that the failure mode for all five boundary conditions without a chord preload is characterized by chord face failure. The chord axial loading (N_o /(A_o f_{yo})) influences the load capacity of the joint considerably. Table 4 indicates that for the particular case investigated the multiplanar effect reduction factor may be less than 0.9 due to the chord loading effect.

The support reaction forces along the chord axis are shown in figure 7 for different boundary conditions. It shows that the support reaction force caused by boundary conditions MBC1, MBC3 and MBC5 tends to increase the secondary bending moment in the chord, leading to a lower capacity of the joint, while the support reaction force caused by boundary conditions MBC2 and MBC4 tends to reduce the secondary bending moment, leading to a higher capacity of the joint.

3.2.2 *Discussion for the joint with a tensile chord preload*

As indicated in Figure 5 the failure mode for the joint modelled with boundary conditions MBC2 and MBC4, subjected to a tensile chord preload N_{OP} $=2N_1COS(\pi/4)$ or $N_{OP}=3N_1COS(\pi/4)$, is characterized by chord global yielding caused by the high tensile chord reaction force.

The numerical results [11] indicated that the failure mode for the joint modelled with boundary conditions MBC1, MBC3 and MBC5, subjected to a tensile chord preload ($N_{OP}=2N_1COS(\pi/4)$ or $N_{OP}=3N_1$ $COS(\pi/4)$), is characterized by chord face failure. The strength behaviour for the joints modelled with these boundary conditions is basically the same. Table 4 indicates that the difference in the capacities obtained in the multiplanar model in comparison with those obtained in the uniplanar model is negligible. The ultimate capacities based on the deformation limit are very close to each other despite the fact that the chord reaction in compression is in the case of N_{OP} = $2N_1COS(\pi/4)$ twice as high as the chord reaction in the case of $N_{OP}=3N_1COS(\pi/4)$ (see Table 2), however in both cases the chord compressive load is rather low and does not exceed 0.5 times the squash load of the chord.

3.2.3 Discussion for the joint with a compressive chord preload

As indicated in Table 4 and Figure 5 the failure mode for the joint modelled with boundary conditions MBC1, MBC3 and MBC5, subjected to a compressive chord preload N_{OP}= $-2N_1COS(\pi/4)$, is characterized by chord global yielding caused by the high compressive chord reaction force.

Table 1 FE capacities N_u for different boundary conditions with different chord preloads N_{OP}

BOUNDARY CONDITION	N_u (kN)			
	$N_{OP} = -2N_1COS(45^0)$	$N_{OP} = 0.0$	$N_{OP} = 2N_1COS(45^0)$	$N_{OP} = 3N_1COS(45^0)$
MBC1	443	574	678	673
MBC3	443	574	677	675
MBC5	443	574	677	675
MBC2	678	610	448	387
MBC4	679	635	472	407

Table 2 Theoretical chord reaction (axial loading) $N_{0,t}$

BOUNDARY CONDITION	$N_{0,t}$							
	$N_{OP}=-2N_uCOS(45°)$		$N_{OP}=0.0$		$N_{OP}=2N_uCOS(45°)$		$N_{OP}=3N_uCOS(45°)$	
	L	R	L	R	L	R	L	R
M/UBC1	2xC	6xC	0	4xC	2xT	2xC	3xT	1xC
M/UBC3	2xC	6xC	0	4xC	2xT	2xC	3xT	1xC
M/UBC5	2xC	6xC	0	4xC	2xT	2xC	3xT	1xC
M/UBC2	2xC	2xT	0	4xT	2xT	6xT	3xT	7xT
M/UBC4	2xT	2xC	4xT	0	6xT	2xT	7xT	3xT

C : Compression, $C = N_uCOS(45^0)$

T : Tension, $T = N_uCOS(45^0)$

L : Left part of the Chord; **R** : Right part of the chord

Table 3 Comparison between the numerical and theoretical chord reactions (axial loading)

BOUNDARY CONDITION	$N_{OP} = -2N_uCOS(45^0)$		$N_{OP}=0.0$		$N_{OP} = 2N_uCOS(45^0)$		$N_{OP} = 3N_uCOS(45^0)$	
	$N_{o,n}$	$N_{o,n}/N_{o,t}$	$N_{o,n}$	$N_{o,n}/N_{o,t}$	$N_{o,n}$	$N_{o,n}/N_{o,t}$	$N_{o,n}$	$N_{o,n}/N_{o,t}$
MBC1	1874 (-)	1	1624 (-)	1	931 (-)	0.97	479 (-)	1.01
MBC3	1881 (-)	1	1636 (-)	1.01	966 (-)	1.01	465 (-)	0.98
MBC5	1882 (-)	1	1636 (-)	1.01	967 (-)	1.01	468 (-)	0.98
MBC2	954 (+)	1	1732 (+)	1	1901 (+)	1	1913 (+)	1
MBC4	954 (+)	0.99	1701 (+)	0.95	1892 (+)	0.95	1880 (+)	0.93

$N_{o,n}$: Numerical value; $N_{o,t}$: Theoretical value; **(+)** : Tension **(-)** : Compression

The failure mode for the joint modelled with boundary conditions MBC2 and MBC4, subjected to a compressive chord preload $N_{OP} = -2N_1COS(\pi/4)$, is characterized by chord face failure. The numerical results [11] show that the strength and behaviour of the joints modelled with these two boundary conditions is basically the same. As indicated in Table 4, the difference in the strength behaviour between the uniplanar K-joint and the multiplanar KK-joint is only about 2%. The ultimate capacities for these two particular boundary conditions are very close to the ultimate capacities obtained for the joint modelled with boundary conditions MBC1, MBC3 and MBC5 subjected to a tensile chord preload $N_{OP} = 2N_1$

Table 4 Multiplanar effect (the capacities of the multiplanar joint, $N_{u,m}$, in comparison with the capacities of the uniplanar joint, $N_{u,u}$, with N_{OP}=0.0 and the same boundary conditions)

BOUNDARY CONDITION	N_{OP} = $-2N_uCOS(45^o)$		N_{OP}=0.0		N_{OP} = $2N_uCOS(45^o)$		N_{OP} = $3N_uCOS(45^o)$	
	$N_{u,m}$	$N_{u,m}/N_{u,u}$	$N_{u,m}$	$N_{u,m}/N_{u,u}$	$N_{u,m}$	$N_{u,m}/N_{u,u}$	$N_{u,m}$	$N_{u,m}/N_{u,u}$
M/UBC1	443 [1]	----	574	0.85	678	1.01	673	1.00
M/UBC3	443 [1]	----	574	0.85	677	1.00	675	1.00
M/UBC5	443 [1]	----	574	0.85	677	1.00	675	1.00
M/UBC2	678	0.98	610	0.88	448 [1]	----	387 [1]	----
M/UBC4	679	0.98	635	0.91	472 [1]	----	387 [1]	----

[1] Chord global yielding for high chord reaction (axial loading), as indicated in Figure 5.
$(N_o + N_{OP})/(A_o * f_{yo}) = 0.98$ to 1.00

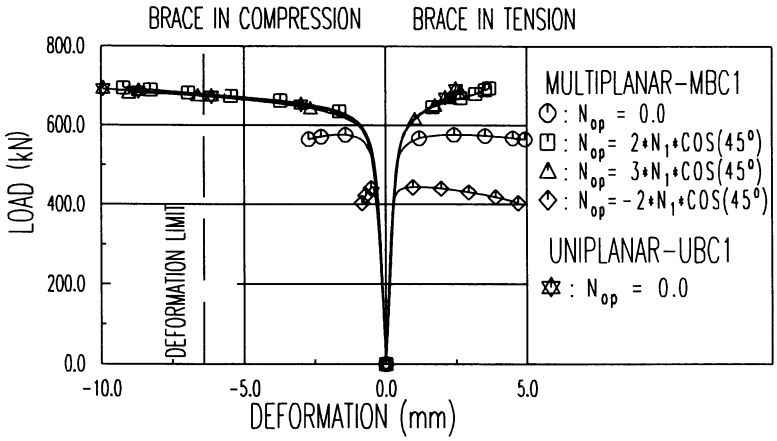

Figure 4 Load vs deformation plots for boundary condition MBC1 with different chord preloads.

$COS(\pi/4)$ or $N_{OP} = 3N_1COS(\pi/4)$, despite the fact that the chord reaction force for these two cases is different (see Table 2).

4 CONCLUSIONS

In this paper the effect of boundary conditions and the chord preload on the strength behaviour of RHS multiplanar gap KK-joint has been investigated for the joint shown in Figure 1.

(a) For this particular joint (β=0.6, θ=45°, 2γ=15 and e=0.0), the effect of boundary conditions on the joint strength is highly dependent on the chord reaction forces (axial loadings).

(b) For this particular joint, the ratio between the strength of the multiplanar joints and that of the uniplanar joints varies between 0.85 to 1.0 depending on the chord force.

(c) The current study shows that the effect of the chord reaction force N_o on the joint strength appears to be very significant and might even be higher for joints with higher chord width to thickness ratio (2γ). It is noted that for the multiplanar KK-joint the chord reaction force N_o in fact is a combination of the reaction forces from two sides of a chord.

(c) More detailed investigations are required for other chord width to thickness ratios before general overall conclusions can be drawn.

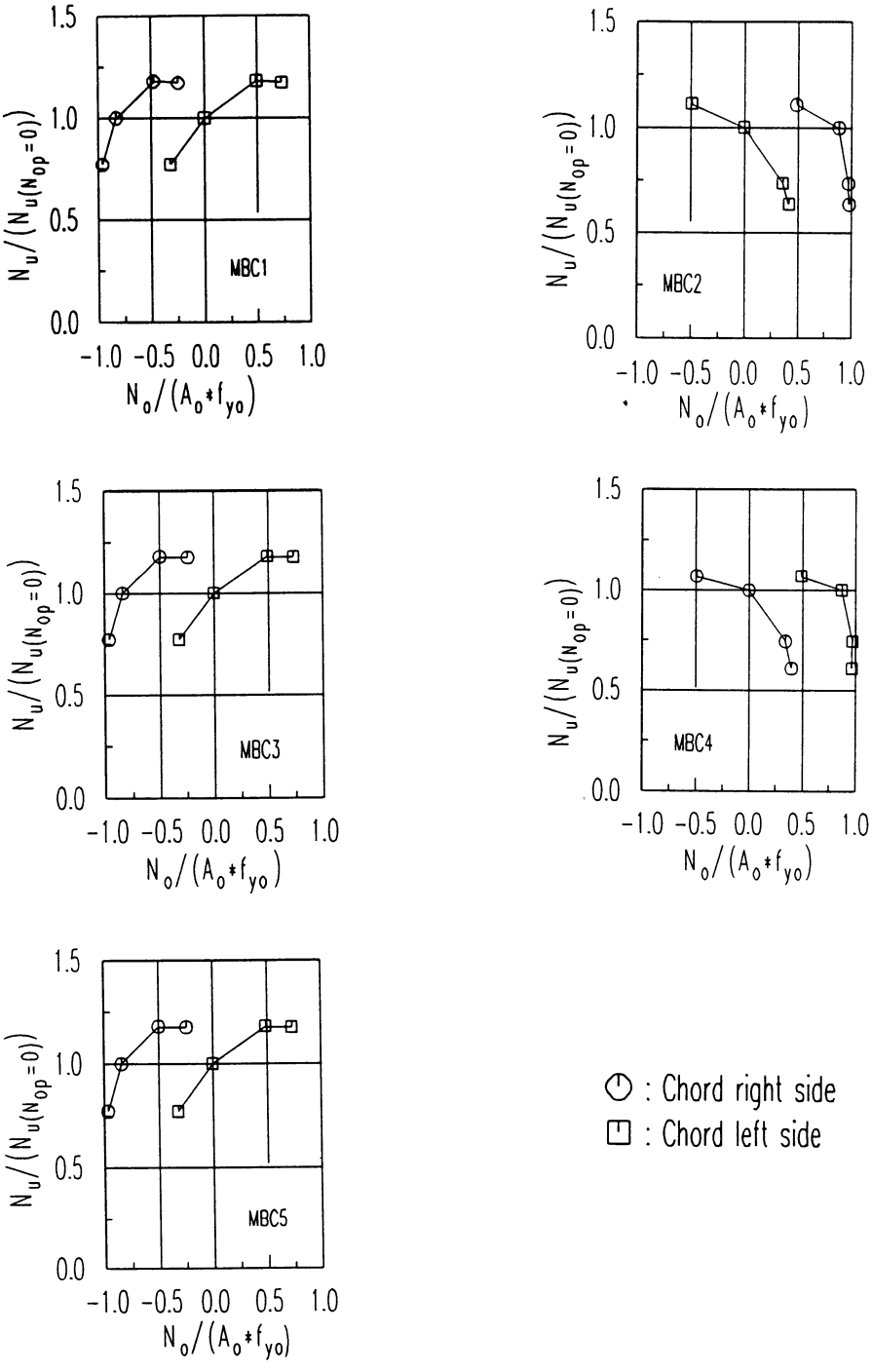

Figure 5 Capacity vs chord reaction (axial loading) plots for different boundary conditions and different chord preloads.

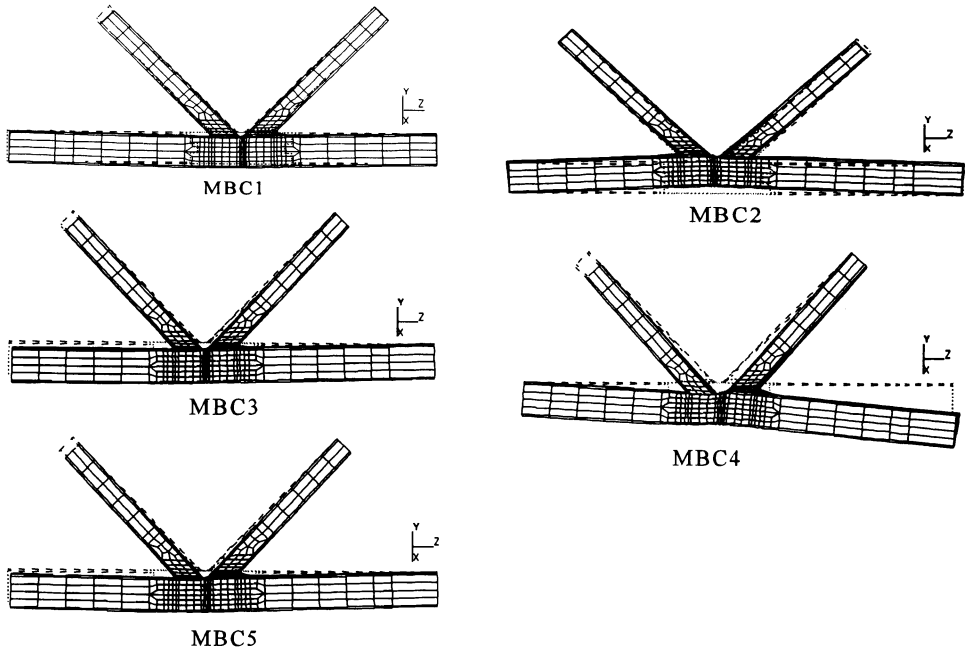

Figure 6 Deformation modes for the different boundary conditions. ($N_{OP} = 0.0$).

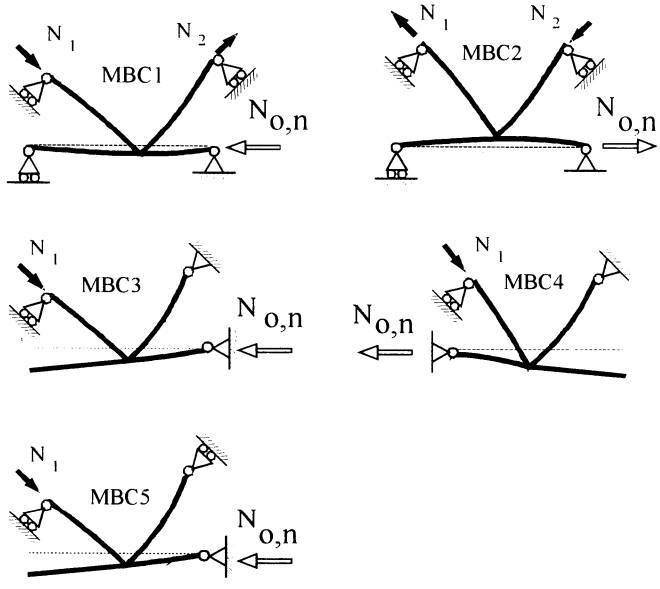

Figure 7 Support reaction forces $N_{o,n}$

5 LIST OF SYMBOLS

A_o	Cross-section area of chord
N_o	Axial reaction force in chord member
$N_{o,p}$	Chord preload
N_1, N_2	Axial force applied to brace
$N_{o,n}$	Numerical axial reaction force in chord member
$N_{o,t}$	Theoretical axial force in chord member
N_u	Connection resistance (general)
$N_{u,m}$	Connection resistance for multiplanar KK-joint
$N_{u,u}$	Connection resistance for uniplanar K-joint
b_o	External width of square hollow section chord
b_i	External width of square hollow section brace i
e	Noding eccentricity for a connection
f_{yo}	Yield stress of chord
f_{yi}	Yield stress of brace i
g	Gap between the bracing members of a K-(KK-)connection
t_o	Thickness of square hollow section chord
t_i	Thickness of square hollow section brace i
β	Width ratio between bracing member(s) and chord
γ	Half width to thickness ratio of the chord
θ	Included angle between bracing member and the chord

6 REFERENCES

[1] D. K. Liu et al. 1997 "Effect of boundary conditions and chord loads on the strength of RHS uniplanar gap K-joints", Stevin Report No. 6-97-21, Faculty of Civil Engineering and Geosciences, Delft University of Technology.

[2] E.M. Dexter et al. 1994. "Effect of overlap on strength of K-joints in CHS tubular members", Tubular structures VI, Proceedings of Sixth International Symposium on Tubular Structures, Australia.

[3] O.H. Bjornoy 1991. "Static strength of tubular joints, Phase II. Analyses and tests of gap and overlap K-joints", Veritec Report No. 91-3393, A.S. Veritec.

[4] M. Connelly et al. 1989. "Frame behaviour effects on tubular joint capacity", Tubular Structures III, Proceedings of Third International Symposium on Tubular Structures, Finland.

[5] B.E. Healy 1994. "A numerical investigation into the capacity of overlapped circular K-joints", Tubular Structures VI, Proceedings of Sixth International Symposium on Tubular Structures, Australia.

[6] G. Davies et al. 1996. "Effect of angle on the strength of overlapped RHS K- and X-joints", Tubular Structures VII, Proceedings of Seventh International Symposium on Tubular Structures, Hungary.

[7] M.A. O'connor 1993. "Static strength of multipanar K-joints in rectangular hollow sections", Tubular Structures V, Proceedings of Fifth International Symposium on Tubular Structures, United Kingdom.

[8] N. F. Yeomans 1993. "Rectangular hollow section double K-joints - Experimental tests and analysis", Tubular Structures V, Proceedings of Fifth International Symposium on Tubular Structures, United Kingdom.

[9] J. Packer et al. 1992. CIDECT - Design guide for rectangular hollow section (RHS) joints under predominantly static loading. Verlag TÜV Rheinland GmbH, Koln.

[10] D. K. Liu et al. 1993. "Static strength of multiplanar DX joints in rectangular hollow sections", Tubular Structures V, Proceedings of Fifth International Symposium on Tubular Structures, United Kingdom.

[11] D. K. Liu et al. 1997. "Effect of boundary conditions and chord loads on the strength of RHS multiplanar gap KK-joints", Stevin Report No. 6-97-24, Faculty of Civil Engineering and Geosciences, Delft University of Technology.

[12] Y. Yu 1997. "The static strength of uniplanar and multiplanar connections in rectangular hollow sections", Ph. D thesis, Delft University Press, The Netherlands.

Tubular Structures VIII, Choo & Van der Vegte (eds) © 1998 Balkema, Rotterdam, ISBN 90 5809 001 9

Current understanding of completely overlap tubular joints

T.C.Fung, C.K.Soh & W.M.Gho
School of Civil and Structural Engineering, Nanyang Technological University, Singapore
L.Y.Cheung
McDermott South East Asia Pte Limited, Singapore

ABSTRACT: Requirements for the design of completely overlap tubular joints are insufficiently covered in the codes and guides. No background information is available. However, this configuration could provide easy fabrication and may have better static strength than simple gap joints. Savings in material costs and construction manhours can be realized. In the current paper, a limited publication is reviewed. A simple calculation based on the current understanding of the joint is presented. It is concluded that more detailed investigations should be performed so that the true behaviour of the joint can be accurately described.

1 INTRODUCTION

Offshore tubular structures are massive and consist of numerous congested connections. Joints with various geometrical properties can easily be found within a structure. These joints are generally multiplanar with braces lying in different planes. Therefore, to design a tubular connection with the centrelines of the braces meeting at the same point and intersecting with the axis of the main member is not always feasible. Under this particular condition, overlapping the braces provides one of the possible solutions. In the completely overlap joint, the braces are overlapped before joining to the chord. Because of the overlapping, the stress distributions are difficult to determine and evaluate. As the joint no longer behaves as a simple joint, it is considered a complex joint.

Uses of completely overlap joints as primary connections are rare. It is more commonly seen in the location where additional clearances between structural members are required. Owing to inadequate coverage in the codes and guides and lack of understanding on the behaviour, the joint is designed carefully and is only adopted when other joint configurations are undesirable.

Unlike simple gap joints where loads are travelling from the brace to the chord prior to another member, in the completely overlap joint (Fig. 1), the load is predominantly transferred from the through brace to the lap brace without passing through the chord. As a result, punching shear stresses on the chord wall can be reduced. A thinner wall and a shorter length of joint-cans is generally sufficient to accommodate the braces. However, the outstanding feature of the joint is the short member between the intersection of the two braces and the chord. The actual behaviour of this link is not well understood yet. The characteristic could have a significant role in defferentiating the joint from the two T&Y-joint behaviour. Furthermore, the joint may have potential to be used effectively in designing structures economically and to resist against intensive dynamic excitations (but this is yet to be justified).

The current paper described the current understanding of the completely overlap joint through the review of a limited publication. Two design codes namely API (1993) and CIDECT (1991) are referenced. Simple calculations are given to demonstrate the distribution of forces and stresses. Research on the structural behaviour of the joint is currently carried out at the Nanyang Technological University. More detailed findings will be reported in the subsequent papers.

2 GEOMETRY OF COMPLETELY OVERLAP JOINTS

A completely overlap joint consists of a through brace and a lap brace. As depicted in Figure 2, the through brace is joined to the chord while the lap brace is fully welded onto the through brace. A gap is maintained from the lap brace towards the chord to facilitate welding and to provide access for non destructive testing. The joint has two work points.

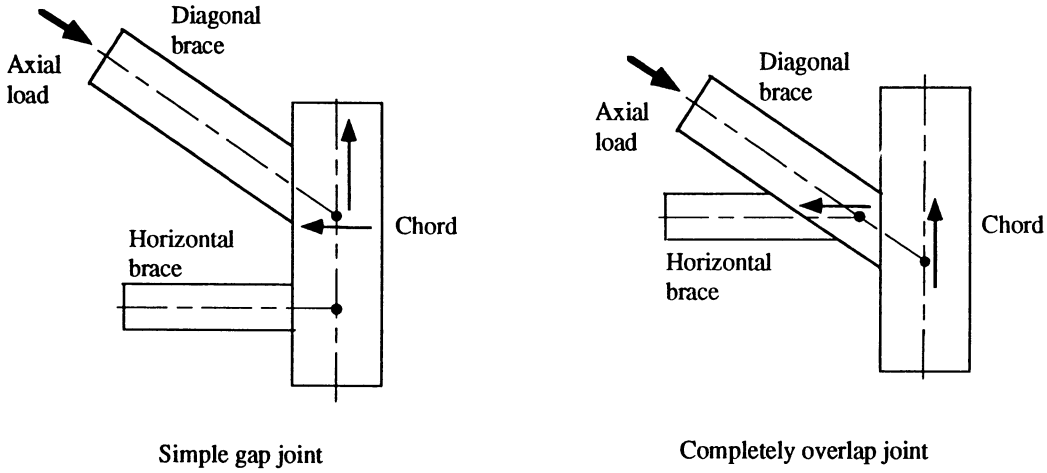

Figure 1. Tubular joints.

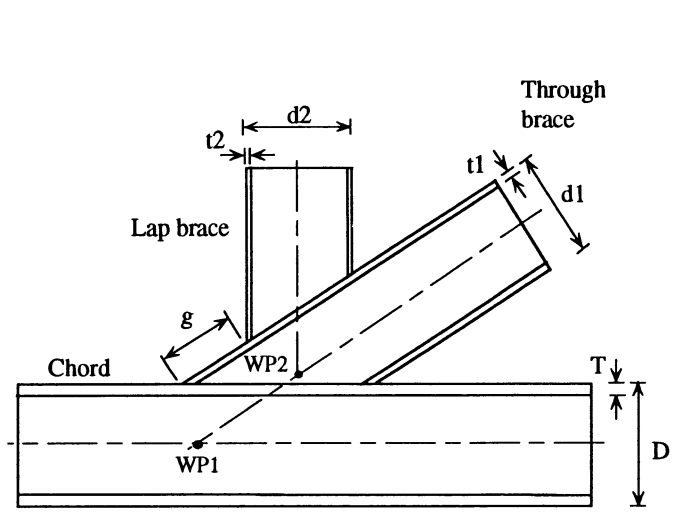

$\gamma = D/2T$
$\beta = d1/D$
$\tau = t1/T$
$\gamma 1 = d1/2t1$
$\beta 1 = d2/d1$ $\quad d1 \geq d2$
$\tau 1 = t2/t1$ $\quad t1 \geq t2$

D : Chord diameter
d1 : Through brace diameter
d2 : Lap brace diameter
T : Chord wall thickness
t1 : Through brace wall thickness
t2 : Lap brace wall thickness
g : Gap length
WP1 : Work point 1
WP2 : Work point 2

Figure 2. Geometric parameters for completely overlap joints.

One is at the intersection between the two braces (WP2) and the other is between the through brace and the chord (WP1). A short member is therefore existed between the two work points.

A proper design of the joint requires the heavily loaded brace to be the through brace. If the loads between the two braces are balanced such as a K-joint, the member with a thicker wall and a larger diameter will be fully welded to the chord surface. However, for a K(N)-joint, the diagonal member is usually chosen to be the through member. This is because it is generally more slender and is subjected to a higher load that requires greater section modulus than the other member.

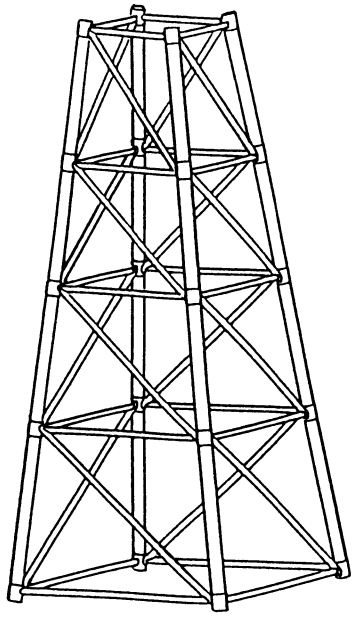

Figure 3. Eccentric jacket.

(Cheung, Gho, Fung & Soh 1997)

3 CURRENT LITERATURE ON COMPLETELY OVERLAP JOINTS

3.1 *Cheung, Gho, Fung & Soh (1997)*

Cheung, Gho, Fung & Soh had proposed an innovative jacket structure which was designed to suit the roll-up fabrication and was suitable to be used in the earthquake sensitive area. As shown in Figure 3, the special feature of the jacket was the inclusion of two T&Y joint configurations at every connection. A link member which was a small segment of the diagonal brace welded to the chord had been adopted. In the content of that paper, two objectives had been specified. One was to propose an easy-to-fabricate jacket to cut down the fabrication cost and the temporary erection braces, and the other was to provide an alternative to the conventional X-braced structure (Fig. 4).

A typical project cost analysis had been carried out with reference to the labour rates in the south east Asia region. The approach of assessing the cost was considered to be more accurate than the conventional method which was based on the steel weight and standard fabrication rates. The cost of equipment, installation and hook-up for the construction of structures was high. A list of 70 activities representing the fabrication of a typical four legs jacket and their estimated manhours associated with

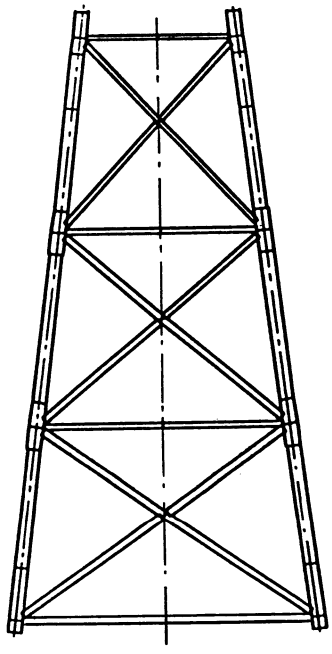

Figure 4. Conventional X-braced framing.

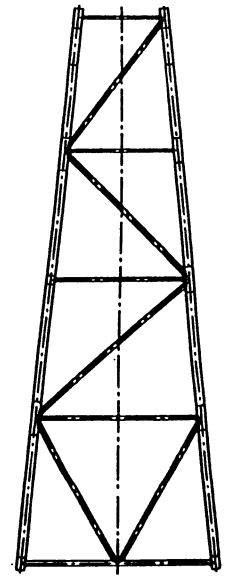

Figure 5. Conventional S-braced framing.

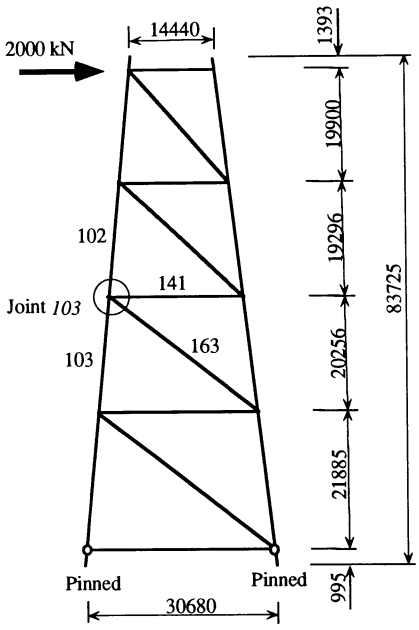

Figure 6. Structure with concentric K(N) - joint.

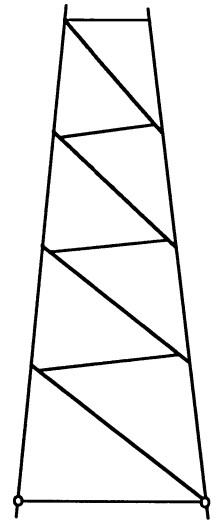

Figure 7. Structure with completely overlap joints. (Two T&Y joint configurations)

Table 1. Section and material properties.

Section properties :

Member	Diameter (mm)	Wall thickness (mm)
Joint can	1219.2	38.1
Jacket leg	1181.1	19.05
Diagonal	660.4	19.05
Horizontal	457.2	19.05

Material properties :

Young's modulus (E)	200 kN/m^2
Shear modulus (G)	77 kN/mm^2
Tensile stress (Ft)	400 kN/mm^2
Yield stress (Fy)	250 kN/mm^2

the job was presented. It had addressed that a heavier structure with simple construction details could be cheaper than a lighter structure with increased fabrication manhours due to complex details.

Conventional approach of fabricating a jacket structure such as the roll up procedure was reviewed and was briefly described. During the construction

stage, a jacket was usually subdivided into several plane frames. The main reason was to maximize ground works and to reduce the work which was needed to be done in the air. The difficulty increased with the height of the structure. Thus, the roll-up operation was adopted to speed up the job. Temporary erection braces were provided to control the self weight deflection of the jacket cantilever members. The fixing and the removing of these braces could increase the total fabrication cost considerably.

With respect to the fabrication consideration, an eccentric jacket was proposed. This jacket required fewer temporary braces during the fabrication. The connections to be welded in the air were also reduced. More detailed works could be done on the ground. Since the jacket had identical bracing pattern in every bay, a shorter length of joint-cans was sufficient to accommodate the braces. This was different from the usual S-braced jacket (Fig. 5). The joint in the eccentric jacket could have a smaller stress concentration factor as the punching shear stress had been reduced. Two weld locations had to be checked. One was at the intersection between the two braces and the other was at the chord-brace intersection. The axial load components at the joint was mainly transferred from one brace to the other brace without travelling to the chord via the punching shear mechanism. Hence, the wall thickness of the joint-can could be reduced. However, the increased of the eccentricity moment could be resulted in an increased of the joint-can wall thickness. The magnitude of this primary moment was related to the magnitude of the eccentricity and thus the length of the short member at the joint.

For the earthquake consideration, that paper had referenced the specifications in American Institution of Steel Construction (AISC, 1992) for the design of onshore Eccentric Braced Frames (EBF). In the EBF, a short beam member which was known as a shear link was deliberately designed to dissipate energy in ductile failure mode. With this member, the EBF had included large built-in eccentricities in the connection details. In order for the structure to undergo a large inelastic deformation without collapse, the plastic yielding was forced to take place on the shear link.

However, in the offshore industry, X-braced jacket was recommended. This structure had equal number of compression and tension diagonal members. It had been designed to redistribute horizontal shear loads in the vertical frames through the buckling of the diagonal braces.

In the eccentric jacket, the short member at the joint was a tubular section. It was an element that contributed to the formation of the connection. These considerations had made the difference from the shear link in the EBF. A short length of tubular member had a very high rotational capacity. In addition, the tubular member possessed a high and a uniform shear capacity. Therefore, the authors had commented that if the short member could be designed to sustain a large inelastic deformation, the eccentric jacket could have potential to replace the X-braced jacket.

It was concluded that the proposed eccentric jacket was lighter, cheaper to fabricate, easier to install and could be functioned as well as the conventional jacket. Savings in main steel fabrication manhours could be as much as 25 percent. A shorter length of joint-cans could be provided. Wall thickness of the chord could also be reduced. In comparison to the X-braced jacket, the eccentric jacket could achieve a saving in fabrication manhours of 15-20 percent for static and 40-50 percent for earthquake design considerations. The authors had also stressed the importance of the energy absorption capacity. The link member at the joint might be able to control the formation of plastic hinges. In overall, the work by Cheung, Gho, Fung & Soh had highlighted indirectly the significant impact for the design of economical offshore structures. Detailed investigations should be carried out to assess the effectiveness of the proposed jacket.

3.2 *Dexter, Lee & Kirkwood (1996)*

Recent numerical investigations on the static strength of completely overlap K-joints were carried out by Dexter, Lee & Kirkwood. The study was based on finite element analyses. Various factors, such as boundary restraints, hidden welds, loading hierarchy and failure mode, which were regarded to have major influences to the relationship between the strength and the amount of overlap were examined. The authors had highlighted the limited research works on overlapped joints and the information was inadequately described in the codes and guides. They had commented that there was an urgent need for new reliable data to derive the capacity equations.

In that paper, a comment with respect to the strength of completely overlap joint had made. They stated that "*Lap joints are expected to exhibit strength increases as the amount of overlap increases. However, strength should peak at a certain amount of overlap and then decrease until the joint becomes completely overlapped, when it is expected to behave as two Y joints with the through brace also acting as a chord.*"

The analysis results had revealed that the effect of boundary conditions was important. With balanced axial loads (through brace under compression), the fully lapped joint was less stronger than the gap joint. However, in single compression brace load, it was opposite. The difference of behaviour was also related to the geometry parameters. The joint between the two braces was found weaker than the joint of the through brace and

the chord.

In the consideration of loading reversal, the tension loaded through brace showed a lower ultimate load capacity than when it was compression loaded. This was explained as the difference of support condition that the through brace received from the lap brace. For the failure mode, γ was found to be an important parameter. The ultimate load for completely overlap joint was 42 percent higher than the gap joint when γ was 30. On the other hand, the gap joint was stronger when γ was 13.7. This was due to the change of failure mechanisms from chord plastification for high γ to local buckling of braces for low γ value.

In the completely overlapped joint, the load was made to transfer directly through the brace to brace intersection and was not by passing the gap in the chord. As a result, the brace local buckling took place. This was different from the gap joint where chord bending failure mode was observed. It could be seen that the chord with thinner wall had a higher ultimate capacity than a simple gap joint. From practical viewpoints, in the offshore structure design, chord failure which would cause the collapse of a structure was strictly not permitted.

That paper had provided a useful information on the strength of completely overlap joints. However, the characteristic of the short member at the joint was excluded and was not addressed.

3.3 *Marshall (1992)*

The advantages of partially overlap joints were given in this statement. "*The principal advantage of such joint connections is that they make efficient use of large diameter, thin wall tubular chords, without joint-cans, since the chord no longer is required to transfer the entire load.*" On the other hand, Marshall commented fully overlapped connections as a poor practice. He addressed that "*The connection between the braces would need to be checked for punching shear as a simple joint, losing the benefit of load transfer by membrane shear. The short length of diagonal between this joint and the chord carries a combination of reduced axial load and massive beam shear, for which it is less efficient than with the axial load alone. At the intersection with the chord, the elimination of radial loads means that projected length should be used to check longitudinal shear, rather than the full footprint length.*"

3.4 *American Petroleum Institute, API (1993)*

The API code had recommended a minimum clearance of two inches (51mm) between non-overlapping braces. The work points (intersections between the centrelines of braces and chord) were allowed to offset of not more than one quarter of the chord diameter to satisfy the 51mm gap. The bending moment induced by the offset of these work points could be neglected if the diameter of the chord was substantially greater than the brace (for example, jacket leg joints). No specific value was given for the β value. But for K and X joints with members of similar diameter, the bending moment could be important.

The code had suggested that if the 51mm minimum clear distance could not be achieved within the allowable offset of the work points, overlapped joints should be designed. Here, the overlap joint was referred to the partially overlapped. An equation was provided to calculate the allowable axial load component perpendicular to the chord, taking into account the shear stress of weld sharing between the two braces. The code also required the overlap to resist at least 50 percent of the allowable load component. In addition, the wall thickness of the brace must not exceed the chord, and the through brace must not be thinner than the lap brace with its full circumference welded to the chord. Capacity checks for the gap and the partially overlap joints had been defined. However, the requirement for the design of the completely overlap joint were not included.

3.5 *International Committee for the Development and Study of Tubular Structures : Design guide for circular hollow section (CHS) joints under predominantly static loading, CIDECT (1991)*

The CIDECT had recommended a gap of not less than the sum of the wall thicknesses of the two separated branch members for simple gap joints. For overlap joints (partially overlapped), the amount of overlap was not less than 25 percent of the projected footprint length on the chord surface. The toe of the overlapped member (hidden part) was usually not welded but it required the heavily loaded brace, which was the through brace, with the full circumference welded to the chord, if the brace load components perpendicular to the chord wall were unbalanced by a factor of 1.5. It also specified that if the eccentricity was between -0.55 and +0.25 of the chord diameter, the resulting bending moments could be neglected for chord members loaded in tension.

In the guide, a completely overlapped joint was defined when the eccentricity was approximately -0.55 of the chord diameter. With regarded to this joint configuration, the guide had made the following two comments.

"*Full overlapping results in an eccentricity* $e \approx -0.55 d_0$ *but provides a more straight forward fabrication than partial overlap joints and a better girder behaviour than gap joints.*" (e and d_0 were referred to the eccentricity and the chord diameter respectively).

"*Gap joints are preferred to partial overlap joints since the fabrication is easier with regard to end*

cutting, fitting and welding. However, fully overlap joints provide better joint strength with similar fabrication than gap joints."

4 CHANGES IN MEMBER END FORCES

Comparison of member end forces and stresses are made between the completely overlap joint (treated as two T&Y-joint) and the simple gap joint. The objective is to assess the effect of load distributions due to the change of joint configurations. The joints are investigated according to the requirements specified in the API design code. Distribution of member end forces and member code checks are discussed and presented in the following.

In the study, a jacket with concentric connections (K(N)-joint) which is commonly found in the region of south east Asia water is referenced. The structure is modified and simplified to a two-dimensional frame with identical section and material properties for all the horizontals, diagonals and legs (Fig. 6 and Table 1). To simulate the actual situation, axial eccentricities are generated for all the braces with their ends joining at the face of the chord. The jacket is assumed to be pinned supported at the base. A horizontal force of 2000kN is applied at the top horizontal framing in one direction. The self weight of the jacket is neglected. The joint 103 as indicated in the Figure 6 is selected for investigation. All the diagonal members are in compression while the horizontal members are in tension.

As shown in figure 7, completely overlap joints are incorporated into the same jacket model. This is accomplished by creating nodes at the diagonals with a short distance (230 mm) away from the chord surface. All the horizontal members are reconnected to the node points along the two diagonal members. Hence, the joint is formed with two typical T&Y configurations which is commonly adopted in the design. Only the horizontal members at the top and bottom framings of the structure remain intact. Comparison of the structure with the concentric joints and the completely overlap joints is performed.

For a braced frame structure such as an offshore jacket, forces are mainly transmitted and balanced by axial action among the members. Since the member axial stiffness is greater than its bending stiffness, the assumption of being pinned or rigid will not significantly affect the load distribution. Consequently, in the analysis of such structure, secondary bending moments due to eccentricities at the joints are generally ignored. This is, however, only valid for structures with concentric connections and for joints with chord diameter substantially greater than the braces. In most of the codes and design guidelines, an allowable eccentricity has been specified, for example, the API code(1993) stipulates the maximum eccentricity to be one quarter of the chord diameter. The amount of overlapping for an overlap joint affects the eccentricity. Increasing the eccentricity will result in an increase of additional bending moments at the joint. Hence, considering the jacket with completely overlap joints as a pinned frame structure may result in a significant error. In this study, rigid joints are considered.

Distribution of member end forces for the two different joint configurations are given in Figure 8. A completely overlap joint involves a large negative eccentricity. Bending moments have increased. These moments are necessary for the moment equilibrium at the joint. In the current example, the maximum change in axial forces in the chords is 1.27 percent. Although there is a considerable increased in shear forces, the impact is insignificant due to large beam shear areas. The bending moment has caused an increase of the overall stresses at the chord sections.

For concentric joints, forces are distributed among the chord, diagonal and horizontal members at a common point according to their stiffness and geometry. However, the forces are distributed at two points for completely overlap joints. One is at the intersection between the two braces (WP2) and the other is between the chord and the through brace (WP1). The changes of stresses in horizontal members are not critical. A remarkable change in forces is at the short member between the intersection of the two braces and the chord. Though it is a small segment of the through brace, the axial force has cut down to 38.2 percent. The bending moment has increased drastically (approximately 6 times). The most noticeable effect is the beam shear. The shear which is negligible for the diagonal at concentric joints has a stress ratio as high as 0.44. The shear stress has become the controlling factor in comparison to the strength. The stress ratios for all the members at the joint is presented in figure 9.

5 DISCUSSIONS

Treating a completely overlap joint as two T&Y-joint configurations may lead to a significant error in the analysis of structures. The effect of stress distribution between the two braces (through brace and lap brace) does not cause any effect to the behaviour of the joint between the chord and the brace visa versa. This is true if the member lying between the two joint components is long enough such that nominal stress exists as in a typical structural member. For the completely overlap joint, the gap between the lap brace to the chord surface is very small. It can be just only 51mm (minimum gap between the two braces of K joint as specified by the API code). In another word, the stresses induced at a joint will affect the distribution of stresses of another joint. The existing punching shear equations stated in the codes (for example, the API recommendations)

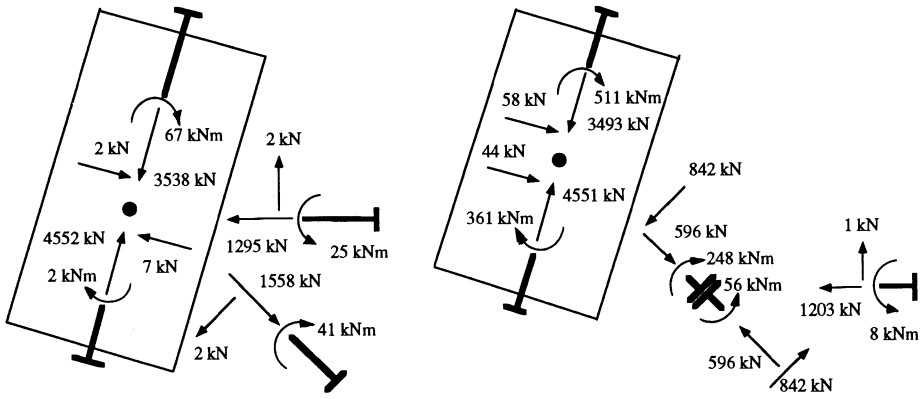

Concentric K(N) - joint

Completely overlap joint
(treated as two T&Y-joint)

Figure 8. Member end forces at joint 103.

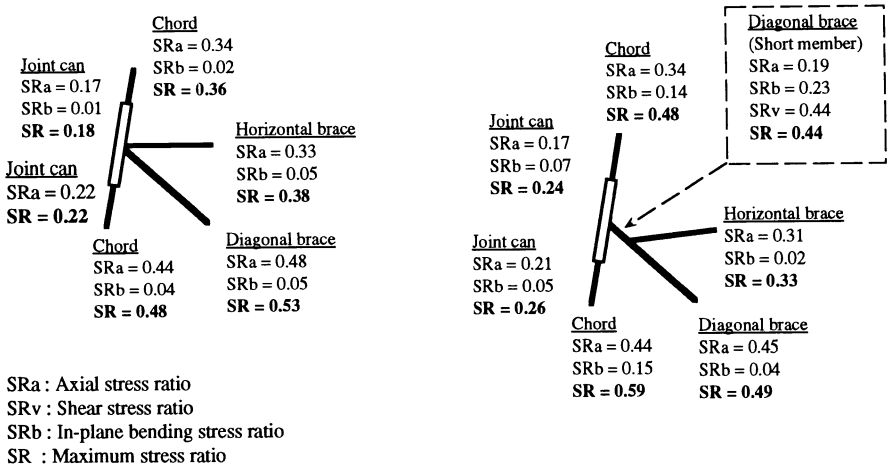

SRa : Axial stress ratio
SRv : Shear stress ratio
SRb : In-plane bending stress ratio
SR : Maximum stress ratio

Figure 9. Member code check at joint 103.

may not be applicable to this kind of connection detail. This is mainly due to the boundary condition. For the punching shear check between the two braces, the result is inappropriate because the chord may act like a diaphragm reinforcing the through brace. On the other hand, for the joint check at the chord-brace intersection, the short member is restraint by the lap brace.

In the analysis of many types of tubular joint structures, only one joint is examined at a time. For the completely overlap joint, the two joint components have to be assessed together and the short member should be accounted for as well. The interaction between the distribution of stresses and the effect of shell membrane and bending stresses is to be investigated. Formulae and parametric equations for the design of simple joints as given in the codes and guides do not necessarily represent the true behaviour of the completely overlap joint. Current information is obviously insufficient. Formulations and precise criteria are required. Items to be included are the minimum and the maximum

gap length between the lap brace and the chord surface for static and dynamic design considerations, classification of joints based on load patterns, various designs parametric equations for joint flexibility, stress concentration factors, ultimate capacities, chord plastifications, etc.

With an increasing emphasis in today economic design of offshore structures for dynamic forces, joints must also be designed to exhibit adequate deformation and rotation capacity. It must be able to show adequate energy absorption capacity in order for the structure to achieve the required level of ductility. Understanding on the behaviour of completely overlap joint is certainly lacking. Many areas are yet to be looked into before conclusions can be drawn with confidence.

6 CONCLUSIONS

The main objective of the current paper is to draw attention on the completely overlap tubular joint. In the present design codes, no specific guideline is given for this kind of connection details. Due to insufficient information on the behaviour, the joint is sometime interpreted as two separated T&Y configurations. However, it is still not known whether the interpretation is appropriate. As early as in 1984, Department of Energy has already stated a statement to described the joint. "*If the overlap is large or complete, the through brace effectively be a chord member and must be considered as such in the analysis of the joint.*" Unfortunately, it is not clearly defined. Uses of direct calculation methods as stipulated in the codes may not necessary yield conservative results.

In the completely overlap joint, the two joint components should be assessed together. The short member (a small segment of the through brace) could also have a significant influence to the overall behaviour of the joint. The actual local effect of shell membrane and bending stresses to the load interaction among the members at the joint is yet to be determined. Understandings on the behaviour of completely overlap tubular joints required a considerable amount of experimental and analytical work. Extensive research in this scope is certainly required. For offshore jacket structures, attempting to avoid completely overlap of braces in some congested connections may result in the design of less economical and inefficient structure.

REFERENCES

American Petroleum Institute 1993. Recommended practice for planning, designing and constructing fixed offshore platforms - working stress design (RP2A-WSD). Washington D.C.: API

American Institute of Steel Construction 1992. Seismic Provisions for Structural Steel Buildings. AISC. Chicago. USA.

Cheung, L.Y., Gho, W.M., Fung, T.C. & Soh, C.K. 1997. Design economics of offshore structures - eccentric jacket', Journal of the Institution of Engineers, Singapore. To appear.

CIDECT 1991. Design guide for circular hollow section (CHS) Joints under Predominantly Static Loading, Verlag TÜV Rheinland GmbH, Köln, Germany.

Department of Energy 1984. Offshore installations: guidance on design and construction. London. HMSO.

Dexter, E.M., Lee, M.M.K. & Kirkwood, M.G. 1996. Overlapped K joints in circular hollow sections under axial loading. Journal of Offshore Mechanics and Arctic Engineering: 53-61.

Marshall, P.W. 1992. Design of Welded Tubular Connections - Basic and Use of AWS Code Provisions New York: Elseviers Science Publishers.



Taylor & Francis
Taylor & Francis Group
http://taylorandfrancis.com

Tubular Structures VIII, Choo & Van der Vegte (eds) © 1998 Balkema, Rotterdam, ISBN 90 5809 001 9

Effect of overlap on the behaviour of axially loaded CHS K-joints

E. M. Dexter & M. M. K. Lee
University of Wales Swansea, UK

ABSTRACT: This paper reports the results of an extensive Finite Element study into the behaviour of statically axially loaded K-joints in circular hollow sections. The emphasis of the study was on the effect of overlap on the behaviour of the joints, though small-gap K-joints were also included for comparative purposes. A companion paper (Dexter & Lee 1998) reviews the ultimate capacity results and their significance in the light of available design guidance. The study reveals new insight into how the behaviour of axially loaded overlapped K-joints varies across the practical range of geometric parameters. Certain overlapped geometries were seen to be 100% efficient – the joints reaching the brace member squash load capacity. Other failure modes of chord bending, brace local buckling and, in particular, combined chord bending and brace local buckling were evident. Examination of the load-deformation characteristics for the sharp falls in post-peak load – reflecting sudden joint failures, which have been a suggested cause for concern in the past – has revealed that few overlapped geometries exhibit such behaviour.

1 INTRODUCTION

K-joints (Figs. 1 and 2) are one of the fundamental joint configurations utilised in on- and offshore tubular structures. An understanding of the behaviour of K-joints under balanced axial brace loading – whereby the brace loads on the joint are balanced in the direction perpendicular to the chord – is important for the quantification of the strength of joints of more complex geometry and/or loading conditions. Nevertheless, despite some three decades of tubular joint research, there are still areas of dispute among researchers and code-drafting authorities regarding the behaviour of gap K-joints, and very little research has been conducted into the behaviour of overlapped joints.

The failure mechanism of balanced axially loaded non-overlapped K-joints (Fig. 1) largely depends on the gap size between the two brace members (HSE 1990b). With a large gap, a K-joint behaves as two independent Y- (or T-) joints. As the gap reduces, the inward push of the compression brace is balanced by the outward pull of the tension brace to offset any chord ovalising effects, and the strength of the joint increases due to the increased bending stiffness of the chord wall between the braces. The failure mode is generally plastic deformation of the chord and crack initiation in the chord side weld toe of the tension-loaded intersection in the gap region. High shear leads to alignment of the chord gap region with the tension brace, which causes direct tension across the gap region and, eventually, rupture. An overlapped joint is one in which the braces intersect each other as well as (or, in extreme cases, instead of) the chord (Fig. 2), which allows a more efficient transfer of the load directly between the two braces through their common weld. One advantage of such joints is that since the chord no longer transfers the entire load, its thickness can be reduced. However, a greater fabrication effort is needed, since the brace end of the overlapping brace must be doubly coped.

The aim of the current research is to investigate the ultimate behaviour of K-joints and, in particular, the effects of overlap, by means of a parametric Finite Element study.

2 JOINT GEOMETRY

The notation and non-dimensional parameters describing the geometry of gap and overlapped K-joints are shown in Figures 1 and 2 respectively. For simple gap joints, ζ ($=g/D$) is the usual non-dimensional gap measurement parameter. For overlapped joints, the overlap amount may be measured using ζ, resulting in negative values. This can be useful for strength equations that attempt to account for both gap and overlapped joints in a single

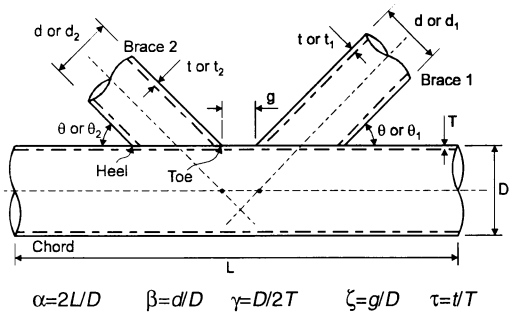

Figure 1. Gap K-joint geometry

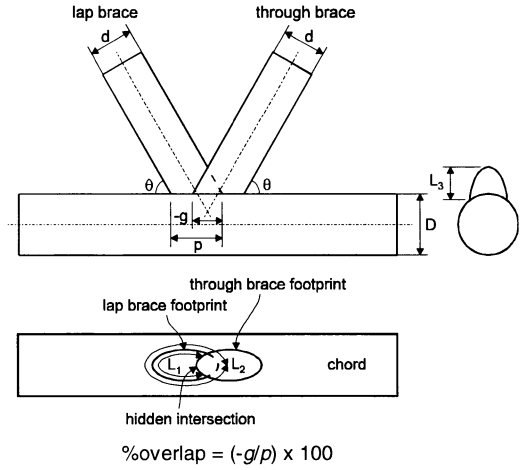

Figure 2. Overlapped K-joint geometry

expression. In this paper, however, the overlap amount will be expressed in the form of a percentage, as defined by CIDECT (1991) and illustrated in Figure 2. Joints may be overlapped by more than 100%, in which case the lap brace is welded entirely to the through brace, and the behaviour of the 'gap' region of the through brace may have a substantial effect on the mode of failure and strength of the joint. The 'hidden intersection' in the overlapped joint, again depicted in Figure 2, is usually not welded when overlapped joints are utilised onshore. Current offshore design guidance dictates that the hidden intersection should be welded, though in older structures it is often not known whether or not hidden welds are present.

The research reported in this paper is concerned only with the case of balanced axial load.

3 REVIEW OF PREVIOUS WORK

3.1 *Design Guidance*

Most onshore design guidance for the capacity of overlapped joints is essentially equivalent to that of CIDECT (1991). CIDECT's design recommendations are based on the data collation and research of Ochi et al. (1984) and Kurobane et al. (1984, 1986). For K-joints, CIDECT present a single expression covering the 'chord plastification' strength of both gap and overlapped K-joints by assigning negative 'gap' values for overlapped joints. The joint efficiency is then checked for brace local buckling, using an expression derived from the brace local buckling equation of Kurobane et al. (1986). Fuller details are given in the companion paper (Dexter & Lee 1998). The majority of the database of overlapped joints used to produce the onshore guidance is considered by the offshore code drafting bodies to be either unreliable or not representative of offshore joints. Due to the lack of data on the strength of overlapped joints, provisions in offshore design codes (API 1993, HSE 1990a), for failure in the lap brace only, are based on principles of structural mechanics, assuming that the loads perpendicular to the chord are carried partly in shear transfer across the common brace weld and partly through the brace-chord intersection, depending on the relative intersection lengths L_1, L_2 and L_3 (shown in Figure 2, as defined by the API (1993)). However, the assumption that joint failure is governed by failure under the brace-chord intersection, combined with shearing at the common brace weld, has been called into question. One of the findings of the BOMEL Frames Project (1992) was that the failure modes of overlapped joints are typically more complex, involving local brace buckling as a direct result of action at the intersection. This failure mode was recognised much earlier in onshore circles by Kurobane et al. (1986) but is not fully accepted as a valid (non-premature) failure mode in offshore circles.

3.2 *Experimental Research*

Well-documented experimental investigations into the behaviour and strength of overlapped joints have been conducted by Kurobane et al. (1986) and BOMEL (1992). A study has also been performed by Bjornoy (1993), though it is confidential and hence unobtainable. The investigations by Kurobane et al. (1986) – three gap and eight overlapped K-joint tests – specifically recognised and investigated the failure mode of brace local buckling. BOMEL's experiments highlighted the efficiency of an isolated, heavily overlapped K-joint, which failed by member failure of the compression-loaded brace, and the presence of brace local buckling in a lesser overlapped K-joint within a frame.

3.3 *Numerical Research*

A limited amount of numerical research into the behaviour and strength of overlapped joints has been conducted in recent years. Some has been concerned with investigating the differences between framed and isolated joint test results and the inherent importance of boundary condition choice for isolated joint tests.

The remaining studies have been mainly small investigations concerned with the relative effects of loading hierarchy or the presence or absence of the hidden weld. van der Valk (1991) reported a series of Finite Element (FE) analyses carried out by Shell, prompted by and in parallel with the BOMEL Frames Project. The effect of loading hierarchy reversal (tension or compression to the through or overlap brace) was investigated for one geometry. A series of FE analyses performed by Exxon for the BOMEL Frames Project Group (BOMEL 1992) included two geometries for which loading hierarchy was investigated, and two further geometries for which the effects of the presence or absence of the hidden weld were determined. For the case of the through brace loaded in tension, joint strengths were found to be up to one-third less when the hidden intersection was modelled as not-welded than when in the connected condition. Loading hierarchy effects were difficult to determine because of the probable differences in the chord stress states for the two cases, caused by the chord boundary conditions used. Nevertheless, Exxon's results indicate that the effect of loading hierarchy may be dependent on the amount of overlap, with the through-brace-in-compression case being weaker for a concentric (zero eccentricity) joint, and the through-brace-in-tension case being weaker for a heavily overlapped joint.

In 1994, Healy reported results from a large FE investigation into the strength of overlapped joints in CHS, mainly under in-plane bending but also including 60 analyses for axial brace loading. Six joint configurations for one gap and two overlapped geometries were analysed using four sets of boundary conditions (including both loading hierarchies). All were modelled as if the hidden weld were present. The through-brace-in-compression joints were consistently weaker than the through-brace-in-tension joints. The latter apparently showed less tendency for brace local buckling, though all joints included an element of brace local buckling, at or beyond failure. The geometries that were dominated by brace local buckling exhibited approximately constant strength with overlap amount, whereas the others increased in strength as the overlap amount increased. Healy also noted a reason for the concern about local brace buckling is that such a failure mode could precipitate sudden failure, and thus require a greater safety factor. None of Healy's results showed such a tendency, though it was reported that one of the test results of Bjornoy (1993) did so.

Research published previously by the present authors (Dexter et al. 1994, 1996) described some preliminary numerical investigations into strength-overlap relationships, including the effects of different boundary conditions, the presence/absence of the hidden weld, loading hierarchy and failure mode changes. 'Single' type brace loading conditions (in which the tension brace is restrained rather than physically loaded) were found to be unsuitable for applying balanced axial load to the more heavily overlapped joints. The absence of the hidden weld served to reduce the joint capacity by approximately 5% across the range of overlap geometries when the through brace was loaded in compression. The effects of loading hierarchy reversal were also investigated. As found by the previous researchers, for the small-to-medium overlaps, the through-brace-in-compression was marginally the weaker case, but for the heavily overlapped joints, the through-brace-in-tension was weaker, by some 10%. Forcing a change of failure mode by changing the joints' geometric parameters and materials also significantly affected the behaviour and strength of the joints. For full details, the reader is referred to Dexter (1996).

4 SCOPE OF THE STUDY

From the results of the foregoing research, the following areas have been highlighted as requiring in-depth investigation:

- The effects of varying the joint geometry require full investigation. The joint parameters β and γ are generally accepted to affect the strength of simple (gap) joints, and the additional parameter τ appears to have a large influence on the capacity of overlapped joints, due to its effect on the important failure mode of brace local buckling. The fourth parameter – the amount of overlap – is the main parameter of interest.
- The effects of the relative material strengths of the braces and chord have also been shown to influence joint strength.
- The case of the through brace in compression appears to be generally the weaker, limiting loading hierarchy case, though not necessarily so for very large amounts of overlap. Selective analyses of heavily overlapped joints are required to determine the weaker, limiting case for any given geometry.
- The absence of the hidden intersection weld is recognised to cause a reduction in the joint capacity. For the case of the through brace being loaded in compression, this reduction appears to

Table 1. Scope of the parametric study

Variable	Description	No.
Geometry		
Joint type	60°–60°K, braces of equal geometry, D=1000 mm	1
Overlap	1 gap (ζ=0.1) 3 intermediate overlaps (10%, 50%, 90%) 1 overlap >100% (ζ=0.1)	5
β	0.4 0.7 1.0	3
γ	8 20 35 50	4
τ	0.4 1.0 1.5	3
Hidden weld	present	1
Load hierarchy	through brace in comp'n	1
Loading	balanced axial	1
Material (chord & brace)	ASTM A36 σ_y=254 N/mm^2 σ_u=405 N/mm^2	1
	analyses =	180

be of little significance. However, further selective analyses of various joint geometries are required to determine the significance for the case of the through brace being in tension, for use onshore, or for the re-assessment of older offshore platforms where the presence of hidden intersection welds is not always a certainty.

The scope of the study completed so far has encompassed only the first of the above, namely geometrical parameter variations, though many of the above areas not covered here are ongoing, or planned for inclusion in the future. The scope of the research reported here is summarised in Table 1. Members with γ ratios of less than 30 are most common in service, though ratios of up to 50 are allowable within buckling limits and may be specified. It was considered important to extend the parametric study to include these thinner members, since the act of overlapping is expected to produce joints that are more efficient and is thus able to utilise such members without compromising joint strength. Although a τ value of 1.5 is outside the range recommended by the design codes, it was included since τ values of between 1.0 and 1.5 have been specified in the past for overlapped joints offshore, in order to enhance joint strength by precluding brace local buckling. To ignore the effects of τ>1.0 when re-assessing joint strength may result in the unnecessary specification of costly strengthening measures.

5 VALIDATION OF THE MODEL

Validation of the numerical model is a prerequisite for any FE study, because the ability of the FE procedure to accurately, yet economically, model the behaviour of real-life structures has to be established. A description of the successful validation of the FE modelling strategy used for the present study – against one gap and three overlapped K-joints tested by Kurobane et al. (1986) – was published previously by the authors (Dexter et al. 1996).

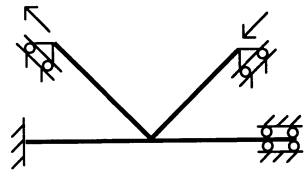

Figure 3. Loading and boundary conditions

6 METHODOLOGY

6.1 *FE Modelling Strategy*

The mid-surfaces of the joint member walls were modelled using meshes of four-noded, linear, shell elements. Shell 'weld' elements were included at the intersections for the joints with significant 'gap' regions, i.e. the gap and >100% overlapped joints, to simulate the stiffening effect provided by welds in actual joints. The 'weld' leg lengths were sized to conform to AWS specifications.

The chord length was specified such that α=14, to preclude end effects. The brace lengths were equal to half the length of the chord. The loading and boundary conditions used are depicted in Figure 3. The brace end conditions are both 'supported', i.e. constrained to displace only along their own axis, and were chosen so that the model behaviour would best represent the behaviour of joints in a frame situation.

The non-linear Finite Element software ABAQUS (1995) was used for the analysis and post-processing. The thin shell element S4R5 (a linear element employing reduced integration, and five degrees of freedom per node) with five integration points through the shell thickness, was utilised. A modified RIKS algorithm was used to apply equal, opposite loads to the two braces, enabling post-peak load shedding to be simulated.

6.2 *Failure criteria*

Four potential failure criteria were considered and checked for each joint, with the joint load at the first, limiting criterion taken to be the ultimate capacity. The criteria are:

- peak load on the brace load-displacement plot
- member squash load (Member Failure)

The axial load in the compression loaded brace or the reaction in the chord may potentially reach the member squash load before true joint failure for the most efficient overlapped joints. In such a situation the member squash load (given by $\sigma_y A$, where σ_y is the yield stress and A the cross-sectional area of the member) may be attained first in either the brace or the chord, or in both approximately simultaneously, depending on the relative cross-sectional areas of the members.

- 20% tensile strain in the outer surface
  This failure criterion crudely (and conservatively) represents the onset of cracking in the outer surface of the joint. Although FE joint models may continue to carry increased loads beyond the point of 'first crack', this criterion is included because any load-displacement path beyond this point, being obtained from a numerical analysis in which cracking and lamellar tearing are not an integral part of the modelling, is potentially unconservative.
- Yura's deformation limit = $60\sigma_y d/E$ for axial brace loading (Yura et al. 1980)

6.3 *Failure mode determination*

A variety of failure modes were expected:

- For the gap joints and for the joints overlapped by >100%, failure was generally expected to be associated with high shear deformation and plastic strains visible in the gap region (denoted as Chord Bending (CB) for the gap joints, and Brace Bending (BB) for the >100% overlapped joints) with the failure criterion of 20% tensile strain (determined by scanning the values of maximum principal strains at the element Gauss points) indicating the onset of Cracking (C).
- For intermediate overlapped joints (10%, 50% and 90%), failure modes of Brace Local Buckling (BLB), or Chord Bending (CB), or a combination of both, had all been identified from previous research. The determination of these failure modes was assessed by visually checking the deformed model, stress and strain plots. Such failure modes were expected to occur in association with peak load or Yura's limit failure criteria.
- Joints with low γ ratios (thick chords) were expected to fail by member failure – Brace Member Failure (BMF) of the compression loaded brace, or Chord Member Failure (CMF) due to the compressive reaction from the boundary condition or, on occasion, both. These failure modes are technically not 'joint' failure modes, but indicate that the strength of the joints in question are limited by their individual member capacities. Such failure modes were determined by the attainment of a substantial proportion of the member squash load, and by global buckling and high stress contours (greater than the yield stress value) observed when post-processing the loaded model.

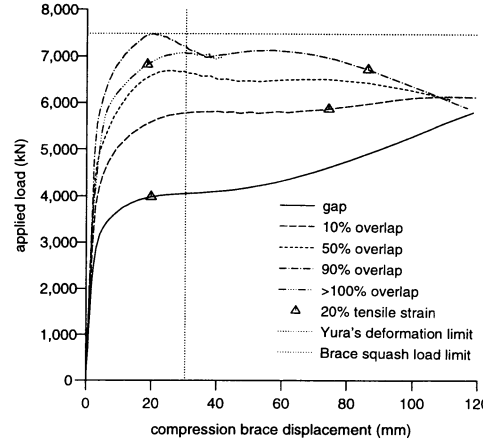

Figure 4. Load-displacement behaviour for β=0.4, γ=20, τ=1.0 joints

7 RESULTS

The results of the parametric study are presented in Table 2. For each joint, the failure criterion, capacity and the failure mode at ultimate load are detailed. Secondary failure modes are included in parentheses. More detailed results, namely joint flexibility, yield load, compression-brace displacement at ultimate load, more detailed categorisation of failure mode(s), mode(s) of failure beyond ultimate load and the location of potential cracks for each joint are reported by Dexter (1996).

Load-displacement plots for all of the joints were reported by Dexter (1996). Plots for one set of joints (β=0.4, γ=20, τ=1.0) are reproduced in Figure 4 by means of example. All applicable failure criteria are included on the plots, in order that their relative proximity may be ascertained. Beyond the point of 20% tensile strain (defining the probability of the onset of cracking in the outer surface) the curves should be regarded as potentially unconservative. The consequences of this are probably insignificant for the intermediate overlapped joints (10%, 50% and 90%), since the point of 20% tensile strain generally occurred well beyond the incidence of the critical criterion, if at all. For the gap and the >100% overlapped joints, which commonly failed by cracking, the load-deformation response curves showed the criterion to be not unduly conservative.

For the gap joints in particular, the point of 20%ε failure criterion often occurred just before, or on, a plateau or minimum gradient of the response curve.

8 ANALYSIS OF JOINT BEHAVIOUR

8.1 *Brace Load-Displacement Behaviour*

All the load-displacement curves were scrutinised for a sharp drop-off in load, reflecting the possibility of sudden failure, as discussed by Healy (1994). Of the joints analysed, relatively few exhibited such sudden post-peak collapse:

- Most marked were the gap, 10%, 50% and 90% overlapped joints where:
  β=1.0, τ=0.4, γ=20, 35 and 50
  All failed with peak loads at very low displacements, by BLB. No CB was evident in any of these joints, though some BMF occurred at later stages of the loading for the more compact brace members. Although similar failure modes were observed for τ=0.4 joints for β=0.7, such

Table 2. Results of the parametric study

Joint geometry			Gap joint results			10% overlapped joint results			50% -
β	γ	τ	Failure Criterion	Capacity (kN)	Failure mode	Failure criterion	Capacity (kN)	Failure mode	Failure criterion
		0.4	MF	7,480	BMF	MF	7,480	BMF	MF
	8	1.0	MF	16,800	BMF	MF	16,800	BMF	MF
		1.5	20%ε	17,500	C(CB)	MF	22,900	BMF	MF
		0.4	MF	3,110	BMF	peak	3,110	BMF	peak
	20	1.0	20%ε	3,980	C(CB)	δ_{Yura}	5,780	BLB,CB	peak
0.4		1.5	20%ε	3,620	C(CB)	peak	7,560	CB(BLB)	δ_{Yura}
		0.4	peak	1,320	BMF,CB	peak	1,510	BLB(CB)	peak
	35	1.0	20%ε	1,510	C(CB)	δ_{Yura}	2,610	CB,BLB	peak
		1.5	20%ε	1,500	C(CB)	δ_{Yura}	3,440	CB,BLB	δ_{Yura}
		0.4	peak	760	CB	peak	863	BLB	peak
	50	1.0	20%ε	804	C(CB)	δ_{Yura}	1,560	CB,BLB	peak
		1.5	20%ε	814	C(CB)	δ_{Yura}	2,070	BLB,CB	δ_{Yura}
		0.4	MF	13,500	BMF	MF	13,500	BMF	peak
	8	1.0	20%ε	29,300	C(CB)	MF	31,800	BMF,CB	MF
		1.5	20%ε	24,600	C(CB)	δ_{Yura}	41,700	BMF,CMF,CB	δ_{Yura}
		0.4	peak	5,330	BLB,BMF	peak	5,480	BLB,BMF	FE halted
	20	1.0	20%ε	6,780	C(CB)	δ_{Yura}	10,000	CB,BLB	peak
0.7		1.5	20%ε	5,910	C(CB)	δ_{Yura}	12,600	CB,BLB	δ_{Yura}
		0.4	peak	2,320	BLB(CB)	peak	2,400	BLB	peak
	35	1.0	20%ε	2,740	C(CB)	δ_{Yura}	4,600	CB,BLB	peak
		1.5	20%ε	2,660	C(CB)	δ_{Yura}	5,840	CB,BLB	peak
		0.4	peak	1,330	BLB	peak	1,330	BLB	peak
	50	1.0	20%ε	1,540	C(CB)	peak	2,660	CB,BLB	peak
		1.5	20%ε	1,540	C(CB)	δ_{Yura}	3,630	BLB,CB	δ_{Yura}
		0.4	peak	19,400	BMF	peak	19,400	BMF	peak
	8	1.0	20%ε	35,400	C(CB)	MF	46,800	CMF,BMF	MF
		1.5	20%ε	31,000	C(CB)	peak	44,300	CMF	MF
		0.4	peak	7,490	BLB	peak	7,330	(BLB)	peak
	20	1.0	20%ε	10,200	C(CB)	peak	15,100	BLB,CB	peak
1.0		1.5	20%ε	8,800	C(CB)	peak	17,900	CB(BLB)	MF
		0.4	peak	3,450	BLB	peak	3,310	BLB	peak
	35	1.0	20%ε	4,950	C(CB)	peak	6,780	CB,BLB	peak
		1.5	20%ε	4,660	C(CB)	peak	8,090	CB	peak
		0.4	peak	2,140	BLB	peak	1,910	(BLB)	peak
	50	1.0	peak	2,900	CB	peak	3,960	CB,BLB	peak
		1.5	20%ε	3,080	C(CB)	peak	4,830	CB	peak

sudden load shedding did not occur.

- The four other joints for which there was a sudden drop-off in load just beyond the peak were:
  90% overlap, β=1.0, τ=1.0, γ=35 and 50
  90% overlap, β=1.0, τ=1.5, γ=35
  >100% overlap, β=1.0, τ=1.5, γ=50
  The failure modes for the τ=1.0 joints involved both large amounts of chord bending and buckling and collapse of the compression brace, whereas for the τ=1.5 joints, failure is due to chord collapse.

The results of the current study certainly do not show that BLB failure modes for overlapped joints lead to sudden joint collapse. Such concerns would probably only appear to be relevant for the joints of highest β and lowest τ (i.e. the highest *d/t* ratios). At lower β and/or higher τ ratios, the BLB failure modes have not been seen to precipitate sudden failure.

overlapped joint results		90% overlapped joint results			>100% overlapped joint results		
Capacity (kN)	Failure mode	Failure criterion	Capacity (kN)	Failure mode	Failure criterion	Capacity (kN)	Failure mode
7,480	BMF	MF	7,480	BMF	20%ε	6,530	C
16,800	BMF	MF	16,800	BMF	MF	16,800	BMF
22,900	BMF	MF	22,900	BMF	MF	22,900	BMF
3,040	BMF	peak	2,980	BMF,BLB	20%ε	2,360	C
6,690	CB(BLB)	peak	7,470	BMF,CB	20%ε	6,820	C
9,410	CB	peak	10,800	BMF,CB	20%ε	10,200	C,BMF
1,500	BLB(BMF)	peak	1,470	BLB	20%ε	1,310	C
3,200	BLB,CB	peak	3,780	BLB,CB	20%ε	3,490	C,BB
4,760	BLB(CB)	peak	5,780	CB,BLB	20%ε	5,220	C,BB
897	CB,BLB	peak	927	BLB	20%ε	898	C,BB
1,910	CB,BLB	peak	2,360	CB(BLB)	20%ε	2,290	C,BB
2,940	CB,BLB	peak	3,720	CB(BLB)	20%ε	3,510	C,BB
13,400	BMF	peak	13,300	BMF	20%ε	10,300	C
31,800	BMF(CB)	MF	31,800	BMF	MF	31,800	BMF,C
44,400	(CB)(CMF)(BMF)	MF	45,400	BMF,CMF(CB)	MF	45,400	BMF(CB)
4,750	(BMF)(BLB)	peak	4,800	BLB(BMF)	20%ε	3,910	C
10,600	CB,BLB	peak	12,200	BLB	20%ε	10,400	C
15,500	CB	δ_{Yura}	17,800	CB(C)	20%ε	15,200	C
2,320	BLB	peak	2,310	BLB	20%ε	2,170	C,BB(BLB)
4,580	BLB(CB)	peak	5,710	BLB(CB)	20%ε	5,320	C
6,880	BLB,CB	peak	8,830	BLB,CB	20%ε	7,950	C,BB
1,350	BLB	peak	1,410	BLB	peak	1,320	BLB
2,750	BLB,CB	peak	3,680	BLB(CB)	20%ε	3,530	C,BB(BLB)
4,080	BLB,CB	peak	5,360	CB(BLB)	20%ε	5,290	C,BB
19,300	BMF	MF	19,500	BMF	20%ε	12,800	C
46,800	BMF,CMF	MF	46,800	BMF,CMF	20%ε	41,100	C
45,800	CMF	MF	49,700	CMF	MF	50,900	C,CMF
6,820	(BLB)	peak	6,600	(BLB)	20%ε	4,670	C(BB)
14,600	CB(BLB)	20%ε	16,700	BLB,C	20%ε	12,200	C(BB)
19,300	CMF	MF	20,600	CMF	20%ε	17,700	C
3,330	BLB	peak	3,110	(BLB)	peak	2,130	BB,BLB
6,450	BLB(CB)	20%ε	8,210	BLB,CB,C	20%ε	6,230	C,BB
9,080	CB(BLB)	peak	10,600	CB	20%ε	9,100	C,BB
2,120	(BLB)	peak	1,890	BLB	peak	916	(BLB)
3,840	CB(BLB)	peak	5,200	BLB,CB	20%ε	3,740	C,BB
5,380	CB(BLB)	peak	6,670	BLB,CB	20%ε	5,910	C,BB,CB

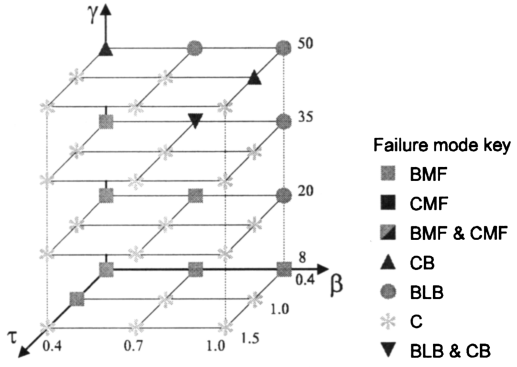

Figure 5. Failure mode distribution for gap K-joints

8.2 *Failure Mode Distribution*

The failure mode for each joint was categorised as one of:

- Brace Member Failure (BMF)
- Chord Member Failure (CMF)
- combined Brace Member Failure and Chord Member Failure (BMF & CMF)
- Chord Bending (CB)
- Brace Local Buckling (BLB)
- Cracking (C)
- combined Brace Local Buckling and Chord Bending (BLB & CB)

and their distributions plotted in three dimensions – β, γ and τ – for each joint type; gap, 10% overlap, 50% overlap, 90% overlap and >100% overlap. The plot for the gap joints is reproduced in Figure 5.

Cracking (in the chord gap region) is seen to be the most common mode of failure for the gap joints. Cracking was never the failure mode for τ=0.4 joints though, where failure generally occurred in the brace. BMF was the dominant mode of failure for seven of the 36 joints, clustered at low β, low γ and low τ ratios, when the members are sufficiently compact to resist bending and buckling at the intersection, but the cross sectional area of the brace was relatively much smaller than that of the chord. No CMF was observed. BLB occurred for only four gap joints, clustered at high β, high γ and low τ, i.e. at high *d/t*, when the brace members are most slender. CB arose rarely, and only for the joints with high γ values, i.e. the most slender chords.

For the >100% overlapped joints, only four failure modes were discerned, and the distribution of each was well defined. No CB or combined CB & BLB occurred since the majority, or all, of the load is transferred directly between the two braces up to the point of ultimate load. Cracking of the 'gap' region of the through brace was the most common mode of failure. This occurred for all but the most slender

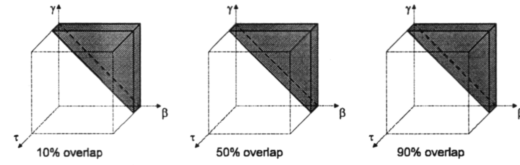

a. Brace Local Buckling only

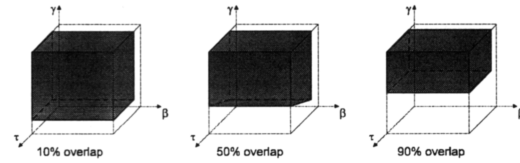

b. Combined Brace Local Buckling and Chord Bending

Figure 6. Generalised failure mode distributions

braces, which failed by BLB, and the most compact members, which failed due to member failure.

For the intermediate overlapped joints, the distributions of the four major failure mode clusters were further generalised. The distributions of BLB and combined BLB & CB, in β, γ and τ are reproduced in Figures 6a and b respectively.

Referring to Figure 6a, the joints failing by BLB only were distinctly clustered in the region of high β and/or high γ, and low τ, i.e. when *d/t* is high, irrespective of the overlap amount. Two typical examples of deformed meshes exhibiting brace local buckling are depicted in Figure 7. Figure 7a clearly shows the in-plane spreading of the compression (through) brace and necking of the tension brace. In Figure 7b, a typical concavity in the compression-loaded through brace (the right-hand brace in the figure) can be seen.

Combined CB & BLB (Fig. 6b) was the most common mode of failure, occurring for 44 of the 108 intermediate overlapped joints. It was most prominent for joints with high γ and high τ, and showed a slightly higher incidence at lower overlaps, when the joints were generally less efficient.

The single failure mode of CB was limited to only six joints (of 108) (all occurring for joints where τ=1.5), highlighting the importance of the brace behaviour on the overall joint behaviour.

The member failure modes of failure (distinguishing the most efficient joints) are clustered at low γ, when the members are sufficiently compact to resist local bending and buckling at the intersection. All γ=8 joints failed by member failure. For γ=20, selected joints failed by member failure, depending mainly on the β and τ ratios (since for the

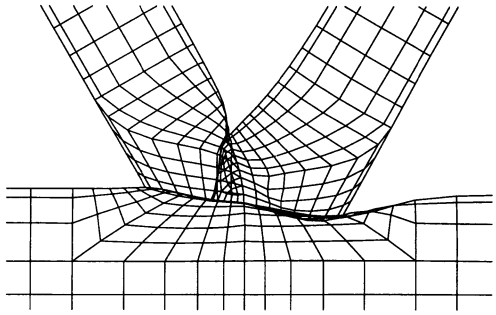

Figure 7a. Typical brace local buckling failure mode

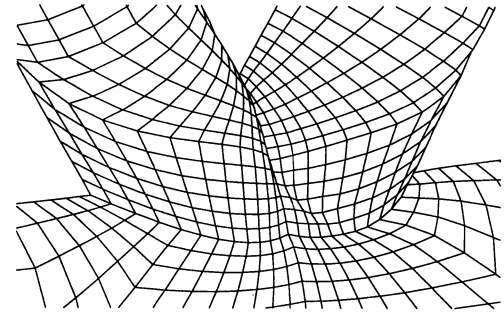

Figure 7b. Typical brace local buckling failure mode

most slender brace members, the brace may fail due to local buckling), but also on the amount of overlap. At lower overlaps, the longer brace footprints allowed load redistribution, with brace punching action causing chord bending, whereas at the higher overlap the reduced brace footprint configuration was more efficient.

9 CONCLUSIONS

The effects of variation of the principal geometrical parameters on the behaviour of axially loaded overlapped K-joints in steel circular hollow sections have been investigated by a review of previous research and by means of calibrated non-linear Finite Element analyses – the only substantial, systematic investigation carried out to date. The ultimate strength results and their significance in the light of available design guidance are examined in the companion paper.

Certain geometries were seen to be 100% efficient, i.e. the joint capacity attained the brace member squash load. Other modes of failure can be categorised as chord bending, brace local buckling (in the compression loaded through brace), or, for a substantial number of joints, combined chord bending and brace local buckling. Brace local buckling certainly appears to be a valid and common failure mode for overlapped joints, occurring locally to the intersection as a direct result of the load transfer between the brace members and the chord.

Examination of the load-deformation behavioural characteristics has confirmed that a sharp fall in post-peak load, reflecting sudden joint failure, should only be of concern for the most slender braces (β=1.0, τ=0.4) which fail by brace local buckling only, and for the very heavily overlapped β=1.0 joints for which chord collapse figures prominently. In the main, however, brace local buckling failure modes do not cause sudden joint collapse and thus should not be a cause for concern.

The distribution of all the various modes of failure may be attributed to the interactive effects of varying the geometrical parameters β, γ, τ and overlap amount and, as such, the failure modes of overlapped joints of arbitrary geometry are predictable.

As discussed in earlier sections, other factors are known, or expected, to affect the behaviour, and consequently the strength, of overlapped K-joints. For example, the effect of overlap on the change in joint strength due to loading hierarchy reversal (recognised from previous research) is clearly due to some critical change in the joint failure mode with increasing overlap amount. Changing the relative strengths of the brace and chord materials, in particular, will certainly affect the mode of failure (and hence joint strength) in many cases. Specifying a stronger chord material, for example, would enhance the strength of any joints failing wholly or partly by chord bending, though not for those joints where failure already occurs solely in the brace. Investigations into such effects, crucial to a more complete understanding of the ultimate behaviour of overlapped joints, are currently underway at Swansea.

10 NOMENCLATURE

D = chord diameter
d = brace diameter
E = Young's Modulus
g = gap length
L = chord length
Ov = % overlap/100 = $g\sin\theta/d$
T = chord wall thickness
t = brace wall thickness
α = joint geometry ratio $2L/D$
β = joint geometry ratio d/D
ε = strain
γ = joint geometry ratio $D/2T$

θ = in-plane brace angle
σ_u = ultimate tensile stress
σ_y = yield stress
τ = joint geometry ratio *t/T*
ζ = joint geometry ratio *g/D*

11 REFERENCES

ABAQUS Users' Manuals I and II (1995), Hibbit, Karlsson and Sorensen Inc.

American Petroleum Institute (API) (1993) API RP 2A: *Planning, Designing and Constructing Fixed Offshore Platforms*, 20th edition, Section E, Connections

Bjornoy O.H. (1993) "Static strength of tubular joints, Phase II. Analyses and tests of gap and overlap K-joints", Veritec Report No. 91-3393, A.S.Veritec

BOMEL (1992) "Joint Industry funded research programme. Analytical and experimental investigation of the behaviour of tubular frames, Phase II." Part 2 - Testing and analysis of frame behaviour, Vol. 1, Test programme, analysis and results

Comité International pour le Developpement et l'Étude de la Construction Tubulaire (CIDECT) (1991) *Design guide for circular hollow section (CHS) joints under predominantly static loading*

Dexter E.M., Lee M.M.K., Kirkwood M.G. (1994) "Effect of overlap on strength of K joints in CHS tubular members", *6th International Symposium on Tubular Structures*, Melbourne, Australia, pp 581-589

Dexter E.M., Lee M.M.K., Kirkwood M.G. (1996) "Overlapped K joints in circular hollow sections under axial loading", *Journal of Offshore Mechanics and Arctic Engineering*, ASME, February 1996, Vol. 118, pp53-61

Dexter E.M. (1996) "Effects of overlap on behaviour and strength of steel circular hollow section joints", PhD thesis C/Ph/200/96 University of Wales Swansea

Dexter E.M., Lee M.M.K. (1998) "Ultimate capacity of axially loaded K-joints in CHS", *8th International Symposium on Tubular Structures*, Singapore

Health and Safety Executive (HSE) (1990a) *Offshore Installations: Guidance on design, construction and certification*, Appendix A21, Steel. 4th edition

HSE (1990b) "*Background to new static strength guidance for tubular joints in steel offshore structures*" OTH 89 308

Healy B.E. (1994) "A numerical investigation into the capacity of overlapped circular K-joints", *6th International Symposium on Tubular Structures, Melbourne*, Australia, pp 563-571

Kurobane Y., Makino Y., Ochi K. (1984) "Ultimate resistance of unstiffened tubular joints", *Journal of Structural Engineering*, Vol. 110, No 2, February 1984, pp 385-400

Kurobane Y., Ogawa K., Ochi K., Makino. (1986) "Local buckling of braces in tubular K-joints", *Thin-Walled Structures*, pp 23-40

Ochi K., Makino Y., Kurobane Y. (1984) "Basis for design of unstiffened tubular joints under axial brace loading." IIW Annual Assembly, Doc. XV-561-84

Valk C.A.C. van der (1991) "New aspects related to the ultimate strength of tubular K- and X- joints", *Offshore Mechanics and Arctic Engineering* Conference Proceedings, Stavanger, Norway, Vol. III-B, pp 417-422

Yura J.A., Zettlemoyer N., Edwards I.F. (1980) "Ultimate capacity equations for tubular joints", *Offshore Technology Conference* 3690, Houston, USA

Tubular Structures VIII, Choo & Van der Vegte (eds) © 1998 Balkema, Rotterdam, ISBN 90 5809 001 9

Ultimate capacity of axially loaded K-joints in CHS

E. M. Dexter & M. M. K. Lee
University of Wales Swansea, UK

ABSTRACT: The ultimate capacity results from an extensive Finite Element study of balanced axially loaded K-joints are reviewed here and compared with predictions from the available design guidance. Both overlapped and small-gap K-joints are included. This paper complements the companion paper (Dexter & Lee 1998), in which an assessment of the joints' behaviour was presented. Overlapping the braces was shown to have a beneficial effect on joint strength for the joints with relatively thick brace walls; the overlapped K-joints having strengths of up to 4½ times that of the corresponding gap joints. The performance of the onshore and offshore design guidance for predicting the joint capacities was found to be poor. Interactive effects of varying the geometric parameters were not fully accounted for, generally resulting in high levels of conservatism. A new strength equation has therefore been proposed for the overlapped joints, providing a robust platform onto which the results of further selective research can be added.

1 INTRODUCTION

1.1 *Background*

Despite many years of research into the static capacity of simple tubular joints, there remain areas of dispute among researchers and code-drafting authorities regarding the effects of various geometric parameters (e.g. β, γ, ζ, θ) on the strength of gap K-joints.

Regarding the ultimate behaviour of overlapped K-joints, the small amount of existing research has been reviewed in the companion paper (Dexter & Lee 1998). Only two studies included investigation of the effects of overlap on joint strength. Healy (1994) conducted FE analyses of six different configurations – with varying β, τ and γ ratios and different brace and chord material properties – each for one gap and two overlapped K-joints. All the overlapped joints were found to be stronger than the corresponding gap joints by a factor of approximately 1.25 to 2.25. Three geometries exhibited approximately constant strength with increasing overlap, whereas the other three increased in strength as the overlap amount increased. The joint strengths were all conservatively predicted by the CIDECT (1991) guidance. Previous numerical research by the present authors (Dexter et al. 1994, 1996a) revealed a reduction in joint strength with increasing overlap amount, for a joint configuration with a relatively thick chord, and thin, weak braces. Other factors briefly investigated included the effects of hidden weld presence and absence, and loading hierarchy. In Dexter & Lee (1996b), selected results from the current study were used to investigate the relative capacities of canned gap and overlapped K-joints. It is evident from even these limited previous studies that the effects of joint geometry and material on overlapped K-joint strength are complex and inter-related.

1.2 *Parametric Study*

The scope of the numerical study thus initiated was tabulated in the companion paper. In essence, the range of practical joint geometries used both onshore and offshore were included, except that the brace angles were maintained at 60° throughout. Of the other possible geometric variables, hidden welds were modelled as if present, as demanded nowadays offshore, and the through brace was loaded in compression, as is deemed the weaker limiting case at least for low to medium overlap amounts. As regards the gap K-joints, the small gap size was chosen to represent the strongest gap joint configuration possible, in order that any resulting strength enhancements due to overlapping would not be unconservative. Joints with an overlap of more than 100% were included as it was believed that they might be particularly efficient. The FE modelling strategy, which had been thoroughly validated against reliable experimental test data (Dexter et al. 1996), was described in the companion paper.

The joint strength results, tabulated in the companion paper, are not reproduced here for reasons of space.

1.3 *Joint Strength Comparisons*

In this paper, the joint strengths obtained from the parametric study, are reviewed. For gap joints, the effects of β, γ and τ are examined and the results used to assess the accuracy of the gap K-joint strength equations recommended by Kurobane et al. (1984, 1986), CIDECT (1991), HSE (1990a) and API (1993). The effect of overlapping is then investigated by comparing the strengths of the overlapped joints with the gap joints of otherwise equivalent geometry. For the overlapped joints, the effects of β, γ, τ and overlap amount are then examined and compared with the available joint strength predictions of Kurobane et al. (1984, 1986) and CIDECT (1991). Finally, a new strength equation is proposed for the intermediate (10% – 90%) overlapped joints.

2 RELEVANT DESIGN GUIDANCE

2.1 *Onshore Guidance*

Kurobane et al. (1984) compiled a screened database and carried out multiple regression on axially loaded K-joint test results where significant ductile chord plastic deflection occurred. Tests where the ultimate load was controlled by brace local buckling were excluded.

The prediction model for mean K-joint strength included both gap and overlapped joints, although the resulting strength distribution was virtually constant with overlap. The mean strength P_u is given (for no chord prestress) as

$$P_u = \sigma_y T^2 f_0 f_1 f_2 f_4 f_6 \tag{1}$$

where

$$f_0 = 2.11(1+5.66\beta) \qquad f_1 = (2\gamma)^{0.209}$$

$$f_2 = 1 + \frac{0.00904(2\gamma)^{1.24}}{e^{\left(\frac{0.508}{T}(g-3.04)-1.33\right)}+1} \qquad f_4 = \frac{1-0.376\cos^2\theta}{\sin\theta}$$

$$f_6 = \left(\frac{\sigma_y}{\sigma_u}\right)^{-0.723}$$

This equation is valid for

$$\begin{cases} 0.19 \le \beta \le 1.0 & \text{for} \quad 7.5 \le \gamma < 30 \\ 0.19 \le \beta \le 0.6 & \text{for} \quad 30 < \gamma \le 51 \end{cases}$$

$$-30 \le \frac{g}{T} < 40 \quad \text{i.e.} \quad -15 \le \zeta\gamma < 20 \tag{2}$$

$$30^\circ \le \theta \le 90^\circ \qquad 0.56 \le \frac{\sigma_y}{\sigma_u} \le 0.94$$

The alternative failure mode of brace local buckling was investigated by Kurobane et al. (1986). It was recognised that for K-joints with overlapped braces, both brace local buckling and chord bending appear simultaneously in many cases. Brace local buckling was considered a valid joint failure mode since, unlike member failure, it occurs locally to the joint and may also involve some deformation of the chord and/or the tension-loaded brace. The local buckling strength, non-dimensionalised by the brace yield stress, was determined as

$$\frac{\sigma_{blb}}{\sigma_y} = 0.433\alpha_b^{0.244}\left(\frac{\sigma_{sb}}{\sigma_y}\right)^{0.446} \tag{3}$$

where

σ_{blb} is the joint capacity due to brace local buckling, represented in terms of an average stress on a cross section of the compression brace,

σ_{sb} is the joint capacity due to shell bending, represented in terms of an average stress on a cross section of the compression brace, and

$$\alpha_b = \frac{E}{\sigma_y}\frac{t}{d} \tag{4}$$

The equation is valid for

$$10 \le \alpha_b \le 30 \tag{5}$$

and it was further recommended that $\alpha_b \ge 10$, to prevent joint failure by local brace buckling due to insufficient ductility.

In the CIDECT (1991) recommendations, for the brace in compression, the chord plastification design strength is given by

$$P^* = \frac{\sigma_y T^2}{\sin\theta_1}(1.8+10.2\beta)\gamma^{0.2}\left(1+\frac{0.024\gamma^{1.2}}{e^{\left(0.5\frac{g}{T}-1.33\right)}+1}\right) \tag{6}$$

for the case of no chord prestress. The ranges of validity for this equation are:

$$\begin{array}{ll} 0.2 < \beta \le 1.0 & g \ge t_1 + t_2 \quad \text{for gap joints} \\ 30^\circ \le \theta \le 90^\circ & \sigma_y \le 355\ \text{N/mm}^2 \\ \text{overlap} \ge 25\% & -0.55D \le e < 0.25D \\ \gamma \le 25 & \frac{d}{2t} \le 25 \quad \text{i.e.} \quad \frac{\beta\gamma}{\tau} \le 25 \end{array} \tag{7}$$

Except for small gaps and overlaps, the predicted gap or overlapped K-joint strengths are virtually constant, with the level of increase in strength for overlapped joints over the gap joints depending on γ. For gap K-joints, the joint strength may be limited by the punching shear capacity

$$P^* \le \frac{\sigma_y}{\sqrt{3}} T\pi d\left(\frac{1+\sin\theta}{2\sin^2\theta}\right) \tag{8}$$

Gap or overlapped joint strength may also be limited by brace local buckling in the compression loaded brace when the brace diameter to wall thickness ratio

d/t is high. CIDECT expresses these limits as

$$\text{efficiency} \le 0.22\sqrt{\frac{E}{\sigma_y}\frac{t}{d}} \le 1.0 \qquad (9)$$

2.2 *Offshore Guidance – Gap Joints*

The API (1993) formula for allowable gap K-joint strength, with the safety factor of 1.7 removed, for no longitudinal chord load is

$$P_a = \frac{F_y T^2}{\sin\theta}(3.4 + 19\beta)Q_g \qquad (10)$$

where

$$Q_g \begin{cases} = 1.8 - 0.1 g/T & \text{for } \gamma \le 20 \\ = 1.8 - 4 g/D & \text{for } \gamma > 20 \\ \ge 1.0 \end{cases} \qquad (11)$$

There are no validity limits as such to this equation. However, it is assumed that the joint members should satisfy certain criteria relating to maximum allowable tensile and compressive stresses in the members.

The HSE (1990a) formula for the characteristic strength of gap K-joints, with no longitudinal chord load, is

$$P_k = \frac{F_y T^2}{\sin\theta}(2 + 20\beta)Q_g\sqrt{Q_\beta} \quad \text{in compression} \qquad (12)$$

$$P_k = \frac{F_y T^2}{\sin\theta}(8 + 22\beta)Q_g \quad \text{in tension} \qquad (13)$$

where

$$Q_g \begin{cases} = 1.7 - 0.9\zeta \\ \ge 1.0 \end{cases} \qquad (14)$$

and

$$Q_\beta \begin{cases} = 1.0 & \text{for } \beta < 0.6 \\ = \dfrac{0.3}{\beta(1 - 0.833\beta)} & \text{for } \beta \ge 0.6 \end{cases} \qquad (15)$$

valid for

$$9 \le \gamma \le 50 \qquad 30° \le \theta \le 90° \qquad (16)$$
$$0.15 \le \beta \le 1.0 \qquad F_y \le 400\ \text{N/mm}^2$$

Allowable stress limits again exist for the members. The limiting case is for the brace loaded in compression, i.e. Equation 12.

2.3 *Offshore Guidance – Overlapped Joints*

The majority of the database of overlapped K-joints used to produce the onshore guidance is considered by the offshore code drafting bodies to be either unreliable or not representative of offshore joints. Provisions in the offshore design codes are therefore based on principles of structural mechanics. Failure is assumed to occur in the lap brace, with loads perpendicular to the chord being carried partly in shear transfer across the common brace weld, and partly through the lap brace-chord intersection, depending on the relative intersection lengths. The lap brace-chord intersection strength is dependent on the code strength for a notional Y-joint between the lap brace and the chord. Various formulae for the intersection lengths exist in the literature, but all are valid only for small to medium overlap amounts, and even then, none are accurate across the full range of β (Dexter 1996). Both codes require that $\tau \le 1.0$, though joints with τ values of up to 1.5 are common on older offshore structures. HSE further require that for heavily overlapped joints, the strength of the lap brace should be limited to that of a Y-joint with the through brace acting as the chord.

The available offshore design guidance is very limited and fails to embody all of the failure modes of brace local buckling and/or chord plastification. In particular, for the geometries analysed here, failure was associated with the compression-loaded brace, which was the through brace, and hence the strength prediction provisions described above are not valid.

No guidance exists for joints overlapped by more than 100%.

3 GAP K-JOINT CAPACITY – TRENDS WITH GEOMETRY

The effects of β, γ and τ on the non-dimensional gap joint strength can be discerned from Figure 1, where the joint strengths have been non-dimensionalised in the usual manner, by multiplying by $\sin\theta/F_y T^2$. In the figure, lines have been drawn linking the datapoints of equivalent geometry, in order to easily show the resulting trends. It is not implied that the strength-parameter relationship between the known datapoints is necessarily linear. The following trends can be observed:

- Strength trends with β

Joint strengths increase significantly with β. The rate of increase is dependent on γ; the strength increases being greater with higher γ. Although there are insufficient datapoints to investigate the applicability of the Q_β parameter (Equation 15) it can be seen that the rate of strength increase between $0.7 \le \beta \le 1.0$ is greater than that between $0.4 \le \beta \le 0.7$, but only for the higher γ ratios of 35 and 50.

- Strength trends with γ

The non-dimensionalised joint strength has already been divided by T^2, hence a γ^2 effect is already included. All geometries show increases in non-dimensional strength with increasing γ ratio, indicating that the increase in absolute capacity due to the change in γ is actually less than γ^2.

- Strength trends with τ

Each of the τ=1.0 joints is at least as strong as the

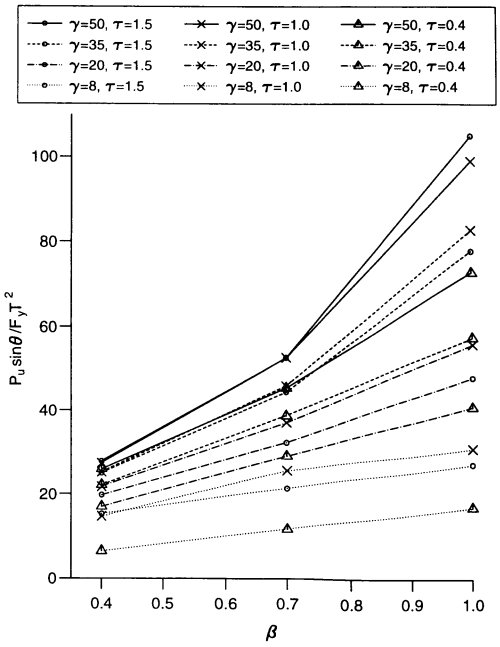

Figure 1 Effects of non-dimensional parameters on gap K-joint strength

equivalent τ=0.4 joint. The τ=1.5 joints are generally of approximately equal strength or weaker than the equivalent τ=1.0 joints. This is not of significant concern, since τ>1.0 is not generally specified in practice for gap joints.

4 GAP K-JOINT CAPACITY – COMPARISON WITH PREDICTIONS

4.1 *Predictions of API (1993) and HSE (1990a)*

The relative provisions and performance of these two offshore codes may be directly compared with the FE joint capacities. Figure 2a depicts the non-dimensional strengths plotted against β for selected geometries. Figure 2b depicts the variation with γ, for the β=0.7 joints. Similar trends were seen for the β=0.4 and β=1.0 joints. The γ=8 joints are outside the validity range of the HSE equation and also violate the allowable stress limits for members of both codes. Regarding the β effects (Fig. 2a), the API linear function (Equation 10) best predicts the trends for lower γ joints, while the HSE function (Equation 12), which is non-linear for β>0.6, better predicts trends of the higher γ joints. As for the γ trends, Figure 2b shows the non-dimensional strength to increase with γ, while the HSE prediction is constant, and that of the API is constant for γ>20, and predicts the wrong trend for γ<20. The results of the present study show that γ has a positive effect on the non-dimensionalised joint strength, i.e. non-dimensionalising by T^2 has over-compensated for the effects of γ.

4.2 *Predictions of Kurobane et al. (1984, 1986)*

Many of the parametric study joints fall outside the validity ranges and allowable failure mode criteria of the Chord Bending (CB) equation (1). Indeed there are few gap K-joints in the matrix for which both this and the Brace Local Buckling (BLB) equation (3) is valid. Ignoring the validity limits, and applying the two equations to all the FE gap joint geometries, the BLB equation capacity was the limiting capacity for all the τ=0.4 joints. The performance of the two mean capacity formulae of Kurobane et al. for the τ=0.4 and τ=1.0 joints is plotted against β in Figure 3a. The trend of increase in strength with increasing β is not fully captured by the formulae and a slight γ trend also remains, though the largest under-predictions are for the high β - high γ combinations, which are outside the CB equation validity ranges.

4.3 *Predictions of CIDECT (1991)*

All the joints were compared with the CIDECT predictions, despite the fact that the joints with higher γ values fall outside the validity limits of the chord plastification equation (6). The joint strengths were then additionally checked for punching shear limits (Equation 8) and efficiency limits (Equation 9). The final predicted joint capacity was never limited by the punching shear check and only limited by the brace buckling efficiency for four gap K-joints (for low τ and low γ). The CIDECT performance is plotted against β in Figure 3b. The combined checks under-predict the capacity of all the gap K-joints, partly due to the efficiency limit of unity limiting the joint strength to that of the brace member squash load and partly as a consequence of the extra conservatism over the equations of Kurobane et al. Although the CIDECT equations are based on the formulae of Kurobane et al., the β and γ trends have not been as well predicted as those in Figure 3a. Very high conservatism is seen for the high β - high γ combinations (though again they are outside the validity ranges of the formulae).

5 EFFECT OF OVERLAPPING ON K-JOINT CAPACITY

The effect of overlapping on K-joint strength is depicted in Figures 4a and b for τ=1.0 and τ=1.5 respectively. The joint strengths are each non-dimensionalised by the strength of the corresponding gap K-joint. Overlapping had no beneficial effect on joint strength for the τ=0.4 joints due to the dominance of the brace buckling and brace member failure modes of failure for these joints (recall the discussion in the companion paper (Dexter & Lee

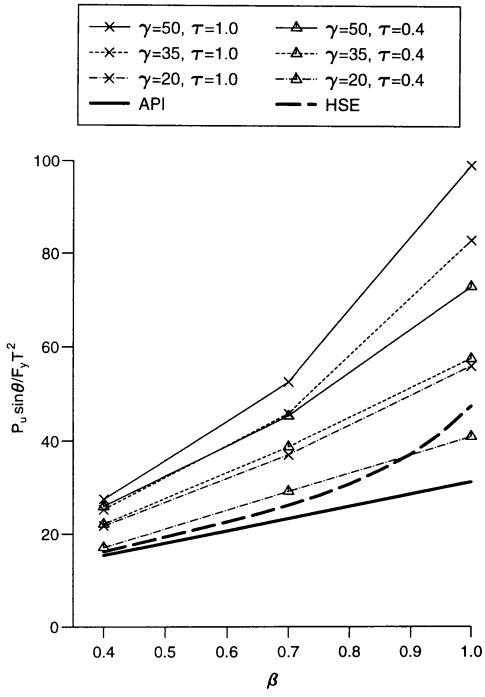

Figure 2a Relative provisions of API and HSE – Effect of β on strength of γ≥20 gap K-joints

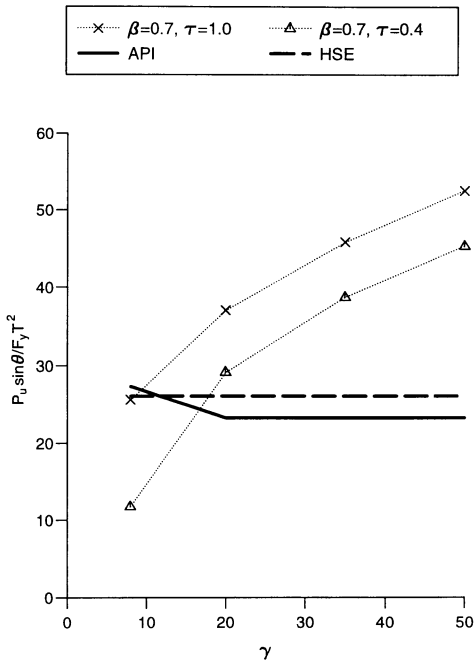

Figure 2b Relative provisions of API and HSE – Effect of γ on strength of β=0.7 gap K-joints

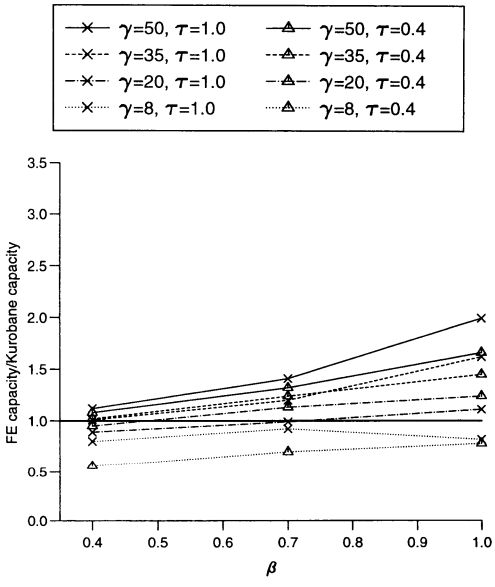

Figure 3a Performance of mean strength equations of Kurobane et al. for gap K-joints

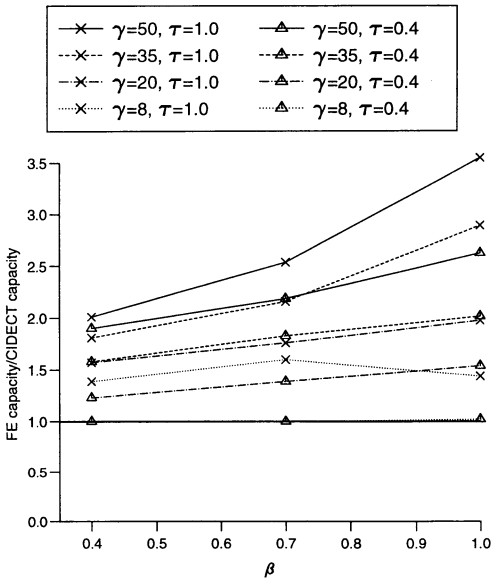

Figure 3b Performance of design strength equations of CIDECT for gap K-joints

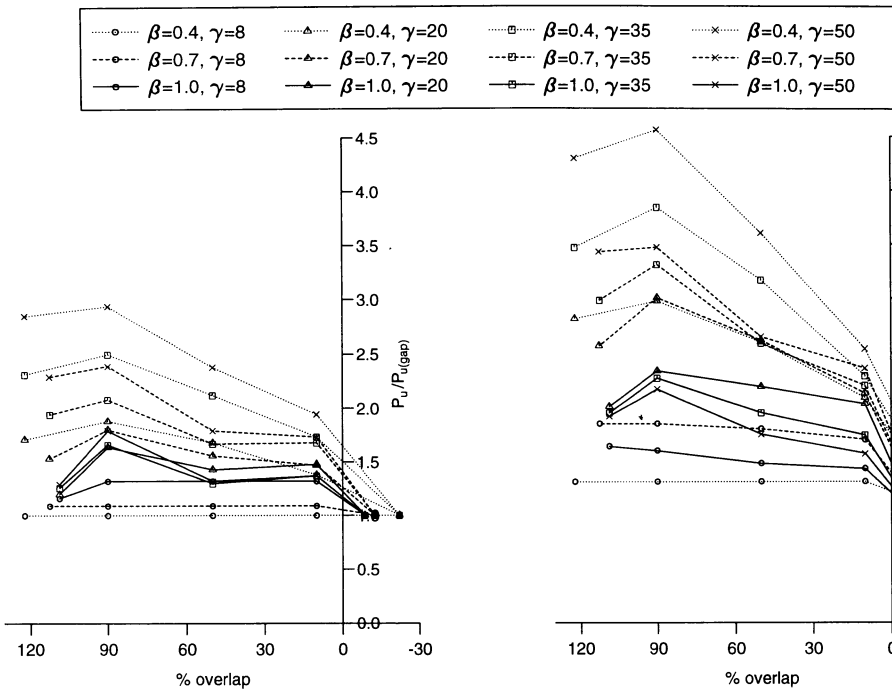

Figure 4a Effect of overlapping on the strength of τ=1.0 K-joints

Figure 4b Effect of overlapping on the strength of τ=1.5 K-joints

1998)). Overlapping does have an increasingly beneficial effect on strength for the higher τ geometries for most of the joints, with the overlapped joints being up to 3 times the strength of the corresponding gap joint for τ=1.0, or up to 4½ times the gap joint strength for τ=1.5. The influence of the chord on gap K-joint failure, particularly for the higher γ ratios (and lower βs), ensures that overlapping causes joint capacity increases when the relatively weak chord gap area is bypassed. However, for the lowest γ ratio of γ=8, there are generally still little strength increases due to the member failure modes of failure.

For the joints overlapped by more than 100%, the joint capacity is, in virtually all cases, less than that of the corresponding 90% overlapped joint – the 'gap' region of the through brace being subjected to high shear stresses and usually failing by cracking at a relatively low load level.

6 OVERLAPPED K-JOINT CAPACITY – TRENDS WITH GEOMETRY

The examination of the trends in overlapped joint strength was limited to the intermediate (10%–90%) overlapped joints. The overlapped joint strength varies with each of the geometric parameters β, γ, τ and overlap amount. Figure 5 depicts the decrease in strength with increasing γ ratio, for the 10% overlapped joints. Similar effects are observed for the 50% and the 90% overlapped joints. On the plot, the joints failing by member failure are marked in bold. Distinct trends in the joint strengths can be seen, particularly with the variation in β and γ, though in the cases of 'premature' member failure, the trends are often interrupted by unusually low capacities.

7 OVERLAPPED K-JOINT CAPACITY – COMPARISON WITH PREDICTIONS

7.1 *Predictions of Kurobane et al. (1984, 1986)*

Again, most of the joints fall outside the validity ranges of the CB equation (1). The BLB equation (3) was also applied though the formula is not valid for all the brace α_b ratios. The BLB prediction was the limiting capacity for all the τ=0.4 joints, and for the other joints with the most slender braces. These joints did indeed all fail by either Brace Member Failure (BMF), BLB or mixed BLB & CB. The CB prediction was the limiting capacity for the remainder of the joints, although a few of these did fail by BLB, and were not picked up by the BLB equation.

The performance of the combined Kurobane et al. predictions is plotted against γ for the 50% overlapped joints in Figure 6. Those for the 10% and

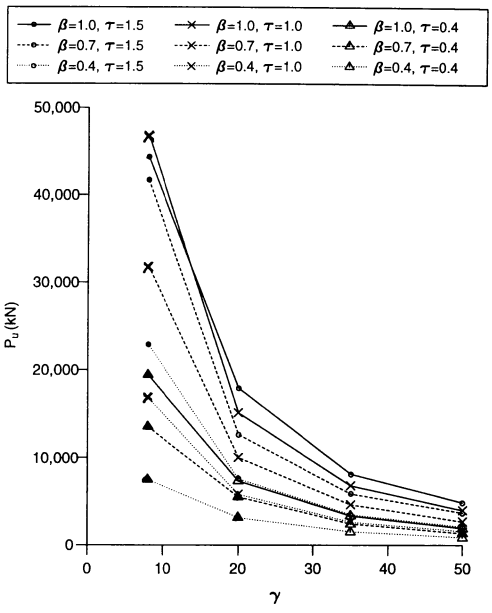

Figure 5 Effects of non-dimensional parameters on 10% overlapped K-joint strength

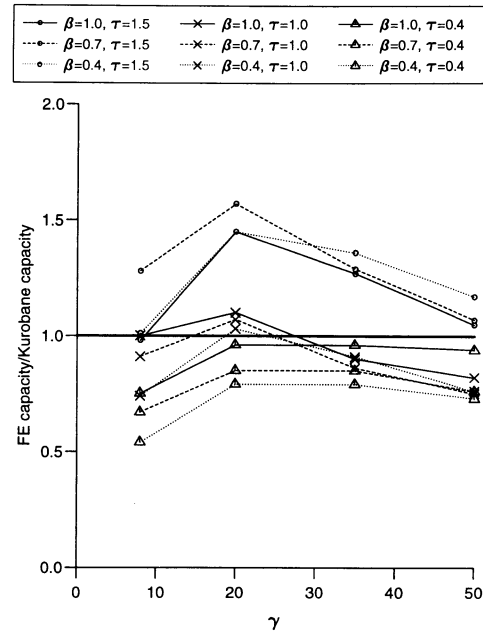

Figure 6 Performance of mean strength equations of Kurobane et al. for 50% overlapped K-joints

the 90% overlapped joints showed similar trends, though generally there was less data spread for 10% overlap, and more for 90% overlap. It should be noted that the plot includes all the joints, whether the CB or BLB equation was the limiting predicted capacity, and hence the trends in performance are not consistent. In general, the formulae adequately captured the effects of β on the joint strength. Joint strengths around γ=20 have been under-predicted relative to those at the lower and higher γ values. The formulae have not captured the strong positive effect of τ on joint strength.

Figure 7 compares the absolute CB equation predictions of Kurobane et al. (1984) (Equation 1) with the β=0.7 joint capacities for which the CB equation was critical. Similar plots were observed for the β=0.4 and β=1.0 joints. The equation (1) predicts negligible strength increases with increasing overlap beyond approximately 10%. The consequent 'flat top' distribution predicts the constant strength distributions of the joints failing by BMF, although this failure mode is not valid for this equation. The strength increases with overlap, seen for the higher γ joints, are not captured. The formula tends to over-predict the capacities of the τ=1.0 joints, and under-predict those of the τ=1.5 joints.

7.2 *Predictions of CIDECT (1991)*

Many of the parametric study joints fall outside the validity ranges of the chord plastification equation (6). The BLB check (Equation 9) only proved critical for the τ=0.4 joints, which all failed by BMF or BLB. However, there were other joints which failed by BMF or BLB for which the brace buckling efficiency check did not prove critical. The CIDECT reliabilities are plotted in Figure 8 against β for the 50% overlapped joints. The trends for the 10% and the 90% overlapped joints were similar, though again there was less data spread for 10% overlap and more for 90% overlap. Generally there were no consistent β trends missed by the formulae for the joints not failing by member failure. From the figure, it can be seen that for the joints with higher τ ratios, the γ=20 joints are again relatively under-predicted; however, for the τ=0.4 joints for which the buckling efficiency equation was critical, this phenomenon was not apparent. Whilst allowing for the fact that the τ=0.4 joint strengths were predicted by the buckling efficiency equation, there is a general positive strength trend with τ which has not been allowed for by the CIDECT equations, though a τ value of 1.5 is beyond the expected limitations of the formula.

When the chord plastification equation predictions were compared with the joint capacities measured in the present study over the range of overlaps, similar trends were seen as plotted in Figure 7 for Kurobane's CB equation predictions, except that all the joint strengths were under-predicted. The 'flat-top' distribution anticipated by CIDECT predicted the constant strength distributions of the joints failing by member failure (i.e. γ=8) but increasingly under-predicted the strength increases obtained at higher γ.

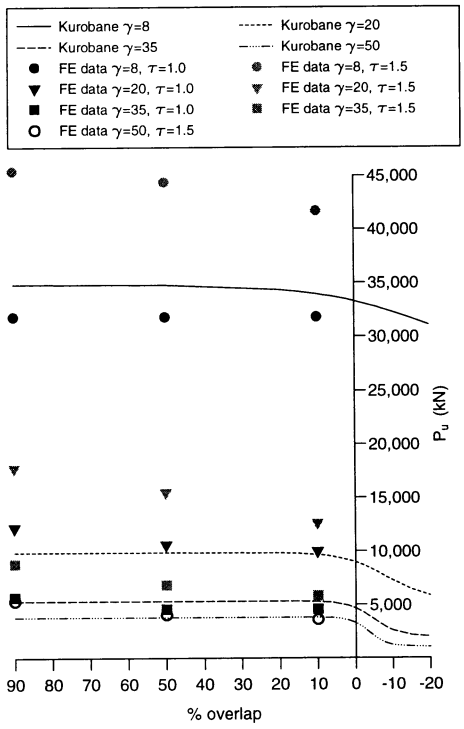

Figure 7 Measured and predicted joint capacities for the chord bending equation of Kurobane et al. for β=0.7 joints

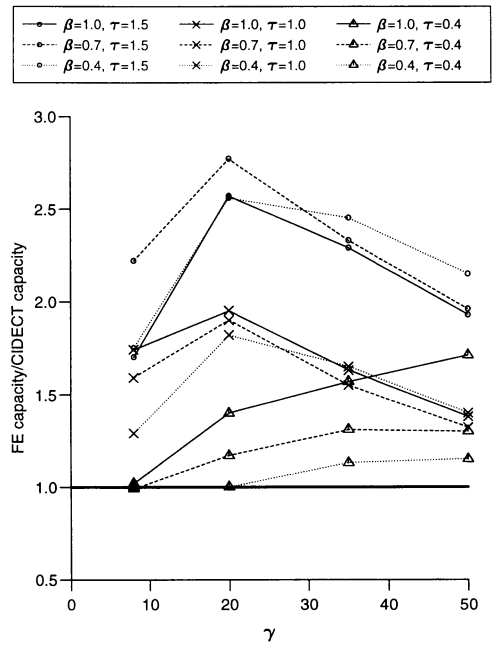

Figure 8 Performance of the design strength equations of CIDECT for 50% overlapped joints

8 NEW STRENGTH EQUATION PROPOSAL FOR OVERLAPPED K-JOINTS

8.1 *Included Failure Modes*

Previous overlapped joint capacity formulae have either attempted to allow for the different failure modes with separate capacity checks, or have assumed the occurrence of one particular mode of failure. However, the current research has shown the existence of a number of failure modes for overlapped joints, which may often occur simultaneously (as reported in the companion paper). Examination of the strength trends with geometry variations showed the data to follow consistent trends across the three failure modes of CB, BLB and mixed CB & BLB. Certainly, for these three modes of failure, the formulation of a single capacity equation, encompassing the interactive effects of β, γ, τ and overlap amount, would appear to be appropriate. However, the joints failing by member failure would not be expected to follow these same trends.

8.2 *Included Joint Types*

The K-joint capacity formulae of Kurobane et al. and CIDECT attempt to include both gap and overlapped K-joint capacities in one continuous equation. However, the arguments against this approach are strong. Firstly, zero gap lengths are not advised or allowed by any of the codes, due to the inherent fabrication problems, hence the requirement for continuous equations would appear academic. The instinct that gap and overlapped capacity equations should be continuous across g=0 may be questioned due to the abrupt change in behaviour and failure mechanism occurring at that point. Consequently, the application of a strength equation for overlapped joints should, for the present at least, be limited to intermediate overlapped joints (0% < % overlap < 100% or, in practice, 10% < % overlap < 90%).

8.3 *Non-dimensionalisation*

Joint capacity (under axial brace loading) is generally non-dimensionalised by $F_y T^2$, the format being based on a theoretical ring analogy. While this method is appropriate for T- and DT-joints, and has some significance for gap K-joints failing by chord plastification, its applicability to overlapped K-joints for which failure may be entirely governed by brace behaviour, is questionable. As an allowance for scale effects, non-dimensionalisation by D^2 would appear to be an appropriate factor; additionally the 'γ effect' issue would not be clouded. Transformation between the two methods of non-dimensionalisation may be achieved by simply multiplying by $4\gamma^2$.

8.4 *New Strength Equation*

The equation was developed using non-linear regression techniques on all the non-member failure data for the 10%, 50% and 90% overlapped joints. The simple equation

$$\frac{P_u \sin\theta}{F_y D^2} = 3.41\frac{\tau^{0.72}\beta^{0.98}}{\gamma^{1.43}} + 0.29\frac{\tau^{1.77} Ov^{1.57}}{\gamma^{1.13}} \qquad (17)$$

predicted the non member failure data with acceptable accuracy, with measured/predicted capacity ratios such that

mean = 1.00 CoV = 5.5%
max = 1.15 min = 0.87

The resulting histogram of measured FE / predicted joint capacities indicated a normal-type distribution.

The new equation (17) may be used to back-predict the capacities of all the intermediate overlapped FE data, including the joints failing by member failure, with the additional check for an efficiency limit of unity

$$\text{i.e.} \quad P_u \le \sigma_y A \qquad (18)$$

limiting the joint strength to the squash load of the compression brace. Additionally, due to the compressive state of stress in the chord, chord member failure must be considered similarly. When Equation 17 was applied to the entire FE database of intermediate overlapped joints, the capacities of most of the joints failing by member failure were over-predicted by the equation, but the efficiency restriction ensured the capacity predictions were then reduced to that of the limiting member squash load.

8.5 *Evaluation of the New Equation vs. Test Database*

The performance of the new strength equation (17) was investigated by comparing the predicted joint strengths with those available in the static strength database recently published by Makino et al. (1996), obtainable on the internet at

http://www.arch.kumamoto-u.ac.jp/Maki_lab/database.html

57 joints were 60°-60° overlapped axially loaded K-joints, obtained from five Japanese sources.

For the comparison, the brace material properties were used, rather than the more usual chord properties. F_y was limited to $0.8\sigma_u$. The statistics for the measured/predicted capacity ratios of the 57 test joints were

mean = 0.98 CoV = 11.2%
max = 1.36 min = 0.82

The strengths of only two joints were particularly under-predicted, since the database reports ultimate capacities well in excess of the brace squash load for both these joints. Otherwise, the strength predictions were all within 18%.

Some of the scatter may be attributed to known or suspected differences between the test set-ups and the conditions under which the FE joints were analysed. Details of boundary conditions, loading hierarchy and hidden weld presence or absence are not included in the database. The close predictions obtained may in fact imply that the effects of these unknown variations are relatively insignificant. Such extra information should be included in the database wherever possible in order to aid data analysis for future formulation of improved guidance.

9 CONCLUSIONS

For gap K-joints the two offshore codes, API (1993) and HSE (1990a), generally safely under-predict the capacities within the validity limits, but fail to account completely for the interactive effects of β and γ. The equations of Kurobane et al. (1984, 1986) predicted the effects of β and γ with better accuracy and made some allowance for the effects of τ on brace buckling. However, when these equations were adopted and simplified by CIDECT (1991), increased conservatism was in-built. Relatively few of the parametric study joints were within the validity limits of these onshore formulae.

The act of overlapping was shown to have a beneficial effect on joint strength for the higher values of τ, with the overlapped joints being up to 3 times the strength of the corresponding gap joint for τ=1.0, or 4½ times gap joint strength for τ=1.5; these highest increases being seen for the low β and high γ joint combinations. Overlapping by more than 100% generally caused a decrease in strength relative to that of the corresponding 90% overlapped joint.

The onshore approach to predicting overlapped K-joint strength by applying both chord plastification and brace buckling checks fails to separate and capture the failure mode of BLB completely. The chord plastification equation fails to predict all the interactive effects of β, γ and overlap amount, due to the limited database from which it was developed. The end result is high levels of conservatism in the CIDECT predicted capacities.

A new strength equation has been proposed for intermediate overlapped K-joints. Although the practical ranges of β, γ, τ and overlap have been completely covered, the equation has limited use in practice at present. It does, however, provide a robust platform onto which the results of further selective research may be added. Specifically:

- Geometry
  - the study has been limited to 60°-60° K-joints with braces of equal geometry
  - the equations are expected to be unconservative if the hidden weld of a joint is absent. A suitable capacity de-rating factor is then required
- Material
  - the effects of varying either σ_y or σ_y/σ_u are unknown
  - the effects of varying the relative brace:chord material strengths are unknown but may be expected to be particularly significant – as

discussed in the previous paper, joint strength may be expected to decrease with overlap if a joint's braces are relatively weak

- Loading
  - the equations are valid only for the case of balanced axial loading
  - the study was limited to the case of the through brace being in compression, which is thought to be the weaker case, at least for small to medium overlaps. For heavily overlapped joints, the equation could be unconservative if the through brace is in tension

9.1 *Final Note*

Work is currently in progress at Swansea to extend the research reported here. For gap K-joints, the FE database has been extended to investigate the effect of the gap parameter. For overlapped joints, initial results suggest that the effect of loading hierarchy reversal is relatively insignificant – although at high overlaps, the through-brace-in-tension case is indeed weaker than the reverse case, the strength difference is less than 10%. An investigation of the effects of varying the brace angle θ, (including some 45°-90° cases) and the absence of the hidden weld for through-brace-in-tension joints is also underway.

10 NOMENCLATURE

A = member cross-sectional area
D = chord diameter
d = brace diameter
E = Young's Modulus
F_y = $\min\{\sigma_y, 2/3\ \sigma_u\}$ (API 1993), or $\min\{\sigma_y, 0.7\ \sigma_u\}$ (HSE 1990a)
g = gap length
L = chord length
Ov = % overlap/100 = $g\sin\theta/d$
P_a = allowable (lower bound) ultimate capacity
P_k = characteristic ultimate capacity
P_u = mean ultimate capacity
P^* = joint design strength (CIDECT) = P_k/γ_m
T = chord wall thickness
t = brace wall thickness
α = joint geometry ratio $2L/D$
α_b = buckling parameter = $Et/\sigma_y d$
β = joint geometry ratio d/D
γ = joint geometry ratio $D/2T$
γ_m = partial material safety factor
θ = in-plane brace angle
σ_{blb} = average ultimate brace stress due to brace local buckling
σ_{sb} = average ultimate brace stress due to shell bending
σ_u = ultimate tensile stress
σ_y = yield stress
τ = joint geometry ratio t/T
ζ = joint geometry ratio g/D

11 REFERENCES

American Petroleum Institute (API) (1993) API RP 2A: *Planning, Designing and Constructing Fixed Offshore Platforms*, 20th edition, Section E, Connections

Comité International pour le Developpement et l'Étude de la Construction Tubulaire (CIDECT) (1991) *Design guide for circular hollow section (CHS) joints under predominantly static loading*

Dexter E.M., Lee M.M.K., Kirkwood M.G. (1994) "Effects of overlap on strength of K-joints in CHS tubular members", *6th International Symposium on Tubular Structures*, Melbourne, Australia, pp 581-589

Dexter E.M., Lee M.M.K., Kirkwood M.G. (1996a) "Overlapped K-joints in circular hollow sections under axial loading", *Journal of Offshore Mechanics and Arctic Engineering*, ASME, February 1996, Vol. 118, pp53-61

Dexter E.M., Lee M.M.K. (1996b) "Effects of chord can length and overlap on the strength of K-joints in CHS tubular members", *7th International Symposium on Tubular Structures*, Miskolc, Hungary, pp 131-138

Dexter E.M. (1996) "Effects of overlap on behaviour and strength of steel circular hollow section joints", PhD thesis C/Ph/200/96 University of Wales Swansea

Dexter E.M., Lee M.M.K. (1998) "Effect of overlap on the behaviour of axially loaded CHS K-joints", *8th International Symposium on Tubular Structures, Singapore*

Health and Safety Executive (HSE) (1990a) *Offshore Installations: Guidance on design, construction and certification*, Appendix A21, Steel. 4th edition

Healy B.E. (1994) "A numerical investigation into the capacity of overlapped circular K-joints", *6th International Symposium on Tubular Structures*, Melbourne, Australia, pp 563-571

Kurobane Y., Makino Y., Ochi K. (1984) "Ultimate resistance of unstiffened tubular joints", *Journal of Structural Engineering*, Vol. 110, No 2, February 1984, pp 385-400

Kurobane Y., Ogawa K., Ochi K., Makino. (1986) "Local buckling of braces in tubular K-joints", *Thin-Walled Structures*, pp 23-40

Makino Y., Kurobane Y., Ochi K., van der Vegte G.J., Wilmshurst S.R. (1996) "Introduction to unstiffened CHS tubular joint database", *7th International Symposium on Tubular Structures*, Miskolc, Hungary, pp 157-164

Tubular Structures VIII, Choo & Van der Vegte (eds) © 1998 Balkema, Rotterdam, ISBN 90 5809 001 9

Static strength tests of CHS KT-joints under axial loading

S. R. Wilmshurst, M. Morita, S. Sakae & Y. Makino
Kumamoto University, Japan

Y. Kurobane
Kumamoto Institute of Technology, Japan

ABSTRACT: This paper reports the results of three static strength tests on uniplanar KT-joints made from circular hollow sections subjected to axial loading. The main geometric parameter variations within the specimens were the diameter ratio, β, and the chord thinness ratio, γ. The aims of the tests were to compare the test strengths with code predictions, and to investigate the post-ultimate load behaviour of the joints as load redistribution occurred. The test rig was designed for this purpose and induced a primary load path along the inclined members. The results of these tests showed some load redistribution to the centre brace after the failure of the chord wall under the inclined compression brace. Eventual collapse of one of the specimens was the result of crack formation at the base of the inclined tension brace, and not due to the failure of the chord wall under the compression braces. Comparison of the joint capacities with strength predictions from leading codes and guidance showed that, where applicable, KT-joints could be conservatively designed using K-joint estimation formulae.

1 INTRODUCTION

In the last thirty to forty years CHS joint research has seen many test programmes and finite element parametric studies devoted to understanding joint behaviour and enhancing static strength formulae. Much of this work has been performed on uniplanar joints. However, a joint configuration that has design guidance but little substantiating data in the public domain is the KT-joint (see Figure 1). Previous test programmes on KT-joints have been carried out by Wardenier and de Koning (1977), and Milani and Grundy (1996). A summary of each is given in the next section. However, the tests did not investigate the post-ultimate load behaviour.

The KT-joint is the uniplanar component of the KTKT-joint, which is often found in the leg nodes of structures constructed from circular hollow sections such as masts, towers, and offshore jackets. The design guidance for KTKT-joints is based upon uniplanar estimation formulae and, to the authors' knowledge, there are no available static strength data. Therefore as part of the ongoing study (Morita *et al* (1996, 1997)) to produce a continuous design formula for uniplanar and multiplanar joints, a test programme investigating the ultimate load behaviour of KT-joints was initiated. This is a preliminary study to future test programs and numerical studies aimed at investigating the ultimate load behaviour of KT- and KTKT-joints.

2 PREVIOUS KT-JOINT TEST PROGRAMS

2.1 Wardenier and de Koning (1977)

Ten KT-joints were tested to determine the influence of γ upon the joint ultimate capacity. Three γ ratios were studied (10.6, 11.25, and 15.15) with a constant β ratio (~0.4) used throughout the test programme. The influence of the joint eccentricity was also studied using two values of e (0 and 0.25D). Three loading conditions were used, which involved individually loading either brace 2 or brace 3, or loading both brace 2 and brace 3 together by a specified ratio. (*Note*: the brace numbering has been altered from original report for consistency herein). Essentially, this meant that the loading placed upon the joint was force-controlled and did not lend itself to the study of the post-ultimate behaviour.

Of the results, six joints yielded in the tension brace, three failed due to chord wall deformation with cracks formed on the chord wall at the tension brace weld toe, and one specimen was not loaded to failure. The specimens that failed in the chord all had a γ ratio of 15.1. Based upon the results of the test programme it was concluded that the strength of KT-joints could conservatively be calculated on the same basis as Warren (K-) or Pratt (T-) type joints. It was also concluded that if the two brace members were loaded in compression both loads should be taken into account.

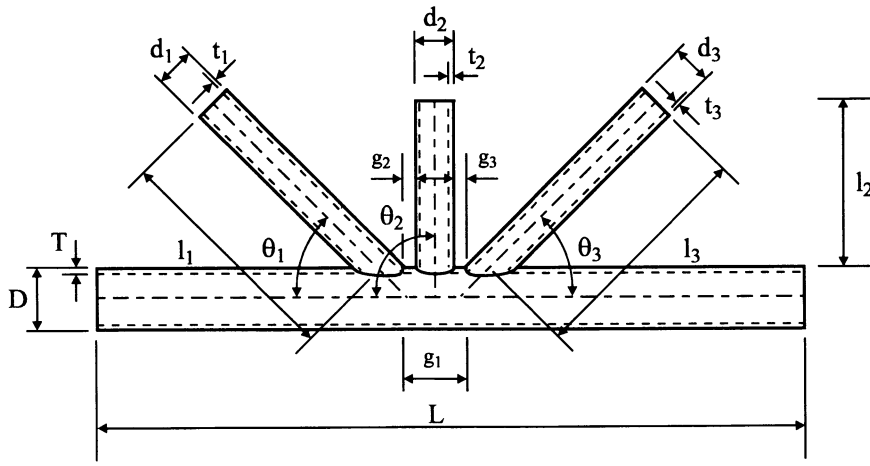

Figure 1 CHS KT-joint specimen showing nomenclature

Although many of the specimens did not reach the full joint capacity due to member failure, the study does provide a valuable insight into considerations that must be made with respect to both the specimen sizing and the loading system.

2.2 *Milani and Grundy (1996)*

As part of a study into the incremental collapse of axially loaded CHS joints in offshore structures, four KT-joints were tested under slow varying high amplitude cyclic loading. The aims were to determine the shakedown loads beyond which incremental collapse of the joints would occur, and to compare the results with the static collapse load determined from monotonic tests on the same specimens after the cyclic loading tests. All specimens had γ of 14, and two β ratios (0.64 and 0.73) were used in two cyclic loading regimes.

The test-rig was set up to allow a constant ratio (P_2=0.7P_3) of the loads in the compression braces (braces 2 and 3 in Figure 1) to be maintained. A description of the procedure for the cyclic tests is beyond the scope of this paper and can be found in the original literature. However, after the incremental collapse tests the joints were subjected to monotonic static tests. The load ratio was maintained as for the cyclic tests, and after the onset of plastic deformations were detected the load increments were reduced to allow the correct detection of the static collapse limit.

Their results showed for both of loading regimes that the shakedown limit was about 15-17% lower than the static collapse limit. A feature of their test rig was that significant reversal of the axial force in the brace members could not be introduced.

3 TEST SPECIMENS AND GEOMETRY

The dimensions of the test specimens are given in Table 1. The lengths of the chord and the brace members were designed to fit the test rig, which is described in the next section. However, the chord length was greater than 8×D in order to prevent end effects In total, three specimens were tested. In each KT-joint, brace 1 and brace 3 were inclined at 45° to the chord member and brace 2 was inclined at 90° to the chord . The member sizes for the specimens were chosen to provide two variations in β and γ between the specimens.

The material properties of the specimens are given in Table 2. These were obtained from tensile coupon and stub column tests performed on specimens from the same tubes. The material testing was carried out in accordance with Japanese Industrial Standards, which follow the usual practice of using a strain rate of 10^{-4}/sec and determination of the yield stress based on a 0.2% offset.

End profiles of the braces were prepared by automatic flame cutting, and the weld details were designed in accordance with the Recommendations for the Design and Fabrication of Tubular Structures in Steel (AIJ, 1990).

4 TEST PROCEDURE

4.1 *The test rig*

The test set-up is shown in Figure 2. It was designed with the intention of simulating the loading pattern that could occur within a KT-joint in framework. The loading was applied to the right hand end of the universal beam by a 100-ton hydraulic ram. The end of the beam was displaced downwards to induce the

Table 1 Geometry of specimens

Specimen	θ_1,θ_3	θ_2	l_1,l_3	l_2	D	T	d	t	g_1	g_2	g_3	e
	[°]	[°]	[mm]	[mm]	[mm]	[mm]	[mm]	[mm]	[mm]	[mm]	[mm]	[mm]
KT-1	45	90	723	383	215.7	5.7	101.7	5.3	183.7	40.0	42.0	54.0
KT-2	45	90	723	383	216.4	8.1	101.7	5.3	179.7	39.0	39.0	54.0
KT-3	45	90	691	360	215.7	5.7	76.3	3.9	169.3	46.5	46.5	27.0

For all specimens L = 2420 mm

Table 2 Material properties of the specimens

Specimen Nominal Size	σ_y (Nmm^{-2})	σ_u (Nmm^{-2})	E (Nmm^{-2})	Elongation (%)	Steel Grade	Specimen Designation
Chord ($216.3^{\varnothing}\times6.0$)	398	496	207440	29.9	STK 400	KT-1, KT-3
Chord ($216.3^{\varnothing}\times8.0$)	407	490	207810	34.5	STK 400	KT-2
Brace ($101.6^{\varnothing}\times5.0$)	461	543	182040	31.7	STK 400	KT-1,KT-2
Brace ($76.3^{\varnothing}\times4.0$)	426	502	190240	27.0	STK 400	KT-3

STK400 tubes are cold-finished ER-welded tubes.

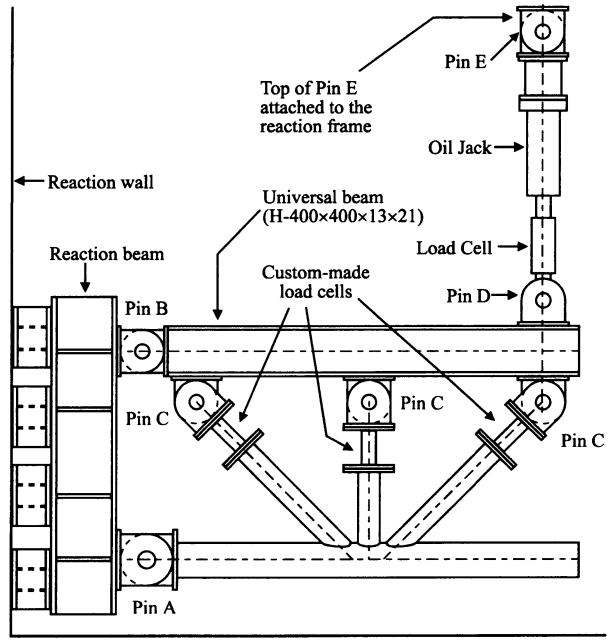

Figure 2 The test set-up

loading in the braces. As the tests are uniplanar, lateral bracing was connected to the free ends of both the chord and the universal beam to prevent out-of plane deflections of the test rig and thereby provide stability. The other end of the bracing was fixed to the reaction frame, which is not shown in Figure 2. The length of the bracing was continuously adjusted during the testing as the beam and the chord ends were deflected downwards.

4.2 Measurement of the loads and deformations

Loads were measured by a dynamometer mounted at the hydraulic ram end and by purpose built load cells attached to the brace ends. A purpose built load cell

is shown in Figure 3. The material used was SS400, which is a solid section with a minimum ultimate tensile strength of 400 Nmm^{-2}. This was welded to two 22mm thick steel plates. Strain gauges were accurately positioned around the section as shown in the figure. Each load cell was accurately calibrated prior to being used in the tests. These load cells were used due to the high shear forces that could be induced at the brace ends, which could have damaged the end fittings of standard load cells. They also have the advantage of being able to measure the bending stresses and hence any shear loading in the braces. In addition to the load cells, the loads were also measured using rings of strain gauges placed at two positions along the length of each member.

Displacements and deformations were measured at several positions in the test rig. The deformations of the chord wall under the braces were measured using wire displacement gauges attached to bolts welded level with the centre-line of the chord member and attached to each side of the braces. The bolt positions are shown in Photographs 1(a) to 2(b). A schematic diagram of the set-up for the wire displacement gauges is shown in Figure 4.

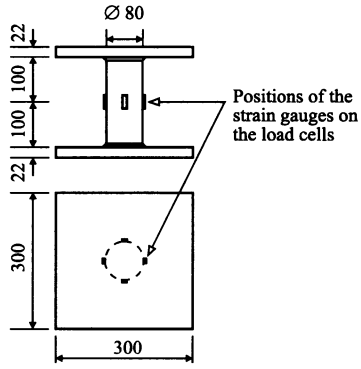

Figure 3 A purpose-built load cell

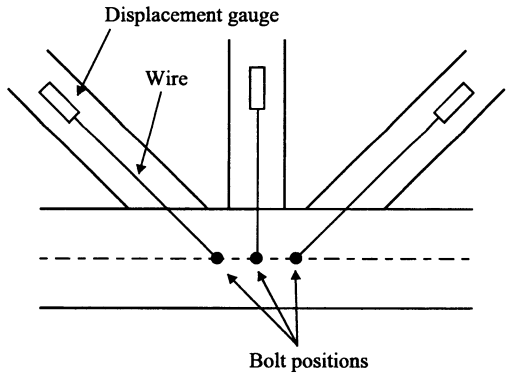

Figure 4 Wire displacement gauge set-up

5 TEST RESULTS

Figure 5 presents graphs of force against the displacement of the beam end for each of the specimens. The load-deformation curves of the test specimens are shown in Figure 6. The loads in the braces are those measured by the purpose-built load cells, and the 'deformation' refers to the deformation of the chord wall under the respective braces. These are the average deformations measured by the wire displacement gauges. The conventions for the brace loads are as follows:

a) Brace 1 – Tension +ve, Compression –ve.
b) Brace 2 – Compression +ve, Tension –ve.
c) Brace 3 - Compression +ve, Tension –ve.

The directions of the deformations follow the loading conventions. Table 3 presents the loads in the brace members at the first peak load and the corresponding deformation of the chord wall under brace 3. The following sub-sections give a summary of the observed joint behaviour during each test:

Specimen KT-1

From Figure 5(a) it can be seen that as the load was applied to the end of the beam it was balanced by axial loads in braces 1 and 3. Brace 2 did not begin to carry any notable axial load until failure of the chord wall occurred under brace 3 at a beam displacement of 26.2mm. Although the chord wall under brace 3 had failed, joint stability was maintained by the load transfer into brace 2. This stability continued during further loading until a through crack formed in the chord wall near the weld toe at the base of brace 2. The position of the crack was at the crown nearest to brace 2 (see Photograph 2(a)) and was due to the high tensile stresses caused by the chord wall deformation in the gap between braces 2 and 3 (see Photograph 1(a)). Inspection of the specimen after the test revealed a ductile fracture surface, accounting for the gradual drop in the axial loads measured in braces 1 and 3. The eventual collapse of the specimen was due to a crack in the chord wall at the base of the brace 1 which caused a sudden drop of the loads in all three braces (see Photograph 2(a) and Figure 5(a)).

Specimen KT-2

A stable hairline crack initiated in the chord wall at the base of the tension brace when the beam end displacement was 20.7mm (corresponding to δ_3 of 1.51mm). However, as the joint stiffness under brace 3 did not appear to suddenly change, this crack probably did not affect the overall joint behaviour. Up to the first maximum, the tension and compression brace axial loads were balanced to within 6%, with a low tensile load in brace 2. After the failure of the chord wall under brace 3, this gradually changed to a compressive load in order to

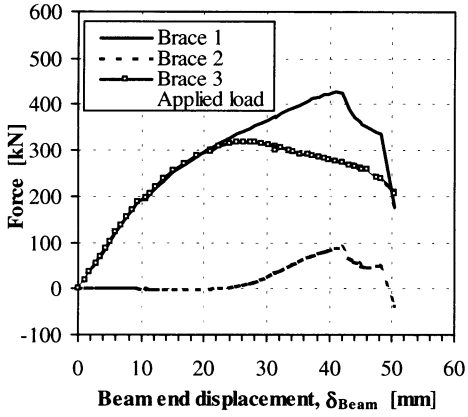

(a) KT-1

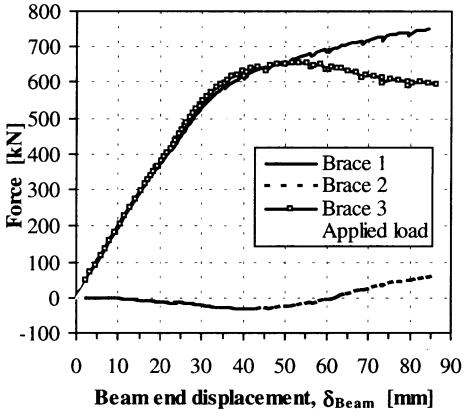

(b) KT-2

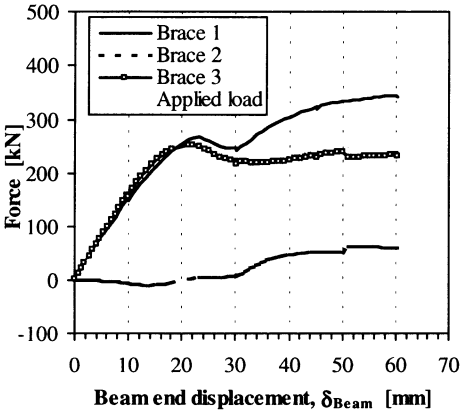

(c) KT-3

Figure 5 Force vs. beam end displacement relationships

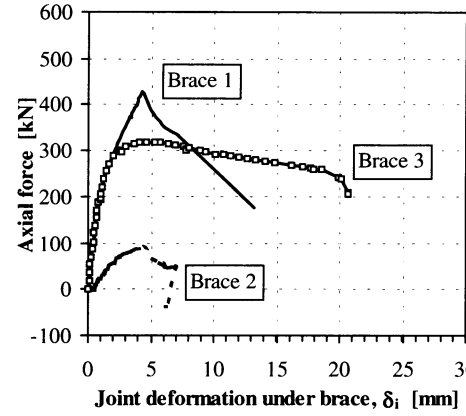

(a) KT-1

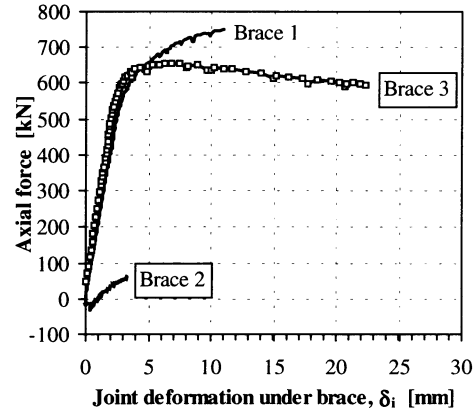

(b) KT-2

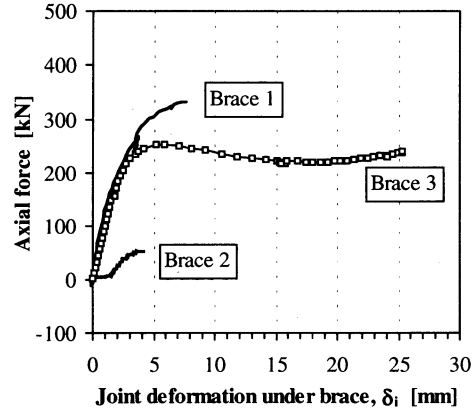

(c) KT-3

Figure 6 Load-deformation relationships

Table 3 Results of the tests

Specimen	Brace loads at first maximum $P_{u,i}$ [kN]			$\delta_{u,3}$ [mm]	$P_{u,Beam}$ [kN]	$\delta_{u,Beam}$ [mm]	Failure mode
	1	2	3				
KT-1	341.2	6.6	319.5	4.6	283.4	26.2	a, c2, c1
KT-2	678.3	-15.5	655.8	7.5	560.9	55.0	c1, a, c2
KT-3	263.9	1.2	253.7	5.2	227.0	21.3	a, c2

Failure modes: a Chord wall deformation
c1 Crack in chord wall at base of brace 1
c2 Crack in chord wall at base of brace 2

Table 4 Comparison of joint capacities with strength predictions

Specimen	$P_{u,3}$ [kN]	Strength predictions [kN] and ratios					
		$P_{u,API}$	Ratio	$P_{u,HSE}$	Ratio	$P_{u,K,Kur}$	Ratio
KT-1	319.5	187.8	1.70	297.9	1.07	288.0	1.11
KT-2	655.8	373.7	1.75	613.6	1.07	538.1	1.22
KT-3	253.7	153.8	1.65	236.6	1.07	235.7	1.08

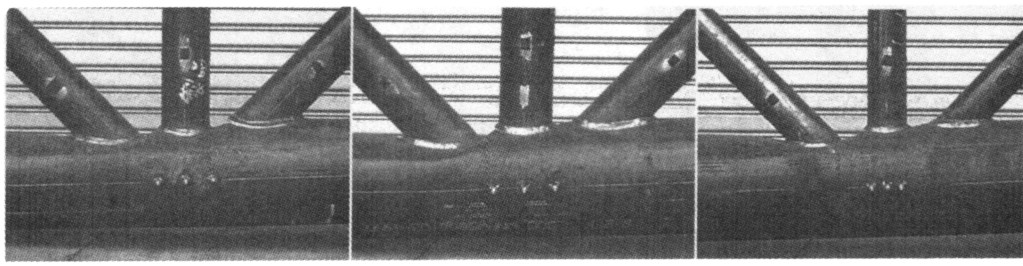

(a) KT-1 (b) KT-2 (c) KT-3

Photograph 1 Joint deformation of specimens after testing

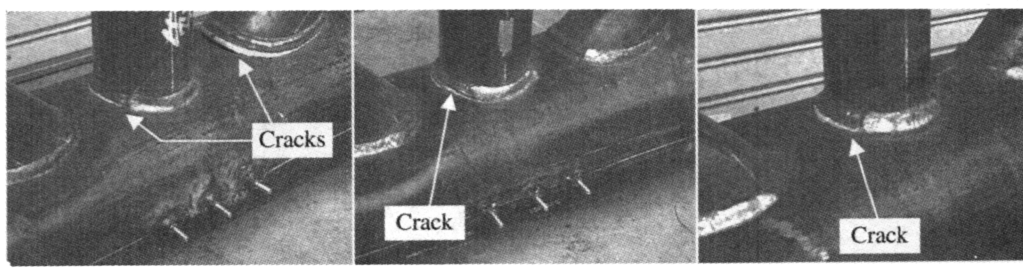

(a) KT-1 (b) KT-2 (c) KT-3

Photograph 2 Positions of cracks in the specimens

balance the loads in braces in 1 and 3. In addition, a crack initiated at the base of brace 2 in the gap between braces 2 and 3 (see Photograph 2 (b)). The formation of this crack was due to the high tensile stresses induced in the gap by the deformation of the chord wall under brace 3. The joint deformation can be seen in Photograph 1 (b). The test was terminated before an overall collapse of the specimen occurred.

Specimen KT-3

Up to the first maximum, the tension and compression brace axial loads were balanced to within 3% with a very low tensile load recorded in brace 2. This tensile load decreased due to compressive axial stresses acting in the brace as the first maximum load was approached. The first maximum occurred when the beam end

displacement was 21.3mm and was the result of failure of the chord wall under brace 3. Soon after the peak, a crack initiated at the base of brace 2, occurring in the same position as the other two specimens. However, unlike the other specimens, increased displacement of the beam end did not increase the axial loads in the braces. Indeed, it can be seen from the graph of axial load against beam end displacement (Figure 5(c)) that there was a decrease in the overall joint stiffness. Subsequently, there was an increase in the joint stiffness with the increase of the tensile axial load in brace 1 balanced mainly by an increase of the compressive axial load in brace 2.

A comparison of the joint strengths with predictions from API (1993), HSE (1995), and the K-joint mean strength prediction formula of Kurobane *et al* (1984) are shown in Table 4. (*N.B.* no load resistance factors were used in the assessment of the API code predictions, and any safety factors were removed from all the prediction formulae). It can be seen that all the predictions are conservative. The formula of Kurobane *et al* is considered by many researchers to give accurate predictions of K-joint mean strengths. The joint capacity was an average of 14% higher than the predictions from this formula. It is possible that this higher joint strength was due to the presence of the centre brace, which could serve to stiffen the chord wall between brace 1 and brace 3.

6 CONCLUSIONS

This paper reports the results of three static strength tests on KT-joints. The aim of the test programme was to provide information regarding the ultimate strength and the post-ultimate behaviour of KT-joints. The test rig was designed to allow load redistribution within the joint after failure of the chord wall under the braces. The following conclusions can be drawn from this study:

1. Until the first maximum load was reached for each specimen, the axial loading in braces 1 and 3 remained more or less balanced. It was observed that throughout the test the axial load in brace 2 was low in comparison to the axial loads in the inclined braces. The primary load path acted along the diagonal bracing.
2. The first failure within each specimen was due to plastification of the chord wall under brace 3. This resulted in load redistribution between braces 2 and 3 in order to balance the tensile load in brace 1.
3. In each specimen a crack formed in the chord wall at the base of the centre brace.
4. Cracks initiated at the chord weld toes of braces 1 and 2 due to the high tensile membrane stresses in the gaps caused by the local deformation of the joints. The eventual collapse of specimen KT-1 was a result of the crack formation at the base of brace 1. From the results, it would appear that overall collapse of KT-joints is more likely to be due to a combination of crack formation and chord wall plastification, rather than due solely to chord wall plastification under both compression braces.

The comparison of strength predictions from leading codes and estimation formulae indicate that the strengths of axially loaded KT-joints where the centre brace is unloaded can be designed conservatively using K-joint strength formulae.

The test results show that the first failure within the joint is a ductile failure of the chord wall under the primary compression brace. The joint ductility continues well beyond the first peak load recorded in the joint, with the possibility of cracks forming at the base of the centre brace well beyond the first peak load. Load redistribution allows the centre brace to carry some of the compressive loading required to maintain joint stability. However, it was observed from the tests that the overall collapse of a KT-joint could be the result of a combination of cracking and chord wall plastification.

7 ACKNOWLEDGEMENTS

The first author would like to thank the Japan Society for the Promotion of Science for the opportunity to carry out tubular joint research in Japan. All the authors would like to extend their sincere gratitude to the following people for their diligent assistance in the testing laboratories: Chief Technician, Mr. M. Hayashida, and students, Messrs. Y. Yamada, M. Honda, Y. Kubota, and T. Higashikosono.

The first author would also like to extend his appreciation to colleagues at Advanced Mechanics and Engineering Ltd., Mott MacDonald Group, for their review comments on this work.

8 NOMENCLATURE

e	Joint eccentricity
σ_y	Yield stress
σ_u	Ultimate tensile stress
E	Elastic modulus
β	Diameter ratio (d/D)
γ	Chord thinness ratio (D/2T)
δ_i	Chord deformation under brace i (i=1...3)
$\delta_{u,i}$	Chord deformation under brace i (i=1...3) at ultimate load
δ_{Beam}	Beam end displacement

$\delta_{u,Beam}$ Beam end displacement at ultimate load
$P_{u,i}$ Ultimate load in brace i (i=1...3)
$P_{u,Beam}$ Applied load at beam end at ultimate load
$P_{u,API}$ Joint capacity predicted by API (1993)
$P_{u,HSE}$ Joint capacity predicted by HSE (1995) (mean strength)
$P_{u,K,Kur}$ Joint capacity predicted by K-joint formula of Kurobane *et al* (1984) (mean strength)

9 REFERENCES

American Petroleum Institute, Recommended practice for planning, designing and constructing fixed offshore platforms, API RP2A 1991 and API RP2A-LRFD 1993.

Architectural Institute of Japan (1990), Recommendations for the design and fabrication of steel structures in steel, AIJ, Tokyo, Japan (in Japanese).

Health and Safety Executive (1995), "Offshore Installations: Guidance on design, construction and certification", 4th Edition, Health and Safety Executive, UK.

Kurobane Y., Makino Y., and Ochi K. (1984), Ultimate resistance of unstiffened tubular joints, *Journal of Structural Engineering*, ASCE, Vol. 110, No. 2, pp. 385-400.

Milani N.K. and Grundy P. (1996), Incremental collapse of KT-joints under variable repeated loading, *Proceedings of the 7th International Symposium on Tubular Structures*, Miskolc, Hungary.

Morita M., Makino Y., Kurobane Y., and van der Vegte G.J. (1996), A new ultimate capacity formula for unstiffened CHS joints under compression – continuous formula between T, TT an X-joints, *Proceedings of the 7th International Symposium on Tubular Structures*, Miskolc, Hungary.

Morita M., Yamada Y., Makino Y., Wilmshurst S.R., Kurobane Y., and Lee M.M.K. (1997), "A new ultimate capacity formula for unstiffened CHS K-joints under axial brace loads", *Proceedings of the 7th International Offshore and Polar Engineering Conference*, Honolulu, Hawaii, U.S.A.

Wardenier J. and de Koning C.H.M. (1977), Investigation into the static strength of welded joints with three bracings made of RHS or CHS, Stevin Report No. 6-77-6, TNO-IBBC Report No. BI-77-37/35.3.51210.

Tubular Structures VIII, Choo & Van der Vegte (eds) © 1998 Balkema, Rotterdam, ISBN 90 5809 001 9

The effects of weld size on the ultimate strength of a double-tee tubular joint under brace axial compression or bending

C.T. Kang, D.G. Moffat, J. Mistry & K.T. Ong
Department of Engineering, The University of Liverpool, UK

ABSTRACT: The effects of weld size on the ultimate capacity of a Double-Tee (DT) tubular joint under brace axial compression, in-plane bending (IPB) and out-of-plane bending (OPB), have been assessed using the general purpose finite element program ABAQUS. Non-linear effects have been included in the modelling. Three models were created for this study: one model without the weld and the other two with welds of different sizes. The results suggest that the joint ultimate load carrying capacities are influenced significantly by the weld sizes. The predicted bending strengths are generally higher than the lower bound or characteristic strength values calculated from API RP 2A and DEn rules, respectively.

NOMENCLATURE

d	brace outside diameter
D	chord outside diameter
E	Young's modulus
F_y	tensile yield stress
H_c	weld height at crown
H_s	weld height at saddle
l_b	length of unconnected brace member
L	chord total length
M_{ib}	in-plane brace moment
M_{iub}	ultimate in-plane brace moment
M_{ki}	DEn characteristic brace IPB moment
M_{ko}	DEn characteristic brace OPB moment
M_{ob}	out-of-plane brace moment
M_{oub}	ultimate out-of-plane brace moment
P_b	brace axial compression
P_k	DEn characteristic brace axial load
t	brace thickness
T	chord thickness
W_b	transverse uniform distributed load
W_c	weld width at crown
W_s	weld width at saddle
α	length parameter (= $2L/D$)
β	diameter ratio (= d/D)
Δ	Yura deformation limit
ε_y	uniaxial yield strain
γ	chord radius to thickness ratio (= $D/2T$)
ν	Poisson's ratio
θ_{rl}	Yura rotation limit
τ	wall thickness ratio (= t/T)

1 INTRODUCTION

A double-tee (DT) tubular joint, which is considered in the present work, consists of two brace members intersecting the chord member at 90°. The parameters used in designing DT tubular joints, as illustrated in Fig. 1, are chord outer diameter (D), chord thickness (T), chord length (L), brace outer diameter (d) and brace thickness (t). The corresponding non-dimensional geometrical parameters used to describe the tubular joints are α (= $2L/D$), β (= d/D), γ (= $D/2T$) and τ (= t/T).

Over the past three years a combined experimental and numerical study has been undertaken on such DT joints at Liverpool. The main objectives of this work have been to assess the effects of chord compression on the ultimate strength of DT joints under brace axial loading (Kang et al 1998) and brace out-of-plane bending (OPB) (Kang et al). The Finite Element (FE) procedures used to model the joints have been described by Kang et al (1996) and the influence of chord length and thickness on the ultimate strength of OPB loaded DT joints is presented by Kang et al (1998). The present paper is an extension

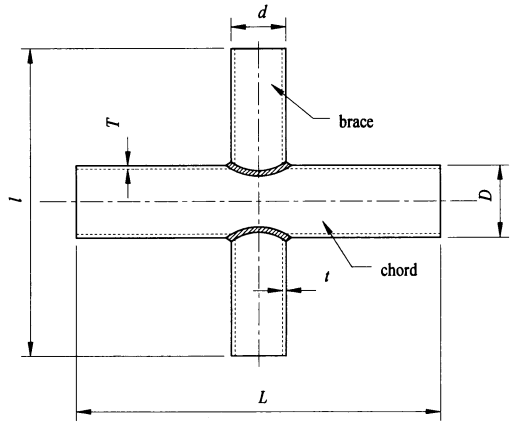

Fig. 1 DT Tubular Joint

Table 1. Model dimensions and geometrical parameters

Geometric Parameters	Values (mm)	Non-dimensional Parameters	Values
D	169	α	16.56
T	7.42	β	0.61
L	1400	γ	11.39
d	102	τ	0.84
t	6.27		

Table 2. Weld Sizes Selected in the Study

Model	H_s/T	W_s/t	H_c/T	W_c/t
W2	2.75	0.99	1.68	0.99
W3	3.61	1.99	1.68	1.99

of this work and is concerned with the influence of the size of the brace/chord weld on the strength of a DT joint.

In non-linear analysis the joint stiffnesses and ultimate loads are dependent to a greater or lesser extent on the joint parameters listed above. However, it seems clear that the size and proportions of the brace/chord weld will also influence joint behaviour. Liaw et al (1976) pointed out the potential benefits of using three dimensional isoparametric finite elements for modelling welded tubular connections. van der Vegte et al (1991) and van der Vegte and Wardenier (1994) used modified shell elements to model the welds in X- and T-joints. However, the authors are not aware of any previous work that specifically examines the influence of weld size on tubular joint design.

The present paper uses 20-noded isoparametric brick elements to model a β = 0.61 DT tubular joint including the brace/chord weld. Three models were created for the study, one with no weld and the other two with welds of different sizes. Results are presented for brace axial compression, brace in-plane-bending (IPB) and brace out-of-plane (OPB), in each case the load being transmitted via the chord from one brace to the other.

2 JOINT GEOMETRY AND MATERIAL PROPERTIES

The geometry and the corresponding non-dimensional parameters of the FE models are given in Table 1. The 1400 mm chord length was selected on the basis of the previous work carried out at Liverpool. This showed that chord end effects are eliminated if α is greater than 15 (Moffat et al 1992).

Three models were used for this study. Model W1 was generated without a weld. In models W2 and W3 the weld size parameters shown in Fig.2 were selected as given in Table 2. The weld of model W2 has similar dimensions to those of the experimental components used by the authors (Kang et al, 1998), but with constant width (i.e. $W_s = W_c$) around the joint to simply FE modelling. The main difference between the welds W2 and W3 was that the width W of W3 was twice that of weld W2. Though model W1 is considered unrealistic, it was included for comparison purposes to assess the effects of the weld on the load carrying capacity.

The material properties of the model were represented by a true stress-strain relationship (Fig. 3). The material for the joint, including the weld, was taken to be structural steel with yield stress F_y = 340 MN/m^2, Young's modulus E = 210 GN/m^2 and Poisson's ratio ν = 0.3. The von Mises effective stress was employed in all FE analyses. Each model was subjected to all three different loads: axial compression, IPB and OPB of the brace members. To avoid premature failure of the brace under IPB loads, the

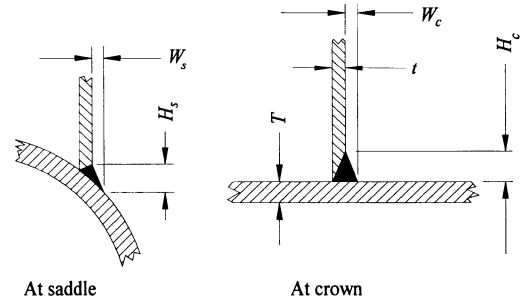

Fig. 2 Weld Notation for Models W2 and W3

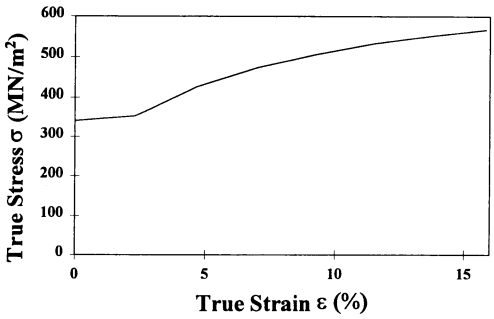

Fig. 3 True Stress-Strain Material Model

yield stress of the brace material was selectively increased to 1000 MN/m^2 to ensure that it remained intact throughout the analyses.

3 FINITE ELEMENT MODELLING

The models were created using the PATRAN (PDA Engineering 1993) mesh generation program and the static strength of the models was assessed using the ABAQUS (Hibbitt et al 1995) general purpose finite element program. The FE models were generated using 20-noded reduced integration isoparametric brick elements (ABAQUS element type C3D20R). These elements can be degenerated into wedge elements (C3D15) where necessary. However, the use of wedge elements was minimised and restricted to the region away from the brace/chord intersection. Each node of the elements has three mutually perpendicular displacements as degrees of freedom. The analysis allows for both geometric and material non-linearities.

Mesh convergence studies of the DT joint subjected to brace axial compression (Kang et al 1996) showed that the use of two elements through the thickness at the brace/chord intersection region produced acceptable ultimate loads. Hence, the same mesh arrangement has been employed in the present study.

The non-linear solution in the FE analyses is achieved through load increments and iterations based on the modified RIKS procedure implemented within the ABAQUS program. Default tolerances for the convergence of iterations were utilised in all cases. In order to take advantage of the symmetry of the structure and its loading, the half model shown in Fig. 4 was adopted for the FE modelling. The normal displacement in the plane of symmetry of the chord together with all displacements at one of the ends of the chord were constrained for the boundary conditions of the models.

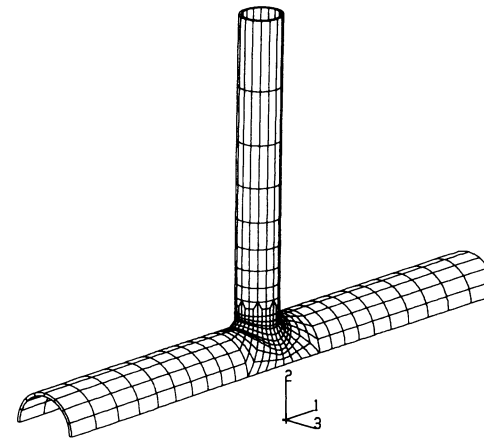

Fig. 4 Half Model used in the FE Analyses

For axially loaded joints, Yura et al (1980) proposed a deformation limit beyond which joints should not be used. The Yura deformation limit Δ is taken to be equivalent to the change in length of an unconnected brace member of length $l_b = 30d$ under axial loading and with a strain of twice the uniaxial yield strain ε_y, i.e.

$$\Delta = 2\varepsilon_y l_b \tag{1}$$

For brace length of $30d$ and $\varepsilon_y = F_y / E$, Equation (1) can be written as

$$\Delta = \frac{60dF_y}{E} \tag{2}$$

For a DT joint, the deformation limit will be 2Δ. Hence, the total deformation limit Δ_{tot} for the present joint is 19.9 mm.

For bending (IPB or OPB) loaded joints, the Yura rotation limit is taken to be equivalent to that occurring at the ends of a simply-supported, unconnected brace member of length l_b = 30d subjected to transverse, uniformly distributed load W_b of sufficient magnitude to cause beam bending strain of $4\varepsilon_y$. Using the Yura recommendation that $l_b = 30d$, the resulting rotation limit θ_{rl} is

$$\theta_{rl} = \frac{80F_y}{E} \tag{3}$$

It should be noted that the Yura rotation limit for brace bending is independent of brace dimensions and is dependent only on the two uniaxial material properties F_y and E. The calculated useful rotation limit θ_{rl} for the present DT components is 0.13 rad (i.e. 7.4°). This value, or the previously determined

Table 3: Joint capacities for axially loaded joints

	Non-dimensional ultimate axial brace load $\frac{P_{ub}}{T^2F_y}$ or $\frac{P_k}{T^2F_y}$					
Model	FE prediction	% increase	API RP 2A (1993) Lower Bound Prediction	% difference*	DEn (1990) Characteristic Strength Prediction	% difference*
W1	13.55	-		19.6		22.7
W2	14.92	10.1	11.33	31.7	11.04	35.1
W3	15.82	16.8		39.6		43.3

Table 4 : Joint Capacities for OPB loaded joints

	Non-dimensional ultimate brace OPB load $\frac{M_{oub}}{dT^2F_y}$ or $\frac{M_{ko}}{dT^2F_y}$					
Model	FE prediction	% increase	API RP 2A (1993) Lower Bound Prediction	% difference*	DEn (1990) Characteristic Strength Prediction	% difference*
W1	6.00	-		-2.3		2.2
W2	7.30	21.7	6.14	18.9	5.87	24.4
W3	7.84	30.7		27.7		33.6

Table 5 : Joint capacities for IPB loaded joints

	Non-dimensional ultimate brace IPB load $\frac{M_{iub}}{dT^2F_y}$ or $\frac{M_{ki}}{dT^2F_y}$					
Model	FE prediction	% increase	API RP 2A (1993) Lower Bound Prediction	% difference*	DEn (1990) Characteristic Strength Prediction	% difference*
W1	9.42	-		-21.4		-8.5
W2	12.08	28.2	11.99	0.75	10.30	17.3
W3	14.50	53.9		20.9		40.8

$$* \%\ \text{difference} = 100 \times \left(\frac{\text{FE prediction}}{\text{Code value}} - 1 \right)$$

useful deformation limit for brace axially loaded joints, is shown here in all load-displacement curves as dashed vertical lines.

4 RESULTS AND DISCUSSION

The load-displacement and moment-rotation curves for Models W1, W2 and W3 under brace axial compression, OPB and IPB loads are presented in Figs 5 to 7, respectively. The loads are non-dimensionalised in the usual way. A summary of the ultimate strengths (i.e. the maximum values or the Yura values, whichever are achieved first) obtained from the FE analyses for the three brace loads are given in Tables 3 to 5. The lower bound strengths and the characteristic strengths calculated from American Petroleum Institute (API) (1993) and Department of Energy (DEn) (1990) codes, respec-

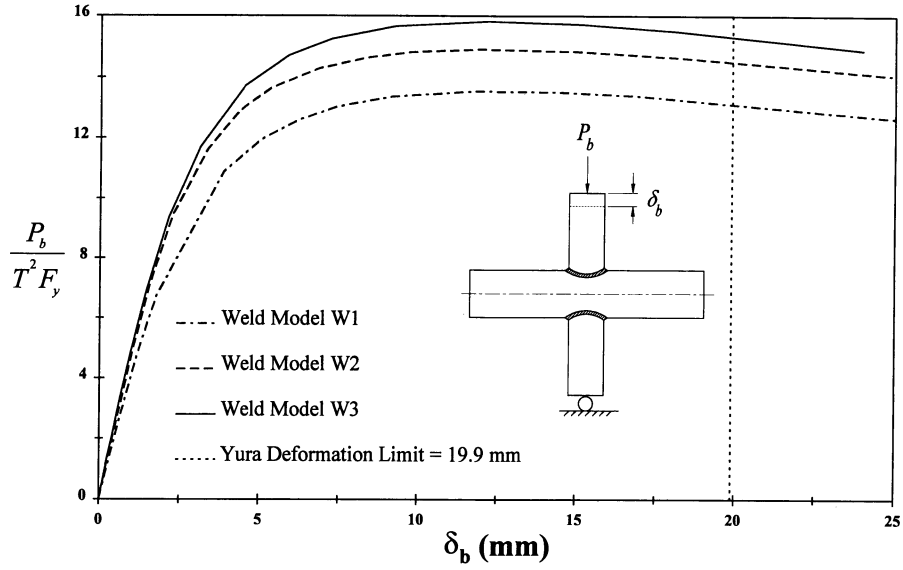

Fig. 5 Effect of Weld size on Behaviour of DT Joints under Brace Axial Compression

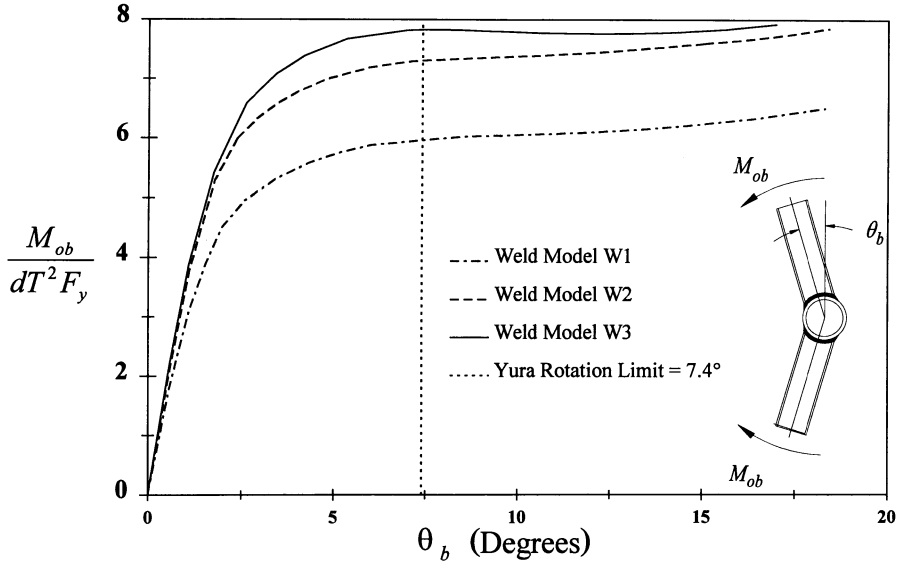

Fig. 6 Effect of Weld Size on the Behaviour of DT Joints under Brace OPB Load

tively, are also presented for comparison. The API lower bound values are obtained from the code equations with the 1.7 "joint safety factor" removed in each case, i.e. the following expressions apply:

$$\frac{P_{ub}}{T^2F_y} = (3.4+13\beta)Q_\beta \qquad (4)$$

$$\frac{M_{iub}}{dT^2F_y} = 0.8(3.4+19\beta) \qquad (5)$$

$$\frac{M_{oub}}{dT^2F_y} = 0.8(3.4+7\beta)Q_\beta \qquad (6)$$

where $Q_\beta = \frac{0.3}{\beta(1-0.833\beta)}$

The DEn characteristic values are obtained directly from the Department of Energy (1990) equations, i.e.

$$\frac{P_k}{T^2 F_y} = (2.5 + 14\beta) Q_\beta \tag{7}$$

$$\frac{M_{ki}}{dT^2 F_y} = 5\beta\gamma^{0.5} \tag{8}$$

$$\frac{M_{ko}}{dT^2 F_y} = (1.6 + 7\beta) Q_\beta^{0.5} \tag{9}$$

where Q_β is the same expression given above for the API equations.

In each case, it was found that the API lower bound values are higher than the corresponding DEn characteristic values. The results show, as expected, that Model W1 (with no weld) has the lowest ultimate loads among the three models. High stresses (not reported here) at the brace/chord intersection of model W1, together with the absence of weld reinforcing, weaken the joint significantly. The % increases in ultimate strength of the welded, as compared to the unwelded models are shown in Tables 3 to 5.

For IPB loaded joints (Table 5), the predicted FE ultimate moment for model W1 is low compared to API and DEn design values, but high for models W2 and W3. For joints under brace OPB load (Table 4), the FE ultimate moments are overall higher than the DEn values, but for Model W1, the predicted FE value is slightly lower than the API value by 2.3%.

The results generally show that, when welds are included in the FE models, the FE predictions are greater than the values calculated from API and DEn. That is, if the FE method is employed to determine the ultimate strength of tubular joints, the welds should be included in the FE models. Also, the present FE results show that the variation of ultimate loads between models W1 and W3 is highest for brace IPB load (54%), followed by brace OPB load (31%) and brace compression (17%). The conclusion is, therefore, that the weld can play an important role in DT joint behaviour, resulting in an increase in joint strength with increasing weld size, with the proviso, of course, that joint failure by cracking does not precede the mode of failure defined herein.

CONCLUSIONS

1. The results presented show that the weld size can have a significant influence on the ultimate load carrying capacity of DT tubular joints. The maximum variation of ultimate loads between Model W1 (with no weld) and W3 (with the largest dimensions defined in Table 2) are highest for brace IPB (54%), followed by brace OPB (31%) and brace compression (17%).
2. All three FE models, with different weld sizes,

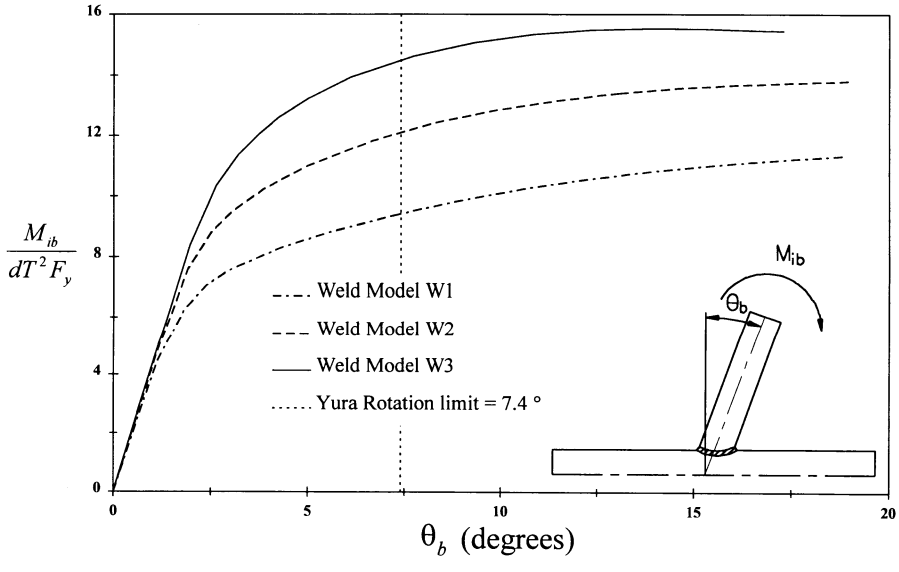

Fig. 7 Effect of Weld Size on the Behaviour of DT Joints under Brace IPB Load

gave ultimate loads in brace compression that were higher than the API and DEn equivalent values. For both IPB and OPB loading the unwelded joint tended to give lower ultimate loads than the equivalent API and DEn values whereas the two welded joints gave higher values.

3. If the FE method is employed to assess the ultimate behaviour of tubular joints, the weld should be included in the models and ideally three-dimensional elements should be used to generate the FE meshes.

ACKNOWLEDGEMENT

The work reported herein was part of the Ph. D. work of C. T. Kang who was part sponsored by the UK Committee of Vice Chancellors and Principals on an Overseas Research Student Award.

REFERENCES

American Petroleum Institute 1993. *Recommended Practice for Planning, Designing and Construction of Fixed Offshore Platforms*, API RP 2A, 20th edition.

Department of Energy, (UK) 1990. *Offshore Installations: Guidance on Design, Construction and Certification*, 4th edition.

Hibbitt, Karlsson and Sorenson Inc. 1995. *ABAQUS Version 5.5 User's Manual, Vols. 1 & 2.*

Liaw, C.Y., Litton, R.W. and Reimer, R.B. 1976. Improved Finite Elements for Analysis of Welded Tubular Joints, *Proceedings: Offshore Technology Conference*, Paper No. OTC 2642, 267-282.

Kang, C.T., Mistry, J. and Moffat, D.G. 1996. A numerical study of a DT tubular joint under combined brace and chord compression, *Proceedings: 11th UK ABAQUS User Group Conference*, Keele University, UK.

Kang, C.T. Moffat, D.G. and Mistry, J. The effect of chord compression on the ultimate strength of a DT tubular joint under brace out-of-plane bending moment, under preparation.

Kang, C.T., Moffat, D.G. and Mistry, J. 1998.The effect of chord compression on the ultimate strength of a DT tubular joint under brace compression loading, accepted for publication in *J. Structural Engineering, ASCE.*

Moffat, D.G., Kruzelecki, J. and Blachut, J. 1992. The effects of chord length and boundary conditions on the static strength of a tubular T-joint under brace compression loading", *Marine Structures*, 9, 935-946.

PDA Engineering 1993. *P3/PATRAN User Manual, Vols. 1 - 4*, PATRAN Division, Costa Mesa, California.

van der Vegte, G.J. and Wardenier, J. 1994. "An Interaction Approach based on Brace and Chord Loadings for Uniplanar Tubular T-joints", *Proceedings of 6th International Conference on Tubular Structures*, Rotterdam, Netherlands, 589-596.

van der Vegte, G.J., Puthli, R.S. and Wardenier, J. 1991. "The influence of the chord and can length on the static strength of uniplanar tubular steel X-joints", *4th International Symposium on Tubular Structures*, Delft, Netherlands, 435-447.

Yura, J., Zettlemoyer, N. and Edwards, I.F. 1980. "Ultimate capacity equation for circular tubular joints", *Proceedings of Offshore Technology Conference*, Paper OTC 3690, Texas, 113-126.



Taylor & Francis
Taylor & Francis Group
http://taylorandfrancis.com

Tubular Structures VIII, Choo & Van der Vegte (eds) © 1998 Balkema, Rotterdam, ISBN 90 5809 001 9

Load-displacement characterisation and prediction for combined loading of a YT tubular joint with and without fillet weld

T.H. Hyde & S.B. Leen
Department of Mechanical Engineering, University of Nottingham, UK

ABSTRACT: This paper describes the elastic-plastic finite element analyses of simply-supported YT tubular joint models, with and without a weld profile, under the action of combined Y- and T-brace axial loads, for a range of radial load paths, to determine non-linear force-displacement responses. The results of experimental tests on model joint castings (with and without the weld) are used to validate the numerical investigations. An elastic-plastic displacement prediction procedure, using energy methods, is applied to the joint, with and without weld, to illustrate the prediction of responses to arbitrary radial load paths.

1 INTRODUCTION

In order to develop an understanding of the non-linear, elastic-plastic behaviour of tubular joints under static loads it is necessary to analyse and study the response of such joints to a range of load paths in the load space, paying particular attention to likely in-service load paths (if known). The need for research in this area is generally accepted (Lalani 1993) and technological developments, especially non-linear finite element (FE) analyses capabilities, provide a basis for such work. The motivation for this research is the need for more accurate prediction of framework static collapse (pushover) loads, with the potential for more optimum design of new structures and more reliable estimation of remaining strength of existing and possibly damaged structures.

The paper is particularly concerned with illustrating that the energy-based, elastic-plastic force-displacement prediction procedure of Hyde & Leen (1997) can be used effectively for YT-joints (and consequently other joint types also) with and without the weld profile. Experimental testing of joint castings are used to validate the non-linear force-displacement response determination process, which is based on extensive FE analyses, for joints both with and without the weld profile. The work described is part of a more general study to tackle the issue of non-linear tubular joint behaviour, using both FE analyses and experimental techniques, to develop global representations of local elastic-plastic behaviour; in this context, the prediction procedure provides the basis for the development of a single elastic-plastic joint element. The work described here thus illustrates that the prediction procedure could be used to evaluate the global effect (on overall framework behaviour) of including local features, such as the weld profile used in this case.

The present work is based on the use of tin-lead alloy casting models of YT-joints, with dimensionless geometrical parameters typical of offshore steel joints; the testing of such joints for static strength determination has been previously described (Fessler et al. 1992). Three-dimensional FE models of the joint with and without weld profile have been generated; model joints with and without weld profile have also been produced (the mould for casting joints was modified to produce model joints with an accurate representation of the weld profile). The castings are homogeneous, i.e. there is no difference between weld and 'parent' plate and there are no heat-affected zones. The model castings are therefore representative of structural joints which have been heat-treated after making full-penetration welds without defects.

2 GEOMETRY OF JOINT AND WELD PROFILE

The geometry and dimensions of the YT joint without the weld profile are shown in Figure 1a; the dimensionless geometrical parameters are also shown. The weld profile is defined here by the parameters d_c^T and d_b^T for the T-brace (Fig. 1b) and d_c^Y and d_b^Y for the Y-brace (Fig. 1c). In this case, both of d_c^T and d_b^T increase from T at the crown position to $1.15T$ at the saddle position. d_c^Y varies from $1.44T$ at the non-gap crown position, to T at a

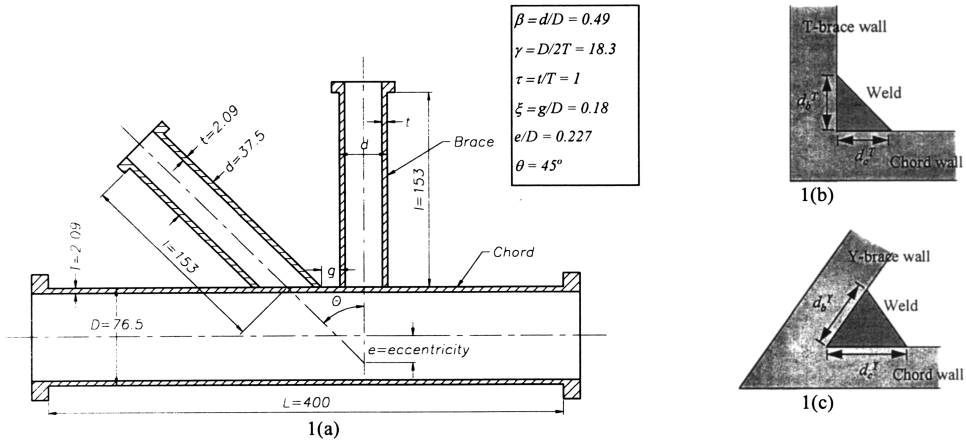

Figure 1. (a) Drawing of the model YT tubular joint (all dimensions in mm.).
(b) Definition of weld geometry parameters for T-brace.
(c) Definition of weld geometry parameters for Y-brace.

60° angular position, to 1.48T at 135°, to 1.44T at the gap crown position. d_b^Y varies from 1.44T at the non-gap crown position, to 1.53T at a 90° angular position, to 1.44T at the gap crown position. It is important to note that the weld profile used here is not intended to be an accurate representation of typical industry-standard welds; the dimensions used, especially d_c^T and d_c^Y, are larger than those typically prescribed for 'standard flat' welds. However, as mentioned above, the primary objective is to illustrate that the force-displacement prediction procedure of Hyde and Leen (1997) can be used to incorporate the non-linear effect of local features (of which the weld is an example) in global framework analyses.

3 FINITE ELEMENT ANALYSES

The FE models of the joint with and without the weld profile are shown in Figures 2a, 2b and 2c. Only one half of the joint is modelled due to geometrical and loading symmetry and appropriate symmetry boundary conditions are applied along the plane of symmetry. For both FE models the mesh was designed according to the recommendations of Saad (1997), paying particular attention to the mesh density and elements sizes in the brace-chord intersection regions. 20-noded, reduced integration isoparametric, 3-D brick elements are used throughout most of the model, apart from the chord ends and the brace footprints, where 15-noded wedge elements are used. Because of the importance of accurate simulation of local elastic-plastic behaviour and of accurate modelling of the intersection geometry for the present work, 3-D brick elements are considered to be most suitable (see Crockett 1994).

The most important mesh factor (using brick elements) influencing FE static strength predictions was found to be the width of the first chord element adjacent to the brace-chord intersection (Saad 1997) and one element through the thickness is sufficient. The brace mesh was found to have no significant effect due to the small deformation of the brace during axial loading. As shown in Figures 2b and 2c, the mesh on the chord is finest at the intersection (for the no-weld case) and at the weld toe (for the weld case), with the smallest width chord element occurring exactly at the junction in Figure 2b and at the toe in Figure 2c; the meshes on the chord around the junction are almost identical in both cases. The experimental tests (see below) show that failure of the no-weld case occurs at the junction on the chord and failure of the weld case occurs at the weld toe on the chord, i.e. the centres of mesh focusing in each case. In the experimental tests, the chord is simply-supported at its ends via steel end closures. Young's modulus of the material is taken as 33 kN/mm^2 and Poisson's ratio as 0.4. The stress-strain data are derived from experimentally-determined, normalised curves presented by Fessler et al. (1996), using the mean ultimate tensile strength (UTS) of the specimens cast with each model (determined by tensile tests); in this paper a UTS of 58 MPa is used for all FE analyses. The brace ends are constrained to move as a plane in the brace axial directions.

In each analysis the applied T- and Y-brace forces are increased proportionally from zero to failure corresponding to radial load paths in the two-

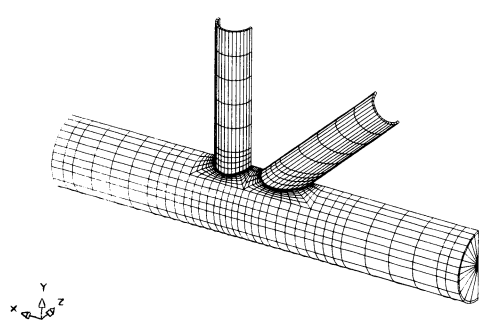

2(a)

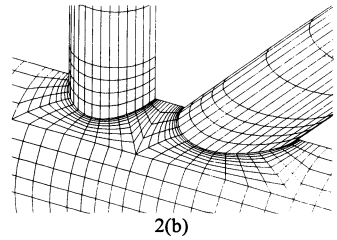

2(b)

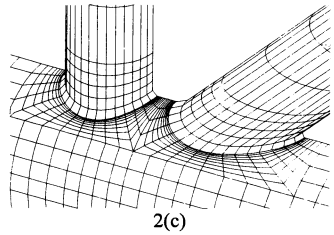

2(c)

Figure 2. (a) FE model of YT joint without weld.
(b) FE model (detail) of joint without weld.
(c) FE model (detail) of joint with weld.

dimensional load space of the two (in-plane) brace forces, F_Y and F_T. For both FE models (i.e. without and with weld) a set of twenty-four basis analyses were carried out, each analysis having a different (F_Y:F_T) load ratio with the load ratios distributed approximately uniformly over the F_Y-F_T load space. The general-purpose, non-linear, FE code ABAQUS (HKS Inc. 1995) is used for the analyses and the modified Rik's solution method (NAFEMS 1991) is employed within ABAQUS, to permit the negotiation of highly non-linear features such as limit points and snap-through behaviour. Geometric non-linearity (i.e. large displacements) as well as material non-linearity (with finite strains) are included in the analyses. The failure loci determined from the FE analyses are compared in Figure 3 in terms of the non-dimensionalised applied brace forces F_Y* and F_T*, where:

$$F_Y^* = \frac{F_Y}{\sigma_u . T^2} \qquad F_T^* = \frac{F_T}{\sigma_u . T^2} \qquad (1)$$

and σ_u is the UTS of the material and T is the chord wall thickness. Figure 4 shows the T- and Y-brace force-displacement responses of both models for the (F_Y:F_T) = (-0.5:1) load ratio, as an example of the effect of the weld profile on the force-displacement response. The failure loads of the analyses are taken as the first peak in the force-displacement curves.

4 EXPERIMENTAL VALIDATION

The testing of tin-lead alloy models of tubular joints for static strength, including YT joints, has been described in detail by Khalid (1993). In contrast, the objective of the present experimental work is to obtain the force-displacement responses of the YT joint and thus to validate the FE analyses. Khalid (1993) describes the use of a steel frame to support the joint between the moving crosshead and the load cell of an Instron 1195 tensile testing machine during the tests. The ends of the joint chord were simply supported by the steel frame, the bottom of which was rigidly clamped to the crosshead of the machine; the ends of the braces were attached via chains and pulleys to a horizontal lever bar which was pivoted at the load cell. The (F_Y:F_T) load ratio during each experiment was determined by the relative horizontal positions of the points of attachment of the load chains to the lever bar; variation of these positions from test to test allowed different force ratios to be applied. A similar method was used for the present tests with the addition of linear bearings to guide the ends of the T and Y braces, thus ensuring pure axial motion. This latter constraint is introduced in order to facilitate accurate comparison of the FE and experimental results, since clearly defined and

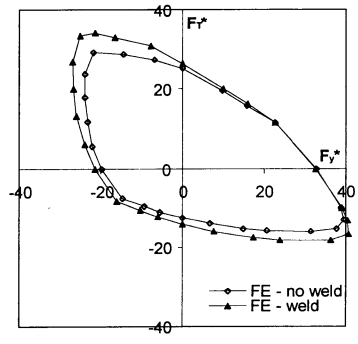

Figure 3. Comparison of FE failure loci in F_Y*-F_T* load space for model with and without weld.

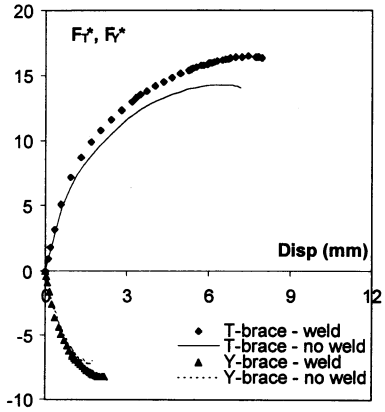

Figure 4. FE responses of joint with/without weld for load ratio (-0.5:1).

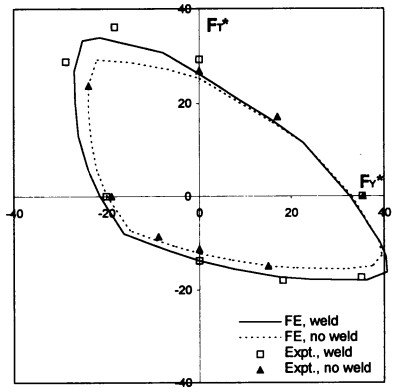

Figure 5. Comparison of FE and experimental failure loci in F_Y*-F_T* load space for model with/without weld.

consistent brace-end conditions are important in this regard. Although this may lead to the development of reaction shear forces at the brace-ends, this is consistent for both the FE and experimental models. The central issue here is to validate the FE models, so that the latter can then be used confidently as the basis of the displacement prediction procedure.

Conductive, plastic, linear-motion potentiometers with 50 mm stroke length were used to measure the brace end displacements. The tin-lead alloy material used in the casting process has an ultimate tensile strength $\sigma_u \approx 60$ N/mm^2, a yield/ultimate strength ratio $\sigma_y/\sigma_u \approx 0.7$ and a ductility of 30% ± 10%; the last two properties are within the range of structural steels used in offshore structures, making it a suitable model material. Errors due to variations in the σ–ε curve were eliminated by testing tensile specimens (cast with the models); further details about this material have been presented by Fessler et al. (1992).
In the present work, both numerically and experimentally, the combined loads are increased proportionally, so that when one load drops, due to sudden loss of structure load-carrying capacity, the other load drops also; this is defined as the failure point. The experimental failure loads for the joints with and without weld profile are compared to the FE loci in Figure 5; the results agree to within 10% for both weld and no-weld cases. The numerical results slightly underpredict the failure loads in the (+,+) quadrant and slightly overpredict them in the (-,-) quadrant. Experimental and FE force-displacement responses of the joint without weld profile to load ratios (-1:1) and (1:-1) are compared in Figures 6a and 6b. Experimental and FE responses of the joint with weld for load ratios (1:-1) and (1:-0.5) are compared in Figures 7a and 7b. The FE model predictions shown correlate closely to the test results and comparisons for other validation load ratios are generally of similar quality. Appropriate checks confirmed that nominal brace or chord failure did not occur for any of the FE or experimental load cases.

5 EFFECT OF WELD PROFILE ON JOINT BEHAVIOUR

In terms of static strength, referring to Figure 5, the smallest effect of the weld is in the (+,+) quadrant of the F_Y*-F_T* load space and the largest effect is in the (+,-) and (-,+) quadrants. According to the FE model the strength increase is from 8% to 16% for load paths in the latter two quadrants, while test results indicate the increase to be from 18% to 22%. It seems reasonable to conclude that strength increases of between 10% and 20% are possible due to the presence of the weld, depending on the applied load ratio. Van der Vegte (1995) used shell elements to model an axially-loaded multiplanar XX-joint with a butt weld and calculated an increase in ultimate load prediction of 24%. Dexter et al. (1994) calculated a 10% increase in peak load due to the inclusion of a weld in the shell element model of a K joint under balanced axial loading.

The failure modes remain unchanged with inclusion of the weld. For tensile-dominated responses cracking occurs in the experimental model joints, initiating at the chord crown position, at the junction itself for no-weld joints but at the weld toe for weld joints. On the other hand, although cracking/tearing is clearly not explicitly simulated in the FE analyses, the use of 3D brick elements, with finite strain capability, allows the modelling of extreme chord wall thinning, and comparison between the post-failure test joints and the FE deformed shapes reveals that the FE models predict this chord wall thinning at the locations of crack initiation, i.e. at the junction for the no-weld joints and at the weld toe for the weld joints (crown position in both cases). Nonetheless, the differences between the FE and experimental static strengths and

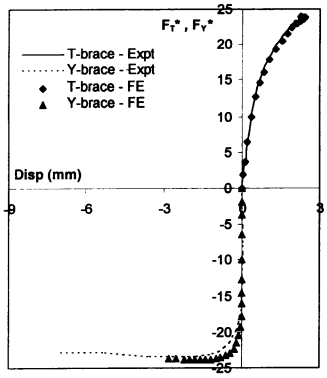

6(a)

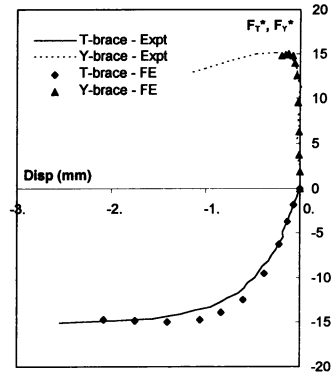

6(b)

Figure 6. FE and experimental response of joint without weld for (a) (F_Y:F_T) = (-1:1), and (b) (F_Y:F_T) = (1:-1).

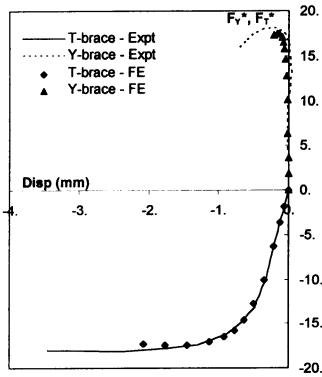

7(a)

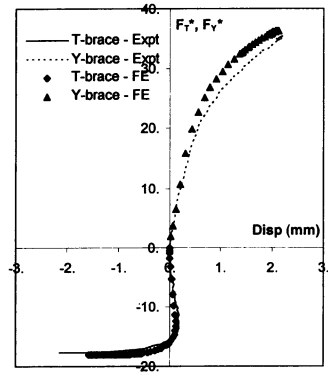

7(b)

Figure 7. FE and experimental response of joint with weld to (a) (F_Y:F_T) = (1:-1), and (b) (F_Y:F_T) = (1:-0.5).

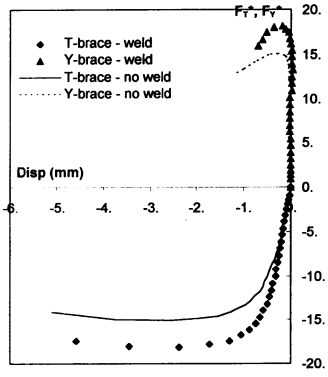

8(a)

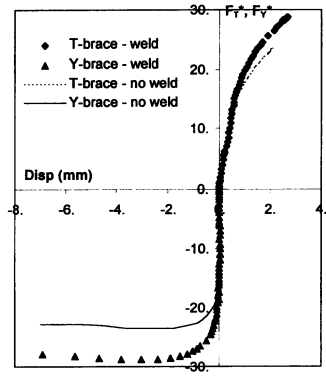

8(b)

Figure 8. Experimental response of joint with and without weld to (a) (F_Y:F_T) = (1:-1), and (b) (F_Y:F_T) = (-1:1).

force-displacement responses for tension-dominated cases are, at least partly, attributable to this limitation of the FE analyses; note that the experimental responses of Figures 6 and 7 are not tension-dominated and do not involve cracking.

Two examples of the effects of the weld on the experimental response of the joint are illustrated in Figures 8a and 8b for the (1:-1) and (-1:1) load ratios, respectively. The most obvious effect is that the forces required for specific brace-end displacements are increased, by up to 20% in the non-linear regions. The general shape of the response is unaffected, although the initial stiffness of the joint is increased by about 7% and 5% for the (1:-1) and (-1:1) cases, respectively.

6 DISPLACEMENT PREDICTION PROCEDURE

The energy-based method of Hyde & Leen (1997) can be used to predict the elastic-plastic axial displacements of the brace ends of the joint under the action of combined Y- and T-brace axial forces for arbitrary radial load paths. It is based on the principle of complementary energy (Langhaar 1962) which is applicable to non-linear elastic materials. The behaviour of the joint under elastic-plastic behaviour with no unloading is equivalent to non-linear elastic behaviour. The fundamental equations used are as follows:

$$u_Y = \frac{\partial W^*}{\partial F_Y} \qquad u_T = \frac{\partial W^*}{\partial F_T} \tag{2}$$

where W^* is the total complementary work done on the joint, u_Y and u_T are the Y- and T-brace end axial displacements and F_Y and F_T are the brace axial forces. Equations (2) express normality of the displacement 'vector' (u_Y,u_T) to the level curves of W^*. The implementation of these equations is achieved by calculating the level curves of W^* using the results of the set of 24 FE basis (radial) load paths of Section 1 above, judiciously distributed over the four quadrants of the F_Y-F_T load space to approximate the level curves appropriately for evaluation of the partial derivatives of equations (2). With increasing deformation the level curves evolve non-uniformly from a rotated ellipse for Hookean behaviour to a more distorted shape. Further details of the procedure are given by Hyde & Leen (1997). In addition to comparisons with the basis load paths (as a minimum check), the prediction procedure was also applied to (F_Y:F_T) load ratios of (1:-0.445), (0.75:1), (-0.75:-1), (-0.87:1) and (-0.625:1), all of which are intermediate to the basis load paths. Additional FE analyses have been carried out for these load ratios, not for use as input to the prediction procedure, which uses only the (W^*,F_Y,F_T) level curve data of the basis load paths, but purely to validate the predictions. In the present case the level curves are calculated from FE results; they could alternatively be calculated from experimental test results if a sufficient range of load paths were tested. It is worth pointing out that the brace-end reaction shear forces, resulting from the 'axial displacement only' constraint on the brace-ends (see Section 4), do not have any associated work or complementary work and consequently do not affect the prediction procedure.

The motivation for the prediction procedure stemmed from the search for a normality rule for the incremental joint force-displacement response, analogous to the normality of the incremental plastic strain tensor to the current yield surface in the principal stress space; it is also known that the incremental plastic displacement 'vector' (δu_Y^p,δu_T^p) at collapse is normal to the collapse locus in the F_Y-F_T load space. The latter fact has been used here, in conjunction with linear interpolation between the FE failure loads and displacements, to effect an improvement of the basic procedure of Hyde & Leen (1997), whereby the displacement predictions are extrapolated right up to the predicted failure load. Figures 9a to 9e show comparisons of the predicted and calculated responses for the above five validation load paths. These load paths were specifically chosen as representing a severe test of the procedure since they correspond to regions of the load space in which the level curves show considerable distortion from the initial elliptical shape (see Hyde & Leen, 1997).

7 CONCLUSIONS

Numerical force-displacement responses (for both no-weld and weld cases) were shown to simulate accurately test joint behaviour and static strengths correlated to within 10%, both for loading combinations leading to cracking failure of the test joints and for other loading combinations. Strain and/or displacement limits are not used in the present work, since the main objective is to study and develop prediction methods for the force-displacement response; clearly, the implementation of an appropriately chosen displacement limit within the prediction procedure would be a straightforward matter. The FE analyses and experimental tests predicted strength increases of up to 16% and 22%, respectively, dependent on (F_Y:F_T) load path, due to inclusion of the weld. However, it must be again stressed that the weld geometry used is larger than those typically used, especially along the chord.

The particular weld geometry used was chosen as an example, chiefly to demonstrate the application of the prediction procedure, and the associated FE/experimental validation methodology, to the case of local tubular joint features. The elastic-plastic prediction procedure (using energy methods) was shown to successfully predict force-displacement

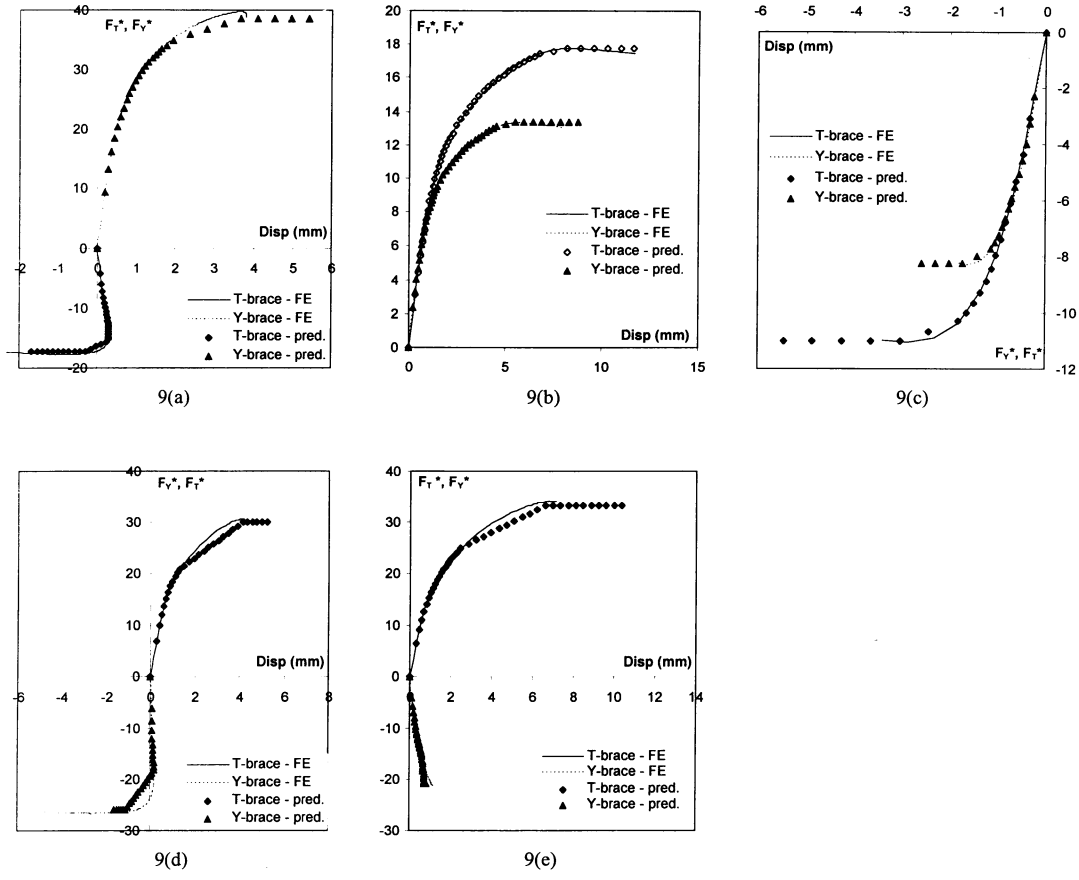

Figure 9. Predicted responses of joint with weld for: (a) load ratio (F_Y:F_T) = (1:-0.445), (b) load ratio (F_Y:F_T) = (0.75:1), (c) load ratio (F_Y:F_T) = (-0.75:-1), (d) load ratio (F_Y:F_T) = (-0.87:1), and (e) load ratio (F_Y:F_T) = (-0.625:1).

responses and failure loads of the joint with and without the weld for a range of arbitrary radial load paths, thus illustrating that the displacement prediction procedure of Hyde & Leen (1997) can be used for YT joints with additional features such as welds, cracks, joint cans, stiffeners, local defects (e.g. due to corrosion). This is significant as it shows that such local features could be included in the 3D solid element joint model and thence, via the prediction procedure, in a framework analysis, so that the global impact of local features or defects could be evaluated in terms of system strength. The issue of more accurate modelling of industry-standard weld profiles, using the 3D brick element approach of the present work, represents an area of detailed work, which is considered more appropriate to an actual design scenario, involving a particular framework and tubular joint design, and subsequent to the further development of the single elastic-plastic joint element, which is the primary motivation of this work.

Finally, a unique and reliable synthesis of numerical and (convenient) experimental investigative capabilities for non-linear tubular joint strength and force-displacement response prediction has been demonstrated with considerable potential for further research into different joint/loading types. The usefulness of the tin-lead alloy technique as a cost-effective method for validation of numerical models has been underlined. The method has already been used extensively for strength predictions but its capability for force-displacement response has been illustrated here, as well as its capability to validate FE models involving local features such as weld profiles, cracks etc.

8 ACKNOWLEDGEMENTS

The authors would like to thank the EPSRC for funding the present research and Mr. R. Pickard and other staff of the Department of Mechanical Engineering for their patient help and assistance.

9 REFERENCES

HKS Inc., ABAQUS User's and Theory Manual., Rhode Is., U.S., Version 5.5, 1995.

Crockett, P. Finite element analysis of welded tubular connections. PhD thesis, University of Nottingham, U.K., 1994.

Dexter, E.M., Lee, M.M.K, and Kirkwood, M.G., Effect of overlap on strength of K joints in CHS tubular members. *Proceedings of 6th International Symposium on Tubular Structures*, Melbourne, Australia, 1994, 581-588.

Fessler, H., Hassell, W. and Hyde, T.H. A model technique for bending strength of tubular joints. *J. Strain Analysis*, 1992, 27, 197-210.

Fessler, H., Hyde, T.H. and Khalid, Y.A. The effect of adjacent braces on the static strength of a corner YT joint. *Proc. Instn. Civil Engrs. Structures and Buildings*, 1996, 116, Feb., 44-53.

Hyde, T.H., and Leen, S.B. Prediction of elastic-plastic displacements of tubular joints under combined loading using an energy-based approach. *J. Strain Analysis*, 1997, 32(6), 435-454.

Khalid, Y.A. Static strength of tubular joints. PhD thesis, University of Nottingham, U.K., 1993.

Lalani, M. Post-yield and post-peak behaviour of tubular joints in offshore structures. *Proceedings of 5th International Symposium on Tubular Structures*, Nottingham, U.K., Aug. 1993, 446-454.

Langhaar, H.L. *Energy Methods in Applied Mechanics*, 1962 (John Wiley & Sons, Inc.).

NAFEMS, *An Introduction to Non-linear Finite Element Analysis*, 1991.

Saad, S.B. Finite element determination of the static strength of cracked and uncracked tubular joints. PhD thesis, University of Nottingham, U.K., 1997.

Van der Vegte, G.J. The static strength of uniplanar and multiplanar tubular T- and X-joints. PhD thesis, Delft University of Technology, The Netherlands, 1995.

Tubular Structures VIII, Choo & Van der Vegte (eds) © 1998 Balkema, Rotterdam, ISBN 90 5809 001 9

A critical assessment of the finite element method for predicting the static strength of tubular T- and YT-joints

T.H. Hyde, S.B. Saad, Y. Khalid, S.B. Leen & N.A. Warrior
Department of Mechanical Engineering, University of Nottingham, UK

ABSTRACT: This paper is concerned with the investigation of the various factors which affect the finite element calculation of the static strength of tubular joints. Two types of tubular joints are studied, a T-joint and a YT-joint, the dimensionless parameters of which correspond to typical offshore joints. Both sets of numerical results are compared with experimental test results. Practical recommendations are made as a consequence of the investigations.

1 INTRODUCTION

Welded tubular joints are widely used in the construction of offshore structures, such as oil and gas platforms. Such joints represent structural weakspots and consequently it is necessary to develop reliable methods of determining their static collapse loads.

Experimental testing of tubular joints has produced much useful information and has resulted in the development of calculation procedures for determining joint strength. However, testing can be expensive and time-consuming. Also, it is not generally feasible to test a wide range of full-scale joints for offshore structures under all possible loading modes and so scaled steel models of the joints are usually tested. This introduces the problem of relating the test results to the behaviour of full-size joints. The use of other materials can also produce useful results, but this introduces the additional problem of how to relate these results to the behaviour of steel joints.

The finite element (FE) method is commonly used as an alternative to experimental testing, and if validated by comparison with appropriate test results, reliable FE solutions can be obtained relatively quickly and cheaply. Also, parametric surveys to investigate the effects of various geometric and material parameters can be easily performed. However, the accuracy of FE results may depend critically on such factors as mesh design, element types/formulations used and accuracy of material data. Although FE analyses are used extensively for the static strength determination of tubular joints, relatively little has been published on the detailed validation of FE modelling for such cases.

This paper describes the results of a series of detailed FE calculations using 3D elements to obtain large deformation, elastic-plastic solutions for the static strength of simply-supported T- and YT-joints, subjected to a range of brace loading modes including axial tension and compression (or combinations thereof for YT), in-plane bending and out-of-plane bending (see Figs. 1b,c). Firstly, a series of analyses of the T-joint are used to determine the effects of various input parameters such as material model, mesh design, number of elements through the chord wall, number/sizes of elements on the surface of the chord and brace, support conditions and changes of geometry. There follows a series of analyses of the YT-joint, based on the conclusions of the T-joint analyses, to investigate issues such as the appropriate type of 3D element (i.e. shell or solid) and the most efficient element formulation, as well as additional convergence studies to confirm applicability of the T-joint mesh study conclusions to the YT-joint. The YT-joint is representative of more complex joint types, and consequently is considered of greater practical significance than the T-joint. The numerical results are compared to experimental data obtained by the authors. In this paper, joint failure is associated with the attainment of maximum load in the joint force-displacement or moment-rotation response curve.

Recommendations are made in relation to the choice of element type, the material model and the mesh design to be used for accurate failure load calculations.

2 EXPERIMENTAL TESTS

Figure 1a shows the YT joint geometry, dimensions and dimensionless parameters chosen for the present work; the T-joint geometry is identical except for the absence of the Y-brace.

The chords were simply-supported, as indicated in Figures 1b and 1c. The four loading modes (applied to brace ends) used for the T-joint experimental and numerical investigations were axial tension (+A), axial compression (-A), in-plane bending (B_0) and out-of-plane bending (B_{90}), as shown in Figure 1b. The YT-joint is subjected to a series of combined T- and Y-brace axial load ratios (A_Y:A_T), including both compression and tension loads.

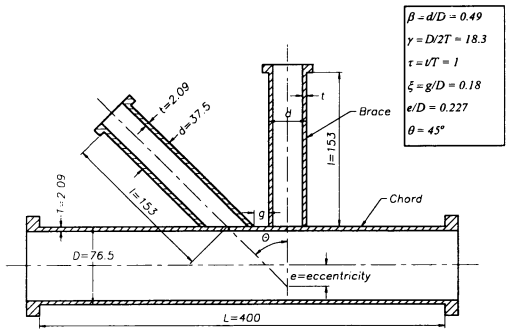

Figure 1a. Experimental model dimensions of YT-joint and T-joint.

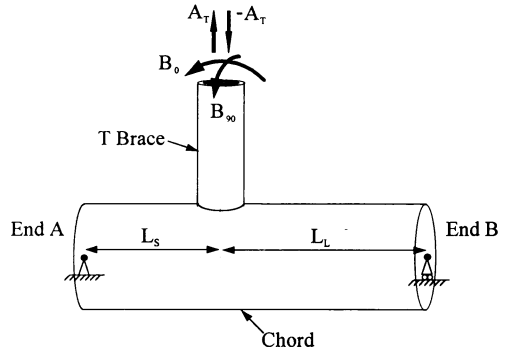

Figure 1b. T-joint loading modes and supports.

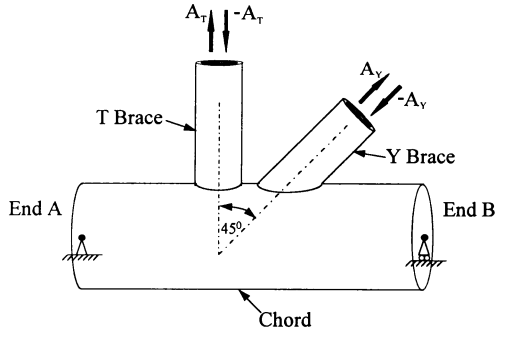

Figure 1c. YT-joint loading modes and supports.

Extensive experimental static strength data have been obtained for these geometries by the authors (Fessler et al. 1992, Khalid 1993). These tests were performed on die-cast, tin-lead alloy models; full details of the manufacturing process and material properties have been published (Fessler & Hassell 1990, Fessler et al. 1996). The test results for the T-joint are presented in terms of average normalised axial force and bending moment static strengths, A^* ($=A/\sigma_u T^2$) and B^* ($=B/\sigma_u T^2 d$), respectively, where σ_u is the ultimate tensile stress (UTS); these are shown in Table 1 (Khalid 1993). Table 2 presents the YT-joint results in terms of normalised T- and Y-brace axial force static strengths, A_T^* ($=A_T/\sigma_u T^2$) and A_Y^* ($=A_Y/\sigma_u T^2$), respectively. Since joint failure, in this paper, is defined as the attainment of maximum load, σ_u is considered the most appropriate measure for failure load normalisation. The distances of the T-brace axis from the chord ends A and B are designated L_S and L_L respectively; in the experimental model joint of Figure 1a, these are equal to 178 mm and 268 mm, respectively.

3 DETAILS OF FE ANALYSES

The T- and YT-joint FE models were generated using FEMGEN (Femsys Ltd. 1994) and the analyses were performed using ABAQUS (HKS Inc. 1995), the general-purpose non-linear FE code. 3D isoparametric parabolic (brick) elements with reduced integration are used throughout although the effects of alternative element types and formulations

Table 1. Average experimental T-joint results.

Loading mode	# tests	A^* or B^*
+A	2	23.52
-A	3	10.8
B_0	4	9.2
B_{90}	5	5.82

Table 2. Experimental YT-joint results (σ_u = 58 MPa).

(A_Y:A_T) load ratio	(A_Y^*:A_T^*) maximum load
(0:1)	(0:26.4)
(1:1)	(17.2:17.2)
(1:0)	(34.7:0)
(1:-1)	(15.4:-15.4)
(0:-1)	(0:-11.4)
(-1:-1)	(-8.7:-8.7)
(-1:0)	(-17.6:0)
(-1:1)	(-23.7:23.7)

are examined and discussed. Elements were concentrated in regions where high stress gradients were expected, i.e. at the brace-chord junction; 20-noded elements are used everywhere apart from the brace footprints and chord end closures where 15-noded wedge elements are used (Saad 1997).

Both material and geometric non-linearity were modelled in the analyses. For the T-joint, three types of assumed stress-strain curve (all with E = 33 GPa) were investigated, namely, elastic-perfectly plastic (EPP) with $\sigma_y = \sigma_u$, bilinear (BL) elastic-plastic with $\sigma_y = 0.7\sigma_u$ and $\varepsilon_p = 0.02$ at the onset of σ_u, and a more accurate multi-linear (ML) elastic-plastic curve, all shown in Figure 2. The von Mises yield criterion was used with the Prandtl-Reuss flow rule and isotropic hardening. Geometric non-linearity was included to allow for the significant shape changes of the chord wall during deformation. The modified Riks method in ABAQUS was used to avoid numerical problems near limit points, i.e. at maximum load; although displacement-controlled loading could be used for single-brace loading cases, it is not convenient for the radial loading paths associated with combined loading of the YT-joint, which represents more closely actual joints in terms of complexity. The 3D solid elements used allow for finite strain and rotation under large displacements.

4 T-JOINT FE RESULTS

4.1 Axial loading

Details of the T-joint analyses performed are given in Table 3. It can be seen that various material behaviour idealisations, FE models and mesh refinements were used in the investigation.

Preliminary analyses were performed using nominal dimensions (i.e. D = 77 mm, d = 38.5 mm, T = 2 mm, t = 2 mm) and quarter models of the T-joint, as shown in Figures 3a and 3b. Unlike the experimental T-joint models, the lengths L_S and L_L were modelled as equal in the preliminary quarter-joint models. The models of this section were used to assess the relative effects of mesh refinement, material behaviour idealisations and chord length on the predicted static strength. Analyses 1 to 5 and 8 to 10 of Table 3 investigate these effects for tensile brace loading. Typical brace-end load-deflection responses for these cases are shown in Figure 4; it is important to note that the responses of Figure 4 do not represent 'converged' mesh results. The corresponding ultimate loads A^* are tabulated in Table 3.

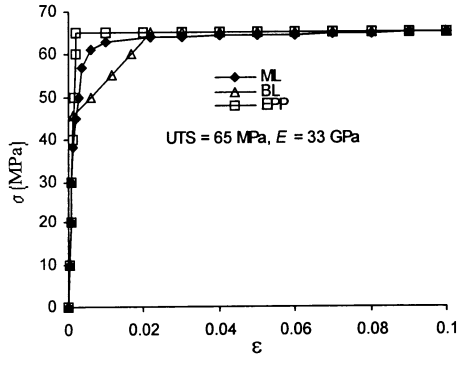

Figure 2. Different assumed stress-strain curves.

The following points are made in relation to the tension load analyses of Table 3, referring to the results of Figure 4 and the meshes of Figures 3a and 3b:

1) Comparison of analyses 1 and 2 shows the effect of halving the Young's modulus; the initial linear elastic (LE) slope is reduced but the maximum loads agree to within 0.7%.

2) The effect of using the BL stress-strain curve instead of the EPP one, but with the same UTS of 65 MPa, can be seen by comparing the results of analyses 1 and 4 in Figure 4. The initial slopes are the same but the BL case shows larger displacements with increasing load, due to the fact that it gives larger strains for equal stress levels. Nonetheless the maximum loads are within 1%.

3) The effect of using a ML curve instead of the EPP one (again with equal UTS values) is shown by analyses 3 and 8 of Figure 4. Once again the maximum loads agree to within 1%, and the ML model predicts larger displacements (but smaller than the BL case) with increasing plasticity.

4) The maximum loads obtained using one or two elements through the wall thickness are identical (see results of analyses 1 and 3 in Table 3); the force-displacement responses are also identical up to maximum load as shown in Figure 4, but they diverge after maximum load with the two-element case predicting a more rapid load drop-off. This indicates that one through-thickness element is sufficient to model the non-linear deformation of the critical junction region, especially the chord wall thinning, and the associated 3D stress distribution, as well as for calculating the non-linear Jacobian (stiffness) matrices.

5) Analysis 9 of Table 3 examines the effect of increasing the mesh density from that of Figure 3a (and analysis 3) to that of Figure 3b. Although not shown, the force-displacement responses are very close up to 90% of maximum load after which they begin to diverge and the resulting predicted maximum load of the finer mesh is 6% lower.

6) As expected the chord length was found to have a significant effect on predicted maximum loads, while the brace length was found to have

Table 3. FE results for brace axial loading of T-joint.

Analysis	Loading mode	σ–ε law	UTS (MPa)	Model type & dims.	L_S, L_L (mm)	# element through thickness	Fig.	A^*
1	$+A$	EPP	65	1/4 & N	165,165	2	3a	36.07
2	$+A$	EPP	65	1/4 & N #	165,165	2	3a	35.80
3	$+A$	EPP	65	1/4 & N	165,165	1	3a	36.08
4	$+A$	BL	65	1/4 & N	165,165	2	3a	35.93
5	$+A$	EPP	65	1/4 & N	255,255	2	3a	24.57
6	$+A$	EPP	61	1/2 & N	178,268	2	3c	28.10
7	$+A$ \$	EPP	61	1/2 & N	178,268	2	3c	28.05
8	$+A$	ML	65	1/4 & N	165,165	1	3a	35.85
9	$+A$	EPP	65	1/4 & N	165,165	1	3b	33.97
10	$+A$	EPP	65	1/4 & N ##	165,165	1	3a	36.08
11	$+A$	EPP	61	1/2 & E	178,268	2	3c	29.67
12	$-A$	EPP	65	1/4 & N	165,165	2	3a	14.45
13	$+A$	ML	61	1/2 & E ##	178,268	1	3c	26.17
14	$-A$	ML	61	1/2 & E ##	178,268	1	3c	12.18
15	$+A$	ML	61	1/2 & E ##	178,268	1	5a	25.03
16	$-A$	ML	61	1/2 & E ##	178,268	1	5a	11.84
17	$+A$	ML	61	1/2 & E ##	178,268	1	5b	22.83
18	$+A$ \$\$	ML	61	1/2 & E ##	178,268	1	5b	23.44
19	$-A$	ML	61	1/2 & E ##	178,268	1	5b	11.18
20	$-A$ \$\$	ML	61	1/2 & E ##	178,268	1	5b	11.14

Poisson's ratio taken as 0.4 throughout.
N signifies nominal dimensions and E signifies experimental model dimensions.
# denotes Young's modulus of 16 GPa used instead of 33 GPa.
$ denotes end B pinned, end A on roller.
denotes brace length of 153 mm instead of 143 mm.
$$ denotes uniform brace-end displacement with load instead of uniform end pressure.

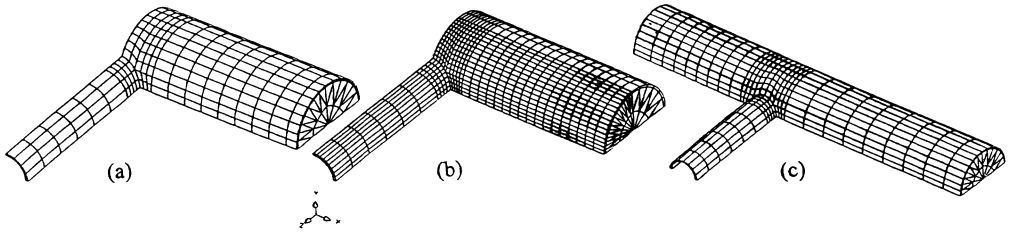

Figure 3. FE meshes used for brace axial loading of T-joint.

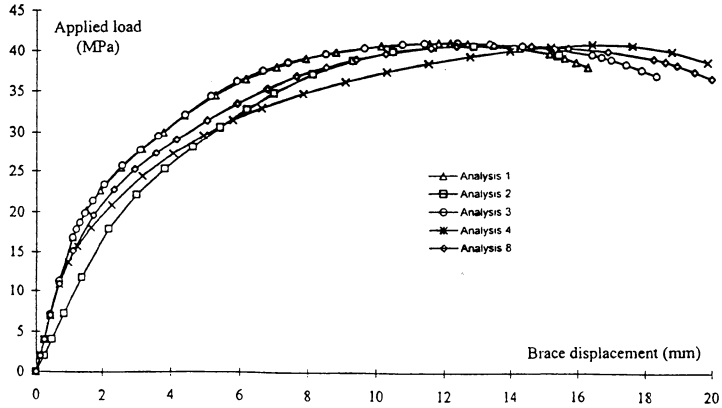

Figure 4. Brace force-displacement responses of T-joint for analyses 1 to 4 and 8 of Table 3.

negligible effect. The results of analysis 5, with a 50% longer chord than that of analysis 1 but identical intersection region mesh, shows a decrease of 32% in maximum load and larger displacements. Analyses 10 and 3 show the effect of brace length.

A comparison of the results of analyses 12 and 1 show that the maximum load under compressive load is about 60% lower than the tensile value. Having carried out similar investigations for compression loading to those discussed above for tension, the effects were found to be similar in trend though less pronounced.

The half-joint model of Figure 3c was used for further investigations as follows:

1) The effect of interchanging the chord support conditions of Figure 1b for the half-joint model of Figure 3c, so that end A (short chord end) was on a roller and end B pinned, is illustrated by comparing the results of analyses 7 (latter support conditions) and 6. Clearly the effect on static strength is negligible as shown in Table 3.

2) The effect of using the experimental model dimensions of Figure 1a instead of the nominal dimensions indicated above is seen by comparing the results of analyses 11 and 6; the 6% increase in strength is considered to be due mainly to the increased chord wall thickness from 2 mm to the more exact 2.09 mm. Note that the brace-end displacements for the latter case were also smaller.

3) The effect of changing the mesh design from that of Figure 3c to that of Figure 5a, which is intuitively more appropriate, is shown by comparing the results of analyses 15 and 13 (for tension), and by comparison of analyses 16 and 14 (for compression); the latter mesh design resulted in predicted strength decreases of 4% and 3%, respectively.

4) In addition to change of mesh design, analyses 15 and 16 also effect a significant reduction in the widths of the first row chord elements adjacent to the junction (and an increase in intersection region mesh density) compared to those of analyses 13 and 14, respectively. This is clearly seen from Figures 3c and 5a. The mesh used for analyses 17 and 19 effects an additional decrease of chord first row element widths, compared to that of analyses 15 and 16. These results indicate a marked effect of chord first row element width on predicted strength: as element width decreases the strength decreases. The effect of changing from the mesh of Figure 5a to that of Figure 5b is to reduce the predicted strengths by 9% and 6% for the tension and compression loading cases, respectively.

5) In the analyses so far the brace-end axial load was applied by uniform end pressure, which remains normal to the brace-end during deformation. An alternative is uniform brace-end displacement with a concentrated/distributed end load via constraint equations; this is investigated for the tension and compression cases using analyses 18 and 20, respectively. Comparison of the results of these cases with those of analyses 17 and 19 indicate negligible effect for the compression case but a 3% increase for the tension case. The latter effect is due to the fact that the uniform end pressure method of loading has greater freedom at the brace-end; this effect is more pronounced for the tension case due to the larger associated contribution from beam bending of the chord.

6) Comparison of the half-joint model tension analyses (15, 17 and 18) with the corresponding compression analyses (14, 16 and 19) shows the compression predicted strengths to be consistently about 50% lower.

The mesh of Figure 5b with the ML stress-strain law and with the joint dimensions of Figure 1a predicts tensile and compressive joint static strengths which correlate with the test results of Table 1 to within 3%. This is taken as the 'converged' mesh, since although it appears that further reduction of the chord first row element width might lead to further small decrease of joint strength predictions until 'complete' convergence, element aspect ratios in the critical regions would then have approached recommended limits and may have interfered with the beneficial effect of further mesh refinement.

4.2 In-plane bending

Details of the in-plane bending (IPB) analyses are given in Table 4. For the preliminary IPB analyses (I1 to I4) the base-case model was a half-joint model with almost identical mesh design to that of Figure 3c, but with equal L_S and L_L lengths of 165 mm. Otherwise, this model had nominal joint dimensions (see above), an EPP stress-strain law and the chord was simply-supported. The moment was applied as a force-couple of two equal and opposite forces at the brace-end, both parallel to the brace axis, with a carefully designed ring of 'rigid' elements on the end, to avoid interference by local brace-end failure. A Young's modulus of 33 GPa is used for all analyses of Table 4.

Figure 6 shows the brace-end moment-rotation responses of this model for analyses I1 and I4. In general the IPB moment-rotation responses have two maxima; the first, normalised (see above) as B_1*, is associated with elastic-plastic instability of the compression side of the chord and the second, normalised as B_2*, with the achievement of a limit load on the chord.

Analysis I2 examines the effect of using a shorter brace length of 143 mm, instead of 153 mm, as used

Table 4. FE results for in-plane brace moment loading of T-joint.

Analysis	σ–ε law	UTS (MPa)	Model type & dims.	L_S, L_L (mm)	# elem. through thickness	Fig.	B_1*	B_2*
I1	EPP	59.3	1/2 & N	165,165	1	3c	8.74	9.48
I2	EPP	59.3	1/2 & N #	165,165	1	3c	9.00	10.2
I3	ML	59.3	1/2 & N	165,165	1	3c	8.68	9.53
I4	EPP	59.3	1/2 & N	165,165	2	-	9.03	9.63
I5	EPP	59.3	1/2 & N	178,268	1	-	9.00	9.74
I6	EPP	59.3	1/2 & N ##	178,268	1	-	9.00	9.74
I7	EPP	59.3	1/2 & N $	178,268	1	-	8.93	9.67
I8	ML	59.3	1/2 & N	178,268	1	3c	8.31	9.05
I9	ML	59.3	1/2 & N	178,268	1	5a	7.77	7.99
I10	ML	59.3	1/2 & N	178,268	1	5b	7.38	7.32

Poisson's ratio taken as 0.4 throughout.
# denotes brace length of 143mm instead of 153mm.
denotes end B pinned, end A on roller.
$ denotes reversal of direction of applied moment.

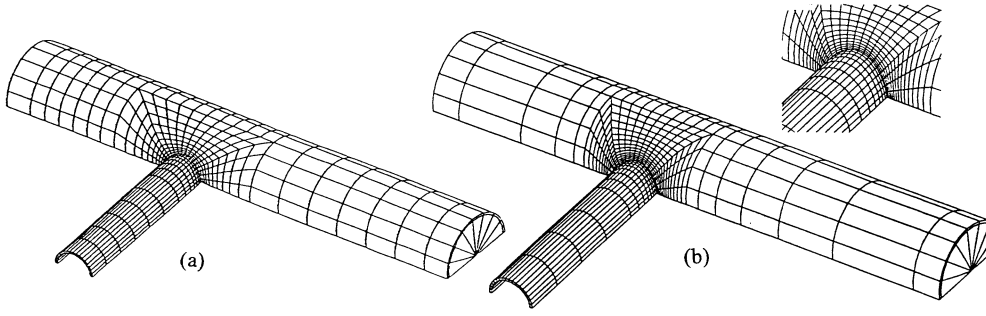

Figure 5. FE fine meshes used for axial force, in-plane and out-of-plane moment analyses of T-joint.

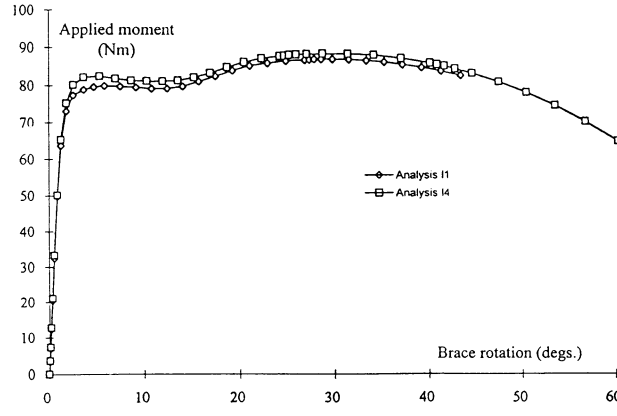

Figure 6. Typical moment-rotation responses of T-joint for in-plane bending.

in analysis I1; the effect is to increase the values of B_1* and B_2* by 3% and 8%, respectively. This effect is consistent with the method used to apply the brace moment and illustrates the dependency of predicted collapse moment on brace length; consequently the importance of FE model dimensional accuracy for brace length in moment loading is underlined. Analysis I3 (compared to I1) shows that the use of a ML stress-strain curve instead of the EPP curve has negligible effect on the predicted collapse moment.

Analysis I4 examines the effect of using two elements through the wall thickness instead of one, as in analysis I1. The effect is shown in Figure 6; the responses are very close until plastic deformation at which point they begin to diverge. The predicted first maximum for the two-element case is 3% higher than that of the one-element case; after this point the responses converge a little again and thereafter maintain an almost constant moment difference of about 1.5% for corresponding rotation values.

Analyses I5 to I7 of Table 4 are based on a half-joint model which has the correct L_S and L_L lengths of 178 mm and 268 mm, but otherwise is identical to the model of analyses I1 to I4, including the same mesh design of Figure 3c. Comparison of the results of analysis I5 and I1 show the effect of this change to be increases of 3% in both B_1* and B_2*. The effect of interchanging the pinned and roller restraints of the chord is examined in analysis I6 and found to be negligible. The effect of reversing the direction of the applied moment is examined in analysis I7; a 1% decrease of both B_1* and B_2* is predicted.

Analyses I8 to I10 are concerned with evaluating the effect of progressive mesh refinement, again paying particular attention to the intersection region; these analyses use the dimensions of Figure 1a and meshes corresponding to those of Figures 3c, 5a and 5b, respectively. The conclusion is that progressive refinement of the chord intersection region mesh leads to gradual reduction of the predicted collapse moment to a converged case with maximum normalised moment of 7.38, which is about 20% lower than the experimental value of Table 1.

4.3 Out-of-plane bending

A series of OPB analyses for the T-joint were performed to investigate the effect of mesh design and refinement on the predicted OPB capacity of the joint. The data and results pertaining to these analyses are presented in Table 5. As it is necessary to use a full-joint model for OPB analyses, such analyses are more computationally-intensive than the axial load and IPB cases. Six meshes were developed for this mode; the first and second meshes are full-joint versions of the quarter-joint model of Figure 3a with one and two elements through the wall, respectively; the third, fourth, fifth and sixth meshes are full-joint versions of Figures 3b, 3c, 5a and 5b, respectively. These meshes are used in the same order by analyses O1 to O6 of Table 5; Figure 7 shows the final mesh which was used in analysis O6. The moment loading was implemented similarly to the in-plane moment case. Analyses O1 to O3 use nominal dimensions and equal L_S and L_L lengths of 165 mm and an EPP stress-strain law; the other analyses use experimental model dimensions with an ML stress-strain law. Figure 8 shows the moment-rotation responses for analyses O1 and O2; some of the responses showed two maxima and others only one clear maximum. The rotations are generally larger than for IPB cases; brace rotations at maximum load for the IPB and OPB cases are about 25^0 and 45^0, respectively.

Analyses O1 and O2 show that two elements through the wall caused a 4% drop in predicted moment capacity. Increasing the mesh density from that of Figure 3a (analysis O1) to that of Figure 3b (analysis O3) caused a 1% drop in predicted strength. Analysis O4 shows that adoption of experimental dimensions and ML stress-strain law caused an 18% drop in predicted strength; this is considered to be due mainly to the extra sensitivity of the out-of-moment loading results to the precise form of stress-strain law used due to the larger rotations and deformations predicted. Analyses O5 and O6 show the gradual reduction of predicted capacity with progressive mesh refinement in the

Table 5. FE results for out-of-plane bending of T-joint.

Case	σ–ε law	Model type & dims.	L_S, L_L (mm)	#elems across wall	Fig	B_1*	B_2*
O1	EPP	Full & N	165,165	1	3a	-	9.53
O2	EPP	Full & N	165,165	2	3a	5.26	9.16
O3	EPP	Full & N	165,165	1	3b	-	9.44
O4	ML	Full & E	178,268	1	3c	5.12	7.85
O5	ML	Full & E	178,268	1	5a	4.70	7.47
O6	ML	Full & E	178,268	1	6	4.62	7.30

Note: σ_u = 60 MPa, E = 33 GPa, ν = 0.4 for all of above analyses.

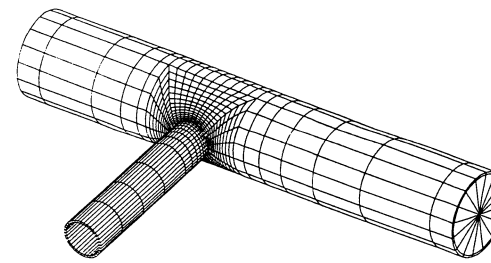

Figure 7. FE model used for OPB analysis O6.

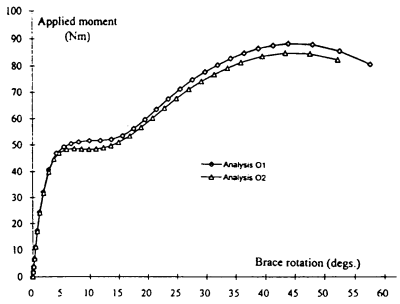

Figure 8. Typical T-joint OPB responses.

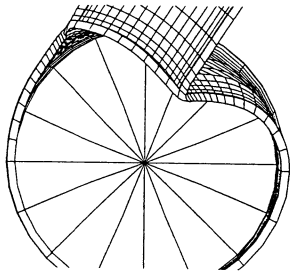

Figure 9. T-brace section view of deformed mesh at maximum load for OPB analysis O6.

intersection region, with the mesh of O6 representing the finest 'reasonable' mesh before introducing aspect ratio problems.

The prediction of analysis O6 is about 25% higher than the experimental value of Table 1; the analyses do not model tearing of the joint which was noted to have begun at approximately 30^0 experimental brace rotation. At a brace rotation of about 30^0, the FE predictions are accurate to within approximately 10% of the test results. Figure 9 shows the deformed mesh at maximum load, as predicted by analysis O6.

5 YT-JOINT FE RESULTS

5.1 Introduction

In this section a series of FE analyses of the simply-supported YT-joint (see Figs. 1a,c) subjected to different combinations of T- and Y-brace axial loads are described. The purpose of these analyses was to determine the most suitable FE mesh for static strength prediction of YT-joints, using the 3D solid isoparametric parabolic elements (with reduced integration) of the T-joint analyses, but also considering additional issues such as comparisons with shell element predictions and evaluation of the difference between the reduced integration, full integration and hybrid formulation variants of the same 3D parabolic (brick) elements.

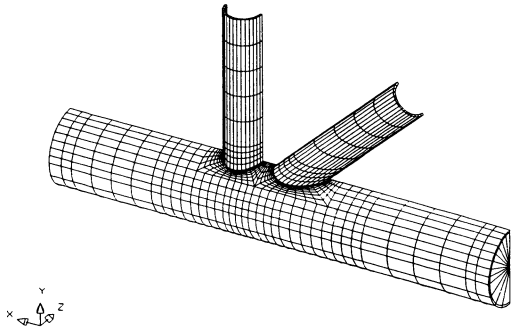

Figure 10. Mesh 5 for FE model of YT-joint.

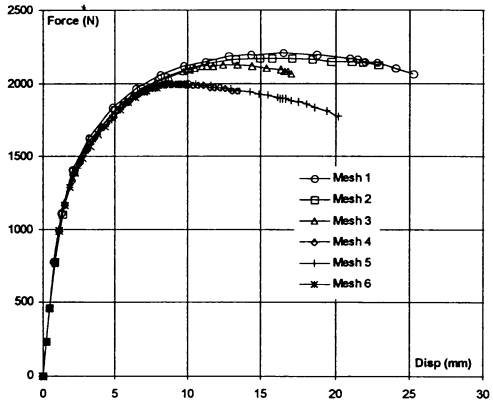

Figure 11. T-brace force-displacement responses for meshes used in YT-joint convergence study.

5.2 Mesh convergence

In order to validate extrapolation of the mesh studies of the T-joint intersection region to the YT-joint a series of six progressively more refined meshes were developed. The 'converged' mesh (mesh 5) is shown in Figure 10. All six meshes used the same pattern; meshes 1 to 4 were less refined than mesh 5 throughout and mesh 6 was more refined in the intersection regions but less outside; mesh 4 is identical to mesh 5 in the intersection regions. Table 6 lists the mesh details and the failure loads for an applied (A_Y:A_T) load ratio of (1:1), i.e. equal T- and Y-brace tensile forces; the parameters r and c define the number of elements in the circumferential and radially-outward directions for the intersection region mesh patches of the chord. The force-displacement responses of the six meshes for the (1:1) load ratio are compared in Figure 11; the failure load of mesh 5 is 9% lower than the experimentally measured failure load.

Further analyses were performed with meshes 4, 5

Table 6. Mesh sensitivity data and results for YT-joint under (A_Y:A_T) load ratio of (1:1).

Mesh	Total # elements	(r, c)	W/T	A_T*
1	292	(2,8)	3.3	17.4
2	324	(4,8)	1.7	17.2
3	672	(8,16)	0.84	16.8
4	672	(8,16) $	0.26	15.8
5	1112	(8,16) $	0.26	15.8
6	736	(10,16) $	0.21	15.8

$ denotes that mesh is biased towards junction.
W/T is the ratio of width (in radially outward direction) of first element on chord at the junction to chord wall thickness T.

and 6 for the range of (A_Y:A_T) load ratios shown in Table 2 to confirm convergence of mesh 5 over the range; the results showed general agreement between the three meshes to within 2%. The results of mesh 5 for the range of load ratios correlated to the experimental results of Table 2 to within 10%.

5.3 Integration order/formulation

The mesh of Figure 10 (mesh 5) was then used to study the differences between full integration, reduced integration and hybrid formulation variants of the 3D isoparametric, parabolic brick element, for the (1:1) load ratio analysis. The full integration elements are generally not recommended for non-linear analyses involving plasticity and limit load type behaviour because of the possibility of 'locking' under incompressible plastic flow. The hybrid elements used here have quadratic displacement interpolation and separate linear pressure interpolation and thus avoid the problems caused by incompressibility; however they are computationally expensive. The reduced integration elements are not susceptible to 'locking' either and are computationally inexpensive relative to the other two variants; however they can be susceptible to 'hourglassing' and consequently caution must be exercised in their use. Reduced integration elements also generally perform better than fully integrated under large displacements, as the latter can exhibit 'locking' there also.

The T-brace force-displacement responses for the three cases are shown in Figure 12. The responses of the hybrid and reduced integration elements are coincident up to a load of 2000 N; the hybrid continues to carry load to 2050 N while the reduced integration element peaks at 2000 N. However, the fully integrated version has a different response to the others above approximately 1500 N and predicts a maximum load of 2100 N. The reduced integration and hybrid elements thus predict maximum loads within 2.5% of each other and the displacements agree also; the reduced integration version therefore gives good accuracy compared to the hybrid

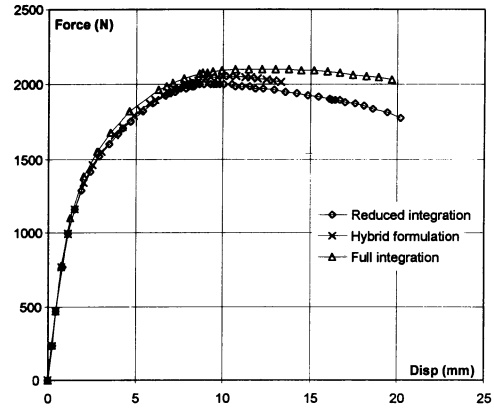

Figure 12. T-brace force-displacement responses for reduced/full integration and hybrid elements.

formulation as well as much better computational efficiency.

5.4 Comparison with shell elements

In order to compare the present 3D brick elements to shell elements, for the static strength prediction of tubular joints, two commonly-used shell element types were used, namely, an 8-node thin-shell element and a 4-node (finite membrane strain) shell element (HKS Inc. 1995). The present structural dimensions fall well within the limits recommended for using the thin-shell elements (HKS Inc. 1995). The 8-node shell element mesh is identical to the brick element mesh (Figure 10) except that mean chord and brace surfaces and dimensions are used; the mesh used for the 4-node element was obtained by replacing each 8-node element by four 4-node elements for most of the joint and especially around the junctions (elsewhere the mesh was slightly more coarse). For both shell elements, five integration points through the thickness were used.

The T-brace force-displacement responses of the YT-joint shell-element models for the (1:1) load ratio are compared to the brick element results in Figure 13; the 8-node shell elements predict a 13% higher maximum load than the brick elements while the 4-node finite strain elements predict a 2% lower maximum load. In both cases the inelastic responses are quite different from that of the brick elements. The 8-node shell element was also analysed for (A_Y:A_T) load ratios of (-1:-1) and (1:-0.4), for both of which it predicted 12% lower maximum loads than the brick elements, again with quite different inelastic force-displacement responses; the 4-node element gave convergence problems for both of these cases well before peak load. The differences between the shell and brick element results may be due to either the different formulations or differences in the associated geometrical representations; the

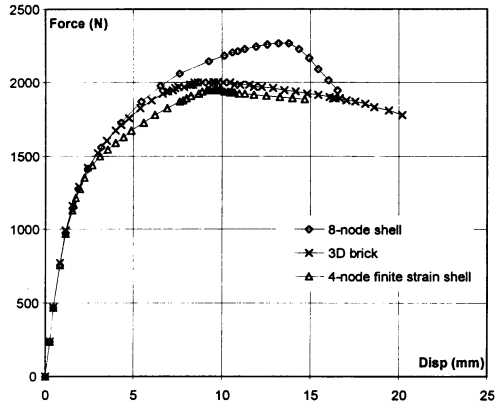

Figure 13. T-brace force-displacement responses of shell and brick element models of YT-joint.

latter point is particularly significant where multi-brace joints, with gaps, are concerned, and the brick elements are considered to be geometrically more accurate in this context. For this reason the YT-joint is considered a more severe and realistic test for the shell/brick element comparison, than the T-joint.

6 CONCLUSIONS

The following conclusions and recommendations are made from the results presented:

i) For accurate FE calculation of the static strength of tubular T-joints using a brick-element model, under axial loading, IPB or OPB, particular attention must be paid to the element sizes on the chord at the junction; 20-noded, isoparametric, parabolic, reduced integration (brick) elements were shown to give good agreement with test results.

ii) The most suitable type of mesh design for all T-joint loading modes was that shown in Figure 5b, with full-joint versions being used for OPB.

iii) One element through the chord wall was found to give accurate strength predictions for axial loading but two elements gave slightly different results for IPB and OPB cases.

iv) The UTS was found to be the important material property governing failure load for axial loading and IPB, whereas the precise form of stress-strain law (i.e. EPP or ML) had greater effect on OPB results.

v) The outcome of the T-joint mesh convergence study was extrapolated to the YT-joint and the resulting mesh was shown be satisfactory for the YT-joint by comparison with results from a range of other meshes and for different T- to Y-brace load ratios.

vi) The reduced integration variants of the brick elements were shown to give solutions in close agreement with the hybrid formulation variants for static strength of YT-joints and at a much lower cost.

vii) Shell element inelastic force-displacement responses were shown to be at variance with parabolic brick element results for the YT-joint; in terms of static strength, the difference was typically about 12% (higher or lower depending on applied load ratio) for 8-node shells; the 4-node finite strain shells predicted a 2% lower maximum load than the brick elements for an (A_Y:A_T) load ratio of (1:1).

viii) Although the force-displacement results presented clearly do not simulate precisely typical welded steel joint tension responses, especially in the near-failure segment, the primary objective of the present work was to establish experimental and FE static strength correlation in the context of the tin-lead alloy joints, as a potential basis for the development of FE models of steel joints.

7 ACKNOWLEDGEMENTS

The authors would like to thank the EPSRC and HSE for funding the present research as well as Mr. R. Pickard, Mr. J. Simpson and other staff of the Department of Mechanical Engineering for their patient help and assistance.

REFERENCES

Femsys Ltd., FEMGEN/FEMVIEW User Manual V.2, Leicester, 1994.

Fessler, H. and Hassell, W. A model technique for static strength of tubular joints. *Steel Construction Today*, 1990, 4, 104-112.

Fessler, H., Hassell, W. and Hyde, T.H. A model technique for bending strength of tubular joints. *J. Strain Analysis*, 1992, 27, 197-210.

Fessler, H., Hyde, T.H. and Khalid, Y.A. The effect of adjacent braces on the static strength of a corner YT joint. *Proc. Instn. Civil Engrs. Structures and Buildings*, 1996, 116, Feb., 44-53.

HKS Inc., ABAQUS User's and Theory Manual., Rhode Is., U.S., Version 5.5, 1995.

Khalid, Y.A. Static strength of tubular joints. PhD thesis, University of Nottingham, U.K., 1993.

Saad, S.B. Finite element determination of the static strength of cracked and uncracked tubular joints. PhD thesis, University of Nottingham, U.K., 1997.

Fatigue strength



Taylor & Francis
Taylor & Francis Group
http://taylorandfrancis.com

Tubular Structures VIII, Choo & Van der Vegte (eds) © 1998 Balkema, Rotterdam, ISBN 90 5809 001 9

Prediction of stress concentration factors in in-plane moment loaded tubular K-joints

M.M.K.Lee & M.R.Morgan
University of Wales, Swansea, UK

ABSTRACT: A parametric study on the distributions of stress concentration factors in tubular K-joints under in-plane moment loading is presented. The new database of finite element results was then used to develop parametric equations for predicting stress concentration factors at key locations around the intersection on the outer as well as the inner surfaces of the chord. The reliability of the proposed and existing parametric equations was then assessed using an acrylic test joint database and some published test data measured from a steel model. Fracture mechanics fatigue calculations were also performed to demonstrate that the information provided from the proposed equations could be utilised to obtain accurate, and safe, fatigue life estimates.

1 INTRODUCTION

Circular hollow section joints in offshore steel jacket structures are subjected to cyclic wave loading and are thus susceptible to fatigue damage. The various methodologies for determining stress intensity factors in tubular joints, which are needed for accurate fatigue lives estimates, require information on the stresses around the joint intersection as well as through the thickness of the chord member, expressed in terms of the distributions of the stress concentration factor (SCF) and the degree of bending (DoB). [Note that the DoB can be determined from the inner (σ_i) and the outer (σ_o) surface stresses – DoB = 0.5 (1-(σ_i/σ_o)).]

This paper presents a comprehensive study on SCFs in gap K-joints under balanced in-plane bending loading. The finite-element results obtained are used to assess the parametric equations of Efthymiou & Durkin (1985) and Smedley & Fisher (1991) [hereafter referred to as the Efthymiou and the Lloyds equations, respectively], which have been regarded by the UK Department of Energy (1995) as the most consistent, overall, in meeting certain criteria (detailed later). New parametric equations are then presented for the maximum SCFs on the outer surfaces of the chord and the brace; equations are also proposed for the inner and the outer surface SCFs at key locations on the chord side. The distributions of stresses around the intersections, obtained using the proposed parametric equations and the strategy outlined in previous work (Morgan & Lee 1996a), are compared with both the finite-element database from which the equations were derived and some recently published test data (Soh & Soh 1996). Comparisons are also made between the fatigue life estimates obtained using the predicted and the finite-element stress distributions for a selected sample of joints in the database.

2 SCOPE OF STUDY

The study, which consists of 254 analyses, was conducted as several sub-studies investigating the effects of various geometric parameters (see Fig. 1 and notation for the definitions of the geometric ratios):

- Effects of the geometric ratios γ, β, τ and ζ: γ=10, 25, 40; β=0.3, 0.5, 0.8, τ=0.4, 0.7, 1.0 and ζ=0.2, 0.6, 0.8. For these models α=12 and θ_A=θ_B =45°.
- Effects of varying θ_A:θ_B and their interaction with other parameters.
- Effects of α
- Effects of β_A:β_B
- Effect of varying τ_A:τ_B.

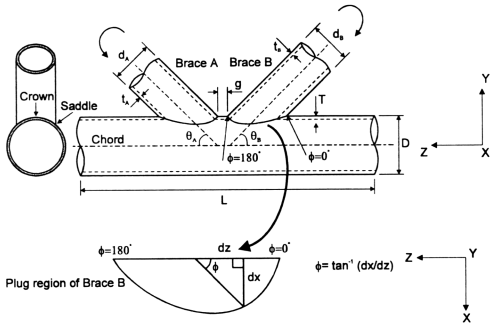

$\alpha = 2L/D$; $\beta_A = d_A/D$; $\beta_B = d_B/D$; $\gamma = D/2T$;
$\tau_A = t_A/T$; $\tau_B = t_B/T$; $\zeta = g/D$;
ϕ = angle around the intersection (measured from the acute crown)

Figure 1 Geometric parameters for a K-joint

3 FE MODELLING AND VALIDATION

The finite-element modelling approach adopted in this study is similar to that used for the balanced axial loading work and has been reported in detail in Morgan & Lee (1996a,b). The finite-element models were generated using ANSYS (1994) and the elastic analyses were performed with ABAQUS (1994). An eight noded doubly curved thin shell element (element S8R5), with a five-point integration through the thickness was used. The Young's Modulus E = 200 KN/mm^2 and the Poisson ratio ν = 0.3 were used. A typical finite-element mesh is shown in Fig. 2.

The loading applied created an opening moment (illustrated in Fig. 1) with the chord end circumferences given full fixity conditions. The nominal stress in the brace was derived from simple beam theory using a moment arm measured, along the axis of the brace, from the point of application of the brace load to the outer surface of the chord. The SCFs reported herein were obtained by dividing the maximum absolute principal stress at any given point around the intersection by the extreme fibre stress in the reference brace.

The finite-element model was validated against eight joint results from the original Efthymiou database (Smedley 1995). These joints had β=0.6 or 0.8, γ=16, 20 or 30, τ=0.3, 0.5 or 1.0, $\theta_A=\theta_B=45^\circ$ and ζ=0.4 or 0.7. The ratio of the SCF from the finite-element model to the SCF recorded in the Efthymiou database had a mean of 1.053 and a coefficient of variation (CoV) of 0.039 for the chord side, and a mean of 1.053 and a CoV of 0.076 for the brace side. In light of the possible variability of SCFs that can

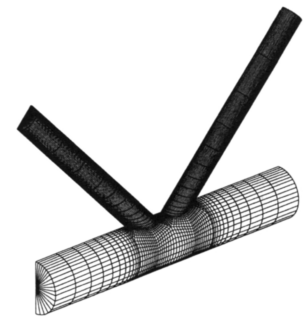

Figure 2 A typical finite element mesh

be obtained using different finite-element modelling techniques, the level of agreement obtained was considered to be satisfactory. And since the Efthymiou data are generally accepted to be of a high quality, the finite-element mesh was also considered to be adequate to produce valid results.

4 ASSESSMENT CRITERIA

The UK Department of Energy (1995) recommends the following assessment criteria regarding the applicability of the commonly used SCF parametric equations (P/R stands for the ratio of the *Predicted* SCF from a given equation to the *Recorded* SCF from test or analysis):

- For a given dataset, if % SCFs underpredicting ≤25%, i.e. [%P/R<1.0]≤25%, and if % SCFs considerably underpredicting ≤5%, i.e. [%P/R<0.8]≤5%, then accept the equation. If, in addition, the percentage SCFs considerably overpredicting ≥50%, i.e. [%P/R>1.5]≥50%, then the equation is regarded as generally conservative.
- If the acceptance criteria is nearly met i.e. 25%<[%P/R<1.0]≤30%, and/or 5%<[%P/R<0.8] ≤7.5%, then the equation is regarded as borderline and engineering judgement must be used to determine acceptance or rejection. Otherwise reject the equation as it is too optimistic.

In view of the fact that for a mean fit equation, there is always a large percentage of underprediction, the requirement for joint underprediction, i.e. P/R<1.0, was completely removed in a subsequent assessment of parametric equations (Smedley, 1995).

The maximum SCF equations of Efthymiou (Efthymiou & Durkin 1985) and Lloyds (Smedley &

Table 1 Assessment of existing equations with the new finite-element data - chord side

Equation	Mean	CoV	%P/R<0.8	%P/R<1.0	%P/R>1.5	Minimum P/R	Maximum P/R
Efthymiou	1.01	0.13	0.70	57.75	0.70	0.78	1.51
Lloyds	0.97	0.17	9.43	62.89	4.40	0.65	2.30
Equation (1)	1.01	0.07	0.00	44.95	0.00	0.80	1.30

P/R = Predicted/Recorded

Table 2 Assessment of existing equations with the new finite-element data - brace side

Equation	Mean	CoV	%P/R<0.8	%P/R<1.0	%P/R>1.5	Minimum P/R	Maximum P/R
Efthymiou	1.16	0.35	3.52	41.55	11.27	0.77	3.49
Lloyds	0.78	0.21	64.15	90.57	1.89	0.59	1.76
Equation (2)	1.01	0.09	0.99	47.78	0.00	0.76	1.34

Fisher 1991) were assessed using the finite-element data produced in this study and the criteria mentioned in the foregoing to determine their reliability (see Tables 1 and 2). Only data falling within the validity range of the equations, i.e. results for joints with α=12 and both braces having the same diameter and thickness, were used in the assessment.

For the chord side, Table 1, although both existing equations provide a mean P/R ratio very close to unity, the predictions exhibit significant scatter, giving CoVs of 13% and 17%. With regard to the assessment criteria, the Efthymiou equations are shown to be the better performer of the two sets. The Lloyds equations give a maximum P/R ratio of 2.3, which represents a gross SCF overprediction.

For the brace side, Table 2, the Efthymiou and the Lloyds equations provide mean P/R ratios of 1.16 and 0.78, respectively, which are substantially worse than those for the chord side. It should be noted that the Efthymiou equations for the brace side SCF are identical to those used for T/Y-joints and it is therefore not surprising that they generally overpredict the SCFs and generate a large amount of scatter, giving a CoV of 0.35 and a maximum P/R ratio of 3.49.

In summary, the assessment using the new finite-element data has highlighted the inadequacy of the existing equations and the need for new, more accurate parametric equations.

5 PARAMETRIC EQUATIONS

Using the database generated in this finite-element study [the entire database is reported in Morgan & Lee (1996c)], new parametric equations were derived for the maximum outer surface SCFs on the chord and the brace. Equations were also derived for the inner and the outer surface SCFs at various key locations on the chord – ϕ=0°, 45°, 90°, 135° and 180° (Fig. 1 shows how ϕ was measured). Multiple regression analyses were carried out using the spreadsheet program Microsoft Excel (1993). The parametric equations are listed in the Appendix.

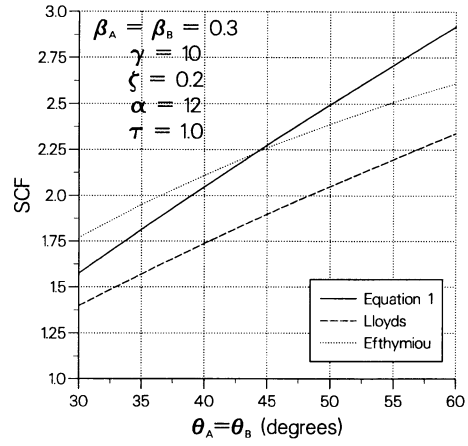

Figure 3 Effect of θ on the chord outer surface SCF

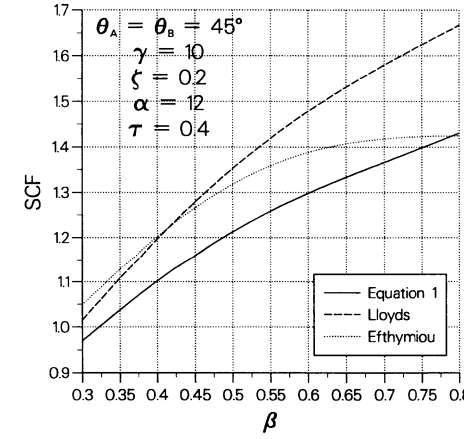

Figure 4 Effect of β on the chord outer surface SCF

5.1 Observations from the new equations for maximum SCF

The predictions from eqns. (1) and (2) were compared with those from the Efthymiou and the Lloyds equations to examine the general applicability of the new equations. The comparison revealed a number of trends, which are highlighted in Figs. 3-6.

The variation of the chord outer surface SCFs with brace inclination (for joints with equal brace inclinations) is shown in Fig. 3. The predictions from (1) fall between the existing equations for low θ values. As θ increases, the Lloyds and the Efthymiou equations become increasingly unconservative; for θ=60°, the underpredictions are 19.7% and 9.7%, respectively. This underprediction for joints with large brace inclinations is common to all other geometries.

It should be noted that for joints with β=1.0, the Lloyds equations predict that the chord SCF will reduce with increasing brace inclination. The opposite effect, however, has been observed from the finite-element data and the Efthymiou equations.

Fig. 4 shows the variation of the chord outer surface SCF with β for joints with equal brace inclinations of θ=45°. Whilst both the Lloyds equations and (1) follow a trend of increasing SCF with β, the predictions from the Efthymiou equations begin to saturate when β≈0.65. When β=0.8, the Lloyds equations predict an SCF 16% higher than that from the Efthymiou equations and (1). These observations were, again, found to be common to other geometries.

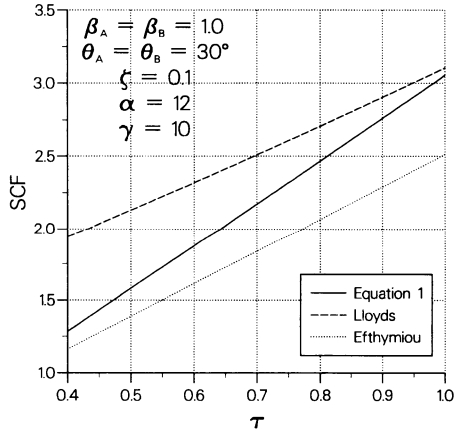

Figure 5 Effect of τ on the chord outer surface SCF

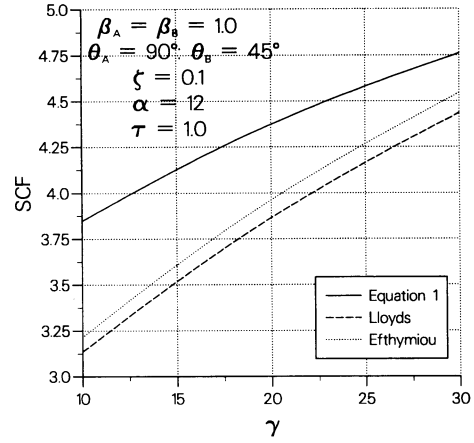

Figure 6 Effect of γ on the chord outer surface SCF

All three sets of equations predict a linear increase in SCF as τ increases, Fig. 5, although (1), with a steeper slope, shows the effect of τ to be more significant than the existing equations. (1) gives good agreement with the Efthymiou equations for low τ values, and with the Lloyds equations for high τ values.

For joints with unequal brace inclinations, all three sets of equations exhibit similar trends in the variation of SCF with γ, Fig. 6. (1) predicts SCF values that are consistently higher than those of the existing equations for the entire range of γ values. These observations only apply to joints with θ_A=90°, θ_B=45°, τ=1.0 and β=1.0, however.

5.2 Assessment of the maximum SCF equations using the acrylic joint database

The UK Department of Energy (1995) includes databases of SCFs measured on steel and acrylic joints. For K-joints under balanced in-plane moment loading, no steel joint data are available. The acrylic joint database consists of 35 results, which were used for the development of the Lloyds equations and, hence, it is expected that these equations would perform well in this assessment. The acrylic database was used to assess the proposed and the existing equations using the criteria detailed previously. To compare the equations on the same footing, the Lloyds equations were converted back to their mean format by removing the design factor. The results of the assessment are presented in Tables 3 and 4.

For the chord side, (1) gives a mean P/R ratio of 1.13, which is near the Efthymiou value of 1.16, but substantially higher than the Lloyds value of 0.92. The CoVs obtained for all three equations are very

Table 3 Assessment of the proposed and existing equations using the acrylic database - chord side

Equation	Mean	CoV	%P/R<0.8	%P/R<1.0	%P/R>1.5	Minimum P/R	Maximum P/R
Efthymiou	1.16	0.16	3.13	18.75	3.13	0.68	1.50
Lloyds	0.92	0.15	15.63	78.13	0.00	0.64	1.25
Equation (1)	1.13	0.17	6.25	28.13	0.00	0.75	1.40

Table 4 Assessment of the proposed and existing equations using the acrylic database - brace side

Equation	Mean	CoV	%P/R<0.8	%P/R<1.0	%P/R>1.5	Minimum P/R	Maximum P/R
Efthymiou	1.32	0.29	2.94	8.82	17.65	0.79	2.97
Lloyds	0.79	0.20	61.77	94.12	0.00	0.52	1.33
Equation (2)	1.33	0.36	2.94	20.59	20.59	0.65	3.43

Table 5 Assessment of the proposed equations

Equation Number	R^2	Mean	CoV	%P/R<0.8	%P/R>1.5	Minimum P/R	Maximum P/R
(3)	0.991	1.003	0.061	0.0	0.0	0.854	1.250
(4)	0.992	0.989	0.094	1.07	0.0	0.789	1.350
(5)	0.986	0.985	0.110	0.0	0.0	0.800	1.319
(6)	0.992	1.017	0.120	3.45	0.0	0.718	1.338
(7)	0.991	1.006	0.072	0.00	0.0	0.841	1.372
(8)	0.968	1.014	0.113	3.65	0.0	0.750	1.300
(9)	0.993	0.982	0.083	1.07	0.0	0.762	1.250
(10)	0.993	0.989	0.107	3.57	0.0	0.754	1.300
(11)	0.994	1.007	0.099	2.84	0.0	0.700	1.350
(12)	0.976	0.993	0.128	5.59	0.0	0.678	1.361

similar. Although the Efthymiou equations are the only ones to meet all of the assessment criteria, it is reasonable to say, overall, that (1) can be considered just as good.

For the brace side, (2) gives the highest mean P/R ratio of 1.33 as well as the highest CoV of 0.36, indicating that it is the most conservative of the three sets. It is interesting to note, though, that (2) still meets all of the assessment criteria.

5.3 Assessment of equations for the SCFs at key locations

Table 5 shows the results of the assessment of eqns. (3)-(12). Eqns. (3)-(7) give correlation coefficients (R^2) in the range of 0.986-0.992 and CoVs in the range of 6.1%-12%. The minimum and the maximum P/R ratios are 0.718 and 1.372, respectively, which, along with the high R^2 and relatively low CoV values, indicate that the equations are a good fit to the finite-element database.

The assessment of eqns. (8)-(12) clearly shows that all of the equations except (12) meet the assessment criteria. (12) also gives a relatively poor R^2 value of 0.976, indicating that it only provides an average fit to the finite-element data. The use of a design factor (to be discussed later) will increase the mean P/R value and hence ensure that the equation meets the assessment criteria. The equations give R^2 and CoVs in the ranges of 0.968-0.994 and 0.083-0.128, respectively. The minimum and maximum P/R ratios are 0.678 and 1.361, respectively. These values, together with the high R^2 and relatively low CoV values, confirm that the equations are a good fit to the finite-element database and they should, therefore, provide accurate SCF estimates.

6 DESIGN FACTORS

Design factors may be applied to mean equations to ensure that certain criteria are satisfied. For example, the Lloyds equations use a factor of one standard deviation from the mean to increase the predicted SCFs, thus reducing the probability of the SCFs being underpredicted.

The ratios of the predicted SCF to the recorded SCF for (1)-(12) were found to give an approximately normal probability distribution when investigated using the χ^2 test at the 5% level of

Table 6 Design factors for the proposed equations

Equation Number	Design Factor	Revised Design Factor
(1)	1.045	1.115
(2)	1.050	1.134
(3)	1.038	1.097
(4)	1.075	1.166
(5)	1.089	1.196
(6)	1.064	1.180
(7)	1.043	1.112
(8)	1.063(0.909)	1.173(0.800)
(9)	1.074(0.962)	1.156(0.881)
(10)	1.084(0.938)	1.187(0.835)
(11)	1.060(0.927)	1.156(0.830)
(12)	1.094(0.920)	1.218(0.797)

Note: When using (8)-(12), if the resulting SCF is of the opposite sign to the corresponding one on the outer surface, the design factor in the parenthesis should be used

significance. Design factors were developed for the proposed outer surface equations to ensure that the condition [%P/R<1.0]≤25% was satisfied. Similarly, design factors were also applied to the proposed inner surface SCF equations. In a previous study on axially loaded K-joints by the writers (Morgan & Lee 1996a), where design factors were included in the outer surface SCF equations as well as for the DoB equations (here the design factors increased the SCF and reduced the DoB), shorter, or more conservative, fatigue lives were predicted.

For the outer surface, the design factors should always increase the SCFs as, on the outer surface, a larger SCF gives a shorter fatigue life (irrespective of whether the outer surface is in tension or compression). The situation on the inner surface is more complex – the design factor should increase the absolute SCFs for cases where both the inner and the outer surface SCFs are of the same sign, and should reduce the absolute SCF for cases when the inner and the outer surface SCFs are of the opposite sign.

The design factors for (1)-(12) are given in Table 6. The use of these factors results in either increasing or decreasing the SCFs by a maximum of 9.4% and should result in more conservative fatigue life estimates.

7 PREDICTION OF DISTRIBUTIONS OF STRESSES

The writers, in their previous work on axially loaded K-joints (Morgan & Lee 1996a), have proposed simple circular functions to predict the circumferential distributions of SCFs or DoBs. Such equations require the magnitude of the predicted parameter to be known at key locations and they predict the distributions over a maximum interval of 45° or 90°. However, it was found that, although the predicted trends were reasonable, the predictions at certain locations could deviate significantly from the

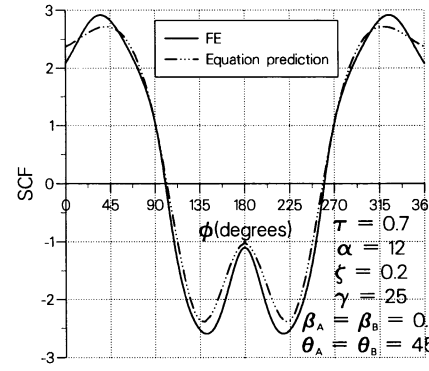

Figure 7 Outer surface stress distribution for joint IPB50

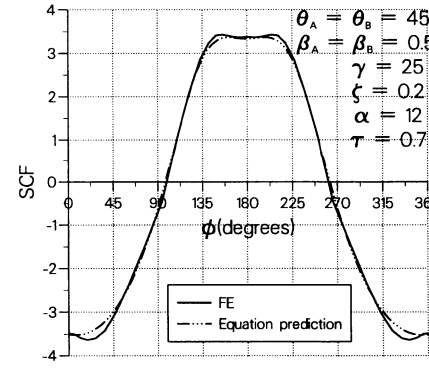

Figure 8 Inner surface stress distribution for joint IPB50

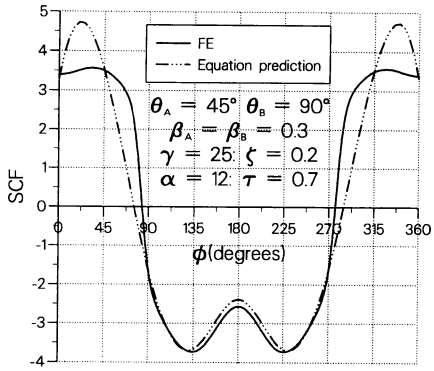

Figure 9 Outer surface stress distribution for joint IPB192

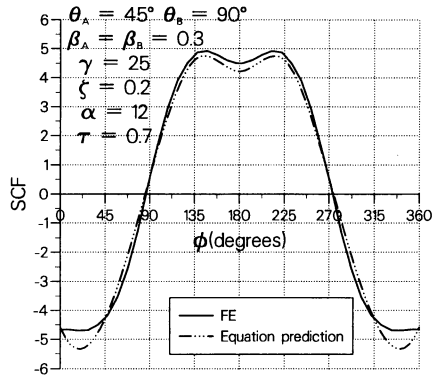

Figure 10 Inner surface stress distribution for joint IPB192

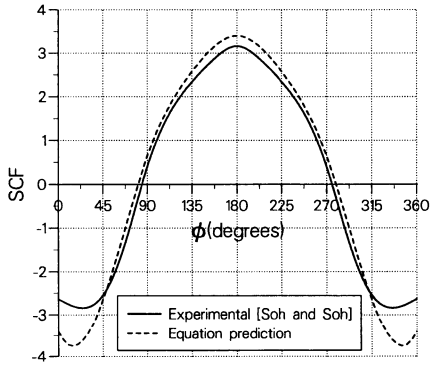

Figure 11 Comparison between the predicted distribution and the experimental measurements by Soh & Soh (1996)

finite-element results. Consequently, the writers, in the same work, also proposed an alternative way of predicting distributions using a cubic spline that might be used to fit through a number of equally or unequally spaced data points. For each interval, a polynomial equation is used to approximate the distribution. At the boundary of the interval, there is continuity in both gradient and the dependent variable. This continuity in slope, unlike the distribution obtained using the circular functions, ensures that the distribution is smooth. All of the intervals are then connected by a smooth curve. The subroutines EO2BAF and EO2BBF from the Numerical Algorithms Group (NAG) library (1983) were used to fit the data points.

7.1 Comparison with the finite-element data

Using the technique adopted in previous work (Morgan & Lee 1996a), the distributions of the inner and the outer surface SCFs were approximated by fitting a cubic spline through the data points obtained from (3)-(12). To confirm the validity of (3)-(12), the finite-element distributions are compared, in Figs. 7-10, with the equation predictions for a number of geometries. Figs. 7 and 8 show the outer and the inner surface SCF distributions, respectively, of a typical joint with 45° brace inclinations. It can be seen that there is good agreement between the finite-element and the equation predictions around the entire intersection. The outer surface SCF distributions of a typical joint with θ_A:θ_B = 45°:90° brace inclinations, Fig. 9, shows that the finite-element and the equation predictions agree well except at ϕ=20° and 340°, where the finite-element distribution is underestimated by ≈12%. The inner surface SCF distribution for the same joint, Fig. 10, shows large discrepancies between the two predictions in the regions $0° \le \phi \le 90°$ and $270 \le \phi \le 360°$. These discrepancies are the result of the relatively poor fit to the data provided by the cubic spline.

In conclusion, (3)-(12) were found to provide reasonably good fits to the finite-element data for the cases investigated, and when used in conjunction with a cubic spline, predict stress distributions which generally agree well with the finite-element distributions.

7.2 Comparison with published test data

Having established that the equation predictions are a good fit to the finite-element data, comparisons are now made with the results from a steel model tested

Table 7 Fatigue life estimates using the proposed equations

Method	Fatigue Endurance (Predicted/Recorded) Mean	CoV	%P/R<0.8	%P/R>1.5	Minimum P/R	Maximum P/R
1	0.92	0.19	20	25	0.68	1.30
2	0.71	0.19	80	5	0.48	1.05

Note: Method 1 – SCFs calculated using the original design factors
Method 2 – SCFs calculated using the revised design factors

by Soh & Soh (1996). In this test the model was loaded by a closing moment and the angle ϕ was measured in a slightly different way to that used in the current study. Fig. 11 compares the experimentally measured outer surface stress distribution with the equation prediction. The agreement between the two distributions is very good except for the regions $0^\circ \le \phi \le 45^\circ$ and $315^\circ \le \phi \le 360^\circ$, where the equation prediction underestimates the experimental measurement by a maximum of about 33%. This underestimation is due to the difference in SCFs at $\phi = 0^\circ$.

The equations proposed in this study, which were derived from opening moment loading, can also be used for the closing moment load case if the predicted SCFs from (3)-(12) are multiplied by -1.

8 FATIGUE LIFE ESTIMATES USING THE PROPOSED SCF EQUATIONS

An algorithm to perform numerical integration of the Paris crack growth law in fracture mechanics calculations was developed by Bowness (1996). The use of this algorithm to predict residual fatigue lives in tubular joints has been previously reported by the writer (Morgan & Lee 1996a).

In this section, an assessment is carried out on the fatigue life estimates obtained for a random sample of 20 joints from the finite-element database which were thought to be representative of the entire population. The results of this assessment are shown in Table 7.

The predicted fatigue lives (P) were obtained using the following procedure:

- The SCF values at the key locations on both the inner and the outer surfaces were obtained using (3)-(12), with each SCF obtained multiplied by the corresponding design factor (Table 6).
- The distributions of SCF were obtained by fitting a cubic spline through the SCF values at the key locations.
- The maximum outer surface SCF and the corresponding inner surface SCF were obtained directly from the predicted distribution, allowing the components of the bending and the membrane stress to be calculated.

The predicted fatigue lives were divided by the recorded life (R), which was obtained using the SCFs obtained from the finite-element calculations. For the sample of joints investigated, the mean P/R value obtained is 0.92, which indicates that, on average, the method gives safe fatigue life estimates. The CoV of 19% was found to be similar to that obtained for the balanced axial loading case (Morgan & Lee 1996a). The predicted fatigue lives, however, were found to exceed the recorded values for 25% of the cases investigated (this is considerably worse than the case the case of balanced axial loading investigated previously), with a maximum overprediction of 30%. The accuracy of the fatigue life estimates was found to be influenced by the complexity of the stress distributions, with the more complex distributions from the in-plane moment loadings producing rather less reliable fatigue life estimates.

To reduce the probability of fatigue life overpredictions, it is recommended that the design factors are revised to ensure that underprediction of SCFs is less than 5% (or for the inner surface SCF, if it is of the opposite sign to that on the outer surface, overprediction is less than 5%). The revised design factors are shown in Table 6. Using the revised design factors, the mean P/R fatigue endurance value obtained is 0.71, which is significantly lower than the value obtained using the original design factors, Table 7. The predicted fatigue lives were found to exceed the recorded values for only 5% of the cases investigated, i.e. 1 in 20 of the joints investigated (this is considerably better than the value of 25% obtained using the original design factors).

In summary, the outlined methodology proposed to calculate the remaining fatigue life has been found to be reliable, although it is recommended that the revised design factors are used, which ensure that the fatigue life is only overpredicted for 5% of the cases investigated.

9 CONCLUSIONS

The existing parametric equations of Efthymiou and Lloyds predict only the maximum outer surface SCF on the chord and the brace. For the in-plane bending load case investigated in the current work, the equations were developed from a very limited database (only 39 and 69 results for the Efthymiou and the Lloyd's equations, respectively) and, as a result, do not capture accurately the effects of all the geometric ratios. In this study an extensive parametric study was performed using thin shell finite-element models. New equations are proposed for the maximum SCFs on the chord and the brace, and they have been found to provide a good fit to the large finite-element database and to meet the proposed assessment criteria.

Equations are also developed for the inner and the outer surface SCFs at intervals of 45° on the chord side; from such surface stresses the DoB may easily be calculated. Using a cubic spline to fit through these points allows accurate predictions of the distribution of stresses around the intersection. Comparisons with published data from a full scale steel test show that the predictions of the stress distributions using this method are valid. Finally, fatigue life calculations performed using the predicted stress distributions were found to give safe fatigue life estimates.

REFERENCES

ABAQUS User's Manual 1994. Hibbit, Karlsson and Sorenson Inc., Providence, RI, Version 5.3..

ANSYS User's Manual 1994. Swanson Analysis Systems Inc., Version 5.0a.

Bowness, D. 1996. Fracture mechanics based assessment of weld toe cracks in offshore tubular structures. *PhD Thesis*. C/PH/201/96, University of Wales Swansea, UK.

Department of Energy 1995. Draft Background to New Fatigue Design Guidance for Steel Joints and Connections in Offshore Structures. Department of Energy.

Efthymiou, M. 1988. Development of SCF formulae and generalised influence functions for use in fatigue analysis. *Proc. Conference on Recent Developments in Tubular Joints Technology*, Surrey, 2-1 - 2-33.

Efthymiou, M. & Durkin, S. 1985. Stress concentrations in T/Y and gap overlap K-joints. *Proc. Int. Conf. on Behaviour of Offshore Structures*, Amsterdam, 429-441.

Microsoft Excel 1993. Microsoft Corporation, Version 5.0.

Morgan, M.R. & Lee, M.M.K. 1996a. A parametric study for the prediction of the stress distribution in tubular K-joints subjected to balanced axial loading. *Report No. CR/936/96*, University of Wales Swansea, UK.

Morgan, M.R. & Lee, M.M.K. 1996b. Prediction of stress concentration factors in K-joints under balanced axial loading. *Proc. Seventh International Symposium on Tubular Structures*, Hungary, 301-308.

Morgan, M.R. & Lee, M.M.K. 1996c. Numerical results for stress concentration factors and degrees of bending in tubular K-joints. Research *Report No. CR/948/96*, University of Wales Swansea, UK.

Numerical Algorithms Group 1983. FORTRAN Library Manual, Mark 16, Volume 1.

Smedley, P. 1995. Private communication.

Smedley, P. & Fisher P. 1991. Stress concentration factors for simple tubular joints. *Proc. 1st Int. Offshore and Polar Engineering Conf., Int. Society of Offshore and Polar Engineers*, Edinburgh, UK, 475-483.

Soh, A. & Soh, C. 1996. Stress concentrations of K tubular joints subjected to basic and combined loadings. *Proc. Institution Civ. Engrs*: Structs and Bldgs, 19-28.

Underwater Engineering Group 1985. Design guidance on tubular joints in steel offshore structures. *Report UR33*, UEG, Westminster, London.

APPENDIX

(Note: All values for θ are in radians)

Equations for Maximum SCF — Eqn. No.

Chord side:

$$SCF_{Ch} = 1.949\,\beta\,\tau^{0.947}\,\gamma^{(1-0.803\beta)}\sin^{(1.339-0.682\beta)}\theta\left(1+0.627\beta^{3.06}\exp(-1.029\zeta)\right) + 6.908(\beta_{MAX}-\beta_{MIN})(\beta-\beta_{MIN}) \quad (1)$$

Brace side:

$$SCF_{Br} = 0.934\tau^{(0.015\gamma+0.032)}\,\gamma^{(0.984-0.718\beta)}\beta^{(-0.075+0.324\tau)}\left(0.289+0.810\beta+0.590\beta^2\right)\left(\frac{\tau_A}{\tau_B}\right)^{0.116} \sin^{(1.256-0.664\beta)}\theta\left(1-1.208\beta^{79.855}\exp(-33.36\zeta)\right)+10.311(\beta_{MAX}-\beta_{MIN})(\beta-\beta_{MIN}) \quad (2)$$

Equations for SCFs at key locations on the chord side – outer surface

$$SCF^{Out}_{Ch0} = \left(-4.667\,\beta^{(-0.005-0.008\gamma)}\,\tau^{1.025}\,\gamma^{-0.875}\sin^{(0.727-0.314\beta)}\theta\,(-2.282+0.817\gamma)\right) -\left(0.719\beta^{1.301}\zeta^{0.268}\right) \quad (3)$$

$$SCF^{Out}_{Ch45} = -1.550\,\beta\,\tau^{1.103}\,\gamma^{(1-0.508\beta\theta)}\sin^{(1.628+1.557\beta)}\theta\left(\frac{\theta_{MAX}}{\theta}\right)^{-0.065}\left(\frac{\theta_{MIN}}{\theta}\right)^{-0.245} \quad (4)$$

$$SCF^{Out}_{Ch90} = -0.229\beta\tau^{1.234}\,\gamma^{(1-0.082\beta)}\sin^{(0.371+0.116\beta)}\theta\left(1-0.348\beta^{47.967}\exp(0.147\zeta)\right)\left(0.344+0.073\beta+0.241\beta^2\right)f(\theta)$$

With $f(\theta) = -1.544\gamma^{-0.030}$ *for cases where* $\beta \neq 1.0$ *and* $\theta_A/\theta_B = 45°/90°$

$f(\theta) = 1.0$ *for all other cases* (5)

If $\beta \le 0.3, \gamma \le 10$ *and* $\theta_A = \theta_B \neq 45°$ *then* $SCF^{Out}_{Ch90} = 0$

If $\beta = 1.0$ *and* $\theta_A/\theta_B = 45°/90°$ *then* $SCF^{Out}_{Ch90} = 0$

$$SCF^{Out}_{Ch135} = 0.237\left(0.468+4.716\beta+0.150\beta^2\right)\tau^{1.130}\,\gamma^{(1-0.497\beta)}\sin^{(1.424+0.299\beta)}\theta\left(1-0.456\beta^{3.549}\exp(-1.466\zeta)\right) \quad (6)$$

Use $\beta^* = 1.647\,\theta^{0.226}\tau^{-0.052}$ *in place of* β *for cases where* $\beta = 1.0$ *and* $\theta_B \le 45°$

$$SCF^{Out}_{Ch180} = 1.528\beta\tau^{0.996}\,\gamma^{(1-0.792\beta)}\sin^{(1.348-0.654\beta)}\theta\left(1+0.913\beta^{2.339}\exp(-1.013\zeta)\right)+0.374\left(\sin\left(\frac{\theta}{\theta_{MAX}}\right)\right)^{0.971} \quad (7)$$

Equations for SCFs at key locations on the chord side – inner surface

$$SCF^{In}_{Ch0} = \left(0.377\beta^{(-0.101-0.01\gamma)}\tau^{0.915}\,\gamma^{0.294}\sin^{(0.577-0.254\beta)}\theta\,(3.897-0.031\gamma)\right)-0.388\beta^{0.233}\zeta^{2.642} \quad (8)$$

$$SCF^{In}_{Ch45} = 1.162\,\beta\tau^{1.100}\,\gamma^{(1-0.452\beta\theta)}\sin^{(1.468+1.184\beta)}\theta\left(\frac{\theta_{MAX}}{\theta}\right)^{-0.009}\left(\frac{\theta_{MIN}}{\theta}\right)^{-0.254} \quad (9)$$

$$SCF^{In}_{Ch90} = 0.991\beta\tau^{0.970}\,\gamma^{(1-0.382\beta)}\sin^{(1.951-1.464\beta)}\theta\left(1+0.005\beta^{-4.825}\exp(0.009\zeta)\right)\left(-0.263+1.695\beta-1.144\beta^2\right)f(\theta)$$

With $f(\theta) = -2.462\gamma^{-0.232}$ *for cases where* $\beta \neq 1.0$ *and* $\theta_A/\theta_B = 45°/90°$

$f(\theta) = 1.0$ *for all other cases* (10)

If $\beta = 1.0$ *and* $\theta_A/\theta_B = 45°/90°$ *then* $SCF^{In}_{Ch90} = 0$

$$SCF^{In}_{Ch135} = -0.162\beta\tau^{1.177}\gamma^{(1-0.354\beta)}\sin^{(1.831-0.778\beta)}\theta\left(1+0.118\beta^{-2.557}\tau^{-1.780}\exp(-22.680\zeta)\right)\left(7.661-5.074\beta+0.004\beta^2\right)$$

Use $\beta^* = 1.927\,\theta^{0.241}\tau^{-0.009}$ *in place of* β *for cases where* $\beta = 1.0$ *and* $\theta_B \le 45°$ (11)

$$SCF^{In}_{Ch180} = -0.213\beta\tau^{1.774}\,\gamma^{(1-0.503\beta)}\sin^{(2.302-0.174\beta)}\theta\left(1+0.608\beta^{-1.187}\tau^{-0.785}\arctan(6.684\zeta)\right)-2.337\left(\sin\left(\frac{\theta}{\theta_{MAX}}\right)\right)^{13.503} \quad (12)$$

If $\beta = 1.0$, $\theta_{MAX} \neq \theta_{MIN}$ *and* $\theta = \theta_{MIN}$ *then* $SCF^{In}_{Ch180} = 0$

Tubular Structures VIII, Choo & Van der Vegte (eds) © 1998 Balkema, Rotterdam, ISBN 90 5809 001 9

Fatigue design and secondary bending moments in RHS K-joints with gap

S. Herion & R. Puthli
Research Centre for Steel, Timber and Masonry, University of Karlsruhe, Germany

ABSTRACT: For the prediction of the fatigue life of a girder it is essential to know the exact load distribution in the structure. For use of the hot spot stress concept, this paper presents formulae for stress concentration factors on uniplanar as well as multiplanar K-joints with gap, between rectangular hollow sections (RHS). Both sets of formulae are for axial forces as well as moments in the braces. Although, K-joints in lattice girders made of hollow sections predominantly carry axial loads, the secondary bending moments are not insignificant. Therefore, as opposed to static loading, where loads are redistributed under ultimate load, moments have a significant influence on the fatigue life of a K-joint. However, there is no simple method for determining these moments at present, apart from using complex finite element modelling. Therefore, present practice is to determine these moments approximately, such as the factors between bending and axial stresses given in tables in Eurocode 3. This paper presents a new approach, simple and more reliable, of calculating these moments using a frame analysis program.

SYMBOLS

IPB	in-plane bending
N_f	number of cycles to failure
OPB	out-of-plane bending
SCF	stress concentration factor
$S_{R,h.s.}$	hot spot stress range
e	eccentricity
t	wall thickness
θ	angle between chord and braces

1 INTRODUCTION

In the past few years, extensive theoretical evaluation and experimental tests have been performed at the University of Karlsruhe to investigate the fatigue behaviour of uniplanar and multiplanar K-type square hollow section joints, leading to design formulae for this type of joint.
Additional tests as well as parametric finite element studies have been carried out in Karlsruhe within the scope of two research programmes sponsored by the German Research Foundation (Deutsche Forschungsgemeinschaft, DFG). Also, several other research projects including parametric studies for uniplanar and multiplanar joints have been completed in Karlsruhe.
In order to determine the influence of combined axial force and in-plane and/or out-of-plane bending moment on the hot spot stress in multiplanar and uniplanar K-joints, static tests with strain measurements using strain gauges and strip gauges have been performed. Following the static strain measurements, fatigue tests on joints with various geometrical parameters have been made plotting $S_{r,h.s.}$ (hot spot stress range) versus N_f (load cycles to failure) diagrams.
All these investigations resulted in parametric formulae for the determination of the maximum stress concentration factors (SCF) for the chord and the braces for the 3 basic load cases (axial load, in-plane bending, out-of-plane bending).
In fatigue design, secondary bending moments can contribute significantly to fatigue life. Frame analysis computer programs cannot determine these values because they occur due to local variations in joint stiffness. It will be shown that commercially available frame analysis computer programs can be used by suitably adapting the joint details, so that a more realistic local distribution can be obtained, giving the secondary bending moments that actually occur in girders with such joints.
This paper presents a practical fatigue design method for uniplanar and multiplanar K-joints with gap as part of complete girders, using frame analysis, SCF data and the $S_{R,h.s.}$-N_f-diagrams. Also, examples to clarify the procedure will be presented.

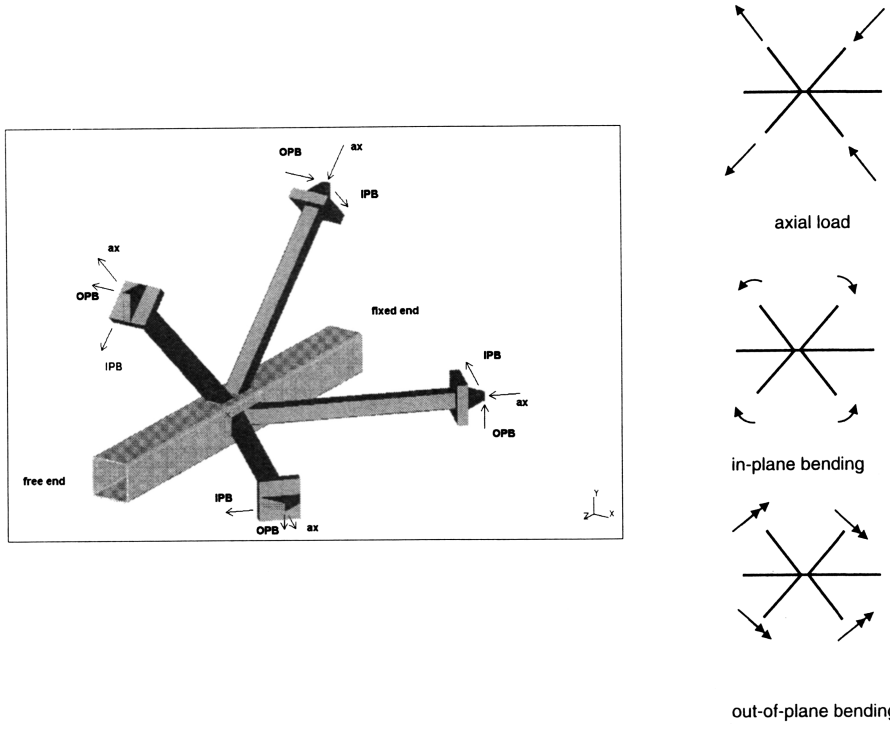

Fig. 1: Load conditions for multiplanar KK-Joints with gap

2 MULTIPLANAR KK-JOINTS WITH GAP

To the authors´ knowledge the fatigue behaviour of multiplanar KK-Joints with gap have only been investigated by two authors, Panjeh Shahi (1994) and Herion (1994). In his work, Panjeh Shahi has investigated joints with no eccentricity (e = 0). Balanced load in the braces is considered (two braces in tension, two braces im compression), with unloaded chord and a constant angle $\theta = 45°$. All the results are given in a database for hot spot stresses along fixed extrapolation lines. Since there is a lot of SCF data given in this database it is very complicated to apply this in practice.

The formulae given by Herion in his Ph.D. work deal with the *maximum* SCFs for chord and brace for the load cases axial load, in-plane bending (IPB) and out-of-plane bending (OPB). The joints are loaded as shown in Fig. 1.

These load conditions have been chosen to obtain safe but not very conservative results, by using the maximum of the stress concentrations in each member (brace or chord).

The formulae for brace and chord are given in Table 1. They are also valid for joints with eccentricity. Design graphs for these formulae are also available.

For multiplanar joints, no thickness correction is neccessary.

As a part of a study on this subject at Karlsruhe University the comparison of SCFs determined by both authors is made separately for chord and brace, Puthli and Herion (1996). The results by Panjeh Shahi (1994) have been taken directly out of his database. A good agreement of both, database and formulae, has been found.

The comparisons have been made using the test results for multiplanar KK-Joints with gap and with overlap found for isolated joints in Karlsruhe and for complete girders in Delft in the scope of an ECSC research programme (Mang et al. 1993). For the comparison only the axial stresses (measured with strain gauges) have been considered, in order to check the validity of the numerical work. These stresses have been multiplied with the SCFs from formulae to get the $S_{R,h.s.}$ for use on the vertical axis of Fig. 2. Fig. 2 gives the design curve (class 114.6) obtained from the ECSC research (Mang et al. 1987). For Eurocode 3, class 112 ($S_{R,h.s.}$ = 112 N/mm² at 2 million cycles, with a slope of m=3) has been proposed on the bases of this research.

The horizontal axis gives the number of load cyles to failure (N_f) found in the tests. In this $S_{R,h.s.}$ - N_f diagram the experimentally determined design line for multiplanar KK-Joints with gap has also been drawn (see Fig. 2).

Table 1: Maximum SCF formulae for multiplanar KK-joints with gap (RHS)

	axial load
chord	$SCF = -0.546 + 42.205 \cdot \xi \cdot \tau^2 + 37.117 \cdot \xi \cdot \beta^3 - 34.580 \cdot \xi \cdot \tau^3 + 0.0597 \cdot \beta \cdot \gamma^2 + 0.0229 \cdot \gamma^2 \cdot \tau^3 + 0.003 \cdot \xi^2 \cdot g'^3 - 4.55 \cdot \beta^3 \cdot g' - 0.0051 \cdot \xi^3 g'^3$
brace	$SCF = 1.462 - 4.74 \cdot \tau^2 + 4.701 \cdot \beta \cdot \tau^2 - 1.449 \cdot \gamma \cdot \beta^3 + 3.819 \cdot 10^{-4} \cdot \tau \cdot \gamma^3 + 0.182 \cdot \tau \cdot g' + 1.263 \cdot \beta \cdot \gamma - 7.7 \cdot 10^{-4} \tau \cdot g'^3$

	in-plane bending (IPB)
chord	$SCF = 89.681 \cdot \beta \cdot \xi^2 + 0.0356 \cdot \beta \cdot \gamma^3 - 8.2649 \frac{\xi^3}{\tau} - 1.646 \cdot 10^{-3} \frac{\gamma^3}{\tau} - 76.127 \cdot \beta^2 \cdot \xi^3 - 0.0332 \cdot \beta^2 \cdot \gamma^3 - 0.195 \cdot g' \cdot \gamma + 2.759 \cdot 10^{-3} \frac{g'^3}{\tau^2} - 0.436$
brace	$SCF = \tau\,(3.607\,\beta - 5.335 \cdot 10^{-4} \gamma^3 - 3.006) + g'^2\,(0.0145 - 1.418 \cdot 10^{-3} g') + \beta\gamma^2 (0.08162 - 0.1114\,\beta^2) + 1.577$

	out-of-plane bending (OPB)
chord	$SCF = 3.9569\,\beta^3\,(12.7993\,\xi\,(1 - 0.3314\,\xi) + 0.4662\,\tau - g'(1 - 0.02427 g')) + 0.0038\gamma^3 (0.273\beta + \tau\,(1 - 0.484\tau)) - 0.4282$
brace	$SCF = \tau^3 (6.437 + 1.623\,\beta - 1.828\,\gamma) + 0.244\,\xi\,\beta - 0.09557\,\gamma^2 (0.00994\,\gamma - 0.796\,\beta + 0.86\,\beta^3 - \tau^3) + 2.213$

range of parameters:

$$0.40 \le \beta = b1/b0 \le 0.80$$
$$12.50 \le 2\gamma = b0/t0 \le 25.0$$
$$0.25 \le \tau = t1/t0 \le 1.15$$
$$0.30 \le \xi = g/b_1 \le 1.10$$
$$2.00 \le g' = g/t_0 \le 11.0$$
$$\theta = 45°$$

3 UNIPLANAR K-JOINTS WITH GAP

For this type of joint, some more information is now available. Soh & Soh (1989), Herion and van Wingerde have given formulae to determine the SCF. Herion has presented two sets of formulae, an older one (Mang et al. 1987) and a new, revised one (Mang and Herion 1995). Van Wingerde gives two sets of formulae, one set of 36 formulae for all the extrapolation lines (van Wingerde et al. 1996) and one set of three simplified formulae for the maximum values (van Wingerde et al. 1997). The results of Panjeh Shahi (1994) are listed in a database on a diskette. Niemi's method (Niemi 1996) is based on the nominal stresses.

Similar to the work for multiplanar joints, the comparisons between experimental and numerical work have been carried out as part of a study on this subject at Karlsruhe University (Puthli and Herion 1996).

The results of van Wingerde (van Wingerde et al. 1997) are for SCF due to axial stresses as well as stresses due to in-plane bending moments. Also, an alternative thickness correction for $t < 4$ mm has been presented in there.

In most publications, except in van Wingerde et al. (1996) and in van Wingerde et al. (1997), the following thickness correction has been used:

$$S_{R,h.s.} = S_{R,h.s.}(16\text{ mm}) \cdot (16/t)^{0.11 \log(N_f)}$$

Comparing the resulting curves with the tests and also in consideration of the scatter bands, the best

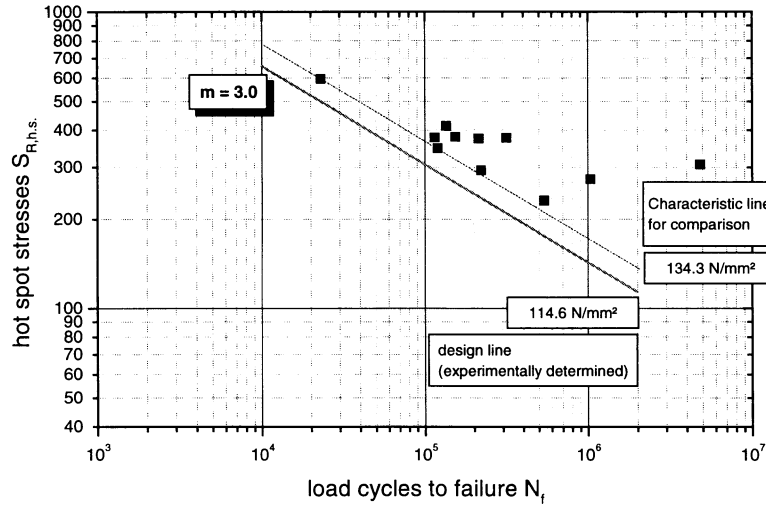

Fig. 2: Comparison of test results and results found by using formulae (multiplanar KK-joints with gap)

results using SCF formulae have been found for the new formulae of Herion (Mang and Herion 1995) and van Wingerde (van Wingerde et al. 1997). Fig. 3 shows the steps for evaluation of the Herion formulae. The formulae found are given in Table 1 and Table 2.

Comparing the two sets of formulae, the range of validity given by van Wingerde is wider with respect to β and θ. But the accuracy has only been proved for the range of parameters investigated in the tests (Mang et al. 1987). On the other hand, the Herion formulae deal with larger gaps and also include eccentricity and have been checked according to the approach given in Fig. 3. Finally, van Wingerde provides no formulae for IPB. The Herion formulae have the advantage of having the same format for uniplanar K-Joints as for multiplanar KK-Joints, because they are a simplification of the multiplanar case.

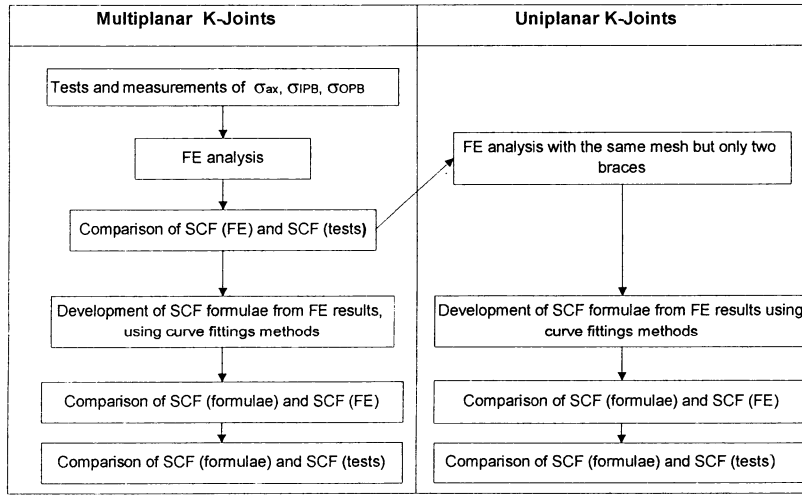

Fig. 3: Flow chart for evaluating the SCF formulae by Herion

Table 2: Maximum SCF formulae for uniplanar KK-joints with gap (RHS), range of validity see Table 1.

	axial load
chord	$SCF = -1.819 + 26.639 \cdot \xi \cdot \tau^2 + 51.33 \cdot \xi \cdot \beta^3 - 22.364 \cdot \xi \cdot \tau^3 + 0.08175 \cdot \beta \cdot \gamma^2$ $+0.02743 \cdot \gamma^2 \cdot \tau^3 + 0.00679 \cdot \xi^2 \cdot g'^3 - 5.752 \cdot \beta^3 \cdot g' - 0.00693 \cdot \xi^3 \cdot g'^3$
brace	$SCF = 1.4324 - 5.602 \cdot \tau^2 + 5.9027 \cdot \beta \cdot \tau^2 - 1.5792 \cdot \gamma \cdot \beta^3 + 4.778 \cdot 10^{-4} \cdot \tau \cdot \gamma^3$ $+ 0.04456 \cdot \tau \cdot g' + 1.412 \cdot \beta \cdot \gamma$

	in-plane bending (IPB)
chord	$SCF = -7.982 - 0.7906 \cdot \gamma + 10.0932 \cdot \xi + 0.01088 \cdot \tau \cdot \gamma^3 - 5.043 \cdot \xi^2 \cdot \beta^3$ $- 0.4435 \cdot \gamma^2 \cdot \beta^3 - 0.00584 \cdot \tau^2 \cdot \gamma^3 - 0.985 \cdot \gamma \cdot \xi + 4.301 \cdot \beta\gamma$
brace	$SCF = -0.425 + 0.598 \cdot \gamma - 0.273 \cdot \xi^3 + 1.8152 \cdot \beta \cdot \tau^2 + 6.139 \cdot 10^{-4} \cdot \tau^2 \cdot \gamma^3$ $-0.469 \cdot \gamma \cdot \tau$

	out-of-plane bending (OPB)
chord	$SCF = -10.729 + 20.763 \cdot \beta + 0.277 \cdot \gamma + 3.46 \cdot \xi^3 - 2.083 \cdot \gamma \cdot \beta^3 - 0.296 \cdot \xi^3 \cdot g'$ $+ (5.72 - 2.974 \cdot \tau) \cdot 10^{-3} \cdot \tau \cdot \gamma^3$
brace	$SCF = 2.572 - 2.976 \cdot \tau^3 - 1.626 \cdot 10^{-4} \cdot \gamma^3 + \left(0.1036 - 0.0934 \cdot \beta^2\right) \cdot \beta \cdot \gamma^2$ $+ \left(1.6077 \cdot \beta^2 + 0.4682 \cdot g' - 0.0303 \cdot g'^2\right) \cdot \tau^3$

Table 3: Influence of secondary bending moments - coefficients according to EC 3

Coefficients to account for secondary bending moments in joints of lattice girders made from rectangular hollow sections				
Type of joint		Chords	Verticals	Diagonals
Gap joints	K type	1.5	1.0	1.5
	N type	1.5	2.2	1.6
Overlap joints	K type	1.5	1.0	1.3

4 DETERMINATION OF SECONDARY BENDING MOMENTS

4.1 *Procedure according to Eurocode 3*

In Eurocode 3 (1992) as well as in IIW recommendations (1985) the member forces in a lattice girder may be analysed neglecting the effect of eccentricities and joint stiffness, assuming hinged connections. In this case, the effects of secondary bending moments on stress ranges should be considered.

In the absence of an exact stress analysis and modelling of the joint, the effects of secondary bending moments may be taken into account by multiplying the stress ranges due to axial member forces by appropriate coefficients.

In Eurocode 3 these coefficients for K-joints made of RHS are given in Table 9.6.5 which is shown in the following Table 3.

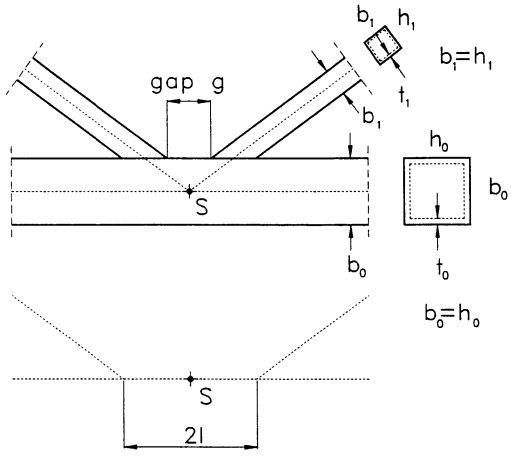

Fig. 4: Real joint geometry and framework model using parameter "l"

4.2 *Alternative Procedure*

Another possible method to get a realistic moment distribution in a K-joint in a real girder is to modify the beam model in an adequate manner. Preliminary studies on this approach have been done in Karlsruhe (internal paper). The main influence on the moment distribution has been found for the gap g. Therefore, a parameter "l" has been introduced, representing half of the "modified" gap. For definition of parameter "l" see Fig. 4.

This modified gap length can be calculated as a function of $g' = g/t_0$ and $\beta = b_1/b_0$. An overview of the procedure to find this function is described in Fig. 5. The procedure described in this figure leads to mean values. To get reliable and safe results, a correction factor KF has been introduced. This is described in Fig. 6. For calibration of the models, tests carried out at TNO in Delft on complete girders have been used (de Koning and Wardenier 1979).
A final comparison of the ratio of bending stresses to axial stresses is plotted in Fig. 7.

4.3 *Guidance for obtaining realistic bending moments using the alternative procedure*

As a result of these preliminary studies a possibility has been shown to obtain realistic bending moments using a framework program. In the following, a short description on how to proceed is given:

- Use any proprietary framework program

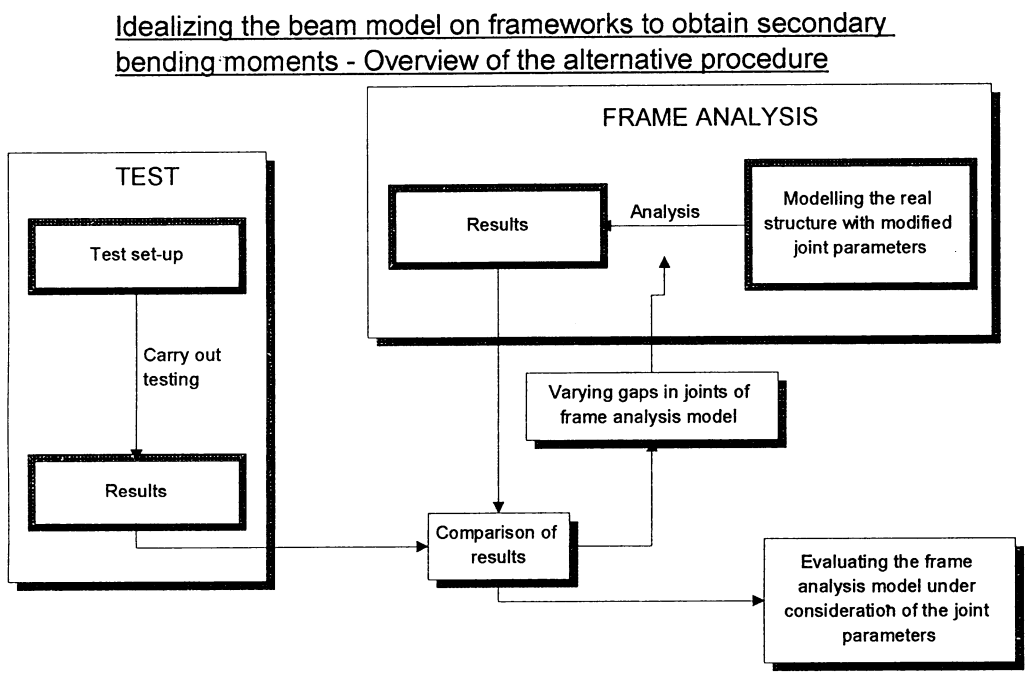

Fig. 5: Overview of the whole procedure

- All connections have to be rigid connections
- Determine the parameter "l" as follows: $l / t_0 = 1.5\ g' + 296\ ß^2 - 398\ ß + 129$
- Use this parameter "l" in the framework program by modifying the gap accordingly Fig. 4
- Run the framework program and obtain the stresses σ_{ax} and σ_{ip}
- Multiply (σ_{ip} / σ_{ax}) with correction factor 1.5 to obtain the final ratio between the stresses.

With these stresses the maximum hot spot stress $S_{R,h.s.}$ in the braces is to be calculated as follows:

$$S_{R,h.s.} = SCF_{ax} \cdot \sigma_{ax} + SCF_{IPB} \cdot \sigma_{IPB}$$

5 SUMMARY

In this paper work on determination of SCF and the fatigue design of RHS K-joints with gap has been revised. Also, new investigations on the determination of secondary bending moments have been presented. The method given is to analyse the framework with a modified fictitious gap. This gap can be calculated with an easy to use function using geometrical parameters. This new model can not only be used to calculate the secondary bending moments for fatigue design, but also give accurate results of member stresses needed in static design of members (where necessary). Finally, more test results and strain gauge measurements on complete girders are necessary to give statistically reliable generalised formulae for this procedure.

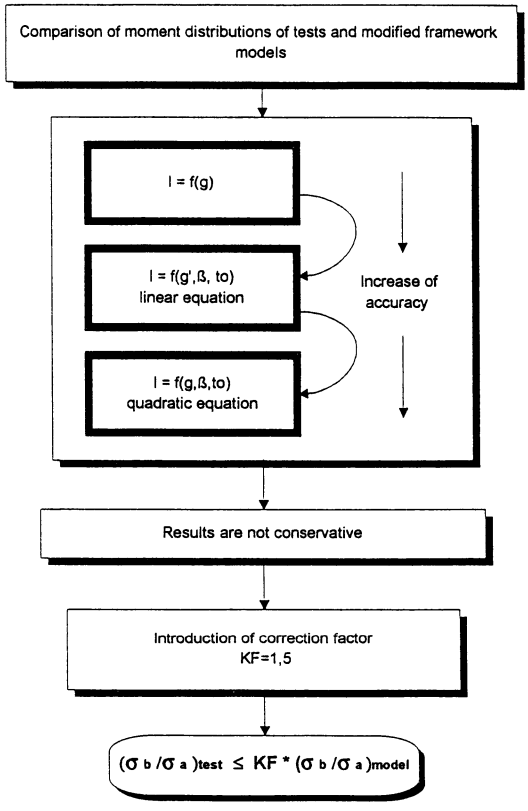

Fig. 6: Introduction of a correction factor KF

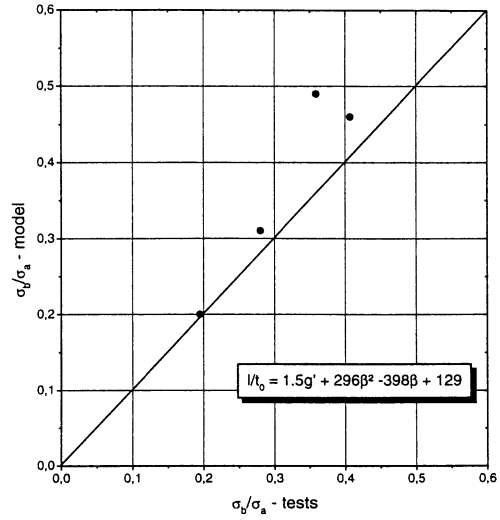

Fig. 7: Comparison of test results and results of alternative procedure using correction factor KF

REFERENCES

Eurocode 3 1992. *Design of steel structures*, Part 1.1: Gerneral rules and rules for buildings.

Herion, S. 1994. *Räumliche K-Knoten aus Rechteck-Hohlprofilen* (Multiplanar K-Joints made of RHS). Ph.D. thesis, University of Karlsruhe, Faculty of Civil Engineering.

IIW, International Institute of Welding 1985: IIW-XVE, *Recommended fatigue design procedure for hollow section joints*. Doc. SC-XV-582-85, XIII-1158-85, Strasbourg, France.

de Koning, C.H.M., Wardenier, J. 1979. Tests on welded joints in complete girders made of square hollow sections. TNO-IBBC report BI-79-19.

Mang. F., S. Herion, Klingler, J., Bucak, Ö. 1987. ECSC research programme 7210-SA/111. *Fatigue behaviour of joints between rectangular hollow sections*. Final Report Part 2: K-joints with gap and overlap (in German language),

University of Karlsruhe, Versuchsanstalt für Stahl, Holz und Steine.

Mang, F., Bucak, Ö., Herion, S. 1993. ECSC research programme 7210-SA/114: Fatigue Strength of Multiplanar Welded, Unstiffened Circular and Rectangular Hollow Sections and Reinforcement Measures for repair (in German language), Final Report Part 3. University of Karlsruhe, Versuchsanstalt für Stahl, Holz und Steine.

Mang, F.; Herion, S. 1995. Deutsche Forschungsgemeinschaft DFG (German Research Foundation) Programm MA 761-10-1: *Uniplanar Hollow Section Joints* (in German language). University of Karlsruhe, Versuchsanstalt für Stahl, Holz und Steine.

Niemi E. 1996: Fatigue Resistance Predictions for RHS K-Joints, Using Two Alternative methods. In: J. Farkas & K. Jarmai (Eds.), *Proceedings of VII International Symposium on Tubular Structures*, pp. 309-314. Miskolc 28-30 August, 1996. Rotterdam: Balkema.

Panjeh Shahi 1994. Stress and Strain Concentration Factors of Welded Multiplanar Joints between Square Hollow Sections. Ph.D. Thesis, Delft University of Technology.

Puthli, R., Herion, S. 1996. *Stress concen-trations and secondary moment distribution in RHS joints for fatigue design.* Background document for the CIDECT Fatigue Design Guide, University of Karlsruhe, Versuchs-anstalt für Stahl, Holz und Steine.

Soh, A., Soh, C. 1989. *A Parametric Stress Analysis of T / Y and Square to Square Tubular Joints.* School of Civil and Structural Engineering, Nanyang Technological Institute, Singapore.

van Wingerde, A., Packer, J.A., Wardenier. J., Dutta, D. 1996. *The Fatigue Behaviour of K-Joints Made of Square Hollow Sections.* CIDECT Final Report 7P-19/96.

van Wingerde, A.M., Packer, J.A., Wardenier, J. 1997. IIW Intern. Conference on *Performance of dynamically loaded welded structures*, July 14-15, San Francisco.

Tubular Structures VIII, Choo & Van der Vegte (eds) © 1998 Balkema, Rotterdam, ISBN 90 5809 001 9

Nominal stress range fatigue of stainless steel fillet welds

K.E. Lahti
Oy Esab, Helsinki, Finland
E. Niemi
Lappeenranta University of Technology, Finland
H. Hänninen
Helsinki University of Technology, Finland

ABSTRACT: 3-point bending nominal stress range fatigue of stainless steel fillet welds was shown to be in good agreement with suggested fatigue classes of Eurocode 3 design standard. However, if the size of the weld was increased, and the failure location could be moved to the weld toe instead of the weld root, a significant increase in fatigue strength was observed.

1. INTRODUCTION

The fatigue strength of a material, as well as that of weldments, are the key factors which are studied when selecting materials for applications which are prone to fatigue. The design of a structure under fluctuating loading needs careful consideration of applicable design guidelines and joint types of any detail of the structure. For example, in order to produce a fatigue tolerant transportation vehicle, the use of suitable design standard, such as Eurocode 3 (1992), is needed.

In transportation vehicle structures fatigue is the main criterion in design. These structures are subjected to both static and dynamic loads during their expected operating life. In manufacturing of the stuctures, welding is typically used. Therefore, the fatigue strength of weldments is of great importance. In fatigue design, existing design codes (e.g., SFS 2378 or BS5400) can be used. In case of stainless steels there is, however, no specific design code at the moment. It has been customary to apply the same design guidelines to stainless steel structures as for conventional carbon steel structures. As a matter of fact, fatigue behaviour of stainless steel welds has indicated a broad similarity with the behaviour of carbon steel welded joints (e.g., Koskimäki & Kyröläinen 1993, Maddox 1991, Marquis 1994, Tubby 1984). For example Koskimäki and Kyröläinen (1993) did not find any difference between the fatigue properties of three different stainless steel grade welds (austenitic, duplex and ferritic) compared with corresponding structural steel welds. Therefore, it is assumed that the same fatigue design rules apply for structural carbon-manganese steels at temperatures up to 375 °C, for austenitic stainless steels up to 430 °C and for aluminium alloys up to 100 °C. However, if the environment is corrosive, these upper limits for operating temperature are too high (Maddox 1994).

2. NOMINAL STRESS APPROACH BY EUROCODE 3

Fatigue data for stainless steels are very similar to those of carbon steels and, thus, the S-N approach should be valid for stainless steels. In principle the fatigue life for a given stress range is obtained from:

$$\log N = \log a - m\log\left(\Delta\sigma_R\right) \tag{1}$$

alternatively expressed as:

$$N = \frac{a}{\left(\Delta\sigma_R\right)^m} \tag{2}$$

The constants a and m are derived empirically from experimental data and are particular to different types of welded joints. For example, for the studied detail, corresponding value for *log a* is 10.951 if slope m is 3, and 13.786 with a shallower slope of 5 (Eurocode 3, 1992). They include the effects of:

- local stress concentrations due to the weld geometry,
- size and shape of acceptable discontinuities,
- the stress direction,

- residual stresses,
- metallurgical conditions,
- the welding process and postweld improvement procedures.

Equations (1) and (2) relate to constant amplitude loading. Welded structures are more commonly subjected to variable amplitude loading caused by non-permanent actions like movement of loads along the structure or changes in loading directions (Niemi 1995). For assessing the effects of variable amplitude loading, use is made of the *Palmgren-Miner* rule for cumulative damage:

$$\sum \frac{n_i}{N_i} \leq 1 \qquad (3)$$

Fatigue data for some joint types of austenitic stainless steels in air has been analysed (Design manual for structural stainless steel, 1994) to discern trends and their recommended classifications to be used with two carbon steel codes, Table 1. The two codes are HSE, i.e., *Health & Safety Executive Guidance Notes for Offshore Installations* and EC3, i.e., *Eurocode 3 Part 1*. Depending on which carbon steel code is used, the joint classification may or may not be downgraded for austenitic stainless steel. In the absence of further stainless steel data, it is recommended that for all other joint types the carbon steel classification should be downgraded by at least one category for application to austenitic stainless steel. (Design manual for structural stainless steel, 1994)

Table 1. Comparison of joint classification for carbon steel and austenitic stainless steel. (Design manual for structural stainless steel, 1994)

Joint description and requirements	Joint classification			
	Carbon steel		Stainless steel	
	HSE	EC3	HSE	EC3
Transverse butt welds	D	90	E	80
Non-load carrying attachments (fillet welded to surface)				
Transverse welds	F	80	F	71
Longitudinal welds	F	71	G	56
Load carrying cruciform and T-joints (fillet welded)	F2	71	F2	63

Eurocode 3 (1992) design code permits the use of code for the design of stainless steel structures under non-corrosive conditions at ambient temperatures. Unfortunately, from the standards' point of view, stainless steels are typically used in corrosive conditions, therefore making the use of stainless steels in non-corrosive environments questionable. However, same classified details can be used for both carbon steels and stainless steels. In Table 2 some classified details for rectangular hollow sections (RHS) are introduced. Detail used

Table 2. Classification of various weld details for rectangular hollow sections. (Eurocode 3, 1992)

Fatigue class	Detail	Remarks
140	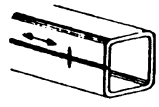	Automated continuous longitudinal welds. No start or stop positions. Free from defects according to tolerances in the reference standard 9 - quality level 3.
56		Butt joint using butt welds. Height of the weld is less than 10% of the weld width, smooth joint. Welded in flat position, and found free from defects according to reference standard 9 - quality level 3.
45	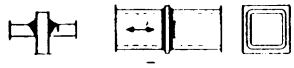	Butt weld using intermittent plate. Load-carrying welds. Welds inspected and found free from defects according to reference standard 9 - quality level 3. If plate thickness is more than 8 mm, welds can be classified to one fatigue class higher, i.e., 50.
36	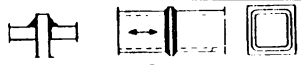	Fillet weld using intermittent plate. Load carrying welds. Plate thickness <8 mm.

Table 3. Summary of test series

Welding performed at	Material	Process	Consumable / shielding gas
Carrus Oy, Vantaa, Finland	EN 1.4003 -"-	Gas Metal Arc Welding Flux Cored Arc Welding	OK Autrod 16.52 / Mison 2 OK Tubrod 14.22 / Robinon
Simo Sainio Technics Ltd., Jämsänkoski, Finland	EN 1.4310	Manual Metal Arc Welding	OK 61.30 OK 67.30
Plasma Modules Oy, Vantaa, Finland	EN 1.4310	Powder Plasma Arc Welding	AISI 316L powder / AGA MIX H 5
Helsinki University of Technology, Espoo, Finland	EN 1.4310 EN 1.4310 EN 1.4310 EN 1.4003	Flux Cored Arc Welding Flux Cored Arc Welding Gas Tungsten Arc Welding Gas Metal Arc Welding	OK Tubrod 14.20 / Mison 2 Filarc PZ 6176 / Robinon OK Tigrod 16.10 / Argon S OK Autrod 16.52 / Mison 2

in this study is in the last row of the table having fatigue class 36, which is the lowest of the Eurocode design curves. As can be seen, butt-welds are graded higher than fillet welds, and also full penetration welds are ranked higher than partial penetration welds. This is in good agreement with the severity of stress concentration factor at the weld toe and root of the weld.

In this study application of stainless steel is seen from the manufacturer's and designer's point of view. This means, that welded stainless steel structures fabricated for use in transport vehicle applications have been studied.

3. TEST ARRANGEMENT

Two stainless steel grades were selected for study because of the increasing interest for their use in transportation vehicles structures: work-hardened austenitic EN 1.4310 (17%Cr - 7%Ni, AISI 301), and 12%Cr low-carbon martensitic EN 1.4003, which corresponds to EN 10088-2:1992 standard steel. The corrosion properties of these steels have been found appropriate for use in mildly corrosive environments typical for operating conditions of various transport vehicles (Vilpas et al., 1995). Also corrosion properties of the weldments are adequate if proper post-weld treatment is carried out. Pickling of the welds is highly recommended (e.g., Lahti & Hänninen, 1995).

EN 1.4310 is an austenitic stainless steel with 17%Cr and 7%Ni. It work hardens vigorously to high yield- and tensile strength levels. The carbon content of this steel is typically low (<0.03 %) in order to decrease the susceptibility to sensitization during welding. The weldability of this steel is good, as it is with all austenitic stainless steels.

EN 1.4003 is modified from conventional 12%Cr stainless steel by decreasing the carbon content to well below 0.03 which is regarded as the limit for low-carbon steels. Also the amount of titanium is limited due to the tendency of titanium to form brittle carbide phases in the heat affected zone of a welded joint (Lokka 1996). Mechanical properties and chemical compositions of the studied RHS steels are shown in Table 4.

Test welds were produced in many different locations by various welders, and also the welding equipment varied at different places. The consumables, shielding gases and materials remained unaltered between the different welding locations. Table 3 presents a summary of the welds produced at each location.

Structural detail chosen for this study consisted of 2 RHS-beams, which were fillet welded to an intermittent plate between the beams as shown in Table 2. The structural detail was taken from Eurocode 3 design standard. An annealed grade (thickness 5-6 mm) of matching material was used as an intermittent plate. Thicker plate was used in order to create the maximum stress concentration to the RHS-beam side of the weld, not to the plate. Intermittent plate also made the detail stiffer, i.e., preventing the contraction at the welded joint.

In Eurocode 3 (1992) numerous structural details are divided into different fatigue classes and a number of corresponding design curves are also presented. Fatigue class 36 or FAT 36 refers to a characteristic fatigue life of 2 million cycles at stress range of 36 N/mm^2. In order to improve the fatigue class, full penetration weld should be used as is seen in Table 2. In case of transportation vehicle manufacturing, this is rarely possible, and therefore it was not tested.

Eurocode 3 design curves have 2 slopes. Down to 5 million cycles the slope is 3, and from 5 million to the fatigue limit it is 5. The use of dual slopes is justified by assuming that after crack initiation and some propagation, lower and lower stress cycles become effective. Therefore the fatigue limit is somewhat lower for variable amplitude loaded

Table 4. Chemical compositions and mechanical properties of the studied steel grades. Note the high $R_{p0.2}$ values of RHS beams representing a highly work hardened condition.

	Chemical composition					Mechnanical properties		
Steel grade	**%C**	**%Cr**	**%Ni**	**%Si**	**%Mn**	**$R_{p0,2}$ (N/mm^2)**	**R_m (N/mm^2)**	**A5 (%)**
EN 1.4310	0.11	16.8	7.0	0.85	1.21	583	956	41
EN 1.4003	0.018	11.0	0.4	0.35	1.16	531	553	22

structures, than purely constantly loaded specimens. In this study, tests were performed at constant amplitude loading, eventhough that is not the case in real transportation vehicle structures.

In fatigue analysis, the nominal stress approach was used. Stresses were calculated using linear elastic stress calculations according to equation (4)

$$\sigma = \frac{M}{I} * e \text{, where} \qquad (4)$$

M is the bending moment;

I is the moment of inertia of the cross-section;

e is the distance from centroid to the point considered.

All fatigue tests were performed as 3-point bending fatigue tests with a stress ratio R of 0.1. The stress was first calculated in the cross-section of the RHS wall, at a distance of 2.5 mm from the centerline of the intermittent plate. Depending on the actual fracture, stress was recalculated after the test either:

1. if fracture did occur from the weld root side through the weld throat, calculated stress was multiplied with a factor of (*RHS wall thickness / throat thickness at fracture*), or

2. if fracture occurred at the weld toe, the stress was calculated at the weld toe.

4. RESULTS

A total of 102 specimens were tested for 3-point bending fatigue endurance. Specimens which lasted for more than 5 million cycles were not used in the determination of the fatigue curve slope. Also specimens, which did not fail by the dominating failure mode in each material/welding process - pairs, i.e., root or toe failure, were not included in the analysis. This left a total of 85 specimes to be used in the analysis of material/welding process - pairs. When the specimens which did last less than 5 million cycles but did not fail by the dominating failure mode were included to the analysis, a total of 94 specimens were qualified. Only those specimens

Table 5. Summary of the S-N test results.

Material/welding process/consumable	**Number of observations used in slope determination**	**Failure location**	**Slope**	**R^{2***}**	**$\Delta\sigma_c$ (2E6) MPa**	**Throat thickness (mm) range median**
EN 1.4003/GMAW/ OK Autrod 16.52*	13	weld toe	2.65	0.913	84	3.2-6.3 4.4
EN 1.4003/GMAW/ OK Autrod 16.52**	12	weld toe	2.93	0.955	65	4.6-5.8 5.2
EN 1.4310/FCAW/ PZ 6176	10	weld toe	3.37	0.875	83	4.8-6.5 5.4
EN 1.4310/PPAW/ AISI 316L powder	14	weld root	3.34	0.855	43	1.4-3.5 1.8
EN 1.4310/GTAW/ OK Tigrod 16.10	11	weld root	2.99	0.951	53	2.5-3.1 2.9
EN 1.4310/SMAW/ OK 61.30	10	weld root	2.78	0.812	40	2.6-4.2 3.0
EN 1.4310/FCAW/ OK Tubrod 14.20	15	weld root	2.90	0.913	45	3.6-4.9 4.3

*= manufacturing quality welded at Carrus, **= laboratory quality welded at HUT, ***= value describing the goodness of the calculated slope (scale 0...+1, +1 being the best).

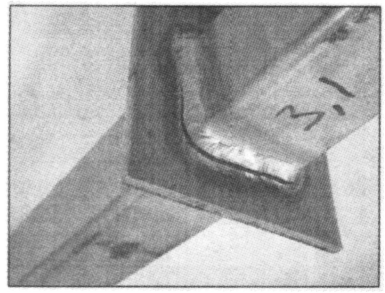

Figure 1. Typical weld root failure. EN 1.4310, GTAW, OK Tigrod 16.10, a = 3,1 mm.

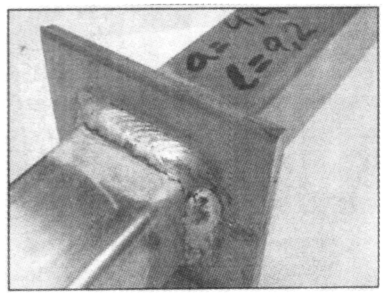

Figure 2. Typical weld toe failure. EN 1.4003, GMAW, OK Autrod 16.52, a = 4,4 mm.

which failed after 5 million cycles, or did not fail at all, were excluded in the latter analysis. Fatigue test results for material/welding process - pairs are summarized in Table 5.

Test specimens can be divided into two separate classes depending on the fracture location: weld toe failures and weld root failures, Figure 1 and Figure 2. Figures 3 and 4 show the S-N data for each class, respectively. Slopes fitted to the S-N data are 2.77 for the weld toe failure (37 observations) and 2.90 for the root failures (57 observations). Both curves are quite close to the slope of 3.0 suggested in Eurocode 3. Characteristic fatigue classes ($\Delta\sigma_c$) for the failure cases had more difference compared to $\Delta\sigma_c$ = 36 MPa suggested in Eurocode 3. Namely, $\Delta\sigma_c$ for toe failures was 59 MPa, and for root failures 38 MPa. Failure location and throat thickness (*a*) had a correlation as showed in Figure 5 and Table 5. As the throat thickness increased, failure was more probable at the weld toe. On the basis of the average throat thickness values, it can be observed that from an approximate value of 4,5 mm upwards the dominant failure location was the weld toe.

5. DISCUSSION

Based on the test results, difference in the fatigue endurance between the two tested stainless steel grades was not large. Since root failure describes mainly the fatigue strength of the weld metal, weld toe failures should be evaluated if any comparisons of fatigue strengths of different materials are to be made. Therefore, if a comparison of GMA welded EN 1.4003 and FCA welded EN 1.4310 is made, there is a difference in the slopes, Figure 6. This implies that there is a difference in fatigue resistance in favour of EN 1.4003 in the low-cycle fatigue regime. One possible explanation may be that the martensitic microstructure in the heat affected zone of EN 1.4003 steel results in a beneficial compressive residual stress state.

On the other hand, recrystallized austenitic microstructure in the HAZ of EN 1.4310 steel will work harden due to loading. At high stresses, i.e., in the low-cycle regime, the beneficial effect of martensitic transformation on fatigue crack growth rate is offset by large amounts of martensite formed due to strain hardening. At lower crack growth rates, i.e., in the high-cycle regime, the formation of deformation-induced martensite within the crack-tip plastic zone results in retarding of the crack growth rate. This observation is in agreement with the studies of Khan and Ahmed (1996) on AISI 301 type stainless steel. At the lower stress ranges, i.e., with increasing number of cycles to failure, martensite formation in the crack-tip plastic zone of EN 1.4310 takes place resulting in volume change associated with martensitic transformation and decreasing the crack propagation rate. Therefore, it can be concluded, that in the low-cycle regime, there is some difference in the fatigue endurance of the studied stainless steels in favour for EN 1.4003, but at lower stress levels, i.e., with higher number of cycles the difference is in favour for EN 1.4310.

If the failures are studied based on failure mode, i.e., toe failure or root failure, there is a clear difference between the two groups (see Figure 3 and Figure 4). Weld root failures with a characteristic stress range $\Delta\sigma_c$(2E6) 38 MPa are in good agreement with Eurocode 3, where the value of $\Delta\sigma_c$(2E6) 36 MPa is given for the detail studied. Since Eurocode 3 does not set any specific requirements for the weld quality, it can be stated that Eurocode 3 gives quite good design curve for the detail studied, if the failure occurs at the weld root.

If the throat thickness is increased, the failure is more likely to occur at the weld toe. Weld toe failures have a $\Delta\sigma_c$(2E6) of 59 MPa, which is fairly

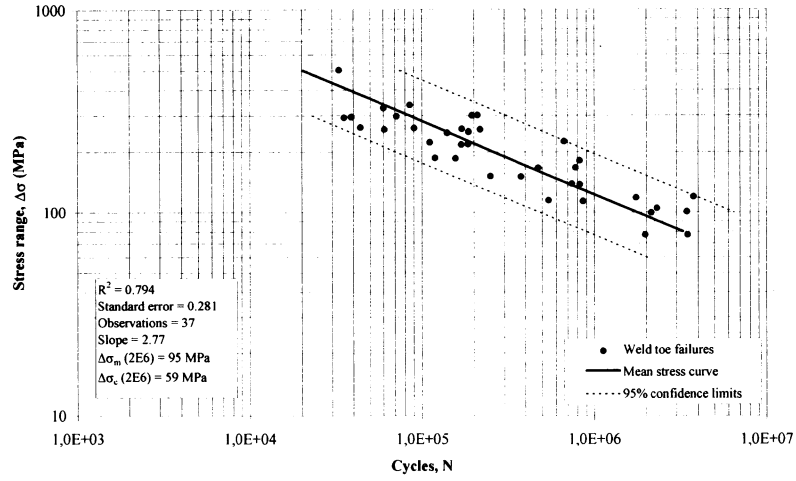

Figure 3. S-N data for weld toe failures.

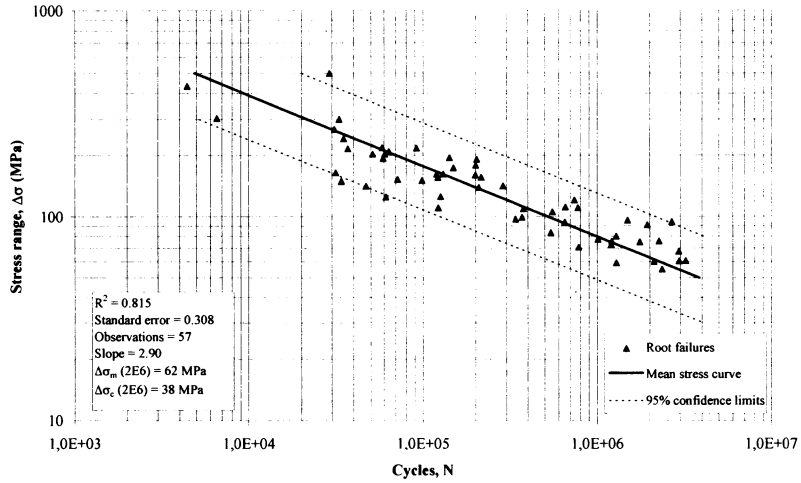

Figure 4. S-N data for weld root failures.

close to the Eurocode 3 class 56 for a butt welded RHS-joint. Therefore, it can be suggested that the severity of the weld root stress concentration decreases as the throat thickness increases. This results in weld toe failure, which is also "more safe" by means of detecting the crack before failure. In practice this means, that increasing the throat thickness, i.e., the weld size, from 3 mm to 5 mm, the fatigue strength of the structure can be increased. For example, at the stress level $\Delta\sigma$ of 100 MPa, mean root failure life is approximately 500 000 cycles, but for mean toe failure endurance is almost 2 million cycles! Therefore, slight overwelding may result in a prolonged life of a structure.

6. SUMMARY

Structural detail chosen from Eurocode 3 was studied in 3-point bending fatigue tests. The studied stainless steels EN 1.4003 and EN 1.4310 were selected because of their increasing use in transportation vehicle structures. A total of 8 different material/welding process -pairs were studied.

The main factor dominating the fatigue endurance of the studied detail was shown to be the throat thickness of the weld. With increasing throat

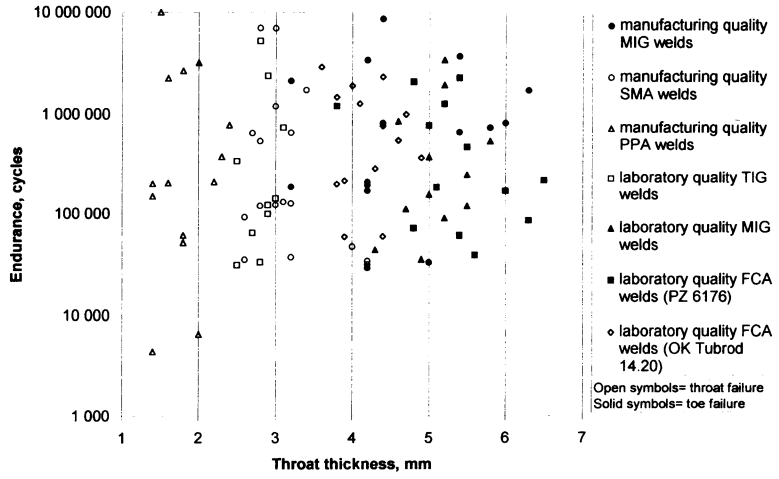

Figure 5. Effect of throat thickness to the failure location. Endurance and throat thickness do not correlate.

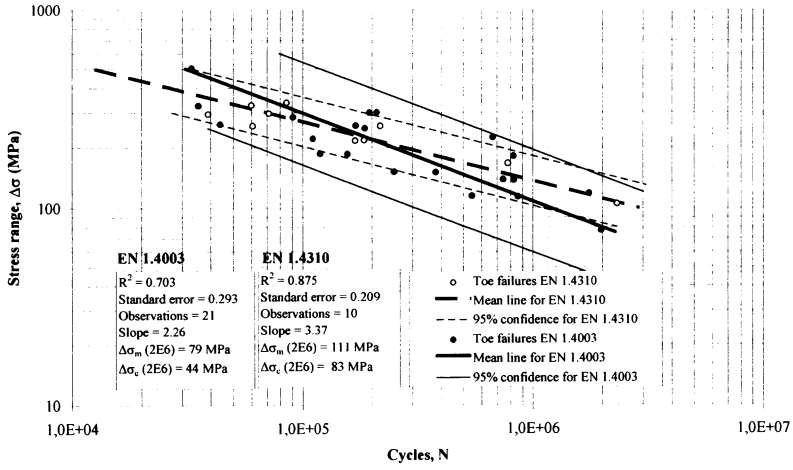

Figure 6. Fatigue strengths for EN 1.4003 and EN 1.4310 weld toe failures in 3-point bending.

thickness, the stress concentration factor at the weld root decreases and the fatigue failure occurs at the weld toe.

Suggested fatigue class of 36 in Eurocode 3, describes well the situation in the case of root failure. Based on the investigation, a higher fatigue class of 56 may be used for the studied detail, if a sufficient weld size is quaranteed. Sufficient throat thickness is ca. twice the wall thickness of the RHS.

In low-cycle fatigue, the fatigue strength of EN 1.4003 is slightly better than that of the EN 1.4310. At 200 000 cycles and more the situation is vice versa. This may be explained by formation of compressive residual stresses to the HAZ of EN 1.4003, and by the differences in the cyclic work hardening properties of the recrystallized and softened HAZ of EN 1.4310 steel in the high- and low cycle regimes.

REFERENCES

Design Manual for Structural Stainless Steel. European Stainless Steel Development and Information Group (EURO INOX). Nickel Development Institute, June 1994. 114 p.

ENV 1993-1-1:1992. Eurocode 3: Teräsrakenteiden suunnittelu. Osa 1-1: Yleiset säännöt ja rakennuksia koskevat säännöt. Comité Européen de Normalization (CEN).

Khan Z., Ahmed M. Stress-Induced Martensitic Transformation in Metastable Austenitic Stainless Steels: Effect on Fatigue Crack Growth Rate. Journal of Materials Engineering and Performance 5(1996)2. pp. 201-208.

Koskimäki, M., Kyröläinen, A. The Fatigue Endurance of Stainless Steels. In: Asko Kähönen, Sisko Sipilä (Ed.), Väsymismitoitus (Fatigue Design) 1993, VTT Symposium 137, Espoo, Finland. pp. 217 - 238.

Lahti, K., Hänninen, H., The Effect of Post-weld Surface Treatment on Corrosion Resistance of Stainless Steel Welds. Kunnossapitolehti 7(1995). p. 36-41. (in Finnish).

Lokka, M. Properties of 12%Cr stainless steel welds. Ph.D. thesis, Helsinki University of Technology, Espoo, 1996. 87 p. + app.

Lokka, M., Hänninen, H. Life Cycle Costing and Assessment and their Application in Materials Selection, Helsinki University of Technology, Laboratory of Engineering Materials, Publication MTR 2/94, 48 p. (in Finnish).

Maddox, S. J. Fatigue Strength of Welded Structures 2nd Ed. Abington Publishing, Abington, England. 1994. 198 p.

Marquis, G. High Cycle Spectrum Fatigue of Welded Components, App. II, Long-life Spectrum Fatigue of Carbon and Stainless Steel Welds. Doctoral Thesis, Helsinki University of Technology, Espoo, 1995. 83 p. + app.

Niemi, E. (ed.). Stress Determination for Fatigue Analysis of Welded Components. IIS/IIW-1221-93. Abington Publishing, England. 1995. 70 p.

Tubby P.J. The Fatigue Strengths of Fillet Welded Joints in 3CR12 Corrosion Resisting Steel (In Air). In: Proceedings of Inaugural International 3CR12 Conference, Johannesburg, March 1984. pp. 264-285.

Vilpas, M., Lahti, K., Lokka, M., Hänninen, H., Stainless steels in transportation vehicles. Hitsaustekniikka 45(1995)4, s. 44-52. (In Finnish)

Tubular Structures VIII, Choo & Van der Vegte (eds) © 1998 Balkema, Rotterdam, ISBN 90 5809 001 9

Effects of weld profile on the fatigue life of thin-walled cruciform joint

F.R. Mashiri, X.L. Zhao & P.Grundy
Department of Civil Engineering, Monash University, Clayton, Vic., Australia

ABSTRACT: Thin-walled cold-formed square hollow sections (SHS) are widely used in road transport and in the agricultural industry. Most of the sections have a wall thickness less than 4mm. Some fatigue failures of these sections have been observed. A welding procedure for thin-walled cold-formed tubular T-joint is determined. The connections consist of square hollow sections with wall thicknesses less than 3mm. Connections for the weld procedures have been done using the MIG and TIG welding methods. The weld profiles of the two welding methods are measured using the silicon imprint technique. As a preliminary investigation, modelling of a thin-walled cruciform joint is carried out using the Boundary Element Analysis System software (BEASY), to determine the effect of weld profile on fatigue propagation life. The cruciform joint is non-load carrying and consists of 3mm thick plates. This program uses fracture mechanics theory and carries out 2D- automatic crack propagation analysis.

1 INTRODUCTION

Thin-walled structural sections offer a good ratio between weight and resistance of longitudinal and lateral forces from all directions. Compared to open sections, hollow structural sections also have a large torsional resistance which prevents lateral buckling. They also have a better cross-sectional area to exposed area compared to open sections resulting in cheaper protection against corrosion and better fire-resistance. Aesthetically their shape and joints appeal to architects (Wardenier 1982).

Cold-formed tubular members are used more and more in modern steel construction such as the new Olympic Aquatic Centre at Homebush bay in Sydney, which has a steel structural roof consisting of mainly tubular members, and the Melbourne Central where about 13 kilometres of tubular sections are used (Zhao et al 1996).

Tubular sections are suitable for construction of steel communication towers (Dean & Bennett 1994), truss bridges (BHP 1995), crane booms, lighting poles and highway sign supports. These types of constructions are under fatigue loading. Thin walled hollow sections are now widely used in road transport and in the agricultural industry. Most of the sections have a wall thickness less than 4mm. Some fatigue failures of these sections have been observed (BHP & Monash University 1997). Failure of welded connections under fatigue loading is a result of the stress concentrations resulting from the overall joint and weld geometry. It is important therefore to study the influence of weld defects and weld geometry on fatigue life as background to setting up design rules, as they may significantly affect fatigue life.

Although a lot of research has been done on fatigue of welded connections (Verheul & Noordhoek 1987, van Wingerde et al 1996, 1997), little has been done on the fatigue of thin-walled sections below 4mm.

This paper investigates the effect of weld profile on the fatigue life of a cruciform welded joint made of thin-walled plates of 3mm thickness. Connections for weld procedures have been carried out by the MIG and TIG welding methods. A comparison of the weld profiles resulting from the two different weld procedures will be attempted to determine which welding profile might be better for connections under fatigue loading. Modelling of the thin-walled cruciform joint is carried out and an analysis done through the Boundary Element

Analysis System software (BEASY). This program uses fracture mechanics theory to carry out crack propagation analysis. This software performs 2D automatic crack propagation. Since the elements in a boundary element method are defined on the boundaries of the model, BEASY gives surface stresses of high accuracy, which makes it a very useful technique for the study of fracture mechanics problems (Computational Mechanics BEASY Ltd 1996a) . Studies will be carried out to show the sensitivity of fatigue life to weld profile.

2 WELDING PROCEDURE

The welding procedure is determined for a T-joint shown in Figure 1 and a base plate connection shown in Figure 2 below. It is made up of cold-formed square hollow section steel of grade C450LO conforming to AS1163-1991. Table 1 and 2 shows

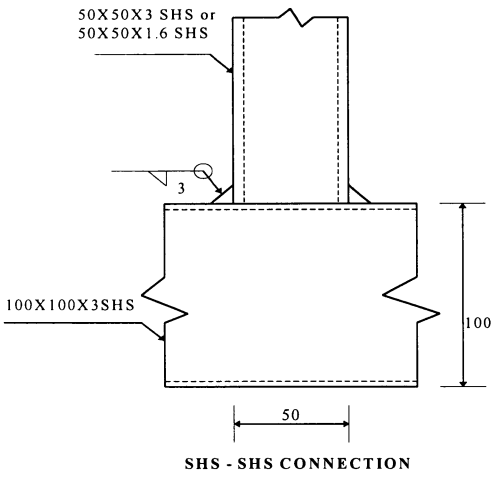

Figure 1: Fillet welded T-joint

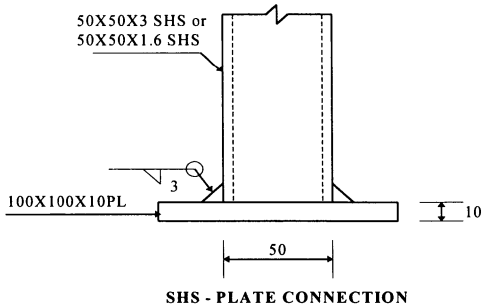

Figure 2: Base-plate connection

the chemical composition and the mechanical properties of the steel respectively.

The minimum size of fillet welds for welded connections complying with AS4100-1991 are prescribed in Table 9.7.3.2 of that code. The minimum size of fillet weld depends upon the thickness of the thickest part in the joint (SAA 1991a). The minimum size of fillet weld for a joint where the thickness of the thickest part is less than 7mm is given as 3mm. Category SP (structural purpose) welds are used, as recommended by AS 1554.1-1991 (SAA 1995), where a statically loaded weld is stressed above 50% of the maximum permissible stress or where the stress range in the welded joint complies with the permissible stress range of weld categories lower than or equal to detail category 112 of AS4100-1991.

All the welding should start and stop in the middle of the flat part of the branch member. Starting and stopping weld runs at corners is detrimental to connections subjected to fatigue loading since this is where the maximum stresses occur. Weld starts and stops introduce irregularities which cause stress concentrations (van Wingerde 1992).

The welding procedure sheets for MIG and TIG welding are shown in Table 3 and 4 respectively.

2.1 Macro test: cross-section examination

The macro cross-section examination tests were carried out in accordance with the Australian Standard AS2205.5.1-1988: Macro Test - Cross-section Examination (Zhao & Hancock 1993), which forms part of the Australian Standard 2205-1988: Methods of Destructive Testing of Welds in Metal.

Table 1: Chemical properties of AS1163-1991, grade C450LO steel

Chemical Composition, %max						
C	Si	Mn	P	S	Al	CE
0.20	0.05	1.60	0.040	0.030	0.10	0.39

TABLE 2: Mechanical Properties of AS1163-1991, grade C450LO steel

Grade and Mechanical Properties			
Grade	Minimum Yield Stress (MPa)	Minimum Tensile Strength (MPa)	Minimum elongation %
C450LO	450	500	16

Table 3: Welding Procedure Sheet for MIG Welding

Reference Specification	AS1554.1-1995
Welding Machine	Miller Dimension 400
Joint Type and Preparation	F1, Table 4.4(C) of AS1554.1-1995
Position	Multiple Position-5F, ANSI/AWS D1.1-1994
Material	AS1163-1991, C450LO
Thickness Range Qualified	1.6mm to 3.0mm
Process	GMAW
Weld run	One
Current (A)	138
Voltage (V)	24
Welding Speed (mm/min)	320
Electrode Trade Name Designer's Requirement Electrode Size (mm)	AustMIG ES6 W502 0.8
Weld Metal Yield Stress (MPa) Weld Metal Tensile Strength (MPa)	480 580
Gas Trade Name Gas Classification Gas Flow Rate (L/min)	M1 Air Liquid Argon-CO_2, 82% Argon 15
Welder	Paul Calcinai, Crossline Engineering Pty Ltd, Melbourne, Australia

Table 4: Welding Procedure Sheet for TIG Welding

Reference Specification	AS1554.1-1995
Welding Machine	Miller Syncrowave
Joint Type and Preparation	F1, Table 4.4(C) of AS1554.1-1995
Position	Multiple Position-5F, ANSI/AWS D1.1-1994
Material	AS1163-1991, C450LO
Thickness Range Qualified	1.6mm to 3.0mm
Process	GTAW
Weld run	One
Current (A)	150
Voltage (V)	14
Welding Speed (mm/min)	90
Electrode Trade Name Designer's Requirement Electrode Size (mm)	Comeweld Super Steel R2 W502 2.4
Weld Metal Yield Stress (MPa) Weld Metal Tensile Strength (MPa)	425 520
Gas Trade Name Gas Classification Gas Flow Rate (L/min)	Argon Welding Grade 99.99% 8
Welder	Paul Calcinai, Crossline Engineering Pty Ltd, Melbourne, Australia

The test from Method 5.1 of AS 2205-1988 reveals the weld shape, the extent of penetration and the soundness of the welded joint (SAA 1988a). Six test pieces each were examined for both MIG and TIG welding. Three specimens were taken from the corners while the other three were taken from the flat portions of the welded square hollow section.

The thickness of the test piece was approximately 10mm. The surface of the test piece was prepared for etching. The smooth filed surface was abraded on successively finer grades of waterproof silicon carbide paper (AS 1863), with the following sequence, 100grit, P240, P600 and finally by P1200.

The specimen was carefully abraded against each grade of paper using a unilinear motion and applying moderate pressure until all surface indications from the previous treatment was removed. Abrasive paper was lubricated with water before and during abrasion. The specimen was washed after each grade of abrasive paper to remove the abrasive. The direction of abrasion with the next finer grade of abrasive paper was at right angles to the marks made by the previous paper.

After the above preparation the test piece was etched. Etching was carried out by immersion in the etchant until a good definition of structure was obtained. The etchant used was nitric acid in alcohol (2 percent nital). This is prepared by adding 2mL of nitric acid to 98mL of alcohol (ethanol or methylated spirit).

After etching the test piece was washed thoroughly with water and then rinsed in ethanol. It was then quickly dried with a hot air blast. To preserve it permanently, it was coated with a thin clear lacquer.

The macro-section was examined for soundness and the etched surface revealed satisfactory penetration and fusion and freedom from weld defects.

2.2 Weld joint hardness test

The test is intended to measure the hardness of the weld metal, heat-affected zone (HAZ) and the parent metal on the prescribed traverses located in the regions of expected maximum and minimum hardness (SAA 1988b).

The hardness was measured by means of the Vickers Hardness Test. The equipment and method of test complied with AS 1817-1991 (SAA 1991b). The test equipment was the Hardness Tester by

Table 5: Vickers Hardness results for Tig welded joint sample

Metal	d_1 (mm)	d_2 (mm)	d (mm)	Hardness (HV 5)
Parent	0.227	0.248	0.238	166
Parent	0.256	0.273	0.265	133
Parent	0.257	0.262	0.260	138
Parent	Mean	-	-	146
HAZ	0.237	0.242	0.240	162
HAZ	0.232	0.271	0.252	150
HAZ	Mean	-	-	156
Weld	0.220	0.228	0.224	185
Weld	0.202	0.218	0.210	211
Weld	0.198	0.212	0.205	220
Weld	Mean	-	-	205

Table 6: Vickers Hardness Results for Mig Welded Joint Sample

Metal	d_1 (mm)	d_2 (mm)	d (mm)	Hardness (HV 5)
Parent	0.252	0.245	0.249	150
Parent	0.241	0.245	0.243	157
Parent	0.246	0.249	0.248	152
Parent	0.240	0.243	0.242	159
Parent	Mean	-	-	155
HAZ	0.227	0.248	0.238	166
HAZ	0.238	0.241	0.240	162
HAZ	Mean	-	-	164
Weld	0.224	0.225	0.225	184
Weld	0.222	0.220	0.221	190
Weld	Mean	-	-	187

Matsuzawa Seiki Company Limited, dated 9-1978. The location of the weld metal, heat-affected zone and the parent metal was through identifying the different microstructures. A nominal force of 49N (HV5) was used. The distance between centres of adjacent HV5 indentations was about 0.5mm. Measurement of hardness consisted of pressing the diamond indenter into the surface of the test piece under force and measuring the diagonals d_1 and d_2 of the indentation, and then determining the mean value, d from d_1 and d_2. The indenter is a right pyramid with square base whose angle between opposite faces is 136°. Vickers Hardness is given by,

$$HV = \frac{2F\sin\frac{136}{2}}{9.806 \bullet 65d^2}$$

$$HV \cong 0.1891\frac{F}{d^2}$$

where
HV = Vickers Hardness,
F= Force in N,
d= mean diagonal of indentation in mm.

The results of Vickers Hardness Tests for TIG and MIG welding are shown in Tables 5 and 6 respectively. The welding procedure can also be qualified by testing according to Section 4.10 of AS1554.1-1991. Hardness tests (according to AS1817.1) containing consumables not qualified shall show that the weld metal does not exceed the parent metal hardness by more than 100HV10. Hardness tests (according to AS 2205.6.1) shall reveal that the hardness of the heat-affected zone shall be not more than 350HV10. The results in Tables 5 and 6 show that these conditions are satisfied.

3 MEASUREMENT OF WELD PROFILE

The silicon imprint technique was used to determine the weld shape (convex or concave), the weld toe radius, the weld flank angle and the shape of the undercut, see Figure 3. Oil for removing rust (KURE CRC 5-56) was sprayed on the weld and cleaning done using a wire brush and a cloth. The impression material (vinyl polysiloxane impression material) was prepared through mixing equal parts of exafine putty type base and exafine putty type catalyst. The mixed material was placed on the weld so that it covered it and was pushed firmly so that a negative of the weld profile was obtained. After the material had hardened it was then removed and cut into test pieces of approximately 1 mm in thickness. The required profile of the weld was measured using a Nikon Profile Projector, Model V-16.
A schematic diagram of the measurements which were obtained is shown in Figure 3.

104 test pieces from each welding method were prepared and measured. The test pieces were prepared from the test joints shown in Figures 1 and 2. The statistical results of the weld profiles from the MIG welds and the TIG welds are shown in Tables 7 and 8 respectively.

Undercut was found in 5 samples out of the 104 that were measured for MIG welding. Out of the 104 measurements for TIG welding profile 14 were found to contain undercut. The dimensions of the undercut found for the two welding methods are

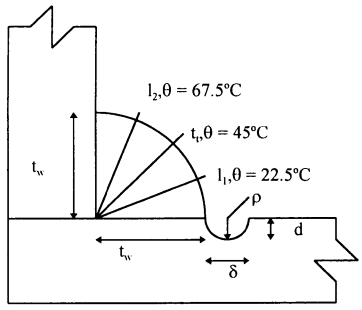

Figure 3: Weld Profile Parameters for a Fillet-welded Joint (Note that although the undercut has been shown on one of the toes of the weld, in practice it can occur in either of the weld toes)

Table 7: Statistical Analysis of MIG results, N=104,

	Max	Min	Mean	Coefficient of Variation (COV)
t_w (mm)	8.7	3.5	5.8	0.138
l_1 (mm)	5.7	3.1	4.4	0.136
t_t (mm)	5.3	3.1	4.1	0.122
l_2 (mm)	6.7	2.7	4.4	0.136
Toe Radius (mm)	3.0	0.3	1.4	0.429
Toe Angle (°)	79.0	20.0	46.3	0.231

Table 8: Statistical Analysis of TIG results, N=104

	Max	Min	Mean	Coefficient of Variation (COV)
t_w (mm)	6.8	1.7	4.3	0.163
l_1 (mm)	4.3	1.6	2.4	0.167
t_t (mm)	3.2	1.6	2.2	0.136
l_2 (mm)	3.8	1.6	2.5	0.160
Toe Radius (mm)	5.8	1.0	3.0	0.400
Toe Angle (°)	58.0	11.0	29.4	0.303

Table 9: Dimensions of undercut from MIG welds

No.	d (mm)	δ (mm)	ρ (mm)
1	0.06	0.77	0.76
2	0.13	0.82	0.51
3	0.16	0.97	0.25
4	0.12	0.47	0.25
5	0.15	0.92	0.25

Table 10: Dimensions of undercut from TIG welds

No.	d (mm)	δ (mm)	ρ (mm)
1	0.18	2.50	3.56
2	0.19	1.56	0.51
3	0.10	1.20	1.52
4	0.19	1.94	0.76
5	0.15	1.49	2.03
6	0.21	1.87	1.27
7	0.06	0.66	0.25
8	0.07	0.50	0.25
9	0.13	1.31	0.51
10	0.12	1.27	1.12
11	0.20	2.00	3.81
12	0.30	1.30	0.51
13	0.20	2.00	3.81
14	0.08	0.60	0.51

shown in Tables 9 and 10, see Figure 3. In both cases the undercut was found to occur at the corners of the welded square hollow sections. Just one incidence of undercut occurred on the flat face of the square hollow section in TIG welding.

4 CRACK PROPAGATION

4.1 General

Fracture mechanics based fatigue assessment is a powerful, yet often under-utilised methodology. One of the key advantages of the fracture mechanics approach to fatigue over the conventional S-N approach is the ability to examine analytically the effect of geometric and loading variables on the fatigue performance of a structure (Grover 1989). For welded joints, it is often assumed that there is no initiation period due to the presence of weld defects. Small fatigue cracks actually initiate at an early stage of fatigue in the welded joints, where crack-like defects or high stress concentrations exist. These reduce the initiation stage of the fatigue and make it relatively less important than the propagation stage (Yamada & Kainuma 1996). The small crack-like discontinuities, termed intrusions, exist at the weld toe. They are a product of conditions during welding which arise with most of the arc processes (Maddox 1991). Therefore it is necessary to investigate the parameters affecting crack propagation.

In order to accurately predict fatigue of welded structures it has been determined that the following factors have to be considered in modifying Paris' equation (Yamada & Kainuma 1996):

(i) The fatigue crack growth rate gradually deviates from Paris' equation, $da/dN = C \cdot \Delta K^n$ when ΔK decreases. The fatigue crack does not propagate when ΔK is less than the threshold stress intensity factor range, ΔK_{th}.

(ii) Fatigue crack growth rates and ΔK_{th} are largely influenced by the stress ratio, residual stresses and crack closure. Crack closure occurs when plastic elongation, which develops near the crack tip, remains at the crack surface after crack propagation, and closes the crack during the unloading stage.

4.2 Fatigue propagation life estimation used in BEASY (Computational Mechanics BEASY Ltd 1996b).

The boundary element analysis system software (BEASY) uses the NASGRO equation for predicting fatigue life:

$$\frac{da}{dN} = \frac{C \cdot (1-f)^n \cdot \Delta K^n \cdot \left(1 - \frac{\Delta K_{th}}{\Delta K}\right)^p}{(1-R)^n \cdot \left(1 - \frac{\Delta K}{(1-R)K_c}\right)^q}$$

$$\Delta K = K_{max} - K_{min} = K_{max}(1-R); \qquad R = K_{min}/K_{max}$$

The crack only grows when ΔK is greater than ΔK_{th}. For a 2D model which is subjected to mode I and mode II loading:

$$K_{max} = \sqrt{K_I^2 + 2K_{II}^2}$$

where

a - crack length (mm)
ΔK - Stress intensity factor range ($N.mm^{-3/2}$)
ΔK_{th} - Threshold stress intensity factor range ($N.mm^{-3/2}$)
f - crack opening function
K_c - critical stress intensity factor ($N.mm^{-3/2}$)
K_{max} - maximum stress intensity factor ($N.mm^{-3/2}$)
K_{min} - minimum stress intensity factor ($N.mm^{-3/2}$)
K_I - stress intensity factor for mode I ($N.mm^{-3/2}$)
K_{II} - stress intensity factor for mode II ($N.mm^{-3/2}$)
C - crack growth rate coefficient
n,q,p- exponents
N - number of cycles to failure

The program takes into account fatigue crack closure analysis for calculating the effect of the stress ratio on crack growth rate under constant amplitude fatigue loading (Computational Mechanics BEASY Ltd 1996b). Experiments and analyses on metallic materials have shown that fatigue cracks, under constant and variable amplitude loading, remain closed during part of the load cycle (Newman Jr 1984).

5 BOUNDARY ELEMENT ANALYSES

5.1 Elements

The fatigue propagation analyses were carried out using a boundary element analysis system software (BEASY). Two dimensional models were used in these analyses. In boundary element analysis, elements must be placed on all external boundaries and on any interface surfaces or lines between sub-regions of the model. For 2D models, boundary elements are lines. More elements or nodes were placed in the part of the model around the toe of the weld from which the crack was propagated. This is the stress concentration region because of the crack, the weld and the undercut. Elements can be constant (1 node), linear (2 nodes) or quadratic (3 nodes).In this analysis quadratic elements were used. All line elements have three mesh points, which are geometric points to define the position and curvature of the line element. Every element also has three nodes, where the values of the problem variables are calculated. Quadratic elements produce the most accurate results, although they require large disk space and require high run-times (Computational Mechanics BEASY Ltd 1996c).

5.2 Parameters

Non-load carrying cruciform joints with 3mm plate thickness are modelled. An initial crack of 0.1 mm in depth was used. The stress ratio, R used was 0.1. The plates are of grade C450LO conforming to AS1163-1991. The values of n and C of 3 and $3x10^{-13}$ respectively have been adopted (Maddox 1991). The values of C and n are similar to the values in PD 6493: 1991 (BSI 1991). The value of exponents p and q is 0.5 (Computational Mechanics BEASY Ltd 1985-1991). The value of ΔK_{th} used was $91.7Nmm^{-3/2}$, that recommended by the Japanese Society of Steel Construction for mean propagation life (JSSC 1995). This value takes into account tensile residual stress conditions. da/dN is calculated in mm/cycle. A detailed discussion on different equations for estimating fatigue propagation life was reported in Mashiri et al 1997.

5.3 Symmetry

If the loading and the cracks are not considered, the cruciform joint is symmetrical about both the x- and y- axes. However this is not the case when the crack is taken into account. The model becomes unsymmetrical. To reduce the disk space and amount of run-time required for analysing a full model, a half model, Figure 4 can be adopted instead of a full model, Figure 5. The percentage difference between the half and full models in the number of cycles to failure is 0.3% (Mashiri et al 1997).

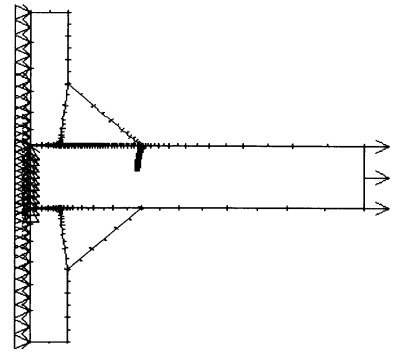

Figure 4: Half Model, with 3mm thick plates.

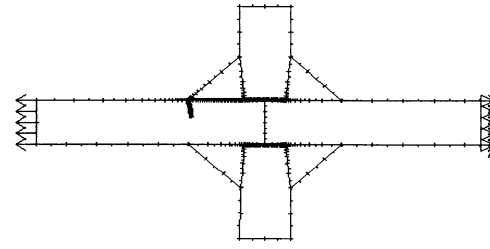

Figure 5: Full Model, with 3mm thick plates.

6 RESULTS AND DISCUSSION

The half models were used to determine the fatigue propagation life. Fatigue failure was assumed to occur when the depth of propagation was at 40% of the plate thickness. It has been shown that after this depth the increase in fatigue life is insignificant (Mori et al, 1997). However other researchers have defined the total fatigue life as the number of cycles at which the crack depth propagated to a depth equal to half the thickness of the plate (Bell et al 1989, Swamidas et al 1989). The mean values of the weld profile results of the MIG and TIG welds shown in Tables 7 and 8 are modelled so that their effect on fatigue life is determined. The shape of the weld profiles are shown in Figure 6 and 7. The MIG weld profile is convex shaped while the TIG weld profile is concave shaped. It has also been decided to compare the fatigue strength of the measured profiles to the weld profile which is normally assumed when no measurements of weld shape are available. This is the triangular shaped fillet weld of equal leg length shown in Figure 8 named the Ideal weld profile. The Ideal weld profile does not incorporate weld toe radius and has a size in leg length of 3mm.

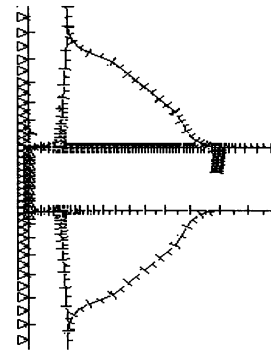

Figure 6: MIG weld profile

Figure 9 also shows the plot of normal stress at distances from the weld toe at an applied tensile cyclic stress of 150MPa, for the MIG, TIG and Ideal weld profiles without undercut.

It shows the differences in stress concentration which occurs from the different weld shapes. The ratio of peak stress at weld toe to the nominal stress applied gives an indication of the stress concentration. The ratios are given in Table 10. The higher ratio occurs in the Ideal weld profile which has no weld toe radius and in the MIG weld profile which has a small weld toe radius.

Figure 10 shows the plot of effective stress intensity factor against the crack length for the three profiles without undercut, at an applied tensile cyclic stress of 150MPa. The effective stress intensity factor increases as the depth of the crack increases since it is depended on crack length. The effective stress intensity factor at a crack length of 0.1mm and an applied tensile stress of 150MPa, decreases from $161Nmm^{-3/2}$ for the Ideal weld profile to $119Nmm^{-3/2}$ for the MIG weld profile and to $108Nmm^{-3/2}$ for TIG weld profile. As the crack propagation progresses the difference in effective stress intensity factor for the three weld profiles decreases. At depths greater

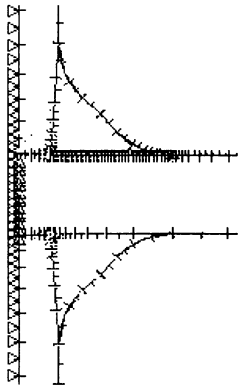

Figure 7: TIG weld profile

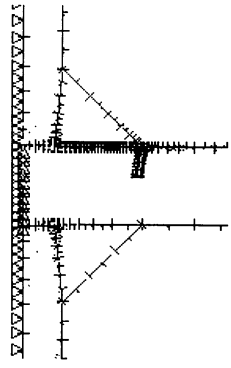

Figure 8: Ideal weld profile

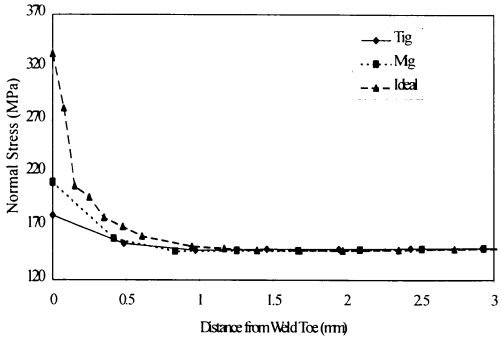

Figure 9: Normal stress (perpendicular to the weld toe) against distance from the weld toe for an applied tensile stress of 150MPa.

than 0.8mm the effective stress intensity factor becomes almost equal for the three weld profiles. The difference in fatigue crack propagation life thus occurs at depth close to the surface where the stress raisers are situated. The effect of the stress concentration resulting from the stress raisers decreases as the depth of the crack increases.

The resultant S-N curves for the MIG, TIG and Ideal weld profiles without undercut are shown in Figure 11. The fatigue life of the three weld profiles at a cyclic tensile stress of 150MPa is shown in Table 11. There is an increase in fatigue life from the Ideal profile to the MIG profile and to the TIG profile. The fatigue life of the MIG weld profile is about 2.3 times that of the Ideal weld profile. The fatigue life of the TIG weld profile is 3.3 times that of the Ideal weld profile and about 1.4 times that of the MIG weld profile. The weld profile from TIG welding results in a joint which is more fatigue resistant. This is due to the fact that there is a reduction in stress concentration for the weld profile with a larger toe radius. However care should be taken to make certain that the design throat thickness is achieved when a concave weld profile is achieved. The TIG weld profile has the same effect on fatigue as TIG arc remelting and plasma dressing.

It can also be realised that there are more occurrences of undercut in the TIG welds than the MIG welds. This may be enough to upset the advantage which has been observed from the concavity of the TIG weld profile. Mashiri et al 1997 has shown that the fatigue life of a thin-walled cold-formed cruciform joint decreases with the depth of undercut for the Ideal weld profile. The maximum value of undercut depth in the TIG weld profile was found to be 0.3mm compared to 0.16mm in the MIG weld profile, see Tables 9 and 10. The larger values of depth of undercut in the TIG weld profile means that there is a greater risk of reduction in fatigue life in this profile. Figure 12 shows the S-N curves of MIG and TIG weld profiles without undercut compared to the same profiles with undercut of maximum depth. There is a significant reduction in fatigue strength as a result of the introduction of undercut to each of the weld profiles. The reduction in fatigue strength is greater for the TIG weld profile with an undercut depth of 0.3mm compared to that of the MIG weld profile with an undercut depth of

Table 10: Ratios of Peak Stress to Nominal Stress

Weld Profile	Peak Stress (MPa)	Peak/Nominal Stress
Ideal	333.1	2.2
MIG	211.3	1.4
TIG	180.3	1.2

Table 11: Number of cycles to failure at cyclic tensile stress of 150MPa.

Weld Profile	Number of Cycles to Failure
Ideal	855,038
MIG	1,959,994
TIG	2,814,659

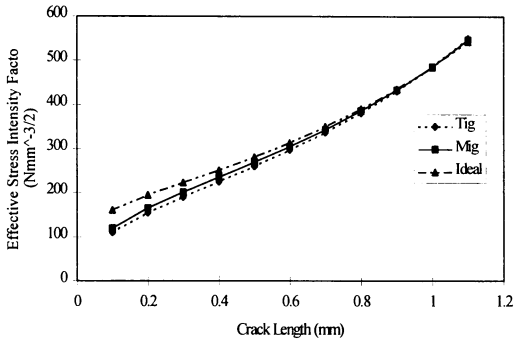

Figure 10: Effective stress intensity factor against crack length for a cyclic tensile stress of 150MPa.

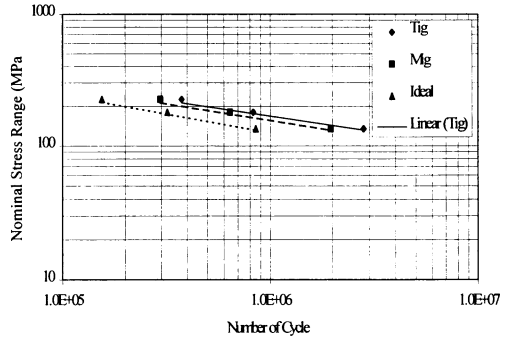

Figure 11: S-N curve for weld profiles

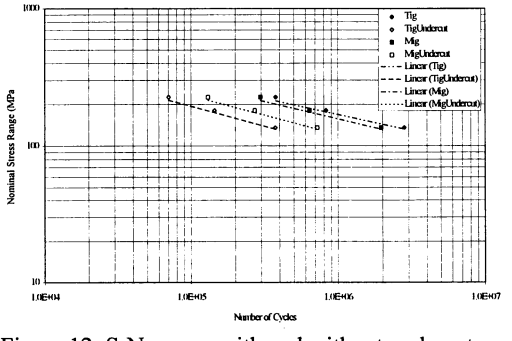

Figure 12: S-N curves with and without undercut

0.16mm. However more numerical results need to be obtained with the measured values of undercut to determine the effect of the overall undercut dimensions on fatigue life.

ACKNOWLEDGEMENTS

Thanks to the Materials Engineering Laboratory, Monash University staff for providing equipment for the cross-section examination and hardness tests, to Professor Takeshi Mori for his help with the silicon imprint technique, and to BHP Steel-Structural and Pipeline Products for supplying cold-formed SHS tubes. This project is sponsored by the Australian Research Council (ARC) Large Grant number A89701933.

REFERENCES

Bell R, O. Vosikovsky O. & S.A. Bain 1989. The significance of weld toe undercuts in the fatigue of steel plate T-joints. *International Journal of Fatigue*, Vol. 11, No. 1, pp 3-11

BHP 1995. *Spanning History in Walhalla.* Steel Structures, Issue No. 8, BHP Structural Steel Development Group, Melbourne.

BHP Structural and Pipeline Products and Monash University 1997. Application for CIDECT Sponsorship, Research into the Fatigue Behaviour of Thin-walled, High-strength Steel Hollow Sections. September 1997 (Successful).

BSI 1991. *Guidance on methods for assessing acceptability of flaws in fusion welded structures* British Standards published Document PD 6493: 1991, BSI, London

Computational Mechanics BEASY Ltd 1996a. *BEASY Version 6.0, Unix Installation Guide.* Computational Mechanics, Southampton, U.K.

Computational mechanics BEASY Ltd 1996b. *BEASY Version 6, Crack Growth Guidebook.* Computational Mechanics, Southampton, U.K.

Computational Mechanics BEASY Ltd 1996c. *BEASY Version 6.0, Fundamentals.* Computational Mechanics, Southampton, U.K.

Computational Mechanics BEASY Ltd 1985-1991. *BEASY Version 6.0, Programme.* Computational Mechanics, Southampton, U.K.

Dean, B.K. & J.D. Bennett 1994. Roof Top Communication Towers, in *Tubular Structures VI*, Grundy P., et al (eds), Balkema, Rotterdam, pp 41-44

Grover J.L. 1989. Thickness, weld profile and initial flaw considerations for tubular joints.

Presented at the Eighth international Conference on Offshore Mechanics and Arctic Engineering, The Hague, march 19-23, pp39-47

Japanese Society of Steel Construction (JSSC) 1995. *Fatigue Design Recommendations for Steel Structures*. English Version, Tokyo, Japan

Maddox S.J. 1991. *Fatigue strength of welded structures*. Second Edition, 1991, Abington Publishing, Cambridge, England.

Mashiri F.R., X.L. Zhao & P Grundy 1997. Crack propagation analysis of welded thin-walled cruciform joint using boundary element method. *Materials Research Forum 1997 Conference Proceedings*, Institute of Metals and Materials Australasia Ltd, Australia, 20-21 November 1997.

Mori T, X.L. Zhao and P. Grundy 1997. Fatigue strength of transverse single-sided fillet welded joints. *Australian Civil/Structural transactions*, Vol. C39, No. 2 and 3, 1997, pp 95-105.

Newman Jr J.U.C. 1984. A crack opening stress equation for fatigue crack growth. *International Journal of Fracture*, Vol. 24, No. 3, pp131-135.

SAA 1988a. *Methods of Destructive Testing of Welds in Metal, Part 5: Metallographic Tests, Method 5.1: Macro Test - Cross-Section Examination*, Australian Standard AS 2205.5.1-1988, Standards Association of Australia, Sydney.

SAA 1988b. *Methods of Destructive Testing of Welds in Metal, Part 6: Hardness Tests, Method 6.1: Weld Joint Hardness Test, Australian Standard AS 2205.6.1-1988*, Standards Association of Australia, Sydney.

SAA 1991a. *Steel Structures, Australian Standard AS 4100-1991*, Standards Association of Australia Sydney.

SAA 1991b. *Metallic materials-Vickers hardness test*, Australian Standard AS 1817-1991, Standards Association of Australia, Sydney

SAA 1995. *Structural Steel Welding (known as the SAA Structural Steel Welding Code), Part 1: Welding of Steel Structures*, Australian Standard AS 1554.1-1995, Standards Association of Australia, Sydney.

Swamidas A.S.J., P.J. Cheema & D.B. Muggeridge 1989. Fatigue strength of fillet welded cruciform joints. *Canadian Journal of Civil Engineering*, Vol. 16, No. 2, pp 162-171

van Wingerde A.M. 1992. *The fatigue behaviour of T- and X-joints made of SHS.* vol 37, No. 2.

van Wingerde, A.M., J.A. Packer & J. Wardenier 1996. New guidelines for Fatigue Design of HSS Connections. *Journal of Structural Engineering*, ASCE, Vol. 122, No. 2, pp 125-132

van Wingerde A.M., D.R.V. van Delft, J. Wardenier & J.P. Packer 1997. Scale Effects on the Fatigue Behaviour of Tubular Structures. *IIW International Conference on Performance of Dynamically Loaded Welded Structures*, July 14-15, San Francisco, U.S.A

Verheul A. & C. Noordhoek 1987. *Fatigue behaviour of joints between rectangular hollow sections, T-joints Part 1.* TNO-IBBC report BI-87-118/63.5.3.820, Delft, Netherlands.

Wardenier, J. 1982. *Hollow Section Joints*, Delft University Press, Delft, The Netherlands.

Yamada K & S. Kainuma 1996. Practical aspects of fracture mechanics applied to fatigue. Key note Paper, *The Fourth International Symposium on Structural Engineering for Young Experts*, Tsinghua University, Beijing, China, 1996

Zhao X.L. and G.J. Hancock 1993. *Tests and Design of Butt Welds and Transverse Fillet Welds in Thin Cold-formed RHS Members*, Research Report No. R681, The University of Sydney, NSW 2006, Australia.

Zhao X.L., G.J. Hancock & R. Sully 1996. Design of Tubular Members and Connections using Amendment Number 3 to AS4100. *Journal of the Australian institute of Steel Construction*, Vol. 30, No. 4, pp 2-15

Tubular Structures VIII, Choo & Van der Vegte (eds) © 1998 Balkema, Rotterdam, ISBN 90 5809 001 9

Analysis of cracked T-tubular welded joints using finite and boundary element methods

S.T. Lie & G. Li
School of Civil and Structural Engineering, Nanyang Technological University, Singapore

ABSTRACT: This paper demonstrates a kind of coupling scheme of finite elements (FE) to boundary elements (BE) for the analysis of T-tubular welded joints frequently encountered in the offshore industry. At the high stress concentration region between the brace and the chord, BE are used to discretize the domain. This domain is further subdivided into two subdomains along the interface containing the semi-elliptical crack found at the saddle point. The rest of the welded tubular joint is then discretised using the standard 20-nodes isoparametric FE. The efficiency and accuracy of this technique is demonstrated by analyzing T-tubular welded joints, and comparison of the results are made with the experimental tests and finite element method.

1 INTRODUCTION

For many years the application of the finite elements (FE) method has become very popular in calculating the stress concentration factor (SCF), load displacement behavior and ultimate capacity of different types of uncracked welded circular tubular joints. Recently, more and more attention has been paid to the analysis of cracked tubular joints. Different models have been used to analyze the fracture behavior of cracked joints by Kristiansen & Turner (1993), Burdekin & Yang (1997) and other researchers. Very fine meshes are usually used for modelling the cracks, so the transition between the fine mesh for a crack and the coarse mesh for the region outside the crack is complicated.

To model the 3-dimensional cracks at the intersection between the chord and the brace, Cao, Yang & Packer (1997) developed a special mesh generation for any circular tubular joints with or without cracks. A typical T-tubular joint without a crack has 8645 nodes and 1380 elements using 20 node brick element. The use of this mesh generator reduces the time taken to prepare the input data significantly.

The boundary element (BE) method is suitable for analyzing any crack problems (Lie, 1994). But it is not efficient to use BE alone to model the full structure with an initial crack because the tubular joint behaves as a thin shell structure. The combination of FE to BE can be an efficient technique for this kind of engineering application. It can preserve the advantages of both methods but reduce the disadvantages from using either method alone. In this paper, a kind of coupling scheme of FE to BE originally proposed by Cen et al. (1986,1988) was suggested. The relationship between nodal displacements and tractions on the interface from FE equations can be introduced into boundary integral equation as a natural boundary condition. The scheme was applied to the analysis of T-tubular welded joint with initial crack. The BE were used for stress intensity factor computations in the domain with crack at high stress gradients, and FE were used in other parts of the structure with low stress gradients. Since the BE method had been adopted for the domain with crack, the quarter-point elements and transition elements were used in neighborhood of the crack front. Some numerical results and discussion on the effects of varying the crack sizes in T-tubular welded joints are given.

2 DISCRETIZATION OF THE CRACKED BODY USING BOUNDARY ELEMENTS

The mathematical treatment of coupling between these two methods for elastic body can be found in the work of Du & Cen (1994). In the boundary element domain, body Γ is divided into n_e isoparametric elements with 4 or 8. In general,

$$\Gamma = \bigcup_{e=1}^{n_e} \Gamma_e \qquad (1)$$

and all the fields, displacements, tractions, as well as geometry can be approximated in each element by products of the interpolation functions, **N**, and the nodal values. In particular, the global coordinates, displacements and tractions are approximated, locally on the element Γ_e, by,

$$x_i(\xi_1,\xi_2) = \sum_{k=1}^{8} N_k(\xi_1,\xi_2)x_i^k,$$

$$u_i(\xi_1,\xi_2) = \sum_{k=1}^{8} N_k(\xi_1,\xi_2)u_i^k, \qquad (2)$$

$$t_i(\xi_1,\xi_2) = \sum_{k=1}^{8} N_k(\xi_1,\xi_2)t_i^k$$

where k is the nodal number in the element, ξ_1, ξ_2 are the local coordinates, x_i^k, u_i^k, t_i^k are the nodal values of the global coordinate, displacement and traction respectively. The interpolation functions N_k are given by :

$$N_k(\xi_1,\xi_2)=\frac{1}{2}(1-\xi_1^2)(1+\xi_2^k\xi_2)$$

where k is 5 or 7.

$$N_k(\xi_1,\xi_2)=\frac{1}{2}(1-\xi_2^2)(1+\xi_1^k\xi_1)$$

where k is 6 or 8.

$$N_1(\xi_1,\xi_2)=N_1^*-\frac{1}{2}(N_8+N_5),$$

$$N_2(\xi_1,\xi_2)=N_2^*-\frac{1}{2}(N_5+N_6),$$

$$N_3(\xi_1,\xi_2)=N_3^*-\frac{1}{2}(N_6+N_7),$$

$$N_4(\xi_1,\xi_2)=N_4^*-\frac{1}{2}(N_7+N_8),$$

$$N_k^* = \frac{1}{4}(1+\xi_1^k\xi_1)(1+\xi_2^k\xi_2) \qquad (3)$$

where k is equal to 1,2,3,4.

It is well known that the behaviour of displacements and stresses near the crack tip are $O(\sqrt{r})$ and $O(1/\sqrt{r})$ respectively. Using two kinds of special elements as shown in Figure 1, quarter-point elements and transition elements, the correct variation of displacements can be obtained near the crack front or crack tip.

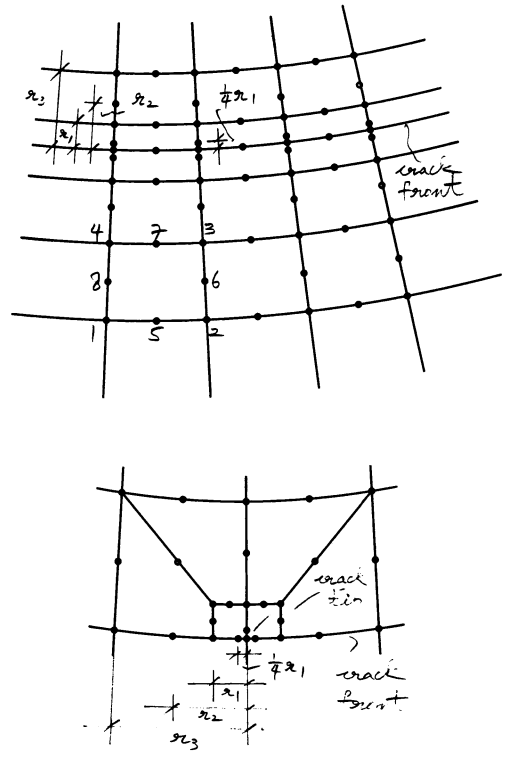

Figure 1. Quarter-Point and Transition Element Used at the Crack Front and Crack Tip.

By shifting the mid-node to the quarter-point from the crack tip, the element will be a quarter-point element. For the transition element the mid-node can be put at the point with the distance r_2 from the crack front. The distance r_2 must be governed by following formula,

$$r_2 = \frac{1}{4}(\sqrt{r_1}+\sqrt{r_3})^2 \qquad (4)$$

If $r_1 = 0$, the transition element will change to a quarter-point element.

Whenever the elasticity solution is available, the stress intensity factors can be evaluated at any point on the crack front from the asymptotic behavior of the displacements near the crack front. For the quarter-point elements employed on the crack front the stress intensity factors K_I and K_{II} (Aliabadi & Brebbia, 1994) can be evaluated as,

$$K_I = \frac{\mu}{\kappa+1}\sqrt{\frac{2\pi}{L_i}}\left[4(u_2^B - u_2^C) - (u_2^D - u_2^E)\right] \quad (5)$$

$$K_{II} = \frac{\mu}{\kappa+1}\sqrt{\frac{2\pi}{L_i}}\left[4(u_1^B - u_1^C) - (u_1^D - u_1^E)\right] \quad (6)$$

where u_2 and u_1 are the opening and shearing displacements at the end-nodes D,E, and at the ¼-nodes B,C in the quarter-point element, L_i is the length of the side of the element internally adjacent to the front, $\mu = E/2(1+\nu)$ is the shear modulus of elasticity and $\kappa = (3-4\nu)$ for plane strain and $\kappa = (3-\nu)/(1+\nu)$ for plane stress.

3 FINITE AND BOUNDARY ELEMENT MODEL OF THE T-TUBULAR WELDED JOINT

To verify the accuracy of the above technique, a typical T-tubular welded joint with the basic dimensions as shown in Figure 2, is modelled using FE and BE. It was axially loaded with a force of 470 kN in the direction of y and clamped at the end of the chord. The dimensions of the model are the same as those used by Huijskens (1988) experimentally. It was found that the fatigue crack always starts from the high stress concentration region at the saddle point. Huijskens (1988) had measured the crack profiles using the beachmarking technique and the observed crack depths at the deepest point are presented again in Table 1.

Due to the symmetry in the x-y and y-z planes, only a quarter of the joint is model using FE and BE. At the region of high stress concentration along the intersection between the brace and the chord, two layers of BE are used to model this region (Figure 3).

Table 1. The Observed Crack Profiles for the T-Tubular Joint.

Chord	∅ 914 mm	Wall Thickness 32 mm	
Brace	∅ 457 mm	Wall Thickness 16 mm	
Profile No.	Cycles	Depth *a* (mm)	Length *2c* (mm)
1	883000	6.5	30.2
2	1077000	11.2	60.9
3	1182000	14.3	91.0
4	1285000	18.0	123.3
5	1448000	24.2	202.2

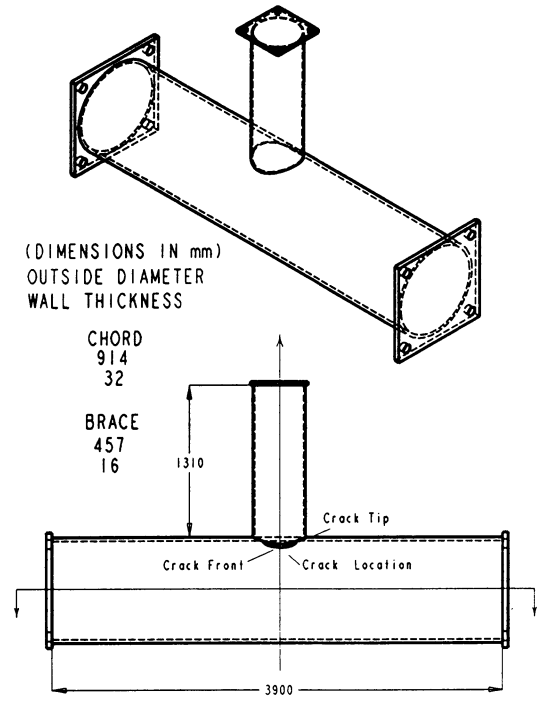

Figure 2. Basic Dimensions of the T-Tubular Welded Joint.

The BE region is further subdivided into two subdomains BE1 and BE2 along the semi-elliptical crack surface (Figure 3). Five different values of crack depth *a* and crack length *2c* from Table 1 are used in this study to determine the accuracy of the stress intensity factors at the deepest on the crack front.

The subdomain BE1 is then connected to FE1 and likewise BE2 to FE2 as shown in Figure 3. Because modelling the crack front is quite complex, many C++ codes were written to generate the mesh of the model. For a crack depth *a* and crack length *2c* equal to 18.0 mm and 123.0 mm, there are 515 nodes and 210 elements in FE1, 334 nodes and 116 elements in BE1, 210 nodes and 75 elements in BE2, and 553 nodes and 226 elements in FE2. Figures 4 shows the enlarged deflected model at the saddle point of the joint.

4 DISCUSSION

The same beachmarked crack profiles from Table 1 were used in the fatigue life prediction model to calculate the stress intensity factors. Figure 5 shows the results from this study and also from the

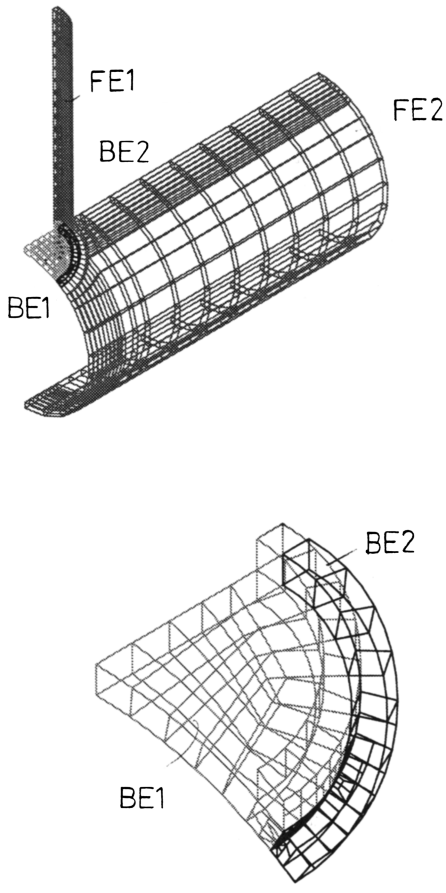

Figure 3. Finite Element and Boundary Element Mesh Used in the Model.

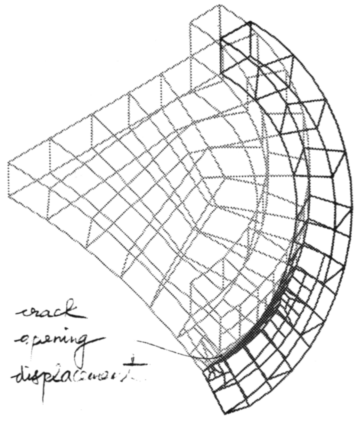

Figure 4. Deflected Shape of the Crack at the Saddle Region of the T-Tubular Joint.

approximate line spring finite element used by Ritchie & Huijskens (1989), and other experimental results at the deepest point of the crack.

It can be seen that the results obtained from this study are within the bandwidth, and they are lower than the results obtained from the line spring finite element. This is may be due to the fact that in the line spring finite element, the adjacent area used was a thin shell element, and hence the joint is more flexible resulting in slight increase in the crack opening displacement. In the present study, 20 node isoparametric nodes are used to model the adjacent area, and hence it is closer to the real behaviour of the joint. Using the same mesh, further calculations were carried out on the same geometry but with increased brace wall thickness of 24.0 mm and 32.0 mm. The objective is to determine whether the brace wall thickness has any influence on the stress intensity factors. It can be seen from Figure 6 that the trend of the results are comparable except that the values obtained from the present study are higher than that obtained by Ritchie & Huijskens (1989).

Surface values of stress intensity factors of Figure 7 show a difference of up to 50% between the line spring finite element and the three-dimensional finite element results. The boundary and finite element results are slightly lower than the three-dimensional

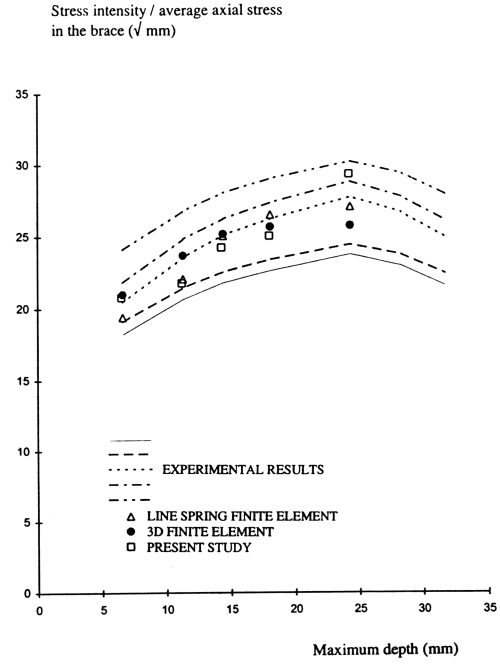

Figure 5. Comparison of Stress Intensity Factors at the Deepest Point of the Crack.

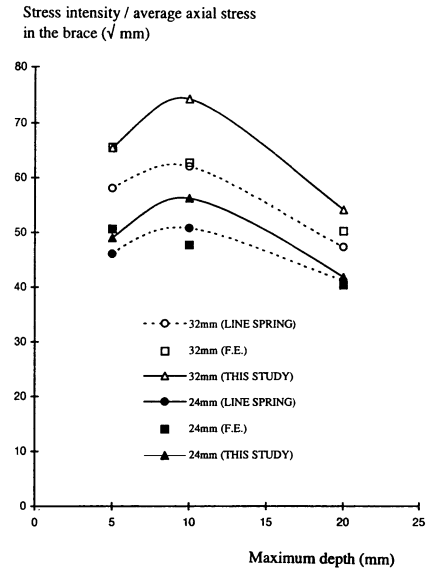

Figure 6. SIF's at the Deepest Point of the Crack for Brace Wall Thickness of 24.0 mm and 32.0 mm.

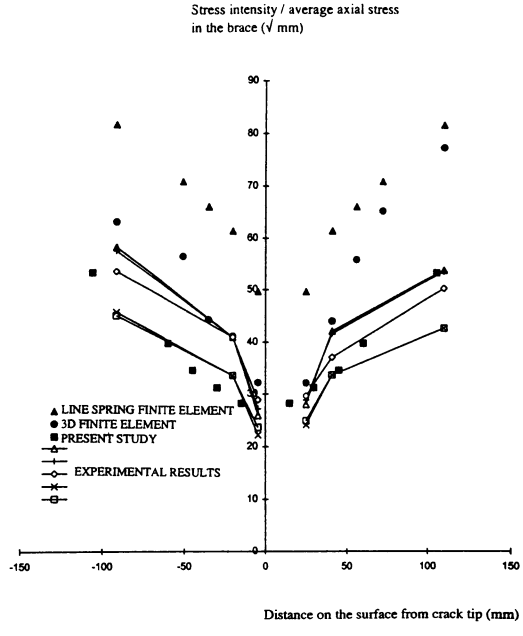

Figure 7. Comparison of Stress Intensity Factors at the Surface Points of the Crack.

finite element results, but they are within the bandwidth of experimental results. Plane stress state conditions are assumed to prevail at the surface. As stated by Huijskens (1988), the line spring finite

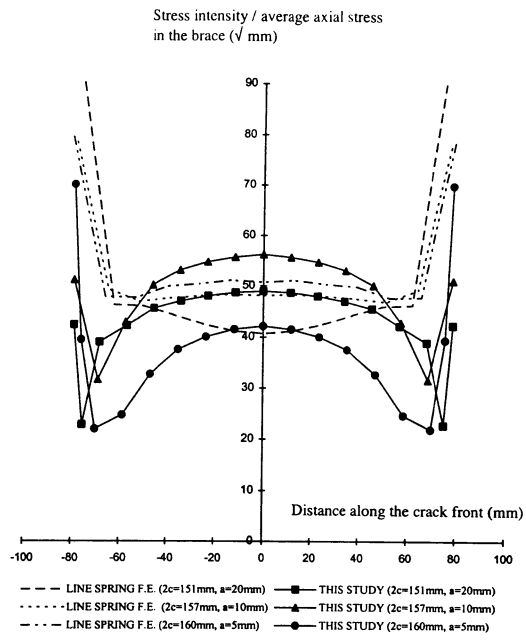

Figure 8. Distribution of Stress Intensity Factors Along the Crack Front for Brace Wall Thickness Equal to 24 mm.

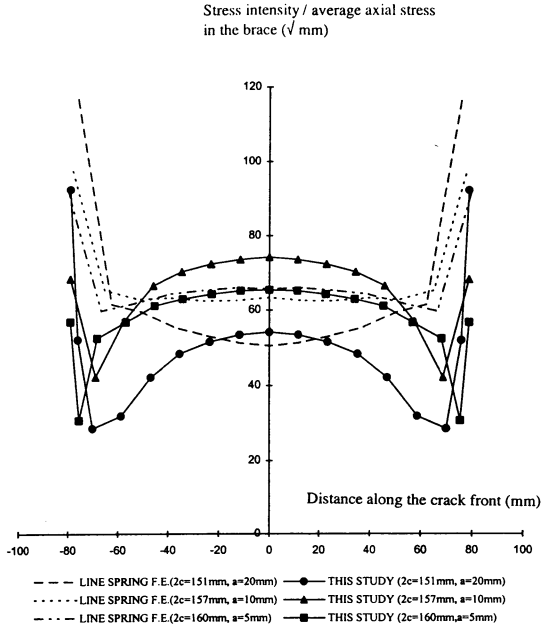

Figure 9. Distribution of Stress Intensity Factors Along the Crack Front for Brace Wall Thickness Equal to 32 mm.

element method is not valid at the end of surface cracks due to its theoretical limitations.

In Figures 8 & 9, the stress intensity factor distributions along the crack front are presented and compared with the line spring finite element method. Again it can be seen that the line spring finite element method has overestimated the surface stress intensity factors by as much as 50% especially for the lower aspect ratio of the semi-elliptical crack. The three-dimensional finite element results are not available.

5 CONCLUSION

It is demonstrated that the proposed coupling scheme of finite element method to boundary element method can be used in estimating the stress intensity factor along the crack front. The deepest point stress intensity factors of shallow semi-elliptical cracks at the saddle region of T-tubular welded joints are in agreement with that of the line spring, three-dimensional finite elements and experimental results. The present results are closer to the experimental results especially for the surface stress intensity factors. This coupling scheme can be used to study the effects of geometrical parameters of other types of tubular cracked welded joints such as the K, KT and X-joints more rapidly because modelling the 3-dimensional cracks at the intersection region can be done faster.

REFERENCES

Kristiansen, N. & Turner, C.E. 1993. Defect assessment of tubular T-joints using R6 failure analysis diagram. *ASME J. Pressure Vessel Technology*, 115:373-380.

Burdekin, F.M. & Yang, G.J. 1997. Failure assessment diagrams for mixed loading and cracked tubular joints. *Proceedings of the Ninth International Conference on Fracture*, Sydney, Australia.

Cao, J.J., Yang, G.J. & Packer, J.A. 1997. FE mesh generation for circular tubular joints with or without cracks. *Proceedings of the Seventh International Offshore and Polar Engineering Conference*, Honolulu, USA, 125-105.

Lie, S.T. 1994. Analysis of fatigue strength on non-load-carrying and load-carrying fillet welded joints. *Journal Of Strain Analysis*, Publishers for the Institution Of Mechanical Engineers, 29/4:243-255.

Cen, Z.Z. et al. 1986. A coupled finite element-boundary element method for three-dimensional elasto-plasticity analysis. *Proceedings of the International Conference on Boundary Elements*, Beijing, Pergamon Press, 311-318.

Cen, Z.Z. et al. 1988. The elastoplastic analysis by the coupling of boundary element method to finite element method. *Journal of Tsinghua University*, 28:34-43.

Du, Q. & Cen, Z.Z. 1994. Two types of displacements elastic schemes for coupling of boundary elements and finite elements. *Proceedings of the Sixth China-Japan Symposium on BEM*, Shanghai, International Academic Publishers, 103-107.

Aliabadi, M.H., Brebbia, C.A. & Parton V.Z. 1994. *Static and dynamic fracture mechanics*. Computational Mechanics Publications, Southampton, UK.

Huijskens, H.A.M. 1988. Fracture mechanics based predictions of the effect of size of tubular joint test specimens on their fatigue life. *Master Thesis*, Department of Civil Engineering, University of Technology Delft, Delft, Netherlands.

Ritchie, D. & Huijskens, H.A.M. 1988. Fracture mechanics based predictions of the effects of the size of tubular joint test specimens on their fatigue life. *Eight International Conference on Offshore Mechanics and Arctic Engineering*, The Hague, Netherlands, 121-126.

Tubular Structures VIII, Choo & Van der Vegte (eds) © 1998 Balkema, Rotterdam, ISBN 90 5809 001 9

J estimation method for through cracked tubular T-joints

Bo Wang & Ning Hu
Department of Engineering Mechanics, Tsinghua University, People's Republic of China
Yuji Makino
Department of Architecture and Civil Engineering, Kumamoto University, Japan
Yoshiaki Kurobane
Kumamoto Institute of Technology, Japan

ABSTRACT: Following the original handbook, the J integral elastic-plastic solution for a through crack in tubular T-joints is developed by combining an elastic solution and a fully plastic solution. The linear elastic solution for a crack in tubular T-joints is obtained by taking the solution for the plane plate with a curved crack, and the h_1 function in the fully plastic solution is calculated by using the finite element analyses. The constitutive relation of the material is described by a set of Ramberg-Osgood material parameters. In FE analyses, collapsed elements near the crack tip are used to reproduce the singularity of stress and strain field and the blunting of the crack tip. This paper presents h_1 functions in the plastic J-integral solution for through cracks with different lengths in tubular T-joints. Finally, the simple J estimation solution for a through crack in tubular T-joints is proposed for the extension of the J estimation handbook.

1. INTRODUCTION

During the earthquake, a lot of steel structures were damaged due to the crack initiation and propagation (Kurobane et al. 1997, Wang et al. 1996, 1997a). Therefore, it is necessary to investigate the fracture behaviour of the structure. In the previous work, based on the J-integral fracture parameter, the structural safety assessment approach has been proposed to assess defected tubular joints. In the modified Central Electricity Generating Board (CEGB) approach (Harrison et al. 1976, Bloom 1995, Wang et al. 1997b), the ultimate collapse load and the crack driving force of cracked structures are used as two assessment parameters. Usually, the J-integral represents the crack driving force for the crack growth. With the emergence of readily available simple J solutions for various types of structures through J estimation techniques, J-integral-based elastic-plastic fracture mechanics has become a common tool for analyzing ductile materials. In this J estimation method (Kumar et al. 1981), elastic-plastic J-integral solutions are estimated as the sum of a linear solution for an effective crack length and a fully plastic solution based on the nonlinear Ramberg-Osgood power hardening law. However, because of the complexity of real structures, the original J estimation handbook did not include the through crack in tubular T-joints. The J-integral values for cracked tubular joints were computed by using the finite element method. Since FE analysis is difficult in engineering application, the estimation formulation of J-integral for cracked tubular joints must be achieved.

In the present paper, the elastic solution for cracked tubular T-joints will be approximately substituted by that from the plane plate with a curved crack. The h_1 function in the fully plastic solution will be computed in FE analyses and will be listed in tabular form. These results are only applicable to cracked tubular T-joints loaded by the axial load on the brace. The EPRI original handbook will be expanded by the additional flaws in tubular T-joints.

2. J ESTIMATION SOLUTION

In the Electric Power Research Institute (EPRI) handbook (Kumar et al. 1981), J estimation solutions have been presented for several types of flaws and structures. In this way, elastic-plastic J solutions response of a flawed structure can be estimated as the sum of a linear solution for an Irwin effective crack length and a fully plastic solution based on the Ramberg-Osgood power hardening law. For a through crack in the tubular T-joint, the combined elastic-plastic J solution can be written as:

$$J(a, P) = J^e(a_e,P) + J^p(a,P) \qquad (2\text{-}1)$$

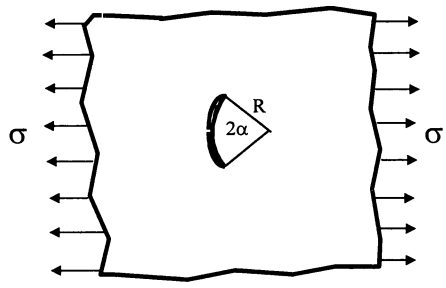

Fig.1 A curved crack under the uniform stress

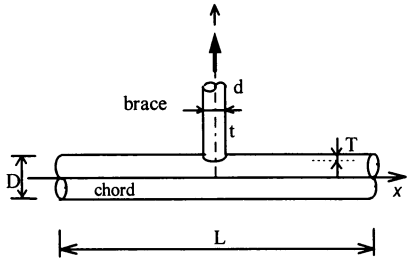

Fig.2 A Tubular T-joint specimen

where J^e is the elastic solution for an effective crack length, a_e, which takes into account Irwin's small-scale yielding correction for strain hardening materials, and J^p is the fully plastic solution.

Eq. (2-1) is derived from the deformation plasticity theory, in which a Ramberg-Osgood power hardening law is used as the material model, which is described as

$$\varepsilon / \varepsilon_0 = \sigma / \sigma_0 + \alpha(\sigma/\sigma_0)^n \qquad (2\text{-}2)$$
$$\varepsilon_0 = \sigma_0 / E$$

where σ is the stress, ε is the strain, α is the "yield offset" constant, n is the power hardening exponent, E is Young's modulus, and ε_0 is the yield strain corresponding to the yield stress σ_0.

J^e (a_e, P) is the elastic part of the solution, and can be obtained from the following equation

$$J^e(a_e, P) = K_I(a_e, P)^2(1-\nu^2)/E \qquad (2\text{-}3)$$

where K_I is the stress intensity factor in the linear elastic fracture mechanics. Because of the complexity of tubular structures, the solutions of stress intensity factors for these structures are not yet available. In this paper, the stress intensity factor solution for the plane plate with a curved crack is taken as the approximate solution for a cracked tubular T-joint and is represented by (Tada et al. 1973)

$$K_I = \sigma\sqrt{\pi R \sin\alpha_0}\,\frac{\cos\frac{\alpha_0}{2}}{1+\sin^2\frac{\alpha_0}{2}} \qquad (2\text{-}4)$$

where α_0 and R are geometric sizes for a curved crack and σ is the applied stress, as shown in Fig.1. In fact, there are some errors between real structure and two-dimensional model. In elastic situation (n=1), the error, which is between the two results separately from eq.(2-4) and FE analyses on T-joint, is in the range of 0.5-3%.

From Kumar et al.(1981), the effective crack length is given by

$$a_e = a + \psi r_y$$

where

$$r_y = \frac{1}{\beta\pi}\frac{n-1}{n+1}\frac{K_I(a,P)^2}{\sigma_0^2}$$

$$\psi = \frac{1}{1+(P/P_0)^2}$$

$\beta = 2$ (plane stress)
$\quad 6$ (plane strain)
$a = 2\alpha_0 R$

P represents a general applied load and P_0 is the reference limit load for a uncracked tubular T-joint given by (Department of Energy, 1990)

$$P_0 = (7.57 + 17.95\beta + 1.18\beta\gamma).\sigma_y T^2 \qquad (2\text{-}5)$$

where $\beta = d/D$, $\gamma = D/2T$, d and D are the diameters of the brace and the chord respectively, T is the thickness of the chord, shown in Fig.2.

The plastic part of the solution, J^p, is written in terms of the h_1 function as

$$J^p(a, P) = 2\alpha\sigma_0\varepsilon_0 R\alpha_0 h_1(\alpha_0 R/T, n)\,(P/P_0)^{n+1} \qquad (2\text{-}6)$$

Where R is the radius of the brace and T is the thickness of the brace, h_1 is the function of material and geometry for the flawed configuration and will be determined from the elastic-plastic J-integral in FE analyses.

Table 1. Test specimens (measured)

Specimen	$D \square T$	$d \square t$	L	Chord σ_y	Chord σ_u	Chord ε_u	Brace σ_y	Brace σ_u	d/D	D/T
	(mm)		(mm)	*(N/mm^2)*			*(N/mm^2)*			
T-joint	323.9□6.4	141.3□6.6	1219	274	451	18.5	274	451	0.44	50.6

Table2 h_1 Functions (n=2)

Crack size (α_0)	h_1 function
2^0	3.5
4^0	4.2
6^0	4.0
8^0	4.2

3. FINITE ELEMENT ANALYSES

Non-linear finite element analyses were performed by using ABAQUS (1995) FE package on cracked tubular T-joints. Because of the symmetry, only one half part was analyzed for the T-joint model. The geometric parameters are presented in Table 1. The constitutive relation of the material satisfies the Ramberg-Osgood power hardening law in Eq.(2-2). Eight nodded thin isoparametric shell elements were used to simulate the chord, brace and weld. The Von Mises yield criterion and isotropic strain hardening have been used in the numerical procedure. The geometry of the weld elements is in agreement with the weld sizes recommended by the AWS (1994).

For the cracked model, collapsed elements around the crack tip were used to reproduce the crack tip singularity, 1/r singularity, and the crack tip blunting at the crack tip in Fig.3. One side, which is made up by three nodes (a, b, c), of an 8-node isoparametric element is collapsed so that all three nodes have the same geometric location at the crack tip. When the three nodes (a,b,c) on the collapse side can displace independently and mid-side nodes remain at mid-points, then $\varepsilon \propto r^{-1}$. For materials being in between linear elastic and perfectly plastic it is better to have a stronger singularity than necessary if the correct singularity cannot be reproduced. The numerics in ABAQUS (1995) will force the coefficient of this singularity to be small.

Meshes have been refined sufficiently to model the very high strain gradients around the crack tip. The evaluation of fracture parameter, the J-integral, can be accurately obtained. A detailed mesh layout near the crack tip of cracked T-joint models is shown in Fig.4. Two kinds of meshes have been used for tubular T-joints and the error between the two results is less than 3%. Fig.4 shows the fine one. It means that the accuracy of this mesh is enough and the result is convergent.

The tubular T-joint is subjected to the axial tensile load on the brace and is simply supported at the two ends of the chord, shown in Fig.2. In the process of calculation, the load control option was used to obtain the corresponding J-integral. The load-

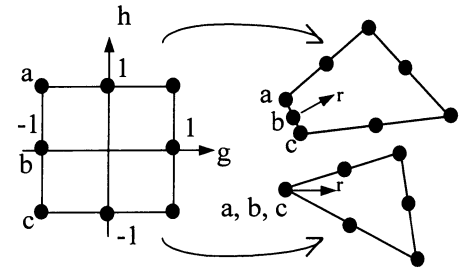

Fig.3 Collapsed elements around the crack tip

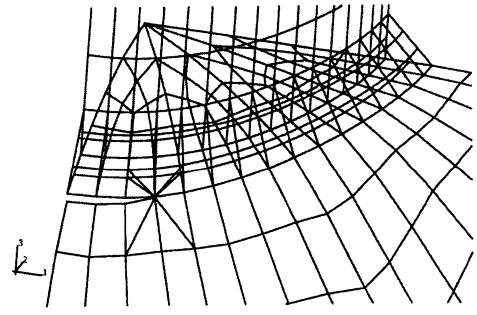

Fig.4 Deformed meshes for cracked T-joint

displacement curve is plotted in Fig.5. Numerical results show that there is a few difference between the uncracked and cracked T-joints. The elastic-plastic J-integral vs the applied load for different crack lengths is shown in Fig.6. It means that the J-integral increases with the crack length.

4. h_1 FUNCTION

In the EPRI handbook (Kumar et.al., 1981), elastic-plastic J-integral solutions are estimated as the sum of a linear elastic solution for an effective crack length and a fully plastic solution based on the Ramberg-Osgood power hardening law, as described by Eq. (2-1). The elastic solution is obtained from Eq. (2-3) and Eq.(2-4) and the plastic solution from Eq.(2-6). Elastic-plastic J-integrals, J^{e+p}, calculated by the FE analyses can be used to formulate h_1 functions in Eq. (2-6). h_1 function is derived from Eq. (2-3), Eq.(2-4) and Eq.(2-6) as the following:

$$h_1(\alpha_0 R/T, n) = \frac{J^{e+p} - J^e(a_e, P)}{2\alpha\sigma_0\varepsilon_0\alpha_0 R(P/P_0)^{n+1}} \qquad (4.1)$$

For a given crack size in tubular T-joints, the h_1 functions calculated from Eq. (4-1) show a dependence on the axial load that is governed by the reference limit load, P_0, and the strain hardening parameters, n. The relation between h_1 and the load is shown in Fig.7. Table 2 presents the h_1 functions calculated for each flaw size using the load of 400kN. These h_1 values can be used to estimate the elastic-plastic J solutions for tubular T-joints with a through crack. Interpolation can be used to obtain h_1 functions for other flaw sizes between 0 and 400kN.

5. DISCUSSION AND CONCLUSIONS

Non-linear finite element analyses have been carried out to obtain elastic-plastic J-integrals for tubular T-joints with a through crack. These J-integrals were used to calculate the h_1 functions utilized in elastic-plastic estimation procedures that combine linear elastic and fully plastic solutions. The h_1 functions for a through crack in tubular joints have been presented in the tabular form and can be used to derive elastic-plastic J-integrals for cracked tubular T-joints. Although h_1 functions were calculated for several flaw sizes, they can be used as a basis for interpolating for diffenent cracks. h_1 functions in this paper only can be applied to analyze cracked tubular joints. Fig.8 indicates that elastic-plastic estimation curves for J-integrals computed from the h_1 functions listed in the table 2 for the entire range from 0 to 400 KN. The elastic components of the

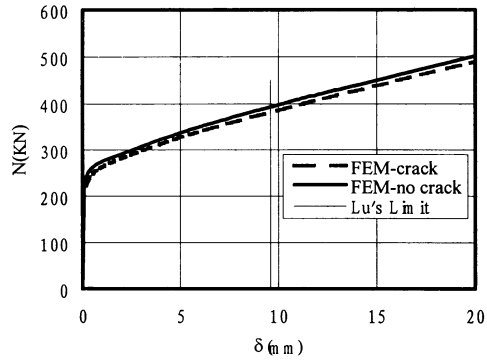

Fig.5 The load-displacement curve

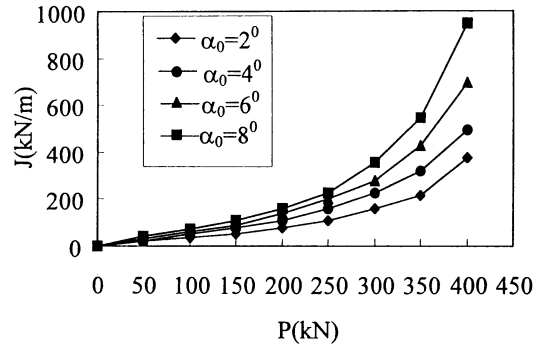

Fig.6 J-integral versus load for different cracks

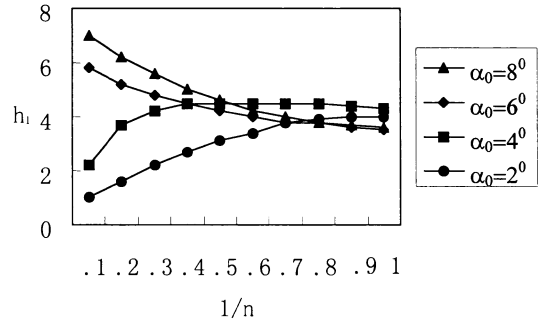

Fig.7 The h_1 function with strain hardening exponent n

estimated J-integrals are also shown in Fig.8, revealing the method is reasonable for both the elastic and elastic-plastic portions of the curves. In conclusions, the estimation solutions of elastic-plastic J-integral for cracked tubular T-joints have been developed in this paper as the expansion for the original EPRI handbook.

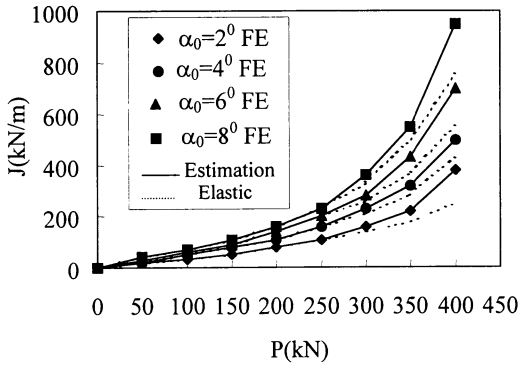

Fig.8 Elastic-plastic estimation curves

REFERENCES

ABAQUS 1995, ABAQUS v5.5 Manuals, Hibbitt, Karlsson and Sorenson Inc.

American Welding Society 1994, Structural Welding Code, AWS D1.1-94.

Bloom, J. M. 1995, Deformation plasticity failure assessment diagram (DPFAD) for materials with non-Ramberg-Osgood stress-strain curves, Journal of Pressure Vessel Technology, Vol. 117, pp346-356.

Department of Energy 1990, Background to new static strength guidance for tubular joints in steel offshore structures, Offshore Technology Report OTH89 308, HMSO, London, UK.

Harrison, R. P., K. Loosemore & I. Milne 1976, Assessment of the integrity of structures containing defects, CEGB R/H/6, Central Electricity Generating Board, UK.

Kumar, V., M. D. German & C. F. Shih 1981, An engineering approach for elastic-plastic fracture analysis, NP-1931, EPRI.

Kurobane, Y., B. Wang, K. Azuma & K. Ogawa 1997, Brittle fracture in steelframes, Proceedings of Int. Conference on Behaviour of Steel Structures in Seismic Areas STESSA'97, Kyoto, Japan.

Tada, H., P. C. Paris&G. R. Irwin 1973, The stress analysis of cracks handbook, Del Research Corporation Hellertown, Pennsylvania.

Wang, B., Y. Kurobane & Y. Makino 1996, Damage criterion and safety assessment for welded T-joints, Journal of Constructional Steel, Vol.4, pp105-112.

Wang, B., Y. Kurobane & Y. Makino 1997a, Damage criterion and ultimate strength for tubular joints, Proceedings of the 7th International Offshore and Polar Engineering Conference, Hawaii, USA.

Wang, B., Y. Kurobane & Y. Makino 1997b, A modified CEGB assessment approach to flawed tubular joints, Proceedings of the 7th International Offshore and Polar Engineering Conference, Hawaii, USA.



Taylor & Francis
Taylor & Francis Group
http://taylorandfrancis.com

Tubular Structures VIII, Choo & Van der Vegte (eds) © 1998 Balkema, Rotterdam, ISBN 90 5809 001 9

Factors affecting the fracture mechanics assessment of a cracked offshore tubular joint

D. Bowness & M. M. K. Lee
University of Wales Swansea, UK

ABSTRACT: Primary fatigue design of tubular joints in offshore installations is performed using the stress-endurance (S-N) approach, because of its simplicity and efficiency. This approach, however, is not suitable for assessing the remaining life of already defective joints during their service life, or for designing joints which are expected to behave differently to those tested in the laboratory, on which the S-N curve was based. For such situations fracture mechanics may be used. The Background to New Fatigue Design Guidance (1995) suggests the use of PD6493 (1991) as a framework of acceptable procedures for performing fracture mechanics analyses. In this paper, some of the input parameters for a fracture mechanics analysis, which are inherent in an S-N curve, are considered to illustrate their effects on a fatigue prediction.

KEYWORDS: Fracture mechanics, fatigue, tubular joints, remaining life, stress intensity factors.

1 INTRODUCTION

The fatigue design of a tubular connection is most commonly carried out by using the stress-endurance (S-N) approach, which only requires a knowledge of the stress at the hot spot because most other factors are inherent in the S-N design curve. By contrast, the fracture mechanics approach, used to assess the significance of any cracking found during in-service inspection programmes and to predict the remaining life of such cracked joints, requires very detailed information.

In this paper, three factors which affect the results of fracture mechanics assessments of tubular joints are examined. The first is multiple crack growth and coalescence — multiple crack initiation and growth are common phenomena at tubular joint weld toes, especially in a corrosive marine environment. A procedure for multiple crack growth calculations is given and used to compare life predictions from multiple and single defects. The effect of the initial crack dimensions is the second factor examined — at the design stage the joint is intact and so there is no initial crack, but in a remaining life assessment the defect dimensions must be determined from the actual cracked joint under consideration. But uncertainties in the inspection process can mean that the size of the defect is under- or over-estimated. The final factor examined is the Degree of Bending (DOB), which quantifies the stress distribution through the thickness of the chord wall at the hot spot. This through thickness stress distribution is ignored in the S-N approach, but it is seen to make a significant difference to the predicted remaining life a of tubular joint.

2 FATIGUE CALCULATION DETAILS

The Paris crack growth law was used to perform the fatigue calculations presented in this paper. Numerical integration of the Paris law is, in general, carried out in accordance with the recommendations of the IIW (PD6493 1991; International Institute of Welding 1990). This entails incrementing the crack depth by Δa and calculating the number of load cycles ΔN consumed in the increment. When dealing with a semi-elliptical surface crack, such as that shown in Figure 1, it is also desirable to update the crack aspect ratio a/c by allowing the crack to grow in the width direction. Therefore,

$$\Delta a = \Delta a \quad (1)$$

$$\Delta c = \Delta a\left(\Delta K_c / \Delta K_a\right)^m \quad (2)$$

$$\Delta N = \Delta a \Big/ \left(C\left(\Delta K_a\right)^m\right) \quad (3)$$

and so

$$a_{\text{new}} = a_{\text{old}} + \Delta a \quad (4)$$

$$c_{\text{new}} = c_{\text{old}} + \Delta c \quad (5)$$

$$N_{\text{new}} = N_{\text{old}} + \Delta N \quad (6)$$

$$[a/c]_{\text{new}} = a_{\text{new}}/c_{\text{new}} \quad (7)$$

where C is the Paris crack growth constant, m the Paris exponent (≈ 3 for steel), K the stress intensity factor (SIF) and the subscripts a and c denote the deepest point of the crack and crack ends, respectively.

This IIW numerical integration procedure, however, is not suitable for all crack growth situations (Thurlbeck 1991; Bowness 1996). Firstly, if the stress intensity factor at the deepest point is close to or less than the threshold SIF, the increase in crack width (equation 2) tends to infinity. The other problem with this numerical integration procedure is that it cannot be used for multiple crack growth problems; this is because when the crack depth is incremented, each of the cracks may not have accumulated the same number of cycles at the time of coalescence. To resolve these problem, the number of cycles may be incremented and used to 'drive' the numerical integration, as follows:

$$\Delta N = \Delta N \quad (8)$$

$$\Delta a = \Delta N\left(C\left(\Delta K_a\right)^m\right) \quad (9)$$

$$\Delta c = \Delta N\left(C\left(\Delta K_c\right)^m\right) \quad (10)$$

With this method applied to all the defects simultaneously, each crack is grown in its own right and the cracks may be compared at any time because the number of cycles, N, for all cracks is the same. For the crack growth calculations presented in this paper, ΔN was 10 load cycles.

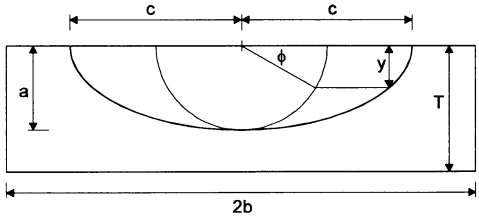

Figure 1. Notation for a semi-elliptical crack

The SIF solutions used in the fatigue crack growth calculations were those of Bowness & Lee (Bowness 1996; Bowness & Lee 1996). These solutions, derived from 3-D T-butt geometries, are presented in the form of weld toe magnification factors Mk, which are defined as

$$Mk = \frac{K_{(\text{in plate with attachment})}}{K_{(\text{in same plate but with no attachment})}} \quad (11)$$

Bowness and Lee's solutions are as follows:

$$Mk_{ma} = -0.08761\left(\frac{a}{c}\right)^{0.5864} + 0.07279\left(\frac{a}{T}\right)^{\left(-0.007556(a/c)-0.6198\right)} + 0.8066\exp\left(0.2675\left(\frac{a}{T}\right)\left(\frac{a}{c}\right)\right) \quad (12)$$

$$Mk_{ba} = 0.5854\left(\frac{a}{c}\right)^{-0.09484} + 0.1019\left(\frac{a}{T}\right)^{\left(-0.06640(a/c)-0.5238\right)} - 0.0003621\exp\left(10.30\left(\frac{a}{T}\right)\left(\frac{a}{c}\right)\right) \quad (13)$$

$$Mk_{mc} = 1.164\left(\frac{a}{c}\right)^{\left(0.1822(a/T)-0.3163\right)} + 1.839\left(1.0+\left(\frac{a}{T}\right)\right)^{-9.759} \quad (14)$$

$$Mk_{bc} = 1.070\left(\frac{a}{c}\right)^{\left(0.07225(a/T)-0.3034\right)} + 1.720\left(1.0+\left(\frac{a}{T}\right)\right)^{-7.167} \quad (15)$$

where the subscript a denotes the deepest point of the crack, c the crack ends and m and b, membrane and bending loading, respectively. To calculate the stress intensity factors, the weld toe magnification factors must be applied to plain plate solutions such as those of Newman & Raju (1981):

$$K_a = \left[Mk_{ma}M_{ma}\sigma_m + Mk_{ba}M_{ba}\sigma_b\right]\sqrt{\pi a} \quad (16)$$

$$K_c = \left[Mk_{mc}M_{mc}\sigma_m + Mk_{bc}M_{bc}\sigma_b\right]\sqrt{\pi a} \quad (17)$$

where M is the plain plate shape factor and σ the applied stress.

The Paris crack growth data used in the calculations were $C = 1.832\times10^{-13}$ and $m = 3.0$ (units in N and mm) which represent mean crack growth data for steel (PD6493 1991).

3 MULTIPLE CRACK GROWTH

Typically, several small cracks initiate in the early stages of fatigue crack growth. These eventually coalesce to form one (or possibly more) dominant crack which then propagates through the chord wall. Multiple defects are particularly common for steel joints freely corroding in sea water.

Many researchers who have investigated the effects of multiple growth and coalescence of coplanar cracks have also tried to replicate their experimental results using fracture mechanics. Disregarding small differences in the various approaches, two main methods are commonly used to account for these effects in a crack growth simulation. The first approach is where the crack shape (*a/c*) development is pre-defined by using a 'forcing function', usually derived from experimental observations. Such a method is advocated by Bell & Vosikovsky (1992) and Monahan & Dover (1995).

The second method is more general and may be referred to as a 'multiple crack model'. In this case, multiple cracks are grown in the crack growth simulation and interaction conditions are imposed when the cracks approach one another. Also, if two cracks touch or come within a certain distance of one another, they may be merged into one crack. Such an approach is allowed in PD6493 (1991), and is advantageous because empirical forcing functions are restricted to a particular loading mode and geometry. However, more detailed information is required on the defect sizes and spacings for the multiple crack model. In this paper, the multiple crack model is adopted.

The condition for interaction between coplanar cracks, and the revision of the interacting cracks into a new effective crack, have been the subject of much research. The PD6493 (1991) condition is illustrated in Figure 2. For two adjacent cracks of dimensions a_1, c_1 and a_2, c_2, respectively ($c_1 < c_2$), interaction is said to occur when $s \leq 2c_1$. On interaction, the revised crack depth is the greater of a_1 and a_2, and the total crack width ($2c$) becomes $2c_1+2c_2+s$. This condition is based on the criterion that the stress intensity factor is increased by 20% or more as a result of the presence of an adjacent crack (International Institute of Welding 1990). Other research and experimental work, however, suggest

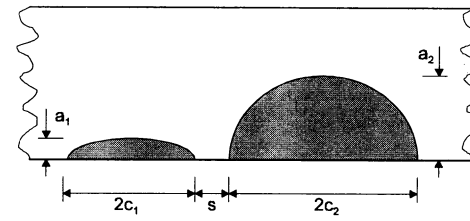

Figure 2. Criterion for interaction of surface cracks according to PD 6493

that the PD6493 condition for interaction is highly conservative. Detailed experimental and numerical work on coplanar cracks in plain plates was carried out by Soboyejo et al. (1990), who noted that "coplanar semi-elliptical cracks grow almost independently until coalescence". Experimental work by Pang (1993) on cruciform type joints also reveals that interaction effects between coplanar cracks are only significant when the cracks are nearly touching. Hence, Pang, in a numerical simulation of his own experimental work (1993), found it acceptable to allow the cracks to grow independently until they touched, when the crack dimensions were revised. Pang's multiple crack model may therefore be treated in the same manner as for PD6493 but with an interaction condition of $s = 0$. With respect to the accuracy of the crack life prediction, both Pang and Soboyejo et al. stated that the instantaneous revision of the two cracks to one with the combined width and deepest depth upon touching, is a conservative assumption because the time taken for the coalescence process has not been accounted for.

In the multiple crack model adopted in this paper, any number of different size and shape cracks may be specified, along with their location along the weld toe. This is depicted in Figure 3, where d_{aw} is the distance along the weld to the centre of a particular crack, measured from an arbitrary datum. The condition for interaction is that the crack ends touch, upon which the crack dimensions are revised and a new location is calculated. For example, in Figure 3, if cracks 1 and 2 touch, a new crack is formed having depth a_1 (since $a_1 > a_2$) and total width $2(c_1+c_2)$. The location of this new crack is then $d_{aw1}+c_2$. Growth of the new crack would then be continued until it touched crack 3, and so on.

4. FATIGUE SIMULATIONS

In the fatigue simulations, a tubular joint with three weld toe defects is considered. Using the notation

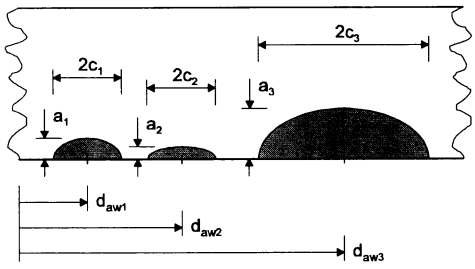

Figure 3. Multiple crack model adopted in this paper

given in Figure 3, the three defects are as follows:

a_1 = 1.0mm	a_2 = 2.5mm	a_3 = 1.5mm
c_1 = 1.5mm	c_2 = 3.5mm	c_3 = 5.0mm
d_{aw1} = 62mm	d_{aw2} = 79mm	d_{aw3} = 100mm

The nominal brace stress σ_{nom} and hot spot SCF were assumed to be 20.0Nmm^{-2} and 6.58, respectively, whilst the DOB ($=\sigma_b/(\sigma_b+\sigma_m)$) was set to a typical tubular joint value of 0.79. The bending and membrane stresses, for equations 16 and 17, may be calculated from

$$\sigma_m = \sigma_{\text{nom}}.SCF.(1-DOB) \quad (18)$$

$$\sigma_b = \sigma_{\text{nom}}.SCF.DOB \quad (19)$$

4.1 *Multiple crack growth*

The results of the first crack growth simulations are shown in Figure 4. In this figure, the solid line denotes the multiple crack growth simulation where each crack is grown separately until coalescence takes place. For the multiple cracks, the progress of the deepest defect is plotted. Also included in this figure are the results of a simulation for a single defect having the biggest dimensions of the three cracks, i.e. a = 2.5mm and c = 5.0mm, and an effective defect which encompasses the three cracks, i.e. a = 2.5mm and $2c$ = left edge of crack 1 to right edge of crack 3 = 44.5mm.

The upper bound to the remaining life predictions (Figure 4a) is from the single crack with the biggest dimensions of the three cracks. The lower bound is from the effective crack which produces a conservative prediction. The multiple crack growth simulation starts off close to the crack with the biggest dimensions but the gradient of the crack depth curve changes just before 200,000 cycles where the three cracks coalesce into one dominant crack. From then on, the curve is similar to that of the effective crack but displaced to the right.

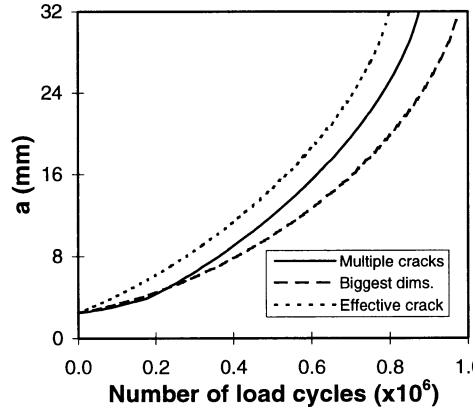

(a) Remaining life

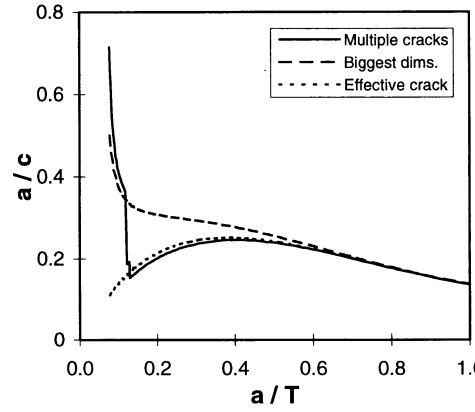

(b) Crack shape development

Figure 4. Multiple cracks versus single cracks

The crack shape development (Figure 4b) also shows that the multiple crack is approximately bounded by the single cracks. The deepest of the multiple cracks (crack 2) is rounded to begin with (large a/c) and becomes wider up until about a/T = 0.1. At this point it coalesces with crack 1 to its left and the aspect ratio drops dramatically. Almost immediately afterwards, this crack coalesces with crack 3 forming a single crack with an aspect ratio of around 0.15. This very wide crack then grows faster in the depth direction with a/c increasing up to a depth of 40% of the chord wall thickness before widening again. The crack with the biggest dimensions is rounded to begin with and the effective crack starts off very wide, but as they grow they converge on a preferred crack shape development curve. Beyond 60% of the chord wall thickness, the aspect ratio is virtually the same for all three simulations.

4.2 *Effect of initial crack dimensions*

The results shown in Figure 5 are based on the crack with the biggest dimensions of the three cracks, i.e. a = 2.5mm and c = 5.0mm, and illustrate the effect of changing the initial dimensions in the simulations. This also highlights any discrepancies that would occur in a remaining life prediction if the initial dimensions of a defect had been under or over estimated from an in-service inspection. The crack dimensions for the four cases are

Case 1	a = 2.5mm	c = 5.0mm
Case 2	a = 2.5mm	c = 10.0mm
Case 3	a = 5.0mm	c = 5.0mm
Case 4	a = 5.0mm	c = 10.0mm

where Case 1 is the base case, and in the other cases, one or both of the crack dimensions have been doubled.

As one might expect, increasing the crack dimensions shortens the predicted remaining life of the joint (Figure 5a). Comparing Cases 2 and 3, it may be seen that the increase in the initial crack depth has a greater effect than the increase in crack width. And when both the width and the depth dimensions of the crack are doubled (Case 4), the fatigue life is shortened by just under 20%. With regard to the crack shape development, as with the multiple crack example, all of the curves converge on the preferred *a/c* variation for this joint configuration and loading.

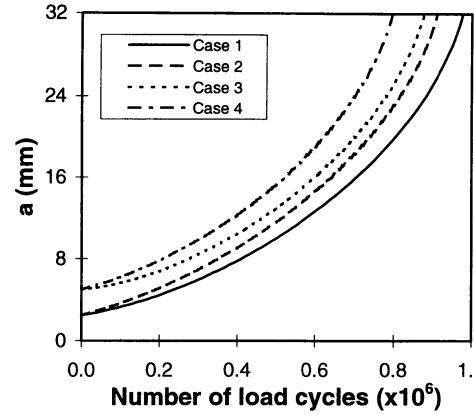

(a) Remaining life

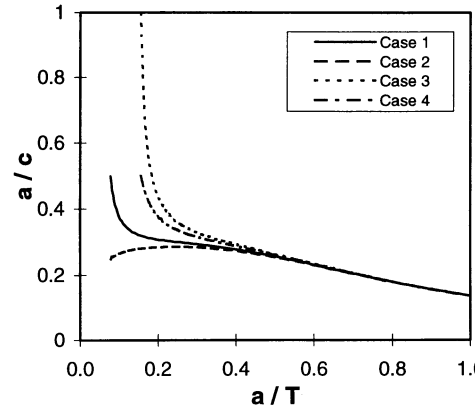

(b) Crack shape development

Figure 5. Effect of initial crack dimensions

4.3 *Effect of the DOB*

The DOB defines the variation in the geometric stress field through the thickness of the chord wall. In the fatigue design of tubular joints, the DOB is usually ignored and the fatigue life is based mainly on the hot spot stress σ_{hs} (= σ_{nom}.SCF).

To investigate the sensitivity of the fatigue crack growth to the DOB, the effective crack (a = 2.5mm and c = 22.25mm) from section 4.1 was used. Four DOB values were chosen for investigation: 0.0 (i.e. $\sigma_b = 0$), 0.5, 0.79 (the actual value) and 1.0 ($\sigma_m = 0$). In all cases, the hot spot stress was kept constant ($\sigma_{hs} = \sigma_m + \sigma_b$). The results of the comparison are shown in Figure 6.

The results clearly show that the higher the DOB, and hence the bending stress component, the higher the remaining fatigue life. This is expected since, under bending, as the crack grows through the chord wall, the deepest point of the crack moves into a region of lower stress, keeping the crack growth rate in the depth direction low (Figure 6a) which results in a much wider crack (Figure 6b). Assuming that the hot spot stress is constant through the plate thickness (DOB = 0.0) causes an acceleration in the growth rate in the depth direction (Figure 6a) producing a more rounded crack (Figure 6b), and results in a remaining life of as little as one third of that predicted by the correct DOB (= 0.79). In practice, most tubular joints appear to have a DOB of between 0.5 and 1.0 (Haswell 1991; Thurlbeck 1991; Bowness 1996). If the DOB for a joint were not known, a generally safe assumption would, therefore, be to assume a DOB of 0.5. But if higher values were to be used, they must be evaluated with a reasonable degree of certainty, as Figure 6a illustrates the sensitivity of fatigue life predictions to the DOB.

At this point, it is interesting to draw a comparison between the S-N and the fracture

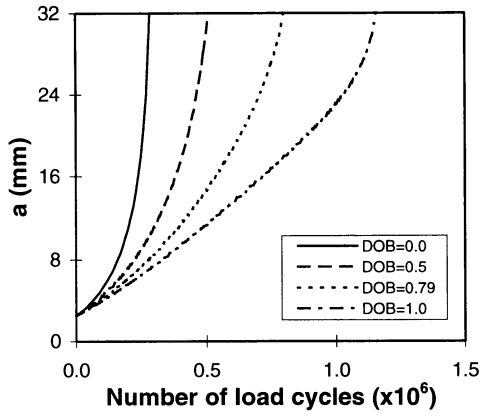

(a) Remaining life

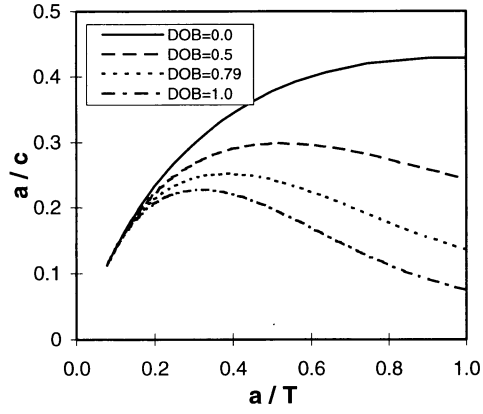

(b) Crack shape development

Figure 6. Effect of the DOB

mechanics approaches. The S-N approach takes no account of the chord wall through thickness stress distribution. Hence, all of the DOB values used in this section would have produced the same design life because the hot spot stress is the same in all cases. The effect of the DOB must therefore be one of the reasons for the large scatter in the experimental databases from which the S-N curves are regressed. In contrast, fracture mechanics can easily incorporate this effect, along with many others, with the main limitation being the availability and accuracy of the more detailed information.

5. DISCUSSION AND CONCLUSIONS

A multiple crack growth model has been outlined in this paper and successfully used in a simulation with three initial fatigue cracks. It was noted that because the cracks, on touching, are allowed to coalesce instantaneously, the model has a certain amount of in-built conservatism because the time taken for the coalescence process is neglected.

When comparing the multiple and the single crack simulations, it was shown that taking one defect even with the largest a and c of the three cracks produced an unsafe fatigue prediction. A single effective defect, of dimensions which encompass all of the multiple cracks, was seen to yield a conservative prediction. The use of a single effective crack is, therefore, recommended when multiple defects are detected along a weld toe but their individual dimensions cannot be ascertained with a high degree of certainty.

Increasing the initial crack dimensions resulted in a reduction of the fatigue life. Hence, factoring the estimated defect size could be used as a way of incorporating a safety factor into the crack growth simulation, but there is no formal guidance on doing this at the present time.

Of the factors affecting fatigue crack growth calculations examined in the paper, the DOB was found to have the greatest influence. For tubular joints, the DOB realistically can range from 0.5 to 1.0, which may easily alter the fatigue life prediction by a factor of two. The DOB, therefore, appears to be more critical than even the initial crack dimensions and whether or not multiple cracks are simulated.

6. REFERENCES

Background to New Fatigue Design Guidance 1995 Draft copy from the UK Health and Safety Executive.

Bell, R. & Vosikovsky, O. 1992 A fatigue life prediction model for multiple cracks in welded joints for offshore structures. *International Conference on Offshore Mechanics and Arctic Engineering*, ASME, Vol. III-B.

Bowness, D. 1996 Fracture mechanics based fatigue assessment of weld toe cracks in offshore tubular structures. Ph.D. Thesis, Department of Civil Engineering, University of Wales Swansea, C/PH/201/96.

Bowness, D. & Lee, M.M.K. 1996 Stress intensity factor solutions for semi-elliptical weld-toe cracks in T-butt geometries. *Fatigue and Fracture of Engineering Materials and Structures*, Vol. 19, No. 6, pp. 787-797.

Haswell, J.V. 1991 A fracture mechanics methodology for the assessment of fatigue cracks

in tubular joints. Ph.D. Thesis, Teeside Polytechnic.

International Institute of Welding 1990 Guidance on assessment of the fitness for purpose of welded structures: Draft for development. IIW/IIS-SST-1157-90.

Monahan, C.G. & Dover, W.D. 1995 Early fatigue crack shape development in welded tubular joints. *International Conference on Offshore Mechanics and Arctic Engineering,* ASME, Vol. III.

Newman, J.C. & Raju, I.S. 1981 An empirical stress intensity factor equation for the surface crack. *Engineering Fracture Mechanics*, Vol. 15, No. 1-2, pp. 185-192.

Pang, H.L.J. 1993 Fatigue crack growth and coalescence of surface cracks. *International Conference on Offshore Mechanics and Arctic Engineering*, ASME, Vol. III-B.

PD6493 1991 Guidance on Methods for Assessing the Acceptability of Flaws in Fusion Welded Structures. British Standards Institution.

Soboyejo, W.O., Knott, J.F., Walsh, M.J. & Cropper, K.R. 1990 Fatigue crack propagation of coplanar semi-elliptical cracks in pure bending. *Engineering Fracture Mechanics*, Vol. 37, No. 2.

Thurlbeck, S.D. 1991 A fracture mechanics based methodology for the assessment of weld toe cracks in tubular offshore joints. Ph.D. Thesis, UMIST.



Taylor & Francis
Taylor & Francis Group
http://taylorandfrancis.com

Tubular Structures VIII, Choo & Van der Vegte (eds) © 1998 Balkema, Rotterdam, ISBN 90 5809 001 9

Guidance on the selection of stress intensity factor solutions for fracture mechanics assessment of cracked offshore tubular joints

D. Bowness & M. M. K. Lee
University of Wales Swansea, UK

ABSTRACT: The revised United Kingdom Health and Safety Executive Design Guidance now recommends the use of BSI PD6493 for assessing defects in tubular joints of offshore structures. But despite the detailed guidance provided by these documents, little information is given on the choice of stress intensity factor (SIF) solutions, which are fundamental to any fracture mechanics assessment. In this paper, an assessment is carried out of the existing SIF solutions that may be applied to semi-elliptical weld toe cracks in tubular joints. The solutions reviewed include the few tubular joint solutions that are currently available as well as the many T-butt solutions. Fatigue calculations are performed to demonstrate the effects that the differences in the SIF solutions have on remaining fatigue life predictions. Based on these comparisons, recommendations are then given on the applicability, and accuracy, of each of the existing SIF solutions for remaining fatigue life assessment of tubular joints.

KEYWORDS: Stress intensity factors, fatigue, tubular joints, remaining life, fracture mechanics.

1 INTRODUCTION

Throughout the operational life of a North Sea installation, its structural integrity must be ensured to a high degree of reliability. This integrity may, however, be compromised by the presence of constructional defects and fatigue cracks which develop with repeated wave loading. Ever since the loss of the drilling rig Sea Gem in 1965, such defects have been recognised as an important problem by operators of North Sea installations. In fact, a quarter of all damage to North Sea structures requiring repair over the period 1974-92 was as a result of fatigue (Stacey & Sharp 1995). Because such defects are so common and their presence and development cannot be avoided, it is essential to be able not only to assess their significance, but also to predict their future development. Such knowledge means that inspection effort may be optimised and repairs carried out when necessary, ensuring structural reliability.

Fracture mechanics is the tool used to assess structural defects. For a given or postulated defect, it may be used to predict the development and the rate of growth of that defect, taking into account the operating, environmental and structural conditions. It can also be used to determine the likelihood of fracture. The principal input parameter in fracture mechanics based assessments is the stress intensity factor (SIF). For simple geometries, well established solutions are readily available, but for weld toe cracks in tubular joints, the range of possible configurations and the geometric complexity means that there are no universally applicable or widely accepted solutions. There are, however, many sets of solutions that may be applied to weld toe cracks in tubular joints. Some of these were inferred from experimental test results whilst others were derived from finite element parametric studies of tubular joint geometries. Solutions from simplified geometries such as T-butts are also commonly used to predict tubular joint SIFs, by using the uncracked stress field at the location of the crack. Naturally, the choice of solutions will have a large effect on the SIF, and in fatigue calculations any differences will be magnified because the crack growth rate is proportional to the cube of the SIF. Yet despite the large discrepancies that can occur in these

assessments, there is no guidance on the choice of SIF solutions to be found in the literature.

In this paper, the main SIF solutions that may be applied to weld toe cracks in tubular joints are reviewed. The solutions are then compared by performing crack growth calculations, using the Paris Law. From these comparisons, guidance on the use of such solutions is given.

2 EXISTING SIF SOLUTIONS

In this section, existing stress intensity factor solutions which may be applied to fatigue cracks in tubular joints are reviewed (a compendium of the stress intensity factor solutions can be found in Bowness (1996)). Also, a summary of the solutions is given in Table 1.

2.1 *Solutions from 2-D based simplified geometries*

The solutions based on 2-D simplified geometries are all approximations of semi-elliptical weld toe cracks in 3-D T-butts (the standard notation for semi-elliptical cracks and T-butts is given in Figures 1 and 2, respectively).

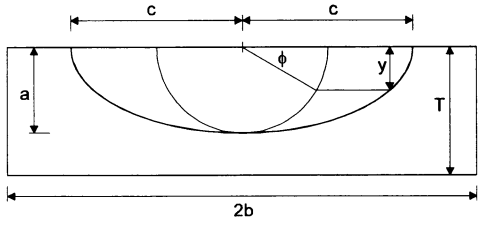

Figure 1. Notation for a semi-elliptical crack

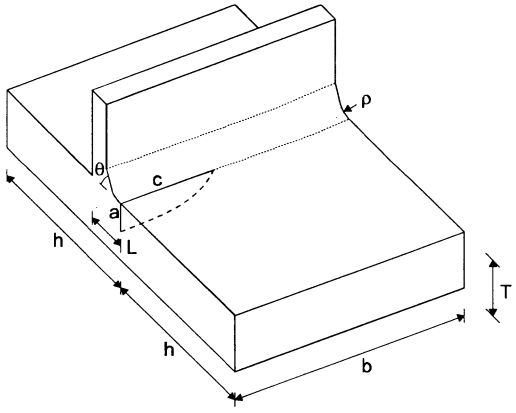

Figure 2. Notation for a T-butt (total width = 2*b*)

They are presented in the form of weld toe magnification factors, after Maddox (1975), which are defined as

$$Mk = \frac{Y_{(\text{in plate with attachment})}}{Y_{(\text{in same plate but with no attachment})}} \qquad (1)$$

where Y is the shape factor for the geometry and loading. The Mk's may then be applied to plain plate solutions, such as those of Newman & Raju (1979a, b; 1981), to account for the effect of the weld and the attachment so that

$$K_{\text{T-butt}} = \left(Mk_m M_m \sigma_m + Mk_b M_b \sigma_b\right)\sqrt{\pi a} \qquad (2)$$

where K is the SIF, M the plain plate shape factor, σ the applied stress and subscripts m and b denote membrane and bending loading, respectively.

The first weld toe magnification factors are those given in PD6493 (1991), which were derived from plane strain analyses of weld toe edge cracks. When performing fatigue calculations on semi-elliptical cracks, it is desirable to apply the Paris Law to the crack ends as well as the deepest point so as to update the crack aspect ratio a/c. However, since the Mk factors are based on a 2-D plane strain slice, they are only directly applicable to edge cracks. Therefore, PD6493 suggests using either an Mk for a small crack depth, e.g. a = 0.15mm, or the elastic stress concentration factor at the crack ends.

Fracture mechanics calculations using solutions such as PD6493 generally produce very conservative (low) life predictions when compared with experimental results. Using such comparisons, Aaghaakouchak et al. (1989) argued that this discrepancy was due to load shedding. Based on a study of plain plates containing edge cracks, they proposed the following linear moment release model

$$\sigma_b = \sigma_b^{\text{uncracked}}\left(1 - a/T\right) \qquad (3)$$

which allows the bending stress σ_b to decay as the crack deepens. This implies that for a through thickness crack, only membrane stresses may be transmitted, which is analogous to a pin joint or a hinge. Studies on the fracture mechanics analysis of tubular joints (Berge et al. 1994; Maddox 1996), however, have shown that whilst this linear moment release model improves the qualitative trends given by simplified geometries, the load shedding characteristics of tubular joints are more complex than the model can accommodate.

Such arguments about load shedding fail to

Table 1. Summary of the stress intensity factors reviewed (continued overleaf)

Solutions of	Geometry	Derived from	Use in conjunction with	*a/T*	*a/c*	Other validity limits
Dover et al.	Tubular T, Y and K joints	Inferred from experimental fatigue tests	—	full range	inherent	none specified†
Newman and Raju	Plain plates containing semi-elliptical cracks	3-D finite element analyses	—	0.2 - 0.8	0.2 - 1.0	—
PD6493	Weld toe edge cracks	2-D finite element analyses	Plain plate solutions (e.g. Newman and Raju)	full range	N/A	$\rho/T = 0.0$ $\theta = 45°$
Aaghaakouchak et al.	Linear moment release model to correct weld toe edge crack solutions	Difference between inferred stress intensity factors and those from weld toe edge cracks	Plain plate solutions and 2-D *Mk* factors (e.g. PD6493)	full range	N/A	none specified†
Dijkstra et al.	Approximation of semi-elliptical weld toe cracks in T-butts	Mainly 2-D with a limited number of 3-D finite element analyses	Plain plate solutions and 2-D *Mk* factors	0.16 - 0.4	0.64 at $a/T = 0.16$ to 0.39 at $a/T = 0.4$	$L/T = 1.3$ $\rho/T = 0.125$ $\theta = 70°$
Bell et al.	Semi-elliptical weld toe cracks in T-butts	3-D finite element analyses	Plain plate solutions	0.01 - 0.4	0.25 - 1.0	fixed L/T $\rho/T = 0.0$ $30° \leq \theta \leq 70°$
Pang	Approximation of semi-elliptical weld toe cracks in T-butts	2-D finite elements for the deepest point and Bell et al.'s work for the crack ends	Plain plate solutions and 2-D *Mk* factors	0.01 - 0.5	0.25	$\rho/T = 0.0$ $\theta = 45°$

Table 1 continued

Fu et al.	Semi-elliptical weld toe cracks in T-butts	3-D finite element analyses	Plain plate solutions	0.05 - 0.4	0.0 - 1.0	fixed L/T $\rho/T = 0.0$ $\theta = 45°$
Thurlbeck et al.	Approximation of semi-elliptical weld toe cracks in T-butts	2-D finite elements with a correction factor based on the 3-D work of Fu et al.	Plain plate solutions	0.001 - 1.0	0.0 - 1.0	$0.375 \le L/T \le 3.0$ $22.5° \le \theta \le 90°$ $0.01 \le \rho/T \le 0.5$
Bowness and Lee	Semi-elliptical weld toe cracks in T-butts	3-D finite element analyses	Plain plate solutions	0.05 - 0.7	0.1 - 0.95	$L/T = 1.0$ $\rho/T = 0.0$ $\theta = 45°$
Haswell	Hot spot cracks in various tubular joint configurations including multiplanar joints	Thin shell finite elements with line-spring cracks	—	0.2 - 0.8	0.2	none specified[†]
Rhee et al.	Saddle cracks in tubular T joints	3-D finite element analyses	—	0.05 - 0.8	$0.0625/\beta\gamma$ - $1.5/\beta\gamma$ for $a/T = 0.05$ and $1.0/\beta\gamma$ - $24.0/\beta\gamma$ for $a/T = 0.8$	$0.4 \le \beta \le 0.8$ $10.0 \le \gamma \le 20.0$ $0.3 \le \tau \le 1.0$ $\alpha = 12.0$
Ho et al.	Hot spot cracks in tubular Y joints	3-D finite element analyses	—	0.1 - 0.8	0.1 - 0.4	$0.6 \le \beta \le 0.8$ $10.0 \le \gamma \le 35.0$ $0.2 \le \tau \le 1.0$ 60° brace angle

[†] No validity limits were specified but accuracy may depend the data used to derive the solutions

account for the inaccuracies in the SIF solutions. Recognising the inadequacies of the 2-D solutions for an essentially 3-D geometry, Dijkstra et al. (van Straalen et al. 1988; Dijkstra et al. 1989; van Straalen & Dijkstra 1991; Dijkstra et al. 1993) carried out eight finite element analyses of 3-D T-butts to investigate the ratio of the 3-D to 2-D *Mk*'s. They then proposed two blanket correction factors: $\omega = 0.9$ at the deepest point of the crack and $\omega = 0.8$ at the crack ends ($Mk_{3\text{-}D} = \omega Mk_{2\text{-}D}$).

The SIF solutions of Pang (Pang 1991; Pang 1993a, b; Pang & Gray 1993) are also based on correcting 2-D *Mk* factors. Pang used the 3-D results of Bell et al. (described in the next section) to improve the prediction at the crack ends by defining a correction factor based on the maximum difference between *Mk* at the crack ends and at the deepest point. The constant crack depth assumed at the crack ends in PD6493 yields a constant *Mk* with crack depth, but Pang's modification incorporates the variation seen in full 3-D solutions.

One of the most recent, and by far the most comprehensive, set of solutions currently available are those of Thurlbeck et al. (Thurlbeck 1991; Thurlbeck & Burdekin 1992; Cheaitani et al. 1995). They produced weld toe magnification factors for 2-D plane strain T-butt slices covering a wide range of weld angles, toe radii and attachment footprint widths. Realising the deficiencies in using 2-D *Mk* factors for 3-D geometries, Thurlbeck et al. then developed the *Ma* correction factor which modifies the 2-D *Mk*'s to produce 3-D T-butt *Mk*'s. *Ma* is based on the 3-D results of Fu et al. (described in the next section), the corrections of Dijkstra et al. and some assumptions which allow *Ma* to be extended over the full parameter range. Like PD6493, crack end *Mk*'s are calculated with a constant shallow crack depth.

2.2 *Solutions from 3-D based simplified geometries*

All the solutions derived from 3-D simplified geometries are based on T-butts and, like the 2-D solutions, are presented in the form of weld toe magnification factors. To supplement the Canadian Offshore Steels Research Program, Bell (1987) analysed a large number of semi-elliptical crack geometries in 3-D T-butts. The results are presented in the form of tabulated 3-D *Mk* factors. Notably, the crack end *Mk* factors vary with crack depth, whereas the use of a small crack depth at the crack ends with 2-D *Mk*'s, as suggested in PD6493, produces a constant *Mk*.

Fu et al. (1992; 1993) also performed a number of finite element analyses of 3-D T-butts. To evaluate the stress intensity factors, Fu et al. used the virtual crack extension method. However, they found that where the crack meets the weld toe, the virtual crack extension produced values that were not path independent, with successive contours differing by as much as 300%. They attributed this to the weld toe notch stress singularity, which alters the crack tip stress field around the weld intersection. Consequently, they ignored the SIF values at the crack ends and extrapolated the rest of the crack front distribution back to this location. The crack end *Mk* factors must, therefore, be calculated in a similar fashion to PD6493, i.e. by using a small crack depth.

Bowness & Lee (Bowness 1996; Bowness & Lee 1996) conducted a finite element study of 3-D T-butts using the method of displacement extrapolation to avoid the problems experienced by Fu et al. with the virtual crack extension method. Their results are presented in the form of *Mk* factor equations applicable at the deepest point and the crack ends, for both membrane and bending loading.

2.3 *Solutions from tubular joint geometries*

The three fatigue assessment models proposed by Dover et al. (Dover & Dharmavasan 1982; Dover & Connolly 1986; Kam & Dover 1987) are based on inferred SIFs from experimental fatigue tests. The first is the Inherent Flaw Model in which both the shape factor *Y* and the crack growth rate are assumed to be constant. A more realistic variation in *Y*, with crack depth, is included in the Average Stress Model. In this model, *Y* is also calculated as a function of the average intersection stress ratio (= hot spot stress / average intersection stress) which was incorporated to account for the fact that different experimental test joints with the same hot spot stress can have different fatigue lives. Finally, the Two Phase Model contains a further refinement where the crack initiation and propagation phases are considered separately. It is worth noting that all of these models were derived from a limited experimental database of T, Y and K joints.

The SIF solutions from Haswell (1990; 1991; 1992a, b) are for cracks at the hot spot location in tubular joints. They were derived from thin shell finite element analyses of a range of cracked and uncracked tubular joint configurations and geometries under various loading modes. Semi-elliptical cracks were incorporated into the models using line-spring elements. As the line-spring elements do not give accurate solutions at the crack ends (ABAQUS 1995), the SIFs obtained there were disregarded. The solutions for the shape factor *Y* are

Table 2. Input data for the first crack growth simulation

Crack data:	a_0 = 0.1mm	- initial crack depth (minor axis of the ellipse)
	c_0 = 0.1mm	- initial crack half width (major axis of the ellipse)
	a_f = 3.2mm	- final crack depth
Paris crack growth data:	C = 1.832×10^{-13}	- Paris crack growth constant for units of N and mm
	m = 3.0	- Paris crack growth exponent
T-butt geometry:	L/T = 1.0	- attachment footprint width for T-butts
	θ = 45°	- attachment weld angle for T-butts
	ρ/T = 0.01	- attachment weld toe radius for T-butts
	a at c = 0.1mm	- crack depth at the crack ends for 2-D T-butt based solutions
Tubular joint geometry:	T = 32.0mm	- main plate or chord thickness
	β = 0.5	- ratio of the brace to chord diameter for tubular joints
	γ = 14.29	- ratio of the chord diameter to twice the chord thickness
	τ = 0.5	- ratio of the brace to chord thickness for tubular joints
Stress field data:	σ_{nom} = 20.0Nmm^{-2}	- nominal axial stress applied to the brace
	SCF = 6.58	- stress concentration factor at the hot spot of the tubular joint
	DOB = 0.79	- degree of bending at the hot spot location
	S = 1.62	- average intersection stress ratio for Dover et al.'s solutions

presented as linear functions of the uncracked stress field parameters SCF stress concentration factor and DOB degree of bending (= bending stress / hot spot stress).

Ho et al. (1995) performed 1200 3-D finite element analyses of axially loaded, cracked tubular Y-joints. They related their stress intensity factors to the SCF and found that the effect of the DOB was negligible. The four resulting curves (one for each a/c) are only applicable to the deepest point of the crack and are valid only for β = 0.6 and 0.8, 60° Y-joints.

The most complex of all the solutions reviewed in this paper are those of Rhee et al. (1991), who were the first to develop parametric equations for tubular joint SIFs. 120 3-D finite element analyses of tubular T-joints containing semi-elliptical saddle cracks were performed and the results regressed into equations that are functions of the standard tubular joint geometric ratios. They are valid for T-joints subjected to axial loading and in- and out-of-plane bending, and are applicable to the crack ends as well as the deepest point.

3 COMPARISON OF SIF SOLUTIONS

In this section, the results from the crack growth simulations are reported so that the effect of the differences in the SIF solutions on fatigue calculations may be quantified. The crack growth calculations were performed using the Paris crack growth law and, to simplify the comparisons, no account was taken of the threshold SIF, crack closure and the loading ratio. A single semi-elliptical crack was assumed in the calculations, with the integration performed at both the deepest point and the crack ends. Each increment of the simulation comprised of 10 load cycles and the changes in the crack depth and width were calculated accordingly. For those solutions which cannot be applied to the crack ends, the integration was carried out at the deepest point only.

In the first crack growth simulation, the performance of the SIF solutions for very shallow cracks was tested. Shallow cracks are important because the majority of the total fatigue life is consumed in this phase. From the Background to New Fatigue Design Guidance (HSE 1995), it was suggested that an initial flaw of depth 0.1mm - 0.25mm yields a fracture mechanics prediction comparable to laboratory fatigue tests. Hence, an initial semi-circular flaw of depth 0.1mm was used. Details of the input data are given in Table 2.

The results of the fatigue calculations are summarised in Table 3, where the number of load cycles is that taken for the crack to propagate to a depth of 3.2mm (a/T = 0.1). The solutions of Bell et al. are not included in the comparisons because they are not in equation form and those of Haswell cannot be extended to such shallow cracks. It should be noted that many of the solutions have been used beyond their validity ranges.

The experimentally inferred solutions of Dover et al. give predictions ranging from a third to one and two third of a million cycles (the Inherent Flaw

Table 3. Crack growth calculation results for a shallow crack

Solutions of	Cycles ($N \times 10^6$)	Final a/c
Dover et al. (Inherent flaw model)	1.68	—
Dover et al. (Average stress model)	0.36	—
Dover et al. (Two phase model)	0.48	—
Newman & Raju	6.87	0.84
PD6493	0.75	0.29
Aaghaakouchak et al.	0.80	0.27
Dijkstra et al.	1.18	0.34
Pang	0.77	0.52
Fu et al.	0.69	0.21
Thurlbeck et al.	0.74	0.34
Bowness & Lee	0.73	0.31
Rhee et al.	The crack grows infinitely large after one increment	
Ho et al.	18.27	1.0 (constant = initial a/c)

Model is, strictly, valid only for T = 16mm joints). When compared to the numerically derived solutions, the Average Stress Model and Two Phase Model give a much lower number of load cycles. This could, in part, be due to multiple initiation and crack growth and crack coalescence which are all inherent in the inferred solutions. The solutions from PD6493, Aaghaakouchak et al., Thurlbeck et al. and Bowness & Lee all produce predictions close to three quarters of a million cycles and a final aspect ratio near to one third. The solutions of Pang and Fu et al. also predict a similar number of load cycles, although the former produces a final crack that is more rounded, whilst the latter predicts the opposite. The blanket reductions in the solutions of Dijkstra et al. result in a high (unconservative) fatigue prediction. The plain plate results of Newman & Raju, which yield a highly unsafe (large) prediction of nearly seven million cycles, illustrate how important it is to account for the stress raising effect at the weld toe for shallow cracks. The remaining two solutions are even worse – Ho et al. gives a life of over eighteen million cycles, and Rhee et al. are unable to give any prediction at all because the crack grows infinitely large in the first growth increment. The problem with Ho et al.'s solutions is that they cannot be applied to the crack ends and so a/c cannot be updated from its original value, unless a predetermined variation is assumed. Rhee et al.'s equations, for an axially loaded T-joint, give an almost infinite stress intensity factor for such a small crack depth leading to an infinitely large growth in the crack depth and width.

The second crack growth simulation was designed to compare the solutions over the remainder of the crack depth range. All crack data are the same as those in the previous simulation, except for those given in Table 4. The results for the predicted number of load cycles are given in Figure 3 and the crack shape development is shown in Figure 4.

In Figure 3a, the tubular joint solutions may be seen to predict very different propagation lives. The Inherent Flaw Model yields the most conservative (lowest) life although, as already mentioned, it is strictly valid only for a chord thickness of 16mm. The solutions of Haswell also produce a low prediction due to the constant aspect ratio (a/c = 0.2). At the other extreme, the solutions of Ho et al. never reach the final crack depth as the crack stops growing at a/T = 0.83. This is due to the constant aspect ratio (= a/c initial) used throughout the fatigue simulation. The Average Stress Model and Two Phase Model are in very close agreement, yielding a life of around 900,000 cycles, whilst the solutions of Rhee et al. slightly under predict this.

The results from the solutions derived from simplified geometries, shown in Figure 3b, exhibit a lesser, but nevertheless still large, spread in propagation lives. Comparing with the results from

Table 4. Input data for the second crack growth simulation

Crack data:	a_0 = 3.2mm	- initial crack depth (a/T = 0.1)
	c_0 = 6.4mm	- initial crack half width (a/c = 0.5)
	a_f = 28.8mm	- final crack depth (a/T = 0.9)

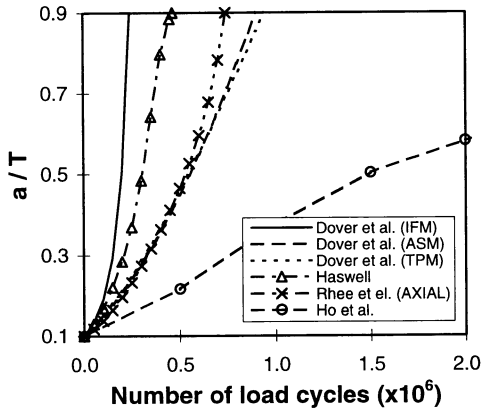

(a) tubular joint solutions

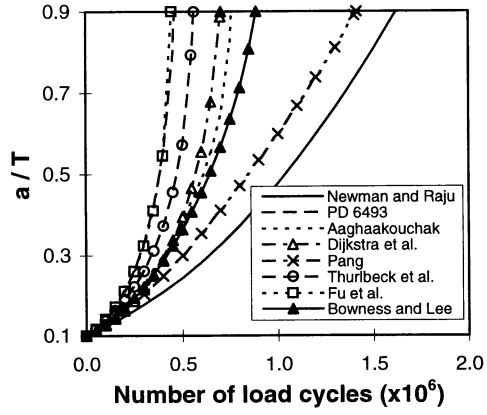

(b) solutions from simplified geometries

Figure 3. Crack growth comparisons - predicted number of load cycles

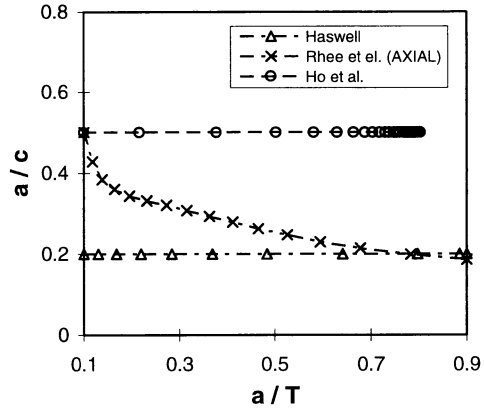

(a) tubular joint solutions

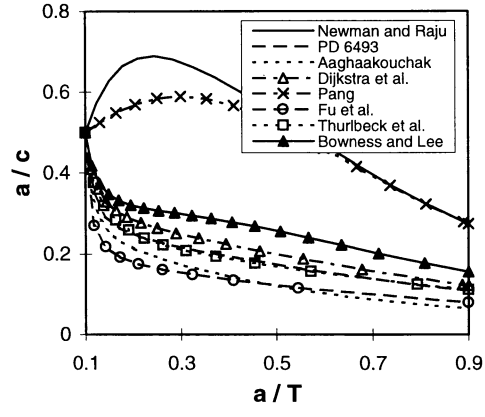

(b) solutions from simplified geometries

Figure 4. Crack growth comparisons - crack shape development

the tubular joint solutions (Figure 3a), the solutions of Dijkstra et al. and Aaghaakouchak et al. give a life close to that of Rhee et al. and Bowness & Lee's prediction is close to that of Dover et al's Average Stress Model and Two Phase Model. Thurlbeck et al.'s result is slightly lower, at just over half a million cycles, and the Fu et al. and PD6493 results are lower still. As expected, the plain plate results of Newman & Raju, used without correction, produce the largest life prediction because the stress raising effect of the weld toe is not included. Pang's difference function results in a life closest to that for the plain plate, which is not surprising as it is effectively unity when the crack depth ratio *a/T* exceeds 0.25.

With regard to crack shape development, Figure 4a, the aspect ratio does not change when using the solutions of Haswell and Ho et al.. The solutions of Rhee et al., which are the only tubular joint solutions to incorporate crack end SIF values, predict the aspect ratio to drop, from its initial value of 0.5, to just below 0.2 at 90% of the chord wall thickness.

For the solutions from simplified geometries, those of Newman & Raju and Pang again produce similar results suggesting that the crack should become more rounded in the early stages of crack growth before it widens. In contrast, all the other solutions predict the crack to widen throughout its propagation life. Aaghaakouchak et al. and Fu et al.'s solutions result in the widest final crack shape of below $a/c = 0.1$. The solutions of Thurlbeck et al., PD6493 and Dijkstra et al., produce a slightly narrower crack of around 0.12, and Bowness &

Lee's solutions suggest the crack may be narrower still, at an *a/c* of around 0.17.

4. CONCLUSIONS

The conclusions that can be drawn from this study are:

- Dover et al. – the Average Stress Model and Two Phase Model perform well but their accuracy for more complex joints is unknown.
- Newman & Raju – yield very unsafe fatigue predictions for tubular joints.
- PD6493 – perform reasonably well but are conservative.
- Aaghaakouchak et al. – perform quite well in the comparisons conducted here, but other studies have shown that they are unreliable.
- Dijkstra et al. – perform reasonably well but are unsafe for shallow cracks.
- Bell et al. – their data needs to be regressed into equation form.
- Pang – good for shallow cracks but unsafe over the rest of the crack range.
- Fu et al. – perform reasonably well but are conservative.
- Thurlbeck et al. – perform reasonably well but are conservative.
- Bowness & Lee – perform well over the whole crack range.
- Haswell – cannot be used for shallow cracks and are very conservative over the rest of the crack range.
- Rhee et al. – cannot be used for shallow cracks but otherwise perform very well.
- Ho et al. – perform very poorly.

5. FURTHER WORK

New SIF solutions are currently being developed at Swansea for an extensive range of full 3-D T-butt geometries. This project, which is sponsored by the EPSRC, HSE and Chevron, will significantly improve upon the accuracy and extend the validity ranges of the solutions reviewed in this paper.

6. REFERENCES

Aaghaakouchak, A., Glinka, G. & Dharmavasan, S. 1989 A load shedding model for fracture mechanics analysis of fatigue cracks in tubular joints. *International Conference on Offshore Mechanics and Arctic Engineering*, ASME.

ABAQUS 1995 User's Manual. Version 5.5, Hibbitt, Karlsson and Sorenson Inc.

Bell, R. 1987 Stress intensity factors for weld toe cracks in welded T plate joints. CANMET Project No. 708803, Carleton University, Ottawa, Canada.

Berge, S., Haswell, J.V. & Engesvik, K. 1994 Fracture mechanics analysis of tubular joint tests degree of bending effects. *International Conference on Offshore Mechanics and Arctic Engineering*, ASME, Vol. III.

Bowness, D. 1996 Fracture mechanics based fatigue assessment of weld toe cracks in offshore tubular structures. Ph.D. Thesis, Department of Civil Engineering, University of Wales Swansea, C/PH/201/96.

Bowness, D. & Lee, M.M.K. 1996 Stress intensity factor solutions for semi-elliptical weld-toe cracks in T-butt geometries. *Fatigue and Fracture of Engineering Materials and Structures*, Vol. 19, No. 6, pp. 787-797.

Cheaitani, M.J., Thurlbeck, S.D. & Burdekin, F.M. 1995 Fatigue, fracture and plastic collapse of offshore tubular joints using BSI PD6493:1991. *International Conference on Offshore Mechanics and Arctic Engineering*, ASME, Vol. 3.

Dijkstra, O.D., Snijder, H.H. & van Straalen, I.J. 1989 Fatigue crack growth calculations using stress intensity factors for weld toe geometries. *International Conference on Offshore Mechanics and Arctic Engineering*, ASME.

Dijkstra, O.D., van Straalen, I.J. & Noordhoek, C. 1993 A fracture mechanics approach of fatigue of welded joints in offshore structures. *International Conference on Offshore Mechanics and Arctic Engineering*, ASME, Vol. III-B.

Dover, W.D. & Dharmavasan, S. 1982 Fatigue fracture mechanics analysis of T and Y joints. *Offshore Technology Conference*, OTC 4404.

Dover, W.D. & Connolly, M.P. 1986 Fatigue fracture mechanics assessment of tubular welded Y and K-joints. *International Conference on Fatigue and Crack Growth in Offshore Structures*, C141/86, Institution of Mechanical Engineers.

Fu, B., Haswell, J.V. & Bettess, P. 1992 Shallow surface cracks in welded T butt plates – a 3D linear elastic finite element study. *Conference on Shallow Crack Fracture Mechanics*, Paper 22, The Welding Institute.

Fu, B., Haswell, J.V. & Bettess, P. 1993 Weld magnification factors for semi-elliptical surface cracks in fillet welded T-butt joint models. *International Journal of Fracture*, 63, pp. 155-171.

Haswell, J.V. 1990 A defect assessment methodology for offshore jacket structures including complex joints subject to complex loading. *Integrity of Offshore Structures 4*, Glasgow.

Haswell, J.V. 1991 A fracture mechanics methodology for the assessment of fatigue cracks in tubular joints. Ph.D. Thesis, Teeside Polytechnic.

Haswell, J.V. 1992a A general fracture mechanics model for a cracked tubular joint derived from the results of a finite element parametric study. *International Conference on Offshore Mechanics and Arctic Engineering*, ASME, Vol. III-B.

Haswell, J.V. 1992b The safe operation of offshore jacket structures containing fatigue cracks. *International Conference on Offshore Mechanics and Arctic Engineering*, ASME, Vol. III-B.

Health and Safety Executive 1995 Background to new fatigue design guidance: For steel joints and connections in offshore structures. Draft copy from the UK Health and Safety Executive.

Ho, C.M. & Zwerneman, F.J. 1995 Assessment of simplified methods. Joint Industry Project on Fracture Mechanics Investigation of Tubular Joints: Phase II, Oklahoma State University.

Kam, J.C.P. & Dover, W.D. 1987 Structural integrity of welded tubular joints in random load fatigue combined with size effects. *Third International Conference on the Integrity of Offshore Structures*, Glasgow.

Maddox, S.J. 1975 An analysis of fatigue cracks in fillet welded joints. *International Journal of Fracture*, Vol. 11, No. 2.

Maddox, S.J. 1996 Fatigue crack growth in tubular T-joints under in-plane bending. *Seventh International Symposium on Tubular Structures*, Miskolc, Hungary.

Newman, J.C. & Raju, I.S. 1979a Stress-intensity factors for a wide range of semi-elliptical surface cracks in finite-thickness plates. *Engineering Fracture Mechanics*, Vol. 11, pp. 817-829.

Newman, J.C. & Raju, I.S. 1979b Analyses of surface cracks in finite plates under tension or bending loads. NASA Technical Paper 1578.

Newman, J.C. & Raju, I.S. 1981 An empirical stress intensity factor equation for the surface crack. *Engineering Fracture Mechanics*, Vol. 15, No. 1-2, pp. 185-192.

Pang, H.L.J. 1991 A literature review of stress intensity factor solutions for a weld toe crack in a fillet welded joint. National Engineering Laboratory, Report No. 721.

Pang, H.L.J. 1993a A review of stress intensity factors for a semi-elliptical surface crack in a plate and fillet welded joint. *The Welding Institute Journal*, Vol. 2, No. 4, pp. 377-385.

Pang, H.L.J. 1993b Fatigue crack growth and coalescence of surface cracks. *International Conference on Offshore Mechanics and Arctic Engineering*, ASME, Vol. III-B.

Pang, H.L.J. & Gray, T.G.F. 1993 Fatigue analysis of surface cracks at fillet welded toes. *Fatigue and Fracture of Engineering Materials and Structures*, Vol. 16, No. 2, pp. 151-164.

PD6493 1991 Guidance on Methods for Assessing the Acceptability of Flaws in Fusion Welded Structures. British Standards Institution.

Rhee, H.C. 1991 Reliability of solution method and empirical formulas of stress intensity factors for weld toe cracks of tubular joints. *International Conference on Offshore Mechanics and Arctic Engineering*, ASME, Vol. III-B.

Stacey, A. & Sharp, J.V. 1995 The revised HSE fatigue guidance. *International Conference on Offshore Mechanics and Arctic Engineering*, Volume III.

van Straalen, I.J., Dijkstra, O.D. & Snijder, H.H. 1988 Stress intensity factors and fatigue crack growth of semi-elliptical surface cracks at weld toes. *International Conference on Weld Failures*, The Welding Institute, London.

van Straalen, I.J. & Dijkstra, O.D. 1991 Application of the fracture mechanics approach to the fatigue behaviour of welded tubular steel structures. *Fourth International Symposium on Tubular Structures*, Delft.

Thurlbeck, S.D. 1991 A fracture mechanics based methodology for the assessment of weld toe cracks in tubular offshore joints. Ph.D. Thesis, UMIST.

Thurlbeck, S.D. & Burdekin, F.M. 1992 Constant and variable amplitude LEFM fatigue assessment for tubular joints incorporating threshold effects. *International Conference on Offshore Mechanics and Arctic Engineering*, ASME, Vol. III-B.

Members and columns



Taylor & Francis
Taylor & Francis Group
http://taylorandfrancis.com

Tubular Structures VIII, Choo & Van der Vegte (eds) © 1998 Balkema, Rotterdam, ISBN 90 5809 001 9

Dynamic failure of bent tubular cantilevers under dynamic tip loading

B.Wang
School of Engineering and Technology, Deakin University, Australia
M.H.Yang
Flour Daniel, Melbourne, Vic., Australia
W.C.Fok
School of Mechanical and Production Engineering, Nanyang Technological University, Singapore

ABSTRACT: A theoretical model is constructed for a large deflection analysis of a rigid-perfectly plastic bent cantilever with a tip mass loaded by a dynamic transverse follower force applied to its tip. The purpose of constructing and analysing such a model is to provide an analytical basis for studying unconstrained pipe whip. The equations for travelling hinge phases are derived and solved numerically. Pipe kinetics and deformation are deducted and comparisons are made to one pipe wipe test.

1 INTRODUCTION

In many structural and mechanical systems, two dimensional components, such as a bent joint are used extensively. Recently, attentions have been given to bent tubular components under in-plane impact loading. The phase "in-plane" indicates that the applied force acts in the plane of the bent segments of a two dimensional configuration. Many works have been carried out in this area. Based on a small deflection assumption, the in-plane impact problem of curved beams was addressed by Owens & Symonds (1955), Yu & Johnson (1981), Yu et al (1985, 1986). More recently, an extensive study was made by Stronge et al (1990) on curved cantilevers, rings and arches. They found that displacement constraints which make the tangential force increases with the applied force result in an indefinitely large number of failed segments for the mode during the impulsive loading. This is unrealistic and could be due to the ignorance of shear interactions which might have led to an alternative yield mechanism.

In this paper, a large deflection analysis is reported for a closing mode under a suddenly applied follower force at the tip in the plane of the beam. This means the beam segments are forced to move closer to each other (thus being termed a closing mode". One key feature of a large deflection analysis is the influence of the axial force caused by the centrifugal effect, which does not exist in a small deflection analysis. Numerical results reveal that a hinge will be formed in the first segment of the beam and moved towards the bend. It then crosses the bend and moves into the second segment. The hinge will travel along the second segment towards the root, but may not arrive there. It may stop somewhere inside the second and the value of this stopping position, indicated by a distance from the bend, depends on the value of the bend and the magnitude of the input force.

In this analysis, it is assumed that the beam material is rigid, perfectly plastic and rate independent, and the dynamic load at the beam tip is a follower one, i.e., fixed in its direction relative to the beam axis it is applied onto, but its magnitude may be time dependent, simulating the close up of the tube cross section. Under a combined bending-stretching load, the yield criterion of the beam is given as

$$\frac{M}{M_0}+\left(\frac{N}{N_0}\right)^2=1 \qquad (1)$$

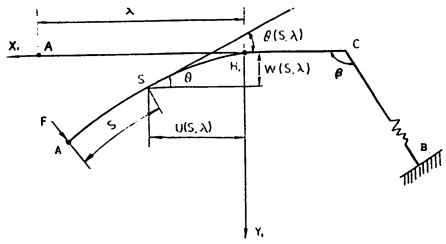

Fig.1 coordinates and displacements during phase i

where M and N are the bending moment and axial force applied on the beam, respectively. M_0 and N_0 are dynamic fully plastic bending moment and axial capacity of the beam. As discussed in a previous study (Wang, 1991), the influence of the axial strain rate due to N is negligible, thus it is not considered here for simplicity.

2. THEORETICAL MODELLING

Consider a β-angled bent tubular beam ACB with the length of each segment L_1 and L_2, as shown in Figure. 1. The cantilever beam is subjected to a suddenly applied transverse follower force F acting at its tip A, perpendicular to the segment AC in the plane of the beam. The beam is allowed to undergo finite deformation.

For a dynamic force of a relatively low magnitude (but still higher than the static limit load of the beam), a plastic hinge may appear at the beam root B or in segment CB. Here we only consider the case with a dynamic force with a higher magnitude resulting in a hinge formed in AC. As may be seen in the following, this covers every feature of the "in-plane" problem.

Figure 1 shows the variables used to describe the beam deflection. s is an intrinsic coordinate for an arbitrary point S in the deformed segment AH measured along the central axis from the tip. λ is the position of the plastic hinge formed in AC, measured from the tip. u and w, the coordinates of S measured from the hinge in the X and Y directions, are thus given by,

$$u(s,\lambda) = \int_s^\lambda \cos\vartheta(\xi,\lambda)d\xi \tag{2}$$

$$w(s,\lambda) = \int_s^\lambda \sin\vartheta(\xi,\lambda)d\xi \tag{3}$$

where the inclination of the beam at S when the hinge is at λ is defined as

$$\vartheta(s,\lambda) = \int_s^\lambda \kappa(\xi)d\xi \tag{4}$$

$\kappa(\xi)$ being the curvature of the neutral axis.

These definitions are quite similar to those used in the large deflection analyses of a straight beam by Ting (1964), Stronge & Shioya (1984) and Wang (1991).

2.1 *Travelling hinge in AC*

This is the first phase of the response when a high magnitude transverse force is suddenly applied at the beam tip, in the plane of the beam segments. As a plastic hinge H is formed in AC and there is no deformation in CB, by applying the D'Alembert's principle, the equation of the translational motion for segment AH in y direction can be derived using the definitions in Eqns. (2) to (4):

$$\begin{aligned}&\left[Gu(\lambda)+\mu i_1(\lambda)\right]\ddot{\vartheta}+(G+\mu\lambda)\dot{\lambda}\dot{\vartheta}\\&-\left[Gw(\lambda)+\mu i_2(\lambda)\right]\dot{\vartheta}^2 = F\cos\vartheta\end{aligned} \tag{5}$$

where G is a concentrated mass at the tip of A, μ is the mass per unit length of the beam segment, u and w are coordinates of the tip with respect to the current hinge position in AC, λ is the hinge position from the tip. i_1 and i_2 are the first moments of the deformed beam segment about axes X and Y, respectively, being defined as

$$i_1(\lambda) = \int_0^\lambda u(s,\lambda)ds \quad \text{and} \quad i_2(\lambda) = \int_0^\lambda w(s,\lambda)ds.$$

Similarly, we have the equation of the translational motion in x direction,

$$\begin{aligned}&\left[Gw(\lambda)+\mu i_2(\lambda)\right]\ddot{\vartheta}+\left[Gu(\lambda)+\mu i_1(\lambda)\right]\dot{\vartheta}^2\\&= F\sin\vartheta + N\end{aligned} \tag{6}$$

where N is the axial force at the hinge due to the centrifugal motion of the deformed segment.

The equation of the rotational motion about the current hinge is

$$\left\{G\left[u(\lambda)^2 + w(\lambda)^2\right] + \mu i_0(\lambda)\right\}\ddot{\vartheta}$$
$$+\left[Gu(\lambda) + \mu i_1(\lambda)\right]\dot{\lambda}\dot{\vartheta} \qquad (7)$$
$$= F\left[u(\lambda)\cos\vartheta + W(\lambda)\sin\vartheta\right] - M$$

where i_0 is the second moment of the deformed segment about the current hinge,

$$i_0(\lambda) = \int_0^{\lambda}\left[u(s,\lambda)^2 + w(s,\lambda)^2\right]ds.$$

At hinge H, the yield criterion is defined by Eqn. (1). The initial hinge position λ_0 at the beginning of the motion is determined by a small deflection analysis which gives

$$\lambda_0 = \frac{3\mu M_0 + \sqrt{9\mu^2 M_0^2 + 24\mu G M_0 F_0}}{2\mu F_0}.$$

F_0 is the magnitude of the dynamic force at time zero. This value of λ_0 can be derived from the above governing equations by letting $\vartheta = 0$, $M = M_0$ and $N = 0$.

Due to the large deflection of the beam, the hinge will travel along AC towards bend C. Eventually the hinge will reach C and this ends the first phase of the response. The complexity of the equations prevents closed-formed solutions being achieved. Standard numerical procedures, such as a fourth order Runge-Kutta approach can be applied to solve the equations. Numerical results will be discussed later in the paper.

2.2 *Hinge in segment CB*

When the hinge crosses the bend and moves into segment CB, AC stops deforming and starts to rotate about the travelling hinge as a rigid body, continuously closing the angle between the two segments. This is the second phase of the response.

In order to describe the motion of the deformed beam segment, a more complicated coordinate system has to be set up compared with that used in Phase one.

Let η be the position of the hinge in CB and system X_1CY_1 fixed at C moving with segment AC, as shown in Figure 2. A global system XBY has its origin at B and X in the direction of the un-deformed CB. While local moving system $X_2H_2Y_2$ has its origin at H_2 in CB and X_2 in the direction of

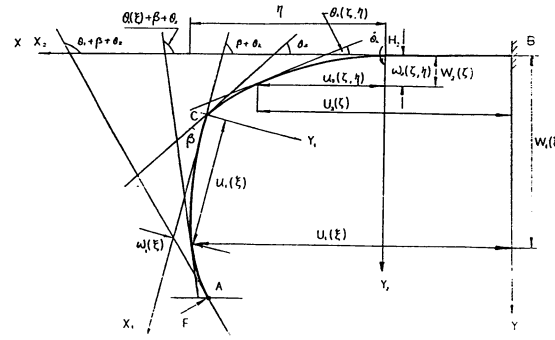

Fig.2 Coordinates and displacements during phase ii

X. Note that system $X_2H_2Y_2$ only moves linearly with H_2 without any rotation. Let ξ be an arbitrary point in the deformed AC, it has coordinates $u_1(\xi)$ and $w_1(\xi)$ in the local system X_1CY_1 which is faxed at C and follows the motion of C. These local coordinates of ξ are time independent because segment AC ceases to deform and they are obtained at the final moment of the fist response phase when the hinge reaches the bend C.

For an arbitrary point ζ in CB, its coordinates in the local moving system $X_2H_2Y_2$ are given as

$$u_2(\zeta) = \int_0^{\eta}\cos\vartheta_2(\zeta,\eta)d\zeta \qquad (8)$$

$$w_2(\zeta) = \int_0^{\eta}\sin\vartheta_2(\zeta,\eta)d\zeta \qquad (9)$$

$\vartheta_2(\zeta,\eta)$ being the rotation of segment CH_2 about hinge H_2 due to bending. It is not difficult to find expressions for coordinates of ζ in the global system XBY:

$$U_2(\zeta,\eta) = L_2 - \eta + u_2(\zeta,\eta) \qquad (10)$$

$$W_2(\zeta,\eta) = w_2(\zeta,\eta) \qquad (11)$$

Clearly, bend C has its coordinates with ζ being zero in the above two equations. For simplicity, let $u_2(0,\eta) = u_2(\eta)$, $w_2(0,\eta) = w_2(\eta)$ and $\vartheta_2(0,\eta) = \vartheta_2$. The global coordinates of point ξ in segment AC can then be written as

$$U_1(\xi,\eta) = L_2 - \eta + u_2(\eta) + u_1(\xi)\cos(\beta + \vartheta_2) - w_1(\xi)\sin(\beta + \vartheta_2) \qquad (12)$$

$$W_1(\xi,\eta) = w_2(\eta) + u_1(\xi)\sin(\beta+\vartheta_2) + w_1(\xi)\sin(\beta+\vartheta_2) \quad (13)$$

Note that subscripts 1 and 2 represent values in segments AC and CB, respectively. $u_1(\xi)$ and $w_1(\xi)$ are constants and the coordinates of point A can be obtained by substituting ξ with zero in Eqns. (12) and (13).

Differentiating equations (10) to (13) gives the absolute velocities and accelerations of points ζ and ξ, then the governing equations of motion can be obtained, in a similar approach as for the Phase I response. The equations for Phase II are listed as follows:

$$I_1\ddot{\vartheta}_2 + \left[G + \mu(L_1+\eta)\right]\dot{\vartheta}_2\dot{\eta} - I_2\dot{\vartheta}_2^2 = F_1 \quad (14)$$

$$I_2\ddot{\vartheta}_2 + I_1\dot{\vartheta}_2^2 = F_2 + N_2 \quad (15)$$

$$I_0\ddot{\vartheta}_2 + I_1\dot{\vartheta}_2\dot{\eta} = F_3 - M_2 \quad (16)$$

where

$$I_1 = G\left[u_2(\eta) + u_1(0)\cos(\beta+\vartheta_2) - w_1(0)\sin(\beta+\vartheta_2)\right] + \mu\left[L_1 u_2(\eta) + i_{1,1}\cos(\beta+\vartheta_2) - i_{1,2}\sin(\beta+\vartheta_2)\right]$$

$$I_2 = G\left[w_2(\eta) + u_1(0)\sin(\beta+\vartheta_2) + w_1(0)\cos(\beta+\vartheta_2)\right] + \mu\left[L_1 w_2(\eta) + i_{1,1}\sin(\beta+\vartheta_2) + i_{1,2}\cos(\beta+\vartheta_2)\right]$$

$$I_0 = G\left\{\begin{array}{l} u_1^2(0) + w_1^2(0) + u_2^2(\eta) + w_2^2(\eta) \\ +2u_2(\eta)\left[\begin{array}{l} u_1(0)\cos(\beta+\vartheta_2) \\ -w_1(0)\sin(\beta+\vartheta_2)\end{array}\right] \\ +2w_2(\eta)\left[\begin{array}{l} u_1(0)\sin(\beta+\vartheta_2) \\ +w_1(0)\cos(\beta+\vartheta_2)\end{array}\right]\end{array}\right\}$$

$$+\mu\left\{\begin{array}{l} i_{1,0} + \left[u_2^2(\eta) + w_2^2(\eta)\right]L_1 + i_{2,0} \\ +2u_2(\eta)\left[\begin{array}{l} i_{1,1}\cos(\beta+\vartheta_2) \\ -i_{1,2}\sin(\beta+\vartheta_2)\end{array}\right] \\ +2w_2(\eta)\left[\begin{array}{l} i_{1,1}\sin(\beta+\vartheta_2) \\ +i_{1,2}(0)\cos(\beta+\vartheta_2)\end{array}\right]\end{array}\right\}$$

$$F_1 = F(t)\cos(\vartheta_1+\beta+\vartheta_2)$$

$$F_2 = F(t)\sin(\vartheta_1+\beta+\vartheta_2)$$

$$F_3 = F(t)\left[\begin{array}{l} u_2(\eta)\sin(\vartheta_1+\beta+\vartheta_2) \\ +w_2(\eta)\sin(\vartheta_1+\beta+\vartheta_2) \\ +u_1(0)\cos\vartheta_1 + w_1(0)\sin\vartheta_1\end{array}\right]$$

The following are the first and second moment of the deformed segments to their corresponding local coordinates and the hinge, respectively.

$$i_{1,1}(\lambda) = \int_0^{L_1} u(s,L_1)ds$$

$$i_{1,2}(\lambda) = \int_0^{L_1} w(s,L_1)ds$$

$$i_{1,0}(\lambda) = \int_0^{L_1}\left[u(s,L_1)^2 + w(s,L_1)^2\right]ds$$

$$i_{2,1}(\lambda) = \int_0^{\eta} u(s,\eta)ds$$

$$i_{2,2}(\lambda) = \int_0^{\eta} w(s,\eta)ds$$

$$i_{2,0}(\lambda) = \int_0^{\eta}\left[u(s,\eta)^2 + w(s,\eta)^2\right]ds .$$

M_2 and N_2 are the bending moment and axial force at the hinge in CB. The yield condition in CB remains the same as in AC. Combined with Eqn. (1), Eqns. (14) to (16) form the basic set of equations for solutions of the travelling hinge in CB. They can be solved by standard numerical procedures.

3. NUMERICAL SOLUTIONS AND COMPARISONS WITH TESTS

For numerical calculations, the structural parameters of the beam were set as M_0=*310Nm*, N_0=*36714N*, μ=*0.971kg/m*, G=*0.3kg*, L_1=*1.36m* and L_2=*2.16m*, based on the data of tube specimens used in the laboratory tests. The numerical procedure used was a standard fourth-order Runge-Kutta approach.

Numerical simulations show three response steps under a step load (a suddenly applied constant force) of *2,000N*. First in Phase one, a hinge forms in segment AC following the application of the dynamic force at tip A. The position of the initial hinge depends on the

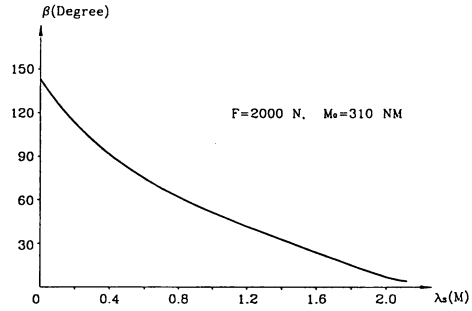

Fig.3 Stationary hinge position in segment CB versus bend angle

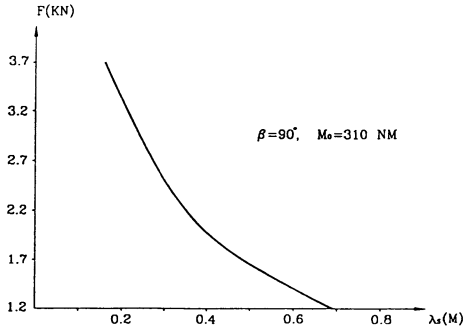

Fig. 4 Stationary hinge position in segment CB versus load level

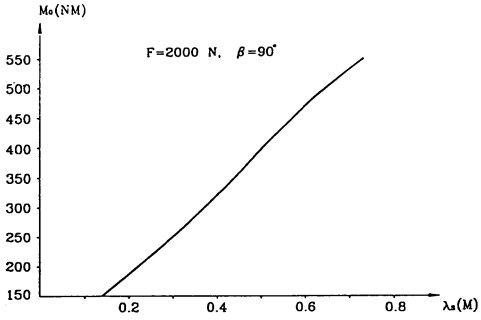

Fig. 5 Stationary hinge position in segment CB versus bending moment

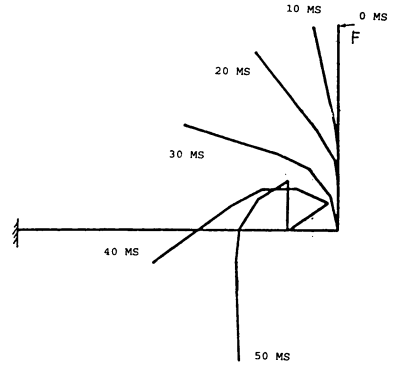

Fig.6 Deformed configurations of a bent cantilever undergoing a closing mode

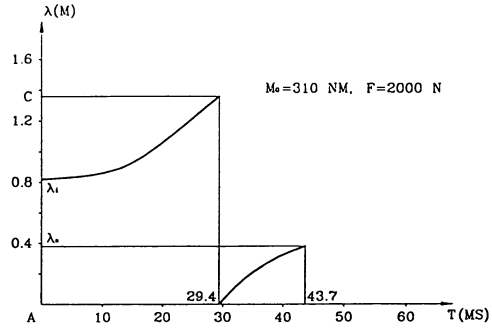

Fig. 7 Hinge position versus time

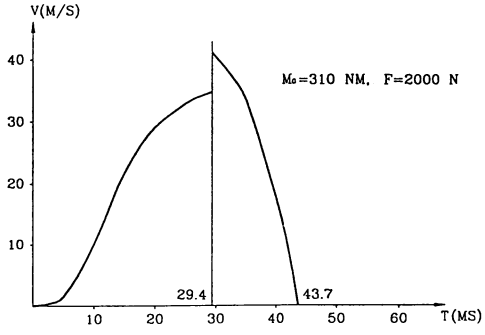

Fig. 8 Hinge velocity versus time

magnitude of the load. The hinge then moves towards the bend of the cantilever. After it reaches there, AC stops deforming and becomes rigid. This completes Phase One. Values of all variables obtained at the end of Phase One become the initial condition of Phase Two.

Phase II starts after the hinge crosses the bend and moves into CB. It travels towards the beam root B with the deformed AC and deforming BH_2 rotating about the moving hinge H_2. Calculations show that while the hinge travels towards B, it does not reach the root but stops somewhere inside the segment CB, then the beam rotates about the stationary hinge in a rigid body

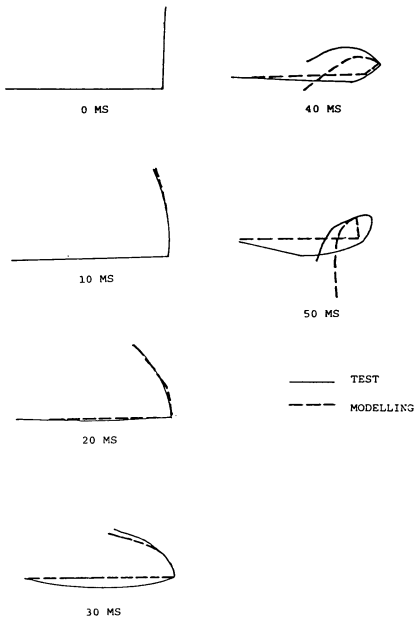

Fig.9 Comparisons between the analytical and test results

motion without further configuration changes. This is Phase III. It is shown that the stopping position of the hinge λ_s measured from C is determined by the value of the bend angle, the magnitude of the applied force and the value of M_0. The relationship between the value of the stopping position and the bend angle is illustrated in Figure 3. When the bend angle is close to zero, the stopping position tends to infinitive from the bend. This is in agreement with a large deflection analysis on straight beams (Wang, 1991). When the bend angle is big, the travelled distance of hinge in CB is shorter. And when the bend angle is more than 143° and the load is *2,000N*, the hinge stays at C and does not move into CB at all, giving a zero stopping distance. It is also noted that when the applied load is higher, the travelled distance in CB is shorter. Figure 4 shows the hinge stopping distance from the bend against the load magnitude for a right-angled bent cantilever. The stopping distance is also influenced by M_0 as illustrated by Figure 5 in an almost linear manner.

Figure 6 shows the calculated response of a right-angled bent cantilever. In the last phase of the response, Phase III, the hinge rests at its limiting stationary position in CB and segment ACH_2 rotates rigidly about the hinge. In the calculation, the applied force was set to be removed when the local rotation reaches $\pi/2$, as the seal-off of the tube for escaping liquid. This enables the remaining kinetic energy to be dissipated at the plastic hinge, and eventually to stop the beam. Figures 7 & 8 give the history of the hinge position and velocity. It is seen that the hinge speed decreases dramatically soon after it moves into segment CB. Figure 9 shows the comparison of the analytical solution to one of the tests reported by Reid (1991). The simulation agrees reasonably well with the test. The stopping of the travelling hinge in CB is clearly shown.

4. SUMMARY AND CONCLUSIONS

The dynamic responses for an in-plane closing mode of a tubular bent cantilever has been analysed. Compared with test results, it shows that a single hinge mechanism can provide a reasonable description of the response for the in-plane deformation problem.

A large deflection analysis reveals that a travelling hinge will appear close to the beam tip following the application of a suddenly applied constant force. The hinge will move along the beam segment, cross the bend, then move towards the beam root. In a closing mode, the hinge may stop somewhere inside the second segment of the beam and become a stationary hinge. The stopping position, measured as the distance from the bend, is determined by the bend angle, the magnitude of the applied force and the value of the dynamic fully plastic bending moment of the beam. If the force is high and the angle is big, the hinge may remain at the bend and never move into the second segment. It is also noted that manipulations with the value of the yield stress of the beam, or the value of M_0 (though simulation results appear not sensitive to the value of N_0) may produce deformed configurations closer to the test, indicating that material hardening and geometric softening (collapse of the cross-section leading to a lower load-bearing capacity) may happen during the dynamic response.

The results presented in this paper demonstrates that in terms of the deformed configuration, a single hinge mechanism can describe reasonably well the motion of a bent tube undergoing a finite in-plane deflection compared with the test result. However, a more careful study reveals that during Phase I of the response while the hinge is travelling in segment AC, in addition

to M_0, the centrifugal force N due to the moving AH will produce additional bending moment in CB and cause the yield condition in it to be violated. Thus this single hinge mode is not a complete solution. An additional stretch-bending hinge may appear in CB when the rotating velocity is high and the magnitude of N cannot be neglected. This double-hinge mechanism is yet to be studies.

ACKNOWLEDGEMENT

The authors acknowledge Professor S. R. Reid for his encouragement and guidance throughout this work.

REFERENCES

Owens, R. & Symonds, P.S. 1955. Plastic deformation of a free ring under concentrated dynamic loading, J. Appl. Mech., 22:523-539.

Reid, S.R. 1991. Final report to National Nuclear Corporation Plc (UK) on Contract CON/BC/2273.

Stronge, W.J., Shu, D. & Shim, V. P-W., 1990: Dynamic modes of plastic deformation for suddenly loaded curved beams, Int. J. Impact Engng., 9:1-18.

Stronge, W.J. & Shioya, T. 1984. Impact and bending of a rigid-plastic fan blade, J. Appl. Mech., 32: 84-Wa/APM-14.

Ting, T.C.T. 1964. Large deformation of a rigid, ideally plastic cantilever beam, J. Appl. Mech.: 64-WA/APM-25.

Yu, T.X. & Johnson, W. 1981. The location of the plastic hinge in a quadrant circular curved beam struck in its plane by a jet at its tip, ASME Advan. Aero. Struc. Mater. Conf., Washington, Wang, S.S. & Benton, W.J. (eds):175-180.

Yu, T.X., Symonds, P.S. & Johnson, W. 1985. A quadrant circular beam subjected to radial impact in its own plane at its tip by a rigid mass, Proc. Roy. Soc., A400:19-36.

Yu, T.X., Symonds, P.S. & Johnson, W. 1986. A reconsideration and some new results for the circular beam impact problem, Int. J. Impact Engng., 4:221-228.

Wang, B. 1991. Response of two-dimensional piping system during pipe whip, Ph.D Thesis, UMIST.



Taylor & Francis
Taylor & Francis Group
http://taylorandfrancis.com

Tubular Structures VIII, Choo & Van der Vegte (eds) © 1998 Balkema, Rotterdam, ISBN 90 5809 001 9

Cyclic inelastic behavior of compact steel tubular columns

I. H. P. Mamaghani & Y. Kajikawa
Department of Civil Engineering, Kanazawa University, Japan

ABSTRACT: The present study is concerned with the cyclic inelastic behavior of compact steel tubular columns of cantilever type subjected to combined constant axial load and cyclic lateral displacement. The two-surface plasticity model is employed for material nonlinearity in the beam-column finite element formulation used in the analysis. First, the cyclic plasticity performance of the formulation is verified and is found to be good when compared with the results of experiments. Later, based on the results of an extensive numerical analysis using the developed formulation, the effects of some important parameters, such as column slenderness ratio, steel grade, loading history, and cross-section shape on the cyclic behavior and energy absorption capacity of compact steel tubular columns are discussed and evaluated.

1 INTRODUCTION

Steel tubular columns are widely used as cantilever bridge piers and columns in buildings and offshore structures. During extreme loading conditions, such as severe earthquakes, winds and ocean waves, the tubes are subjected to cyclic lateral loads in addition to the constant axial load of the supported structures. This leads to their damage and consequent collapse of the structures. For example, during the Hyogoken Nambu Earthquake on January 17, 1995 severe damage and even total collapse of such bridge piers occurred in and around Kobe city in Japan resulting in a considerable disruption to the transportation and relief works (*IGNTSDSS* 1996). Therefore, clear understanding of the inelastic cyclic behavior of steel tubular columns is important to prevent their collapse under severe earthquake loading.

During the last few years a large number of experiments have been conducted to study the inelastic behavior of steel tubular columns of cantilever type, modeling bridge piers, under the combined action of the dead load along the axial direction and the cyclic lateral loads (among others, Tsuji & Nakatsuka 1986, Usami et al. 1992, Tominaga & Yasunami 1994, Sueda et al. 1997). However, an accurate analytical study of the cyclic inelastic behavior of steel tubular columns has attracted limited attention (Mamaghani et al. 1996a). From the experimental studies, it was found that the main factors influencing the inelastic behavior of steel tubular columns are the cyclic mechanical properties of material, column slenderness ratio, radius-to-thickness ratio, and magnitude of the axial load (Usami et al. 1992, Mamaghani 1996a, Sueda et al. 1997).

On the other hand, energy absorption through hysteretic damping is one of the great interest in seismic design. Because it can reduce the amplitude of seismic response, thereby reducing the ductility demand on the structure (Usami et al. 1992). Therefore, further investigation is still needed to clarify the interaction effects of the steel grade (material properties, such as, yield plateau, Bauschinger effect and cyclic strain hardening), loading history and structural parameters on the hysteretic behavior and energy absorption capacity of the steel tubular columns under cyclic loads.

The present paper is concerned with the cyclic inelastic large displacement analysis of compact steel tubular columns of cantilever type. The study has been confined to compact design and ignores local buckling. An elastoplastic finite element formulation for beam-columns, considering geometrical and material nonlinearities, was coded and implemented in the computer program FEAP

(Zienkiewics 1977) used in the analysis. The two-surface plasticity model(2SM) (Mamaghani et al. 1995, Shen et al. 1995), was adopted for material nonlinearity.

The developed beam-column element formulation incorporating the 2SM for material nonlinearity accounts for the cyclic behavior of structural steels within the yield plateau, Bauschinger effect, cyclic strain hardening as well as gradual variation of section properties in line with the spread of plasticity across the section and along the member length. It has the advantage of avoidance of generating the moment-curvature curve required in the lump plasticity method of analysis. The cyclic plasticity performance of the formulation is examined by comparing with experiments. It is found that the beam-column formulation (2SM) can predict with a high degree of accuracy the experimentally observed cyclic behavior of steel tubular columns.

Using the developed formulation (2SM), a series of numerical experiments on hypothetical specimens is carried out to investigate the cyclic behavior of cantilever type compact steel tubular columns subjected to the combined constant axial load and cyclic lateral displacements. The main parameters considered are: (1) Steel grade; (2) column slenderness ratio, $\bar{\lambda}$; (3) axial load; (4) lateral loading history; and (5) cross-section shape. The effects of these parameters on the cyclic behavior and energy absorption capacity of the compact steel tubular columns are discussed and evaluated.

2 ANALYTICAL METHOD

An elastoplastic analysis based on the finite element method (Clarke 1994), using a conventional beam-column element of three displacements at each node, is employed in the analysis of compact steel tubular columns. The analysis accounts for the spread of plasticity through the cross-section and along the length of member. In this approach, the member analyzed is divided into several beam-column elements along its length, and the cross-section is further subdivided into elemental areas, as shown in Figure 1 for the hollow circular section. Each of the elemental areas is identified by, area dA_i, distance from the section centroid y_i, residual stress and strain, and stress-strain history. The incremental stress-strain relation for each elemental area is described by the 2SM.

In this study, local buckling effect is not consid-

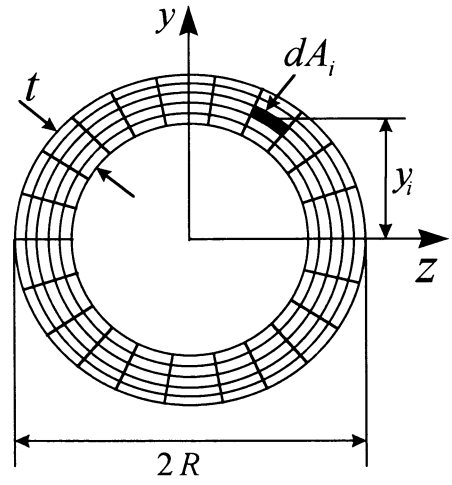

Figure 1. Subdivision of section.

ered so that uniaxial stress-strain relationship (2SM) has been used in the analysis. That is, only longitudinal strain (ε_x) is considered and so at any elemental area in the cross-section (Fig. 1) yielding is assumed to occur as a result of longitudinal stress (σ_x) only. The stress resultants of axial force and bending moment are calculated simply by summing the contribution of each elemental area over the cross-section (Mamaghani et al. 1996b). The material properties and corresponding 2SM parameters for structural steels JIS SS400, SM490 and SM570 (equivalent to ASTM A36, A242 and A572) are given in Table 1. With respect to detailed information regarding 2SM

Table 1. Material properties and 2SM parameters for steel grades SS400, SM490 and SM570.

Parameter	SS400	SM490	SM570
$E(GPa)$	206.7	205.8	215.6
$\sigma_y(MPa)$	274.4	357	524.3
ν	0.29	0.25	0.25
E_{st}^p/E	2.49×10^{-2}	3.40×10^{-2}	1.02×10^{-2}
ε_{st}^p	1.53×10^{-2}	1.24×10^{-2}	0.00
a	-0.505	-0.528	-0.553
b	2.17	1.88	6.47
c	14.4	18.7	34.8
α	0.191	0.217	0.175
ϵ	5.00×10^2	3.16×10^2	7.00×10^2
f/E	0.30	0.484	0.361
M	-0.37	-0.522	—
E_0^P/E	8.96×10^{-3}	1.01×10^{-2}	7.85×10^{-3}
$\omega\cdot\sigma_y$	3.08	4.0	2.67
$\bar{\kappa}_0/\sigma_y$	1.15	1.13	1.06
σ_u/σ_y	1.81	1.61	1.22
$\zeta\cdot\varepsilon_y^2$	9.89×10^{-4}	1.52×10^{-3}	8.04×10^{-3}

parameters and symbols in Table 1, please refer to the literatures (Mamaghani et al. 1995, Shen et al. 1995).

In all analysis, the column is divided into ten elements along its length and the circular cross-section is subdivided into 5 and 22 layers in the radial and circumferencial directions, respectively (Fig. 1). Initial geometrical imperfection and residual stress are not considered.

The details of the element formulation for beam-column and the procedures of the numerical analysis can be found in the work by Mamaghani (1996). In the following sections, the numerical results will be presented and discussed.

3 VERIFICATION

A series of numerical studies on the cyclic behavior of steel tubular columns is carried out using the developed formulation (2SM) and the results are compared with the experiments. The results for a typical example (test C1, Sueda et al. 1997) presented hereafter are intended to verify the accuracy of the current implementation of the 2SM.

The tested column, shown in Figure 2, had a slenderness ratio parameter of $\bar{\lambda} = 0.38$, radius-to-thickness ratio of $R/t = 15$. The parameter $\bar{\lambda}$ controls the global instability and is defined as

$$\bar{\lambda} = \frac{2h}{r}\frac{1}{\pi}\sqrt{\frac{\sigma_y}{E}} \tag{1}$$

in which, E = the Young's modulus, r = the radius of gyration, h = the height of the column $= 3073mm$; R = the outer radius of the tube $= 300mm$; and t = the thickness of the tube $= 20mm$. The material used was SS400 with the measured yield stress of $\sigma_y = 285MPa$ (Sueda et al. 1997).

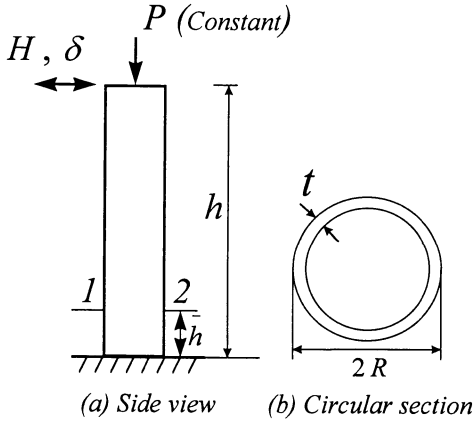

Figure 2. Steel tubular column.

The tested column was subjected to a constant axial load of $P/P_y = 0.086$ (P_y is the squash load) and cyclic lateral displacement of increasing amplitude at the tip. The R/t ratio inhibits local buckling of the tube. Owing to the smaller value of R/t ratio, local buckling did not occur until lateral displacement reaches at $\delta/\delta_{y0} = 6$. During the test a slight local buckling appeared in the compression side at loading point $\delta/\delta_{y0} = 6$, however, the strength did not deteriorate until lateral displacement of $\delta/\delta_{y0} = 9$, as shown in Figure 3(a) (Sueda et al. 1997).

3.1 *Cyclic behavior*

Figure 3 shows the normalized lateral load H/H_{y0} versus lateral displacement δ/δ_{y0} responses from the experiment and the 2SM. The notations H_{y0} and δ_{y0} indicate, respectively, the yield load and yield displacement (neglecting shear deformation)

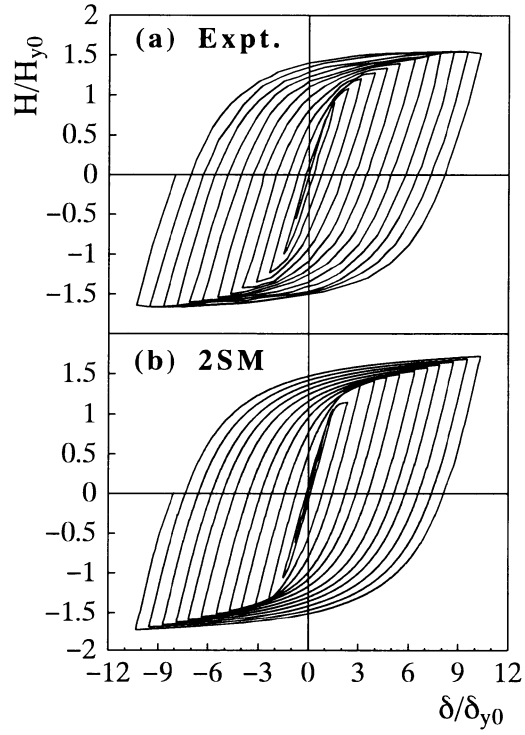

Figure 3. Comparison of the normalized lateral load H/H_{y0} versus lateral displacement δ/δ_{y0} (SS400, $\bar{\lambda} = 0.38$, $R/t = 15$, $P/P_y = 0.086$).

corresponding to zero axial load as follows

$$H_{y0} = \frac{M_y}{h} \tag{2}$$

and

$$\delta_{y0} = \frac{H_{y0}h^3}{3EI} \tag{3}$$

in which , M_y = elastic yield moment; and I = moment of inertia.

Figure 3 shows that the overall shape of the hysteresis loops from the developed formulation (2SM) are significant close to the experimental results mainly owing to the accuracy of the 2SM. These results indicate that the developed formulation is accurate enough. An observed small discrepancy between experimental and analytical (2SM) hysteresis loops is that the predicted cyclic load capacities (Fig. 3), in both directions of loading, are slightly larger than those of the experiment. The two possible reasons are: (1) The initial residual and geometrical imperfections are not considered in the analysis; (2) the effect of local buckling is ignored in the analysis.

3.2 *Energy absorption capacity*

Energy absorption through hysteresis damping can reduce the amplitude of seismic response and, thereby, reduce the ductility demand on the structures. Therefore, it is one of the great interest in seismic design (Usami et al. 1992). In order to account for the displacement history to which the inelastic performance of a structure is highly sensitive, a cumulative normalized energy absorption, $\bar{E}$, defined as

$$\bar{E} = \frac{1}{E_y}\sum_{i=1}^{n} E_i \tag{4}$$

$$E_y = \frac{1}{2}H_{y0}\delta_{y0} \tag{5}$$

is considered to be a more objective measure of the cyclic inelastic performance of a member (Usami et al. 1992). In which, E_i =energy absorption in the i-th half-cycle, n = number of half-cycles (here, one half-cycle is defined from any zero lateral load to the subsequent zero lateral load). Using the above definitions, Figure 4 compares the normalized cumulative energy absorption capacity, $\bar{E}$, versus the number of half cycles, n, obtained from experiment and analysis using the 2SM. From this comparison it is clear that the predicted

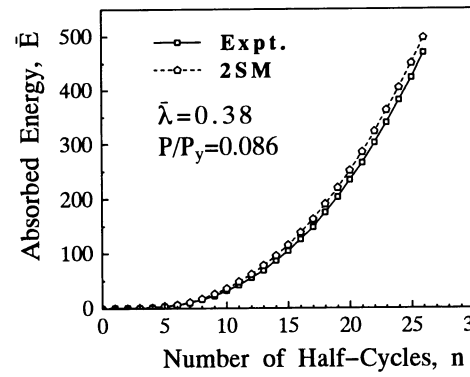

Figure 4. Comparison of absorbed energy.

energy absorption capacity agrees well with experimental results. The reason for this is that the 2SM takes accurately into account the yield plateau, Bauschinger effect and cyclic strain hardening of the material (Mamaghani 1996). This results in an accurate prediction of the cyclic behavior and energy absorption of the column (Figs 3, 4).

4 PARAMETRIC STUDY

In this section, the developed formulation(2SM) is used to investigate the effects of some important parameters on the cyclic behavior and energy absorption capacity of steel tubular columns of compact circular section. A series of numerical experiments is carried out on hypothetical specimens subjected to combined constant axial load and cyclic lateral displacement. The main parameters considered are: (1) Steel grade; (2) column slenderness ratio, $\bar{\lambda}$; (3) axial load; (4) lateral load history; and (5) cross-section shape (circular section and square box section). Four values of $\bar{\lambda}$, namely, 0.2, 0.4, 0.6 and 0.8, and three values of P/P_y ratios, namely, 0.0, 0.2 and 0.4 which are almost in the practical range are used. For each combination of $\bar{\lambda}$ and P/P_y, three materials, namely, SS400, SM490 and SM570, with material properties and corresponding two-surface model parameters given in Table 1, are assumed in the analysis. For each material, two type of lateral displacement histories, with constant and variable displacement amplitudes, are applied.

4.1 *Specimens*

All of the assumed specimens have circular sections

of outer radius $R = 300mm$; and thickness $t = 20mm$, as shown in Figure 1. The height of each specimen h, is calculated using equation (1) for the corresponding value of $\bar{\lambda}$ and material properties given in Table 1.

4.2 *Load sequences*

After applying the prescribed constant axial load, lateral displacement histories which consists of fully reversed displacement cycles are applied. The lateral loading history of type 1 is described for 10 half-cycles with a constant peak displacement of $\delta/\delta_{y0} = \pm 4$. In the loading history of type 2, the peak displacement is increased stepwise after three successive cycles at each displacement level; $\delta/\delta_{y0} = \pm 2, \pm 4$ and ± 6. In the analysis, initial geometrical imperfection, residual stress and local buckling are not considered. Also, the axial strain is monitored in the outermost fiber of the cross section at points 1 and 2 near the base of the column (Fig. 2; $\bar{h} = R = 300mm$), in order to check cyclic response of the material under different loading conditions. In the following sections, some typical results will be presented and discussed.

4.3 *Cyclic behavior*

Figure 5 compares the normalized lateral load H/H_{y0}-lateral displacement δ/δ_{y0} and the normalized axial stress σ/σ_y-axial strain $\varepsilon/\varepsilon_y$ responses for specimens of $\bar{\lambda} = 0.4$ subjected to varying axial loads and lateral displacement of type 1.

Figure 5(a) shows that the lateral load carrying capacity decreases as the axial load increases. Also, it can be observed that the stabilized state for the lateral load-displacement hysteresis loops is achieved after two cycles. The hysteresis loop becomes thinner after the first cycle and later it does not change significantly. The possible reasons for this behavior are: (1) The length of plastic zone stabilizes after the second cycle, because the yield plateau disappears and the material experiences cyclic strain hardening [thinning out of the hysteresis loops in Figure 5(b)]. Consequently the spread of plasticity slows down and stabilizes; (2) the Bauschinger effect (reduction in the elastic range) of the material along the plastified zone, which causes the slope of hysteresis curves to decrease [consequently leading to thinner hysteresis loops in Figure 5(a)], is more apparent in the first two cycles than in the subsequent cycles, see Figure 5(b). This effect is as a consequence of the larger rate of spread of plasticity in the first two cycles; and (3) since local buckling is not considered in the analyses, no degradation of the load carrying capacity is observed as the number of cycles increases.

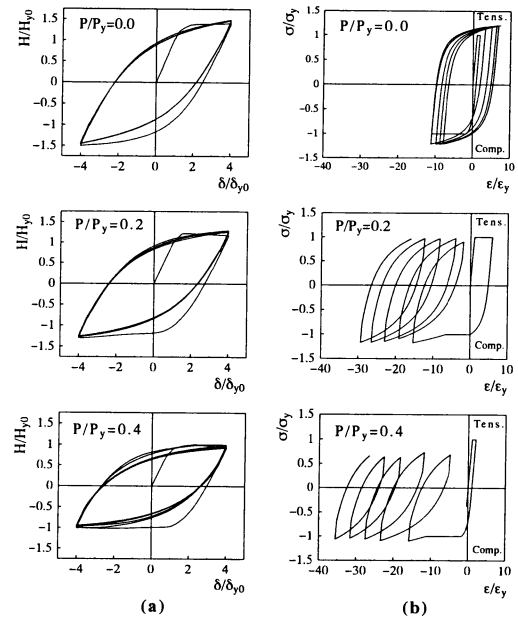

Figure 5. Axial load effect (SS400, $\bar{\lambda} = 0.4$): (a) normalized lateral load H/H_{y0}-lateral displacement δ/δ_{y0}; (b) normalized axial stress σ/σ_y-axial strain $\varepsilon/\varepsilon_y$ at point 1.

Figure 5(b) shows that due to lateral cycling in the absence of the axial load ($P/P_y = 0.0$) there is almost no accumulation of the inelastic axial strain (inelastic deformation), conversely, the axial strain increases in the direction of axial load (compression) under constant axial load (ratcheting effect), see Figure 5(b) for $P/P_y = 0.2$ and $P/P_y = 0.4$. It is worth noting that similar behavior was observed from the experiments for steel box columns which was accurately simulated by the developed formulation (2SM) (Mamaghani et al. 1996a, 1997).

As shown in Figure 5(b), the rate of ratcheting slows down as the number of cycles increases and the material experience cyclic strain hardening. Also, comparison between the results in Figure 5(b) shows that the rate of ratcheting increases with the increase in axial load.

Figure 6 compares the effect of slenderness ratio

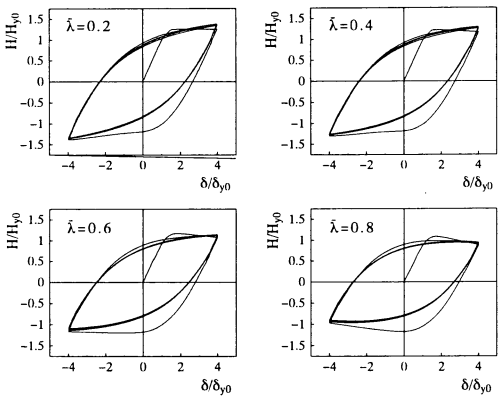

Figure 6. Effect of column slenderness ratio (SS400, $P/P_y = 0.4$): normalized lateral load H/H_{y0}-lateral displacement δ/δ_{y0}.

parameter $\bar{\lambda}$, on the normalized lateral load H/H_{y0}-lateral displacement δ/δ_{y0} responses for specimens of steel grade SS400 subjected to lateral displacement of type 1 under constant axial load $P/P_y = 0.2$. The results in this figure show that as the slenderness ratio increases, the load carrying capacity of the column decreases. The hysteretic loops stabilize after two cycles under various slenderness ratios (Fig. 6).

Figure 7(a) compares the normalized lateral load H/H_{y0}-lateral displacement δ/δ_{y0} responses for specimens of steel grade SM490 and SM570 subjected to lateral displacement of type 2 under constant axial load of $P/P_y = 0.2$. Figure 7(b) shows the corresponding normalized axial stress σ/σ_y-axial strain $\varepsilon/\varepsilon_y$ responses at point 1 (see Fig. 2). The main objective of these results is to compare the effect of steel grades and loading histories on the cyclic behavior.

Comparison of the hysteresis loops in Figure 7(a) shows that: (1) Degradation in load carrying capacity, for both steel grades, occurs when cycling is carried out within a small displacement range, $\delta/\delta_{y0} = \pm 2$; (2) stabilized state of the hysteresis loops is achieved after the second cycle for steel SM490, while the loops stabilize after the first cycle for steel SM570; and (3) the hysteresis loops are much fatter for SM570 than the corresponding ones for SM490.

All these observations may be mainly attributed to the reason that steel grade SM570 does not exhibit yield plateau in contrast to SM490 (Mamaghani 1996), see Table 1 for material properties.

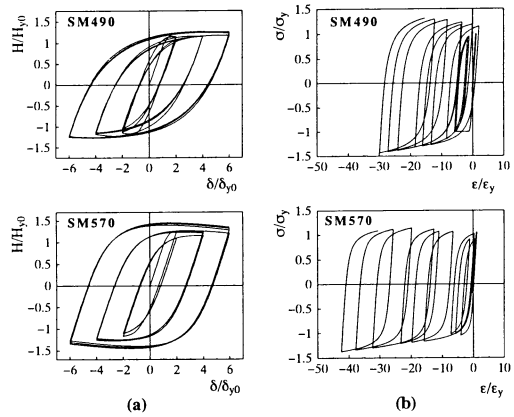

Figure 7. Effect of steel grade and loading history ($\bar{\lambda} = 0.6$, $P/P_y = 0.2$): (a) normalized lateral load H/H_{y0}-lateral displacement δ/δ_{y0}; (b) normalized axial stress σ/σ_y-axial strain $\varepsilon/\varepsilon_y$ at point 1.

The existence of the yield plateau causes a larger plastified zone in SM490 specimen compared to SM570, which in turn increases the Bauschinger effect. As a consequence, the hysteresis loops for steel SM490 become thinner.

Comparison of hysteresis loops in Figure 7(b) indicates that the ratcheting effect is more apparent in the case of steel SM570 as a result of severe stress reversals. However, cyclic load carrying capacity does not degrade due to cyclic stain hardening, see Figure 7(a) for SM570. In the second and third steps of loading, the hysteresis loops for the steel grade SM570 exhibit a larger descending behavior than that of the steel grade SM490 for which it is not so significant. This is, possibly, because of the larger ratcheting effect and further

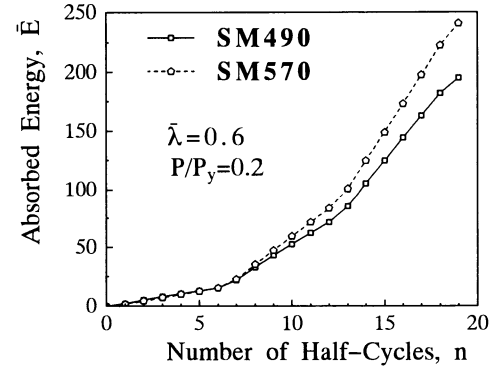

Figure 8. Normalized absorbed energy under three-cycle loading.

spread of plastic zone due to higher peak load in the case of SM570, see Figure 7.

Figure 8 shows that the normalized cumulative energy absorption capacity for steel grade SM490 is lower than that for the steel grade SM570. This implies that the existence of yield plateau has a reducing effect on the normalized cumulative energy absorption capacity under the same loading history.

4.4 *Energy absorption capacity*

Using the above definitions, the results of numerical analysis regarding energy absorption capacity are summarized in Figures 9-12 for the above discussed three steel grades, various $\bar{\lambda}$, P/P_y ratios and loading history of type 1. In what follows, it is aimed to illustrate the effects of these parameters on the energy absorption capacity under constant displacement amplitude cycling.

Figure 9 compares the normalized cumulative energy absorption capacity, $\bar{E}$ versus the number of half-cycles n, for steel grade SS400. It can be observed that all the curves corresponding to a specific P/P_y, say $P/P_y = 0.2$, and various $\bar{\lambda}$ values almost coincide. It implies that the column slenderness parameter, $\bar{\lambda}$, has almost no effect on the normalized cumulative energy absorption capacity. Another observation from these results is that an increase in axial load P/P_y decreases the energy absorption capacity, especially when the number of cycles increases. However this effect is less significant in the case of $P/P_y \leq 0.2$, see Figure 9. Similar results have been obtained for steel grades SM490 and SM570. However, the reduction of normalized energy absorption capacity due to increase in axial load is not as significant for steel grade SM570 as for steel grade SS400, see Figure 10.

As described before, the existence of yield plateau considerably reduces the stiffness of the column and affects the shape (thinning out) of hysteresis loops, see Figure 7(a), which in turns causes reduction in the normalized energy absorption capacity under the same loading condition.

Figures 10 and 11 compare the normalized

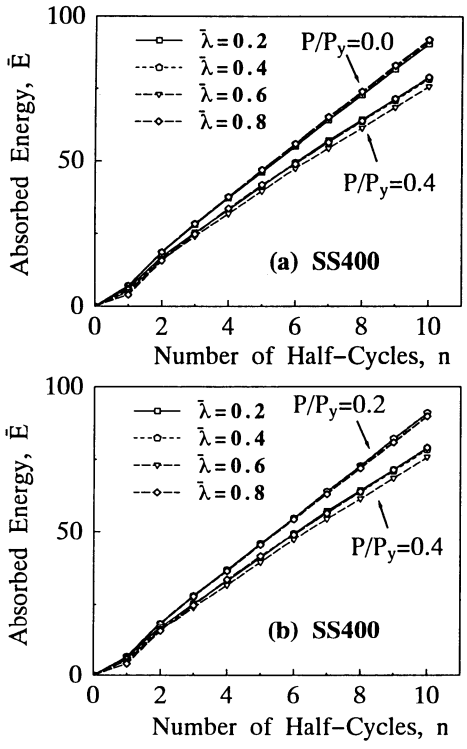

Figure 9. Effect of column slenderness ratio and axial load on absorbed energy (steel grade SS400).

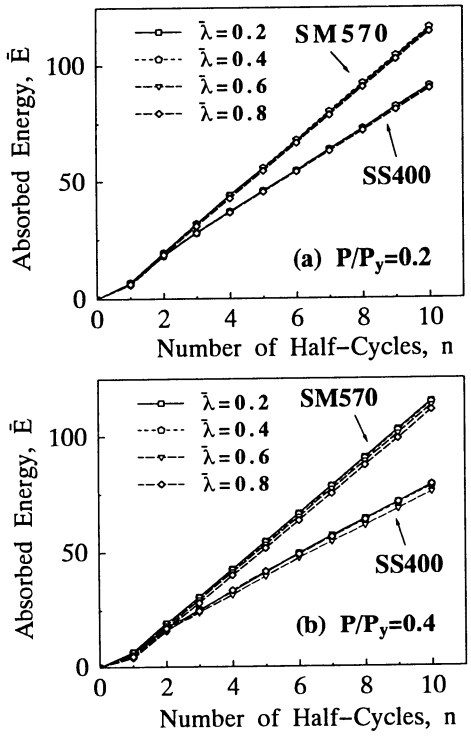

Figure 10. Effect of steel grade and loading history on absorbed energy (steel grades SS400 and SM570).

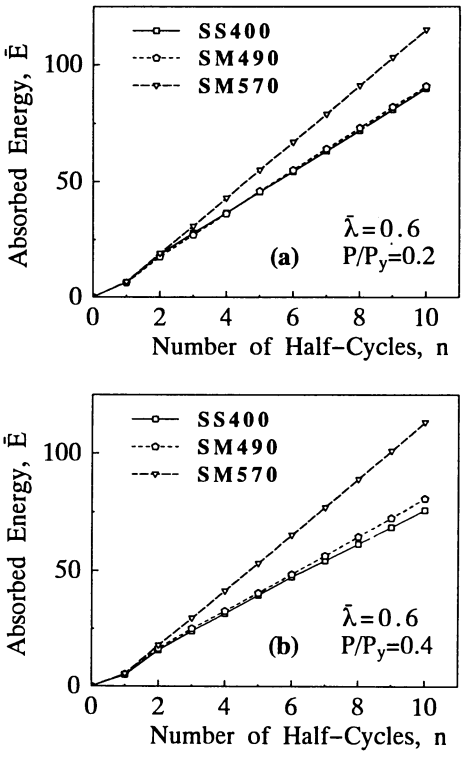

Figure 11. Effect of steel grade on absorbed energy (steel grades SS400, SM490 and SM570).

energy absorption capacity for the steel grades SS400, SM490 and SM570. The results shown in these figures reveal that the normalized energy absorption capacities for steel grades SS400 and SM490 are very close to each other and are lower than that of steel grade SM570. The difference in normalized energy absorption capacities increases as the axial load and the number of cycles increases (Figs 10, 11). These observations are mainly attributed to the fact that steel grades SS400 and SM490 exhibit yield plateau, while it is not the case for steel grade SM570.

4.5 *Effect of cross-section shape*

Figure 12 compares the normalized energy absorption capacity, $\bar{E}$, versus the number of half cycles, n, for the cantilever steel columns of compact circular section (Fig. 1) and compact square box section (Mamaghani et al. 1997) corresponding to the three steel grades of SS400, SM490 and SM570, column slenderness ratio of $\bar{\lambda} = 0.6$, applied constant axial load of $P/P_y = 0.4$, and lateral cycling displacement of type 1. The compact square box section have size and wall thickness equal to the diameter ($2R = 600mm$) and wall thickness ($t = 20mm$) of the compact circular section, respectively. From Figure 12 it can be observed that the normalized absorbed energy capacities regarding each steel grade are very close and almost coincide for both of the circular and square box sections. This implies that the shape of cross-section, to be taken as a compact circular section or a compact square box section, does not significantly affect the normalized absorbed energy capacity under the same loading history.

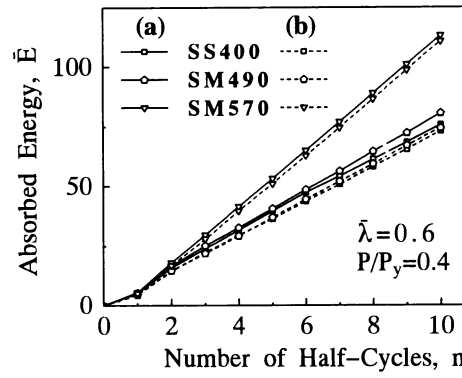

Figure 12. Effect of cross-section shape on normalized absorbed energy: (a) compact circular section; (b) compact rectangular section.

5 CONCLUSIONS

The present paper was concerned with the cyclic inelastic behavior of compact steel tubular columns. An elastoplastic finite element formulation for beam-columns, accounting for both material nonlinearity and geometrical nonlinearity, used in the analysis. The two-surface plasticity model (2SM) was adopted for material nonlinearity.

The developed formulation, after being verified by experiments, was used to carry out a series of parametric studies on compact steel tubular columns. The effects of some important parameters, such as, column slenderness ratio, steel grade, axial load, lateral loading history, and shape of cross-section on cyclic behavior and energy absorption capacity were pointed out and evaluated. It was concluded that:

- the column slenderness parameter, $\bar{\lambda}$, has al-

most no significant effect on the normalized cumulative energy absorption capacity;

- the stabilized state for the lateral load-displacement loops is achieved after two cycles in the absence of local buckling;

- the yield plateau considerably affects the shape of hysteretic loops and has the effect of reducing the normalized energy absorption capacity;

- due to lateral cycling in the absence of the axial load there is almost no accumulation of the inelastic axial strain, conversely, under constant axial load and lateral cycling the axial strain increases (ratcheting effect) in the direction of axial load (compression);

- the rate of ratcheting increases with the increase in axial load and it slows down as the number of cycles increases and the material experiences cyclic strain hardening;

- the shape of cross-section, to be a compact circular section or a compact square box section, does not significantly affect the normalized absorbed energy capacity under the same loading history.

This study has been confined to compact design and ignores local buckling effect, though it is extremely important when the behavior of thin walled tubular columns under severe earthquake loads is investigated. The research is now underway by the authors.

REFERENCES

Clarke, M. J. 1994. Plastic-zone analysis of frames. In Chen, W.F. & Toma, S. (eds), *Advanced analysis of steel frames*, Fl: 259-319, CRC Press, Boca Raton.

Mamaghani, I.H.P., Shen, C., Mizuno, E. and Usami, T. 1995. Cyclic behavior of structural steels. I: Experiments. *J. Engng Mech., ASCE*, 121(11): 1158-1164.

Mamaghani, I.H.P., Usami, T. and Mizuno, E. 1996a. Cyclic elastoplastic large displacement behaviour of steel compression members. *Journal of Structural Engineering, JSCE*, March, 42A: 135-145.

Mamaghani, I.H.P., Usami, T. and Mizuno, E. 1996b. Inelastic large deflection analysis of steel structural members under cyclic loading. *Engineering Structures*, UK, 18(9): 659-668.

Mamaghani, I.H.P. 1996. Cyclic elastoplastic behavior of steel structures: Theory and experiment. *Doctoral Thesis*, Department of Civil Engineering, Nagoya University, Nagoya, Japan.

Mamaghani, I.H.P., Usami, T. and Mizuno, E. 1997. Hysteretic behavior of compact steel box beam-columns. *Journal of Structural Engineering, JSCE*, March, 43A: 187-194.

Interim Guidelines and New Technologies for Seismic Design of Steel Structures (IGNTS-DSS) 1996. In Usami, T. (eds), Committee on New Technology for Steel Structures (CNTSS), Japan Society of Civil Engineers (JSCE).

Shen, C., Mamaghani, I.H.P., Mizuno, E. & Usami, T. 1995. Cyclic behavior of structural steels. II: Theory, *J. Engng Mech., ASCE*, 121(11):1165-1172.

Sueda, A., Yasunami, H., Mizutani, S., Kobayashi, Y. & Nakagawa, T. 1997. A study on ductility of steel pier under cyclic loading. In Usami, T. (eds), *Proc. 5th Int. Coll. stability and ductility of steel structures:* 29-31 July: 237-244, Nagoya, Japan.

Tominaga, T., & Yasunami, H. 1994. An experimental study on ductility of steel bridge piers with thick walled cross section and small number of stiffeners. *Journal of Structural Engineering, JSCE*, March, 40A:189-200 (in Japanese).

Tsuji, B., & Nakatsuka, T. 1986. Inelastic strength and deformation behavior of tubular beam-columns. In Kurobane & Makino (eds), *Safety criteria in design of tubular structures:* 27-35, Tokyo, Japan.

Usami, T., Mizutani, T. Aoki & Itoh, Y. 1992. Steel and concrete-filled steel compression members under cyclic loading. In Fukumoto, Y. & Lee, G.C. (eds), *Stability and ductility of steel structures under cyclic loading:*Fl:123-138, CRC Press, Boca Raton.

Zienkiewicz, O. C. 1997. *The finite element method, 3rd Ed.*, McGraw-Hill, New York.



Taylor & Francis
Taylor & Francis Group
http://taylorandfrancis.com

Tubular Structures VIII, Choo & Van der Vegte (eds) © 1998 Balkema, Rotterdam, ISBN 90 5809 001 9

Void-filled SHS beams subjected to high amplitude cyclic bending

Xiao Ling Zhao, Raphael Grzebieta & Elizabeth Sironic
Department of Civil Engineering, Monash University, Clayton, Vic., Australia

ABSTRACT: Local buckling and plastic hinges may occur in the compression flange of Square Hollow Section (SHS) beams under high amplitude cyclic bending arising from earthquakes, waves, storms and heavy traffic. Once a local mechanism forms residual strength rapidly reduces within a few cycles. This is even true for compact sections which have adequate rotation capacity under static bending. This paper compares the behaviour of empty and void-filled cold-formed square hollow sections subjected to large deformation cyclic bending. The filler material used was normal concrete, light-weight concrete and polyurethane. Experimental results show that void filling significantly increases ductility and thus the number of bending cycles SHS beams can be subjected to in overloaded situations.

1 INTRODUCTION

1.1 *General*

Cold-formed tubular steel members and connections are widely used in domestic houses, industrial and high rise buildings, bridges and offshore structures. These structures can be subjected to static or dynamic loading. The dynamic loading can be classified as low amplitude cyclic loading, which causes elastic deformation in the structure, and high amplitude cyclic loading, which causes inelastic deformation in the structure. The structural behaviour of cold-formed tubular members and connections under static loading has been well investigated (Wardenier 1982, Packer & Henderson 1992, Kitpornchai et al. 1993, Zhao et al. 1996, Zhao & Mahendran 1998, Zhao & Hancock 1998). The structural behaviour of cold-formed tubular members and connections under low amplitude dynamic loading such as fatigue and floor vibration is under investigation (Mashiri et al. 1997,1998, Alikhail et al. 1998). However, there is relatively little research reported on tubular structures under high amplitude dynamic loading which may cause unexpected and significant failures (Kurobane & Ogawa 1996). This paper forms part of a research project on Tubular Structures under High Amplitude Dynamic Loading currently running at Monash University. Only cold-formed SHS beams under cyclic gross pure bending will be discussed in this paper.

1.2 *Empty SHS beams subjected to static bending*

Local buckling in the flange of a SHS beam may occur if the flange width-to-thickness ratio (b/t) is larger than a certain value. This cut-off value of b/t for SHS sections was determined using stub column tests (Key et al. 1988, Zhao & Hancock 1991, Hancock & Zhao 1992). Similarly the plastic bending moment of a SHS beam may not be achieved or maintained if the flange width-to-thickness ratio (b/t) is larger than a certain value. This cut-off value of b/t for SHS beams was determined using plastic bending tests and a rotational capacity criterion (Zhao & Hancock 1991, Hancock & Zhao 1992, Korol & Hudoba 1972, Hasan & Hancock 1989, Stranghoner et al. 1994). A SHS section can therefore be classified as a compact section, non-compact section or slender section in accordance with the Australian Standard for Steel Structures AS4100-1990 (SAA 1990) and the American Institute of Steel Construction Specification (AISC 1993). A similar approach has been adopted in Eurocode 3 (Eurocode 3 1992), British Standard BS5950 Part 1 (BSI 1990), Japanese Standard AIJ-1990 (AIJ 1990) and the Canadian Standard CSA-S16.1-M89 (CSA 1989)

where a SHS section can be classified from class 1 to class 4, ie. from a plastic (deformation) section to a slender (buckling) section.

1.3 *Empty SHS beams subjected to cyclic bending*

Local buckling and plastic hinges may occur in the compression flange of Square Hollow Section (SHS) beams under high amplitude cyclic bending. Early research at Monash University on low cycle fatigue of cold-formed SHS beams (Grzebieta et al. 1997) showed that once a local mechanism forms in the flange of SHS sections, the residual strength rapidly reduces after a few cycles. This is even true for compact sections which have adequate rotation capacity under static bending. A similar phenomenon was observed in the case of empty RHS bracing members subjected to cyclic tension and compression (Sherman & Sully 1995, Walpole 1995) and for empty thin-walled box beams under cyclic bending (Fukumoto & Kusama 1985, Sohal & Chen 1987). The ductility in steel beams under cyclic bending was also studied by Daali & Korol (1996).

1.4 *Void-filling*

Void-filling is an efficient way to prevent local buckling and to increase ductility of steel hollow sections. Existing research has covered members and connections under static loading (Zhang & Brahmachari 1994, Lu & Kennedy 1994, Shakir-Khalil 1997, Packer & Fear 1991, Bergmann et al. 1995, Zhao & Goldberg 1997) and columns and connections under cyclic loading (Liu & Goel 1988, Ge & Usami 1996, Nakai et al.1994, Ricles 1995). Most of the tubular sections in these studies were either hot-rolled or welded box sections. Very little research was performed on void-filled SHS beams under cyclic bending. Most of the research was limited to tubular sections filled with normal concrete. Research has been performed at Monash University on thin-walled box sections filled with light-weight materials such as polyurethane (Sironic et al. 1996, Sironic & Grzebieta 1996, Grzebieta & White 1994, Grzebieta et al. 1995) to improve the bending capacity as well as the energy dissipation (crashworthiness) of box sections.

This paper investigates the behaviour of void-filled cold-formed square hollow sections subjected to large deformation cyclic bending. Three sizes of SHS sections are selected, which correspond to compact section, non-compact section and slender section. The filler material is normal concrete, light-weight concrete and polyurethane. The test results are compared with those for empty SHS beams under cyclic bending (Grzebieta et al. 1997).

2 MATERIAL PROPERTIES

The SHS sections were supplied by BHP Steel - Structural Pipeline and Products (Newcastle, NSW). They are the "in-line" galvanised Square Hollow Section tubes (also called "Duragal SHS"), which are manufactured using roll forming with electric resistance welding (ERW) to close the section. These sections are similar to those used in previous research (Zhao & Hancock 1992a,b,1996, Alikhail et al. 1998, Grzebieta et al. 1997, Zhao & Goldberg 1997). The nominal dimensions and measured properties (0.2% proof stresses from flat faces) for the SHS sections used in this project are shown in Table 1 where a cross-section number (1, 2 or 3) is given. The measured properties for the filler material are listed in Table 2.

3 TEST SPECIMENS AND TEST SET UP

Twenty one specimens were tested. They are summarised in Table 3 where the specimen

Table 1. Dimensions and properties for SHS sections

Cross-Section Number	Nominal Dx Bxt (mm)	Ratio (B-2t)/t (compact-ness)	Yield Stress (MPa)
1	65x65x2.0	30.5 (slender)	444
2	65x65x2.5	24.0 (non-compact)	467
3	65x65x3.0	19.7 (compact)	454

Table 2 Properties for Filler Material

Filler Material	Density (kg/m^3)	Compression Strength (MPa)
Normal Concrete	2400	60.4
Light-Weight Concrete	1200	12.4
Polyurethane	867	34.4

identification number, test type, filler material and cross-section sizes are given. The first letter (S or C) in the specimen label refers to the test type (Static or Cyclic), the second letter (C, L or P) in the label refers to the filled material (Concrete, Light-weight concrete or Polyurethane), the last letter (1, 2 or 3) in the label refers to the cross-section number defined in Table 1.

A pure bending test rig was used. The rig was designed and built at Monash University and is described in detail by Cimpoeru (1992). The rig has been successfully utilised in previous research work (Grzebieta et al. 1995,1997, Cimpoeru & Murray 1993). Each specimen was subjected to cyclic bending. A complete cycle is defined as the following four steps: (1) bend from the flat position to an angle (θ) in one direction, (2) bend back to the original flat position, (3) bend from the flat position to the same angle (θ) in a reversed direction, (4) bend back to the original flat position. Each void-filled specimen was bent to a maximum angle (θ) of 20 degrees, so that they could be compared with results from previous tests on empty SHS beams (Grzebieta et al. 1997).

Table 3 Detail Information about Tested Specimens

ID No.	Test Type	Filler Material	SHS Size DxBxt (mm)
SC1	static	concrete	65x65x2.0
SC2	static	concrete	65x65x2.5
SC3	static	concrete	65x65x3.0
SL1	static	light weight concrete	65x65x2.0
SL1 repeat	static	light weight concrete	65x65x2.0
SL2	static	light weight concrete	65x65x2.5
SL3	static	light weight concrete	65x65x3.0
SP1	static	polyurethane	65x65x2.0
SP2	static	polyurethane	65x65x2.5
SP3	static	polyurethane	65x65x3.0
CC1	cyclic	concrete	65x65x2.0
CC2	cyclic	concrete	65x65x2.5
CC3	cyclic	concrete	65x65x3.0
CL1	cyclic	light weight concrete	65x65x2.0
CL1 repeat	cyclic	light weight concrete	65x65x2.0
CL2	cyclic	light weight concrete	65x65x2.5
CL2 repeat	cyclic	light weight concrete	65x65x2.5
CL3	cyclic	light weight concrete	65x65x3.0
CP1	cyclic	polyurethane	65x65x2.0
CP2	cyclic	polyurethane	65x65x2.5
CP3	cyclic	polyurethane	65x65x3.0

Table 4. Comparison of ultimate moment capacity

Section Size	M_{uC}/M_{uE}	M_{uL}/M_{uE}	M_{uP}/M_{uE}
65x65x2.0	1.387	1.184	1.254
65x65x2.5	1.320	1.108	1.281
65x65x3.0	1.335	1.137	1.158
MEAN	1.347	1.143	1.231

Table 5. Comparison of rotation angle

Section Size	θ_{uC}/θ_{uE}	θ_{uL}/θ_{uE}	θ_{uP}/θ_{uE}
65x65x2.0	3.429	2.857	2.867
65x65x2.5	2.700	3.200	>3.200
65x65x3.0	2.857	>2.500	>2.500
MEAN	2.995	>2.852	>2.856

4 TEST RESULTS

4.1 *Static bending*

The ultimate moment capacity obtained for the void-filled SHS beams are compared in Table 4 with those for the empty SHS beams. The increase in ultimate moment capacity is found to be about 35% for concrete-filled SHS beams, 14% for light-weight concrete filled SHS beams and 23% for polyurethane filled SHS beams. It can be seen the void-filling increases the ultimate moment capacity of SHS beams. The different percentage of increase may be due to the different compressive strength of the filler material. The rotation angle when the ultimate moment is reached for the void-filled SHS beams are compared in Table 5 with those for the empty SHS beams. The increase in the rotation angle at ultimate moment is about 300%. It seems that void-filling significantly increases the ductility of SHS beams.

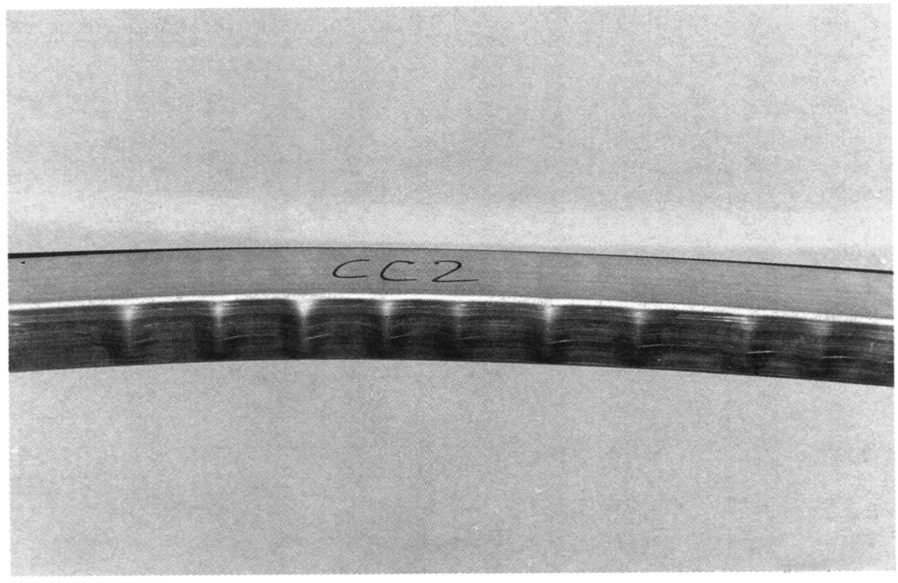

Figure 1 Uniform Buckling Mode

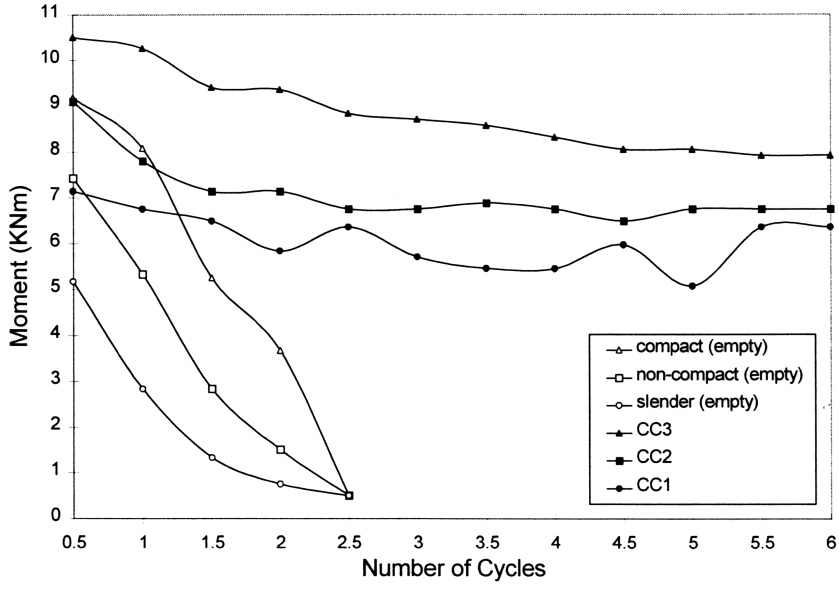

Figure 2 Maximum Bending Moment Reached in Each Cycle Versus Number of Cycles (SHS Filled With Concrete)

4.2 *Cyclic bending*

For SHS beams filled with normal concrete, uniform buckling was observed as shown in Figure 1. No cracking occurred after 6 cycles. The maximum moment reached in each cycle is plotted in Figure 2 against the number of cycles. The results for empty SHS beams are also plotted in Figure 2 for comparison.

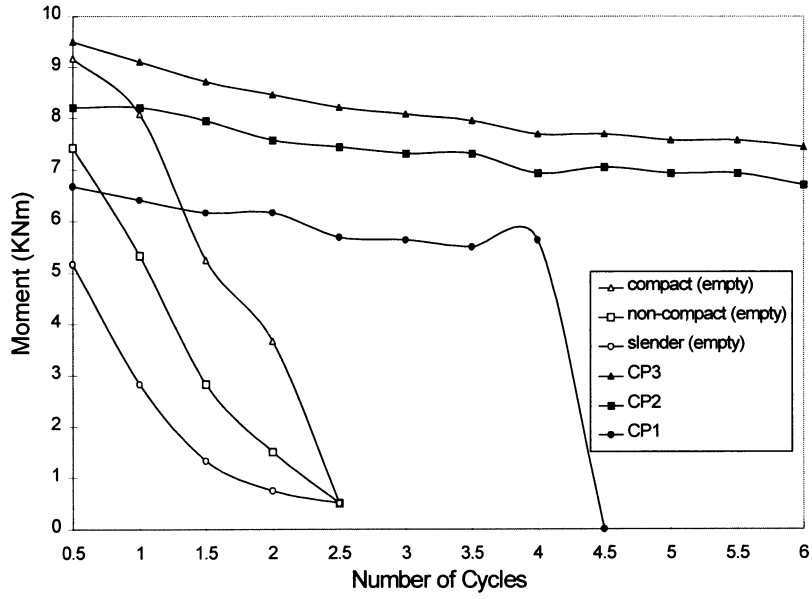

Figure 3 Maximum Bending Moment Reached in Each Cycle Versus Number of Cycles (SHS Filled with Light Weight Concrete)

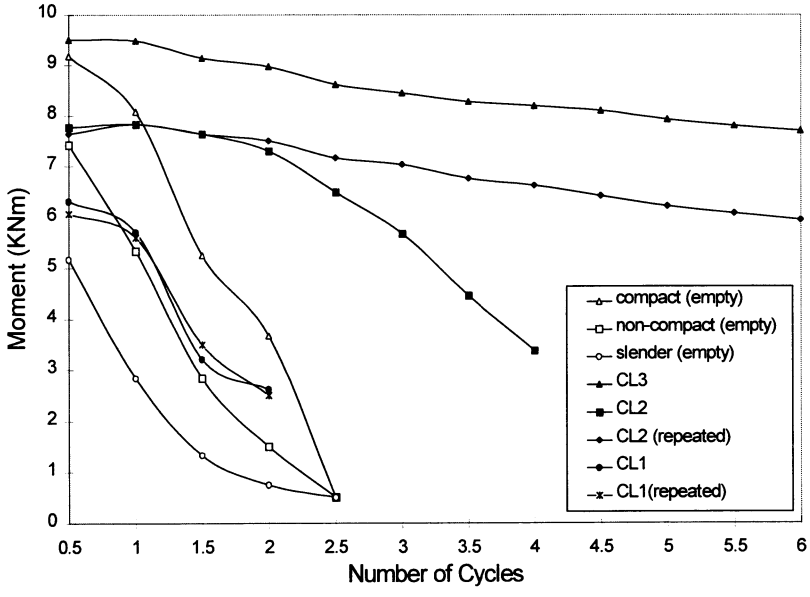

Figure 4 Maximum Bending Moment Reached in Each Cycle Versus Number of Cycles (SHS Filled with Polyurethane)

For SHS beams filled with light-weight concrete, the maximum moment reached in each cycle is plotted in Figure 3 against the number of cycles. The results for empty SHS beams are also plotted in Figure 3 for comparison. For the slender section (SHS 65x65x2.0) beam filled with light-weight concrete, a local mechanism formed after one cycle. The tube split after the second cycle. For the compact section (SHS 65x65x3.0), no cracking was observed after 6 cycles. For the non-compact section (SHS 65x65x2.5), a local mechanism formed after two cycles. The tube split after four and a half cycles. A second specimen was tested for the non-compact section. No crack was observed after 6 cycles. It was found that the failure of the first non-compact section beam may have been due to the poor quality of the concrete mix.

For SHS beams filled with polyurethane, the maximum moment reached in each cycle is plotted in Figure 4 against the number of cycles. The results for empty SHS beams are also plotted in Figure 4 for comparison. For the slender section (SHS 65x65x2.0) filled with polyurethane, a local mechanism started to form after one cycle. During the 4.5 cycles of bending (loading time), the tension flange cracked and the whole section tore apart. For the compact section and non-compact section filled with polyurethane, uniform buckling was observed and no crack occurred after 6 cycles of bending.

5 CONCLUSIONS

- For void-filled SHS beams under static bending, the increase in ultimate moment capacity was found to be about 35% for concrete-filled SHS beams, 14% for light-weight concrete filled SHS beams and 23% for polyurethane filled SHS beams. The increase in the rotation angle at ultimate moment is about 300%. It can be concluded that void-filling significantly increases the ductility of SHS beams.
- For SHS beams filled with normal concrete subjected to gross deformation cyclic bending, uniform buckling was observed and no cracking occurred after 6 cycles of bending.
- For SHS beams filled with light-weight concrete, the slender section split after 2 cycles of bending, the compact section survived without cracking after 6 cycles and the non-compact section may survive 6 cycles if the quality of the concrete mix is assured.
- For SHS beams filled with polyurethane, the slender section split after 4.5 cycles of bending, the compact section and non-compact section survived without cracking after 6 cycles.

6 ACKNOWLEDGMENT

The authors would like to thank Mr. Roger Doulis, Ms. Filicia Purza, Mr. Sunny Tam and Mr. Lee Dowler for performing the tests. The project was sponsored by an Australian Research Council Large Grant and a Monash University New Staff Member Research Fund. The SHS tubes were supplied by BHP Steel - Structural Pipeline and Products.

REFERENCES

1. AIJ (1990). *Standard for Limit State Design of Steel Structures*, Draft, Architectural Institute of Japan, Tokyo, Japan
2. AISC (1993). *Load and Resistance Factor Design Specification for Structural Steel Buildings*, American Institute of Steel Construction, Chicago, Ill., USA
3. Alikhail, M. Zhao, X.L., Koss, L., Grundy, P. , Dagg, H. and Shield, A. High Strength Steel RHS Domestic Flooring System, *Proc. 8th Int. Symposium on Tubular Structures*, August, Singapore
4. Bergmann, R. et al. (1995). *Design Guide for Concrete-Filled Hollow Section Columns under Static and Seismic Loading*, CIDECT, Verlag TUV Rheinland GmbH, Koln, Germany
5. BSI (1990). *Code of Practice for Design in Simple and Continuous Construction: Hot-Rolled Sections - Structural Use of Steelwork in Building*, BS5950 Part 1, London
6. Cimpoeru, S.J. (1992), The Modelling of the Collapse During Roll-Over of Bus Frames Consisting of Square Thin-Walled Tubes, *PhD Thesis*, Dept. Civil Engineering, Monash University, Clayton, Australia
7. Cimpoeru, S.J. and Murray, N.W. The Lage-Deflection Pure Bending Properties of a Square Thin-Walled Tube, *Int. J. Mech. Sci*, 1993, 35(3/4), 247-256
8. CSA (1989). *Steel Structures for Buildings (Limit State Design)*, CSA-S16.1-M89Canadian Standards Association, Rexdale, Ontario

9. Daali, M.L. and Korol, R.M. Adequate Ductility in Steel Beams under Earthquake-Type Loading, *Engineering Structures*, 1996, 18(2), 179-189
10. Eurocode 3 Part 1.1 (1992*). Design of Steel Structures: Part 1.1 - General Rules and Rules for Buildings,* DD ENV, Eurocode 3 Editorial Group
11. Fukumoto, Y. and Kusama, H. Cyclic Bending Tests of Thin-Walled Box Beams, *Proc. JSCE Structural Eng./Earthquake Eng.,* 1985, 2(1), 141-151
12. Ge, H. B. and Usami, T. Cyclic Tests of Concrete Filled Steel Box Columns, *Journal of Structural Engineering*, ASCE, 1996, 122(10), 1169-1177.
13. Grzebieta, R.H. and White, G. J. (1994), "Void-Filled Square Cantilever Steel Tubes Subject to Gross Plastic Deformation", in Tubular Structures VI, Grundy, Holgate and Wong (eds), Balkema, Rotterdam, 255-262.
14. Grzebieta, R.H., Kilner, A.A. and Murray, N.W. (1995), Gross Bending Deformation of Void-Filled Square Tubes, in *Structural Stability and Design*, Kitipornchai, Hancock and Bradford (eds), Balkema, Rotterdam, 397-403
15. Grzebieta, R.H., Zhao, X.L. and Purza, F. (1997), Multiple Low Cycle Fatigue of SHS Tubes subjected to Gross Pure Bending Deformation, *5th Int. Colloquium on Stability and Ductility of Steel Structures*, Nagoya, Japan, July, 847-854
16. Hancock, G.J. and Zhao, X.L. Research into the Strength of Cold-Formed Tubular Sections, *Journal of Constructional Steel Research*, 1992, **23**, 55-72
17. Hasan, S.W. and Hancock, G.J. Plastic Bending Tests of Cold-Formed Rectangular Hollow Sections, *J. Australian Institute of Steel Construction*, 1989, **23**(4), 2-19
18. Key, P.W., Hasan, S.W. and Hancock, G.J. Column Behaviour of Cold-Formed Hollow Sections, *Journal of Structural Engineering*, ASCE, 1988, 114(2), 390-407
19. Kitipornchai, S. , Al-Bermani, F.G.A. and Murray, N.R. Eccentrically Connected Cleat Plates in Compression, *J. Struct. Engineering*, ASCE, 1993, 119(3), 767-781
20. Korol, R.M. and Hudoba, J. Plastic Behaviour of Hollow Structural Sections, *J. Struct. Engineering*, ASCE, 1972, 98(ST5), 1007-1023
21. Kurobane, Y. and K. Ogawa (1996), Kobe Earthquake Damage to High-Rise Ashiyahama Apartment Buildings: Brittle Tensile Failure of Box Sections Columns, in *Tubular Structures VII*, Farkas and Jamai (eds), Balkema, Rotterdam, 277-284.
22. Liu, Z.Y. and Goel, S. Cyclic Load Behaviour of Concrete-Filled Tubular Braces, *Journal of Structural Engineering,* ASCE, 1988, 114(7), 1488-1506.
23. Lu, Y. Q. and Kennedy, D.J.L. The Flexural Behaviour of Concrete-Filled Hollow Structural Sections, *Can. J. of Civil Engg.,* 1994, 21(1), 111-130
24. Mashiri, F. , Zhao, X.L. and Grundy, P. (1997), Crack Propagation Analysis of Welded Thin-Walled Cruciform Joint using Boundary Element Method, *Proc. Materials Research Forum'97 - Materials Conservation,* November, Melbourne, Australia
25. Mashiri, F. , Zhao, X.L. and Grundy, P. (1998), Effects of Welded Profile on the Fatigue Life of Thin-Walled Cruciform Joint, *Proc. 8th Int. Symposium on Tubular Structures*, August, Singapore
26. Nakai, et al. Experimental Study on Ultimate Strength and Ductility of Concrete Filled Thin-Walled Steel Box Columns After Receiving Seismic Loading, *J. Struct. Engineering*, JSCE, 1994, 40A, 1401-1412
27. Packer, J.A. and Fear, C.E. Concrete-Filled Rectangular Hollow Section X and T Connections, in *Tubular Structures IV*, 1991, Wardenier and Shahi (eds), Delft University, 382-391
28. Packer, J.A. and Henderson, J.E. (1992), *Design Guide for Hollow Structural Section Connections*, Canadian Institute of Steel Construction, Ontario, Canada.
29. Ricles, J.M. Seismic Performance of CFT Columns-to-WF Beam Moment Connections, Proc. 3rd International Workshop on Connections in Steel Structures, Trento, Italy, 1995
30. SAA (1990). *Steel Structures*, Australian Standard AS 4100, Standards Association of Australia, Sydney, Australia
31. Shakir-Khalil, H. Connection of Steel Beams to Concrete-Filled Tubular Columns, *Proc. Int. Confrence on Composite Construction-Conventional and Innovative,* Innsbruck, Austria, September, *1997,* 878-879
32. Sherman, D. and Sully, R. M. (1995), Tubular Bracing Members Under Cyclic Loading, *Proc., 3rd Pacific Structural Steel Conference*, Singapore, May.

33. Sironic, E.,Grzebieta, R.H. and Murray, N.W. (1996), "A Study of Form Filled Thin-Walled Tube Sections: Effect of Filler on the Section Local Elastic Buckling Capacity", Proc. Monash Industry Geomechanics and Structures Symposium, Melbourne, 119-120.
34. Sironic, E. and Grzebieta, R.H. (1996), "Should Car Roof Pillars be Epoxy-Filled for Increased Roll-Over Strength?", Proc. 15th Int. Technical Conf. on the Enhanced Safety of Vehicles, Melbourne.
35. Sohal, I.S. and Chen, W. F. Local Buckling and Inelastic Behaviour of Tubular Members, *Thin-Walled Structures*, 5 (1987), 455-475
36. Stranghoner, N., Sedlacek, G. and Boeraeve, Ph. Rotation Requirement and Rotation Capacity of Rectangular, Square and Circular Hollow Sections, in *Tubular Structures VI,* Grundy, Holgate & Wong (eds), 1994, Balkema, Rotterdam
37. Walpole, W.R. (1995), Behaviour of Cold-Formed Steel RHS Members under Cyclic Loading, *Technical Conf.,* New Zealand National Society for Earthquake Engineering, Waikanae, April.
38. Wardenier, J. (1982), *Hollow Section Joints*, Delft University Press, Delft, The Netherlands.
39. Zhang, Q. and Brahmachari, K. Flexural Behaviour of Rectangular Tubular Sections Filled with Fibrous High Strength Concrete, in *Tubular Structures VI*, Grundy, Holgate & Wong (eds), Balkema, Rotterdam, 1994, 247-254
40. Zhao, X.L. and Goldberg, E. (1997). Web Crippling of Partially Stiffened RHS Sections, *5th Int. Colloquium on Stability and Ductility of Steel Structures*, Nagoya, Japan, July, 173-180
41. Zhao, X.L. and Hancock, G.J. Tests to Determine Plate Slenderness Limits for Cold-Formed Rectangular Hollow Sections of Grade C450, *Steel Construction*, Australian Institute of Steel Construction, 1991, **25**(4), 2-16
42. Zhao, X.L. and Hancock, G.J. (1992a), Tests to Determine the Reliability of Stub Columns of DuraGal RHS, *Investigation Report*, No. S916, January, Centre for Advanced Structural Engineering, The University of Sydney, Sydney, Australia
43. Zhao, X.L. and Hancock, G.J. (1992b), Tests to Determine the Reliability of Beams of DuraGal RHS, *Investigation Report*, No. S917, January, Centre for Advanced Structural Engineering, The University of Sydney, Sydney, Australia
44. Zhao, X.L., Hancock, G.J. and Sully, R. Design of Tubular Members and Connections Using Amendment No.3 to AS4100, *Steel Construction*, AISC, 1996, Vol.30, No.4, 2-15
45. Zhao, X.L. and Hancock, G.J. (1996). Welded Connections in Thin Cold-Formed Rectangular Hollow Sections, in *Connections in Steel Structures III,* Bjorhovde, R., Colson, A., Zandonini, R. (eds), Pergamon, Oxford, 89-98
46. Zhao, X. L. and Mahendran, M. (1998), Recent Innovations in Cold-Formed Tubular Sections, *2nd World Conference on Constructional Steel*, Spain, May
47. Zhao, X.L. and Hancock, G.J. (1998), Recent Research on Cold-Formed Tubular Structures, *2nd World Conference on Constructional Steel*, Spain, May

Tubular Structures VIII, Choo & Van der Vegte (eds) © 1998 Balkema, Rotterdam, ISBN 90 5809 001 9

Optimum design and comparison of hollow flange beams

K.Jármai, J.Farkas & T.Liszkai
University of Miskolc, Hungary

ABSTRACT: A hollow flange beam (HFB) consists of a straight web and two hollow flanges. The shape of flanges can be triangular, circular or square one. To compare these structural versions with welded I-beams an optimization procedure is developed. The optimum cross-sectional dimensions are determined which minimize the cross-sectional area and fulfil the design constraints on stress due to bending and on local buckling of web and compression flange. The comparison shows that a HFB has smaller cross-sectional area (weight), larger moment of inertia (smaller deflection) and larger critical bending moment of lateral-torsional buckling.

1 INTRODUCTION

Hollow flanges can be used instead of simple plate flanges in welded beams (Fig.1). The shape of hollow flanges can be triangular, circular or rectangular (square). A special triangular hollow flange beam (TFB), called also „dogbone", was developed by the Australian firm Palmer Tube Technologies Ltd (Dempsey 1993), but this steel section was subsequently cancelled and is not manufactured.

The section is cold-formed from flat strip. The triangular flanges are closed by two electric resistance welded seam. They have used higher-strength steel of ultimate tensile strength 520 MPa and a yield strength 450 MPa.

They have not used any optimization procedure. We have worked out an optimization method to compare the TFB-s with circular CFB and square SFB and with welded I-beam.

The main advantages of HFB over simple welded I-beams are as follows: (a) the local buckling strength of beam parts is higher, therefore the thicknesses can be smaller; (b) the whole beam is higher, therefore the beam deflection is smaller; (c) the torsional stiffness is much larger, therefore the lateral-torsional buckling strength is larger.

The problem of lateral-torsional buckling of TFB is investigated by Pi & Trahair (1997). They have proposed a reduction of the torsional stiffness due to web distortion. We show that the Eurocode 3 (EC3) formulae give smaller values for lateral-torsional buckling factors, thus, the EC3 method can be used for comparison.

In the optimization the optimum cross-sectional dimensions are sought which minimize the cross-sectional area and fulfil the design constraints on maximum stress due to bending as well as on local buckling of the web and the compression flange.

First the cross-sectional characteristics are derived for an arbitrarily hollow flange shape and the optimization procedure is described, then the optimum cross-sectional areas and moments of inertia are expressed and compared for the above mentioned four beam shapes.

The lateral-torsional buckling strengths are characterized by buckling factors in the function of L/h for simply supported beams of span length L and web height h subject to uniformly distributed normal load.

It should be mentioned that Avery & Mahendron (1997) have investigated the effect of transverse stiffeners on the lateral-torsional buckling of TFB.

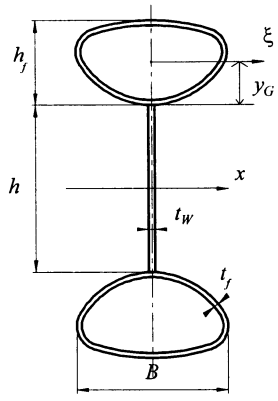

Figure 1. General hollow flange beam

A graphical optimization procedure is worked out for the design of welded I-beams against lateral-torsional buckling by Farkas (1997).

The calculation of the torsional constants of closed thin-walled beams is treated e.g. in the book Farkas & Jármai (1997).

2 SECTIONAL CHARACTERISTICS OF A GENERAL HOLLOW FLANGE BEAM

A general hollow flange beam is shown in Figure 1. Introducing the ratio between the flange depth and web depth as the main variable:

$$\varsigma = \frac{2h_f}{h} \tag{1}$$

and the slenderness:

$$\beta = \frac{t_w}{h} \tag{2}$$

the flange height can be expressed as:

$$h_f = \frac{\varsigma h}{2} \tag{3}$$

The second moment of inertia, the cross-sectional area of the flange and the location of the gravity centre y_G of the flange can be expressed as a function of web depth h or flange depth hf.

$$I_{f\varsigma} = P_1 h_f^4 = P_1 \varsigma^4 \frac{h^4}{16} \tag{4}$$

$$A_f = P_2 h_f^2 = P_2 \varsigma^2 \frac{h^2}{4} \tag{5}$$

$$y_G = P_3 h_f = P_3 \varsigma \frac{h}{2} \tag{6}$$

where $P1$, $P2$ and $P3$ are constants

The properties of the whole cross-sectional area can be written in the following forms:

$$A = ht_w + 2A_f = ht_w + P_2 \varsigma^2 \frac{h^2}{2} \tag{7}$$

$$I_x = \frac{h^3 t_w}{12} + 2\left[I_{f\varsigma} + A_f \left(\frac{h}{2} + y_G \right)^2 \right] \tag{8}$$

Substituting equations (2), (4), (5) and (6) into equation (8), one obtains the following for the moment of inertia

$$I_x = \frac{\beta h^4}{12} + 2\left[P_1 \varsigma^4 \frac{h^4}{16} + P_2 \varsigma^2 \frac{h^4}{16} (1 + P_3 \varsigma) \right] \tag{9}$$

and the elastic section modulus can be written as:

$$W_x = \frac{I_x}{\frac{h}{2} + h_f} = \frac{I_x}{\frac{h}{2}(1+\varsigma)} \tag{10}$$

From (9) and (10) we get the final form of the elastic section modulus:

$$W_x = \frac{\beta h^3}{6(1+\varsigma)} + \frac{\varsigma^2 h^3}{4(1+\varsigma)} \left[P_1 \varsigma^2 + P_2 (1 + P_3 \varsigma)^2 \right] \tag{11}$$

3 GENERAL OPTIMUM DESIGN

The objective function is the cross-sectional area (7).

The constraint on maximum normal stress due to bending moment M_{max} according to EC3 (1992) is defined by:

$$\sigma_{\max} = \frac{M_{\max}}{W_{el.x}} \le f_{y.1} = \frac{f_y}{\gamma_{M.1}} \tag{12}$$

$$\gamma_{M.1} = 1.1 \tag{13}$$

where $\gamma_{M.1}$ is a safety factor,
or expressed by the required section modulus W_0:

$$W_{el.x} \ge W_0 = \frac{M_{\max}}{f_{y.1}} \tag{14}$$

Local buckling constraints
For the web:

$$t_w \ge \beta h \tag{15}$$

where

$$\frac{1}{\beta} = 124 \sqrt{\frac{235}{\sigma_f}} \tag{16}$$

where β is the ultimate plate slenderness for the web and σf is the absolute value of the normal stress at the upper and the lower end of the web. Expressing

the ratio of σ_f and σ_{max},

$$\sigma_f = \sigma_{\max} \frac{\frac{h}{2}}{\frac{h}{2} + h_f} = \sigma_{\max} \frac{1}{1+\varsigma} \tag{17}$$

The final form of the plate slenderness for the web provided that the maximum normal stress σ_{max} in the extreme fibre is equal to the yield stress:

$$\frac{1}{\beta} = 124\sqrt{\frac{235}{f_y}(1+\varsigma)} = 124\varepsilon\sqrt{1+\varsigma} \tag{18}$$

$$\varepsilon = \sqrt{\frac{235}{f_y}} \tag{19}$$

For the upper part of the flange:

$$t_f \geq \frac{B}{\delta} \tag{20}$$

where B depends on the shape of the flange and δ is the ultimate plate slenderness for a flange according to EC3.

Converting the objective function (7)

$$A = \beta h^2 + P_2\varsigma^2 \frac{h^2}{2} = h^2\left(\beta + \frac{P_2\varsigma^2}{2}\right) \tag{21}$$

$$h^3 = \frac{A^{\frac{3}{2}}}{\left(\beta + \frac{P_2\varsigma^2}{2}\right)^{\frac{3}{2}}} \tag{22}$$

and substituting (22) into (11) the stress constraint gets the following form:

$$\frac{A}{W_0^{\frac{2}{3}}} = \frac{\beta + \frac{P_2\varsigma^2}{2}}{\left\{\frac{\beta}{6(1+\varsigma)} + \frac{\varsigma^2}{4(1+\varsigma)}\left[P_1\varsigma^2 + P_2(1+P_3\varsigma)^2\right]\right\}^{\frac{2}{3}}} \tag{23}$$

As W_0 is a constant the only variable is ζ, so the task is to find the optimum ζ which gives the minimum cross-sectional area.

4 TRIANGULAR FLANGE BEAM (TFB)

The dimensions of a TFB can be seen in Figure 2. The flange details of TFB are shown in Figure 3. Because of the production technology of TFB its thickness has to be a constant along its circumference. Instead of using both buckling constraints (local buckling for the web and for the flange) we introduce only one buckling constraint:

$$t \geq \beta h \tag{24}$$

For the web:

$$\frac{1}{\beta_w} = 124\varepsilon\sqrt{1+\varsigma} \tag{25}$$

For the upper part of the flange:

$$t \geq \beta_{f0} B \tag{26}$$

Expressing the flange width B by means of the web depth h we get another form of (26):

$$B = \frac{2h_f}{\tan\alpha} = \frac{\varsigma h}{\tan\alpha} \tag{27}$$

$$t \geq \beta_{f0} \frac{\varsigma h}{\tan\alpha} = \beta_f h \tag{28}$$

According to EC3(1992) $\frac{1}{\beta_{f0}} = 42\varepsilon$ (29)

$$\frac{1}{\beta_f} = 42\varepsilon\frac{\tan\alpha}{\varsigma} \tag{30}$$

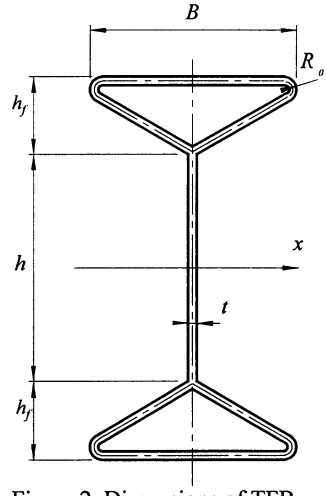

Figure 2. Dimensions of TFB

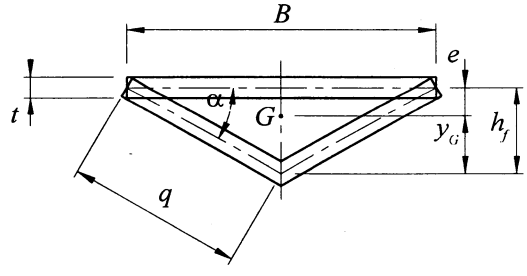

Figure 3. Flange details of TFB

Since the web and flange have the same thickness, the larger value from $\beta_w h$ and $\beta_f h$ is governing. The symbol β is used, but the optimization has to be performed either with $\beta_w h$ and with $\beta_f h$.

The solution of (31) gives the value of ζ at which web and flange buckling constraints are active.

$$\beta_w h = \beta_f h \tag{31}$$

$$\frac{h}{124\varepsilon\sqrt{1+\zeta}} = \frac{\zeta h}{42\varepsilon tan\alpha} \tag{32}$$

It can be seen from (32) that the solution for ζ does not depend on the yield stress of the material. The only factor which affects the solution of ζ is the angle of the flange α.

Solving (32) for given flange angles for the interval $0.1 \leq \zeta \leq 1$:

for α=30° $\zeta_{opt} = 0.180020$ (33)

for α=35° $\zeta_{opt} = 0.215149$ (34)

for α=40° $\zeta_{opt} = 0.253818$ (35)

Below the limit of ζ_{opt} the web buckling constraint is active and defines the thickness of TFB. Above ζ_{opt} the flange buckling constraint is active.

The sectional properties can be expressed as follows: the cross-sectional area of a triangular hollow flange:

$$A_f = Bt + 2qt = \frac{2h_f t(1+\cos\alpha)}{\sin\alpha} \tag{36}$$

considering that the local buckling constraint is active:

$$t = \beta h \tag{37}$$

$$A_f = \frac{4\beta h_f^2(1+cos\alpha)}{\zeta sin\alpha} = P_2 h_f^2 \tag{38}$$

The location of the gravity centre G of the flange is described by the distance:

$$e = \frac{2qt\frac{h_f}{2}}{A_f} = \frac{h_f}{2(1+\cos\alpha)} \tag{39}$$

and

$$y_G = h_f - e = \frac{h_f(1+2\cos\alpha)}{2(1+\cos\alpha)} = P_3 h_f \tag{40}$$

The moment of inertia of the flange section is:

$$I_{f\xi} = \frac{t^3 B}{12} + Bte^2 + \frac{2q^3 t\sin^2\alpha}{12} + \left(\frac{h_f}{2} - e\right)^2 2qt \tag{41}$$

The first member of (41) can be neglected in comparison with the other members.

$$I_{f\xi} = P_1 h_f^4 \tag{42}$$

The design constants P_1, P_2 and P_3 can be expressed from (41), (38) and (40), respectively:

$$P_1 = \frac{\beta}{\zeta\sin\alpha(1+\cos\alpha)^2}\left[\cos\alpha + \cos^2\alpha + \right.$$

$$\left. + \frac{(1+\cos\alpha)^2}{3}\right] \tag{43}$$

$$P_2 = \frac{4\beta(1+\cos\alpha)}{\zeta\sin\alpha} \tag{44}$$

$$P_3 = \frac{1+2cos\alpha}{2(1+cos\alpha)} \tag{45}$$

Substituting the design constants into (23), and iterating this equation we can get the optimum value of ζ.

The cross-sectional area of TFB can be calculated as follows:

For steel with a yield stress of 355 MPa:

α=30° $A_{optTFB} = 0.536347 \cdot W_0^{\frac{2}{3}}$ (46)

α=35° $A_{optTFB} = 0.531289 \cdot W_0^{\frac{2}{3}}$ (47)

α=40° $A_{optTFB} = 0.526035 \cdot W_0^{\frac{2}{3}}$ (48)

The optimum dimensions for TFB are as follows:

$$h_{opt} = \sqrt{\frac{A_{optTFB}}{\beta + P_2\frac{\zeta_{opt}^2}{2}}} \tag{49}$$

$$h_f = \frac{\zeta_{opt} h_{opt}}{2} \tag{50}$$

$$B_{opt} = \frac{2h_f}{\tan\alpha} \tag{51}$$

$$t_{opt} = \beta h_{opt} \tag{52}$$

5 CIRCULAR HOLLOW FLANGE BEAM (CFB)

The dimensions of a CFB can be seen in Figure 4. The design constants (P_1, P_2 and P_3) can be expressed by means of the ultimate plate slenderness of the flange.

The ultimate plate slenderness according to EC3 (1992) for the flange, considering that the local buckling constraint for the flange is active:

$$\delta_c = \frac{2r}{t} = \frac{D}{t} = 90\varepsilon^2 = 90\frac{235}{f_y} \tag{53}$$

$$h_f = 2r \tag{54}$$

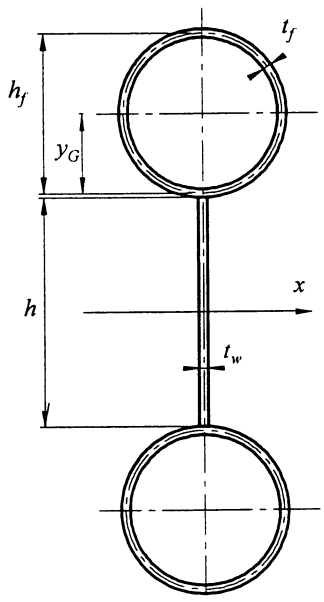

Figure 4. Dimensions of a CFB

The P_1, P_2, P_3 design constants can be expressed from (4):

$$I_{f\xi} = \pi r^3 t = \frac{2\pi r^4}{\delta_c} = P_1 h_f^4 = P_1(2r)^4 = 16P_1 r^4 \tag{55}$$

$$P_1 = \frac{\pi}{8\delta_c} \tag{56}$$

from (5):

$$A_f = P_2 h_f^2 = P_2 4r^2 = 2\pi rt = \frac{4\pi r^2}{\delta_c} \tag{57}$$

$$P_2 = \frac{\pi}{\delta_c} \tag{58}$$

from (6):

$$y_G = P_3 h_f = P_3 2r = r \tag{59}$$

$$P_3 = \frac{1}{2} \tag{60}$$

Substituting P_1, P_2, P_3 into (23) we can get its final form

$$\frac{A}{W_0^{\frac{2}{3}}} = \frac{\beta + \frac{\pi}{2\delta_c}\varsigma^2}{\left\{\frac{\beta}{6\beta(1+\varsigma)} + \frac{\varsigma^2}{4(1+\varsigma)}\left[\frac{\pi}{8\delta_c}\varsigma^2 + \frac{\pi}{\delta_c}\left(1+\frac{\varsigma}{2}\right)^2\right]\right\}^{\frac{2}{3}}} \tag{61}$$

The optimum value of ζ can be calculated by the iteration of ζ. The optimum value of ζ is 0.92, 0.81, 0.75 for steel with a yield stress of 235 MPa, 355 MPa, 450 MPa, respectively.

The minimum cross-sectional area of CFB can be calculated as follows:

For steel with a yield stress of 355 MPa:

$$A_{opt,CFB} = 0.513517 \cdot W_0^{\frac{2}{3}} \tag{62}$$

The optimum dimensions of CFB are as follows:

$$h_{opt} = \sqrt{\frac{A_{optCFB}}{\beta + P_2\frac{\varsigma_{opt}^2}{2}}} \tag{63}$$

$$t_{w,opt} = \beta h_{opt} = \frac{h_{opt}}{124\varepsilon\sqrt{1+\varsigma_{opt}}} \tag{64}$$

$$D_{opt} = \frac{1}{2}\varsigma h \tag{65}$$

$$t_{opt} = \frac{D_{opt}}{\delta_c} \tag{66}$$

6 SQUARE HOLLOW FLANGE BEAM (SFB)

The dimensions of a SFB can be seen in Figure 5. The design constants P_1, P_2 and P_3 can be expressed by means of the ultimate plate slenderness of the flange.

The ultimate plate slenderness, according to EC3 (1992) for the flange, considering that the local buckling constraint for the flange is active, is:

$$\delta_L = \frac{b_s}{t} = 42\varepsilon = 42\sqrt{\frac{235}{f_y}} \tag{67}$$

$$h_f = b_s \tag{68}$$

The P_1, P_2, P_3 design constants can be expressed from (4):

$$I_{f\xi} = \frac{2b_s^3 t}{3} = \frac{2b_s^4}{3\delta_L} = P_1 h_f^4 = P_1 b_s^4 \tag{69}$$

$$P_1 = \frac{2}{3\delta_L} \tag{70}$$

from (5):

$$A_f = P_2 h_f^2 = 4 b_s t = \frac{4h_f^2}{\delta_L} \tag{71}$$

$$P_2 = \frac{4}{\delta_L} \tag{72}$$

from (6):

$$y_G = P_3 h_f = P_3 b_s = \frac{b_s}{2} \tag{73}$$

$$P_3 = \frac{1}{2} \tag{74}$$

Substituting P_1, P_2, P_3 into (23), we can get its final form

$$A / W_0^{2/3} = \frac{\beta + \frac{2}{\delta_L}\varsigma^2}{\left\{\frac{\beta}{6\beta(1+\varsigma)} + \frac{\varsigma^2}{4(1+\varsigma)}\left[\frac{2}{3\delta_L}\varsigma^2 + \frac{4}{\delta_L}\left(1+\frac{\varsigma}{2}\right)^2\right]\right\}^{\frac{2}{3}}} \tag{75}$$

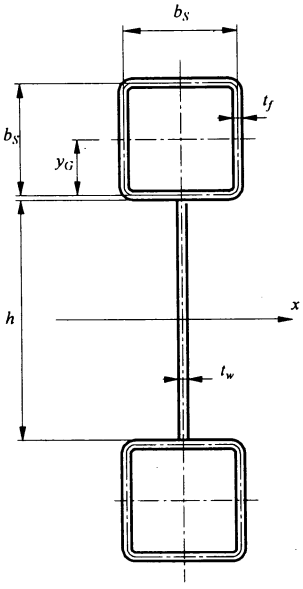

Figure 5. Dimensions of a SFB

The optimum value of ζ can be calculated by the iteration of ζ. The optimum value of ζ for steels of yield stress of 235 MPa, 355 MPa, 450 MPa is 0.5.

The cross-sectional area of SFB can be calculated as follows:

For steel with a yield stress of 355 MPa:

$$A_{opt\,SFB} = 0.536256 \cdot W_0^{\frac{2}{3}} \tag{76}$$

The optimum dimensions for HFB with CHS flange:

$$h_{opt} = \sqrt{\frac{A_{optSFB}}{\beta + P_2 \frac{\varsigma_{opt}^2}{2}}} \tag{77}$$

$$t_{w,opt} = \beta h_{opt} = \frac{h_{opt}}{124\varepsilon\sqrt{1+\varsigma_{opt}}} \tag{78}$$

$$b_{sopt} = \frac{1}{2}\varsigma_{opt} h_{opt} \tag{79}$$

$$t_{fopt} = \frac{b_{sopt}}{\delta_L} \tag{80}$$

7 WELDED I-SECTION

The objective function is

$$A = ht_w + 2bt_f \tag{81}$$

the stress constraint is

$$\frac{M}{W_x} \le \frac{f_y}{\gamma_{M1}} \tag{82}$$

the web buckling constraint is

$$\frac{t_w}{h} \ge \beta = \frac{1}{124\varepsilon} \tag{83}$$

the flange buckling constraint is

$$\frac{t_f}{b} \ge \delta = \frac{1}{42\varepsilon} \tag{84}$$

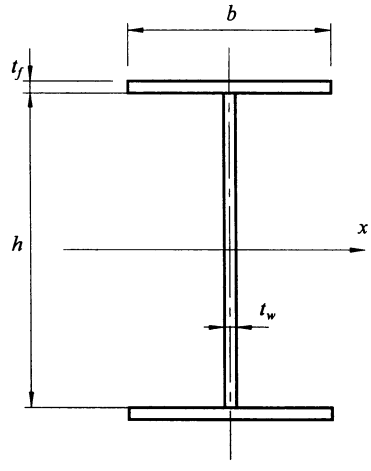

Figure 6. Dimensions of a welded I-section

The optimal solution of the problem is the following (Farkas 1984, Farkas & Jármai 1997):

$$A_{opt} = 2\beta h_{opt}^2 = \sqrt[3]{18\beta W_0^2} \tag{85}$$

$$h_{opt} = \sqrt[3]{\frac{1.5W_0}{\beta}} \tag{86}$$

$$t_{wopt} = \beta h_{opt} \tag{87}$$

$$t_{fopt} = h_{opt}\sqrt{\frac{\beta\delta}{2}} \tag{88}$$

$$b_{opt} = \frac{t_{fopt}}{\delta} \tag{89}$$

The minimum cross-sectional area of welded I-section for steel of 355 MPa yield stress

$$A_{optI} = 0.554165 \cdot W_0^{\frac{2}{3}} \tag{90}$$

The above obtained results are summarized in Table 1.

Table 1. Cross-sectional area and moment of inertia of optimized TFB, CFB, SFB and welded I-beams

beam type	$A_{\min} / W_0^{2/3}$	$I_x / W_0^{4/3}$
TFB	0.536347	2.95464
CFB	0.513517	4.12001
SFB	0.536256	3.64304
I-beam	0.554165	2.70677

It can be seen that the HFB-s have smaller cross-sectional area and larger moment of inertia than the welded I-beam. The CFB has the smallest cross-sectional area and the largest moment of inertia.

8 LATERAL-TORSIONAL BUCKLING STRENGTH

8.1 *The EC3 method*

The design buckling resistance moment of a laterally unrestrained beam shall be taken as:

$$M_{b,Rd} = \chi_{LT}\beta_w W_{pl,y}\frac{f_y}{\gamma_{M1}} \tag{91}$$

where

$$\beta_w = \frac{W_{el,x}}{W_{pl,x}} \qquad \text{for Class 3 cross-sections}$$

and χ_{LT} is the reduction factor for lateral-torsional buckling

$$\chi_{LT} = \frac{1}{\phi_{LT} + \sqrt{\phi^2 - \bar{\lambda}^2}} \quad \text{but } \chi_{LT} \le 1 \tag{92}$$

in which

$$\phi_{LT} = 0.5\left[1 + \alpha_{LT}\left(\bar{\lambda}_{LT} - 0.2\right) + \bar{\lambda}_{LT}^2\right] \tag{93}$$

The values of the imperfection factor α_{LT} for lateral torsional buckling should be taken as: $\alpha_{LT} = 0.49$ for welded sections.

The formula of $\bar{\lambda}_{LT}$ is as follows:

$$\bar{\lambda}_{LT} = \frac{\lambda_{LT}}{\lambda_1}\beta_w^{\frac{1}{2}} \tag{94}$$

where

$$\lambda_1 = \pi\left(\frac{E}{f_y}\right)^{\frac{1}{2}} = 93.9\varepsilon \tag{95}$$

$$\varepsilon = \sqrt{\frac{235}{f_y}} \tag{96}$$

$$\lambda_{LT} = \frac{L\left(\frac{W_{pl,x}^2}{I_y I_\omega}\right)^{0.25}}{C_1^{0.5}\left(1 + \frac{GL^2 I_t}{\pi^2 E I_\omega}\right)^{0.25}} \tag{97}$$

for beams with pinned ends with uniformly disributed loads $C_1 = 1.132$, I_t is the torsion constant, I_ω is the warping constant, I_y is the moment of inertia about the minor axis, L is the beam length between points which have lateral restraint.

8.2 *The method of Pi & Trahair (1997)*

They have proposed a calculation method which considers also the effect of web distortion. Their formula for the design bending moment is

$$\frac{M_{bdx}}{M_{Sx}} = \alpha_{Sd}\alpha_m = 0.6\alpha_m^2\left(\sqrt{\lambda_d^4 + \frac{2.8}{\alpha_m^2}} - \lambda_d^2\right) \tag{98}$$

where α_m is the factor for the effect of loading, for uniformly distributed normal load it is 1.1662. Values of $\alpha_{Sd}\alpha_m$ in the function of λ_d are compared with the lateral-torsional buckling factors χ_{LT} given by EC3 in function of $\bar{\lambda}_{LT}$ in Table 2.

Table 2. Comparison of lateral-torsional buckling factors given by Pi & Trahair as well as by EC3

λ_d or $\bar{\lambda}_{LT}$	$\alpha_{Sd}\alpha_m$	χ_{LT}
0.5	0.9845	0.8430
1.0	0.6111	0.5399
1.5	0.3416	0.3145
2.0	0.2036	0.1962

It can be seen that the buckling factors given by EC3 are smaller than those of Pi & Trahair, thus, the EC3 method is suitable for comparison.

8.3 *Comparison of lateral-torsional buckling factors using the EC3 formulae*

We calculate the buckling factors in the function of $\varphi = L/10h$ in the range of $\varphi = 1-10$.
(a) Using the formulae given in Section 4, the characteristics of a TFB, expressed in terms of the web height are as follows:

with $\varsigma_{opt} = 0.18$, f_y = 355 MPa and $\alpha = 30^0$ one obtains

$$W_{pl.x} = \beta h^3\left[0.25+\frac{\varsigma(1+\varsigma)}{\tan\alpha}+\frac{\varsigma(1+\varsigma/2)}{\sin\alpha}\right] =$$

$$= 0.9218*10^{-2}h^3,$$

$$W_{el.x} = 0.79608*10^{-2}h^3 \;;\; \beta_w^{0.5} = 0.9293$$

$$I_y = \frac{\varsigma^3 h^3\beta}{64\tan^3\alpha}\left(1+\frac{1}{\cos\alpha}\right) = 9.9279*10^{-5}h^4$$

$$I_t = \frac{\varsigma^3\beta\cos^2\alpha}{2\sin\alpha(\sin\alpha+\cos\alpha)}h^4 = 2.9218*10^{-5}h^4$$

$$I_\varpi = \frac{\varsigma^3\beta}{24\tan^3\alpha}\left(1+\frac{1}{\cos\alpha}\right)\left(1-\frac{\varsigma}{1+\cos\alpha}\right)^2 =$$

$$=2.0263*10^{-5}h^6$$

It should be mentioned that we use the symbol ϖ instead of ω, since the hollow flanges are closed sections.

According to (94) and (97)

$$\bar{\lambda}_{LT} = \frac{1.63875\varphi}{\left(1+5.6193\varphi^2\right)^{025}}$$

(b) Formulae for CFB with $\varsigma_{opt} = 0.81$ and f_y = 355 MPa:

$$W_{pl.x} = \frac{\beta h^4}{4}+\frac{\pi\varsigma^2 h^3(1+\varsigma/2)}{4\delta_C} = 1.3994*10^{-2}h^3$$

$$W_{el.x} = \frac{2I_x}{1+\varsigma} = 1.0503*10^{-2}h^3$$

$$I_y = \frac{\pi\varsigma^4 h^4}{64\delta_C} = 0.35466*10^{-3}h^4$$

$$I_t = \frac{\pi\varsigma^4 h^4}{32\delta_C} = 7.09315*10^{-4}h^4$$

$$I_\varpi = \frac{2}{3}h_f t_f\left(3\varpi_{T1}^2+2\varpi_{T1}\varpi_{T2}+3\varpi_{T2}^2\right)$$

where

$$\varpi_{T1} = -\frac{h_f^2}{2}\left(\frac{1}{\varsigma}+\frac{1}{2}\right);\quad \varpi_{T2} = -\frac{h_f^2}{2}\left(\frac{1}{\varsigma}-1\right)$$

Since the exact calculation of the warping constant for the closed sectional parts of CFB leads to very complicated integrals, we use the formula of the warping constant derived for SFB with the approximation that $h_f = D\sqrt{2}/2$, this means that, instead of the circle, a square is used inscribed inside the circle. This approximation gives the following value:

$$I_\varpi = 2.18333*10^{-5}h^6.$$

$$\bar{\lambda}_{LT} = \frac{1.34385\varphi}{\left(1+126.6051\varphi^2\right)^{0.25}}$$

(c) Formulae for SFB with $\varsigma_{opt} = 0.5$ and f_y = 355 MPa:

$$W_{pl.x} = \frac{\beta h^4}{4}+\varsigma h^2 t_f(2+\varsigma) = 1.11688*10^{-2}h^3$$

$$W_{el.x} = 0.872368*10^{-2}h^3$$

$$I_y = \varsigma^3 h^3 t_f / 6 = 1.52425 * 10^{-4} h^4$$

$$I_t = \varsigma^3 h^3 t_f / 4 = 2.28637 * 10^{-4} h^4$$

The formula for warping constant is the same as for CFB:

$$I_\varpi = 6.99612 * 10^{-5} h^6;$$

$$\bar{\lambda}_{LT} = \frac{2.01048\varphi}{\left(1 + 12.7356\varphi^2\right)^{0.25}}.$$

The results of calculations are summarized in Table 3.

It can be seen that the lateral-torsional buckling strength of HFB-s is larger than that of welded I-beam. The high values for CFB show that the torsional stiffness of circular hollow flanges is very large because of the high value of $\varsigma_{opt} = 0.81$ compared with the lower ς_{opt}-values for TFB and SFB.

9 CONCLUSIONS

The minimum cross-sectional area design of four welded beam types considering the maximum stress due to bending and the limiting local buckling slendernesses gives a basis of comparison relating to the beam weight, deflection and lateral-torsional buckling strength.

The cross-sectional area (weight) of HFB-s is smaller than that of I-beams. The moment of inertia about the major axis of HFB-s is larger, therefore the beam deflection is smaller than that of I-beams (Table 1).

The lateral-torsional buckling factor in function of $\varphi = L/10h$ is larger for HFB-s than that for I-beams (Table 3). These realistic comparisons give designers a basis for selection of suitable structural versions.

Table 3. Comparison of lateral-torsional buckling factors

φ	χ_{LT} TFB	χ_{LT} CFB	χ_{LT} SFB	χ_{LT} I-beam
1	0.5275	0.8974	0.5146	0.3536
2	0.3181	0.8052	0.3153	0.1346
3.33	0.2075	0.7052	0.2068	0.0702
10	0.0769	0.4031	0.0769	0.0216

ACKNOWLEDGEMENTS

This work has been supported by grants OTKA 19003 and 22846 of the Hungarian Fund for Scientific Research.

REFERENCES

Avery,Ph. & M. Mahendran 1997. Finite-element analysis of hollow flange beams with web stiffeners. *J. Struct. Engng ASCE* 123: 1123-1129.

Dempsey,R.I. 1993. *Hollow flange beam member design manual.* Palmer Tube Technologies Pty Ltd. Queensland, Australia.

Eurocode 3. 1992. *Design of steel structures. Part 1.1.* CEN European Committee for Standardization, Brussels.

Farkas,J. 1984. *Optimum design of metal structures.* Budapest: Akadémiai Kiadó, Chichester: Ellis Horwood.

Farkas,J. & K. Jármai 1997. *Analysis and optimum design of metal structures.* Rotterdam: Balkema.

Farkas,J. 1997. Optimum design of welded I-beams with constraint on lateral-torsional buckling. *Publ. Univ. of Miskolc, Series C. Mechanical Engineering.*47: 27-35.

Mahendran,M. & Ph.Avery 1997. Buckling experiments on hollow flange beams with web stiffeners. *J. Struct. Engng ASCE* 123: 1130-1134.

Pi, Y.L. & N.S. Trahair 1997. Lateral-distortional buckling of hollow flange beams. *J. Struct. Engng ASCE* 123: 695-702.



Taylor & Francis
Taylor & Francis Group
http://taylorandfrancis.com

Tubular Structures VIII, Choo & Van der Vegte (eds) © 1998 Balkema, Rotterdam, ISBN 90 5809 001 9

Compact or Class 1 limits for rectangular hollow sections in bending

Tim Wilkinson & Gregory J. Hancock
Centre for Advanced Structural Engineering, The Department of Civil Engineering, The University of Sydney, N.S.W., Australia

ABSTRACT: This paper describes a series of bending tests to examine the influence of web slenderness on the rotation capacity of cold-formed rectangular hollow sections (RHS) for use in plastic design. Some sections, which are classified as Class 1 or Compact by current steel specifications, do not demonstrate rotation capacity suitable for plastic design. There is considerable interaction between the webs and flange which influences the rotation capacity which is shown by approximate iso-rotation curves. A proposal for a linear interaction formula between the web and flange slenderness for the Compact limits of RHS is given.

KEYWORDS: cold-formed steel, hollow sections, plastic design, slenderness ratio, bending, rotation capacity, beams

1 INTRODUCTION

Local buckling may affect the bending behaviour of steel sections. Steel design specifications define different classes of cross sections, depending on the point at which local buckling occurs during bending. Sections can be classified as Compact, Non-Compact or Slender, or Class 1, 2, 3, or 4. A Compact or Class 1 section is deemed suitable for plastic design.

Figure 1 illustrates various types of behaviour of steel beams mentioned above. The curvature (κ) is non-dimensionalised with respect to κ_p, where $\kappa_p = M_p/EI$, M_p is the plastic moment and EI is the elastic rigidity. The rotation capacity (R) is a measure of rotation between reaching M_p and the point where the moment falls below M_p. R is defined as κ/κ_p - 1, where κ/κ_p is the dimensionless curvature at which the moment drops below M_p. The decrease in moment is usually associated with an inelastic local buckle. Width - thickness (b/t) or slenderness limits are normally given to classify the effect of local buckling of sections and to determine suitability for plastic design.

There has been research on the flange slenderness limit for rectangular hollow sections (RHS) and square hollow sections (SHS) (Dwyer and Galambos (1965); Korol and Hudoba (1972); Hasan and Hancock (1988); and Zhao and Hancock (1991)). More recently, RHS have been produced with higher aspect ratios (depth/width), such as 3.0 (Tubemakers (1994)). The webs of these sections are considerably more slender than the flange, and the possibility of web local buckling before flange buckling is increased. Zhao and Hancock ((1991a) and (1992)) observed inelastic web local buckling in some RHS and provided the impetus for this test series.

2 CURRENT SPECIFICATIONS

Steel design codes from Europe, America and Australia are considered in this paper: the American Institute of Steel Construction Metric Load and Resistance Factor Design Specification for Structural Steel Buildings (AISC (1994)) (henceforth referred to as "AISC LRFD"), Eurocode 3 Part 1.1: Design of Steel Structures (European Committee for Standardisation (1992)) ("Eurocode 3"), and Australian Standard AS 4100 Steel Structures (Standards Australia (1990)) ("AS 4100").

The web and flange slenderness limits for cold-formed RHS bending about the major principal axis are listed in Table 1 for each standard for the RHS shown in Figure 2. Figure 2 defines the dimensions d, b, and t (depth, width and thickness) of the section. The web and flange slenderness limits in Table 1 are independent of each other since no interaction between the webs and flange is considered. Table 1 indicates that the AISC LRFD web slenderness limits are significantly higher than AS 4100 and Eurocode 3 web slenderness limits. The flange slenderness limits in the three standards are very similar.

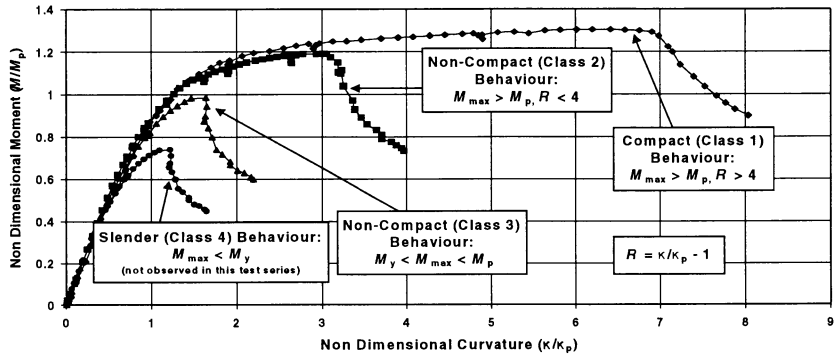

Figure 1: Classes of behaviour for cold-formed RHS beams

Table 1: Summary of RHS Slenderness Limits

Standard	Web slenderness (λ_w)	Flange slenderness (λ_f)	Web / *Flange* slenderness limits							
			Class 1 Compact		Class 2		Class 3		Non-Compact	
			λ_w	λ_f	λ_w	λ_f	λ_w	λ_f	λ_w	λ_f
AS 4100	$\frac{d-2t}{t}\sqrt{\frac{f_y}{250}}$	$\frac{b-2t}{t}\sqrt{\frac{f_y}{250}}$	82	*30*	-		-		115	*40*
AISC LRFD	$\frac{d-2r_c}{t}\sqrt{\frac{f_y}{E}}$	$\frac{b-2r_c}{t}\sqrt{\frac{f_y}{E}}$	3.76 106*	*1.12* *31.7**	-		-		5.7 161*	*1.4* *39.6**
Eurocode 3	$\frac{d-3t}{t}\sqrt{\frac{f_y}{235}}$	$\frac{b-3t}{t}\sqrt{\frac{f_y}{235}}$	72	*33*	83	*38*	124	*42*	-	

Notes: Sections exceeding the Class 3 or Non-Compact limit are Class 4 or Slender respectively.
* Applies to f_y = 250 MPa for direct comparison with the AS 4100 limits.
Values in *italics* refer to flange limits, values in plain text refer to web limits.

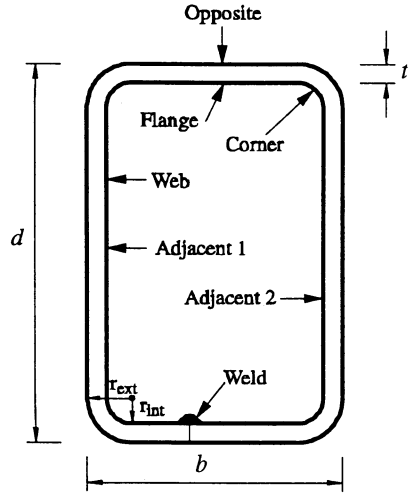

Figure 2: Typical RHS

Steel design specifications have varying rotation capacity requirements for plastic design. The wide variety of loading patterns and structural frame shapes results in a large range of required plastic rotations. However it is appropriate to adopt a representative value of rotation capacity which is satisfactory for most practical situations. Korol and Hudoba (1972) put forward a recommendation of $R = 4$. Eurocode 3 Class 1 and AISC LRFD Compact limits are based on a rotation capacity of $R = 3$. However AISC LRFD states that greater rotation capacity may be required in seismic regions. A value of $R = 4$ was adopted in the determination of the RHS flange slenderness limit in AS 4100 (Hasan and Hancock (1988), Zhao and Hancock (1991b)) as appropriate for plastic design and is deemed suitable in this paper.

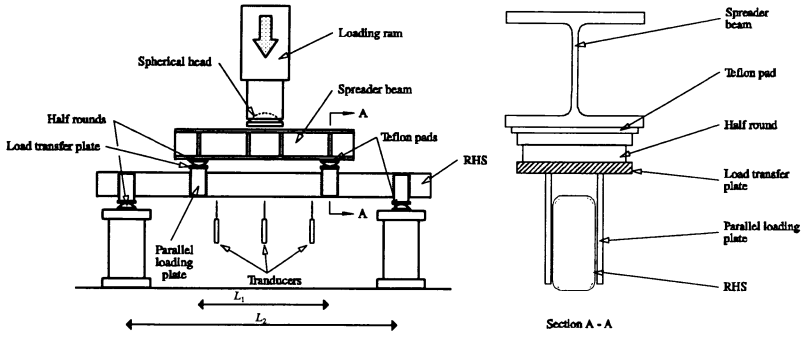

Figure 3: Test rig for plastic bending tests

3 TEST SPECIMENS

The RHS in this test series were manufactured by BHP Structural and Pipeline Products. Two strength grades were selected, Grade C350L0 and C450L0 (nominal yield stress of 350 MPa and 450 MPa respectively), manufactured to Australian Standard AS 1163 (Standards Australia (1991)). The Grade C450 specimens are known as *DuraGal* sections, produced using a unique cold-forming and in-line galvanising process. In-line galvanising provides extra strength enhancement compared to cold-forming alone.

4 TENSILE COUPON TESTS

Three coupons were taken from the centre of the flats of each tube. One was cut from the face opposite the weld, and one from each of the sides adjacent to the weld (refer to Figure 2). Corner coupons were cut from selected RHS. The coupons were prepared and tested in accordance with AS 1391 (Standards Australia (1991)) in a 250 kN capacity INSTRON Universal Testing Machine.

Since the steel was cold-formed, the yielding was gradual, so that the yield stress used was the 0.2% static proof stress. The average of the yield stress from both of the adjacent faces was used in the determination of plastic moment and slenderness values. The average of the Young's modulus of elasticity from both of the adjacent faces was used in stiffness calculations. The yield stress of the opposite face was on average 10% higher than that of the adjacent faces. This was a result of the cold-forming process and has been identified previously (CASE (1990)). The yield stress obtained from the corner coupons was on average 10% higher than that of the opposite face. Full details on the tensile coupon tests are given in Wilkinson and Hancock (1997).

5 PLASTIC BENDING TESTS

5.1 *Procedure*

The bending tests were performed in a 2000 kN capacity DARTEC testing machine, using a servo-controlled hydraulic ram. A diagram of the test set-up is shown in Figure 3. The four point bending arrangement provided a central region of uniform bending moment and zero shear force. Specimens were supported on half rounds resting on greased Teflon pads. The members were loaded symmetrically at two points via a centrally loaded spreader beam.

The initial loading method ("parallel plate" method) adopted is one that has been used previously (Hasan and Hancock (1988), Zhao and Hancock (1991)) and involved welding plates parallel to the webs of the RHS beam as shown in Figure 3. A greased teflon pad was placed between the bottom of the spreader beam and the half round, to allow for axial shortening of the beam caused by curvature. The half round ensured that the applied loads were vertical. The half round bore upon a thick load transfer plate, which transmitted the force to the loading plates. The lengths of the specimens were chosen to avoid lateral buckling (Zhao, Hancock and Trahair (1995)), and shear failure in the end spans. For RHS with depth $d \geq 100$ mm, the length between the loading points (L_1) was 800 mm, and the distance between the supports (L_2) was 1700 mm. For sections with $d \leq 75$ mm, L_1 was 500 mm, and L_2 was 1300 mm. Two other loading methods ("perpendicular plate" and "pin loading") were used in some tests. It was found that the loading method did not have a significant effect on the rotation capacity (Wilkinson and Hancock (1997)).

5.2 *Results*

The results of the plastic bending tests are presented in Table 2. This table lists the section size, the ratio M_{max}/M_p, and R. M_{max} is the maximum static moment reached during the test and M_p is the plastic moment of

Table 2: Summary of Results of Plastic Bending Tests

Specimen	Section	Loading method	$\frac{M_{max}}{M_p}$	R
BS01B	150x50x5.0 C450	Parallel	1.23	>13.0
BS01C		Parallel	1.17	>9.0
BS02B	150x50x4.0 C450	Parallel	1.27	6.6
BS02C		Parallel	1.19	7.7
BS02A		Pin	1.24	7.2
BF02		Parallel	1.17	9.5
BS03A	150x50x3.0 C450	Parallel	1.15	2.7
BS03B		Parallel	1.16	2.3
BS03C		Parallel	1.13	2.9
BS04B	150x50x2.5 C450	Parallel	1.02	1.4
BS04C		Parallel	1.00	1.2
BS04A		Perp.	1.10	2.2
BS16A		Pin	1.11	1.1
BS05A	150x50x2.3 C450	Parallel	0.98	0.0
BS05B		Parallel	1.01	0.6
BS05C		Parallel	0.98	0.0
BS06B	100x50x2.0 C450	Parallel	1.07	0.8
BS06C		Parallel	1.01	0.8
BS06A		Perp.	1.07	1.3
BS17A		Pin	1.08	1.6
BS07B	75x50x2.0 C450	Parallel	1.04	1.7
BS07C		Parallel	1.02	1.9
BS08B	75x25x2.0 C450	Parallel	1.11	5.7
BS08C		Parallel	1.13	n/a
BS09B	75x25x1.6 C450	Parallel	1.08	2.2
BS09C		Parallel	1.13	2.5
BS09A		Perp.	1.09	2.5
BS10B	75x25x1.6 C350	Parallel	1.03	1.9
BS10C		Parallel	1.00	2.6
BS11B	150x50x3.0 C350	Parallel	1.21	4.1
BS11C		Parallel	1.15	3.6
BS20A		Perp.	1.18	3.2
BS20B		Pin	1.21	3.6
BS12B	100x50x2.0 C350	Parallel	1.00	1.2
BS12C		Parallel	1.00	1.3
BS13B	125x75x3.0 C350	Parallel	1.03	1.5
BS13C		Parallel	1.04	1.6
BS13A		Perp.	1.03	1.4
BS21A	125x75x2.5 C350	Pin	1.06	1.1
BS19A	100x100x3.0 C450	Parallel	1.02	0.8
BS19B		Pin	0.95	0.7
BS19C		Perp.	1.03	0.9
BJ07	150x50x4.0 C350	Parallel	1.28	12.9
BF01		Parallel	1.19	10.7

the section based on the measured dimensions and the measured yield stress. The static moment is obtained when the test machine is halted for approximately one minute in the vicinity of the ultimate load. Measured dimensions are tabulated in Wilkinson and Hancock (1997).

All specimens except the two 150 x 50 x 5.0 C450 (BS01B and BS01C) specimens and the 100 x 100 x 3.0 C450 (BS19A, BS19B and BS19C) samples experienced web local buckling, which produced a rapid shedding of load with increased deflection. Each web buckled and compatibility of rotation at the corner caused deformation of the flange. The local buckle always formed adjacent to one of the loading plates. BS01B and BS01C exhibited large deflections and inelastic lateral deformation was observed at high curvatures (κ/κ_p) greater than 6. There was no sudden unloading associated with the lateral deflection. BS19A, BS19B and BS19C were SHS and, as expected, failed by flange buckling. Specimen BS08C was not loaded to failure. No specimen failed due to insufficient material ductility.

Four typical non-dimensional moment-curvature curves are shown in Figure 1, and are representative of the performance of the test specimens. Compact and Non-Compact behaviour, as shown in Figure 1, was observed. No specimen behaved as a Slender section, but a typical slender member's behaviour is shown in Figure 1 for completeness.

The web slenderness is calculated slightly differently in AS 4100, Eurocode 3, and AISC LRFD (refer to Table 1). The results calculated according to Eurocode 3 are shown in Figure 4, which also compares the results of the different steel grades. Figures 5 displays the rotation capacity versus web slenderness for AISC LRFD and differentiates between the different aspect ratios. In each figure, the slenderness is calculated with the measured dimensions and yield stress.

6 DISCUSSION

The results in Figures 4 and 5 clearly indicate that the current web slenderness limits for Compact or Class 1 sections are non-conservative. There is a large number of sections which are currently classified as Compact or Class 1 which demonstrate insufficient rotation capacity for plastic design. The Compact limit for the AISC LRFD specification is the most unconservative. The trend in Figure 5 suggests it may be possible that sections defined as Compact by AISC LRFD may not even be able to reach the plastic moment M_p let alone maintain the plastic moment for significant rotations. Many of the sections classified by Eurocode 3 as Compact or Class 1 failed to reach the required rotations of $R = 3$ or $R = 4$ as shown in Figure 4.

Figure 4 also compares the different steel grades. Separate linear regression lines for the Grade C350 and Grade C450 are plotted in Figure 4. It can be seen that to achieve a rotation capacity of approximately $R = 4$, a similar web slenderness is required from both Grade C350 and Grade C450 RHS. At higher web slenderness, less rotation capacity is generally available for the Grade C450 RHS compared to the Grade C350.

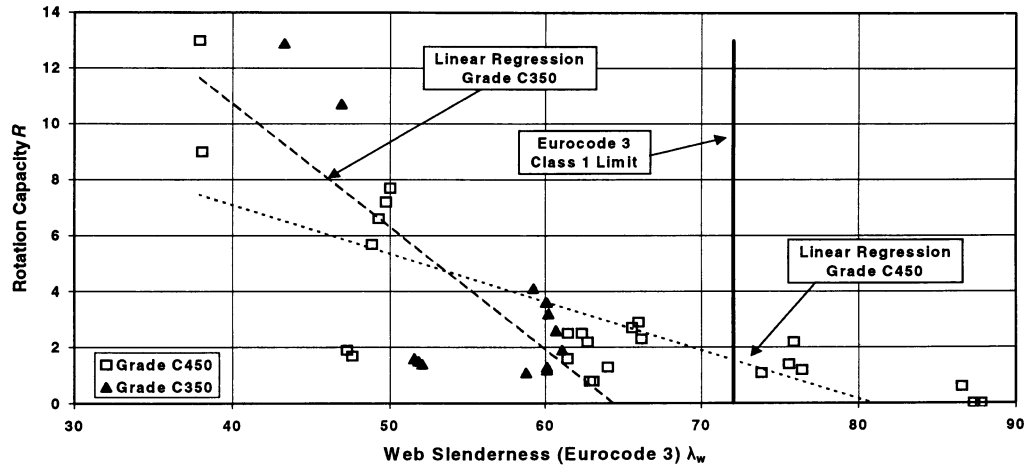

Figure 4: Web Slenderness - Rotation Capacity Curve (Eurocode 3) with respect to Steel Grade

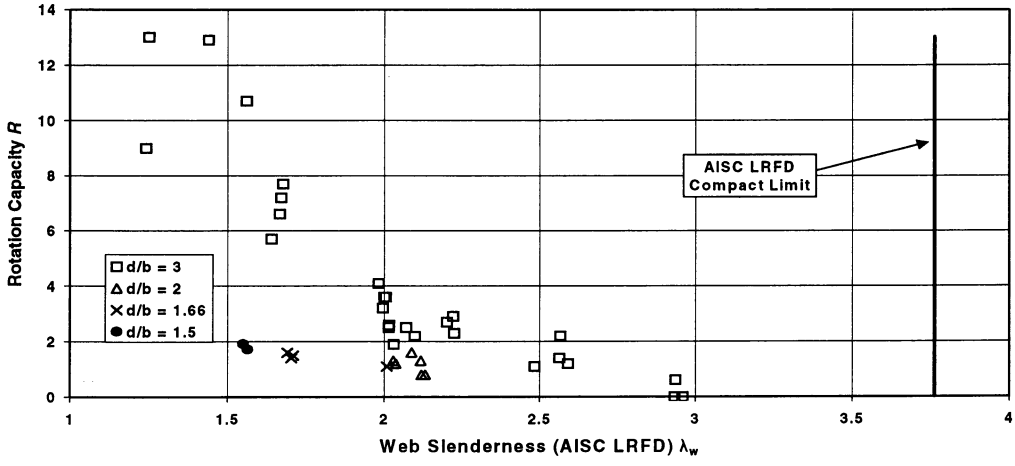

Figure 5: Web Slenderness - Rotation Capacity Curve (AISC LRFD) with respect to Aspect Ratio

From Figure 5, it can be noted that for sections with the same web slenderness, the RHS with higher aspect ratios (which correspond to a lower flange slenderness) exhibit higher rotation capacities. For example, one may compare the 150x50x3 C450 RHS (d/t = 50, b/t = 17, d/b = 3, $R \approx 2.5$), with the 100x50x2 C450 RHS (d/t = 50, b/t = 25, d/b = 2, $R \approx$ 1.0). Hence flange - web interaction may affect the rotation capacity of RHS.

An appropriate way to illustrate the interaction between the flange and the web is with iso-rotation curves (contours of equal rotation capacity) plotted with respect to the web and flange slenderness. Figure 6 shows approximate iso-rotation curves for the RHS tested. Since some tests were repeated, the rotation capacity shown in Figure 6 is the average rotation from the two (or three) tests performed on a given RHS size. Only the results of sections tested by the parallel plate method are shown in Figure 6. To incorporate the effects of flange buckling, the results of Hasan and Hancock (1988) and Zhao and Hancock (1991b) are included. All tests used the parallel plate method of loading.

The iso-rotation curves in Figure 6 display a definite interaction between the flange and the web so that the flange and web slenderness values required to reach a given R are related. The sections with higher aspect ratio have a relatively stiffer flange which provides restraint against web buckling. A section with a similar web but having a less stiff flange has

less restraint against buckling and hence a lower rotation capacity. The smooth elliptical nature of the rotation contours is not unexpected once it is recognised that the flange and web interact. The current "rectangular" independent flange and web limits assume no interaction.

Figure 6 also distinguishes the two steel grades. It can be seen that near the contour $R = 4$, there is not much difference between the two steel grades. However, in the higher rotation contour regions, the Grade C350 RHS achieve a higher rotation than the Grade C450 RHS of similar flange and web slenderness. Hence for most stocky sections with high rotation capacities, steel grade does appear to affect the rotation capacity, but in the vicinity of $R = 4$, the steel grade does not have considerable effect.

Figure 6 indicates that the Compact flange limit accurately models the behaviour for RHS and SHS with stocky webs which buckle predominately in the flange. However there is a significant region for members with more slender webs in which the standard is non-conservative. A simple bi-linear interaction formula may be appropriate and is shown in Figure 7 and Equation 1. Similar proposals would be suitable for Eurocode 3 and the AISC LRFD. Since the proposed limit is based on a rotation capacity of $R = 4$, then the effect of steel grade (detailed above) has no notable impact on the value of the compact limit. The bi-linear curve has been chosen initially due to its simplicity, while still accounting for the flange web interaction. A multi-linear curve or an elliptical compact limit may also be appropriate, and could be less conservative than the proposed bi-linear limit.

$$\lambda_w \le 70 - \frac{5\lambda_f}{6}, \quad \lambda_f \le 30 \qquad (1)$$

The cold-formed RHS do not satisfy the material ductility requirements of AS 4100 (Clause 4.5.2) or Eurocode 3 (Clause 3.2.2.2) for plastic design. However local instability (web buckling) was the failure mode of the sections, not material failure. Section BS01B, which did not experience local buckling, exhibited large rotations and strains, indicating that ductility may not present a problem. Hence the limitation on cold-formed RHS for plastic design on reduced material ductility may be incorrectly based.

7 CONCLUSION

The results of the plastic bending tests on a range of cold-formed RHS with different plate slenderness, aspect ratio and yield stress grade have been presented. The major finding of the study is that the Compact (or Class 1) web slenderness limits for RHS, which were based on tests of I-section beams, are non-conservative for RHS. The three methods of loading the RHS did not have a considerable effect on the rotation or moment capacity of the sections. Many Compact or Class 1 sections which satisfy the requirements of the AS 4100, Eurocode 3 and AISC LRFD do not exhibit the rotation capacity suitable for plastic design. There is interaction between the flange and the web in the failure mode so that the flange and web slenderness

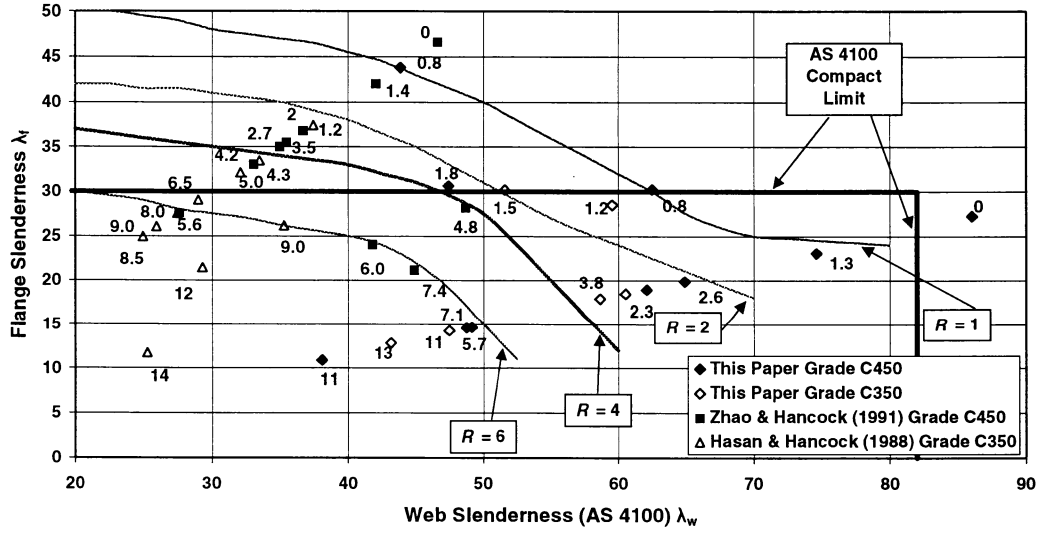

Figure 6: Iso-rotation curves

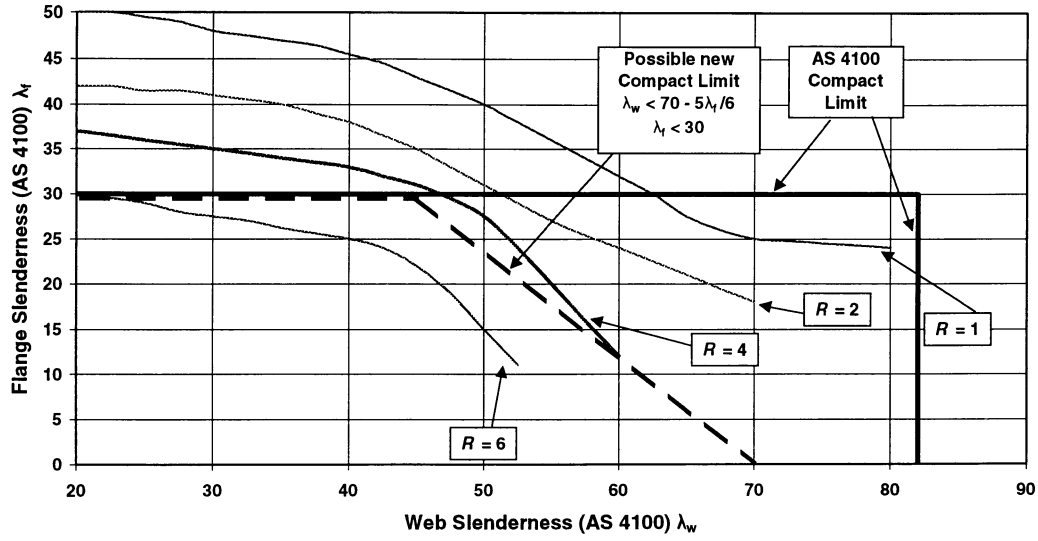

Figure 7: Proposed compact limits for cold-formed RHS

limits must be correlated. This has been identified in the iso-rotation plot from which a simple bi-linear interaction curve for the Compact limits of RHS has been proposed. The bi-linear interaction curve has been drawn at a rotation capacity of $R = 4$, where it has been shown that the effect of steel grade is not significant.

8 REFERENCES

AISC, (1994), *Metric Load and Resistance Factor Design Specification for Structural Steel Buildings*, (AISC LRFD), American Institute of Steel Construction, Chicago, Il.

Beg D. and Hladnik L., (1996), "Slenderness Limit of Class 3 I Cross-sections Made of High Strength Steel", *Journal of Constructional Steel Research*, 38(3), pp 201-217.

CASE, (1992), "Tests on Rectangular Hollow Sections to Investigate the Effect of Variation of Yield Stress Around a Section", *Investigation Report S885*, Centre for Advanced Structural Engineering, School of Civil and Mining Engineering, University of Sydney, Sydney, Australia.

Daali M.L. and Korol R. M., (1995), "Prediction of Local Buckling and Rotation Capacity at Maximum Moment", *Journal of Constructional Steel Research*, 32(1), pp 1-13.

Dwyer T. J., and Galambos T.V., (1965), "Plastic Behaviour of Tubular Beam-Columns", *Journal of the Structural Division*, ASCE, 91(4), pp 153-168.

European Committee for Standardisation, (1992), "Design of Steel Structures: Part 1.1 - General Rules and Rules for Buildings", (known as "Eurocode 3"), *DD ENV. 1993-1-1*, Eurocode 3 Editorial Group, Brussels, Belgium.

Hasan S. W., and Hancock G. J., (1988), "Plastic Bending Tests of Cold-Formed Rectangular Hollow Sections", *Research Report*, No. R586, School of Civil and Mining Engineering, The University of Sydney, Sydney, Australia.

Korol R. M., and Hudoba J., (1972), "Plastic Behaviour of Hollow Structural Sections", *Journal of the Structural Division*, ASCE, 98(5), pp 1007-1023.

Standards Australia (1990a), "Steel Structures", *AS 4100*, Sydney, Australia.

Standards Australia, (1990b), "Methods for Tensile Testing of Metals", *AS 1391*, Sydney, Australia. Standards Australia, (1991), "Structural Steel Hollow Sections", *AS 1163*, Sydney, Australia.

Sedlacek G. And Feldmann M., (1995), "The b/t ratios Controlling the Applicability of Analysis Models in Eurocode 3, Part 1.1", *Background Document 5.09 for Chapter 5 of Eurocode 3, Part 1.1*, Aachen, Germany.

Tubemakers, (1994), *Design Capacity Tables for DuraGal Steel Hollow Sections*, Tubemakers of Australia Limited, Structural Products Division, Newcastle, Australia.

Wilkinson T., and Hancock G. J., (1997), "Tests for the Compact Web Slenderness Limits of Cold-Formed Rectangular Hollow Sections", *Research Report*, No. R744, Department of Civil Engineering, The University of Sydney, Sydney, Australia.

Zhao X. L. and Hancock G. J., (1991a), "T-Joints in Rectangular Hollow Sections Subject to Combined Actions", *Journal of Structural Engineering*, ASCE, 117(8), pp 2258-2277.

Zhao X.L. & Hancock G. J. (1991b), "Tests to Determine Plate Slenderness Limits for Cold-Formed Rectangular Hollow Sections of Grade C450", *Steel Construction*, Journal of Australian Institute of Steel Construction, 25 (4), pp 2-16.

Zhao X. L. and Hancock G. J., (1992), "Square and Rectangular Hollow Sections Subject to Combined Actions", *Journal of Structural Engineering*, ASCE, 118(3), pp 648-668.

Zhao X. L., Hancock G. J., and Trahair N. S., (1995), "Lateral Buckling Tests of Cold-Formed RHS Beams", *Journal of Structural Engineering*, ASCE, 121(11), pp 1565-1573.

9 NOTATION

A_g	Gross cross section area
b	Width of RHS, or width of plate
d	Depth of RHS
E	Young's modulus of elasticity
f_y	Yield stress
f_{yn}	Nominal yield stress
I	Second moment of area
k	Plate buckling coefficient
L_1	Length between loading plates
L_2	Length between supports
M_{max}	Maximum bending moment
M_p	Plastic bending moment
M_y	Bending moment at first yield
R	Rotation capacity
t	Thickness of RHS, or plate
κ	Curvature
κ_p	Plastic curvature (= M_p/EI)
λ_f	Flange slenderness
λ_w	Web slenderness

10 ACKNOWLEDGEMENTS

This research project is funded by CIDECT (Comité International pour le Developpement et l'Étude de la Construction Tubulaire). Tube specimens were provided by BHP Steel Structural and Pipeline Products. The experiments were carried out in the J. W. Roderick Laboratory for Materials and Structures, Department of Civil Engineering, the University of Sydney.

Tubular Structures VIII, Choo & Van der Vegte (eds) © 1998 Balkema, Rotterdam, ISBN 90 5809 001 9

Influence of boundary conditions on the modeling of steel CHS columns

Y.X. Dong & S.P.Chiew
School of Civil and Structural Engineering, Nanyang Technological University, Singapore

ABSTRACT: It is usual to take advantage of symmetry in the numerical modeling of physical structures that possess symmetrical planes. Only a part of the original structure needs to be modeled by imposing proper symmetrical conditions at the boundaries. While the transposition symmetric conditions are relatively easy to impose, there are several ways to impose the rotational symmetric conditions, especially for a circular symmetric section. In this paper the suitability of various rotational symmetric conditions for the nonlinear analysis of a CHS steel tube are examined with reference to the available experimental results. The ultimate load, load-displacement curve and local buckling shape have to be considered in determining the influence of various approximate rotational symmetric condition. It is found that the rotational boundary condition on the vertical symmetric plane has little influence on the result, while the rotational boundary condition on the horizontal plane is essential for a realistic numerical model of CHS columns.

1 INTRODUCTION

With the rapid development of the finite element technique and computer hardware, numerical simulation has become one of the most powerful and practical techniques in structural analysis and design, especially in the nonlinear or dynamic analysis where the histories of the loading and the deformation are of the main concern. Often in these kinds of analysis, a large number of time/load steps and iterations are necessary for the simulation of the history of deformation, strain and stress of the structure. This requires immense amount of disk and memory space that are often limited by the computing machines. In order to reduce the required amount of disk and memory space, as well as the CPU time, the symmetric conditions of the structures are often utilized, where applicable, so that only a part of the structure is modeled with finite element mesh and appropriate symmetric boundary conditions to simulate the behavior of the whole structure. When modeled in this way, the symmetric conditions should be applied correctly to ensure that the numerical model simulate the same behavior as the actual structure. While the transposition symmetric conditions are obvious and easy to apply, the rotational ones are often hard to determine (Zienkiewicz, 1977, Kleiber & Wozniak, 1991 and Trahair, 1993).

In this paper, different rotational symmetric boundary conditions are applied to a circular steel column model to examine the effect of approximate symmetric boundary conditions. For the calibration of the failure mode predicted by numerical models with different symmetric conditions, a full scale circular hollow section (CHS) steel tube was tested. Its ultimate load was recorded and failure mode fully documented. Numerical results are compared with the experimental ones.

2 EXPERIMENT ON THE PRACTICAL SIZE COLUMN

One 3500 mm long CHS column was tested. The column was subjected to an eccentric axial load. A summary of the geometrical and material properties for the specimen is presented in Table 1.

The 500T Schenck-Trebel RBU Universal Testing Machine was used to test the column. A schematic drawing of the experimental setup is shown in

Table 1 Geometrical and material properties of the tested column

Column No.	Type(DxtxM) (mmxmmxkg/m)	Length (mm)	A_s (mm^2)	f_y N/mm^2
CFC1	168.3x7x25.5	3500	3600	390

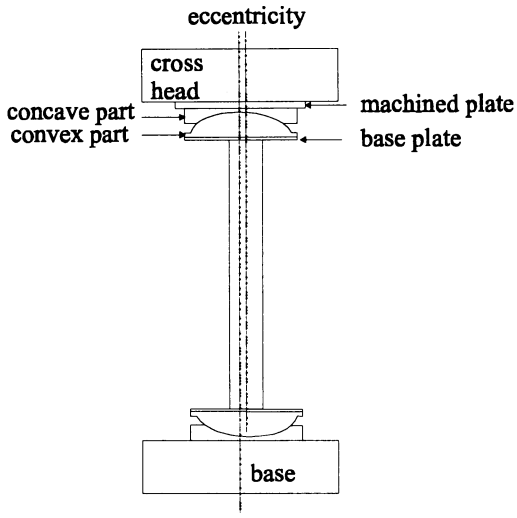

Figure 1. Experimental setup

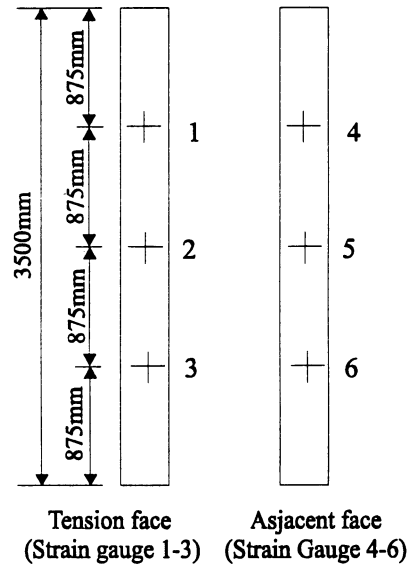

Figure 1. Two identical end attachments were fabricated for the testing in order to ensure that uniaxial bending is predominant. The attachments helped to minimize the effect of biaxial bending since they only allowed rotation in one direction. The eccentric distance was set to be 20 mm. FLA-5-11 strain gauges were used in the experiment program.

The strain gauges had a gauge length of 5 mm and a gauge resistance of 120Ω. A set of six gauges were used to measure the strain in the outer face of the column. Three gauges were placed on the tension face and another three gauges were placed on the adjacent face of the column. The position of the strain gauges are shown in Figure 2.

Three transducers were used to monitor the lateral deformation of the tension face of the column under different incremental loads. The transducers used were capable of measuring deflections up to 50 mm. Axial deformation for the column was measured by the testing machine. Figure 3 shows the arrangement of the transducers.

Stroke control mode was used throughout the test so as to observe the post-peak behavior of the column. This mode allows the load to decrease with increasing axial deformation. The rate of stroking was set at 0.3 mm/min. The tested failure load, P_t, is 910 kN.

It is observed that the column failed suddenly after exhibiting some ductility. An obvious inward curling of the steel towards the center was observed on the compressive side and at the mid-height of the column. This indentation caused the moment of inertia of the hollow section steel column to reduce significantly and thus caused it to fail suddenly. A close up view of the indentation is shown in Figure 4.

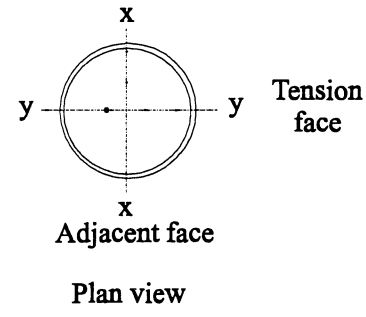

Figure 2. Strain gauge positions

The axial load-axial strain curves for the column are plotted and presented in Figure 5.

The axial load-axial deformation relationship for the column is shown in Figure 6. The load-lateral displacement curves are plotted and shown in Figure 7 and Figure 8. The graphs show that the maximum lateral deflection occurs at the mid-height of the column. The common feature of these graphs is that the strain gauges placed at the tension side and the adjacent side were subjected to compressive forces before and just after peak-load. During loading, the tension side was initially subjected to increasing compressive load. As the applied load increases, the tension side was subjected to less compressive forces. Up to the point of peak-load, the tension side was still under compressive force. But as loading continues and the lateral deformation increases, the tension side became subjected to tensile force.

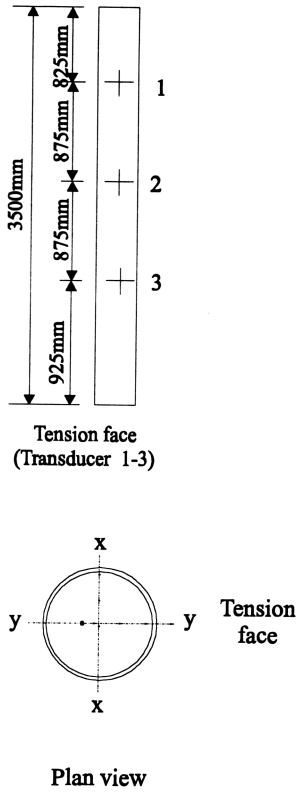

Figure 3. Transducer positions

3 NUMERICAL MODELING AND THE SYMMETRIC CONDITIONS

The numerical simulation is done with MARC -- a general purpose finite element analysis software (MARC research analysis corporation, 1995). The elasto-plastic finite element analysis is performed to simulate the pre- and post-peak behavior of the steel tube column under eccentric axial load.

Two types of elements are used in the analysis: the 8-node doubly-curved thick shell element is used to model the steel tube and the 20-node isoparametric three-dimensional element is used for the end plate.

Steel is modeled as elastic-plastic material. Strain hardening is considered with the hardening modulus being 1/250 of the elastic modulus. The Von Mises yield criterion with kinematic hardening rule is adopted.

As mentioned previously, the column is allowed to have lateral deformation only in one direction. The column had two symmetric planes. One is formed by the longitudinal axis and the direction of lateral deformation (the vertical symmetric plane) and the other is the cross-section at the mid-height of the column (the horizontal symmetric plane). So only a quarter of the column is modeled and the symmetric boundary conditions are applied. At each load step the axial displacement at the top of the column is increased by a constant amount to simulate the displacement control condition used in the experiment. The step displacement is applied on the nodes that are on top plate and are in a line 20 mm away from the X axis.

A total of 76 thick shell elements for the steel tube and 6 three dimensional elements for the end plate and a total of 340 nodes are used in the model. The finite element mesh is shown in Figure 9.

As for the symmetric conditions, the zero displacement in Y direction is applied to the nodes on the vertical symmetric plane and the zero displacement in Z direction is applied to the nodes on the horizontal symmetric plane (see Figure 9). In order to examine the effect of the rotational symmetric boundary conditions, various types of rotational symmetric conditions are applied. Experience shows that, for the considered column and load, the rotational boundary condition in the vertical symmetric plane does not matter much in terms of its influence on the failure mode and ultimate load of the column. So the theoretical boundary condition for the vertical symmetric plane is applied while the following four types of rotational boundary conditions on the horizontal symmetric plane are applied and examined separately (see Figure 9):

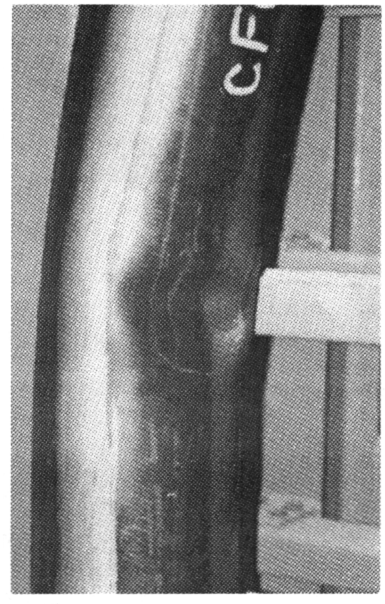

Figure 4. Indentation of the test column

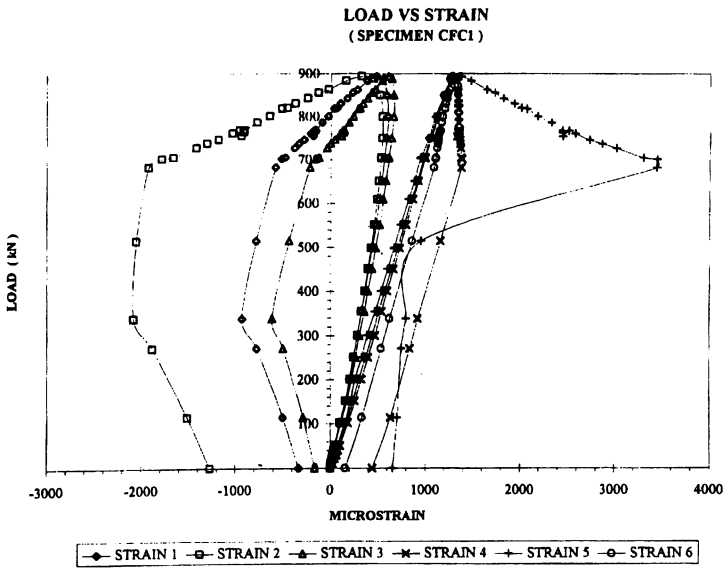

Figure 5. Experimental load-strain curves

Type 1: the nodes in the horizontal symmetric plane are not allowed to have rotations around X, Y and Z axes;

Type 2: the nodes in the horizontal symmetric plane are free to have rotation around the X, Y and Z axes;

Type 3: In the horizontal symmetric plane, the nodes on X axis are not allowed to rotate around X, Y and Z axes and the node on Y axis is not allowed to rotate around X and Y axes.

Type 4: Theoretically, the symmetric boundary conditions are:

$u_y = \varphi_x = \varphi_z = 0$ for the nodes on vertical symmetric plane; and

$u_z = \varphi_x = \varphi_y = 0$ for the nodes on horizontal symmetric plane, where u_i is the transposition displacement in direction i and φ_i is the rotational displacement in direction i.

This symmetric condition is also considered in the calculation.

For the purpose of comparison, a finite element model of the whole column, with the same mesh density, is also analyzed.

4 EFFECTS OF SYMMETRICAL BOUNDARY CONDITIONS ON THE NUMERICAL RESULTS

The experimental and FEM predicted values of the ultimate load of the column are listed in Table 2. The squash load of the corresponding short column, $P_y = f_y A_s$, is 1404 kN, where f_y is the yield strength of the steel and A_s is the area of the cross section of the column. The results of the ultimate load show that due to local buckling, the bearing capacity of the column is less than 65% of the squash load.

It is seen from Table 2 that numerical models with the four types of symmetrical condition all yield an ultimate load smaller than but quite close to the test value. Among the four types of rotational symmetric boundary conditions, Type 1 gives the largest ultimate load because it has the strongest restriction on the rotational movement of the nodes. Type 2 has the weakest restriction and hence the lowest ultimate load. Although Type 3 sets up the correct boundary condition only for the nodes on the axes, it produced quite close result as compared with Type 4, the case where the theoretical boundary conditions are applied. It is also noticed that although the rotational symmetric boundary condition are quite different in each type, the difference in ultimate loads they produced are not obvious.

The computed axial load-axial deformation curves of this column are compared with the experimental

Table 2 Ultimate loads of the hollow section column

Col. No.	Test P_t (kN)	Boundary condition			
		Type1 (kN)	Type2 (kN)	Type3 (kN)	Type4 (kN)
CFC1	910	871	863	864	865
%of P_t	100	95.7	94.8	94.9	95.1

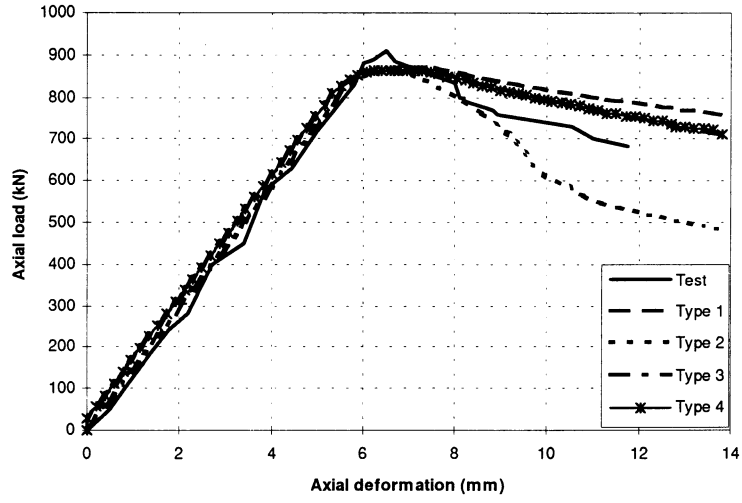

Figure 6. Axial load vs Axial deformation

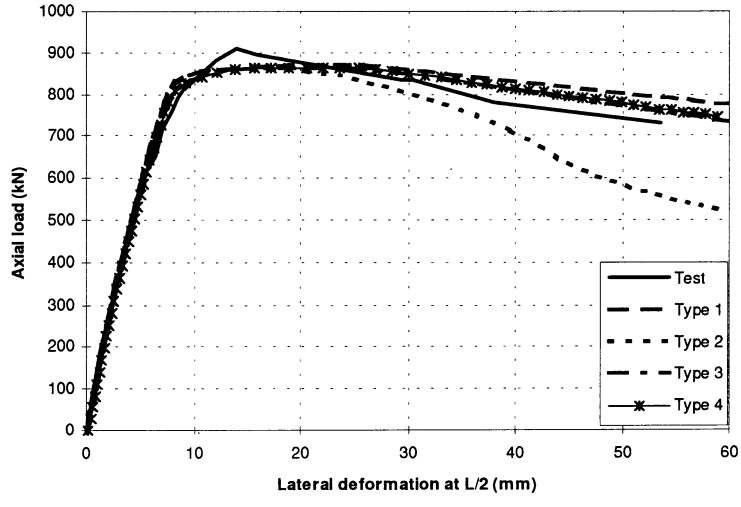

Figure 7. Axial load vs Lateral deformation at L/2

curve as shown in Figure 6.

It can be seen from Figure 6 that FEM simulated axial load-axial deformation curves have quite the same ascending slopes but different descending slopes. Under Type 1 rotational symmetric condition, the descending slope is the flattest; Under Type 2 rotational symmetric conditions the descending slope is the stiffest and the Type 3 symmetric condition produces a descending slope in the midst of the above two, and is quite close to the curves produced by Type 4 symmetric condition.

It is apparent that the stronger the restriction on the rotational degree of freedom the flatter the descending slope will be.

Due to the eccentricity of the applied load, the lateral displacement of the column is quite obvious. The lateral displacements at two points, one at the mid-height and another at the 3/4 height of the column, are shown in Figure 7 and Figure 8. Good agreement on the post-peak lateral deformation can also be seen between the FEM simulation with Type 3 and Type 4 rotational symmetric conditions and the experimental results.

The shape of the local buckling is different under different types of rotational symmetric conditions. Figure 10 to Figure 13 show the different shapes of

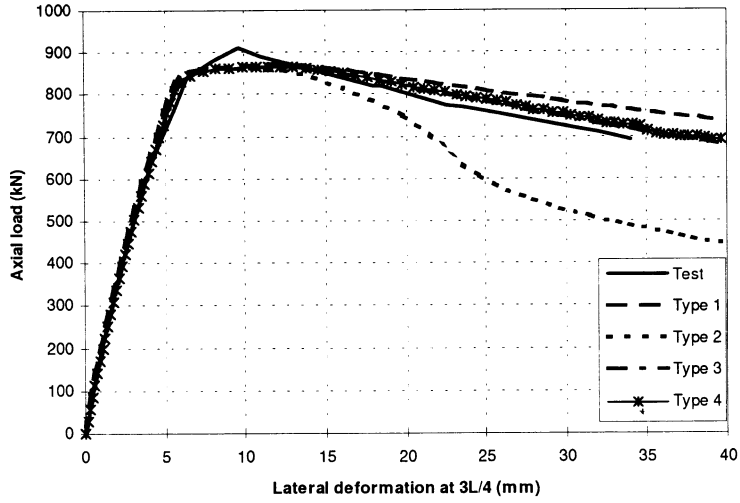

Figure 8. Axial load vs Lateral deformation at 3L/4

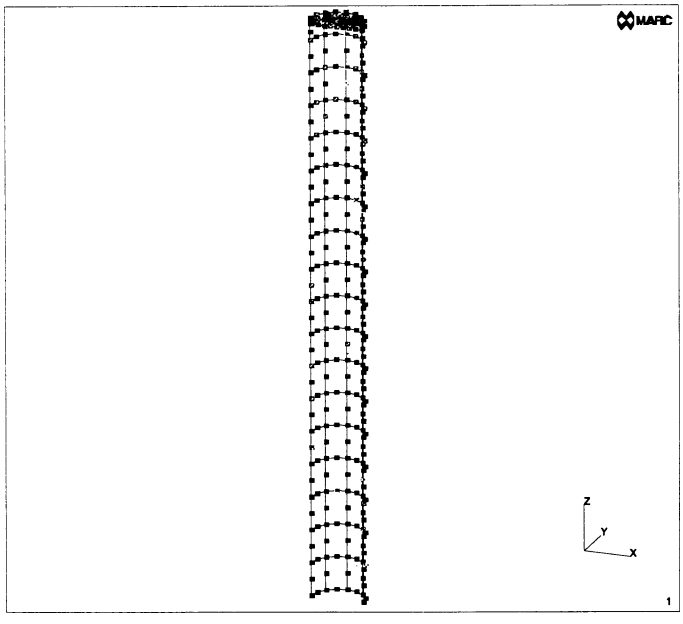

Figure 9. Finite element mesh

the local buckling. It can be seen that the shapes of the inward curling of the steel tube are different under the four types of rotational symmetric conditions.

With the Type 1 rotational symmetric condition, since all nodes on the horizontal symmetric plane are not allowed to have any rotation, the inward curling is forced to occur at a place away from the symmetrical plane (see Figure 10), indicating that there will be two inward indentations occur in the tube, which is not in accordance with the inward curling shape observed from the experiment (Figure

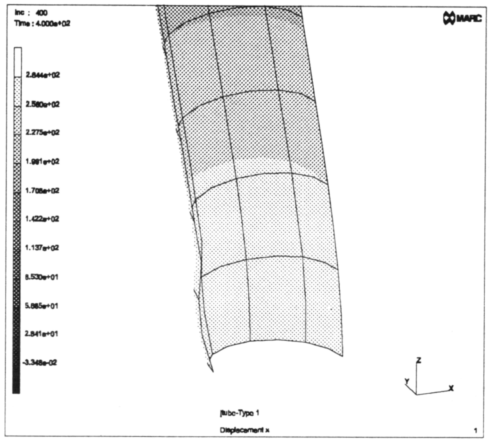

Figure 10 Failure mode (Type 1)

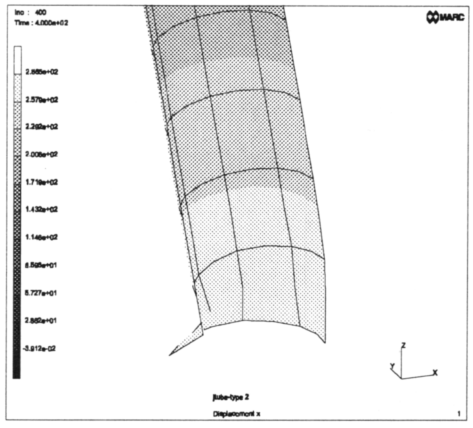

Figure 11 Failure mode (Type 2)

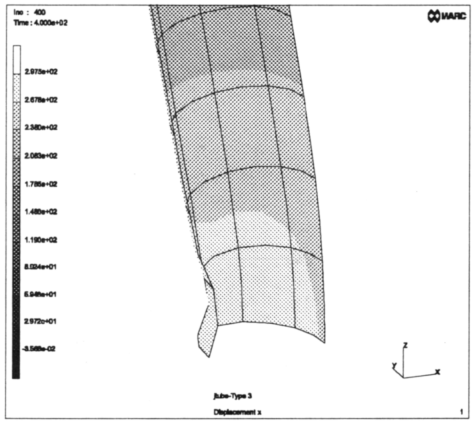

Figure 12 Failure mode (Type 3)

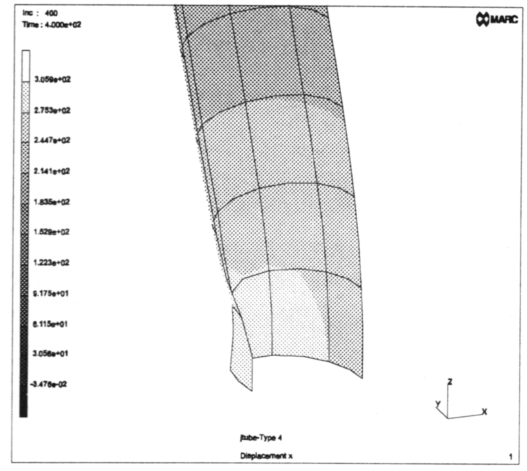

Figure 13 Failure mode (Type 4)

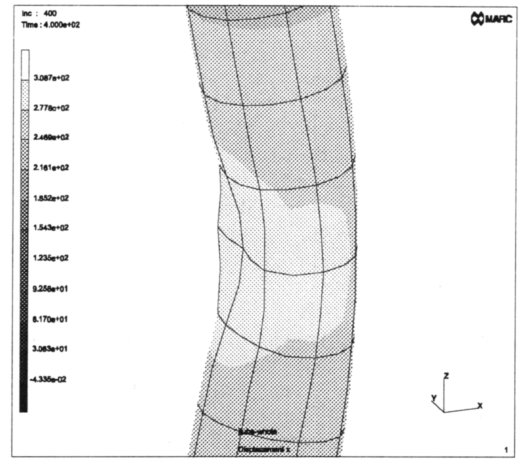

Figure 14 Failure mode (Whole column model)

4). It is also known that this type of boundary condition is the same as the one used to simulate fixed end and so it is not quite suitable for the symmetric condition.

With the Type 2 rotational symmetric condition no rotational restriction is applied to the nodes on the symmetric plane. The inward curling is deeper than that with Type 1 rotational symmetric condition (see Figure 11). The buckling shape also indicates that there will be two inward indentations near the symmetric plane, which is also contradicting the experimental observation. This type of boundary condition assumes that the column is linked by hinges, which is not true for the continuous steel column tube.

With the Type 3 rotational symmetric condition, although the boundary condition is quite the similar

to the theoretical one and the ultimate load and the load-deformation curves are quite close to the ones of the theoretical symmetric condition, the inward curling is not similar to the experimental result (see Figure 12).

The shape of the inward curling under theoretical symmetric condition (Type 4) is quite the same as the tested shape (see Figure 13). Compared with the numerical simulation of the whole column model shown in Figure 14, it is seen that they are of the same inward curling shape and almost the same displacements in X direction. So we see that the correct rotational symmetric condition is critical for a realistic numerical modeling.

5 CONCLUSION

In this paper, an eccentrically loaded hollow section steel tube is studied to examine the four types of rotational symmetric conditions in the horizontal symmetric plane. With the experimental results, as well as a complete column finite element model as references, the influences of three types of approximate rotational symmetric boundary conditions are shown. It is found out that the fully restricted and fully free types of rotational symmetric conditions will produce unrealistic buckling shape and inaccurate load-displacement curves as compared with the experimental results. Although partial restricted rotational symmetric condition (Type 3) can produce quite closed ultimate load and load-displacement curves as the theoretical symmetric boundary condition (Type 4), the local buckling shape is not the same as that predicted by theoretical symmetric boundary condition and by the experiment. It is thus concluded that careful and correct application of rotational symmetric boundary condition is very important for the realistic simulation of structural behaviors by numeric modeling.

REFERENCES

Kleiber M. and Wozniak C., Nonlinear mechanics of structures, *Kluwer Academic Publishers*. 1991

MARC Analysis Research Corporation, Vol. A-E, 1995.

Trahair N. S., Flexural-torsional buckling of structures. *E & FN Spon*, London, 1993

Zienkiewicz O. C., The finite element method (3rd Edition). *McGraw-Hill Book Company (UK) Limited*, England, 1977

Tubular Structures VIII, Choo & Van der Vegte (eds) © 1998 Balkema, Rotterdam, ISBN 90 5809 001 9

Service load deformations of concrete-filled steel RHS sections

M.A. Bradford
The University of New South Wales, Sydney, N.S.W., Australia

ABSTRACT: Composite columns in high-rise buildings may be constructed by filling thin-walled RHS sections with concrete. Under normal service loads, the walls of these sections should not buckle locally, although the RHS section classification is that of slender. It is shown that in the time domain, creep and shrinkage of the concrete core shed compressive force into the steel, and this may precipitate local buckling. An analytical model is presented for predicting this time-dependent buckling, and this is illustrated by using a thin-walled SHS section as an example.

1 INTRODUCTION

Modern construction practice in high-rise buildings is making increasing use of concrete-filled steel tubes as columns. These composite sections allow for rapid erection of the steel skeleton prior to filling the tubes with concrete. There are a number of examples of this practice in Australasia, and particularly in Australia.

Earlier practice was to use reasonably thick steel tubes, so that local buckling of the steel did not present a difficulty in design. However, it is recognised that the column members are reasonably slender, and that they will fail by flexural buckling at loads less than their squash loads. Because of this, it is not imperative the steel section be compact, and as a result economies are achieved by using much thinner-walled steel tubes (Uy 1998). Hence, at the strength limit state, failure will occur in a flexural mode when the stress in the steel tube is less than its yield stress f_y. Compactness of the steel tube is thus not a necessary requirement.

At service load levels, the concrete core shrinks, and in particular creeps. Although these time-dependent mechanisms are arrested somewhat by the prevention of moisture egress through the steel tube, Terrey *et al.* (1994) demonstrated in careful experimental observations that creep and shrinkage do occur in concrete-filled tubes, irrespective of whether the tube contains holes to allow the egress of steam in the event of fire. The effects of creep and shrinkage are to shed compressive load into the steel tube. The compressive forces build up with time, and may lead to eventual local buckling of the steel tube at service load levels. This phenomenon was observed by Uy & Bradford (1995) in long-term composite profiled beam experiments, and has been quantified by Bradford & Wright (1998) and by Bradford *et al.* (1998) for composite profiled walls.

This paper presents an analytical solution for the time-induced local buckling of concentrically-loaded thin-walled concrete-filled steel tubes at service loads. The local buckles are unilateral (Smith *et al.* 1998), in that they may only form away from the concrete core. This is known as a contact problem. The Rayleigh-Ritz method is used to firstly derive the unilateral buckling stress of a plate in a concrete-filled RHS section, and then the Age-Adjusted Effective Modulus Method (Bazant 1972) is invoked to determine the time-dependent compressive stress that is shed into the walls of the RHS section. The buckling solution may be determined easily by hand or spreadsheet calculation. Some illustrative examples are presented to demonstrate the propensity of a thin-walled SHS to buckle due to creep and shrinkage in the time domain.

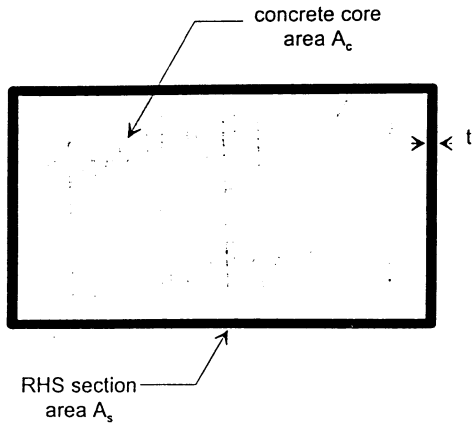

Figure 1. Concrete-filled RHS section

2 LOCAL BUCKLING ANALYSIS

Figure 1 shows an RHS section filled with concrete, and Fig. 2 shows the buckling mode in which the sheeting buckles away from the concrete core under a uniform stress σ_o. The buckling displacement w is assumed to be represented as a sine squared function, so that

$$w = q \sin^2 \frac{m\pi x}{L} \sin^2 \frac{n\pi y}{b} \tag{1}$$

where q is the buckling degree of freedom.

The strain energy store during buckling U is written as (Timoshenko & Gere 1961)

$$U = \frac{1}{2} D \int_0^L \int_0^b \left\{ \left(w_{,xx} + w_{,yy} \right)^2 - 2(1-\nu) \left(w_{,xx} w_{,yy} - w_{,xy}^2 \right) \right\} dy dx \tag{2}$$

where the plate rigidity is given by

$$D = \frac{E_s t_p^3}{12\left(1-\nu^2\right)} \tag{3}$$

where E_s and ν are the Young's modulus and Poisson's ratio of the steel plate of thickness t_p. Substituting Eqn. 1 into Eqn. 2 and integrating produces

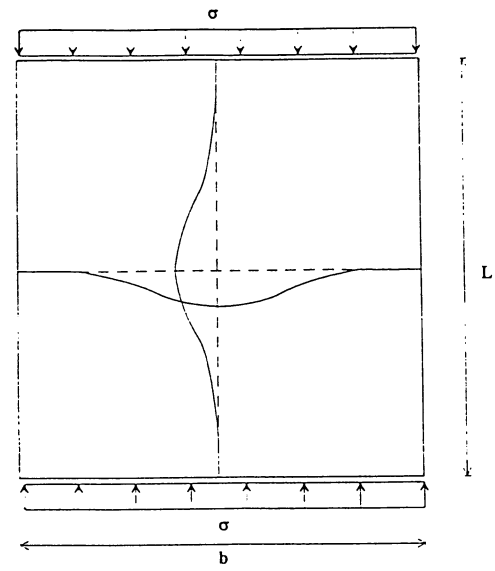

Figure 2. Unilateral buckling mode

$$U = q^2 \pi^4 D \left(\frac{3m^4}{8} \frac{b}{L^3} + \frac{3n^4}{8} \frac{L}{b^3} + \frac{m^2 n^2}{4Lb} \right) \tag{4}$$

The work done during buckling V may be written as (Timoshenko & Gere 1961)

$$V = \frac{\sigma t_p}{2} \int_0^L \int_0^b w_{,x}^2 \, dy dx \tag{5}$$

and substituting Eqn. 1 into Eqn 5 and integrating produces

$$V = q^2 \frac{3}{32} \sigma t_p m^2 \pi^2 \frac{b}{L} \tag{6}$$

The change in total potential is thus U - V, and applying the Rayleigh-Ritz method of minimising with respect to the arbitrary degree of freedom q produces

$$\frac{d(U-V)}{dq} = 0 \tag{7}$$

Hence substituting Eqns. 4 and 6 into Eqn. 7, and ignoring the trivial prebuckling solution $q = 0$, leads to the expression given in Eqn. 8 for the critical stress in the form given by Trahair & Bradford (1997).

$$\sigma_{cr} = k\frac{\pi^2 E_s}{12(1-\nu^2)}\frac{1}{(b/t_p)^2} \tag{8}$$

In Eqn. 8 above, k is the local buckling coefficient given by

$$k = \frac{4m^2}{\varphi^2} + \frac{4\varphi^2}{m^2} + \frac{8}{3} \tag{9}$$

where $\varphi = L/b$ is the plate aspect ratio.

Figure 3 shows the variation of k with φ for different values of m. The minimum value of k occurs when

$$\frac{dk}{d\varphi} = 0 \tag{10}$$

in Eqn. 9. Performing this minimisation leads to $\varphi = m$, and

$$k_{\min} = 10.67 \tag{11}$$

3 ANALYSIS FOR CREEP AND SHRINKAGE

3.1 *General*

Figure 1 shows the concrete core of area A_c surrounded by the steel skin of the RHS section of area A_s. This composite element is assumed to acted upon by a constant sustained service-load stress of magnitude σ_o. The steel is assumed to be bonded to the concrete, so that both materials share the load.

3.2 *AEMM Analysis*

The method developed herein has been adopted from the treatment in Gilbert's text (1988). When the stress σ_o is applied gradually to the concrete and then held constant after time $t = \tau_1$, the effect of creep is more pronounced than if the stress was applied at time $t = \tau_o$ and then held constant (Fig. 4). Due to the effects of aging, the creep coefficient $\phi(t, \tau_o)$ is reduced by the aging coefficient $\chi(t, \tau_o)$ to $\chi\phi$. The aging coefficient is often taken to be 0.8 (Gilbert 1988). As the steel RHS section restrains the creep and shrinkage, the stress in the concrete σ_o reduces with time, as shown in Fig. 5. This stress change $\Delta\sigma(t)$ is tensile or negative, and is given by

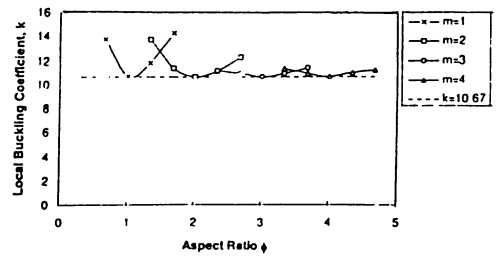

Figure 3. Variation of k

$$\Delta\sigma(t) = \sigma_c(t) - \sigma_o \tag{12}$$

where $\sigma_c(t)$ is the time-varying stress in the concrete.

The total strain in the concrete $\varepsilon_c(t)$ is the sum of the instantaneous, creep and shrinkage strains, and is also equal to the strain in the steel $\varepsilon_s(t)$ by the assumed compatibility condition. Hence

$$\varepsilon_c(t) = \varepsilon_s(t) = \frac{\sigma_o}{E_c(\tau_o)}\{1+\phi(t,\tau_o)\} + \frac{\Delta\sigma(t)}{E_c(\tau_o)}\{1+\chi\phi(t,\tau_o)\} + \varepsilon_{sh} \tag{13}$$

where E_c is the elastic modulus of the concrete and $\varepsilon_{sh}(t)$ is the shrinkage strain in the concrete (taken as positive). Equation 13 may be simplified to yield

$$\varepsilon_c(t) = \frac{\sigma_o}{E_e(t,\tau_o)} + \frac{\Delta\sigma(t)}{\bar{E}_e(t,\tau_o)} + \varepsilon_{sh}(t) \tag{14}$$

where the effective modulus is given by

$$E_e(t,\tau_o) = \frac{E_c(\tau_o)}{1+\phi(t,\tau_o)} \tag{15}$$

and the age-adjusted effective modulus is given by

$$\bar{E}_e(t,\tau_o) = \frac{E_c(\tau_o)}{1+\chi\phi(t,\tau_o)} \tag{16}$$

The sustained force acting on the cross-section P is

$$P = A_s\sigma_s(t) + A_c\sigma_c(t) \tag{17}$$

where $\sigma_s(t)$ is the time-varying stress in the RHS section. In addition,

$$P = \sigma_o(1+np)A_c \tag{18}$$

where $p = A_s/A_c$ and n is the short-term modular ratio (not to be confused with the harmonic number in Eqn. 1), and also

$$\varepsilon_s(t) = \frac{P - A_c(\sigma_o + \Delta\sigma_o)}{A_s E_s} \tag{19}$$

Hence from Eqns. 14, 18 and 19,

$$\sigma_c(t) = \sigma_o\left\{1+\frac{p(n-n_e)}{1+\bar{n}_e p}\right\} - \left\{\frac{E_s p}{1+\bar{n}_e p}\right\}\varepsilon_{sh} \tag{20}$$

where the effective modular ratio is

$$n_e(t,\tau_o) = \frac{E_s}{E_e(t,\tau_o)} \tag{21}$$

and the age-adjusted effective modular ratio is

$$\bar{n}_e(t,\tau_o) = \frac{E_s}{\bar{E}_e(t,\tau_o)} \tag{22}$$

Rearranging Eqn. 17 produces the stress in the steel as

$$\sigma_s(t) = \frac{P - \sigma_c(t)A_c}{A_s} \tag{23}$$

and substituting Eqns. 18 and 20 into Eqn. 23 yields

$$\sigma_s(t) = \frac{\sigma_o(n\bar{n}_e p + n_e) + E_s\varepsilon_{sh}}{1+\bar{n}_e p} \tag{24}$$

3.3 *Models for Creep and Shrinkage*

National concrete standards present empirical formulae for calculating the creep coefficient ϕ and the shrinkage strain ε_{sh}. These formulae are generally not for concrete whose moisture egress is retarded by the presence of an impermeable barrier in the form of the RHS section. The creep and shrinkage in circular concrete-filled steel tubes was investigated by Terrey *et al.* (1994). This study concluded that there are indeed quite substantial creep and shrinkage strains in the concrete, but nevertheless they are somewhat lower than those encountered in 'free' concrete specimens. It also showed that the strain-time relationship for constrained concrete was similar to that for unconstrained concrete. Terrey *et al.* Suggested that the maximum long-term shrinkage strain $\varepsilon_{sh}(\infty)$ be taken as 200×10^{-6} and that the maximum long-term creep coefficient $\phi(\tau,\infty)$ be taken as 1.2. Based on the relationship in the Australian AS3600-1994, the time-dependent parameters may be assumed to be

$$\phi(t,\tau_o) = 1.2G(t) \tag{25}$$

and

$$\varepsilon_{sh}(t) = 200\times10^{-6}G(t) \tag{26}$$

where

$$G(t) = \frac{t^{0.7}}{t^{0.7}+32} \tag{27}$$

A plot of the time-varying function $G(t)$ which is adopted in this study, is given in Fig. 5. The coefficients in Eqns. 25 and 26 of this time-varying function were also adopted herein.

4 TIME-DEPENDENT LOCAL BUCKLING

It can be seen from Fig. 3 that if the plate buckles in a few half-wavelengths, which would be the case in a long RHS column, then the buckling coefficient may be taken as 10.67. Under an applied stress in the concrete of σ_o, buckling will therefore take place when $\sigma_s(t)$ in Eqn. 24 equals σ_{cr} in Eqn. 8. Rearranging this equality, and using E_s = 200 kN/mm^2 and ν = 0.3, produces the critical width to thickness ratio at which time-dependent buckling occurs $(b/t_p)_{cr}$ as

$$\left(\frac{b}{t_p}\right)_{cr} = \left\{\left(\frac{\sigma_o}{1.30\times10^6}\right)\left(\frac{n\bar{n}_e + n_e}{1+\bar{n}_e p}\right) + \frac{0.104\varepsilon_{sh}}{1+\bar{n}_e p}\right\}^{-1/2} \tag{28}$$

in which σ_o is in N/mm^2. The right hand side of Eqn. 28 is clearly as function of the time t since ε_{sh} is a function of t, as are n_e and $\bar{n}_e$.

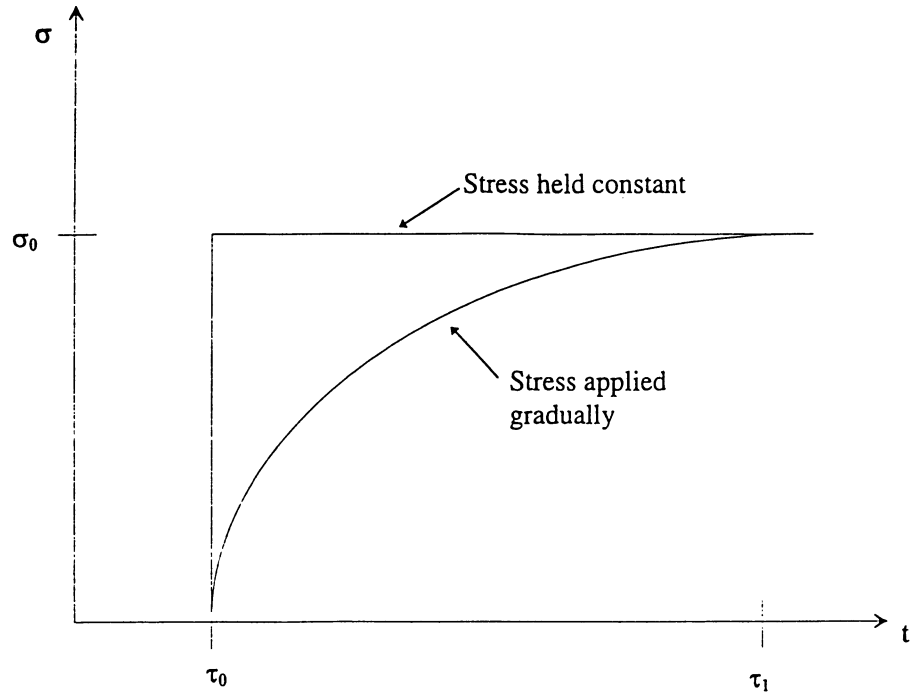

Figure 4. Stress regimes

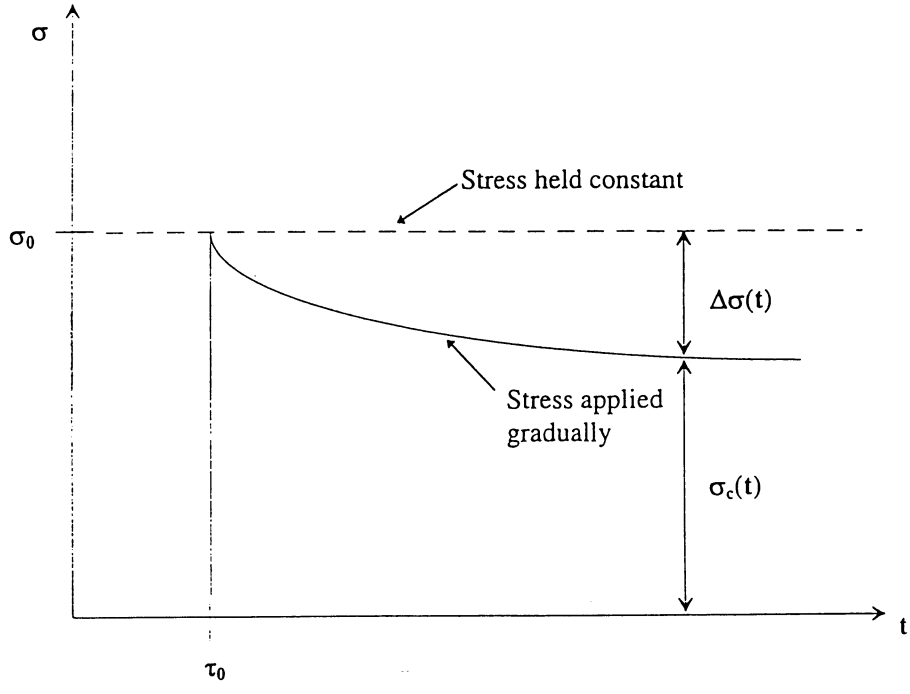

Figure 5. Reduction in concrete stress

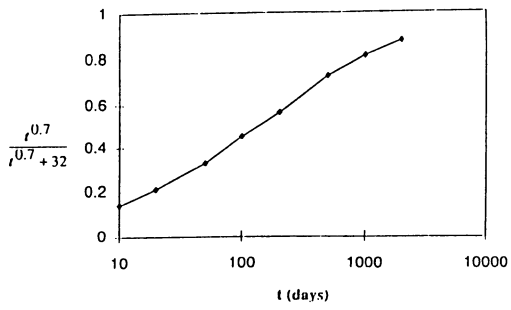

Figure 6. Time-varying function

It is worth noting that even when there is no applied stress (ie. $\sigma_o = 0$), the critical width to thickness ratio still depends on t through the shrinkage strain, and decreases as ε_{sh} increases. It is thus possible in theory that shrinkage-induced local buckling of the thin-walled RHS section may occur.

5 APPLICATION TO SHS SECTIONS

Equation 28 is in a form that may be programmed on a spreadsheet. Consider firstly a SHS with sides 400 mm wide and a plate thickness of t_p, which is filled with concrete with a short-term elastic modulus of E_c = 25 kN/mm^2 and subjected to a sustained service-load stress of σ_o = 20 N/mm^2. Figure 6 shows the critical width to thickness ratio for unilateral buckling as a function of the time in days, plotted logarithmically. At $t \rightarrow 0$, the short-term value of $(b/t_p)_{cr}$ is 90.1, and this value of the critical depth to thickness ratio decreases as t increases. The reduction in the time-domain is not so marked as the base value of b/t_p decreases. In the range of the latter ratio given (ie. 100 to 400), the critical depth to thickness ratio is less than the corresponding base depth to thickness ratio, indicating that, even in the short-term, the side of the RHS would have buckled locally. While values of b/t_p of 400 are probably unrealistic in practice, those of 100 are not (Uy 1998).

Figure 7 shows the same plot for σ_o = 10 N/mm^2. For b/t_p = 200 and 400, the critical width to thickness ratios are less than these corresponding ratios, indicating again that the sides of the SHS would have buckled both in the short and long-terms. However, for b/t_p = 100, the critical value $(b/t_p)_{cr}$ = 127 in the short-term, indicating that the side plate of the SHS would not have buckled. However, this drops down to about 90 in the long-term, so that time-dependent buckling would be expected to occur. The transition when $(b/t_p)_{cr}$ reaches 100 occurs between $t = 10^2$ and 10^3 days, indicating indeed that creep and shrinkage will precipitate local buckling in the time domain.

Finally, for a SHS, the value of the ratio p may be expressed as

$$p = \frac{A_s}{A_c} \approx \frac{4bt_p}{b^2} = \frac{4}{\left(b/t_p\right)} \tag{29}$$

This value of p may be substituted into Eqn. 28 and then solved iteratively for $(b/t_p)_{cr}$. This procedure was undertaken when the concrete core was subjected to σ_o = 10 N/mm^2 and 20 N/mm^2, both in the short-term ($t \rightarrow 0$) and long-term ($t \rightarrow \infty$). The results are presented in Table 1. It can be seen that in the long-term, unilateral local buckling of the plates of the SHS can occur for b/t_p = 69 under a sustained concrete stress of 20 N/mm^2, which is not an unreasonable scenario. The designer of welded thin-walled box sections that are intended to be infilled with concrete should therefore be aware of the propensity of the buckle with time.

6 CONCLUDING REMARKS

Concrete-filled RHS sections may deploy steel plates whose width to thickness ratios are in the 'slender' range, so that elastic local buckling will precede the yield stress f_y. At ultimate strength, this proportioning is satisfactory, since the column usually fails by flexural buckling well before the stress in the steel skin reaches f_y.

Although the elastic buckling coefficient is increased to a value of 10.67 for unilateral buckling, buckling may still occur at service load levels, since creep and shrinkage of the concrete core shed compressive load into the steel skin. A theoretical model showed by invoking the Rayleigh-Ritz method that the minimum elastic local buckling coefficient is indeed 10.67, and by using the AEMM the critical width to thickness ratio of the sides of an RHS section at which local buckling occurs was determined as a function of the concrete properties and time. An illustrative example was given. For a SHS section, it was shown further that the critical depth to thickness ratio may be obtained by iterative

Table 1. Values of $(b/t_p)_{cr}$ for a SHS section

σ_o (N/mm^2)	Short-term	Long-term
10	127	97
20	91	69

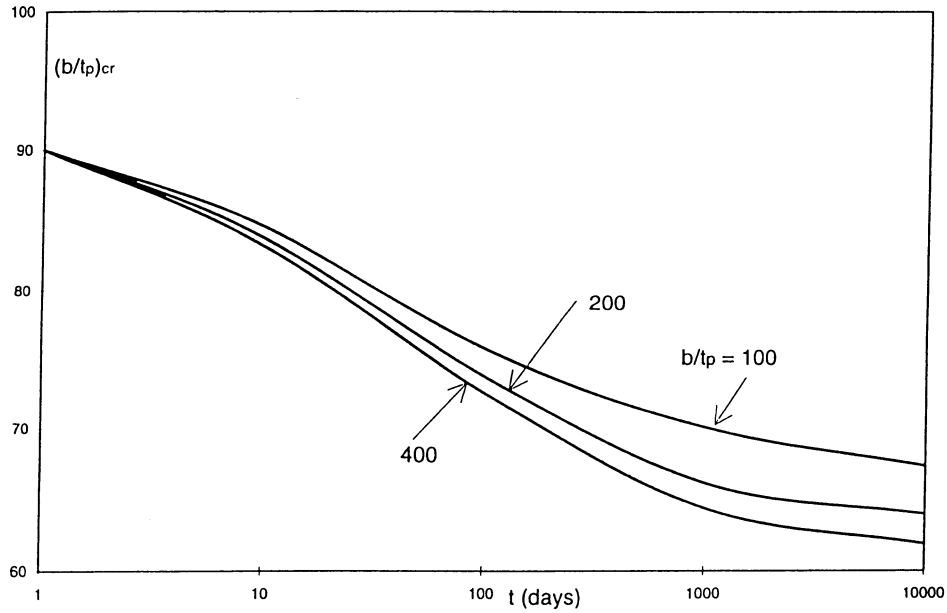

Figure 7. Critical slendernesses for $\sigma = 20$ N/mm^2

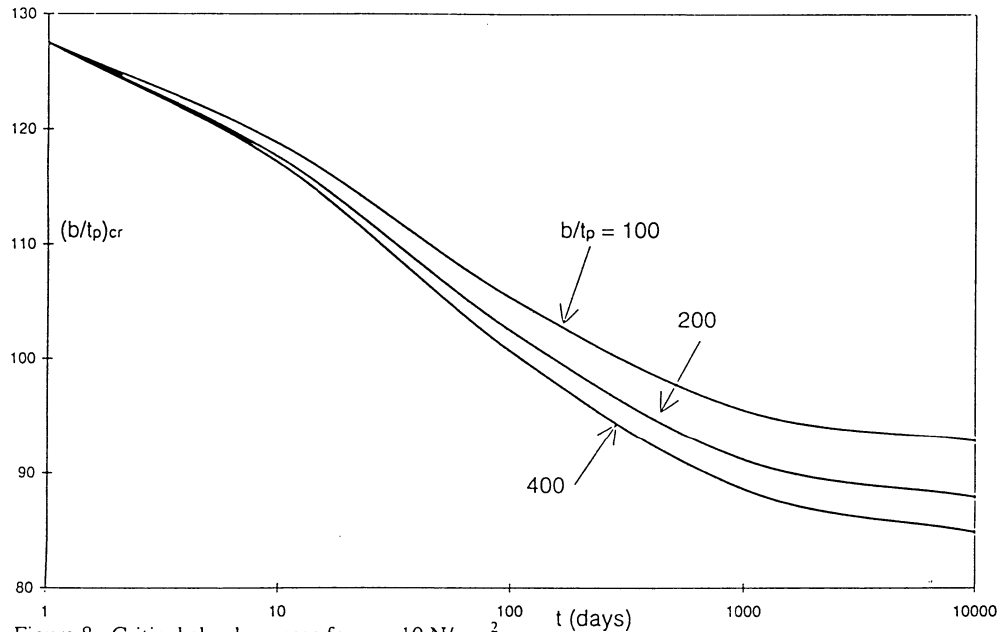

Figure 8. Critical slendernesses for $\sigma = 10$ N/mm^2

solution of a simple equation. For the example cited, local buckling may occur under high sustained stresses with depth to thickness ratios that may be typical in fabricated box columns. The critical width to thickness ratio was shown to decrease by 24 percent due to time-induced local buckling in the long-term.

7 ACKNOWLEDGEMENT

The work reported in this paper was financially supported by the Australian Government through a Royal Society Visiting Fellowship awarded to the author.

REFERENCES

Bazant, Z.P. 1972. Prediction of concrete creep effects using Age-Adjusted Effective Modulus Method. *ACI J.* 69(2): 212-217.

Bradford, M.A. & Wright, H.D. 1998. Time-dependent local buckling in lightweight composites. *Proc. 2nd World Conf. on Constr. Steel Res.,* San Sebastian, Spain, May.

Bradford, M.A., Wright, H.D. & Uy, B. 1998. Local buckling of the steel skin in lightweight composites induced by creep and shrinkage. Submitted for publication.

Gilbert, R.I. 1988. *Time effects in concrete structures*. Amsterdam: Elsevier.

Smith, S.T., Bradford, M.A. & Oehlers, D.J. 1998. Elastic buckling of unilaterally constrained rectangular plates in pure shear. *Eng. Structs.* (in press).

Standards Australia 1994. *AS3600-1994 Concrete structures*, Sydney: SA.

Terrey, P.J., Bradford, M.A. & Gilbert, R.I. 1994. Creep and shrinkage in concrete-filled steel tubes. *Proc. 6th Int. Conf. on Tubular Structs.*, Melbourne, Dec., 293-298.

Timoshenko, S.P & Gere, J.M. 1961. *Theory of elastic stability.* New York: McGraw Hill.

Trahair, N.S. & Bradford, M.A. 1997. *The behaviour and design of steel structures.* 3rd Australian edn., London: Chapman and Hall.

Uy, B. 1998. Local and post-local buckling of fabricated thin-walled steel-concrete filled box columns. *J. Constr. Steel Res.,* in press.

Uy, B. & Bradford, M.A. 1995. Local buckling of cold-formed steel sheeting in profiled composite beams at service loads. *Struct. Eng. Rev.* 7(4): 289-300.

Tubular Structures VIII, Choo & Van der Vegte (eds) © 1998 Balkema, Rotterdam, ISBN 90 5809 001 9

Use of tubular steel columns for high rise construction – A case study

Huen Poh Lai
RSP Architects Planners and Engineers (Pte) Limited

ABSTRACT: The development of structural concept with specific reference to Republic Plaza to illustrate the design and construction aspects which will be discussed.

Specifically, the design of the steel columns will be illustrated as these inclined columns are of particular interest. The details of the joints between the tubular section columns and the I beams will be discussed to illustrate how these joint problems are solved.

1 Introduction

Republic Plaza is a recent example of a spectacular use of tubular steel for high rise construction.

The Republic Plaza is located at the corner bound by Cecil Street, D'Almeida Street, Market Street and Malacca Street. It has a 66-storey office block with one basement and a 10-storey podium with 8 levels of carpark. The tower has a floor to floor height of 3.95m except at the mechanical floors where it is increase to 7.90m. It rises from the street level to a height of 280m to share the limelight with the other two adjacent buildings as being the tallest building in Singapore.

2 Structural System of the Tower

The floor system consists of a composite reinforced concrete slab with thickness varying from 125mm on the typical floor to 135mm on the 4th to 25th storey to cater for a flush floor trunking system introduced as an added flexiblity for the tenants. A thicker concrete slab of 150mm is adopted for the 1st storey and the mechanical floors to meet the design loading requirements. The slab is cast with the ribbed steel deck supported on structural steel beams spaced at approximately 2 metres centre.
The tower structural layout as shown in Figures 3 to 6 consists of a reinforced concrete central core and concrete infill structural steel columns located at the perimeter of the building. These members are connected by steel beams and composite reinforced concrete slabs to form the overall framing system for the tower. In addition, out riggers are introduced on the mechanical floors at 28th and 47th floor to enhance the rigidity of the building frame under lateral loads (See Fig.2).

3. Basis of Design of Tubular Steel Columns

3.1 Codes of Practice

In general, the design of the structure follows local and British codes of practice. In the areas where recommendations are silent in these codes, American and Japanese codes are used as reference.

The design of composite columns follows the recommendations of BS 5400 and AISC-LRFD (American Institute of Steel Construction, 1986 - Load Resistance Factored Design Method). The load factors of the BS and AISC (American Institute Steel Construction) are used to obtain the design loads under serviceability and ultimate limit states.

The design of the beam-column rigid connections using ring stiffeners are based on the AIJ (Architectural Institute of Japan) recommendations since an equivalent design guideline or recommendation was not given in BS or AISC.

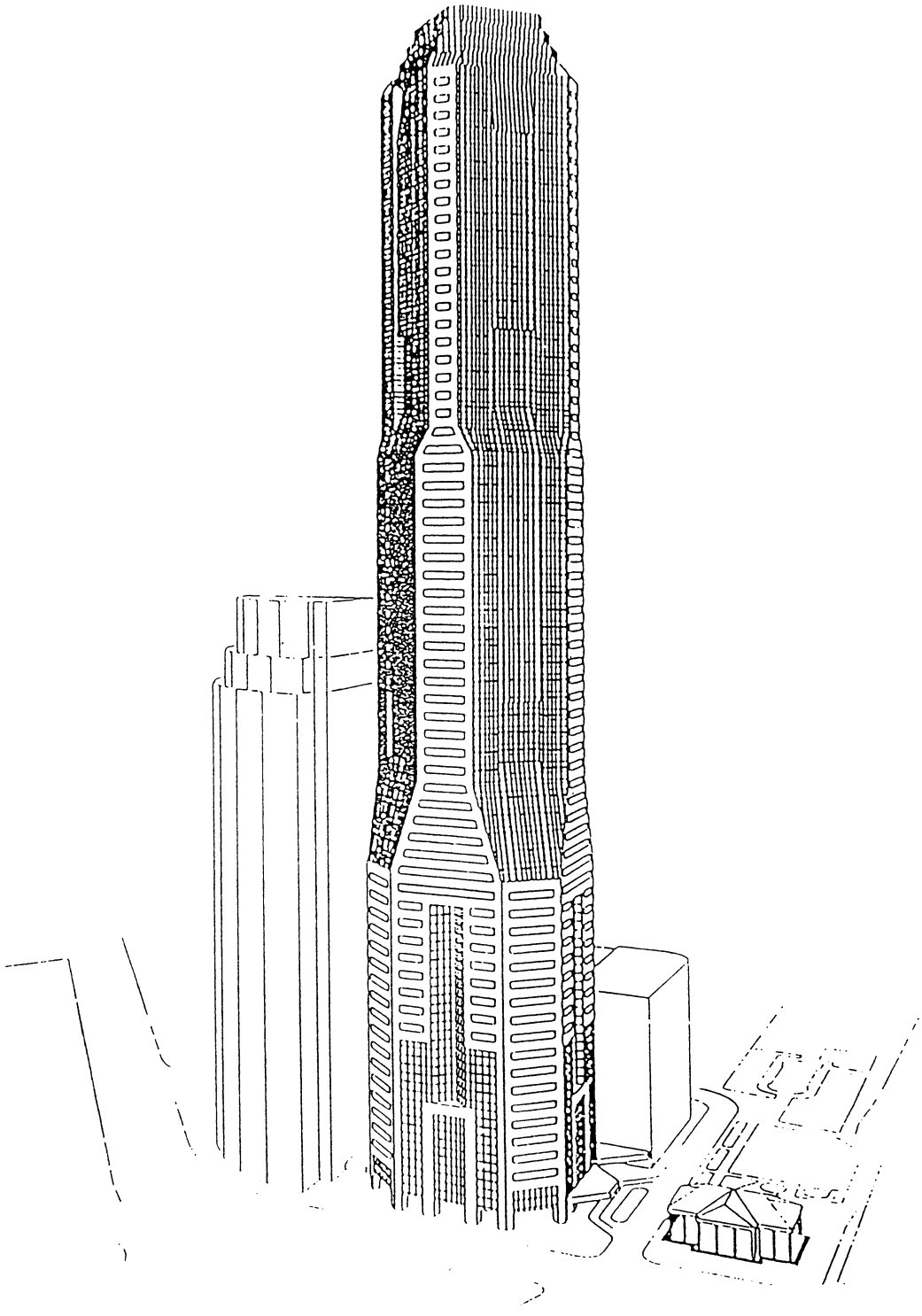

Figure 1 : Perspective View of Republic Plaza

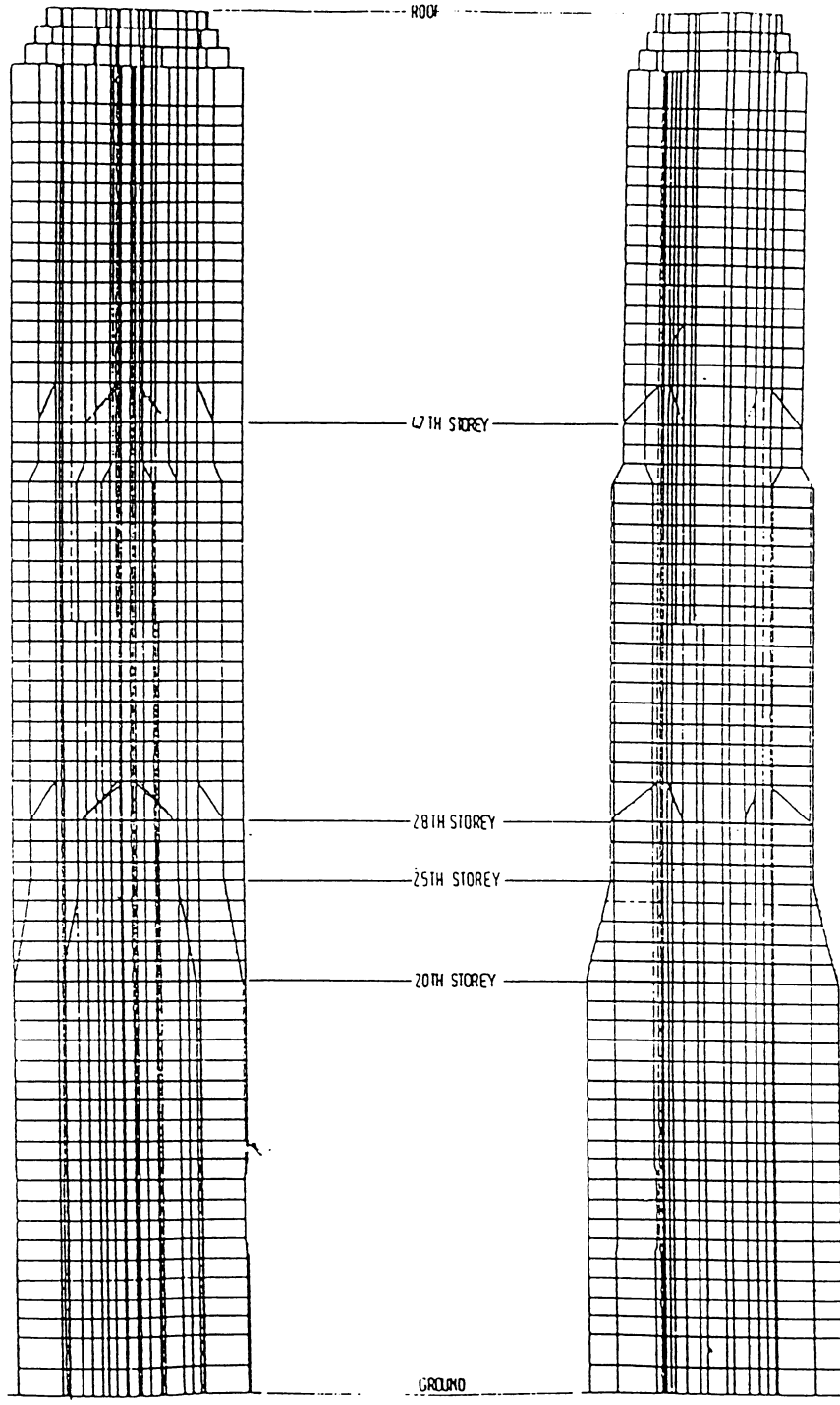

Figure 2 : Elevation of Tower Frame

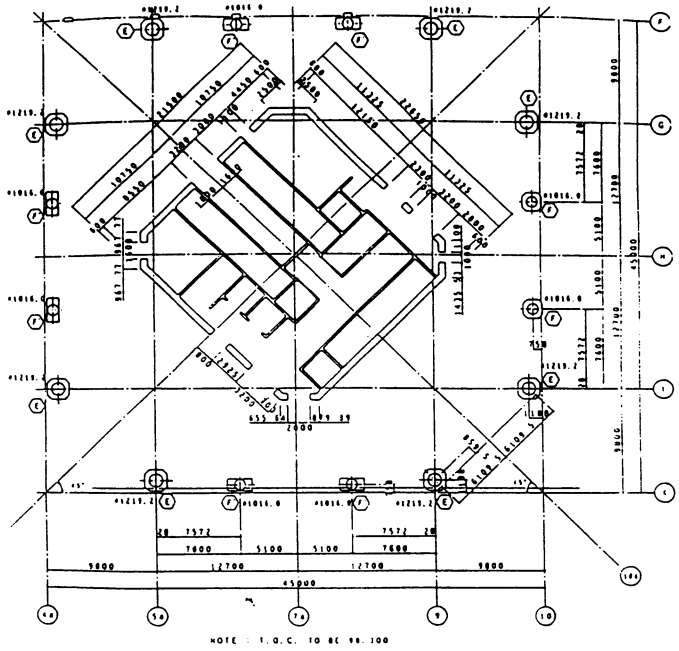

Figure 3 : Base Plate Layout

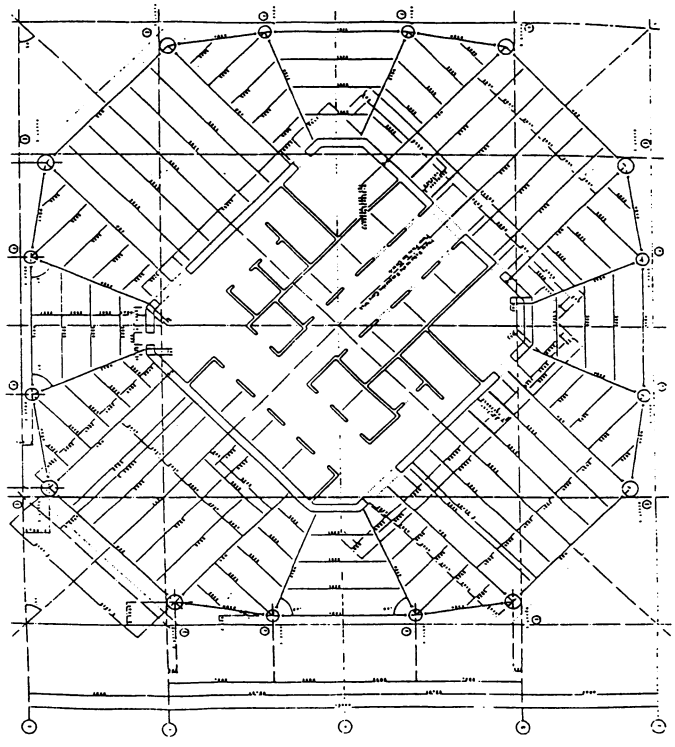

Figure 4 : Typical Floor Layout 1st - 37th Storey

3.2 Structural Performance

Vertical deflection	L/360 for beams as specified by BS 5950 where L is the span of the member.
Lateral deflection	H/500 for finishes and cladding (Section 3.2.2.2 Part 2, BS 8110) under a 50-year return period wind load.

Acceleration Peak horizontal acceleration at the uppermost occupied floor was not to exceed 0.01g (10 milli g). This was taken as the accepted level of occupancy comfort.

3.3 Design Loads

Superimposed dead and live loads follow the recommendations given in the Fourth Schedule of the Building Control Regulations 1989.

Wind loads were determined from the wind tunnel test using a mean wind velocity of 35.4 m/s from a 3-second gust with a mean return period of 100 years.

3.4 Materials

Concrete	
Column infill	Grade 55
Core walls	Grade 50
Composite slab	Grade 30
Steel Reinforcement	
Mild steel bar	Grade 250
High yield bar	Grade 460
Structural Steel	
Universal beams	Grade 43A, 50B ($t < 25$ mm) and columns 50C ($t > 25$ mm)
Plates	JIS G3106: SM 490YA and SM 490YA
Pipes	JIS G 490YA
High Strength bolts	JIS B1186 (TC - Type)
Hold down Bolts	BS 4190 Gr. 4.6
Shear studs	Section 3.1 BS 5950 Part 3

4. Structural Analysis

In the analysis of the tower structure, the lateral loads are assumed to be applied at the respective floor levels on the building and are resisted by the lateral load resisting system comprising the central concrete core and the moment resisting frame with out-riggers at 28th and 49th floor. The structural model is idealized as follows:

4.1 The stiffiness of the steel members for the main frame analysis consists of:

a) Perimeter columns below 49th storey - Composite tubular columns

b) Perimeter columns above 49th storey - Steel tubular columns

c) Inner columns above 63rd storey - Encased steel H columns

d) Beams - Steel beams

e) Out riggers - Steel bracings

4.2 The connection of main beams to the perimeter column is assumed as a rigid joint. From the 1st to 59th storey, the connections of main beams to the core walls, and to the columns are assumed as pinned and fixed respectively. Other beam-column connections and those of the out-riggers are assumed as pinned connections.

4.3 The out-riggers on the 28th and 47th storey are effective only under live and wind loads as these were installed after the completion of the tower main frame.

4.4 The base of the building frame are assumed to be pinned. The same assumption is adopted for the design of foundation and substructure. As a result, the base plates are only designed for axial and shear forces only.

4.5 The resistance to the axial forces and overturning moment at the base of the building caused by lateral loads are provided by the reaction forces of the caissons and passive soil pressure on the sides of transfer girders below the basement level.

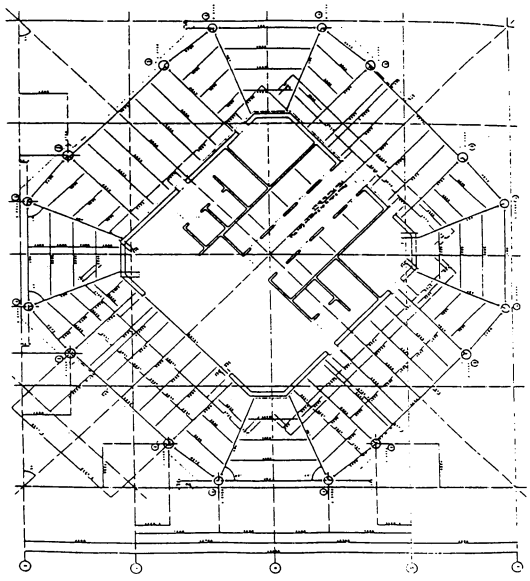

Figure 5 : Typical Floor Layout 38th - 62nd Storey

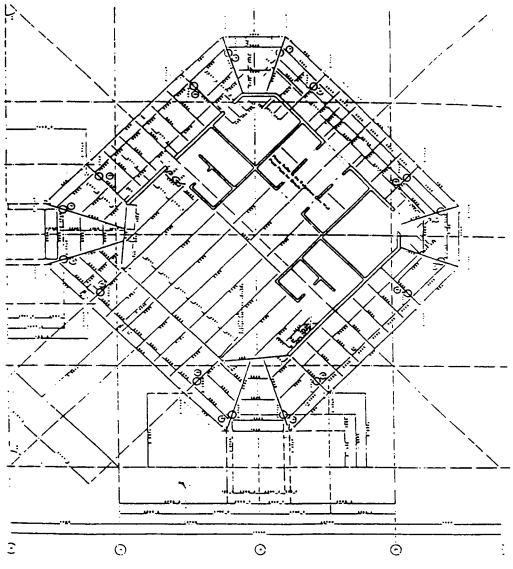

Figure 6 : Typical Floor Layout 63rd - 66th Storey

5 Computer Modelling

The design calculation was based on GT STRUDL space frame and finite element programmes for the tower block analysis and Micas Plus 3-D finite element for the foundation analysis.
In all cases, the structural model comprises an assembly of the core wall system, RC tie beams, main steel beams, out-rigger braces and the perimeter composite and steel columns. The out-riggers at the mechanical floors as shown in Fig. 9 and the inclined columns installed from 20th and 25th storey, and 43rd to 45th storey (see Fig. 7 and Fig. 8) are also included in the computer model to enable the local forces at these levels be determined for design purposes. Peak wind pressure envelopes obtained from Tunnel Test were adopted for the frame analysis.

The core walls system is modelled as one wall section having an equivalent section property similar to the concrete core and with stiffened beams at the floor levels. The model is analysed by the GT STRUDL space frame programe using modular ratios of 1:6.83 for the steel sections cast in the core walls and 1:15 for the composite columns.

Results of the analyses were extracted from the computer runs and were then compiled and factored before they were combined to form the various load cases in accordance with the recommendation of BS 8110 or BS 5950. The load cases were adopted for design and checking of the tower structure.

6 Design of Tubular Columns

The design of structural members was carried out based on the results obtained from the GT STRUDL space frame analyses. For the design of key members, the upper bound results from the Sway Frame model with an amplification factor of 1.138 as specified in Sections 5.1.2.3 and 5.6.3 of BS 5950: Part 1 are adopted. Special features in the design include:

6.1 Composite Column Design

The composite columns are designed in accordance with the requirements as stated in BS 5400 and are checked against the AISC-LRFD requirements using the appropriate load factors. It was found that the AISC-LRFD requirements are more stringent and control the design of composite columns.

The composite columns at the tower block from basement level to the underside of the 49th storey are designed using Grade 55 concrete infill.

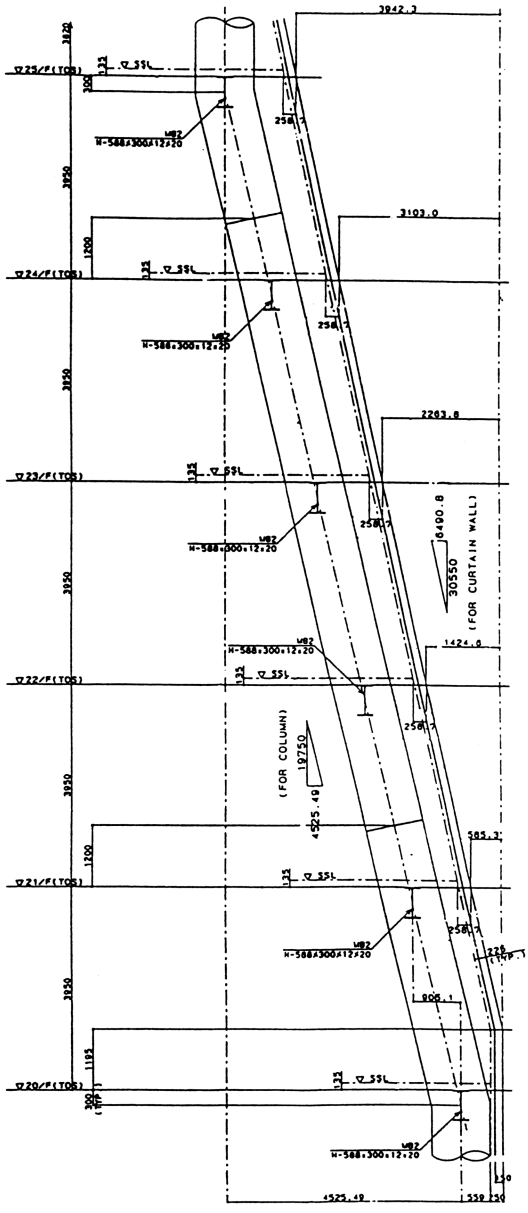

Figure 7 : Detail of Inclined Columns from 20th to 25th Storey

However, Grade 60 concrete was adopted at the site for absolute quality control reasons. The design of inclined columns was carried out in the same way except the loading was based on the results from the finite element analysis.



Photo 1 - Republic Plaza under-construction. Note the inclined steel columns from the 20th to 25th storey.

6.2 Column splices

The stress at a column splice joint is calculated as P/A ± M/Z. If no tension stress exists, then a minimum partial penetration (P.P) butt weld of ($2\sqrt{t} + 3$) is used, where, t is the wall thickness of the steel column. If tension exists, then, the weld is designed to provide full tension capacity for this condition.

The eccentric loading at the joints caused by the incorporation of columns of different diameters in the design is resisted by web stiffeners, the detail of which is shown in Fig. 10.

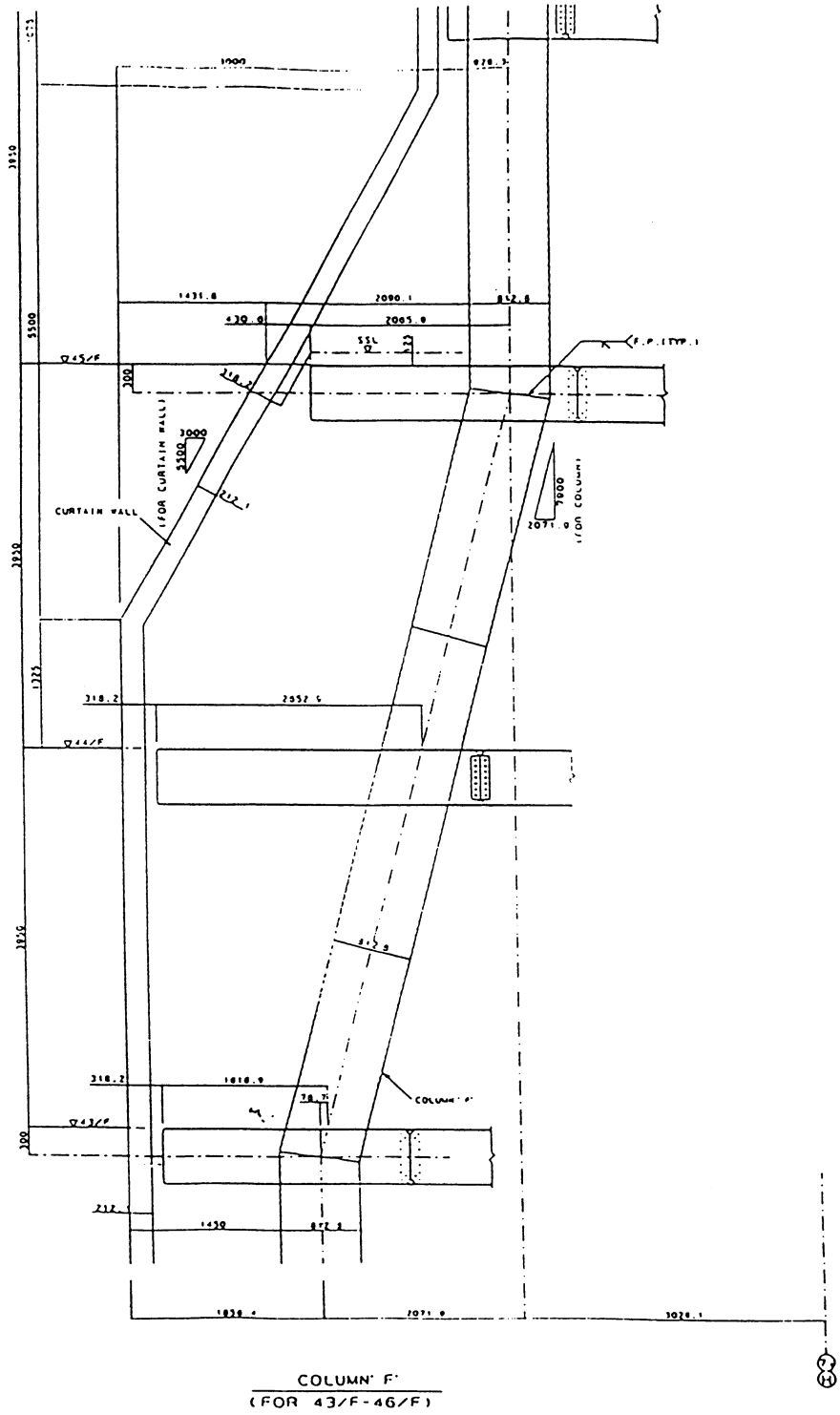

Figure 8 : Detail of Inclined Columns from 43rd to 45th Storey

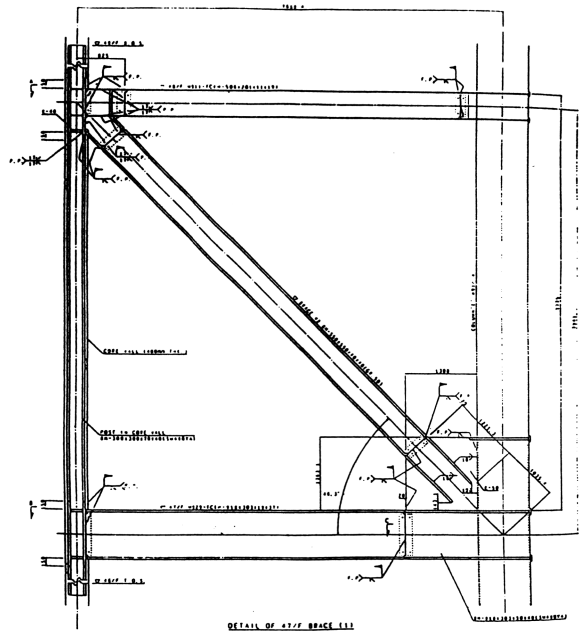

Figure 9 : Out-rigger Detail on M & E Floors

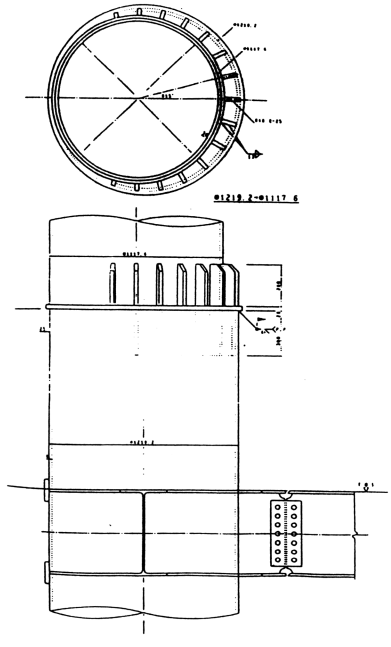

Figure 10 : Column Splice Connection

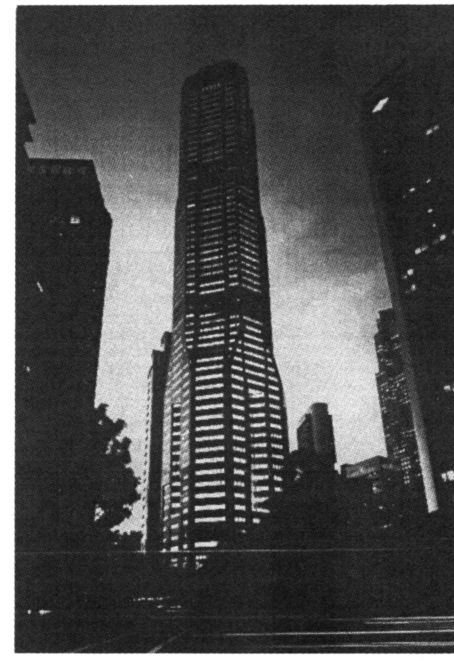

Photo 2 - The completed Republic Plaza

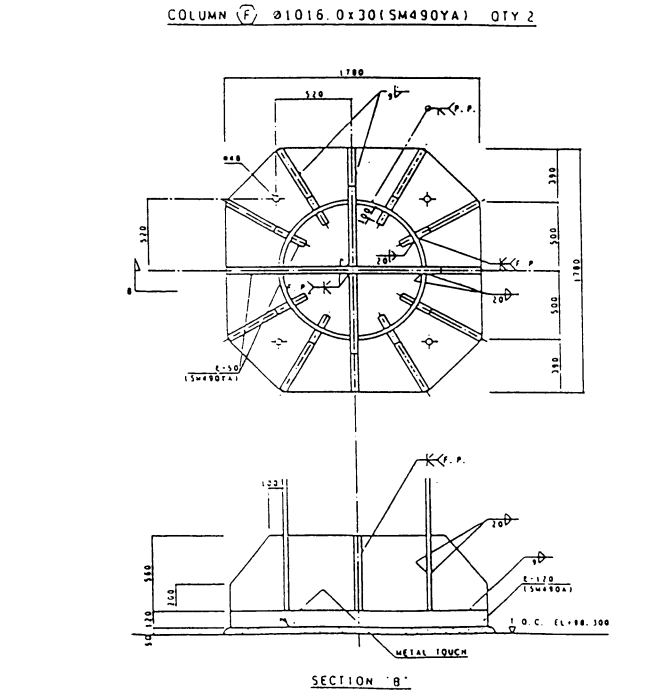

Figure 11 : Typical Base Plate Detail

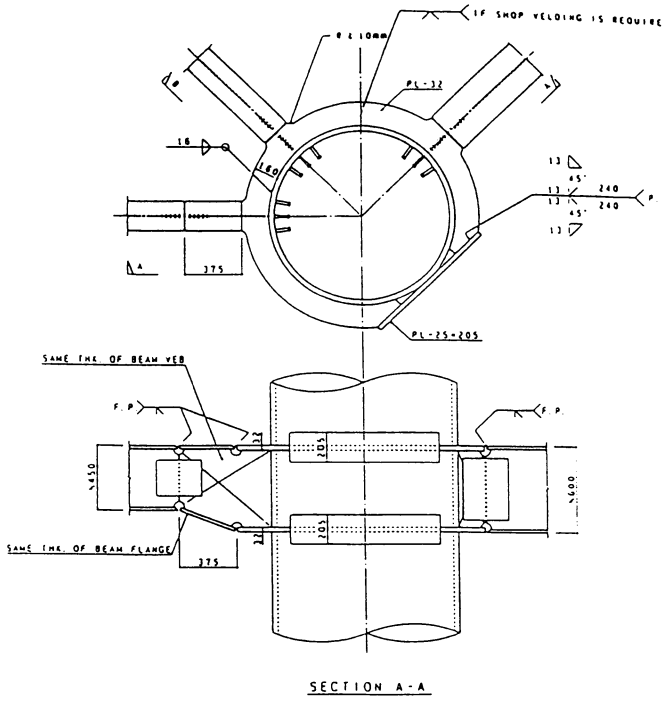

Figure 12 : Beam to Column Connection

6.3 Column base plate

The base plate as shown in Fig. 11 does not transfer any moment as it is modelled as a pin connection in the computer models. It is designed to resist bearing and local bending only. The forces on the base plate are transferred to the foundation by the means of holding down bolts.

6.4 Beam-column rigid connection

The design and checking of the ring stiffener plate connections are based on the recommendations givne by the Architectural Institute of Japan (AIJ) as no other reference is available at the design stage. The procedure is based on working stress method and the design forces are obtained by dividing the ultimate loading cases by a factor of 1.50. The typical detail of the beam-column joint connection is shown in Fig. 12.

The design of the beam-column connection is based on the actual beam forces obtained from the computer output with a 10% redistribution allowance for the peak elastic moment as permitted in Section 5.4.1 of BS 5950: Part 1. Friction bolts are used for all the on-site connections. In addition, beams forming part of the steel truss system for the inclined columns are jointed by full penetration butt welds.

7 Conclusion

The structural design of the Tubular Steel Columns was described.

7.1 The core wall system resisted approximately 90 to 95 percent of the lateral shears at the lower floors and particularly at the base level. At the top storeys, the resistance to storey shear was mainly taken by the steel frame.

7.2 The out-riggers introduced at 28-storey and 47-storey were effective in controlling the inter-storey drifts.

7.3 In view of the high stiffness of the central concrete core and the pinned joint detail adopted for the main seel beam and core wall connection, the steel frame acted more like a gravity frame. This had two advantages. First, it helped to bring down the structural steel content. Secondly, it enhanced buildability for the project.

7.4 The tower structure featured the use of inclined steel columns from 20th to 25th storey and 43rd to 45th storey, which is an economical solution to account for the shifting of column positions at these floors. Otherwise, transfer system will be required, which can be time consuming, expensive and difficult to build given the height of this building.



Taylor & Francis
Taylor & Francis Group
http://taylorandfrancis.com

Tubular Structures VIII, Choo & Van der Vegte (eds) © 1998 Balkema, Rotterdam, ISBN 90 5809 001 9

The behaviour of cold-formed slender square hollow section beam-columns

R.M.Sully
Hyder Consulting, Sydney, Australia
G.J.Hancock
Department of Civil and Mining Engineering, University of Sydney, Australia

ABSTRACT: A test programme was conducted into the behaviour of cold-formed square hollow section (SHS) beam-columns of slender cross-section. This experimental programme follows an earlier test programme on compact SHS beam-columns. The tests were conducted in a purpose built testing rig capable of applying load and moment in a constant ratio. The test specimens were pin ended and were loaded at two different ratios of end moment. The results of the testing programme are compared with the current design rules in the Australian Steel Structures Standard AS 4100, the American Institute of Steel Construction Specification (AISC-LRFD), and Eurocode 3.

1 INTRODUCTION

At present in Australia, the design rules applicable to cold-formed slender tubular beam-columns are simple linear interaction curves (Amendment No. 3 to AS4100 (SAA 1995)). However within the same standard, advanced interaction rules are available for doubly symmetric, compact I-sections and tubular sections. In the U.S.A., in the AISC Specification (AISC 1994), there is a bilinear rule that does not change with the ratio of end moments, β, but is applicable to SHS sections whether compact, non-compact or slender. However, the interaction curves are non-dimensionalised with values of column capacity and moment capacity that account for local buckling of slender sections. Eurocode 3 (EC3 1990) follows an approach similar to that used in AS 4100, however the moment amplification factor used is quite different.

From previous research (Sully and Hancock 1996), it was evident that the advanced rules for doubly symmetric I-sections (from AS 4100) were applicable to compact SHS beam-columns. It was believed that by non-dimensionalising these rules with values of column capacity and moment capacity that accounted for local buckling, the advanced rules would be applicable to slender SHS sections as well. A test programme was therefore conducted to assess; (i) the behaviour of cold-formed, slender square hollow sections, under varying load/moment ratios, for two end moment conditions, and (ii) the applicability of the current interaction design rules, in AS4100 (advanced rule), the AISC Specification (chapter H), and Eurocode 3, for cold-formed slender square hollow sections.

2 TEST RIG LAYOUT AND OPERATION

2.1 Test Rig

A test rig was purpose built for this test programme. It consisted of a 2000 kN hydraulic actuator used to apply compressive axial force and a 250 kN hydraulic actuator used to apply bending moment to the specimen. The moment was applied to the specimens by the bending actuator via lever arms attached to each end of the specimen. The layout of the rig allowed for a range of end moment ratios (β) from $\beta = -1/4$ to $\beta = -1$ (i.e. specimens bent in single curvature). The rig does not allow for positive values of β (i.e. specimens bent in double curvature). A full description of the test rig can be found in Sully and Hancock 1996.

2.2 Test Programme

The slender sections described in this report are 200x200x5 SHS, with a nominal yield stress of 350 MPa. Two lengths of specimen were used for the

interaction tests. The long test specimens were all 5100 mm in length. This gave the specimens an effective length (L_e) between the pinned bearings of 5550 mm. This length was chosen because it gave a non-dimensionalised column slenderness (λ) of approximately 1, when the nominal yield stress (f_y = 350 MPa), and nominal dimensions were used (Equation 1).

$$\lambda = \left(\frac{L_e}{r}\right)\sqrt{\frac{f_y}{\pi^2 E}} \quad (1)$$

Previous research (Key et al 1988) had shown that the effects of section slenderness were more pronounced in shorter sections. Consequently it was decided to also conduct several interaction tests on short specimens to investigate fully the effect of local instability on beam-column behaviour. The short interaction test specimens were 1000 mm long (i.e. the same length as the stub column test specimens).

3 ANCILLIARY TESTS

3.1 Material Tests

In order to correctly compare the test results with design rules and gain a clearer understanding of actual behaviour material tests were conducted. They included tensile coupon tests of both the corner and flat material and residual stress measurements.

The tensile coupon tests showed an average yield stress for the flat material of 343 MPa with an ultimate tensile strength of 489 MPa. The corner material had values of 425 MPa and 524 MPa for yield stress and ultimate tensile strength respectively. A full description of the method is described in Sully and Hancock 1995.

The results of the residual stress measurements show a small net compressive residual stress in the flat material of 24 MPa. The bending residual strains averaged 920 microstrain. Both of the values are substantially less than those observed for the compact sections (Sully and Hancock 1996). This is to be expected given that the thinner sections experience less cold-work during the forming process. A full description of the results is described in Sully and Hancock 1995.

3.2 Geometric Tests

Overall geometric imperfections were measured for four of the long test specimens. The test specimens show a maximum imperfection of approximately 0.4 mm or 1 in 12750 (higher than, i.e. more straight than, but still comparable to, the earlier compact tests (Sully & Hancock 1996 and Key et al 1988)). In addition to the overall geometric imperfections, local imperfections existed at the ends of the specimens, and are suspected to have come from local plate distortions associated with the welding of the moment plates. These imperfections bow out from the tube, are equal on both sides, and are of the order of 2 mm which is clearly greater than the overall member imperfections.

In addition to measuring the overall imperfection, the cross sectional dimensions were measured using a micrometer and a digital vernier. The comparison of nominal versus actual dimensions is set out in Table 1 which also includes values of actual and nominal computed section properties. The actual section properties were calculated using the measured flat dimensions and corner radii, and are gross values not effective values.

4 TEST RESULTS

4.1 Stub Column Tests

Two stub column tests were carried out in a 2000 kN hydraulic actuator in order to determine the axial section capacity of the specimens. A plot of axial displacement versus axial load for both tests is shown in Figure 1. The tests are designated STC1 and STC2 for reference within this paper. As can be seen, both specimens reached similar ultimate loads (1359 kN (STC1) and 1361 kN (STC2)). Similarly both tests show almost identical unloading behaviour; both had very steep unloading characteristics associated with local buckling at or just prior to reaching the ultimate load as was

Table 1. Section Properties for 200x200x5 SHS.

Dimension or Property	Nominal Value	Actual Value
B,D	200.0 mm	199.4 mm
t_{flange}	5.0 mm	5.03 mm
Corner radius	10.0 mm	8.5 mm
Area	3810 mm^2	3858 mm^2
I	23.9E6 mm^4	24.1E6 mm^4
Z	239.0E3 mm^3	242.0E3 mm^3
S	277.0E3 mm^3	279.9E3 mm^3

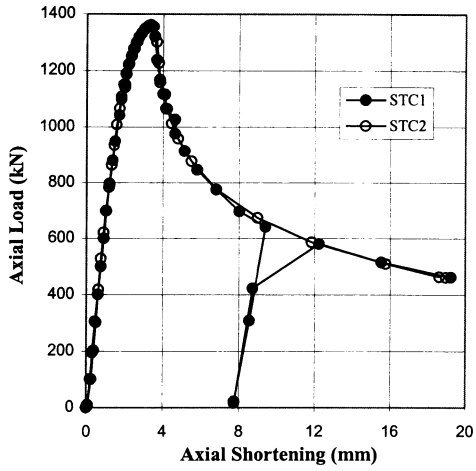

Figure 1. Stub Column Test Results

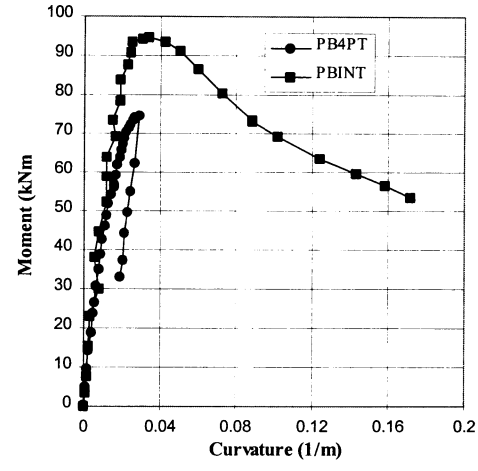

Figure 2. Plastic Bending Test Results.

expected given their slender cross-section.

4.2 Plastic Bending Test

In order to non-dimensionalise correctly the interaction tests, it was necessary to obtain a reference plastic bending capacity and column strength. Two plastic bending tests were conducted. The first was conducted using a 2000 kN hydraulic actuator in a four point bending test configuration. This test is designated PB4PT. A more complete description of the test rig is described in Sully and Hancock 1995.

The second test was conducted in the interaction test rig, and is designated PBINT. The 250 kN bending jack was used in compression thereby applying a moment at each end and inducing a small tension in the specimen. At the same time, the 2000 kN compression jack was used to apply the same force in compression to the specimen, negating the axial load. Plots of curvature versus moment for both tests are shown in Figure 2.

The four point bending test reached an ultimate moment, M_{pt}, of 94.6 kNm at which time the specimen buckled locally in the region of constant moment. Some amount of local buckling may have been present before the ultimate load was reached but it was not observable. The interaction bending test failed suddenly at a moment of 74.6 kNm. The specimen formed a local buckle at the southern end just next to the welded moment plates. It is thought that the specimen failed prematurely due to the local distortions and stress concentrations induced in the specimen from the heavy welding used to attach the moment plates. This behaviour was evident in one of the interaction tests described in Section 4.5.

4.3 Column Test

An interaction test (designated LC1) was conducted in the test rig by application of the compression actuator only. The column specimen was 5100 mm long giving it an effective lengths (L_e) of 5550 mm (the same as for the long interaction test specimens). An eccentricity of 5 mm was added at each end in the plane of bending to create an approximate

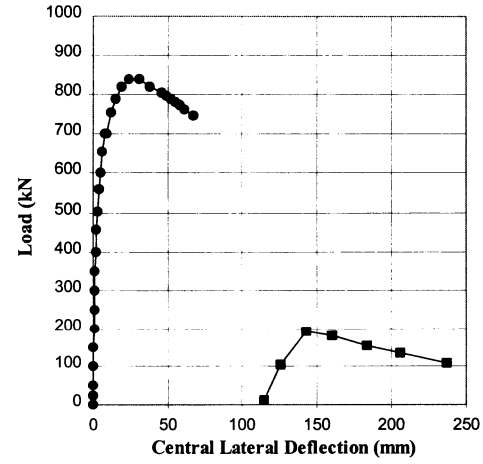

Figure 3. Column Test Results.

eccentricity of 1/1000 of the specimen length. This eccentricity was considerably greater than the maximum measured geometric imperfection of approximately 0.3 mm.

A graph showing load versus central lateral deflection is shown in Figure 3. The column specimen reached an ultimate axial load, P_{uc}, of 840 kN. Shortly after reaching ultimate the specimen collapsed suddenly leaving the discontinuity in the load deflection graph shown in Figure 3. The collapse occurred as a local buckle formed at mid-span. The loading rig and/or control electronics were not stiff enough to control the unloading of this specimen as was also observed in tests described in Key et al (1988).

4.4 Long Interaction Tests

Two series of interaction beam-column tests were conducted. For the first series with $\beta = -1$ (referred to as B1 series), four tests were conducted with varying ratios of applied load and moment. In order of descending applied load/moment ratio they are B1R1 to B1R3. For the second series with $\beta = -0.5$ (referred to as the B2 series), three tests were conducted, known as B2R1 to B2R3, again in descending order of applied load/moment ratio.

Plots of load versus central moment for the B1 series of tests are shown in Figure 4. The central moment is the sum of the moment applied directly from the bending actuator and the moment indirectly applied via the P-Δ effect from both the compression and bending actuators.

From the plots, it is evident that local buckling affected the beam-column behaviour of these specimens. In comparison to the compact sections (Sully & Hancock 1996) the slender sections show a distinct maximum moment with rapid unloading associated with the formation of a local buckle. The local buckles did however, occur after the maximum load had been reached. In all four cases, the local buckle occurred at midspan. Test B1R2a was conducted as a repeat of B1R2. As B1R2 approached its maximum load, the electronic coupling mechanism between the loading actuators lost stability, giving a somewhat erratic loading path. It was thought this could have affected the results adversely and so the test was repeated, and designated B1R2a. Test B1R2a was controlled manually through the region of maximum load to avoid any instability. As can be seen, the two tests gave very similar results.

The results of the B2 series are shown in

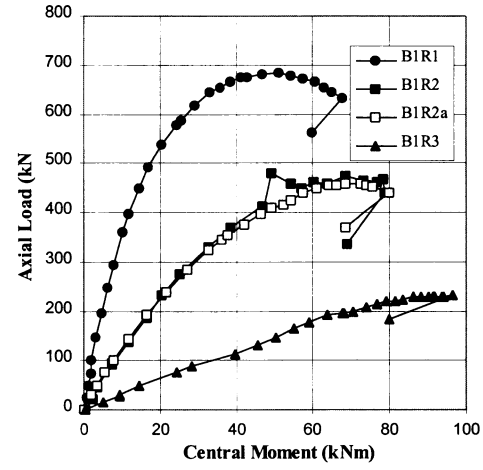

Figure 4. Long Interaction Tests, $\beta = -1$.

Figure 5. Here the graph is of load versus maximum moment instead of central moment because the location of the maximum moment shifted during the tests. For B2R1, it started at the southern end (the point of application of maximum moment) and traversed north to the centre, where the specimen buckled locally. The same is true for B2R2, however the speed at which the traverse of the maximum moment happened is slower. For B2R3, with a lower applied load, the maximum moment stayed at the southern end (this specimen failed locally about 100 mm north of the moment plates). This was still within the area of large local distortions caused by

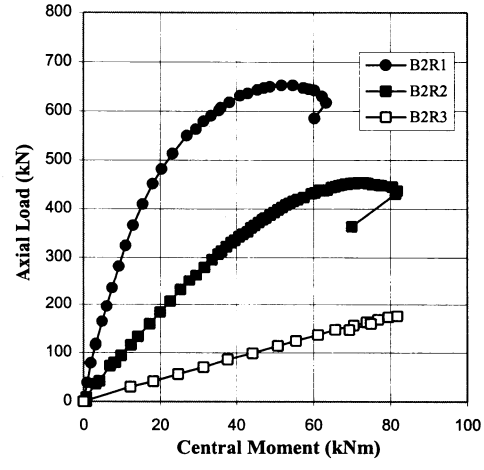

Figure 5. Long Interaction Tests, $\beta = -1/2$.

the welding of the moment plates, as described in Section 3.2. Test B2R3 failed in a similar fashion to the interaction-bending test described in Section 4.3, locally buckling at the same location, at a very similar moment (B2R3 at 75.9 kNm, the interaction bending test, PBINT, 74.6 kNm).

It is thought that in both cases the failure occurred prematurely because of local distortions and stress concentrations due to the heavy welding associated with the moment plates. This problem was not observed in the compact sections and so it is the authors opinion that the problem is directly associated with the plate slenderness of the slender section. It should be pointed out that such connections with slender sections are possible in practice and the occurrence of these failures is a concern to the authors, and the subject of on-going research at the University of Sydney.

4.5 Short Interaction Tests

Three short interaction tests were performed, designated SIT1, SIT2, and SIT3. All three interaction tests were performed in a 2000 kN vertical testing machine by application of an eccentrically located axial load. The eccentricities used in the three test were 50 mm for SIT1, 125 mm for SIT2, and 400 mm for SIT3. These eccentricities were chosen in order to get a broad range of interaction values between the stub column capacity and pure bending strength. A full description of the testing rig is found in Sully and Hancock 1995.

Load versus central lateral deflection for the three short interaction tests is shown in Figure 6. Test SIT1 failed by locally buckling close to the centre of the specimen, as expected, precipitating a sharp fall in load. Unlike the long interaction tests however, it appears that the local buckling occurred prior to the maximum load being reached. The local buckles appeared similar to the buckles that formed in the long interaction tests. The maximum applied load was 847 kN, giving a maximum applied end moment of 42.4 kNm.

Tests SIT2 and SIT3 did not fail in the same manner. Both tests failed, when a local plastic collapse mechanism formed at one end, preceeded by small but visible local buckles at each end. SIT2 reached a maximum applied load 495 kN (giving an applied moment of 61.9 kNm), while SIT3 reached 197.3 kN (giving an applied moment of 78.9 kNm). There is evidence that the failures may have been induced by the connections used in a similar fashion to the problem outlined in Section 4.5.

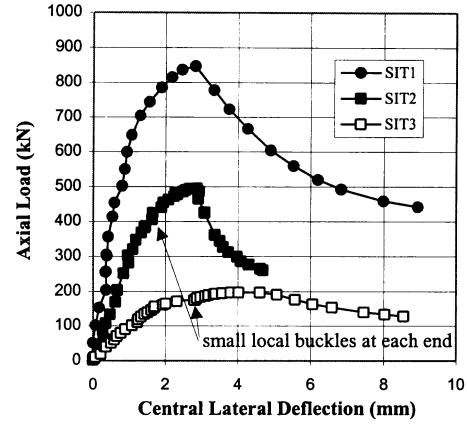

Figure 6. Short Interaction Tests, β =-1.

For both tests (SIT2 and SIT3) the collapse mechanism was similar, although more pronouced in SIT3. At about 75 % of the maximum load, small local buckles were observed to form at the top and bottom of both specimens. They were observed to be the same size top and bottom and in the same relative positions on the specimens. The buckles, once formed, remained unchanged until the ultimate load was reached. At this point, one of the small buckles formed into a plastic collapse mechanism, and the specimen failed.

The point at which the small local buckles formed in SIT3 is shown in Figure 6. The specimen 'softened' with the formation of the buckles and then stiffened again to take the additional load. The ability of the section to take increased load after the formation of these local buckles is probably due to the restraint at the ends offered by the welded end plates.

The reason the local buckles formed was not apparent until test SIT3 was completed. During this test, the loading beam began to yield locally around the bolts in tension as the load approached maximum. The yielding in the loading beam caused the loading beam to separate from the end plates in the tension region. This led to an uneven loading configuration and some plastic deformation in the end. It is thought that this flexibility in the connection caused the local buckles to form prior to the ultimate load being reached, and that these local buckles, once formed, led to the appearance of a local plastic collapse mechanism. It is also possible that the load at failure was lower than would have been reached if the specimens had not locally buckled at the ends but had failed in the middle as

SIT1 did. This problem appears to be more evident for SIT3 than SIT2. In Figure 6 the point at which the local buckling occurs is marked by a discontinuity in the plot for SIT3, not as evident in the plot for SIT2.

5 DESIGN

Comparison of the test results is made to the three standards; AS4100, the AISC specification, and Eurocode 3. The design rules for combined actions for each are as follows.

The AS4100 design rule (Clause 8.4.2.2) for doubly symmetric compact I-sections;

$$M_x^* \le M_s \left[\begin{array}{l} \left[1-\left(\frac{1+\beta}{2}\right)^3\right]\left(1-\frac{N}{N_c}\right)+ \\ 1.18\left(\frac{1+\beta}{2}\right)^3\sqrt{1-\frac{N}{N_c}} \end{array} \right] \qquad (2)$$

where; M_x^* = Member moment capacity, or maximum member design moment, M_s = Section moment capacity, N = Applied axial load, N_c = Member axial capacity, β = Ratio of applied end moments.

The AISC specification design rules; Chapter H;

$$\frac{P}{P_n} + \frac{8}{9}\left(\frac{M_{ux}}{M_{nx}}+\frac{M_{uy}}{M_{ny}}\right) \le 1.0, \qquad (3)$$

$$\text{For } \frac{P}{P_n} \ge 0.2, \text{and}$$

$$\frac{P}{2P_n} + \left(\frac{M_{ux}}{M_{nx}}+\frac{M_{uy}}{M_{ny}}\right) \le 1.0, \qquad (3a)$$

$$\text{For } \frac{P}{P_n} < 0.2$$

where; M_{ux}, M_{uy} = applied moments about the major and minor axes respectively, M_{nx}, M_{ny} = Section moment capacities about the major and minor axes respectively, P = Applied axial load, P_n = Member axial capacity, β = Ratio of applied end moments.

The Eurocode 3 rule;

$$\frac{N_{Sd}}{N_{c.Rd}}+\frac{k_y M_{y.Sd}}{M_{y.Rd}}+\frac{k_z M_{z.Sd}}{M_{z.Rd}} \le 1 \qquad (4)$$

where, N_{Sd} = the applied axial load, $N_{c.Rd}$ = the axial load capacity, $M_{y.Sd}$, $M_{z.Sd}$ = the applied moments about the major and minor axes respectively, $M_{y.Rd}$, $M_{z.Rd}$ = the section moment capacities about the major and minor axes respectively, and for slender tubular sections;

$$k = 1-\frac{\mu N_{Sd}}{N_{c.Rd}} \le 1.5 \qquad (5)$$

$$\mu = \bar{\lambda}(2\beta_M - 4) \le 0.9, \qquad (6)$$

here β_m = 1.8 - 0.7ψ, where ψ is the ratio of end moments taken as positive for single curvature, which is the opposite convention used in AS 4100 and the AISC specification and λ is the effective slenderness.

The values of moment from the AS 4100 and AISC interaction rules (M_x^* and M_{ux} respectively) are maximum second order elastic moments. These therefore should be equivalent to the product $k_y M_{y.Sd}$ in Eurocode 3, although the amplification factors used are different. Consequently in order to compare the three design rules with the test values, values of applied load and moment are compared to values of applied first order moments from each of the design rules adjusted to account for the different amplification factors; $M_x^*/\delta_b = M_{ux}/\delta_b = k_y M_{y.Sd}/\delta_b$, where δ_b is the amplification factor used in both the Australian and AISC specifications.

The results of the comparison are shown in figures 7 to 12. Figure 7 shows the results for the long interaction tests for β = -1 and Figure 8 for β = -1/2. In both cases the values of column capacity, and moment capacity were derived from code rules using actual dimensions, and material properties. The design values incorporated reductions for section slenderness as appropriate to each code. Figures 7 and 8 have been redrawn as Figures 9 and 10 respectively with the design curves using the test values of column and moment capacity. This was done to more accurately compare the design curves with actual behaviour.

Figures 7 and 8 show all three design curves to be quite conservative. The Eurocode 3 rule being more conservative than the other two. This is partially a result of the low estimation of column capacity made by Eurocode 3. Both design curves applicable in Eurocode 3 were used; that is the higher curve using the 'base' material properties and the lower curve using the higher 'actual' material properties (resulting from the cold working process). The difference between the values of capacity was only 1%.

Figures 9 and 10 show much closer agreement by all three curves. The Eurocode 3 rule is still the most conservative. In all four graphs it is clear that the as β increases from -1 to -1/2 the interaction envelope moves out. It is also clear that for β = -1 the AISC specification rule is the closer approximation, while for β = -1/2 the AS4100 rule appears to be a better fit.

Figures 11 and 12 show comparisons for the short interaction rules. Figure 11 with design curves plotted against code values for stub column and moment capacity, and Figure 12 with design curves plotted against actual column and moment capacity. If PB4PT is taken as the section moment value all

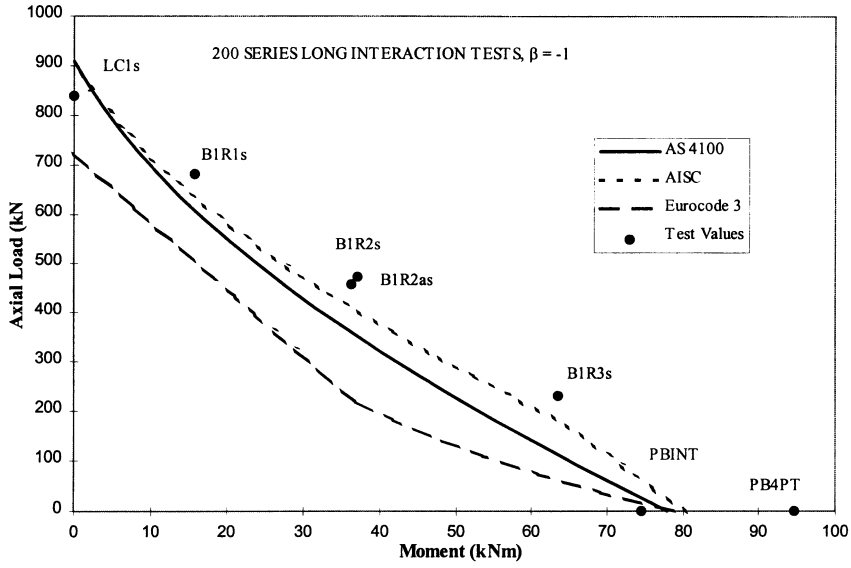

Figure 7. Test results compared with design rules for β = -1, non-dimensionalised against code rules.

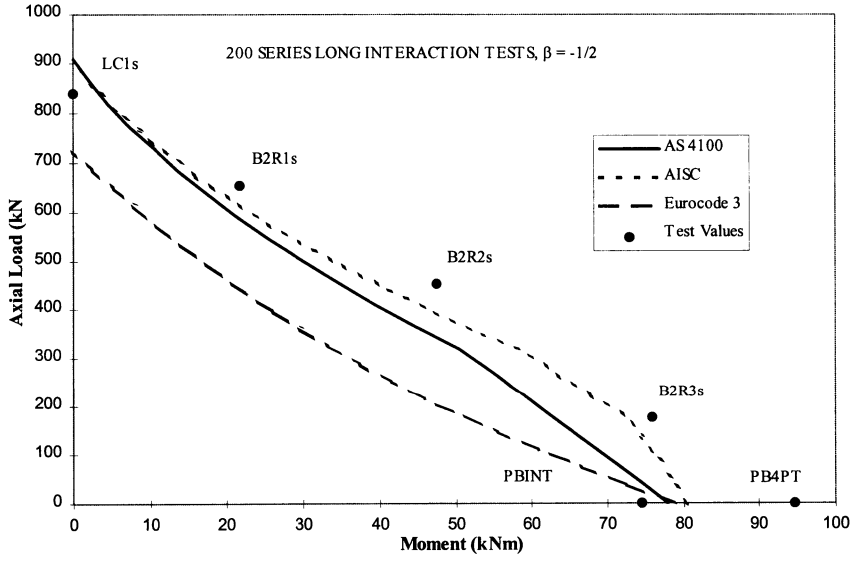

Figure 8. Test results compared with design rules for β = -1/2, non-dimensionalised against code rules.

three design curves are very conservative when viewed in Figure 11. Figure 9 shows much better agreement by all three design curves with the AS 4100 rule being closer to test results in the high moment regions, and the AISC rule being closer in regions of high axial load. The Eurocode 3 rule is again conservative, while in high moment regions the AISC rule is unconservative.

6 CONCLUSIONS

From the interaction and column tests it is clear that the slender sections collapse more suddenly as a

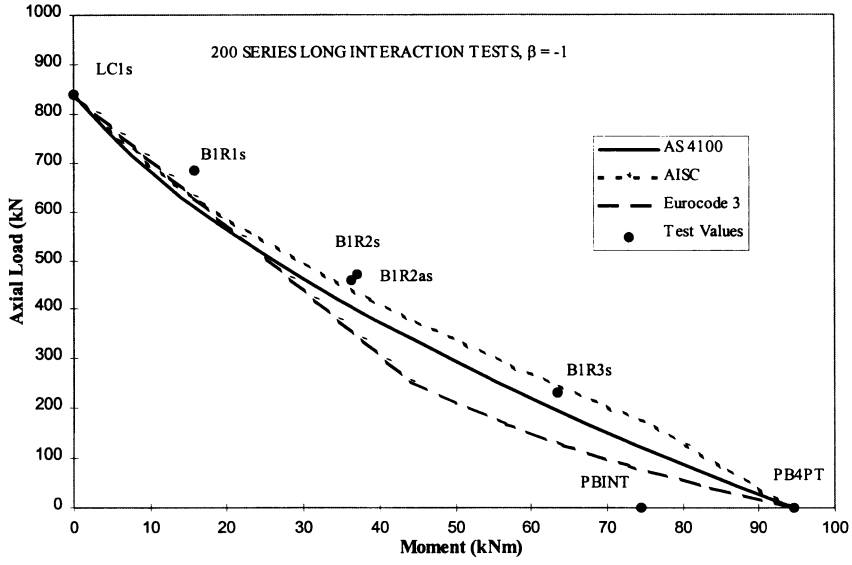

Figure 9. Test results compared with design rules for β = -1, non-dimensionalised against test values for column and bending capacity.

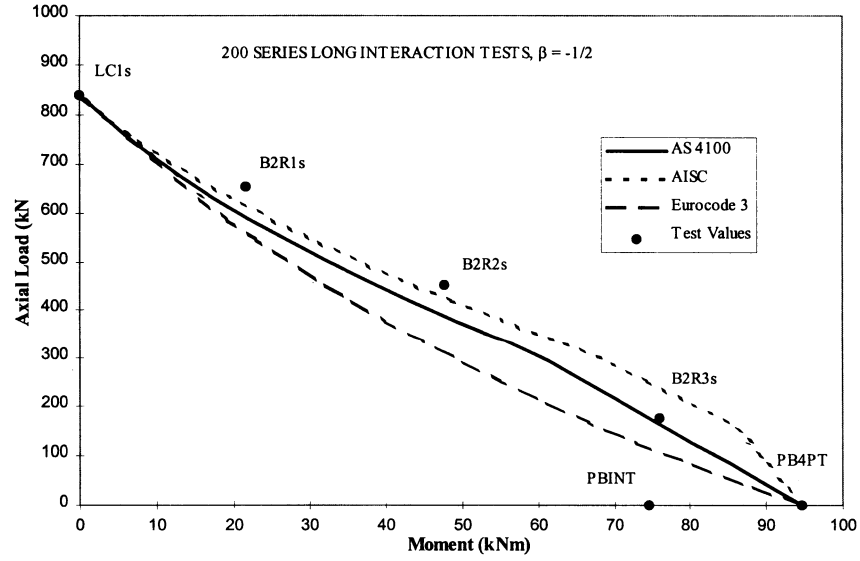

Figure10. Test results compared with design rules for β = -1/2, non-dimesionalised against test values for column and bending capacity.

result of inelastic local buckling than do compact sections. The long yielding plateau and associated high curvatures observed in the compact tests (Sully & Hancock 1996) were not evident for the slender sections.

Local imperfections are more easily formed in the slender sections particularly from the welding of connection components. These local imperfections can have a detrimental effect on the section bending capacity of the member causing premature collapse through local instability. In addition, the tests show that flexibility within connections may also cause premature failure within the section. The possibility of this type of failure

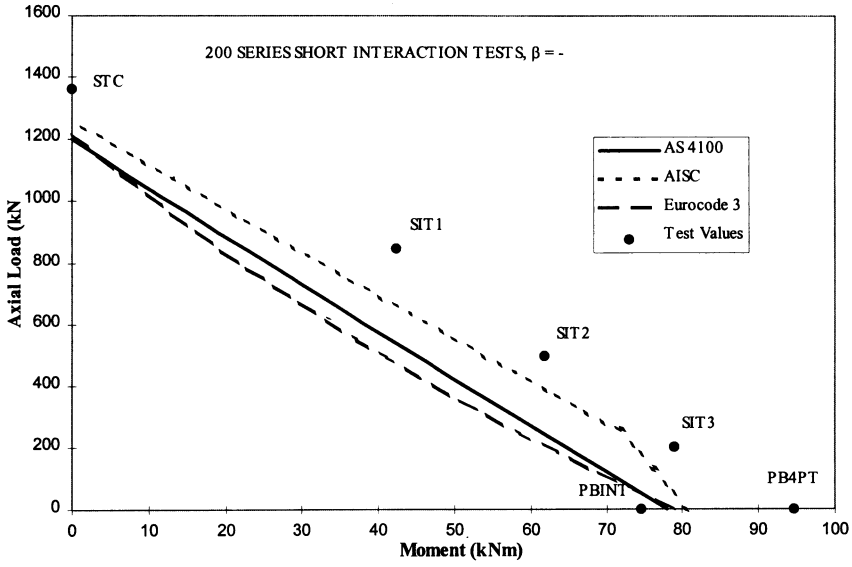

Figure 11. Test results for short interaction tests compared with design rules, for β = -1.

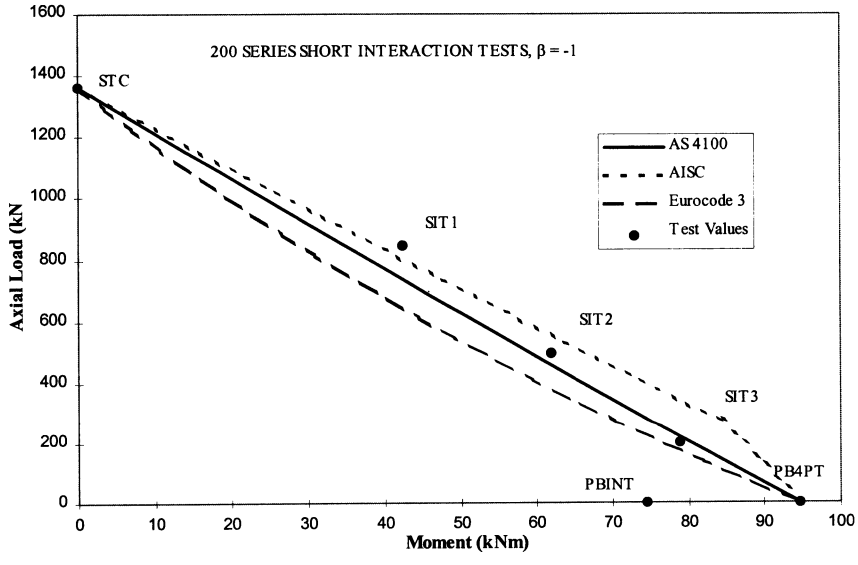

Figure 12. Test results for short interaction tests compared with design rules for β = -1, non-dimensionalised against test values for column and bending capacities.

occurring is of particular concern in structures where maximum moments occur at the member connections, and is the subject of continuing research by the authors at The University of Sydney.

For the long interaction tests with $\beta = -1$, and $\beta = -1/2$, where the maximum load was reached prior to local instability, the current design rules in AS4100 for compact doubly symmetric I-sections are applicable. However this does not preclude the case of more slender sections than those tested which may locally buckle before reaching maximum load. Further investigation is required to determine if the AS4100 interaction rules are appropriate for greater values of β. The short interaction tests indicated that local instability affects the beam-column strength more severely for short length specimens. Again further investigation is required to determine if this is true for other values of β. The bi-linear AISC rule appears to be unconservative in high moment regions of interaction, particularly for the short length slender beam-columns, while the Eurocode 3 rule is very conservative.

7 ACKNOWLEDGEMENTS

The authors wish to thank Tubemakers (Aust) Pty Ltd for the tube sections used in this experimental investigation. The first author also wishes to make known his appreciation for the financial support provided by the J.W. and I.C.M. Roderick Research Bequest and The Centre For Advanced Structural Engineering. Funding for the test rig was provided by the Australian Research Council under a grant entitled "Thin-Walled Structural Members Subject to Combined Compression and Bending"

8 REFERENCES

AISC 1994, Manual of Steel Construction, Load & Resistance Factor Design, American Institute of Steel Construction, Volume 1, Second edition, 1994.

EC3, 1990, Eurocode No.3, Design of Steel Structures, Part 1. Commision of European Communities, Draft issue 5th November.

Key, P.W., Hasan, S.W., and Hancock, G.J. 1988, Column Behaviour of Cold-Formed Hollow Sections, Journal of Structural Engineering, ASCE, Vol 114, No. 2, Feb 1988 pp390-407.

SAA 1995, Steel Structures, Standards Association of Australia, AS4100-1990, Amendment 3.

Sully, R.M., & Hancock, G.J. 1995, behaviour of Cold-Formed Slender SHS Beam-Columns. Research Report R707, School of Civil and Miming Engineering , University of Sydney, September 1995.

Sully, R.M., & Hancock, G.J. 1996, Behaviour of Cold-Formed SHS Beam-Columns. *Journal of Structural Engineering*, ASCE, Vol. 122, No.3, pp326-336.

Frames



Taylor & Francis
Taylor & Francis Group
http://taylorandfrancis.com

Tubular Structures VIII, Choo & Van der Vegte (eds) © 1998 Balkema, Rotterdam, ISBN 90 5809 001 9

Study on out-of-plane rotational stiffness of CHS joints and effective column length of web members in CHS lattice girder

Y. Furukawa & Y. Makino
Department of Architecture and Civil Engineering, Kumamoto University, Japan
Y. Kurobane
Department of Architecture, Kumamoto Institute of Technology, Japan

ABSTRACT: The equations for effective column length of web members in CHS lattice girder are presented in the existing design guidance (CIDECT, AIJ and DNV). In each of these design recommendations, the rotational stiffness equations are based on different experiment / numerical analysis results, causing major differences between the available rotational stiffness equations. Since the out-of-plane rotational stiffness of CHS joints is directly related to the effective column length, this parameter is also largely influenced by the choice of the rotational stiffness equation. The aim of this investigation is to estimate the existing equations regarding the effective column length of web members and devise a more reliable column length formula based on the joint geometrical parameters.

1 COMPARISON BETWEEN EXISTING OUT-OF-PLANE ROTATIONAL STIFFNESS EQUATIONS

1.1 *Existing out-of-plane rotational stiffness equation*

The existing out-of-plane rotational stiffness equations used for calculating the effective column length of web members in CHS lattice girder are as follows.

CIDECT equation (M. Efthymiou 1985)
for T-joints:

$$\frac{K_0}{ED^3} = 0.2875\left(\frac{d}{D}\right)^{2.12}\left(\frac{D}{2T}\right)^{\left[0.7\left(0.55-\frac{d}{D}\right)^2-2.20\right]} \quad (1)$$

for Y, K-joints:

$$\frac{K_0}{ED^3} = 0.2875\left(\frac{d}{D}\right)^{2.12}\left(\frac{D}{2T}\right)^{\left[0.7\left(0.55-\frac{d}{D}\right)^2-2.20\right]} * \sin^{-\left(\frac{d}{D}+1.3\right)}\theta \quad (2)$$

AIJ equation (Sakamoto & Minoshima 1990):

$$\frac{K_0}{ED^3} = 2040\exp\left[\left(2.65\frac{d}{D}-11\right)\left(\frac{D}{T}\right)^{0.15}\right] \quad (3)$$

DNV equation (Det Norske Veritas 1977):

$$\frac{K_0}{ED^3} = 0.0002\left(215-135\frac{d}{D}\right)\left(\frac{2T}{D}-0.02\right)^{2.45-1.6\frac{d}{D}} \quad (4)$$

where

K_0	:	out-of-plane rotational stiffness of CHS joints
E	:	Young's modulus
D	:	chord diameter
d	:	brace diameter
T	:	chord thickness
θ	:	angle between brace and chord

1.2 *Comparison of T-joints stiffness equations*

A parameter study has been carried out to compare the recommended stiffness equations for T-joints. In this study, the validity range of parameters extended as $0.3 \le \beta \le 1.0, 8 \le \gamma \le 30$, although this range exceeds the validity ranges specified in some of the design equations (CIDECT: $0.3 \le \beta \le 0.8$, $10 \le \gamma \le 30$, AIJ: $0.6<\beta<1.0$, $6.3<\gamma<15.6$, DNV: $0.33 \le \beta \le 0.8$, $10<\gamma<30$).
where $\beta=d/D$, $\gamma=D/2T$.

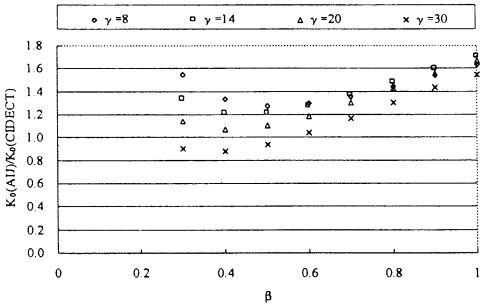

Fig. 1 Comparison between CIDECT and AIJ (parameter : β)

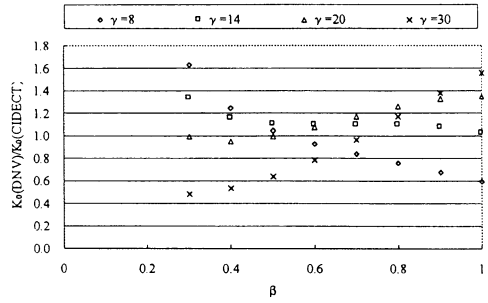

Fig. 2 Comparison between CIDECT and DNV (parameter : β).

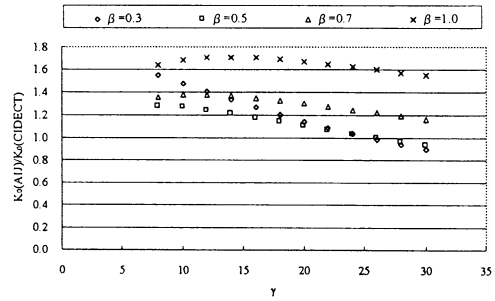

Fig. 3 Comparison between CIDECT and AIJ (parameter : γ).

1.3 *Comparison with available experimental results*

The results of the comparison between the estimated out-of-plane rotational stiffnesses using the existing equations and the test results from the database for tubular joints (Makino et al 1996) are summarized in Table 2 and shown in Figs. 5-10. Further more, the mean values and the standard deviations of test to prediction ratios are shown in Table 2. In Figs. 5-7,

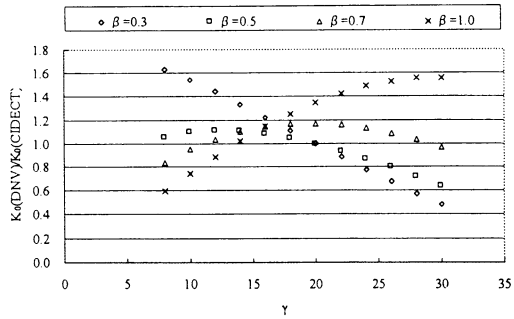

Fig. 4 Comparison between CIDECT and DNV (parameter : γ).

Table 1. Comparison between CIDECT, AIJ and DNV

	AIJ/ CIDECT		DNV/ CIDECT		DNV/ AIJ	
	min	max	min	max	min	max
γ=8	1.28	1.63	0.59	1.63	0.36	1.05
γ=14	1.21	1.71	1.02	1.33	0.60	1.00
γ=20	1.07	1.67	0.95	1.35	0.81	0.90
γ=30	0.88	1.55	0.48	1.56	0.54	1.01
β=0.3	0.90	1.55	0.48	1.63	0.54	1.05
β=0.5	0.94	1.28	0.64	1.11	0.68	0.92
β=0.7	1.16	1.38	0.84	1.17	0.62	0.91
β=1.0	1.55	1.71	0.59	1.56	0.36	1.01
total	0.88	1.71	0.48	1.63	0.36	1.05

the ratios between the test and the estimation of the stiffnesses are shown as a function of β, while in Figs. 8-10, the ratios are shown as a function of γ.

1.4 *Correction factor for K-joints*

In the CIDECT design code, it is recommended to determine the rotational stiffness of K-joints by multiplying the stiffness equation for T-joints by a factor $\sin^{-(\beta+1.3)}\theta$. For examining the influence of correction factor, $\sin^{-(\beta+1.3)}\theta$, a comparison is made

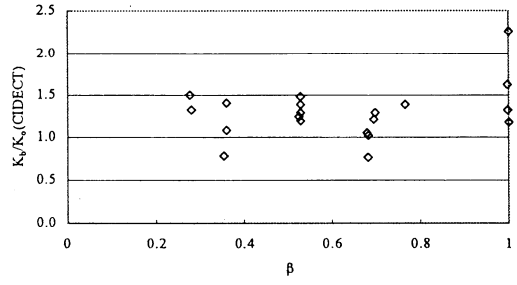

Fig. 5 Comparison between the test results and CIDECT Equation (parameter : β).

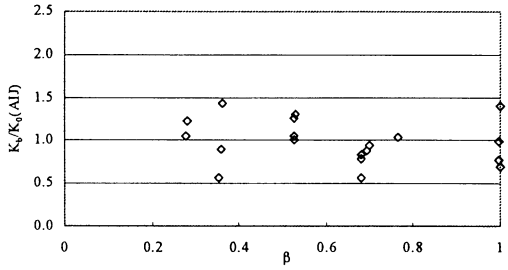

Fig. 6 Comparison between the test results and AIJ Equation (parameter : β).

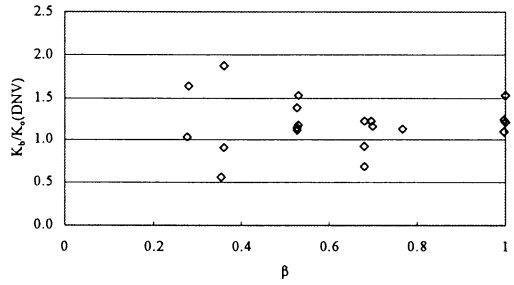

Fig. 7 Comparison between the test results and DNV Equation (parameter : β).

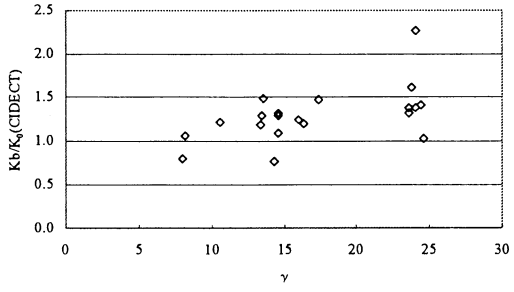

Fig. 8 Comparison between the test results and CIDECT Equation (parameter : γ).

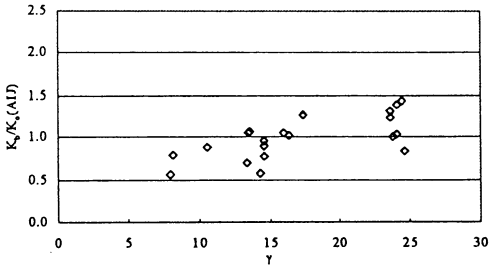

Fig. 9 Comparison between the test results and AIJ Equation (parameter : γ).

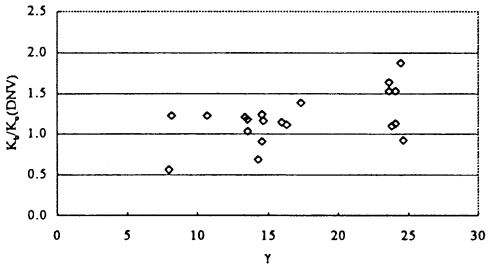

Fig. 10 Comparison between the test results and DNV Equation (parameter : γ).

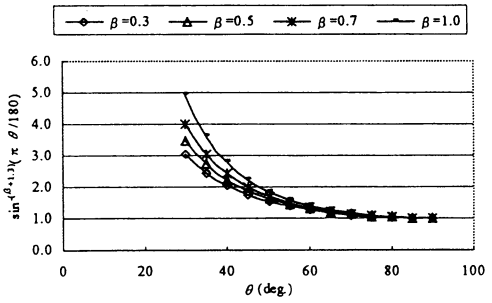

Fig. 11 Correction factor for K-joint.

for $0.3 \le \beta \le 1.0, 30 \le \theta \le 90$. The results are shown in Fig. 11. In the AIJ and the DNV, the rotational stiffness for K-joints is not provided. According to CIDECT correction factor, the rotational stiffness for K-joints with 45 degree brace angle becomes 1.7-2.2 times greater than that for T-joints.

2 EQUATION FOR OUT-OF-PLANE EFFECTIVE COLUMN LENGTH

In Ogawa et al (1988), the following equation is used for calculating the out-of-plane effective column length of web members for CHS lattice girders.

$$\left(\alpha^2 EIs - G_0\right)\left\{K_0 \tan\alpha\left(\frac{l}{2} - s\right) + \alpha EI\right\} - \alpha EIK_0 = 0 \quad (5)$$

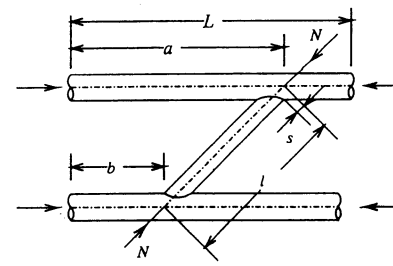

Fig. 12 Examined web member.

Table 2. Comparison between the existing test results and calculated stiffnesses.

No.	D (mm)	T (mm)	d (mm)	β	γ	K_b (kN*m/rad)	K_b/K_0 (CIDECT)	K_b/K_0 (AIJ)	K_b/K_0 (DNV)
TM-1	216.4	4.5	216.4	1	24.04	1954	2.27	1.40	1.52
TM-2	216.5	4.5	165.6	0.765	24.06	478	1.39	1.04	1.13
TM-3	216.3	4.58	114.3	0.528	23.61	205	1.39	1.31	1.52
TM-4	216.3	4.58	60.7	0.281	23.61	60	1.32	1.23	1.63
TM-5	216.5	6.24	114.2	0.527	17.35	429	1.47	1.26	1.38
TM-6	217.8	6.83	114.4	0.525	15.94	441	1.25	1.05	1.15
TM-7	217.3	6.65	114.6	0.527	16.34	402	1.20	1.01	1.11
TM-8	216.5	8.12	216.5	1	13.33	3440	1.18	0.69	1.21
TM-9	216.6	8.02	114.3	0.528	13.50	653	1.29	1.05	1.18
TM-10	216.7	8.01	60.2	0.278	13.53	222	1.50	1.06	1.04
TM-23	168.7	10.55	59.8	0.354	8.00	270	0.78	0.56	0.57
TM-24	168.4	10.28	114.5	0.680	8.19	1320	1.05	0.78	1.22
TM-25	168.3	5.78	60.6	0.360	14.56	104	1.09	0.89	0.92
TM-26	168.3	5.9	114.6	0.681	14.26	286	0.77	0.57	0.69
TM-27	168.6	5.79	168.3	0.998	14.56	1500	1.32	0.77	1.25
TM-28	168.5	3.45	60.8	0.361	24.42	44	1.41	1.43	1.87
TM-29	168.5	3.42	114.7	0.681	24.63	115	1.02	0.84	0.93
TM-30	168.8	3.55	168.3	0.997	23.77	670	1.62	1.00	1.10
TM-42	456.4	15.6	319	0.699	14.63	9709	1.29	0.95	1.16
TM-44	457.1	21.5	317.4	0.694	10.63	17946	1.20	0.88	1.23
mean							1.29	0.99	1.19
S.D.							0.32	0.25	0.30

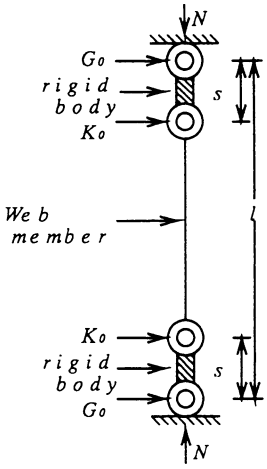

Fig. 13 Analyzed model of web member.

where

- α : $\alpha=\pi/l_k$
- l_k : the out-of-plane effective column length
- E : Young's modulus of web member
- I : geometrical moment of inertia of web member
- s : the length between the center of joint and surface of chord
- G_0 : $G_0=4GI_P/L$
- G : shear modulus
- I_P : polar moment of inertia
- L : the whole chord length
- K_0 : T-joint out-of-plane rotational stiffness
- l : the system length between joints of web member

α is determined by solving the above equation. Hence l_k, the out-of-plane effective column length, is obtained by substituting the value of α in the equation, $l_k=\pi/\alpha(0.5l \le l_k \le l)$. The equation (5) estimates an upper bound value of an effective column length.

3 COMPARISON BETWEEN OUT-OF-PLANE BUCKLING STRENGTHS

3.1 *Influence on out-of-plane effective column length by rotational stiffness equation*

The out-of-plane effective column lengths are calculated using the rotational stiffness equations for T-joints (CIDECT, AIJ and DNV). In a parameter study, the differences between the various equations have been investigated. The range of geometric parameters considered is similar to the range mentioned earlier. The results are shown in Figs. 14-17.

3.2 *Comparison with existing test results*

The results of the comparison between the out-of-plane buckling strength calculated using the various rotational stiffness equations for T-joints and the test

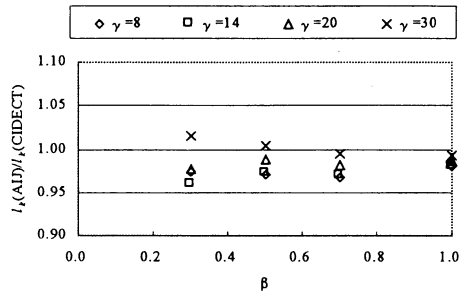

Fig. 14 Comparison of effective column length between CIDECT and AIJ (parameter : β).

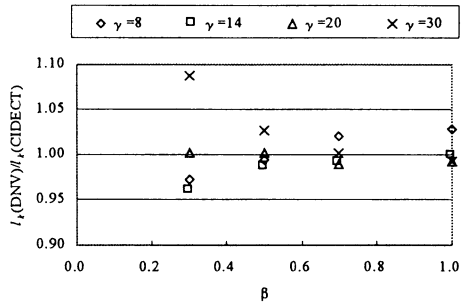

Fig. 15 Comparison of effective column length between CIDECT and DNV (parameter : β).

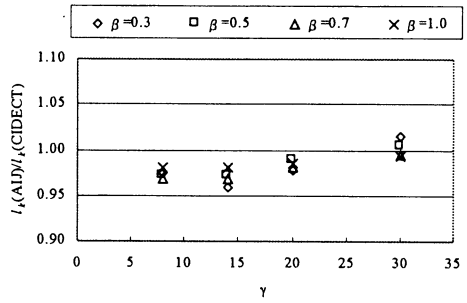

Fig. 16 Comparison of effective column length between CIDECT and AIJ (parameter : γ).

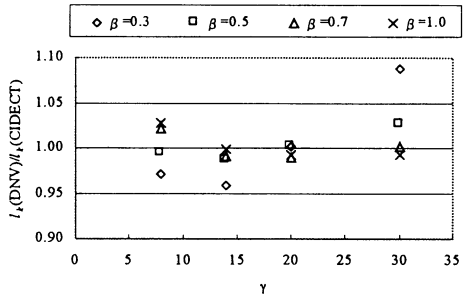

Fig. 17 Comparison of effective column length between CIDECT and DNV (parameter : γ).

results are shown in Table 4. The out-of-plane buckling stresses are calculated using the SSRC Curve 1P, 2P and 3P formulas. The test configuration is roughly shown in Fig. 18, and the details are shown in Ogawa (1988).

3.3 *Comparison between out-of-plane buckling strength using rotational stiffness equations for K-joints and test result*

The correction factor for K-joint stiffness suggested by CIDECT, has been applied to the other equations, AIJ and DNV. The buckling strengths obtained from these equations have been compared with the test results. The results are shown in Table 5.

Table 3. Comparison of effective column length between CIDECT, AIJ and DNV.

	AIJ/ CIDECT		DNV/ CIDECT		DNV/ AIJ	
	min	max	min	max	min	max
γ=8	0.97	0.98	0.97	1.03	1.00	1.05
γ=14	0.96	0.98	0.96	1.00	1.00	1.02
γ=20	0.98	0.99	0.99	1.00	1.01	1.02
γ=30	0.99	1.01	0.99	1.09	1.00	1.07
β=0.3	0.96	1.01	0.96	1.09	1.00	1.07
β=0.5	0.97	1.00	0.99	1.03	1.01	1.02
β=0.7	0.97	0.99	0.99	1.02	1.01	1.05
β=1.0	0.98	0.99	0.99	1.03	1.00	1.05
total	0.96	1.01	0.96	1.09	1.00	1.07

CONCLUSIONS

1. When both β and γ are in the middle of the validity range, the T-joint stiffnesses calculated by CIDECT, AIJ and DNV are almost identical. When β and γ take values in the extreme of the validity range, the stiffness varies more widely with the recommended equation. Of the existing out-of-plane rotational stiffness equations, the AIJ equation gives highest estimations for the stiffness.
2. When β and γ are not in the middle of the validity range, the T-joint stiffness using the existing equation is far from the test results.
3. The out-of-plane effective column length calculated by AIJ and by CIDECT are almost identical when β is in the middle of the validity range and γ close to the upper limit of the validity range.

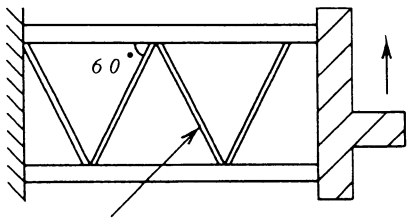

Specimen A-1, A-2, A-3 and B-2

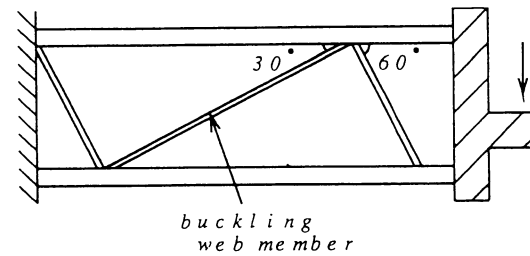

Specimen C-1

Fig. 18 Specimens for tests.

Table 4. Comparison between the calculated out-of-plane buckling strengths and the test results.

specimen	measure length (mm) L	measure height (mm) h	section upper chord (mm) D	section upper chord (mm) T	section lower chord (mm) D	section lower chord (mm) T	buckling web member (mm) d	buckling web member (mm) t	β	γ	yield stress of web member σ_y (kN/mm^2)
A-1	3628	1500	165.57	4.27	165.47	4.29	60.62	2.12	0.37	19.4	0.364
A-2	3628	1500	165.53	5.73	165.52	5.72	60.57	2.18	0.37	14.4	0.364
A-3	3485	1500	165.55	4.28	165.58	4.3	60.58	2.2	0.37	19.3	0.364
B-2	2474	1000	165.42	5.73	165.45	5.74	60.57	2.19	0.37	14.4	0.364
C-1	4247	1500	165.52	3.8	165.52	3.8	76.5	2.54	0.46	21.8	0.349

system length between joints l (mm)	out-of-plane rotational stiffness of joint K_0 (kN*mm) CIDECT	AIJ	DNV	buckling length of web member l_k (mm) CIDECT	AIJ	DNV	slenderness ratio of web member λ_b	λ CIDECT	AIJ	DNV
1732.1	503.7	550.2	493.5	1199.4	1182.3	1203.4	83.7	58.0	57.1	58.1
1732.1	954.0	1162.7	1127.5	1079.8	1045.0	1050.3	83.8	52.3	50.6	50.8
1732.1	505.7	553.1	496.6	1204.5	1187.2	1208.0	83.9	58.3	57.5	58.5
1154.7	954.7	1163.6	1128.3	740.0	715.8	719.5	55.9	35.8	34.7	34.8
3000.1	605.2	634.1	551.2	2166.8	2151.5	2197.2	114.7	82.8	82.2	84.0

max. axial force N_{exp}	SSRC formula N_{exp}/N_u(CIDECT)			N_{exp}/N_u(AIJ)			N_{exp}/N_u(DNV)		
(kN)	1P	2P	3P	1P	2P	3P	1P	2P	3P
118.7	0.947	1.068	1.351	0.942	1.061	1.337	0.949	1.070	1.355
134.4	1.009	1.128	1.387	0.999	1.114	1.359	1.001	1.116	1.363
130.4	1.008	1.137	1.441	1.002	1.129	1.425	1.009	1.139	1.444
141.2	0.986	1.066	1.209	0.983	1.059	1.194	0.983	1.060	1.197
182.4	1.259	1.490	2.051	1.249	1.475	2.035	1.279	1.519	2.082

4. DNV/AIJ ratios for effective column length are almost equal to 1 or bigger, which means that the length recommended by DNV is larger than the value recommended by AIJ.

5. According to the comparison between the experimental values of the buckling strength and the estimated values using the SSRC Curve 1P, 2P and 3P, it becomes clear that the SSRC Curves are below the test results. There are almost no differences in the buckling strength between recommended equations in the range of the test specimens.

6. The correction factor for K-joint stiffness equation suggested by CIDECT gives better accuracy for the buckling strength when the angle of intersection between the chord and brace becomes 30 degree.

Table 5. Comparison between out-of-plane buckling strengths calculated using the existing rotational stiffness equation with correction factor for K-joints and the test results.

specimen	β	γ	N_{exp}/N_u(CIDECT)			N_{exp}/N_u(AIJ)			N_{exp}/N_u(DNV)		
			1P	2P	3P	1P	2P	3P	1P	2P	3P
A-1	0.37	19.4	0.933	1.049	1.313	0.929	1.042	1.299	0.935	1.051	1.315
A-2	0.37	14.4	0.998	1.111	1.353	0.990	1.100	1.330	0.991	1.102	1.333
A-3	0.37	19.3	0.993	1.117	1.399	0.987	1.109	1.385	0.994	1.119	1.402
B-2	0.37	14.4	0.982	1.058	1.192	0.980	1.052	1.178	0.980	1.053	1.180
C-1	0.46	21.8	1.078	1.228	1.669	1.074	1.223	1.657	1.087	1.238	1.694

REFERENCES

AIJ 1990. Recommendations for the Design and Fabrication of Tubular Structures in Steel.

Det Norske Veritas 1977. Rules for the Design, Construction and Inspection of Fixed Offshore Structures.

J. Rondal, K. –G. Wurker, D. Dutta, J. Wardenier & N. Yeomans 1992. Structural Stability of Hollow Section. CIDECT. Verlag TUV Rheinland.

K. Ogawa, Y. Makino, M. Yamanari & Y. Kurobane 1988. Effective Length for Web Members in Tubular Trusses. Transaction of AIJ. (in Japanese)

M. Efthymiou 1985. Local Rotational Stiffness of Unstiffened Tubular Joints. KSEPL Report RKER 85. 199.

Y. Makino, Y. Kurobane, K. Ochi, G. J. van der Vegte & S. R.. Wilmshurst 1996. Database of Test and Numerical Analysis Results for Unstiffened Tubular Joints. IIW Doc. XV-E-96-220, pp1-116, Miskolc, Hungary.



Taylor & Francis
Taylor & Francis Group
http://taylorandfrancis.com

Tubular Structures VIII, Choo & Van der Vegte (eds) © 1998 Balkema, Rotterdam, ISBN 90 5809 001 9

Advanced inelastic analysis for the design of tubular structures

J.Y.R.Liew & L.K.Tang
Department of Civil Engineering, National University of Singapore, Singapore
Y.S.Choo
CAE/CAD/CAM Centre, Faculty of Engineering, National University of Singapore, Singapore

ABSTRACT: This paper describes the methodology of a nonlinear plastic-hinge based program for studying collapse behaviour of tubular space frame structures. One beam-column element is used to model each physical member in the structure and to obtain a realistic representation of material and geometrical nonlinear effects. Material nonlinearity is modelled by yield hinges, which are allowed to form at the element ends and at the mid-length section. Gradual yielding is modelled using a bounding surface theory. Member initial imperfection effects are studied and they are calibrated to fulfil the code's provisions for member capacity checks. A large-span lattice domes is analysed to illustrate the qualities and limitations of the analyses in predicting the ultimate strength behaviour of three-dimensional frameworks.

1 INTRODUCTION

Structural engineers have been exploring various approaches for assessing member and frame stability in the design of tubular structures for decades. Contrasted with hand calculation approaches based on member capacity checks, computer-based advanced analysis considers the interdependent effects between member and frame stability. This paper is primarily to introduce an analysis method that can be used for analysing three-dimensional tubular structures within the context of advanced inelastic analysis. The work is part of the research program to extend the advanced analysis method from two-dimensional frame structures (Chen et al., 1996; Liew et al., 1993) to space frames (Liew et al., 1997).

The contents of the paper are organised as follows. A brief review of the basic theories of the advanced inelastic analysis program is provided in Section 2. Special emphasis is placed on the yield hinge formulation. To allow for gradual plastification effect, the bounding surface theory in force space is used, and two interaction surfaces representing the states of the stress resultants on a cross-section are employed. In Section 3 the effects from "enlarged" initial imperfections are studied and calibrated to fulfil the code's provisions for member capacity checks. The "calibrated" value of initial imperfection is then adopted for the following studies. Advanced plastic hinge analysis is carried out on a compression member in Section 4. This is to demonstrate both the fundamental concept and the basic and advanced features of the program. Finally in Section 5, collapse analysis is carried out on a 50-m span lattice dome. The capability of the advanced analysis program for designing large-scale three-dimensional structures is accordingly illustrated and validated. Meanwhile, the influence of the initial member imperfection upon the structural behaviour is discussed.

2 THEORIES OF THE PLASTIC-HINGE BASED ADVANCE ANALYSIS

2.1 *Element Formulation*

A finite element program, USFOS (1993), developed primarily for analysing offshore structures, is used for studying the collapse behaviour of tubular space frames in this work. The basic philosophy of the program is to use one element per member to model each structural

component and to obtain a realistic representation of nonlinear material and geometric effects. The program non-linear formulation is based on Navier beam theory (plane sections remain plane after deformation). The motion of material is described by an updated Lagangian formulation and referred to a Cartesian co-ordinate system. The stiffness matrix is derived from potential energy consideration.

The beam-column element consists of three transitional and three rotation degrees of freedom at each node. Thus it is strictly applicable for closed section or for other sections in which warping effects have negligible influence on the deformation and strength of the members and the overall framework. The incremental stiffness is obtained by introducing interpolation functions relating general displacements of a material point to the nodal displacements. The elastic stiffness matrices contain the influence of large lateral deformations as the form of stability functions (Hellan, 1995).

2.2 *Plasticity Formulation*

The advanced analysis considers material nonlinear behaviour by introducing yield hinges at the element ends and mid-length sections. If a plastic hinge is formed at the mid-length, the element is divided into two. The mid-length plastic hinge is then modelled as an end hinge at one of the sub-element. Inelastic stiffness properties for the two sub-elements are then determined. The inelastic stiffness properties of the original element are obtained by static condensation of the "extra" node at the mid-span.

Plastic hinges are introduced when the section forces exceed the plasticity criterion. For a thin-walled tubular cross section, neglecting torsion and shear forces, the plastic interaction function is expressed by

$$\Gamma = \cos\left(\frac{\pi}{2}\frac{N}{N_p}\right) - \frac{\sqrt{M_y^2 + M_z^2}}{M_p} = 0 \qquad (1)$$

N, M_y, M_z and N_p, M_{py}, M_{pz} are the applied loads and plastic capacities for axial force and bending moments. $\Gamma = 0$ represents full plastification of the cross section. A state of forces characterised by $\Gamma > 0$ is illegal.

Associated flow rule is assumed, which defines the state of forces moving from one legal plastic state to another plastic state, following the yield surface so that $\Gamma = 0$. The flow rule is given by

$$\Delta v^P = \begin{bmatrix} g_1 & 0 \\ 0 & g_2 \end{bmatrix} \begin{bmatrix} \Delta\lambda_1 \\ \Delta\lambda_2 \end{bmatrix} = G\Delta\lambda \qquad (2)$$

stating that plastic displacement increments are normal to the cross sectional yield surface, Γ, multiplied by a scalar, $\Delta\lambda$. The surface normal g_i is given by

$$g_i^T = \frac{\partial\Gamma}{\partial S_i} = \left[\frac{\partial\Gamma}{\partial N}, \frac{\partial\Gamma}{\partial Q_y}, \frac{\partial\Gamma}{\partial Q_z}, \frac{\partial\Gamma}{\partial M_x}, \frac{\partial\Gamma}{\partial M_y}, \frac{\partial\Gamma}{\partial M_z}\right]_i \qquad (3)$$

and index i refers to beam end 1 and end 2. For an elastic-perfectly-plastic material model, this can be expressed as

$$\Delta\Gamma = \frac{\partial\Gamma}{\partial N}\Delta N + \frac{\partial\Gamma}{\partial Q_y}\Delta Q_y + \frac{\partial\Gamma}{\partial Q_z}\Delta Q_z + \frac{\partial\Gamma}{\partial M_x}\Delta M_x + \frac{\partial\Gamma}{\partial M_y}\Delta M_y + \frac{\partial\Gamma}{\partial M_z}\Delta M_z = g^T\Delta S_i = 0 \qquad (4)$$

2.2.1 *Elastic-Perfectly-Plastic Stiffness Matrix*

The elastic stiffness expression for the beam element is expressed as

$$\Delta S = K_T \Delta v^E \qquad (5)$$

The total displacement increment is separated into elastic and a plastic component

$$\Delta v = \Delta v^E + \Delta v^P \qquad (6)$$

Hence the stiffness equation (Eq. 5) can be expressed as

$$\Delta S = K_T(\Delta v - \Delta v^P) = K_T\Delta v - K_T G\Delta\lambda \qquad (7)$$

Pre-multiplying with G^T, the right-hand side of Eq. 7 takes the form of

$$G^T\Delta S = G^T K_T\Delta v - G^T K_T G\Delta\lambda = 0 \qquad (8)$$

and the plastic increment can be solved as

$$\Delta\lambda = (G^T K_T G)^{-1}(G^T K_T \Delta v) \qquad (9)$$

Substituting $\Delta\lambda$ back into (7), the elastic-perfectly-plastic stiffness equation becomes

$$\begin{aligned}\Delta S &= K_T\Delta v - K_T G\Delta\lambda \\ &= K_T\Delta v - K_T G(G^T K_T G)^{-1} G^T K_T \Delta v \\ &= (K_T - K_T G(G^T K_T G)^{-1} G^T K_T)\Delta v \\ &= K_T^{EP}\Delta v \end{aligned} \qquad (10)$$

2.2.2 *Elasto-Plastic Stiffness Matrix*

The bounding surface theory in force space is adopted to account for gradual plastification effect. Two interaction surfaces representing the state of the

stress resultants on a cross section are employed. The yield surface bounds the region of elastic cross sectional behaviour, while the bounding surface defines the state of full plastification of the cross-section. The bounding surface encloses the cross sectional force state and the yield surface at any stage during the yielding process. To avoid intersection of the surfaces, the yield and bounding surfaces are given the same shape. The yield surface for a tubular cross section is given by

$$\Gamma_y(N,M_x,M_y,M_z,\beta_i,Z_y) = \sqrt{1-m_x^2}\times\cos\left(\frac{\pi}{2}\times\frac{n}{\sqrt{1-m_x^2}}\right)-\sqrt{m_y^2+m_z^2}=0 \qquad (11)$$

where

$$n=\frac{N-\beta_1}{N_pZ_y} \qquad m_x=\frac{M_x-\beta_4}{M_{px}Z_y}$$

$$m_y=\frac{M_y-\beta_5}{M_{py}Z_y} \qquad m_z=\frac{M_z-\beta_6}{M_{pz}Z_y}$$

The bounding surface is defined as

$$\Gamma_b(N,M_x,M_y,M_z,\alpha_i) = \sqrt{1-m_x^2}\times\cos\left(\frac{\pi}{2}\times\frac{n}{\sqrt{1-m_x^2}}\right)-\sqrt{m_y^2+m_z^2}=0 \qquad (12)$$

Where

$$n=\frac{N-\alpha_1}{N_p} \qquad m_x=\frac{M_x-\alpha_4}{M_{px}}$$

$$m_y=\frac{M_y-\alpha_5}{M_{py}} \qquad m_z=\frac{M_z-\alpha_6}{M_{pz}}$$

M_x and M_{px} are the section force and plastic capacity for the torsional moment. α and β are the surface offsets in force space and Z_y is the yield surface size. The value of Z_y is the inverse of the shape factor of the cross-section and it can be shown that Z_y =0.79 for circular cross sections.

Γ_y is the yield function. Γ_y=-1 corresponds to a stress-free cross section, $\Gamma_y < 0$ corresponds to elastic behaviour, and $\Gamma_y = 0$ corresponds to an initial yielding or any subsequent yielding state. Once the yield is reached, it starts to translate so that the current force state remains on the yield surface during subsequent loading.

When the force state just reaches the yield surface, the stiffness should equal to k^e. To obtain a smooth transition between the two, a distance parameter, δ, is introduced. δ is taken as the distance between the current state of forces on the yield surface, S, and the corresponding force state, on the bounding surface, $\bar{S}$. The distance at first yield is denoted δ_{in}, and the hardening moduli are expressed as:

$$k_{ii}^h=\frac{k_{ii}^e}{f_i}\left(c_i+a_i\frac{\delta}{\delta_{in}-\delta}\right) \qquad (13)$$

In the elastic region, the plastic modulus is infinite, i.e. $k^h=\infty$. When the force state has reached the bounding surface, the modulus k^h becomes constant c_i. The plastic hardening parameter c_i and transition parameter a_i are specific for each force component and they may be determined from experiments or numerical calibrations. These parameters are crucial for the inelastic behaviour of the element.

It is again assumed that the increment of element displacements may be decomposed into an elastic and a plastic contribution, $\Delta v = \Delta v_e + \Delta v_p$, and that the total element force increment can be decomposed into a term tangential to the yield surface and a term corresponding to the material hardening: $\Delta S = \Delta\bar{S}_t + \Delta\bar{S}_h$. The refined elastic-plastic element stiffness relationship may then be written as

$$\Delta S=\left[k_e-k_p\right]\Delta v+k_f\Delta\bar{s}_f \qquad (14)$$

where $\Delta\bar{S}_f$ is the incremental consistent load vector.

The plastic reduction matrix k_p, and the load matrix k_f, are given by:

$$k_p=k_eG\left(G^T\left(k_e+k_h\right)G\right)^{-1}G^Tk_ek_f=I-k_eG\left(G^T\left(k_e+k_h\right)G\right)^{-1}G^T$$

I = unity matrix (15)

The two-surface plastic hinge method, which is referred here as the refined plastic hinge analysis, will be illustrated in the numerical examples given later, and the results will be compared with those obtained from the elastic plastic hinge analysis.

2.3 *Load Increment Procedure*

Different load increment sizes may be specified at different stages in the non-linear loading history. The program automatically scales back the increment size based on the following criteria: a) plastic hinges are encounter between the load increment; b) user defined maximum displacement increment is exceeded; c) arc length iterations are exceeded.

If yielding occurs in any cross section, the load step is scaled so that the element forces of that cross section comply 'exactly' with those on the yield surface. To avoid small step length in case of frequent occurrence of yield hinges, a lower limit is specified for the increment for the scaling. In this way, 'exact' scaling to the yield surface is not always possible and several yield hinges may be

inserted during one particular load increment. To control exceedingly large displacement increments for a softening structure, a maximum displacement increment can be specified. A characteristic displacement is calculated as a weighted sum of specified degrees of freedom. At each load increment, the characteristic displacement is limited by a factored characteristic displacement in the initial load step.

The size of the load increment is governed by the Current Stiffness Parameter and by the determinant of the tangential stiffness matrix. The Current Stiffness Parameter at step i is defined by

$$S_p^i = \frac{(\Delta r_1)^T \Delta R_1}{(\Delta \lambda_1)^2} \times \frac{(\Delta \lambda_i)^2}{(\Delta r_i)^T \Delta R_i} \qquad (16)$$

where Δr and ΔR are the incremental displacements and forces. $\Delta\lambda$ is the load increment size (fraction of the external load R) at each load step. The Current Stiffness Parameter is a normalised parameter representing the stiffness of the structure during the deformation. It has an initial value of 1.0. The value increases when the structure stiffens and it decreases when the structure softens. Zero determinants signify a global instability point or a bifurcation point. Negative determinant (one or more negative terms on the stiffness matrix diagonal) represents an unstable structure. The load increment is reversed if S_p changes sign or if the system stiffness matrix has one or more negative pivot elements in the solution step.

3 CALIBRATION OF MEMBER INITIAL IMPERFECTIONS

In order to fulfil the code's provisions for member capacity checks, some calibration works are required to compute the required magnitude and the direction of member initial out-of-straightness based on some defaulted values for plasticity parameters. In the refined plastic hinge analysis, the plasticity parameters comprise the transition parameters (a_1 to a_6) and the hardening parameters (c_1 to c_6) for each force component in addition to the extension of the yield surface from the bounding surface (Z_y). There are in total 13 plasticity variables. Since many combinations of initial imperfections and plasticity parameters may produce the same compression resistance of the member, it is necessary to develop an approach to reach the required values for initial imperfections for ease of design implementation. In this work, all the plasticity parameters are set to be the default values of the program but the magnitude of the member initial out-of-straightness is varied.

A pin-ended column of circular section CHS 244.5mm x 6.3mm with modulus of elasticity 205kN/mm^2 and yield strength 275N/mm^2 is considered for calibration purpose. The length of the column L is varied from 5.0m to 10.0m with 0.25m increment to provide various slenderness ratios. The column is assumed to have initial out-of-straightness with a maximum mid-length deflection of L/1000, L/750 and L/500. The out-of-straightness magnitude is applied at the mid-length about any principle plane. The default values for the transition parameters, a_1 to a_6, are taken as 0.25, while the hardening parameters, c_1 to c_6, are 0.002. The yield surface extension parameter Z_y is 0.79. For each case of the initial imperfection ratios, the limit load of the column is computed and the results are presented in Figure 1 in the form of column strength curves. The Axial load is non-dimensionalised by the ratio of P/P_y, where P_y is the squash load. The slenderness ratio is non-dimensionalised as

$$\bar{\lambda} = \frac{L}{\pi r}\sqrt{\frac{\sigma_y}{E}} \qquad (17)$$

The column strength curve computed based on curve 'a' in Eurocode 3 is also shown in Fig. 1 for comparison. The investigation shows that the refined plastic hinge analysis can predict the Eurocode's column strength within 5% error if the following imperfection magnitudes are adopted:

$\delta_o = L/750$ for $\lambda \le 0.92$
$\delta_o = L/500$ for $\lambda > 0.92$

The above recommendations are conservative for members in space frames in which end restraints are provided by rigid joints. The resistance of a rigid-jointed space frame member to load is characterised by the availability of axial, shear, flexural and torsional restraints at their ends.

4 ANALYSIS OF AN AXIALLY LOADED COLUMN WITH INITIAL IMPERFECTION

Advanced analyses are carried out on a 10 m pin-ended column with tubular cross-section CHS 241x5mm, as shown in Figure 2. The Young's modulus and yield strength are assumed to be 205kN/mm^2 and 330N/mm^2. The non-dimensional reduced slenderness is calculated as 1.46. Hence the

Reduced Slenderness Value	P/P_y as per EC3	Predicted P/P_y values with imperfection ratios equal to			% difference of predicted P/P_y from EC3 for		
		0.002	0.0013	0.001	0.002	0.0013	0.001
0.4661	0.9345	0.860	0.874	0.890	-8.0	-6.5	-4.8
0.5827	0.8964	0.820	0.840	0.852	-8.5	-6.3	-5.0
0.6992	0.8481	0.777	0.810	0.820	-8.4	-4.5	-3.3
0.8158	0.7866	0.732	0.757	0.789	-6.9	-3.8	0.3
0.9323	0.7124	0.672	0.716	0.745	-5.7	0.5	4.6
1.0490	0.6314	0.616	0.655	0.679	-2.4	3.7	7.5
1.1650	0.5522	0.551	0.587	0.610	-0.2	6.3	10.5
1.2820	0.4806	0.492	0.523	0.541	2.4	8.8	12.6
1.3980	0.4187	0.436	0.460	0.474	4.1	9.9	13.2

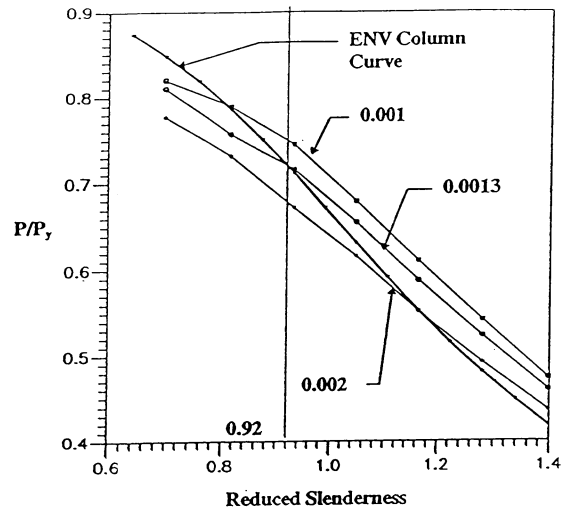

Fig. 1 Comparison of column curves with Eurocode 3

initial out-of-straightness magnitude at the mid-length is taken as L/500, in according with the recommendation given in Section 3. The column is analysed using the refined plastic hinge analysis, and the results are presented in axial-load versus axial displacement curves as shown in Figure 2.

The analysis shows that first yield takes place at the mid-span when the compression load reaches 489kN and the overall buckling occurs at 491kN. After the maximum load is reached, the axial displacement of the load-imposed end keeps increasing when the column is unloaded. The results are compared with those obtained from the elastic-perfectly-plastic hinge analysis. The maximum load obtained is 500kN, which is 2% higher than that from the refined elastic-plastic hinge analysis. The buckling resistance predicted by the Eurocode 3 is 479kN, which is 2.5% lower than the limiting value predicted by the refined plastic hinge analysis.

Figure 3 shows the axial force-bending moment interaction at the mid-length cross section. The gradual plastification occuring from the yield surface towards the bounding surface can be seen. This is in contrast with the more abrupt plastification effect from the elastic-perfectly-plastic analysis.

5 ANALYSIS OF A LATTICE DOME

A 50-meter span single-layer lattice dome, as shown in Fig 4, is considered in the present work to investigate the collapse behaviour of 3-D tubular structure. The height to span ratio of the dome is 1:5 and all members are circular hollow section CHS 180 x 5mm. The Young's modulus and yield strength are assumed to be 205kN/mm^2 and 375N/mm^2. The boundary nodes of the dome are simply supported and all members are rigidly connected to each other. The dome is subjected to concentrated vertical loads of 386.51kN applied at

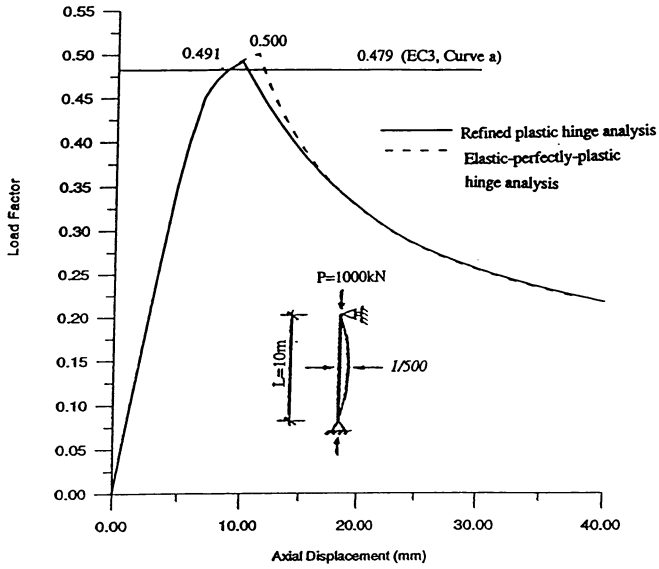

Fig. 2 Load displacement curves of an axially loaded column

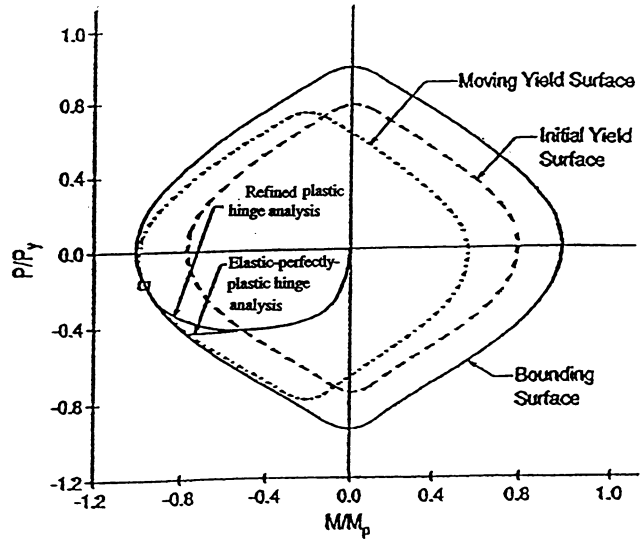

Fig. 3 Axial force and moment interaction at the midspan cross-section of the column

the node points. Horizontal load combinations have also been included in the analyses by they are found to be less critical in comparison with the gravity load combination.

Figure 5 shows the vertical load-deflection curves of three nodes at the region where the maximum deflection takes place at collapse. The positions of these three nodes are shown in Figure 4. Load-displacement analysis shows that first yield occurs at a load ratio of 0.540. The maximum resistance of the dome is reached when one of the member buckles at a load ratio of 0.608. Figure 6 shows the deformed mode of the dome at the limit load point.

Analysis is also carried on the same structure,

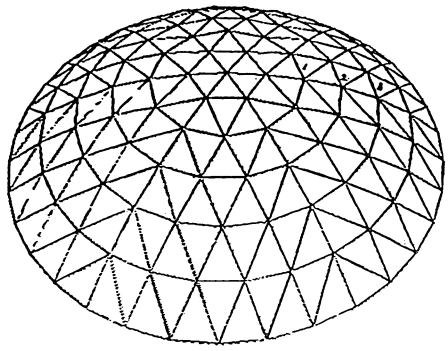

Fig. 4 Initial geometry of a 50-meter span lattice dome

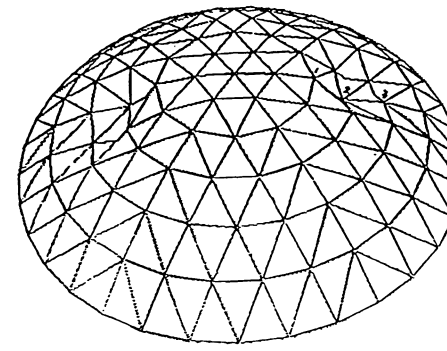

Fig. 6 Deformed shape of the lattice dome at ultimate load

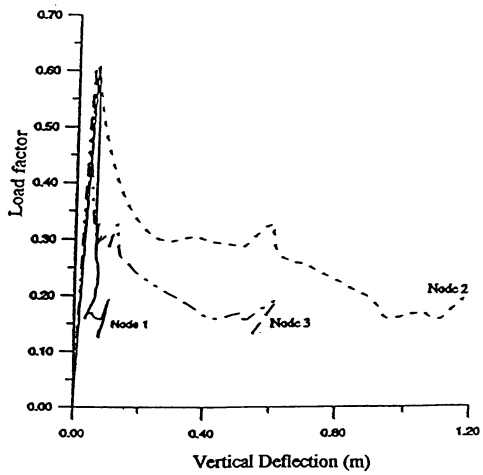

Fig. 5 Vertical load-deflection curve of the lattice dome

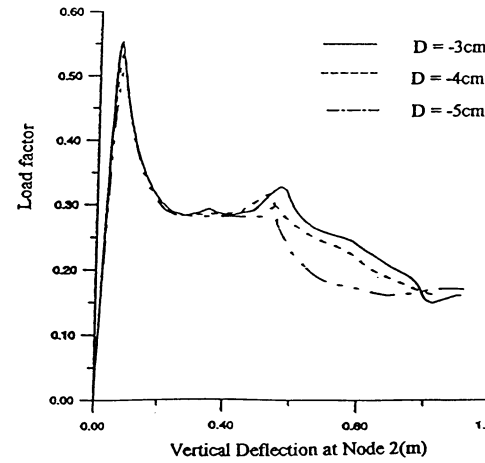

Fig. 7 Vertical load-displacement curves of lattice dome with different magnitude of geometric imperfections

assuming that the Z co-ordination of Node 2 is 3 cm, 4 cm or 5 cm lower than its idealised position. This might happen because of the construction error, and the percentage error in term of the deviated deflection with respect to the total height of the node is less than 0.64%. Such construction error is considered to be stringent, but it was discovered from the refined plastic hinge analysis that the capacity of the dome decreases to 0.553, 0.535 and 0.514 respectively, as shown in Figure 7. These represent a decrease in capacity of 9.0%, 12.0% and 15.5% as compared with the frame with idealised geometry. Hence in the design and analysis of such lattice dome, the effect of overall geometric imperfection due to the possible construction error on the ultimate load is rather significant and cannot be ignored. Further studies are required to quantify the effects of imperfection magnitudes and directions for the design of dome structures.

6 CONCLUSIONS

The basic philosophy of the refined elastic-plastic hinge analysis program is presented, focusing on the beam-column formulation and the plasticity models. The program is also calibrated to fulfil the code's provisions for member capacity check. The analysis

has been applied to study the behaviour of a large-span lattice dome. It is illustrated that the practical and reliable tools are available for static collapse analysis of tubular structures. It is possible to determine system collapse strength accurately with careful consideration of member and system imperfection effects. This is in line with the modern design codes such as Eurocode 3, which allows the use of advanced analysis for designing steel structures.

For slender structures such as the large-span lattice dome, the limit state of system collapse coincides with the limit-state for first member failure, and the global limit load is sensitive to the initial geometrical imperfection of the nodes. The analysis of other three-dimensional braced frame (not reported n this paper) shows that the evaluation of strength limit-state based on 3-D system's limit load will be less conservative compared with the conventional approach based on 2-D limit load analysis. Design economy can be realised if the inelastic reserved strength built into the 3-D system can be assessed through inelastic analysis. Further studies also show that the capacity enhancement from 3-D analysis over 2-D's is significant for the braced frame example. However, the effects of member initial imperfection on the system strength are not as noticeable as those on the slender dome structure. The resistance of the lattice dome decreases dramatically due to the possible construction error and global geometric imperfections, which require careful consideration in either analysis or design work.

7 REFERENCES

Chen W F, Goto Y and Liew J Y R (1996) *Stability Design of Semi-rigid Frames*, John Wiley& Sons, N.Y., 468pp.

Eurocode 3 *: Design of steel structures, Part 1.1:General Rules and Rules for Buildings,* DD ENV 1993-1-1:(1992).

Hellan, O (1995) *Nonlinear pushover and cyclic analysis in ultimate limit state design and reassessment of tubular steel offshore structures*, PhD thesis, Div. of Marine Structures, The Norwegian Institute of Technology.

Liew, J.Y.R., White, D.W. and Chen, W.F. (1993) Second-order refined plastic hinge analysis for frame design: Parts 1&2, *J. Structural Engineering, ASCE* 119(11), 3196-3237.

Liew, J Y R and Tang, L K (1997a), *Advanced Analysis of Space Frame Systems*, International Symposium on Shell and Spatial Structures, International Association of Shell and Spatial Structures, 10-14 November, 1997, Singapore.

Liew J.Y.R., Punniyakotty, N.M. and Shanmugam, N.E. (1997b), Advanced analysis and design of spatial structures, *J constructional Steel research*, Vol. 42, No. 1, Elsevier Science, pp 21-48..

Punniyakotty, N.M. (1998), Nonlinear analysis and design of spatial-truss ad flexible structures, Ph.D thesis, National University of Singapore, Dept. of Civil Engineering.

USFOS, (1993), *A Computer Program for Progressive Collapse Analysis of Steel Offshore Structures*, SINTEF, The Foundation for Scientific and Industrial Research, Norwegian Institute of Technology, Trondheim, Norway.

Tubular Structures VIII, Choo & Van der Vegte (eds) © 1998 Balkema, Rotterdam, ISBN 90 5809 001 9

The elastic buckling behaviour of cellular columns

S.J.Wilkinson & K.Roodbaraky
The Nottingham Trent University, UK

G.Davies
The University of Nottingham, UK

ABSTRACT: The elastic critical failure load of a cellular column is not obtainable directly from classical structural theory because of its inherent cross-section non-uniformity. In the past the load capacities for cellular or castellated columns have generally been obtained from rigorous empirical laboratory testing procedures. The finite element method (FEM) provided a technique that was able to efficiently model the complex structural behaviour of this type of non-uniform section. Initially such investigations were calibrated by modelling a standard universal column (UC) section, with further detailed investigations based on a modified UC section with twin symmetrical webs. A parametric study was undertaken for a range of hole diameters and pitch spacings. From an evaluation of the critical load capacities, it was possible to calculate the effective section properties of a specific cellular column. Additional investigations showed that the calculated effective section properties were independent of the overall section length.

Notation.

P_{cr}	Euler critical load for elastic failure.
P	initial load on structure.
EI	flexural rigidity of section.
L_e	effective length of section.
K	linear or elastic stiffness matrix.
$\mathbf{K_G}$	non-linear or geometric stiffness matrix.
λ_E	scaling factor or Eigenvalue
λ	slenderness ratio
ϕ	eigenvector, the evaluation of failure mode.
FE(M)	finite element, finite element method.
UC	Universal column section

1 INTRODUCTION

The classical theory of Euler (1759) provides an exact solution for the critical failure load for a number of simple flexural buckling problems involving columns of uniform cross-section.

The elastic failure load of a pin-ended slender column, is given by:

$$P_{cr}=\frac{\pi^2 EI}{L_e^2} \qquad (1.1)$$

However, exact solutions for many problems, particularly for sections of non-uniform cross-section are not available. It is for this reason that a number of approximate numerical techniques were developed. Early techniques presented by Rayleigh (1945), Ritz (1909), Timoshenko (1961), Galerkin (1915) and the modifications to these methods by Thomson (1950), Schmidt (1982), and Bert (1984), are generally based on the assumption that the deformed shape of the structure may be determined from a set of predetermined displacement functions. These numerical techniques effectively replace the real structure with its infinite number of degrees of freedom with an idealised structure that is constrained to behave within the bounds of its prescribed displacement function.

The idealisation of a structure in this way forms the basis of another numerical approximation, the finite element method (FEM), in which a continuous structure is replaced with an assemblage of discrete elements. This method of analysis allows the behaviour of the structure to be fully represented by the displacement of the interconnected element nodes.

2 THE CELLULAR COLUMN

The buckling behaviour of specific cellular type sections was of interest to Mabey Hire Limited, a manufacturer and supplier of temporary works systems.

One of their products, the System 160 soldier may be categorised as cellular, and although originally

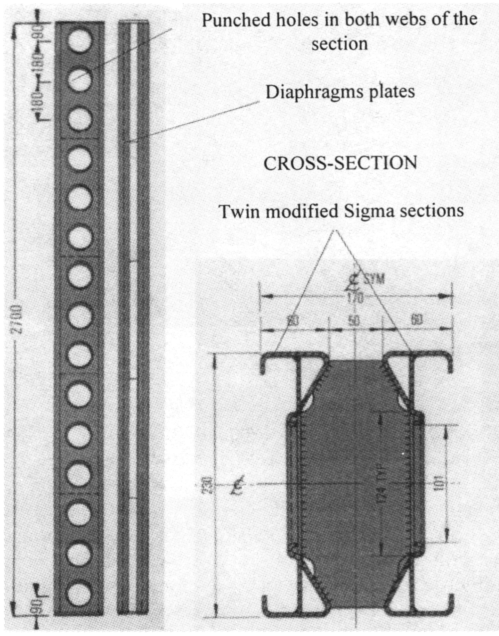

All Dimensions in mm.

Figure 1. Typical System 160 soldier section.

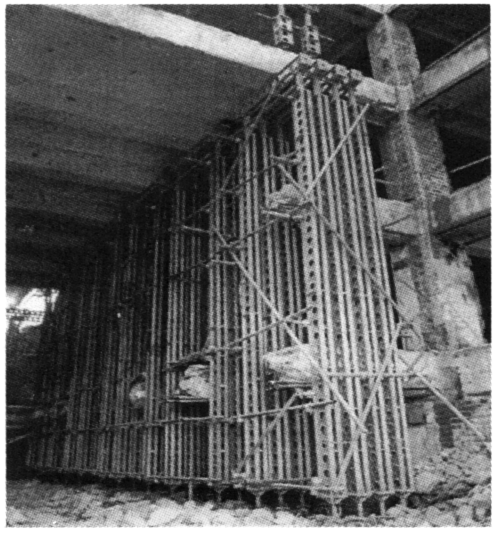

Figure 2. Soldier section used in prop application.

designed for general use as a beam in concrete formwork schemes, it has been increasingly used in prop or column applications.

The inherent cross-section non-uniformity of the cellular column prevents the elastic critical load of the section being calculated from classical theory and must be obtained from the approximate techniques outlined above . The structural form of the cellular column with its multiple variation in cross-sectional area is ideal for the application of FEM because of its ability to solve for the large number of unknowns required in the problem formulation.

2.1 The finite element software package

The cellular sections were analysed by the eigenvalue extraction method incorporated into the LUSAS finite element package.

The use of the eigenvalue extraction method to solve stability problems involves the formation of a incremental procedure typically reserved for the solution of non-linear structural problems. However, the equations for linear buckling theory are formulated as a special case.

The assumptions made in this form of analysis are that the elastic stiffness matrix, which is calculated from the geometry and section properties of the structure does not change prior to buckling and the geometric or non-linear stiffness matrix, which for linear buckling analysis is calculated from the effects of high axial load, is simply a multiple of its initial value. In addition, the pre-collapse displacements are considered to be small and therefore have a negligible influence on the structural behaviour of the section.

As the structure reaches the point of collapse, small incremental increases in load result in relatively large displacements and a significant reduction in stiffness. At failure, the structure will have zero stiffness, which is represented numerically by the structure stiffness matrix being singular:

$$\det (\mathbf{K} + \lambda_E \mathbf{K_G}) = 0 \qquad (2.1)$$

or

$$(\mathbf{K} + \lambda_E \mathbf{K_G})\phi = 0 \qquad (2.2)$$

and the buckling load may be given by:

$$P_{cr} = \lambda_E P \qquad (2.3)$$

The subspace iteration method within LUSAS was used to evaluate the lowest eigenvalue and its corresponding eigenvector. This gave the collapse load and first mode of failure for each model.

2.2 The finite element model

The main aim of the study was to formulate a general understanding of the structural behaviour of this type of cellular section. The behaviour of the soldier sections shown in Figures 1-2 are influenced

not only by the change in cross-sectional area due to their cellular form, but also by the effects of composite action between the two sigma sections. Therefore, this initial study considered the buckling behaviour of a standard universal column (UC) and a modified UC section. These sections were geometrically similar to the soldier section, but eliminated the influence of composite action. The UC section would also provide a more general pattern of structural behaviour because the soldier geometry was specific only to the Mabey soldier.

The three dimensional shell group of elements were the most suited to model this type of section because of their ability to represent the required geometric form. Of the family of shell elements, the quadratic eight noded thick and thin shells were used initially. Both types of element can accommodate generally curved geometry with varying thickness, anisotropic material properties, and element formulations are able to account for both membrane and flexural deformation.

The differences in the two element types lie in the ability to model shear deformation and the element restraint condition at the nodes.

The semi-loof thin shell (after Irons, 1976) excludes the effects of shear deformation from its formulation and the degrees of freedom at the nodes are the three orthogonal translations U, V, & W, and the two mid-side semi-loof rotations θ_1 & θ_2.

The thick shell element does accommodate shear deformation in its formulation, and the degrees of freedom are the three orthogonal translations U, V, & W, and the orthogonal rotations θ_U, θ_V & θ_W.

2.3 Validity of the solutions

A comparative study of the elastic critical load of the cellular sections modelled by FE could not be obtained directly because of the absence of appropriate literature. However, a range of sections were analysed with a solid uniform cross-section to enable comparisons with Euler to be made.

3 PRELIMINARY INVESTIGATIONS

3.1 Convergence test

In order to acquire a sufficient degree of confidence in the accuracy and performance of the method, a simple convergence test was performed by the FE model using the geometry of a suitable UC section.

A 254 x 254 x 107 kg/m UC section, 6000mm in length was chosen because its section geometry in regard to both the flange and web thickness' ensured local elastic buckling effects could be ignored.

An identical model was analysed for fifteen runs, with the number of elements varied from 60 up to 480. Translational nodal restraints in the three orthogonal directions were applied along the minor axis at the column base, and in two directions at the column head, allowing the column to displace vertically. No rotational restraints were applied, effectively pinning the two ends of the column.

Figure 4 shows that both element types converge to within 1% of the Euler solution, and that the thick shell element models produce a closer degree of convergence, with a difference of only 0.6%. Convergence using thick shell was also achieved with a significantly smaller number of elements.

As a result of the thick shell's enhanced performance, this element type was used to model all the cellular sections.

3.2 The Twin web model

Once confidence in the FE model was achieved, it was possible to approach the analysis of the cellular column.

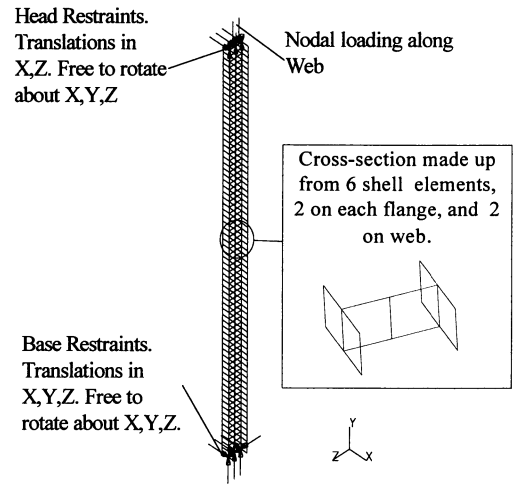

Figure 3. The 408 element Universal Column model.

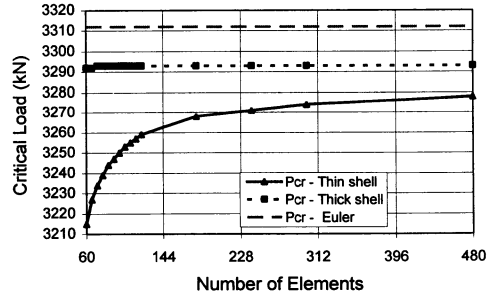

Figure 4. Convergence Test for Shell Elements.

The initial tests for convergence were undertaken using the geometry of a standard UC section. The web cellularisation of this type of section would have a negligible effect on its elastic buckling strength because of the webs geometric position on minor neutral axis.

To enable an effective study of the effects of web cellularisation, a modification to the standard UC section was introduced. An identical second web was incorporated into the model with both webs positioned symmetrically at a specific spacing from the minor neutral axis.

Initially the relationship between the spacing of the twinwebs and critical load capacity was investigated using a solid web section and a cellular section with a 160mm hole diameter and a pitch along the web of 200mm. This gave a quadratic relationship associated directly with the parallel axis theorem, and therefore it was unnecessary to continue the investigation into the effects of web spacing on the buckling strength of the section.

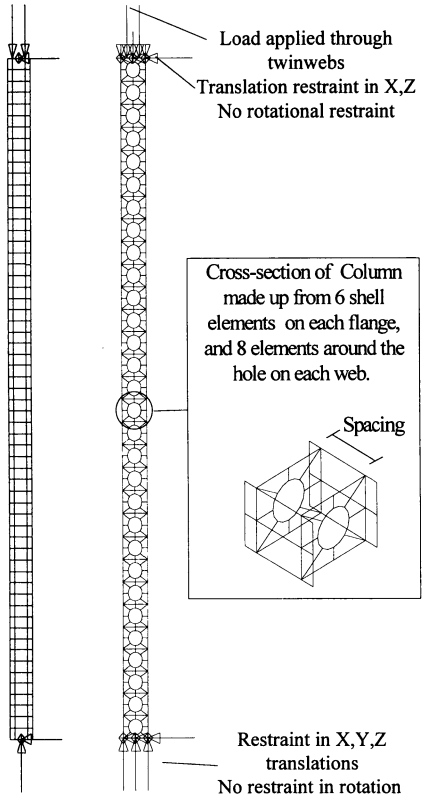

Figure 5. The Twinweb model

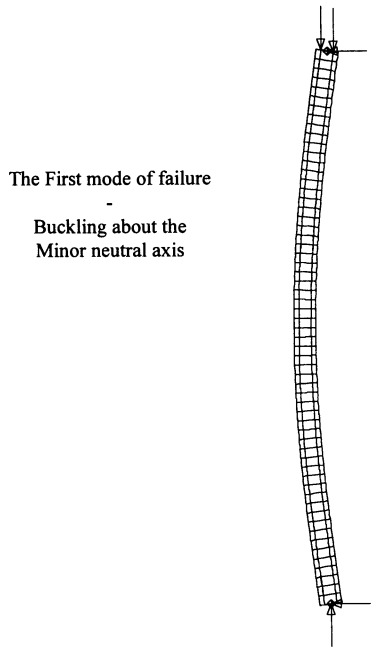

Figure 6. The first failure mode of Twinweb model.

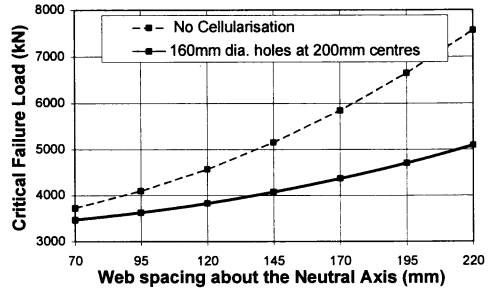

Figure 7. Variation to twinweb spacing

4. THE DETAILED STUDY.

The modified UC section was analysed for a number of hole diameters, pitch spacings and three selected web spacings. In addition, a solid web section was analysed to provide a benchmark for the effects of cellularisation and to provide a check with Euler.

The reduction in critical load capacity is presented in figure 8. At a twinweb spacing of 70mm, the section capacity was reduced by a maximum of only 7%. The twinweb spaced at 220mm had a more marked reduction in capacity of 33%.

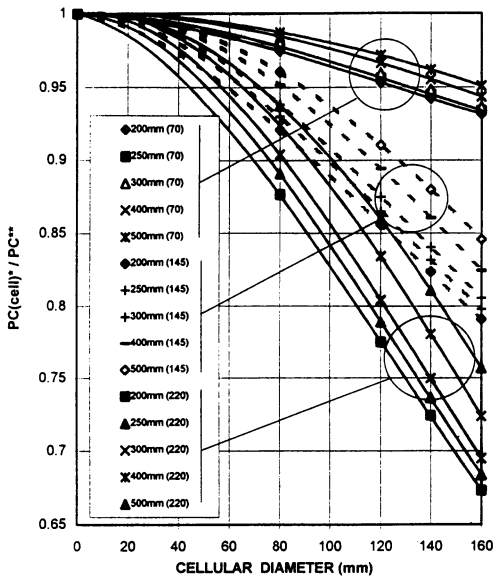

*Critical load for a cellular section.
**Critical load for equivalent solid web section.

Figure 8. Reduction in Critical load capacity.

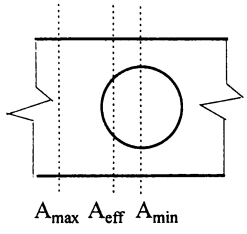

Figure 9. Effective Cross-section

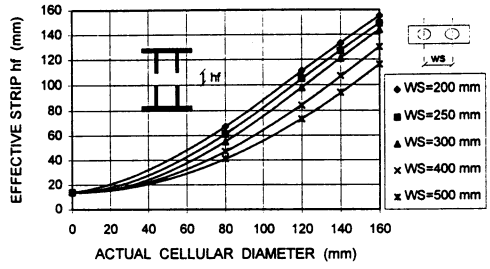

(a) Twinweb spacing 70mm.

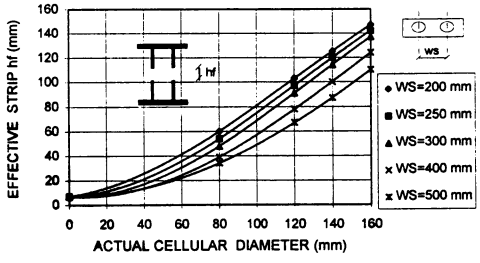

(b) Twinweb spacing 145mm.

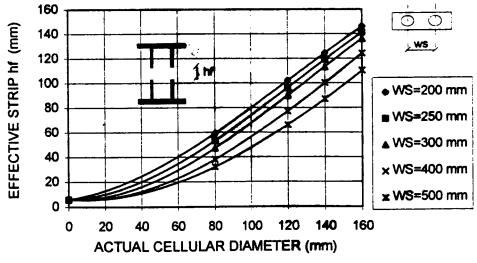

(c) Twinweb spacing 220mm.

Figure 10. Effective Cross-section area.

The FE results enable the calculation of the effective second moment of area I_{eff}, for a specific cellular section. It would be of great benefit for the purposes of design to be able to compute the other section properties, the effective cross-sectional area A_{eff}, and the effective radius of gyration r_{eff}.

Considering figure 9, the effective cross-sectional area of the cellular section would lie at a position between the maximum and minimum area of the section.

By relating the reduction in critical load to the apparent change in cross-sectional area from the solid web to the cellular web, it was possible to calculate this reduction in area. Furthermore, it was possible to convert a cellular section with specific hole diameter and pitch spacing to a corresponding uniform cross section with a central missing strip in both webs of the section. This conversion to an effective uniform cross-sectional area with an effective central missing strip is presented in figure 10.

The accuracy of the effective area calculation may be quantified by considering the 'zero errors' shown in figure 10.

The effective area has been calculated from the combination of the FE results and the section geometric properties. Consider the variation between Euler and the FE results for the solid web model, 0.7 to 1.4% for the 70mm and 220mm twinweb sections respectively. These differences are responsible for the presence of the zero errors, and the accuracy of the calculations must therefore be taken in this context.

Table 1. Errors in effective Strip calculation.

	Error in depth of strip calculation (mm)		
Variation in Critical Load Euler - FE (%)	70mm web	145mm web	220mm web
0.5	10.4	3.4	2.2
1.0	20.8	6.8	4.3
1.5	31.2	10.2	6.6

5. THE EFFECTS OF SECTION LENGTH

The section properties obtained were for one specific 6000mm length of section. It was necessary to investigate whether these properties were unique for any length of section, and consequently independent of length.

The effect of overall section length was investigated using the 220mm twinweb model, two cellular diameters, pitch spacings, and two additional section lengths of 12000mm and 18000mm.

Considering the results presented in tables 2 &3. For a range of column lengths, with approximate slenderness ratio's between 70 and 200, the effective second moment of area calculated from the FE results varied by less than 1%. It is therefore valid to suggest that the effective second moment of area of this type of cellular section with a particular hole diameter and pitch is independent of overall length.

6. CONCLUSIONS

This study has shown that the finite element method can readily be adopted to solve difficult elastic stability problems involving complex sections of non-uniform cross-section.

A standard UC section was modelled and convergence was achieved to within 1% of the Euler solution. In addition, the uniform solid twinweb section converged to within 1.4% of Euler.

The cellular twinweb section was successfully analysed and the effective section properties for each model were obtained. The inherent non-uniform cross-section of the cellular column could be transformed into an equivalent uniform section with a missing central strip in the two symmetrical webs.

The section properties calculated for a particular pitch and hole diameter were independent of length.

The web slenderness ratio for a number of sections analysed in this parametric study indicate that localised plastic buckling in the web hole region would occur before the elastic failure load was reached. If the true buckling capacities of these sections were required, then the effects of geometric and material non-linearities would need to be investigated, and refinements to the FE model undertaken. However, this study was purely concerned with the calculation of the theoretical elastic buckling load from which the effective section properties could be quantified. Therefore, although these loads are purely theoretical, they are valid for this application.

Table 2. Benchmark for Solid web sections.

Section Length mm	Euler Load kN	FE Load kN	Variation %
6000*	7667	7563	1.4
12000*	1917	1910	0.4
18000*	852	851	0.1

*The Slenderness ratio of solid web sections: $\lambda_{6000} = 67$, $\lambda_{12000} = 134$, $\lambda_{18000} = 201$.

Table 3. Variation in Section properties for sections with twinweb spacing of 220mm.

Section Length mm	Hole Dia. mm	Pitch mm	FE Load kN	$I_{effective}$ $10^7 mm^4$	Variation %
6000	120	200	5861	10.428	--
12000	120	200	1477	10.509	0.8*
18000	120	200	657	10.523	0.9*
6000	160	200	5090	9.056	--
12000	160	200	1281	9.116	0.7*
18000	160	200	570	9.128	0.8*
6000	120	300	6082	10.821	--
12000	120	300	1533	10.909	0.8*
18000	120	300	682	10.925	0.9*
6000	160	300	5256	9.352	--
12000	160	300	1323	9.418	0.7*
18000	160	300	589	9.430	0.8*

*Variation between I_{eff} for 6000mm length and the value for the new lengths.

ACKNOWLEDGEMENTS

The authors wish to thank Mabey Hire Limited for their support of this work.

REFERENCES

Bathe, K.J. 1982. *Finite element procedures in engineering analysis*. London : Prentice-Hall International Inc.

Bert, C.W. 1984. Improved technique for estimating buckling loads. *Journal of Engineering Mechanics, ASCE.* 110(12): 1655-1665.

Euler, L. 1744. *De Curvis elasticis*: Lausanne and Geneva.
Euler, L. 1759. *Sur la force de colonnes' memoires de l'Academie de Berlin.*
Finite Element Analysis Limited. 1997. *The Lusas finite element system.* Kingston upon Thames, Surrey, United Kingdom.
Galerkin, B.G. 1915. Series solutions of some problems of elastic equilibrium of rods and plates. *Vestnik Inzhenerov.* 1: 879-908.
Irons, B.M. 1976. The Semiloof shell element. *Finite elements for thin shells and curved members.* London: Wiley.
Rayleigh. 1945. *The theory of sound.* (2nd Ed) Vol.1&2. New York: Dover.
Ritz,W. 1909. Uber eine neue methode zur Losung gewisser Variations- probleme der mathematischen Physik. *J fur reine und angewandte Mathematik.* 135: 1-61.
Schmidt, R. 1982. Estimation of Buckling loads and other Eigenvalues via a Modification of the Rayleigh -Ritz Method. *Journal of Applied Mechanics.* 49: 639-640.
Strutt, J.W. 1870. On the theory of resonance. *Trans. Roy. Soc.* A161: 77-118. London
Thomson, W.T. 1950. Critical load of columns of varying cross-sections. *Journal of Applied Mechanics.*17:132-134.
Timoshenko, S.P & Gere, J.M. 1961. *Theory of elastic stability* (2nd ed.) New York: McGraw-Hill.



Taylor & Francis
Taylor & Francis Group
http://taylorandfrancis.com

Tubular Structures VIII, Choo & Van der Vegte (eds) © 1998 Balkema, Rotterdam, ISBN 90 5809 001 9

Optimum design of a statically indeterminate tubular truss

J. Farkas & K. Jármai
University of Miskolc, Hungary

ABSTRACT: The minimum weight design of a two-span truss is treated. The truss is welded from square hollow section rods and the height at the middle support is linearly increased. The cross-sectional areas of all chords are the same and two different cross-sectional areas are considered for bracing, since the bracing forces near the middle support are higher than those in other parts. Thus, in the optimization procedure three cross-sectional areas and two factors for height are sought, which minimize the structural volume and fulfil the stress and buckling constraints. For the calculation of the flexural buckling strength of compression members closed formulae are applied, which can be derived from the buckling curves of the Japanese Road Association. First the cross-sectional areas are calculated using an iterative process for constant height factors, then these factors are varied. Finally the strength of overlapped nodes are checked according to CIDECT design formulae. The illustrative numerical example shows that the optimum truss geometry depends on the number of different cross-sectional areas.

1 INTRODUCTION

Tubular trusses are widely applied in various structures. Their main advantage is the economy in weight because of high flexural buckling strength of compressed rods. The authors have published a lot of articles dealing with the optimum design of tubular trusses. The economy of higher strength steels in trusses has been treated in Farkas (1984).

The role of fatigue constraints has been studied in Farkas (1987a,b). The minimum cost design has been worked out taking into account buckling and fatigue constraints in Farkas (1990). The absorbed energy of tubular braces has been determined in Farkas (1993).

In the article of Farkas and Jármai (1994) roof trusses welded from circular (CHS) or square (SHS) hollow section as well as double-angle section rods have been compared to each other and it has been shown that the structural weight of CHS or SHS trusses is much smaller than that of double-angle trusses. In this article, it has been verified that the optimum truss geometry depends on the cross-sectional shape of compressed members.

The optimum truss topology of a simply supported belt-conveyor bridge structure has been determined in Jármai and Farkas (1994).

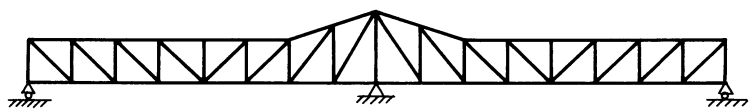

Figure 1. A two-span truss with increased height at the middle support

The optimum height of a statically determinate tubular truss with parallel chords has been calculated taking into consideration also the CIDECT rules for the strength of nodes in Farkas and Jármai (1995).

The minimum cost design of a Vierendeel truss welded from SHS rods has been worked out in Farkas and Jármai (1996). In the book Farkas and Jármai (1997) the optimum design of tubular trusses is treated in a separate chapter.

In the present study the minimum weight design of a statically indeterminate tubular truss shown in Figure 1 is treated. It is well-known that the strut forces in this case depend on the cross-sectional area of members, thus, the design of struts should be performed by an iterative process. Another problem is that, in a two-span truss the strut forces are the largest near the middle support, thus, the height should be increased here (Fig.1).

In the optimum design of this representative truss the following unknowns are sought, which minimize the weight of the structure and fulfil the design constraints: the cross-sectional areas A_C of all chords and two different profiles A_{B1} and A_{B2} for bracing as well as the two height factors $\Omega = H/a$ and $\omega = h/a$.

2 CALCULATION OF ROD FORCES

The unknown force X acting on the statically determinate basic structure (Fig.2) can be calculated from the displacement equation expressing that the horizontal displacement of node 17 should be zero

$$u_0 - Xu_1 = 0 \qquad X = u_0 / u_1 \tag{1}$$

where

$$u_0 = \sum_i \frac{S_{0i} s_i L_i}{EA_i} \quad \text{and} \quad u_1 = \sum_i \frac{s_i^2 L_i}{EA_i} \tag{2}$$

S_{0i} and s_i are the strut forces from external load and from $X = 1$, respectively, L_i and A_i are the length and the cross-sectional area of i-th strut, E is the modulus of elasticity.

For the structure shown in Figure 2 the horizontal displacements are as follows:

$$u_0 = \frac{Fa\Omega}{8\omega^2 A_C}\left[251 + \frac{98\left(1+\varsigma_1^3\right)\omega^2}{\left(\Omega+\omega\right)^2} + 36\varsigma_1^3\right] +$$

$$+\frac{Fa\Omega}{A_{B1}}\left(\frac{7.5\omega}{8} + \frac{\omega_1^3}{\omega^2}\right) + \frac{Fa\Omega}{A_{B2}}\left[-\frac{3.5\Omega}{8} - \frac{\omega_1^3}{4\omega^2} + \left(\frac{3\Omega}{\omega} - 4\right) *\right.$$

$$* \frac{6\Omega - 3\omega}{16} + \frac{6\Omega - \omega}{\Omega + \omega}\frac{0.75\Omega - \omega}{2} - \frac{\varsigma_2^3\left(6\Omega - \omega\right)\left(4 - \frac{3\Omega}{\omega}\right)}{4\omega\left(\Omega+\omega\right)^2} -$$

$$\left. - \frac{7\Omega_1^3}{\left(\Omega+\omega\right)^2\Omega}\left(-0.75\Omega + \omega\right)\right] \tag{3}$$

$$u_1 = \frac{\Omega^2 a}{64\omega^2 A_C}\left[146 + \frac{196\omega^2}{\left(\Omega+\omega\right)}\left(1+\varsigma_1^3\right) + \frac{64\omega^2}{\Omega^2} +\right.$$

$$\left. +36\varsigma_1^3\right] + \frac{\Omega^2 a}{64\omega^2 A_{B1}}\left(5\omega^3 + 4\omega_1^3\right) + \frac{\Omega^2 a}{64\omega^2 A_{B2}}\left[\left(-4 +\right.\right.$$

$$\left. + \frac{3\Omega}{\omega}\right)^2\omega^3 + 2\omega_1^3 + \frac{32\left(0.75\Omega - \omega\right)^2\omega^2}{\Omega+\omega} + \Omega\omega^2 +$$

$$\left. + \frac{4\varsigma_2^3\omega^2}{\left(\Omega+\omega\right)^2}\left(-4 + \frac{3\Omega}{\omega}\right)^2 + 64\frac{\left(0.75\Omega - \omega\right)^2\Omega_1^3\omega^2}{\left(\Omega+\omega\right)^2\Omega^2}\right] \tag{4}$$

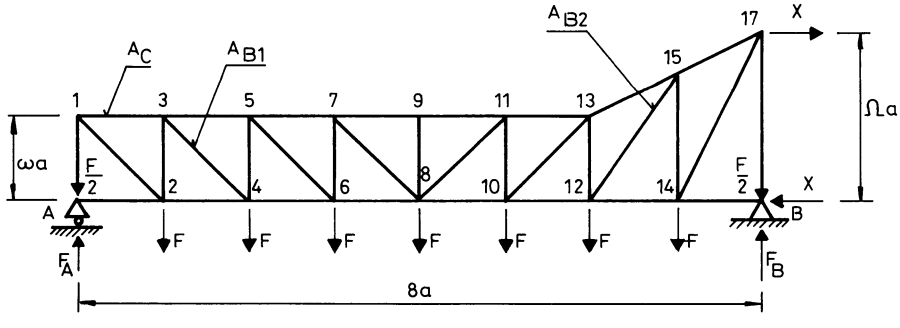

Figure 2. Forces acting on the half structure of the numerical example

The actual rod forces are given by

$$S_i = S_{0i} + Xs_i .$$

It can be seen that these displacements depend on cross-sectional areas.
It should be mentioned that for parallel chords ($\Omega = \omega$) and only two different cross-sectional areas ($A_{B1} = A_{B2}$) the formulae (3) and (4) take the following form:

$$u_0 = 336F / \omega \qquad (3a)$$

$$u_1 = \left(\omega^3 + \omega_1^3\right) A_C / A_B + 43 \qquad (4a)$$

In the above formulae the following symbols are used: $\omega_1 = \sqrt{1+\omega^2}$; $\Omega_1 = \sqrt{1+\Omega^2}$;

$$\varsigma_1 = \sqrt{1+\frac{(\Omega-\omega)^2}{4}}; \qquad \varsigma_2 = \sqrt{1+\frac{(\Omega+\omega)^2}{4}}$$

The rods of bracing are separated to two groups, the cross-sectional area A_{B2} is considered for rods 8-11, 10-13, 12-13, 12-15, 14-15, 14-17 and B-17 (Fig.2), the cross-sectional area for other rods is A_{B1}.

3 THE OBJECTIVE FUNCTION AND THE DESIGN CONSTRAINTS

The objective function is defined by

$$V / a = 2A_C\left(7+\varsigma_1\right) + A_{B1}(6\omega + 4\omega_1) +$$

$$+A_{B2}\left[2\omega_1 + 1.5(\Omega+\omega) + \varsigma_2 + \Omega_1\right] \qquad (5)$$

where V is the volume of the half structure.

To simplify the design of compression members for flexural buckling, the formulae of the Japanese Road Association (JRA) are applied (Hasegawa et al. 1985), which give near the same buckling factors as the Eurocode 3 (EC3) curve "b". From JRA formulae closed expressions can be derived for the required cross-sectional area as detailed below.

The flexural buckling constraint for the compression members subject to compressive force N is expressed as

$$N / A \le \chi f_{y1} \qquad f_{y1} = f_y / \gamma_{M1} \qquad (6)$$

f_y is the yield stress, $\gamma_{M1} = 1.1$ is the partial safety factor according to EC3. For the buckling factor JRA formulae are as follows:

$$\chi = 1 \qquad \text{for} \quad \bar{\lambda} \le 0.2 \qquad (7a)$$

$$\chi = 1.109 - 0.545\bar{\lambda} \qquad \text{for} \quad 0.2 \le \bar{\lambda} \le 1 \qquad (7b)$$

$$\chi = 1/\left(0.773 + \bar{\lambda}^2\right) \qquad \text{for} \quad \bar{\lambda} \ge 1 \qquad (7c)$$

where $\bar{\lambda} = KL / r\lambda_E$, K is the effective length factor. According to Packer et al (1992), in tubular trusses, for chords K=0.9, for bracing K = 0.75.

The radius of gyration for SHS of width b is

$r = b/\sqrt{6}$. $\lambda_E = \pi\sqrt{E / f_y}$, for the modulus of elasticity of steels $E = 2.1*10^5$ MPa and yield stress f_y = 355 MPa λ_E = 76.41.
Introducing symbols $\vartheta = 100b / L$, the limiting local slenderness $\delta_L = (b/t)_L$, $c = 100K\sqrt{6} / \lambda_E$ and $\nu = 10^4 N\delta_L / \left(4L^2 f_{y1}\right)$ and solving (6) with (7b) one obtains (Farkas and Jármai 1997)

$$\vartheta = 0.24572c\left(1+\sqrt{1+\frac{14.93475\nu}{c^2}}\right) \quad \text{for} \quad \vartheta \ge c \qquad (8)$$

and for $\vartheta \le c$ with (7c)

$$\vartheta = \left[0.3865\nu\left(1+\sqrt{1+\frac{6.69424c^2}{\nu}}\right)\right]^{1/2} \qquad (9)$$

Considering the relationship

$$A = 4bt = \frac{4b^2}{\delta_L} = \frac{4\vartheta^2 L}{10^4\delta_L} \qquad (10)$$

with (8) we get

$$A = \frac{0.4830L^2}{10^4\delta_L}\left(c^2 + 7.4644\nu + c^2\sqrt{1+\frac{14.93475\nu}{c^2}}\right) \qquad (11)$$

It should be noted that, for our numerical example (7b) is valid for all compression members. When $\vartheta \le c$ another formula for A should be derived.

The design constraint for tension force is given by

$$N / A \le f_{y1} \qquad (12)$$

4 NUMERICAL EXAMPLE

Data: a = 3000 mm, f_y = 355 MPa, the static concentrated forces F = 450 kN act on lower nodes representing the factored load of a belt-conveyor bridge.

On the basis of preliminary calculations the following rods are selected for each rod groups:

Table 1. Results of the numerical example for three different profiles (A and V/a in mm^2)

Ω	ω	A_C	A_{B1}	A_{B2}	$10^{-5} V/a$
2.2	1.0	7580	3446	8780	2.687
2.2	0.9	7631	3347	8795	2.632
2.2	0.8	7655	3258	8795	2.574
2.2	0.7	7658	3177	8795	2.517
2.2	0.6	8177	3099	8795	2.598
2.0	0.9	8284	3356	8504	2.649
2.0	0.8	8357	3255	8523	2.601
2.0	0.7	8397	3165	8534	2.551
2.0	0.6	8409	3084	8534	2.500
2.0	0.5	9907	3005	9004	2.743
1.8	0.9	8990	3385	8200	2.680
1.8	0.8	9144	3268	8237	2.646
1.8	0.7	9247	3164	8261	2.607
1.8	0.6	9306	3072	8275	2.564
1.8	0.5	9805	2988	9043	2.668
1.6	0.9	9732	3442	7877	2.722
1.6	0.8	10012	3302	7935	2.708
1.6	0.7	10221	3180	7979	2.686
1.6	0.6	10365	3073	8009	2.658
1.6	0.5	10451	2979	9066	2.715
1.4	1.4	7539	4536	7001	2.675
1.4	1.3	8121	4330	7099	2.683
1.4	1.2	8729	4123	7208	2.700
1.3	1.3	8132	4424	6892	2.657
1.3	1.2	8788	4216	6995	2.680
1.2	1.2	8815	4316	6777	2.658
1.2	1.1	9567	4104	6892	2.701
1.1	1.1	9621	4209	6678	2.685
1.1	1.0	10488	3993	6793	2.749
1.0	1.0	10604	4102	6694	2.754
1.0	0.9	11674	3875	7072	2.875

(a) for all rods of chords two compressed rods are selected: rod 14-B subject to $N = S_{14\text{-}B} = X$ and rod 5-7 with force

$$N = S_{5\text{-}7} = \frac{7.5F}{\omega} - \frac{3\Omega}{8\omega} X .$$

The required A_C is calculated for larger compressive force using (11) with values of c = 2.8851 and ν with $L = a$ and, according to CIDECT rules (Packer et al 1992), $\delta_L = 30$;

(b) for rods of bracing excluding the rods near the middle support (mentioned at the end of Section 2): rod A-1, subject to $N = S_{A\text{-}1} = 3.5F - X\Omega/8$ compressive force, A_{B1} is calculated with (11) considering $c = 2.4043$ and $L = \omega a$;

Table 2. Results for two different profiles

Ω	ω	A_C	A_B	$10^{-5} V/a$
2.0	1.2	7523	8302	3.332
2.0	1.1	7762	8365	3.285
2.0	1.0	7951	8415	3.228
2.0	0.9	8093	8453	3.162
2.0	0.8	8191	8479	3.088
2.0	0.7	8251	8495	3.008
2.0	0.6	8559	8509	2.970
2.0	0.5	10102	8933	3.212
1.8	0.9	8749	8143	3.148
1.8	0.8	8933	8187	3.094
1.8	0.7	9062	8217	3.031
1.8	0.6	9244	8237	2.961
1.8	0.5	10009	8968	3.141
1.6	1.2	8106	7538	3.138
1.6	1.1	8592	7639	3.147
1.6	1.0	9037	7732	3.148
1.4	1.4	7078	6916	2.956
1.4	1.3	7652	7018	2.986
1.4	1.2	8261	7127	3.021
1.3	1.3	7652	6810	2.915
1.3	1.2	8301	6917	2.958
1.3	1.1	8988	7031	3.008
1.2	1.2	8316	6706	2.893
1.2	1.1	9056	6818	2.953
1.1	1.1	9092	6602	2.893
1.1	1.0	9949	6721	2.975
1.0	1.0	10033	6587	2.943
1.0	0.9	11091	6999	3.113

(c) for rods of bracing near the middle support:
rod B-17 of compressive force

$N = S_{B-17} = 3.5F + X\Omega/8$, A_{B2} is calculated with (11) considering $c = 2.4043$ and $L = \Omega a$;
rod 12-15 of tension force

$$S_{12-15} = F\varsigma_2 \frac{6\Omega - \omega}{\omega(\Omega + \omega)} + X\left(4 - \frac{3\Omega}{\omega}\right)\frac{\varsigma_2 \Omega}{4(\Omega + \omega)}$$

calculated with (12),
rod 10-13 of tension force

$$S_{10-13} = 1.5F\omega_1/\omega + X\Omega\omega_1/(8\omega).$$

The results are summarized for three different profiles in Table 1, for two different profiles in Table 2.

5 THE OPTIMIZATION METHOD

This method is a direct search one without derivatives. Rosenbrock's (1960) method is an iterative procedure that bears some correspondence to the exploratory search of Hooke and Jeeves in that small steps are taken during the search in orthogonal coordinates. However, instead of continually searching the co-ordinates corresponding to the directions of the independent variables, an improvement can be made after one cycle of co-ordinate search by lining the search directions up into an orthogonal system, with the overall step on the previous stage as the first building block for the new search coordinates. Rosenbrock's method locates $x^{(k+1)}$ by successive unidimensional searches from an initial point $x^{(k)}$ along a set of orthonormal directions.
The method is executed as follows:
Minimize the objective function $f(x_i) \rightarrow$ min.
Design constraints are:

explicit $x_i^L \le x_i \le x_i^U$ $(i = 1,2,...,N)$,

implicit $g_j(x_i) \ge 0$ $(j = 1;2,..,M)$. (13)

(i) Before starting the minimization process, define a set of 'initial' step lengths S_i, to be taken along the search directions M_i, i= 1,2,..,N. The starting point must satisfy the constraints and should not lie in the boundary zones.
(ii) After each function evaluation, the following steps are carried out: Define by f^o the current best objective function value for a point where the constraints are satisfied, and $f(x)$ where in addition to this the boundary zones are not violated. f^o and $f(x)$ are initially set equal to the objective function value at the starting point.
(iii) The first variable x_1 is stepped a distance S_1 parallel to the axis and the function evaluated. If the current point objective function value, f, is worse (greater or less) than f^o or if the constraints are violated, the trial point is a failure and S_1 decreased by a factor β, $0 < \beta \le 1$, and the direction of movement reversed. If the move is termed a success, S_1 increased by a factor α, $\alpha \ge 1$. The new point is retained, and a success is recorded. The values of α and β are usually taken as 3,0 and 0,5 respectively.
(iv) Continue the search sequentially stepping the variables, x_i, a distance S_i parallel to the axis. The same acceleration or deceleration and reversal procedure is followed for all variables, until at least one step has been successful and one step has failed in each of the N directions. Perturbations are continued sequentially in the search directions until a success is followed by a failure in every direction, at which time the kth stage is terminated. Since an equal value of a function counts as a success, a success is eventually reached in each direction as the multipliers of reduce the magnitude of the step length. The final point obtained becomes the initial point for the succeeding stage $x^{(k+1)} = x^{(k)}$. The normalized direction $S_i^{(k+1)}$ is chosen parallel to $x_0^{(k+1)} - x_0^{(k)}$, and the remaining directions are chosen orthonormal to each other and to $S_i^{(k+1)}$.
(v) Compute the new set of directions rotating the axes. In general, the orthogonal search directions can be expressed as combinations of all the co-ordinates of the independent variables.
(vi) Search is made in each of the x directions using the new co-ordinate axes. In each x direction the variables are stepped a distance S_i parallel to the axis and the function is evaluated.
(vii) If the current point lies within a boundary zone, the objective function is modified as follows;

$$f(new) = f(old) - (f(old) - f^*)(3\lambda - 4\lambda^2 + 2\lambda^3) \quad (14)$$

where
The boundary zones are defined as follows:

$$\lambda = \frac{distance\ into\ boundary\ zone}{width\ of\ boundary\ zone} \quad (15)$$

At the inner edge of the zone, $\lambda = 0$, i.e., the function is unaltered (f(new) = f(old)). At the constraints, λ=1, and thus f(new) = f^*.
For a function which improves as the constraint is approached, the modified function has an optimum in the boundary zone.
(viii) f^* is set equal to f^0 if an improvement in the objective function has been obtained without violating the boundary zones or constraints.
(ix) The search procedure to find the continuous values of the variables is terminated when the convergence criterion is satisfied.
(x) The procedure was modified by a secondary search to find the discrete values of the variables.
The procedure stops if the convergence criterion or the iteration limit is reached. The procedure is very quick, but it gives usually local optima, so it is advisable to use more starting points. The Turbo/Borland C version of Hillclimb technique can be found in Farkas & Jármai (1997).

6 CHECK OF THE OPTIMUM VERSION
($\Omega = 2.0, \omega = 0.6$, three different profiles)

From Table 1 we get A_C = 8409, A_{B1} = 3084 and A_{B2} = 8534 mm^2. According to (1), (3) and (4) one obtains X = 2501 kN. Using European Standard prEN 10219 (1996) SHS 250*10 with A = 9260 mm^2 and radius of gyration r = 97 mm is selected for all rods of chords. According to Section 4
$S_{14\text{-}B} = X = 2501$ kN,
$S_{5\text{-}7} = 2449$ kN, thus, the rod 14-B is governing and should be checked for flexural buckling with formulae (6) and (7).

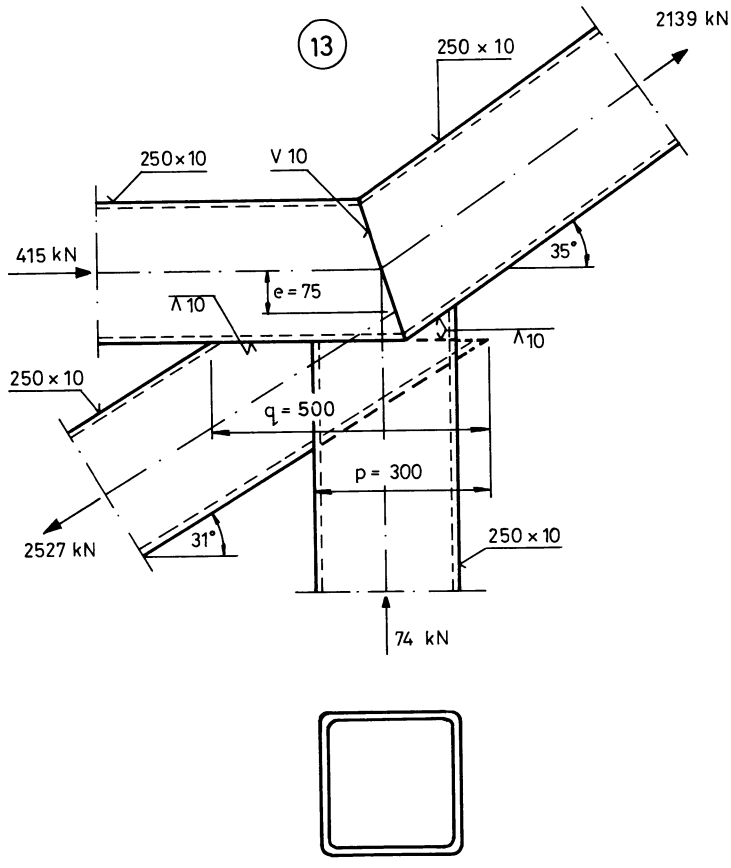

Figure 3. A characteristic node of the optimum structure ($\Omega = 2.0, \omega = 0.6$)

$$\bar{\lambda} = \frac{0.9 * 3000}{76.41 * 97} = 0.3643, \quad \chi = 0.9105$$

N/A = 2501000/9260 = 270 < 0.9105*323 = 294 MPa, OK.

For smaller rods of bracing the section of 150*6 is selected with A = 3360 mm^2 and r = 58.4 mm. According to Section 4 $S_{A\text{-}1}$ = 950 kN,

$$\bar{\lambda} = \frac{0.75 * 0.6 * 3000}{76.41 * 58.4} = 0.3025, \quad \chi = 0.9441,$$

N/A = 283 < 0.9441*323 = 305 MPa, OK.

For larger rods of bracing the section of 250*10 is selected with A = 9260 mm^2 and r = 97 mm.

$S_{B\text{-}17}$ = 2200 kN, $\bar{\lambda} = 0.6071$, $\chi = 0.7781$, N/A = 238 < 251 MPa, OK. Since this section is valid only for the half truss, rod B-17 should be designed for double force 4400 kN and should have a cross-sectional area 2*8534 = 17068 mm^2. Section 300*16 can be used with A = 17100 mm^2 and r = 114 mm. $\bar{\lambda} = 0.5166$, $\chi = 0.8275$, N/A = 440000/17100 = 257 < 0.8275*323 = 267 MPa, OK. To enable the fabrication of node 17, the width of chords 15-17 and 14-B should be increased to 300 mm.

The formula given in Section 4 yields for this case a tension force $S_{12\text{-}15}$ = 660 kN, N/A = 660000/9260 = 71 < 323 MPa, OK.

To illustrate the SHS nodes in the optimum structure the drawing of node 13 is given in Figure 3.

Check the node 13 for effective width according to Packer et al (1992). For the rod 10-13 a section of 250*10 should be used (A = 9260 mm^2). The tension force in this rod is

$$S_{10\text{-}13} = 1.5F\omega_1 / \omega + X\Omega\omega_1 / (8\omega) = 2527 \text{ kN},$$

N/A = 2527000/9260 = 273 < 323 MPa, OK. According to the Figure 3 the overlapping factor is $Ov = (p/q)100 = (300/500)100 = 60\%$,

$$b_e = b_{e.ov} = \frac{10}{b_0 / t_0}\frac{t_0}{t_1}b_1 = \frac{10}{250/10}\frac{10}{10}250 = 100 \text{ mm},$$

$$N_1 = f_y t_1\left[\frac{Ov}{50}(2b_1 - 4t_1) + b_e + b_{e.ov}\right] =$$

$$= 355 * 10\left[\frac{60}{50}460 + 2 * 100\right] = 2670 > 2527 \text{ kN, OK.}$$

7 CONCLUSIONS

The evaluation of the results of the numerical example gives the following conclusions.

(a) designing the truss with three different cross-sectional areas, i.e. all chords with the same profile and bracing divided into two profile groups, the structure of increased height at the middle support gives the minimum structural weight for $\Omega = 2.0$ and $\omega = 0.6$ ($V/a = 2.500*10^5$ mm^2);

(b) designing the truss with three different profiles, for the optimum version of parallel chords is the solution of $\Omega = \omega = 1.3$ (V/a = $2.657*10^5$ mm^2), 6% larger than that for the version with increased height;

(c) designing the truss with only two different profiles, i.e. one profile for all chords and other for all bracing rods, the best non-parallel solution is $\Omega = 2, \omega = 0.6$ (V/a = $2.970*10^5$ mm^2) and the parallel chord solution of $\Omega = \omega = 1.2$ gives the minimum weight ($V/a = 2.893*10^5$ mm^2). The non-parallel chord solution gives 19% larger weight than that of three different profiles.

The main conclusion is that the optimum truss geometry depends on the number of different rod profiles.

It should be noted that the optima are not very sensitive to the change of height parameters, although the weight difference between the best and worst ($\Omega = 2.0, \omega = 1.2$, $V/a = 3.332*10^5$) structural version is 33%.

ACKNOWLEDGEMENTS

This work has been supported by grants OTKA 19003 and 22846 of the Hungarian Fund for Scientific Research.

REFERENCES

European Standard prEN 10219. 1996: *Cold formed welded structural hollow sections of non-alloy and fine grain steels.* Draft. Brussels: European Committee for Standardization.

Farkas,J. 1984. Economy achieved by using higher strength steels in trusses welded from square hollow sections. *Welding of tubular structures. Proceedings 2nd International Conference, Boston, Mass. USA:* 137-144. IIW, Oxford: Pergamon Press.

Farkas,J. 1987a. Optimum design of welded tubular trusses including fatigue constraints.. *Proceedings International Meeting on Safety Criteria in Design of Tubular Structures, Tokyo 1986:* 309-318. IIW, Tokyo: Architectural Institute of Japan.

Farkas,J. 1987b. Optimum design for fatigue of trusses welded from circular hollow sections. *Acta Technica Acad. Sci.Hung.* 100(1-2):51-65.

Farkas,J. 1990. Minimum cost design of tubular trusses considering buckling and fatigue constraints. *Tubular Structures.* Niemi,E., Mäkeläinen,P. (eds): 396-400. London-New-York, Elsevier Applied Science.

Farkas,J. 1993. Absorbed energy of CHS and SHS braces cyclically loaded in tension-compression. *Tubular Structures V.* Coutie,M.G., Davies,G. (eds): 607-617.London: E&FN Spon.

Farkas,J.&Jármai,K. 1994. Savings in weight by using CHS or SHS instead of angles in compressed struts and trusses. *Tubular Structures VI.* P.Grundy, A.Holgate, B.Wong (eds): 417-422. Rotterdam: Balkema.

Farkas,J.&Jármai,K. 1995. Stability constraints in the optimum design of tubular trusses. *Proceedings of International Colloquium on Stability of Steel Structures, Budapest.* Budapest: Akadémiai Kiadó, 1996. Vol.2. 783-790.

Farkas,J.&Jármai,K. 1996. Minimum cost design of SHS Vierendeel trusses. *Tubular Structures VII.* Farkas,J. & Jármai,K. (eds): 469-474. Rotterdam: Balkema.

Farkas,J. & Jármai,K. 1997. *Analysis and optimum design of metal structures.* Rotterdam: Balkema.

Hasegawa,A. et al. 1985. Optimum cross-sectional shapes of steel compression members with local buckling. *Proceedings JSCE Structural Engineering/Earthquake Engineering* 2:121-129.

Jármai,K. & Farkas,J. 1994. Application of expert system at the optimum design of tubular trusses of belt-conveyor bridges. *Tubular Structures VI.* P.Grundy, A.Holgate, B.Wong (eds): 405-410. Rotterdam: Balkema.

Packer,J.A. et al. 1992. *Design guide for rectangular hollow section (RHS) joints under predominantly static loading.* Köln: TÜV Rheinland.

Rondal,J. et al. 1992: *Structural stability of hollow sections.* Köln: TÜV Rheinland.

Rosenbrock,H.H. 1960: An automatic method for finding the greatest or least value of a function. *Computer Journal,* 3: 175-184.

Fire



Taylor & Francis
Taylor & Francis Group
http://taylorandfrancis.com

Tubular Structures VIII, Choo & Van der Vegte (eds) © 1998 Balkema, Rotterdam, ISBN 90 5809 001 9

The performance in fire of concrete filled SHS columns protected by Intumescent paint

M. Edwards
Technical Marketing, British Steel Tubes and Pipes, UK

ABSTRACT Filling a Structural Hollow Section column with concrete will increase its load carrying capacity. The concrete infill will also improve the thermal characteristics of the composite column and reduce the amount of external fire protection necessary. However, only limited design advice is presently available on how to quantify this effect. British Steel in collaboration with the intumescent paint manufacturer Nullifire have undertaken a series of investigative fire tests on a range of unloaded SHS specimens. The test data has produced a specific assessment method to predict the performance of an intumescent paint in fire. Generalised expressions have also been developed to assess the Effective Section Factors of protected filled SHS in fire that can be used with any type of external protection. Additional fire tests on fully loaded columns have also confirmed that the same ULS limiting temperatures can be used with both filled and unfilled SHS columns.

1 INTRODUCTION

Filling a Structural Hollow Section (SHS) column with concrete can markedly increase its load carrying capacity. The characteristic performance of such a structural member is well understood. Over the last two decades, various ambient temperature design manuals have been produced based on both UK (British Steel 1992) and European (CIDECT 1995) Ultimate Limit State (ULS) Design codes.

It is also known that a concrete infill will improve the thermal characteristics of a composite column and reduce the amount of external fire protection necessary when such a column is fully utilised as a load carrying member. However, at present, only limited deeply conservative design advice is available on how to utilise this (see Table 1). The need to quantify this effect became more urgent after the introduction in of a new UK ULS Fire Design code (British Standards 1990) for steel structural members based on a variable limiting temperature steel temperature obtained by reference to a reduced fire design load.

Accordingly, in 1995, British Steel Tubes and Pipes, in collaboration with the intumescent paint manufacturer Nullifire, initiated a series of indicative furnace tests (Edwards & Wainman , in prep) on a range of unloaded SHS sections.

2 PRESENT SPECIFICATION METHODOLOGY

In the UK, the required thickness of external fire protection to a steel member is specified by reference to the Section Factor of the SHS shell, where;-

$$\text{Section Factor (Hp/A)} = \frac{\text{Exposed Perimeter}}{\text{c.s.a. of the SHS}}$$

A Circular Section is a uniform pure shape, so when fully exposed to a fire, the Section Factor will be based on the full perimeter and cross-sectional area, i.e;-

$$Hp/A = \frac{\pi.D}{\pi/4.D^2 - \pi/4.(D - 2.t_s)^2} = \frac{1}{t_s.(1 - t_s/D)}$$

An unprotected Hot Finished SHS has rounded corners, but ignoring the corner effects will still produce a closely accurate assessment of its Section

Factor, so;-

$$Hp/A = \frac{1}{t_s.[1 - 2t_s/(B + D)]}$$

For a square section this simplifies to;-

$$Hp/A = \frac{1}{t_s.(1 - t_s/B)}$$

The Section Factor is intended for use with tables giving specified thicknesses of both generic and proprietary inert protection systems. A table for assessing the permissible reduction in external protection thickness due to the presence of a concrete core is given in BS 5950 Part 8, viz;-

Table 1. Protection modification factor (C)

$Hp/A_{(e)}$	C	$Hp/A_{(f)}$
50-75	1.00	50-75
100	0.92	92.0
125	0.88	110.0
150	0.81	121.5
175	0.75	131.8
200	0.69	138.0
260 -300	0.55	143 -175

i.e, if the specified thickness of protection by reference to the EMPTY SHS shell = ti , then the reduced thickness required = ti_r = C.ti This is equivalent to reducing the Section Factor by the same proportion (also see Table 1). In practice, it has been observed during real fire tests (Edwards 1998) that filled sections appear to have substantially lower Section Factors.

3 MODELLING THE BEHAVIOUR OF PROTECTED CONCRETE FILLED SHS SECTIONS

Figure 1 shows the observed temperature time profile of a 150 sq x 6.3 concrete filled SHS column heated to the ISO curve while externally protected by a layer of Nullifire S605 intumescent paint with an initial thickness of 1819 microns. Figure 2 shows the measured temperature developments within the concrete along the diagonal. It can be seen that once intumescence has occurred, the temperature time development of the SHS is relatively linear (as is to be expected for a protected section with a low effective Section Factor). Moreover, the individual layers of concrete all appear to have a similar rate of temperature increase once the free water in each layer has been boiled off. This suggests that the temperature profiles of the column interiors can be simply modelled in terms of an underlying uniform heating rate without explicit reference to the external fire regime or the thermal behaviour of the protection layer.

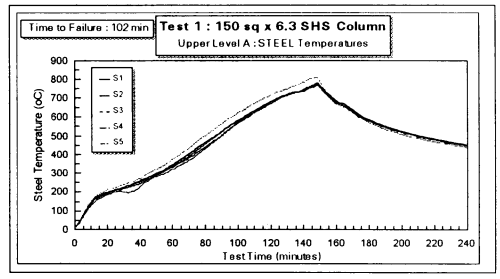

Figure 1 Temperature development in the SHS shell of a protected filled SHS

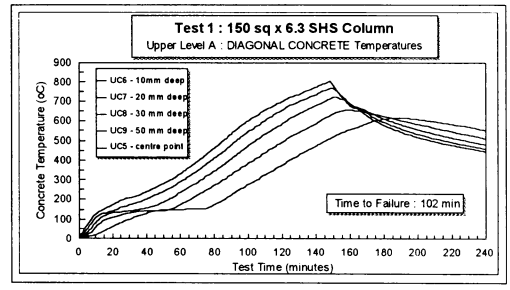

Figure 2 Temperature development within the concrete core of a protected filled SHS

3.1 *Protected Circular Section Cores*

For a circular core, the underlying heating rate of the concrete can be quantified as;-

$$\Delta Q_c = \rho_c.c_c.A_c.\frac{(\theta_t - \theta_i)}{(T_t - T_{wd})}$$

$$\text{with;-} \quad T_{wd} = \frac{T}{[1 + c_c.(\theta_t - \theta_i)/(p_w.L_h)]}$$

where;- θ_t = Limiting temperature of the SHS
θ_i = Initial temperature of the SHS
ρ_c = density of the concrete (taken as 2300 kg/m^3)
c_c = specific heat of the concrete (see below)
A_c = csa of concrete core
T_t = Time to reach limiting temperature
T_{wd} = Water Dwell Time (minutes)
L = Latent heat of water (2150 kJ/kg)
p = unit water content of the concrete by weight (taken as 0.04)

The temperature gradient through the core can now be estimated as a one-dimensional heat flow by dividing the core up into N annuli of equal area. Each annlus will then, in turn, absorb a constant proportion ($1/N^{th}$) of the heat while allowing the remainder to be conducted through it towards the centre. So for the nth annulus;-

$$\Delta\theta_n = \Delta Q_c.(\eta - n/N).(1/2\pi k).[1 - (N - n)/(N+1-n)]^{0.5}$$

$$\text{while } \eta \geq n/N \qquad (1)$$

and $$\theta_n = \theta_t - (\Delta\theta_n)/2 - \sum_0^{n-1}(\Delta\theta_x)$$

where;- $\Delta\theta_n$ = Temperature gradient across the nth annulus
θ_t = Limiting temperature of the SHS
θ_n = Temperature of the nth annulus
θ_x = Temperature of the nth annulus
η = proportion of the concrete area actually being heated
k = conductivity of the concrete (see below)

The temperature profile through the circular core can be simply obtained on a spread sheet by summing the contents of N cells using trial values of η. This can be done using an iterative macro, with conditional checks. Once these conditions have been satisfied, the average temperature of the core (θ_{av}) and a resulting core utilisation factor (γ) can be calculated as;-

$$\gamma = \frac{(\theta_{av} - \theta_i)}{(\theta_t - \theta_i)}$$

3.2 *Protected Square Section Cores*

For a square section, the underlying heating rate of the concrete can be based on heat flow through one side face of the section and quantified as ;-

$$\Delta Q_c = \rho_c.c_c.A_c/4.\frac{(\theta_t - \theta_i)}{(T_t - T_{wd})}$$

The temperature differential through the core can now be initially estimated as a one-dimensional heat flow by dividing the core up from the side face to the centre line into N vertical strips of equal area. Each strip will then, in turn, absorb a constant proportion ($1/N^{th}$) of the horizontal heat flow from that face, while allowing the remainder to be conducted through it towards the centre. However, there will also be an identical vertical heat flow from the horizontal faces. The only way to satisfy both conditions simultaneously is to subdivide the a quadrant of the core into an N x N grid and place the resulting temperature differentials along the grid diagonal.So at position (n,n) on the core diagonal-

$$\Delta\theta_{(n,n)} = \Delta Q_c.(\eta - n/N).(1/2Nk) \text{ while } \eta \geq n/N \quad (2)$$

There will be a secondary temperature differential between the the core diagonal and core centre line. this can be closely approximated by assuming that;-

$$\Delta\theta_{(n,N)} = \Delta\theta_{(n,n)}.(1 + (N - n)/\sum_1^{N-1} n) \qquad (3)$$

The temperature profile along the diagonal of a square core can now be simply obtained on a spread sheet by using equation (2) to sum the contents of N cells using trial values of η. Again this can be done using an iterative macro, with a conditional check. Temperature off-sets within the core quadrant can then by assigned to the individual elements of the N x N grid using equation(3). The average temperature of the core (θ_{av}) and the resulting utilisation factor (γ) can then be calculated.

3.3 *Unprotected Filled Sections*

Within limits, the temperature of an unprotected section after a given ISO heating time can be obtained using the published formula;-

$$T = 0.54.(\theta_s - 50)/(Hp/A)_e^{0.6}$$

In fact, a more accurate estimate can be made using the modification;-

$$T = 0.135 .[\theta_s^2/(Hp/A)_e]^{0.604} \quad (4)$$

This formula can be incorporated into the procedures given above for protected sections by continually replacing θ_t with θ_s and recalculating as the iteration progresses. It is then possible to assess the both the final steel section temperature and effective section factor after a fixed heating time (15, 30 or 45 minutes).

3.4 *Concrete Thermal parameters*

The specific heat and conductivity of concrete vary markedly with temperature. According to the base document of Eurocode 4.0 part 1.2 ;-

$$c = 0.90 + 0.08.(\theta_c/120) - 0.004.(\theta_c/120)^2 \text{ kJ/kg/°C}$$

$$k = 2.0 - 0.24.(\theta_c/120) + 0.012.(\theta_c/120)^2 \text{ W/m/°C}$$

Comparison between assessed and measured temperature profiles showed that only average values need be used for these parameters during the iteration processes described above and that these could be quantified using the temperature at the 1/2 area depth on the centre line.

4 INDICATIVE TEST SPECIMENS

A total of 34 indicative specimens were heated to the ISO temperature-time using a private test gas fired furnace owned by the Nullifire Company at Coventry. These specimens can be divided into three groups;-

a) *Specimen Group 1 - Empty/Protected Sections*

Test group 1 comprised seven empty SHS specimens coated with Nullifire S605 intumescent paint. These specimens were used to initialy assess the performance of the paint. Table 2 gives details of these specimens including the time taken for each to reach the average temperature of 550°C used to quantify the paint performance. An initial regression was performed on these specimens using the standard formula for inert external protection, viz;-

$$T = C. \frac{ti^{0.77}}{(Hp/A)_e^{0.77}}$$

It was found that this formula had to be modified to include a size effect, i.e;-

$$T = A + \frac{B + C.(1 + s/D).ti^{0.77}}{(Hp/A)_e^{0.77}} \quad (5)$$

where; - s = section size

This additional parameter probably reflects the actual pattern of intumescence that occurs on an SHS, namely a corner/diameter effect that becomes less pronounced as section size increases.

Values for the coefficients and the resulting correlation are given as regression group r1 in Table 4

Table 2. Test Group 1 (7 Specimens)

Spc	Size	ti	Hp/A	Time to 550°C (min)		
		mcrns	m^{-1}	test	reg 1	reg 3
nk1	114.3 x 3.6	471	286.8	21.0	21.3	14.9
nl2	114.3 x 6.3	2111	168.0	38.0	40.7	32.8
na1	100 x 4.0	481	260.4	21.0	22.0	15.9
nc1	100 x 10.0	2230	111.1	53.0	51.1	44.6
nd4	200 x 6.3	2730	163.9	54.0	50.9	41.5
ne2	200 x 10.0	617	105.3	35.5	34.6	34.3
nf3	200 x 16.0	2810	67.9	86.5	88.1	81.4

b) *Specimen Group 2 - Filled/Protected Sections*

Test group 2 comprised twenty three filled SHS specimens, again coated with Nullifire S605 intumescent paint. These specimens were used to quantify the performance of the paint on filled sections and compare preformance with the empty sections.. Table 3 gives details of these specimens, again including the time taken for each to reach the average temperature of 550°C .

An initial regression was performed using equation (5), then a second, more conservative regression performed that excluded the three best specimens. The coeffients and correlations obtained are given as regression groups r2 and r3 in Table 4.

Table 3. Test Group 2 (23 Specimens)

Spec No.	Size	ti	Hp/A (m^{-1})		Time to 550°C (min)	
		mcrns	empty	full	test	reg3
nk2	114.3 x 3.6	670	286.8	68.04	40.0	45.5
nk3		1534	-"-	61.35	61.0	61.9
nl3	114.3 x 6.3	1110	168.0	56.46	59.0	59.5
nl4		2139	-"-	54.10	80.0	76.9
na2	100 x 4.0	2580	260.4	66.00	67.5	69.9
na3		1440	-"-	66.30	66.0	56.3
nb2	100 x 6.3	1050	169.4	62.69	57.0	53.4
nb3		2130	-"-	60.53	75.0	69.2
nc2	100 x 10.0	690	111.1	56.47	56.0	52.0
nc3		1870	-"-	55.60	67.0	70.3
nd1	200 x 6.3	622	163.9	54.29	56.0	56.3
nd2		1730	-"-	43.21	111.0	93.0
nd3		2800	-"-	41.80	120.0	117.5
ne3	200 x 10.0	1810	105.3	38.69	111.0	103.0
ne4		2870	-"-	37.64	122.0	128.8
nf1	200 x 16.0	634	67.9	36.92	74.5	75.6
nf2		1800	-"-	32.82	121.0	116.5
nf4		2790	-"-	31.97	141.0	143.9
ng4	300 x 8.0	818	128.4	41.86	77.0	79.7
ng2		2660	-"-	36.05	144.0	145.0
nh1	300 x 10.0	417	103.4	41.22	63.0	66.9
nh2		1420	-"-	36.43	113.0	108.3
nh3		1910	-"-	35.24	129.0	126.1

Table 4. Regression Coefficients and Correlations

Case	No.	A	B	C	D	r^2
r1 - unfilled	7	14.0	219	2.49	401	0.984
r2 - filled	23	2.5	795	1.66	287	0.964
r3 - filled	20	1.5	792	1.60	264	0.985
r4 - all spec.	30	10.6	559	1.61	243	0.984

c) *Specimen Group 3 - Filled/Unprotected Sections*

A small group of 4 specimens were filled with concrete but left unprotected. Details are given Table 5 which shows their assessed effective Section Factors after heating to 550°C ; the predicted time it should take for them to reach this temperature according to regression 3 and the actual measured time for them to do so.

Table 5. Test Group 3 (4 specimens)

Spec.	Size	Hp/A (m^{-1})		Time to 550°C (minutes)	
		empty	filled	test	predict
nl1	114.3 x 6.3	168.0	74.13	19.5	20.8
nb1	100 x 6.3	169.4	76.70	19.5	19.9
ne1	200 x 10.0	105.3	55.15	23.0	24.9
ng1	300 x 8.0	128.4	56.22	24.0	24.6

4.1 *Comparative Performance*

In practice, all three regressions give similar significance to each component of the formula. Figure 3 shows the estimated fire times for all 30 protected specimens calculated using the most conservative prediction formula.

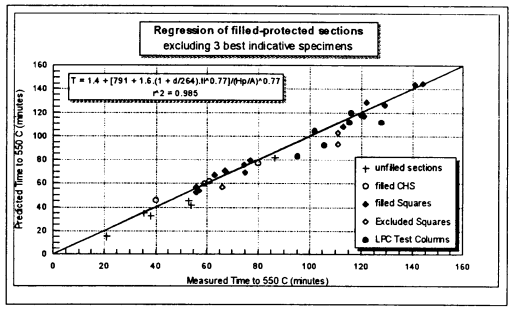

Figure 3 Predicted v Measured Times to 550°C

5 GENERAL PERFORMANCE EQUATIONS

Modified versions of the simple assessment spread sheets and their macros were used to obtain discrete values for the effective Section Factors for the full range of Circular and Square British Steel Hollow Sections at 540°C , the standard limiting temperature of fully utilised columns.

Figure 4 shows a comparison of the assessed effective factor obtained for protected Circular Sections. It can be seen that these values are substantially lower than those given in Table 1 according to the present existing recommendations.

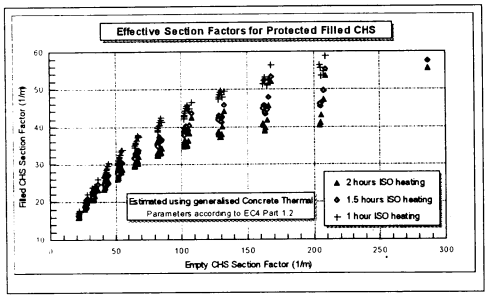

Figure 4 Comparative Section Factors of Filled v Empty SHS

Using the following approach, the discrete values of effective Section Factors obtained from these spread sheets were also regressed to obtain simple expressions that would directly evaluate effective Section Factors.

i) The Effective Section Factor for a section can be defined as;-

$$(Hp/A)e = \frac{\text{Exposed Perimeter of the SHS}}{\text{Effective csa of the filled SHS}}$$

ii) This can formula be simplified to;-

$$(Hp/A)e = \frac{1}{(t_s + t_{ce}).[1 - (t_s + t_{ce})/D]}$$

where;- t_{ce} = apparent increase in CHS wall thickness due to the presence of the concrete

iii) The value of t_{ce} is time dependent and has been quantified to a high accuracy for filled CHS as;-

either $t_{ce} = 1.858.T^{0.5}$ when $di > 24.717.T^{0.5}$

or $t_{ce} = 0.1206.di.(2 - di/17.955/T^{0.5})$

when $di \geq 24.717.T^{0.5}$

where;- T = the ISO heating time in minutes
di = the internal CHS diameter in mm

iv) The apparent increase in the wall thickness of SQUARE sections has also been explicitly quantified in tabular form. Explicit formulae are still being developed to take account of the two dimensional heat flow. However, a slightly conservative set of expressions have been developed using CHS style formulae, namely;-

either $t_{ce} = 1.810.T^{0.5}$ when $bi > 20.972.T^{0.5}$

or $t_{ce} = 0.1193.bi.(2 - bi/16.422/T^{0.5})$

when $bi \geq 20.972.T^{0.5}$

where;- T = the ISO heating time in minutes
di = the Internal Square section size in mm

6 COLUMN TESTS

While the indicative series was continuing, a series of six full size protected SHS column specimens were fabricated and fire tested at the Loss Prevention Centre in order to investigate if the existing load ratio method/limiting temperature method could be safely applied to protected composite SHS columns (Edwards, in prep)

Five test specimens were designed using SHS of markedly differing sizes but with the same wall thickness and SHS Section Factor so as to produce a clear indication of the mass cooling effect of the concrete and how the presence of load bearing concrete would modify the failure temperatures in fire. A sixth specimen using the maximum possible wall thickness (16.0 mm) was also introduced.

6.1 *Fire Test Load Ratio and Limiting Temperature*

The actual Load Ratio of a member in fire (and the resulting Limiting Temperature) depends both on the type of member and the relative magnitude of the Permanent and Live Loads.

Assuming that the member is being used with 100% efficiency in a room temperature design; that the Permanent Load is Equal to the Imposed Load; that the Imposed Load will reduce in fire and that Wind Load can be discounted, then;-

$$\text{Fire Test Load Ratio (R)} = \frac{D + 0.8.L}{1.4.D + 1.6.L}$$

with D = L

so, $R = \frac{1.8}{3.0} = 0.6$

The table below, reproduced from BS5950 Part 8 , shows the Limiting Temperatures to be used with protected steel columns for the generalised range of possible Fire Design Load ratios ;-

Table 6. Limiting Temperatures for steel columns

Column Slenderness	Limiting Temp. at Load Ratio of: 0.7	0.6	0.5	0.4	0.3	0.2
	°C	°C	°C	°C	°C	°C
$\lambda \leq 70$	510	540	580	615	655	710
$> 70\ \lambda \leq 180$	460	510	545	590	635	635

NOTE: column slenderness λ = effective length divided by radius of gyration

6.2 *Test Details*

The six columns were fabricated and filled with a commercial structural grade concrete at the Loss Prevention Centre, Elstree. The axial capacity of each column was calculated using BS 5400 part 5 procedures based on measured SHS material properties and the concrete 28 day cube strength and the normal material strength reduction factors. The concrete contribution (α) to the axial capacity was also assessed. The fire test load was taken as 60% of this capacity. Each column would then have a limiting temperature of 540°C, if they behaved in an identical fashion to steel columns.

Table 7. LPC Column Tests- Failure Temperatures

Sp.	SHS Size	Time to Failure	Contrib. Factor α	SHS Limiting Temperature (°C Nominal | Actual
		min		°C	°C
C1	168.3 x 6.3	116.5	0.288	540	610
C2	323.9 x 6.3	165.8	0.465	539	692
S1	150 x 6.3	101.5	0.217	540	613
S2	200 x 6.3	108.8	0.250	540	616
S3	200 x 16.0	116.5	0.117	540	550
S4	300 x 6.3	145.5	0.417	540	661

The temperature -time developments of these columns were also measured and so that estimates could be made of their effective Section Factors for a limiting temperature of 550°C. These and the resulting predicted times for the LPC columns to attain this temperature are given in Table 8 and included in Figure 3

Table 8. LPC Column Tests- Actual and Predicted Times to 550°C

Spec No.	Size	ti	Hp/A (m^{-1})		Time to 550°C (min)	
		mcrn	empty	full	test	reg3
C1	168.3 x 6.3	2444	164.9	42.76	102.0	104.2
C2	323.9 x 6.3	1785	161.9	41.08	115.5	115.5
S1	150 x 6.3	1819	165.7	47.81	95.0	82.9
S2	200 x 6.3	1783	163.9	44.07	105.5	92.8
S3	200 x 16.0	1940	67.93	33.00	116.0	119.6
S4	300 x 6.3	1791	162.1	39.67	128.0	112.0

7 CONCLUSIONS

The indicative test data has produced a specific method to predict the performance of an intumescent paint in fire, In addition, generalised expressions were also obtained for the Effective Section Factors of protected filled SHS that can be used with any type of external protection. Moereover, the full size column tests have confirmed that the same ULS limiting temperatures can be used with both filled and unfilled SHS columns. This should allow full advantage to be taken of the load carrying capacity and improved Section Factor of composite SHS columns in fire.

REFERENCES

British Steel 1992.*Design Manual for Concrete Filled SHS Columns Part 1*, TD 296: Part 1/3E/92, British Steel Tubes and Pipes, Corby, Northants, 1992

The Steel Construction Institute 1994.*Composite Column Design to Eurocode 4, (based on DD ENV 1994-1-1:1994 Part 1.1, with reference to the UK NAD)*, SCI Publication No. 142, The Steel Construction Institute, Ascot, 1994

CIDECT 1995. *Design Guide for Concrete Filled Hollow Section Columns under Static and*

Seismic Loading, Verlag TUV, Rheinland, Koln, 1995

British Standards Institution 1990. *BS 5950 Structural use of Steelwork in building, Part 8. Code of Practice for fire resistant design*, British Standards Institution, London, 1990

.Edwards M. 1998. *Reinstatement of Concrete Filled Structural Hollow Section Columns following Short Duration Fires, Phase 2 - Standard Fire tests on Full Size Columns*, British Steel Tubes and Pipes, Corby, Northants, 1998

Edwards M. in prep. *British Steel Project S2808: Fire Tests on Concrete Filled SHS Indicative Specimens protected by Intumescent Paint,* British Steel Tubes and Pipes, Corby, Northants. (to be published)

Loss Prevention Council 1998. *TE89574; Fire Resistance test on a Loaded SHS Column (168.3 dia x 6.3) filled with concrete and protected by a Nullifire paint system*, Loss Prevention Council, Borehamwood, UK, 1998

Loss Prevention Council 1998. *TE89575; Fire Resistance test on a Loaded SHS Column (323.9 dia x 6.3) filled with concrete and protected by a Nullifire paint system*, Loss Prevention Council, Borehamwood, UK, 1998

Loss Prevention Council 1998. *TE89576; Fire Resistance test on a Loaded SHS Column (150 x 150 x 6.3) filled with concrete and protected by a Nullifire paint system*, Loss Prevention Council, Borehamwood, UK, 1998

Loss Prevention Council 1998. *TE89577; Fire Resistance test on a Loaded SHS Column (200 x 200 x 6.3) filled with concrete and protected by a Nullifire paint system*, Loss Prevention Council, Borehamwood, UK, 1998

Loss Prevention Council 1998. *TE89578; Fire Resistance test on a Loaded SHS Column (200 x 200 x 16.0) filled with concrete and protected by a Nullifire paint system*, Loss Prevention Council, Borehamwood, UK, 1998

Loss Prevention Council 1998. *TE89579; Fire Resistance test on a Loaded SHS Column (300 x 300 x 6.3) filled with concrete and protected by a Nullifire paint system*, Loss Prevention Council, Borehamwood, UK, 1998

Edwards M. in prep. *British Steel Project S2940: Fire Tests on Fully Loaded Concrete Filled SHS Columns protected by Intumescent Paint,* British Steel Tubes and Pipes, Corby, Northants. (to be published)

Tubular Structures VIII, Choo & Van der Vegte (eds) © 1998 Balkema, Rotterdam, ISBN 90 5809 001 9

The effects of fire curves on the temperature of steel tubular members

M. B. Wong
Department of Civil Engineering, Monash University, Melbourne, Vic., Australia
J. I. Ghojel
Department of Mechanical Engineering, Monash University, Melbourne, Vic., Australia

ABSTRACT: The calculation of the thermal response of steel tubular members is based on the heat transfer mechanism between fire and steel. Charts relating the response time of steel tubular members with different shape factors to the temperature of steel in a standard fire have been published, for instance, in CIDECT design guide. It has generally been recognised that standard fire curve is not intended to be used to simulate the real fire situation but to compare performance between structural members. Thus, a structure which fails in a fire according to the standard fire curve may survive in a real fire. In this paper, a method to calculate the thermal response of steel tubular members subject to various fire curves, including both standard and real ones, is presented. This method is based on the heat transfer mechanism between fire and steel. The importance of the gaseous products as a result of combustion which affects the resulting steel temperature is described. Comparison of results based on this method and the CIDECT design charts for standard fire curve is also presented.

1 INTRODUCTION

The trend for fire engineering design is to assess the fire resistance of individual members or sub-assemblies through analytical means. Various methods for calculating the fire resistance of structural members have been proposed in fire engineering design codes in many countries around the world. Among these codes are the AS4100 (1990) for steel structures composed mainly of I-sections, ECCS (1983), FCRC (1996) and CIDECT (1994), the latter of which deals with the fire engineering design for tubular columns only.

Fire resistance calculation consists primarily of two steps : (i) to determine the critical temperature at which individual members or sub-assemblies fail; (ii) to determine the time required for the individual members or sub-assemblies to reach the critical temperature. According to the Eurocodes on structural fire design, assessment can be carried out either through simple calculations with the aids of design tables and diagrams or through general calculation procedures which require detailed knowledge of the thermal and mechanical properties of materials and may require sophisticated computer programs to perform the analysis. FCRC (1996) provides details, to the extent that includes heat transfer and material property equations, to enable general calculation procedures to be carried out whereas CIDECT (1994) provides charts and diagrams for simple calculation procedures.

The advantages and disadvantages of both approaches are obvious : the general approach caters for variations in material and thermal properties, fire curves or even configurations of the structures; the simple approach enables efficient calculations but is restricted to specified parameters such as the use of standard fire curve and heat transfer model. CIDECT (1994) provides charts and diagrams, though without background information for their formulation, to relate the fire resistance, in terms of time, to critical temperatures in terms of members' shape factors. Similar approach is adopted by AS4100 (1990) where regression equations are given to assess the fire resistance.

This paper adopts the general calculation procedures to calculate the thermal response of steel tubular members. It emphasises the importance in having an accurate heat transfer model to predict the steel temperature which may be used to produce charts and diagrams for simple calculation procedures. The heat transfer model adopted in this paper is different from the conventional one (for instance, FCRC (1996)) in that the fire is treated as a participating medium that emits and radiates energy. It will be shown that the gaseous products as a result

of combustion play an important role in transferring the heat flux from the fire to the steel members. This model has been shown (Wong and Ghojel 1997) to give accurate results for I-sections. Its application to steel tubular members under both standard and real fire curves will be shown here.

2 HEAT TRANSFER MECHANISM BETWEEN FIRE AND STEEL

Suppose that a fire occurs in a compartment where a particular steel tubular column is subject to the rising temperature. The heat flux is transferred to the column mainly in two parts, namely the convection part q_c and the radiation part q_r. The temperature rise in the column can be evaluated as a function of the shape factor A_m/V:

$$q_c + q_r = f(A_m/V)\dot{T} \qquad (1)$$

where $\dot{T}$ is the rate of temperature rise and the shape factor is defined as the ratio of the exposed area A_m to the volume V of the member. For a thin-walled tubular member, it can be shown that the shape factor can be approximated as

$$A_m/V = 1/t \qquad (2)$$

where t is the wall thickness of the tube.

The heat flux due to convection is given as

$$q_c = h_c(T_f - T_s) \qquad (3)$$

where h_c = coefficient of convective heat transfer, and T_f and T_s are the respective fire and steel temperatures. In most design codes, for instance FCRC (1996), the heat flux due to radiation is usually given as

$$q_r = \varepsilon\sigma(T_f^4 - T_s^4) \qquad (4)$$

where ε = emissivity of the fire and σ = Stefan-Boltzmann constant. Equation (4) is based on the assumption that combustion products are perfectly transparent to thermal radiation during the heat transfer process between the fire and the column. This process is shown schematically in Figure (1a).

However, the reality in a fire situation is that gases exist in the compartment as a result of combustion. These gases absorb and emit heat energy and act as a transfer medium between the fire and the steel column as shown in Figure (1b). The crux of the current investigation is to assess the way the gases transfer the heat energy. It is found that the gases possess emissivity ε_g and absorptivity α_g, both of which are temperature dependent. Data for ε_g and α_g can be found from Edwards and Matavosian (1984, 1990). The data used here is based on 10% carbon dioxide, 10% water vapour and 80% nitrogen. The resulting equation for heat flux due to radiation can now be modified as

$$q_r = \sigma(\varepsilon_g T_f^4 - \alpha_g T_s^4) \qquad (5)$$

Equation (5) is nonlinear in temperature and, together with equations (1) and (3), can be solved iteratively for the rate of temperature rise in the members.

3 STANDARD FIRE CURVE

Most design codes specify the use of standard fire curve as the basis for prescribed design requirements. This fire curve represents more or less the extreme cases for fires in buildings. Although the curve may vary from one country to another, the difference is not significant. The standard fire curve adopted here is that given in ISO 834 (1975).

Use of the proposed heat transfer model described in the previous section for steel I-sections has been presented in Wong & Ghojel (1997) in which temperatures predicted by equations (4) and (5) in the model are compared. If equation (4) is used for calculating radiation heat flux, the maximum error is about 200°C when compared with observed values whereas the temperatures predicted by equation (5) give excellent match with observed values.

For demonstration purposes, the temperature-time curves of the three SHS columns under standard

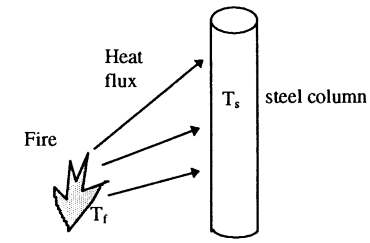

(a) Radiation without heat loss

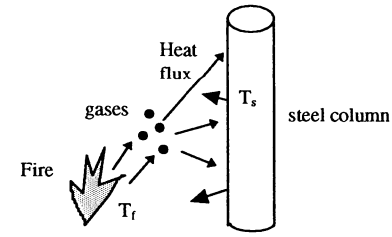

(b) Radiation through gases

Figure 1. Heat transfer model.

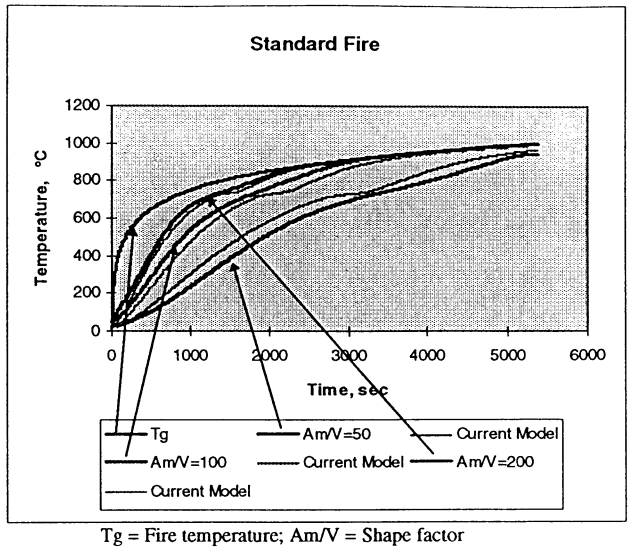

Tg = Fire temperature; Am/V = Shape factor

Figure 2. Temperature comparison between CIDECT (thick line) and current model using standard fire curve.

fire curve given in CIDECT (1994), Fig. 3.4, are compared with the results obtained from the current model. The comparison is given in Figure (2) in which the thick lines represent the results given in CIDECT (1994) and the thin lines represent the corresponding curves predicted in the current model. Both results match reasonably well. Since no information on CIDECT's heat transfer model is given, accuracy due to both methods cannot be compared.

It should be noted from Figure (2) that a sudden delay in temperature rise occurs at a temperature of around 700°C. This phenomenon is due to the sudden surge of the specific heat value of steel at that temperature and is in agreement with the CIDECT curves.

CIDECT (1994), Fig. 3.5, provides a method to estimate the critical time for steel sections with known shape factors if the critical temperature is known. An alternative way to calculate the critical time is to plot curves for the yield strength ratio as a function of time for each given shape factor. This can be done by using the following equation for yield strength ratio, $f_y(T)/f_y$ (20°C):

$$f_y(T)/f_y(20^\circ C) = 1.0 \quad for \quad 0^\circ C \le T \le 215^\circ C$$

$$= (905 - T)/690 \quad for \quad 215^\circ C \le T \le 905^\circ C \qquad (6)$$

The variation of time with the yield strength ratio for a shape factor of 50 m^{-1} is shown in Figure (3).

The main advantage of using this type of curves is that the ratio of action and capacity for a member section is usually proportional to the yield strength ratio as given in equation (6). Hence, the critical time can be readily found from curves similar to that in Figure (3) without even finding the critical temperature.

For example, if a member section with $A_m/V = 50$ m^{-1} is subject to a maximum moment M* of 250 kNm and its moment capacity M is 400 kNm. Hence,

$$\frac{M^*}{M} = \frac{f_y(T)}{f_y(20^\circ C)} = 0.63 \qquad (7)$$

From Figure (3), the critical time for the member section to reach the critical temperature is about 25 minutes.

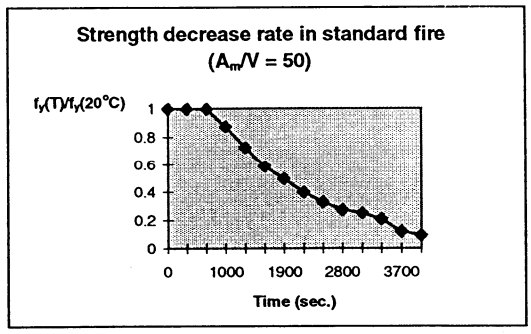

Figure 3. Yield strength in standard fire.

4 REAL FIRE CURVES

Although standard fire curve prescribes a fire scenario which may result in a safe design, it may not be a general representation of what is actually happening during a real fire. For instance, a real fire usually exhibits a peak temperature after which the temperature will drop. In contrast, the standard fire gives an ever increasing temperature curve, representing fire fuel load which will never diminish. This implies that the steel temperature will only increase until the material fails. A structure which fails in a standard fire may survive in a real fire. Thus, it is more realistic to use real fire curves for design of structures which may be cheaper to construct. In fact, many design codes permit the use of real fire curves provided that the steel temperature is properly assessed. It should be emphasised that the real fire curve represents only a simplified but extreme temperature distribution for structural members. In reality, temperature varies at different locations within the compartment in a real fire situation and the difference could be quite significant between the areas aound the floor and the ceiling. Another assumption made in the current analysis is that the tubular member is exposed to the real fire uniformly

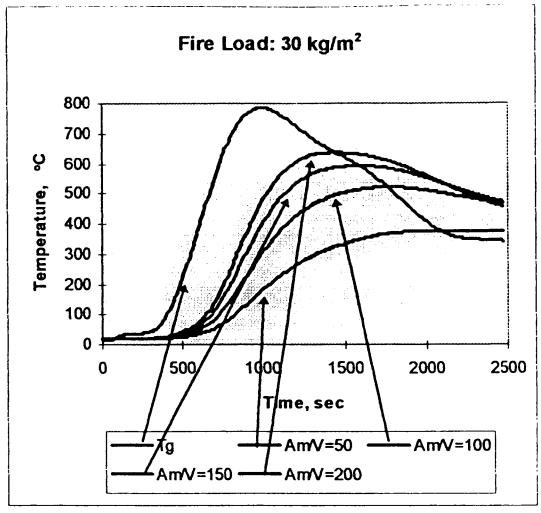

Figure 4. Temperature of steel tubular members under real fire curve.

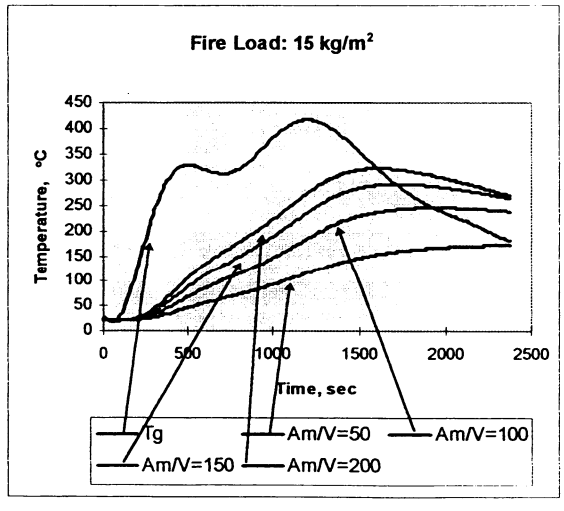

Figure 5. Temperature of steel tubular members under real fire curve.

along its surface. This is indicated by a constant value of A_m/V being adopted in the analysis. This practice is also adopted in CIDECT (1994). The following shows the results of the predicted steel temperature using the proposed heat transfer model in a real fire situation.

Again, for demonstration purposes, two real fire curves of fire loads of 30 kg/m^2 and 15 kg/m^2 as given in CIDECT (1994), Fig. 2.1, are used. Figures (4) and (5) show the predicted temperatures of four steel tubular members with A_m/V = 50, 100, 150 and 200 m^{-1}. It can be seen from Figures (4) and (5) that the higher the fire load, the higher the maximum temperature of the steel members.

For example, the member with A_m/V = 200 m^{-1} shows a peak temperature of about 630°C at about 23 minutes for a fire load of 30 kg/m^2 which is likely to cause failure for the member. However, for the same member under a fire load of 15 kg/m^2 the peak temperature is about 330°C and the member is likely to survive.

It is also noted that the shape factor, hence the thickness of the tubes, is essential in determining the peak temperature. As shown in Figure (4), an increase in thickness of about four times (A_m/V = 200 m^{-1} to A_m/V = 50 m^{-1}) reduces the peak temperature by about 300°C.

5 CONCLUSIONS

A method for calculating the temperature variation with time for steel tubular sections under fire is proposed. This method is based on the general calculation procedures using a heat transfer model which takes into account the effects of gaseous combustion products in fire. This heat transfer model has been shown to give results which are in good agreement with that given in CIDECT design guide for standard fire. Its application to strength determination of members under fire using simple calculation procedures is also demonstrated. The model has been extended for real fire curves and some results are presented.

6 REFERENCES

Standards Australia (1990). *AS4100 - Steel Structures.*

ECCS (1983). *European recommendation for the fire safety of steel structures, ECCS Technical Committee 3 - fire safety of steel structures.* Elsevier, Amsterdam.

Fire Code Reform Centre Limited (1996). *Fire engineering guidelines.* Australia.

CIDECT (1994). *Design guide for structural hollow section columns exposed to fire.* Ed. by Comite International pour le developpement et l'Etude de la construction tubulaire, Rheinland.

Wong, M.B. & Ghojel, J.I. (1997). Time effects on the behaviour of steel structures under elevated temperatures. *Proceedings of the 15th Australasian Conference on the Mechanics of Structures and Materials,* Melbourne, Australia, 8-10 December 1997: 297-302.

Edwards, D.K. & Matavosian, R. (1984). Scaling rules for total absorptivity and emissivity of gases. *J. Heat Transfer,* 106, 684-689.

Edwards, D.K. & Matavosian, R. (1990). Emissivity data for gases. *Hemisphere Handbook of Heat Exchange Design,* Ed. G.H. Hewitt.

ISO, (1975). *Fire resistance tests - Elements of building construction.* International standard ISO 834.



Taylor & Francis
Taylor & Francis Group
http://taylorandfrancis.com

Tubular Structures VIII, Choo & Van der Vegte (eds) © 1998 Balkema, Rotterdam, ISBN 90 5809 001 9

Buckling strength of steel tubular frames under fire

N. L. Patterson & M. B. Wong
Department of Civil Engineering, Monash University, Melbourne, Vic., Australia

ABSTRACT: This paper looks into the elastic buckling strength of slender frames composed of steel tubular members under fire. The mechanical and thermal properties of steel at elevated temperatures are first described. These properties are used to calculate the structural actions induced by the temperature rise. A method is then described for the calculation of the buckling load of frames under fire situation. The method is essentially that of eigenvalue extraction. In carrying out eigenvalue extraction, it is recognised that the buckling load factor should be applied to the static loads only which are separated from the thermal loads. The buckling load calculation leads to a "Unit Load Factor Method" by which the critical temperature of the frame can be calculated. This method assumes that the temperature distribution between the members remains at fixed ratios at all temperatures. Examples are then given to demonstrate the use of this method.

1 INTRODUCTION

Due to their generally low fire resistance, bare steel sections are particularly susceptible to structural degradation when subjected to a fire environment. Even so, where a bare steel structure satisfies regulatory design standards, it is rare that it will collapse in fire, although, depending on the severity of the fire, it may need substantial repair.

The strength degradation of a steel tubular member under fire can be assessed in terms of its mechanical and thermal properties at elevated temperatures. For a structure composed of steel tubular members under fire, the continuous degradation of the members' mechanical and thermal properties may eventually lead to the failure of the structure. For slender structures, failure is likely to be due to frame buckling prior to the onset of material yield.

The buckling load factor in frame buckling analysis may be used to reflect the safety factor of a steel structure at different temperature levels. For fire safety design it is also important to assess the critical temperature at which the structure fails by elastic buckling when the external imposed loads remain constant. It is always the case that the loads will not vary while the temperature is rising in a real fire situation. Previous research (Wong & Patterson 1996a) has been conducted on the critical elastic buckling load factor for I-sections at elevated temperatures. The current investigation focuses on the performance of steel frames consisting of structural hollow sections which, unlike many other section types, have many advantages in construction. Hollow sections possess a high strength to weight ratio and a high stiffness. They are very efficient in resisting both compressive forces and lateral torsional instability. Structural hollow sections are also favoured for aesthetic reasons as well as their versatility. The application of external fire protection to hollow section members is made somewhat easier due to the shape of the cross-section. Not only due to the fact that they have a smaller exposed surface area and a uniformly smooth surface as compared to I-sections but in many cases the hollow part of the section can also be utilised by infilling the tube with certain materials. These materials may be load bearing, ie. concrete, and may therefore effectively reduce the space which the member occupies while maintaining adequate member strength. Also, water may be used as infill material so that the fire resistance level of the member may be increased as the infill may act as a heat sink. BISRA (1990) describes how to design fire protection for structural hollow sections, including concrete-filling, water-cooling and external insulation. CIDECT(1994) and BISRA (1990) have also produced guidelines for the fire resistance calculations of hollow section members under elevated temperatures. Design tables for SHS members have also been published by both the AISC (1991) and DuraGal (1996) in Australia.

2 MECHANICAL & THERMAL PROPERTIES OF STEEL AT ELEVATED TEMPERATURES

The accuracy of structural analysis for steel frames under fire conditions is partly dependent on the accuracy of the relationships which describe the variation in the mechanical and thermal properties of the material at temperatures between 20°C and 1000°C. Uddin & Culver (1975) reviewed past investigations which had been conducted on the mechanical and thermal properties of steel and concrete. BISRA(1992) produced tables for the variations in the mechanical and thermal properties of steel tubes at elevated temperatures.

In this paper, the mechanical properties of steel under elevated temperatures are modelled according to Australian Standard AS4100-1990 Steel Structures Code. The three main steel properties which are usually taken into account for elevated temperature analysis are the yield stress, the modulus of elasticity and the coefficient of thermal expansion. The degradation of yield stress with temperature is omitted in the determination of the elastic response of a structure even though plastic deformation commences before the occurrence of instability. This may result in an overestimation of the elastic buckling load capacity for lower temperatures. The variation in mechanical properties for the elastic response of steel are defined as follows:

2.1 *Variation of modulus of elasticity*

AS4100 models the variation of modulus of elasticity of steel with temperature according to recommendations by CTICM (1982). This variation for the modulus of elasticity has been adopted in the current investigation.

Where a temperature gradient exists in the cross-section of a member, the effective modulus of elasticity for the whole cross-section can be approximated by using the value of the modulus of elasticity which corresponds to the average of the temperatures at the top and bottom of the cross-section. Although this may be a simple and efficient approximation it is not necessarily an accurate one. In fact the variation in the values of the modulus of elasticity with temperature is not linear and therefore the average temperature does not specifically relate to the average modulus of elasticity. Therefore a more accurate representation may be necessary to take into account the variation of the temperature across the cross-section. The mathematical expression for the effective modulus of elasticity being used in the current work for the whole cross-section is given in Equation 1, where I is the strip number in the section and I_i and $E(T)_I$ are respectively the second moment of area and modulus of elasticity at temperature T of the individual strips.

$$E(T)_{effective} = \frac{\sum (E(T)_i I_i)}{I_{effective}} \qquad (1)$$

In the case of circular hollow sections the subdivision of the cross-section is as shown in Figure 1 for a linear variation of temperature from T1 to T2.

In Figure 1, the section is divided into elements such that there is a horizontal boundary between adjacent elements for every two-degree angle subtended at the geometric centroid, thus creating ninety horizontal elements throughout the section. For this method, each element is assigned with the appropriate temperature which varies linearly along the vertical axis of the cross-section as shown in Figure 1.

2.2 *Coefficient of thermal expansion*

The value of the coefficient of thermal expansion is based on tests carried out by BISRA (1953) and the ECCS. Although the coefficient of thermal expansion for steel, α_t, varies with temperature as recommended by these two authorities, AS4100 adopts a constant value of 11.7×10^{-6} /°C. At higher temperatures this may result in an over-estimation of thermal expansion effects, leading to an earlier system collapse. The validity of a constant value for α_t as recommended by AS4100 regardless of the temperature variation has been investigated by Patterson & Wong (1997), who found that there was no significant effect on the buckling strength for steel frames at elevated temperatures compared with values for which α_t varies with temperature. Therefore in the current investigation, a constant coefficient of thermal expansion as recommended by AS4100 is adopted.

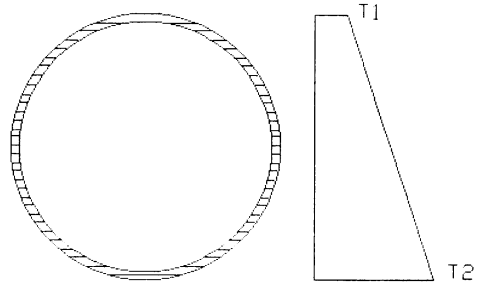

Figure 1. Subdivision of section for temperature gradient.

3 STRUCTURAL ACTIONS INDUCED BY A TEMPERATURE RISE

In general, an increase in temperature of a steel member will produce expansion according to Equation 2, where α_t is the coefficient of thermal expansion and $\Delta T(y)$ is the increase in temperature for a particular point at a distance y from the extreme fibre in the cross-section. The value adopted for α_t was detailed in the previous section.

$$\varepsilon_T = \alpha_t \Delta T(y) \qquad (2)$$

When a member is not restrained, it will undergo free expansion under fire conditions without inducing stresses in the cross-section. However, when the member is restrained, axial force will be induced. The induced axial force N_T within the member can be calculated according to Equation 3.

$$N_T = \int_A \sigma_T \, dA \qquad (3)$$

where $\sigma_T = E(T)\varepsilon_T$, the stress induced by the temperature rise, E(T) is the temperature-dependent modulus of elasticity, and A is the cross-sectional area of the member.

If the temperature in the steel member varies across the cross-section, a bending moment will also be induced by the thermal expansion of the steel. This bending moment, M_T, can be calculated according to Equation 4.

$$M_T = \int_A \sigma_T \, y \, dA \qquad (4)$$

The calculations of these self-straining forces N_T and M_T are essential in the buckling analysis for steel structures at elevated temperatures as detailed below.

4 ELASTIC BUCKLING ANALYSIS

The calculation of the elastic buckling load factor λ for a slender frame consisting of steel hollow sections under fire is essentially an eigenvalue extraction process.

The equilibrium equation of a structure can be described by P = [K]x where P is the force vector, [K] is the stiffness matrix and x is the displacement vector of the frame. In elastic buckling analysis for structures at elevated temperature, the stiffness matrix [K] is modified so that the axial forces in the members due to the effects of the static loads are separated from those due to the thermal loads. In the usual manner where static loads are multiplied by the elastic buckling load factor λ in formulating the eigenvalue problem, Equation 5 can be obtained, where $[K_e]$ represents the elastic stiffness

$$\left| \lambda \left[K_G^1 \right] + \left[K_G^2 \right] + \left[K_e \right] \right| = 0 \qquad (5)$$

matrix and $[K_G]$ the geometric stiffness matrix of the frame. In Equation 5, the superscript 1 denotes the geometric stiffness matrix assembled from those of the members with axial forces induced by the static loads whereas the superscript 2 denotes the same with axial forces induced by the thermal loads.

It is more convenient to express Equation 5 in the following form for eigenvalue extraction:

$$\beta x = \left[K \right]^{-1} \left[K_G^1 \right] x \qquad (6)$$

where

$$\left[K \right] = \left[K_e \right] + \left[K_G^2 \right] \qquad (7)$$

and β is the inverse of the elastic buckling load factor, λ.

The axial forces in the members due to the thermal loads are obtained from linear analysis in response to the forces calculated from Equations 3-4.

5 UNIT LOAD FACTOR METHOD

Fire resistance is a design requirement where the structure is required to withstand the effects of fire without failure within a specified time. One of the crucial parameters in calculating the fire resistance is the critical temperature at which collapse of the structure is imminent. Unlike the usual plastic analysis where the critical collapse load factor is obtained on the basis of a set of proportionally increasing loads, the critical temperature is obtained when the external loads are constant. In other words, the critical temperature of the structure corresponds to a structural state when the collapse load factor, in the present case λ, is equal to one. This concept for evaluating the critical temperature leads to the development of the 'Unit Load Factor Method' which has been used to predict critical temperature for elastic steel frames consisting primarily of I-sections (Wong & Patterson 1996b). This method assumes that the temperature distribution between the members remains the same or at fixed ratios for all temperatures. The technique in using this method requires the determination of the critical temperature (for members with the same temperature) or critical temperature multiplier (for members with temperatures at fixed ratios) for which there will be a corresponding zero determinant for the structure stiffness matrix. The main difficulty in using this method is to match a critical temperature with a unit load factor because the

properties of steel change invariably with temperature. In order to overcome this difficulty, an interpolation technique is adopted to determine the critical temperature corresponding to a unit elastic buckling load factor, $\lambda = 1.0$. This technique is exemplified in Figure 2 where T_D and T_E are two temperatures corresponding to two values of λ below and above 1.0. The critical temperature which corresponds to $\lambda = 1.0$ for the frame is denoted by $T_{1.0}$ which can be obtained by linear interpolation. The technique requires the calculations of a number of elastic buckling load factors at different temperatures as described in the previous section.

6 EXAMPLES

A report produced by BHP (1990) found that in an office which consisted of bare steel structural members, the maximum temperature reached in the steel in a fire was about 600°C. Temperatures above this maximum are therefore considered unlikely to occur. In the following examples, analysis will be carried out up to 600°C, beyond which the critical temperature will be obtained through extrapolation.

6.1 *Uniform temperature*

Two frames as depicted in Figures 3-4 were used as examples in the current investigation. These frames were analysed by subjecting them to a number of uniform temperatures between 20°C and 600°C at multiples of 100°C. The results of the analyses are shown in Table 1. The critical temperature at which the elastic buckling load factor λ=1.0 is also shown.

The section sizes and properties in the examples were taken from the AISC design capacity tables for structural hollow sections. All steel members used were Grade 350.

For Frame 1 shown in Figure 3, the vertical members are 4m long, 219.1 x 6.4 CHS. The horizontal members are 6m long, 168.3 x 6.4 CHS. The diagonal members are 168.3 x 6.4 CHS.

For Frame 2 shown in Figure 4, the vertical members are 4m long, 219.1 x 6.4 CHS. The horizontal members are 6m long, 114.3 x 4.8 CHS. The diagonal members are 168.3 x 6.4 CHS.

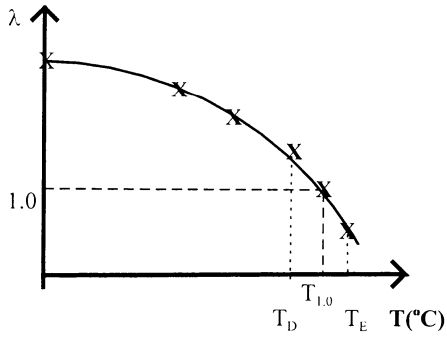

Figure 2. Unit Load Factor Method for critical temperature analysis.

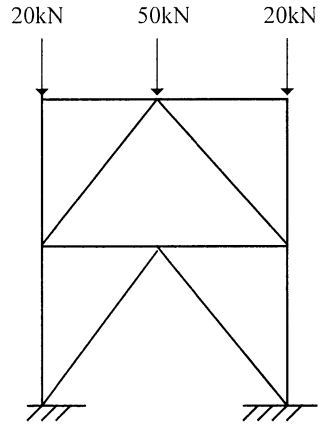

Figure 3. Example: Frame 1.

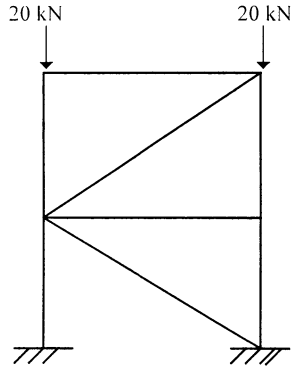

Figure 4. Example: Frame 2.

Table 1. Results of buckling load factor for tubular frames subjected to a uniform temperature increase.

	Elastic Buckling Load Factor (λ)	
Temperature	**Frame 1**	**Frame 2**
20° C	52.049	169.106
200° C	41.181	136.771
300° C	33.504	102.408
400° C	25.103	63.526
500° C	16.176	31.209
600° C	7.094	2.763
λ = 1.0	667.1° C	606.3° C

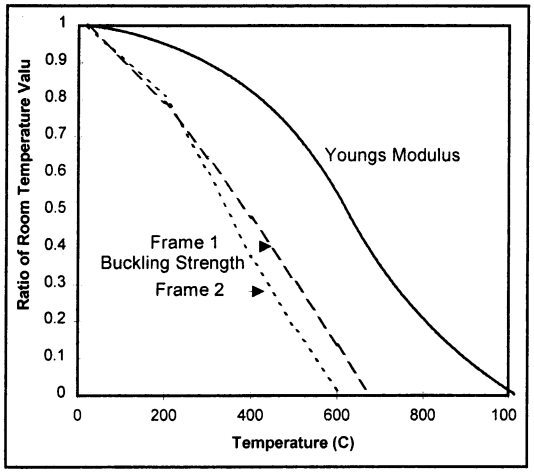

Figure 5. Plot of ratios between elevated temperature and room temperature values for Youngs Modulus and the buckling strengths of Frames 1-2.

As can be seen from the results in Table 1, the increase in temperature corresponds to a decrease in the elastic buckling load factor of the frame. This is due to the fact that while the temperature in steel increases, its material and thermal properties decrease, leading to a decrease in the strength of the frame. This is highlighted in Figure 5 which shows a plot of the degradation in elastic buckling strength of the two frames relative to their room temperature values. In this figure the relative reduction in Youngs Modulus with temperature is also shown.

6.2 *Temperature gradient*

In order to demonstrate the effect of an existing temperature gradient in members on the elastic buckling load factors, two examples were used.

The first example is again Frame 2 as shown in Figure 4 but with modification. The modification is that all members are 168.3 x 6.4 CHS. The original lengths have been retained.

The second example is Frame 3, shown in Figure 6. For this example all members are 114.3 x 4.8 CHS. Both the horizontal and vertical members in this example are 4m. Two concentrated loads of 20 kN are applied on top of the vertical members.

The members in each of the frames were subjected to a linearly varying temperature gradient across their sections, (as illustrated in Figure 1), of 200°C over different temperature ranges.

Two methods were used to calculate the modulus of elasticity of the cross-section. The first method (denoted as method 1) is based on the average temperature of the cross-section. The second method (denoted as method 2) is based on the effective modulus of elasticity as described in section 2.1. The equivalent temperatures which will be used to calculate the effective modulus of elasticity of the cross-section using both methods are shown in Table 2. It can be seen that a maximum difference of about 35°C occurs. These values for the equivalent temperatures were then used in an analysis to obtain the elastic buckling load factor. The results of the analyses are shown in Table 3.

It is obvious from the results shown in Table 3 for frames subjected to different temperature ranges, that
little difference results in the elastic buckling load factor when either method is used for calculating the equivalent modulus of elasticity of the members. It

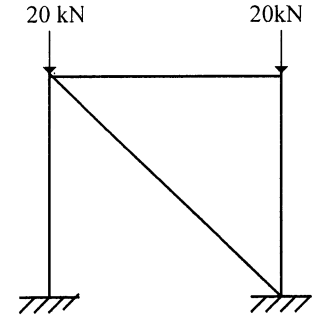

Figure 6. Example: Frame 3.

Table 2. Equivalent temperatures of sections using two different methods.

		Temperature gradient - upper (or outer) to lower (inner) face (°C)					
		20 - 200	**200 - 400**	**300- 500**	**400 -600**	**500 - 700**	**600 - 800**
Method 1 Temperature		110	300	400	500	600	700
Method 2 Temperature	**114.3 x 4.8**	118.13	265.83	384.79	504.47	606.21	691.53
	168.3 x 6.4	119.31	267.16	385.77	505.2	606.66	692.16
	219.1 x 6.4	121.5	269.88	387.79	506.74	607.61	693.51

Table 3. Results of elastic buckling load factor for tubular sections with temperature gradient

Temperature gradient	Elastic Buckling Load Factor (λ)			
	Modified Frame 2		Frame 3	
	Method 1	Method 2	Method 1	Method 2
20°C	214.262		80.010	
20°C - 200°C	177.902	175.743	76.656	76.202
200°C - 400°C	131.071	142.097	61.899	65.029
300°C - 500°C	96.513	101.498	51.564	53.220
400°C - 600°C	61.142	59.266	39.647	39.069
500°C - 700°C	25.572	23.339	25.523	24.580
600°C - 800°C	3.732	4.926	13.878	14.655

can therefore be concluded that both methods will produce a similar critical temperature for a given steel frame.

7 CONCLUSIONS

A method for the calculation of elastic buckling load factor for slender frames consisting of steel hollow sections in fire conditions was presented. This method involves the solution to an eigenvalue problem in which the axial forces due to both the static loads and the thermal loads are calculated separately. The method accounts for the strength degradation of the steel members by including the change in the mechanical and thermal properties of steel at different temperatures.

It has been shown that by progressively increasing the temperature of the structure until a value for the elastic buckling load factor close to unity is found, linear interpolation may be used to calculate the limiting temperature of the structure. This is described as the Unit Load Factor Method.

Investigation was also carried out to examine the effect of using two different methods to calculate the equivalent temperature of a cross-section where a temperature gradient exists. It was found that although there may be a difference in the equivalent temperatures produced using the two methods, the effect on the elastic buckling load factor is minimal.

8 REFERENCES

AISC : *Design capacity tables for structural steel.* 1st edition 1991, DCT/01-1991.

BHP Melbourne Research Laboratories (1990). Fire in Mixed Occupancy Buildings. *Report No. MRL/PS69/89/004* August 1989.

BISRA (1953). *Physical Constants of some commercial steels at elevated temperatures.* Butterworths Scientific Publication, London.

BISRA (1990). *Fire resistance design for SHS to BS5950 Part 8.*

BISRA (1992). Steel Tubes and their high temperature properties. *Report TD 270/5E/87R.*

CIDECT (1994). *Design guide for structural hollow section columns exposed to fire.* Ed. by Comite International pour le developpement et l'Etude de la construction tubulaire, Rheinland.

CTICM (1982). Methode de prevision par le calcul du comportment au feu des structures en acier. *Constr. Metall.*, 19, 39-79.

DuraGal (1996). *Design capacity tables.* Tubemakers structural and pipeline products.

Patterson, N.L. & Wong M.B. (1997). Influence of Coefficient of Thermal Expansion on Steel Frame Strength. *Proceedings of the 15th Australasian Conference on the Mechanics of Structures and Materials*, Melbourne, Australia, 8-10 December 1997: 291-296.

Standards Australia (1990). *AS4100 - Steel Structures.*

Syam, A.A. & Chapman, B. G. (1996). *Design of structural steel hollow sections.* Volume 1: Design models, 1st edition.

Uddin, T. & Culver, C.G. (1975). Effects of elevated temperature on structural members. *Journal of the Structural Division, ASCE*, Vol 101, No. ST7.

Wong, M.B. & Patterson, N.L. (1996a). Buckling strength of steel frames under elevated temperatures. *Third Asian-Pacific Conference on Computational Mechanics*, Seoul, Korea, 16-18 September 1996: 473-478.

Wong, M.B. & Patterson, N.L. (1996b). Unit load factor method for limiting temperature analysis of steel frames with elastic buckling failure mode. *Fire Safety Journal*, Vol. 27, 113-122.

Tubular Structures VIII, Choo & Van der Vegte (eds) © 1998 Balkema, Rotterdam, ISBN 90 5809 001 9

Advanced structural fire design of offshore structures

T. Holmas
SINTEF Civil and Environmental Engineering, Norway
J. Amdahl
Norwegian Institute of Science and Technology (NTNU), Department of Marine Structures, Norway

ABSTRACT: Resistance against extreme loading has to be documented for offshore structures. Fire is a continuos threat as large amounts of oil and gas are passing through the installations. In a conventional design procedure, the 'cold' structure is optimized for the different mechanical loads. The responsibility of the structure is then transferred to the safety department, which normally recommend use of passive fire protection as the only way to avoid structural failure during fire. Including fire in the design process will result in more fire resistant structures which means reduced use of passive fire protection and thereby reduced initial and maintenance costs. Better understanding of the structural behavior under fire exposure opens also for extended use of light alloy structures. Design against accidental fires should be included in the design process conducted by the structural engineers in close cooperation with the safety department.

1 INTRODUCTION

Adequate resistance against extreme loads has to be documented for offshore structures. Accidental fires are a continuos threat as large amounts of oil and gas are passing through the installations. The requirements to the structures are based on general safety studies, and are often expressed as minimum time to failure of the most important structures exposed to on or more fire scenarios.

Structures exposed to fire will be heated up, and the heating rate is dependent on the intensity of the fire, the surface/mass ratio of structural components, the surface properties of the actual material and finally the presence of passive fire protection covering the surface.

The main effects of the heating are thermal expansion, reduced elastic modulus and yield stress and creep. Thermal expansion takes place from the very beginning, and due to the fact that the different components will be heated differently (different exposure and surface/mass ratio), the thermal expansion will vary from one structural component to another. The thermal expansion results in member axial forces and bending moments. Thin walled components are the most vulnerable, and if the ends are restrained member buckling take place even for moderate temperature increase, (ΔT=100°C). As the yield stress and E-modulus reduce, and after a given time the whole structure may collapse.

In a conventional design procedure the 'cold' structure is designed and optimized by the structural engineer for the different loads. The "responsibility" for the structural performance is transferred to the safety department. The major measure to avoid structural failure is by using *passive fire protection,* i.e. thermal insulation slowing down the heating of the structural components. The requirements to the protection is expressed as maximum allowable temperatures after a given time (for instance 400°C after 1 hour). The necessary thickness of the passive fire protection is taken from tables depending on the surface to mass ratio (*HP/A ratio*), the fire exposure, maximum accepted structural temperature and the fire duration. Normally, this work is carried out by safety engineers who seldom have their background

from structural engineering and *thus may have problems to suggest alternative structural design.* One consequence of using the temperature criterion for determining the passive fire protection is that the smallest components get the largest thickness and vice verse.

The fire scenarios used in design are often limited to standardized uniform 'fires' (e.g. 200 kW/m^2) which are assumed to expose all structural members "all way around" from the very beginning to the very end of the fire. Such assumptions are often overly conservative, yielding excessively high costs for fire protection. In some cases it may exclude the use of f ex light weight material such as aluminum alloys.

By contrast to such simplistic considerations, advanced computational fluid mechanics (CFD) codes recently developed allows accurate simulation of the combustion process from the ignition to termination. It is possible to trace differences in exposure of the various structural components giving a far better description of the real fire.

Similarly, advanced non-linear structural analysis tools are available. By simulating the mechanical response of structures exposed to fire it is possible to document and evaluate the consequences of a fire in a much more physically correct manner. It is possible to trace failure of components, force redistribution and global failure during the fire. With this knowledge it is possible for the structural engineer to suggest a more optimum design of the structure with respect to the effects of fire. In particular, alternatives to passive fire protection can be evaluated.

2 FUNDAMENTAL BEAM BEHAVIOR

To describe the behavior of complex structures exposed to fire, it is necessary to understand the fundamental behavior of the structural members.

2.1 *Simplified beam behavior*

The simply supported axially free beam shown in Figure 1 carries the midspan force by bending, and in connection with linear design, no axial forces are introduced.

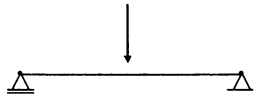

Figure 1. Simply supported beam.

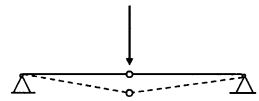

Figure 2. Fixed beam with middle hinge.

The hinged beam described in Figure 2 which is axially fixed in both ends, is assumed to carry the same force through *axial forces* only (pure membrane). In this simple example, the change in geometry due to *stress induced strain* is disregarded.

The two static systems will have a very different behavior during fire.

For the simply supported beam, the elongation of the beam due to thermal expansion will not change the system, but the material degradation due to increased material temperature will reduce the bending capacity.

For the hinged beam the thermal elongation of the beam introduces lateral deflections as indicated by the dotted lines. This deflection changes the load carrying system in a *positive* manner: Increased deflection results in increased capacity.

To demonstrate these effects, the following simple example is given:
Assume a steel pipe with diameter 1.0m and thickness 50 mm spanning 10 m. The steel with initial yield stress 350 MPa is assumed to be degraded according to Eurocode 3, /4/.

For the simply supported beam the ultimate midspan force P_u is taken as:

$$P_u = 4\ \sigma_y\ W_p / L \qquad (1)$$

where

σ_y : Current yield stress
W_p : Plastic sectional modulus
L : Span length

For the hinged beam following ultimate midspan force is taken:

$$P_u = 2\ \sigma_y\ A\ \sin(\varphi) \qquad (2)$$

where

σ_y : Current yield stress
A : Cross section area
φ : Angle = ArcTan ($2\delta/L$)
δ : Midspan deflection

The midspan deflection caused by thermal expansion only is expressed as follows:

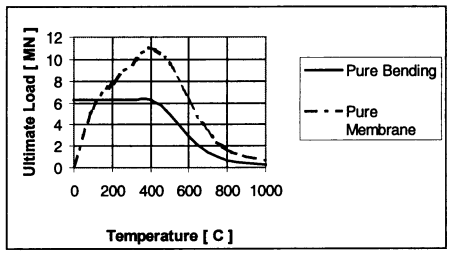

Figure 3. Bending capacity versus membrane as function of temperature.

$$\delta^2 = [\, L/2\,(\,1 + \alpha T\,)\,]^{\,2} - (\,L/2\,)^{\,2}$$
$$= L^2/4\,(\,2\,\alpha T + \alpha^2 T^2\,) \qquad (3)$$

where

α : Thermal expansion coefficient
T : Temperature increase of beam

For the simply supported beam the capacity as given by Equation (1) is governed by the degradation of the yield stress. The equation is used for varying temperature of the beam which means changed yield stress. The initial capacity of 6.3 MN is kept unchanged up to 400° C, and then the capacity drops according to the material degradation curve.
For the axially restrained beam the capacity as given by Equation (2) is governed by the degradation of the yield stress as well as the angle φ. With an initial deflection equal to zero, the capacity curve of the hinged beam starts in zero when the stress induced strain is disregarded, (sin (0)=0). Increasing temperature results in increased deformation which means *improved membrane load carrying*, see equations (2) and (3). When the temperature passes 400°C, however, the material degradation is stronger than the improved geometric stiffness due to further increase of the midspan deformation, and the capacity drops. In Figure 3 the "ultimate" capacity is shown as function of temperature for the two simplified cases. The current maximum of the two cases are plotted in Figure 4.

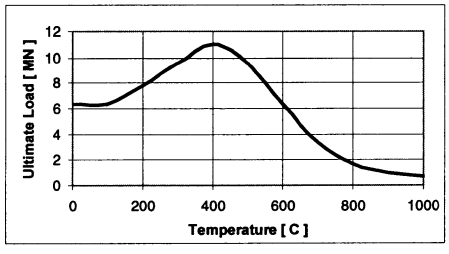

Figure 4. Ultimate capacity of the simplified beam.

This simple "linear" approach shows that membrane effects represents a substantial reserve which should be utilized in connection with extreme load situations where requirement to deflections are less than under normal, service conditions.

2.2 *Advanced beam behavior*

In the above example, pure bending and pure membrane effects have been demonstrated under fire conditions. In a real case both membrane and bending effects take place at the same time limited by current plastic interaction of the cross section. With increasing temperatures, the yield surface shrinks. In the following, the example described in the previous section is used without the middle hinge inserted.

In Figure 5 the plot of midspan bending moment versus axial force at temperature 250°C shows that after pure bending, compression forces are introduced due to thermal expansion.
Due to second order effects, the midspan bending moment increases with the increasing compression force. At same point the member buckles, and the axial force is being relieved. At this point the response is governed by the plastic interaction between axial force and bending moment. Later the response travels through the initial condition with pure bending, see Figure 6. However, by further increase of the deflection the axial force will turn from compression to tension.

The yield surface is reduced continuously. New equilibrium conditions must be established always limited by the current size of the yield surface. The mechanical load which is kept constant during the heating, is carried more and more by membrane effects. The force state at 600°C is shown in Figure 6.

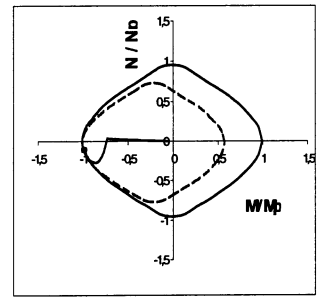

Figure 5. Yield surface and force path at 250° C.

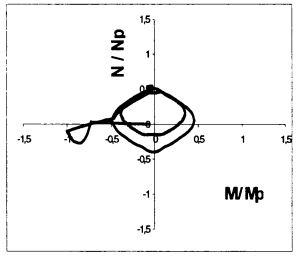

Figure 6. Yield surface and force path at 600° C
Both ends translation fixed

The beam now carries the lateral force by pure membrane action.

Without fully fixation in both ends, the beam will have a very different behavior. No compression forces will be introduced due to thermal expansion, and the beam will carry the load by bending throughout the whole heating process. Figure 7 describes the force state for the simply supported axially free beam at 600°C.
Similar to the simplified case described in 2.1 the *ultimate capacity* of the beam as a function of the temperature with different boundary conditions are calculated utilizing the non-linear computer code *USFOS* /1/. The beams are first heated up to the actual temperature and then the mechanical load is applied. Each calculation terminates when the midspan deflection exceeds 0.75 m in this example. Stress induced strain as well as thermal expansion effects are included. The example demonstrates the much higher capacity of an axially fixed beam compared to one with free ends. *This documents the importance of designing the joints for the ultimate member forces including accidental loading rather than optimizing the connections for the actual forces in "cold" condition.*

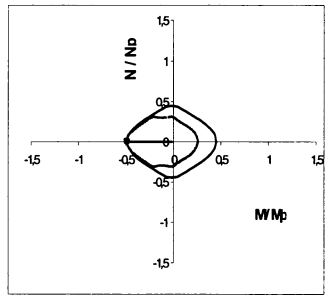

Figure 7. Yield surface and force path at 600° C.
No axial fixation.

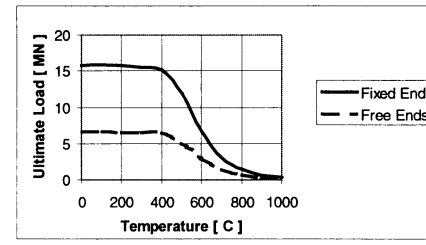

Figure 8. Ultimate beam capacity versus temperature.

2.3 *Column behavior*

Columns have a very different behavior under fire exposure than beams. No inherent reserves are available due to large deformation – rather the opposite is the case as any disturbance from straight configuration will reduce the ultimate capacity.

Several factors influence the ultimate capacity of the column:

- Reduction of yield stress
- Reduction of stiffness (E-modulus)
- Uneven exposure and associated uneven thermal expansion over the cross section causing column curvature
- Thermal expansion which may lead to column buckling depending on the column boundary conditions

Figure 9 describes the ultimate load as function of temperature of a steel column. The temperature is uniform over the cross section (no gradients), and following column data is used:

Outside diameter:	Do	=	355 mm
Thickness:	T	=	25 mm
Length:	L	=	6 m

The material properties are assumed to be degraded according to Eurocode 3, /4/.
The column is first heated up to the actual temperature, then the axial compression force is applied until the column buckles. The ultimate (peak) force level is recorded for each case.

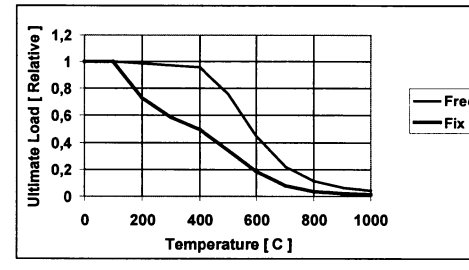

Figure 9. Ultimate load of free and fixed column

In the "free" case, the column is free to expand axially. In the "fixed" case the column upper node is free to move inwards, but is fixed in the outward direction. This means that thermal expansion may cause column buckling before the mechanical load is applied.

The ultimate load is given relative to the initial "cold" situation.

In the "free" case the buckling load is little influenced by temperatures up to 400°C as the ultimate load is primarily governed by the material yield stress. A slight decrease caused by the E-modulus degradation is observed for this particular column.

The "fixed" case the ultimate capacity is influenced by the temperature already from slightly above 100°C. This is mainly caused by thermal expansion forcing the column into a bent configuration. This out-of –straightness reduces the ultimate capacity significantly when the column is subsequently loaded in compression.

The two curves represent the limits for "real life" column behavior; in practice the capacity curve will be somewhere between the two extremes

3 BEHAVIOR OF PLANE FRAMES

The next case to be studied is a portal frame braced with an X-trusswork, Figure 10 and a K-trusswork Figure 11. The frame is loaded with a horizontal force, which is primarily carried by tension and compression in the braces. The X-truss represents an indeterminate structure in the sense that once the compression brace fails, it load can be shed to the tension braces. The K-truss is a determinate structure. Equilibrium requires that the compression brace carries the same force as the tension brace. Hence, failure of the compression brace signifies global failure of the frame.

The frames are first subjected to uniform heating followed by application of the mechanical load. The ultimate strength is recorded for all cases and normalised against the capacity at normal temperature.
During heating very small thermal strains are induced in the K-brace analogous to the axially free case of Section 2.3. Failure of the compression brace is again predominantly governed by the reduction in the yield stress and elastic modulus, but a further

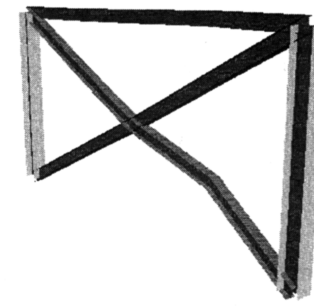

Figure 10. Horizontal loaded X-Truss exposed to fire.



Figure 11. Horizontal loaded K-Truss exposed to fire.

reduction in the buckling strength is also attributed to a frame induced lateral deformation.

Conversely, due to the static indeterminacy significant thermal strains are induced in the X-truss-work, closer to the axially fixed case in Section 2.3 The compression brace fails early in the heating process, but this does not of, course, signify ultimate strength. Global failure occurs when the tension brace reaches yield.

Figure 12 displays the normalised capacities for the frames. It is seen that both curves lies within the domain spanned by the axially free and axially fixed

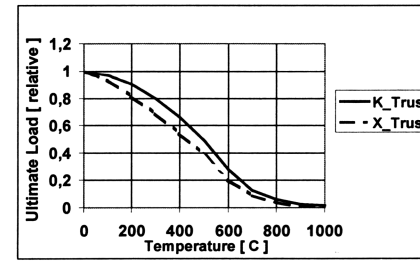

Figure 12. X-Truss versus K-truss behavior during fire.

cases plotted in Figure 9. The X-truss suffers the largest *relative* reduction of ultimate capacity. The *absolute* strength is nevertheless larger.

4 OFFSHORE STRUCTURE EXPOSED TO FIRE

4.1 *Background*

The steel frame bridge composed of tubular members shown in Figure 13 connects two offshore oil platforms in the Northern Sea.

The bridge has two main functions: Supporting hydrocarbon pipelines and human traffic. In connection with fire the bridge is a part of the escape routes which must remain intact for a given time. In addition it is of great importance that the pipelines do not break and then cause escalation of the fire.
From the safety studies the actual heat flux (or gas temperature) associated with the assumed "fire-on-sea" scenario is found. The bridge is not subjected to direct exposure of the fire and is assumed mainly to be exposed to smoke gases, (approx. 40 kW/m^2). It is required that the bridge should withstand the fire with substantial margin at least for 1 hour.

4.2 *Conventional fire design*

In a conventional design procedure, the structural department optimizes the steel based on the mechanical loads only. The structural response due to member heating is disregarded except for checking of necessary clearances in connection with thermal expansion.

The structural engineers presuppose that the member temperatures do not exceed a given temperature, 400°C is a widely used temperature threshold. At this temperature the steel maintain most of the initial (cold) properties.

The "responsibility" of the structure is then transferred to the safety department.

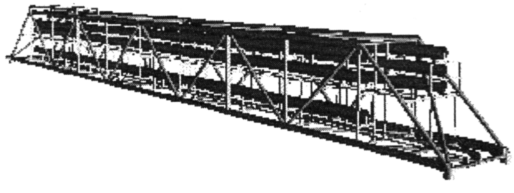

Figure 13. Bridge connecting two offshore oil platforms supporting hydrocarbon pipelines

The safety engineers will normally use *passive fire protection* (PFP) to protect the structure. The thermal insulation will slow down the heating of the structural members avoiding the members to reach f ex 400°C within 1 hour. Correct thickness of the selected PFP product is found by utilizing the surface to mass ratio (*HP/A ratio*) which means in practice that the smaller members (easiest to heat up) get the largest thickness of PFP and vice verse.

In this particular example approx. 1500 m^2 surface was to be protected. With a minimum thickness applied of a typical spray-on product this results in approx. 8 ton passive fire protection.

4.3 *Advanced Fire Design*

Application of passive fire protection on exterior surfaces which are exposed to rough Northern Sea climate represents a maintenance challenge. Covering the whole surface with f ex a spray-on product makes it hard to inspect welds etc for fatigue cracks. Corrosion on the steel surface may cause the PFP to loosen and fall off.

Avoiding use of passive fire protection is then of great interest.

Assuming the heat fluxes from the safety studies to be design requirements, the computer code *FAHTS* (*Fire And Heat Transfer Simulations*) /2/ is used to simulate the individual member temperature histories. The design finite element model of the bridge is automatically transferred to surface shell elements by the code in order to capture the thermal effects over the cross section.

Simulations of the unprotected structure result in member temperatures up to approx. 650°C. At this temperature the steel has "lost" more than 50% of the initial strength. The temperature history for each individual structural member are transferred automatically to the mechanical response module *USFOS*. Both FAHTS and USFOS have been verified against large scale testing of a fire exposed 3D tubular frame /3/.

In connection with the USFOS simulations the following analysis procedure is used:

- Apply deadweight (loadfactor=1.0)
- Apply member heating (results from FAHTS)
- Increase deadweight up to system collapse

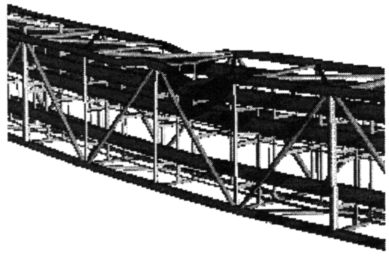

Figure 14. Collapse mode due to fire. Original design

Figure 14 shows the collapse mode of the original design configuration. The compression members in the upper girders at midspan buckle with a load factor of the permanent loads equal to 1. This is an unacceptably small margin.
The first modification is to increase the wall thickness of the upper girder tubular members. The idea is to prevent member buckling.

New simulations are carried out with the modified structure. However, now it is observed that member buckling takes place at the supports, see Figure 15. System failure corresponds to a load factor =1.05.
Increasing the wall thickness of the most exposed diagonal members gives a substantial increase of the collapse load. In Figure 16 the midspan deflection versus load factor is presented for the three cases. Linear behavior is observed for all 3 cases up to a load factor of 1.0 causing a midspan deflection of approx. 0.12 m. The fire is then applied causing the deformation to increase to approx. 0.5m mainly due to reduced E-modus. Further increase of the mechanical load results in a very early system collapse for the two first cases. For the third case (final design), the system does not collapse before a load factor of 1.6 is reached. A rather 'linear' path is observed up to the peak, and the slope is approx. 1/3 of the initial slope which corresponds well with the fact that the E-modulus is reduced to approx. 1/3.

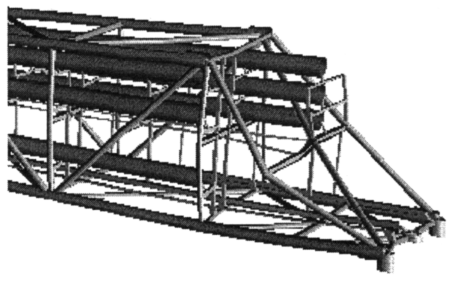

Figure 15. Collapse mode due to fire and with 5% overload. First modification.

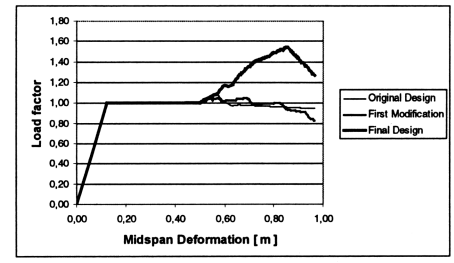

Figure 16. Midspan deflection versus load factor for three design alternatives.

The bridge situation at the peak load level of 1.6 is presented in Figure 17 with unscaled displacements.
The increase of the steel weight caused by the increased wall thickness of some compression members represents 1% of the total permanent load. The saved weight by using no passive fire protection represent the same mass which means that *the total weight of the bridge is unchanged.* The fabrication and maintenance *costs* are, however, *substantially lower.*

5 CONLUSIONS

The importance of including the accidental fire in the design process is documented.

Advanced computer codes which have been verified against large 3D tests simulating structural behavior during fire might be an efficient and reliable tool for the structural engineer.

Increased knowledge about structural behavior under fire opens for more fire resistant structures, reduced fabrication and maintenance costs and extended use of light metal structures.

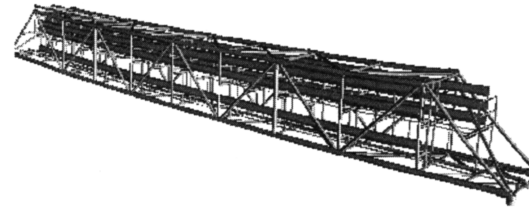

Figure 17. Final Design. Situation after 1 hour fire and 60% overload.

6 REFERENCES

/1/ USFOS. Ultimate Strength of Frame Offshore Structures. User's Manual, SINTEF Report STF71 F88039.

/2/ FAHTS Fire And Heat Transfer Simulations User's Manual, SINTEF Report 1995.

/3/ Laboratory Test of a 3D Steel Frame Exposed to Fire. SINTEF Report, 1995.

/4/ Eurocode 3: Design of Steel Structures Part 1.2: Structural Fire Design

Connections



Taylor & Francis
Taylor & Francis Group
http://taylorandfrancis.com

Tubular Structures VIII, Choo & Van der Vegte (eds) © 1998 Balkema, Rotterdam, ISBN 90 5809 001 9

Tests of portal frames in cold-formed RHS

Tim Wilkinson & Gregory J. Hancock
Centre for Advanced Structural Engineering, The Department of Civil Engineering, The University of Sydney, N.S.W., Australia

ABSTRACT: This paper describes tests on three large scale portal frames manufactured from cold-formed RHS in both Grade C350 and Grade C450 steel. Two different ratios of horizontal to vertical load were used. The connections, lateral restraint mechanism, loading method and test procedure are explained. The results indicate that a plastic collapse mechanism was formed in each frame. The ultimate loads obtained by the frames are similar or slightly smaller than the loads obtained from a simple plastic analysis.

KEYWORDS: cold-formed steel, hollow sections, plastic design, portal frame, bending, rotation capacity, local buckling.

1 INTRODUCTION

Plastic design of statically indeterminate frames, can lead to higher ultimate loads with associated higher deformations compared to traditional elastic design methods. As some point in the frame reaches its plastic moment (M_p), a plastic zone is created. The zone forms a hinge and rotates further, maintaining M_p, while redistributing additional load to other parts of the structure. The hinge process is repeated as other hinges form, until there is a sufficient number of hinges to create a plastic collapse mechanism for the whole structure or part of the structure. All hinges, particularly those which form early, must be able to rotate sufficiently for this mechanism to form.

There are specific requirements for the suitability of sections for plastic design. A Compact or Class 1 section is deemed suitable for plastic design. The flanges and webs of the RHS must be sufficiently stocky to avoid local buckling before large plastic rotations occur. Beam tests have examined the appropriate slenderness limits for cold-formed RHS (Wilkinson and Hancock (1997)). The rotation capacity of knee joints has also been examined (Wilkinson and Hancock (1998a,b), since plastic hinges often form at the connections of portal frames.

Due to the large strains occurring in plastic hinges, material ductility requirements are imposed by design standards. Most cold-formed RHS do not satisfy the requirements of Clause 3.2.2.2 of Eurocode 3 (European Committee for Standardisation (1992)) or Clause 4.5.2 of Australian Standard AS 4100 (Standards Australia (1990)).

This paper describes tests on portal frames manufactured from cold-formed RHS. The aims of the test series included: (1) investigation of the ultimate load capacity of RHS frames; (2) whether a plastic collapse mechanism can form in such a frame; (3) a study of rotation capacity requirements for portal frames.

2 PORTAL FRAME LAYOUT

Three frames were tested under simulated combined gravity and transverse wind loads. The ratio of vertical load (V) to horizontal load (H) is summarised in Table 1. The general layout of each frame is shown in Figure 1. Each frame spanned 7 metres, with an eaves height of 3 metres, and a total height of 4 metres. There was a collar tie which joined the midpoint of each rafter. The frames were constructed from RHS, and the collar tie was made from a pair of channel sections.

The RHS were manufactured by BHP Structural and Pipeline Products. Two strength grades were selected, Grade C350L0 and C450L0 (nominal yield stress f_{yn} of 350 MPa and 450 MPa respectively), manufactured to Australian Standard AS 1163 (Standards Australia (1991a)). The Grade C450 specimens are called *DuraGal*, produced using a unique cold-forming and in-line galvanising process.

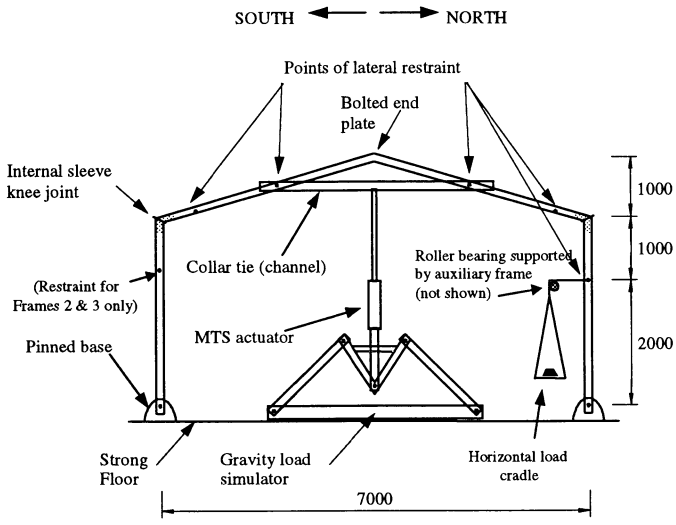

Figure 1: Layout of portal frame

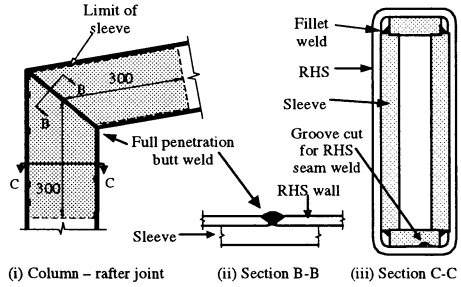

Figure 2: Portal frame knee joint

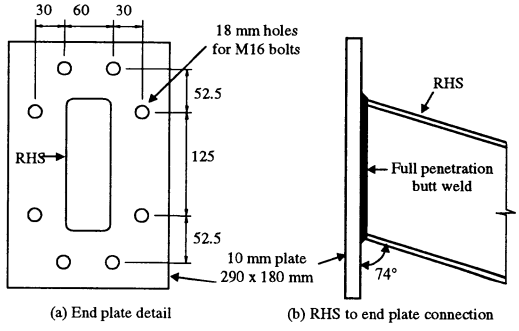

Figure 3: Detail of rafter apex connection

Table 1: Summary of portal frame tests

Frame	Made from section	Load Ratio *V/H*
Frame 1	150 x 50 x 4.0 C350	40
Frame 2	150 x 50 x 4.0 C450	40
Frame 3	150 x 50 x 4.0 C450	4 (3.3)*

Note: * Load ratio varied from 4.0 to 3.3 in Frame 3.

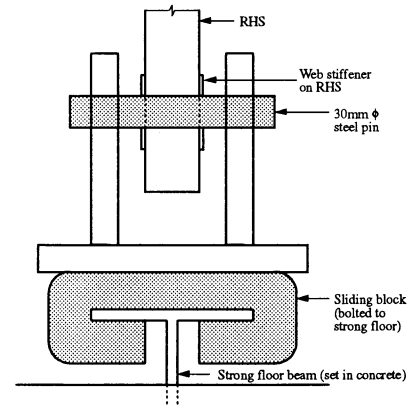

Figure 4: Pinned base connection

3 CONNECTIONS

The welded internal sleeve joint (Wilkinson and Hancock (1998b)), as shown in Figure 2 was selected for the knee joints of the portal frame. A welded box section, cut in an open "V" shape (to match the angle of the portal frame knee), was fabricated from 10 mm Grade 250 plate. The sleeve was sized to fit tightly inside the RHS. The sleeve extended 300 mm into both the column and the rafter of each knee joint and required a sledge hammer to insert the sleeve in place. The sleeve connection forces the plastic hinge at the knee to form away from the connection centreline.

A moment resisting bolted end plate connection (Figure 3) was used at the apex of the frame. A 10 mm plate was butt welded to the end of each rafter, and the two plates were bolted together

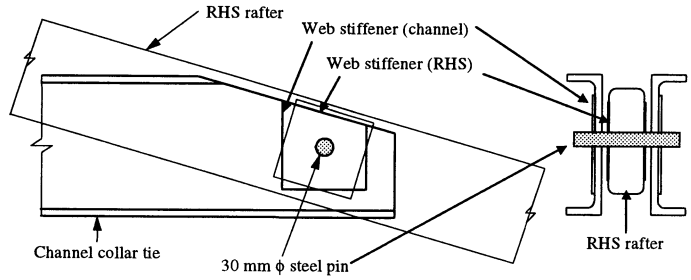

Figure 5: Collar tie - rafter connection

with eight high strength fully-tensioned M16 bolts positioned symmetrically about the *x*-axis of the RHS.

A common connection for portal frames is the bolted base plate connection to a concrete footing. To simulate the column base plate, a pinned connection, as shown in Figure 4, was used. The webs of the RHS were stiffened locally by a steel plate, and a 30 mm diameter high strength steel pin was inserted through the neutral axis of the RHS. A thick steel base plate supported the pin. The base plate was securely fastened to the strong floor of the laboratory. The pin connection was greased to reduce friction.

Many portal frames have a collar tie, which joins the two rafters between their midpoints. The collar tie is usually the same section size as the whole frame. The tie acts in tension for gravity loads, reducing the moment at the apex of the frame. The collar tie supports services in a commercial structure. In the experimental frames, the collar tie transferred the vertical load to the frame. The simulated gravity load acted at the centre of the tie and transferred load to the frame at the ends of the tie. A pair of channels was used, one channel on each side of the RHS frame, as shown in Figure 5. Steel pins inserted through a stiffened hole cut through the centre of the RHS webs and the channels connected the rafters to the channels.

4 LATERAL RESTRAINTS

Plastic design requires that no out-of-plane (lateral) buckling occurs in the frame. In a prototype multi-frame portal structure, purlins and sheeting linking adjacent frames provide some lateral restraint. Often the final two frames in a structure have cross bracing which restrains the entire system against out-of-plane deflections. For the single frame being tested, a system was required which would restrain the frame out-of-plane for the large in-plane deflections expected.

The system chosen has been used previously in large scale frame tests (Yarimci *et al* (1968)) and uses two parallel levers which are pin-jointed together at one end by a coupler. The other end of each lever is spherically pinned to a fixed support. As shown in Figure 6, the midpoint of the coupler traces out an approximate straight line as the mechanism moves. For very large movements the locus of the midpoint deviates only slightly from the straight line. Hence this system can be used as a lateral restraint system if the midpoint of the coupler is connected to the frame.

5 CONSTRUCTION SEQUENCE

The two columns and two rafters were fabricated separately. The RHS was supplied in standard lengths and then saw cut to correct length. The ends of the sections were mitre cut with a band saw at the appropriate angle (for the knee and apex connections). Stiffening plates for the loading points were welded in place and the holes for the pins and restraints were drilled. The end plates for the apex joint were butt welded to the rafters and the internal sleeves were manufactured to fit snugly into the columns and rafters. Strain gauges were placed at the appropriate locations and dimensions measured.

The sleeves were hammered into each rafter. This was a tight fit which required substantial hitting with a sledge hammer. The other end of each sleeve was then hammered into the column. Finally the RHS at each knee joint were welded together. The two halves of the frame were bolted together at the apex joint. At all stages during this sequence, the frame

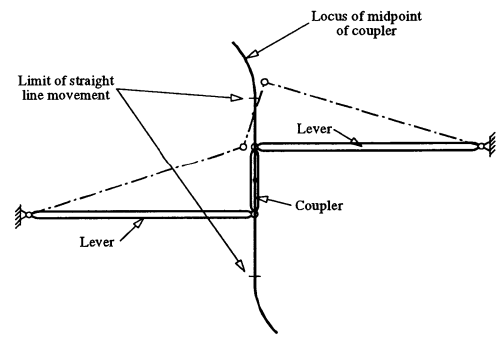

Figure 6: Lateral restraint mechanism

remained in a horizontal position on the ground. Before the pair of channels that made up the collar tie was pinned to the rafters, the exact locations of the pin holes in the channels were identified and cut. This minimised any lack of fit moments induced in the frame during the construction process. The channel tie was connected to the frame with the pins.

The constructed frame was lifted into place by a crane. One pin base had been securely fixed to the laboratory strong floor previously and one column was connected to this base. The other base was then slid into the correct position to avoid lack of fit moments being induced and was fixed to the strong floor. The other column was then pin-connected to this base. The lateral restraints were connected to the frame and overall imperfection measurements were made.

6 INSTRUMENTATION

Strain gauges were placed at important locations on the frame as shown in Figure 7. Curvature and net axial strain were calculated from the strain values on the opposite flanges of the RHS during the tests. Steel tapes were hung from the frame, and viewed through a WILD NA2 automatic level, from which vertical displacements could be calculated. Lateral and horizontal deflections were monitored by separate theodolites.

7 LOADING METHOD

A combination of vertical gravity and transverse wind loads was selected for the test series as listed in Table 1. In a prototype portal frame, gravity and wind loads are transferred to the frame from the sheeting via purlins and girts, similar to a distributed load. It is difficult to replicate distributed loads in a laboratory, and hence the loads were applied as point loads.

The vertical load was applied at the midpoint of the collar tie. Large in-plane sway displacements were anticipated and it was essential that the downwards loads remained vertical to simulate true gravity loading. A hydraulic jack was required to achieve the large vertical load. However, a jack connected directly to the strong floor of the laboratory would produce a non-vertical load as the frame swayed horizontally.

A gravity load simulator (Yarimci *et al* (1967)) was attached to the strong floor of the laboratory. The simulator had two inclined members, pinned together by a rigid triangular unit, and pinned at the other end to the base. The jack was bolted to the top of another vertical member, which was pinned to the base of the triangular section.

As the unit swayed, the instantaneous centre of rotation (ICR) of the two inclined arms moved as

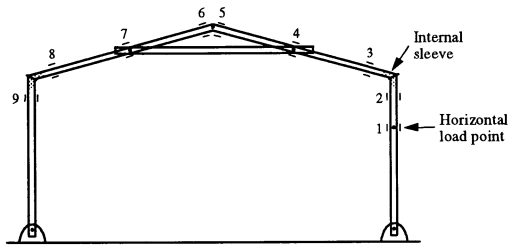

Figure 7: Strain Gauge Locations

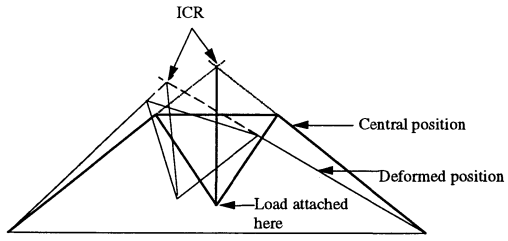

Figure 8: Displaced and undisplaced configurations of gravity load simulator

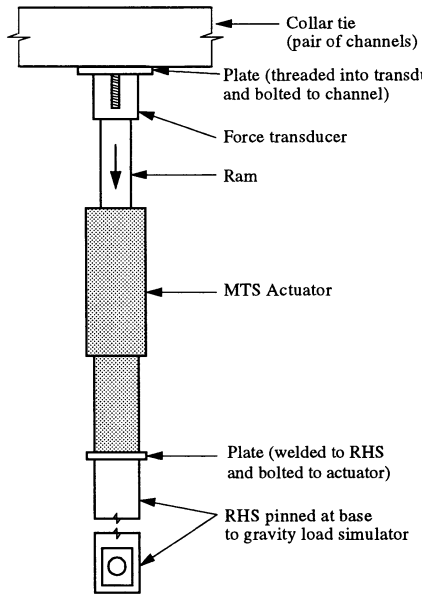

Figure 9: Details of actuator to frame connection

indicated in Figure 8. To maintain equilibrium, the line of action of the force from the jack acted through the ICR. The bottom vertex of the triangle remained almost vertically below the instantaneous centre and hence the direction of the load remained vertical. For very large sways, the line of action deviated slightly from the vertical. The simulator had a range of approximately 250 mm in both directions from the central position.

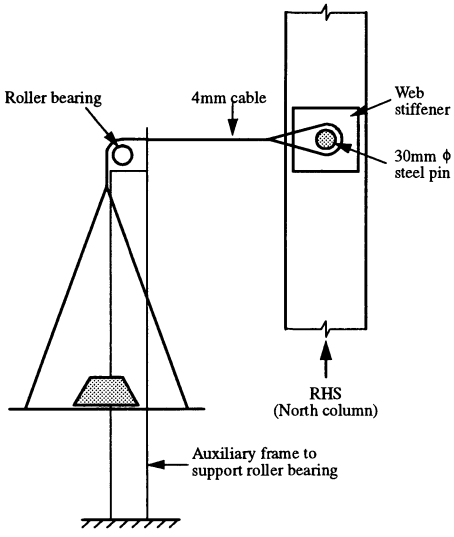

Figure 10: Transverse Load Apparatus

A 150 × 50 × 5.0 C450 RHS was pinned to the bottom vertex of the triangular section of the simulator. The other end of the RHS was bolted to a 250 kN capacity MTS Actuator (Model 244.31). The actuator was bolted to the channel tie of the portal frame.

The transverse load was smaller than the gravity load and was achieved with dead weights as shown in Figure 10. A pin was inserted through the north column of the frame. A pair of cables was attached to the pin and slung over a roller bearing (supported by an auxiliary frame) to a cradle upon which lead weights were placed.

8 TEST PROCEDURE

Before testing, the actuator ram was bolted to the channel tie. The ram was lowered, in stroke control mode, at a constant rate of approximately 0.06 mm/s. At fixed increments of vertical load, lead blocks were added to the side load cradle to maintain the appropriate ratio of vertical to horizontal load.

At regular intervals during the test, the ram was halted for approximately two minutes. After this pause, load measurements were made to obtain a value of the static load. At these times, all displacement measurements were taken.

Each test continued until well past the ultimate load. The actuator ram was near its maximum stroke of 200 mm, and the large sway deflection of about 300 mm was near the limit of sway for the gravity load simulator. The horizontal load was removed and the ram raised until the vertical load was zero.

9 RESULTS

9.1 *Tensile coupon tests*

Three coupons were taken from the flats of each tube. One was cut from the face opposite the weld, and one from each of the sides adjacent to the weld. The coupons were prepared and tested in accordance with AS 1391 (Standards Australia (1991a)) in a 250 kN capacity INSTRON Universal Testing Machine. Since the steel was cold-formed, the yielding was gradual. Accordingly the yield stress (f_y) quoted is the 0.2% proof stress.

At time of publication, only one coupon from each frame has been tested. In each case, the coupon was cut from the flat face adjacent to the weld. As was noted previously (Wilkinson and Hancock (1997)), the yield stress of this face is normally about 10% less than the yield stress of the opposite face, and approximately 20 % less than the yield stress of a corner. Hence using the yield stress of the adjacent face may underestimate the strength of the frame. The results are summarised in Table 2.

9.2 *Plastic analysis*

Simple plastic analysis, using the computer program PRFSA (CASE (1997)), was performed on models of each frame. The analysis assumed no reduction of the plastic moment in the presence of axial force. Only elastic - plastic (no strain hardening) material properties could be considered. Second order effects were not considered. Hence the analysis probably overestimated the ultimate strength of the frame.

Two analyses were made on each frame: (1) based on nominal dimensions and nominal yield stress (either 350 MPa or 450 MPa); (2) based on measured dimensions and measured yield stress (refer to Table 2).

The results of the PRFSA plastic analysis are summarised in Table 3. The hinge locations are shown in Figure 11. Table 3 lists the ultimate load, which is the load at plastic collapse. The pin-based portal

Table 2: Summary of coupon test results

Specimen	Cut from section	f_y[1] (MPa)
Frame 1	150 × 50 × 4.0 C350	411
Frame 2	150 × 50 × 4.0 C450	445
Frame 3	150 × 50 × 4.0 C450	445

Notes:
(1) The value of f_y from one face is used for the whole section.
(2) Nominal strengths:
Grade C450 specimens f_{yn} = 450 MPa and f_{un} = 500 MPa.
Grade C350 specimens f_{yn} = 350 MPa and f_{un} = 430 MPa.

Table 3: Summary of plastic analysis

Frame	Load at ultimate (kN) Vertical	Horizontal	Ultimate load / First hinge load
Frame 1			
nominal	57.6	1.44	1.05
measured	68.3	1.71	1.05
Frame 2			
nominal	74.0	1.85	1.05
measured	74.1	1.85	1.05
Frame 3			
nominal	54.1 (51.0)*	13.6 (15.3)*	1.07 (1.09)*
measured	54.3 (51.2)*	13.5 (15.4)*	1.07 (1.09)*

Note: * values in brackets are for Frame 3 with $V/H = 3.3$.

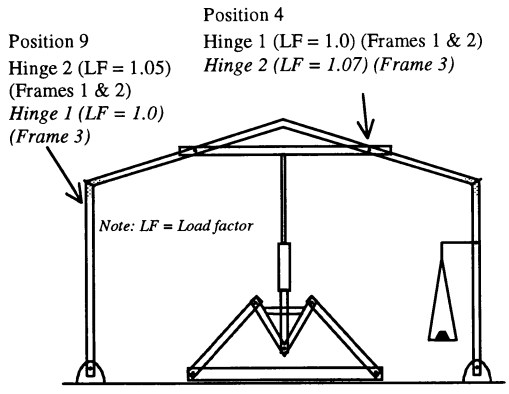

Figure 11: Hinge locations from plastic analysis

frame is a redundant structure, with one degree of static indeterminancy: hence two plastic hinges are required to form a plastic collapse mechanism. The ultimate load occurs at the formation of the second hinge. The ratio of the ultimate load to the load at the formation of the first hinge represents the increase in load capacity afforded by a plastic analysis when compared to an elastic analysis where the section is compact so that the first hinge is allowed to form.

Advanced simulation of the portal frame tests will be performed in the future to include the effects of material non-linearity, member imperfections, gradual yielding, second-order effects, residual stresses, and interaction of moment and axial force.

9.3 *Observations during testing*

A constant stroke rate was applied by the MTS actuator ram. At frequent stages during the test, the ram was halted and deflection measurements were made with a theodolite or level. At appropriate times, dead weight was added to the horizontal load rig, to maintain the ratio of vertical to horizontal load. For Frame 3, the load ratio varied slightly during the test, ranging from $V/H = 4.0$ to 3.3.

Initially deflections increased elastically with the load. Frame 2 was unloaded after the end of the elastic region and reloaded back to the previous position and testing continued. It was noticed that the pin base on the north column was about to stick due to lateral movement, preventing rotation. The load was removed and the joint corrected, allowing rotation.

For both Frame 1 and Frame 2, large rotations became visible at the channel loading point in the north rafter (Position 4 in Figure 12). For all three frames, sway deflections in the frame increased dramatically after the initial elastic region. Large horizontal deflections were visible in the south column. As shown in Figure 12, a local buckle formed at either Position 4 (Frames 1 and 2) or Position 9 (Frame 3) below the limit of the internal sleeve into the column. The local buckle at Position 4 did not form exactly at the loading point (as predicted by the plastic analysis) since there was a small stiffening plate on the RHS at this point (see Figure 12). The buckle formed just past this plate toward the apex of the frame, at the point of lateral restraint. With further increase in stroke, the formation of the second plastic hinge was visible at either Position 9 (Frames 1 and 2), or Position 4 (Frame 3), and the ultimate load was reached. The load then dropped slowly as the stroke increased. A second local buckle formed at Position 9 in Frame 2. No second buckle formed in Frame 1 or 3 before the displacement limit of the gravity load simulator was reached.

In Frame 1, out-of-plane deflections of the south column became visible in the vicinity of the ultimate load. Consequently, Frames 2 and 3 had an additional brace point in the south column. No out-of-plane deflections occurred in the south column in Frames 2 or 3. All three frames unloaded elastically. There was no sign of failure or distress at either the apex joint or the welded internal sleeve knee joint.

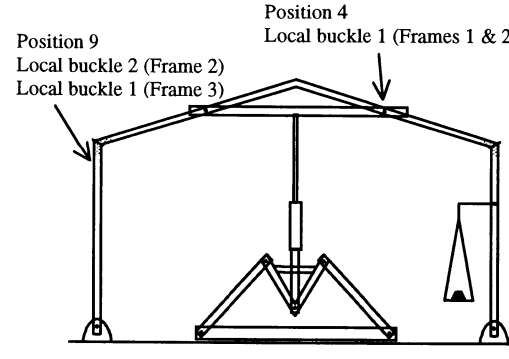

Figure 12: Local buckle/hinge locations

Table 4: Portal Frame Tests: Ultimate Loads

Specimen	Cut from section	Load at ultimate (kN)		Ultimate vertical load
		Vertical	Horizontal	Plastic analysis load[1]
Frame 1	150 x 50 x 4.0 C350	68.2	1.75	1.00
Frame 2	150 x 50 x 4.0 C450	71.5	1.87	0.95
Frame 3	150 x 50 x 4.0 C450	45.7	13.8	0.84 (*0.89*)[2]

Notes: (1) Plastic analysis load based on measured properties (Table 3)
(2) Value in brackets for Frame 3 refers to $V/H = 3.3$, value in plain text refers to $V/H = 4$.

9.4 *Ultimate loads*

The ultimate loads are given in Table 4 and compared with the results of the plastic analysis. As mentioned above, the plastic analysis of the frames did not include second order effects and the reduction of plastic moment to account for interaction with axial force. More useful comparisons will be performed later, when the analysis is completed including these effects and the full set of material properties.

In particular, the ultimate load for Frame 3, is low compared with the simple plastic analysis. However, *preliminary* advanced analysis has shown that the second order effects are substantial and reduce the ultimate load of the frame by approximately 20%. Results of the advanced analysis will be available in the future.

9.5 *Load deflection curves*

The load deflection curves are shown in Figure 13 and Figure 14. Figure 13 represents the vertical deflection at the apex of the frame. The unloading and reloading of Frame 2 has been removed from the data. In each curve the load has been non-dimensionalised with respect to the vertical load at ultimate based on a plastic analysis using the measured section properties (Table 3).

The curves for Frames 1 and 2 have similar shapes, as expected, as the load ratio was the same for both frames. The different stiffness of each frame is identifiable in the curves. The rigidity of the knee and apex connections are important factors in the frame stiffness. Small variations in bolt tension, or the tightness of the fit of the sleeve in the RHS, can affect the entire stiffness. The initial horizontal deflections of Frame 2 were negative. This was caused by the lack of rotation of the pin base connection which was identified and corrected.

10 DISCUSSION

The following important points can be derived from the results:

- Plastic collapse mechanisms were formed in all three frames. Large curvatures (hinges) occurred in (or very close to) the locations predicted by the computer analysis.
- The ultimate loads were similar to or smaller than those predicted by the simple, plastic analysis. More refined, advanced analysis in the future will consider second order effects and material non-linearity. It is the comparison with this advanced analysis that is most important. Preliminary advanced analysis has shown that second order effects are considerable.
- There was no significant difference in the behaviour of the Grade C350 and Grade C450 frames (Frame 1 and Frame 2).
- There was no failure due to insufficient material ductility.
- The welded internal sleeve knee joints performed without any signs of distress.
- The lateral restraints performed adequately and the frame did not buckle out-of-plane.

Further advanced analysis is required to investigate the effects of non-linearity and frame imperfections. Investigation of the rotation capacity required to achieve the plastic collapse mechanism in the three frames will also be carried out.

11 CONCLUSIONS

This paper has described tests on three full scale portal frames manufactured from cold-formed RHS. The connections, lateral restraint mechanism, loading method and test procedure have been summarised. The results indicate that a plastic collapse mechanism was formed in each frame. Local buckles formed at some of the plastic hinge points but there was no failure of the connections or RHS fracture due to lack of material ductility. The ultimate loads obtained by the frames were similar or smaller than the loads obtained from simple plastic analysis, but the plastic analysis did not consider factors such as second order effects and moment-axial force interaction.

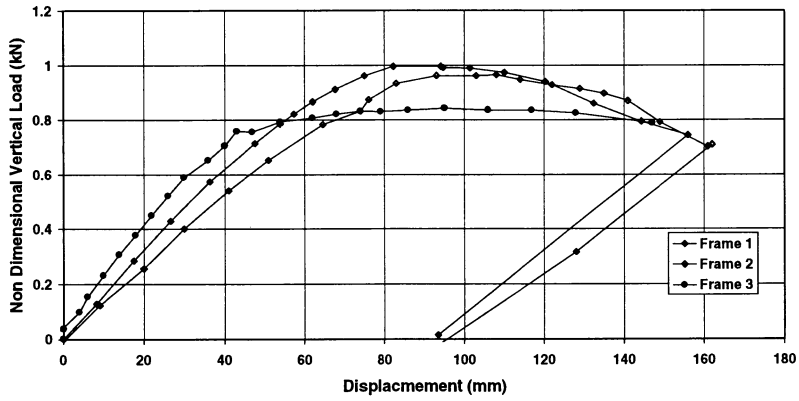

Figure 13: Load - vertical displacement (at apex) graph for portal frame tests

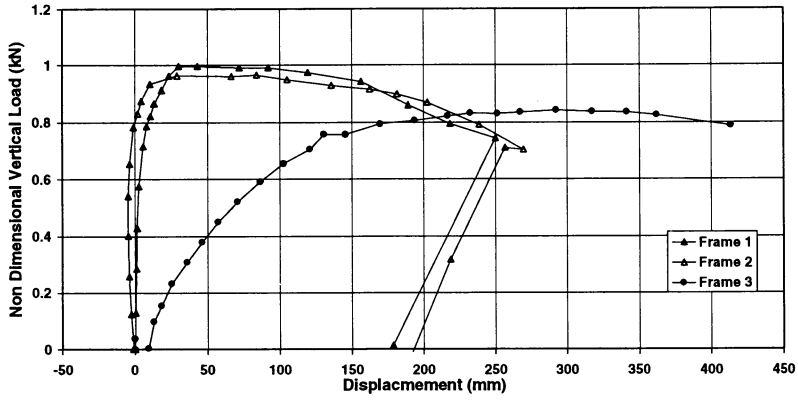

Figure 14: Load - horizontal displacement (at north knee joint) graph for portal frame tests

Note for Figures 13 and 14: The load has been non-dimensionalised with respect to the vertical load at ultimate based on a plastic analysis using the measured section properties (Table 3)

12 ACKNOWLEDGEMENTS

This research project is funded by CIDECT (Comité International pour le Developpement et l'Étude de la Construction Tubulaire). Tube specimens were provided by BHP Structural and Pipeline Products. The experiments were carried out in the J. W. Roderick Laboratory for Materials and Structures, Department of Civil Engineering, The University of Sydney.

13 NOTATION

f_y	Yield stress
f_{yn}	Nominal yield stress
H	Horizontal load
M_p	Plastic bending moment
V	Vertical load

14 REFERENCES

European Committee for Standardisation, (1992), *Design of Steel Structures: Part 1.1 - General Rules and Rules for Buildings*, DD ENV. 1993-1-1, Eurocode 3 Editorial Group.

CASE, (1997), "PRFSA: Plane Rigid Frame Structural Analysis", *Users Manual*, Centre for Advanced Structural Engineering, School of Civil Engineering, University of Sydney, Sydney, Australia.

Standards Australia, (1990), Australian Standard *AS 4100 Steel Structures*, Standards Australia, Sydney.

Standards Australia, (1991), Australian Standard *AS 1163 Structural Steel Hollow Sections*, Standards Australia, Sydney.

Wilkinson T. and Hancock G. J., (1997a), "Tests for the Compact Web Slenderness of Cold-Formed Rectangular Hollow Sections", *Research Report*, No. R744, Department of Civil Engineering, University of Sydney, Sydney, Australia.

Wilkinson T. and Hancock G. J., (1997b), "Plastic Design of Cold-Formed RHS", CIDECT Project 2S, *Interim Report No. 3*, Centre for Advanced Structural Engineering, Department of Civil Engineering, University of Sydney, Sydney, Australia.

Wilkinson T. and Hancock G. J., (1998a), "Tests of Stiffened and Unstiffened Welded Knee Connections in Cold-Formed RHS", *Proceedings*, 8th International Symposium on Tubular Structures, Singapore, (Balkema, publ.).

Wilkinson T. and Hancock G. J., (1998b), "Tests of Bolted and Internal Sleeve Knee Connections in Cold-Formed RHS", *Proceedings*, 8th International Symposium on Tubular Structures, Singapore, (Balkema, publ.).

Yaramici E., Yura J. A., and Lu L. W., (1967), "Techniques for Testing Structures Permitted to Sway", *Experimental Mechanics*, August 1967, pp321-331.



Taylor & Francis
Taylor & Francis Group
http://taylorandfrancis.com

Tubular Structures VIII, Choo & Van der Vegte (eds) © 1998 Balkema, Rotterdam, ISBN 90 5809 001 9

Rotation capacity of joints for beam-to-column RR and RI welded connections

J.Szlendak
Bialystok Technical University, Poland

ABSTRACT: Advanced static analysis of frames should include the inevitable imperfections during the fabrication and erection of real structure. This is simulated by the initial sway of frame (II order theory). Also the prediction of the actual behaviour of the connections, called in this paper II level joints. is necesary. Such joints are described by the following parameters: initial stiffness, design bending moment, design moment resistance and rotation capacity. This last parameter for RI and RR welded beam-to-column connection is studied in this paper.

1 INTRODUCTION

Static analysis of non-sway frames typically is undertaken for their original geometry (I order theory). When they are multi-storey sway frames their actual geometry should be considered. This is often simulated by the initial sway of frames (II order theory). Such model estimates the inevitable imperfections during the fabrication and erection. However, up to now the predictions of the actual joint's behaviour are not satisfactory. Usually it is assumed that they are fixed or pined. Such connections are called in this paper - I level joints. The real behaviour of frame connections is less or more semi-rigid and in this paper they are called - II level joints. The absence of the internationally agreed model of the II level joint's influences the overall calculation model of the frames and leads to the divergence's of the results. It is suggested that advanced calculation model of the multi-storey frame needs taking into consideration the actual geometry of the frame (II order theory) and also the actual behaviour of the connections (II level joints). The II level joint's model has at least the following parameters:

a) initial stiffness of connection $S_{j,ini}$ (or secant S_j)
b) design bending moment $M_{j,Sd}$
c) design moment resistance $M_{j,Rd}$
d) rotation capacity Φ_{Cd}

In this paper the last parameter for RR and RI beam-to-column welded connection is considered.

2 ROTATION CAPACITY FROM THE TEST DATA

In 1995-96 in Bialystok Technical University the twelve two storeys two bay frames had been tested. Series A contains 6 specimens and series B the other 6 ones. Six of them had RHS columns and I sections as the beams. The six other had the columns and beams with RHS. The scale of the specimens is about 1:4 with regard to the nature.

Each of series A specimen has been loaded twice. First time by the asymmetric point load applied to the one upper beam (Fig.1) and the second time by the symmetric point load applied to the inner beams.

The serviceability deflection limit is L/250, where L - is the span of the beam. In tested series A and B this is 1500/250 = 6 mm.

The local rotations in the joints of the tested frame specimen are shown for the series A and B in the Table 1.

It is easy to show that the rotation of the supports for the single-span beam for the L/250 limit, is for the one point central load 1.2x10-2 rad and for continuous load 1.28x10-2 rad.

The data presented in the Table 1 show that the joints are partially rigid. However, for example for frame A6SY and B6 semi-rigid connections are almost pinned.

The geometry of joints is shown in Fig. 2 and 3 and the actual values of their local rotations in Table 2. They are obtained when the connections are loaded up to design bending moments $M_{j,Sd}$ (Szlendak 1996a,b).

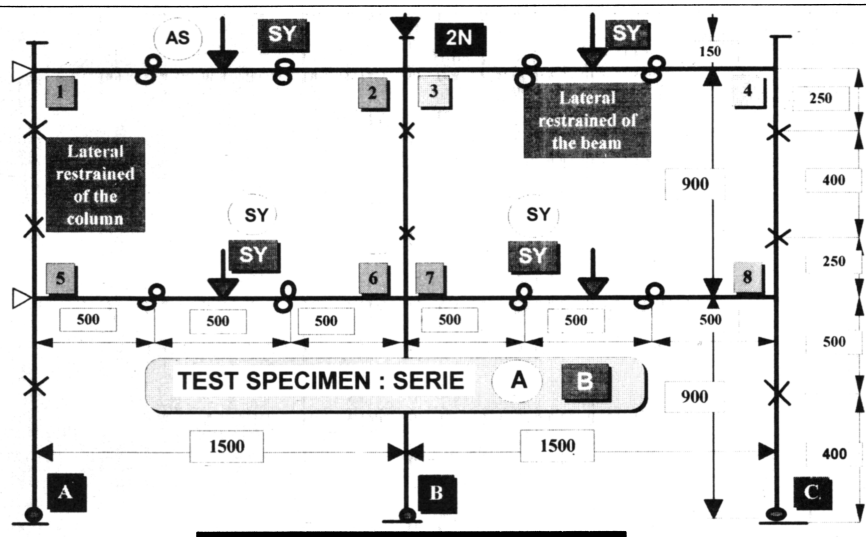

Fig.1 Columns: RHS Beams : RHS or I

RR type welded joint

Fig. 2

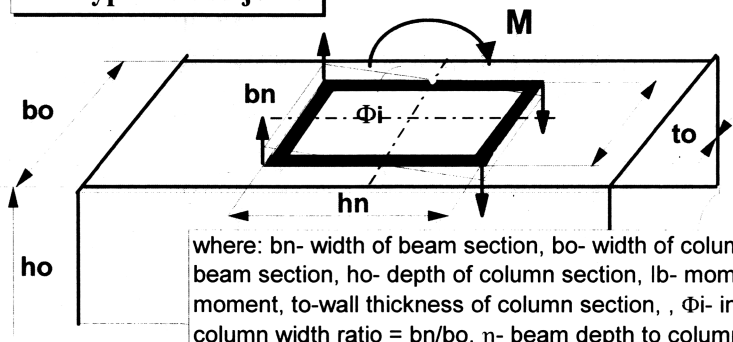

where: bn- width of beam section, bo- width of column section, hn- depth of beam section, ho- depth of column section, Ib- moment of inertia, M- moment, to-wall thickness of column section, , Φi- initial rotation, β- beam to column width ratio = bn/bo, η- beam depth to column width ratio =hn/bo, λo- slenderness of column flange = bo/to, fyo,fyi - column,beam yield stress

RI type welded joint

Fig. 3

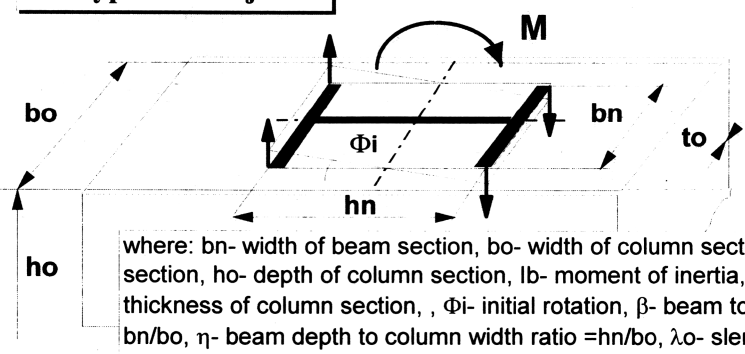

where: bn- width of beam section, bo- width of column section, hn- depth of beam section, ho- depth of column section, Ib- moment of inertia, M- moment, to-wall thickness of column section, , Φi- initial rotation, β- beam to column width ratio = bn/bo, η- beam depth to column width ratio =hn/bo, λo- slenderness of column flange = bo/to, fyo,fyi - column,beam yield stress

Table 1. Joints rotation for the serviceability load limit

Nr of frame specimen	Section of column /section of beam	Type /load value [kN]	Deflection of beam δ = L/250 [mm]	Local rotation of joints x 10-2 rad for the load when the deflection of beam is equal δ =L /250					
				1	**2**	**5**	**6**	**7**	**8**
A1AN	70x70x3/70x70x3	AN/23	6,19	0,345	0,493				
A1SY	70x70x3/70x70x3	SY/28	6,35			0,461	0,765	**0,824**	0,461
A2AN	50x50x3/40x80x3	AN/18	6,67	0,139	0,293				
A2SY	50x50x3/40x80x3	SY/22	6,38			0,131	**0,852**	0,575	0,141
A4AN	40x60x3/I 80	AN/28	6,36	0,339	0,500				
A4SY	40x60x3/ I 80	SY/31	5,97			0,363	**0,877**	0,713	0,327
A5AN	50x50x3/I 80	AN/28	6,48	0,316	0,670				
A5SY	50x50x3/I 80	SY/29	6,45			0,522	**1,017**	0,947	0,366
A6AN	70x70x3/I 80	AN/24	6,44	0,704	0,930				
A6SY	70x70x3/I 80	SY/**25**	6,11			0,777	0,956	**1,162**	0,776
A7AN	70x70x3/40x80x3	AN/19,5	5,95	0,749	0,835				
A7SY	70x70x3/40x80x3	SY/19,5	5,83			0,727	**1,096**	1,012	0,705
B1	70x70x3/70x70x3	SY/26	5,99	0,307	0,652	0,414	**0,907**	0,813	0,492
B2	50x50x3/40x80x3	SY/22,5	6,02	0,150	0,521	0,229	0,797	**0,807**	0,263
B4	40x60x3/I 80	SY/32	6,19	0,128	0,575	0,226	0,722	**0,807**	0,229
B5	50x50x3/I 80	SY/28,8	6,13	0,164	0,869	0,287	0,954	**1,044**	0,204
B6	70x70x3/I 80	SY/**24,5**	6,05	0,711	0,881	0,969	**1,042**	0,813	0,939
B7	70x70x3/40x80x3	SY/18,3	6,02	0,614	0,801	0,754	**0,871**	0,868	0,863

Table 2. Joints rotation for the design load limit

Nr of frame specimen	Section of column /section of beam	Type /load value $M_{j,Sd}$ [kNcm]	Deflection of beam δ [mm]	Local rotation of joints $\Phi_{j,Sd}$ x 10-2 rad for the design bending moment $M_{j,Sd}$, which occurs in one of the joint (bold)					
				1	2	5	6	7	8
A1AN	70x70x3/70x70x3	AN/261,4	10,0	0,615	**0,817**				
A1SY	70x70x3/70x70x3	SY/261,4	7,59			0,594	**0,988**	**1,032**	0,570
A2AN	50x50x3/40x80x3	AN/426,5	13,22	0,277	**0,754**				
A2SY	50x50x3/40x80x3	SY/426,5	7,21			0,186	**1,016**	0,661	0,165
A4AN	40x60x3/I 80	AN/445,2	15,27	0,719	**1,418**				
A4SY	40x60x3/ I 80	SY/445,2	15,00			0,997	2,200	**1,520**	-
A5AN	50x50x3/I 80	AN/296,7	12,76	0,547	**1,357**				
A5SY	50x50x3/I 80	SY/296,7	9,73			0,670	1,331	**1,305**	0,527
A6AN	70x70x3/I 80	AN/172,0	15,38	1,881	**2,319**				
A6SY	70x70x3/I 80	SY/172,0	9,26			**1,244**	1,398	1,660	1,141
A7AN	70x70x3/40x80x3	AN/216,8	-	-	-				
A7SY	70x70x3/40x80x3	SY/216,8	16,80			**2,758**	3,900	3,706	2,295

3 ESTIMATION OF ROTATION CAPACITY OF JOINTS

Only few studies have been undertaken to estimate the rotation capacity of joints in steel frames.
One of such estimation (Bjorhovde et.al 1990) is formula, which after small modification could be written as:

$$\Phi_{rc} = 15(0,9M_p - M)\frac{hn}{EI_b} \qquad (1)$$

After substituting actual moment M, which occurs in the joint, the rotation capacity Φ_{rc} is obtained. Calculated the rotation capacities using the estimation by the equation (1) are given in Table 3 . Other estimation (EC3, Annex J5,1994) suggests that the minimum rotation capacity of welded jointsbetween beam and column should at least be equal 1.5 x 10-2 rad. After described here tests the new formula for Φ_{rc} is suggested :

- for welded RR joints

$$\Phi_{rc} = 32,6\sqrt[6]{\frac{\beta^2\eta}{\lambda_o^7}}\frac{1}{\beta^2\eta^3\lambda_o}\frac{f_{yo}}{f_{yi}}\frac{M_p}{Et_o^3} \qquad (2)$$

- for welded RI joints

$$\Phi_{rc} = 579\sqrt[6]{\frac{\eta}{\beta^4\lambda_o^7}}\frac{1}{\beta\eta^3\lambda_o^2}\frac{f_{yo}}{f_{yi}}\frac{M_p}{Et_o^3} \qquad (3)$$

where: M_p-plastic moment of beam

Calculated from (2) and (3) rotation capacity Φ_{rc} for the joints in the tested frames are given in Table 3.

Table 3. Estimation of the rotation capacity of joints Φrc

Nr of frame specimen	Section of column /section of beam	Maximum rotation in the joint (Nr) x 10-2rad	Estimation **Φrc** by Bjorhovde x 10-2 rad	Estimation**Φrc** by EC3 x 10-2 rad	Estimation **Φrc** by (2) & (3) x 10-2rad
A1AN	70x70x3/70x70x3	4,01(2)	2,59	1,50	4,46
A1SY	70x70x3/70x70x3	8,70(6)	2,50	1,50	4,46
A2AN	50x50x3/40x80x3	6,85(2)	1,18	1,50	3,14
A2SY	50x50x3/40x80x3	6,02(6)	1,30	1,50	3,14
A4AN	40x60x3/I 80	7,60(2)	1,40	1,50	3,61
A4SY	40x60x3/ I 80	4,05(6)	1,75	1,50	3,61
A5AN	50x50x3/I 80	6,68(2)	2,35	1,50	4,24
A5SY	50x50x3/I 80	4,54(5)	1,94	1,50	4,24
A6AN	70x70x3/I 80	9,80(2)	3,48	1,50	6,37
A6SY	70x70x3/I 80	5,33(5)	3,25	1,50	6,37
A7AN	70x70x3/40x80x3	9,70(2)	4,80	1,50	6,76
A7SY	70x70x3/40x80x3	9,80(5)	4,29	1,50	6,76

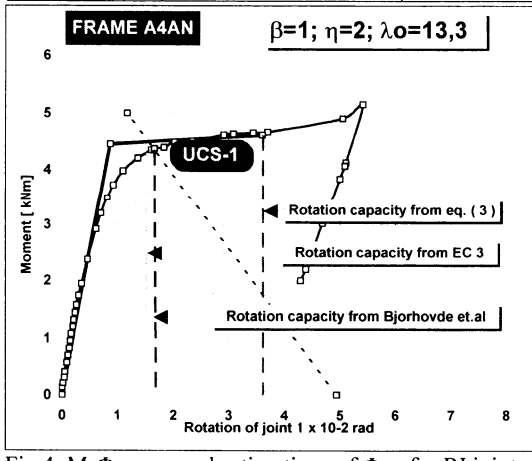

Fig.4 M-Φ curve and estimations of **Φrc** for RI joint

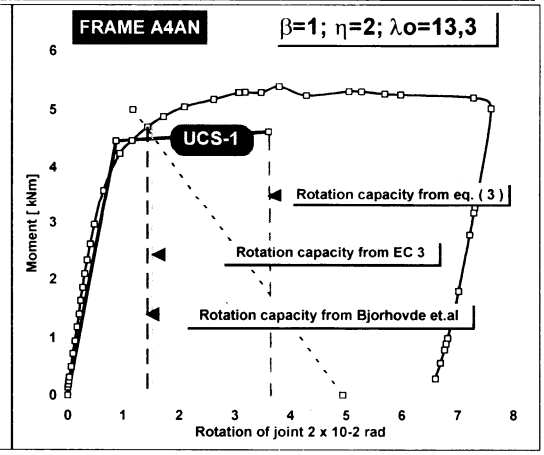

Fig.5 M-Φ curve and estimations of **Φrc** for RI joint

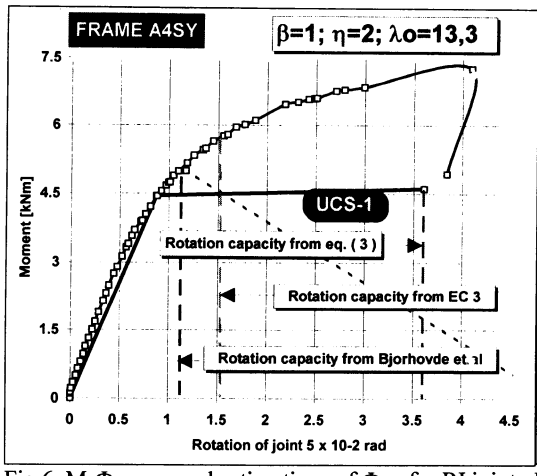

Fig.6 M-Φ curve and estimations of **Φrc** for RI joint

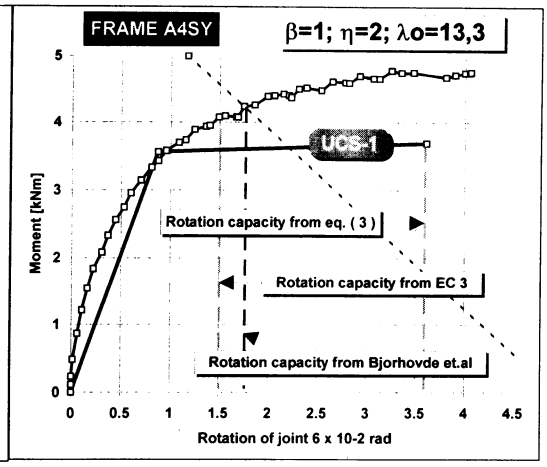

Fig.7 M-Φ curve and estimations of **Φrc** for RI joint

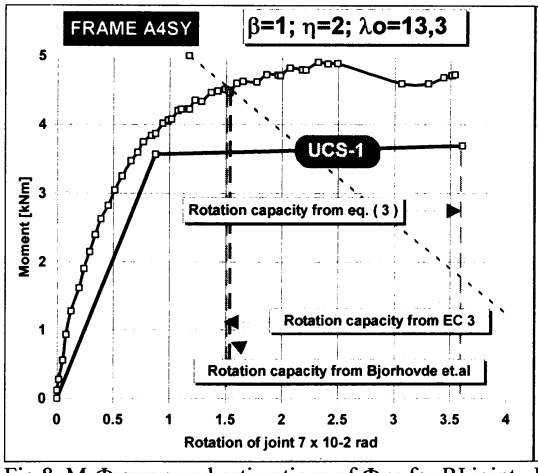

Fig.8 M-Φ curve and estimations of **Φrc** for RI joint

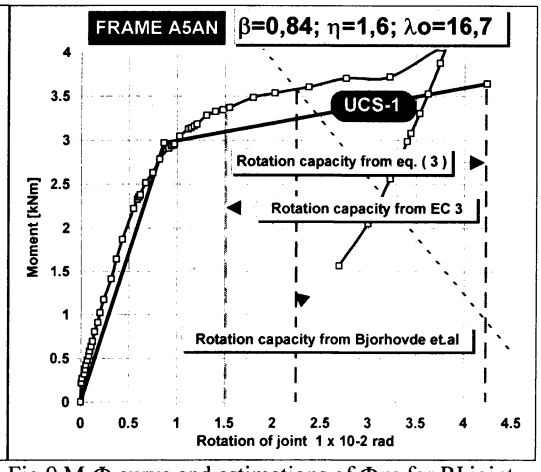

Fig.9 M-Φ curve and estimations of **Φrc** for RI joint

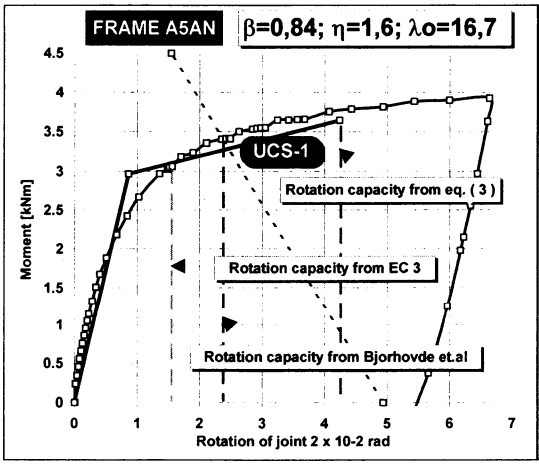

Fig.10 M-Φ curve and estimations of **Φrc** for RI joint

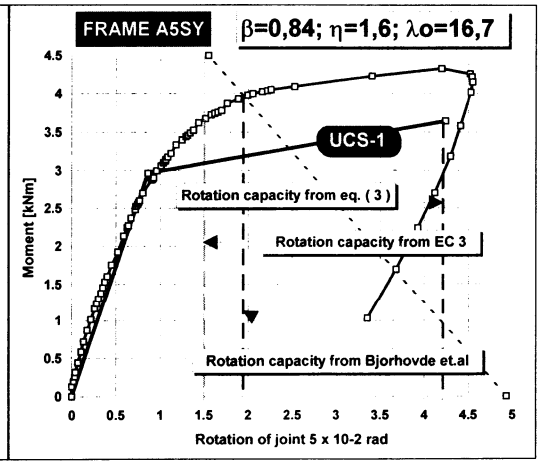

Fig.11 M-Φ curve and estimations of **Φrc** for RI joint

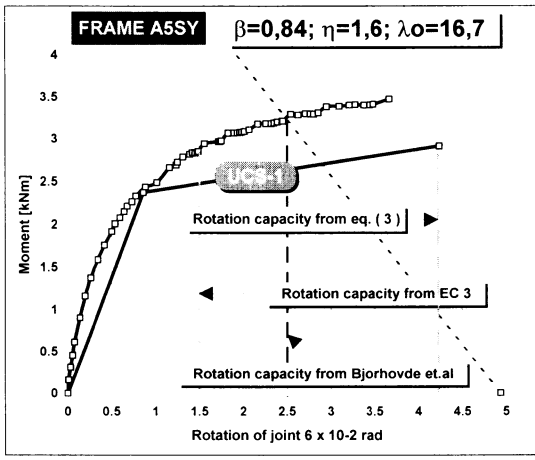

Fig.12 M-Φ curve and estimations of **Φrc** for RI joint

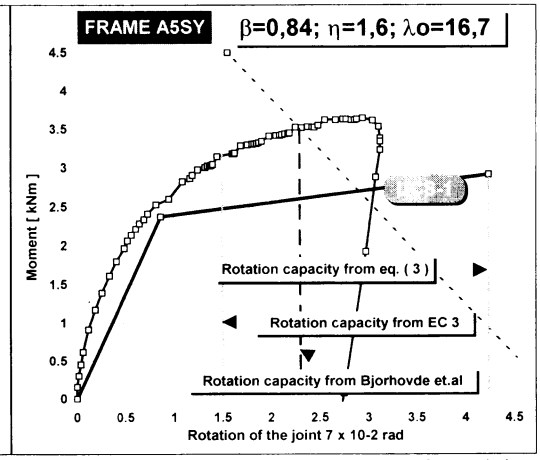

Fig.13 M-Φ curve and estimations of **Φrc** for RI joint

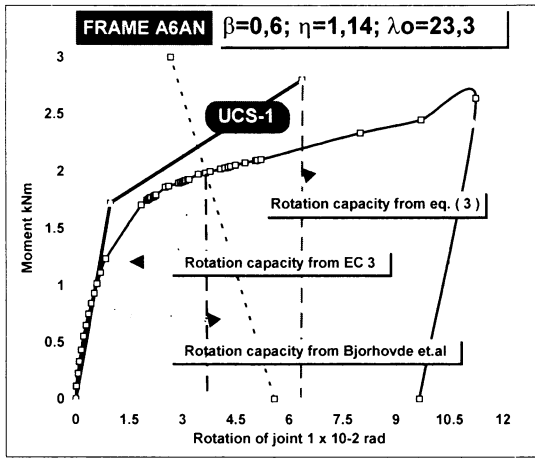

Fig.14 M-Φ curve and estimations of **Φrc** for RI joint

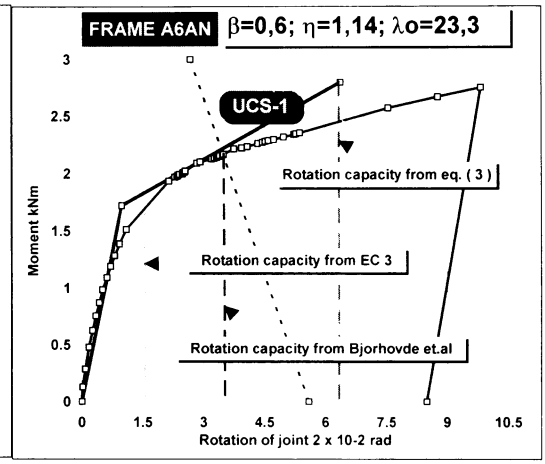

Fig.15 M-Φ curve and estimations of **Φrc** for RI joint

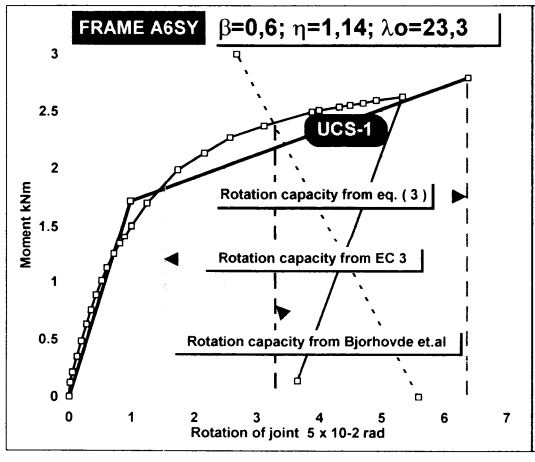

Fig.16 M-Φ curve and estimations of **Φrc** for RI joint

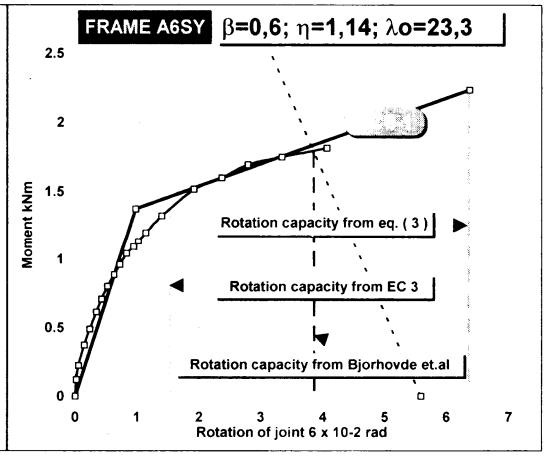

Fig.17 M-Φ curve and estimations of **Φrc** for RI joint

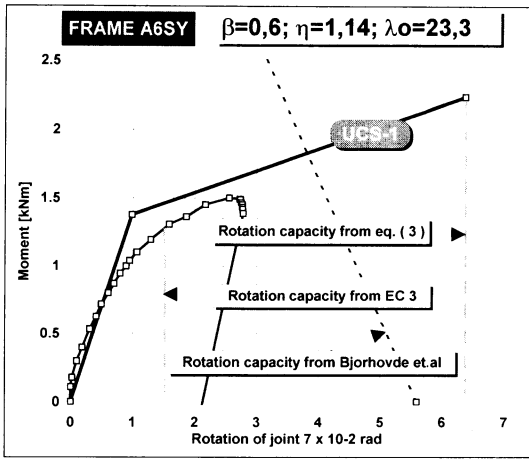

Fig. 18 M-Φ curve and estimations of **Φrc** for RI joint

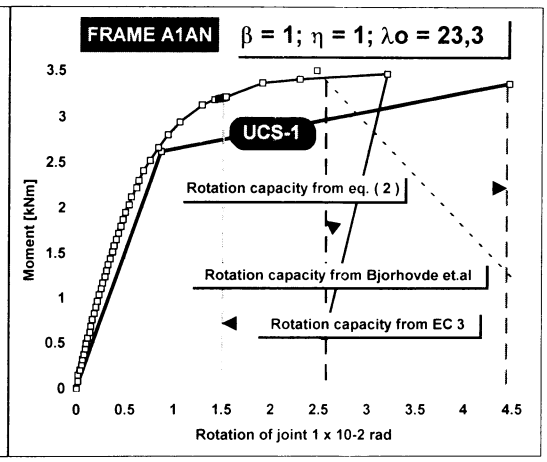

Fig. 19 M-Φ curve and estimations of **Φrc** for RR joint

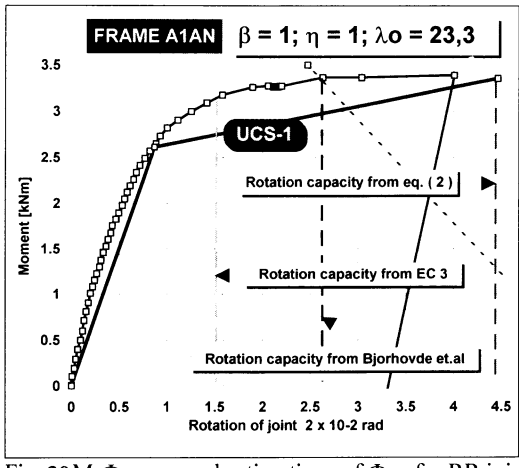

Fig. 20 M-Φ curve and estimations of **Φrc** for RR joint

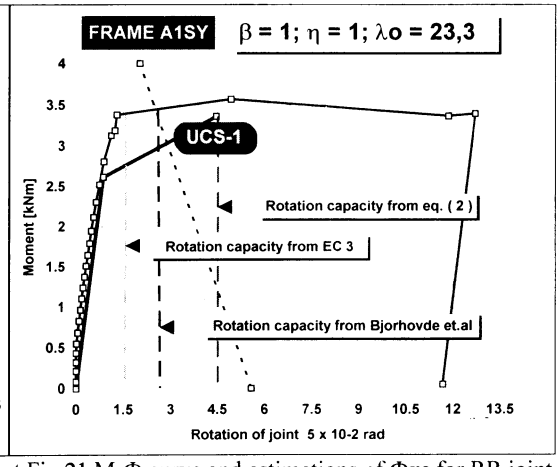

Fig. 21 M-Φ curve and estimations of **Φrc** for RR joint

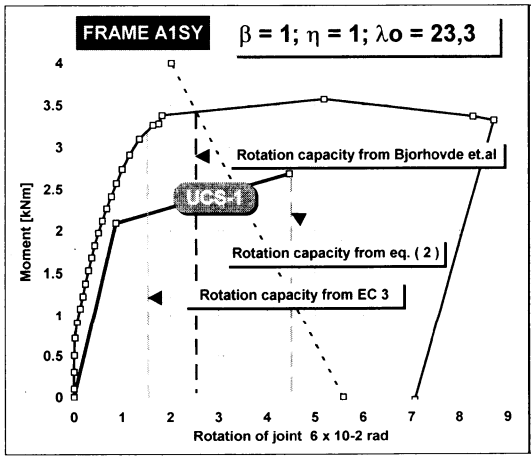

Fig. 22 M-Φ curve and estimations of **Φrc** for RR joint

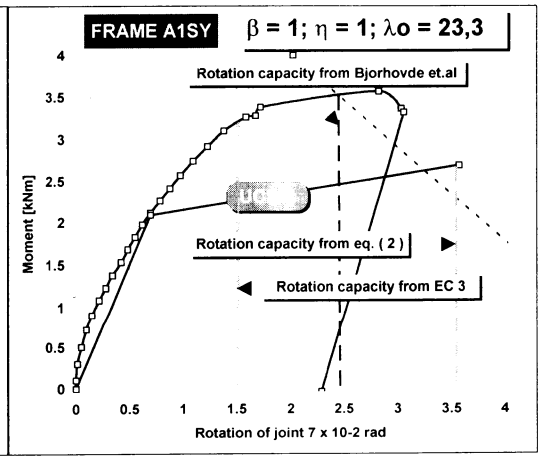

Fig. 23 M-Φ curve and estimations of **Φrc** for RR joint

In this Table are presented moreover, the maximum rotations of joints obtained during the tests.
In Fig. 4-17 the experimental results of moment - rotation (M-Φ) curves are shown. The series A RI joints are presented. Moreover, examples of such results for RR joints are given in Fig.19-23. In above figures the discussed three estimations of rotation capacity of joints are mentioned. The bilinear model UCS-1 (Szlendak 1996a,b) is suggested to estimate the actual behaviour of such connections. This UCS-1 estimation is presented in Fig. 4-23.

4 CONCLUSIONS

1. The EC-3 estimation of the rotation capacity of RI and RR joints seems to be too pessimistic. This estimation could be useful if one want to preliminary predict the moment when elastic work of connections is finished.
2. Bjorhovde et.al estimation is more optimistic then EC-3 but seems to be as well too much conservative.
3. The estimation of Φrc proposed in this paper is derived from the UCS-1 model of connection. It is more optimistic then these two presented above. In certain joints, Fig. 4-23, the predicted rotation capacity seems to be very optimistic. However, before the frame failure i.e. cracks of the welds or instability of the section only one joint in the frame presents its full rotation capacity. So, for the other joints of the same frame the proposed formula will be too optimistic.

REFERENCES

Szlendak J. 1996a. Joints behaviour in the test middle scale steel frames. Proc.7 th Int. Symp. *"Tubular Structures"*, 237-244, Miscolc, Balkema.

Szlendak J. 1996b. Uniform classification system with applications to connections between RHS columns and I beams. Arch. Inż. Ląd.(Poland), Nr 4/96, 447-469

Bjorhovde R., Brozzetti J., Colson A.: Classification system for beam-to-column connections, J.Struct. Engrg., ASCE. 116(11), 1990, 3059-3076.

Eurocode No 3: Design of steel structures: Part 1.1 General rules and rules for buildings. ENV 1993-1-1: 1992/prA2: 1994.

Tubular Structures VIII, Choo & Van der Vegte (eds) © 1998 Balkema, Rotterdam, ISBN 90 5809 001 9

Design model for bolted moment end plate connections joining rectangular hollow sections

A.T.Wheeler, M.J.Clarke & G.J.Hancock
Department of Civil Engineering, The University of Sydney, N.S.W., Australia
T.M.Murray
Department of Civil Engineering, Virginia Polytechnic Institute and State University, Blacksburg, Va., USA

ABSTRACT: The paper presents a model for the determination of the serviceability and ultimate moment capacities of bolted moment end plate connections utilising rectangular hollow sections and two rows of bolts. One row of bolts is positioned above the top flange and the other is symmetrically positioned below the bottom flange. The model considers the combined effects of prying action due to flexible end plates and the formation of yield lines in the end plates. The model is calibrated and validated using experimental data from an associated test program.

The design model constitutes a relatively simple method for predicting the serviceability and ultimate moment capacities for the particular type of bolted moment end plate connection described in this paper. A step-by-step design procedure is given which illustrates how the design model can be applied to practical connection designs.

KEYWORDS: tubular, connections, moment end plate, structural design, yield line, prying.

1 INTRODUCTION

The increase in the use of rectangular hollow sections in mainstream structures coupled with the economics of prefabrication has highlighted the need for simple design methods that produce economical bolted connections for tubular members. Moment end plate connections joining I-section members have been used extensively and considerable documentation on their behaviour exists in the literature (for example, Grundy *et al*, 1980; Murray, 1988, 1990; Kukreti *et al*, 1990). Contrastingly, research on end plate connections joining rectangular and square hollow sections has been limited and furthermore has concentrated primarily on pure tensile loading (Kato & Hirose, 1985; Packer *et al*, 1989), or combined compression and bending (Kato & Mukai, 1991). Although some test programs on tubular end plate connections subjected to flexural loading have been conducted (Mang, 1980; Petit *et al*, 1986), associated theoretical or design models were not presented.

When an end plate connection is subjected to pure flexure, tensile loads are applied to the bolts on the tensile side of the neutral axis through the bending of the plate. Failure of the connection generally occurs when these bolts reach their tensile capacity, which may occur either before or after yielding has occurred in the end plate (Nair *et al*, 1974). When yielding does not occur, the end plate is said to be "rigid". When yielding does occur, the end plate is said to be "flexible". The design of connections with rigid end plates may be less difficult than those with flexible end plates due the need to consider prying effects in the latter. However, flexible end plates invariably provide a more economical and ductile connection.

The effects of end plate bending and the resulting prying action have been studied extensively (Agerskov, 1976; Kato & McGuire, 1973; Nair *et al*, 1974; Kennedy *et al*, 1981), using various methods such as the stub-tee analogy. While the stub-tee method is primarily associated with moment end plate connections joining I-sections, the behaviour of end plate connections utilising rectangular hollow sections is similar. Thus the stub-tee analogy can be adapted to suit rectangular hollow section end plate connections.

Kennedy *et al* (1981) suggested three distinct modes of end plate behaviour based on the plate thickness and magnitude of loading. The first mode is termed *thick plate behaviour* and is characterised by the absence of prying effects and yield lines. At the other extreme, the third mode is termed *thin plate behaviour* and is characterised by yield lines through the bolt positions and a maximum value of the prying force. The second mode, termed *intermediate plate behaviour*, falls between the thick and thin plate behaviour and is characterised

by the prying force ranging from zero to the maximum attainable value.

In this paper, an analytical model to determine the moment capacity of end plate connections joining rectangular hollow sections is presented. The model is based on a modification of the stub-tee analogy originally developed for I-section end plate connections. The model is further refined using yield line analysis to enable the effect of the bolt positions along the tensile face of the end plate to be included. The model described in this paper is limited to the end plate connection containing two rows of bolts as shown in Figure 1. The predictions of the model are compared with the results obtained from an associated experimental program conducted at the University of Sydney (Wheeler *et al*, 1995, 1997a).

2 EXPERIMENTAL STUDY

The general configuration of the connections studied experimentally is shown in Figure 1 together with the relevant terminology. The connections were tested in pure bending by subjecting a beam, containing an end plate (splice) connection at mid span, to four-point bending.

The parameters varied in the test program include the plate size (W_p, D_p), the plate thickness (t_p), the section shape (square (SHS) or rectangular (RHS)), and the position of the bolts with respect to the section flange (s_o) and the section web (c). The dimensions of the end plates used in the experimental program are given in Table 1. The distance from the edge of the plate to the centre of the bolts (a_e) was constant at 30 mm.

All holes were clearance holes (diameter 22 mm) for M20 bolts. The end plate material was 350 grade steel to AS 3678 (SA, 1981b) with a nominal yield stress of 350 MPa. The measured static yield stress (f_y) and ultimate tensile strength (f_u) for each end

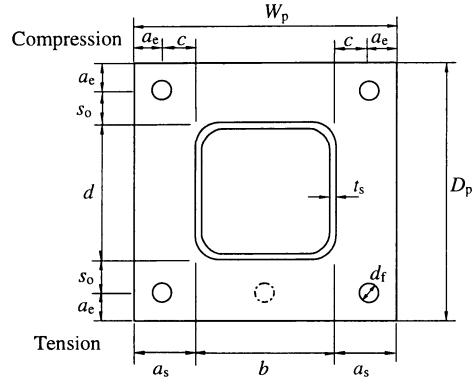

Figure 1. End plate layout

Table 1. End Plate Connection Details

Specimen No.	Plate Dimensions (mm) t_p	W_p	D_p	s_o	c	M_{cu} kNm
11 (SHS)	12	210	280	35	0	48.6
12 (SHS)	16	210	280	35	0	69.0
13 (SHS)	20	210	280	35	0	77.4
14 (RHS)	12	160	330	35	0	57.1
15 (RHS)	16	160	330	35	0	72.5
16 (RHS)	20	160	330	35	0	86.6
17 (SHS)	12	280	280	35	35	38.6
18 (SHS)	16	280	280	35	35	59.5
19 (SHS)	20	280	280	35	35	72.4
20 (RHS)	12	230	330	35	35	48.5
21 (RHS)	16	230	330	35	35	71.3
22 (RHS)	20	230	330	35	35	79.6
23 (SHS)	16	210	300	45	0	58.3
24 (SHS)	16	210	260	25	0	66.6
25 (RHS)	16	160	350	45	0	62.1
26 (RHS)	16	160	310	25	0	86.0

Table 2. Measured End Plate Material Properties

t_p (mm)	f_y (MPa)	f_u (MPa)
12	354	499
16	349	482
20	351	496

plate obtained through coupon tests are listed in Table 2.

The sections sizes used were 150×150×9 square hollow section (SHS) and 200×100×9 rectangular hollow section (RHS) of nominal 350 grade (SA, 1991a). The SHS and the RHS had measured ultimate moment capacities (M_{us}) of 119 kNm and 138 kNm, respectively. The bolt and nut assemblies were M20 structural grade 8.8 assemblies (grade 8.8/T to AS 1252 (SA, 1981a)). The measured yield and ultimate tensile loads of the bolts were 195 kN and 230 kN, respectively.

The connections were prefabricated to AS 4100 (SA, 1990) using a combination fillet/butt weld joining the section to the end plate. This weld was SP category and qualified to AS 1554.1 (SA, 1991c). A nominal leg length of 8 mm for the fillet was used.

Upon assembly of the connection, the bolts were tensioned to the specified pre-load of 145 kN. An incremental load was then applied to the connection by means of a stroke-controlled servo until failure occurred. As the sections were not susceptible to local buckling, the ultimate load of the specimen was limited to connection failure, which occurred either when the tensile bolts fractured, or when the longitudinal deformations of the end plate were deemed excessive. The ultimate moment (M_{cu}) for each test is listed in Table 1.

3 GENERAL THEORETICAL BASIS OF MODEL

Theoretical models for the bolted tubular moment end-plate connection based on yield line analysis and the stub-tee analogy are presented in this section. A generalised connection model for predicting the ultimate capacity of the connection involving the integration of both the yield line and stub-tee analysis is detailed in Section 4.

The yield line analysis, which provides an estimate of the yield moment of the connection (M_{cy}), is described in detail in Wheeler *et al* (1997b). Yield line analysis also facilitates the determination of connection serviceability limit moments and provides a refinement to the stub-tee analysis as discussed in Section 4.

The theoretical model based on the stub-tee analogy considers the effects of prying action and aims to predict the experimental ultimate strength of the connection (M_{cu}). This model is limited by the assumption that the end plate behaves in a one-dimensional fashion due to the formation of yield lines across the width of the end plate (Modes 1 and 2 shown in Figure 2) (Agerskov, 1976; Kato & McGuire, 1973). Since the yield lines invariably undergo significant rotations prior to the connection ultimate strength being reached, much of the material is stressed into the strain-hardening range. For the purpose of predicting the connection *ultimate* moment, it is therefore appropriate to assume the yield lines are fully plastic and stressed to a level denoted by f_p which is greater than the yield stress f_y but less than the ultimate tensile strength f_u (see Equation 12 following).

3.1 Yield Line Analysis

The three yield line mechanisms that were observed in the experimental program are shown in Figure 2. Mode 1 consists of yield lines forming at the top and bottom of the section, coupled with elongation and yielding of the tensile bolts (Figure 2a).

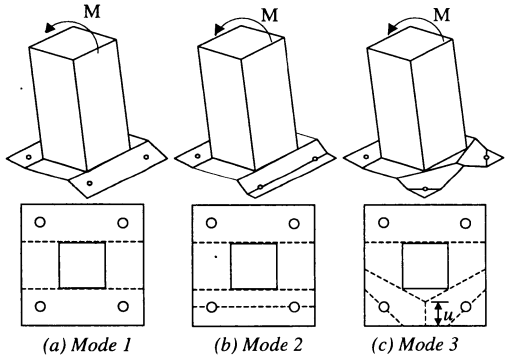

Figure 2. Yield line modes of failure

In Mode 2, an additional yield line forms through the line of bolts on the tension side of the connection (Figure 2b). Once the Mode 2 mechanism has formed, no additional load is transferred to the tensile bolts as the end plate deforms. Mode 3 comprises a more complex arrangement of yield lines (Figure 2c). As for Mode 2, the yield lines pass through the tensile bolts and no additional loads are transferred to the bolts following the yield line formation.

A detailed analysis for each mode is presented in Wheeler *et al* (1997b), with the yield moments (M_{yl}) for Mode 1, Mode 2 and Mode 3 being given by:

Mode 1

$$M_{yl} = \left(\frac{(d'+2(s_o'+a_e))W_p}{(s_o'+a_e)d'} m_p + \frac{B_y a_e}{s_o'+a_e} \right) d \qquad (1)$$

Mode 2

$$M_{yl} = \left(\frac{2(d'+s_o')W_p}{s_o' d'} - \frac{nd_f}{s_o'} \right) m_p d \qquad (2)$$

Mode 3

$$M_{yl} = \left(\frac{W_p}{d'} + \frac{\frac{vW_p}{b}(b^2+4q^2) + \left(\sqrt{r^2+4v^2q^2}\right)d_{34} + 4uqv}{(2qc+s_o'b)d'} \right) d\, m_p \qquad (3)$$

where $W_p = b + 2a_e + 2c$

$v = d'+s_o'$

$q = a_e + s_o'-u$

$r = 2qc - bd'$

$$d_{34} = \frac{a_e(2qv-r)}{qvr}\sqrt{r^2+4q^2v^2} - 2d_f$$

For Mode 3, the yield moment M_{yl} must be minimised with respect to the variable u to obtain the correct lower bound solution.

The terminology used in Equations (1) to (3) is defined in Figure 1, with n being the number of bolts in the tensile zone. In the yield line analysis for Mode 1, $B_y = nB_{yl}$ is taken as the yield load of the tensile bolt group. The yield load of an individual bolt (B_{yl}) was measured to be 195 kN. The plastic moment per unit length (m_p) for yield line analysis is given by

$$m_p = \frac{1}{4} t_p^{\,2} f_y \qquad (4)$$

where f_y is the yield stress of the end plate and t_p is the end plate thickness.

In order to improve the accuracy of the model, the depth of the section (d) and the distance from the line of bolts to the section flange (s_o) are corrected

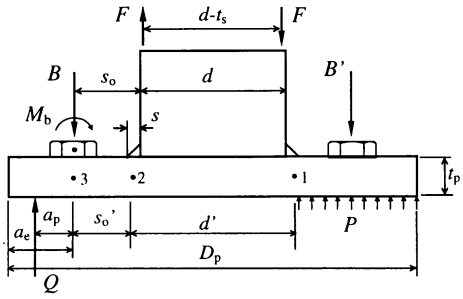

Figure 3. Analytical model used in modified stub-tee analysis

to $d' = d + \sqrt{2}\,s$ and $s_o' = s_o - s/\sqrt{2}$, where s is the leg length (8 mm) of the fillet weld.

3.2 *Modified Stub-Tee Analysis*

General Model

The stub-tee model involves the application of simple rigid plastic (yield line) analysis to an analogous beam that represents the one-dimensional behaviour of the end plate with yield lines parallel to the axis of bending only. This simple representation of the connection is shown in Figure 3, with the equivalent beam having a length equal to the plate depth (D_p), and a depth equal to the plate thickness (t_p).

The model assumes that the plastic hinges that form at Points 1, 2 and 3 (Figure 3) represent yield lines which form transversely across the end plate as demonstrated in Modes 1 and 2 (Figure 2). If the bolts are positioned such that a Mode 3 failure occurs, the model needs to be adjusted using the "equivalent width" concept as discussed in Section 4.

The moment acting on the connection (M) is assumed to be applied to the end plate through equal and opposite flange forces F acting through the centrelines of the flanges, so that

$$M = F(d - t_s) \tag{5}$$

The bolt forces are assumed to act through the centre of the bolts and are denoted B and B' on the tensile and compressive sides of the connection, respectively. The moment generated through bending of all the bolts on the tensile side of the connection, resulting from the end plate deformation, is denoted M_b. The resultant of the contact forces acting on the compressive side of the end plate connection is denoted P, with the prying force on the tension side of the connection being simplified to a point load (Q) acting at a distance a_p from the line of the tensile bolts. Following the approach of Nair *et al* (1974), the quantity a_p is

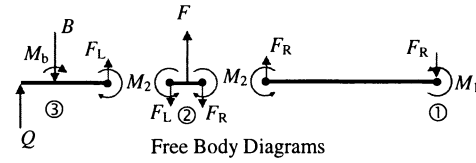

Figure 4. Definition of forces

defined as the lesser of the distance to the edge of the plate (a_e) and twice the end plate thickness ($2t_p$).

The tensile force (F) acting through the tensile flange of the section can be expressed in terms of the shear forces either side of the flange,

$$F = F_R + F_L \tag{6}$$

where F_L is the shear force on the left and F_R the shear force on the right side of the flange as shown in Figure 4. These shear forces can be expressed in terms of the tensile bolt loads (B), the prying force (Q) and the internal moments at Points 1 and 2 (M_1, M_2) using

$$F_L = B - Q \tag{7}$$

$$F_R = \frac{M_1 + M_2}{d'} \tag{8}$$

Combining Equations 5–8, the general expression for the connection moment is obtained as

$$M = F(d - t_s) = \left(B - Q + \frac{M_1 + M_2}{d'}\right)(d - t_s) \tag{9}$$

The plastic moment M_{ip} for each of the "hinges" i shown in Figure 3 is given by

$$M_{ip} = \frac{1}{4} t_p^2 f_p l_i \tag{10}$$

where t_p is the end plate thickness, f_p is the stress along the yield line, and l_i is the length of the yield line. In the case of Points 1 and 2, the yield line length l_i is simply the width of the end plate W_p. Since the yield line at Point 3 forms through the line of the bolts, its length is assumed to be defined by

$$l_3 = W_p - n d_f \tag{11}$$

in which n is the number of bolts in the tensile zone and d_f is the diameter of the bolt holes.

Reflecting the influence of strain-hardening on the ultimate moment capacity of the connection, the stress (f_p) used to calculate the plastic moment capacity of the end plate is assumed to be intermediate in value between the yield stress (f_y) and the ultimate tensile strength (f_u) of the plate material (Packer *et al*, 1989),

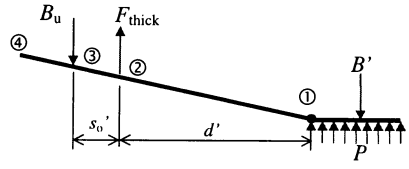

Figure 5. Thick plate behaviour

$$f_p = \frac{f_y + 2f_u}{3} \tag{12}$$

In this paper, f_p is termed the plate design stress.

Thick Plate Behaviour

The mechanism described as thick plate behaviour is shown in Figure 5. The mechanism forms through the combination of a yield line at Point 1, and yielding of the tensile bolts. The ultimate bolt load B_u is the tensile resistance produced by n bolts, each with a tensile strength of B_{u1}.

For the thick plate, the prying force (Q) is zero. Also, since there is little bending in the plate away from Point 1, the resisting moment of the bolts (M_b) is neglected. The moment at Point 2 (M_2) is found by considering moment equilibrium for the left-hand segment of the beam and is expressed as

$$M_2 = B_u s_o' \tag{13}$$

From Equations 9 and 13, setting Q and M_b to zero, and using the plastic moment at Point 1, the moment for the connection can be expressed as

$$M_{thick} = \left(\frac{M_{1p} + B_u(d' + s_o')}{d'} \right)(d - t_s) \tag{14}$$

Thick end plate behaviour is considered to hold as long as the moment at Point 2, as calculated from Equation 13, is less that the plastic moment ($M_2 \le M_{2p}$).

Intermediate Plate Behaviour

The mechanism for intermediate plate behaviour is shown in Figure 6, and is characterised by plastic hinges forming at Points 1 and 2, with the bolts on the tensile side of the connection also yielding.

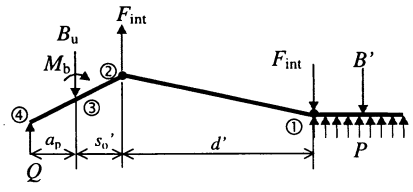

Figure 6. Intermediate plate behaviour

The bolts are assumed to have attained their full plastic moment and so the resistance generated by the bending of n bolts is given by

$$M_b = n\frac{\pi d_b^3 f_{yb}}{32} \tag{15}$$

where d_b is the bolt diameter and f_{yb} is the bolt yield stress.

At the commencement of intermediate plate behaviour, the prying force (Q) is zero. The prying force will attain its maximum value (Q_{max}) at the point of transition from intermediate to thin plate behaviour. As previously discussed, the yield lines characteristic of intermediate plate behaviour form at Points 1 and 2, thus $M_1 = M_{1p}$ and $M_2 = M_{2p}$. In the following description, intermediate behaviour is addressed firstly for the limiting case of zero prying force ($Q = 0$), and then for positive prying force ($Q > 0$).

Case 1: Prying force $Q = 0$. In this case, the end plate is in the transition stage between thick and intermediate plate behaviour. The bolt load (B) can be determined from Figure 6 by taking moments about Point 2 to furnish

$$B = \frac{M_{2p} + M_b}{s_o'} \tag{16}$$

Substituting Equation 16 into Equation 9, and setting the prying force (Q) to zero enables the minimum moment for the connection for intermediate behaviour to be expressed as

$$M_{int} = \left(\frac{M_{2p}(d' + s_o') + M_{1p}s_o' + M_b d'}{s_o' d'} \right)(d - t_s) \tag{17}$$

Case 2: Prying force $Q > 0$. When the prying force (Q) is greater than zero it can be determined through

$$Q = \frac{M_3}{a_p} = \frac{F_L s_o' - M_{2p} - M_b}{a_p} \tag{18}$$

Substituting Equation 7 into Equation 18 enables Q to be determined as

$$Q = \frac{Bs_o' - M_{2p} - M_b}{a_p + s_o'} \tag{19}$$

Further substitution of Equation 19 into Equation 9 results in the following expression for the moment acting on the connection during intermediate behaviour with $Q > 0$:

$$M_{int} = \left(\frac{M_{2p}(d' + s_o' + a_p) + M_{1p} + (Ba_p + M_b)d'}{(a_p + s_o')d'} \right)(d - t_s) \tag{20}$$

The above exposition on intermediate behaviour is valid from the point when the moment at Point 2, as calculated from Equation 13, exceeds the plastic moment, and while the moment at Point 3 is less than the plastic moment. The bolt load B must also be less than or equal to the ultimate bolt load (B_u). These conditions can be expressed in the following inequalities:

$$B_u s_o' \geq M_{2p} \tag{21}$$

$$F_L s_o' - M_{2p} \leq M_{3p} \tag{22}$$

Thin Plate Behaviour

As depicted in Figure 7, thin plate behaviour occurs when the moments at Points 1, 2 and 3 have reached their plastic limits (M_{1p}, M_{2p} and M_{3p}).

Compared to intermediate plate behaviour, for thin plates an additional yield line forms at Point 3. Once this yield line forms, the prying force attains its maximum value Q_{max}:

$$Q_{max} = \frac{M_{3p}}{a_p} \tag{23}$$

The plate behaves as an intermediate plate prior to the yield line forming at Point 3. Using Equation 19 and substituting $Q = Q_{max}$ enables the bolt load B to be expressed as

$$B = \frac{Q_{max}(a_p + s_o') + M_{2p} + M_b}{s_o'} \tag{24}$$

The resulting connection moment for thin plate behaviour is found using Equations 24, 23 and 9, and is given by

$$M_{thin} = \left(\frac{M_{2p}(d'+s_o') + M_{3p}d' + M_{1p}s_o' + M_b d'}{d' s_o'} \right)(d - t_s) \tag{25}$$

4 GENERALISED CONNECTION MODEL

4.1 *Ultimate Strength*

While the stub-tee method assumes that the yield lines form in a one-dimensional fashion across the section, this may not always be the case. The generalised connection model discussed in this section constitutes a modification of the stub-tee analogy to cater for the Mode 3 plastic mechanism (see Figure 2) which involves inclined yield lines.

As yield line analysis is based on virtual work principles, it could be said that for a given connection with a plate of width W_p failing in Mode 3 with inclined yield lines (Figure 2c), there is an "equivalent" connection with an "equivalent"

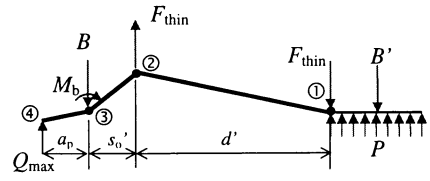

Figure 7. Thin plate behaviour

end plate width w_{eq} that fails according to a Mode 2 mechanism (Figure 2b) with the one-dimensional patterns of yield lines. This equivalent width w_{eq} is determined using Equation 2 and is expressed as

$$w_{eq} = \left(\frac{4M_{yl}}{d t_p^2 f_y} + \frac{n d_f}{s_o'} \right)\left(\frac{d' s_o'}{2(d'+s_o')} \right) \tag{26}$$

where M_{yl} is the yield moment corresponding to the Mode 3 mechanism.

The modified stub-tee method identified two failure modes, which are bolt capacity and end plate capacity. Bolt capacity manifests itself as fracture of the tensile bolts, and may occur in conjunction with thick or intermediate plate behaviour. Plate capacity governs when a plastic mechanism forms in the end plate, and is associated with thin plate behaviour. The plate capacity is independent of the bolt loads.

Utilising the modified stub-tee method with appropriate equivalent widths (w_{eq}), and the plate design stress (f_p) defined by Equation 12, the predicted ultimate moment corresponding to both bolt capacity (M_{cb}) and plate capacity (M_{cp}) for the connections outlined in Table 1 can be determined. These moments, together with the ratio of the predicted ultimate moments (i.e. the lesser of M_{cb} and M_{cp}) to the experimental ultimate moments, are given in Table 5.

The statistical analysis shows a good correlation between the experimental and the predicted results. The mean and standard deviation of the predicted-to-test ratios for all the tests was 0.95 and 0.09 respectively. These results can be further divided into two categories depending on whether the ultimate capacity was limited by plate capacity or bolt capacity. The connections with a tensile bolt failure mode demonstrated an excellent correlation with the test results, having a mean of 1.00 and a standard deviation of 0.07. In these connections, the deformations of the end plates were not as severe as in the thin plates, and the assumption that the end plate behaves in the same manner as a wide beam is appropriate. The connections characterised by an end plate failure mode showed a less accurate correlation with the experimental results, having a mean ratio of predicted to experimental moments of 0.89 and a standard deviation of 0.08. The low average prediction is thought to be a result of the

Table 3 Connection Ultimate Moments Predicted using Modified Tee-Stub Model

Test #	Width w_{eq} (mm)	M_{cb} kNm	M_{cp} kNm	Failure Mode	Ratio Pred./Test
11	210.0	47.6	*41.6*	End Plate (2)	0.85
12	210.0	*60.4*	67.8	Bolt	0.88
13	210.0	*74.8*	103.8	Bolt	0.97
14	160.0	58.3	*42.4*	End Plate (2)	0.74
15	160.0	71.4	*67.6*	End Plate (2)	0.93
16	160.0	*84.8*	102.2	Bolt	0.98
17	189.7	46.2	*37.8*	End Plate (3)	0.98
18	201.8	*59.5*	65.2	Bolt	1.00
19	201.8	*73.3*	99.6	Bolt	1.01
20	168.4	59.0	*44.4*	End Plate (3)	0.92
21	179.1	74.2	*75.6*	End Plate (3)	1.04
22	179.1	*89.1*	114.9	Bolt	1.12
23	210.0	53.2	*53.2*	End Plate (2)	0.91
24	210.0	*70.6*	97.5	Bolt	1.06
25	160.0	62.3	*52.5*	End Plate (2)	0.85
26	160.0	*84.3*	98.4	Bolt	0.98
				Mean	0.95
				S.D.	0.09

* For connections governed by end plate capacity, the relevant yield line mechanism is noted in brackets

fact that the model does not incorporate the membrane stiffening effects which occur in practice when the end plates deform significantly.

4.2 *Serviceability Limits*

To determine the serviceability limit moments (M_{cs}) of the connection, yield line analysis is utilised. The yield line moment capacity per unit length is assumed to be based on the plate yield stress (f_y) rather than the plate design stress (f_p), the latter being appropriate for ultimate strength calculations only. The serviceability limit is defined as when either the tensile bolts commence to yield, or the end plate forms a plastic mechanism. The moment at which the bolts begin to yield (Mode 1 yield line failure) is determined from Equation 1, while the formation of a plastic mechanism in the end plate (without bolt deformation) is described by the Mode 2 and Mode 3 mechanism analyses (Equations 2 and 3).

5 OVERVIEW OF DESIGN MODEL

The design model presented here relates to a bolted moment end plate connection utilising square or rectangular hollow sections. The layout of the end plate is shown in Figure 1, with the depth of the beam section (d) assumed to be no greater than 400 mm.

A major recommendation of this paper is that the end plate should behave in an intermediate manner to achieve an economical and ductile design. The disadvantage of a thin end plate is that it exhibits low stiffness, causing large deformations which reduce the serviceability limit moment of the connection relative to the connection ultimate moment. On the other hand, a connection with an end plate classified as thick can fail in a brittle manner due to bolt fracture and may also be unnecessarily expensive. Thus, the paper suggests that the "ideal" failure mode should involve bolt capacity combined with intermediate plate behaviour.

Following the philosophy of Murray (1990), it is assumed that the bolts in the compressive region resist all the shear loads. It is recommended that the tensile bolts be positioned so that two or more bolts fall on or between the line of the webs (i.e., $c = a_s - a_e \leq 0$, see Figure 1). If this condition is not met, two-dimensional yield line mechanisms may form requiring complicated yield line analysis to calculate the equivalent end plate width (w_{eq}).

The strength limit state moment capacity of the connection (M_{cu}) is the lower value of the ultimate moments computed on the basis of bolt capacity (M_{cb}) and plate capacity (M_{cp}). The connection serviceability moment (M_{cs}) is the lower of the moments that cause yielding of the bolts (M_{cbs}) or yielding of the end plate (M_{cps}).

The resisting moment generated by the bolts (M_b) and the plate design stress in the end plate (f_p) are defined by Equations 15 and 12, respectively. The corresponding material properties should be the nominal values obtained from the appropriate standards.

5.1 *Strength Limit State Design*

The moment capacity of the connection is determined using the modified stub-tee method which includes the effects of prying forces. Equations to calculate the connection capacity based on bolt failure and end plate failure are presented. The moment capacity of the connection is the lower of these two values.

Connection Capacity Limited by Bolt Failure

Bolt failure is premised on intermediate plate behaviour. The bolt load at failure is equal to the nominal tensile strength of all tensile bolts (B_u), and the stress in the end plate yield lines is equal to the plate design stress (f_p) as defined by Equation 12. Since it is assumed that tensile failure of the bolts governs, it is appropriate that the resistance factor for bolts in tension (ϕ_b) be used.

From an adaptation of Equation 20, the connection design moment capacity ($\phi_b M_{cb}$) is given by

$$\phi_b M_{cb} = \phi_b \left(\begin{array}{l} w_{eq}\left(d'+2\left(s_o'+a_p\right)\right)t_p^2 f_p \\ \quad +4d'\left(B_u a_p + M_b\right) \end{array} \right) \frac{(d-t_s)}{4\left(a_p+s_o'\right)d'} \quad (27)$$

Alternatively, if the connection design moment M^* is known, the appropriate end plate thickness (t_{bu}) is given by

$$t_{bu} = \sqrt{\frac{4\left(\dfrac{M^*\left(a_p+s_o'\right)}{\phi_b(d-t_s)} - \left(B_u a_p + M_b\right) \right) d'}{w_{eq}\left(d'+2\left(s_o'+a_p\right)\right)f_p}} \quad (28)$$

To avoid thick plate behaviour, the limit on the plate thickness for the capacity limited by bolt failure is

$$t_p \le \sqrt{\frac{4B_u s_o'}{w_{eq} f_p}} \quad (29)$$

Connection Capacity Limited by End Plate Failure

The equations for end plate capacity are based on thin plate behaviour using the plate design stress (f_p). Since the capacity of the plate is assumed to govern, with no significant contribution from the bolts, it is appropriate that the resistance factor for the plate in bending (ϕ_p) be used.

From an adaptation of Equation 25, the connection design moment capacity is given by

$$\phi_p M_{cp} = \phi_p \left(\begin{array}{l} t_p^2 f_p w_{eq}\left(d'+2s_o'\right) \\ \quad +t_p^2 f_p\left(w_{eq}-nd_f\right)d' \\ \quad +M_b d' \end{array} \right) \frac{(d-t_s)}{4d's_o'} \quad (30)$$

Alternatively, for a given connection design moment M^*, the appropriate end plate thickness is given by

$$t_{pu} = 2\sqrt{\frac{\left(\dfrac{M^* s_o'}{\phi_p(d+t_s)} - M_b \right) d'}{\left(w_{eq}\left(d'+2s_o'\right)+\left(w_{eq}-nd_f\right)d'\right)f_p}} \quad (31)$$

5.2 *Serviceability Limit State Design*

The serviceability moment is based on yield line analysis. Serviceability limits for the connection occur when either the bolts or the end plate begin to yield. Equations 32 and 33 following give the serviceability moments for connections whose plate parameters are known, while Equations 34 and 35 enable the appropriate plate thickness to be calculated for a given serviceability moment M_s^*.

The serviceability limit moments based on bolt yielding ($\phi_b M_{cbs}$) and plate yielding ($\phi_p M_{cps}$) are given respectively by

$$\phi_b M_{cbs} = \phi_b \left(\begin{array}{l} \dfrac{\left(d'+2\left(s_o'+a_e\right)\right)w_{eq}t_p^2 f_y}{4\left(s_o'+a_e\right)d'} \\ \quad +\dfrac{B_y a_e}{s_o'+a_e} \end{array} \right) (d-t_s) \quad (32)$$

$$\phi_p M_{cps} = \phi_p \left(\frac{\left(\left(d'+s_o'\right)w_{eq} - nd_f d'\right)t_p^2 f_y}{2s_o'd'} \right) (d-t_s) \quad (33)$$

Alternatively, if the connection design serviceability moment M_s^* is known, the required plate thickness to satisfy the serviceability requirements based on bolt yielding (t_{bs}) and plate yielding (t_{ps}) are given respectively by

$$t_{bs} = 2\sqrt{\frac{\dfrac{M_s^*\left(s_o'+a_e\right)d'}{\phi_b(d-t_s)} - B_y a_e d'}{\left(d'+2\left(s_o'+a_e\right)\right)w_{eq}f_y}} \quad (34)$$

$$t_{ps} = \sqrt{\frac{2M_s^* s_o' d'}{\phi_p(d-t_s)\left(\left(d'+s_o'\right)w_{eq} - nd_f d'\right)f_y}} \quad (35)$$

6 PRACTICAL DESIGN PROCEDURE

The recommended procedure for the design of an end plate connection of the type shown in Figure 1 is as follows:

(1) Estimate the end plate dimensions for initial design based on section size, bolt size and number of bolts.

(2) If two or more bolts are not positioned within the webs of the section ($c \le 0$), yield line analysis is required to determine the equivalent width (w_{eq}). Otherwise the equivalent width is equal to the end plate width (W_p). If the plate thickness is already known, go to Step (6).

(3) Solve for the strength limit state design thicknesses t_{bu} and t_{pu} using Equations 28 and 31. The required plate thickness (t_u) is equal to the maximum of the thickness based on bolt and plate capacity

$$t_u = \max(t_{bu}, t_{pu})$$

(4) Solve for the serviceability design thicknesses t_{bs} and t_{ps} using Equations 34 and 35. The required plate thickness (t_{sv}) is equal to the maximum of the serviceability thicknesses

calculated

$$t_{sv} = \max(t_{bs}, t_{ps})$$

(5) The resulting thickness for the end plate (t_p) must exceed both the serviceability and ultimate limit state thicknesses, but must be less than the maximum allowable plate thickness (t_{max}) given by Equation 29, that is

$$\max(t_{sv}, t_u) \leq t_p \leq t_{max}$$

(6) Solve Equations 27 and 30 using t_p to obtain the design moment capacities of the connection ($\phi_b M_{cb}$ and $\phi_p M_{cp}$). If $\phi_b M_{cb} > \phi_p M_{cp}$, either select an alternative bolting arrangement to lower the bolt capacity, or a thicker plate to increase the plate capacity. Similarly, if $M^* > \phi_b M_{cb}$ the bolt capacity must be increased. Moment capacities should then be recalculated to ensure they exceed the design moment (M^*).

(7) Solve Equations 32 and 33 to ensure that the serviceability limit moments $\phi_b M_{cbs}$ and $\phi_p M_{cps}$ are greater than the serviceability design moment (M_s^*).

(8) The serviceability limit moment is the minimum moment from Step (7), while the connection design capacity for the strength limit state is the minimum moment from Step (6).

Specific design examples are given in Wheeler *et al* (1997b, 1998).

7 CONCLUSIONS

This paper presents a simple and accurate model to predict the strength of a moment end plate connection utilising rectangular hollow sections. The model uses a modified stub-tee analogy coupled with yield line analysis to predict both the ultimate moment capacity and serviceability limit moment for the connection. The modified stub-tee analysis incorporates the effects of the prying forces on the connection strength, while the yield line analysis predicts the failure mechanism of the end plate to enable the calculation of an end plate "equivalent width" to be used in conjunction with the stub-tee model.

The model is limited to square and rectangular sections with two rows of bolts, one of which is above the top flange and the other of which is below the bottom flange. While the connections tested experimentally and used for model verification only contained two bolts in each row, the addition of extra bolts in the tensile (and compressive) bolt rows does not invalidate the model. The use of additional bolts in the tensile row will tend to enforce a Mode 2 end plate failure, for which the model presented in this paper is well suited.

Of the three types of plate behaviour presented (thick, thin and intermediate), it is recommended that the end plate connections should be designed to behave in an intermediate fashion, with connection strength being governed by bolt failure. Thin plate behaviour results in connections that are very ductile and exhibit extremely high rotations, while connections exhibiting thick plate behaviour are very brittle and may be uneconomical. The connection serviceability limit presented is based on first yield of the bolts or the formation of a yield line mechanism in the end plate.

The model demonstrates a good correlation with the associated experimental results, with an overall mean predicted-to-experimental ratio of 0.95, and a corresponding standard deviation of 0.09 for the range of connections tested. The model is effective in its consideration of all relevant failure modes which can occur, including bolt fracture and plastic mechanism formation in the end plate.

8 REFERENCES

Agerskov, H., (1976), "High-Strength Bolted Connections Subject to Prying", *Journal of Structural Division*, ASCE, **102**(1), 161-175.

Grundy, P., Thomas, I. R. & Bennetts, I. D., (1980). "Beam-to-Column Moment Connections", *Journal of Structural Engineering*, ASCE, **106**(1), 313-330.

Kato, B. & Hirose, R. (1985), "Bolted Tension Flanges Joining Square Hollow Section Members", *Journal of Structural Engineering*, ASCE, **111**(5), 163-177.

Kato, B. & McGuire, W. (1973), "Analysis of T-Stub Flange-to-Column Connections", *Journal of Structural Division*, ASCE, **99**(5), 865-888.

Kato, B. & Mukai, A. (1991), "High Strength Bolted Flanges Joints of SHS Stainless Steel Columns", *Proceedings*, International Conference on Steel and Aluminium Structures, Singapore, May 1991.

Kennedy, N. A., Vinnakota, S. & Sherbourne A. N., (1981) "The Split-Tee Analogy in Bolted Splices and Beam-Column Connections", *Joints in Structural Steelwork*, John Wiley & Sons, London-Toronto, pp. 2.138-2.157.

Kukreti, A. R., Ghassemieh, M. & Murray T. M., (1990), "Behaviour and Design of Large-Capacity Moment End Plates", *Journal of Structural Engineering*, ASCE, **116**(3), 809-828.

Mang, F., (1980), "Investigation of Standard Bolted Flange Connections for Circular and Rectangular Hollow Sections", CIDECT Programme 8A Final Report, Steel Construction Institute, Ascot, U.K.

Murray, T. M. (1988), "Recent Developments for the Design of Moment End-Plate Connections", *Journal of Constructional Steel Research*, (10), pp 133-162.

Murray, T. M., (1990), "Design Guide for Extended End Plate Moment Connections", Steel Design Guide 4, American Institute of Steel Construction.

Nair, R. S., Birkemoe, P. C. & Munse, W. H., (1974), "High Strength Bolts Subject to Tension and Prying", *Journal of the Structural Division*, ASCE, **100**(2), 351-372.

Packer, J. A., Bruno, L. & Birkemoe, P. C. (1989), "Limit Analysis of Bolted RHS Flange Plate Joints", *Journal of Structural Engineering*, ASCE, **115**(9), 2226-2241.

Petit, L., Plumier, A. and Rondal, J., (1986), "Tests on T Type Bolted Joints in Hollow Section Intended to Transmit a Moment", CIDECT Programme 6B Final Report, Steel Construction Institute, Ascot, U.K.

SA (1981a), *AS 1252-1981: High-strength Steel Structural Bolts with Associated Nuts and Washers for Structural Engineering*, Standards Australia, Sydney.

SA (1981b), *AS 3678-1981: Structural Steel – Hot-rolled plates, floorplates and slabs*, Standards Australia, Sydney.

SA (1990), *AS 4100-1990: Steel Structures*, Standards Australia, Sydney.

SA (1991a), *AS 1163-1981: Structural Steel Hollow Sections*, Standards Australia, Sydney.

SA (1991c). *AS 1554.1-1991: Structural Steel Welding – Part 1: Welding of Steel Structures*, Standards Australia, Sydney.

Wheeler A. T., Clarke M. J. & Hancock G. J., (1995), "Tests of bolted Moment End Plate Connections in Tubular Members," *Proceedings,* Fourteenth Australasian Conference on the Mechanics of Structures and Materials, Hobart, Tasmania, University of Tasmania, pp 331-336.

Wheeler A. T., Clarke M. J. & Hancock G. J., (1997a), "Bending Tests of Bolted End Plate Connections in Cold Formed Rectangular Hollow Sections," *Research Report*, No. R736, Department of Civil Engineering, The University of Sydney.

Wheeler A. T., Clarke M. J. & Hancock G. J., (1997b), "Design Model for Bolted Moment End Plate Connections using Rectangular Hollow Sections", *Research Report*, No. R745, Department of Civil Engineering, The University of Sydney.

Wheeler A. T., Clarke M. J. & Hancock G. J., (1998), "Design Model for Bolted Moment End Plate Connections using Rectangular Hollow Sections", *Journal of Structural Engineering*, ASCE, 124(2).

Tubular Structures VIII, Choo & Van der Vegte (eds) © 1998 Balkema, Rotterdam, ISBN 90 5809 001 9

Finite element modelling of bolted moment end plate connections in tubular members

A.T.Wheeler, M.J.Clarke & G.J.Hancock
Department of Civil Engineering, The University of Sydney, N.S.W., Australia

ABSTRACT: The increase in the use of rectangular hollow sections in mainstream steel structures coupled with the economics of prefabrication have highlighted the need for design methods that produce economical bolted tubular connections. The development of a design methodology for a particular connection type normally follows the determination of the connection behaviour using experimental or numerical methods.

This paper describes the finite element modelling philosophy employed to analyse bolted moment end plate connections joining square and rectangular hollow sections which are subjected to pure bending. The ABAQUS finite element package (HKS, 1995) is used to simulate the experimental behaviour observed in tests performed at the University of Sydney. The parameters varied in both the experiments and the ABAQUS simulations include the end plate thickness, the section shape (square or rectangular), and the position of the bolts. The results obtained from the finite element analyses are evaluated and the appropriateness of the model assessed by comparing the numerically predicted ultimate loads and moment-rotation responses with those of the corresponding tests.

KEYWORDS: ABAQUS, bolted tubular connections, tubular sections, moment-rotation behaviour.

1 INTRODUCTION

Investigations of connection behaviour are invariably accompanied by an experimental program. Due to the high cost of experimental work, these programs are generally limited to the variation of a few parameters that have the most effect upon the connection behaviour. A partial solution to this problem is to use finite element packages to model the additional variation in parameters.

Rigorous finite element modelling of bolted connections is not straightforward. Such modelling must take account of bolt pre-tensioning, contact between plates, prying action, plate separation, plate yielding, and bolt deformation and failure. Modern commercial finite element packages such as ABAQUS (HKS, 1995) have the capability to model all these phenomena, but there are many subtleties.

In the present work, the ABAQUS finite element package is used to simulate the experimental behaviour of bolted tubular end plate connections subjected to bending. The parameters varied in both the experiments and the ABAQUS simulations include the end plate thickness, the section shape (square or rectangular), and the position of the bolts.

2 DEVELOPMENT OF FINITE ELEMENT MODELS

2.1 Overview

The generation of a three dimensional finite element model of the tubular end plate connection was carried out using the PATRAN pre-processor (PDA Engineering, 1994). The connections were analysed using the ABAQUS finite element software package (HKS, 1995). The analysis incorporated the effects of both material and geometric non-linearities.

The finite element model of a typical bolted tubular end plate connection is shown in Figure 1, with the vertical axis of symmetry along the beam length being utilised to reduce the size of the model. To aid the model verification process, the connection was divided into five individual sub-models, each of which represent the various components of the connection. These components are identified in Figure 1 and are referred to as the end plate, the bolts, the weld, the section, and the rigid end cap.

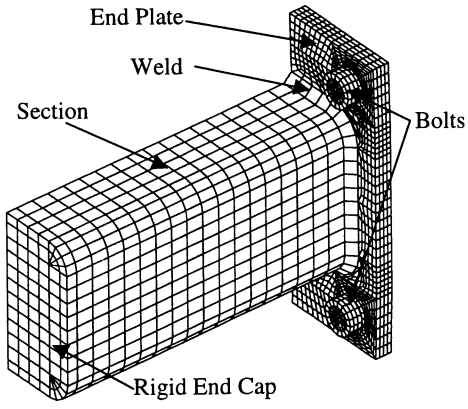

Figure 1. Finite element model

The model employed solid three dimensional brick elements for each of the components, with additional interface elements used to model contact/separation between various surfaces.

The incorporation of material non-linearity in the ABAQUS model requires the use of true stress-strain relationships. These were determined from measured engineering stress-strain curves. The material properties were assigned to the model using the "Elastic Plastic Isotropic Material" definition (HKS, 1995). Full details of the material properties are given in Wheeler and Clarke (1998).

2.2 *Beam Section*

To model the beam section, eight-noded linear brick elements were utilised as shown in Figure 2. These elements are of type C3D8 in ABAQUS terminology. The dimensions of the sections for the respective tests are given in Table 1 and correspond to the nominal values (AISC, 1992). The external radius of the corners of the section is equal to 2.5 times the thickness of the section.

The tubular sections employed in the bolted end plate connections were manufactured using a cold-forming process, and as a result the material in the corners of the section (the shaded portion in Figure 2) is of higher strength than the material on the flats of the section. Consequently, two different material properties were assigned to the corners and flats of the section. The corner material is assumed to extend through 90 degrees circumferentially.

Table 1. Nominal Section Sizes

	D (mm)	B (mm)	t_s (mm)
SHS	150	150	9
RHS	200	100	9

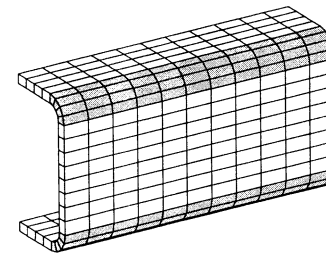

Figure 2. Beam model

2.3 *End Plate*

The layout of the end plates is shown in Figure 3, with the corresponding dimensions given in Table 2. For all tests, the edge distance to the centre of the bolt holes was 30 mm, and the diameter of the holes was 22 mm. The variable s_o is defined as the distance from the flange of the section to the centre of the bolt holes, and c is the dimension from the webs of the section to the centre of the bolt holes. The plate thickness is denoted t_p.

In the finite element simulations, the end plate was modelled using eight noded linear hybrid bricks, corresponding to element type C3D8H in ABAQUS. The linear hybrid elements (constant pressure elements) were selected to prevent possible problems of volume strain locking which can occur in the C3D8 linear elements (HKS, 1995). Following a convergence study, it was decided to use four elements through the thickness of the end plate for all analyses. The measured stress-strain relationships of the end plates follows the classic elastic-plastic-strain hardening pattern; full details are given in Wheeler and Clarke (1998).

2.4 *Bolts*

In many cases, the ultimate strength of the connection depends upon the tensile behaviour of the bolts. Therefore, to simulate the connection behaviour accurately, each bolt was modelled as a

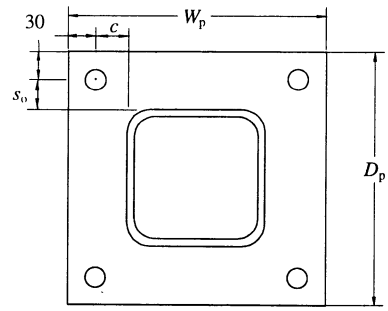

Figure 3. End plate layouts

Table 2. End Plate Details

Test #	Section	t_p (mm)	D_p (mm)	W_p (mm)	s_o (mm)	c (mm)
11	SHS	12	280	210	35	0
12	SHS	16	280	210	35	0
13	SHS	20	280	210	35	0
14	RHS	12	330	160	35	0
15	RHS	16	330	160	35	0
16	RHS	20	330	160	35	0
17	SHS	12	280	280	35	35
18	SHS	16	280	280	35	35
19	SHS	20	280	280	35	35
20	RHS	12	330	230	35	35
21	RHS	16	330	230	35	35
22	RHS	20	330	230	35	35
23	SHS	16	280	210	25	0
24	SHS	16	280	210	45	0
25	RHS	16	330	160	25	0
26	RHS	16	330	160	45	0

separate entity using the nominal cross-sectional areas (Ajax Fasteners Handbook, 1994). The model of a typical bolt constructed using eight noded linear hybrid brick elements (C3D8H) is shown in Figure 4. It can be seen in this figure that a step is included in the bolt diameter to model the decrease in effective cross-sectional area from the unthreaded to the threaded portion of the bolt shank. For all studies reported in this paper, the bolts were 20 mm nominal diameter.

The interaction (i.e. contact and separation) between the bolt and the end plate is modelled using the INTER4 cubic interface elements (HKS, 1995). The interface elements between the underside of the bolt head and the end plate were modelled as a "rough" interface to prevent slippage between the surfaces. The assemblage of interface elements between the bolt shank and the bolt hole modelled a frictionless surface to prevent the "penetration" of the bolt into the end plate at high rotations.

2.5 *Weld*

The connection between the tubular section and the end plate consisted of a combination butt-fillet weld.

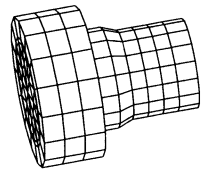

Figure 4. Bolt element layout

In the finite element model, the butt weld was assumed to be an extension of the beam section and therefore had no effect on the connection stiffness. On the other hand, the fillet weld has an effect on the connection strength and stiffness by inhibiting bending of the end plate immediately adjacent to the section, thus stiffening and strengthening the overall response. Consequently, the weld was modelled as an individual component in the connection model using eight noded linear brick elements (C3D8) and six noded linear triangular prism elements (C3D6) for the butt and fillet portions, respectively.

2.6 *Rigid End Cap*

Pure moment loading was applied to the connection using imposed rotations about the neutral axis of a rigid end cap attached to the far end of the beam section.

2.7 *Initial Stresses and End Plate Deformations*

The cold-formed tubular sections used in the end plate connections contain residual stresses as a result of the manufacturing process. Residual stresses and initial deformations of the end plate are also induced when the latter is welded to the tubular section. Bolt pre-tensioning introduces further initial stresses in the connection. These initial stresses and initial end plate deformations have varying effects upon the connection behaviour as discussed in Section 3.5.

Welding the end plate to the tubular section induces bowing deformations in the end plate. These heat induced distortions of the end plate have a significant effect upon the stiffness of connection because the bolt pre-tensioning induces bending stresses into the end plate through the clamping action. In particular, high initial tensile stresses are observed at the toes of the welds. Numerical studies indicate that, although these initial stresses have an appreciable effect upon the connection stiffness and moment-rotation response, the effect upon ultimate strength is negligible.

In practice, the heat-induced deformations of the end plate were modelled by simply displacing the initial geometry as shown in Figure 5. An initial transverse displacement of δ_0 (the magnitude of which depends on the end plate thickness) was applied to the top and bottom edges of the end plate, with a linear variation to zero initial displacement at the flange. The size of the initial deformation used in the numerical analyses was based upon corresponding experimental measurements; details are given in Table 3.

Although the initial deformations can be simply applied to the geometry, the added complexity of sloping contact surfaces creates convergence difficulties, which in turn increases the computation time used to solve the problem.

Table 3. Initial End Plate Deformations

End Plate Thickness t_p (mm)	Initial Deformation δ_0 (mm)
12	3.0
16	1.5
20	1.0

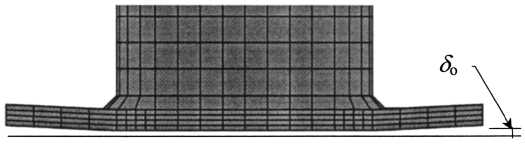

Figure 5. Imposed initial end plate deformations

2.8 Restraints and Loading

The use of three-dimensional elements throughout the model meant that generally only restraints against nodal translations were required, with the exception being reference nodes for the rigid surfaces. The orientation of the model was such that the end plate was located in the *xy* plane, with the *z* axis corresponding to the longitudinal axis of the beam.

The nodes along the axis of symmetry were restrained against movement in the *x* direction but were free to move vertically (*y*) and longitudinally (*z*). The node located on the axis of symmetry and on the neutral axis in the end plate was restrained against vertical movement (*y*). The nodes used as reference nodes for the "rigid surfaces" were restrained against both nodal translations and rotations.

The "Rigid Surface" command (HKS, 1995) was used to define the behaviour of the surface immediately adjacent to and behind the end plate. This surface prevents the penetration of the end plate into a defined plane (representing the adjacent connecting surface) but allows separation of the end plate and rigid surface. The interface properties of the end plate and the rigid surface correspond to a frictionless surface, with zero impedance and zero nodal loads when separation occurs, allowing the end plate to slide up and down the rigid surface.

The loading of the connection was carried out in four steps to model the complete behaviour of the connection. In the first step, infinitesimal displacements were applied to close the nominal gap between the solid elements and the appropriate rigid surfaces. In the second step, a concentrated load was applied to the end of the bolts to produce the pre-load of 145 kN as specified by AS 4100-1990 (SA, 1990). In the third step, the ends of the pre-tensioned bolts were restrained against movement in the longitudinal (*z*) direction. For the final step, the rigid end cap was rotated, thus applying a moment to the beam section, and in turn, the connection.

3 VALIDATION OF FINITE ELEMENT MODEL

The finite element model described in the previous section was verified using a number of numerical analyses. These analyses were initially carried out on various components of the connection to validate the method of loading the connection, the number and type of elements in the end plate, and the type of element used to model the bolt and beam components. Additional numerical tests were conducted to observe the effect on the moment-rotation response of the end plate deformations caused by welding, as discussed further in Section 3.5.

3.1 Beam Section Element Type and Layout

To verify the accuracy of the model of the beam section itself, and to establish the most efficient method of loading the connection, three numerical models were developed. In these models, the element type and layout were varied but the material properties remained constant.

The first model, termed the *Comprehensive Model* (Figure 6a), used three dimensional brick elements, and modelled the beam section and the associated loading plates as used in the experimental program (Wheeler *et al*, 1997). The second model, termed the *Rigid End Cap Model* (Figure 6b), again used three-dimensional brick elements, but only over a short length of the beam adjacent to the end plate. This length of section was capped by a rigid end cap as shown in Figure 6b. Moment loading was achieved by rotating the rigid end cap about its major principal axis. The third model, termed the *Shell Element Model* (Figure 6c), used two-dimensional

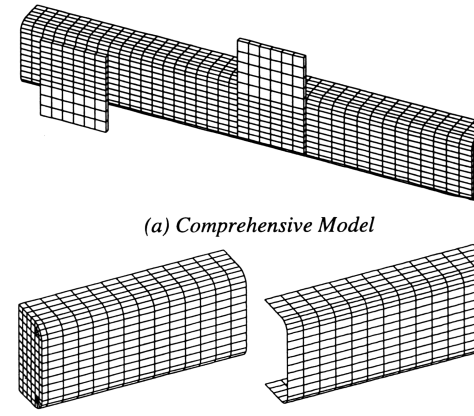

(a) Comprehensive Model

(b) Rigid End Cap Model *(c) Shell Element Model*

Figure 6. Beam model verification

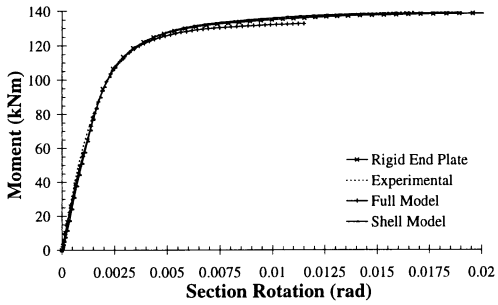

Figure 7. Beam model comparison

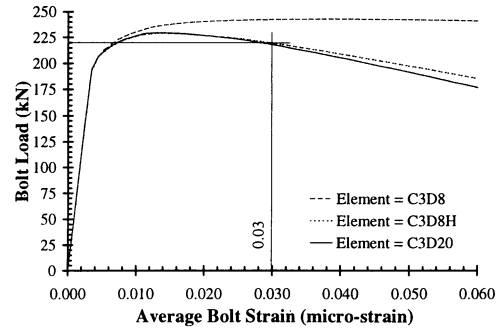

Figure 8. Bolt element type comparison

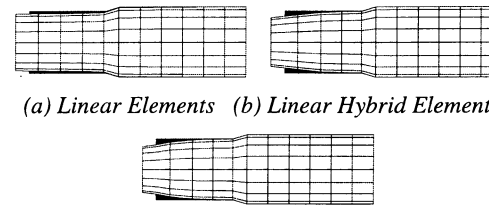

(a) Linear Elements (b) Linear Hybrid Elements

(c) Quadratic Elements

Figure 9. Bolt deformations

shell elements and modelled a short length of the beam adjacent to the end plate. Moment loading was achieved by defining the elements on the end of the section as rigid, and rotating this row of elements in a similar fashion to the rigid end cap.

The moment-rotation behaviour of the three numerical tests corresponding to Figures 6a, 6b and 6c are plotted against the experimental results in Figure 7. In this figure, the section rotation is measured over a 75 mm length immediately adjacent to the plane of zero rotation at the centre of the beam. It can be seen in Figure 7 that the correlation between the experimental curves and the numerical results is very good, with no significant differences resulting from the methods of loading or types of elements used. Consequently, selection of the most suitable connection model was based on efficiency. The *Rigid End Cap Model* was selected on the basis of minimisation of the number of elements used and simplicity of integration into the end plate, which itself is most appropriately modelled using continuum rather than shell elements.

3.2 Bolt Element Selection

The ultimate capacity of the connection is often governed by the strength of the tensile bolts. For this reason, the behaviour of the bolts needs to be modelled accurately. To determine the best type of element to model the behaviour of the bolts, three numerical analyses were carried out using bolts with identical dimensions but different types of elements. Three types of elements were studied, these being the quadratic (C3D20), linear (C3D8) and linear hybrid (C3D8H) brick element types (HKS, 1995). The bolts were subjected to pure tension loading.

The behaviour of the three differing element types is shown in Figure 8. All three analyses produced the same initial stiffness, but as the bolts began to yield the models utilising the quadratic and linear hybrid elements peaked and shed their load substantially more effectively (realistically) than the linear element model.

The difference in the behaviour of the various element types is attributed to the fact that the linear elements are unable to model accurately the effect of changing volume. This is demonstrated in Figure 9 where the deformed shapes of the bolts for each element type are shown. Both the linear hybrid and quadratic elements demonstrated localised reduction in the tensile area (necking), while the linear elements have a more gradual reduction in the cross-sectional area of the bolt.

As the results for the linear hybrid element are nearly identical to those obtained for the quadratic element model, but with significantly fewer degrees of freedom, the former element type was selected to model the bolts in the end plate connection.

To model tensile fracture, the bolts are deemed to have failed when the average strain in the shank exceeds 3 percent, which corresponds to a post ultimate load of approximately 220 kN (see Figure 8).

3.3 End Plate Element Selection

The appropriateness of the type of elements used to model the end plate was assessed by comparing experimental connection test results with simulations using different types of end plate elements. The three types of end plate elements selected for comparison were:

- linear (C3D8)
- quadratic (C3D20)
- linear hybrid, constant pressure (C3D8H).

A number of analyses were carried out using the abovementioned element types. The analysis carried out using the linear elements contained the fewest degrees of freedom, but these elements are prone to "shear locking" which may result in an over stiff response. By contrast, the linear hybrid (constant pressure) elements increase the number of degrees of freedom, but are able to model the large deformation with greater accuracy. Numerical tests comparing the linear and linear hybrid elements were carried out and demonstrated that for the thickest end plate no measurable variation occurred. The tests also demonstrated that for the thinnest end plate, a small amount of stiffening was evident due to the high rotations experienced (Wheeler and Clarke 1998).

To ascertain the accuracy of using the linear hybrid elements, a comparison was made with the quadratic elements as shown in Figure 10. When a sufficient number of linear hybrid elements are included in the end plate, the behaviour of the linear hybrid and quadratic elements demonstrate excellent agreement. When the initial end plate distortions are included, both the quadratic and linear hybrid element results correspond closely to the experimental response.

A comparison of computer run-times demonstrates that for the added accuracy of the second order elements there is a fourfold increase in the computation time relative to that of the linear elements (for the same number of elements). The linear hybrid elements increase the run time twofold, but also remove the possibility of shear locking. For these reasons the linear hybrid elements were selected to represent the end plate for all subsequent numerical analyses. The inclusion of the initial end plate distortions also increases the computation time but, as shown in Section 3.5, also provides a significant increase in the accuracy of the predicted moment-rotation response.

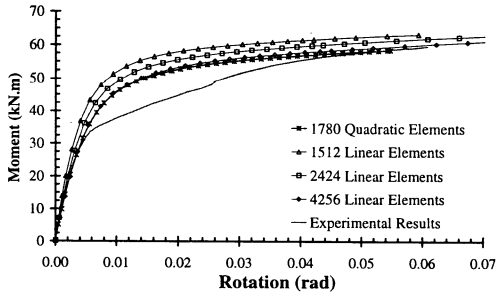

Figure 10. Effect of number of elements

3.4 *Number of Elements*

To obtain the best mesh that accurately models the connection behaviour with minimal computation effort, a number of studies were carried out, varying the number of elements across the end plate and the number of elements through the thickness of the end plate.

The effect of the number of elements in the end plate is shown in Figure 10. An increase in the total number of elements affects the flexibility of the solution, causing the behaviour to approach that obtained using quadratic elements. In the studies described here, all end plates contained four elements through the thickness, resulting in approximately 4000 elements in total.

3.5 *Effects of Initial End Plate Deformations*

The effects of the initial deformations caused by both the heat distortion generated through welding and the applied pretension in the bolts were investigated. The imposition of initial end plate deformations, as described previously, proved to have only a minor effect upon the connection ultimate moment, but a more significant effect on the overall moment-rotation response. The variation in the response is demonstrated in Figure 11 where a number of numerical analyses with varying magnitudes of initial deformation are presented for connections using 16 mm end plates.

It can be seen in Figure 11 that the effect of the initial end plate deformation (δ_0) on the overall response seems to plateau at a value of $\delta_0 = 1.0$ mm for a 16 mm end plate.

Figure 11 demonstrates that although the effect of the deformations on the ultimate strength of the connection is minimal, there is a significantly softer moment-rotation response due to the earlier initiation of yielding.

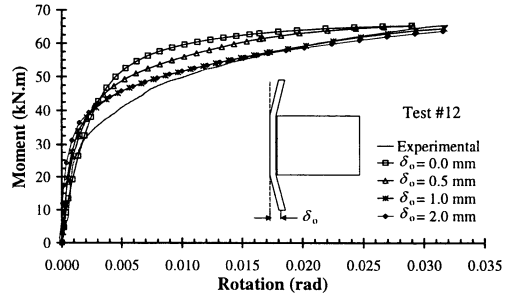

Figure 11. Effect of initial end plate deformations

Table 4. Comparison of Experimental and Numerical Ultimate Loads

Test #	Test M_{cu} (kNm)	ABAQUS M_{ab} (kNm)	M_{cu}/M_{ab}
11	48.6	51.5	1.06
12	69	64.4	0.93
13	77.4	79.1	1.02
14	57.1	62.1	1.09
15	72.5	71.6	0.99
16	86.6	86.1	0.99
17	38.6	39.9	1.03
18	59.5	60.0	1.01
19	72.4	74.8	1.03
20	48.5	49.0	1.01
21	71.3	70.9	0.99
22	79.6	86.1	1.08
23	58.3	61.4	1.05
24	66.6	68.1	1.02
25	62.1	66.2	1.07
26	86	78.4	0.91
		Mean	1.02
		S.D.	0.05

4 SIMULATION OF CONNECTIONS

4.1 Results

Having validated the ABAQUS model and obtained an economical mesh and element type, analyses were carried out on the bolted tubular end plate connections detailed in Table 2.

The ultimate connection moments (M_{ab}) obtained numerically are presented in Table 4. For consistency with the experimental philosophy, the ultimate moment is defined to occur when either the average strain in the bolt shank exceeds a predefined fracture limit (3 percent), or a rotation limit is exceeded (Wheeler and Clarke, 1998).

4.2 Discussion

The numerical analyses demonstrate that flexibility and strength of the connection depends upon the stiffness of the end plate. This stiffness is a function of the end plate thickness and the positioning of the bolts relative to the section perimeter.

The effect of the end plate thickness on the stiffness of the connection is shown in Figure 12, where the connection moment-rotation behaviour is presented for Tests 17, 18 and 19. These three tests differ only in end plate thickness.

The position of the bolts relative to the section webs and flanges also affects the stiffness of the end plate. This conclusion is depicted in Figure 13, which plots the responses for a constant end plate thickness but varying bolt positions.

The position of the bolts with respect to the section flange (s_o) has a significant effect on the stiffness and strength of the connection. As the bolts are moved closer to the flanges (stiffening the end plate), the strength and stiffness of the connection increases (compare Tests 24, 12 and 23 in Figure 13). Moving the bolts away from the line of the section web ($c > 0$) results in a widening of the end plate, which increases its flexibility and thus reduces the strength and stiffness of the connection (compare the results for Tests 12 and 18 in Figure 13).

The numerical analyses indicate that the ultimate mode of failure of the connection depends to a large extent on the stiffness of the end plate. The connections consisting of relatively stiff end plates (thicknesses of 20 mm or 16 mm) were predicted to fail as a result of the bolts exceeding the defined fracture strain. In the physical tests, the actual failure mode for Tests 11 and 14 was fracture of the bolts at excessive deformations, while Tests 17 and 20, with the additional flexibility, showed no signs of bolt failure.

As discussed previously, a significant reduction in strength and stiffness of the connection was observed as the bolts move away from the line of the webs. This decrease in connection capacity and

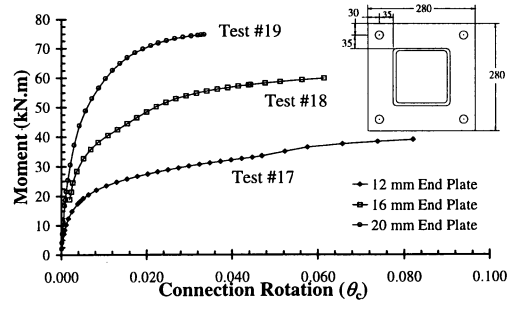

Figure 12. Effect of end plate thickness on connection behaviour

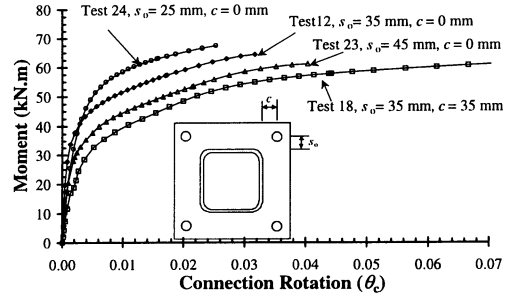

Figure 13. Effect of bolt position on connection behaviour

increase in the flexibility is the result of the formation of an alternative yield line mechanism at lower loads.

The yielding patterns in the end plates are shown in Figure 14 for Tests 12 and 18, both of which comprise a 16 mm end plate. The regions of high stress concentrations in the end plate are equivalent to yield lines. When the bolts are in line with the webs ($c = 0$, Figure 14a) the yield lines form horizontally across the end plate, while when they lie outside the line of the webs ($c > 0$, Figure 14b) the yield lines form diagonally across the corners of the end plate.

The effect of the initial end plate deformations induced by welding can be seen clearly in Figure 15, which plots the stress distributions resulting from the clamping action induced by the "tensioning" of the bolts to 145 kN. Substantial stresses result in the end plate adjacent to the flanges of the section (Figure 15). Figure 16, which plots the stress distribution at ultimate for Test 18, highlights the discontinuity in the stresses in the section at the interface between the corners and flats, which is the result of the use of different material properties in these zones, as discussed in Section 2.2.

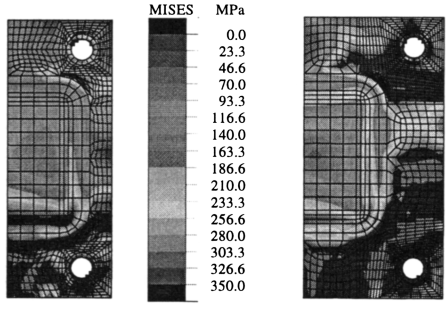

(a) Test 12 $W_p = 210$, $c = 0$ (b) Test 18 $W_p = 280$, $c = 35$

Figure 14. End plate stress concentration patterns

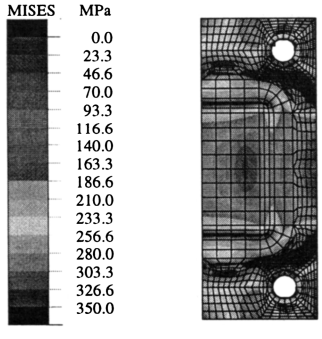

Figure 15. Mises stresses from initial deformations

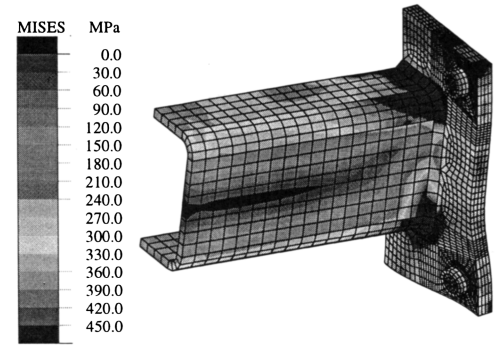

Figure 16. Mises stresses for Test 18 at ultimate

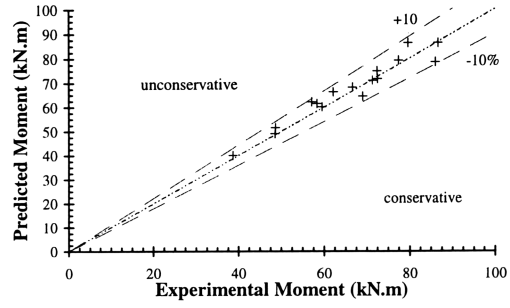

Figure 17. Experimental vs predicted maximum moment

4.3 Comparison of Results

The numerical results for the connections are compared in Table 3 with the corresponding experimental results (Wheeler *et al*, 1997). It should be noted that in the experimental study, the tests with a 12 mm end plate (#11, #14, #17 and #20) were all stopped due to excessive deformations and prior to failure of the bolts. The tabulated ultimate loads are therefore based upon the rotation limit defined in Wheeler and Clarke (1998).

As shown in Table 4 and Figure 17, the experimental and numerical ultimate moments correspond well, with a mean test-to-predicted ratio of 1.02 and a standard deviation of 0.05.

The experimental and numerical moment-rotation responses for Test 12 are compared in Figure 18. The correlation between the experimental and numerical results for this test is very good, with both the ultimate moment and rotation predicted accurately.

Examination of the all moment-rotation curves, as presented in Wheeler and Clarke (1998), reveals that generally the agreement between the experimental and numerical results is reliable. One exception is

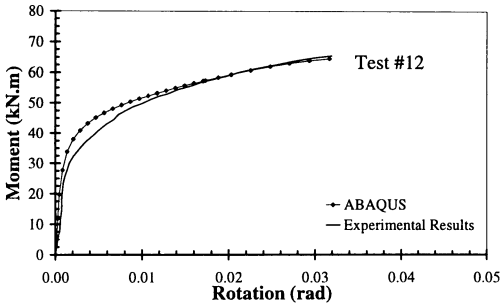

Figure 18. Experimental vs predicted moment

Test 16 where, although the ultimate rotation and moment are similar, the moment-rotation curves differ significantly.

Tangible variations in the experimental and numerical moment-rotation response were also observed in Tests 19, 22, 23, 24, 25 and 26. There are several possible causes for these discrepancies, although time constraints meant they could not be fully investigated for this paper. Tests 23 and 25 were analysed using the meshes from Tests 12 and 15 respectively, adjusted by elongating the elements between the bolts and the tubular section. Refinement of the mesh between the bolts and section may provide moment-rotation curves that are closer to the experimental results. Tests 19, 22, 24 and 26 contain stiff end plates, suggesting that the behaviour of the bolts may not be accurately modelled, thus increasing the stiffness of the connection.

A typical comparison of the behaviour of the bolts is shown in Figure 19. The figure presents the numerical bolt loads for both tensile and compressive bolts, and the measured average strain in the load cells located under the bolt heads in the physical test. It was not possible to calibrate accurately the small "load cell washers" positioned under the bolt heads in the experimental program.

The qualitative behaviour of both the numerical bolt loads and the experimental strains are similar.

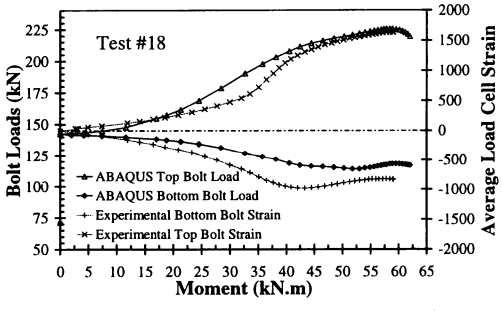

Figure 19. Comparison of bolt behaviour

The tensile bolt loads increase until the ultimate bolt load is reached, at which time load shedding occurs while the moment of resistance of the connection is still increasing marginally. The compressive bolts shed load from the onset of moment loading as a result of the initial tension being relaxed, and this reduction in bolt load continues until the stresses in the end plate are fully relaxed.

5 CONCLUSIONS

A numerical study of the behaviour of bolted moment end plate tubular connections has been described in this paper. The analyses were conducted using the commercially available finite element package ABAQUS. Brick elements were used almost exclusively as this type of element is easily adapted to model interfaces between the connecting surface and the end plates and bolts.

To validate the model, a series of numerical analyses were carried out to determine the most efficient configuration for the components of the connection. These included the type and arrangement of elements in the beam section, the type of elements for the bolts, and the type of elements for the end plate. A number of analyses were also conducted to determine the most efficient number of elements in the end plate to provide an appropriate simulation of the test results.

Sixteen tests were simulated numerically, and these tests encompassed variations in plate thickness, section type and positions of the bolts. The model included the individual modelling of the bolts, and the complex contact surfaces, as well as the introduction of initial deformations to model the heat distortions generated through the welding process. The model simulated the moment-rotation behaviour of the connections sufficiently well for it to be used with confidence in wider-ranging parametric studies.

6 REFERENCES

AISC (1992), "Design Capacity Tables for Structural Steel Hollow Sections", Australian Institute of Steel Construction, Sydney, Australia.

Ajax Fasteners (1992), "Fasteners Handbook - Bolt Products", Richmond, Victoria, Australia.

HKS (1995), "ABAQUS/Standard Users Manual", *Version 5.5*, Hibbitt, Karlsson and Sorensen, Inc.

PDA Engineering (1994), "PATRAN 3", PDA Engineering, Costa Mesa, California.

SA (1990), *AS 4100-1990: Steel Structures*, Standards Australia, Sydney.

Wheeler A. T., Clarke M. J. & Hancock G. J., (1997), "Bending Tests of Bolted End Plate Connections in Cold Formed Rectangular Hollow Sections," *Research*

Report, No. R736, Department of Civil Engineering, The University of Sydney.

Wheeler A. T., Clarke M. J., (1998), "Finite Element Modelling of Bolted Moment End Plate Connections in Rectangular Tubular Members", *Research Report*, Department of Civil Engineering, The University of Sydney (in preparation).

Tubular Structures VIII, Choo & Van der Vegte (eds) © 1998 Balkema, Rotterdam, ISBN 90 5809 001 9

Rectangular hollow section column connections using the Lindapter HolloBolt

N.F.Yeomans
Technical Marketing, British Steel Tubes and Pipes, UK

ABSTRACT : The paper gives a brief review of the development of the HolloBolt insert, describes the experimental work carried out on typical I-beam to structural hollow section column connections and present initial design recommendations. The development of the HolloBolt insert describes its evolution from Lindapter's previous blind bolting system, the HolloFast insert. The experimental work, which was carried out in the United Kingdom and Italy, covers shear tests, individual and group tension tests and some moment test on typical semi-rigid beam to column connections.

1 INTRODUCTION

One of the remaining areas of difficulty regarding the use of structural hollow sections is that of bolting to the face of the section, since access to the inside of the section to tighten a normal bolt and nut is difficult, if not impossible. This has meant that in most cases, unless a blind (single sided) bolting system could be used, some sort of expensive intermediate fabrication has to be used between the column and the beam. Such a fabrication could be, for instance, a plate extending beyond the outside of the section, a welded on channel, etc.

At the 5th and 6th International Symposia on Tubular Structures, the basic concept of the Flowdrill system, friction drilling with a tungsten carbide bit, with structural hollow section members (Banks 1993) and semi-rigid joints using the Flowdrill system (Yeomans 1994) were presented. This paper presents the results of a further series of work on another type of bolting system, the Lindapter HolloBolt. The HolloBolt is another blind (single sided) bolting system, which can also be used successfully to overcome this bolting problem.

Unlike the Flowdrill system, which is a two stage process involving friction drilling a hole and then tapping a thread for a standard bolt, the HolloBolt is a one stage system using a normally drilled hole and a special expanding insert. The original Lindapter blind bolting system was the HolloFast insert. This worked well structurally, but could be initially difficult to insert and fix into the relatively flexible walls of a structural hollow section. Development work on the system has resulted in the HolloBolt insert, which while retaining the same expanding mechanism, is much easier to apply in practice.

2 HOLLOBOLT DEVELOPMENT

In a connection to a structural hollow section, the Lindapter HolloFast insert was fixed into the face of the hollow section using a hammer to force it into an interference fit hole. This often proved difficult due to the flexible and springy nature of the hollow section face. In addition when the connection was being torqued up it very often slipped round in the hole, despite the knurled surface, making it difficult to expand the legs of the insert. Another problem was that the insert could be pushed through the hollow section wall if a lever was used in one of the holes to line the holes up during erection.

To overcome these problems, and to make the insert more user friendly, Lindapter has carried out a development programme, which has resulted in the new HolloBolt insert. This HolloBolt insert, while still retaining the same expansion mechanism of splaying out the legs of the insert, is now inserted

through both thicknesses of material to be connected together and is then torqued up to complete the connection.

Individual shear and tension tests on the original design of the HolloBolt insert showed that it performed well. However, while investigating inconsistencies in the results of tests on moment connections, it was discovered that, in several cases, the plates were not being clamped together by the insert as it was torqued up and the legs were being splayed out. A resulting investigation showed that if a small gap (about 3 mm) was deliberately left between the plates, then even after the insert had been fully torqued up a gap of 1 to 2 mm still remained between the plates. An examination of the expanding mechanism, during the torquing up process, showed that as the legs were splayed out, the inner edge of the hole in the inner ply dug into the legs and locked them in position relative to the top of the insert. This caused the compression, induced by the bolt tension, to be taken by the body of the insert rather than by the plies of material being connected and as a result the plies were not being clamped together. This had not been a problem with the original HolloFast insert because it was fixed to the inner plate (the hollow section face) and the torquing up and tensioning of the bolt directly clamped the plies together.

Rather than completely redesigning the insert to overcome this problem, it was decided to incorporate a short undercut into the body of the insert, which would collapse under a predetermined load. This predetermined load being set above that required to splay out the legs of the insert, but below that generated by the prescribed torque to fully set the insert. This modification was incorporated into some previously manufactured inserts and its effect on the clamping force investigated by making up some simple plate to plate connections. It was found that this small modification worked well and completely overcame the clamping problem.

The production version of the insert, illustrated in figure 1, is supplied as a complete unit made up from three parts, the main insert body, a tapered and threaded cone and a standard grade 8.8 fully threaded bolt. The insert is shown in figure 1, where the left hand side shows the insert in the as supplied condition, before any torque has been applied, and the right side after torquing sufficient to splay out the legs but before the undercut, situated immediately under the head of the insert, has collapsed.

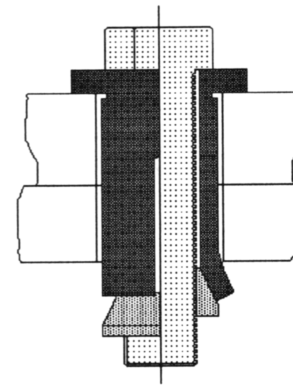

Figure 1. The HolloBolt insert
Left side un-torqued *Right side torqued up*

3 TESTS ON INDIVIDUAL INSERTS

These shear and tension tests were carried out at Trento University in Italy (Ballerini 1996 and Occhi 1996) and by Lindapter International in the UK (Harvey 1996). In all cases the hollow section material was hot finished 140 x 140 in various thicknesses to EN 10210-1 in steel grade S275J2H (yield strength of 275 N/mm^2)

3.1 *Shear Tests*

The individual shear tests were carried out as illustrated in figure 2. During the tests the load was increased continuously until either shear failure of one of the inserts occurred or until a noticeable gap appeared between the RHS and the plates due to rotation of the inserts. The results are summarised in figures 3.

It was thought that several different failure modes could be possible. Some of these would be simple to calculate, for example bearing on the hollow section or plate. Others, however, would be more difficult, for example the crushing of the HolloBolt body, because of the slots, and the shear of the body, because it would have to shear in combination with the bolt. For simplicity, it was eventually decided that, for comparison with the test results, the calculated shear capacity should be based on that of the bolt, acting alone, and that bearing capacity in the hollow section or the plate would also be checked. Crushing of the HolloBolt body and combined shear of the body and the bolt would not, initially, be considered.

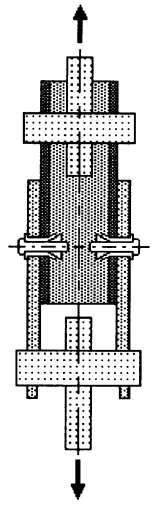

Figure 2. Individual shear test set-up

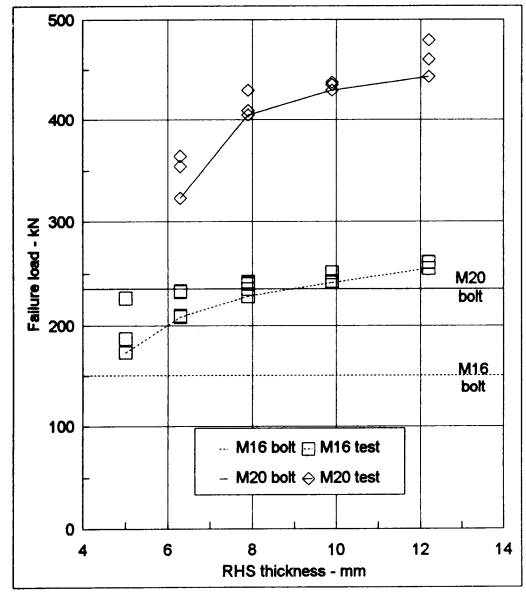

Figure 3. Shear test results

The calculated shear capacity per bolt was therefore based on the following formulae, according to Eurocode no 3 :

$$\text{Bolt shear, } F_{v,R} = 0.6\, A_s\, f_{ub} \quad (1)$$

$$\text{Bolt bearing, } F_{b,R} = 2.5\, t\, d_i\, f_u \quad (2)$$

where:

A_s = shear area of one bolt
f_{ub} = nominal tensile strength of bolt (800 N/mm^2)
t = thickness of hollow section or plate
d_i = HolloBolt insert diameter
f_u = tensile strength of hollow section or plate

In all cases the lowest calculated capacity was the shear of the bolts, and this is also shown in figure 3 for comparison purposes.

The most general failure mode was crushing of the insert body by the closing up of the slots, followed by some initial shearing of the insert and bolt. In several cases, especially on the thinner hollow sections, after the initial crushing of the insert body, rotation of the insert in the hole occurred and when this became excessive the tests were stopped. These tests were completed before the problems related to the clamping force (see section 2, above) were discovered and it is probable that much of the rotation encountered in these tests was due to the lack of clamping force in the specimens. If these tests were repeated with the later collapsing undercut under the head of the insert, one would expect slightly higher failure loads.

It can be seen in figure 3 that all of the test results were above the respective bolt shear capacities, so designing for shear based on the capacity of a grade 8.8 bolt will be safe for the thicknesses of hollow section tested. However, there is a definite thickness effect and with thinner sections (less than 5mm) a check for bearing in the wall of the hollow section would also be required.

3.2 *Tension Tests*

The individual tension tests were carried out as illustrated in figure 4, with a summary of the results shown in figure 5.

Also shown in this figure are the calculated tension capacity of the bolts and the calculated capacity of the hollow section based on the face plastification of the hollow section. The formula used to calculated the bolt capacity is that given in Eurocode 3 and that for the hollow section face plastification is a modification (Yeomans 1994) of the standard formula for a rectangular to rectangular hollow section T-joint (Eurocode 3, annex K).
These formulae are shown below, together with a formula to check the hollow section punching shear capacity, however, in these tests this never became the critical failure mode and, therefore, is not shown in figure 5

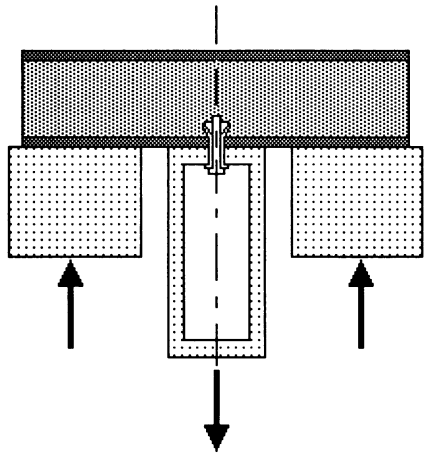

Figure 4. Individual tension test set-up

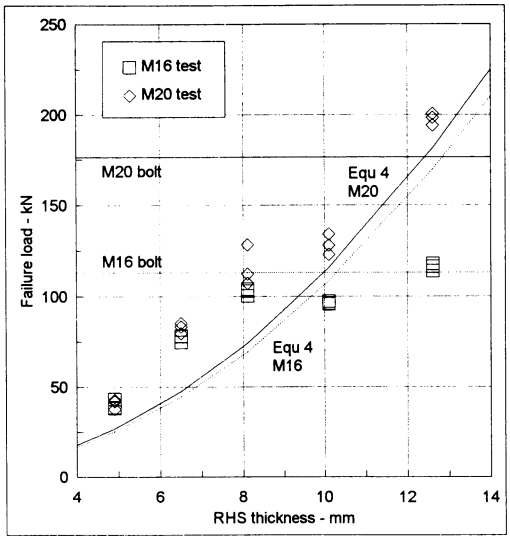

Figure 5. Individual tension test results

Bolt tension capacity, $F_{t,R} = 0.9\ A_s\ f_{ub}$ (3)

Hollow section face plastification capacity, $F_{def,R}$

$$= \pi\ f_y\ t^2\ [2\ d_i/b' + 4\ (1 - d_i/b')^{1/2}]\ /\ [4\ (1 - d_i/b')]\ f(n) \quad (4)$$

Hollow section punching shear capacity, $F_{p,R}$

$$= 0.6\ \pi\ t\ d_i\ f_u \quad (5)$$

where:

f_y = hollow section yield strength
f_u = hollow section tensile strength
b' = hollow section flat face width function = (b - t)
t = hollow section thickness
f(n) = 1.3 (1 + n) but not greater than 1.0
n = factored applied stress in RHS / RHS yield strength, negative for compression, in these tests n = 0, so f(n) = 1

It can be seen from figure 5 that for the thinner sections the chord face plastification criterion is the critical one, but for the thicker sections, at about 10mm thick for M16 and about 12mm for M20, this changes to the bolt capacity.

The results for the 10mm thick section with the M16 insert are low and the only ones to fail at a load below that predicted by the above formulae. The fact that they are lower than those for the next thinner section (8mm thick material) would suggest that there is something wrong with them, since in all other tests the failure loads have increased with material thickness. The results of the M20 tests with 10mm thick hollow section material, although above their calculated capacity, are also slightly lower than would be expected, when compared to the failure loads for the similar specimens with 8 and 12.5mm material. The reason for this is not clear at the moment, however, since the 10mm thick hollow section is the only common factor, it is likely that this, and not the insert, was the cause.

The failure mode for specimens with thinner sections (5 mm to 8 mm) was by large deformation of the hollow section wall, which caused the hole in it to open up, which in turn resulted in the insert pulling through. In the thicker sections, the hollow section face plastification is much smaller, and failure was by shearing of the splayed legs of the insert, resulting in the eventual pull through of the remainder of the insert

4 GROUP TENSION TESTS

This group of tests was carried out to give a better understanding of the behaviour of moment connections. It was thought that the critical area of design for a moment connection would be associated with the area around the tension flange of the beam. They would also be used to satisfy the requirement, in the UK, covering structural integrity. This is the ability of a simple shear connection to withstand a specified tension load, which is related to the actual shear load acting on the beam.

A number of these tests had already been conducted on the earlier HolloFast insert. As a result

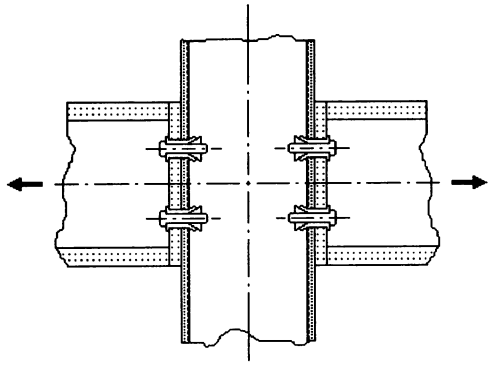

Figure 6. Group tension test set-up

only a few tests were carried out using the HolloBolt insert to confirm that they behaved either the same as or better than the HolloFast insert. The tests were carried out as illustrated in figure 6, with four bolts on each side of the connection.
All the tests were carried out on 150 x 150 materials in various thicknesses and with a nominal yield strength of 275 N/mm^2. The length between hole centres along the axis of the hollow section (h) remained constant at 120 mm for all specimens. The across face dimension (c), however; was varied; both 60 mm and 90 mm were used for the HolloFast connections and for the HolloBolt connections 90 mm was also used for the M16 insert, but, because of the larger clearances required, this dimension was 75 mm for the M20 insert.
Two typical load/deflection curves from the group

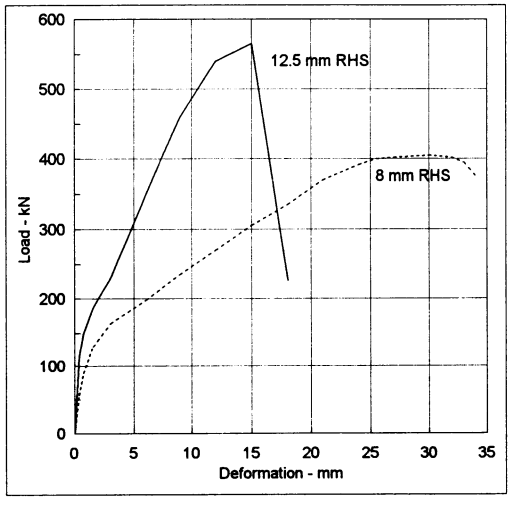

Figure 7. Typical group tension load/deflection plots

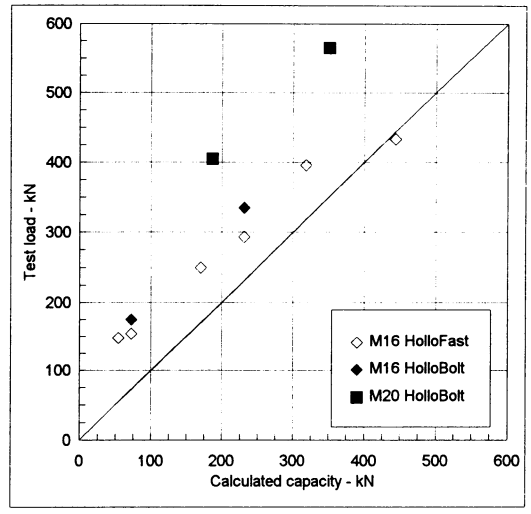

Figure 8. Group tension test results

tension tests are shown in figure 7 for specimens incorporating M20 HolloBolts with 8 and 12.5mm thick hollow sections. The deflections shown are for the combined deflection for both sides of the connection. The effect of the hollow section thickness on the relative stiffnesses and capacities of the connection is easily seen in this figure.
The results of the group tension tests are shown in figure 8, which also includes the results of the previous tests on the HolloFast insert. For comparison purposes the results are shown against the calculated capacity based on the minimum value calculated from the following formulae. The formula for hollow section face plastification was developed during previous work (Occhi 1996 and Yeomans 1994) on Flowdrill and HolloFast connections and is a modified version of a similar formula for rectangular to rectangular hollow section T- and X-joints (CIDECT 1992 and Eurocode 3, 1992)

Bolt tension capacity, $F_{t,R} = 4\ (0.9\ A_s\ f_{ub})$ (6)

Hollow section face plastification capacity, $F_{def,R}$

$$= f_y\ t^2\ [2\ (h - d_i)/b' + 4\ (1 - c/b')^{½}(1 - d_i/b')^{½}] / [1 - c/b']\ f(n) \quad (7)$$

Hollow section punching shear capacity, $F_{p,R}$
$= 4\ (0.6\ \pi\ t\ d_i\ f_u)$ (8)

where:

b' = b - t
h = length between insert centres along the hollow section axis
c = length between insert centres across the hollow section face
f(n) = 1.3 + 0.4 n b/c, but not greater than 1.0, in these tests n = 0, so f(n) = 1

Based on these calculated capacities, in all cases the critical failure criterion was hollow section face plastification.

A comparison of the results obtained from the two identical M16 HolloBolt and HolloFast specimens shows that in both cases the failure load of the HolloBolt connection was about 14% higher than that of the HolloFast specimen and all of the HolloBolt specimens, both M16 and M20, have a capacity well above the calculated values.

The failure modes were very similar to those for the individual bolt tension tests, consisting of deformation of the hollow section allowing the insert to pull through for the thinner specimens and shearing of the splayed legs of the insert body in the thicker sections.

It was concluded that the HolloBolt connections had a higher capacity than the identical HolloFast connection and, as a result, no further tests of this type would be made.

5 MOMENT ROTATION TESTS

A series of nine moment tests was made, the details of which, around the tension flange area, were very similar to the layout of the tests for the group tension tests described above. However, in these tests the bolt spacing along the hollow section face was 100 mm, instead of the 120 mm used previously. Sketches of the test set-up are shown in figures 9 and 10.

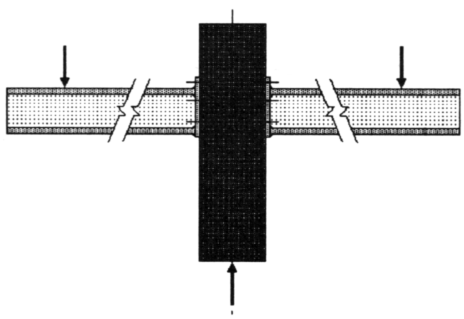

Figure 9. General view of moment test set-up

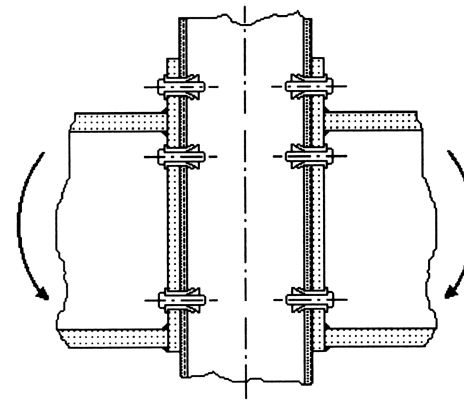

Figure 10. Detail of moment test set-up

Typical moment/rotaion plots are shown in figure 11 for the specimens incorporating M20 HolloBolts with hollow section thicknesses of 5, 8 and 12.5mm. A significant increase in the moment /rotation characteristics as the thickness increases can easily be seen.

The results of these tests are shown in figure 12, where they are compared to the minimum calculated capacities of the connection. In order to determine the minimum calculated capacity of each connection six different failure modes were examined.

In the tension flange area of the connection the shear, tension and bearing capacity of the bolt, and the punching shear and face plastification capacity of the hollow section were considered. In the compression area of the connection, since the beam end plate was the same width as the hollow section, only the web bearing capacity of the hollow section was considered If the end plate had been less than the width of the hollow section face plastification would have needed to be considered, using an effective load area based on the dispersion of the load in the compression flange of the beam through the end plate.

The formulae used to determine these capacities were based on (1), (2) and (6) to (8), suitable modified by the relevant lever arm. In all cases the hollow section face plastification around the tension flange area of the beam was found to be the critical one.

The formula used to calculate the hollow section face plastification capacity was as follows:

$$M_{def,R} = f_y\, t^2\, h_c\, [2\,(h - d_i)/b' + 4(1 - c/b')^{1/2} (1 - d_i/b')^{1/2}] / [1 - c/b']\, f(n) \qquad (9)$$

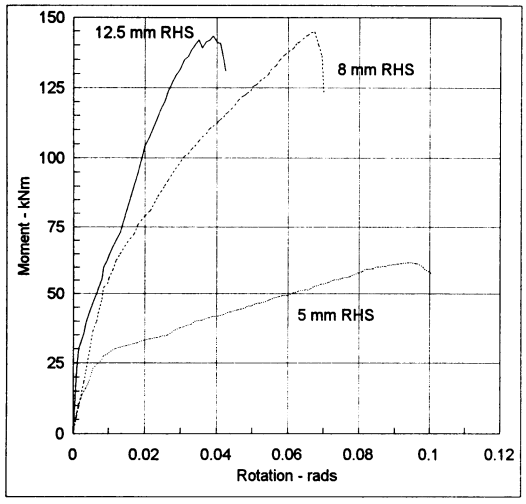

Figure 11. Typical moment/rotation plots

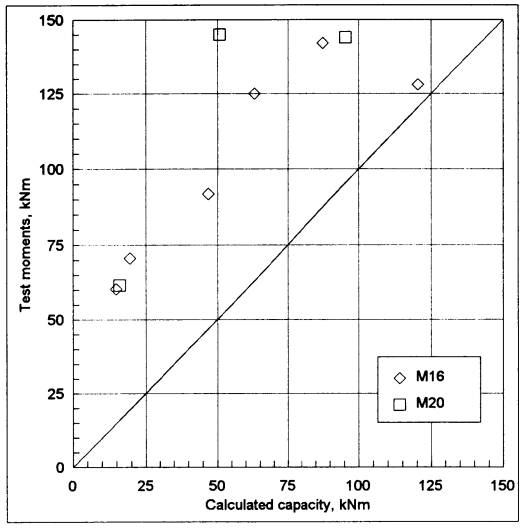

Figure 12. Moment test results

where

h_c = depth of beam between flange centres

Although two of the results were unexpected low, in comparison with others, all of the failure moments were somewhat above the calculated capacities.

For basically identical joint geometries, except for hollow section thickness and bolt spacing, it would be expected that as either the thickness or bolt spacing increased the failure load would also increase. In two instances in these tests the opposite happened, as shown in figure 12 by the two highest test values for both the M16 and M20 inserts. In the case of the M20 inserts the joint with 12.5 mm thick hollow section failed at a moment of 144 kNm while the 8.0 mm thick one failed at 145 kNm. With M16 inserts the specimen with a bolt spacing of 60 mm failed at 142 kNm while that with a 90 mm bolt spacing failed at only 128 kNm.

It was during the analysis of these test results and subsequent examination of the failed specimens that the lack of clamping force between the hollow section face and the beam end plate became apparent. The anomaly in these test results led to a further inspection of the failed specimens. On close inspection it could be seen that, in some instances, there was a gap between the beam end plate and the face of the hollow section. However, at adjacent bolts the plate and hollow section were still clamped tightly together, even though they should have been subjected to the same loads. It was at this point that the further development work on the HolloBolt insert, described in section 2, was undertaken.

6 CONCLUSIONS

It can be concluded that the Lindapter HolloBolt insert can be used as an efficient structural connector for simple shear connections. The shear capacity should be based on that of the grade 8.8 bolt supplied with the insert and the bearing capacity in the normal way, but based on the diameter of the insert, rather than that of the bolt. If any tie force capacity is required, this should be based on a modified version of the standard RHS/RHS T-joint face plastification formula.

The insert can also be used for semi-rigid moment connections provided that adequate clamping between plates can be assured. These can be designed using similar formulae to those used for the simple shear connection, but with additional checks for the tension flange and compression flange areas where again a modified version of the standard RHS/RHS T-joint face plastification formula should be used. For almost full width beam end plates a check for side wall crushing and buckling of the RHS at the location of the beam compression flange should be added.

REFERENCES

Ballerini, M. et al 1996. Shear capacity of blind bolted connections to RHS steel structural elements. *Tubular Structures VII*, 99-106, A A Balkema publishers, Rotterdam, August 1996.

Banks, G 1993. Flowdrilling for tubular structures. 117-124, *Tubular Structures V*, E & F N Spon publishers, August 1993.

CIDECT 1992. *Design guide for rectangular hollow section (RHS) joints under predominantly static loading.* Verlag TUV Rheinland, Koln, Germany, 1992.

ENV 1993-1-1:1992: *Eurocode 3: Design of steel structures: Part 1.1 General rules and rules for buildings.* CEN, Brussels, Belgium, 1992

Harvey, S. 1996. *HolloBolt product development report, shear/slip tests and tensile tests.* Confidential report, Lindapter International, 21 October 1996.

Occhi, F. 1996. *Hollow section connections using (HolloFast) HolloBolt expansion bolting.* CIDECT report no 6G-14E/96, July 1996.

Yeomans, N. 1994. I-beam/rectangular hollow section column connections using the Flowdrill system. *Tubular Structures VI*, 381-388, A A Balkema publishers, Rotterdam, December 1994.

Yeomans, N. 1996. *HolloFast and HolloBolt system for hollow section connections.* CIDECT report no 6G-14A/96, June 1996.

Tubular Structures VIII, Choo & Van der Vegte (eds) © 1998 Balkema, Rotterdam, ISBN 90 5809 001 9

CHS column connections without stiffener

T.Kamba
Department of Architecture and Civil Engineering, Kobe University, Japan
C.Taclendo
Graduate School of Science and Technology, Kobe University, Japan

ABSTRACT: The paper describes a numerical study on CHS steel column semi rigid connections. Connections here are that gusset plates (flange plates) or I-beams are welded to columns. The numerical work was carried out by FEA with a 1/8 model for the gusset plates type specimen subjected to tension or compression loads through gusset plates and a 1/4 model of the subassemblage specimens under symmetrical loading. It involved 90 numerical analyses of Finite Element models with parameters of the diameter to thickness ratio (*D/t*) and the flange width to diameter ratio (*Bf/D*). Evaluations of the numerical results showed as follows: (1) the affective parameters on the behaviour of the connections are the *D/t* and the *Bf/D* ratio, (2) the compression strength is less than the tension one in case of *D/t* >27, and it is almost the same as the tension strength in case of $D/t \leq 22$, (3) the estimated formulae obtained by regression analysis estimates well the elastic-plastic behaviour of the connections.

1 INTRODUCTION

Recently, there are many studies that have tried to make new design format for semi rigid connections considering some deformation of the connections against usual rigid connections.
The authors have already proposed the design format for CHS column to wide flange beam connections with exterior diaphragms that has been adopted in the AIJ Recommendations (AIJ, 1990). The investigation on the elastic plastic behaviour of a CHS column-to-beam connection without diaphragms in which the thickness of column at the connection is increased has already been reported (Kamba, 1995). It is capable to restrain local flexural deformation of the heavy column wall without diaphragms and its experimental formulae predicts the local strengths of these connections with high accuracy. Such connections are assumed as rigid connections, so the reports being considered concerning only the strength provide many unclear points in the deformation of the connections. Especially, there is no systematic information on the rigidty of the CHS column connection with no diaphragm.
The numerical study on CHS steel column semi rigid connections focuses on two types of models, namely, 1) gusset plates (calling after "simple model") and 2) wide flange beams (called hereafter "subassemblage model") are welded directly to columns. The numerical work is carried out by FEA with the 1/8 model of the simple model subjected to tension or compression loads through flange plates in Figure 1 and the 1/4 model of the subassemblage model under symmetrical loading. It involves 90 numerical analyses of Finite Element models with parameters of the diameter to thickness ratio (*D/t*) and the flange width to diameter ratio (*Bf/D*). The purpose of this paper is to obtain the design information on such type of connections considering test results already reported (Kamba 1982 and 1984) and FEA results.

2. TENSION SIMPLE MODEL

2.1 Outline of FEA

In numerical analyses, the finite element program "ABAQUS/Standard /Ver.5.5" is used (Hibbitt. 1986). The model specimen consists of a column (*D*=216.3 mm; constant) and flange plates. The plastic part of the material and the mesh of the model are the following:

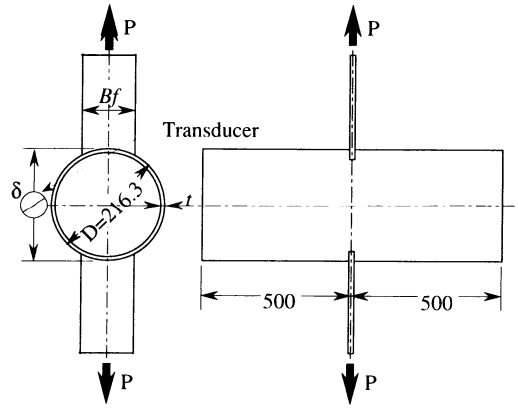

Figure 1 Gusset plates type specimen

1) An one eighth model is assumed to be made up of an isotropic material with Young's modulus 205,800 N/mm^2 and Poisson's ratio of 0.3 in elastic range, with the Mises yield condition. The stress-strain curve is assumed as a bilinear model. In defining hardening, true (Cauchy) stress, σ, and log plastic strain, ε, values are needed. Here, the mechanical properties are assumed as follows; the yield and the maximum stress of the column are σ_{yp}=354 N/mm^2 σ_{up}=519 N/mm^2. The yield and the maximum stress of the flange plate are σ_{yf}=382 N/mm^2 and σ_{uf}=520 N/mm^2. And the strain at the maximum stress is ε_u=10%. These are the average values of test results (Kamba, 1983).
2) A mesh of the model is shown in Figure 2. Element used is a 4-node thick shell element (S4R in ABAQUS) for the column and a 4-node plane strain element (CPE4 in ABAQUS) for the flange. The 4-node thick shell element does not model stresses very well at the intersection of flange plate and tubes. Here, this factor is ignored, because the FEA results agree well with the test results as describe later.

2.2 FEA results

The number of FEA specimens is 30. The parameters of specimen are the diameter-to-thickness ratio (D/t =13, 18, 22, 27, 36, 54) and the flange width to diameter ratio (Bf/D =0.69, 0.58, 0.46, 0.35, 0.23). The FEA results are shown in Table 1. The symbols, ${}_tP_{max}$, ${}_tP_y$ are the maximum and the yield load, ${}_t\delta_{max}$, ${}_t\delta_y$ are the maximum and the yield local deformation, ${}_tK_o$, ${}_tK_f$ are the initial and the second stiffness (=$({}_tP_{max}-{}_tP_y)/({}_t\delta_{max}-{}_t\delta_y)$), and η_u (= ${}_tP_{max}/\sigma_{uf}A_f$; A_f =section area of flange plate) is the joint efficiency. The 5 specimens (st13-series and st18-23) with $\eta_u \geq 1.0$ are recalculated with higher maximum stress to obtain the local maximum strength, ${}_tP_{max}$. The yield load ${}_tP_y$ is defined as the load required for the stiffness of the P-δ curves to become one third of the initial stiffness.
Four FEA results of test specimens reported are also shown in Table 1(Kamba, 1982). Those are noted with the mark * at specimen's column. Their parameter is only the D/t ratio (=18, 22, 27, 36), and the B_f/D ratio (=0.46) is constant. The mechanical properties used are their own tensile coupon test results. Such four specimens failed with crack at the corner between the column and the flange plate propagating to the column wall at the final stage. There is no unloading in the load vs. deformation curves obtained by the numerical analysis, because the FEA cannot pursuit the crack initiation. The maximum strength of the FEA, here, is defined as 1.31${}_tP_y$, because the ratio of ${}_tP_{max}/{}_tP_y$ of four test results ranges from 1.28 to 1.35, and their average value is 1.31.
Comparison of load-deformation (δ in Figure 1) curves of the test (Test) to the FEA result (FEA(tens.)) are shown in Figure 3. It can be seen that there is good

Table 1 Dimensions and FEA results (Tension)

Specimen	t	Bf	${}_tPmax$	${}_tPy$	${}_t\delta max$	${}_t\delta y$	${}_tKo$	${}_tKf$	ηu	σ_y
	mm		kN		mm		kN/mm			N/mm^2
st54-69	4	150	130.1	99.3	22.3	8.5	18.9	2.2	0.19	354
st54-58	4	125	118.9	90.7	24.1	11.1	12.3	2.2	0.20	354
st54-46	4	100	105.2	80.3	28.6	13.3	8.8	1.6	0.22	354
st54-35	4	75	94.7	72.3	34.9	16.1	6.7	1.2	0.27	354
st54-23	4	50	85.6	65.3	39.8	19.4	5.3	1.0	0.37	354
st36-69	6	150	204.6	156.2	10.2	5.1	47.0	9.5	0.29	354
st36-58	6	125	193.2	147.4	15.3	6.9	31.8	5.4	0.33	354
st36-46	6	100	170.6	133.6	19.5	8.4	23.4	3.8	0.36	353
st36-46*	6	100	164.8	127.5	17.9	5.7	24.5	3.1	0.35	353
st36-35	6	75	151.1	115.3	20.0	9.5	18.1	3.4	0.43	354
st36-23	6	50	124.9	95.3	18.2	10.1	14.5	3.6	0.53	354
st27-69	8	150	301.1	229.8	8.4	4.0	87.2	16.3	0.43	354
st27-58	8	125	279.8	213.6	11.9	5.1	61.0	9.8	0.48	354
st27-46	8	100	257.2	190.4	14.0	6.1	45.9	7.4	0.55	355
st27-46*	8	100	264.8	196.1	15.7	4.8	56.0	6.3	0.57	355
st27-35	8	75	209.9	160.3	13.3	6.5	35.9	7.3	0.60	354
st27-23	8	50	171.2	130.7	13.0	6.7	29.0	6.4	0.73	354
st22-69	10	150	406.6	310.3	7.7	3.4	137.8	22.6	0.58	354
st22-58	10	125	367.6	280.6	9.4	4.1	99.6	16.4	0.63	354
st22-46	10	100	321.4	245.3	10.9	4.7	76.4	12.6	0.69	355
st22-46*	10	100	327.5	255.0	11.3	4.1	90.2	10.1	0.70	355
st22-35	10	75	272.1	207.7	10.3	4.9	60.5	11.9	0.78	354
st22-23	10	50	222.9	170.2	10.7	5.1	49.5	9.4	0.95	354
st18-69	12	150	521.0	397.7	6.9	3.0	197.7	30.5	0.74	354
st18-58	12	125	463.3	353.7	8.8	3.6	147.7	20.9	0.79	354
st18-46	12	100	390.9	304.6	9.1	3.9	114.2	18.3	0.84	349
st18-46*	12	100	448.2	343.2	8.3	2.9	150.9	19.4	0.96	349
st18-35	12	75	336.9	257.2	8.7	4.0	92.7	17.0	0.96	354
st18-23	12	50	285.0	217.6	9.2	4.3	77.2	13.6	1.22	354
st13-69	16	150	715.8	546.4	4.7	2.3	348.9	72.4	1.02	354
st13-58	16	125	662.3	505.6	5.6	2.8	272.8	54.8	1.13	354
st13-46	16	100	614.7	469.2	7.2	3.3	220.7	37.3	1.31	354
st13-35	16	75	538.4	411.0	7.6	3.4	183.3	30.7	1.53	354
st13-23	16	50	464.2	354.4	7.8	3.5	157.0	25.2	1.98	354

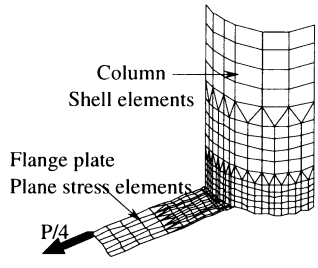

Figure 2 Tensile simple model (Gusset plate type)

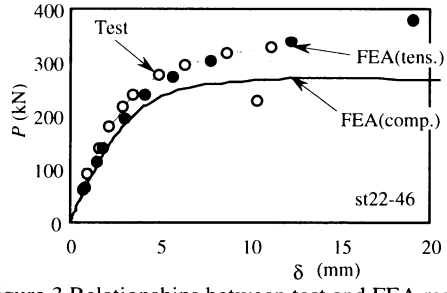

Figure 3 Relationships between test and FEA results (Load-deformation curves)

agreement between them. In the figure, the FEA result of the same specimen subjected to compression load (FEA(comp.)) are also shown.

The load-deformation curves of the specimens with the variation of the D/t ratio (B_f/D= 0.46; constant) and the B_f/D ratio (D/t = 27; constant) are shown in Figure 4 and Figure 5, respectively. In the figures, marks with an arrow and a double circle show the maximum and yield strength.

From both figures, the load-deformation curves show inelastic behaviour before reaching the yield strength, and almost the constant rigidity after P_y, that is, they show the trilinear behaviour. The more the D/t ratio and the less the B_f/D ratio, the less the strength and the stiffness. Especially, the variation of the D/t ratio affect the strength and the stiffness. The comparison of the initial stiffness and the maximum strength of Specimen st54-46 (D/t=54) to Specimen st13-46 (D/t=13) are 1/25 and 1/6, respectively.

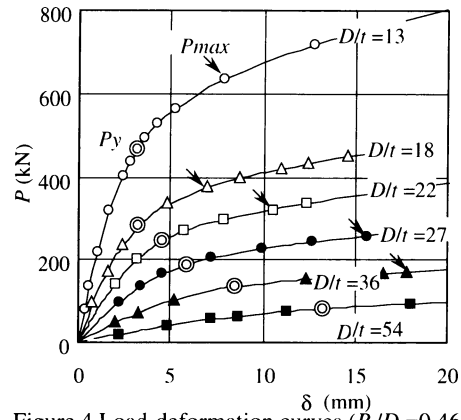

Figure 4 Load-deformation curves (B_f/D =0.46)

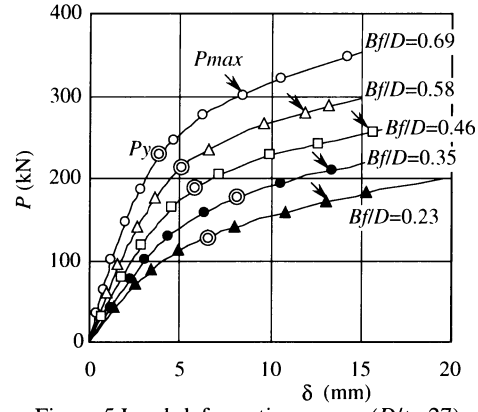

Figure 5 Load-deformation curves (D/t =27)

2.3 Evaluation of connection parameters

It is evaluated quantitatively due to the FEA results how the connection parameters (D/t and B_f/D) affect the elastic-plastic behaviour of the connection. Mechanical properties of the connections are the initial stiffness, the yield strength, the maximum strength, the yield deformation, the maximum deformation, and the second stiffness shown in Table 1. It is possible to assume the elastic-plastic behaviour of the connection by evaluating the mechanical properties of the connections quantitatively. Here, the model of the load-deformation curve is assumed as a trilinear model connecting the origin, point A, B, and C shown in Figure 6. The load and the deformation at the point A are assumed as two-third of the yield strength and ${}_t\delta^* = (2{}_tP_y/3)/{}_tK_o$). The point B is the yield point, and its load and deformation are the yield strength, ${}_tP_y$, and the yield deformation, ${}_t\delta_y$. The point C is the maximum point, and its load and deformation are the maximum strength, ${}_tP_{max}$, and the maximum deformation, ${}_t\delta_{max}$. The relationships between the mechanical properties (${}_tP_y$, ${}_tP_{max}$, ${}_t\delta_y$, ${}_t\delta_{max}$, ${}_tK_o$, and ${}_tK_1$) and the D/t ratio with the variation of the B_f/D ratio are shown in Figures 7-12. Test results are shown in the figures,

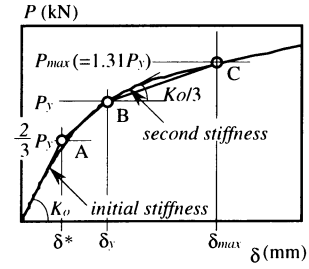

Figure 6 Model of load-deformation curve

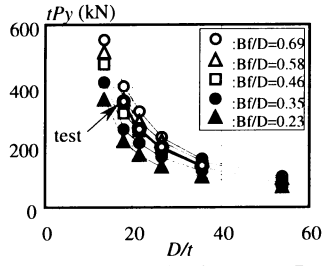

Figure 7 Relationships between ${}_tP_y$ and D/t

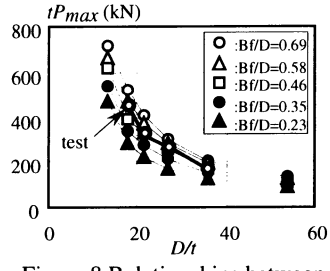

Figure 8 Relationships between ${}_tP_{max}$ and D/t

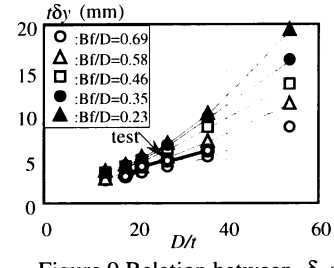

Figure 9 Relation between ${}_t\delta_y$ and D/t

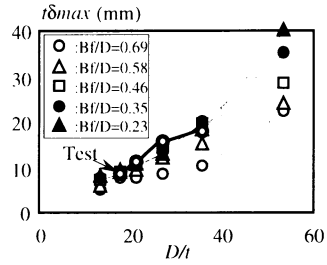

Figure 10 Relationships between ${}_t\delta_{max}$ and D/t

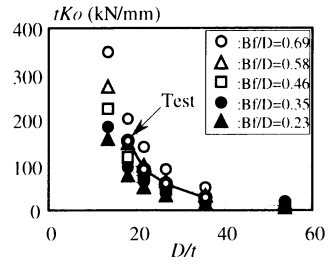

Figure 11 Relationships between ${}_tK_o$ and D/t

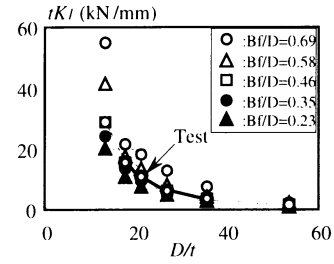

Figure 12 Relation between ${}_tK_i$ and D/t

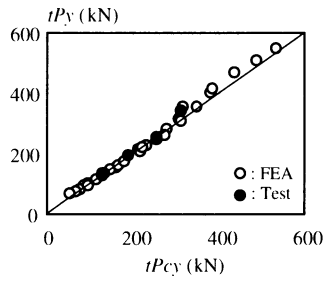

(a) Yield strength

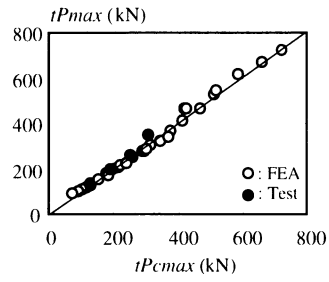

(b) Maximum strength

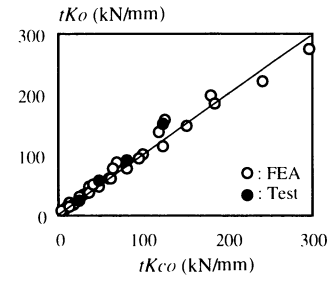

(c) Initial stiffness

Figure 13 Relationships between FEA and estimated results

too. There are good agreement between the test and the FEA results except for the yield deformation (the test results (B_f/D =0.46) are plotted between B_f/D =0.58 and B_f/D =0.69).

The larger the D/t ratio and the smaller the B_f/D ratio, the less strength and the larger the deformation.

According to the theory of the dimensional analysis, a physical quantity is represented non-dimensionally by a non-dimensional product of all the physical quantities related to it. The physical quantities related to the initial stiffness, ${}_tK_o$, of the connection are mechanical properties of the material and its dimensions. The elastic modulus is selected as an index of the mechanical properties of the material, the initial stiffness appears as;

$$ {}_tK_o = f(D, t, B_f, E) \qquad (1) $$

Considering the non-dimensional parameters shown in Figures 7-12, the mathematical model is assumed as follows;

$$ {}_tK_{co}/E = X_1(D/t)X_2\,(B_f/D)X_3\varepsilon \qquad (2) $$

where, variable ε is the error. The numerical variables X_1, X_2, and X_3 are determined by the method of least squares with the 30 FEA results in Table 1. The numerical variables of each mechanical properties of the connections (${}_tP_y/\sigma_yR^2$, ${}_tP_{max}/\sigma_yR^2$, ${}_t\delta_y/D$, ${}_t\delta_{max}/D$, ${}_tK_i/E$) are shown in Table 2. Each range of the ratio of the test to estimation value and the coefficient of

Table 2 List of estimated formulae of simple model subjected to tension load

	Estimation	*Eq.*
tPy	$tPcy/\sigma yR^2 = 5.6\,(D/t)^{-1.32}(Bf/D)^{0.48}$	(3)
	$0.94 \leqq tPy/\,tPcy \leqq 1.15$, COV=0.047	
$tPmax$	$tPcmax/\sigma yR^2 = 7.3\,(D/t)^{-1.32}(Bf/D)^{0.48}$	(4)
	$0.95 \leqq tPmax/\,tPcmax \leqq 1.15$, COV=0.047	
$t\delta y$	$t\delta cy/D = 0.00054\,(D/t)^{1.07}(Bf/D)^{-0.45}$	(5)
	$0.79 \leqq t\delta y/\,t\delta cy \leqq 1.22$, COV=0.112	
$t\delta max$	$t\delta cmax/D = 0.0013\,(D/t)^{1.07}(Bf/D)^{-0.37}$	(6)
	$0.71 \leqq t\delta max/\,t\delta cmax \leqq 1.24$, COV=0.125	
tKo	$tKco/E = 959\,(D/t)^{-2.3}\,(Bf/D)^{0.92}$	(7)
	$0.87 \leqq tKo/\,tKco \leqq 1.30$, COV=0.117	
tKi	$tKci/E = 149\,(D/t)^{-2.3}(Bf/D)^{0.78}$	(8)
	$0.81 \leqq tKi/\,tKci \leqq 1.56$, COV=0.176	

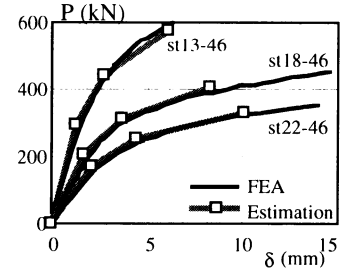

Figure 14 Comparison of Load-Deformation Curves

variation are also shown in the table.
The relationships of the maximum strength, the yield strength, and the initial stiffness between the FEA and the estimated results are shown in Figures 13(a), 13(b), and 13(c). These are the comparison of the test to the estimated results with the symbol ● . There is good agreement between the test and the estimated results. The load-deformation curves of the FEA results (st13-46, st18-46, and st22-46) and the trilinear models by the estimation are shown in Figure 14. The trilinear models are plotted by using the estimation results, ${}_tP_{cy}$, ${}_tP_{cmax}$, ${}_tK_{co}$, ${}_t\delta_{cmax}$, and ${}_t\delta_{cy}$ in Table 2. It can be seen that the estimated mechanical properties of the connections by the formulae in Table 2 agree with the FEA results well.

3. COMPRESSION SIMPLE MODEL

3.1 FEA results

The 30 FEA models subjected to compression load through the flange plates are carried out. The dimensions and mechanical properties of the FEA models are the same as those in Chapter 2. The model name and the FEA results are shown in Table 3.
The difference of the initial stiffness between the compression and the tension model is small (${}_tK_o/{}_cK_o$=0.93-1.18), but the compression load-deformation curves fell compared with the tension one in inelastic range (refer to Figure 3). The unloading in the load-deformation curves of simple models with the smallest D/t ratio (=13, otherwise except for sc13-69) or the smallest B_f/D ratio (=0.23, otherwise except for sc18-23) is not confirmed. The maximum deformation, ${}_c\delta_{max}$, where the unloading is confirmed is very large. The ratio of the maximum deformation to the thickness of columns of each D/t ratio are ${}_c\delta_{max}/t$ = 1.53-1.74 (D/t =13), ${}_c\delta_{max}/t$ = 1.29-2.0 (D/t =18), ${}_c\delta_{max}/t$ = 1.47-1.75 (D/t=22), ${}_c\delta_{max}/t$ = 1.39-2.05 (D/t=27), ${}_c\delta_{max}/t$ = 1.75-2.35 (D/t=36), and ${}_c\delta_{max}/t$ = 2.87-4.43 (D/t=54). The ${}_c\delta_{max}$ of models with D/t = 54 is two or three times of the thickness of columns. If the maximum load is defined as the load at the ${}_c\delta_{max}$, it means to permit the excessive deformed condition in design format. Hence, the maximum strength is defined as ${}_cP_{max}$ in the following item (i).
The trilinear load-deformation curve of the model subjected to the compression load is defined as the same as the tension one in Figure 6. The difference points are as follows:
(i) maximum load, ${}_cP_{max}$, is defined as the load at the ${}_t\delta_{max}$ (note that this value is the maximum deformation of the model subjected to the tension load) of the P-δ curves.
(ii) But, the deformation increases to the maximum deformation, ${}_c\delta_{max}$, with the same load.
The relationships between the strength of the models under tension or compression loading are shown in Figure 15. The abscissa shows the B_f/D ratio, and the ordinate shows the ${}_tP_{max}/{}_cP_{max}$ and the ${}_tP_y/{}_cP_y$ ratio.
From the figures, it can be seen that the larger the D/t ratio or the smaller the B_f/D ratio, the larger the strength ratio of the tension to the compression. The ${}_tP_{max}/{}_cP_{max}$ and ${}_tP_y/{}_cP_y$ ratios of the D/t = 54 series ranges from 1.62 to 2.49 and from 1.54 to 2.03, respectively. The compression strength of the connections with D/t = 54 is 40-60% less than the tension one. On the other hand, the compression strength of the connections with $D/t \leq$ 22 is only 20% less than the tension one.

Table 3 Dimensions and FEA results (Compression)

Specimen	$cPmax$	cPy	$c\delta max$	$c\delta y$	cKo	cKI
	kN		mm		kN/mm	
sc54-69	80.4	62.1	17.7	5.5	11.2	1.50
sc54-58	69.2	58.7	16.5	7.8	7.5	1.21
sc54-46	57.7	52.1	15.0	9.4	5.6	1.00
sc54-35	44.6	41.4	15.0	10.9	3.8	0.76
sc54-23	34.3	32.2	11.5	8.8	3.6	0.83
sc36-69	160.6	120.8	13.0	4.0	30.5	6.39
sc36-58	137.9	114.9	11.8	5.6	20.6	3.70
sc36-46	114.5	102.5	14.1	6.8	15.1	1.63
sc36-35	90.6	82.5	14.0	6.7	12.3	1.10
sc36-23	71.4	61.8	10.5	6.4	9.6	2.37
sc27-69	254.8	195.9	16.7	3.4	57.0	11.97
sc27-58	221.5	181.7	15.6	4.5	40.5	5.35
sc27-46	186.0	157.9	12.6	5.2	30.6	3.79
sc27-35	150.8	129.4	11.1	5.3	24.5	3.66
sc27-23	121.7	103.0	13.5	5.3	19.5	2.42
sc22-69	361.1	279.3	16.2	3.1	90.2	17.96
sc22-58	314.1	253.8	14.7	3.8	66.8	10.84
sc22-46	267.4	220.4	15.3	4.3	51.6	7.12
sc22-35	220.1	179.2	16.4	4.3	41.9	6.73
sc22-23	180.1	143.5	17.5	4.2	34.0	5.56
sc18-69	464.5	360.8	21.0	2.8	129.6	25.11
sc18-58	409.8	323.4	15.5	3.3	97.3	15.82
sc18-46	347.2	280.3	20.1	3.5	81.1	11.93
sc18-35	289.8	231.3	18.9	3.6	64.0	11.60
sc18-23	245.6	188.0	24.0	3.5	54.3	9.96
sc13-69	679.1	520.2	25.9	2.2	233.7	64.76
sc13-58	617.4	476.8	27.9	2.6	183.1	46.60
sc13-46	557.2	423.4	27.5	2.9	147.8	31.09
sc13-35	482.5	380.6	24.5	3.2	119.6	23.34
sc13-23	413.3	328.5	24.9	3.2	101.4	18.57

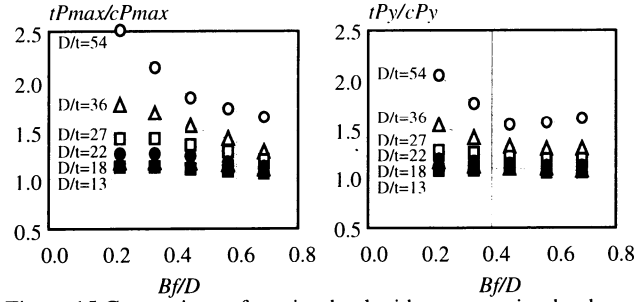

Figure 15 Comparison of tension load with compression load on strength

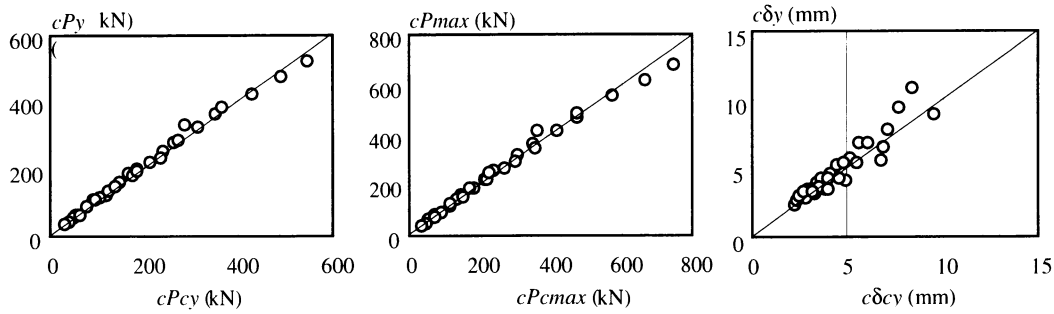

(a) Yield strength (b)Maximum strength (c) Yield deformation

Figure 16 Comparison of FEA results with estimated results (Compression load)

3.2 Evaluation of connection parameters (Compression load)

It is evaluated quantitatively due to the FEA results how the connection parameters (D/t and B_f/D) affect the elastic-plastic behaviour of the connection subjected to the compression loads.

The numerical variables X_1, X_2, and X_3 are determined by the method of least squares with the 30 FEA results. The numerical variables of each mechanical properties of the connections (${}_cP_y/\sigma_yR^2$, ${}_cP_{max}/\sigma_yR^2$, ${}_c\delta_y/D$, ${}_c\delta_{max}/D$) are shown in Table 4. Each range of the ratio of the test to estimation value and the coefficient of variation is shown in the table, too.

The relationships of the maximum strength, the yield strength, and the yield deformation between the FEA and the estimated values are shown in Figures 16(a), 16(b), and 16(c), respectively. There is good agreement between the FEA results and the estimated results.

The load-deformation curves of the FEA results with B_f/D= 0.46 and the trilinear models by the estimation are shown in Figure 17. The trilinear models are plotted by the estimation values, ${}_cP_{cy}$, ${}_cP_{cmax}$, ${}_tK_{co}$, ${}_c\delta_{cmax}$, and ${}_c\delta_{cy}$ in Tables 2 and 4. When the $D/t \leq 22$, the maximum compression deformation, ${}_c\delta_{cmax}$, is less than the maximum tension deformation, ${}_t\delta_{cmax}$. In this case, this trilinear model is different from the tension model. That is, the compression load after the yield strength increases by the ${}_t\delta_{cmax}$, and thereafter the deformation increases by the maximum compression deformation, ${}_c\delta_{cmax}$, with the same load. It can be seen that the estimated mechanical properties of the connections by the formulae in Table 4 agree with the FEA results well.

4. SUBASSEMBLAGE MODEL

A subassemblage model with wide flange beams (H-300 × B_f × 6 × 9) are welded directly to columns is shown in Figure 18. The 30 FEA models subjected to

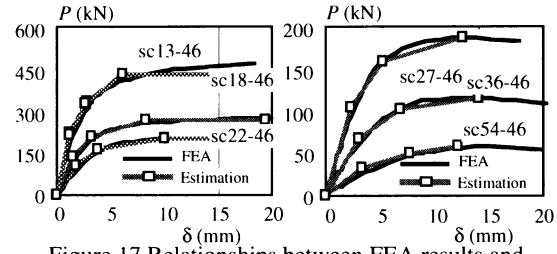

Figure 17 Relationships between FEA results and estimation

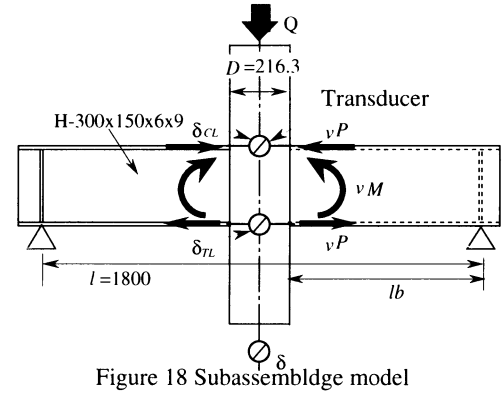

Figure 18 Subassembldge model

Table 4 List of estimated formulae of simple model subjected to compression load

	Estimation	*Eq.*
cPy	${}_cP_{cy}/\sigma_yR^2 = 14\,(D/t)^{-1.65}(B_f/D)^{0.58}$ $0.95 \leqq {}_cP_y/{}_cP_{cy} \leqq 1.14$, COV=0.039 comment; load when the stiffness become one third of the initial stiffness	(9)
$cPmax$	${}_cP_{cmax}/\sigma_yR^2 = 25\,(D/t)^{-1.74}(B_f/D)^{0.65}$ $0.90 \leqq {}_cP_{max}/{}_cP_{cmax} \leqq 1.12$, COV=0.05 comment; load when the local deformation reach to to the tension maximum local deformation, ${}_t\delta_{max}$	(10)
$c\delta y$	${}_c\delta_{cy}/D = 0.0012\,(D/t)^{0.79}(B_f/D)^{-0.31}$ $0.80 \leqq {}_c\delta_y/{}_c\delta_{cy} \leqq 1.29$, COV=0.115	(11)
$c\delta max$	${}_c\delta_{cmax}/D = 0.325\,(D/t)^{-0.42}(B_f/D)^{0.084}$ $0.70 \leqq {}_c\delta_{max}/{}_c\delta_{cmax} \leqq 1.40$, COV=0.207 comment; local deformation when the compression load decreases	(12)

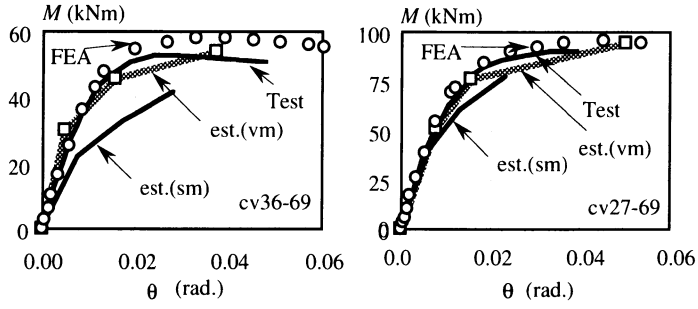

Figure 19 Comparison between test and FEA results

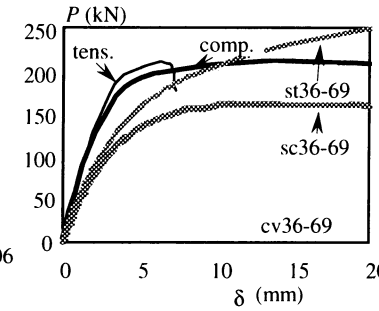

Figure 20 Comparison of local deformation

Table 5 Comparison of the experimental results with calculated results (Subassembldge model)

Specimen	t mm	Bf mm	σ_y N/mm^2	σ_u N/mm^2	$_vM_{max}$ kNm	$_vM_{cmax}$ kNm	$\frac{_vM_{max}}{_vM_{cmax}}$	$_vM_y$ kNm	$_vM_{cy}$ kNm	$\frac{_vM_y}{_vM_{cy}}$	$_v\theta_{max}$ rad.	$_v\theta_{cmax}$ rad.	$\frac{_v\theta_{max}}{_v\theta_{cmax}}$	$_v\theta_y$ rad.	$_v\theta_{cy}$ rad.	$\frac{_v\theta_y}{_v\theta_{cy}}$
cv36-69T	5.8	150	355	489	52.3	53.7	0.98	42.7	45.5	0.94	0.029	0.037	0.80	0.012	0.015	0.81
cv36-69F	5.8	150	355	489	57.9	53.7	1.08	48.0	45.5	1.15	0.039	0.037	1.08	0.015	0.015	0.98
cv27-69T	8	150	386	486	89.5	94.2	0.95	66.0	76.3	0.87	0.056	0.048	1.16	0.012	0.014	0.85
cv27-69F	8	150	386	486	95.0	94.2	1.01	72.1	76.3	0.95	0.045	0.048	0.94	0.014	0.014	0.99

symmetrical moment through the wide flange beams are carried out. The dimensions of columns (D=216.3 mm) and the mechanical properties of the members are the same as those in Chapter 2.

The comparison between the test (Kamba, 1986) and the FEA results are shown in Table 5. The 30 model names and the FEA results are shown in Table 6. The strengths in Table 5, The $_vP_{max}$ and $_vP_y$ show the local strength which are the moment at the beam ends, $_vM_{max}$ and $_vM_y$, divided by the distance between the gravity centre of the flange plates. The deformations, $_v\theta_{max}$ and $_v\theta_y$, show the rotation angle of the beam which is the deformation at the beam ends, $_v\delta_{max}$ and $_v\delta_y$, divided by the beam length. The maximum moment, $_vM_{max}$, in Table 6 is the moment at θ =1/20 in the case where there is no unloading until then. The comparison of the yield strength to the plastic moment of the beam are shown in the column of the $_vM_y/M_p$. The larger the D/t ratio, the less the $_vM_y/M_p$ ratio.

The comparison of typical moment-rotation curves of the test (cv36-69 and cv27-69) to the FEA results are shown in Figure 19. The ratios of the yield and the maximum strength of the test to the FEA results are 0.82 and 0.89 for cv36-69, and 0.83 and 0.92 for cv27-69, respectively. The FEA results, however, overestimate a little to the test results, it can be seen that the FEA results follow substantially the test results.

The relationships between the compression and the tension local deformations, δ_{CL} and δ_{TL}, of the subassemblage model and those of the simple model are shown in Figure 20. In the figure, the compression and the tension local deformations at the compression and the tension flange level of the subassemblage model (cv36-69) are shown as "comp." and "tens.". And, the local compression deformations of the simple model subjected to the compression load is shown as "sc36-69" and the tension one is shown as "st36-69". The compression local deformation of the subassemblage model increases rapidly compared with its tension local deformation after reaching the yield load. The initial stiffness of the compression and the tension local deformation of the subassemblage model are almost the same, but those are larger than the initial stiffness of the compression and the tension local deformation of

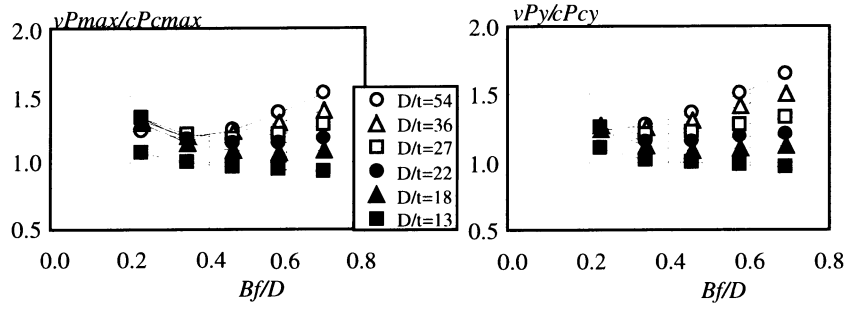

Figure 21 Comparison of strength of subassembldge model to estimated compression load of simple model

the simple model due to the stiffening effect by the beam web and the interaction of tension and compression load from the flange plates. And the initial yield load that the stiffness starts to decrease from the initial stiffness is larger than that of the simple model, too.

The trilinear load-deformation curve models for the subassemblage models are shown in Figure 19 as "est.(sm)". These are obtained by using the above formulae in Table 4 which estimate the mechanical properties of the simple model connections subjected to compression load, that is, the models are obtained by converting the trilinear local load vs. local deformation curve into the moment-rotation angle curves using the beam length and the distance between the centre of gravity of the flange plates. Here, elastic

Table 7 List of estimated formulae of subassembldge model

	Estimation	*Eq.*
vPy	$vPcy/\sigma yR^2 = 8.2\,(D/t)^{-1.41}(Bf/D)^{0.62}$	(14)
	$0.86 \leqq vPy/vPcy \leqq 1.12$, COV=0.066	
$vPmax$	$vPcmax/\sigma yR^2 = 16\,(D/t)^{-1.55}(Bf/D)^{0.61}$	(15)
	$0.83 \leqq vPmax/vPcmax \leqq 1.11$, COV=0.076	
$v\theta y$	$v\theta cy = 0.0087\,(D/t)^{0.13}(Bf/D)^{-0.18}$	(16)
	$0.90 \leqq v\theta y/v\theta cy \leqq 1.06$, COV=0.044	
vKo	$vKco/(Elb) = 47.4\,(D/t)^{-1.97}(Bf/D)^{0.85}$	(17)
	$0.84 \leqq vKo/vKco \leqq 1.17$, COV=0.091	
$vK1$	$vKc1/(Elb) = 0.51\,(D/t)^{-1.49}(Bf/D)^{0.6}$	(18)
	$0.69 \leqq vK1/vKc1 \leqq 1.26$, COV=0.14	

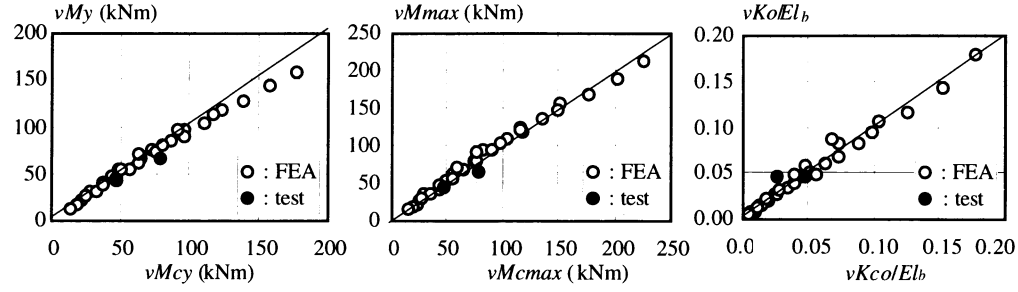

(a) Yield strength (b) Maximum strength (c) Initial stiffness

Figure 22 Relationships between FEA results and estimated values

Table 6 FEA results and estimated values (Subassembldge model)

Speci-men	t	Bf	vMmax	vMcmax	vMmax/vMcmax	vMy	vMcy	vMy/vMcy	vθmax	vθy	vθcy	vθy/vθcy	vKo	vKco	vKo/vKco	vK1	vKc1	vK1/vKc1	vMy/Mp
	mm		kNm						rad.				kNm/rad.			kNm/rad.			
cv54-69	4	150	33.9	29.4	1.15	30.3	28.6	1.06	0.028	0.016	0.015	1.02	2541	2181	1.17	227	170	1.17	0.15
cv54-58	4	125	27.4	26.3	1.04	25.1	25.6	0.98	0.029	0.017	0.016	1.05	1979	1865	1.06	143	153	1.06	0.15
cv54-46	4	100	21.7	22.9	0.95	20.1	22.4	0.90	0.028	0.017	0.017	1.02	1353	1539	0.88	132	134	0.88	0.14
cv54-35	4	75	17.1	19.2	0.89	15.9	18.9	0.84	0.028	0.018	0.018	0.99	1081	1202	0.90	94	113	0.90	0.13
cv54-23	4	50	13.7	15.0	0.91	12.8	14.8	0.87	0.035	0.021	0.020	1.04	735	848	0.87	52	89	0.87	0.13
cv36-69	6	150	62.6	54.2	1.15	53.9	49.5	1.09	0.036	0.014	0.014	0.99	5278	4656	1.13	398	320	1.13	0.28
cv36-58	6	125	52.0	48.5	1.07	46.1	44.4	1.04	0.031	0.016	0.015	1.06	4173	3980	1.05	395	287	1.05	0.27
cv36-46	6	100	42.5	42.4	1.00	38.9	38.8	1.00	0.031	0.017	0.016	1.09	3298	3285	1.00	254	252	1.00	0.27
cv36-35	6	75	34.7	35.5	0.98	30.0	32.7	0.92	0.039	0.017	0.017	0.97	2534	2565	0.99	205	212	0.99	0.25
cv36-23	6	50	28.5	27.8	1.03	24.9	25.6	0.97	0.032	0.018	0.019	0.97	1872	1810	1.03	257	167	1.03	0.26
cv27-69	8	150	93.3	83.4	1.12	74.7	72.7	1.03	0.050	0.013	0.014	0.92	9354	7973	1.17	468	499	1.17	0.38
cv27-58	8	125	79.0	74.6	1.06	65.1	65.1	1.00	0.047	0.014	0.014	0.99	6953	6816	1.02	388	448	1.02	0.38
cv27-46	8	100	66.4	65.1	1.02	54.1	57.0	0.95	0.044	0.015	0.015	0.98	5654	5626	1.00	375	393	1.00	0.37
cv27-46	8	75	56.5	54.6	1.03	45.5	47.9	0.95	0.050	0.016	0.016	0.98	4329	4393	0.99	292	332	0.99	0.38
cv27-23	8	50	48.0	42.6	1.13	37.6	37.6	1.00	0.044	0.016	0.018	0.91	3613	3099	1.17	325	261	1.17	0.39
cv22-69	10	150	124.7	115.8	1.08	96.5	97.4	0.99	0.050	0.012	0.013	0.93	13429	12101	1.11	697	706	1.11	0.49
cv22-58	10	125	107.5	103.6	1.04	84.7	87.3	0.97	0.050	0.014	0.014	0.99	9965	10345	0.96	582	634	0.96	0.50
cv22-46	10	100	92.7	90.4	1.02	72.7	76.4	0.95	0.050	0.015	0.015	1.01	8152	8539	0.95	517	555	0.95	0.50
cv22-35	10	75	80.0	75.9	1.05	62.1	64.3	0.97	0.050	0.016	0.016	1.00	6400	6667	0.96	474	469	0.96	0.51
cv22-23	10	50	69.5	59.2	1.17	53.4	50.4	1.06	0.050	0.017	0.017	0.97	5041	4704	1.07	440	369	1.07	0.56
cv18-69	12	150	155.1	150.9	1.03	116.5	123.3	0.94	0.050	0.012	0.013	0.93	17204	17017	1.01	959	936	1.01	0.59
cv18-58	12	125	135.6	135.0	1.00	104.5	110.5	0.95	0.050	0.014	0.014	1.01	13183	14548	0.91	798	840	0.91	0.61
cv18-46	12	100	118.6	117.9	1.01	90.3	96.7	0.93	0.050	0.014	0.014	1.00	11040	12008	0.92	732	737	0.92	0.62
cv18-35	12	75	104.3	98.9	1.05	79.6	81.4	0.98	0.050	0.016	0.015	1.03	7960	9376	0.85	676	622	0.85	0.66
cv18-23	12	50	91.5	77.2	1.18	70.0	63.8	1.10	0.050	0.017	0.017	1.02	7663	6616	1.16	576	489	1.16	0.73
cv13-69	16	150	211.0	227.3	0.93	158.2	177.3	0.89	0.050	0.013	0.012	1.02	29150	29143	1.00	1412	1462	1.00	0.81
cv13-58	16	125	188.8	203.3	0.93	143.4	158.9	0.90	0.050	0.014	0.013	1.06	23297	24913	0.94	1251	1313	0.94	0.84
cv13-46	16	100	167.7	177.5	0.94	128.1	139.0	0.92	0.050	0.015	0.014	1.07	18692	20563	0.91	1116	1151	0.91	0.88
cv13-35	16	75	145.8	148.9	0.98	114.0	117.0	0.97	0.050	0.016	0.015	1.07	15365	16056	0.96	923	971	0.96	0.94
cv13-23	16	50	120.8	116.3	1.04	97.0	91.7	1.06	0.050	0.016	0.016	0.98	14013	11329	1.24	692	765	1.24	1.01

flexural deformation calculated by the beam theory is added to the rotation angle. From the figures, it can be seen that the estimated results by the formulae in Table 4 much underestimate the FEA results of the subassemblage model. The comparison of the local strength of the subassemblage connections ($_vP_y$, $_vP_{max}$) to the estimated strength by the equations (9) and (10) in Table 4 ($_cP_{cy}$, $_cP_{cmax}$) are shown in Figure 21. When the smallest D/t =13, the equations (9) and (10) estimate well the FEA results ($_vP_y/_cP_{cy}$= 0.89-1.06 and $_vP_{max}/_cP_{cmax}$ = 0.93-1.04). But, the larger the D/t ratio, the more the estimated results underestimate the FEA results (for D/t =54; $_vP_y/_cP_{cy}$= 1.28-1.61, $_vP_{max}/_cP_{cmax}$ = 1.22-1.54). The reason is that the stiffening effect of the beam web against the local deformation is more notable because the out-of-plane stiffness of the column decreases as the D/t ratio increases.

It is obvious that the elastic-plastic behaviour of the subassemblage model cannot be estimated directly by the formulae in Table 4 from the above consideration. Here, the estimation of the mechanical properties of the subassemblage model are carried out using the regression analysis and the FEA results.

The formulae estimating the mechanical properties of the subassemblage model subjected to the symmetrical moment are shown in Table 7. The relationships between the test and the estimated results are shown in Figure 22. The trilinear load-deformation curve models by the formulae in Table 7 are shown in Figure 19 as "est.(vm)". Obtaining the initial stiffness, it needs to add the elastic flexural deformation to the rotation angle.

From the figures and the tables, the estimated results agree well with the FEA results.

The results of the connections subjected to symmetrical loading can be applied to the connections subjected to asymmetrical loading. Because, the symmetrical loading condition is severe one against the local deformation of tubes. On the other hand, the asymmetrical loading condition restrict the local deformation due to the interaction of tension and compression force from the flange plates.

5. COMPARISON WITH DESIGN FORMULAE

The allowable strength in short term ($1.5Pa$ or $1.5Ma$) which corresponds to the yield strength and the ultimate strength (Pu or Mu) of the tubular connections are shown in AIJ, Recommendations for the Design and Fabrication of Tubular Structures in Steel (1990). Those are the empirical formulae which the connections is replaced by the simple mechanical model. The followings are the design formulae:

i) Allowable and ultimate strength of simple connections subjected to tension load

$$1.5P_a = 1.5\times1.9(D/(2t))^{0.1}/(1\text{-}0.81(B_1/D))t^2F' \quad (19)$$

$$P_u = 1.87(D/(2t))^{0.1}P_a \quad (20)$$

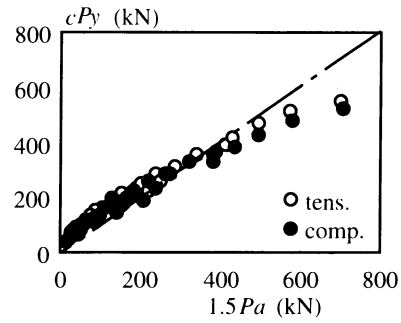

Figure 23(a) Relationships between FEA results and estimated values by design formulae (Yield)

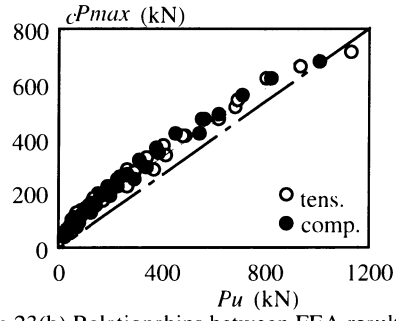

Figure 23(b) Relationships between FEA results and estimated values by design formulae (Maximum)

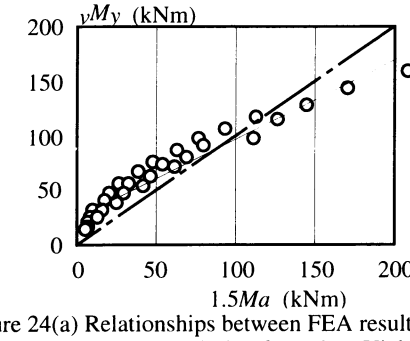

Figure 24(a) Relationships between FEA results and estimated values by design formulae (Yield)

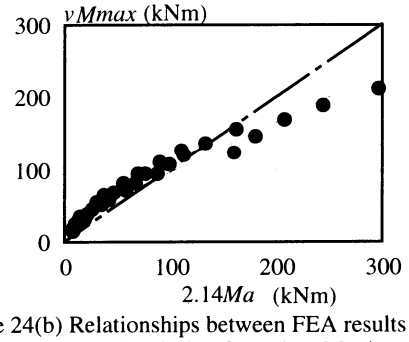

Figure 24(b) Relationships between FEA results and estimated values by design formulae (Maximum)

ii) Allowable and ultimate strength of simple connections subjected to compression load

$$1.5P_a = 1.5\times2.8(D/(2t))^{-0.1}/(1-0.81(B_f/D))t^2F' \quad (21)$$
$$P_u = 2.14P_a \quad (22)$$

iii) Allowable and ultimate strength of column to wide flange beam connections subjected to symmetrical moment

$$1.5M_a = 1.5\times2.8H(D/(2t))^{-0.1}/(1-0.81(B_f/D))t^2F' \quad (23)$$
$$M_u = 2.14M_a \quad (24)$$

where, F' is specified minimum yield strength of the column material. Comparing the estimated results with the design formulae, F' is replaced by the yield stress of the column.

The results of comparing the maximum and the yield strength of the FEA models subjected to the tension and the compression load with the design formulae (19)-(22) are shown in Figures 23(a) and 23(b). Straight lines in the figures show regression lines between the FEA results and the design formulae. It can be seen that there is good correlation between them (each coefficient of correlation is 0.99). But, the design formulae do not estimate well the FEA results. When $D/t \leq 22$, the tension yield strength, ${}_tP_y$, is almost equal to the estimated results by Equation (19) (${}_tP_y/1.5P_a$ = 0.78-1.22 ; average =1.01), but the larger the D/t ratio, the more the Equation (19) underestimate the ${}_tP_y$ (D/t =54 ; ${}_tP_y/1.5P_a$ = 1.94-2.37). For the maximum strength, ${}_tP_{max}$, the less the D/t ratio, the more the Equation (20) overestimate the ${}_tP_{max}$ (D/t =13 ; ${}_tP_{max}/P_u$ = 0.63-0.77), and the larger the D/t ratio, the more the Equation (20) underestimate the ${}_tP_{max}$ (D/t =54 ; ${}_tP_{max}/P_u$ =1.37-1.67).

The relationships between the design formulae and the FEA results with compression load are almost the same as those above mentioned. When the smallest D/t =13, the estimated results by the design formulae (21) and (22) overestimate a little the yield and the maximum strength, ${}_cP_y$ and ${}_cP_{max}$ (${}_cP_y/1.5P_a$ = 0.74-0.87, ${}_cP_{max}/P_u$ = 0.74-0.87). On the other hand, When the largest D/t =54, the estimated results by the design formulae (21) and (22) underestimate the yield and the maximum strength (${}_cP_y/1.5P_a$ = 1.53-1.91, ${}_cP_{max}/P_u$ = 1.14-1.51). The results of comparing the maximum and the yield strength of the subassemblage FEA models with the design formulae (23) and (24) are shown in Figures 24(a) and 24(b). It can be seen that there is good correlation between them (the coefficient of correlation is 0.97). The relationships between them are almost the same as those of the simple models. When the smallest D/t =13, the estimated results by the design formulae (23) and (24) overestimate a little the yield and the maximum strength, ${}_vM_y$ and ${}_vM_{max}$ (${}_vM_y/1.5M_a$ = 0.76-0.90, ${}_vM_{max}/M_u$ = 0.75-0.80). And, when the largest D/t =54, the estimated results by the equations underestimate the yield and the maximum strength (${}_vM_y/1.5M_a$ = 2.1-2.67, ${}_vM_{max}/M_u$ = 1.57-2.09).

6. CONCLUSION

The following conclusions can be drawn from this research:

(1) The dimension parameters of the D/t and the B_f/D ratios affect significantly the mechanical properties of such types of connections without stiffening.

(2) The mechanical properties of the connections can be estimated well by the formulae obtained by the regression analysis.

(3) The estimated trilinear load-deformation curve models agree not only with the FEA results but also with the test results.

(4) There is good correlation between the FEA results and the design formulae in AIJ recommendation. But, when the D/t ratio is smaller, the design formulae overestimate by 20 or 30% the strength of the connections. And when the D/t ratio is larger, the design formulae underestimate by almost twice the strength of the connections.

ACKNOWLEDGEMENTS

The author is greatly indebted to Hibbitt, Karlsson & Sorensen, INC. for providing ABAQUS program.

REFERENCES

AIJ, Recommendations for the Design and Fabrication of Tubular Structures in Steel, 1990

T. Kamba, H. Kanatani, K. Fujiwara, and M. Tabuchi 1982. Test on the local failures of tubular column to H-beam connections in steel structures, Transaction of AIJ, No. 322, pp.44-51, Tokyo (in Japanese)

T. Kamba, H. Kanatani, K. Fujiwara, and M. Tabuchi 1983. Empirical formulae for strength of steel tubular column to H-beam connections, Transaction of AIJ, No. 325, pp.67-73, Tokyo (in Japanese)

T. Kamba, H. Kanatani, and M. Tabuchi 1984. Local strength of tubular column to H-beam connections - Study of connections subjected to vertical and horizontal loading, Transaction of AIJ, No. 360, pp.147-156, Tokyo (in Japanese)

T. Kamba, H. Kanatani, M. Tabuchi, and T. Wakida 1984. Local strength of the centrifugal cast steel tubular columns to H-beam connections -Study of connections subjected to vertical or horizontal loading, Transaction of AIJ, No. 370, pp.81-91, Tokyo (in Japanese)

T. Kamba, H. Kanatani and T. Wakida 1994. CHS Column-to-Beam Connections without Diaphragms, Proc. of 6th Int. Symposium on Tubular Structures, PP.325-334, 1994.12

Hibbitt, Karlsson & Sorensen, Inc. ABAQUS/ Standard User's Manual, Ver. 5.5, 1996.

Hibbitt, Karlsson & Sorensen, Inc. ABAQUS/ Standard Example Problems Manual, Ver. 5.5, 1996.

Tubular Structures VIII, Choo & Van der Vegte (eds) © 1998 Balkema, Rotterdam, ISBN 90 5809 001 9

Study of structural strength of column joints reinforced by welding ring-stiffeners in steel tubular transmission towers

Eijiro Hongo
Tokyo Electric Power Company Incorporated, Japan
Takashi Fukasawa & Yasuhiro Matsuo
Tomoe Corporation, Tokyo, Japan

ABSTRACT: Column joints around the cross arm of large truss transmission steel towers generally reinforced by ring-stiffeners. This paper presents static strength and fatigue strength of this joints. Regarding static strength of column joints reinforced by the ring-stiffeners, these static strength was found by experiments and parametric studies by FEM. Then design specification was proposed corresponding to kinds of loading states of joint taking material properties of the ring-stiffener into consideration. Regarding fatigue strength of welded portion between the ring-stiffeners, or the gusset plate, and the column, these fatigue curve was found experimentally, then obtained fatigue strength was normalized against the static strength.

1 INTRODUCTION

As shown in Figure 1, column joints around the cross arm of a large truss transmission steel tower are generally reinforced by ring stiffeners welded with double-side fillet on the column, of which welding method is adopted to gusset plates. Because these ring-stiffeners are fixed on the outermost line of the column section, bending moment applied to the column section is almost sustained by these ring-stiffeners.

Because the aim of this paper is to discuss a rational method of designing this kind of joint, based on the above consideration, the objective is a simple joint consisting of a column and single ring-stiffener as shown in Figure 2. The items studied are [1] the fatigue strength of the welded portion between the ring stiffener or the gusset plate and the column and [2] the static strength of the welded portion between the ring stiffener and column.

2 YIELD STRENGTH OF WELD BETWEEN RING-STIFFENER OR GUSSET PLATE AND COLUMN

This section describes static loading testing performed to quantitatively clarify the yield strength of the welded portion. The results are compared with those of an FEM analysis.

The specimens are shown in the detailed specimen diagram Figure 3 and the analysis model diagram. The diameter of the steel tube column D = 190.7(mm), the thickness of the steel plate T=5.3(mm) (STK590), and D x T = (190.7 x 5.3). The width of the ring-stiffener R = 30(mm), and the thickness of the steel plate t = 4.5(mm) (SH590P), so R x t = (30 x 4.5). The leg length of the fillet weld is 4.0(mm) (welding wire: SF60T). The loading jig used for the testing was shaped in the form of a gusset plate. Loading was done on a single side gusset plate (single side loading) and on a two side gusset plate (two side loading). The column force - yield strength ratio was assumed to be the axial force N / yield strength Ny ratio, and the testing was done for two ratios, N/Ny=0 and N/Ny=0.8. In the case of

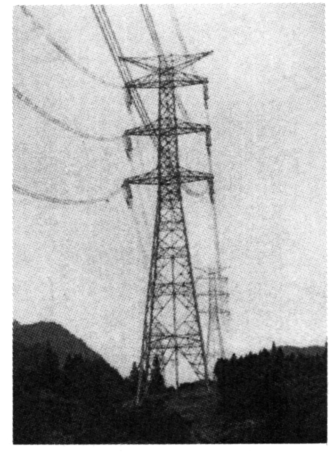

Photo.1

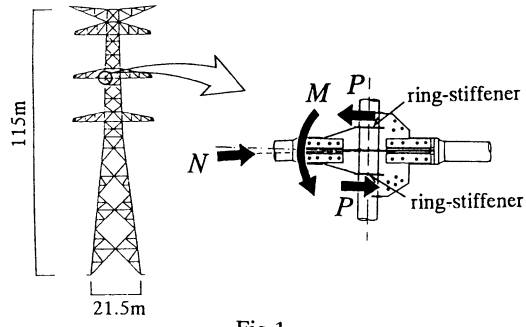

Fig.1

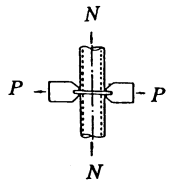

Fig.2

the FEM analysis, the stress-strain relationship is assumed to be bi-linear, and a yield stress of σ_y=6.0(tonf/cm^2). The fillet weld portion was assessed as a triangle element so it would coincide with the real thing, and incomplete penetration was not evaluated because the plate was thin.

Figure 4 shows the relational curves for the load P and the load direction displacement δ of the ring-stiffener from the test results and from the FEM analysis. The load direction displacement δ is considered macroscopically, the quantity of deformation is local deformation of the steel tube superimposed on the shearing deformation of the ring-stiffener. This reveals that regardless of the form of loading and the steel pipe yield strength ratio N/Ny, the FEM based analysis results correspond closely to the experimental results. And the fracturing are fractures which progress from cracks starting at the toe of the fillet weld between the ring-stiffener and the loading jig, and at this time, the local deformation of the steel tube is also clearly revealed.

The yield strength is difficult to point out load-displacement relation in this case, otherwise its value is scattered by the general yield point method. Therefore, the yield strength Pyo is obtained by 0.5% offset method. In addition, obtained value by this method is almost equal to value by 1/3 stiffness method unexpectedly regarding to this specimens. Figure 5 presents the relationship of R/D with the dimensionless strength obtained by dividing the yield strength Py (N/Ny = 0) based on the one-sided and two-sided loading and on FEM analysis when N/Ny = 0 for each material by the product of the T-shaped cross section (Rt + BeT)

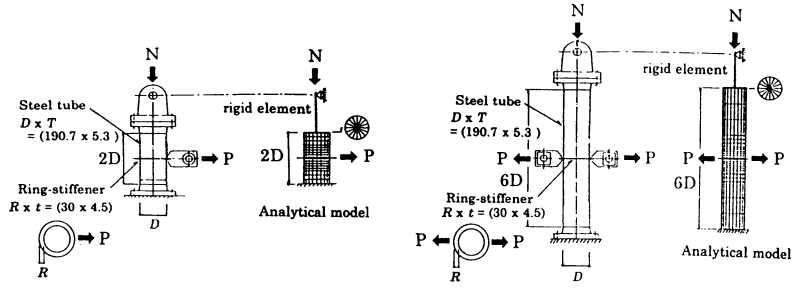

Fig.3 Specimens of the static load testing

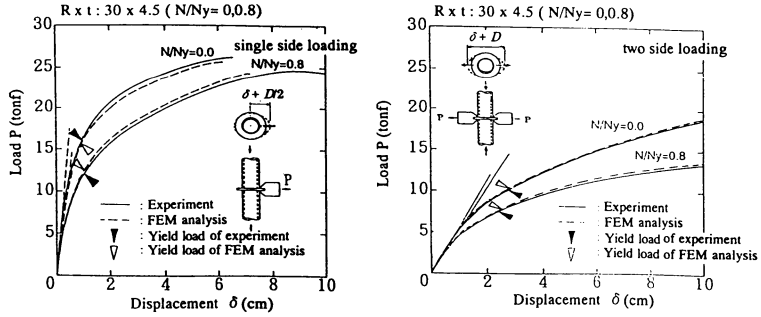

Fig.4 P-δ relationship

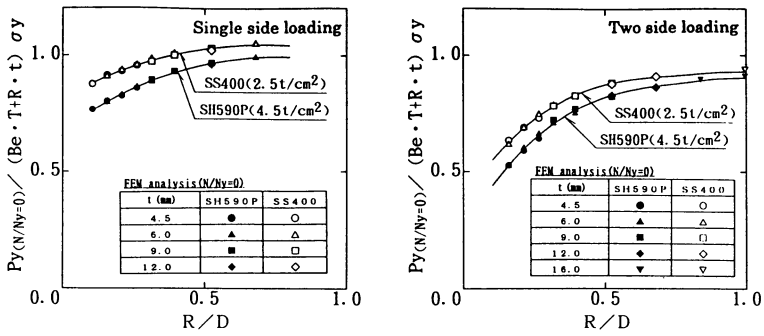

Fig.5 $Py_{(N/Ny=0)}/(Be \cdot T+R \cdot t)\sigma y$-$R/D$ relationship

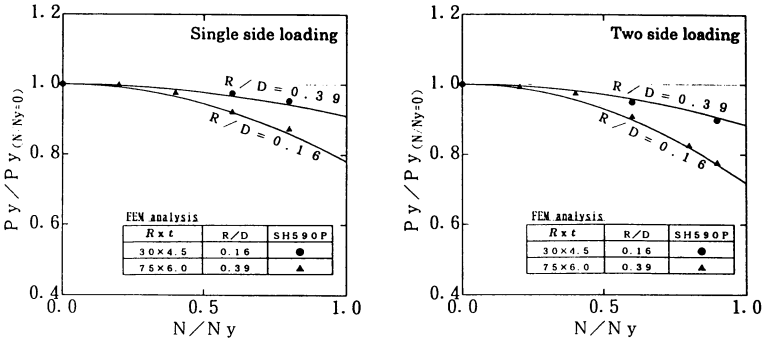

Fig.6 $Py/Py_{(N/Ny=0)}$-N/Ny relationship

and the yield stress σ_y of the ring. It also shows the multiple regression curve. At this time, the effective width "Be" is considered to be the range in which the steel pipe bears the shearing force. And with the width of the ring-stiffener R constant, the dimensionless strength was also almost constant in a case where the ring plate thickness t was varied, and it was confirmed that the effect on $Py_{(N/Ny=0)}$ that is a combination of R/t and R/D is small enough to be ignored.

Figure 6 presents the relationship of N/Ny with the ratio $Py/Py_{(N/Ny=0)}$ of the yield strength Py at N/Ny time for both one-side and two-side loading and of $Py_{(N/Ny=0)}$ that is the yield strength when $N/Ny = 0$. It also shows the multiple regression curve. It indicates that the greater N/Ny, or the smaller R/D, the greater the extent of the decline of $Py/Py_{(N/Ny=0)}$. And even when the material was SS400 or SH590P, the extent of the strength decline caused by the axial force ratio N/Ny was identical.

These yield strength of single side loading Pyo_1 and yield strength of two side loading Pyo_2 are represented by following formula,

SH590P:

$$Pyo_1=\beta_1\left\{-0.540(R/D)^2+0.821(R/D)+0.683\right\}\times(B_e \cdot T+R \cdot t)\cdot\sigma_y \quad (1)$$

$$Pyo_2=\beta_2\left\{1.050(R/D)^3-2.508(R/D)^2+2.127(R/D)+0.251\right\}\times(B_e \cdot T+R \cdot t)\cdot\sigma_y \quad (2)$$

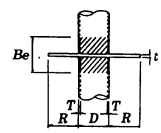

SS400:

$$Pyo_1=\beta_1\left\{-0.445(R/D)^2+0.638(R/D)+0.818\right\}\times(B_e \cdot T+R \cdot t)\cdot\sigma_y \quad (3)$$

$$Pyo_2=\beta_2\left\{1.032(R/D)^3-2.390(R/D)^2+1.924(R/D)+0.379\right\}\times(B_e \cdot T+R \cdot t)\cdot\sigma_y \quad (4)$$

$$\beta_1=-0.035(D/R)\left(N/N_y\right)^2+1.00 \quad (5)$$

$$\beta_2=-0.045(D/R)\left(N/N_y\right)^2+1.00 \quad (6)$$

where,

Pyo_1 :Yield strength of single side loading ,
Pyo_2 :Yield strength of two side loading ,
σ_y :Yield Stress,
D :Diameter of the steel tube ,
T :Thickness of the steel tube ,
R :Width of the ring stiffener ,
Be :Effective width of the steel tube

$=1.52\sqrt{T(D-T)/2}+t$,

N :Axial force of the steel tube, and
Ny :Yield force of the steel tube.

3 FATIGUE TESTING

In this study, the fatigue strength of the welded portion between the ring- stiffener or gusset plate and the column is normalized against the yield strength, because an evaluation of its stress amplitude would be vague due to the complex details of the joint.

3.1 *Specimens*

Figure 7 shows the load - strain relationship at the point where the maximum strain in the peripheral direction of the ring-stiffener is generated, which is the result of FEM. The parameters for the fatigue test specimens were narrowed based on following factors which effect on the maximum strain.

[1] *N/Ny*: Because the maximum strain at the time of yield strength of the ring- stiffener weld portion is greater in a case where $N/Ny = 0$ than in a case where $N/Ny \neq 0$, the value of *N/Ny* was constant at $N/Ny = 0$.

[2] *R/D*: Because the maximum strain at the time of yield strength of the ring- stiffener weld portion is greater in a case where *R/D* is small than in a case where *R/D* is large, the value of *R/D* was constant at $R/D = 0.16$ ($R \times t = 30 \times 4.5$) which is the minimum value in an actual large steel tower.

[3] Ring-stiffener material: Because the maximum strain at the time of yield strength of the ring-stiffener weld portion is greater in a case the material is SH590P than when it is SS400, the material was constant at SH590P.

[4] Steel tube size: Because the stress amplitude *P* of the fatigue curve is assessed based on the amplitude ratio *S* (=*P*/*Py*) made nondimensional by the yield strength *Py* which was obtained by the static strength testing described in the previous paragraph, the steel tube size was the same size (diameter of 190.7 x 5.3 (STKT590)) as that used in the static strength testing.

[5] Loading method: Because the maximum strain at the time of yield strength of the ring-stiffener weld portion is almost identical with no dominance by either case observed for both single side and two side loading, both single side and two side loading were performed.

[6] Stress amplitude: Because it is forecast from the results of past research that the fatigue life *Nf* will decrease almost in proportion to the power of the reversed stress amplitude *S*, the minimum level of 3 was set to obtain the *S* - *Nf* relationship curve.

From the above study results, two types of loading--single side and two side loading-were performed for three stress amplitude levels, with a total of 8 specimens, 2 x (3+1) including static loading test specimens to provide the yield strength which normalize the amplitude of fatigue testing. The ring-stiffener welded fatigue specimens are shown in Figure 8. The welding was performed in the same way as conventional joints and as shown in Figure 8, the cross section of the bead was almost identical to that of conventional joints.

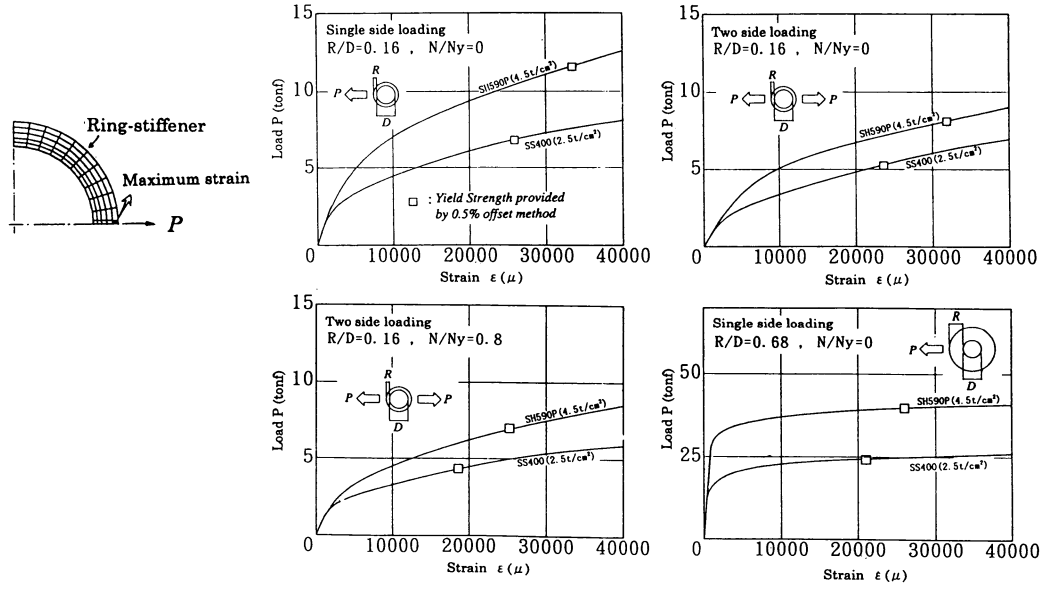

Fig.7 P-ε relationship

3.2 *Loading and Measurement Method*

During static strength testing, the force acting on the weld was a tensile load and loading was applied until the weld was fractured. During the fatigue testing, cyclic stress loading was applied until loading was impossible. During both the static strength testing and the fatigue testing, the axial force N acting on the steel tube was set at N=0.

During the fatigue testing, magnetic particle testing was performed with a cycle 1/10 the fatigue life Nf in order to study the way in which cracks begin and develop. And the fatigue life Nf was set as the number of cycles until immediately before load control became impossible. And in order to study changes in the strain of the ring-stiffener weld portion for each number of cycles, strain gauges were installed at parts of the ring-stiffener where the generation of the maximum strain was forecast to occur. During static strength testing, the yield strength of the joint was assessed from the load direction displacement - load relationship of the ring-stiffener.

3.3 *Fatigue Test Results*

(1) *S-Nf Relationship Obtained From Fatigue Testing*

Table 1 shows the results of static strength testing and fatigue testing. During fatigue testing of all specimens, initial cracking appeared in the weld between the ring and the gusset plate, developed along the weld portion, and when it reached the weld between the ring and the steel tube, loading became impossible and a fracture occurred.

Figure 9 shows the *S-Nf* relation obtained from the fatigue testing results (under complete reversed tension and compression), in which S = Amplitude normalized by the yield strength Py and Nf = fatigue life. So for the following reasons, the test results for single side and two side loading were assessed together. [1] Because it is generally impossible for factors such as the shape of the toe of the weld and others which influence the fatigue strength to be kept constant through a test series, the assessments of the fatigue testing results are scattered. [2] The value of the strain

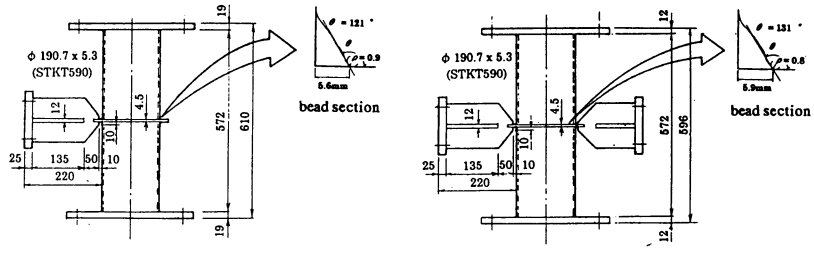

Fig.8 Specimens of the fatigue testing

Table 1 Results of the static load testing and the fatigue testing

	Size of steel tube	Size of ring-stiffener	Loading direction	Yield strength Pye(tonf)	Load P(tonf)	S $=P/Pye$	Fatigue life Nf
Single side loading	φ 190.7x5.3 (STKT590)	30x4.5 (SH590P)	P	14.0	14.0	-	-
				-	8.7	0.62	470
				-	7.3	0.52	1378
				-	5.8	0.41	7250
Two side loading	φ 190.7x5.3 (STKT590)	30x4.5 (SH590P)	P P	10.0	10.0	-	-
				-	7.0	0.70	238
				-	6.0	0.60	962
				-	5.0	0.50	8018

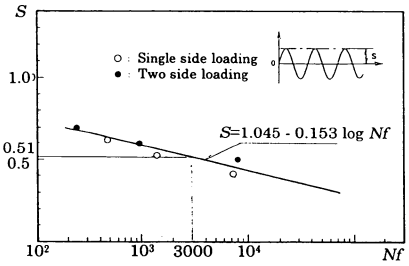

Fig.9 *S-Nf* relationship under complete reversed tension and compression

at yield strength in the load - strain relationship obtained from FEM analysis is almost identical during single side loading and two side loading. The regression formula is obtained as follows from the results of the above tests.

$$S=1.045-0.153\log Nf \qquad (7)$$

(2) *Setting the Strength Reduction Coefficient*

Figure 10 shows examples of the results of full-scale wind response measurements of a transmission tower such as the response strain of the member, or the orbit of response displacement at the top of the tower. From these, it is possible to view the wind response of a steel tubular transmission tower as a partially pulsating stress. This means that the strength reduction coefficient needed to evaluate fatigue strength is determined based on the fatigue curve of a complete pulsating stress evaluated on the safe side. Here, the completely reversed fatigue life is transformed into completely pulsating fatigue life based on the Goodman Line.

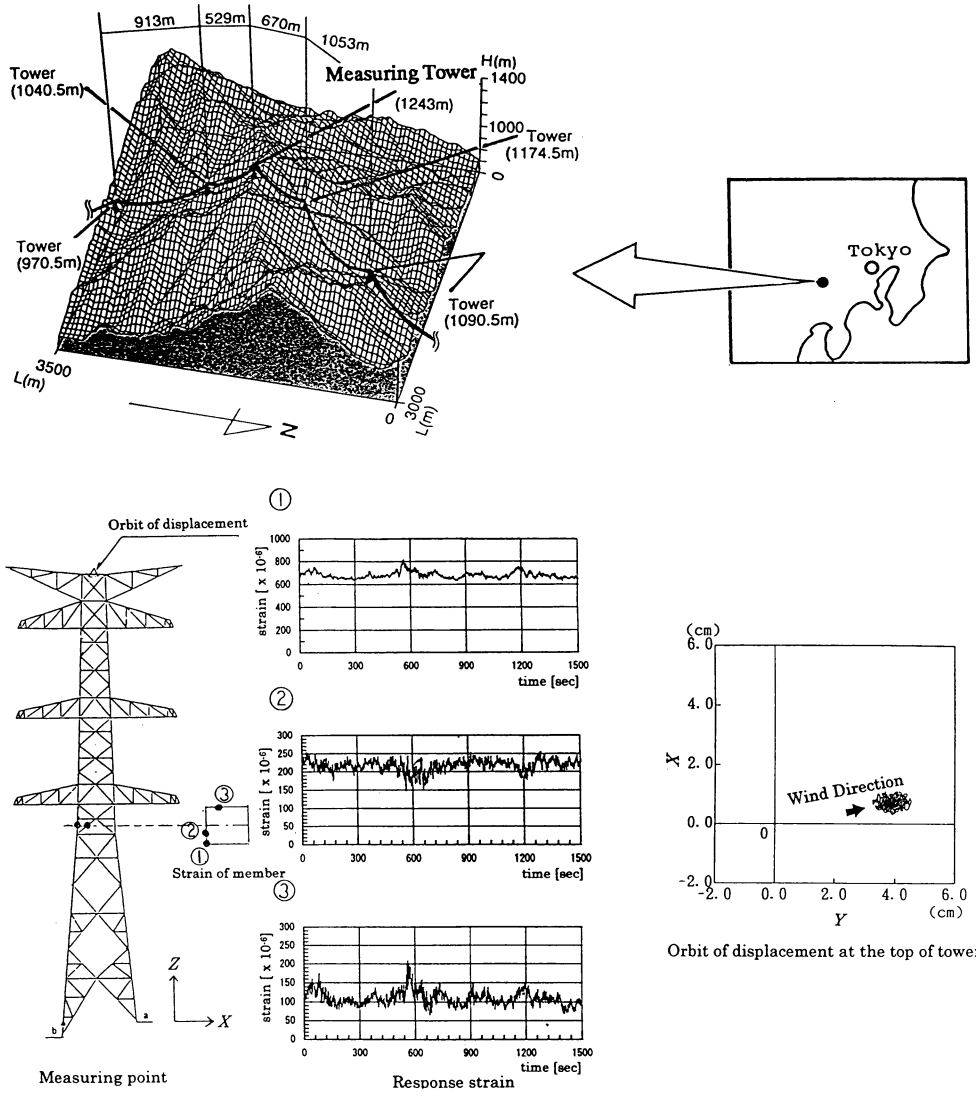

Fig.10 The result of full-scale wind response measurements of the transmission tower

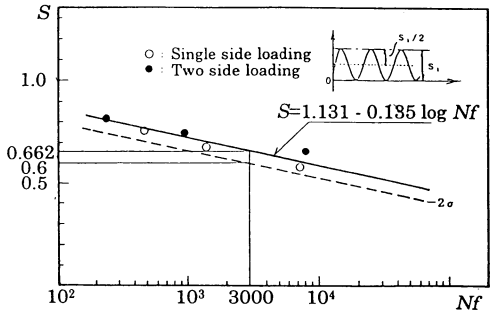

Fig.11 *S-Nf* relationship under complete pulsating stress

Figure 11 shows the *S-Nf* relationship obtained by converting the experimental results into completely pulsating stress. If, considering the scattering of the test results, twice the standard differential of the residual (2σ) for the regression formula of the experimental values is reduced to evaluate the amplitude, the strength reduction coefficient α_0 for Nf = 3,000 cycles (Value of *Nf* for *P/Py* = 1.0 stipulated based on a cyclic load which is estimated from wind loads for fifty years in the design of steel towers for electric power transmission) is 0.6.

4 CONCLUSIONS

1. Experiments and FEM analysis were performed to clarify quantitatively the yield strength of the welded portion between the ring-stiffener and the column in a joint around the cross arm of a steel tubular transmission tower reinforced with ring-stiffeners.

2.Then the fatigue strength of the welded portion is evaluated with the reduction coefficient of yield strength from the results of experiment.

3.Additionally, these obtained results have been reflected in designing the steel tower and standards of the fabrication.

REFERRENCES

B. Thürlimann, R.O. Bereuter and B.G. Johnston : The Effective Width of a Circular Cylindrical Shell Adjacent to a Circumferential Reinforcing Rib, Proc. 2nd U.S. Natl. Conf. Applied Mechanics, pp.347 ~ 356, 1954



Taylor & Francis
Taylor & Francis Group
http://taylorandfrancis.com

Tubular Structures VIII, Choo & Van der Vegte (eds) © 1998 Balkema, Rotterdam, ISBN 90 5809 001 9

Experimental study of structural behavior of beam-to-column connections reinforced by increasing plate thickness of column without diaphragms

Koji Morita & Kazumasa Ebato
Chiba University, Japan
Keizo Furusawa, Kenichi Fujita & Kimio Hamano
Yokogawa Bridge Corporation, Chiba, Japan

ABSTRACT: The structural behavior of beam-to-column connections reinforced by increasing the plate thickness of column at the connection area without inner diaphragms seems to be different from those of connection with inner diaphragms. The structural behavior of beam-and-column subassemblages with increased column thickness at the connection area in addition to the horizontal haunch of beam at the connection side are investigated by the cyclic reversal loading test. The case studies are presented to discuss the structural performance of beam-to-column connections by using finite element analysis and yield line theory with respect to two types of connection, that is, (1) the beam-to-column connection reinforced by increasing the column thickness at the connection area, and (2) the beam-to-column connection reinforced by increasing the column thickness at the connection area with the horizontal haunch of beam at the connection side.

1 INTRODUCTION

High-rise steel structures in Japan are usually constructed by assembling rectangular hollow section (RHS) columns and wide flange beams. To reinforce the beam-to-column connections of the structure, inner diaphragms are used. Fabrication of the columns with inner diaphragms requires many production processes. To reduce the fabrication process of columns, the following reinforcement of connections may be considered: (1) increasing the column thickness at the connection area. (2) horizontal haunch of the beam flanges at the connection side in addition. When the structural performance of the proposed beam-to-column connections is the same as that of the inner diaphragm connections, a reasonable connection system may be proposed.

The structural behavior of beam-to-column connections reinforced by increasing the column thickness seems to be considerably different from those of inner diaphragm connections because the working force such as bending moment and shearing force on the connections has to be resisted by the out-of-plane bending resistance of the column wall at the connection. The structural performance of such connections has to be fully discussed in structural analysis.

In this study, the structural behavior of beam-and-column subassemblages whose connection is reinforced by increasing the column thickness at the connection area in addition to the horizontal haunch of beam at the connection side is investigated and compared with those of the inner diaphragm connection by the cyclic reversal load testing. Case studies are carried out using finite element analysis and yield line theory to determine whether the structural performance of the proposed beam-to-column connections can be given the same performance of the inner diaphragms connection.

2 BEAM-AND-COLUMN SUBASSEMBLAGE TEST

2.1 *Test program*

The half-scale beam-and-column subassemblage specimens corresponding to the lower part in high-rise steel structures are projected to the cyclic reversal loading test. The dimensions of the built-up RHS column and the built-up wide flange beam are □-300×300×19 and BH-400×150×9×14, respectively. Test parameters are the detail of beam-to-column connection. A total of four specimens shown in Figure 1 are tested in this study:

1. Specimen DU: Prototype model in this study. The beam-to-column connection is reinforced with inner diaphragms.
2. Specimen NU: The difference of connection detail from DU is the removal of the inner diaphragms.

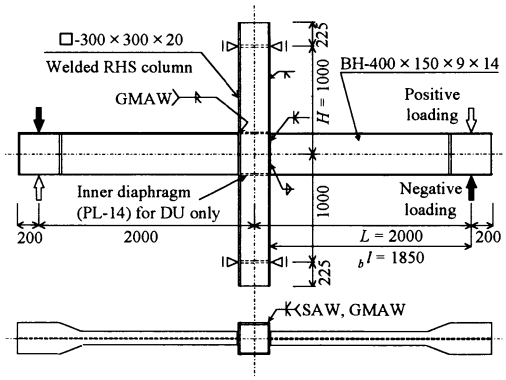

(a) Specimens DU and NU

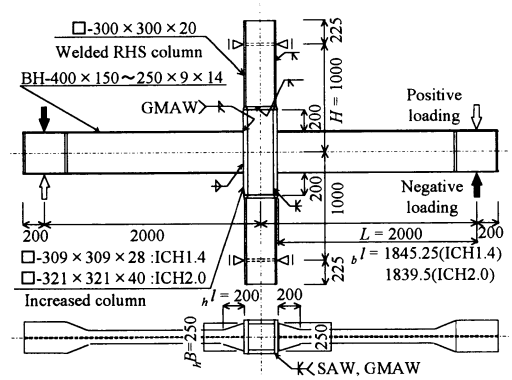

(b) Specimens ICH1.4 and ICH2.0

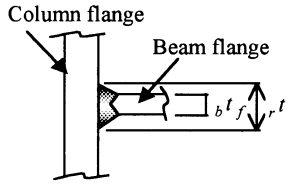

Measured value of $_{r}t$ (mm)

	DU	NU	ICH1.4	ICH2.0
$_{r}t$	34.2	35.2	35.6	32.8

(c) Total weld leg length of beam

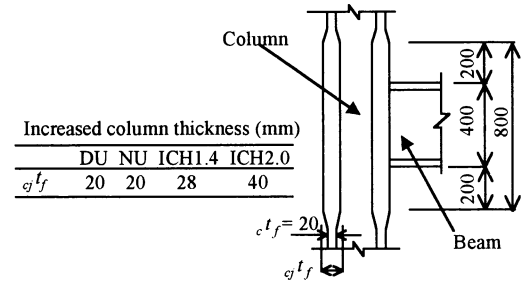

(d) Increased column thickness

Figure 1. Dimensions of subassemblage specimens

Table 1. Mechanical properties of materials

	Yield point σ_y (N/mm²)	Tensile strength σ_t (N/mm²)	Elongation El. (%)
PL-40 (40.3)	343	513	32
PL-28 (28.3)	330	519	31
PL-20 (19.6)	340	524	28
PL-14 (14.5)	364	532	27
PL-9 (9.1)	389	539	25

( ) measured thickness (mm)

Table 2. Welding condition

	GMAW	SAW
Wire (mm)	1.2	4.0
Current (A)	290 - 320	800
Voltage (V)	36 - 44	38 - 40
Heat input (kJ/mm)	1.7 - 2.7	6.1 - 6.4
Interpass tempereture (°C)	100 - 150	-

GMAW: Gas metal arc welding
SAW : Submerged arc welding

3. Specimen ICH1.4: The column thickness at the connection area is increased to be 309×309×28, which is 1.4 times as large as that of NU. In addition, the beam at the connection side is horizontally haunched to be 400×250 ×9×14 without any inner diaphragms.

4. Specimen ICH2.0: The difference of connection detail from ICH1.4 is the column thickness at the connection area. The column thickness is increased to be 321×321×40, which is almost 2.0 times as thick as that of NU.

Specimen NU is projected to estimate the strength of beam-to-column connection without any diaphragms. Specimens ICH1.4 and 2.0 proposed in this study are projected to compare the full plastic strength and stiffness of beam-and-column subassemblage with those of DU.

The cyclic reversal loading $_{b}Q$ is applied to the end of beam which is reinforced to resist the lateral buckling of beam. The axial load acting on the column is not considered. The mechanical properties of materials used and the welding condition are shown in Table 1 and Table2, respectively.

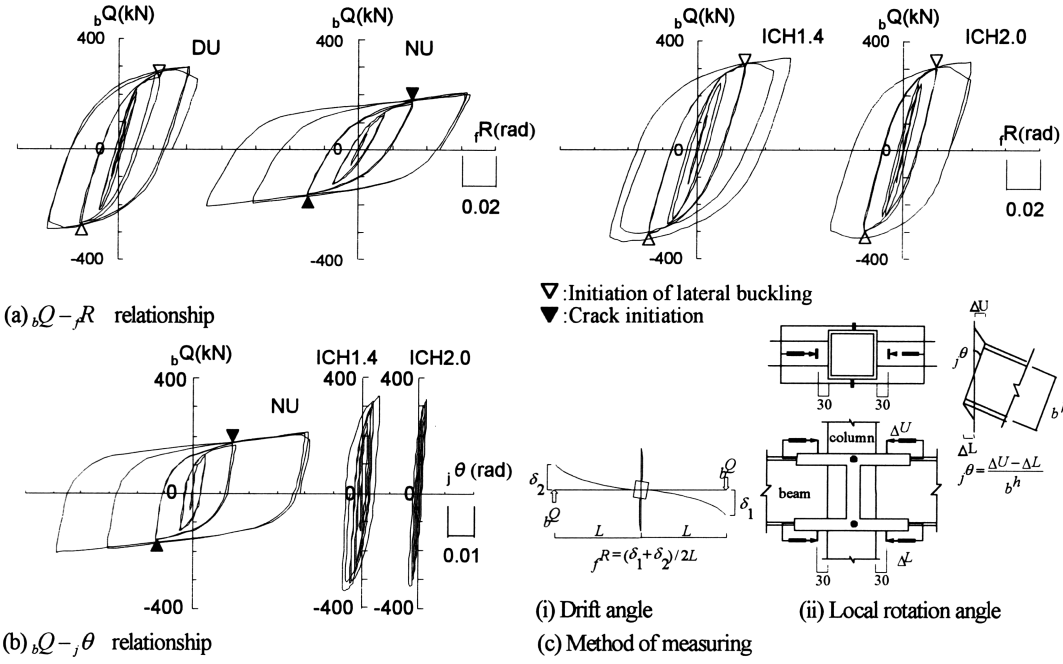

Figure 2. Hysteretic characteristics of subassemblage specimens

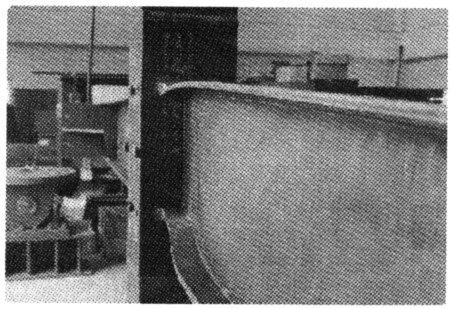

(a) Lateral buckling of beam

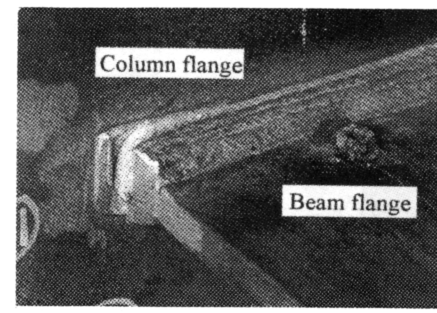

(b) Cracks at beam-to-column connection

Figure 3. Failure mode of subassemblage specimens

2.2 *Test results*

The applied load ($_bQ$) - drift angle ($_fR$) and the applied load ($_bQ$) - local rotation angle of beam-to-column connection ($_j\theta$) relationships are shown in Figure 2, respectively. For the specimen DU, the lateral buckling of beam is observed in the drift angle of $\pm$0.02rad. The strength capacity is deteriorated in the drift angle of $\pm$0.04rad because of the coupled local buckling of beam web and out-of-plane deformation of beam flange as shown in Figure 3(a). The hysteretic curve is stable spindle type until the second cycle in the drift angle of 0.04rad. For the specimen NU, cracks

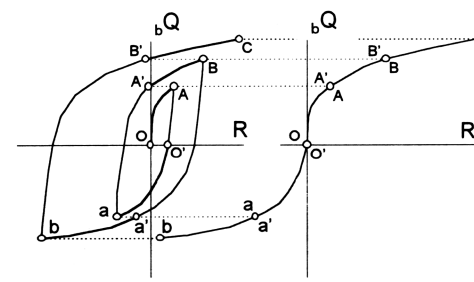

Figure 4. Relation between hysteretic curve and synthetic curve

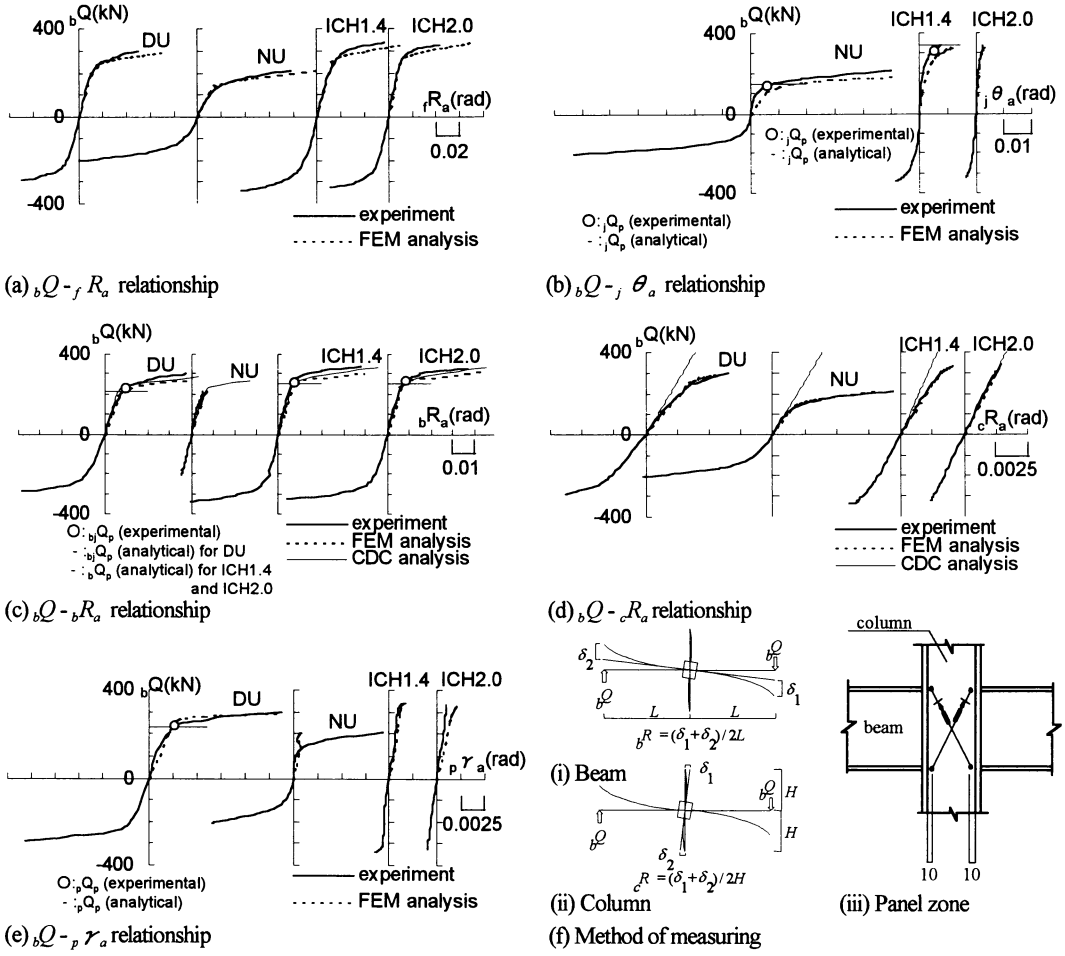

Figure 5. Synthetic curves of subassemblage specimens

are initiated in the column wall at both sides of beam flange in the drift angle of ±0.03rad. The cracks are extended into the column flange around the beam flange as shown in Figure 3(b), however, the decrement of the strength capacity can not be observed until the drift angle of −0.09rad. In the case of the specimens ICH1.4 and ICH2.0, the lateral buckling of beam is observed in the drift angle from ±0.02rad to ±0.025rad. The hysteretic curves of ICH1.4 and ICH2.0 are stable spindle type until the drift angle of ±0.05rad and ±0.04rad, respectively. The strength capacity is deteriorated at the second cycle of the drift angle of ±0.05rad and ±0.04rad for ICH1.4 and ICH2.0, respectively. Based on the relationship between the hysteretic curve and synthetic curve as shown in Figure 4 (Kato, 1982), the synthetic curves of drift angle ($_fR_a$), local rotation angle of beam-to-column connection ($_j\theta_a$), rotation angle of beam ($_bR_a$), rotation angle of column ($_cR_a$) and shear deformation angle of panel zone ($_p\gamma_a$) are shown in Figure 5.

The initial stiffness of column and panel zone of ICH1.4 is larger than that of DU, moreover, the local full plastic strength of beam-to-column connection for ICH1.4 is stronger than the full plastic strength of beam end connection for DU as shown in Figures 5(b), 5(c), 5(d) and 5(e). As the result, the initial stiffness and full plastic strength of beam-and-column subassemblage for ICH1.4 become larger than those for the prototype specimen DU as shown in $_bQ$-$_fR$ relationship in Figure 2 and Figure 5(a).

The initial stiffness of column, panel zone and local rotation angle of beam-and-column subassemblage of ICH2.0 is larger than that of ICH1.4 as shown in Figures

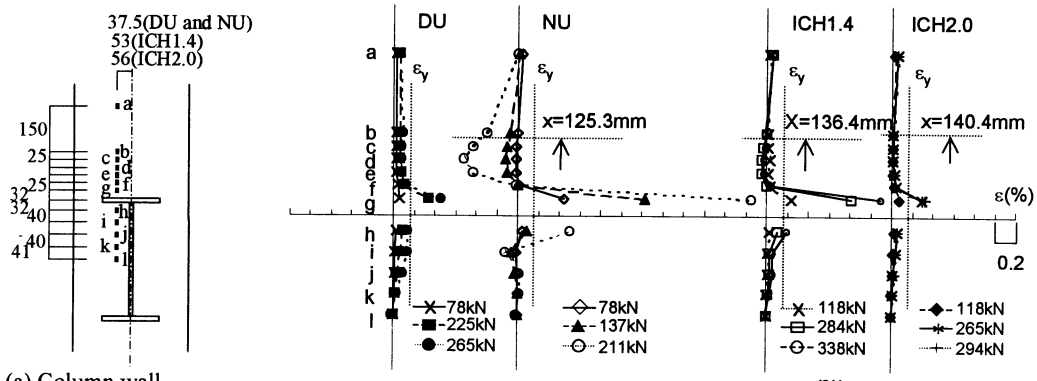

(a) Column wall

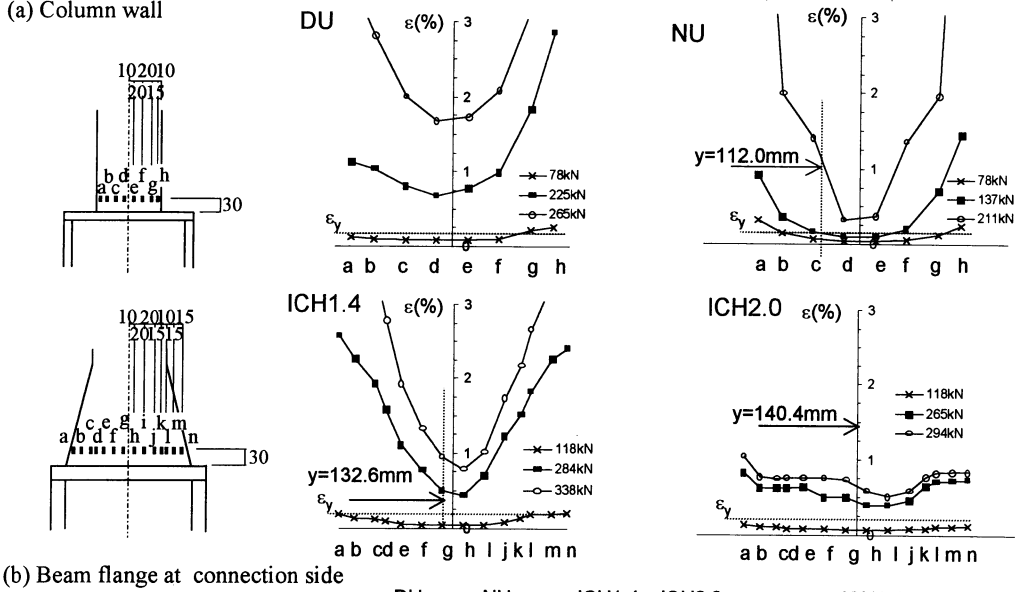

(b) Beam flange at connection side

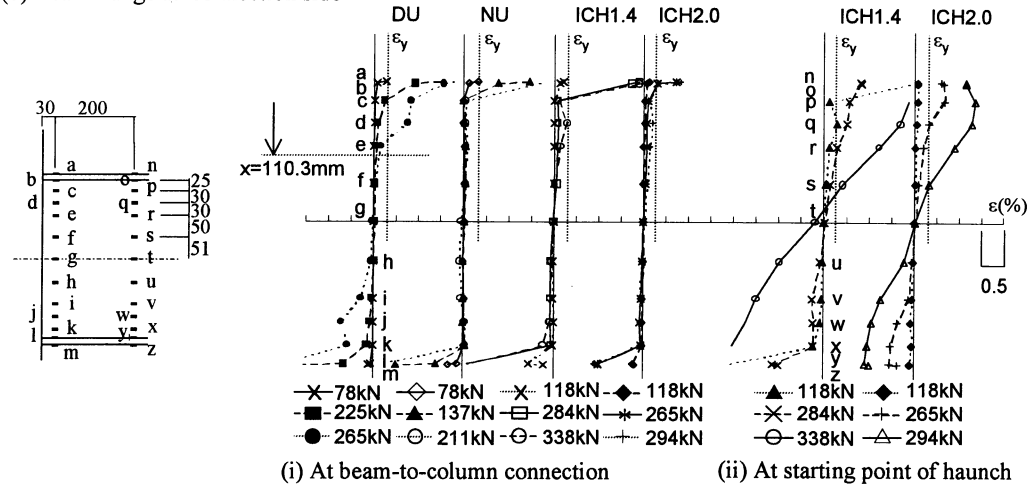

(i) At beam-to-column connection (ii) At starting point of haunch

(c) Beam

Figure 6. Strain distributions of each element in specimens

Table 3. Experimental and analytical strengths of each specimens

(a) Local strength of beam-to-column connection

Specimen	Full plastic strength ${}_jQ_p$ (kN)			Ultimate strength ${}_jQ_u$ (kN)		
	Exp.	Ana.	Exp./Ana.	Exp.	Ana.	Exp./Ana.
DU	-	230.8	-	-	309.6	-
NU	138.1	144.3	0.96	210.7	207.1	1.02
ICH1.4	317.5	337.5	0.94	-	461.1	-
ICH2.0	-	578.0	-	-	803.4	-

(b) Strength of beam end connection

Specimen	Full plastic strength ${}_{bf}Q_p$ (kN)			Ultimate strength ${}_{bf}Q_u$ (kN)		
	Exp.	Ana.	Exp./Ana.	Exp.	Ana.	Exp./Ana.
DU	228.5	222.9	1.03	299.9*	299.3	1.00
NU	-	(222.9)	-	-	(299.3)	-
ICH1.4	260.0	(342.0)	-	339.0*	(469.7)	-
ICH2.0	262.5	(347.1)	-	329.0*	(475.2)	-

* Lateral buckling of beam

5(b), 5(d) and 5(e) because the column thickness of ICH2.0 is more thick than that of ICH1.4. The hysteretic behaviors of column and panel zone for both ICH1.4 and ICH2.0 are remained in the elastic region.

The initial stiffness and full plastic strength of beam-and-column subassemblage of NU are much smaller than those of DU, however, the plastic deformation capacity of NU becomes larger than that of DU as shown in Figure 2 and Figure 5(a).

The full plastic strengths of each element obtained by the experimental results using general yield point method are shown in Table 3, in which ${}_jQ_p$ and ${}_{bj}Q_p$ are the local full plastic strength of beam-to-column connection and the full plastic strength of beam end connection, respectively. ${}_jQ_u$ and ${}_{bj}Q_u$ are the local ultimate strength of beam-to-column connection and the ultimate strength of beam end connection, respectively. The full plastic strength of panel zone of the specimen DU is 237.6kN. The experimental strengths of each specimen is indicated by the shearing force at the beam end.

The strain distributions of the axial direction of column flange, beam flange and web around the beam-to-column connection are shown in Figure 6.

The out-of-plane bending behavior of column flange is observed clearly for NU, however the degree is not so remarkably for ICH1.4 as compared with that of NU as shown in Figure 6(a). The plastic region at both sides of beam flange is progressed. But the central part of beam flange is remained in the elastic region for NU, however, the full section of beam flange is in the yield region finally for ICH1.4 as shown in Figure 6(b).

In the case of ICH2.0, the out-of-plane bending behavior of column flange and the strain concentration at both sides of beam flange can not be observed as shown in Figures 6(a) and 6(b).

The plastic region of beam web for DU is larger than that for other specimens as shown in Figure 6(c).

For both ICH1.4 and ICH2.0, the full section of beam at the starting point of the horizontal haunch is progressed almost in the full plastic range as shown in Figure 6(c).

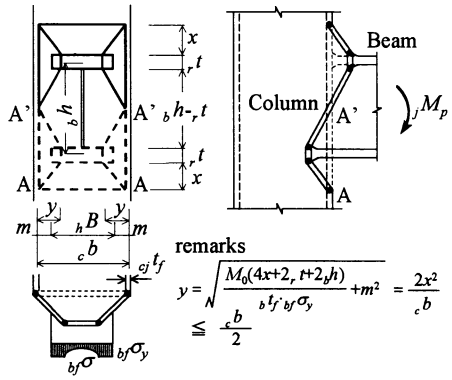

Figure 7. Yield mechanism of beam-to-column connection

3 Discussion

3.1 *Yield line theory*

Local full plastic strength of beam-to-column connection

The estimation procedure of the local full plastic strength of beam-to-column connection without any diaphragms (${}_jM_p$) has been proposed by the authors (Morita *et al.*, 1989A). The yield mechanism shown in Figure 7 is assumed. The local full plastic strength of beam-to-column connections is given by:

$$ {}_jM_p={}_bh\cdot M_0[{}_cb\{(4x+{}_bh+{}_rt)/x^2+2/({}_bh-{}_rt)\} $$
$$ +2\{x-m\cdot{}_cb/(2x)\}^2{}_bt_f\cdot{}_{bf}\sigma_y/(M_0\cdot{}_cb)] \quad (1) $$

where x satisfies the following equation:

$$ 4{}_bt_f\cdot{}_{bf}\sigma_y\cdot x^4-4M_0\cdot{}_cb^2\cdot x $$
$$ -{}_cb^2\{2M_0({}_bh+{}_rt)+m^2\cdot{}_bt_f\cdot{}_{bf}\sigma_y\}=0 \quad (2) $$

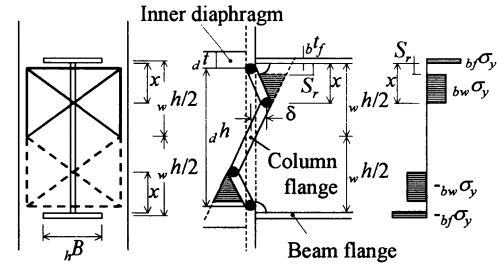

Figure 8. Yield mechanism of beam end connection

where ${}_c b$ is the distance between center axis of column web, ${}_h B$ is the width of horizontal haunch, ${}_b h$ is the distance between center axis of beam flange, $M_0 = {}_q t_f^2 \cdot {}_c \sigma_y / 4$ is the out-of-plane full plastic moment of column flange per unit length, m is the distance between horizontal haunch side and center of column flange, ${}_b t_f$ is the thickness of beam flange, ${}_q t_f$ is the thickness of column wall, ${}_r t$ is the total weld leg length of beam flange, ${}_{bf} \sigma_y$ is the yield point of beam flange material and ${}_c \sigma_y$ is the yield point of column material.

The estimation procedure of the local ultimate strength of beam-to-column connection without any diaphragms (${}_j M_u$) is proposed to replace the yield point of column material (${}_c \sigma_y$) to the tensile strength (${}_c \sigma_t$).

The analytical local full plastic and ultimate strengths of beam-to-column connection calculated by Equation (1) are shown in Table 3(a). These strengths are evaluated as the shearing forces acting on the beam end.

The ratio of the experimental local full plastic strength to the analytical one is 0.96 for NU and 0.94 for ICH1.4 respectively, and that of the local ultimate strength is 1.02 for NU, showing a good correspondence.

The location of yield line AA is within the increased area of column thickness showing a good agreement with the experimental results as shown in Figure 6(a) (Murakami *et al.*, 1994). The analytical yield area of beam flange agrees relatively well with the experimental results as shown in Figure 6(b). The local yielding of beam-to-column connection can not be observed for ICH2.0 because ${}_j Q_p$ is much larger than ${}_{bj} Q_p$.

Full plastic strength of beam end connection

The estimation procedure of the full plastic strength of beam end connection reinforced by inner diaphragms has been proposed by the authors (Morita *et al.*, 1989B). The yield mechanism shown in Figure 8 is assumed. The following assumptions are considered:

(1) The beam flanges are assumed to be axial yielding.
(2) The beam web of flange side is assumed to be axial yielding as shown in Figure 8 in conjunction with the moment yield line assumed in the column flange.

The full plastic strength of beam end connections (${}_{bj} M_p$) is given by:

$$ {}_{bj} M_p = {}_b h \{ {}_h B \cdot {}_b t_f \cdot {}_{bf} \sigma_y + {}_b t_w (x - S_r)({}_w h - x - S_r) {}_{bw} \sigma_y \} \quad (3) $$

where x satisfies the following equation:

$$ x = (-c_2 - \sqrt{c_2^2 - 4 c_1 c_3}) / (2 c_1) \quad (4) $$

The coefficients c_1, c_2 and c_3 are given by the following equations, respectively:

$$ c_1 = -\{16 M_0 + {}_c b \cdot {}_b t_w \cdot {}_{bw} \sigma_y\} {}_d h \quad (5a) $$

$$ c_2 = 2\{4 {}_d h (4 {}_s t + {}_d h) M_0 - 2 {}_c b^2 M_0 + {}_d h \cdot {}_c b \cdot {}_b t_w \cdot {}_{bw} \sigma_y \cdot S_r \} \quad (5b) $$

$$ c_3 = -8 {}_d h \cdot {}_s t (2 {}_s t + {}_d h) M_0 + 4 {}_c b^2 ({}_s t + {}_d h) M_0 - {}_d h \cdot {}_c b \cdot {}_b t_w \cdot {}_{bw} \sigma_y \cdot S_r^2 \quad (5c) $$

where ${}_d h$ is the distance between center axis of diaphragms, S_r (= 0) is the radius of weld access hole, ${}_b t_w$ is the thickness of beam web, ${}_d t$ is the thickness of inner diaphragm, ${}_s t = ({}_d t - {}_b t_f) / 2$ and ${}_{bw} \sigma_y$ is the yield point of beam web material.

The estimation procedure of the local ultimate strength of beam end connection (${}_{bj} M_u$) is proposed to replace the yield point of the beam material (${}_{bf} \sigma_y$) to the tensile strength (${}_{bf} \sigma_t$).

The analytical strengths of beam end connection calculated by Equation (3) are shown in Table 3(b). These strengths are evaluated as the shearing forces acting on the beam end.

The ratio of the experimental full plastic and ultimate strengths to the analytical ones is 1.03 and 1.00 for DU respectively, showing a good correspondence. The analytical plastic region of beam web (x) agrees relatively well with the experiment result for DU as shown in Figure 6(c).

But the analytical strengths overestimate the experimental ones for ICH1.4 and ICH2.0. For both ICH1.4 and ICH2.0, the shearing forces at the beam end equivalent to the full plastic moment ${}_b M_p$ and ultimate moment ${}_b M_u$ at the starting point of horizontal haunch are ${}_b Q_p = 252.0$kN and ${}_b Q_u = 334.8$kN, respectively.

These values agree well with the experimental strengths of beam end connection because of ${}_b Q_p < {}_{bj} Q_p$ and ${}_b Q_u < {}_{bj} Q_u$.

The ultimate strength ${}_b M_u$ is estimated by assuming that the stress of beam flange is reached to the tensile strength of material and the beam web is remained in the full plastic state:

$$ {}_b M_u = {}_b B \cdot {}_b t_f \cdot {}_b h \cdot {}_{bf} \sigma_t + {}_b t_w \cdot {}_w h^2 \, {}_{bw} \sigma_y / 4 \quad (6) $$

where ${}_b B$ is the beam width, ${}_w h$ is the height of beam web.

3.2 *Elasto-plastic analysis of subassemblage specimen using finite element method*

The monotonic elasto-plastic behavior of beam-and-column subassemblage specimens is calculated taking account of both material and geometrical nonlinear by the three-dimensional elasto-plastic finite element package ANSYS 5.1.

The symmetric model is used to the finite element analysis because of the loading condition and symmetry of the subassemblage specimens. The finite meshing of ICH1.4 is shown in Figure 9. Eight-node elasto-plastic solid elements are used for each element. The total weld leg

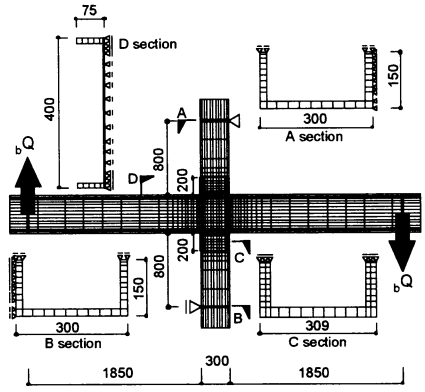

(a) Finite element meshing and boundary conditions

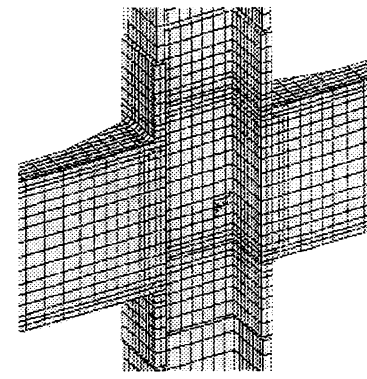

(b) Finite element meshing at beam-to-column area

Figure 9. Finite element model (ICH1.4)

length is taken into account in the analysis. The yield criterion by Von Mises and the Prandtl-Reuss flow equation are used for steel materials. The stress and strain curve obtained from the material test is modeled by multi-linear.

The hysteretic curves of beam-and-column subassemblage specimen calculated by the finite element analysis are shown in Figure 5.

For the ${}_bQ - {}_fR_a$ relationship of the specimen DU, the analytical result agrees well with the experimental result until the drift angle of 0.03rad. as shown in Figure 5(a). And as for the initial stiffness and full plastic strength of ${}_bQ - {}_bR_a$, ${}_bQ - {}_cR_a$ and ${}_bQ - {}_p\gamma_a$ relationships, the analytical results agree relatively well with those of experimental results as shown in Figures 5(c), 5(d) and 5(e).

For the specimen NU, as for the ${}_bQ - {}_fR_a$, ${}_bQ - {}_bR_a$ and ${}_bQ - {}_cR_a$ relationships, the analytical results agree well with the experimental results as shown in Figures 5(a), 5(c) and 5(d). But as for the ${}_bQ - {}_j\theta_a$ relationship, the analytical initial stiffness and strength capacity after yielding are slightly smaller than the experimental results as shown in Figure 5(b).

For the ${}_bQ - {}_fR_a$ and ${}_bQ - {}_bR_a$ relationships of both specimens ICH1.4 and ICH2.0, the analytical full plastic strength is slightly smaller than the experimental results. And as for the ${}_bQ - {}_j\theta_a$ relationship, the analytical result is slightly smaller than the experimental result for ICH1.4, while, it agrees well with the experimental result for ICH2.0. As for the ${}_bQ - {}_cR_a$ and ${}_bQ - {}_p\gamma_a$ relationships, the analytical results agree relatively well with the experimental results as shown in Figure 5(d) and 5(e).

The hysteretic curves of column and beam of each specimen calculated by the column deflection curve (CDC) numerical method are shown in Figure 5. The initial stiffness of ${}_bQ - {}_bR_a$ relationship calculated by the CDC analysis agrees well with those of experimental result for each specimen, however, the analytical full plastic strength is slightly underestimated comparing with the experimental result. The initial stiffness and full plastic strength of ${}_bQ - {}_cR_a$ relationship calculated the CDC analysis tend to overestimate the experimental results for each specimen except for ICH2.0.

Table 4. Dimensions and full plastic strength ratio of analytical model

Model	Column size at connection	Beam size at connection side	${}_jM_p / {}_{bj}M_p$	${}_jM_p(1-{}_hl/{}_bl) / {}_bM_p$
DU	300×300×20	400×150×9×14	—	—
IC1.25	305×305×25		0.99	—
IC1.5	310×310×30	400×150×9×14	1.34	—
IC1.75	315×315×35		1.75	—
ICH1.0	300×300×20		0.66	0.85
ICH1.25	305×305×25	400×250×9×14	0.89	1.15
ICH1.4	308×308×28		1.03	1.33

4 STRUCTURAL PERFORMANCE OF BEAM-TO-COLUMN CONNECTION

Two types of beam-to-column connections are considered in the case studies: (1) the beam-to-column connection

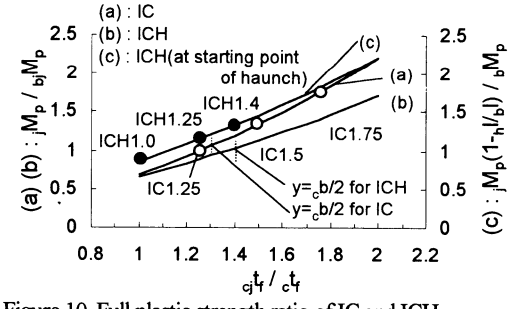

Figure 10. Full plastic strength ratio of IC and ICH

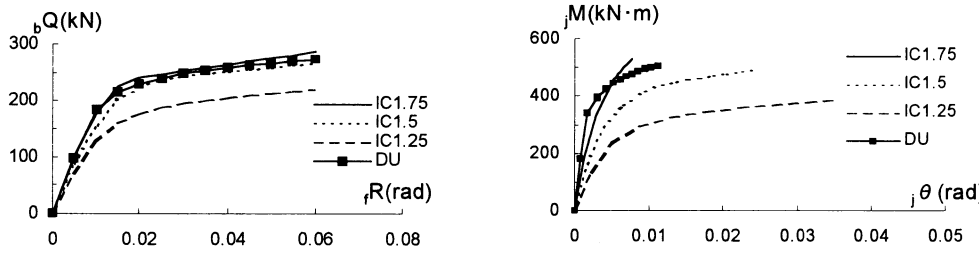

(a) ${}_bQ-{}_fR$ relationship (b) ${}_jM-{}_j\theta$ relationship

Figure 11. Hysteretic curves of subassemblage models without haunch (IC)

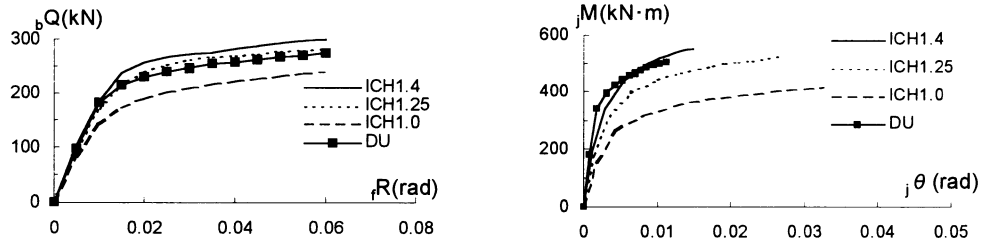

(a) ${}_bQ-{}_fR$ relationship (b) ${}_jM-{}_j\theta$ relationship

Figure 12. Hysteretic curves of subassemblage models with haunch (ICH)

reinforced by increasing the column thickness. (2) the beam-to-column connection reinforced by increasing the column thickness with horizontal haunch of beam. The dimensions of column and beam for the prototype model in the case studies is the same with the specimen DU in the experimental studies except for neglecting the reinforcement of welding seam. The analytical parameter is the ratio of the local full plastic strength of beam-to-column connection to the full plastic strength of beam end connection (${}_jM_p/{}_{bj}M_p$). The details of beam-to-column connections in the case studies are shown in Table 4.

Beam-to-column connection reinforced by increasing column thickness

The ${}_jM_p/{}_{bj}M_p-{}_gt_f/{}_ct_f$ relationship for the beam-to-column connection reinforced by increasing the column thickness calculated by the yield line theory is shown in Figure 10. The full plastic strength ratio ${}_jM_p/{}_{bj}M_p$ of beam-to-column connection is rapidly increased after ${}_gt_f/{}_ct_f = 1.3$, where ${}_gt_f/{}_ct_f$ is the increasing ratio of column thickness.

The finite element analysis is carried out for the models IC1.25, IC1.5 and IC1.75 whose ${}_gt_f/{}_ct_f$ is 1.25, 1.5 and 1.75, respectively.

The ${}_bQ-{}_fR$ relationship calculated by the finite element analysis is shown in Figure 11(a). The solid line with square marks in Figure 11(a) is the analytical result of the prototype model DU. The full plastic strength and local full plastic strength of each model are evaluated by the general yield point method in the case studies.

The full plastic strength ratio ${}_jM_p/{}_{bj}M_p$ of IC1.25 becomes 0.99. The initial stiffness and full plastic strength of beam-and-column subassemblage of IC1.25 are reduced to 80% and 85% values of DU.

The full plastic strength ratio of IC1.5 becomes 1.34. The initial stiffness of IC1.5 is slightly reduced to 89% value of DU, however, the full plastic strength is almost the same with that of DU.

The full plastic strength ratio of IC1.75 becomes 1.75. The initial stiffness and full plastic strength of IC1.75 are 1.01 and 1.03 times those of DU.

The bending moment at the beam-to-column connection (${}_jM$) – local rotation angle of beam-to-column connection (${}_j\theta$) relationship calculated by the finite element analysis is shown in Figure 11(b). The solid line with square marks in the figure is the analytical result of DU.

The initial rotational stiffness and local full plastic strength of beam-to-column connection of IC1.25 are reduced to 26% and 79% values of DU, respectively. And those values of IC1.5 are also reduced to 41% and 91% values of DU, respectively. The initial rotational stiffness of the beam-to-column connection of IC1.75 is deduced to 61% of DU, however, the local full plastic strength is more than that of the prototype model DU.

Beam-to-column connection reinforced by increasing column thickness with horizontal haunch of beam

The ${}_jM_p/{}_{bj}M_p-{}_gt_f/{}_ct_f$ in addition to ${}_jM_p({}_bl-{}_hl)/({}_bM_p\cdot{}_bl)-$

${}_gt_f / {}_ct_f$ relationships calculated by the yield line theory are shown in Figure 10, respectively, where ${}_bl$ is the length of beam, ${}_hl$ is the length of horizontal haunch and ${}_bM_p$ is the full plastic strength of beam at the starting point of horizontal haunch. The degree of increment of ${}_jM_p/{}_{bj}M_p$ is smaller than that of the model without horizontal haunch, however, the degree of increment of the ratios becomes larger after ${}_gt_f / {}_ct_f = 1.4$.

The finite element analysis is carried out for the models ICH1.0, ICH1.25 and ICH1.4 whose ${}_gt_f/{}_ct_f$ is 1.0, 1.25 and 1.4, respectively.

The ${}_bQ - {}_fR$ relationship calculated by the finite element analysis is shown in Figure 12(a). The solid line with square marks in the figure denotes that of the prototype model DU.

The full plastic strength ratios ${}_jM_p / {}_{bj}M_p$ and ${}_jM_p\,({}_bl - {}_hl) / ({}_bM_p \cdot {}_bl)$ of ICH1.0 become 0.66 and 0.85 respectively. The initial stiffness and full plastic strength are reduced to 85% and 82% values of the prototype model DU, respectively.

The full plastic strength ratios ${}_jM_p / {}_{bj}M_p$ and ${}_jM_p\,({}_bl - {}_hl) / ({}_bM_p \cdot {}_bl)$ of ICH1.25 becomes 0.89 and 1.15, respectively. The initial stiffness and the full plastic strength are almost the same with those of DU.

The full plastic strength ratios ${}_jM_p / {}_{bj}M_p$ and ${}_jM_p\,({}_bl - {}_hl) / ({}_bM_p \cdot {}_bl)$ of ICH1.4 become 1.03 and 1.33, respectively. The initial stiffness of ICH1.4 is 1.07 times that of DU and the full plastic strength is 1.1 times that of DU. The full plastic strengths of each model calculated by the finite element analysis agree well with the full plastic strength calculated at the starting point of horizontal haunch.

The ${}_jM - {}_j\theta$ relationship calculated by the finite element method is shown with the broken lines in Figure 12(b). The solid line in the figure is the analytical result of DU. For ICH1.0, the initial rotational stiffness and local full plastic strength are reduced to 39% and 85% values of DU, respectively. As for ICH1.25, those values are also reduced to 59% and 96% values of DU, respectively. In the case of ICH1.4, the initial rotational stiffness is reduced to 73% value of DU, however, the local full plastic strength becomes equivalent to that of DU.

As shown in the case studies, The application of the horizontal haunch of beam at the connection side is useful to reduce the value ${}_gt_f / {}_ct_f$ to get the structural performance equivalent to that of the prototype model with inner diaphragm.

5 CONCLUSIONS

The results of experimental and analytical studies on the structural behavior of beam-to-column connection reinforced with increasing the column thickness can be summarized as follows:

1. The initial stiffness, full plastic strength and plastic deformation capacity of subassemblage specimens ICH1.4 and ICH2.0 are larger than those of DU with inner diaphragms.
2. The local full plastic strength of NU and ICH1.4 without any diaphragms can be estimated well by the yield line theory. Also, the full plastic strength of beam end connection of DU can be estimated well by the yield line theory.
3. The elasto-plastic behavior of beam-and-column subassemblage specimens can be predicted by the finite element analysis.
4. The column thickness at the beam-to-column connection area (${}_gt_f$) required to get the structural performance equivalent to that of the prototype specimen DU with inner diaphragms, whose column thickness is ${}_ct_f$, is as follows: (i) ${}_gt_f / {}_ct_f$ should not less than 1.5 for the beam-to-column connection reinforced by increasing the column thickness without any diaphragms, and (ii) ${}_gt_f / {}_ct_f$ should not less than 1.25 for the beam-to-column connection reinforced by increasing the column thickness in addition to the horizontal haunch without any diaphragms.

ACKNOWLEDGEMENTS

The authors express their thanks to Messrs. Akira Fukuda, Kenji Furumi for Daiwa House Industry Co., LTD., Yoichi Matsubara for Dai-ich High Frequency Co., LTD., Keiji Yokoi and Hideaki Takamura for Chiba Univ. for their contributions.

REFERENCES

Kato, B. 1982. Beam-to-Column Connection Research in JAPAN, *J. of the Structural Division, ASCE*, Vol.108, No.ST2, pp.343-360.

Morita, K., Yamamoto, N. & Ebato, K. 1989A. Analysis on the Strength of Unstiffened Beam Flange to RHS Column Connections Based on the Combined Yield Line Model, *Tubular Structures, The Third International Symposium*, pp.164-171.

Morita, K., Ebato, K., Funabashi, A., Kominami, T. & Satomi, T. 1989B. Study on Structural Behaviors of Beam-to-Column Connections –In case Corner Weld of Box Column is Partial Penetration Weld-, *J. Struct. Constr. Eng., AIJ*, No.463, pp.115-124. (in Japanese)

Murakami, Y., Yamamoto, N. & Morita, K. 1994. A Study on the Design of Semi-Rigid Frames with Beam-to-Column Connections Reinforced by Increasing Thickness of Columns, *Steel Construction Eng.*, Vol.1, No.4, pp.53-64. (in Japanese)

Tubular Structures VIII, Choo & Van der Vegte (eds) © 1998 Balkema, Rotterdam, ISBN 90 5809 001 9

Study on beam to box column connections with split diaphragms

K. Fukuda & F.Otake
Structural Engineering Department, Sumitomo Metal Industries Limited, Japan
M.Tabuchi
Faculty of Engineering, Kobe University, Japan

ABSTRACT:The elasto-plastic behavior of H shaped beam to box column connections with split diaphragms is predicted. It is supposed that the load-deformation curve of the connection could be obtained from the behavior of the diaphragms part and the column part. The load-deformation curve of each part is simplified as tri-liner curve.The comparison between experimental results and analytical results shows that the supposition seems to be valid , and the load-deformation curves of the connections can successfully predict both in weak direction and strong direction.

1 INTRODUCTION

It is suitable to use split diaphragms to prevent local deformation at the beam to column connections made by two channels. In this connections, the split diaphragms can not be welded eachother. Therefore,strength and stiffness of the connections are different in the loading direction (Fig.1).
In this paper,the prediction of elasto-plastic behavior of the connection both in the weak direction and the strong direction is tried. It is supposed that the load-deformation curve of the connection could be obtained from the behavior of the diaphragms part and the column part. As shown in Figure 2,the diaphragm part is composed of the diaphragm and a piece of the column with the effective width B_l which corresponds to the weld metal of beam flange to column flange. The effective width B_l is supposed to be equal to $2 \cdot t_{bf}$. Here, t_{bf} is the thickness of the beam flange. On the other hand,the column part is the box column which is removed the diaphragms part.

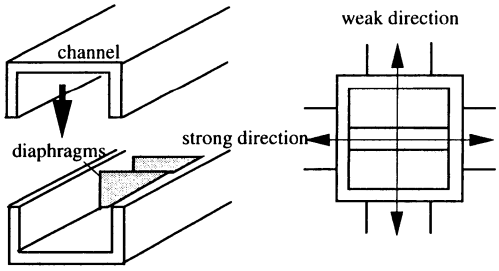

Figure 1. Beam to column connection with split diaphragms

2 BEHAVIOR OF THE DIAPHRAGM PART IN WEAK DIRECTION

2.1 Analytical model

As shown in Figure 3, the diaphragm part in weak direction is supposed as a simply supported T-section beam model subjected to two shear forces derived from the axial force of the beam flange.The section is composed of the diaphragm and a piece of the column with the effective width B_l. The distance between the two shear forces is equal to that of beam flange B_b. Its load-deformation curve will be simplified as a tri-liner curve.

2.2 Yield strength

The yield strength of the diaphragm part is assumed as the load when the plastic hinge at the loading points occurs. Here, full plastic moment is calculated considering the relationships between bending moment and shear force denoted as follows (Fig.3).

$$q^2+m^2=1.0 \quad (1)$$
$$(q=Q \diagup Q_p,\ m=M \diagup M_p)$$

where Q= shear force;M=bending moment;Q_p=yield shear force$(=H_d \cdot t_d \cdot \tau_y)$; M_p=full plastic moment $(=Z_p \cdot \sigma_y)$;H_d=diaphragms depth; t_d;diaphragms thickness ;Z_p=plastic modulus; σ_y; yield stress and $\tau_y = \sigma_y \diagup \sqrt{3}$
On the other hand, the relationships between shear

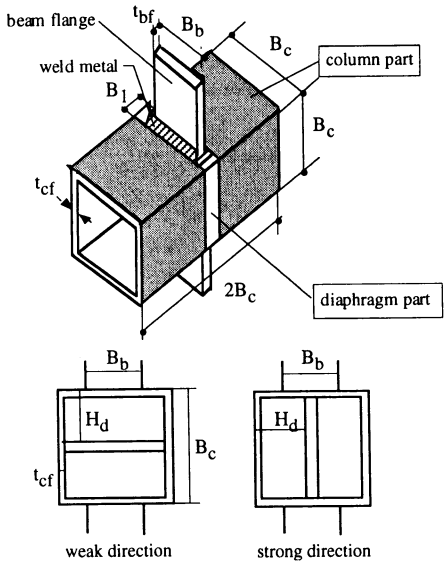

Figure 2. Definition of the diaphragm part and the column part

force and bending moment at the plastic hinge turn to be as follows.

$$q=S_{1y}\cdot m \tag{2}$$

Here, S_{1y} , the slope coefficient of the q-m relationship , is expressed as follows.

$$S_{1y}=\frac{2M_p}{(B_c-B_b)Q_p} \tag{3}$$

where B_c=column width B_b=beam flange width

Yield strength of the diaphragm part N_{dy} is obtained on referring to equation (1) and (2).

$$N_{dy}=\frac{2Q_p}{\sqrt{1+1/S_{1y}^2}} \tag{4}$$

2.3 Ultimate strength

Ultimate strength of the diaphragm part N_{du} can be expressed replacing Q_p by Q_u and M_p by M_u respectively.

$$N_{du}=\frac{2Q_u}{\sqrt{1+1/S_{1u}^2}} \tag{5}$$

$$S_{1u}=\frac{2M_u}{(B_c-B_b)Q_u} \tag{6}$$

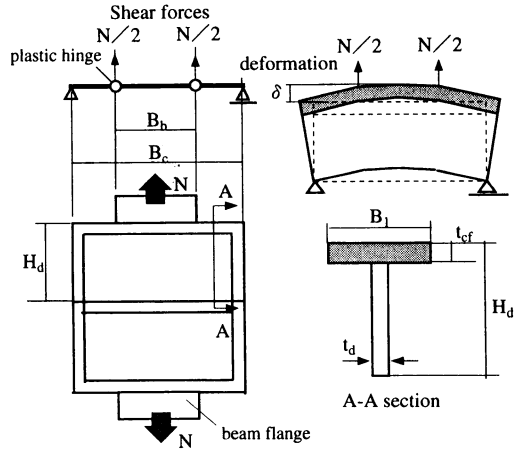

Figure 3. Beam model for the diaphragm part in weak direction

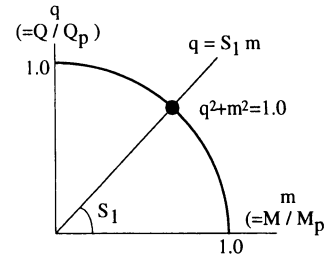

Figure 4. Relationships between bending moment and shear force of T-section

where Q_u=ultimate shear force(=$H_d \cdot t_d \cdot \tau_u$) ; M_u= ultimate moment (=$Z_p \cdot \sigma_u$) σ_u; tensile strength and $\tau_u=\sigma_u/\sqrt{3}$

2.4 Initial stiffness

Initial stiffness of the diaphragm part K_{dl} will be expressed as follows supposed that the deformation of diaphragm part can be represented by that of beam center.

$$K_{dl}=\frac{N}{\delta_b+\delta_s} \tag{7}$$

where δ_b=bending deformation at beam center, and δ_s=shear deformation at beam center

δ_b and δ_s are shown as follows.

$$\delta_b=\frac{B_c^3\ \alpha\ (3-\alpha^2)}{48EI} \tag{8}$$

$$\delta_s = \frac{\alpha B_c}{2 H_d t_d G} \quad (9)$$

where I=geometrical moment of inertia;E=Young's modulus;G=modulus of rigidity; $\alpha = (B_c - B_b) / 2B_c$

2.5 Second stiffness

Second stiffness K_{d2} of diaphragms part K_{d2} is supposed to be 2% of the initial stiffness K_{d1}.

$$K_{d2} = 0.02 K_{d1} \quad (10)$$

3 BEHAVIOR OF THE DIAPHRAGM PART IN STRONG DIRECTION

3.1 Analytical model

As shown in Figure 5, the diaphragm part in strong direction is supposed as a simply supported T-section beam model subjected to axial force derived from the beam flange and additional bending moment caused by the difference between center of gravity of axial force and neutral axis of diaphragm part. The section is composed of the diaphragm and a piece of the column with the effective width B_1.Its load-deformation curve will be simplified as a tri-liner curve.

The additional bending moment M_A will be expressed as follows supposed that the axial force from beam flange is the uniform load.

$$M_A = N(e1/2 - D/4) \quad (11)$$

where M_A=additional bending moment;N=axial force from beam flange;e_1=location of neutral axis of diaphragm part;D=width of the uniform load

The axial force from the beam flange is uniformly distributed on the diaphragm part with width D expressed as.

$$D = (B_b - B_c + 2H_d + t_{cf}) / 2 \quad (12)$$

where t_{cf}=column thickness;B_b=beam flange width;B_c=column width;H_d=diaphragm depth

3.2 Yield strength

The yield strength of the diaphragm part is assumed as the load when the plastic hinge at the loading points occurs. Here, full plastic moment is calculated considering the relationships between bending moment and axial force denoted as follows (Fig.6).

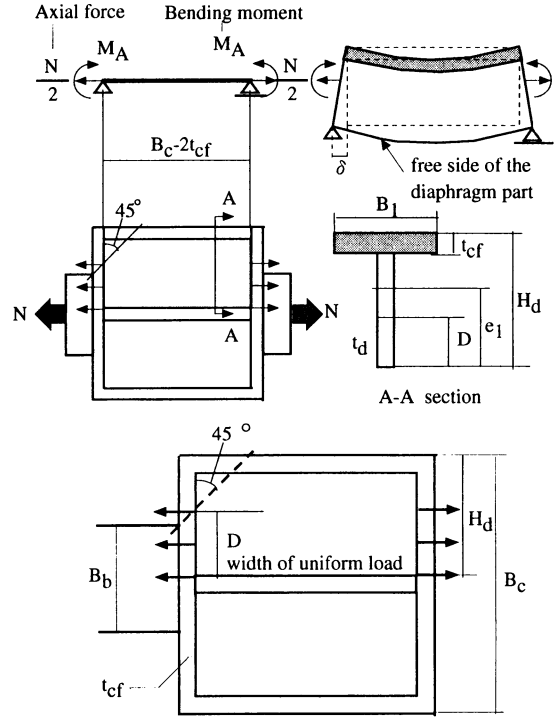

Figure 5. Beam model for the diaphragm part in strong direction

$$\begin{cases} n = 1 + \beta m & (1 + \beta \leqq n \leqq 1.0) \\ m = 1.0 & (0.0 \leqq n \leqq 1 + \beta) \end{cases} \quad (13)$$

$$(n = N / 2N_y,\ m = M_A / M_p)$$

where N_y=yield axial force(=$A \cdot \sigma_y$) ; M_p=full plastic moment (=$Z_p \cdot \sigma_y$) ;A=cross sectional area On the other hand,the relationships between axial force and bending moment at the plastic hinge turn to be as follows.

$$n = S_{2y} \cdot m \quad (14)$$

Here,S_{1y} , the slope coefficient of the n-m relationship , is expressed as follows.

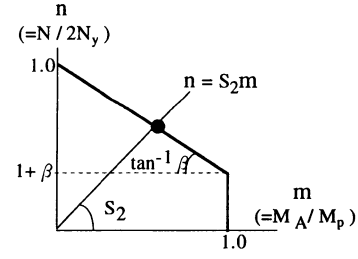

Figure 6. Relationships between bending moment and axial force of T-section

$$S_{2y}=\frac{M_p}{N_y(e_1-D/2)} \tag{15}$$

Yield strength of diaphragms part N_{dy} is obtained on referring to equation (13) and (14).

$$\begin{cases} N_{dy}=2\dfrac{S_{2y}\cdot N_y}{S_{2y}-\beta} & (1+\beta \leqq n \leqq 1.0) \\ N_{dy}=2S_{2y}\cdot N_y & (0.0 \leqq n \leqq 1+\beta) \end{cases} \tag{16}$$

The value β which is gradient of n-m relationships is obtained by regression analysis.

$$\beta=-0.48-0.05\frac{B_1}{t_d}-0.88\frac{t_{cf}}{H_d} \tag{17}$$

$(B_1/t_d=1.0\sim5.0,\ t_{cf}/H_d=0.02\sim0.20)$

3.3 Ultimate strength

Ultimate strength of the diaphragm part N_{du} can be expressed replacing N_y by N_u and M_p by M_u respectively.

$$\begin{cases} N_{du}=2\dfrac{S_{2u}\cdot N_u}{S_{2u}-\beta} & (1+\beta \leqq n \leqq 1.0) \\ N_{du}=2S_{2u}\cdot N_u & (0.0 \leqq n \leqq 1+\beta) \end{cases} \tag{18}$$

$$S_{2u}=\frac{M_u}{N_u(e_1-D/2)} \tag{19}$$

where N_u=tensile axial force$(=A\cdot\sigma_u)$; M_u= ultimate moment $(=Z_p\cdot\sigma_u)$ σ_u; tensile strength

3.4 Initial stiffness

Initial stiffness of the diaphragm part K_{d1} will be expressed as follows supposed that the deformation of diaphragm part can be represented by the axial deformation at the free side of diaphragms (Fig.5) .

$$K_{d1}=\frac{N}{2(\delta_b+\delta_n)} \tag{20}$$

where δ_b=axial deformation caused by additional bending moment M_A and δ_n=axial deformation caused by axial force N.

δ_b and δ_n are shown as follows.

$$\delta_b=\frac{B_c\cdot M_A}{Z\cdot E} \tag{21}$$

$$\delta_n=\frac{B_c\cdot N}{2A\cdot E} \tag{22}$$

where Z= section modulus

3.5 Second stiffness

Second stiffness of diaphragms part K_{d2} is supposed to be 2% of the initial stiffness K_{d1}.

$$K_{d2}=0.02K_{d1} \tag{23}$$

4 BEHAVIOR OF THE COLUMN PART

4.1 Analytical model

The load-deformation curve of the column part is directly obtained from FEA because of the difficulty of evaluating its behavior with beam theory. As shown in Figure 7, the FEA model is three dimensional solid model.The FEA model is subjected to uniform deformation with width B_b which corresponds to the beam flange width.
The analytical values are ratio of beam flange width-to -column flange width B_b/B_c(from 0.4 to 0.6) and width-to-thickness ratio of column B_c/t_{cf} (from 10 to 40). Table1 shows the analytical values and results of FEA.Its load-deformation curve will

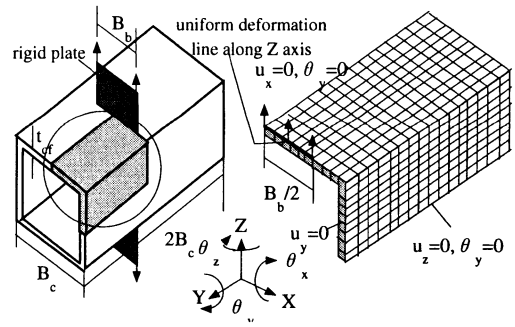

Figure 7. Analytical model for loading condition and boundery condition of column part

be simplified as a tri-liner curve.
Here,the yield strength of FEA is supposed to be the load at the crossing point between initial stiffness line and tangent line,which passes the crossing point between 1/3 of initial stiffness line and load-deformation curve(Fig.8). And the initial stiffness of FEA,$_cK_{cl}$,is secant modulus of elasticity when the load reaches 1/2 of the limit analysis load N_L.

4.2 *Yield strength*

As shown in Table 1, the average value of yield strength of FEA shows 0.76 times as much as that of the limit analysis load N_L which corresponds to the mechanism shown in Fig.9. Therefore, the yield strength of column part N_{cy} will be expressed as follows.

$$N_{cy}=0.76\,N_L \tag{24}$$

Here, the limit analysis load N_L is shown as follows.

$$N_L = 16.0\,M_{pc}\sqrt{\frac{B_c - t_{cf}}{(B_c - t_{cf} - B_b)}} \tag{25}$$

where $M_{pc}=\sigma_y^{\,2}\,t_{cf}/2$; σ_y=yield stress of column;t_{cf}=column thickness;B_b=beam flange width

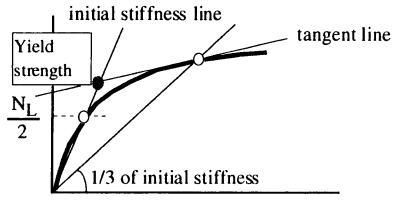

Figure 8. Definition of the yield strength of column part by FEA

4.3 *Ultimate strength*

The ultimate strength of the column part N_{cu} is supposed to be equal to the limit analysis load N_L.

$$N_{cu}=N_L \tag{26}$$

4.4 *Initial stiffness*

The initial stiffness of the column part,K_{cl}, can be predicted by that of a unit rahmen frame,K_r. As shown in Figure 10,the unit rahmen frame is composed of unit-width and t_{cf}-hight square section,having rigid parts with width B_b.

$$K_{cl}=W\cdot K_r \tag{27}$$

where K_{cl}=initial stiffness of the column part;K_r=initial stiffness of the unit rahmen frame

Here, W is the effective width of unit rahmen frame and it will be expressed as the following equation which is obtained by the regression analysis.

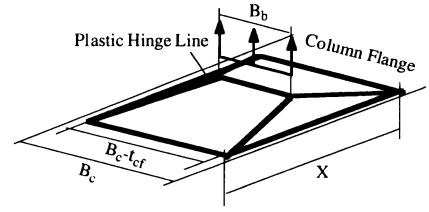

Figure 9. Supposed mechanism at column flange for limit analsys

Table 1. Analytical the values and results by FEA

FEA model			Results of FEA			Limit analysi	Comparison between FEA and limit analysis	Proposal			Comparison between FEA and proposal		
Bc	tcf	Bb	cNcy	cKc1	cKc2	NL	cNcy	Ncy	Kc1	Kc2	cNcy	cKc1	cKc2
cm	cm	cm	tf	tf/cm	tf/cm	tf	NL	tf	tf/cm	tf/cm	Ncy	Kc1	Kc2
35.0	3.50	14.0	157.3	830.1	55.7	221.4	0.71	167.8	994.8	74.4	0.94	0.83	0.75
35.0	3.50	21.0	195.7	2762.2	204.7	271.2	0.72	205.5	1857.3	111.8	0.95	1.49	1.83
35.0	3.50	28.0	292.9	2884.6	189.7	383.5	0.76	290.7	2469.5	112.6	1.01	1.17	1.68
35.0	2.50	14.0	83.2	324.3	25.2	113.0	0.74	85.6	345.1	32.7	0.97	0.94	0.77
35.0	2.50	21.0	104.8	569.2	46.6	138.3	0.76	104.9	696.9	55.9	1.00	0.82	0.83
35.0	2.50	28.0	145.3	1106.3	82.4	195.7	0.74	148.3	1345.9	88.3	0.98	0.82	0.93
35.0	1.75	14.0	43.3	112.9	11.8	55.4	0.78	42.0	111.5	13.9	1.03	1.01	0.85
35.0	1.75	21.0	54.9	206.0	19.6	67.8	0.81	51.4	231.3	25.5	1.07	0.89	0.77
35.0	1.75	28.0	73.4	496.4	49.3	95.9	0.77	72.7	605.9	57.9	1.01	0.82	0.85
35.0	1.17	14.0	18.4	35.3	7.9	24.6	0.75	18.6	31.1	5.4	0.99	1.13	1.46
35.0	1.17	21.0	23.5	66.6	10.9	30.1	0.78	22.8	64.5	10.3	1.03	1.03	1.06
35.0	1.17	28.0	33.2	184.4	21.8	42.6	0.78	32.3	201.8	29.4	1.03	0.91	0.74

cKc1:initial stiffness cKc2:second stiffness cNcy:yiled strength (FEA)
Kc1:initial stiffness Kc2:second stiffness Ncy:yiled strength (Proposal)

$$W=23.2 - 24.4 \left(\frac{B_b}{B_c}\right) \quad (28)$$

The initial stiffness of the unit rahmen frame K_r will be expressed as follows.

$$K_r = \frac{1}{1/K_{rb} + 1/K_{rs} + 1/K_{rn}} \quad (29)$$

$$K_{rb} = \frac{192\, E\, I_r\, (2B_c - 2t_{cf} - B_b)}{(B_c - t_{cf} - B_b)^3\, (5B_c - 5t_{cf} - B_b)} \quad (30)$$

$$K_{rs} = \frac{4\, G\, t_{cf}}{(B_c - t_{cf} - B_b)} \quad (31)$$

$$K_{rn} = \frac{4\, E\, t_{cf}}{(B_c - t_{cf})} \quad (32)$$

where

K_{rb}=stiffness caused by bending moment;

K_{rs}=stiffness caused by shear force;

K_{rn}=stiffness caused by axial force;

$I_r = t_{cf}^3/12$

4.5 Second stiffness

Second stiffness of column part K_{c2} will be expressed as the following equation which is obtained by regression analysis.

$$K_{c2} = \left\{0.054 + 0.005 \frac{B_c}{t_{cf}} - 0.073 \frac{B_b}{B_c}\right\} K_{c1} \quad (33)$$

Fig.11 shows the comparison between the load-deformation curve of FEA and that of proposal. The proposed curves are almost the same as that of FEA .

5 PREDICTION FOR THE ELASTO-PLASTIC BEHAVIOR OF THE CONNECTION

The authors supposed that the load-deformation curve of the connection could be obtained from the behavior of the diaphragms part and the column part . As confirmation of this supposition ,tension beam flange test results (K.Fukuda,1994,1996) have been carried out.

The test parameters are ratio of beam flange width-to -column flange width B_b / B_c(from 0.4 to 0.6) ,width-to-thickness ratio of column B_c / t_{cf} (from 14 to 39), diaphragm thickness and the loading direction.

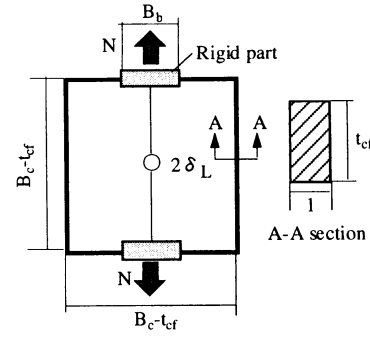

Figure 10. Unit rahmen frame

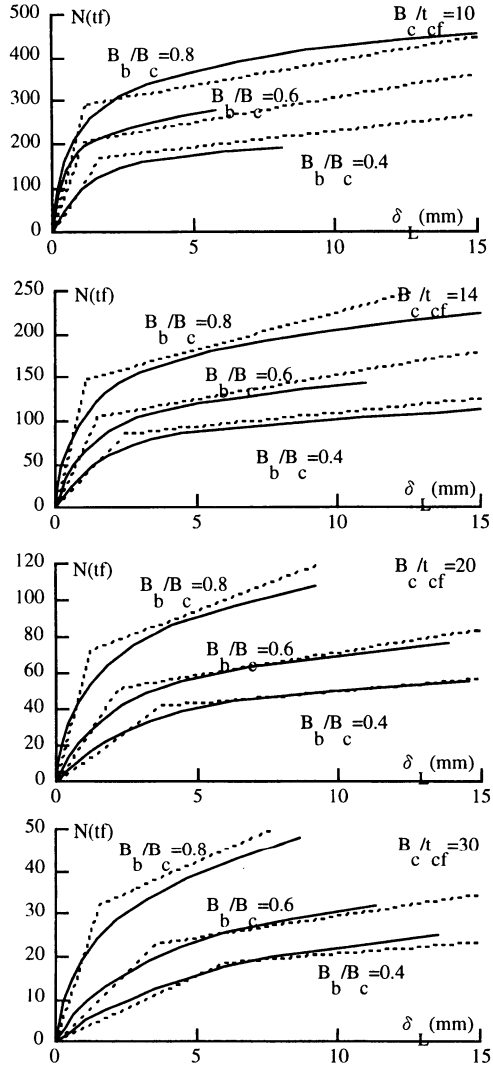

Figure 11. Comparison between FEA and proposal

Table 2 shows the member sections and mechanical properties of material. Here,the yield strength of the analysis is supposed to be the load at the second point on the prediction curve.On the other hand, that of the test result is supposed to be the load at crossing point between initial stiffness line and tangent line which passes the point on the load-deformation curve when the deformation reaches 1/2 of δ_m defined as the deformation at maximum load (see Fig.12).

Fig.13 and table 3 show the comparison between the test results and analysis.All predicted curves are almost the same as that of the test results. And the yield strength and the ultimate strength of the test results are close to that of the analysis.

As a result ,the supposition seems to be vaild, and the load-deformation curve of the connection can successfully be predicted both in weak direction and strong direction.

Table 4 shows the ratio of the diaphragm part strength to the total strength obtained by the analysis. These ratios show about 90% of all speciments in an elastic state. But , these tend to decrease according to the yield of the connection and the finally become 50~80% at the ulitimate strength state.

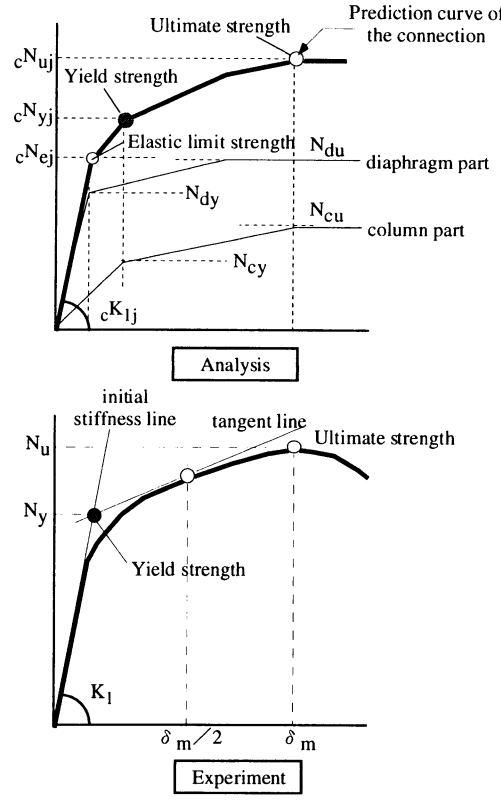

Figure 12. Definition of strength and stiffness

6 CONCLUSION

The elasto-plastic behavior of H shaped beam-to-box column connection with split diaphragms is discussed here in.

The authors supposed that load-deformation curve of the connection could be obtained from the behavior of the diaphragms part and that of the column part .The diaphragm part is supposed as a simply supported T-section beam model.On the other hand, the behavior of the column part is

Table 2. Member sections and mechanical properties of material

specimens	member section				mechanical properties of material						
					column		beam		diaphragms		
	Bcxtcf	Bbxtbf	td	Hd	YS	TS	YS	TS	YS	TS	
	(mm)	(mm)	(mm)	(mm)	(tf/cm2)						
NO1W	350x16	210x32	12	150	3.58	5.58	3.42	5.41	3.77	5.60	weak direction
NO2W			19						3.65	5.49	
NO3W			22						3.24	5.14	
NO4W		140x32	19		3.56	5.57			3.65	5.49	
NO5W		280x32									
NO6W	350x9	210x32			3.76	5.77	3.34	5.44			
NO7W	350x25				3.54	5.51					
NO1S	350x16	210x32	19	150	3.49	5.32	3.10	5.11	3.28	5.26	strong direction
NO2S			22						3.30	5.31	
NO3S		140x32	19						3.28	5.26	
NO4S		280x32	19								
NO5S	350x25	210x32	19		3.26	5.12					
NO6S	350x16	210x16	19		3.49	5.32	3.49	5.32			

Bc:width of column tcf:thickness of column td:thickness of diaphragms
Bb:width of beam flange tbf:thickness of beam flange
Hd:hight of diaphragms
YS:yield strength TS:tensile strength

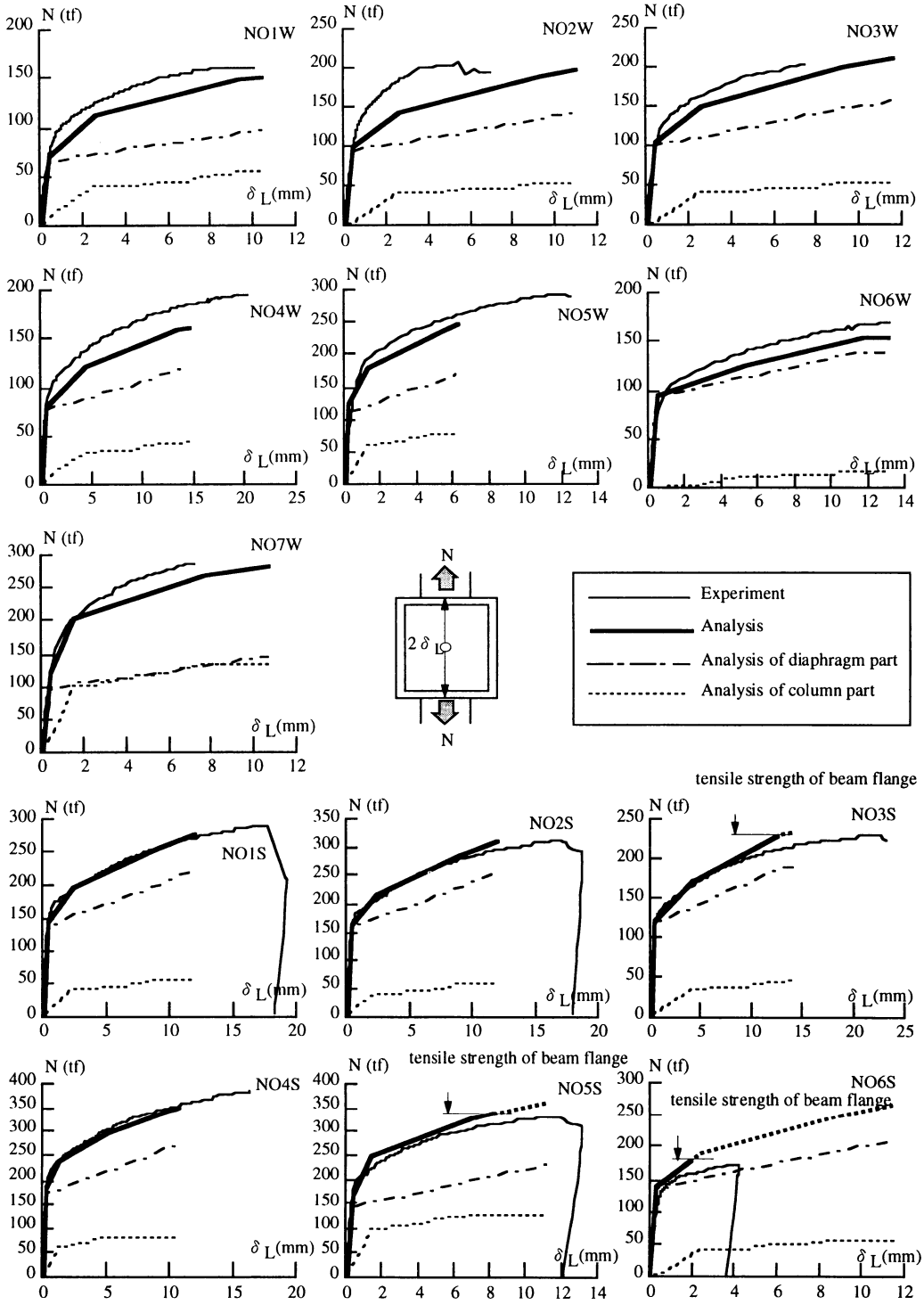

Figure 13. Comparison between test results and analysis

Table 3. Comparison between the test results and the analysis

specimens	Experiment			Analysis								
	Ny	Nu	K1	cNej	cNyj	cNuj	cK1j	cNub	cNu	Ny/cNyj	Nu/cNu	K1/cK1j
	(tf)	(tf)	(tf/mm)	(tf)	(tf)	(tf)	(tf/mm)	(tf)	(tf)			
NO1W	123	160	172	71	113	151	176	364	151	1.09	1.06	0.98
NO2W	151	205	214	100	145	197	245	364	197	1.04	1.04	0.88
NO3W	144	203	238	105	152	211	274	364	211	0.95	0.96	0.87
NO4W	118	196	166	81	123	162	164	242	162	0.96	1.21	1.01
NO5W	210	291	272	122	180	246	518	485	246	1.16	1.18	0.52
NO6W	113	170	160	93	126	156	210	366	156	0.90	1.09	0.76
NO7W	210	288	276	123	205	282	309	366	282	1.03	1.02	0.89
NO1S	210	292	396	145	196	279	378	343	279	1.07	1.05	1.05
NO2S	224	312	362	166	220	313	436	343	313	1.02	1.00	0.83
NO3S	171	230	280	121	174	234	293	229	229	0.99	1.00	0.95
NO4S	225	388	582	186	239	351	540	458	351	0.94	1.10	1.08
NO5S	250	329	424	170	251	362	477	343	343	0.99	0.96	0.89
NO6S	146	174	356	139	191	270	379	179	179	-	0.97	0.94

Test results－Ny:yield strength, Nu:ultimate strength, K1:initial stiffness
Analysis－cNej:elastic limit strength, cNyj:yield strength, cNuj:ultimate strength, cNub:tensile strength of beam flange , cNu=Min (cNuj,cNub) ,cK1:initial stiffness

Table 4. The ratio of the diaphragm part strength to the total strength

specimens	elastic limit strengh			yiled strength			ultimate strength		
	cNde	cNce	Rde	cNdy	cNcy	Rdy	cNdu	cNcu	Rdu
	tf	tf		tf	tf		tf	tf	
NO1W	64.6	6.4	0.91	71.7	41.3	0.63	96.8	54.6	0.64
NO2W	93.9	6.6	0.93	103.8	41.3	0.72	142.2	54.5	0.72
NO3W	99.1	6.1	0.94	110.4	41.2	0.73	156.6	54.3	0.74
NO4W	77.1	3.8	0.95	89.2	33.9	0.72	117.1	44.7	0.72
NO5W	111.2	11.1	0.91	120.8	59.2	0.67	168.1	78.1	0.68
NO6W	92.2	1.1	0.99	112.5	12.7	0.90	139.1	16.8	0.89
NO7W	96.5	26.3	0.79	102.1	102.7	0.50	146.2	135.5	0.52
NO1S	138.5	6.7	0.95	153.4	42.8	0.78	222.1	56.5	0.80
NO2S	159.6	6.7	0.96	176.9	42.8	0.81	256.8	56.5	0.82
NO3S	117.3	3.5	0.97	138.6	35.0	0.80	188.0	46.1	0.80
NO4S	169.1	16.6	0.91	178.1	60.6	0.75	271.2	79.9	0.77
NO5S	145.3	24.8	0.85	153.8	97.7	0.61	232.9	128.9	0.64
NO6S	133.0	6.4	0.95	148.0	42.8	0.78	213.2	56.5	0.79

cNd: diaphragms part strength , cNc: column part strength
Rd:the ratio of diaphragm part strength to total strength =cNd ／ (cNd+cNc)

obtained from FEA directly.Both load-deformation curves are simplified as tri-liner curves respectively.

As a result of comparison between the experiment and the analysis,the supposition seems to be valid and the load-deformation curve of the connection can successfully be predicted both in weak direction and strong direction.

Moreover,the ratios of diaphragm part strength to the total strength obtained by the analysis show about 90% of all specimens in an elastic state. But ,these tend to decrease according to the yield of the connection and finally become 50～80% in an ultimate strength state.

REFERENCES

K.Fukuda,Y.Ichinohe,F.Otake,K.Takada.1994.Experimental study on yield strength of H-shaped beam to RHS column connection with split diaphragms.*Summaries of Technical Papers of Annual Meeting Architectural Institute of Japan*:1419-1422.

K.Fukuda,K.Kubota,F.Otake,K.Takada.1996.Experimental study on strength of H-shaped beam to RHS column connection with split diaphragms -Elasto-plastic behavior of connection on strong axis-.*Summaries of Technical Papers of Annual Meeting Architectural Institute of Japan*: 613-614.



Taylor & Francis
Taylor & Francis Group
http://taylorandfrancis.com

Tubular Structures VIII, Choo & Van der Vegte (eds) © 1998 Balkema, Rotterdam, ISBN 90 5809 001 9

A moment-rotation model for connections of H-beams to concrete filled RHS columns

A. Kawano & C. Matsui
Kyushu University, Fukuoka, Japan

ABSTRACT: A connection between an H-beam and a concrete filled RHS (rectangular hollow section) column can not be perfectly rigid even if the connection is fitted with a horizontal diaphragm, because the diaphragm itself must have a fairly large opening to allow the RHS to be filled with concrete. Some effective means is needed to study deformation in such a connection. This paper presents a method for modeling the moment-rotation relationships in beam joints using typical diaphragm-stiffened connections.

1 INTRODUCTION

Under horizontal loading of the sort caused by earthquakes, the principal deformations which occur in a carefully welded connection between an H-beam and an RHS column are the shear deformation in the connection panel and the local deformation at the beam-joint, both of which cause rotation of the beam joint. In this paper, we study the local deformation at a beam-joint (Fig. 1) which we designate the local deformation in a connection.

A connection between a concrete filled RHS column and an H-beam is usually fitted with horizontal diaphragms to increase the rigidity and the strength of the connection. However, the diaphragm does not have perfect rigidity because it must have a substantial hole in it to allow the RHS to be filled with concrete. The connection panel can derive additional rigidity and strength from the encased concrete in the column tube. Therefore, under a horizontal load, the local deformation in the connection would be larger than that in the connection panel.

When the maximum moment in a beam joint depends on the connection strength, the maximum moment is not observed until the rotation angle in the beam joint becomes fairly large. This suggests that structural designs which take into account only the connection strength may involve an inconsistency, because the maximum moment would hardly be realized within a realistic deformation level even in an ultimate limit state.

The earthquake-resistant capacity of an entire framed structure is linked to two aspects of local deformation. One is undesirable: early failure of the beam joint due to strain concentration. The other may be desirable : a relaxation effect which reduces deformations in neighboring beams and columns.

To facilitate structural analysis and the design of framed structures, an effective model of the moment-rotation relations in beam joints should be established. This paper presents a new method for modeling the moment-rotation relations in several typical diaphragm-stiffened connections with concrete filled RHS columns.

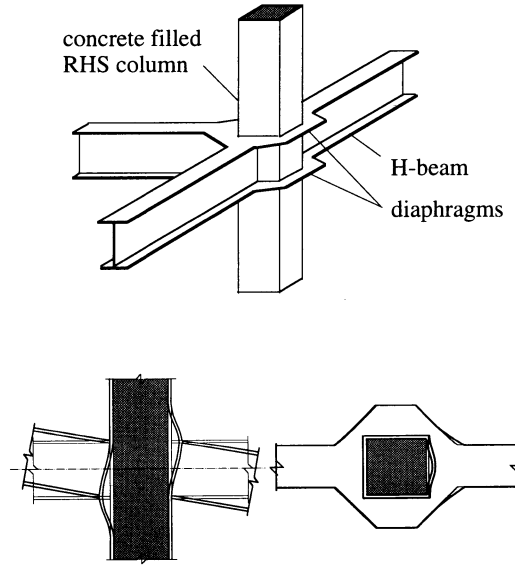

Fig. 1 Local deformation of a connection

2 DERIVATION OF MODEL

2.1 *Modeling load-deformation relations in a connection*

Three typical diaphragm-stiffened connections are investigated in this study: (a) the external diaphragm connection; (b) the internal diaphragm connection with a circular hole and extended flanges (the cut-through diaphragm connection); and (c) the internal diaphragm connection with a circular hole. These are illustrated in Figure 2.

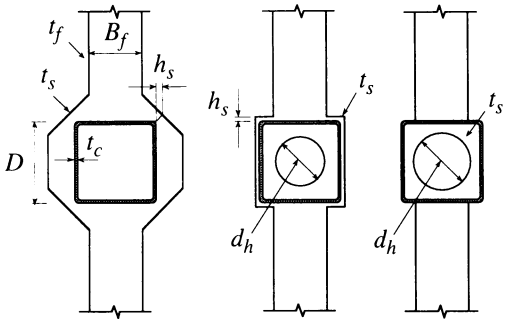

(a) External diaphragm (b) Cut-through diaphragm (c) Internal diaphragm

Fig. 2 Typical diaphragm-stiffened connections

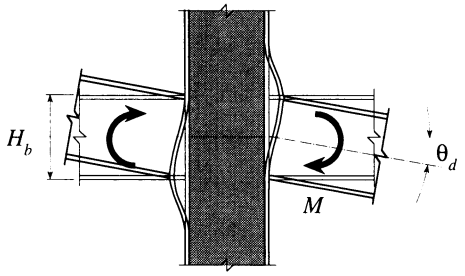

(a) Beam-to-column connection

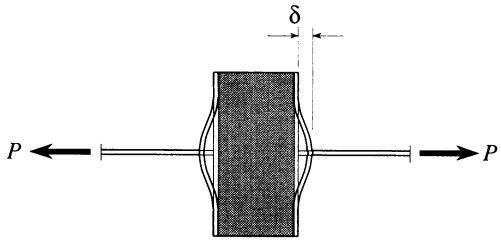

(b) Partial connection model

Fig. 3 Moment-rotation in connection

Local deformation of a connection appears only around the beam flange under tension but not under compression because the concrete encased in the column tube effectively prevents the tube wall from being dented (Fig. 3a). Therefore, the moment-rotation relation in a beam joint is determined by the local deformation of the connection around a beam flange under tension. The local deformation under tension can be studied by a tension test conducted on a partial connection model. The model is composed of two beam flange plates, a diaphragm and a stub of column as depicted in Figure 3b. Once the relationship between the tensile force in beam flange P and the local deformation δ is modeled, the moment-rotation relation in the beam joint is derived by using the following equations in which the contribution of a beam web is ignored because of its negligible quantity.

$$M = H_b \cdot P$$
$$\theta_d = \frac{\delta}{H_b} \tag{1}$$

The relationship between P and δ is designated as the load-deformation relation of the connection. To find the load-deformation relation in a partial connection model, we propose the multi-linear curve shown in Figure 4 as a model of the relation. The model has four constants: the elastic stiffness, EK, the yield load, P_{dy}, the load at $\delta = 0.01D$, $P_{d1\%}$ and the load at $\delta = 0.03D$, $P_{d3\%}$, where D denotes the width of a column flange. The $P_{d3\%}$ may be regarded as the maximum strength of the connection, P_{dmax}, because cracks or the fracture will happen around the beam joints if δ exceeds $0.03D$, and because the increase in the load up to the peak will not be great. The four constants for the model are determined by the material properties and dimensions of the beam, diaphragm and column tube.

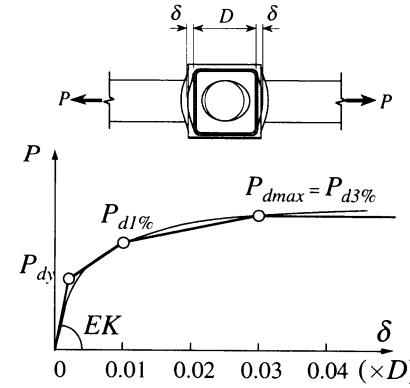

Fig. 4 Load-deformation model of connection

2.2 *FEM analysis of diaphragms and columns*

The load P, corresponding to the local deformation δ can be evaluated approximately by superimposing loads, $P_c + P_d$, where the P_c is the load at δ, resisted by only the column portion and the P_d is resisted only by the diaphragm portion, as shown in Figure 5. Morita et al. (1991) and Fukumoto & Kobayashi (1996) have reported that this approximation does not affect the predicted accuracy of P, so that the mutually potentiating effect of a column and a diaphragm is negligibly small.

To obtain the load-deformation relation for each column portion or diaphragm portion, a numerical analysis based on the finite element method (FEM) was performed. Figures 6a-d shows the analytical models for each. All are one-eighth scale models based on symmetrical conditions. The analytical parameters for the models are listed in Table 1. The total number of calculations was forty-eight for a column portion model, seventy-five for a external diaphragm model, and sixty each for both cut-through and internal diaphragm models. To model the steel plates, the finite element chosen was a shell element with four nodes (#75 in the program MARC K4). The concrete encased in a column tube is modeled as a geometric boundary which prohibits the column tube or the diaphragm from deforming into the space occupied by the concrete. The other assumptions adopted for the analysis were: (1)

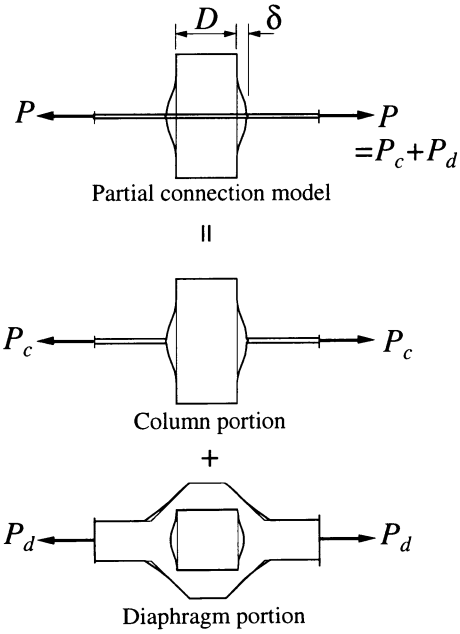

Fig. 5 Superposition of loads

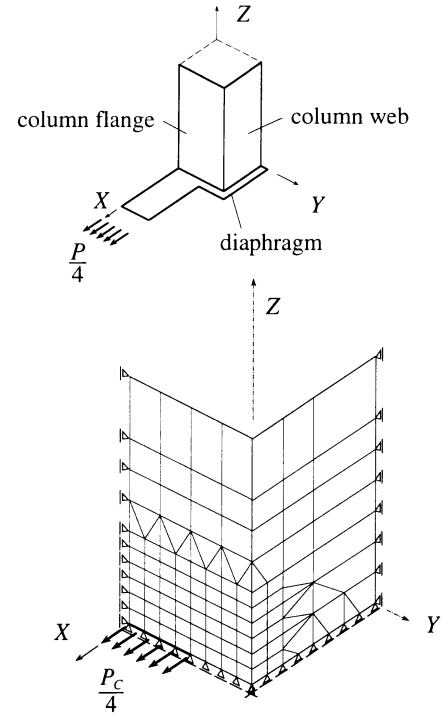

(a) Column portion

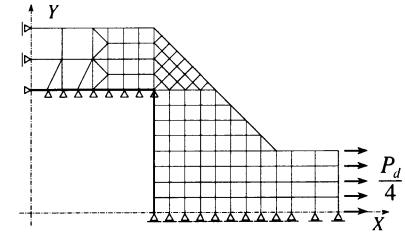

(b) External diaphragm portion

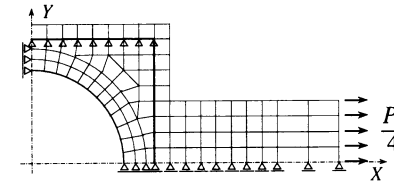

(c) Cut-through diaphragm portion

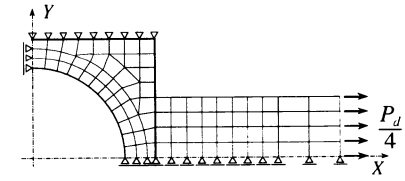

(d) Internal diaphragm portion

Fig. 6 FEM models of a column and diaphragms

Table 1 Analytical parameters for FEM models of column and diaphragm portions

Portion	Analytical parameters
Column	D/T = 20 ~ 80, B_f/D = 0.25 ~ 0.75, $\sigma_u{}^*$ = 500 ~ 600MPa, Y^{**} = 0.8 ~ 0.85, total: 48
External diaphragm	h_s/D = 0.05 ~ 0.25, B_f/D = 0.38 ~ 0.88, σ_u = 430 ~ 600MPa, Y = 0.7 ~ 0.85, total: 75
Cut-through diaphragm	d/D = 0.50 ~ 0.80, B_f/D = 0.38 ~ 0.88, σ_u = 430 ~ 600MPa, Y = 0.7 ~ 0.85, total: 60
Internal diaphragm	d/D = 0.50 ~ 0.80, B_f/D = 0.38 ~ 0.88, σ_u = 430 ~ 600MPa, Y = 0.7 ~ 0.85, total: 60

*σ_u : maximum stress in steel, **Y : yield ratio

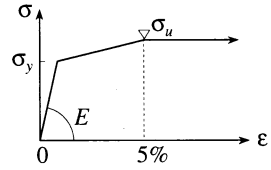

Fig. 7 Equivalent stress-strain relationship

stresses in an element are those in a planar stress field; (2) yielding is judged by von Mises yield criterion; (3) increments in plastic strains are determined by the associated flow rule; (4) strain-hardening is based on the isotropic hardening rule; (5) geometric non-linearities are handled by the updated Lagrangian method, (6) and the equivalent stress-strain relation in a steel element is that as shown in Figure 7.

The analysis was performed by the incremental displacement method in which equal increments of displacements are repeatedly specified at the loading nodes. The result was data on the load-deformation relations for column portions and diaphragm portions possessing various material properties and dimensions. Using the same analytical method, we calculated results for a large number of partial connection models, that is the assemblies consisting of column portion and diaphragm portion models. The results are used to create the FEM database which is referred to in Section 3.2.

2.3 *Formulae for model constants*

The following simple formulae were derived through trial and error so as to give good estimations of the constants of the load-deformation model for each column portion and diaphragm portion. Because priority was given to making the model as simple as possible, the formulae do not necessarily follow rigorous physical or mechanical requirements.

Column portion:

$$EK_c = 12E\,t_c \frac{\left(1-0.7\,b\right)\cdot\frac{D}{t_c}-4.5}{\left[\left(1-0.9\,b\right)\cdot\frac{D}{t_c}\right]^3}$$

$$P_{c1\%} = 0.9\left[1+0.004\left(b-3\right)\cdot\frac{D}{t_c}\right]\cdot P_{c3\%} \qquad (2)$$

$$P_{c3\%} = 0.04\,\sigma_{cu}\,D\,t_c\,\frac{\left(0.5+b+60\,\frac{t_c}{D}\right)}{1.3-b}$$

$b = 0.75$ for external diaphragm,

$b = 0.5\,\frac{B_f}{D}$ for cut-through or internal diaphragm

External diaphragm portion:

$$EK_e = 2\,E\,t_s\,\frac{\left[0.017+\left(0.01+\frac{h_s}{D}\right)\left(1.06-\frac{B_f}{D}\right)\right]}{1.1-\frac{B_f}{D}}$$

$$P_{ey} = Y_s\,P_{e3\%} \qquad (3)$$

$$P_{e1\%} = 0.5\left(Y_s+1\right)P_{e3\%}$$

$$P_{e3\%} = 2.2\,\sigma_{su}\,D\,t_s\left(0.02+\frac{h_s}{D}+0.01\,\frac{B_f}{D}\right)$$

Cut-through diaphragm portion:

$$EK_t = 1.5\,E\,t_s\,\frac{\left(0.95+0.5\,\frac{B_f}{D}-\frac{d_h}{D}\right)}{2-\frac{B_f}{D}}$$

$$P_{ty} = Y_s\,P_{t3\%}$$

$$P_{t1\%} = 0.5\left(Y_s+1\right)P_{t3\%} \qquad (4)$$

$$P_{t3\%} = 1.7\,\sigma_{su}\,D\,t_s\,\frac{\left(1+0.5\,\frac{B_f}{D}-\frac{d_h}{D}\right)}{3-\frac{B_f}{D}}$$

Internal diaphragm portion:

$$EK_i = 1.7\,E\,t_s\,\frac{\left(0.85+0.5\,\frac{B_f}{D}-\frac{d_h}{D}\right)}{2-\frac{B_f}{D}}$$

$$P_{iy} = Y_s\,P_{i3\%}$$

$$P_{i1\%} = 0.5\left(Y_s+1\right)P_{i3\%} \qquad (5)$$

$$P_{i3\%} = 1.8\,\sigma_{su}\,D\,t_s\,\frac{\left(0.9+0.5\,\frac{B_f}{D}-\frac{d_h}{D}\right)}{3-\frac{B_f}{D}}$$

Where EK_x, P_{xy}, $P_{x1\%}$, $P_{x3\%}$ represent the elastic stiffness, the yield load, the load at $\delta = 0.01D$, and the load at $0.03D$, respectively. The subscript "x" represents "c", "e", "t" and "i" which indicate a column portion, an external diaphragm portion, a cut-through diaphragm portion, an internal diaphragm portion, respectively. σ_{cu} and Y_c are the maximum stress and the yield ratio of a column portion, and σ_{su} and Y_s are those of a diaphragm portion, respectively. The constants of the load-deformation model for a complete connection, which is composed of both a column portion and a diaphragm portion, are calculated by the following equations:

$$
\begin{aligned}
EK &= EK_c + EK_x \\
P_{dy} &= EK_c \cdot \delta_{xy} + P_{xy} \\
\delta_{xy} &= \frac{P_{xy}}{EK_x} \\
P_{d1\%} &= P_{c1\%} + P_{x1\%} \\
P_{dmax} &= P_{c3\%} + P_{x3\%}
\end{aligned}
\qquad (6)
$$

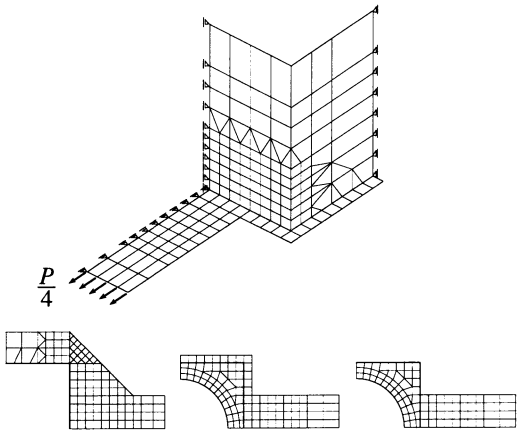

Fig. 8 Analytical model of FEM database

Table 2 Analytical parameters for FEM database

Connection type	Analytical parameters
External diaphragm	$h_s/D = 0.05 \sim 0.25$, $B_f/D = 0.50 \sim 0.75$, $\sigma_{su} = 430 \sim 600$MPa, $Y_s = 0.7 \sim 0.85$
Cut-through diaphragm	$d_h/D = 0.60 \sim 0.80$, $B_f/D = 0.50 \sim 0.75$, $\sigma_{su} = 430 \sim 600$MPa, $Y_s = 0.7 \sim 0.85$
Internal diaphragm	$d_h/D = 0.60 \sim 0.80$, $B_f/D = 0.50 \sim 0.75$, $\sigma_{su} = 430 \sim 600$MPa, $Y_s = 0.7 \sim 0.85$

Column: $D/t_c = 30, 50$, $\sigma_{cu} = 500 \sim 600$MPa, $Y_c = 0.8 \sim 0.85$

The yield load of a column portion is not used in the above equations because the load-deformation curve of a column portion is that of the round house type, and therefore and has no distinct yield point.

3 MODEL ACCURACY

3.1 *Comparison with FEM database*

The accuracy of Equations 2-6 is investigated by comparing their results with those from the FEM database which we mentioned in Section 2.2. The analytical model in the FEM database is a partial connection model, an assembly of a column portion model and a diaphragm portion model as shown in Figure 8. The analytical parameters for the models are listed in Table 2. The total number of calculation cases was thirty-six for each of the external diaphragm connections, the cut-through diaphragm connections, and the internal diaphragm connections.

Figures 9a-d show the comparisons between the model constants from the FEM database and those calculated by means of Equations 2-6. Good agreement can be observed for each constant: EK, P_{dy}, $P_{d1\%}$, and $P_{d3\%}$, as well as for the load-deformation model itself (Figs. 9a-d, respectively). The average and the standard deviation of the ratios of the constants from the FEM database to those from the calculaltion are listed in Table 3. The prediction gives a slight underestimation with the standard deviation of about 5% for every model constant.

3.2 *Comparison with experimental database*

Using data from Iida et al. (1994), Kawano et al. (1997), Matsui & Kondo (1979), and Shiiba et al. (1992), we constructed an experimental database for a tension test of a partial connection model. The model was composed of two beam flange plates, a diaphragm and a stub column as indicated in Figure 10. . The experimental parameters of the database are listed in Table 4. The database does not contain many specimens, but the range of the parameters may cover most of those in practical use.

Figures 11a-d show the results of comparisons between the model constants of the experimental database and those calculated by means of Equations

Table 3 Average and standard deviation for the ratios of the FEM database to the calculations

Connection type		EK	P_{dy}	$P_{d1\%}$	P_{dmax}
External diaphragm	average	1.030	1.054	0.973	0.985
	st. deviation	0.031	0.044	0.024	0.021
Cut-through diaphragm	average	1.047	1.052	1.029	1.056
	st. deviation	0.065	0.031	0.032	0.035
Internal diaphragm	average	1.036	1.049	1.041	1.058
	st. deviation	0.066	0.045	0.038	0.040

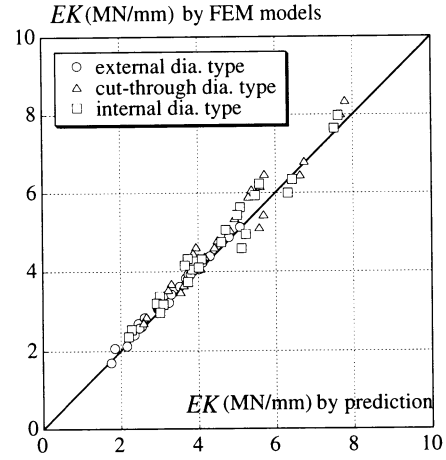

(a) EK

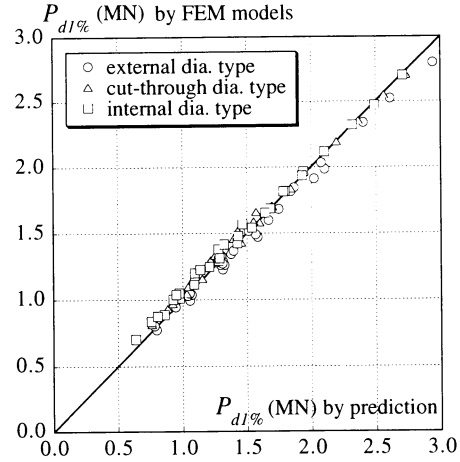

(c) $P_{d1\%}$

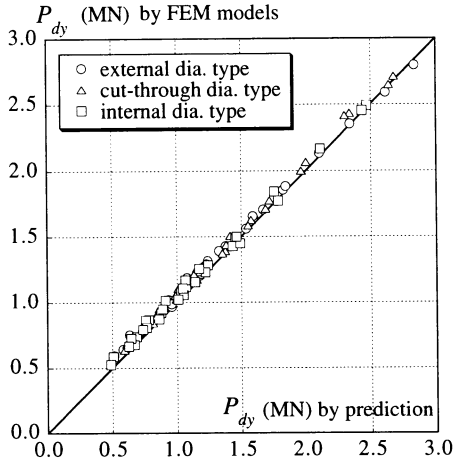

(b) P_{dy}

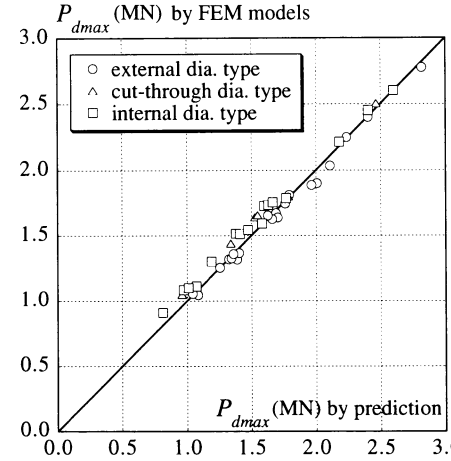

(d) $P_{3\%}$

Fig. 9 Comparison with FEM database (cont.)

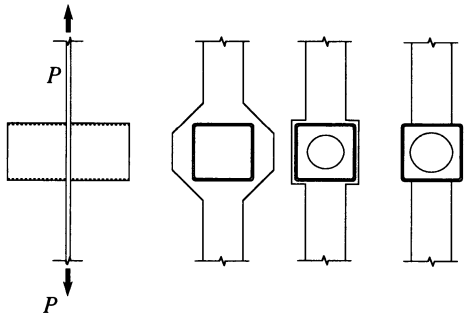

Fig. 10 Partial connection specimens

Table 4 Parameters of an experimental database

Connection type	Experimental parameters
External diaphragm	D/t_c=34～65, h_s/D=0.06～0.25, B_f/D=0.5～1.0, σ_{cu}=304～462MPa, Y_c=0.8～0.88, σ_{su}=398～458MPa, Y_s=0.65～0.70, total: 12
Cut-through diaphragm	D/t_c=34～65, d_H/D=0.45～0.60, B_f/D=0.25～0.75, σ_{cu}=304～503MPa, Y_c=0.7～0.88, σ_{su}=391～479MPa, Y_s=0.65～0.70, total: 17
Internal diaphragm	D/t_c=25～65, d_H/D=0.58～0.75, B_f/D=0.33～0.65, σ_{cu}=304～543MPa, Y_c=0.64～0.84, σ_{su}=433～580MPa, Y_s=0.70～0.72, total: 11

2-6. Table 5 lists the average and the standard deviation of the ratios of the model constants from the experimental database to those from the calculations. The agreement was less than that seen in the comparison with the FEM database. possible reasons may be the welding metal and residual stresses which were not taken into account in the calculations and in the FEM models; and the measuring error in the test procedures especially for the elastic stiffness *EK*. The calculation gives an underestimation in most cases, and the standard deviation of the ratios of the experimental database to the calculations is about 10% for P_{dy}, $P_{d1\%}$, and $P_{d3\%}$. Therefore, it can be concluded calculations using Equations 2-6 are accurate enough for engineering purposes, as the scattering is almost the same as that of structural materials in general use.

Table 5 Average and standard deviation for the ratios of the experimental database to the calculations

Connection type		*EK*	P_{dy}	$P_{d1\%}$	P_{dmax}
External diaphragm	average	1.005	1.253	1.076	1.040
	st. deviation	0.091	0.103	0.085	0.103
Cut-through diaphragm	average	1.158	1.081	1.056	0.962
	st. deviation	0.164	0.088	0.055	0.029
Internal diaphragm	average	1.092	1.209	1.135	1.141
	st. deviation	0.133	0.096	0.118	0.099

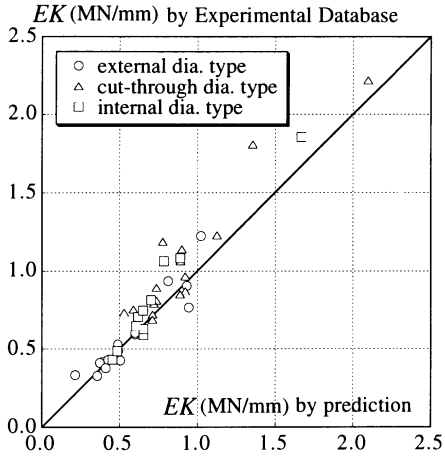

(a) *EK*

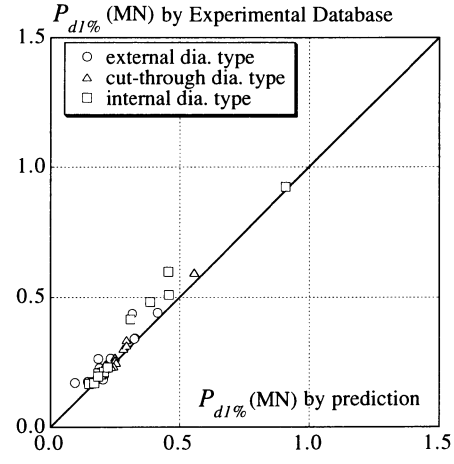

(c) $P_{d1\%}$

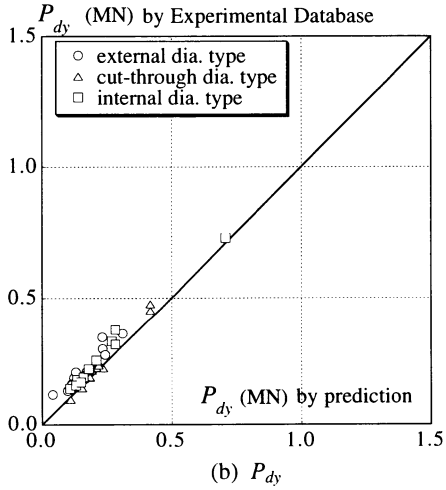

(b) P_{dy}

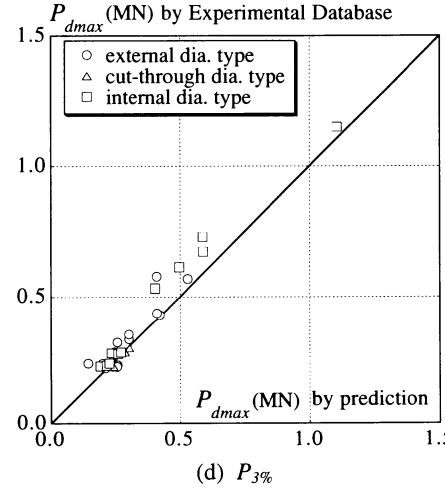

(d) $P_{3\%}$

Fig. 11 Comparison with experimental database

3.3 *Examples of load-deformation relations*

Examples of the relations between load P and deformation ΔL in tension tests of partial connection specimens (Fig. 12, Kawano et al. 1997) are shown in Figures 13a-i. The deformation ΔL is a summation of the local deformation of the connection and the deformation of two beam flange plates. The experimental curve was predicted by a load-deformation model of a connection in which deformation of the beam flanges occurs. The stress-strain relation for the

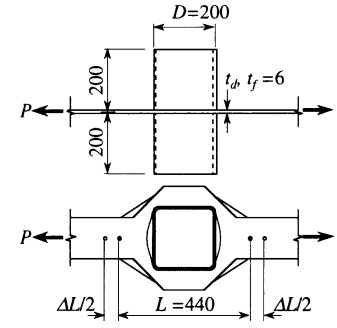

Fig. 12 partial connection specimen

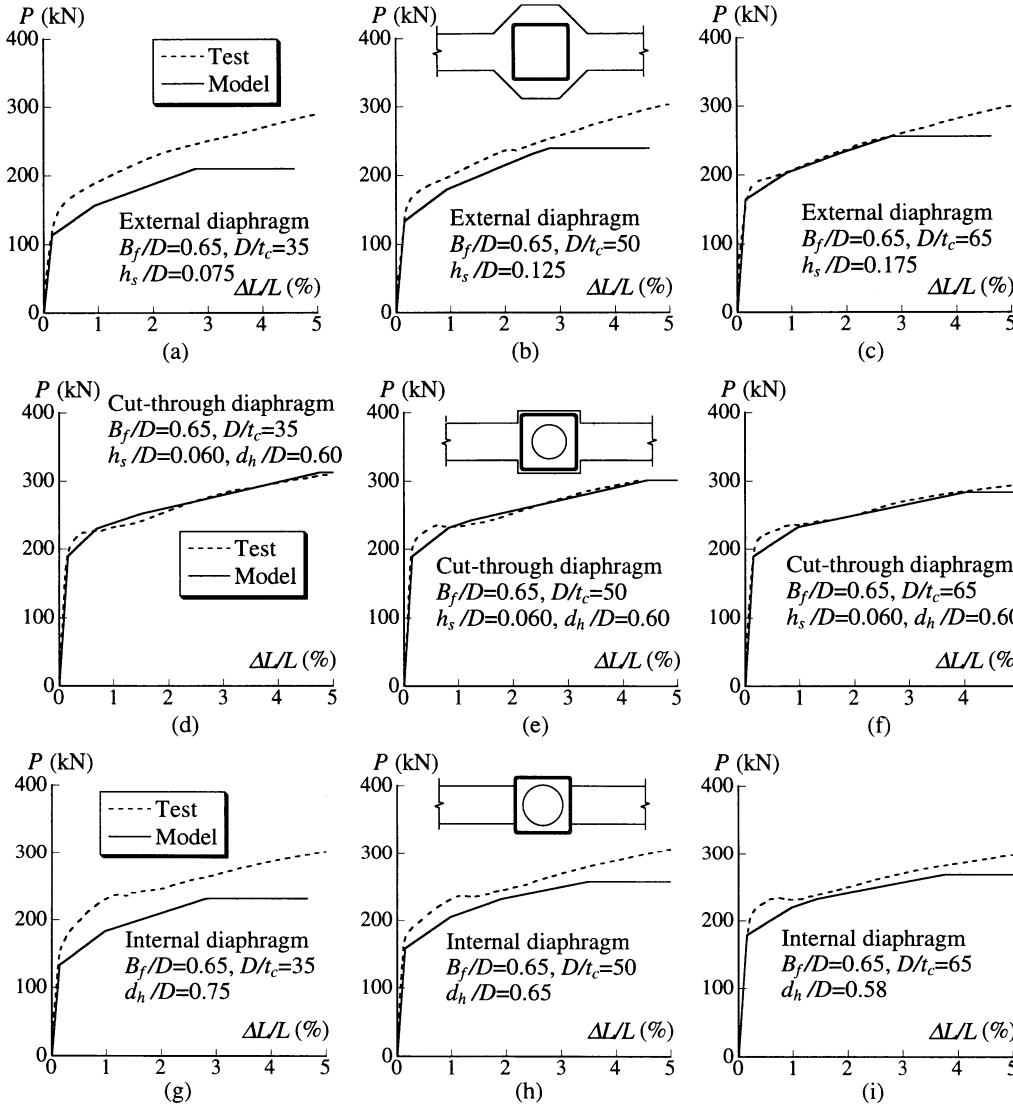

Fig. 13 Examples of load-deformation relations of connections

beam flanges is the same as that for the model shown in Figure 7. The examples are curves of three typical diaphragm connections. It can be seen that each both model and experimental curves are in good agreement.

4 CONCLUDING REMARKS

A load-deformation model has been proposed for predicting local deformation in H-beam connections with concrete filled RHS columns. The moment-rotation relation in a beam joint can be specified by the load-deformation model. The model is available for three typical diaphragm-stiffened connections, and is determined by four constants, EK, P_{dy}, $P_{d1\%}$, and $P_{d3\%}$. In order to predict these model constants, simple and effective formulae have been derived from numerical data on column portion models and diaphragm portion models.

The accuracy of the formulae have been proved through comparison with an FEM database and an experimental database obtained from partial connection models. Some experimental examples of the load-deformation relations in the partial connection models have been shown with the proposed load-deformation models, in which resonable agreement was seen.

ACKNOWLEDGMENT

The study in the paper is supported by the grant of scientific research 1995-1997 by the Ministry of Education Japan, "Steel Structural Design Method Based on Quantifiable Limit States of Connections" (chairman: Takanashi K.) , and the grant of sub-committee of a new design method for steel structures in Japanese Society of Steel Construction, (chairmen: Takanashi K. & Morita K.).

REFERENCES

Fukumoto, T. & Kobayashi H. 1996. Connection between high-strength concrete-filled square tubular steel column and steel beam, reinforced with internal diaphragm. *Journal of structural and construction engineering, Transactions of AIJ* 479: 109-118.

Iida, T., Inai E. & Shimazaki K. 1994. Loading tests of beam-column connections reinforced with the inner stiffener plate with circular holes, Study on steel beam-concrete filled tubular column connections. *Summaries of technical papers of annual meeting, AIJ* : 1547-1548.

Kawano, A., Matsui, C. & Murai N. 1997. Strength and deformabilities of connections in composite structures. In Takanashi, K. (ed.), *Steel Structural Design Method Based on Quantifiable Limit States of Connections*, Report of the grant for scientific research by the Ministry of Education Japan (1995-1997).

Morita, K., Yokoyama, Y., Kawamata, Y. & Matsumura, H. 1991. Effect of inner ring stiffener on the strength of connection between steel beam and concrete-filled square tube column. *Journal of structural and construction engineering, Transactions of AIJ* 422: 85-96.

Matsui, C. & Kondo K. 1979. A study on connections of H-shaped beams to concrete-filled square tubular columns. *Summaries of technical papers of annual meeting, AIJ* : 1661-1662.

Shiiba, K., Harada, N. & Iijima, N. 1992. An experimental study on concrete-filled steel tubular column, part 2 tension loading test on column-to-beam connection. *Summaries of technical papers of annual meeting, AIJ* : 1853-1854.



Taylor & Francis
Taylor & Francis Group
http://taylorandfrancis.com

Tubular Structures VIII, Choo & Van der Vegte (eds) © 1998 Balkema, Rotterdam, ISBN 90 5809 001 9

On the behaviour and design of composite column to beam connections under seismic loads

J.G. Beutel
School of Civil Engineering, Queensland University of Technology, Brisbane, Qld, Australia (Formerly: Robert Bird and Partners, Consulting Engineers, Brisbane, Qld, Australia)

D.P. Thambiratnam
School of Civil Engineering, Queensland University of Technology, Brisbane, Qld, Australia

N.J. Perera
Robert Bird and Partners, Consulting Engineers, Brisbane, Qld, Australia

ABSTRACT: Concrete filled steel tube (CFST) columns and steel beams are becoming increasingly popular in multi-storey buildings located in regions of high seismic activity. Moment resisting frames with ductile connections capable of high energy dissipation are well recognised for their superior performance in resisting earthquake forces. With this in mind a large scale research project has been undertaken at the Queensland University of Technology to study the behaviour of such connections and to develop a deterministic procedure for their design. This paper discusses the current state-of-the-art on the design of full-strength moment-resisting type connections between steel beams and CFST columns, and identifies some of the most suitable connection details for continued study in this project. The models selected for investigation have been chosen and/or developed through practical applications of this connection problem on several major design projects with due consideration for constructability, cost and efficiency.

1 INTRODUCTION

The present trend in the construction of high rise buildings clearly indicates the economic superiority of composite steel/concrete construction techniques and structural systems. Their increasing popularity can be attributed to important technological advances in areas such as shear connection, and the many advantages such as speed and ease of construction, reduction in storey heights and building mass, etc. in utilising this construction technique. One of the more recent advances in the development of composite construction materials and systems has been the emergence of composite columns. These members have many advantages over other column construction types and have many desirable attributes for their application in areas of high seismic risk.

1.1 *The Composite Advantage*

There are two general forms of composite columns in use today ; concrete-encased steel sections, and concrete-filled steel tube sections. The concrete-filled alternative is the more recent of the two varieties, and has many distinct advantages over its encased counterpart. These have been well documented and include:

- Most of the axial load is carried by the concrete core, a concrete member being the most economical way to resist compressive forces. This, combined with significant construction savings results in a column which has been found to cost approximately the same as a reinforced concrete alternative, which is generally acknowledged as the cheapest column type for multi-storey type construction (Webb and Peyton, 1990).
- The outer steel shell enhances the concrete's axial strength by placing the material into a state of tri-axial stress, and the presence of the concrete infill enhances the local buckling capacity of the tube wall. This results in a very efficient and ductile axial load carrying member, which also makes it possible to use smaller column sizes.
- The strength of steel is used more efficiently than in a conventional reinforced column and plate rolled into a tube is a very cost efficient way to use this material (Webb and Peyton, 1990).
- The steel tube acts as formwork for the concrete core and can also take the place of the internal reinforcement cage, reducing labour and material costs.
- Several floors of the building can be constructed simultaneously, without the need to fill the column, removing this activity off the

building's critical path, thus giving the contractor considerable flexibility.
- The columns can be filled over many floors and can be pumped full from the base. This eliminates the need to vibrate the concrete as air entrapment is avoided, the placed concrete is of a higher quality, many floors can be filled in one operation, and this can proceed from a constructed floor thus separating construction activities.
- No special curing treatments or precautions are required as perfect curing conditions exist in the tube.
- If the concrete mix is designed properly, no scabbling of the interface between pours is necessary (Webb, 1993).

Because of these advantages the CFST has become recognised world-wide as being a highly constructable, and very economical axial load carrying member, combining the stiffness, economy and axial load carrying capacity of concrete with the speed of erection and strength of structural steel. The result is a composite member possessing exceptional axial and lateral stiffness, strength, and ductility and the construction techniques which are employed have been described as a technological break-through in high rise construction (Webb, 1993 and Ricles et al, 1995). A large amount of research has been conducted and published on the design of both composite beams and columns such as these, resulting in the publication of codes for their design. However, relatively little work has been conducted on the connection of these elements, particularly full strength moment resisting connections.

1.2 *The Connection Dilemma*

When investigating suitable lateral load resisting systems for structures in areas of high seismic risk, most of these systems involve full moment resisting connections between the beam and column elements. This is because many of these systems rely on the action of these connections to support gravity loads and carry lateral forces to their foundations. The seismic design of modern lateral load resisting systems relies on the ability of this system to dissipate the large amounts of energy imparted onto it during an extreme seismic event.

This design philosophy has increased the popularity of systems which incorporate full moment resisting connections because the preferred energy dissipating mechanism associated with these involves the formation of plastic hinges in the beam elements adjacent to the connection. Beams acting in flexure such as this are capable of excellent ductile behaviour. The formation of such a hinge protects the beam from a possible more brittle shear failure, and also protects the critical axial load carrying columns from failure by limiting the load transmitted into the column. However, the connections in such a system suffer extreme levels of stress during a severe earthquake as the moment across the connection can change from fully plastic in one direction to fully plastic in the other, as the seismic loads reverse. Therefore the column to beam connections must be adequately designed and proportioned to ensure that a ductile flexural hinge forms in the beam, and the system performs as was intended.

A lack of sufficient data and design guidance (principally in the area of connections) has limited the application of CFST technology when attempting to incorporate these into the lateral load resisting system of a structure. Much of the research which has been conducted has focused on joint configurations and details which are extremely difficult to build and do not facilitate the unique construction methods employed with this column type. Also the current design practices for these connections rely heavily on the judgement and experience of individual designers due to the small amount of research and testing information available (Azizinamini and Prakash, 1993). Research is required to develop a highly constructable, ductile, and predictable connection detail, to understand the behaviour of composite members in this application, and develop a procedure for its design.

1.3 *The Industry Partner*

Australian engineering companies of recent have been called upon to actively participate in the design of a large number of structures and facilities to resist earthquakes, particularly in the Asia Pacific Region. Robert Bird and Partners Pty Ltd - the industry partner for this project, has been actively involved in the design and construction supervision of several prestigious high rise projects in earthquake prone areas of this region during the past six years. The company has ultilized CFST's in several such projects with connection configurations based on the magnitude of forces and the performance requirements of the lateral load resisting system. These configurations were:
- Embedded shear connectors and beams welded to the column face.
- Flange plates and web shear connectors extending into the concrete core.
- External stiffening of the steel tube.

Some critical observations based on the experiences of the industry partner were as follows.

- A deterministic procedure for the design of these fairly complex composite connections was not available.
- Research to date provided information and guidelines on the relative merits and demerits of different types of connections. However, these correlations between material strengths, geometry and applied forces that are necessary for practical design applications were inadequate.
- The adopted designs encountered buildability problems due to:
    - ♦ Distortion or damage to embedments due to pumping pressure of concrete
    - ♦ Air entrapment around large embedments that were stiff enough to withstand pumping pressures.
    - ♦ Fabrication access for embedded connections and associated high cost.
    - ♦ High material content and cost of external stiffening.
    - ♦ The need for off and on site welding in the connection zones.

This prompted the industry partner, in conjunction with the Queensland University of Technology to undertake a detailed investigation into such connections.

2 REVIEW OF PREVIOUS RESEARCH

Experimental research on connections involving CFST's has been very diverse, and has only taken place relatively recently. Connections to CFST's can generally be placed into two groups. Those that connect to the external steel tube only (External Connections), and those that attempt to transfer a portion of the girder flange forces into the internal concrete core via embedded fitments (Internal Connections). Some of this research which is most relevant to this project is reviewed below.

2.1 *External Connections*

These can be further categorised into unstiffened and stiffened connections.

(i) Unstiffened - These connections are made up of a simple web cleat plate off the tube and butt welding (FSBW) of the flanges to the tubing (refer to Figure 1). This form of connection is very simple, hence highly constructable and cheap. They offer no internal resistance to the pump-filling of the tube and do not create a compaction problem due to presence

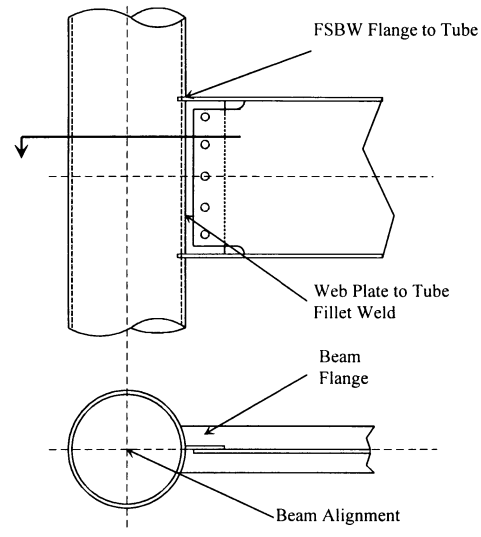

Figure 1
Simple External Connection

of embedded items in the vicinity of the connection. These connections generally suffer from tube distortion and buckling problems, resulting in poor rotational stiffness, and insufficient strength to mobilise the connecting beam's full plastic capacity. This is because no direct load path is provided for the large flange forces to enter into the concrete core.

Shakir-Khalil has conducted tests on web-cleat connections, utilising a plate welded off the tube wall only (1994,1993 and 1992). These tests were carried out on 28 full scale specimens. Parameters tested included, load eccentricity, effect of internal shear devices, ratio of the column load to shear load, and the use of local thickenings around the tube wall. Failure loads for each specimen were predicted based on British Standards for both the column and the connection itself. Tests carried out on connections to circular hollow section (CHS) members (Shakir-Khalil, 1992) found that no premature failure of the connection took place though local yielding of the steel tube did occur in the surfaces parallel to the loading plane within the lower half of the cleat -plate position. This local yielding caused the column stiffness to deteriorate causing large in-plane displacements and eventual column failure. The failure load of the connections tested increased with the presence of shear connectors, using a deeper fin-plate and reducing the eccentricity (hence moment) on the connection. It was found that for the connections subjected to the larger moments, failure was by the

cleat plate pulling out of the steel section wall, tearing the wall at the toe of the connection. For all the specimens tested it was found that the joint effect was very localised with the beam loads transferred to the composite column within a distance of no larger than a column depth above and below the cleat position. It should be noted that these tests were on a equivalent simple support cleat type connection only and these were unable to resist significant bending moments.

Ricles *et al* (1995) conducted an experimental investigation into concrete filled square hollow section panel zones as would be developed in a typical moment resisting connection. A variety of parameters were tested including the width to thickness ratio of the tube, concrete compressive strength, strut angle, tube yield strength etc. and design equations were developed. Test results indicated that shear capacity correlated well with joint capacity strength equations. These were based on superimposing the shear strength of the steel tube and the concrete core in the joint region using a concrete strut model. All specimens tested performed well under monotonic loading, with exceptional ductility. This ductility was attributed to the tension membrane action that the steel tube developed.

Alostaz and Schneider (1996 I and II) conducted a series of analytical and experimental tests on a variety of connections to concrete-filled circular tubes. The six connection details investigated were: Connection type (i), web cleat and full strength butt weld flanges to the steel tube (similar to Figure 1), Connection type (ii), web cleat and external diaphragm plate to top and bottom flanges (similar to Figure 3), Connection type (iii), web cleat and full strength butt weld flanges to the steel tube incorporating weldable reinforcing bars from the beam flanges into the concrete core (similar to Figure 5), Connection type (iv), web cleat and full strength butt weld flanges to the steel tube incorporating headed studs at the level of the beam flanges, Connection type (v), web plate fully embedded into the core incorporating headed studs, Connection type (vi), fully embedded beam into the column.

These connections were investigated for their suitability as a full-strength type connection. Various parameters were investigated including the diameter to wall thickness ratio of the tube, the applied axial load on the column, and the eccentricity of the applied beam load. The findings for each of the connection types tested will be discussed separately in the relevant sections of this document. Figure 2 (Alostaz and Schneider, 1996) shows the moment-rotation behaviour for all of the above connection types.

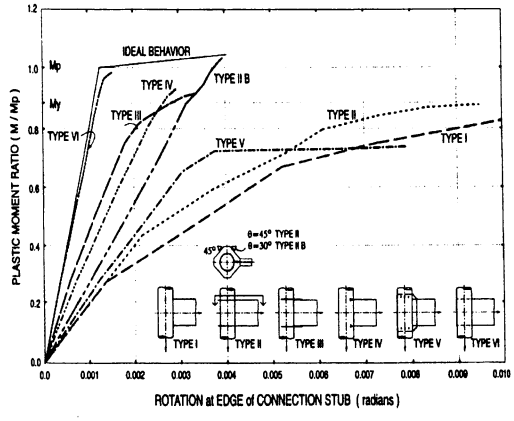

Figure 2
Analytical Moment-Rotation Behaviour
(Alostaz and Schneider, 1996)

Connection type (i) was the simplest, hence cheapest connection type investigated. The design of the beam flange to tube connection was based on the through shear strength of the tube which would be required to generate the full flange force. This detail was able to mobilise only 70% of the beam's full plastic moment capacity with an initial stiffness of only 25% of that of a ideal rigid connection. This was due to very high local distortions of the tube wall around the tension flange. Very little strength and stiffness benefit could be gained from using a thicker tube wall as tube wall distortions still became too large. The experimental results correlated well with those obtained using analytical methods with the cyclic performance of the connection being very poor. The hysteresis for the connection showed a strength degradation after only one cycle and the loops being pinched indicating very poor ductility.

(ii) Stiffened - This type of connection includes local thickening of the tube wall in the area of the connection, and the use of continuous stiffening rings or diaphragms at the top and bottom flange locations, an example of which are given below (refer to Figure 3). These connections attempt to distribute the flange forces into the concrete core by stiffening the steel tube in the vicinity of the connection. From the research conducted it would seem that these connections, when properly detailed, could mobilise the connecting beam's full plastic capacity with adequate rotational stiffness, however the industry partner has found such connections very expensive, requiring excessive material quantities and labour in their fabrication.

Kang *et al* (1995) and Choi *et al* (1995) conducted a series of analytical and experimental

investigations on tensile capacity of a stiffened and unstiffened concrete filled CHS section with a single beam flange welded to the column. It was found that infilling the tube increased the capacity of the connection twofold over the unfilled specimens, and as the tube became thicker it had greater capacity to accept the applied tensile load due to increased direct hoop stiffness and capacity. It was also found that stress concentrated at the flange edges which is produced as the load attempts to distribute into direct hoop stress around the tube.

Kato *et al* (1992) tested the tensile capacity of a beam flange (a single plate only) welded to a stiffener ring which was in turn welded by a fillet weld to a CFST. Design formulae were derived for the ultimate tensile capacity of the connection and validated by specimen tests. It was suggested that the yield and ultimate capacity of the connection can be found by summing the capacities of the stiffener ring and weld in the vicinity of the flange individually. Tests were conducted which verified the proposed expression. The failure of the connection began from a crack at the intersection of the ring and beam flange.

Alostaz and Schneider (1996, I) conducted an analytical investigation into a externally stiffened connection similar to that shown in Figure 3 (referred to as connection type (ii)). It was found that providing the beam flange forces with a more direct load path to flow around the CFST

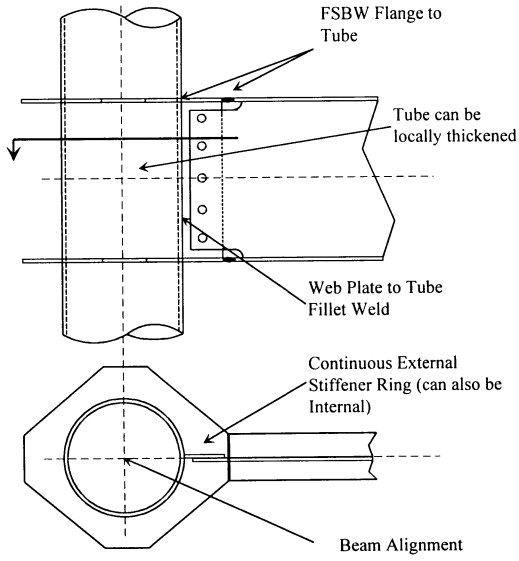

Figure 3
Stiffened External Connection

increased the connections stiffness and its ultimate capacity. The stresses in the stiffener plate were much better distributed, and tube distortions were decreased, improving both the elastic and in-elastic behaviour of the connection

2.2 *Embedded Connections*

This connection type includes proposed details which range from fully embedded beam sections to bolted end-plates, shear studs and reinforcing bar anchored into the concrete core. All of these details are designed to transmit most of the large flange forces directly into the concrete core of the column. This generally has the effect of reducing the required material quantities and labour associated with these connections (with one notable exception) compared to stiffened external connections. It does however introduce a flow restriction into the tube and a point at which voids in the concrete may form. These embedded items are also subjected to very high pumping pressures and could suffer from distortion or damage during the pumping operation.

Hawkins *et al* (1980) conducted a series of 22 tests on connections between wide flange sections to reinforced square concrete columns using steel end plates and embedded studs. The parameters investigated were the influence of stud embedment, stud spacing and edge distances, and the eccentricity of the loading. It was found that the performance of the connection was highly dependent on the eccentricity of the loading as this governed the mode of load transfer and thus connection failure. A brittle type of failure was experienced when the studs failed by pull out due to inadequate embedment length or excessive tensile forces generated by large connection bending forces. Failure due to shear distortion or tensile fracture of the stud (decreased load eccentricity or increased stud embedment) was much more ductile and was therefore the preferred failure mode. Under cyclic loading the connections tested showed a rapid decrease in strength and stiffness and the hysteretic curves were very pinched s-shaped indicating rapid deterioration of the joint.

Alostaz and Schneider (1996, I and II) conducted an analytical investigation into a similar connection to a CFST (connection type (iv)). Their results suggested that the strength of the connection was limited by the strength of the studs and its behaviour was greatly influenced by the moment-shear ratio on the connection as this controlled the failure mode of the connection (similar to the results found by Hawkins *et al*, 1980). It was found that the connection was able to mobilise 50% of the elastic stiffness of a ideal

rigid connection, and responded linearly up to 93% of the ultimate bending strength of the girder.

Dunai *et al* (1996) conducted a series of experiments on end-plate type steel beam to concrete column connections using embedded studs and through bolts. It was found that the failure mode of these connections was one of combined bending and yield of the bolts and end plate, and the eventual crushing of the concrete in the compression zone of the connection due to the opening and closing of gaps between the endplate and the concrete face. The formation of these gaps and their subsequent deterioration, reduced the rotational stiffness of the connection markedly, but the strength of the connection was not affected. However a sharp decrease in the full ductility ratio was experienced due to the appearance of these gaps.

Kanatani *et al* (1987) conducted experiments on concrete-filled RHS column to universal beam connections fabricated with through bolts and tee's or welded endplates. The connections were of a general form similar to the full strength connection tested by Dunai et al (1996) with no shear studs in the region of the beam web. It was found that the connection was capable of transmitting the beams full moment capacity to the columns and that the concrete in the panel zone of the joint was capable of effectively handling the shear forces travelling through the joint

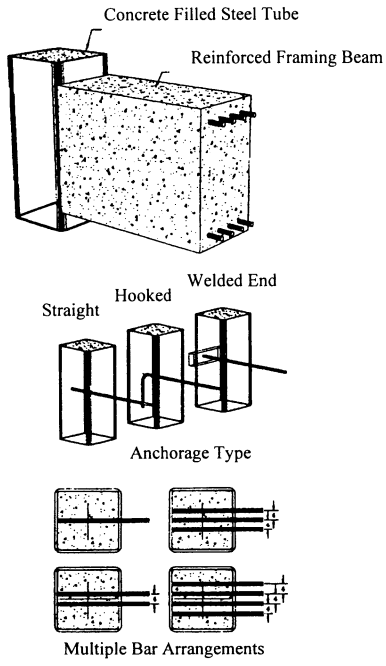

Figure 4
Concrete Beam to CFST Connection
(Ashadi and Bouwkamp, 1995)

Ashadi and Bouwkamp (1995) conducted an experimental study on both interior and exterior beam column joints incorporating concrete-filled SHS columns and reinforced concrete beams (refer to Figure 4). Full moment capacity of the beam section was developed by embedding the tension steel into the concrete filled tube. Failure of all joint types was via the formation of a plastic hinge in the concrete beam (as designed). Various bar shapes were tested and both the welded and hooked anchorage bar types showed excellent hysteretic behaviour, without significant loss of capacity with increasing deflection. Straight anchored bars had significantly lower ductility and poor hysteric behaviour due to bond deterioration and the resulting pinching effect reducing its energy absorption capacity.

Alostaz and Schneider (1996, I and II) conducted analytical and experimental tests on a similar connection as shown in Figure 1 above but reinforced with weldable reinforcing bar off the beam flanges and embedded into the CFST (refer to Figure 5). The initial elastic stiffness was 57% of the ideal rigid connection. The connection was able to mobilise 92% of the full plastic bending capacity of the beam. The deformed bars were found to be very effective in transferring the beam flange forces into the concrete core, with analysis indicating that 71% of the tension flange force was transmitted into the deformed bar (this force was not sensitive to the thickness of the tube), and 65% of the compression flange force was transmitted through the bars into the concrete infill. The bars virtually eliminated the tube wall distortions experienced by connection type (i). The experimental tests found that the connection behaved well under cyclic loads, with stable hysteresis behaviour up to drifts of approximately 3.5%. Eventual failure of the connection was due to the fracture of the deformed bars which would again tend to suggest that this configuration has the potential to initiate a full plastic hinge in the connection beam when it is correctly sized and detailed.

Kanno and Deierlien (1994) conducted a series of experiments on the connection of steel beams to reinforced concrete columns, where the steel beam is completely embedded into the reinforced column. Kanno et al identify two possible failure modes, a joint panel shear failure (shear distortion of the steel web and concrete joint panel), and joint bearing failure (localised crushing of the concrete above and below the beam). It was found that the bearing failure mode was the less desirable of the two due to the

pinching effect being much larger for this failure mode resulting in the hysteresis loops being less stable with greater strength loss under cyclic loading.

Azizinamini and Prakesh (1993) and Alostaz and Schneider (1996 I and II) conducted both analytical and experimental investigations into the behaviour of a connection in which the steel beam extended continuously through the CFST. It was found that this type of connection accurately represented a fully rigid moment resisting connection which was able to develop the connecting beam's full plastic capacity. This connection exhibited increasing elastic stiffness with higher axial load within the column. Experimental tests on the connection showed that the connection exhibited stable inelastic behaviour with no significant post yield stiffness deterioration reported and was able to develop the beam's full plastic capacity. It was also reported that this type of connection was very expensive. Not only is the cost prohibitive, but when considering the construction techniques employed with this column type ie. column pumped full from base with no vibration of the concrete required, it is likely that such a connection would require some form of concrete vibration to guarantee adequate concrete compaction, further increasing its actual on-site construction cost.

3 CONNECTION SELECTION

Upon review of current connection configurations, assessment of their structural suitability and possible economic viability, and with advice from the industry partner, a joint configuration has been selected for this study. The criteria which has been used to assess its suitability was based on-

- Structural Suitability- the selected connection must be capable of satisfying both serviceability and ultimate seismic design criteria. Connection will be assessed based on its rotational rigidity, ductility, and ultimate strength.
- Constructional Suitability- the selected connection must permit easy fabrication, simple erection, access for inspection and fully facilitate the unique construction methods used when erecting a CFST structure ie. pumping the column full from its base with no internal concrete vibration.

With these in mind the connection configuration selected for this study is shown in Figure 5 and is similar to that studied by Alostaz and Schneider (1996 I and II) as connection (iii). This connection has the following characteristics-

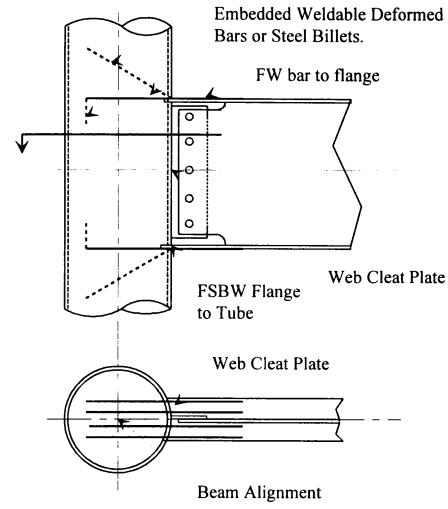

Figure 5
Internally Stiffened Connection with Weldable Reinforcing Bars

- Work on this connection to date (Alostaz and Schneider, and Ashadi and Bouwkamp) would suggest that this connection is capable of mobilising the full plastic capacity of the framing beam, will have good hysteretic behaviour, and behave in a ductile manner. It may however not have the rotational rigidity required to classify it as a full strength connection in its current form and may require some modification.
- This configuration will be highly constructable, and fully facilitate the construction of the CFST. The embedded bars (or steel billets) will offer limited flow restriction to the pumping of the concrete, will not create concrete compaction problems and can be easily installed after the beam has been welded to the tube.
- The weldable reinforcing bars are very effective in transferring the large flange forces into the concrete infill, thus reducing the tube distortion to a minimum. These bars are readily available, cheap and very simple to place.
- The placement of the reinforcing bars will strengthen the beam in the vicinity of the connection, forcing the formation of the plastic hinge to the end of the reinforcing bars.
- From discussions with the industry partner it is expected that this connection will not be cost prohibitive.

The geometry and loading on the connection will be provided from the industry partner to accurately represent column and framing beam member sizes

which can be expected in a tall structure utilising this column type.

4 FINITE ELEMENT MODELLING AND ANALYSIS

The finite element technique will be used initially to optimise the connection configuration and identify critical parameters for its design and behaviour. Little analytical analysis has been conducted on these connections and CFST's to date, likely due to the complex nature of modelling such a system. The main difficulties lie in modelling the various material interfaces and the plastic properties and response of the concrete. There are many commercially available finite element analysis programs on the market today capable of overcoming these difficulties. ABAQUS will be employed for the numerical analysis of this project. MSC/Patran will be used to model the connection and view the results. A discussion of the computer model will now follow.

The concrete core of the column will be modelled using brick elements with three translational degrees of freedom per node. The concrete material model available in ABAQUS will be used to model the core's behaviour. This model can be used to model both plain and reinforced concrete, but has been developed primarily for applications where the concrete is subjected to essentially monotonic loading, with low confining pressures ie. less than four to five times the largest compressive stress that can be carried by the concrete in uni-axial compression. The steel tube will be offering some confinement but the magnitude of this is unclear and it is envisaged that provided the axial load in the column is kept to reasonably low levels it should not be a problem.

The concrete model adopted in ABAQUS models the tensile response based on a smeared crack model. This model does not track individual cracks, rather constitutive calculations are performed independently at each integration point and the presence of a crack is modelled by how it affects the strength and stiffness characteristics of the material associated with each individual integration point. The post cracking behaviour of the concrete is then modelled using orientated damaged elasticity concepts, with the specification of a strain softening parameter (using the *TENSION STIFFENING option). This parameter specifies the post-failure stress as a function of strain across the crack. The value of this parameter is dependant on a large number of variables including the presence and amount of reinforcing, the quality of the bond to the reinforcing bar, the relative size of the aggregate compared to the reinforcing bar, and the mesh density. Once a crack has been detected at a point it is irrecoverable and remains for the rest of the calculation, there is no permanent strain associated with cracking (cracks can completely close if the stress across them becomes compressive) and no more than three cracks can occur at any one point (two in a plane stress case and one in a uni-axial stress case).

The steel tube and beam stub will be modelled using shell elements with 5 degrees of freedom per node and allows for shear deformations. The steel behaviour will be assumed to act the same in tension and compression, and until experimental results are available the assumed stress strain curve will be bilinear with an assumed 2% strain hardening. The embedded reinforcing bar will first be modelled using 3-D brick elements, the same as those used for the concrete.

There are a number of steel-concrete interfaces in this connection which must be accurately modelled to ensure the response of the model, principally the concrete core to the steel tube and the steel reinforcing bars. Both of these interfaces must model the transition between two material types, but the tube to core interface will have the added complexity involved with the transition between different element types ie. 3-d brick to 2-d shell. This interface has been studied by Alostaz and Schneider (1996 I and II) who tested two different approaches. The first approach involved the use of a standard gap element available in ABACUS, which can transfer compression between the elements and the shear force in the gape element represents the bond. It was found that this model experienced convergence problems at large model deformations. The second approach tested used a thin layer of 3-d brick elements with very low strength and stiffness properties. This model exhibited solution convergence at much larger deformations. It is envisaged that both of these approaches will be tested in this project. The second material interface between the reinforcing bar and the concrete has not been studied at this stage but it is expected that some form of nodal compatibility between the materials will be adequate.

The loading onto the connection will be applied in a series of increments. The first loading increment will be the application of the axial column load. Then the moment and shear will be applied in small increments at the girder tip.

5 EXPERIMENTAL TESTING AND PARAMETRIC STUDY

After initial design optimisation and the identification of probable critical connection elements from the initial analytical testing, the selected model will be constructed and tested experimentally. The results of this study will then be used to verify and calibrate the computer model. This model will then be used to numerically expand the results for further study. The end result of this project will be the formulation of design relationships and procedures for a full strength composite beam column connection.

6 CONCLUSIONS

From the research which has been conducted there exists little practical guidance for the design and detailing of full strength moment resisting connections between CFST columns and steel beams. This inadequacy has limited the application of this column type on many projects. It has become apparent that to produce a reliable full strength connection some means of transferring the framing beam's flange forces directly into the concrete core must be provided. How this transfer is achieved will directly control not only the connection's structural performance, but its practicality and hence economical viability.

The connection configuration chosen for this study has been selected based upon the promising seismic performance characteristics which current research findings suggest it would posses, and the highly constructable nature of such a connection configuration. The parameters to be investigated in the project will include the thickness of the steel tube, strength of the concrete, size and embedment length of the steel connector attached to the flanges of the beam and protruding into the column, with the essential condition that the plastic hinge must form on the beam (and not at the connection). It is anticipated that the outcomes of the study will be (i) a better understanding of elasto-plastic behaviour of composite connections under seismic loads, (ii) accurate assessment of energy absorption and ductility of these connections and (iii) provision of simple, but deterministic, design aids.

Analytical work is currently underway and it is envisaged that some of the results from this study will be available for presentation at the conference.

(Beutel, Thambiratnam, and Perera, 11/2/98)

REFERENCES

Alostaz, Y. & Schneider, S. (1996) 'Analytical Behaviour of Connections to Concrete-filled Steel Tubes', *Journal of Constructional Steel Research*, Vol. 40, No. 2, pp. 95-127.

Alostaz, Y. & Schneider, S. (1996) 'Connections to Concrete Filled Tubes', *11th World Conference on Earthquake Engineering*, Acapulco.

Ashadi, H.W. & Bouwkamp, J.G. (1995) 'Behaviour of hybrid composite structural earthquake resistant joints', *10th European Conference on Earthquake Engineering*, Rotterdam, pp.1619-1624.

Azizinamini, A., Prakash, B., Prishtina, B. & Salmon, D.C. (1992) 'New Steel Beam To Composite Column Detail', *Composite Construction in Steel and Concrete II - Proceedings of an Engineering Foundation Conference*, ASCE, Missouri, pp. 854-868.

Azizinamini, A. & Prakash, B. (1993) 'A Tentative Design Guideline for a New Steel Beam Connection Detail to Composite Tube Columns', *Engineering Journal* (AISC), 3rd Qr, pp.108-115.

Azizinamini, A. & Shekar, Y. (1994) 'Rigid Beam-To-Column Connection Detail for Circular Composite Columns', *Structures Congress XII - Proceedings of the Structures Congress 1994*, Atlanta, pp. 1155-1160.

Azizinamini, A. & Shekar, Y. (1995) 'Design of through beam connection detail for circular composite columns', *Engineering Structures*, Vol. 17, No. 3, pp. 209-213.

Choi, S.M., Shin, I.B., Eom, C.H., Kim, D.K. & Kim, D.J. (1995) 'Elasto-Plastic Behaviour of the Beam to Concrete Filled Circular Steel Column Connections with External Stiffener Rings', *Building for the 21st Century - Proceedings of the Fifth East Asia-Pacific Conference on Structural Engineering and Construction*, Griffith University, pp. 451-456.

Dunai, L., Fukumoto, Y. & Ohanti, Y. (1996) 'Behaviour of Steel-to-Concrete Connections under combined Axial Force and Cyclic Bending', *Journal of Constructional Steel Research*, Vol. 36, No. 2, pp.121-147.

Hawkins, N., Mitchell, D. & Roeder, C. (1980) 'Moment Resisting Connection for Mixed Construction', *Engineering Journal* (AISC), Vol 17, 1st Quar, pp 1-10.

Kanatani, H., Tabuchi, M., Kamba, T., Hsiaolien, J. & Ishikawa, M. (1987) 'A Study on Concrete Filled RHS Column to H-Beam Connections Fabricated with HT Bolts in Rigid Frames', Composite Construction in Steel and Concrete - Proceedings of an Engineering Foundaton Conference, New Hampshire, pp. 614-635.

Kang, H.S., Park, J.W., Yoon, M.H., Moon, T.S. & Kim, K.S. (1995) 'Elasto-Plastic Behaviour of Beam - Concrete Filled Circular Column Connections with Internal Stiffeners', *Building for the 21st Century - Proceedings of the Fifth East Asia-Pacific Conference on Structural Engineering and Construction*, Griffith University, pp. 445-450

Kanno, R. & Deierlein, G. (1994) 'Cyclic behaviour of Joints between Steel Beams and Reinforced Concrete Columns', *Structures Congress XXII - Proceedings of the Structures Congress 1994*, Atlanta, pp.1137-1160.

Kato, B., Kimura, M., Ohta, H. & Mizutani, N. (1992) 'Connection of Beam Flange to Concrete-Filled Tubular Column', Composite Construction in Steel and Concrete II - Proceedings of an Engineering Foundation Conference, Missouri, pp. 528-38

Ricles, J.M., Lu, L., Soi, T.K. & Vermaas, G. (1995) 'Seismic Performance of CFT Column - to-WF Beam Moment Connections', *Connections in Steel Structures III, Behaviour, Strength and Design,- Proceedings of the Third International Workshop*, Italy, pp. 99-114.

Shakir-Khalil, H. (1992 - 1) 'Columns of Concrete-Filled Rectangular Hollow Sections', *Composite Construction in Steel and Concrete II - Proceedings of an Engineering Foundation Conference*, ASCE, Missouri, pp. 512-527.

Shakir-Khalil, H. (1992 - 2) 'Full-scale tests on composite connections', *Composite Construction in Steel and Concrete II - Proceedings of an Engineering Foundation Conference*, ASCE, Missouri, pp. 539-554.

Shakir-Khalil, H. (1993) 'Connection of Steel Beams to Concrete Filled Tubes', *Tubular Structures V: Proceedings of the Fifth International Symposium*, pp. 195 - 203.

Shakir-Kahlil, H. (1994) 'Beam connection to concrete-filled tubes', *Tubular Structures VI - Proceedings sixth International Syposium on Tubular Structures*, Melbourne, pp. 357-364.

Webb, J. (1993) 'High-Strength Concrete: Economics, Design and Ductility', *Concrete International*, January, pp. 27-32.

Webb, J. & Peyton, J.J. (1990) 'Composite Concrete Filled Steel Tube Columns', *Second Structural Engineering Conference*, Adelaide, pp. 181-185

Tubular Structures VIII, Choo & Van der Vegte (eds) © 1998 Balkema, Rotterdam, ISBN 90 5809 001 9

High strength steel RHS, domestic flooring system

Masood Alikhail, Xiao Ling Zhao, Lenn Koss & Paul Grundy
Monash University, Clayton, Vic., Australia
Hayden Dagg & Andrew Shield
BHP Steel - Structural and Pipeline Products, Newcastle, Australia

ABSTRACT: A DuraGal floor system consisting of rectangular hollow section (RHS) piers, bearers and joists with particle board deck is studied. A summary of dynamic and subjective tests carried out on different floors and acceptability criteria developed and reported in the literature is presented. Dynamic properties such as natural frequencies, amplitude and damping are reported for a stand alone flooring system. Subjective tests were carried to out to assess the acceptability of the floor. The results from the tests have shown the inconsistency of the available criteria for dynamic acceptability in regard to the system tested.

1 INTRODUCTION

1.1 DuraGal Hollow Sections

DuraGal is a high strength structural product with a light galvanised exterior coating. It consists of steel hollow sections coated on the exterior surface by in-line hot-dip galvanising, which is further protected with a clear polymer coating. The product is typically used in light to medium duty structural fabrication, such as sheds, garages, low rise commercial buildings, etc, where the zinc coating is beneficial as a low cost alternative to paint and primer for corrosion prevention. DuraGal rectangular hollow sections (RHS) have been widely used in Australia. The advantages of DuraGal RHS sections can be summarised as high strength, light-weight, anti-corrosion and aesthetic appeal. Research has been carried out to investigate the member strength (Zhao and Hancock, 1992a, b, c), welded connection strength (Zhao and Hancock, 1996), web crippling capacity (Zhao and Goldberg, 1997) and low cycle fatigue under bending (Grzebieta, Zhao and Sironic, 1997, Zhao, Grzebieta and Sironic, 1998). Ongoing research at Monash University include fatigue of welded connections sponsored by CIDECT, and dynamic performance of light-weight floor system sponsored by APA (Industry). In both cases the industry partner is BHP Steel - Structural Pipeline and Products

1.2 DuraGal Flooring System

A flooring system made from DuraGal rectangular hollow sections (RHS) developed by BHP structural and pipeline products is a light weight high tensile flooring system. This allows a larger joist span compared to timber floor systems. The height of the piers can be adjusted before and after assembly, allowing accurate leveling of the floor, compensating for variations in the footing. Particle boards are usually used for decking of the floor. The system typically has a 90x90x2 piers, 150x50x2 bearers and 100x50x2 joists. The joist span is usually 2.6 m as opposed to the timber joist on brick piers which traditionally spans 1.8m. The steel (cold-formed) hollow sections used in the manufacture of the DuraGal flooring system are in-line hot-dip galvanised and are practically maintenance free (AISC (construct in steel) 1996).

A structural grade particle board (*Structaflor)*, is the decking. This flat pressed, class 1 particleboard decking complies with Australian Standard AS1859-1980. It is made from precision milled wood flakes and bonded with moisture resistant synthetic resin. The upper surface is resin enriched and all edges are sealed for additional protection. Structaflor is sanded on the underside for thickness control, the edges are factory grooved and can be fitted with rigid PVC tongues. The board are supplied at 600 and 900 widths (Introduction and applications 1996).

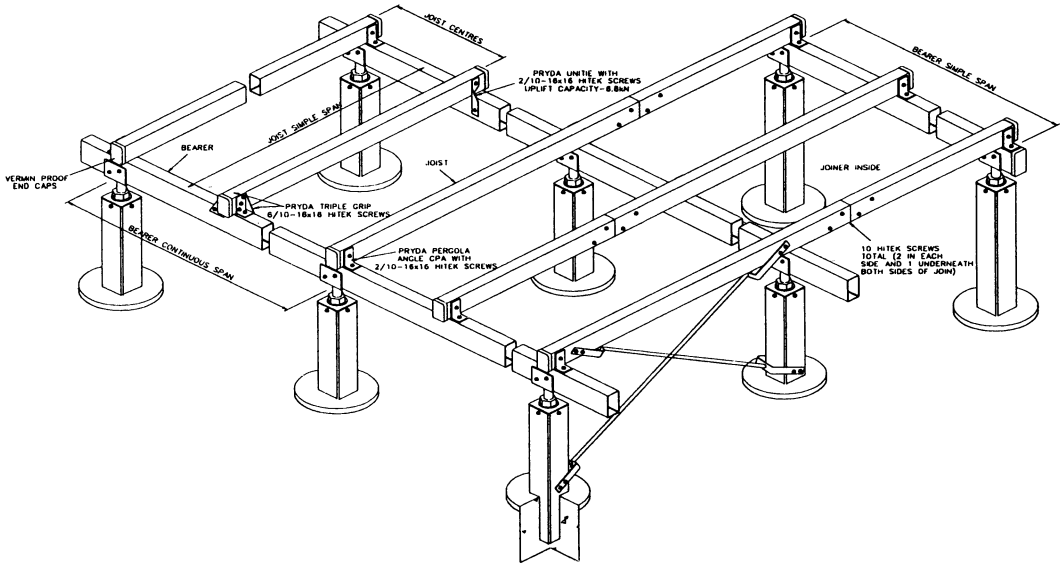

Figure 1 Typical set up of DuraGal Floors (DuraGal flooring systems 1997).

1.3 Existing Research On Floors

A serviceability problem which occurs for floors is "annoying vibration". There have been many studies in this area and these can be divided into two categories (Onysko 1995):

1. Perception based studies in which subjective response of humans to vibration, independent of the type of occupancy, is investigated. The study by Reiher and Meister in 1931 is one of the first investigations of this kind (Reiher and Meister 1931). In their investigation 10 people were subjected to floor vibration at different frequencies and displacement amplitudes and their subjective response or degree of annoyance was recorded.
2. Acceptability based studies in which data from floor testing (or inspection) and subjective evaluation of acceptability form a database for correlation studies. The acceptability based studies search for dynamic or static parameters of floors to correlate with subjective evaluation or acceptability. In dynamic tests it is usually assumed that the person bases his/her opinion on perception of vibration, however it has been suggested that the opinions are rather based on responses to disturbances such as jolts or vibration of objects (Onysko 1995).

An acceptability based study directed by Lenzen (Lenzen 1966) was started in the 60's. This study was continued by Murray (Murray 1981, Murray 1991, Allen and Murray 1993) and was complemented by work from Allen and Rainer (Allen and Rainer 1976).

This paper gives a summary of studies on different floor systems. Table 1 summarises some of the floor tests reported in the literature followed by Table 2 which is a summary of the subjective tests and Table 3 a summary of acceptability criteria developed by different authors.

These studies indicate that no previous research has been undertaken on this type of flooring system. The information given in the tables indicates the order of magnitude of frequency, amplitude and damping one normally encounters in floor serviceability studies.

The different criteria for dynamically satisfactory floors listed in Table 3 can be applied to DuraGal floor systems for comparison with the conclusions of this study.

2 EXPERIMENTAL INVESTIGATION

2.1 Test Floor

This paper reports on the first test of a set of floors that will be investigated in the near future. This is a stand alone floor (Fig 2) with no ceiling and walls which is summarised in Table 4.

Three bearers, 9m long, are fitted on top of 0.6 m high piers and are bolted to concrete ground. The joists are placed 0.45 m apart each 7m long. The floors are covered with 19mm thick Structaflor particle boards.

Table 1. Summary of floor studies.

Reference	Type of floor	Frequency	Damping	Excitation method	Span	Comments
Lenzen 1966	steel beams concrete slabs	only the first mode studied (not available)	not available	heel drop	moderate (~7-10 m)	SDOF* calculation done using idealised heel drop model
Allen &Rainer 1976	concrete slabs on steel joists or beams	fundamental only (3.6-16 Hz)	log-decrement (2-12 %)	heel drop	long span (7-22.3 m)	Conclusion is limited to long span floor using a heel drop only
Ohlsson 1982	timber floors	first 5modes (12-70Hz)	0.5-1.3%	hammer impact, continuous loading, random walking &heel drop	3.5,4.25,5m	Random walk excites the first four modes. Measured data is compared with plate model results of the floor
Ohlsson 1982	Trapezoidal steel sheet, plywood deck	first 7modes (7-30Hz)	0.4-2.8%	as above	7.2m	as above
Murray 1991	concrete slabs steel joists	5-8Hz	1-20 %	heel drop	not mentioned	Criterion: $D>35Af_O+2.5$**. Not for floors with f_O>10 Hz
Allen & Murray1993	one-way and two-way steel joists and concrete slabs	4-8.8 Hz	1-3% bare floor 1-10% duct work and 10-20% partitioned	heel drop	8.7-22.2 m	Equation of steady state acceleration by Rainer is used to calculate the fundamental frequency

* Single Degree of Freedom

** D= percentage damping ratio, A= displacement amplitude in inches, f_O= fundamental frequency

*** Finite Element Analysis

Table 2. Summary of subjective tests

Test	Floor type	Number of people or floors involved	Type of excitation	Amplitude, frequency and damping	Comments
Reiher and Meister 31	vibrating table	10 people	sinusoidal continuous vibrating table	0.0254-1.02mm,5-70Hz	horizontal and vertical vibration for ~5minutes
Wiss and Parmelee 74	vibrating table	40 people	transient vibrating table	0.0254-0.25mm, 2.5-25Hz, 1-16%	empirical formula was developed
Onysko &Bellosilo 78	timber joist span 3-5.1m	646 floors	1 kN concentrated load	n.a.	subjective response of occupants correlated to static deflection
Allen and Rainer 76*	steel and concrete (span >7m)	42 floors	heel drop	0.05-0.2g, 0-30Hz, 3-12%	good correlation between acceptability and amplitude and ξ
Atherton &Polensek76 *	timber floors	24 floors, span: 2.7-5.2 m	heel drop and dropping weight impact	correlation found between amplitude and rating	At equal rating impact amplitude was 4-8 x walking amplitude
Atherton and Cordate 78*	mostly timber floors	telephone survey 687 dwellings	n.a.	confirmation of above correlation	n.a.
Murray 81*	steel beam concrete slab, span > 7m	91 floors	heel drop	not given	criterion: $D>35Af_O+2.5$**
Ohlsson 82	8 timber floors	15 people	heel drop and random walk	12-70 Hz, 0.5-1.3%	span size and ceiling board affected rating
Ohlsson 82	2 steel Trapezoidal sheet floor	15 people	heel drop and random walk	7-30 Hz, 0.4-2.8 %	n.a.

* Source for these tests are Ohlsson 82

Table 3 Summary of floor vibration criteria

Reference	Country, Code	Static Criteria	Dynamic Criteria	Validity	Comments
Ohlsson 1982	Australia, AS3623	Δ* **< 2mm under 1 kN concentrated Load**	$logV_{max}<1.2+2f\zeta$* * under 1Ns impulse	first resonance > 8Hz UDL of 0.3 KPa	Timber and steel floors
Onysko and Bellosillo 1978	Canada	$\Delta<8/(span)^{1.3}$ **under 1kN**	nil	first resonance >15Hz floor span > 2.9 m	Timber floors
Onysko and Bellosillo 1978	Canada	Δ**<2mm under 1kN**	nil	floors with span <2.9 m	Timber floors
Onysko 70	Canada, CSA, S136-94	**0.5-1mm deflection under 1kN**	nil	steel joist, wood deck, 10-25 Hz generally	timber floors criterion used
survey of 100 floor systems by Murray 81	USA	**nil**	$D>35Af_O+2.5$**	first resonances < 10 Hz	Concrete floors
Ohlsson 1988	Swedish Building Code SBN 1980	Δ **< 1.5mm (or span/600) under 1kN**	nil	timber floors	
Ohlsson 1988	Swedish Building Code SBN 1980	**span/400 under 1kN**	nil	steel floors	

* Δ = deflection

** V_{max} =maximum velocity, ζ =modal damping ratio

D= percentage damping ratio, A= displacement amplitude in inches, f_O= fundamental frequency

UDL = Uniformly distributed load

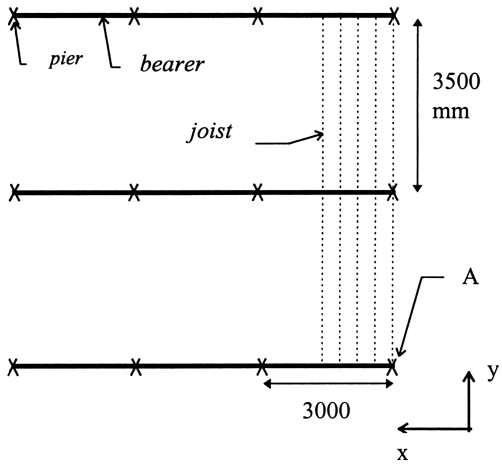

Figure 2 Plan view of floor used in first test. (See Table 4 for details.)

Table 4 Summary of Floor Characteristics.

	Mass kg/m	*Span & spacing (mm)*	*Type & Dimensions(mm)*
Bearers	6.07	3000	RHS, 150x50x2, 3of 9m length
Joists	4.5	3500, 450	RHS, 100x50x2, 20 of 7m length
Piers	5.45	600 (height)	SHS, 90x90x2, 12 of 0.6m length, adjustable height
Decking	10 kg/m^2		19 (thickness) particle boards, 63 m^2, Nailed and glued to joists

2.2 Test Procedure

To perform the test an accelerometer was placed at positions (0,0), (0,3500/2), (0,3500), (1500,0), (1500,3500/2) and (1500,3500) on the floor (Figure2). Origin is marked as point A in the figure. Acceleration was measured after an excitation was applied at each point using three methods:

1. Hammer impact on the floor, with no weight on the floor.
2. Hammer impact with a person standing on the floor very close to the point of application of the impact and
3. A human heel drop test.

The impact hammer is equipped with an in-built force transducer. The accelerometer and the force transducer are connected to a frequency analyser which calculated the frequency response (FRF) of the floor. The resonances were identified with the aid of a dynamic analysis software (Icats) which calculated the damping and uncertainty.

3 RESULTS

3.1 Natural frequencies (Resonances)

In the frequency range of 0-50 Hz there are more than 16 resonances. As lower modes affect human perceptibility significantly (Allen and Rainer 76) only the resonances in the 0-20 Hz range have been considered. The results using different excitation techniques are given in Table 5.

In Table 5 first row shows the coordinate of positions on the floor shown in Figure 2 where M+ and M- refers to the presence or absence of weight in the impact hammer test. Note that heel drop test is only performed for three positions and for last position only test with weight is performed. It should be pointed out that the mode under 10 Hz was not observed using the hammer impact at first, but they were observed, although not very clearly, when a low pass filter was used. The FRFs became more clear when windowing was used to isolate the impulse from hammer impact and the resulting vibration in the floor. The fundamental resonance is taken to be 3.67±0.08 Hz and there is a minimum of 13 resonances in the frequency range of 0-20 Hz. As can be seen from the table 5 the excitation method does not affect the resonance frequency beyond the measurement error but the number of resonances observed is affected. No Particular pattern emerges from the use of different excitation methods. The only observation that can be made is that the presence of mass damps out some of the resonances and heel drops excite the least number of resonances. The empty spaces signify the modes that were observed in one location but were not observed in others.

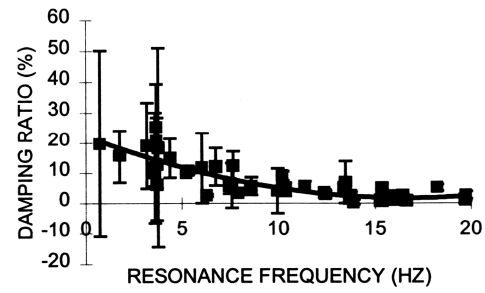

Figure 3 Damping vs their resonance frequency

Table 5 Resonance frequencies in Hz, in the 0-20Hz range for the test floor.

(0, 0)		(0, 3500/2)			(0, 3500)		(1500, 0)			(1500, 3500/2)			(1500,3500)
M+	M-	M+	M-	heel drop	M+	M-	M+	M-	heel drop	M+	M-	heel drop	M+
			0.3			0.2		0.35					
					0.94		0.74						
					1.75	1.28	1.59						
			3.18										
3.75	3.66	3.65	3.7	3.6	~3.6	3.6	3.6	3.7	3.6	3.6	3.63	3.65	3.68
			4.39										
		5.23	5.35	5.9									
		6.76					~6	~6				6.85	6.05
			7.49	7.4			~7.9		7.9	7.6	7.93	7.85	7.66
		~8.6	8.6				~8.6	8.57					
		10.2	10.3				~10	9.95		10.35		10.35	
			11.37									11.95	
		~12.5	12.45				~12.4	12.4					
		13.49	13.4	13.75			13.75	13.7	13.6	13.9	13.51	14.05	13.76
		~15.3	~15.3	15.45			~15.3	15.4	15.25		15.28		15.36
	15.88	15.8	15.85	15.95			15.8	15.8	15.8	15.75	15.8	15.75	
		16.43	16.37	16.6			~16.3	16.3	16.45	16.32	16.44	16.3	
							~18.2	18.23					
		19.72	19.7					19.69	19.6	~19.7	~19.7	19.5	

3.2 Damping Ratio

The calculated damping ratios are plotted vs resonance frequency in Figure 3. It illustrates decrease in damping with increasing frequency.

The analyser damping function was used to calculate damping using the half power method on the frequency spectrum of the response. The result is summarised in Table 6, which shows the effect of different mass and excitation on the magnitude of damping.

The data indicates that the damping values depended on how the system was excited. The empty spaces signify that resonance was not sufficiently prominent to calculate damping. The damping ratios calculated using the software and the analyser are comparable but are not exactly equal. The difference can be due to the use of two different techniques in the calculations and measurement errors.

3.3 Accelerations

Acceleration amplitude was calculated at points (0, 3500/2), (1500, 0) and (1500, 3500/2) as these points have lower stiffness compared to other locations on the floor. As a consequence these points will have the highest deflections and are the points which would cause the highest annoyance. Measurements from heel drop test were used to extract the acceleration amplitude using the sensitivity of the accelerometer (105 mV/g). Results are shown in Table 7

Table 6 Damping values (fraction of critical) for the modes in the 0-20Hz range estimated using the analyser.

	Heel drop	hammer (FRF)	hammer (spec)	hammer + person	people (FRF)	people (spec)
First mode 3.8 Hz	.12	-	-	.07	.06	.07
Second mode 13.8Hz	.02	.01	.01	.02	-	-
Third mode 15.8 Hz	-	.01	.01	-	-	-
Fourth mode 16.8Hz	.07	.01	.01	.04	-	-

Table 7 Acceleration amplitude for the resonances which were identifiable in the heel drop test.

Frequency(Hz)	Acceleration		Frequency(Hz)	Acceleration		Frequency(Hz)	Acceleration	
at (0, 3500/2)	g	$m/s^{2}_{(r.m.s)}$	at (1500, 0)	(g)	$m/s^{2}_{(r.m.s)}$	(1500, 3500/2)	(g)	$m/s^{2}_{(r.m.s)}$
3.6	0.16	1.1	3.6	0.05	0.35	3.65	0.2	1.4
5.9	0.06	0.4				6.2	0.07	0.49
						6.85	0.07	0.49
7.4	0.07	0.49	7.9	0.03	0.2	7.85	0.08	0.55
						10.35	0.08	0.55
						11.95	0.08	0.55
13.75	0.12	0.83	13.6	0.06	0.4	14.05	0.16	1.1
15.45	0.09	0.62	15.25	0.08	0.55			
15.95	0.11	0.76	15.8	0.09	0.62	15.75	0.07	0.49
16.6	0.15	1.0	16.45	0.09	0.62	16.3	0.09	0.62
			19.6	0.05	0.35	19.5	0.16	1.1

3.4 Stiffness Test

The static deflection of the floor as a concentrated load is applied on it was measured using dial gauges. The concentrated load is applied at the mid-span of the central joist at position (4500, 3500x2/4) and the deflections are measured at positions: (4500, 3500x1/4), (4500, 3500x2/4), (4500, 3500x3/4) (figure 2). The results for the above three points called l, c and r are plotted in figure 4.

The right side has a greater deflection than the left side because the right side is close to an end support whereas the left side is close to an interior support (Figure 2).

3.5 Subjective Test

A survey on the acceptability of the floor was undertaken. Thirty five people were given a questionnaire and asked to evaluate the floor while a person was walking on it and during some heel drop tests. The result is plotted in Figure 5.

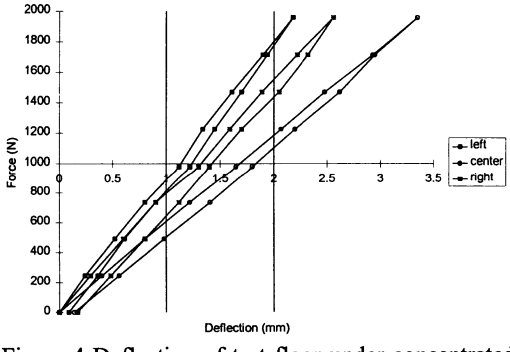

Figure 4 Deflection of test floor under concentrated load.

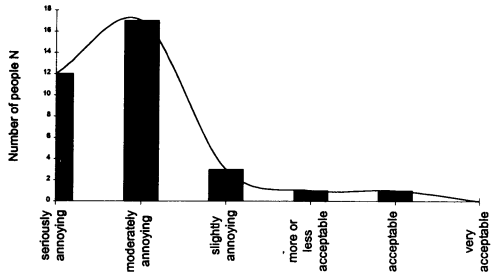

Figure 5 Human sensitivity response to test floor vibration.

4 COMPARISONS

The stiffness of the floor system can be derived from the slope of deflection graph of the floor under concentrated weight. The slope is the stiffness of the floor. Taking the floor as a SDOF system we can predict it's fundamental frequency using $\omega^2=k/m$. From table 4 the total mass of the floor including the piers is 1424 Kg, and stiffness at the centre of the joist and a quarter of length from the left edge is $1.114x10^6$ and $0.583x10^6$ N/m respectively which gives frequencies 3.22 and 4.45 Hz which are comparable to our measured fundamental of 3.8 Hz.

There are two types of performance criteria for a floor: dynamic and static.

The dynamic criterion looks for a limit in velocity, acceleration or any other dynamic characteristic of the floor due to an idealised 1 Ns impulse or from a heel drop test. The static or deem-to-comply criterion limits the deflection or the ratio of span to deflection of the floor due to 1 kN concentrated force or 1.5 kPa of uniformly distributed load (UDL) below a set value.

The Australian criterion seems not to be applicable to the floor as its first natural frequency is less than 8Hz, even though the floor satisfies the static deflection condition ie $\Delta < 2$mm (Figure 4). This floor also satisfies the dynamic criterion ie $log(V_{max}) < 1.2+2f_o\xi$.. V_{max} was found to equal 0.82 (refer to appendix A for calculation) and the values for f_o *and* ξ *are* 3.6Hz and 0.12 taken from Table 5 and Figure 3 respectively. $log(V_{max})$ =-0.086 is smaller than the left side of the above inequality.

The Canadian Criterion by Onysko (Onysko 95)is $\Delta < 8/(span)^{1.3}$, ie a deflection (Δ) limit is set for a concentrated load of 1kN if it applied anywhere on the floor. For span = 3.5m Canadian criterion is $8/1^{1.3}$ = 1.57mm. As Δ=1.7mm for the test floor (figure 4) it does not satisfy the above criterion. This criterion was developed for timber floors.

Murray's criterion ($D>35Af_o+2.5$) which is extensively used in the US sets a minimum limit on percentage damping of the fundamental mode of 2.5%. The displacement amplitude in the floor can be found by dividing the acceleration by $(2\pi f)^2$, using the highest acceleration from table 7 so $35Af_o+2.5=16$. This is higher than the 12% damping shown in Figure 3. This floor satisfies Murray's criterion, which was developed using data from concrete floors.

The Swedish Criterion (Murray and Kraus 1996) at 1 kN load is that the deflection $\Delta < 1.5$ mm or the deflection of the floor due only to live load does not exceed span/600. As the test floor deflection was 1.8 mm at 1 kN the floor did not satisfy the Swedish static criterion. This Criterion is used for timber floors.

5 CONCLUSIONS

DuraGal floors have been introduced and it was shown that most of floor serviceability criteria may not be applicable to these floors. The available criteria and floor test were surveyed and comparisons were made. One test floor was investigated using three different excitation method and the results showed that the excitation method affects the number of modes excited but not the resonance frequency of the mode. The results were applied to available criteria. The results from the test floor showed the inconsistency of available criteria and the need for developing an acceptability criterion for DuraGal type floors.

6 FUTURE RESEARCH

Future work will include

- Experiments on eight more test floors
- FEA modelling
- Design Criterion recommendation

Over all project for producing acceptability criteria can be summarised by the following chart

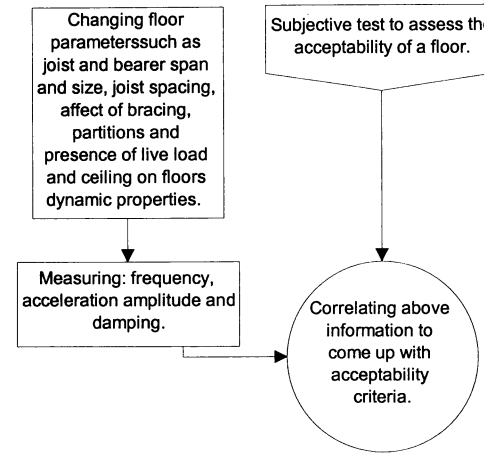

Appendix A

. [Note: According to Australian Standard, Domestic Metal Framing, AS3632-1993, the maximum velocity response to an impact of 1 N-s can be approximated by the following equation:

$$V_{\max} = 4\left(\frac{0.4 + 0.6N_{40}}{wBL + 200}\right)$$

where

$$N_{40} = \sqrt{\left(\frac{r + f^2 - 1}{r}\right)} - 1$$

N_{40} = the number of modes with natural frequency less than 40Hz.

s = joist spacing = 0.45 m

$k_x = E_b I_b/s$ (the flexural stiffness of the main member)=$(2x10^{11}Pa)(2.08x10^{-6}m^4)/(0.45\ m)$

$=0.92x10^6$ Nm

$k_y = E_f t_f^3/12$ (the flexural stiffness of flooring, fort joist-only system)

$=(3x10^9\ Pa)(0.019\ m)^3/12$

$=1.7x10^3$ Nm

r = the ratio of the floor stiffness in two direction ie $k_y/k_x = 1.85x10^{-3}$

f = the frequency ratio $(40/f_1)$

As f_1 (the first natural frequency)is 3.6Hz then f=11.1Hz

w = is the mass of the floor per unit area including the live load mass, in kg/m^2

=22.6 kg/m^2

B = the width of the floor in metres = 7 m

L = span of the joists in metres = 3.5 m

so V_{max} = 0.82 m/s

ACKNOWLEDGMENTS

The floor for this experiment was constructed by the building department of Holmesglen TAFE college. Material and financial help was provided by Structural and Pipeline products BHP and ARC APA(I).

REFERENCES

Allen, D. E. and Rainer, J. H. (1976). Vibration criteria for long span floors, Canadian journal of civil engineering, vol 3 number 2, Pp165-173.

Allen, D. E. and Murray, T. M. (1993). Design criterion for vibration due to walking, engineering journal / American institute of steel construction

Atherton, G., Polensek, A. and Corder, S., (1976) Human response to walking and impact vibration of wood floors, Forest product journal, Vol 26, No 10, Oct 1976, pp 41-47

Atherton, G., and Corder, S. E., (1978) Human response to vibration of floors in occupied dwellings, Forest Res. Lab. Paper No 1.249, School of Forestry, Oregon State Univ., 1978

Australian Standard, Domestic Metal Framing, AS3632-1993, published by Standards Australia (Standard association of Australia) 1 the Crescent, Homebush, NSW 2140.

Australian Standard, AS1859-1980, published by Standards Australia (Standard association of Australia) 1 the Crescent, Homebush, NSW 2140.

AISC (Construct in Steel), Vol 9 No3 September 1996

DuraGal Flooring System, June (1997) BHP Structural and Pipeline Products, An operating business of Tubemakers of Australia, CAN 007 519 646

Grzebieta, R. H., Zhao, X. L. and Purza, F. (1997), Multiple low cycle fatigue of SHS tubes subjected to gross pure bending deformation, 5th Int. Colloquium on stability and ductility of steel structures, Nagoya, Japan, July, 847-854

Haritos, N. (1994), Experimental modal analysis in structural engineering applications, proceedings, Australian Structural Engineering conference, 21-23 September, Sydney

Icats, Modacq/Modent/Modesh/ Couple Reference Manual, Imperial College, analysis, testing and software, Imperial college of Science, Technology and Medicine, Mechanical Engineering Department, Exhibition Road, London SW 7 2BX

Lenzen, K. H., (1966), Vibration of steel joist-concrete slab floors. AISC Engineering Journ., July1966, pp. 133-136

Murray, T. M. (1981). Acceptability criterion for occupant-induced floor vibration,AISC engineering journal / American institute of steel construction, No 2,1981, pp 62-70

Murray, T. M. (1991). Building floor vibration, engineering journal / American institute of steel construction

Murray, T. M., and Kraus, C. A., (1996) Development of design criteria for cold formed c-section supported residential floor systems, National Association of Home Builders, Upper Marlboro, Maryland Sept 1996.

Onysko, D. M.,(1970) Performance of wood joist floor systems- a literature review. Forest Products Laboratory Information Report OP-X-24, Canadian Forestry Service, Department of Fisheries and Forestry, Jan 1970

Onysko, D. M., and Bellosillo, S. B. (1978) Performance criteria for residential floors, Eastern Forest Products lab. Final report to Central Mortgage and Housing Corporation. Grant No 120-74 Ottawa ON.

Ohlsson, S. (1982). Floor Vibration and human discomfort, Ph. D Thesis, Division of steel and timber structures. Chalmers University of Technology, Goteberg Sweden

Ohlsson, S. (1988), Springiness and human-induced floor vibration, A design guide, Swedish Council for Building Research, Stockholm, Sweden

Onysko, D. M.,(1995) Some background on factors affecting performance of floors and setting of performance criteria, presentation to task group, the forintek study on serviceability criteria for floors, 9 July 1995

Reiher, H. and Meister, F.(1931) Eie empfindlickkeit des Menschen gegen erschutterungen, forschung auf dem gebiete des ingenieurwesens, Vol 11, No 2, 1931, pp 38-386

Introduction And Application, Structaflor, May 1996, CSR Wood panel, CSR limited, Level 7, 9 Help street, Chatswood NSW 2057, Lock bag No. 6, Chatswood NSW 2057

Zhao, X. L. and Hancock, G. J. (1992a), Tests on rectangular hollow section to investigate the effect of

variation of yield stress around a section, Investigation report, No. S885, January, Center for advanced structural Engineering, the University of Sydney, Sydney, Australia
Zhao, X. L. and Hancock, G. J. (1992b), Test to determine the reliability of stub columns of DuraGal RHS, Investigation Report, No. S916, January, Center for advanced structural Engineering, the University of Sydney, Sydney, Australia
Zhao, X. L. and Hancock, G. J. (1992c), Test to determine the reliability of beams of DuraGal RHS, Investigation Report, No. S917, January, Center for advanced structural Engineering, the University of Sydney, Sydney, Australia
Zhao, X. L. and Hancock, G. J. (1996), Welded connection in thin cold-formed rectangular hollow sections, in Connections in steel structures III, Bjorhovde, R. Colson, A. Zandonini, R. (eds), Pergamon, Oxford
Zhao, X. L. and Goldberg, E. (1997), Web Crippling of Partially stiffened RHS sections, 5th international colloquium on stability and ductility of steel structures, Nagoya, Japan, July, 173-180
Zhao, X. L., Grzebieta, R. H. and Sironica, E. (1998), Void-filled SHS beams subjected to high amplitude cyclic bending, 8th International symposium on tubular structures, August, Singapore

Tubular Structures VIII, Choo & Van der Vegte (eds) © 1998 Balkema, Rotterdam, ISBN 90 5809 001 9

Experimental study of connections between longitudinal plates and RHS columns

J.J.Cao, J.A.Packer & N.Kosteski
Department of Civil Engineering, University of Toronto, Ont., Canada

ABSTRACT : In order to investigate the behaviour of welded connections between longitudinal plates and RHS columns, 10 specimens, in an X configuration, with four different angles (90°, 60°, 45° and 30°) between plates and columns have been tested. Plate thickness, column cross section and the connection area between plate and column for all the test specimens have been kept constant. Different column compression "preloads" were applied to the RHS columns first and then tension forces were applied to the plates of the specimens. All the specimens were tested to rupture and the load-displacement behaviour of the column connecting face and the stress distribution across the branch plate were obtained from the tests.

1. INTRODUCTION

Rectangular Hollow Sections (RHS) have been used widely as columns in different structures, due to their superior column performance. As a traditional and convenient connecting method, plates are sometimes welded to the faces of columns (or truss chord members), either longitudinally or transversely, to connect beams, braces and other attachments. The flanges of an I-beam connected to an RHS column can be also considered as a pair of transverse plates. Since the connecting face of an RHS member is flexible, special precautions should be taken for the design of plate connections.

A lot of research work has been undertaken for plate connections related to I-beam-to-RHS column connections. In order to study the interaction between I-beam flanges and RHS columns, Lu et al. (1993, 1995) analysed a large number of connections between transverse plates and RHS columns using Finite Element models. Dawe & Guravich (1992) tested 13 connections between transverse plates and RHS columns with stiffening plates on the RHS connecting faces. Sherman (1996) has performed a large number of tests for nine different types of simple connections for I-beams with RHS columns. One type of connection was the "shear tab", which is a longitudinal plate under shear (force parallel to the RHS column). Other types of shear connections using tees or angles can be thought of as longitudinal plate connections with stiffening plates on the RHS connecting faces. Design rules for such simple (shear) connections have been proposed from the work. Dawe & Mehendale (1995) also tested 10 shear connections between tees and RHS columns.

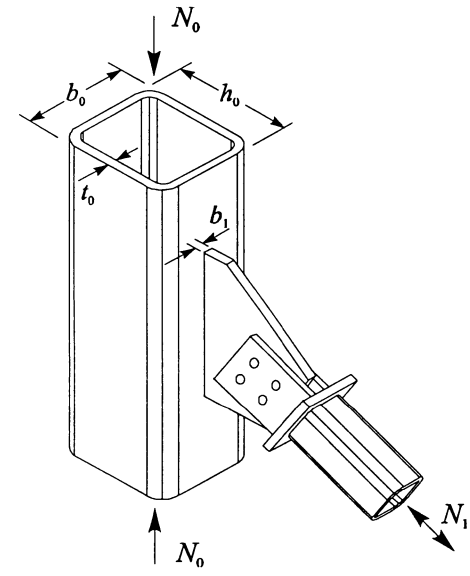

Figure 1 Longitudinal plate connection

On the other hand, not much work has been done for longitudinal plate connections used to connect brace members to RHS members. In Figure 1, a longitudinally oriented plate is welded to an RHS column to connect a brace member. The column is under the action of compression load and the plate is under the action of the axial load from the brace member. Although this connection is very flexible and provides low connection resistance, it is still a popular choice for some braced structures. However, there is not much reliable information available for design of this type of connection.

In order to develop a reliable design method for longitudinal plate connections, experimental tests and Finite Element (FE) analyses have been carried out at the University of Toronto for a large range of longitudinal plate connections. The test program is reported in this paper and the FE analyses are reported in another paper (Cao et al. 1998).

2. SPECIMENS

Ten specimens with four different angles between plates and columns have been tested in the program. Figure 2 shows the assembly for a non-90° specimen. The column of the specimen is RHS 178x127x7.6 and a 13.1mm thick plate was welded to the column. The RHS 127x127x11 opposite to the branch plate was used as a reaction and cut from a previously-tested specimen. Two tongues, at both the plate side and the reaction side, were used to grip the specimen in a tension testing machine so that tension force could be applied to the connection between the plate and the column. In order to avoid any constraint to the deformation of the column top face, the branch plate was connected to the tongue by means of a pin connection.

The hydraulic jack shown on the left hand side was used to apply column preload through a high strength steel rod and the load cell shown on the

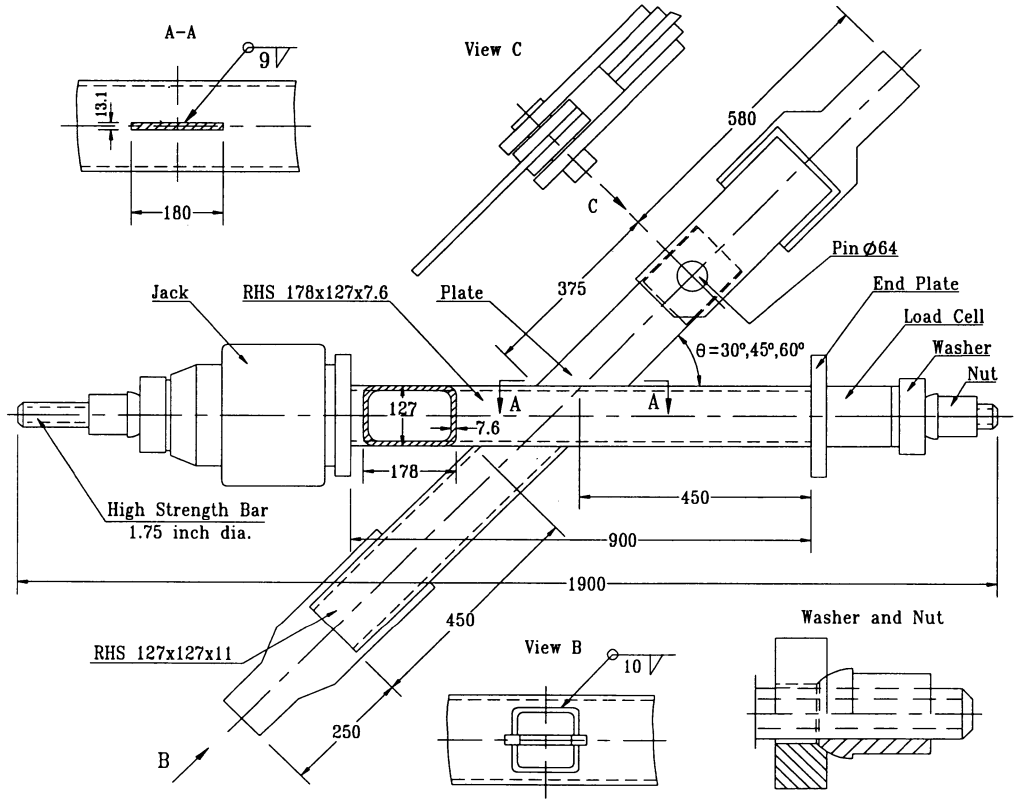

Figure 2 Assembly for 30°, 45°, 60° specimens

right hand side was used to measure the compressive load applied to the column. Two thick end plates were placed at the two ends of the column to ensure uniformly distributed compression load on the column. As shown in the figure, a round head nut with a special washer was used at each end of the rod so that rotation between the washer and the rod was allowed, which occurred for all the tests.

Arrangement for a 90° specimen is the same as that for a non-90° specimen except that a tongue was made at the end of the branch plate without a pin connection. Although the angles between the plates and the columns were changed for different specimens, the "footprint" between a plate and a column was kept to be the same; i.e. the contact length was always 180mm long and oriented along the centreline of the column connecting face.

One length of RHS was used for all the columns and all the branch plates were cut from one sheet of steel plate, so the column cross section, plate thickness and material properties can be thought to be constant. The RHS used was a cold-formed, stress-relieved, Class H 350W section. All the welds were made as fillet welds by MIG welding using metal-cored wire and the branch plates were always placed on the RHS walls opposite to the tube seam. All the welds were visually examined carefully so as to minimize the existence of weld defects.

The dimensions of the RHS cross section, plate thickness and the size of welds connecting the columns and the plates were measured carefully and all the measured properties of the specimens are given in Table 1. The specimens were named based on the angle between the plate and the column, and the preload applied to the specimen. The first two digits of a name for a specimen refer to the angle between the plate and the column and the last one or two digits refer to the amount of column preload as a percentage of the squash load, rounded to the nearest ten percent.

Tensile tests have also been carried out on two coupons for each of the column and plate materials and the average values of several key material properties are also presented in Table 1.

Table 1 Measured geometrical and mechanical properties of test specimens

Specimen	Angle θ (degrees)	Preload N_0 (kN)	Preload Ratio $(N_0/F_{y0}A_0)$ %	Weld Size w (mm)
90LP0	90	0	0	9.5
90LP20	90	-300	-18.7	9.2
90LP40	90	-600	-37.4	8.2
90LP60	90	-900	-56.1	8.9
45LP0	45	0	0	7.3
45LP20	45	-300	-18.7	7.3
45LP40	45	-600	-37.4	8.0
45LP60	45	-900	-56.1	9.0
60LP0	60	0	0	7.2
30LP0	30	0	0	7.7

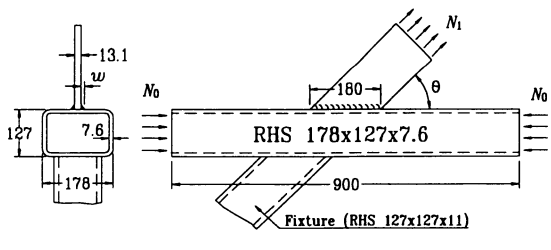

For columns:
Yield strength (F_{y0}) = 378MPa
Ultimate strength = 506MPa
Young's Modulus = 210,600MPa
Cross section (A_0) = 4242mm^2

For plates:
Yield strength (F_{yp}) = 408MPa
Ultimate strength = 540MPa
Young's Modulus = 217,900MPa

3. TEST SET-UP

All the tests were conducted using a 1000kN capacity MTS Universal Testing Machine and a typical testing arrangement is shown in Figure 3. The two tongues of the specimen were gripped by the machine and the upward movement of the cross head exerted a tension load on the branch plate. The column compression load was applied by the hydraulic jack which was operated by a hand pump and could apply a maximum load of 1000kN.

Figure 4 shows typical instrumentation for a specimen. Two Linearly Varying Displacement Transducers (LVDTs) were arranged at the centre cross section of the RHS column (A-A in Fig. 4) and four LVDTs were arranged along the centre line of the RHS top surface. All the LVDTs were mounted on a bar, which was parallel to the column and fixed to the plate, so the deformation of the RHS connecting face, relative to the plate, at different locations could be obtained. Normally the deformation of the column top face, in the direction of the LVDTs, is much larger than the deformation of the branch plate itself and column side walls in this direction, so the LVDTs actually measured the deformation of the column connecting face reasonably accurately. The maximum deformation of the RHS connecting face could be obtained from the LVDT located at the mid-height of the RHS centre cross section. Five strain gauges, parallel to the plate sides, were placed on the plate to measure the stress distribution across the plate.

All data, including the upward movement of the machine cross head, the tension load (N_1) applied to the plate, the column compression load (N_0), measured by the load cell, and readings from the LVDTs and strain gauges, were recorded by a data acquisition system.

After a specimen was set up, all channels recording data were initialised. For a test without column preload tension load could then be applied to the plate. For a test with column preload, the desired column compression load was applied first using a hand pump. After column preload was applied all channels were scanned to record the influence of column preload (for some specimens). The channels were initialised again before tension load was applied to the plate in order to remove the influence of column preload on these measurements. During a test, column preload was monitored and held constant throughout the test. Tension load was increased under displacement control and all specimens were loaded until rupture. Data readings were made at every 0.2-0.25 mm of displacement or at every 5kN of load.

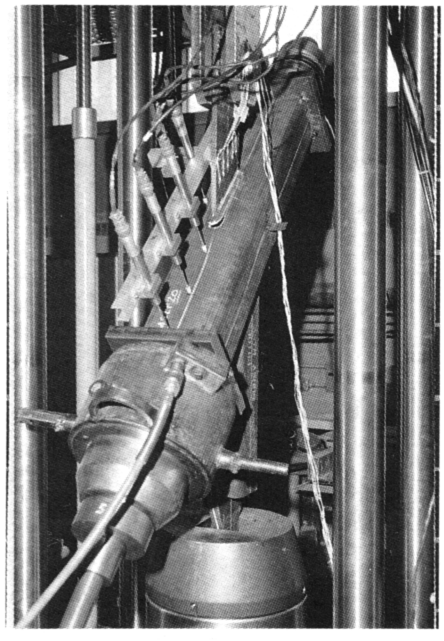

Figure 3 Typical testing arrangement

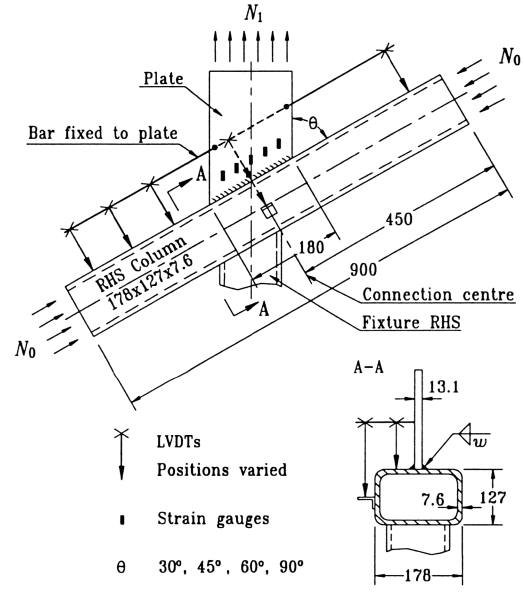

Figure 4 Arrangement of LVDTs and strain gauges

4. TEST RESULTS

From the tests, the failure mode, the deformation profile of the column connecting face, the load - displacement curve and the stress distribution across the branch plate for each of the specimens were obtained.

4.1 *Failure mode*

All specimens tested are shown in Figure 5. The figure also shows clearly the difference between the branch plates for 90° and non-90° specimens. For a 90° specimen, the plate is symmetric to the connection centre, so a tongue was made at the end of the plate and the plate was gripped directly by the testing machine. When deformation was not very high, the connecting face deformed symmetrically to the connection centre. When deformation was high, cracks usually initiated at one or both ends of the plate and propagated along one or both sides at the weld toe. For a non-90° specimen, the plate was connected to the testing machine by a pin connection, so the rotation of the plate was not limited. Rotation did happen to all the plates for non-90° specimens during tests. For a 45° to 60° specimen, a crack always initiated at the toe of the plate (left end of the plate in Fig. 2) and propagated along both side of the plate at the weld toe.

For all the specimens except the 30° specimen (30LP0), final failure was due to punching shear at the toe of the fillet weld between the plate and the column face. The 30° specimen experienced tensile failure of the plate. All the specimens had very large deformations on the RHS connecting faces before they failed.

4.2 *Deformation profile of connecting face*

The deformation profile of the RHS connecting face is very important for the creation of a model for mathematical analysis. From the LVDTs shown in Figure 4, the deformation of the connecting face along the centre line of the column and across the centre cross section for each of the specimens has been measured. Figure 6 shows the deformation profiles along the column centre lines for specimens 90LP20 and 45LP60. The orientation of the columns in the two diagrams is horizontal. It can be seen that, for the 90° specimen 90LP20, the deformed shape at different tension loads is symmetrical about the centre of the connection, except at the ultimate load. The highest curve records the situation when fracture occurred at the left toe end of the connection. For all other 90° specimens their column deformation profiles are similar to that for the specimen 90LP20.

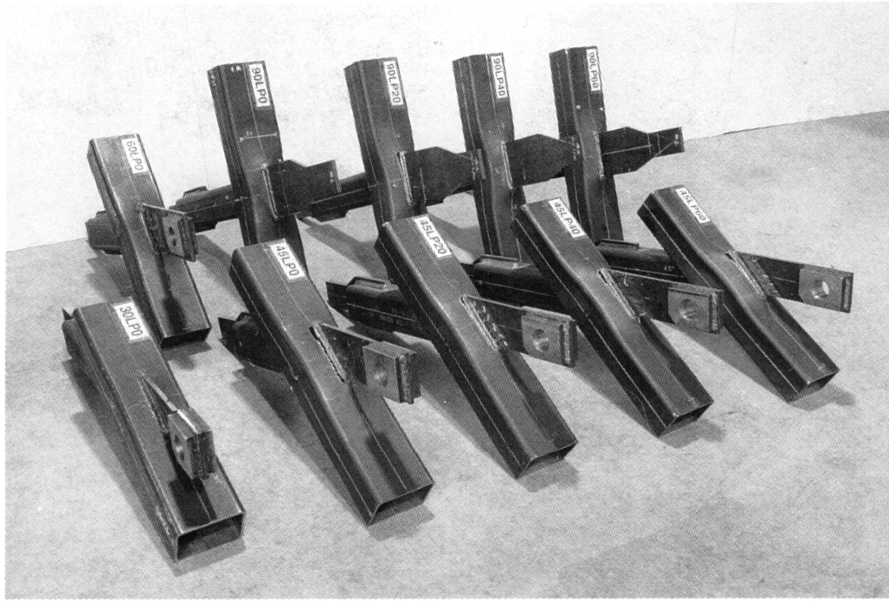

Figure 5 All specimens after testing

For the 45° specimen 45LP60, the toe of the weld is at the left side and the heel is at the right side. As shown in Figure 2, a pin connection was used at the top of the plate, so the plate could rotate around the pin. Due to the rotation the deformation at the toe side was larger than that at the heel side. Hence, for all the 45° to 60° specimens, cracks initiated at toe sides first and final failures were caused by the tearing at the toe. In Figure 6 the deformation near the two ends of the column was caused by the buckling of the column, so the deformation of the column face is also local.

Figure 7 shows the cross sections of some failed specimens (45° and 90°) along longitudinal direction of the column connection face and connection centre. It can be seen that the specimens with different angles have very similar deformation behaviour. The deformation of the connecting face of a specimen was dominated by the outward bulge of the face.

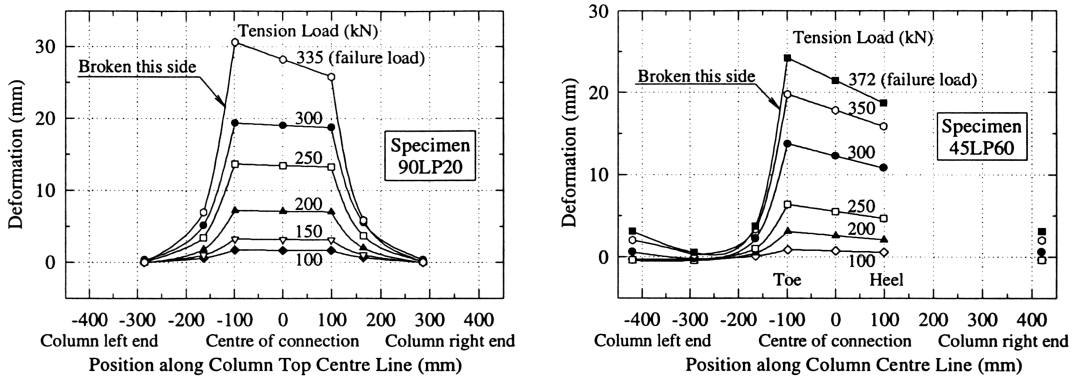

Figure 6 Deformation profiles along centre lines of column connecting faces

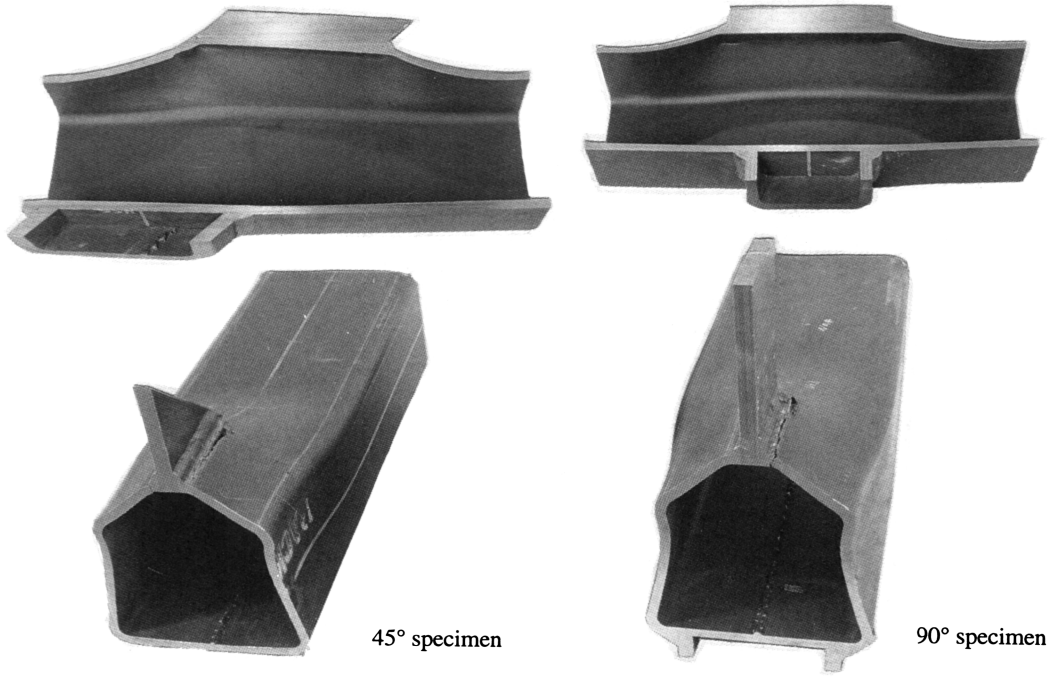

Figure 7 Cross sections of failed specimens

4.3 *Load - displacement curves*

Since failure of a specimen is usually due to excessive deformation of the RHS connecting face, the load - displacement behaviour of the connecting face is the most important data from the tests. The maximum displacement of a specimen can be measured by the LVDT located at the mid-height of the column wall (Fig. 4). Since the deformations of the plate and the column wall are much smaller than the deformation of the column face, the displacement measured by the LVDT closely represents the deformation of the column face.

Figure 8 shows the load - displacement curves for these specimens. The results for four 90° specimens and for four 45° specimens are shown in Figure 8a and Figure 8b, respectively. The results for four specimens with different angles but without column preload are shown in Figure 8c and Figure 8d. Hence the influences of column preload and plate angle can be obtained from the curves.

In Figure 8a, although the differences between the curves are small when the tension load is smaller than 100kN, the effect of the column compression preload is very clear when the tension load is higher than 100kN, i.e., the column preload increases the deformation of the column face significantly.

In Figure 8b, due to the differences between weld sizes, the 45LP60 (with the largest weld as noted in Table 1) seems to be the strongest one when the tension load is low. However, when the tension load is high the effect of the column preload is also clear.

Comparing Figures 8a and 8b, it can be seen that, the tension load sustained by a 45° specimen is higher than that for a 90° specimen, under the same column preload, at the same column displacement value. It can be seen that a 45° specimen is about 1.4 times as strong as a 90° specimen.

In Figure 8c, the results for four specimens with different angles but without column preload are shown in terms of total load applied (N_1) to the plate vs. the displacement. It can been seen that as the angle of θ increases the total tension load decreases, for a particular column face displacement. In Figure 8d the results for the four specimens are shown in

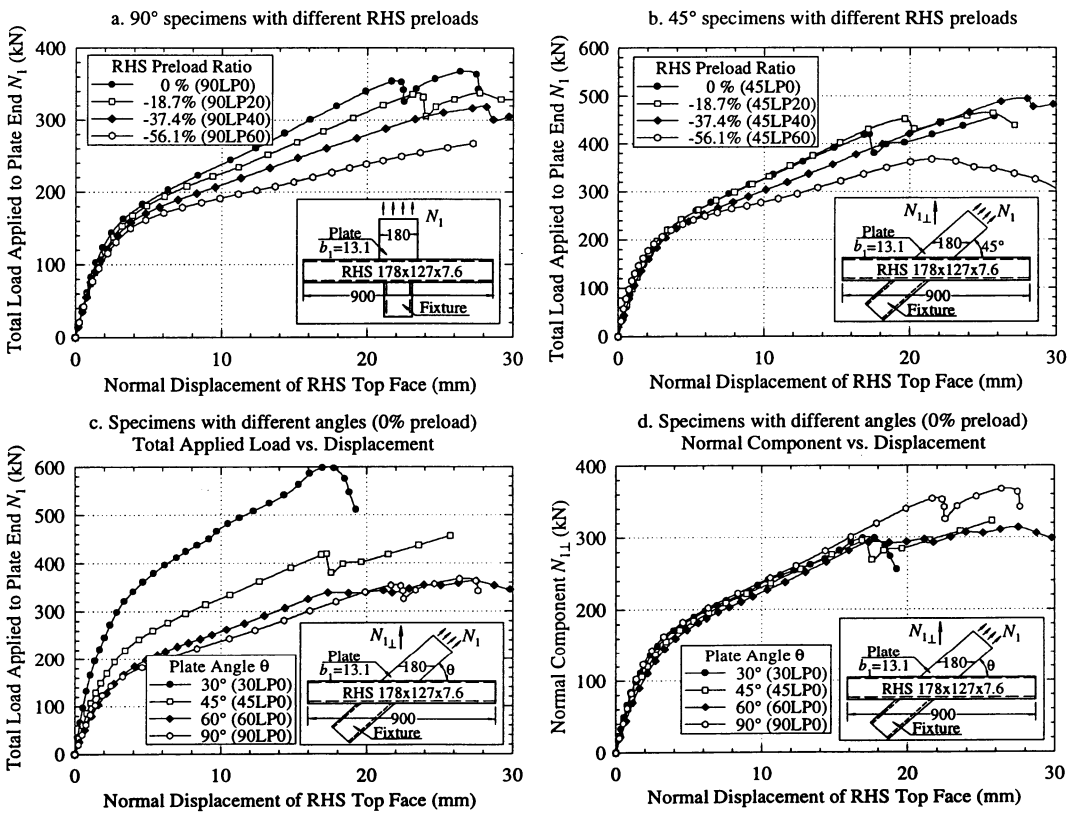

Figure 8 Load - Displacement curves for specimens

terms of the normal component of the applied tension load ($N_{1\perp}$) vs. the displacement. Figure 8d shows that the four specimens have very similar curves, which means that the normal component of the applied tension load dominates the vertical deformation of the column face. This can also be proven by the curves in Figures 8a and 8b, in which a 45° specimen is around 1.4 times as strong as a 90° specimen under the same column preload. Hence, perhaps only the normal component needs to be considered for such connections.

During the tests, cracks occurred around the welds between the plates and the columns, which caused tension loads to drop as displacements became large, as shown in the load-displacement curves in Figure 8. Peak loads occurred when displacements were large and specimens had nearly failed. For connections in real structures, such large displacements are not allowed and connections should be considered failed when displacements attain some limits. Two deformation limits have been used to define the strength of such a connection: these are an ultimate deformation limit and a serviceability deformation limit, which have been used for different types of RHS connections (IIW 1989, Lu *et al.* 1994, Zhao 1996). The ultimate deformation limit restricts the normal deformation of the RHS under the ultimate load to 3% of the RHS width ($0.03b_0$). The serviceability deformation limit restricts the normal deformation of the RHS under the serviceability load to $1\%b_0$.

4.4 *Stress distribution across plate width*

As shown in Figure 4, five strain gauges were arranged across the branch plate width and oriented in the direction of the tension load. Since the plate can be thought to be under the action of unidirectional tension, the stress distribution in the plate can be obtained from the strains measured by the strain gauges. Figure 9 shows the stress distributions in the branch plates of specimens 90LP20 and 45LP60.

The specimen 90LP20 is symmetric about the plate centre so it can be seen that when the tension load is low the curves are nearly symmetric about the plate centre. The stresses near the two ends are higher than those around the plate centre. As the tension load was increased, cracks occurred at the weld toe at the left end first (see Fig. 5) causing the stresses at the right side to increase faster. The uppermost curve corresponds to the peak load of the test and the drop in stress at the left side of this curve was due to the tearing of the crack at the weld toe at the left end.

The orientation of the plate for the specimen 45LP60 is the same as that shown in Figure 2; i.e. the left end of the plate is the toe and the right end of the plate is the heel. When the tension load is low the curves are nearly symmetric about the plate centre. As the tension load was increased the stresses near the two ends increased more quickly than those around the plate centre. Although the stresses near the right heel end were a little bit higher than those near the left toe when the tension load was low, the stresses near the left toe end were higher than those near the right heel end when the tension load was high. The plate broke at the left toe end as shown in Figure 5.

Figure 9 shows that the stress distributions of the two branch plates are very similar and the stresses near the two ends are higher than those around the plate centre. This trend has been verified by other specimens so this effect should be considered in the design of the plate and weld in such a connection.

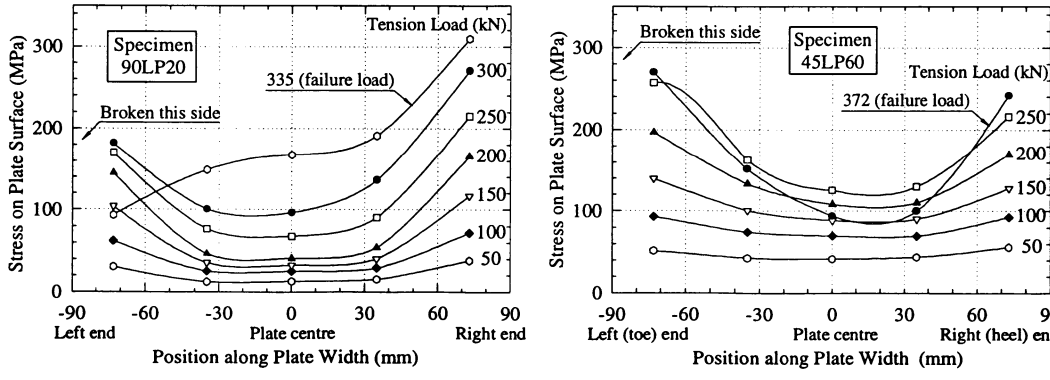

Figure 9 Stress distributions on plate surfaces for specimens 90LP20 and 45LP60

CONCLUSIONS

In the test program reported in this paper for connections between longitudinal plates and RHS members, ten specimens with different angles, between plates and RHS members, have been tested to rupture under different levels of compression loads on the RHS members. These tests indicate that the following points should be considered in the design of connections between longitudinal plates and RHS members:

a. Failure of a connection is usually due to excessive deformation of the RHS connecting face. The deformation of the connecting face is local and dominated by the outward bulge of the face. The strength of a connection should be decided based on deformation limits.
b. Although a plate tension load may be applied to a connection at different angles, the deformation of the RHS connecting face is caused, mainly, by the component of the applied tension force normal to the RHS member.
c. Compression "preload" on the RHS member of a connection reduces the stiffness and design capacity of the connection and has to be considered in the design of a connection.
d. The stress distribution across the branch plate width is not even. The stresses near the two plate ends are generally higher than those around the plate centre.

Although the information obtained from the tests is not sufficient to develop a rational design method for connections between longitudinal plates and RHS members, the test results can be used to calibrate the models used for parametric finite element analysis.

ACKNOWLEDGEMENTS

Financial support from the Steel Structures Education Foundation, the Steel Tube Institute of North America, the Comité International pour le Développement et l'Étude de la Construction Tubulaire (CIDECT), and the Natural Sciences and Engineering Research Council of Canada (NSERC) for this project, is greatly appreciated.

REFERENCES

Cao, J. J.; Packer, J. A. & Kosteski, N. 1998. Parametric finite element study of connections between longitudinal plates and RHS columns. *Proc. Eighth International Symposium on Tubular Structures*, Singapore.

Dawe, J. L. & Guravich, S. J. 1992. Branch plate to reinforced HSS connections in tension and compression. *Canadian Journal of Civil Engineering* 20:631-641.

Dawe, J. L. & Mehendale, S. V. 1995. Shear connections using stub tees between W beams and HSS columns. *Canadian Journal of Civil Engineering* 22:683-691.

International Institute of Welding (IIW) 1989. Design recommendations for hollow section joints - predominantly statically loaded. *IIW Doc. XV-701-89*, 2nd ed, IIW Subcommission XV-E, , IIW Annual Assembly, Helsinki, Finland.

Lu, L. H. & Wardenier, J. 1995. Parametric study on the static strength of uniplanar and multiplanar plate to RHS column connections. *Proc. Fifth International Offshore and Polar Engineering Conference* Vol. IV:21-28. The Hague, The Netherlands.

Lu, L. H., Puthli, R. S. & Wardenier, J. 1993. Semi-rigid connections between plates and rectangular hollow section columns. *Proc. Fifth International Symposium on Tubular Structures*: 723-731. Nottingham, UK.

Lu, L. H., de Winkel, G. D., Yu, Y. & Wardenier, J. 1994. Deformation limit for the ultimate strength of hollow section joints. *Proc. Sixth International Symposium on Tubular Structures*: 341-347, Melbourne, Australia.

Sherman, D. R. 1996. Designing with structural tubing. *AISC Engineering Journal* 33(3):101-109.

Zhao, X. L. 1996. Verification of the deformation limit for T-joints in cold-formed RHS sections. *Proc. Seventh International Symposium on Tubular Structures*: 213-220, Miskolc, Hungary.



Taylor & Francis
Taylor & Francis Group
http://taylorandfrancis.com

Tubular Structures VIII, Choo & Van der Vegte (eds) © 1998 Balkema, Rotterdam, ISBN 90 5809 001 9

Parametric finite element study of connections between longitudinal plates and RHS columns

J.J.Cao, J.A.Packer & N.Kosteski
Department of Civil Engineering, University of Toronto, Ont., Canada

ABSTRACT : A parametric study, covering 120 different cases, has been carried out using Finite Element (FE) models to investigate the behaviour of connections between longitudinal plates and RHS columns (chords). All the connections are in an X-configuration with four different angles (90°, 60°, 45° and 30°) between plates and columns, and different plate thicknesses, plate widths and RHS thicknesses were used for the connections. Both compression and tension "preloads" on the RHS columns were considered and tensile and compressive forces were applied to the plates of the connections. The results from the FE models, which have been confirmed by tests conducted on 10 specimens, can be used to develop design guidelines for connections between longitudinal plates and RHS columns.

1. INTRODUCTION

As a traditional and convenient method, plates are used widely to connect beams and braces to Rectangular Hollow Sections (RHS). Although a lot of research work has been undertaken for plate connections related to I-beams and RHS columns (Lu et al. 1993, 1995, Dawe & Guravich 1992, Sherman 1996, Dawe & Mehendale 1995), not much work has been done for connections between longitudinal plates and RHS members, for connecting braces.

Figure 1 shows such a longitudinal plate connection. The column is under the action of compression load and the plate is under the action of the axial load from the brace member. Although this connection is quite flexible and provides low connection resistance, it is still a popular choice for some braced structures. However reliable design information on this type of connection is scant.

A test program for longitudinal plate connections has been carried out by Cao et al. (1998a) at the University of Toronto, in which 10 specimens have been tested. Since laboratory experiments are costly, only a limited number of specimens can be tested. It is also not easy to apply very high compressive preload and tensile preload to the columns. Hence, the information obtained from the test program is not adequate for developing a rational design method for this type of connection.

In order to explore the behaviour of connections between longitudinal plates and RHS members, a parametric study has been carried out using Finite Element (FE) models, in which 120 different cases have been studied. The FE models have been calibrated by experimental tests and the influence of connection dimensions and loading cases has been

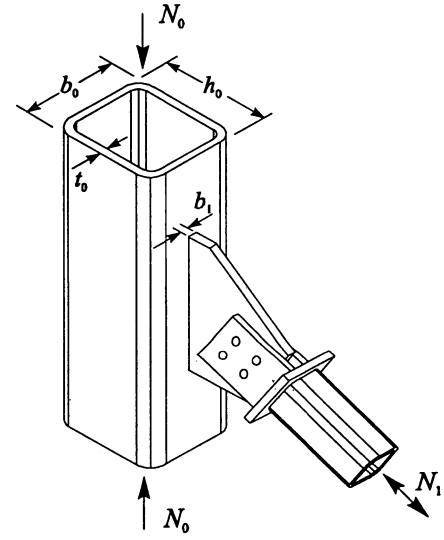

Figure 1 Longitudinal plate connection

investigated thoroughly from the FE analyses of the different cases.

2. CONNECTIONS USED FOR FE ANALYSES

All the connections used for the FE analyses are listed in Table 1. As shown in the diagram in the table, the connections have an X configuration, the same as that for the experimental specimens (Cao et al. 1998a). A plate is welded to one side of the RHS column (or chord, in the following text the term column will be used to represent the two cases) and an RHS branch is welded to the other side of the RHS column as a fixture. The end of the RHS fixture is fixed, and tension and/or compression loads can be applied to the plate and to the two ends of the RHS column. The outside dimensions and length of the RHS were kept constant for all the connections. The angle, θ, between the plate and the RHS, RHS thickness, t_0, plate thickness, b_1, and connecting length, $h_1/\sin\theta$, were varied.

Table 1 Connections Used for FE Analysis

Group	Inclined Angle θ (degrees)	RHS Thickness t_0 (mm)	Plate Thickness b_1 (mm)	Connecting Length $h_1/\sin\theta$ (mm)	Weld Size $w^\dagger$ (mm)	Loading Case	No. of Specimens
90LPA	90	7.6	13.1	180	9		4
90LPB	90	7.6	20	180	12	I, II, III	0
90LPC	90	7.6	13.1	270	9		0
60LPA	60	7.6	13.1	180	9		1
60LPB	60	7.6	20	180	12	I	0
60LPC	60	7.6	13.1	270	9		0
45LPA	45	7.6	13.1	180	9		4
45LPB	45	7.6	20	180	12	I	0
45LPC	45	7.6	13.1	270	9		0
30LPA	30	7.6	13.1	180	9		1
30LPB	30	7.6	20	180	12	I	0
30LPC	30	7.6	13.1	270	9		0
90LPVA	90	11.4	13.1	180	9		0
90LPVB	90	11.4	20	180	12	I	0
90LPVC	90	11.4	13.1	270	9		0
90LPWA	90	4.74	13.1	180	9		0
90LPWB	90	4.74	20	180	12	I	0
90LPWC	90	4.74	13.1	270	9		0

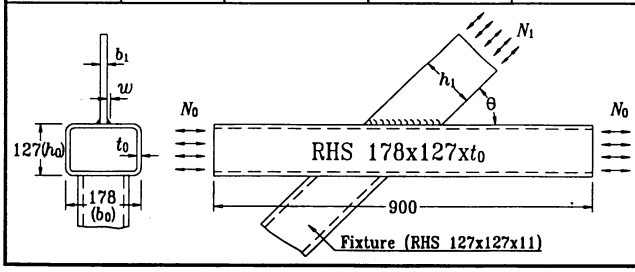

Case	N_0	N_1
I	Comp.	Tension
II	Tension	Tension
III	Comp.	Comp.

RHS Preload Ratio n (N_0/A_0F_{y0} %)‡
Comp. 0, -18.7, -37.4, -56.1, -74.8
Tens. 18.7, 37.4, 56.1, 74.8, 93.5

† The real weld sizes, w, for the specimens vary from 7.2mm to 9.5mm.
‡ A_0 and F_{y0} are cross sectional area and yield stress of the RHS column (chord).

There are 18 groups of connections with different dimensions in Table 1. The first two digits for a group refer to the angle between the plate and the RHS column and four different angles (30°, 45°, 60° and 90°) were used. The last letter for a group (A, B or C) refers to the dimensions of the plate and the weld size. Plate A can be considered as a "standard" plate (13.1mm thick and 180mm long for the connecting area to the RHS column). Plate B is thicker (20mm) than Plate A but its connecting length with the RHS columns is the same as Plate A. Plate C has a longer connecting length (270mm) than Plate A but has the same thickness as Plate A. Two weld sizes were used for the two plate thicknesses.

Three different loading cases were used for the groups. Loading case I was applied to all the groups, in which the RHS column is under compression and the plate is under tension. Loading cases II and III were only applied to the first three groups, in which the RHS and the plate were under tension or compression simultaneously. For each loading case five different column preloads were applied, so, in total, 120 different cases have been studied.

The last column of the table shows the numbers of the specimens tested by Cao et al. (1998a) for each group. It can be seen that the experimental tests cover only 10 cases of these 120 cases. The RHS column preload ratio for the FE analyses ranges from -74.8% to 93.5% and three different thicknesses were used for the RHS columns. Hence the extent of the FE analyses is far beyond the extent of the tests.

3. FE MODELS

The finite element package ABAQUS (Hibbit et al. 1996) has been used for the analyses and all meshes were generated using ABAQUS input files consisting of ABAQUS commands.

3.1 *Models for 90° connections*

Figure 2 shows a mesh for a 90° connection, which represents a quarter of the connection due to symmetry. Twenty noded solid elements were used for all the model except that some 15-noded solid

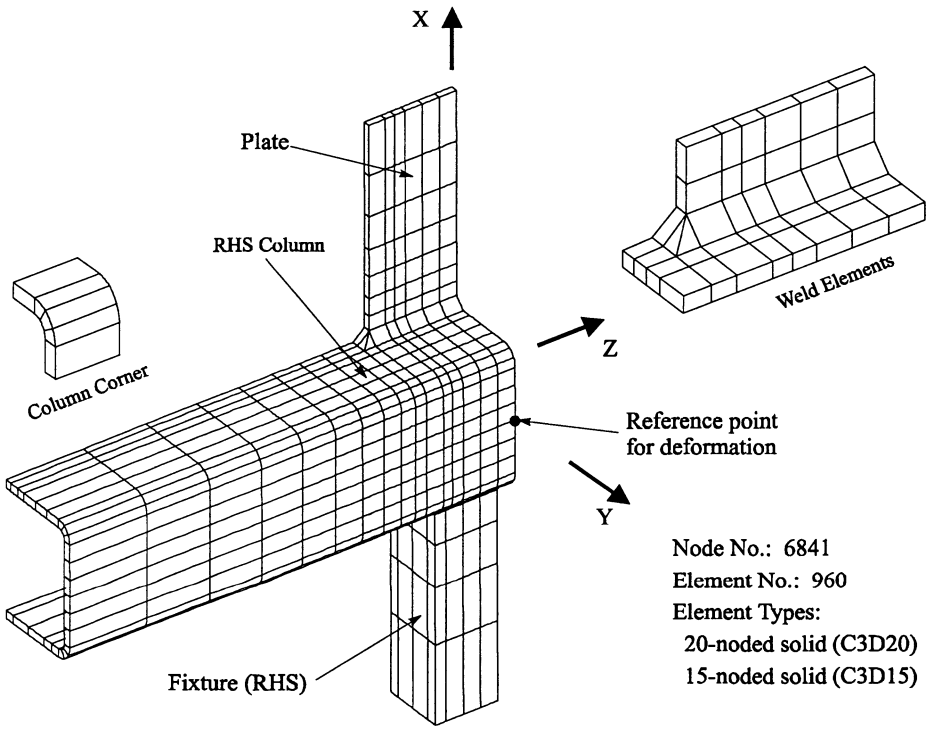

Figure 2 Mesh for a 90° connection

elements were used for the welds between the plate and the column and between the column and the reaction fixture. Detailed modelling of the column round corners and weld sizes was included in the model and the model includes 468 elements and 3441 nodes.

Symmetrical boundary conditions were applied to the plane X-Z (Y=0) and the plane X-Y (Z=0). The bottom of the RHS fixture was fixed. Column axial preload (compressive or tensile) was applied to the left end of the column as a uniformly distributed load. Displacement control was applied to the top of the plate, which simulated the situation during a specimen test. The displacements at the top of the plate were increased (upwards for tension and downwards for compression) step by step and the axial load, applied to the plate, corresponding to each step of displacement could be obtained from the reaction at the bottom of the fixed RHS fixture. The reference point shown in the figure was used to calculate displacement of the plate and deformation of the column connecting face.

Since the meshes were generated using ABAQUS input files, a file for a connection could be modified very easily to compose another file for another connection. All the meshes for the 90° connections listed in Table 1 are very similar to the mesh shown in Figure 2 so the effects of element size and shape for different connections are avoided.

3.2 *Models for 30°, 45° and 60° connections*

Since a non-90° connection is not symmetrical about the X-Y plane (see Fig. 2), half of the connection has to be modelled. Figure 3 shows a mesh for a 45° connection, which includes 960 elements and 6841 nodes. Similarly, all elements in this mesh were 20-noded solid elements except that weld elements were 15-noded solid elements.

A symmetrical boundary condition was applied to the X-Z plane (Y=0) and the bottom of the RHS fixture was fixed. Column compression load was applied to both ends of the column as a uniformly distributed load. The centre of the plate top corresponds to the pin hole in a specimen (Cao et al.

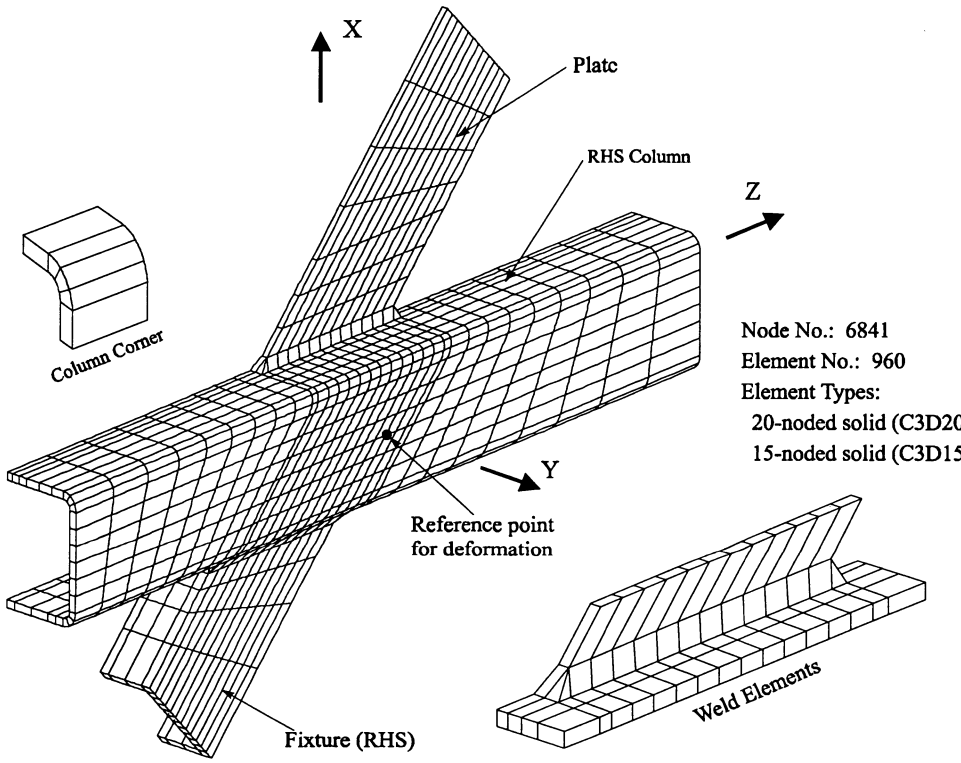

Figure 3 Mesh for a 45° connection

1998a) and displacement control was applied to the centre (exactly the same as in a test). A higher elastic modulus was used for the elements along the top layer of the plate to distribute the tension load to the plate (similar to the stiffener plates used in the test specimens). When a displacement was applied to the centre of the plate top along the direction of the plate, the plate could rotate freely with the deformation of the connecting face. The tension load corresponding to the displacement could be obtained from the reaction at the bottom of the fixed RHS. The reference point for deformation is also shown in the figure.

All the 30° to 60° connections have similar meshes to that shown in Figure 3. As the angle, θ, between the plate and the RHS column increases, the mesh in Figure 3 closes to the mesh in Figure 2. Hence the mesh configurations for connections with different angles were also kept consistent, which is of importance for the investigation of the effect of the angle θ.

3.3 *Material properties and analysis method*

The material properties for RHS columns and plates were from material tests for specimens (Cao et al. 1998a). Several key material parameters for the columns and plates are presented in Table 2. The strain and stress relationships obtained from the material tests were modelled as multi-linear relationships for all the FE analyses for the connections listed in Table 1. The material properties for the RHS fixtures were taken as the same as those for the RHS columns and the material properties for welds were taken as the same as those for the plates. Hence non-linear behaviour for all the materials was considered.

Displacement control was used for all the analyses. The displacements at controlled nodes were increased step by step and the corresponding loads applied to plates, stresses and displacements could be obtained. Geometrical non-linear behaviour was considered in all the analyses.

Table 2 Key material properties (MPa)

	Column	Plate
Yield Stress	378	408
Ultimate Stress	506	540
Young's Modulus	210,600	217,900

4. RESULTS AND ANALYSIS

From the analyses of the cases listed in Table 1, the load-displacement curve, deformed shape and stress distribution for each of the cases were obtained. The models used for the FE analyses can be verified by comparing load-displacement curves obtained from the FE analyses and tests. After the models are verified, the results from the FE analyses can be used confidently.

4.1 *Verification of FE models*

The most important data from the FE analyses is the load-displacement curve for each of the cases. Figure 4 shows the load - displacement curves, obtained from the FE analyses and the tests (Cao et al. 1998a), for four connections with different angles but without column preload (90LPA, 60LPA, 45LPA and 30LPA with 0% RHS preload in Table 1).

During the tests, cracks occurred around the welds between the plates and the RHS columns, which caused loads to drop as displacements became large. Because no cracks were considered in the FE models, the drops could not be predicted by the FE analyses. For defining the strength of an RHS connection, two deformation limits have been used: these are an ultimate deformation limit and a serviceability deformation limit (IIW 1989, Lu et al. 1994, Zhao 1996). The ultimate deformation limit restricts the deformation under the ultimate load to 3% of the RHS width ($0.03b_0$). The serviceability deformation limit restricts the deformation under the

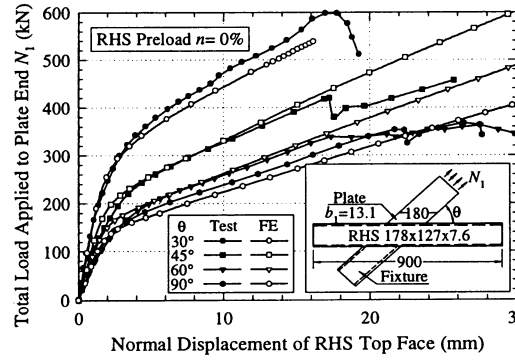

Figure 4 Load - displacement curves for connections with different angles

serviceability load to $1\%b_0$. Since the drops in tension loads in the tests correspond to very large displacements, they are actually out of the range of interest of the investigation. There are also slight differences between the welds for the test specimens and the welds for the FE models (Table 1), which would cause slight differences between the FE results and the test results. However, as a whole, the FE results agree very well with the test results. For the other six specimens (Cao et al. 1998a), the load - displacement curves from the FE analyses are also very close to those from the tests. Hence, the load - displacement curves obtained from the FE analyses for all the connections can be used confidently to analyse the influences of different factors.

4.2 *Load - displacement curves*

Figure 5a and Figure 5b show the load - displacement curves for two groups of connections (90LPA and 45LPA in Table 1), with different levels of RHS compression loading. There are four specimens tested in each of the groups (Cao et al. 1998a) and the load - displacement curves in Figures 5a and 5b have been confirmed by the test results (Cao et al. 1998a). From the two diagrams, it can be seen that a high compression load on the RHS of a connection reduces the stiffness and strength of the connection significantly, so compression "preload" has to be considered in the design of the connection.

The two groups of curves in Figures 5a and 5b have very similar shapes. The vertical scale of Figure 5b is 1.4 times the vertical scale of Figure 5a, so a 45° connection in Figure 5b is a little more than 1.4 times as strong as a 90° connection in Figure 5a with the same column preload. This confirms that the normal component, $N_{1\perp}$, dominates the deformation of the RHS top face.

In Figure 5c, the vertical axis is the normal component, $N_{1\perp}$, of the applied tension load N_1. The load - displacement curves for four connections with different angles under two different RHS preloads

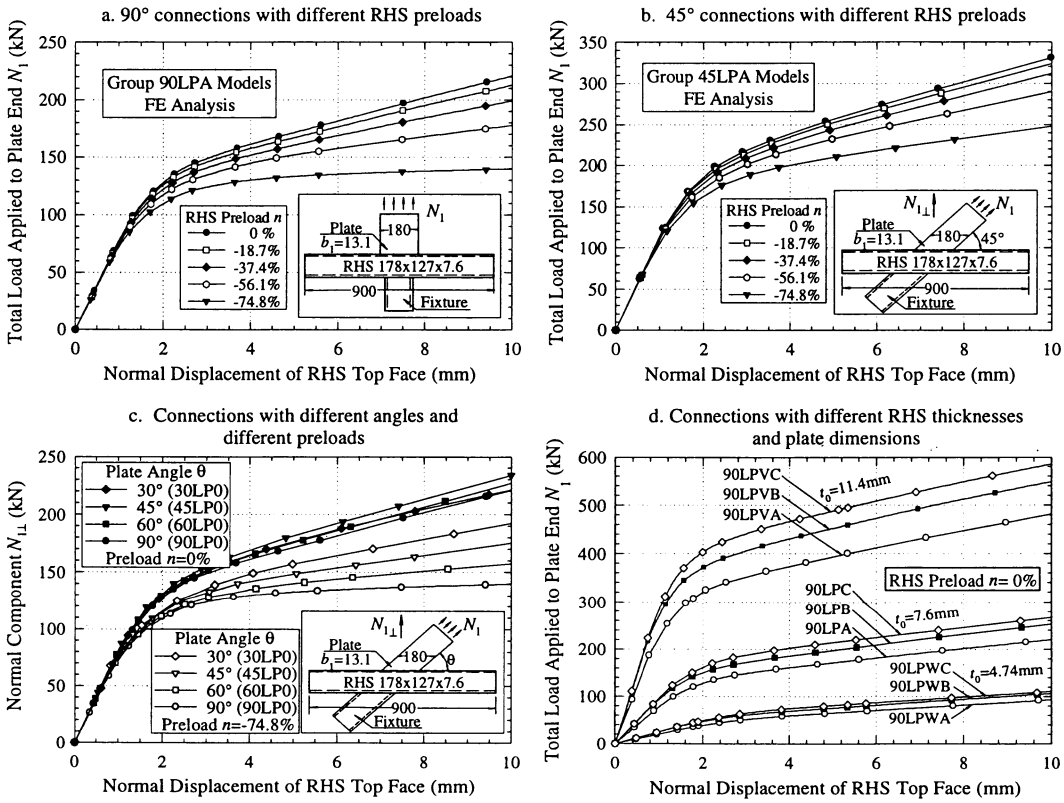

Figure 5 Load - displacement curves for connections with different parameters

are presented in the figure. The curves with solid symbols correspond to 0% RHS preload. It can be seen that the four curves are very close. The curves with hollow symbols correspond to -74.8% RHS preload and the differences between these curves are larger than those for the case of 0% RHS preload. It seems that a non-90° connection is stronger than a 90° connection. Actually, the displacement for a connection in Figure 5 is the displacement at the centre of the plate. It will be shown in the next section that the deformation on the RHS connecting face along the plate width for a non-90° connection is not uniform and the plate rotates as the RHS connecting face deforms. The displacement at one side of a plate is larger than that at the plate centre, which brings the displacement of a non-90° connection close to that of a 90° connection. Hence connections with different angles can be designed based on normal components of their applied loads.

Figure 5d shows the results for nine 90° connections with three different RHS thicknesses (11.4mm, 7.6mm and 4.74mm) but without RHS preload. Three different plates (Plates A, B and C in Table 1) were used for each RHS thickness. It can be seen that the thickness of the RHS is a critical factor for the performance of a connection. A longitudinal plate connecting to a thin RHS has a very low connection strength and the connection strength can not be increased effectively by changing plate dimensions. Hence a stiffener plate on the connecting face may be needed in such a case. Although both the cross-sectional areas of Plates B and C are about 1.5 times the cross-sectional area of Plate A, the increase of connection strength by replacing Plate A by Plate B or Plate C is much less than 50%. The Plates B and C have nearly the same cross-sectional areas but the connection strength using Plate C is always higher than that using Plate B. Therefore, an increase in plate area is best achieved by increasing the plate width/length (along the RHS axis, as for Plate C), not the thickness (transverse to the RHS axis, as for Plate B).

As listed in Table 1, two additional loading cases have been applied to the connection groups 90LPA, 90LPB and 90LPC. In the loading case II, tension preloads were applied to the RHS columns. Although this is not a general case for columns in a building, it is a common case for connections attached to chords under tension in a truss. It has been found that the tension preloads on the RHS main members (column or chord) had very little influence on the strength of the connections. For preload ratios from 18.7% to 74.8% the deformations on the connecting faces of the connections actually decreased a little. For a preload ratio 93.5%, the deformations of the connections increased less than 10%. Since the axial stress ratio (preload ratio) in a main member (column or chord) will not be as high as 0.9, the effect of the tension axial load on the main member can be ignored in the design of RHS connections.

In the loading case III, compressive forces were applied to plates for the three groups of connections (90LPA, 90LPB and 90LPC). The differences between the results for the two plate loading cases (tension and compression) are small, in terms of the load applied vs. the displacement on the connecting face, so the two loading cases can be considered in the same manner.

4.3 *Deformation profile*

Figure 6 shows the deformations along the centre lines of the column connecting faces for two connections, one being a 90° connection and another being a 45° connection, obtained from FE analyses. Test results for the two connections with the same

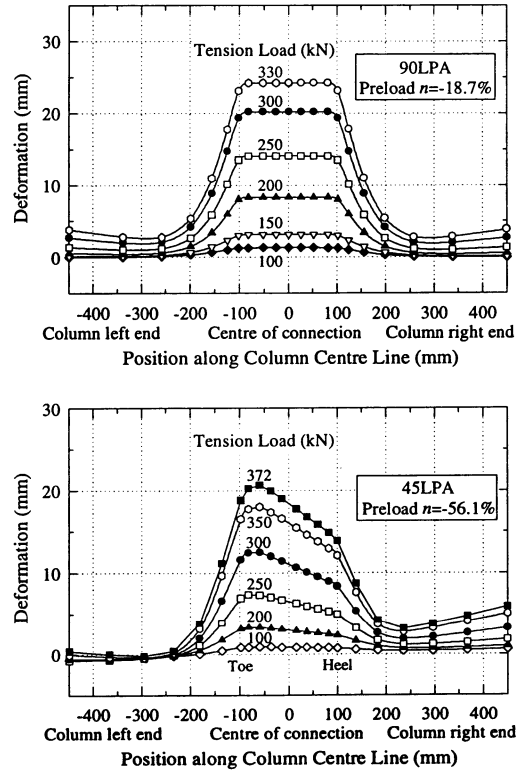

Figure 6 Deformation profiles

RHS preloads have been reported (Cao et al. 1998a) and it can be found that the deformations obtained from the FE analyses agree with the deformations measured from the tests, both in terms of the deformation pattern and the amount of deformation.

As shown in Figures 2 and 3, the reference point for deformation is at the centre of the side wall at the column middle cross section. The two ends of the column moved upwards because the whole column actually "sagged". This effect was caused by the column compression load and has been confirmed by all the tests with column preloads.

The orientation of the connection 45LPA in Figure 6 is the same as that in Figure 3. The deformation for connection 45LPA includes the rotation of the column, which leads to the deformations on the right side end being higher than those on the left side end. The curves also show that the deformation at the toe is higher than that at the heel due to the rotation of the plate.

All the FE analyses confirm that, for a longitudinal plate to RHS column connection, the deformation of the column connecting face is local and dominated by the outward bulge of the face, which is caused, mainly, by the normal component of the applied tension force.

4.4 *Stress distribution across plate width*

Figure 7 shows the stress distributions across plate width for two connections. The distance between the column surface and the line where the stresses are considered is 37mm, the same height as the strain gauges used in specimen tests (Cao et al. 1998a). The stress direction is along the applied load, i.e. along the plate sides.

General agreement between the results from the FE analyses and the tests has been found. The curves in Figure 7 represent typical situations for 90° and non-90° connections. For a 90° connection, the stresses near the two edges of the plate are higher than those around the centre of the plate. For a non-90° connection, although the stresses near the right heel end are higher than those to the right side of the plate centre, the stresses at the left toe side are much higher than those at the right heel side due to the rotation of the plate. Hence the stress distribution across the plate of a connection is not uniform.

From Figure 6, it can be found that the highest loads in Figure 7 for the two connections correspond to very large displacements. Based on the deformation limits, the two connections should be considered to have failed when the tension loads

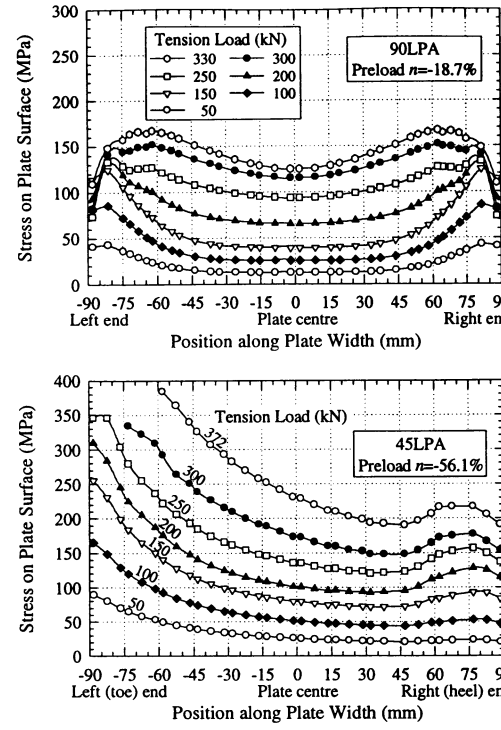

Figure 7 Stress distribution across plate width

were quite low. Hence the non-uniformity of the stress distribution is actually not too important. For all the connections listed in Table 1, the resistance of a connection was limited by deformation limits, not by yielding of the plate. Although plate failure is unlikely to occur for most longitudinal plate to RHS connections, it may become critical for connections with low plate-to-RHS angles or with very high RHS thickness and very low plate thickness. Hence the strength of the plate should be checked for the design of such a connection. From the results of the tests (Cao et al. 1998a) and the FE analysis, the non-uniformity of stress distribution of the plate may be considered by a 20% reduction in plate strength.

5. CONNECTION STRENGTH

From the parametric study, it has been found that the limit state of a connection between a longitudinal plate and an RHS column is usually due to excessive deformation of the RHS connecting face. The ultimate deformation limit and the serviceability deformation limit have been used to define the strength of such a connection. From a known load -

displacement curve, two loads ($N_{1.1\%}$ and $N_{1.3\%}$) corresponding to the serviceability limit and ultimate limit can be obtained. The $N_{1.1\%}$ is the load (or normal component of the load, for a non-90° connection) applied to the branch plate corresponding to an RHS face deformation of $0.01b_0$ (1.78mm in Fig. 5) and the $N_{1.3\%}$ is the load (or normal component of the load, for a non-90° connection) applied to the branch plate corresponding to an RHS face deformation of $0.03b_0$ (5.34mm in Fig. 5). Then, assuming that an overall total load factor around 1.5 is typically applied to the service (or specified) loads to obtain the factored (ultimate) loads, the ultimate limit state of a connection can be deemed to be given by the lesser of $1.5N_{1.1\%}$ and $N_{1.3\%}$. The two deformation limits can be applied to FE analysis results for all the connections listed in Table 1 and results for some of the connections are presented in Table 3.

Based on a new yield line model for an RHS T or X connection, in which the compressive load in the main member has been taken into account, Cao et al. (1998b) developed a general formula for the calculation of the yield strength of a T or X connection, N_1^*, under the influence of compressive load. If only the component of the branch member load normal to the main member is considered, the following formula can be derived for T, Y and X connections

$$N_1^* = \frac{F_{y0}\, t_0^{\,2}}{(1-\beta')\sin\theta}\left(2\frac{h_1'}{b_0'}+4\sqrt{1-\beta'}\right)f(n) \quad (1)$$

Table 3 Connection Strengths Determined by Limit States and Formula

Connection Group	Parameters					Limit States		Eqn. (1)	Comparison†
	β'	b_0/t_0	h_1'/b_0'	t_0 (*mm*)	n (%)	$1.5N_{1.1\%}$ (kN)	$N_{1.3\%}$ (kN)	N_1^* (kN)	$\frac{N_{1,Lim}-N_1^*}{N_1^*}$ %
90LPA	0.183	23.4	1.162	7.6	0.0	180.8	**175.1**	158.7	10.3
					-74.8	156.2	**134.0**	126.2	6.2
90LPB	0.258	23.4	1.197	7.6	0.0	215.0	**201.9**	171.9	17.5
					-74.8	183.8	**153.0**	137.8	11.0
90LPC	0.183	23.4	1.690	7.6	0.0	229.0	**218.0**	186.9	16.6
					-74.8	201.1	**175.4**	154.4	13.6
45LPA	0.183	23.4	1.162	7.6	0.0	263.1	**262.3**	224.5	16.8
					-74.8	233.0	**212.9**	178.5	19.3
45LPB	0.258	23.4	1.197	7.6	0.0	309.8	**300.8**	243.1	23.7
					-74.8	273.6	**243.5**	194.9	24.9
45LPC	0.183	23.4	1.690	7.6	0.0	335.3	**327.0**	264.3	23.7
					-74.8	300.6	**274.7**	218.4	25.8
90LPVA	0.187	15.6	1.19	11.4	0.0	461.7	**399.8**	361.5	10.6
					-74.8	397.9	**310.4**	288.2	7.7
90LPVB	0.264	15.6	1.22	11.4	0.0	537.3	**460.0**	392.5	17.2
					-74.8	459.2	**354.5**	315.5	12.4
90LPVC	0.187	15.6	1.73	11.4	0.0	581.7	**495.5**	426.7	16.1
					-74.8	506.9	**396.1**	353.4	12.1
90LPWA	0.180	37.6	1.14	4.74	0.0	**52.9**	67.1	61.2	-13.6
					-74.8	**45.0**	47.8	48.6	-7.4
90LPWB	0.254	37.6	1.18	4.74	0.0	**64.5**	77.8	66.1	-2.4
					-74.8	55.1	**54.7**	52.9	3.4
90LPWC	0.180	37.6	1.66	4.74	0.0	**67.1**	83.4	71.9	-6.7
					-74.8	**59.2**	63.9	59.3	-0.1

† $N_{1,Lim}$ is the lesser value of $1.5N_{1.1\%}$ and $N_{1.3\%}$.

where:

$$b_0' = b_0 - t_0 \qquad h_1' = h_1 / \sin\theta + 2w$$
$$b_1' = b_1 + 2w \qquad \beta' = \frac{b_1'}{b_0'} = \frac{b_1 + 2w}{b_0 - t_0} \tag{2}$$

$$f(n) = \frac{\frac{h_1'}{b_0'} + 2\sqrt{1-\beta'}\sqrt{1-n^2}}{\frac{h_1'}{b_0'} + 2\sqrt{1-\beta'}} \quad \text{for } n < 0 \tag{3}$$
$$= 1.0 \quad \text{for } n \geq 0$$

The dimensions in the equations are shown in the diagram in Table 1. Equation (1) has been used for the connections in Table 1 and the results have been presented in Table 3. For each group, results for two RHS compression preload ratios (0% and -74.8%) are given. In the last column in Table 3, the connection strength $N_{1,Lim}$, determined by the limit states, is the lesser value of $1.5N_{1,1\%}$ and $N_{1,3\%}$. It can be seen that most connection groups are controlled by $N_{1,3\%}$ and Equation (1) can provide very good predictions for these connections. For groups 90LPW*, which have a high ratio of b_0/t_0 (38), $N_{1,Lim}$ is often controlled by $1.5N_{1,1\%}$ and Equation (1) may not be safe for these connections. However, these connections have very low strengths and should be avoided. This can be enforced by limiting the value of b_0/t_0 to a maximum of 30. Equation (1) can be applied to both plate tension and compression loads and the $f(n)$ for RHS tension cases is 1.0. Plate strength may also be checked based on a 20% reduction.

CONCLUSIONS

From an FE parametric study of longitudinal plate to RHS column connections, the behaviour of these connections has been investigated thoroughly. The results from the FE analyses have been used to confirm a design formula based on a yield line analysis.

ACKNOWLEDGEMENTS

Financial support for this project was provided by the Steel Structures Education Foundation, the Steel Tube Institute of North America, the Comité International pour le Développement et l'Étude de la Construction Tubulaire (CIDECT), and the Natural Sciences and Engineering Research Council of Canada (NSERC).

REFERENCES

Cao, J. J.; Packer, J. A. & Kosteski, N. 1998a. Experimental study of connections between longitudinal plates and RHS columns. *Proc. Eighth International Symposium on Tubular Structures*, Singapore.

Cao, J. J., Packer, J. A. & Yang, G. J. 1998b. Yield line analysis of RHS connections with axial loads. Accepted for publication, *J. Constructional Steel Research.*

Dawe, J. L. & Guravich, S. J. 1992. Branch plate to reinforced HSS connections in tension and compression. *Canadian Journal of Civil Engineering* 20:631-641.

Dawe, J. L. & Mehendale, S. V. 1995. Shear connections using stub tees between W beams and HSS columns. *Canadian Journal of Civil Engineering* 22:683-691.

Hibbit, Karlsson & Sorenson Inc. 1996. *ABAQUS/Standard User's Manual Version 5.6*, USA.

International Institute of Welding (IIW) 1989. Design recommendations for hollow section joints - predominantly statically loaded. *IIW Doc. XV-701-89*, 2nd ed, IIW Subcommission XV-E, , IIW Annual Assembly, Helsinki, Finland.

Lu, L. H. & Wardenier, J. 1995. Parametric study on the static strength of uniplanar and multiplanar plate to RHS column connections. *Proc. Fifth International Offshore and Polar Engineering Conference* Vol. IV:21-28. The Hague, The Netherlands.

Lu, L. H., Puthli, R. S. & Wardenier, J. 1993. Semi-rigid connections between plates and rectangular hollow section columns. *Proc. Fifth International Symposium on Tubular Structures*: 723-731. Nottingham, UK.

Lu, L. H., de Winkel, G. D., Yu, Y. & Wardenier, J. 1994. Deformation limit for the ultimate strength of hollow section joints. *Proc. Sixth International Symposium on Tubular Structures*: 341-347, Melbourne, Australia.

Sherman, D. R. 1996. Designing with structural tubing. *AISC Engineering Journal* 33(3):101-109.

Zhao, X. L. 1996. Verification of the deformation limit for T-joints in cold-formed RHS sections. *Proc. Seventh International Symposium on Tubular Structures*: 213-220, Miskolc, Hungary.

Tubular Structures VIII, Choo & Van der Vegte (eds) © 1998 Balkema, Rotterdam, ISBN 90 5809 001 9

Author index

Alikhail, M. 625
Amdahl, J. 511
Ariyoshi, M. 203

Beutel, J.G. 615
Bowness, D. 353, 361
Bradford, M.A. 425

Cadei, J.M.C. 81
Cao, J.J. 635, 645
Chan, T.K. 131
Cheung, L.Y. 239
Chiew, S.P. 417
Choo, Y.S. 139, 203, 465
Churchman, A.E. 81
Clarke, M.J. 539, 549
Courage, W.M.G. 89

Dagg, H. 625
Davies, G. 167, 473
Dexter, E.M. 249, 259
Dier, A.F. 107
Dong, Y.X. 417

Ebato, K. 585
Edwards, M. 491
Eekhout, M. 51

Farkas, J. 399, 481
Fok, W.C. 373
Fujita, K. 585
Fukasawa, T. 577
Fukuda, K. 595
Fung, T.C. 131, 239
Furukawa, Y. 457
Furusawa, K. 585

Gho, W.M. 239
Ghojel, J.I. 499
Glijnis, P.C. 41
Grundy, P. 331, 625
Grzebieta, R. 391

Haagensen, P.J. 95
Hamano, K. 585
Hancock, G.J. 177, 187, 409, 445, 521, 539, 549
Hänninen, H. 323
Hara, K. 73
Herion, S. 315
Holmas, T. 511
Hongo, E. 577
Hu, N. 347
Hyde, T.H. 285, 293

Ikago, K. 73

Jármai, K. 399, 481

Kajikawa, Y. 381
Kamba, T. 567
Kang, C.T. 277
Karcher, D. 197
Kawano, A. 605
Khalid, Y. 293
Koss, L. 625
Kosteski, N. 635, 645
Kurobane, Y. 3, 269, 347, 457

Lahti, K.E. 323
Lai, H.P. 433
Lalani, M. 107
Lee, M.M.K. 147, 249, 259, 305, 353, 361
Leen, S.B. 285, 293
Leendertz, J.S. 21
Li, B.H. 139
Li, G. 341
Lie, S.T. 341
Liew, J.Y.R. 139, 465
Liszkai, T. 399
Liu, D.K. 157, 223, 231
Llewelyn-Parry, A. 147

Macdonald, K.A. 95
Makino, Y. 203, 213, 269, 347, 457
Mamaghani, I.H.P. 381
Mang, F. 197
Mashiri, F.R. 331
Matsui, C. 605
Matsuo, Y. 577
Mistry, J. 277
Moffat, D.G. 277
Morgan, M.R. 305
Morita, K. 585
Morita, M. 213, 269
Murray, T.M. 539

Niemi, E. 323

Ong, K.T. 277
Otake, F. 595
Owen, J.S. 167

Packer, J.A. 117, 635, 645
Patterson, N.L. 505
Perera, N.J. 615
Puthli, R. 197, 315

Ridley-Ellis, D.J. 167

Roodbaraky, K. 473

Saad, S.B. 293
Sakae, S. 269
Shield, A. 625
Sironic, E. 391
Snijder, H.H. 63
Soetens, F. 89
Soh, C.K. 131, 239
Sully, R.M. 445
Szlendak, J. 531

Tabuchi, M. 595
Taclendo, C. 567
Tang, L.K. 465
Thambiratnam, D.P. 615

Ukai, K. 73

Vákár, L.I. 63
van der Vegte, G.J. 139, 203
van Wingerde, A.M. 117

Wang, B. 347, 373
Wardenier, J. 117, 157, 223, 231
Warrior, N.A. 293
Wheeler, A.T. 539, 549
Wilkinson, S.J. 473
Wilkinson, T. 177, 187, 409, 521
Wilmshurst, S.R. 203, 213, 269
Wong, M.B. 499, 505

Yamada, Y. 213
Yang, M.H. 373
Yeomans, N.F. 559
Yu, Y. 157, 223, 231

Zettlemoyer, N. 139
Zhao, X.L. 331, 391, 625
Zondervan, A. 31